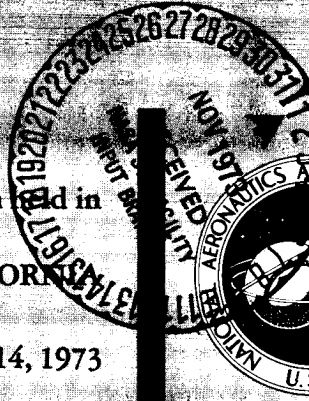


SEVENTH CONFERENCE ON SPACE SIMULATION

A symposium held in
LOS ANGELES, CALIFORNIA
November 12-14, 1973



N74-10232
THRU
N74-10296
Unclas
19526

CSCL 14B

H1/11

(NASA-SP-336) SPACE SIMULATION, 7TH
(NASA) 935 P MF \$1.45; SOL HC \$6.85

SPACE SIMULATION

The proceedings of a symposium held November 12-14, 1973,
at the International Hotel, Los Angeles, California

Sponsored by

The American Institute of Aeronautics and Astronautics
The American Society for Testing and Materials
Institute of Environmental Sciences
and the National Aeronautics and Space Administration

AIAA

ASME

Prepared at Goddard Space Flight Center



Scientific and Technical Information Office 1973
NATIONAL AERONAUTICS AND SPACE ADMINISTRATION
Washington, D.C.

This requirement for the use of the International System of Units (SI) has been waived for this document under the authority of NPD 2220.4 paragraph 5.d.

For sale by the Superintendent of Documents,
U.S. Government Printing Office, Washington, D.C. 20402
Price \$6.85 (Paper) Stock No. 3300-00534

FOREWORD

As a co-sponsor of the Seventh Space Simulation Conference, the National Aeronautics and Space Administration has published these proceedings as a NASA Special Publication so that they would be readily available to the technical community as well as the general public.

This conference provided an international forum for the exchange of meaningful and useful information on the technological advances in the simulation of space environments and the interaction of man and matter with these environments.

The papers in these proceedings represent a significant contribution to our understanding of space problems and our utilization of the knowledge gained.

NASA is again pleased to cooperate with the American Institute of Aeronautics and Astronautics, the American Society for Testing and Materials, and the Institute of Environmental Sciences, in presenting this important work in the fields of space simulation, and making it available to other technical disciplines.



John C. New
Chief, Test & Evaluation Division
Goddard Space Flight Center

PREFACE

These proceedings are for the seventh of a series of conferences jointly sponsored by the American Institute of Aeronautics and Astronautics (AIAA), the American Society for Testing and Materials (ASTM), and the Institute of Environmental Sciences (IES). In addition, the National Aeronautics and Space Administration (NASA) was a co-sponsor for the seventh conference. Responsibility for organizing and conducting the Conference is rotated among the three societies. The cooperative effort of the three societies provides the following benefits:

- 1) Reduces the number of conferences in this field and results in economic savings to both conference participants and the sponsoring societies.
- 2) Provides an up-to-date reference in one published volume of recent technical information associated with space simulation.

Normally, three committees are involved in each conference. These are the Permanent Policy Committee, A General Conference Committee, and the Technical Program Committee. The purpose and functions of these committees are as follows:

The Permanent Policy Committee provides policy and guidance for the organization and conduct of the conference. It is made up of two members from each participating society. These members represent the technical committee of each society most closely related to Space Simulation technology.

These are:

AIAA - Ground Testing and Simulation Committee
ASTM - Committee E-21 on Space Simulation
IES - Solar Radiation Committee

The General Conference is responsible for arranging the facilities for the meeting, conducting the meeting, and publishing the proceedings.

The Technical Program Committee is responsible for the technical program. Their purpose is to review and select papers and arrange sessions for the meeting. Each of the three sponsoring societies is represented on the Technical Committee.

The committees for this conference are listed on the following pages.

The 7th Space Simulation Conference was hosted by the American Institute of Aeronautics and Astronautics and was held in Los Angeles, California, at the International Hotel on November 12-14, 1973. These proceedings were published by the National Aeronautics and Space Administration, who was a co-sponsor for the meeting.

R. E. King
Chairman, Technical
Program Committee

COMMITTEES FOR
SEVENTH SPACE SIMULATION CONFERENCE

GENERAL CONFERENCE COMMITTEE

General Chairman	G. J. Frankel, Grumman Aerospace Corporation
Technical Program Chairman	R. E. King, McDonnell Douglas Astronautics Company
Publications Chairman	R. T. Hollingsworth, Goddard Space Flight Center
Administrative Chairman	Wolfgang Simon

TECHNICAL PROGRAM COMMITTEE

R. E. "Zeke" King, Chairman	McDonnell Douglas Astronautics Company
G. N. Borson	The Aerospace Corporation
P. R. Gauthier	The Boeing Company
T. L. Hershey	Spectrolab Division of Textron
D. H. Orbock	Northrop Services, Incorporated
E.S.J. Wang	McDonnell Aircraft Company
G. F. Wright, Jr.	Sandia Laboratories

JOINT POLICY COMMITTEE

IES

John D. Campbell	Perkin-Elmer Corporation
R. T. Hollingsworth	NASA/GSFC

AIAA

Aleck C. Bond	NASA/JSC
R. E. Covey	Jet Propulsion Laboratory

ASTM

G. N. Borson	The Aerospace Corporation
C. H. Duncan	Envirosin

TABLE OF CONTENTS

SESSION 1

TEST PROGRAMS

- Session Organizer - P. R. Gauthier
The Boeing Company
- Session Chairman - P. R. Gauthier
The Boeing Company
- Session Co-Chairman - E. L. Mulcahy
LTV Aerospace Corporation

<u>Paper No.</u>		<u>Page</u>
1	Space Simulation Testing for the Skylab Waste Tank, C. A. Skinner, R. Gershman, L. C. Kvinge, McDonnell Douglas Astronautics Company	1 ✓
2	A Thermal Vacuum Test of Skylab Orbital Workshop Refrigeration Subsystem, F. W. Sun, R. A. Deak, McDonnell Douglas Astronautics Company	7 ✓
3	General Electric Company Underwater Environmental Laboratories Zero G Techniques Applied to the Environment, Ruth H. Fry, General Electric Company, Space Division	19 ✓
4	Mars Surface Thermal Environment for Viking Lander Design and Test, T. F. Morey, T. R. Tracey, Martin Marietta Aerospace	31 ✓
5	Thermal Testing of the Viking Lander in Simulated Martian Environments, T. Buna, T. R. Tracey, Martin Marietta Corporation, T.W.E. Hankinson, NASA Langley Research Center	41 ✓
6	The "Pressure-Vessel" Spacecraft; An Assessment of Its Impact on Spacecraft Development and Test, W. G. Stroud, Goddard Space Flight Center, D. W. Keller, General Electric Company	63 ✓

SESSION 2

SPACE SIMULATION FACILITIES AND OPERATION I

- Session Organizer - E.S.J. Wang
 McDonnell Aircraft Company
- Session Chairman - E.S.J. Wang
 McDonnell Aircraft Company
- Session Co-Chairman - W. Alexander
 Hughes Aircraft

<u>Paper No.</u>		<u>Page</u>
7	The Radiometric Calibration and Performance Evaluation of the ASET Facility, J. David Shoore, A. B. Dauger, R. P. Day, R. H. Meier, McDonnell Douglas Astronautics Company	65 ✓
8	Increase of the Absorptance of a Shroud for a Thermal Test Facility and Methods of Determination, H. Nuss, J. Reimann, Industrieanlagen-Betriebsgesellschaft, Ottobrunn, Germany . . .	87 ✓
9	Testing for Thermal Fatigue Failures in Solar Arrays, G. J. Antonides, Lockheed Missiles and Space Company, Incorporated	99 ✓
10	A Test Facility for 6000 Hour Life Test of a 30 CM Mercury Ion Thruster, J. J. Caldwell, Hughes Aircraft Company	103 ✓
11	Computer Simulation of Temperatures on the Centaur Standard Shroud During Heated-Jettison Tests, J. A. Hemminger, NASA Lewis Research Center	105 ✓
12	Infrared Simulation and Thermo-Vacuum Facility-ISA/TVA, H. J. Kurscheid, Gessellschaft fur Weltraumforschung mbH Within DFVLR	119 ✓

SESSION 3

SPECIAL TOPICS

- Session Organizer - David Orbock
Northrop Services, Incorporated
- Session Chairman - David Orbock
Northrop Services, Incorporated
- Session Co-Chairman - Raymond Haney
Northrop Services, Incorporated

<u>Paper</u> <u>No.</u>		<u>Page</u>	
13	Comparative Evaluation of Predicted and Measured Performance of a 68m ³ Truncated Reverberant Noise Chamber, H. D. Cyphers, A. N. Munson and F. J. On, Goddard Space Flight Center	127	✓
14	Dynamics of the Skylab Waste Tank System, G. Rupprecht, Bendix Corporation, Navigation and Control Division	155	✓
15	Thermal Scale Modeling of a Spacecraft Radiator with Coupled Forced Convection - Conduction - Radiation Heat Transfer, D. Maples, Louisiana State University; D. Colvin, Becton-Dickinson Research Center	175	✓
16	Simulations of Martian Eolian Phenomena in the Atmospheric Wind Tunnel, J. D. Iversen, B. R. White, Iowa State University; R. Greeley, University of Santa Clara; J. B. Pollack, NASA Ames Research Center	191	✓
17	Simulation of Spacecraft Interaction With a Parallel-Streaming Plasma, A. R. Martin, R. N. Cox, The City University, London	215	✓
18	Simulation As a Computer Design Aid, J. E. Weatherbee, D. S. Taylor, Computer Sciences Corporation; B. C. Hodges, NASA, Marshall Space Flight Center	231	✓

- 19 Development of a Stochastic Simulation Model
for Performance Evaluation, E. Gordon,
P. G. Freese, Aerojet ElectroSystems Company

251 ✓

SESSION 4

SPACE SIMULATION FACILITIES AND OPERATION II

- Session Organizer - E.S.J. Wang
McDonnell Aircraft Company
- Session Chairman - W. Alexander
Hughes Aircraft
- Session Co-Chairman - E.S.J. Wang
McDonnell Aircraft Company

<u>Paper No.</u>		<u>Page</u>
20	Contamination Control in Space Simulation Chambers, B. C. Moore, R. G. Camarillo, L. C. Kvinge, McDonnell Douglas Astronau- tics Company	265 ✓
21	Space Simulation Ultimate Pressure Lowered Two Decades by Removal of Diffusion Pump Oil Contaminants During Operation, A. E. Buggele, NASA Lewis Research Center . .	281 ✓
22	Multi Gas Cryopumping Experiments in a Liquid Helium Cooled Space Simulation Facility, J. F. Cassidy, NASA Lewis Research Center . .	309 <i>WAF</i>
23	Real-Time, Multiprogrammable Computer Opera- ting System for Space Simulation Facility and Test Control, N. T. Selvey, McDonnell Douglas Astronautics Company	311 <i>WAF</i>
24	Experiences in Bringing On-Line A Large Selectively Pumped Thermal Vacuum Space Simu- lation Chamber, E. K. Beck, Sr., A. A. Edwards, Sr., Lockheed Missiles and Space Company . .	313 <i>WAF</i>
25	A Method for Predicting Blast Wave Overpressure Produced by Rupture of a Gas Storage Vessel, P. W. Garrison, McDonnell Douglas Astronautics Company	315 ✓

26

Leak Testing of High Pressure Oxygen and Nitrogen Tank Systems for the Skylab Airlock, R. A. Dutton, G. L. Adlon, R. K. Weinberger, McDonnell Aircraft Company, R. G. Morris, Jr., McDonnell Douglas Astronautics Company

331 ✓

SESSION 5

CONTAMINATION I

Session Organizer - E. N. Borson
The Aerospace Corporation

Session Chairman - C. M. Wolff
Northrop Services, Incorporated

Session Co-Chairman - J. J. Scialdone
Goddard Space Flight Center

<u>Page No.</u>		<u>Page</u>
27	Thermoelectrically-Cooled Quartz Crystal Microbalance, D. McKeown, W. E. Corbin, Jr., Faraday Laboratories, Inc., R. J. Naumann, Marshall Space Flight Center	345 ✓
28	Development of a Miniature Cryogenic QCM for Low Temperature Contamination Measurement, D. A. Wallace, Celesco Industries, Inc.	357 ✓
29	Transient Frequency Effects in Piezoelectric Quartz Crystals Caused by Incident Thermal Radiation, D. A. Wallace, Celesco Industries Inc.	367 ✓
30	Photographic Measurement of Particulate Surface Contamination, O. Hamberg, The Aerospace Corporation	379 ✓
31	Measurement of Condensate Film Contamination on Critical Surfaces by Charged Particle Excited X-Ray Fluorescence, W. Saylor, General Electric Space Company	401 ✓
32	Evaluation of Radio Isotope Tracer and Activation Analysis Techniques for Contamination Monitoring in Space Environment Simulation Chambers, J. B. Smathers, W. E. Kuykendall, Jr., R. E. Wright, Jr., J. R. Marshall, Texas A&M University	421 ✓
33	Outgassing Tests in Support of a Proposed ASTM Specification, J. J. Park, R. S. Marriott, W. A. Campbell, Jr., C. L. Staugaitis, NASA, Goddard Space Center	437 ✓

SESSION 6

REENTRY MATERIALS I

- Session Organizer - G. F. Wright, Jr.
Sandia Laboratories
- Session Chairman - G. F. Wright, Jr.
Sandia Laboratories
- Session Co-Chairman - R. E. Sheldahl
Sandia Laboratories

<u>Paper</u> <u>No.</u>		<u>Page</u>
34	A Shrouded Flow Arc Air Heater for Simulation of a 250 Megawatt Plasma Jet Heater, J. C. Beachler, W. A. Kachel, Air Force Flight Dynamics Laboratory, Wright Patterson AFB . .	449 ✓
35	The Ablation Performance of Foams in a Low Heat Flux, D. H. Smith, D. R. Hender, McDonnell Douglas Astronautics Company	465 ✓
36	Space Shuttle Entry Environment Testing Techniques, E. L. Mulcahy, R. R. Rogers, LTV Aerospace Corporation	477 ✓
37	Response of Candidate Metallic Space Shuttle Materials to Simulated Reentry Environments, I. M. Grinberg, E. S. Bartlett, R. G. Luce, Batelle-Columbus Laboratories	489 ✓
38	Testing of Space Shuttle Thermal Protection System Panels Under Simulated Reentry Thermoacoustic Conditions, C. E. Rucker, R. E. Grandle, NASA Langley Research Center	507 ✓

SESSION 7

REENTRY MATERIALS II

- Session Organizer - G. F. Wright, Jr.
Sandia Laboratories
- Session Chairman - G. F. Wright, Jr.
Sandia Laboratories
- Session Co-Chairman - R. E. Sheldahl
Sandia Laboratories

<u>Paper</u> <u>No.</u>		<u>Page</u>
39	Simulation of Three-Dimensional Coolant Flow Within Transpiration Nosedtips, J. R. Schuster, G. E. Seay, McDonnell Douglas Astronautics Company	523 ✓
40	Investigation of Critical Defects in Ablative Heat Shield Systems, C. C. Miller, W. D. Rummel, Martin Marietta Aerospace	543 ✓
41	Properties of a Closed Pore Insulation Thermal Protection System, A. Tobin, C. Feldman, M. Russak, J. Reichman, Grumman Aerospace Corporation	555 ✓
42	Ablative Heat Shield Design for Space Shuttle, R. W. Seiferth, Martin Marietta Aerospace . .	567 ✓
43	Envolvement of a Sprayable Ablator for Thermal/Cryogenic Applications, J. W. Maccalous, Martin Marietta Corporation	583 <i>WAZZ</i>
44	A Study of Ablator Producibility and Refurbishment Methods, W. E. King, Jr., Martin Marietta Aerospace	585 ✓

SESSION 8

CONTAMINATION II

- Session Organizer - E. N. Borson
The Aerospace Corporation
- Session Chairman - G. N. Borson
The Aerospace Corporation
- Session Co-Chairman - L. Leger
NASA Johnson Space Center

<u>Paper No.</u>		<u>Page</u>	
45	The Study of Molecular Contamination Kinetics Using Ellipsometry, T. H. Allen, McDonnell Aircraft Company	605	<i>WAA</i>
46	Use of Ellipsometry for the Quantitative Detection of Contaminants on Second Surface Mirrors, L. Dormant, The Aerospace Corporation	607	<i>WAA</i>
47	Development of Techniques for Advanced Optical Contamination Measurement with Internal Reflection Spectroscopy, J. D. Hayes, Teledyne-Brown Engineering; R. G. Richmond, NASA Johnson Space Center	609	✓
48	Contamination Effects of Titanium Sublimation-Pumped Systems on Optical Surfaces, J. T. Visentine, R. G. Richmond, NASA Johnson Space Center	635	<i>WAA</i>
49	The Vacuum-Ultraviolet Degradation of Salt-Spray-Contaminated Thermal Control Coatings, J. E. Gilligan, IIT Research Institute; H. M. King, NASA MSFC	637	✓
50	The Far Ultraviolet Photolysis of Polymethylphenylsiloxane Films on Quartz Substrates, P. D. Fleischauer, L. Tolentino, A. R. Calloway, The Aerospace Corporation . .	645	✓
51	Skylab Plume Contamination Experiments, R. L. Bowman, E. W. Spisz, R. D. Sommers, J. R. Jack, NASA Lewis Research Center . . .	651	<i>WAA</i>

SESSION 9

SOLAR SIMULATION I

- Session Organizer - T. L. Hershey
Spectrolab Division of Textron
- Session Chairman - T. L. Hershey
Spectrolab Division of Textron
- Session Co-Chairman - A. Matel
Hughes Aircraft

<u>Paper</u> <u>No.</u>		<u>Page</u>
52	High Intensity Solar Simulation Test for Structure Parts and Experiments for the Helios Solar Probe, P. Kleber, (DFVLR) . .	653 ✓
53	Development of a Heater Post & Spotlight Array for Thermal Vacuum Testing of the Intelsat IV Communications Satellite, L. A. Nelson, M. B. Levine, Hughes Aircraft Company	663 ✓
54	Solar Probe Helios, Mission Requirements & Applied Space Simulation Techniques, H. Schutz, R. A. Karsten, Gesellschaft fur Weltraumforschung mbH Within DFVLR. .	671 ✓
55	The Design & Operation of an Infrared Simulator for Testing of the Shuttle Radiator System, D. J. Skinner, Northrop Services, Inc., J. E. Breiby, NASA Johnson Space Center	679 ✓
56	Method and Results of Infrared Testing of the Helios Solar Probe, W. Lorenz, Joachim Guelpen, ERNO Raumfahrttechnik GmbH . . .	695 ✓
57	Large Solar Beam Testing at Planet Mercury and Greater Intensities in the JPL 25-Ft Space Simulator, J. W. Harrell, Jet Propulsion Laboratory	713 ✓

58 Survey of Solar Simulation Facilities,
T. L. Hershey, Spectrolab Division of
Textron; A. Lunde, the Boeing Company . .

723 *CAAAA*

SESSION 10

VACUUM ENVIRONMENTS

- Session Organizer - P. R. Gauthier
The Boeing Company
- Session Chairman - P. R. Gauthier
The Boeing Company
- Session Co-Chairman - E. L. Mulcahy
LTV Aerospace Corporation

<u>Paper No.</u>		<u>Page</u>
59	Plume Mass Flow and Damage Distributions for an MMH/N ₂ O ₄ RCS Thruster, E. W. Spisz, R. L. Bowman, J. R. Jack, NASA Lewis Research Center	725 <i>CAAAA</i>
60	Determination of a High-Velocity Water-Vapor Plume Profile in a Thermal Vacuum Environment, H.K.F. Ehlers, R. G. Richmond, J. T. Visentine, NASA Johnson Space Center .	727 <i>CAAAA</i>
61	Outgassing Measurements of a Thermal Blanket and Space Chamber Using Quartz Crystal Microbalances, J. J. Scialdone, R. Kruger, NASA Goddard Space Flight Center	729 ✓
62	Molecular Density Determination of Water Vapor in a 10 ⁻⁴ to 10 ⁻² TORR Vacuum Environment by Ultraviolet Absorption, R. G. Richmond, J. T. Visentine, NASA Johnson Space Center . .	749 ✓
63	Mathematical Model of Molecular Flow in the NASA-JSC Thermal Vacuum Chamber A, H.K.F. Ehlers, NASA Johnson Space Center; A. Lee, J. Robertson, Lockheed Missiles & Space Company	757 ✓

SESSION 11

SOLAR SIMULATION II

Session Organizer - T. L. Hershey
Spectrolab Division of Textron

Session Chairman - T. L. Hershey
Spectrolab Division of Textron

Session Co-Chairman - A. Matel
Hughes Aircraft

<u>Paper</u> <u>No.</u>		<u>Page</u>
64	A Unique High Intensity Solar Simulator System, I. N. Serafino, L. Romanowsky, Jr., Northrop Services, Inc., Goddard Space Flight Center	775 ✓
65	Solar Image, Corona and Radiation Simulations for the Apollo Telescope Mount Displays of the Skylab Simulator, A. J. da Silva, Johnson Space Center, Houston, Texas, G. Gause, R. J. Nobilini, Aero Service Corporation, Philadelphia, Pennsylvania	795 ✓
66	A Novel 20 KW Solar Simulator Designed for Air Pollution Research, J. H. Beauchene, Aerospace Controls Corp., P. J. Bekowies, A. M. Winer, J. M. McAfee, L. Zafonte, J. N. Pitts, Jr., University of California, Riverside	811 ✓
67	A Novel Facility for Radiant Heat Transfer Experiments, J. W. Metzger, General Electric Company	827 ✓
68	A Versatile Instrument for Thermal Radiation Measurement, C. M. Wolff, Northrop Services Inc., Houston, Texas	847 ✓
69	Improved Spatial Uniformity of Beam-Plane Interaction by Means of Inverse Rastering C. G. Miller, Jet Propulsion Laboratory . . .	855 ✓

70 An Absolute Total Radiation for Measuring a
Wide Range of Irradiances in Space Simulators,
J. M. Kendall, Sr., Jet Propulsion Laboratory 867 ✓

SESSION 12

MATERIALS AND HEAT TRANSFER

Session Organizer - E. N. Borson
The Aerospace Corporation

Session Chairman - E. Luedke
TRW Systems

Session Co-Chairman - C. Maag
Comsat Corporation

<u>Page</u> <u>No.</u>		<u>Page</u>
71	Qualification of Non-Metallic Materials for the Viking Mars Lander, W. K. Johnson, J.Y.K. Peng, Martin Marietta Aerospace, Denver, Colorado	875 ✓
72	Sphere Forming in Zero-Gravity, W. Aubin, G. Busch, D. Larson, Jr., G. Geschwind, Grumman Aerospace Corporation	893 ✓
73	A New Method for Determining the Absorptivity and Emissivity of Metal Wires, A. Lorenz, H. P. Schmidt (DFVLR)	909 ✓
74	Heat Transfer at Subatmospheric Pressure I, C. M. Wolff, J. Vyas, Northrop Services Incorporated, Houston, Texas	919 ✓
75	A Rocket-Borne, Low Gravity Cryogenic Heat Transfer Experiment, K. D. Williamson, Jr., F. J. Edeskuty, J. F. Taylor, Los Alamos Scientific Laboratory of the University of California	935 ✓
76	Temperature Rise for Spring-Loaded Phase Change Devices, R. A. Farmer, Martin Marietta Corporation	943 ✓

SPACE SIMULATION

ABSTRACT

This volume contains either the final draft or the abstract of most of the technical papers accepted for prime or alternate presentation at the Seventh Space Simulation Conference, which was held at the International Hotel, Los Angeles, California, U.S.A. on November 12, 13, and 14, 1973.

The scope of this Conference included all aspects of space simulation both existing and planned, and encompassed facilities, techniques, effects, measurements, and applications. The range of topics covered is indicated by the session titles which include:

Test Programs

Space Simulation Facilities and Operations

Special Topics (Thermal Scale Modeling,
Predicted vs Measured Data, Computer
Simulation, etc.)

Re-entry Materials

Contamination

Solar Simulation

Vacuum Environments

Materials and Heat Transfer

Two sessions each were held on Space Simulation Facilities and Operations, Re-entry Materials, Contamination, and Solar Simulation. The remainder of the topics were covered in a single session each.

Key Words: space simulation, contamination, ablation, computer simulation, zero-g, weightlessness, thermal testing, vacuum technology, cryopumping, vacuum measurements, contamination detection, thermal vacuum testing, re-entry materials, solar simulation, heat transfer, high energy light sources, spacecraft testing, space chamber, facilities.

INTRODUCTION

As stated in the Call for Papers, the purpose of this Conference was to provide an international forum for the exchange of meaningful and useful information on advances in space simulation technology. This technology encompasses all aspects of simulating the space environment as well as the effects of this environment upon man and matter. Much of this technology is applicable to ecological studies and to the development of methods to monitor and control pollution of the terrestrial environment.

The papers accepted for presentation at the Conference were organized into twelve sessions. In this volume, they are grouped by session in the same order as presented at the Conference. Since time did not permit the Technical Program Committee to review the final drafts of these papers before this volume went to press, each author assumes full responsibility for the content of his paper.

George J. Frankel
Grumman Aerospace Corporation
General Chairman

N74-10233

Paper No. 1

SPACE SIMULATION TESTING FOR THE SKYLAB WASTE TANK

C. A. Skinner, R. Gershman, and L. C. Kvinge, *McDonnell Douglas
Aeronautics Company, Huntington Beach, California*

ABSTRACT

Large scale space simulation testing was accomplished for the Skylab waste tank concept. Investigations included vapor generation rates for liquids dumped into a low pressure tank, sublimation of ice at low pressure, and pressure drop and blockage phenomena for fine mesh filter screens.

The mission of Skylab, America's first space station, will last eight months. Three different three-man crews will inhabit the station: The first crew for one month and the second and third crews for two months each. A wide variety of experiments will be performed including many in the fields of earth resources and astronomy. Because of the need to protect the Skylab external optical environment from contamination which would interfere with these experiments, overboard disposal of waste materials, frequently used in previous missions especially for liquid wastes, had to be avoided. A waste tank concept was established to provide for disposal of all liquid and solid waste material outside of the Skylab habitation area without contaminating the optical environment. This paper describes the waste tank concept with particular emphasis on the small scale and full scale space simulation testing accomplished to develop the hardware necessary to implement the concept.

The structure of the Skylab vehicle is based on the SIVB stage of the Saturn rocket. The crew quarters are built into the 10,000 cubic foot SIVB liquid hydrogen tank and the 2800 cubic foot liquid oxygen tank is used for waste disposal. Solid wastes are transferred from the crew area to the waste tank via a small airlock and liquid wastes are dumped into the waste tank through probes which penetrate the common bulkhead between the two tanks. It was found necessary to vent the waste tank to space since, otherwise, cabin air introduced during trash airlock operations and by leakage would eventually raise the waste tank pressure to a level that would prevent transfer of materials from the crew area. To minimize impact on the Skylab attitude control system, a non-propulsive vent system is used consisting of two short, diametrically opposed ducts located on opposite sides of the vehicle. To avoid venting of liquid, which could

contaminate optical surfaces or result in clouds of ice, the vent system is sized to maintain the pressure in the waste tank below the triple point of water. Since practically all liquid wastes consist of water solutions - e.g., wash water, urine - no liquid phase will be present in the waste tank. In order to minimize venting of solids which would interfere with the optical experiments, fine mesh screens are used as filters to trap solid trash and ice formed from flashing of waste liquids in the waste tank. These screens have a nominal filtering capability of two microns. (See sketch in Figure 1.)

The waste tank concept presented a number of unusual thermophysical problems which required vacuum testing, including establishing liquid dump rates and vent system flow rates which would maintain the waste tank pressure below the triple point of water, investigation of fine mesh screen pressure drop and the possibility of screen blockage resulting from freezing of dumped liquids, demonstration of the filtering capability of the screens, and establishing the sublimation rate for frozen liquids trapped within the waste tank.

The test program involved both small scale testing, performed in a bell jar, and full scale testing, performed in the MDAC 39-foot-diameter space chamber. The small scale testing was mainly for the purpose of investigating screen blockage. The test setup provided the capability for dumping water, urine or dust onto small screen samples and for measuring pressure drop across the screen during the dumping and with a known flow rate of nitrogen after each dump. (See Figure 2.)

The full scale test specimen was designed to duplicate actual waste tank volumes, screen areas, and vent size. A production type dump probe was used and was mounted at the actual distance relative to the screen. To assure maximum ice accumulation on the screen, the screen was mounted in a horizontal position with the dump probe above it. Two methods were used to verify that the screen was filtering out all solid materials: The screen was mounted on load cells to measure the ice accumulation and contamination collection plates were installed facing the vent outlets. The load cells also provide data on sublimation rates. Tank pressure and screen pressure drop were measured using MKS Baratron units. (See Figure 3.)

Prediction of waste tank pressure during a dump, which was necessary in order to establish liquid dump rates that would not increase the pressure to the triple point, was first approached in a rather simplified manner. Uniform phase equilibrium was assumed to exist between the ice and the water vapor throughout the tank. The full scale testing showed that this is a reasonable approximation when starting with an empty tank, but the pressure rise rate was found to be smaller and considerably

less predictable when significant quantities of ice were accumulated in the tank. (See Figure 4.) The vapor generation rate was apparently reduced by heat transfer between the incoming liquid stream and the cold ice in the tank.

The fine-mesh screens used to prevent venting of solid materials overboard were made of stainless steel wire in a Dutch twill weave. Their two micron filtering capability resulted in an open area of only a few percent which led to concern over pressure drop and potential blockage. While considerable test data were available on screen pressure drop at high flowrates, none were found covering the low Skylab flow range. The small scale testing was accomplished to establish dry pressure drop and blockage characteristics of the screen material and large scale testing was run to determine effects of Skylab geometry on potential blockage.

Results of the dry screen pressure drop tests are shown in Figure 5. These results agree with existing correlations for the higher Reynolds numbers tested, but deviate significantly at very low Reynolds numbers.

When water was dumped on the screen in a vacuum, it was found that a thick layer of porous ice formed which did not significantly increase the pressure drop across the screen. On the other hand, dumping of urine resulted in almost complete blockage of the small scale specimen and very significant blockage in the large scale test. (See Figure 6.) As a result of this testing, it was decided to install a baffle which would prevent impingement of the liquid stream directly on the screen.

Another finding of the urine dump testing was that urine dumped onto residual urine ice, which had an increased concentration of salts due to sublimation, would dissolve the residual salts and depress its vapor pressure to the point where it could freeze only at substantially lower pressures.

In summary, the test program demonstrated that liquid dump rates and vent system flowrates can be predicted accurately enough to provide for maintaining the waste tank pressure below the triple point pressure of water, the range of known pressure drop characteristics for fine mesh screen filters was extended and the effect of contamination on pressure drop was quantitatively assessed, and the effectiveness of the fine mesh screens as filters in a low pressure environment was demonstrated.

References

1. J. C. Armour and J. H. Cannon. Fluid Flow Through Woven Screens. AIChE Journal, Vol 14, No. 3, May 1968.
2. Low Gravity Propellant Control Using Capillary Devices in Larger Scale Cryogenic Vehicles. GDA Report No. GDC-DOB70-009, August 1970.

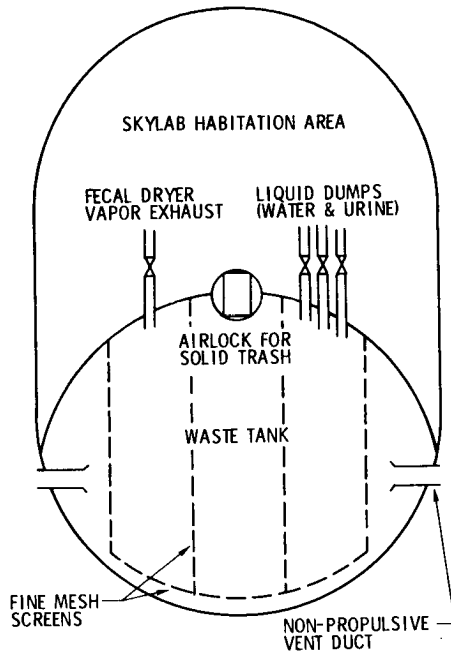


Figure 1. Skylab Overboard Waste Disposal

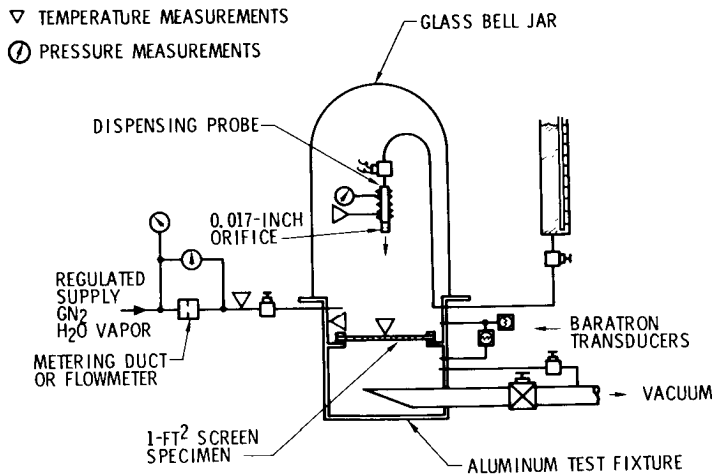


Figure 2. Small Scale Screen Test Setup

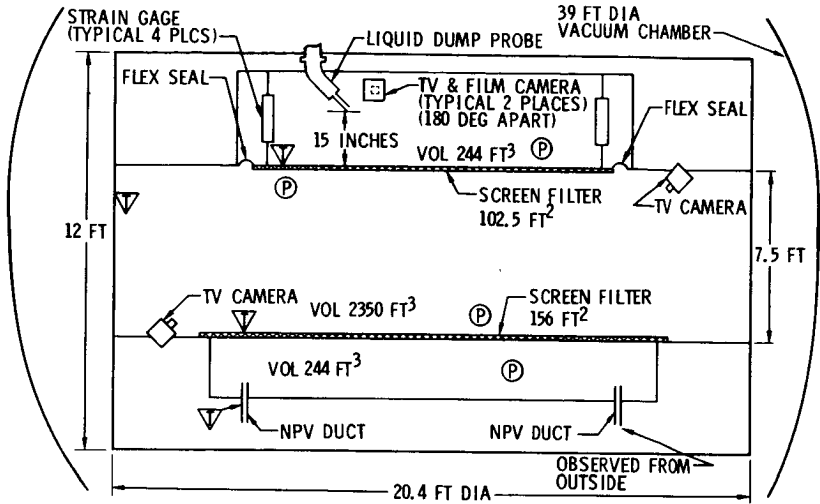


Figure 3. Large Scale Waste Tank Screen Tests

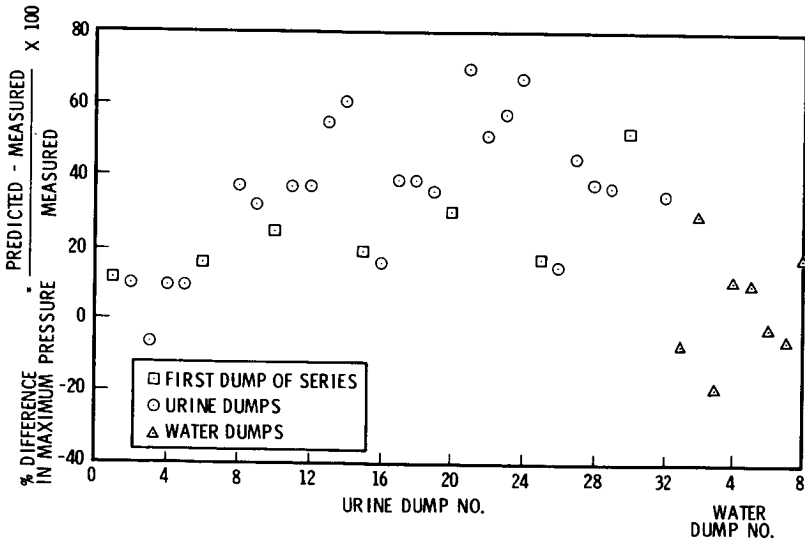


Figure 4. Comparison of Predicted Waste Tank Pressures with Test Results

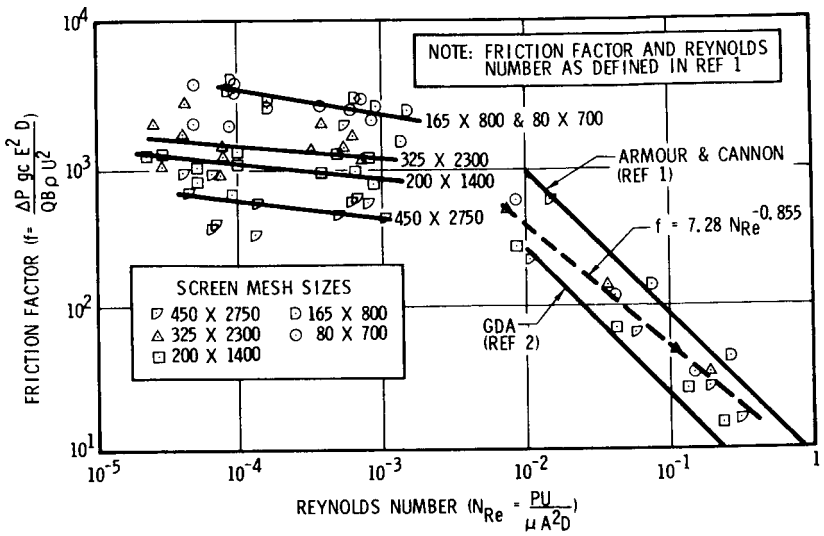


Figure 5. Dutch Twilled Screen ΔP Correlation

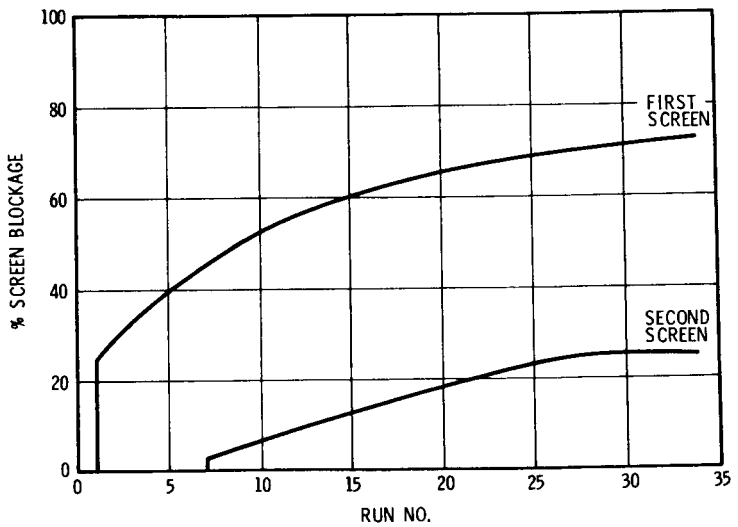


Figure 6. Calculated Screen Blockage

N74-10734

A THERMAL VACUUM TEST OF SKYLAB ORBITAL WORKSHOP REFRIGERATION SUBSYSTEM

F. W. Sun, R. A. Deak, *McDonnell Douglas Astronautics Company, Huntington Beach, California*

ABSTRACT

This paper describes the facilities, test support equipment, and test setup of a thermal qualification test performed on a fully operational Refrigeration Subsystem (RSS). This subsystem consists of a radiator, radiator thermal control unit, pump assembly, wardroom freezer, food freezer, urine freezer, urine chiller (simulated), water chiller, and electrical cold plate. These components and the connecting plumbing comprise one complete coolant loop of the refrigeration system thermally and is functionally equivalent to the flight system. Coolant is circulated through freezers and chillers accepting heat for rejection to space by radiation. Design features and thermal operating characteristics of the test specimen are discussed. Results are presented on radiator heat rejection performance, radiator/thermal capacitor integrated thermal performance, coolant temperature control and temperature control hardware, coolant pumping equipment, regenerative chilling equipment, freezers, chillers, etc. Redundancy features of the flight system are also discussed.

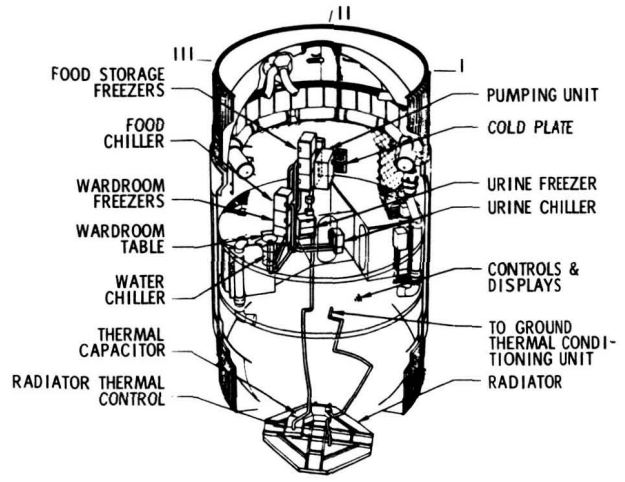


Figure 1. Refrigeration System

System Description

Frozen food, refrigerated food and water and freezing and chilling capability for medical experiments was provided aboard the Skylab vehicle by a circulating coolant refrigeration system (See Figure 1). Low temperature single phase coolant (Coolanol-15) passed through insulated freezer and chiller compartments accepting heat for rejection to space by radiation. The system is required to operate in two temperature ranges, 0°F to -20°F for freezers and $+35^{\circ}\text{F}$ to $+45^{\circ}\text{F}$ for chillers.

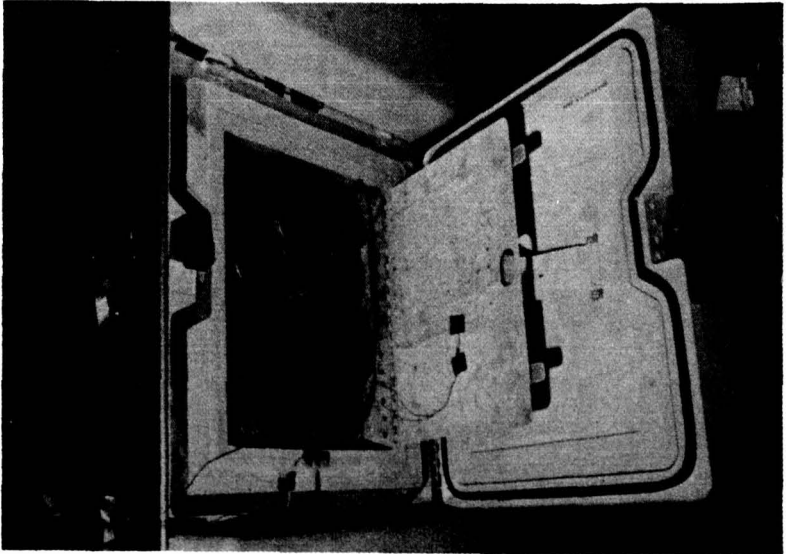


Figure 2. Food Compartment

Food was maintained in a frozen state in two freezer units, the wardroom freezer and in the food storage freezer. The freezers were located inside the spacecraft crew quarters. Each freezer is a rectangular container 21 in. x 21 in. x 76 in. high with an internal storage volume of 6 ft^3 in three equal size cubical compartments. Full face mechanically latching doors with perimeter seals provide maximum access to each compartment. Freezer cooling is achieved by flowing low temperature heat transfer fluid through aluminum tube-plate (dip brazed) heat exchangers which make up the compartment walls. Compartments are insulated from the outer aluminum structure and each other with polyurethane foam insulation. The top compartment of the wardroom freezer was utilized as a chiller where temperatures were maintained from $+35^{\circ}\text{F}$ to $+45^{\circ}\text{F}$. Frozen food was provided in circular pop top cans stored in cylindrical canisters. The canisters were placed in a rack inside the freezer compartment. (See Figure 2).

A medical experiment freezer for freezing urine and blood samples was a single compartment unit similar in construction to the food freezers but much smaller in size. This unit contained trays into which urine and blood samples from the spacecraft crew were frozen. These samples were eventually returned from orbit for medical analysis. The sample trays included a phase change material heat sink to maintain low temperature during deorbit from the time the trays were removed from the medical experiment freezer in orbit until they were placed into an earthbound freezer on the recovery vessel. (See Figure 3 - Urine trays and samples.)

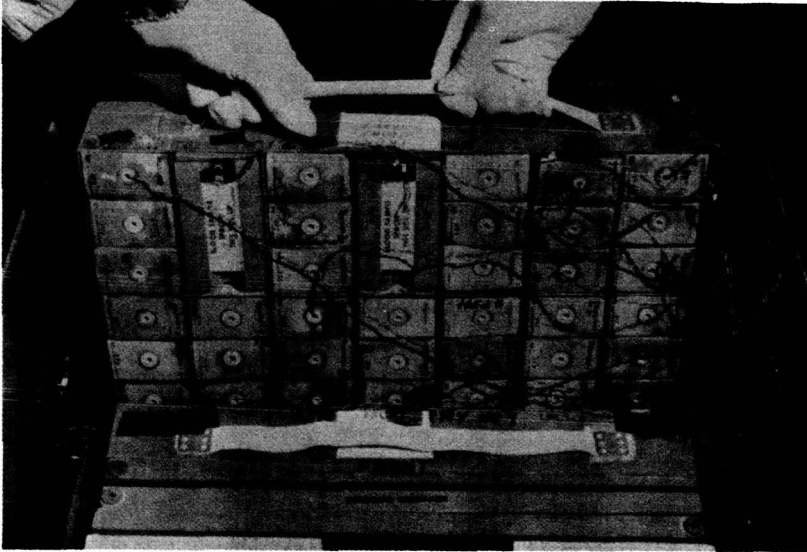


Figure 3. Urine Trays and Samples

Chilled water was provided by passing water through an insulated coiled tube heat exchanger to either a hand-held drinking dispenser or a table mount dispenser for reconstituting foods.

Rejection of system heat load and coolant temperature control were accomplished with the space radiator and the low temperature thermal control equipment located on the aft end of the spacecraft. The radiator is a flat octagonal shaped tube-fin heat exchanger with an effective heat exchange area of approximately 85 square feet. Radiator coolant extrusions are seam-welded to the radiating surface. The radiating surface is finished with a high emissivity low absorption coating. Polyurethane foam insulation, reflective surfaces and glass felt insulation on the radiator back surface minimize heat flow in this region.

During a typical earth orbit cycle, radiator outlet coolant temperature can vary as much as 60°F. A thermal control unit

adjacent to the radiator, controlled and modulated radiator outlet coolant to minimize temperature excursions of the fluid delivered to the freezers.

A coolant temperature modulating device within the thermal control panel called a thermal capacitor 'rectifies' radiator outlet coolant temperature by storing and releasing thermal energy at the heat of fusion point of a phase change material (PCM). The thermal capacitor is a plate-fin coolant coldplate with honeycomb tanks of PCM bonded to either face. The thermal rectification mode of control provides exclusive temperature control when the radiator is operating in a warm or moderate heat rejection environment. For colder radiator operation, the thermal capacitor remains mostly frozen and coolant outlet temperatures can be quite low. For this mode coolant flow is periodically directed to bypass the radiator on a path directly to the thermal capacitor to continue the freezing and thawing cycle in the capacitor. Bypass control is accomplished automatically with an electronic controller and temperature sensors at the thermal capacitor. The temperature sensors provide the positioning command to a solenoid operated two-position valve. Temperature sensors on the radiator surface can also divert flow to bypass in the event of a too warm radiator surface. A relief valve is included across the radiator in the event the coolant freezes in the radiator.

Coolant pumping and chilling equipment is located inside a container in the spacecraft. The interior of the container is vented to vacuum to improve insulation performance and to eliminate the possibility of coolant leaking into the cabin in the event of a leak. Four electric driven gear pumps are included in a single coolant circuit. Only one pump is operated at any one time. The operational time span of each of the four pumps is programmed to allow for the long duration mission. Two independent refrigeration coolant loops are provided onboard the Skylab, a primary system and an alternate backup. Both systems are identical. Loop switching if required may be accomplished manually or automatically, either by the spacecraft crew or from the ground according to various performance parameter fault indications, freezer hi-temperature indication, chiller low temp indication, accumulator low level indication, low pressure indication (causes pump switching in sequence and eventual loop switching).

Temperature operation in the $+35^{\circ}\text{F}$ to $+45^{\circ}\text{F}$ range was achieved with regenerative heat exchangers and a temperature regulated mixing valve set to operate from $+36^{\circ}\text{F}$ to $+42^{\circ}\text{F}$. An electric heater was included in the chiller circuit to prevent low temperature freezeup in the water chiller. The heater functions automatically according to commands from an electronic controller and temperature sensors in the regenerative circuit.

Refrigeration piping was stainless steel seamless tubing. All joints were electro-brazed except for interfaces with major components which were standard boss fittings. Elastomer seals

were used in non-vacuum application where temperatures were above 0°F. Metallic K seals were used for low temperature vacuum applications. The relatively low volume accumulators 106 cubic inches in relation to the total system volume of 900 cubic inches necessitated a leak-tight system. The above piping and joint arrangement provided the desired low leakage characteristics. Piping was insulated with cylindrical polyurethane foam insulation sections sheathed in aluminum for fire protection. Insulation segments were clamped together and joints sealed with tape.

Operation of the Skylab Orbital Work Shop Refrigeration System begins several weeks before launch. The system is activated and chilled down and maintained cold with a water-glycol ground thermal conditioning unit. Frozen food is placed into the freezers. The spacecraft is checked out and sealed off in preparation for launch. Refrigeration system pumps are turned off during boost into orbit. Once in orbit, the radiator assumes the heat rejection job and the system operates continuously throughout Skylab mission. A summary of Refrigeration System design and performance characteristics is given in Table 1.

Table I. REFRIGERATION SYSTEM DESIGN & PERFORMANCE CHARACTERISTICS

Coolant -- Coolanol-15
Total system coolant volume (one loop) -- 900 in³
Total maximum accumulator volume (one loop) -- 106 in³
Coolant operating pressure range -- 18 to 118 psia
Coolant flow rate -- 125 lb/hr
Maximum prelaunch heat load -- 1700 BTU/h
Maximum orbital heat load -- 1300 BTU/h
Minimum orbital heat load -- 750 BTU/h
Food freezers operating temperature range -- 0°F to -20°F
Urine freezer operating temperature range -- -2.5°F to -34°F
Chillers operating temperature range -- +35°F to +45°F
Radiator heat rejection at maximum conditions -- 1500 BTU/h
Thermal capacitor heat of fusion at -14°F -- 1800 BTU
Approximate system operating life -- 9000 hrs
Designated operating life of one pump -- 2250 hrs

Test Facility

To test a subsystem of such magnitude, requires a facility that has two adjoining chambers, one of which is capable of simulating cold black space and pressure below 1×10^{-6} Torr and the other capable of duplicating the Skylab cabin environment. The McDonnell Douglas Space Simulation Laboratory's 39-foot chamber and adjoining manlock were used for this test. (See photograph Figure 4.) Four of the components and the interconnecting plumbing of the RSS were installed in the spherical 39-foot chamber. These were the radiator, radiator thermal control assembly, pump and chiller assembly, and radiator

bypass valve controller. The balance of the RSS system, such as the urine freezer, wardroom freezer, food storage freezer, water chiller, urine chiller (simulated) and electrical cold plate, were installed in the manlock chamber. (See Figure 5 - Test Setup Schematic). The manlock chamber is approximately 10 feet in diameter and 13 feet long, equipped with a separate pumping system so that the pressure in the manlock chamber is independent of that in the 39-foot chamber. Provision also was made to allow this chamber to be pressurized up to 26 psia for simulating the Skylab prelaunch cabin pressure. An aluminum tube/plate extrusion type black thermal shroud was built for the manlock chamber to provide the required Skylab cabin environment temperature. A thermal control cart circulated freon in the shroud to control and maintain a stable temperature.

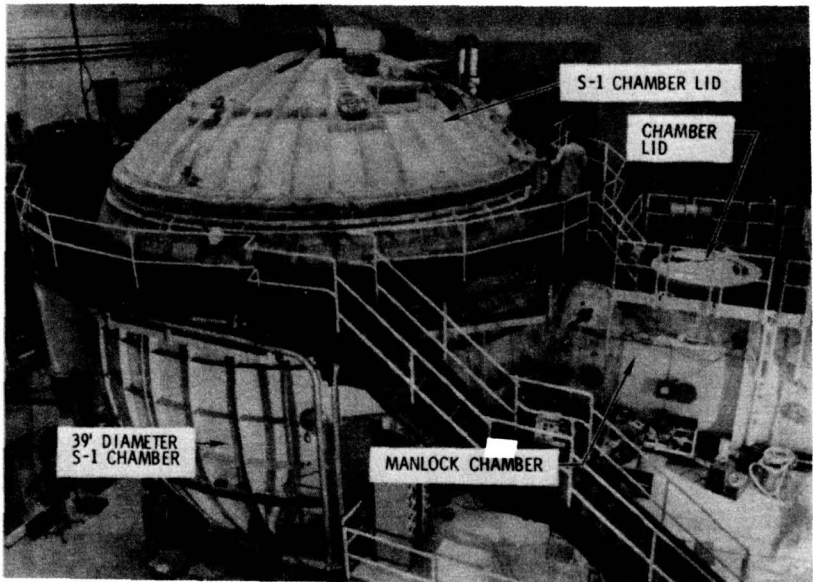


Figure 4. 39-Foot Diameter Space Simulator and Manlock Chamber

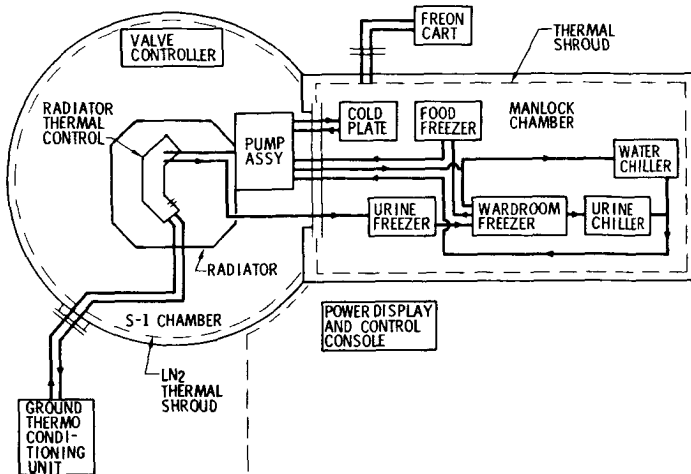


Figure 5. Test Setup Schematic

Test Support Equipment

A modified NASA Model S14-121 Thermal Conditioning Unit, similar to the unit used at the Skylab launch site, was used to provide the refrigeration system initial thermal conditioning (chilldown) and continuous thermal control during the prelaunch interval. Also, a separate refrigeration system service cart was used to perform four basic functions: It evacuated the coolant loop, filled and drained coolant, circulated and flushed the coolant in the system and reduced the air and moisture content of the coolant.

The power, control and display panel was built for proper RSS operation and performance display. Electrical power to the RSS was applied and controlled through this panel. The display parameters were provided for immediate readout to determine the RSS current performance status which allowed quick and accurate monitoring of the system.

To provide the radiant heat flux for the test, an Infrared (IR) Lamp Array was assembled with line reflectors containing twenty 500W quartz lamps each. To cover the approximately 10-foot-square area of the radiator surface, seven lines of these reflectors were used, spaced at 20 inches. The plane of the IR Array was placed 24 inches above the radiator surface. (See Figure 6 - IR Lamp Array and radiator surface.) This array was capable of providing an incident flux of up to 1.4 solar constants at rated voltage. In order to reduce the background effect, the individual reflector lines were cooled with liquid

nitrogen and the reflector bodies painted with 3M Black Velvet paint. The IR lamp array was calibrated and the uniformity determined. Analysis of the flux readings showed that 80% were within $\pm 5\%$ of the average flux for the field, and 98% were within $\pm 10\%$. An ignitron power supply, Thermac Controller and Data Trak programmer and a feedback radiometer were used in a closed control loop to simulate the orbital heat flux cycles. The desired heat flux curve was fed into the Data Trak program chart which rotates at a rate equivalent to the Skylab orbital period. This curve defines the power level supplied to the IR lamp array by the ignitron which in turn is controlled by the Thermal Controller. The Thermal Controller compares the feedback signal from the control radiometer and the Data Trak output to regulate the ignitron power supply.

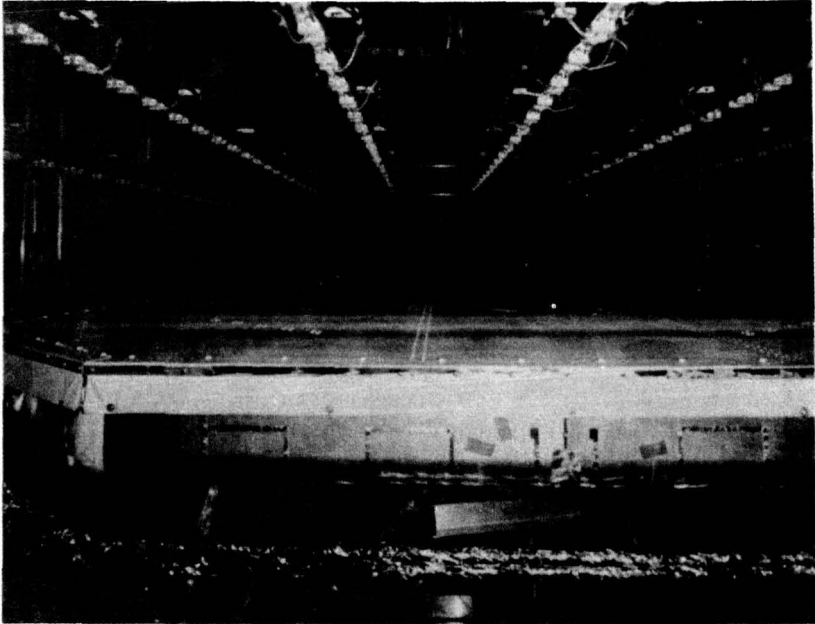


Figure 6. IR Lamp Array and Radiator Surface

Test Specimen Instrumentation

Temperature instrumentation included copper-constantan immersion thermocouples, copper-constantan surface patch thermocouples, and thermistor patches. Differential temperature measurements were obtained with three couple copper-constantan thermopiles. Pressure and differential pressure measurements were obtained with Statham Model PA 822, PL 822 and PL 872 transducers. Flow measurements were made with turbine-type flowmeters.

To measure the heat flux, three high output radiometers, Hy-Cal Engineering Model R-8410-E-01-120, were placed at the cutoff corners of the radiator. The radiometer's sensitive surface was painted with the same coating as used on the radiator surface so that the radiometers would measure the flux that was absorbed by the radiator. One radiometer was used as a feedback as mentioned above for the Data Trak Controller to control the programmed flux. Two radiometers were used for data. The radiometers were cooled by flowing 70°F water through the radiometer cooling tubes. The temperature of each radiometer was measured by a thermocouple imbedded in the radiometer body.

Key measurements were redundantly instrumented. One set was wired to the power, control and display panel where readouts were obtained by digital temperature indicators, pressure gages and light indicators. The others were scanned by the automatic data system.

Data System

Primary data for this test were acquired using a 200-channel HP-Dymec 2010J Data System having a resolution of one microvolt. Data channels were scanned using a crossbar scanner, digitized at a rate of approximately five readings per second by a five-digit integrating digital voltmeter and recorded on an incremental magnetic tape recorder for subsequent post test processing. A printer was used as required to monitor raw data values. At the start of each test, a uniform set of standardizations were recorded to verify the bias and sensitivity of each channel that used signal conditioning external to the data system, such as bridge-type transducers and turbine flowmeters. The on-line computer was programmed to initiate each scan at a specified interval. A local timer was also connected to initiate a scan in the event one was not initiated by the computer within a maximum allowable interval. Data was reduced both on-line and off-line.

The Dymec Acquisition System was coupled to an XDS-930 computer which accepts raw data and outputs calibrated data in engineering units for selected channels to the remote typewriter located at the test site. Reduced data values from a maximum of 56 channels can be typed in groups of eight channels on the remote typer. The XDS-930 program provides for updating the channels in each group and also allows the teletype operator to select which of the groups are to be typed out. The type-out occurs after each time slice of data. Also located at the test site was a Tektronix 611 Scope Display upon which two types of plotted data were available: a) a time history multiple plot previously reduced time slices from 1 to 5 data channels, b) a continuous update multiple plot of current time slices from 1 to 5 channels.

A hardcopy unit attached to the 611 Scope allowed the

operator to make a hard copy of all on-line plots for immediate reference and comparison purposes.

Reduced data, besides being output to the remote typewriter and scope, was being stored on magnetic tape in the Data Reduction Facility. This calibrated data tape was used to obtain all off-line plots.

In the event of an XDS-930 Computer failure while on-line, data can be removed by processing data in an off-line mode. In this case, the Dymec raw data tape can be processed to obtain test data plots.

Test Specimen Performance

Most of the simulated orbital testing was done at maximum cabin environmental temperatures with the radiator operating in the highest absorbed energy flux environment. These conditions established the upper limits of system operation. Tests were also conducted at intermediate and coldest environment and radiator absorbed energy flux conditions to verify temperature control for all operating situations. Refer to Figure 7 for maximum and minimum net lamp flux curves.

Heat loads rejected by the radiator for simulated orbital conditions ranged from 750 BTU minimum to 1300 BTU maximum which corresponded to internal environment temperatures from $+40^{\circ}\text{F}$ to $+79^{\circ}\text{F}$. For the warmest conditions radiator outlet coolant temperature ranged from $+3^{\circ}\text{F}$ to -38°F for an orbital cycle. For the coldest radiator rejection environment, the lowest recorded radiator outlet temperature was -95°F .

Thermal capacitor 'thermal rectification' provided coolant temperature control for the maximum operating conditions. Refer to Figure 8. Coolant delivered to the freezers is at constant temperature for this condition near the fusion point of the PCM. For colder operation, bypass switching resulted in the temperature control of Figure 9. Coolant delivery temperature to the freezers for this condition varied by the amount of the temperature switching limits. This variation is considered acceptable.

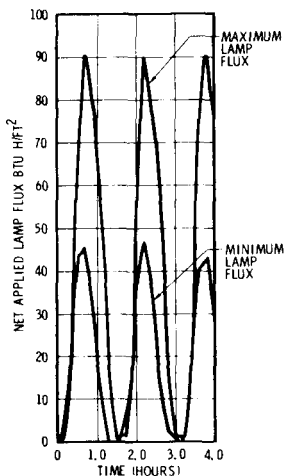


Figure 7. Net Applied Orbital Lamp Flux

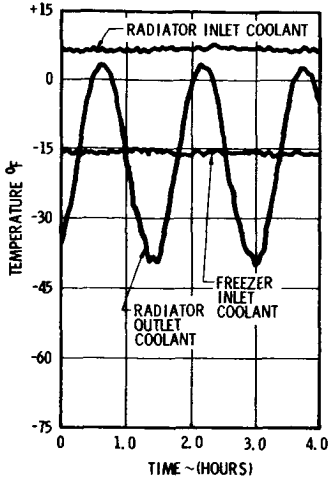


Figure 8. High Heat Load (Maximum) Operating Condition

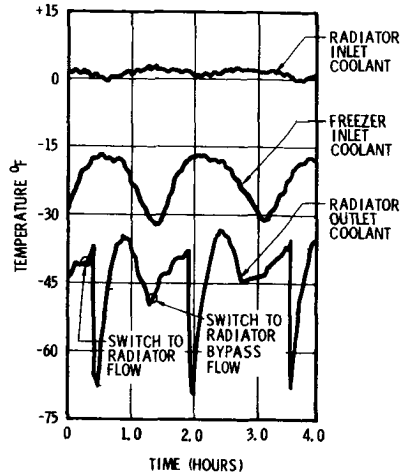


Figure 9. Low Heat Load (Minimum) Operating Conditions

Frozen food was maintained from -3°F to -20°F through the range of operating conditions. With such low temperatures there was concern early in the test program with regard to the amount of ice and frost buildup in and around the freezer doors and food cans. Since there was no provisions for freezer defrosting and the Skylab mission spanned approximately 9 months, it was felt that this could be a potential problem. Frost tests were conducted where temperature, dewpoint and ventilation conditions at the freezer doors were simulated in conjunction with door opening and food can removal operations. Considerable frost and ice buildup did occur during these tests; however, it was relatively soft in consistency and because of the low cooling capacity of the system sufficient heat was added to the affected areas when the freezer doors were opened to further soften the ice for easy removal.

DISCUSSION

The space chamber quartz IR lamp thermal simulation proved to be a good representation of the radiators earth orbit thermal environment. Radiator heat rejection and temperature characteristics were as predicted for the applied conditions. The applied orbital average net heat flux was always within 2 BTU/h/Ft² of the required value. The automatic cycle variation of lamp intensity provided excellent transient environment simulation to permit verification of refrigeration system coolant temperature control modes.

Subsequent Skylab flight data confirmed refrigeration system operation as first demonstrated in the simulation tests. As would be expected, the Skylab refrigeration system reflected

slightly more thermal performance capability than was demonstrated during the conservative simulation tests. During the first few days of Skylab operation when internal environment temperatures were as high as $+125^{\circ}\text{F}$, corresponding maximum food freezer temperatures were $+5^{\circ}\text{F}$. As Skylab internal temperatures returned to normal maximum frozen food temperatures dropped to values lower than -5°F .

N74-10235

Paper No. 3

**GENERAL ELECTRIC COMPANY UNDERWATER ENVIRONMENTAL
LABORATORY'S ZERO G TECHNIQUES APPLIED TO THE
ENVIRONMENT**

Ruth H. Fry, *General Electric Company Space Division,
Valley Forge, Pennsylvania*

ABSTRACT

The Underwater Environmental Laboratory (UEL) was specifically designed for zero G simulation in an underwater environment to test and evaluate astronaut subjects, manned/unmanned vehicles and equipment.

This paper relates particularly to UEL's recent endeavors in the conversion of zero G simulation techniques applicable to water environmental pollution areas such as oil spill clean-up techniques, thermal pollution, solid waste materials, industrial wastes, storm water discharge and radioactive or nuclear waste evaluation, aircraft emergency ejection studies, automotive water impact and submersion studies, buoy/small submersible development, ocean wave/glitter pattern research and similar areas of water-related research and development.

INTRODUCTION

The UEL is an indoor variably controlled environmental or zero G simulation facility. Its unique capabilities enable it to accommodate virtually any water-related research and development project in the industrial, military, medical, commercial, scientific, or Governmental community. Set forth herein is a description of the manner in which the UEL has revised and up-dated its equipment, zero G techniques and capabilities to serve a larger marketplace in new and non-aerospace activities. Also set forth are a few of these recent programs, such as oil/water separator methods and techniques, remotely-controlled manipulation to be used underwater twenty thousand feet beneath the ocean instead of in space, storm water pollution monitoring systems, vehicle water impact and submersion research and development, buoy and small submersible development and checkouts and radioactive

or nuclear waste evaluation. Lastly, described herein are some of the methods in which the UEL evaluated what areas to investigate relative to new business in other industries and fields and how potential customers were approached and apprised of the UEL's existence and unique capabilities.

UNDERWATER ENVIRONMENTAL LABORATORY

The main tank is in-ground 25' deep, 60' long, 28' wide (See Figures 1 and 2), water temperature controlled from approximately 40°F - 120°F - 190°F.

The air temperature in the tank area is controllable from 55°F - 102°F or higher if specifically required. During normal operating conditions the air temperature is maintained at 90°F. The air temperature in other areas of UEL, such as the electronics control room, machine shop, office areas, lounge and medical dispensary, highbay equipment preparation area, conference room, scuba equipment room and locker rooms is maintained at 70°F - 72°F.

The main tank is capable of docking three S-4Bs simultaneously or of performing two or three different experiments simultaneously, dependent upon requirements for each project. The main tank contains 315,000 gallons of water, which is normally completely chlorinated, filtered and purified every 24 hours. However, the UEL presently has the capability of chemically changing 315,000 gallons of fresh water to salt water of almost any density desired for a specific test program.

Built into the main tank is a water manifold pressurization system (a self-contained water supply for water pressurizing Gemini space suits to 3.5 psi). Above this system is an air manifold pressurization system extending 60 feet along one wall of the tank which is used for hookup umbilical helium oxygen deep water (1000-3000') tethered diving experimentation simulated), air pressurization of Apollo suits 3.5 psi, or in performing extended duration submergence physiological testing of selected subjects. To supplement the air pressurization system and to meet NASA, Navy and other customer requirements a two man recompression chamber is available with fully certified Navy trained medical chamber operators. In addition to the above-mentioned air manifold pressurization system and the two-man recompression chamber there is presently tied into the system a

compressed air and/or oxygen system (See Figure 3) used for extended submergence studies on hookah and tethered lines and to replenish scuba and other high pressure bottled gas supplies required on programs.

Adjacent to the main 60' long, 28' wide, 25' deep tank is a smaller circular tank 12' in diameter, 8' deep, water temperature controlled from 33°F to 212°F (See Figure 3) This environmental tank may be used for organic R&D such as growing algae, physiological monitoring in cold water experiments and thermal pollution studies.

The UEL is equipped with both surface and underwater TV capabilities whereby monitoring and/or video recording modes may be utilized. The system comprises two underwater cameras, one mobile and one stationary unit, one topside camera, and three surface monitors; each one can be independently connected to the video recorder if desired. Audio surface and underwater communication systems are also available if required for an individual program. Adjacent to the pool area is an electronics control room where from the comfort of a 70°F environment topside personnel monitor the underwater and pool area activities on two closed circuit TV monitors or through a 6' x 8' viewing window opening into the pool area. (See Figure 2).

The lighting system at the UEL consists of windows lining two sides of the pool area in the overhead bay, a spread of thirty-seven 350 watt highbay reflector lamps over the entire overhead bay section, a movable cross bar of 6 to 8, 1000 watts ea., colortran quartz lights. The cross bar can be raised or lowered to within one foot of water's surface as desired. Also, there is a 25' high photographic catwalk over the tank area. Additional underwater lights, 500 watts each, can be installed at specific locations in the main tank if any underwater supplemental lighting is required. For example, for normal underwater color motion pictures, still photography or TV system utilization, underwater lighting is not a requirement. However, if a test requires spotlighting, backlighting, etc., the underwater lights are excellent for such purposes.

Additional facilities and capability provided are:

- In addition to 315,000 gallon capacity fresh or soft water--murky, dark water can be provided or water visibility from one to sixty feet, capable of reading third to fifth line on standard eye chart.
- This year UEL has the capability of manufacturing 2' simulated waves, fresh or salt water.
- UEL's two ton overhead trolley crane (length of tank area)
- Five ton forklifts (3)
- Highbay area 61' x 25' x 20' high leading from the exterior of the building in the UEL area to the edge of the main tank area for equipment preparation and/or storage for future testing.

Listed below are some typical areas of the marketplace wherein UEL has capability to perform research and development programs and in which areas there is interest, in accomplishing these programs by the customer.

- Simulated "0" gravity for space flight
- Aquanaut equipment development
- Astronaut/aquanaut personnel training
- Environmental pollution studies
- Buoy and small submarine development
- Aircraft emergency ejection studies
- Car submersion rescue techniques
- Nuclear waste containment studies
- Public relations activities
- Underwater TV commercials, special features
- Ocean wave and glitter pattern research

- Coast guard sea rescue equipment development
- Deep sea remote controlled equipment development

All activities and programs at UEL are on a lease basis to General Electric Company components and industrial, military, commercial, scientific, medical and governmental communities alike are subject to a \$25 per hour--\$200 per day minimum.

UEL NON-AEROSPACE PROGRAMS

Several of UEL's recent activities center in the water environmental pollution area.

Oil/Water Separator

GE's Re-Entry and Environmental Systems Division has developed an oil/water separator to be used on land or offshore. It is a self-contained gravity separation system which requires no operator, has high volume capabilities and is adaptable to existing oil production facilities, both on land and offshore. The separator is designed with non-corrosive materials, has no moving parts, and has been proven in months of field operations to be virtually maintenance-free. The system does not have any external power requirements which place utility demands on the installation site. The only power required is 110V AC to push or pull the bilge mixture to the separator and to pump the separated oil to a suitable storage container.

Presently the oil/water separator is being tested at UEL on a regular basis to develop increased volumetric rates from 1,000 gallons/minute to 5,000 gallons/minute. Because of UEL's capacity of 315,000 gallons, these rates per minute and higher rates are entirely feasible.

Separator efficiency is achieved by design which achieves total laminar flow of the mixture from the input manifold, through baffles and then passes through a combination of specially configured coalescent plates and packs.

With a flow of approximately two feet to maintain capacity flow, the unit operates at atmospheric pressure with essentially no pressure drop from inlet to outlet. While the waste water flows horizontally through the separator, the oil adheres to the plates

and moves vertically through the specially configured plate banks. When the oil reaches the liquid surface level in the separator, it is automatically skimmed off by a passive float device that can also control the oil layer thickness to insure that water free oil is removed from the separator.

In addition to utilization in oil production facilities, the separator can also be used for such tasks as ship debilging, refinery and chemical process produced water water clean-up, and assistance in major oil clean-up.

Storm Water Pollution Monitoring System

Another area of water environmental pollution in which UEL has a significant capability is the storm water pollution monitoring system.

Recently a study was conducted by the Environmental Protection Agency to define the water pollution impact of urban storm water discharge. It was discovered that street surface runoff is highly contaminated. In addition, it was found that street cleaning practices and storm drains are ineffective in keeping the fine solids fraction of the street surface contaminants from reaching receiving waters during a storm. The study also showed that the fine solids have the highest pollution potential because they are primarily composed of heavy metals and pesticides which are detrimental to biological systems.

As a result of this study, it was recommended that improved street cleaning practices and newly developed street cleaning equipment could more effectively remove the fine solids from the storm discharge water.

Since the completion of the above study, General Electric has developed a method for monitoring storm water discharge.

In concept, the system is a heavy metals analyzer that is positioned at the desired monitor locations. Prior to a storm the station is automatically operated by remote control using digital codes over a telephone line. The heavy metal data is transmitted by telephone line to a central station where it is recorded and analyzed. Real time heavy metal concentrations in the runoff storm water from many such stations can give a total picture of the storm water in a metropolitan area.

The sensor is an adaptation of a system GE has designed for industrial process line monitoring of the chemical composition of liquids and slurries. The system includes a sensor, recorder, excitation source, power supply and cooling unit.

The sensor operates on the principle of x-ray fluorescence analysis. As the water is circulated through the measurement cell, it is exposed to a source of radiation which causes the elements in the water to emit their characteristic x-rays. The number of x-rays counted by the detector is always proportional to the concentration of each element. In field use each element's x-rays generate discrete voltage pulses in the detector. These pulses are monitored by a programmable single channel analyzer (SCA) and the count rate for each element is transmitted by a data phone line to a central office. Here the data is recorded for future analysis.

A simulated storm drain outfall system will be constructed at UEL for proof testing the water intake designs and pollutant detection sensitivity of the system as a function of water velocity.

Storm water discharges will be simulated by pumping water out of the main test tank of the UEL into the existing storm drain system. (See Figure 4) The main tank of the UEL shown in Figure 1 is 25' x 60' x 28'. The maximum pump-out rate is 315,000 gallons per 24-hour period.

Pollutant detection sensitivity testing under simulated storm conditions will be performed by flushing contaminated street dirt into the UEL existing storm drain system. Contaminated dirt will be collected from streets. The street dirt will be analyzed prior to the storm simulation tests. These tests will then provide sensor detection sensitivity data for various storm water loadings. These data are necessary because the detection sensitivity of the sensor in the storm water monitor is dependent on the total solids contained in the runoff water. The variation in solids will affect the signal to background values. This occurs because the radiation reflected into the sensor by the water plus solids determines the background whereas the characteristic x-rays that are simultaneously generated in the elements contained in the solids determines the detectable signal level.

Additionally, the water intake model will then be constructed to withstand the conditions previously measured in the field. The integrity of the design will be tested at the UEL under conditions equivalent to peak storm conditions.

Lastly, detection sensitivity tests will then be performed under simulated storm runoff conditions in the UEL. Detection sensitivities will be established for each of the heavy metals: Ni, Zn, Cu, Cd, Pb and Hg.

Radioactive or Nuclear Waste Evaluation

A further area of UEL capability and participation is in the radioactive or nuclear waste evaluation problem. Namely, the effect of hydrostatic pressure on the performance of a gamma-ray spectrometer; the passive detection of an isotope source; and, determination of the parameters for using activation analyses to identify materials at a distance in water. UEL has the capability of utilization of these three different measurements.

Water Impact and Vehicle Submersion

A quite different endeavor of the UEL in the non-aerospace marketplace is the development of safety standards and procedures in motor vehicle accidents involving water impact and vehicle submersion.

UEL is presently proposing itself to develop practical ways and means of reducing the numbers of accidents involving water impact and vehicle submersion. Presently, very little is known about the behavior and failure characteristics of a motor vehicle upon impact with the water, or during floatation, submergence and bottom impact phases. Equally unknown are the psychological difficulties experienced by the victims, or the escape difficulties experienced under varying conditions of vehicle type, post-accident conditions, rest attitude of the vehicle, and water depth.

A review of the small amount of data that is readily available indicates that in those accidents which result in total submersion of the vehicle, the fatality rate is abnormally high. This leads to the speculation that by far the largest percentage of these deaths are caused by drowning. The more important factors contributing to death by drowning under these conditions may be: (1) panic, with the attendant in-

ability to think clearly; (2) inability of the victim to hold his breath long enough to permit escape because of the greatly increased demand for oxygen brought on by fear and panic; (3) ignorance of escape procedures; (4) unconsciousness or other disabling injuries sustained in the accident; (5) jammed windows and doors.

The number of accidents, injuries and deaths involving water impact and submersion may be reduced through: (1) improving highways, along areas bordering water, such as the installation or improvement of guardrails; (2) the development of proven escape procedures under the most prevalent conditions to be encountered; coupled with a thorough education program to make these procedures known to the driving public; (3) determine those design features and modifications which can be incorporated in present and future motor vehicles in order to significantly increase the survival chances of persons involved in accidents of this type. Undoubtedly, the most effective of these changes, if practical and feasible, would be to make motor vehicles virtually unsinkable.

Other Non-Aerospace Programs

During the past year, one of UEL's customers (within General Electric Company) has been developing an unmanned manipulator, initially developed for aerospace utilization, for use in oceanic research at depths of 10,000 to 20,000 feet beneath the sea. Other ocean related programs have been: research and underwater testing of undersea cables, checkout of life support systems and maneuverability of small submissiles and submarines, ocean wave and glitter patterns sensed from orbiting satellites, and research and development in closed cycle mixed gas breathing equipment used by aquanauts to ocean depths of 1,500 to 2,000 feet.

POTENTIAL CUSTOMERS

As may be readily understood from the above typical examples of the variation of non-aerospace problems which may be solved with aerospace technology, the UEL has achieved a degree of interest and capability in other areas of technology, especially in the environmental area.

As stated previously, the Underwater Environmental Laboratory now has a capability to perform virtually any water-related research and development program and is more than willing to assist other companies, both aerospace and non-aerospace oriented to solve their particular problems in underwater related research and development and to lease the UEL to these organizations to achieve this very worthwhile result.

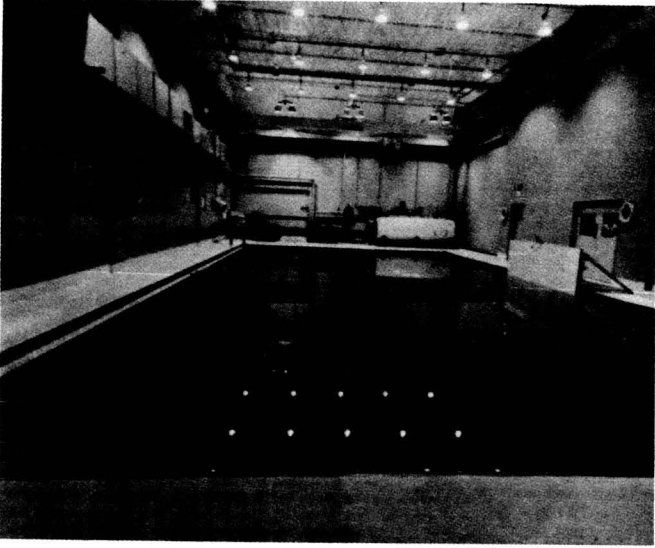


Figure 1

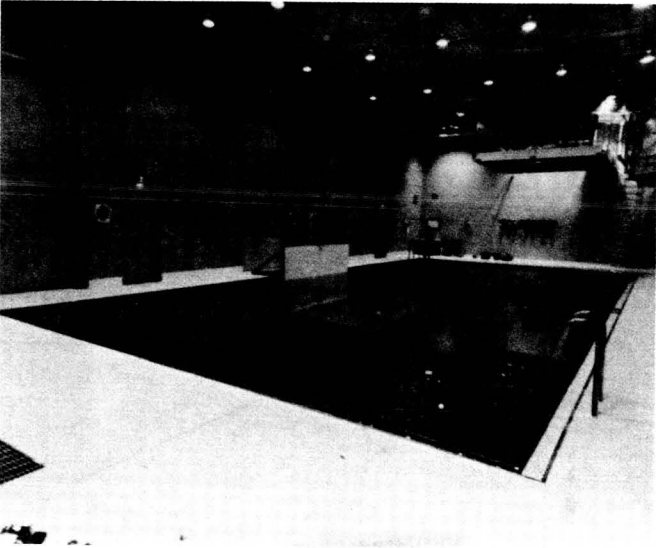


Figure 2

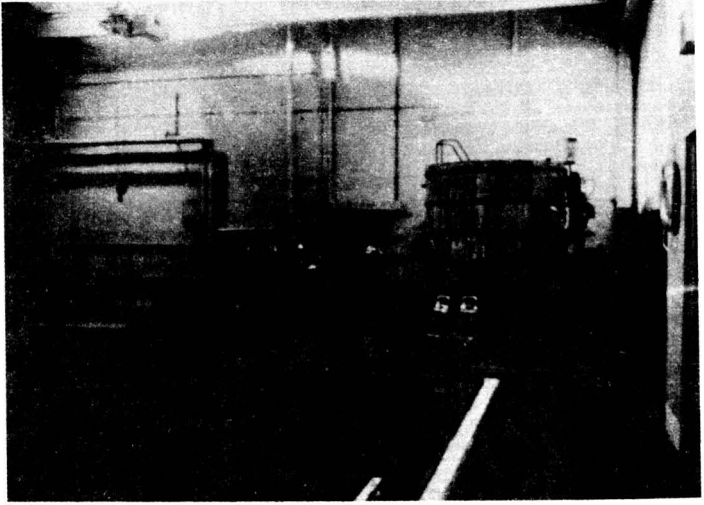


Figure 3

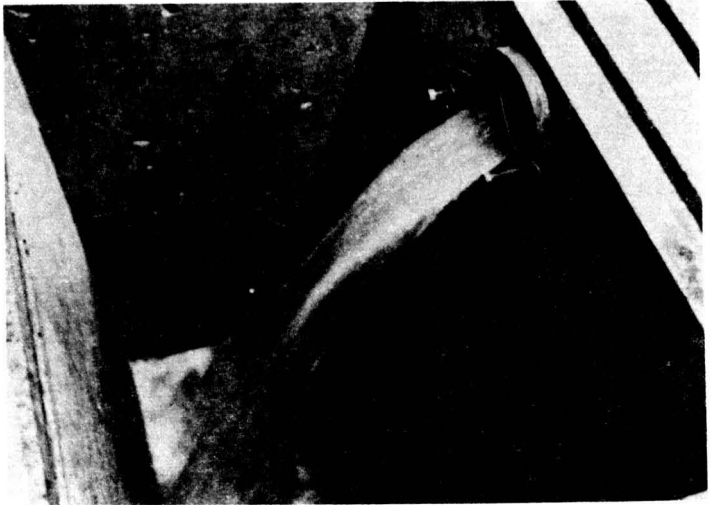


Figure 4

Paper No. 4

MARS SURFACE THERMAL ENVIRONMENT FOR VIKING LANDER DESIGN AND TEST

T. F. Morey and T. R. Tracey, *Martin Marietta Aerospace,
Denver Div., Denver, Colo.*

ABSTRACT

Mars surface thermal environments have been developed for design and testing of the Viking lander, based on mission requirements and available Mars thermal data.

INTRODUCTION

The Viking program is intended to place two soft landers on the surface of Mars during 1976 for extended observations and transmittal of data to Earth. They must be able to survive many days of whatever environments may be encountered. It is well known that the Mars surface environment will vary greatly with season, latitude, and time of day. However, since the Viking landers will be the first weather stations on Mars, there are a great many unknowns.

The purpose of this work was to develop a rationale for defining the probable range of thermal environments, obtain the required Mars thermal data, and then define the specific combination of environments to be used in the design and testing of the Viking lander. The scope of this paper includes the derivation and results of the work of establishing these environments, but not the vehicle thermal design, testing, or performance.

The thermal environment parameters to be specified depend on the general design and mission objectives of the Viking lander. The Viking mission definition determines the ranges of landing sites and mission dates to be considered. The basic data for the surface, atmospheric, and astronomical parameters are taken primarily from the Mars Engineering Model prepared by the NASA Langley Research Center for the Viking program (Reference 2). Many of the parameters used in this study have been continually updated as better information became available.

ENVIRONMENTAL FACTORS

Factors Affecting Lander

The Viking lander is affected by many types and modes of heat transfer, including solar and infrared radiation, forced and free convection and gas conduction. The cyclic and mean

daily thermal conditions and their variations with landing site and time of year are required to establish the design requirements. The environments for specific lander areas or external components are also affected by the specific vehicle configuration and orientation, and must be considered in the detailed lander design, especially for critical exposed components.

The pertinent solar radiation parameters are the solar irradiance, solar angle, daily solar radiation time, and solar radiation absorptivity of Mars and vehicle surfaces. The infrared radiation parameters are the Mars surface and effective sky temperatures and Mars and vehicle surface infrared emissivities. The terrain configuration could also affect both solar and infrared radiation by modifying the vehicle to soil view factors and reflections and introducing solar radiation shadowing. Forced convection depends on the wind speed, free convection on the acceleration of gravity, and both depend on the atmospheric temperature, pressure, and physical properties. The lander insulation performance and internal heat transfer are affected by the atmosphere conductivity and pressure.

Mission Specifications

The mission specifications affecting the environment are the ranges of landed mission dates and landing sites given in Reference 1. The solar radiation, the surface, atmosphere and sky temperatures, and the atmospheric pressure vary with these factors. The landed mission season or time of year on Mars and the landing site latitude are the most important parameters in determining the thermal environment.

The specified range of arrival dates at Mars is June 17 to August 13, the time in orbit is 10 to 50 days, and the landed mission time span is 90 days. Thus, the design landed mission is from June 27 to December 31, 1976. The actual end of mission may occur earlier because of loss of communication caused by occultation of Mars by the sun, but the design requirement extends through December.

The mission landing site latitude range was specified as 30 deg south latitude to 30 deg north latitude. Currently, further north landings are being considered, but none of these has more extreme conditions than the extreme hot and cold cases occurring for the original latitude limits. The range of elevations considered is from 3 km above to 9 km below the mean surface level. Potential landing sites are selected to have anticipated slopes not over 19 deg, and studies have shown that relatively moderate slopes have little effect on the environment. Therefore, for this study the terrain is assumed to be level.

Mars Thermal Data

The pertinent thermal data for Mars are taken primarily from the Mars Engineering Model (Reference 2) with some additional information obtained from other sources (References 3-8).

The required astronomical constants are the mean solar day of 24.66 hrs, the solar constant at one A.U. of $429 \pm 1.5\%$ Btu/hr-ft², and Mars surface gravity of 12.146 ft/sec². The Mars-Sun distance, solar irradiance at Mars, and aerocentric solar declination (angle between Mars equator and sub-solar latitude) vary with Earth date as shown in Figures 1 and 2. The daily solar radiation time span on Mars varies with Earth date and Mars latitude as shown in Figure 3.

The soil properties affecting the environment are the solar absorptivity, infrared emissivity and thermal inertia parameter (the square root of the product of soil density, thermal conductivity and specific heat). The presence of dust on the lander surfaces affects their optical properties. The pertinent atmospheric properties are the composition, pressure at the mean surface level and its variation with altitude, physical and thermal properties, transmissivity to solar radiation, and peak steady state wind speed. The effective sky temperatures are obtained from the other parameters for the various atmospheric models as described in References 7 and 8. Values for some of these surface and atmospheric parameters are given in Table 1. The ranges of most atmospheric parameters such as pressure, composition and thermal conductivity have decreased considerably in significance with each new set of model atmospheres.

The thermal inertia values used in this study are for particulate soils having about 50 percent voids, which are believed to cover much of Mars (Reference 2). Solid rock has a much higher value and would greatly attenuate the daily surface temperature fluctuations. The normal atmospheric transmissivity of nearly 100 percent is used. Martian clouds, especially the dust clouds observed by Mariner '71 have a radical effect on the environment. As in the case of heavy terrestrial clouds, they would attenuate the surface and atmospheric temperature extremes and reduce the incoming solar and outgoing infrared radiation.

DESIGN CONDITION SELECTION

Mars Properties

The mean or most probable values for all parameters are used to obtain the nominal environments. The hot and cold design environments are obtained by using the heating or cooling design limits for these parameters. However, the limiting conditions to be used for certain parameters are not immediately obvious. Moderate variations in soil thermal inertia have very little effect on the mean surface temperature, but the daily peak surface temperature varies inversely with the thermal inertia to a significant degree.

Wind has a cooling effect in the cold case, since the external environment is always much cooler than the lander interior. In the hot case, the mean exterior environment is also

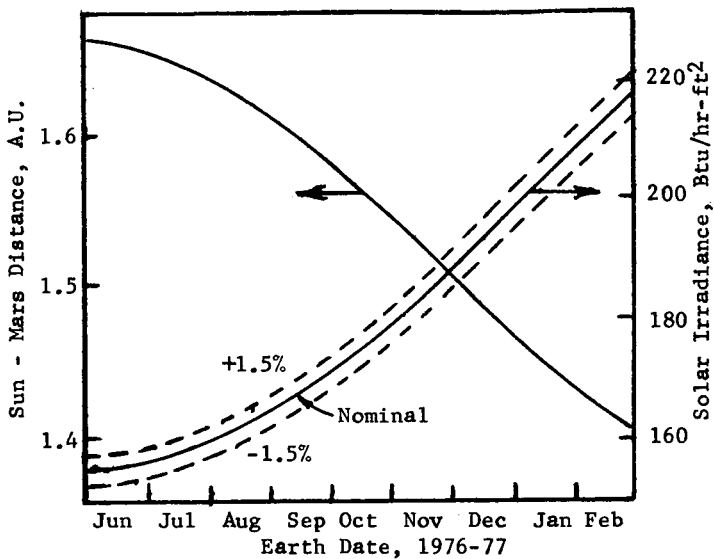


FIGURE 1 - SUN-MARS DISTANCE + SOLAR IRRADIANCE AT MARS

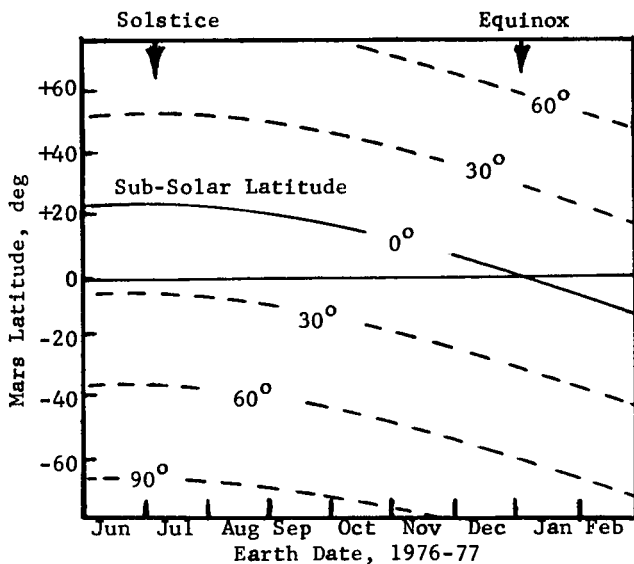


FIGURE 2 - NOON SOLAR ANGLE ON MARS

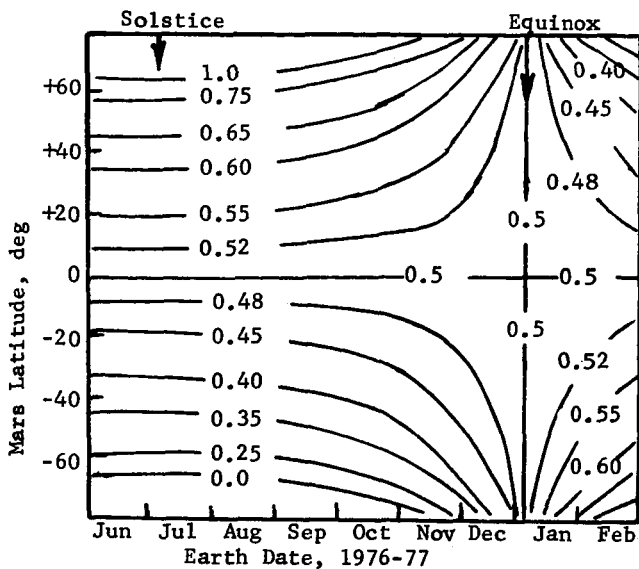


FIGURE 3 - SOLAR RADIATION FRACTION OF DAY ON MARS

TABLE 1 - MARS SURFACE PHYSICAL AND OPTICAL PROPERTIES

<u>Surface Albedo Dependent</u>	<u>Light Area</u>	<u>Average</u>	<u>Dark Area</u>
Surface Albedo (Reflectivity)	0.25	0.23	0.15
Surface Solar Absorptivity	0.75	0.77	0.85
Soil Thermal Inertia, Btu/ ^o F-ft ² -hr ^{1/2}	0.55±0.12	0.59±0.12	0.74±0.12
<u>Atmospheric Model Dependent</u>	<u>Minimum P</u>	<u>Nominal P</u>	<u>Maximum P</u>
Pressure, Mean Surface Level, mb	4.0	5.3	8.0
Atmosphere Composition, wt % CO ₂	100	100	82
wt % Ar	0	0	18
Thermal Conductivity at -46 ^o F Btu/hr-ft- ^o F	0.0074	0.0074	0.0075
Effective Sky Temperature, as Function of Surface T, ^o F	-188.9 +0.664T	-177.3 +0.658T	-177.3 +0.658T
<u>Independent Variables</u>	<u>Minimum</u>	<u>Nominal</u>	<u>Maximum</u>
Surface Infrared Emissivity	0.89	0.93	0.96
Landing Site Elevation, km	-9	-3	+3
Wind Speed at Surface, ft/sec	0	65	130

colder than the lander interior, but wind tends to heat the lander during part of the day. However, a wind that starts and stops in a specific pattern every day is considered sufficiently unlikely to be excluded, and the no wind condition is assumed to be generally hotter. Since the wind is one of the least known and widest varying parameters which may have a major thermal effect, insensitivity to wind speed must be considered in vehicle design.

The values tending to produce the highest mean and/or peak Mars surface and atmospheric and vehicle surface temperatures and the least heat loss from the lander are used for the hot environments. The selected surface properties are dark soil for a high solar absorptivity, low emissivity, and low thermal inertia for a dark area. The atmosphere selected has the lowest thermal conductivity and pressure and the highest effective sky temperature. A plus tolerance on the solar constant, a zero wind speed, and a dust covered lander for high solar absorptivity are also assumed.

The values tending to produce the lowest mean and/or peak temperatures and the greatest heat loss from the lander are used for the cold environments. The selected surface properties are a light soil for a low solar absorptivity, high emissivity, and high thermal inertia for a light area. The atmosphere selected has the highest thermal conductivity and pressure and the lowest effective sky temperature. A minus tolerance on the solar constant, the maximum steady state wind speed, and a bare lander surface are also assumed.

Mars Temperatures

The daily surface temperature cycles for hot, nominal and cold environments were derived for Mars as functions of Earth date and Mars latitude. The atmospheric temperature at Mars surface is assumed equal to the surface temperature. This assumption is generally conservative as the atmospheric temperature normally fluctuates less than that of the surface. The computer model used to obtain these temperatures has several soil layers increasing in thickness with depth. The lowest layer has a nearly constant temperature close to the average surface temperature, which is consistent with actual subsoil conditions. The upper atmosphere temperature and pressure profile shapes are assumed constant throughout the day for a given atmospheric model. Thus, the effective sky temperature used for each case depends only on the average atmospheric temperature at the surface and the model atmosphere used. The parameter values used for the various cases are those described in the preceding section.

The mean daily temperatures for the nominal environments are presented in Figure 4 for the ranges of Earth dates and Mars latitudes of primary interest. This plot indicates the ranges and distributions of mean daily temperatures to be encountered during the mission. Several representative diurnal temperature

cycles, including those for the hot and cold design cases, are shown in Figure 5. These curves indicate the extremely wide ranges of daily temperatures characteristic of these latitudes on Mars.

Mission Design Points

The selected design point for the cold case is on July 4, the time of Mars northern solstice and shortly after aphelion, and at a landing site 30 deg south latitude. This point corresponds to a low solar irradiance, minimum solar elevation angle and shortest daily solar radiation time for this mission. This time was picked rather than the earliest landing date, which could be colder, because the solstice time is fixed and not subject to changes in mission definition, and the environment at 30 degrees south varies little during late June and early July. It is also the goal date for the first Viking landing.

The hot design point is on December 31, the mission time nearest the equinox and approaching perihelion, and at a landing site one deg north latitude, the subsolar point at that time. These conditions correspond to the maximum solar irradiance for this mission, the maximum solar elevation angle, and the nominal daily solar radiation time. The highest temperature occurs at the sub-solar point when it is at the equator.

The nominal case is selected to be on October 2, the latest landing date and end of mission for the July 4 landing date, and at a landing site on the equator, the midpoint of the original landing site range. These conditions produce an environment very close to the median or most probable environment for the specified mission ranges as shown in Figure 4.

DESIGN ENVIRONMENTS

The conditions used for the hot extreme, cold extreme, and several intermediate environments are given in Table 2. The corresponding surface temperature diurnal cycles are given in Figure 5. The nominal case represents the most probable set of conditions and thus the most probable thermal environment anticipated for much of the mission. The cold design case represents the coldest environment to be met during any part of the mission, including the proposed landings near 45 deg north latitude. The hot design case represents the hottest environment to be encountered during any part of the mission.

The intermediate environments are useful in determining most probable conditions and margins, while the extreme hot and cold cases are used for vehicle design and test limits. The cold and hot cases have another major difference besides their wide difference in temperatures. The cold case is convection dominated because of the low temperatures, low solar flux and high wind speed, while the hot case is radiation dominated because of the high temperatures, high solar flux and low atmospheric free convection.

The available Mariner data, such as Reference 9, have been compared with these results and found to fall within the design limits. The Mariner measurements cover relatively wide areas, while the Viking design environments must consider local conditions. The Mariner data indicates that wind and blowing dust do exist on Mars, and that severe dust storms modify the environment by attenuating the radiation and temperature peaks at the surface. The design environments will be reviewed as more Mariner data become available.

TABLE 2 - MARS SURFACE MODEL ENVIRONMENTS

<u>TIME/PLACE</u>	<u>Cold Case</u>		<u>Nominal Case</u>		<u>Hot Case</u>
Event	North Solstice		Late Landing		Mission End
Earth Date, 1976	July 4		Oct. 2		Dec. 31
Solar Latitude, deg	+24.77		+18.45		+0.96
Solar Irradiance, nominal-Btu/hr-ft ²	156.3		170.9		198.3
Lander Latitude, deg	-30.0		0.0		+0.96
Irradiance Time, hr	10.21		12.33		12.33
Lander Altitude, km	-9		-3		+3
<u>THERMAL CONDITIONS</u>	<u>Cold</u>	<u>Nominal</u>	<u>Nominal</u>	<u>Nominal</u>	<u>Hot</u>
<u>Solar Irradiance</u>					
Tolerance, Btu/hr-ft ²	-2.3	0.0	0.0	0.0	+3.0
<u>Surface Properties</u>					
Solar Absorptivity	0.75	0.77	0.77	0.77	0.85
Infrared Emissivity	0.96	0.93	0.93	0.93	0.89
Thermal Inertia, Btu/°F-ft ² -hr ^{1/2}	0.67	0.59	0.59	0.59	0.62
<u>Atmosphere Properties</u>					
Pressure at Site, mb	20.2	6.8	6.8	6.8	2.85
Composition, wt % CO ₂	82	100	100	100	100
wt % Ar	18	0	0	0	0
Conductivity at -46°F Btu/hr-ft-°F	0.0075	0.0074	0.0074	0.0074	0.0074
Wind Speed, ft/sec	130	65	65	65	0
<u>Temperatures</u>					
At Surface, °F Max	-60	-46	+42	+72	+95
Mean	-139	-132	-67	-50	-34
Min	-184	-180	-141	-131	-121
Sky (Effective), °F	-281	-264	-221	-210	-200

CONCLUSIONS

1. The most critical thermal environment parameters and the values to be used depend on the type of vehicle and mission objectives.
2. The thermal environments defined in Table 2 are conservative but reasonable for the thermal design and testing of the

- Viking lander.
3. The most probable variations in parameter values from those used for the extreme design cases will produce less extreme environments.
 4. These Mars thermal environments present very wide ranges of temperatures, solar radiation, wind and dust conditions which must be considered in the Viking lander thermal design.
 5. These environments should be reviewed as more data become available to prevent unnecessary conservatism in the vehicle design and operation.

REFERENCES

1. Viking 75 Project Mission Requirements on System Design, RS-3703001, Appendix A, 1971, NASA Langley Research Center.
2. Mars Engineering Model, NASA-M-75-125-2, April 1972, NASA Langley Research Center,
3. Mars Scientific Model, JPL Document 606-1, 1968, Jet Propulsion Laboratory.
4. Morrison, D; Sagan, C.; and Pollack, J. B.; "Martian Temperatures and Thermal Properties", *Icarus*, Vol. II, pp 36-45, 1969.
5. Hovis, W.A., Jr.; and Callahan, W.R.; "Infrared Reflectance Spectra of Igneous Rocks, Tufts, and Red Sandstones from 0.5 to 20 Microns", *J. of Optical Society of America*, Vol. 56, pp 639, 1966.
6. Space Environmental Criteria Guidelines for Use in Space Vehicle Development (1969 Revision), NASA TM X-53957, Oct. 1969, Marshall Space Flight Center.
7. Wachter, J.P., "Effective Sky Temperatures for Several Martian Atmospheric Models", *J. of Spacecraft and Rockets*, Vol. 7, No. 3, pp 350-352, March 1970.
8. Wachter, J.P., "A Method for Calculating Effective Martian Sky Temperatures for Inclined Planes", to be published.
9. Neugebauer, G., et al, "Mariner 1969; Preliminary Results of Infrared Radiometer Experiment", *Science*, Vol. 166, pp 98-99, Oct. 1969.

**THERMAL TESTING OF THE VIKING LANDER IN
SIMULATED MARTIAN ENVIRONMENTS**

T. Buna and T. R. Tracey, *Martin Marietta Aerospace,
Denver Div., Denver, Colorado*
T. W. E. Hankinson, *NASA Langley Research Center,
Hampton, Virginia*

ABSTRACT

Techniques for the simulation of the Martian Thermal Environment are Verified by Full Scale Test Data

INTRODUCTION

The presence of a dynamic atmosphere on Mars introduces a probabilistic element into the definition of the mission environment of a Martian lander. This precludes the possibility of "mission thermal simulation" in a test facility, in the usual sense applicable to spacecraft testing. The available alternative is to bracket the multitude of possible thermal conditions at the landing site with simulated "hot" and "cold" extremes which guarantee the survival of the lander under all anticipated conditions on Mars. This paper reviews the definitions of thermal test extremes applicable to the Viking Lander, and discusses the criteria, techniques and facilities required for their simulation in light of recent data obtained from Mars Simulation tests conducted with the Viking Thermal Effects Test Model (TETM).

The TETM is a full scale model of the Viking Lander, incorporating the developmental thermal control subsystem, flight type structures, and thermal simulators of science and electronic equipment. The primary objective of the Mars simulation tests was to verify the lander thermal design and supporting analytical models, and to demonstrate the adequacy of the test techniques. The discussion in this paper is limited to the latter aspects of the test results; the thermal response of the vehicle being only considered to the extent necessary to demonstrate the test approach. The relation of the TETM Mars simulation test program to the other Viking thermal tests is illustrated on Figure 1.

In the above context, the TETM tests represent the final link in a chain of developmental efforts initiated early during the Viking program and aimed at the definition of a suitable Mars simulation test approach. These developments included the definition of the test environments and facility requirements (1,2)¹, implementation of the necessary facility modifications,

¹The numbers in parenthesis refer to the list of references appended to this paper.

and investigations related to unique test-operational features of Mars environmental simulation (3,4). The final proof of the proposed technique, however, was dependent on the availability of a full scale thermal model of the Lander, since the simulation techniques are related to convective processes which depend in detail on vehicle-peculiar forcing geometries and heat dissipation profiles. These vehicle-induced convective effects in the test environment impose limitations on both the controllability of the test environment, and the ability to separate the performance of the test facility from that of the test article.

In addition to the precursory developmental effort already mentioned, of particular significance are the "RTG Wind Tunnel Tests" depicted on the left hand side of Figure 1. Their purpose was to provide data for the design of protective wind shields for the RTG's, and to determine the effects of winds on the availability of RTG waste heat for thermal control. The results of the wind tunnel tests served as input in the form of controlled ETG boundary conditions during the TETM cold extreme test.

In the next section, the definition of the simulated thermal extremes is reviewed, and criteria for their simulation are developed. This is followed by descriptions of the simulation approach, the test hardware, and test operations. A discussion of test results as applied to the simulation technique is presented in the last section.

NOMENCLATURE

f	=	parameter defined by Equation (2)
h	=	convective coefficient, Btu/hr-ft ² -°R
h*	=	equivalent convective coefficient defined by Equation (7e), Btu/hr-ft ² -°F
P	=	period of Martian diurnal cycle - 24.66 hours (= 1480 min., approx.)
q	=	heat flux per unit area of skin, Btu/hr-ft ²
t	=	time from Martian midnight, hr
T	=	temperature, °R
\bar{T}	=	average temperature for the Martian diurnal cycle, °R
ΔT_R	=	difference between radiation-equilibrium and skin temperature, °R = $T_{R,M} - T_S$
ϵ	=	vehicle outer surface emissivity
σ	=	Stefan-Boltzmann constant, Btu/hr-ft ² -°F

Subscripts

abs	=	radiation absorbed from the environment (sum of IR, solar and albedo)
em	=	radiation emitted by vehicle outer surface
CH	=	simulation chamber
h	=	convection
min	=	minimum (lower extreme)

- max = maximum (upper extreme)
- M = Mars
- R = radiation-equilibrium (as attained in the absence of convection)
- s = outer surface of the vehicle (vehicle/environment thermal interface)
- ∞ = Martian atmosphere

SIMULATION CRITERIA

In order to arrive at a definition of the simulated extremes, consider the heat balance of the vehicle outer skin in the non-dimensional form derived in Reference 1:

$$(T_{s,M}/T_{R,M})^4 + f(T_{s,M}/T_{R,M}) - f(T_{s,M}/T_{\infty}) - 1 = 0 \quad (1)$$

where: $f = h_M / \epsilon \sigma T_{R,M}^3 \quad (2)$

$$T_R = \left(\frac{q_{tr,M} + q_{abs,M}}{\epsilon \sigma} \right)^{1/4} \quad (3)$$

The above equations may be applied to either local/instantaneous values of the temperatures and heat transfer coefficients, or to averages over time and/or surface areas. In the latter case the averaging should be in accordance with the various components of heat fluxes, hence fourth-power averages apply to the first term in Equation (1), whereas algebraic averaging pertains to the linear terms.

Equation (1) is plotted with f as a parameter on Figure 2, an examination of which indicates the following. For a given vehicle surface, all possible thermal conditions are bracketed by the two intersecting straight lines $f = 0$ and $f = \infty$, and the point of intersection divides the environments into two regimes designated as "convective cooling" and "convective heating" regimes, respectively. In the convective cooling regime, maximum vehicle temperatures are attained in the absence of winds (convection minimized) approaching T_R in the limit. The opposite applies to the convective heating regime.

In the most general case, the various elements of a lander may operate in different thermal regimes at a given time, or may cross over (through the point of intersection at which $T_R = T_{\infty} = T_s$) from one regime to the other during a given period of time.

For given operational modes of the lander, mission span, and landing site, extreme values for both T_{∞} and T_R may be established as functions of diurnal cycle, independently from the convective environments on Mars. The extremes of T_{∞} are defined by the Mars Environmental Models depicted on Figure 5 of Reference 5. The extremes of T_R may be calculated from Equation (3) with good approximation, since neither q_{tr} nor q_{abs} are significantly dependent on wind effects. For the general case where the surface "crosses over" from one thermal regime to the other during the diurnal period, these profiles may look as shown on Figure 3, an examination of which indicates the following.

The theoretical upper limit for the vehicle surface temperature is given by the curve ABCDE. In order for the vehicle surface to approach this limit, it would be necessary that radiation dominated conditions (zero wind) prevail from A through B, and D through E, whereas maximum wind conditions dominate from B through D. This implies a step function increase in wind velocity from zero to maximum at B, and a corresponding decrease at D. This is a highly improbable condition, especially considering the fact, that it would have to repeat itself during two consecutive Martian days, to produce significant thermal effects on the equipment compartment. On the other hand, a "probable" upper limit of the temperatures will be represented by the curve ABFDE on Figure 3, provided that

$$\begin{aligned} \bar{T}_{R,M,max} &= \frac{1}{P} \int_0^P T_{R,M,max} dt \gg \frac{1}{P} \int_0^P T_{oo,max} dt \\ &= \bar{T}_{oo,max} \end{aligned} \quad (4)$$

Similar reasoning establishes the theoretical lower limit of the vehicle temperatures as the curve abfde, and the practical lower limit as abcde, on Figure 3, provided that:

$$\begin{aligned} \bar{T}_{oo,min} &= \frac{1}{P} \int_0^P T_{oo,min} dt \ll \frac{1}{P} \int_0^P T_{R,M,min} dt = \\ &\bar{T}_{R,M,min} \end{aligned} \quad (5)$$

As applied to the thermally significant vehicle/environment interfaces, the success criteria for the latter approach may be summarized as follows:

- (1) The inequalities (4 and 5) must be satisfied,
- (2) The radiation component of the "hot-extreme" environment must be accurately simulated,
- (3) The temperature differences $(T_R - T_{s,CH}) \equiv \Delta T_R$ are within a pre-determined upper limit ($\Delta T_{R,max}$), established from estimates of minimum natural convective cooling on Mars, i.e.,

$$(T_{R,M} - T_{s,CH}) \leq \Delta T_{R,max} \quad (6)$$

In the above inequality, $\Delta T_{R,max} = 10^\circ\text{F}$ (based on estimates of natural convection on Mars), $T_{s,CH}$ is supplied by the test data and $T_{R,M}$ is calculated by the use of Equation (3). Note that, with good radiation-simulation,

$$T_{R,CH} \approx T_{R,M}$$

within the approximation permitted by the compensating features to be discussed under Simulation Approach.

(4) The cold extreme simulation shall satisfy the requirement:

$$T_{s,CH} \leq T_{s,M,min} \quad (7)$$

$T_{s,M,min}$ in Equation (7) may be deduced from the test data as follows:

$$h_M = \frac{q_{h,M}}{T_{s,M} - T_{oo}} \quad (\text{by definition}) \quad (7a)$$

and $q_{h,M} = (q_{tr} + q_{abs} - q_{em})_M$ (from heat balance) (7b)

Furthermore, $(q_{tr})_M = (q_{tr,CH})$ (7c)

and in view of (7) $(q_{em})_M \geq (q_{em})_{CH}$ (7d)

By combining (7a through 7d) we have:

$$h^* \equiv \frac{q_{tr,CH} + q_{abs,M} - q_{em,M}}{T_{s,CH} - T_{oo,min}} \geq h_{M,max} \quad (7e)$$

which is the explicit form of criterion (4) above.

An $h_{M,max} = 1$ was established for these tests from standard forced-convection correlations, as applied to maximum-wind conditions on Mars.

There are two general approaches that can be used to verify compliance with the above criteria for a given test. The first consists of comparing pre-test analytical predictions of $T_{s,M}$ profiles, with the corresponding $T_{s,CH}$ profiles supplied by the test data. This method has the advantage of possible attention to detail characteristic to large analytical models, however, it cannot separate the effects of convection and radiation in the chamber, and lacks the capability of independent verification of the test approach from that of the analytical model.

The second approach concentrates on the vehicle/environment interfaces only, and consists in determining the degree of approach of the $T_{s,CH}$ profiles to the $T_{R,M}$ and $T_{oo,M}$ profiles, as appropriate, per the discussions above. With this method, directly measured values of $q_{tr,CH}$ are all that is required to characterize the internal heat transfer processes of the lander, and the only calculated inputs (viz. q_{em} and q_{abs}), are connected with radiation processes. The convective effects in the chamber can be determined by solving the heat balance equation as applied to the vehicle skin. During the TETM tests, the $q_{tr,CH}$ were measured by commercial heat transfer gauges, and the results presented at the end of this paper are based on those measurements.

In addition to considerations of probability as noted above, a major factor entering into the definition of thermal extremes is the feasibility of techniques, and the availability of facilities, for their simulation. Clearly, an accurate simulation of thermal conditions implied by the curves ABCDE or ~~abfde~~ requires a test

facility combining the principal features of solar simulators, thermal vacuum chambers, and high-altitude wind tunnels, with special equipment required for atmospheric temperature control and for the simulation of the thermal properties of the Martian ground. Such a facility is presently outside the realm of practicality. On the other hand, the radiation-dominated domain represented by ABFDE and the convection domain represented by abcde on Figure 3 can be reproduced with acceptable accuracies, with specially equipped conventional thermal vacuum chambers, as discussed in the next section.

SIMULATION APPROACH

The TETM Mars surface simulation tests were conducted in Martin Marietta's Space Simulation Laboratory in Denver, Colorado, which has recently been equipped with planetary environmental simulation capabilities. The chamber adapted to Mars surface environmental simulation is schematically shown on Figure 4, on which the representative ranges of chamber environmental parameters are also indicated. The solar, planetary, and atmospheric ("sky") radiation components on Mars are reproduced in the facility by a 16-ft. dia. off-axis solar simulator, temperature-controlled ground thermal simulator, and a temperature-controlled shroud, respectively. The ground plane and the test article are mounted on a two-axis gimbal to provide rotation with respect to the solar vector for zenith and azimuth angle simulation (one-axis rotation only was used during the TETM tests). The chamber was "pressurized" with CO₂ to 2 torr during hot-extreme simulation, and with Argon to 35 torr during the cold-extreme tests. Argon was selected in lieu of CO₂ during the cold tests in order to prevent condensation on the cold shroud.

The conditions for the various test runs are summarized in Table 1. The objective of the cold soak runs was to provide steady-state heat transfer data for the purpose of verifying the conductor network in the thermal-analytical models and to evaluate thermal switch performance. They were preceded by a "calibration run" conducted in vacuum with the purpose of verifying the external radiation conductor networks at various simulated zenith angles. Martian diurnal cycle simulation was accomplished during Runs 227, 223 and the second half of Run 231, and these will be the subject of further discussion. Unfortunately, Run 223 was not entirely successful because of partial overheating of the ground simulator, however, the data presented here pertain to areas of the lander not reflecting this anomaly.

Because of the dissimilarities inherent in the finite size of the thermal-vacuum chamber as opposed to the "open" environment on Mars, the following corrective or compensating features have been incorporated into the test approach:

- (1) Compensation for finite ground simulator size by increased ground simulator temperatures,

- (2) Substitution of IR radiation from the ground simulator for albedo on Mars, resulting in additional (although small) increase in required ground simulator temperatures,
- (3) The simulation of dust cover on the lander surfaces, which could result in up to 70 percent increase in their solar absorptivity (with emissivity unchanged) by a 70 percent increase in solar constant in the simulated environment (Run 223).
- (4) Compensation for excessive convective cooling during the hot extreme simulation tests by increased radiation levels in the chamber (as noted above). The higher convective levels are due in part to the higher gravitational constant on Earth, and in part to the colder sink temperatures provided by the shroud (which simulates "sky" temperatures) as compared to the atmospheric temperatures on Mars.
- (5) Compensation for the absence of winds in the chamber during cold extreme simulation by the following:
 - (a) Increased chamber pressure to 35 torr, as opposed to 15.2 torr max. on Mars to enhance natural convection.
 - (b) Reduced chamber heat sink (shroud) temperatures 50 to 100 degrees F below the corresponding levels of $T_{oo,min}$, in order to enhance natural convective and radiation cooling.
 - (c) Reduced thermal output from the RTG simulators to account for the decrease in the availability of RTG waste heat for thermal control during cold extreme conditions.
 - (d) Reduced radiation levels in the chamber.

The ground simulator is a 22-ft diameter disc, covered with 19 individually controlled heater blankets, comprising a central disc, and two concentric rings surrounding the disc. Item (1) above was accomplished by increasing the emissive power of the outer ring by approximately 20 percent above Martian levels.

Items (2) and (3) resulted in increased temperatures of the inner ring as well, however, no further increase in the radiation levels was necessary to account for Item (4).

The upper limit in chamber pressure during the cold extreme simulation was set at 35 torr (Item 5a) to avoid undesirable internal convection within the equipment compartment of the lander. To prevent condensation of the chamber atmosphere on the shroud in view of Item 5b, argon was used as a chamber atmosphere in lieu of CO_2 during these tests. This provided additional conservatism to the test results, since the conductivity of argon (and hence, of the fiberglass insulation in the lander) was somewhat higher than that of CO_2 .

Item 5c was in conformance with the results of the RTG Wind Tunnel Tests referred to earlier. The reduced output was controlled to predetermined RTG fin root temperatures as determined by these tests. Item 5d consisted (in addition to the effects of

the reduced shroud temperatures) in running the cold extreme tests with the solar simulator off, and a thermally passive ground simulator, in a horizontal position.

TEST ARTICLE AND SUPPORT EQUIPMENT

The test article and support equipment comprised several major elements, including: the TETM; Electrical Test Support Equipment (TSE); Space Simulation Laboratory (SSL); Test Fixtures; Data Processing Software; Data Reduction Support, and Assembly, Handling and Support Equipment. The TETM and its subsystems, the TSE, and the Data Processing Software, will be described briefly.

The Thermal Effects Test Model was designed to duplicate the thermal response of the Viking Lander when exposed to the simulated mission environments. It comprised six principal subsystems, including: Thermal Control, Structures, Non-functional Flight Type Equipment, Electrical Subsystem, Thermal Simulators, and an Instrumentation Subsystem. The Thermal Control Subsystem consisted of developmental hardware including multilayer and fiberglass insulation, erosion-resistant external coatings, internal thermal control coatings and finishes, thermal standoffs, and thermal switches. Special attention was given to minimizing test-peculiar thermal effects, such as by isolation of electrical and instrumentation cable feedthroughs.

The Structural Subsystem consisted of flight-type structures, including lander body, equipment mounting plate, and brackets. The non-functional flight-type equipment included cable harness (for heat-leak evaluation), developmental propulsion lines and valves assembly, and mounting brackets. There was no propellant fluid flow or storage requirements associated with the TETM program. Additionally, there was included a prototype unit of the soil sampler boom, and developmental landing legs.

The electrical subsystem comprised the heaters, cabling, and connectors for the thermal simulators of heat-dissipating equipment, including two Electrical Thermoelectric Generators (ETG's), which simulated the RTG's. Power control and monitoring of all electrical heaters within the TETM was accomplished by the TSE.

The function of the thermal simulators was to simulate the primary thermal characteristics of selected flight-type equipment, including: (a) the mounting thermal interfaces, by the use of flight-type mounting provisions; (b) the radiation/convection thermal interfaces, by preservation in the simulators of the geometry, size, and external optical properties of the flight equipment; (c) conduction coupling between the radiation and mounting interfaces, by preservation of the wall-conductances of equipment casings; (d) internal conduction paths; (e) total thermal mass; (f) total internal heat dissipation rate, with capabilities to approximate variable heat dissipation by step functions; (g) internal heat distribution (by the use of more than one heater element, when required), and (h) internal thermal mass distribution. The materials of construction for the simulators included

aluminum, steel, foam, and commercially available heater elements.

The TETM instrumentation consisted of temperature sensors, heat flow gauges, and strain gauges, the latter being included to comply with a secondary objective of the program to evaluate thermal strains within the structures. The vehicle-mounted thermal instrumentation comprised 648 measurements; 188 additional channels were used for monitoring electrical power to the TSE, ground simulator and shroud temperatures, solar intensities, and chamber pressures.

Typical simulator assemblies within the equipment compartment are shown on Figure 5, and the TETM during two consecutive stages of assembly is depicted on Figures 6 and 7, respectively. On Figure 7 the ETG's and the terminal propulsion tank simulators are exposed, the wind shields and the tank insulation being removed.

The function of the Electrical Test Support Equipment (TSE) was to supply, measure, and control electrical power to the thermal simulators and the ETG's. The power levels and distribution within the simulators were controlled by step functions representative of smoothed power profiles of the flight article. The power control was accomplished by the use of a pre-programmed drum switch, the switching from position to position being done manually according to a predetermined schedule.

The TETM Data Reduction Software was designed to provide quasi-real time data reduction and analysis.

The latter included calculations of heat balance, convective parameters, data averaging, data plotting, and predictions of times to stabilization.

TEST OPERATIONS

Preparatory to starting of the tests, a solar simulator calibration was performed, the chamber insulation was installed and several pumpdowns were performed in order to outgass and settle the insulation. The two-axis gimbal and the ground simulator, with the "closure panels" removed for access were installed in the chamber. An end-to-end power and instrumentation checkout was performed on the TETM outside the chamber.

Following the preparatory work, the TETM was installed into the chamber, and secured on the test adapter serving as the structural interface between the lander legs and the gimbal, and the gimbal and the ground simulator. Following the hookup of instrumentation and power cabling, the ground simulator closure panels were installed. This sequence of events is depicted on Figures 8, 9 and 10. The styro-foam insulation between the outer shell and the shroud of the chamber is shown on the lower part of Figure 8. The TETM is shown in the fully-assembled landed configuration, with the ETG's covered by wind shields, and the terminal propulsion tanks (partially covered by the wind shields) insulated.

The TETM was installed with the "science side" (the side closest to the technician on Figure 9) facing the simulated west on Mars, in order to provide worst-case orientation for the hot extreme tests.

Supplementing the quasi-real time monitoring provided by the TETM software, 100 pre-selected data channels were also monitored by the use of a real time data monitoring system which provided data printouts on command, and within five minutes of the actual data bursts.

Solar simulator on-off cycles, gimbil rotation, shroud temperature and ground simulator temperatures were controlled manually and were monitored with the RTM system.

The data were recorded on magnetic tapes by the "Astrodata" System, and the tapes removed on an average of 6-hour intervals for processing by the TETM software. Strict time-discipline was maintained in the data taking process, in order to provide accurate (Martian) day-to-day comparisons of temperatures for stability estimates. The same time-discipline was maintained with regard to all test support operations.

To assure the necessary flexibility for optimizing the simulation technique, in-test parameter modifications were permitted, and the test procedures redlined accordingly.

DISCUSSION OF TEST RESULTS

Typical temperature and heat flux profiles for test runs 227 and 231 are depicted on Figures 11 and 12, respectively. The curves indicate excellent repeatability of test conditions from one simulated Martian day to the other, and that periodic stability was essentially achieved within three Martian diurnal cycles. The heat flux profiles of Figures 11 and 12, represent traces from the same gauge, mounted on the side of the lander. The small fluctuations of heat flow within a Martian diurnal cycle are due to variations in the internal heat dissipation, and to shadowing effects from external components. The negative sign on the ordinate of these figures is in accordance with the convention assigning negative values to outgoing heat from the lander. A comparison of Figures 11 and 12 indicates that approximately twice as much heat was lost to the environment during the cold extreme tests, as compared to the hot extremes, the difference being supplied by the thermal switches from RTG waste heat.

Figures 13 through 17 are indicative of the quality of simulation achieved during the TETM tests. The vehicle skin temperatures closely approached (Martian) radiation equilibrium values during the hot extreme tests, with the temperature depression parameter ΔT_R always smaller than the specified limit of 10°F . It is also evident from the plots that the inequalities (4 and 5) were satisfied.

In order to determine the adequacy of radiation simulation during the hot extreme tests, $q_{\text{abs,CH}}$, averaged over the lander

sides, is compared with its corresponding Martian counter-part determined analytically, on Figure 13. The higher values of the chamber loads, especially during the simulated Martian mid-day, served as "compensation" for excessive convective cooling in the chamber, and did not cause overheating, as evidenced by the temperature profiles applicable to the same locations on Figure 14.

Figure 15 indicates that inclusion of the lander top into the averaging of surface temperatures results in an increase of T_R and in operation within the convective cooling regime. This is due to increased solar absorption on the lander top, as compared to the sides, and to external heating from the RTG's. A similar effect is noted on Figure 16, which applies to the "dust covered lander", i.e. 170 percent solar constant. In this case the approach of $T_{s,CH}$ to $T_{R,M}$ is near-perfect.

Figure 17 shows typical temperature profiles during the cold-extreme simulation. Note that, on the average, the vehicle temperatures are considerably above Martian atmospheric temperatures, as implied by Equation (7e). The following values for h^* have been determined by the use of Equation (7e) from the test data as averaged over the Martian diurnal cycle.

Lander sides, average: $h^* = 1.57$
Lander top, average: $h^* = 1.27$
Lander bottom, average: $h^* = 0.89$

The somewhat lower than "required" h^* for the lander bottom is more than compensated for by the higher values on the sides and the top. It is further noted, that during the actual mission, atmospheric boundary layer effects will result in a decrease in wind speed and heat transfer coefficient near the ground.

CONCLUSIONS

1. The Viking lander thermal environments may be bracketed by a radiation-dominated hot extreme and a convection-dominated cold extreme. Both can be adequately simulated in modified conventional thermal vacuum facilities.
2. The hot extreme is completely defined by the radiation environment at the landing site and the heat dissipation requirements through the external surfaces of the lander. These may be resolved into a set of Radiation Equilibrium Temperature profiles, approached by the lander surfaces during "hot" operating conditions.
3. Due to its non-isotropic character, the Martian radiation environment must be accurately simulated during hot-extreme thermal testing.

4. The principal criterion for success for hot extreme simulation is the approach to radiation-equilibrium.
5. The effects of vehicle-induced convection inside the chamber during hot case simulation may be adequately compensated for by increased radiation levels.
6. The cold extreme is completely defined by the minimum atmospheric temperature profile at the landing site and an upper limit for the forced-convective coefficient, as applied to the lander.
7. The criterion of success for cold extreme simulation is that h^* determined from heat losses in the chamber and the projected vehicle-environment temperature differences on Mars, shall equal or exceed the maximum forced convection coefficient on Mars.
8. Verification of the simulation approach during a test may be accomplished independently from the performance of the test article, provided the heat transferred through the vehicle skin is measured directly at predetermined locations. The correlation and consistency of the TETM data indicate that a limited number of judiciously located gauges suffice for this purpose.
9. The TETM Mars Simulation test program has demonstrated the feasibility and practicality of the test approach to be used on the qualification and flight articles.

REFERENCES

1. Buna, T., "Thermal Testing under Simulated Martian Environment", Progress in Astronautics and Aeronautics, Vol. 21, pp. 391-417, Academic Press, 1969.
2. VER-28, "Mars Surface Thermal Simulation", Martin Marietta Corporation, Denver Division, 27 January 1970.
3. Buna, T., and Ratliff, J.R., "Operation of a Large Thermal Vacuum Chamber at Martian Pressure Levels", National Bureau of Standards Special Publication 336, pp 725-748, October 1970.
4. Buna, T., "Convective Heat Transfer in Simulated Martian Environments", Final Report, TOS T70-48888-001, Martin Marietta Corporation, Denver, Division, 1970.
5. Morey, T. F., and Tracey, T. R., "Mars Surface Thermal Environments for Viking Lander Design and Test", (In this volume).

TABLE 1 - TETM MARS SURFACE SIMULATION TEST PARAMETERS

TEST	COLD SOAK		HOT EXTREME		COLD EXTREME	
	201	202	223	227	231	
DESCRIPTION	ZERO POWER	MIN. POWER	"DUST" COVERED LANDER	NO DUST COVER	STEADY STATE ENV.	CYCLING ENV.
SOLAR BEAM, BTU/HR-FT ²	0		(170%) 346	(100%) 204	0	
ZENITH ANGLE	NA		CYCLING		NA	
GROUND SIM. TEMPERATURE	PASSIVE		CONTROLLED TEMP. CYCLING		PASSIVE	
CHAMBER PRESS. & ATMOSPHERE	17.5 mbs CO2		2.7 mbs CO2		47 mbs ARGON	
SHROUD TEMP.	CONSTANT @ -180 F		CONSTANT @ -200 F		-240 F	CYCLING -240/-160F
ETG THERMAL OUTPUT	2 x 600 w		2 x 640 w		2 x 600 w	
INTERNAL POWER	0	MIN. AVG.	MAXIMUM DAILY DUTY CYCLE		MINIMUM DAILY DUTY CYCLE	

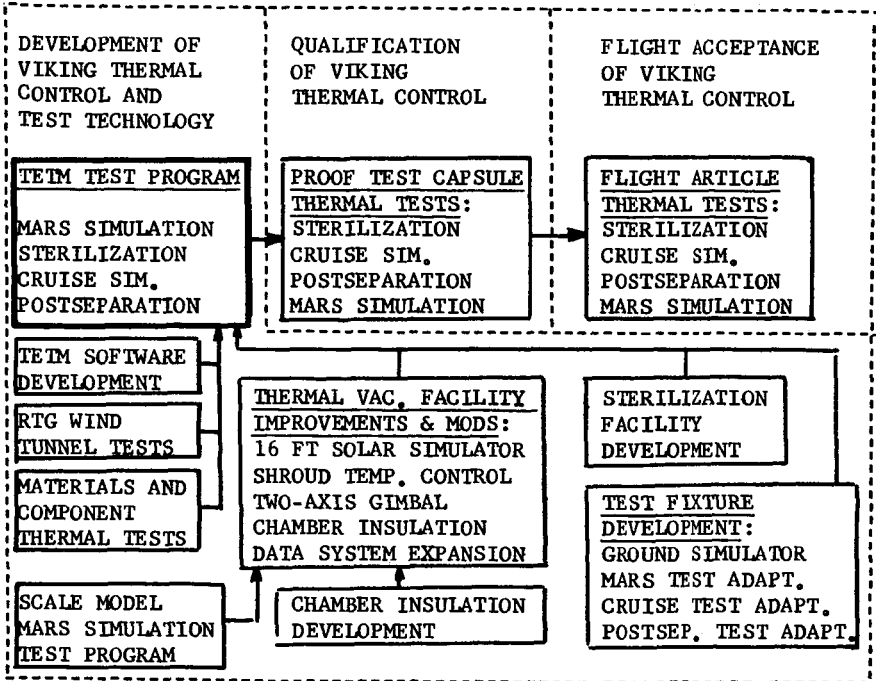


Fig. 1 - Relation of TETM other Viking thermal test programs

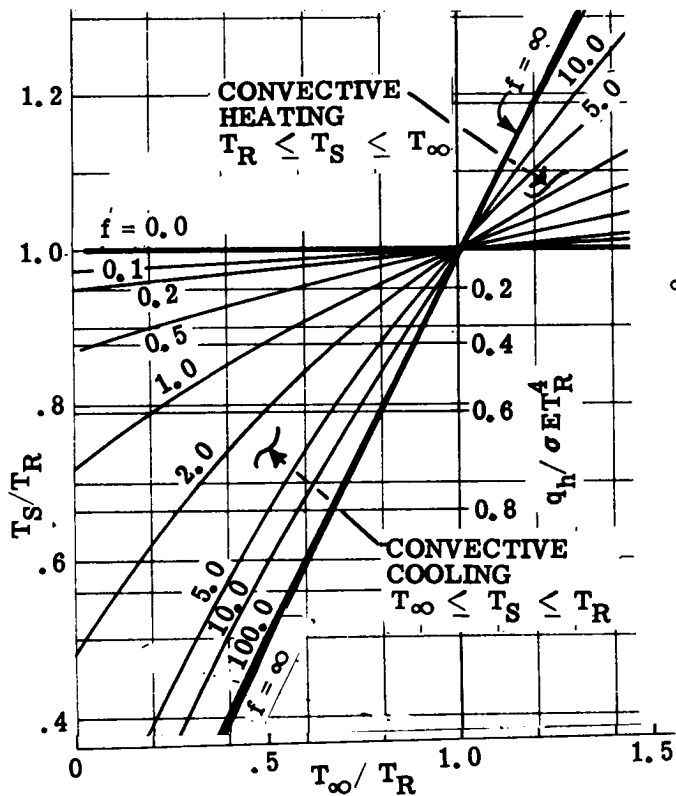


Fig. 2 - Definition of thermal regimes

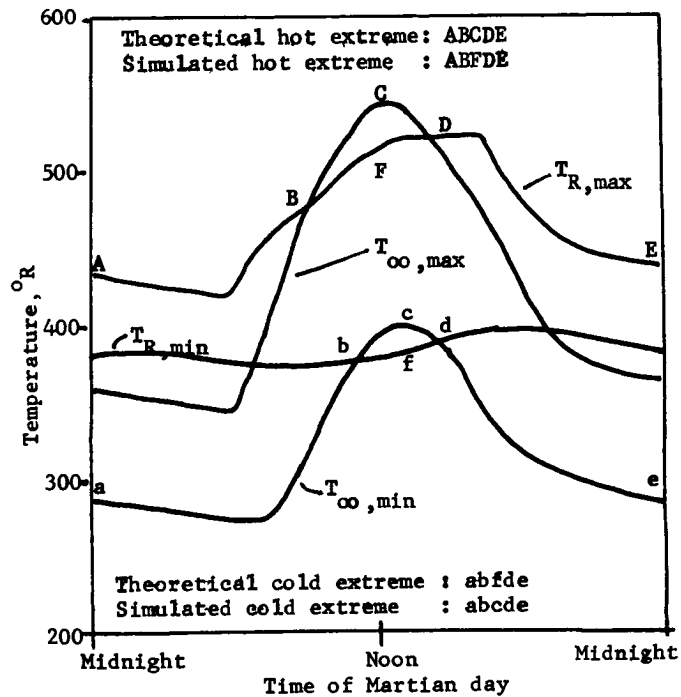


Fig. 3 - Definition of simulated thermal extremes

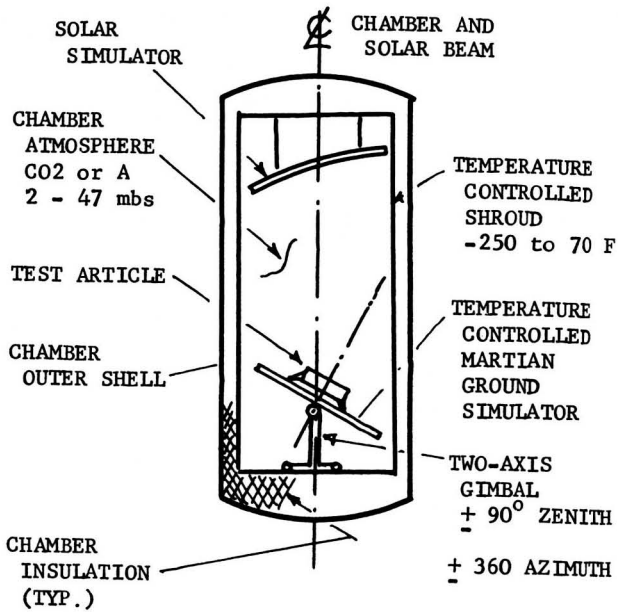


Fig. 4 - Test configuration schematic

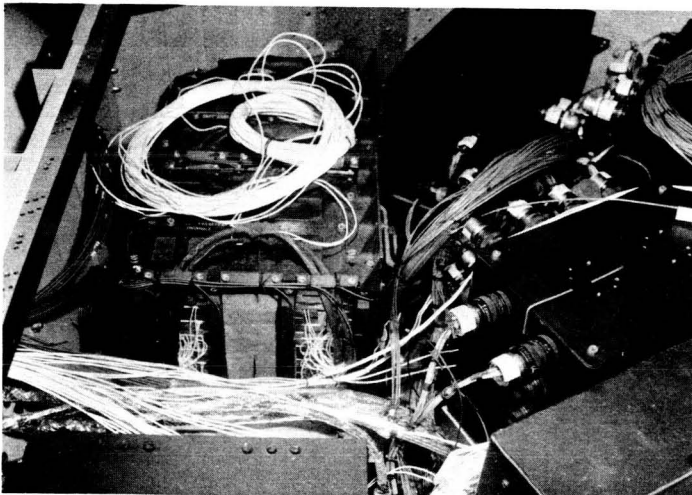


Fig. 5 - TETM thermal simulators during assembly

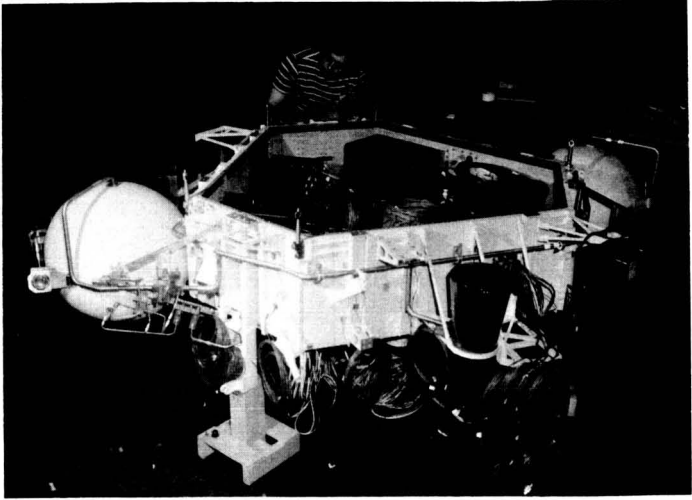


Fig. 6 - TETM during assembly - Internal equipment

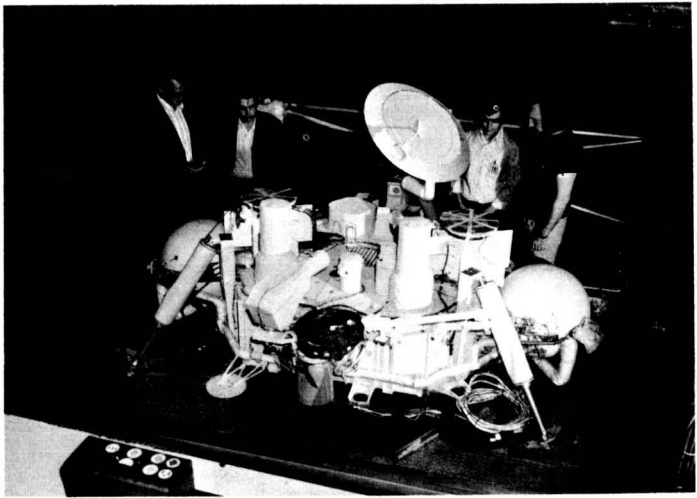


Fig. 7 - TETM during assembly - External equipment

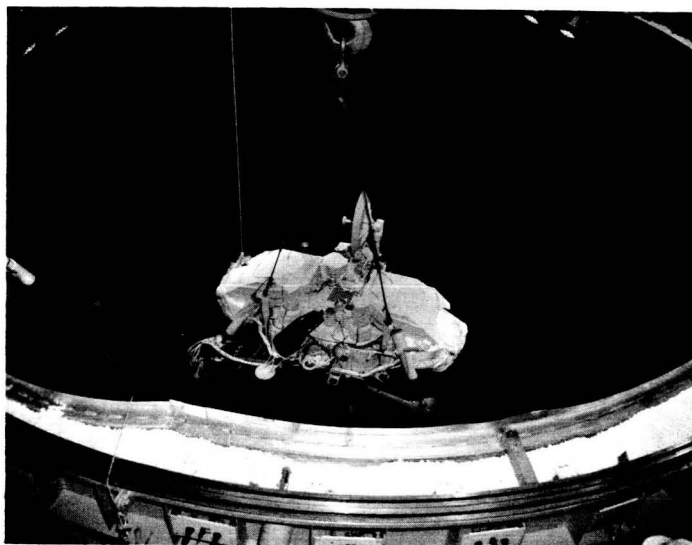


Fig. 8 - TEIM being lowered into the chamber

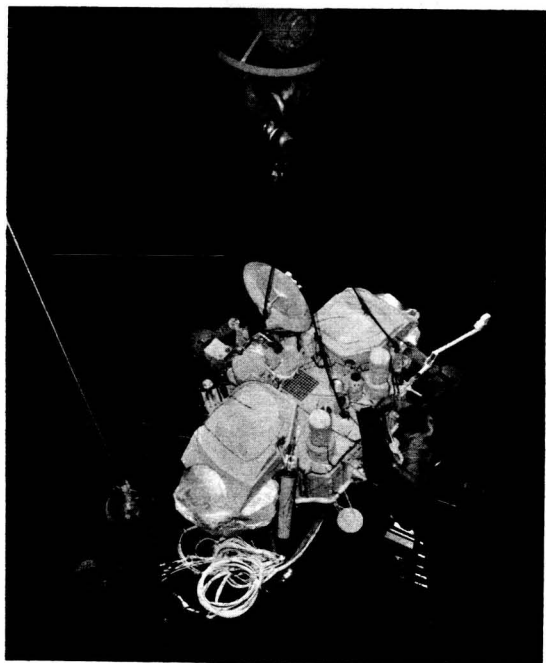


Fig. 9 - Installation and hookup inside the chamber

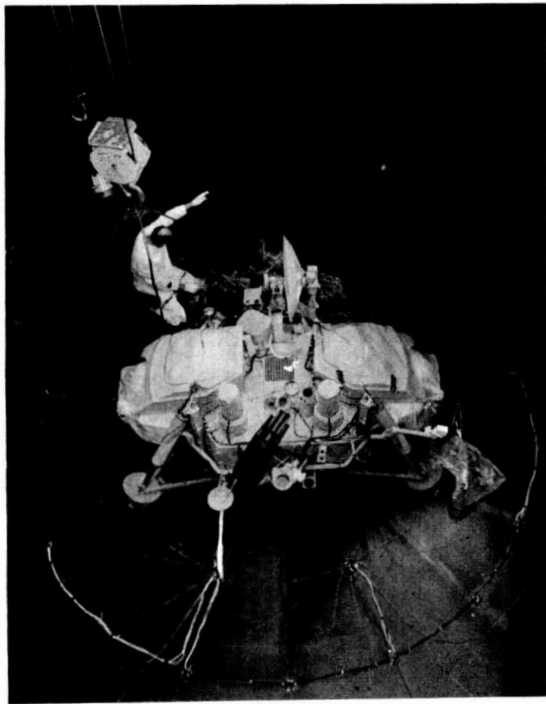


Fig. 10 - Installation complete

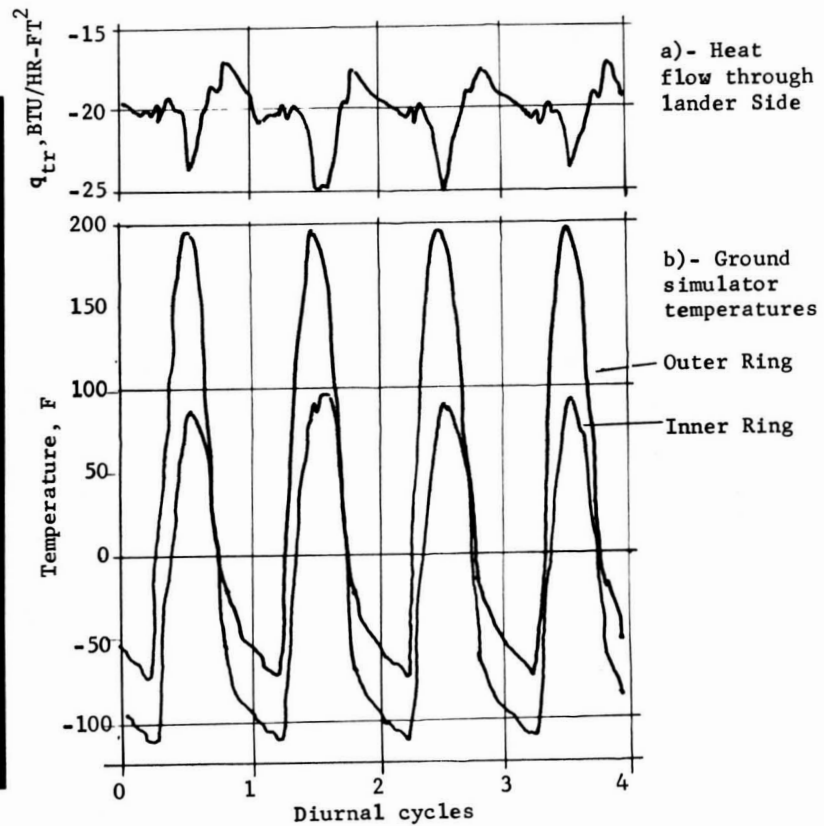


Fig. 11 - Typical data profiles - RUN NO 227

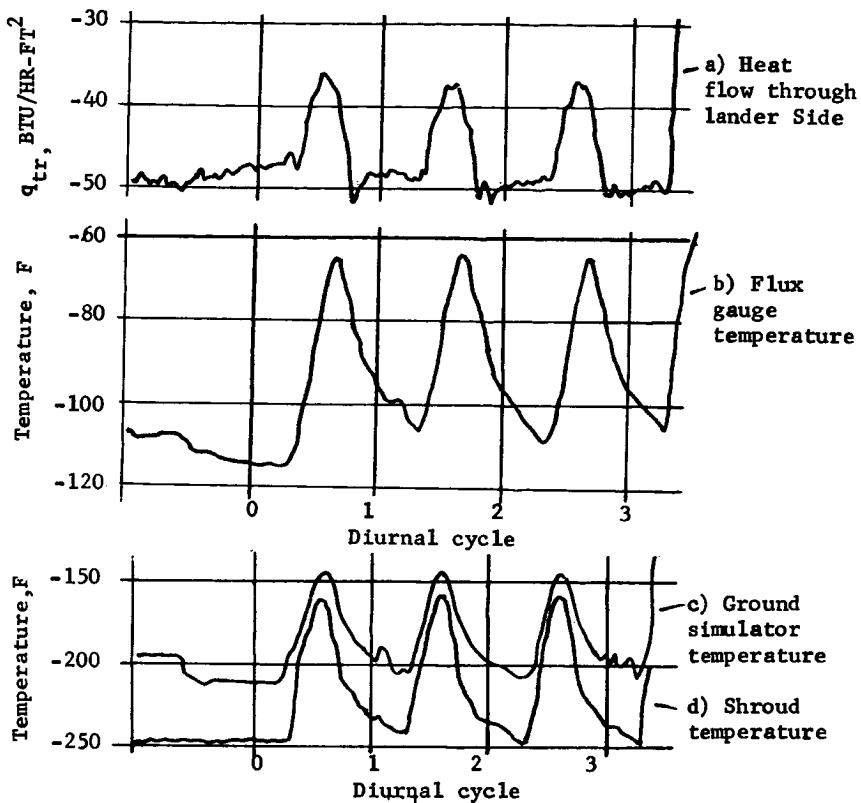


Fig. 12 - Typical data profiles - RUN NO 231

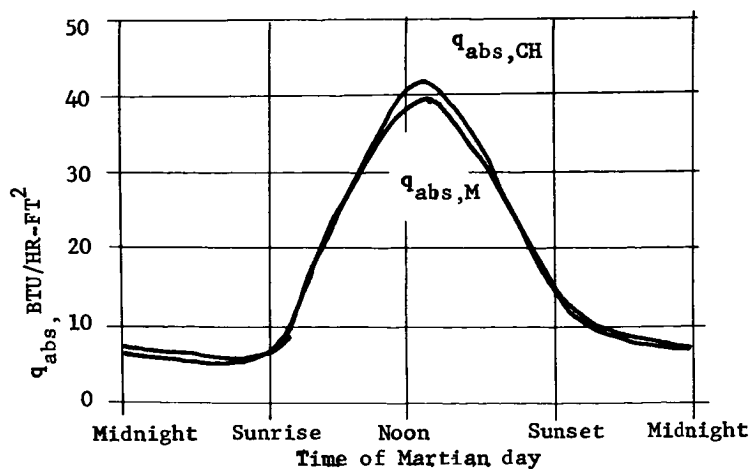


Fig. 13 - Martian vs. simulated absorbed radiation

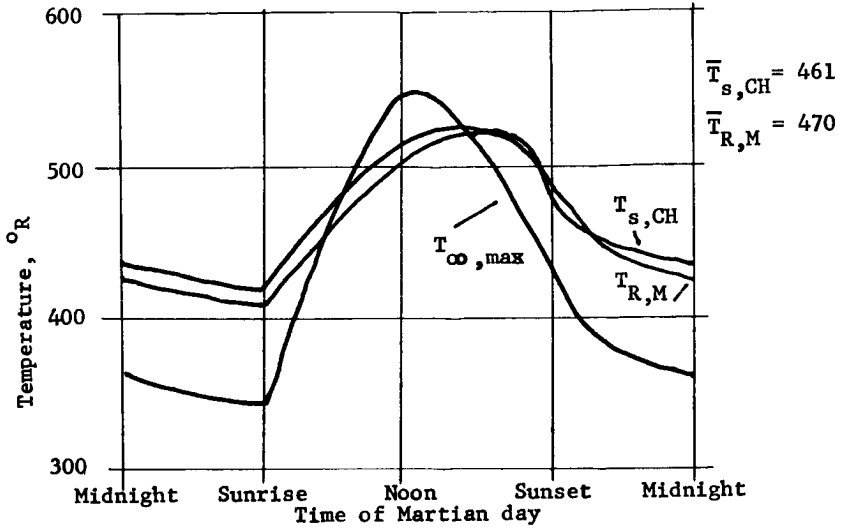


Fig. 14 - Simulated vs Martian hot extreme - Lander side - RUN NO 227

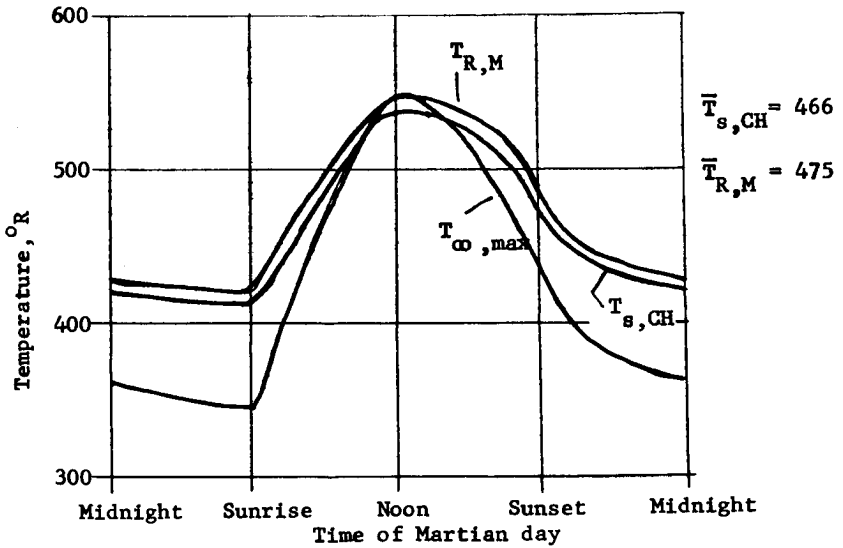


Fig. 15 - Simulated vs Martian hot extreme - Lander sides plus top - RUN NO 227

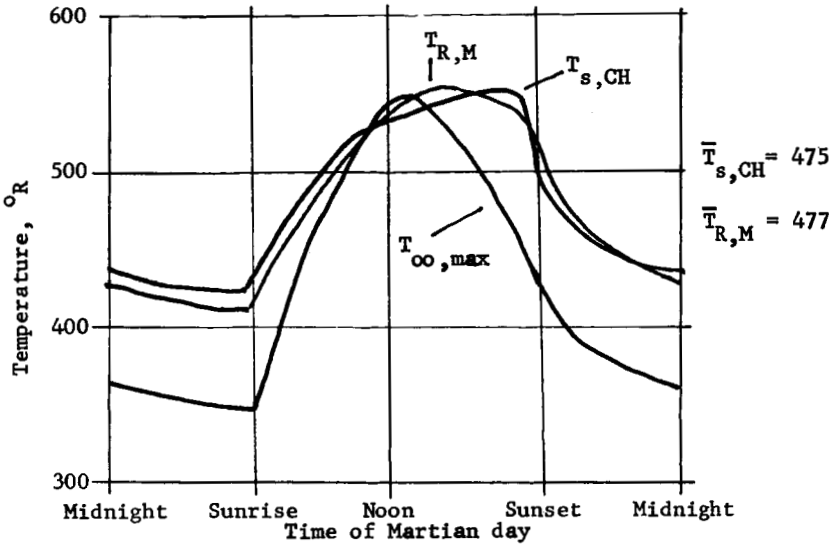


Fig. 16 - Simulated vs Martian hot extreme -
Lander sides - RUN NO 223

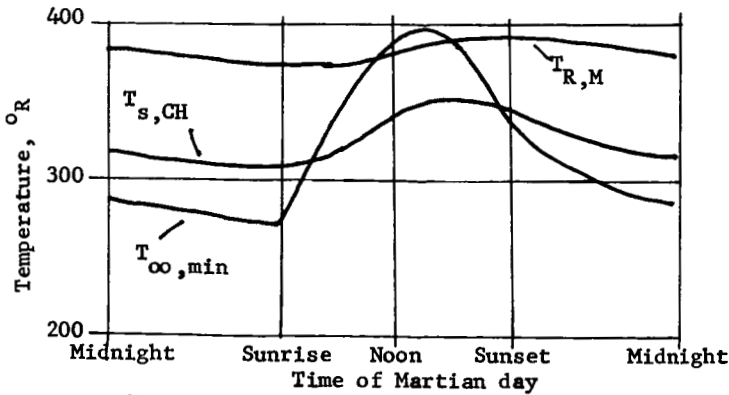


Fig. 17 - Simulated vs Martian cold extreme -
Lander sides - RUN NO 231

Paper No. 6

**THE "PRESSURE-VESSEL" SPACECRAFT; AN ASSESSMENT
OF ITS IMPACT ON SPACECRAFT DEVELOPMENT AND TEST**

W. G. Stroud, *NASA/GSFC* and D. W. Keller, *General Electric Co.*

ABSTRACT

The space shuttle promises significant reduction in the costs of space flight through in-flight serviceability, spacecraft recovery and possibly by reduced constraints on weight and volume of spacecraft. The high technology, sophistication and high costs per unit weight characterizing the US program have not characterized the USSR program because of their greater launch weight capabilities. Also, the USSR spacecraft are invariably one or more pressure vessels so that in all requirements for miniaturization, vacuum operations and test, vacuum thermal control, and materials control can be circumvented. The pressure vessel approach avoids some of the costly elements of the US program.

PRECEDING PAGE BLANK NOT FILMED

Paper No. 7

THE RADIOMETRIC CALIBRATION & PERFORMANCE
EVALUATION OF THE ASET FACILITY

J. D. Shoore, A. B. Dauger, R. P. Day and R. H. Meier,
*McDonnell Douglas Astronautics Company,
Huntington Beach, California*

ABSTRACT

The Advanced Sensor Evaluation and Test (ASET) Facility, which simulates physical and optical exoatmospheric environmental conditions, provides the capability for radiometric calibration of infrared sensors and astronomical telescopes. The techniques and procedures developed and used to calibrate the facility are discussed.

INTRODUCTION

The Advanced Sensor Evaluation and Test (ASET) Facility, Figure 1, was developed by the McDonnell Douglas Astronautics Company (MDAC), Huntington Beach, California, as part of the Space Simulation Laboratory. The facility offers the capability to measure selected performance parameters, providing a radiometric calibration for a variety of infrared sensors in a simulated space environment.

This calibration ensures known and accepted values for the collimator beam irradiance which is the irradiance at the entrance aperture of systems under test.

Any optical measurement system intended for operation in an exoatmospheric environment must receive a meaningful preflight calibration, which provides the basis both for an evaluation to verify the predicted performance capability of the optical system, and for the actual flight test data reduction and analysis.

Reliable techniques and procedures have been established to ensure a controlled measurement process which, under statistical analysis, provides the degree of precision and accuracy with which optical systems can be calibrated within the facility.

Because there are presently no national standards for the unique ASET Facility's operational environment, it is impossible to obtain an absolute measure of the irradiance. However, based upon experiments and calculations, values and limits have been established by MDAC. The precision of measurement is extremely good. When an absolute standard becomes available, the accuracy values presently given can be converted.

ASET FACILITY

The ASET Facility, whose schematic diagram is shown in Figure 2, consists of a stainless steel vacuum chamber with an inner cryoshroud housing an on-axis parabolic collimator, a radiant energy source assembly, a calibration monitor that subtends one portion of the collimated beam, and a pair of scanning mirrors that direct the radiant energy from another portion of the collimated beam into a sensor under test. All the optical elements consist of Kanigen coated aluminum, and their active surfaces are gold coated. Vacuum levels of 10^{-8} torr or better can be achieved with a multistage, contamination-free pumping system. A dense gas helium closed-cycle cooling system cools the cryoshroud and all other interior structures, components, and optical elements to a temperature of approximately 20 Kelvin, thereby producing an extremely low radiation background. Tests have shown that once stabilization at the cold operational temperature has occurred, there is no measurable degradation of the performance of the collimator assembly due to cooling.

Also associated with the facility is a clean room that can maintain the sensor under test in a class-100 clean environment, which is defined as one having no more than 100 particles of 0.5- μ diameter or larger per cubic foot of clean room volume. A special air shower and cover are used to protect the aperture of the sensor from contamination when the sensor is attached to the chamber interface.

COLLIMATOR

The collimator assembly, shown in Figure 2, consists of a 0.81-m parabola having a focal length of 3.02-m, and two 0.81-m by 1.06-m plano-folding mirrors. Its performance was found to be diffraction-limited for wavelengths longer than 8- μ m. During development the spatial distribution of the collimated beam's flux density was assessed and the expected symmetry and uniformity were observed.

STANDARD SOURCE ASSEMBLY

The standard source assembly is shown in Figure 3. It consists of a blackbody-type source with a fixed frequency chopper and a set of stepped limiting apertures located in front of its cavity, with a second set of stepped variable apertures located at its exit aperture, and a special dual-surface reflector mounted inside the integrating cavity. The interior surface texture of the integrating cavity walls and one side of the dual-surface reflector was achieved by peening these surfaces with glass beads of size 20-30 screen mesh. The selected aperture located at the blackbody cavity is imaged, either into the integrating cavity or onto the selected exit aperture of the integrating cavity, with unity magnification via a toric mirror and four folding plano-reflectors and the dual-surfaced reflector located

inside the integrating cavity. The exit aperture of the integrating cavity is located at the back focus of the source projector, which projects a 2.36-times-reduced image into the focal plane of the parabolic collimator.

The source assembly can be operated in three different modes, depending on the angular position of the dual-surfaced reflector inside the cavity. The specular surface reflection mode is used to directly image the blackbody cavity aperture onto the integrating cavity exit aperture, when high irradiance levels are required. In the diffuse reflection mode, the dual-surfaced reflector is rotated 180 degrees so that its peened surface is in position to diffusely deflect the radiant energy onto the integrating cavity's aperture. The lowest irradiance levels are achieved by rotating the dual-surfaced reflector into a position where it does not intercept the beam entering the cavity and where the diffuse side is facing the cavity's exit aperture. In this test mode, called the integrating cavity mode of operation, the beam first strikes a convex diffuse reflecting surface of a button-type insert mounted in the wall of the integrating cavity. The diffuse button reflects the radiant flux toward the front half of the integrating cavity, from which it is again diffusely reflected toward the diffuse surface of the dual-surfaced reflector. This surface now provides a uniform Lambertian radiant background for the integrating cavity exit aperture, and fills the field of view of the source projector.

In the specular mode of operation, the 8-mm blackbody is used exclusively; only the exit apertures of the integrating cavity are varied. In the two other modes, combinations of the two sets of variable apertures can be used to control the beam irradiance. Furthermore, in the integrating cavity mode, an attenuator plate can be rotated into the exit beam from the blackbody to obscure any desired portion from reaching the integrating cavity. The final result is that for any given blackbody temperature this source assembly can provide a range of irradiance values in the collimated beam that spans more than nine orders of magnitude. This is achieved without filters or impractical aperture sizes. The effective attenuation factor between the specular mode and the diffuse mode for a selected set of apertures is approximately 15.4, while the effective attenuation factor between the diffuse mode and the integrating cavity mode is approximately 600.

CALIBRATION MONITOR

The calibration monitor is mounted with the collimator assembly. It consists of a Cassegrainian telescope, referred to as the tester telescope, and a bolometer-type detector assembly. The tester telescope has a primary mirror 0.204 m in diameter, an F-number of 3.5, and an effective collection area of 211.6 cm². The optical performance of the tester telescope was measured and found to be diffraction-limited for all wavelengths greater than 3.5 μ m. The tester telescope is mounted looking downward into the collimated beam of the ASET collimator, with its optical axis

parallel to the axis of the collimated beam. It intercepts a 0.2-m-diameter portion of the collimated beam adjacent to that portion of the beam which is used in testing systems. The bolometer assembly is mounted on a three-axis detector table, and its detector element is placed at the focal plane of the tester telescope.

BLACKBODY-TYPE SOURCE ASSEMBLY

The blackbody source assembly geometry is presented in Figure 4. The source assembly, which consists of the blackbody-type source, the baffling structure, stepped limiting apertures, and the fixed-frequency chopper, is mounted directly on the cooled three-axis source table. The dimensions of the source-limiting apertures vary in six discrete steps from 0.76 to 8.00 mm in diameter. The chopper is mounted on a shaft between the mounting plates and is driven through a nylon gear train by a fixed-frequency motor that mounts on the back side of the aperture plate in an enclosed radiation shield can. To ensure cooling of the apertures and the chopper blade, the blackbody is mounted on a separate mounting structure, with its heat sink achieved through a controlled heat leak directly to the actively cooled source table. The source table temperature is force-cooled to approximately 20-Kelvin. A 25-Kelvin maximum aperture temperature has been measured when the blackbody was operated at 300 Kelvin. The entire source assembly is covered, well baffled, and cooled to eliminate any unwanted energy.

The blackbody cavity is fabricated from ultra-pure aluminum (1100 series). At the time of the bolometer calibration the cavity was assumed to have a surface emissivity of 0.90, resulting in an effective calculated emissivity of 0.9977, determined according to the method of Gouffé. The cavity temperature at that time was monitored using a single copper: constantan thermocouple. Currently, the cavity temperature is monitored by three copper: constantan thermocouples embedded in its wall symmetrically around the apex of the cavity. The reference temperature used for the blackbody is liquid nitrogen.

At the time of the initial ASET Facility bolometer responsivity calibration, the blackbody radiant exitance (M) was determined by measurements of its temperature and calculation of its effective emissivity. The value used for the Stefan-Boltzmann constant was $5.6697 \times 10^{-12} \text{ W-cm}^{-2} \text{ K}^{-4}$, as per NAS-NRC Committee, 1963, NBS, U.S. Technical News Bulletin, No. 10, pp. 175-177.

BOLOMETER CALIBRATION

A high-quality gallium-doped germanium semiconductor bolometer supplied by Infrared Laboratories, Inc., was chosen as a working transfer standard. The philosophy for the ASET Facility calibration is based on the bolometer serving as the working standard, since the total irradiance in the collimated beam is established by bolometer measurements.

Normally, the blackbody and bolometer would be used together as a set of standards, one serving as a cross-check on the other, with the blackbody considered the primary working standard. However, it was decided to use the bolometer as the working transfer standard of total irradiance subsequent to its initial calibration with the blackbody. This decision was based on evidence that the bolometer performance characteristics are highly stable and repeatable over a long period of time, whereas the long-term repeatability of temperature settings of the blackbodies appears to be quite deficient.

The calibration of the bolometer consists of the determination of its blackbody responsivity; i.e., its responsivity with respect to the radiant energy emitted by a blackbody. The ASET blackbody was initially assumed to be the primary laboratory standard in the 100 to 400 Kelvin temperature region, providing standard values of irradiance (w/cm^2) over a range that satisfies the requirements for calibrating the bolometer.

The responsivity of the bolometer is determined from the output signal voltage ($V_{s,rms}$), with the bolometer viewing the blackbody cavity directly. The measured voltage is plotted as a function of the radiant power (ϕ_{BB}) incident upon it. The slope of the resulting calibration curve yields the blackbody responsivity of the bolometer, $R_{BB} = V_{s,rms}/\phi_{BB}$. Figure 5 presents a plot of the measured signal for a 25.5-Hz copper frequency as a function of the modulated radiant power incident on the bolometer. The bolometer responsivity was calculated at each point and was determined to be, $R_{BB} = 1.54 \pm 0.03 \times 10^5$ volts (rms)/watt (peak to peak). The resultant slope of the responsivity varied by ± 0.03 for a 1 σ value. The bolometer has an effective sensitive area of one millimeter diameter and is operated at 2.03 Kelvin by carefully maintaining the vapor pressure in its helium dewar to within $\pm 10^{-3}$ torr.

The rss uncertainty of the radiant power for each of the data points shown in Figure 6 is represented by error bars. Because of the assumed ± 5 -degree measurement uncertainty at all temperatures of the blackbody cavity, a larger uncertainty (longer bars) occurs for lower temperatures. A combination of different blackbody temperatures and various apertures and separation distances was used to obtain the range of radiant power, which accounts for the different-length error bars that occur along the graph.

The single-value bolometer responsivity calibration was accomplished for blackbody temperatures of 100, 200, and 300 Kelvin. As a result, a temperature of approximately 300 Kelvin can be chosen for determining the resulting rss uncertainty in the bolometer responsivity. At the time of the bolometer responsivity calibration, the rss uncertainty was determined to be ± 8.9 percent.

For the various source apertures, Figure 6 can be used to estimate the conversions to the rms value of the radiant power as referenced to the fundamental component of a square wave. The unit of radiant power, watts, refers to the total watts (peak-to-

peak) value of the square-wave-type modulated beam. In general, it is sufficient to multiply the watts peak-to-peak value by 0.45 to convert to watts rms of the fundamental. To convert to the rms value of the bolometer blackbody responsivity, the bolometer responsivity is multiplied by 2.22.

Recent noise measurements were made on the bolometer using the configuration shown in Figure 7. At a bolometer temperature of 2.03 Kelvin, a bias current of 0.5 microamperes (μA), and a QuanTech 304 TDL wave-analyzer noise equivalent bandwidth of 1 Hz, the mean bolometer noise was found to be $46 \text{ nV}/\sqrt{\text{Hz}}$ at 25.5 Hz.

Although the bolometer calibration was carried out at a single chopping frequency, 25.5 Hz, the measured frequency response of the bolometer is included in Figure 8. A typical noise spectrum is presented in Figure 9. This noise spectrum was recorded using a QuanTech 304 TDL spectrum analyzer operating with a 1-Hz bandwidth and a 25-db half-band response.

BEAM IRRADIANCE CALIBRATION THEORY

The bolometer is used as a working transfer standard during the irradiance calibration of the collimated beam. The blackbody responsivity of the bolometer is given by

$$R_{\text{BB}} = \frac{V_{\text{SBN}}}{\phi_{\text{BB}} G_{\text{C}}} \left[\frac{\text{volts (rms)}}{\text{watts (p-p)}} \right] \quad (1)$$

where

- V_{SBN} = the signal resulting from source and background irradiance and noise, referenced at the bolometer, in volts (rms)
- G_{C} = electrical gain during responsivity calibration
- ϕ_{BB} = the radiant power, total watts peak-to-peak value of a square wave, and is given by

$$\phi_{\text{BB}} = \frac{\epsilon_{\text{eff}} \sigma T_{\text{BB}}^4 A_{\text{S}} A_{\text{D}}}{\pi S^2} \text{ [watts (p-p)]} \quad (1A)$$

where

- ϵ_{eff} = effective calculated emissivity of the blackbody cavity, per A. Gouffe, 0.9977
- σ = Stefan-Boltzmann constant, $5.6697 \times 10^{-12} \text{ W cm}^{-2} \text{ K}^{-4}$
- T_{BB} = blackbody cavity measured temperature in degrees Kelvin
- A_{S} = area of source (i.e., area of blackbody variable aperture) in cm^2
- A_{D} = area of bolometer, $7.85 \times 10^{-3} \text{ cm}^2$
- S = separation distance between source and bolometer during the bolometer calibration, cm

The calculated value of the bolometer responsivity, R_{BB} , when operated at 2.03 Kelvin and at a bias current of 0.5 μ A, as given previously, is 1.54×10^5 volts (rms)/watts (p-p).

The radiant power incident on the bolometer when mounted at the focal plane of the tester telescope is given by

$$\phi_{BB} = \frac{V_{SBN}}{R_{BB}} [\text{watts (p-p)}] \quad (2)$$

The total voltage out of the bolometer is a function of more than one variable, and is given by

$$V_{SBN} = \left[(V_S + V_B)^2 + V_N^2 \right]^{1/2} [\text{volts (rms)}] \quad (3)$$

where

V_S = the signal out of the bolometer due to the modulated source in volts (rms)

V_B = the background radiation-contributed noise in volts (rms)

V_N = the bolometer noise in volts (rms)

Therefore, the total irradiance at the entrance aperture of the tester telescope is the same as the total irradiance in the collimator beam, and is given by

$$E_{SB} = \frac{\left(V_{SBN}^2 - V_N^2 \right)^{1/2}}{G_E A_{TT} R_{BB}} \left[\frac{\text{watts (p-p)}}{\text{cm}^2} \right] \quad (4)$$

where

E_{SB} = the total irradiance from the modulated source and the DC background, in watts (p-p)/ cm^2

V_{SBN} and V_N = same as before

G_E = the electrical gain during the irradiance calibration

A_{TT} = the effective area of the entrance aperture of the tester telescope, 211.6 cm^2

R_{BB} = the responsivity of the bolometer, 1.54×10^5 v (rms)/w (p-p), with a ± 8.9 percent rss uncertainty

RESULTS

The total source irradiance, E_{SB} , in the ASET collimator beam is presented for each calibration temperature as a function of the normalized effective aperture diameters and for each mode as defined by the position of the beam deviating mirror mounted within the integrating cavity. The normalized effective aperture

diameters (NEAD) is defined as

$$NEAD = \left[\left(\frac{\text{source aperture diameter}}{8.00} \right) \left(\frac{\text{IC aperture diameter}}{5.88} \right) \right]^2 \quad (5)$$

where each aperture is normalized to the largest aperture in its set.

The average blackbody temperatures at which the beam irradiance calibration was performed were 400.2, 300.1, and 200.6 Kelvin. As explained previously, the three modes defined by the position of the beam-deviating mirror are specular, diffuse, and integrating cavity. The numbers associated with each measured point represent the aperture combination identification. Those points which are solid indicators without the associated rss error bar could not be measured with the bolometer, i.e., $E_{SB} \leq NEI$ (noise equivalent irradiance) of the bolometer. They are included, however, since the area relationships are maintained between apertures, and hence the associated irradiance value can be extrapolated.

The results are presented in Figures 10, 11, and 12. Also, Figure 13 presents the normalized effective diameter code that defines the aperture combinations used to achieve the irradiance levels for the various modes of operation. The measured data points are presented with the rss error bar limits resulting from the geometric and bolometer responsivity uncertainties. Data analysis indicates that the bolometer responsivity appears to be independent of the blackbody temperature. Therefore, the temperature error of the blackbody during the irradiance calibrations is not of prime importance in the error budget for the beam irradiance. As a result, the rss uncertainty in the responsivity of the bolometer calibration is increased only by the additional measurement errors encountered in determining the total beam irradiance. Thus, the rss uncertainty in the total beam irradiance is given as ± 9.22 percent.

A comparison between the graphs generated for the three different blackbody temperatures shows excellent agreement with the Stephan-Boltzmann law, which may be verified by comparing the ratio of the total irradiances to the ratio of the temperatures raised to the fourth power. For the beam-deviating mirror in the diffuse mode, the ratios are performed and presented. As may be seen, the comparison of measured versus ratio differences are less than 1 percent.

$$\left(\frac{400.2}{300.1} \right)^4 = 3.16; \quad \frac{E_{BB} 400.2}{E_{SB} 300.1} = 3.14; \quad \text{percent difference} = 0.63$$

$$\left(\frac{300.1}{200.6} \right)^4 = 5.01; \quad \frac{E_{SB} 300.1}{E_{SB} 200.6} = 5.00; \quad \text{percent difference} = 0.20$$

$$\left(\frac{400.2}{200.6} \right)^4 = 15.84; \quad \frac{E_{SB} 400.2}{E_{SB} 200.6} = 15.70; \quad \text{percent difference} = 0.88$$

Additionally, checks were made to determine the variation between the irradiance levels as established by the beam-deviating mirror positions. The variations were found to remain constant as a function of the temperature and geometric changes. This tends to indicate a lack of dependence upon the wavelength as a function of temperature and variable geometries.

A regression analysis utilizing a two-variable power regression of the form

$$y = A_0 x^{A_1} \quad (6)$$

has been performed to allow for rapid calculation of irradiance levels for sensor calibrations. The relationship is linear on a log-log plot, and the slope of the line is very close to unity. As such, the data are described extremely well. All the measured data were entered to determine the coefficients of the power curve. Once the coefficients were determined, the best-fit line for the data was plotted. As can be seen in Figures 10 through 12, the best-fit calculated curve describes the measured data. The correlation coefficient approaches unity for each case, providing an estimate of the overall precision of the measurements.

REPEATABILITY OF DATA

During the pumpdowns after the calibration run, comparison data were taken with the bolometer to see if there were any variations that could be attributed to test buildup or lapsed time between measurements. Presented in Table 1 is a comparison of the raw voltage data taken on 17 May 1972, during the original calibration, and verification data taken on 30 May and 10 October 1972. As shown, the worst-case percent difference for each beam-deviating mirror position is 3 percent for the low-energy integrating cavity mode measurements.

ERROR ANALYSIS

The total irradiance in the beam of the collimator has been examined in sufficient detail to provide for an rss error uncertainty determination. An estimate of the accuracy of the beam irradiance can be obtained by determining the absolute fractional error in E_{SB} , Equation (4), which is given by the summation of the differential dE_{SB} divided by the true value of E_{SB} . This can be written in equation form and is given by

$$\frac{dE_{SB}}{E_{SB}} = \frac{1}{E_{SB}} \sum_{X_1} \frac{\partial E_{SB}}{\partial S_1} dX_1, \quad (7)$$

where X_1 indicates the set of independent variables of Equation (4). Expanding Equation (4) as a function of all terms in the responsivity equation gives

$$E_{SB} = \frac{(V_{SBN}^2 - V_N^2)^{1/2} G_C \epsilon_{eff} \sigma T_{BB}^4 A_S A_D}{\pi G_E A_{TT} S^2 V_1} \left[\frac{\text{watts (p-p)}}{\text{cm}^2} \right] \quad (8)$$

where all terms are as defined previously except for

V_1 = the bolometer voltage output during the bolometer calibration, in volts (rms)

Before proceeding with the error analysis, some mention should be made of the case where the background-contributed noise voltage exceeds the bolometer noise voltage, i.e., $V_B > V_N$. Normal operating conditions of the ASET Facility are such that $V_B \ll V_N$. However, during unusual measurement conditions there have been occasions when measurable background irradiance was observed. It is for this reason that subscripts denoting background are included in the expression for the total irradiance. Under such adverse conditions, where $V_B > V_N$, it should be recognized that a meaningful error analysis cannot be carried out. The effect of high background is easily observed, and must be corrected before calibration measurement is performed. In typical operation the inherent low background in the ASET Facility does not influence the bolometer calibration. If a very low background is found to be present, the following two criteria for acceptable data in the presence of the background noise can be considered. First, only those data points are considered for which the signal voltage $V_S \geq 9V_B$ (or in terms of measurable quantities, one has $(V_S + V_B) \geq 10V_B$). Secondly, the decision to accept or reject a particular data point must be influenced by the technical judgement of the scientist conducting the measurements. Based upon these criteria, variations of E_{SB} with V_B in the following analysis may be ignored.

Now, performing the substitution of Equation (8) into Equation (7) and evaluating the partial derivative yields

$$\begin{aligned} \left[\frac{dE_{SB}}{E_{SB}} \right] &= \left[\frac{V_{SBN} dV_{SBN} - V_N dV_N}{V_{SBN}^2 - V_N^2} \right] + \left[\frac{d\epsilon_{eff}}{\epsilon_{eff}} \right] + \left[\frac{d\sigma}{\sigma} \right] + \left[\frac{4dT_{BB}}{T_{BB}} \right] \\ &+ \left[\frac{dA_S}{A_S} \right] + \left[\frac{dG_C}{G_C} \right] + \left[\frac{dA_D}{A_D} \right] - \left[\frac{dG_E}{G_E} \right] - \left[\frac{dA_{TT}}{A_{TT}} \right] - \left[\frac{2dS}{S} \right] \\ &- \left[\frac{dV_1}{V_1} \right] \end{aligned} \quad (9)$$

In order to simplify computations, an approximation is considered for the first term of Equation (9). It is desirable to eliminate the relative error in the noise voltage, dV_N/V_N , because measuring

dV_N/V_N with high precision is difficult. Therefore, in general, only those data points for which $V_{SBN}/V_N \geq 2$ are deemed acceptable. Using this assumption, the first term in Equation (9) can be approximated as

$$\frac{V_{SBN} \frac{dV_{SBN}}{V_{SBN}} - V_N \frac{dV_N}{V_N}}{V_{SBN}^2 - V_N^2} = \left[\frac{1}{1 - \left(\frac{V_N}{V_{SBN}}\right)^2} \right] \left[\frac{dV_{SBN}}{V_{SBN}} \right] - \left[\frac{1}{\frac{V_{SBN}}{V_N} - 1} \right] \quad (10)$$

$$\left[\frac{dV_N}{V_N} \right] \approx \frac{dV_{SBN}}{V_{SBN}} \text{ within 1 percent.}$$

Equation (9) can be rewritten as simplified by Equation (10) and then converted in terms of the rss uncertainty in the total irradiance by taking the square root of the sum of the squares of each term. Thus, the rss uncertainty in the total irradiance is given by

$$\begin{aligned} \left[\frac{dE_{SB}}{E_{SB}} \right]_{\text{rss}} = & \pm \left[\left(\frac{dV_{SBN}}{V_{SBN}} \right)^2 + \left(\frac{d\epsilon_{\text{eff}}}{\epsilon_{\text{eff}}} \right)^2 + \left(\frac{d\sigma}{\sigma} \right)^2 + \left(\frac{4dT_{\text{BB}}}{T_{\text{BB}}} \right)^2 \right. \\ & + \left(\frac{dA_S}{A_S} \right)^2 + \left(\frac{dA_D}{A_D} \right)^2 + \left(\frac{dG_C}{G_C} \right)^2 + \left(\frac{dA_{\text{TT}}}{A_{\text{TT}}} \right)^2 + \left(\frac{2dS}{S} \right)^2 \\ & \left. + \left(\frac{dV_1}{V_1} \right)^2 + \left(\frac{dG_E}{G_E} \right)^2 \right]^{1/2} \quad (11) \end{aligned}$$

A summary of the assumed and measured uncertainties in Equation (11) is given in Table 2. As can be seen, the dominant error lies in the assumed ± 5 -degree uncertainty in the blackbody temperature measurement at the time of the responsivity calibration. Since the variation in the responsivity was only ± 0.03 for a 10 value for the various temperatures used in the responsivity calibration, the highest calibration temperature is used in determining the rss uncertainty, i.e., 300 Kelvin. The beam irradiance measurement is dependent upon the bolometer calibration and hence, the blackbody temperature is not found in the beam irradiance uncertainties summary. Solving Equation (11) using the values of Table 2 gives an rss uncertainty in the total beam irradiance of ± 9.22 percent.

SOURCE MONOCHROMATOR

In addition to the total irradiance calibration capability, the ASET Facility has another source assembly capable of producing a scanable monochromatic beam, thus providing the capability for spectral response calibrations. The spectral range covered is from 2.5 to 26 micrometers. The monochromator source assembly replaces the standard source assembly on the source table, with its radiant output projected with the same F-number into the collimator through a single fixed exit aperture. It is an all-reflective grating instrument whose use has important advantages over the use of narrow-band filters to provide the necessary spectral energy distribution. A schematic diagram of the monochromator source is shown in Figure 14. It produces a nearly monochromatic beam that is focused onto the exit aperture and is then collimated by the ASET collimator, thus simulating a monochromatic point source at infinite distance.

The monochromator utilizes a filter wheel containing up to six multiple-layer interference-type longwave-pass filters. They are used to block radiation of shorter than selected wavelength values in order to prevent second-order and higher-order wavelength radiation output from the monochromator. In addition, one position can hold a polystyrene filter to serve as a wavelength calibrator.

Three gratings are available with rulings of 20, 40, and 80 lines per millimeter, corresponding to a line spacing of 50, 25, and 12.5 micrometers, and blaze wavelengths of 4.3, 8.6, and 17.2 micrometers respectively.

MONOCHROMATOR CALIBRATION

The main monochromator parameter to be calibrated is its output wavelength as a function of grating angle. This parameter is important since it remains constant from run to run, whereas the resulting beam irradiance depends on the blackbody-type source temperature. The variability of the irradiance is effectively taken into account by continuously measuring the beam irradiance with the calibration monitor, whose response is spectrally flat. Although three gratings are available, only two were calibrated, the 80 lines per mm and the 20 lines per mm. These two gratings cover the range from 2.5 to 26 micrometers in the first order, with a slight dip in the mid-range.

The expected wavelength values in the first order are given by

$$\lambda = 2d \sin\phi \cos\delta$$

with ϕ being the grating angle, δ the angle of incidence at the specular (zero order) position ($\phi = 0$), and d the line spacing or grating constant. For the 20 lines/mm grating at room temperature $d = 50 \mu\text{m}$, and for the 80 lines/mm grating $d = 12.5 \mu\text{m}$. The value of d is reduced at 20°K by 0.4 percent due to the contraction of the aluminum grating material. The value of $\cos \delta$ is

0.86, based on the geometry of the instrument. It will not change with temperature, since the whole instrument is made of aluminum and should shrink uniformly, keeping angular relationships constant.

At room temperature the calculated wavelength values for each grating are

$$\lambda = 86.0 \sin\phi \text{ (20 lines/mm)}$$

$$\lambda = 21.5 \sin\phi \text{ (80 lines/mm)}$$

and at 20°K, the calculated wavelength values for each grating are

$$\lambda = 85.65 \sin\phi \text{ (20 lines/mm)}$$

$$\lambda = 21.42 \sin\phi \text{ (80 lines/mm)}$$

The grating was directly connected to a rotary resolver, i.e., an angular position transmitter, whose output signals were converted to digital information and input directly to a digital computer, a PDP-15, which calculated the wavelength according to the preceding formulas and displayed it on a terminal at the ASET console in near real time. In addition, the bolometer signal output amplitude from the ASET lock-in amplifier (PAR HR-8) was input to the computer for display along with the wavelength. An X-Y recorder was also set up to plot the resolver analog signal along the X-axis and the lock-in amplifier signal along the Y-axis. This data-taking arrangement during an actual wavelength scan produced an analog plot of sensor signal versus wavelength simultaneous with a digital table of sensor signals as a function of wavelength as provided by the computer.

A typical room temperature monochromator response using the polystyrene filter is given in Figure 15. The corresponding response at 20 Kelvin is given in Figure 16. The wavelengths calculated from the formulas shown were compared with the polystyrene band center wavelengths. The discrepancies were within the monochromator resolution. Similar response curves using the interference type filters showed the expected 1 to 3 percent downward shifts in their characteristic wavelengths as the temperature was lowered to 20 Kelvin.

The measured results are presented in Table 3 for the 80 lines/mm grating and in Table 4 for the 20 lines/mm grating. The grating wavelengths are calculated using the previous formulas.

The monochromatic beam irradiance was measured using the ASET bolometer. The result was a set of typical system response curves of the monochromator and ASET Facility, which are presented in Figure 17. The curves were obtained with a 900 Kelvin source during two test cycles; one with the 80 lines per millimeter grating and the other with the 20 lines per millimeter grating.

The relative spectral response of a Si:As detector was obtained during tests within the facility, and is shown in Figure 18.

MONOCHROMATOR ERROR ANALYSIS

The major error in the monochromator wavelength calibration is due to the monochromator dispersion, which is $0.05 \mu\text{m}/\text{mm}$ for the 80 lines/mm grating and $0.22 \mu\text{m}/\text{mm}$ for the 20 lines/mm grating. During the operational tests in ASET, a 1.1 mm diameter aperture was used as the exit slit, so that the wavelength spread in the ASET beam was $0.055 \mu\text{m}$ and $0.25 \mu\text{m}$ respectively for each grating. During the ambient calibration runs using the thermocouple detector, the wavelength spread was defined by the 0.5 mm thermocouple width that was being used. The resulting expected wavelength uncertainty was therefore estimated to be $0.028 \mu\text{m}$ for the 80 lines/mm grating and $0.11 \mu\text{m}$ for the 20 lines/mm grating.

Other wavelength errors included offset in the analog-to-digital converter and graph reading error. The total wavelength errors due to these and other sources is about $\pm 0.02 \mu\text{m}$ for the 80 lines/mm grating and $\pm 0.08 \mu\text{m}$ for the 20 lines/mm grating. The total error in the monochromator wavelength calibration is therefore about $\pm 0.04 \mu\text{m}$ for the 80 lines/mm grating and $\pm 0.14 \mu\text{m}$ for the 20 lines/mm grating. It is seen in Tables 3 and 4 that the differences between measured and calculated wavelength values for each grating at any point are less than the calibration measurement errors. Therefore, the approach taken is considered sufficiently accurate to define the monochromator wavelength calibration.

REFERENCES

- Day, R. P., Meier, R. H., Shoore, J. D., and Thompson, C. J. C.; Status Report on MDAC's Advanced Subsystem Evaluation and Test (ASET) Facility; MDAC-WD 1525, Nov 1970 (S).
- Meier, R. H., Day, R. P., Shoore, J. D., and Thompson, C. J. C.; An Advanced Test and Evaluation Facility for Space Optical Systems; MDAC-WD 1573, Apr 1971 (C).
- Shoore, J. D. and Day, R. P.; Calibration of the ASET Facility Bolometer; MDAC-G2484, Sept 1971.
- Dauger, A. B., Meier, R. H., and Shoore, J. D.; Irradiance and Spectral Calibration of the MDAC ASET Facility; MDAC-WD 2081, Jan 1973.
- Gauffé, A.; Corrections d'ouverture des corps-noirs artificiels compte tenu des diffusions multiples internes, Revue D'optique, 24, No. 1-3, Paris, France, 1945.
- Holscher, H. H.; Simplified Statistical Analysis, Cahners Publishing Co., Inc., Boston, Mass, 1971.

ACKNOWLEDGMENT

The authors particularly wish to acknowledge the team effort and contributions made by Messrs. J. R. Averett, F. A. Eckhardt, R. A. Edgell, W. A. Fraser, S. Griffith, R. M. Hartman, J. T. Morrow, R. E. King, B. C. Moore, E. J. Pisa, H. Popick, R. W. Powell, R. E. Schatzmann, I. Richman, E. H. Schwiebert, J. P. Theriault, and C. J. C. Thompson for their efforts in solving several unusual engineering problems in optics, mechanics, cryogenics, and vacuum technology which has greatly contributed to the successful completion of this unique facility. Also, we wish to express our appreciation for many fruitful discussions with Drs. R. H. McFee and S. Zwerdling. The work described here was conducted by the McDonnell Douglas Astronautics Company as part of the Company-sponsored research and development program.

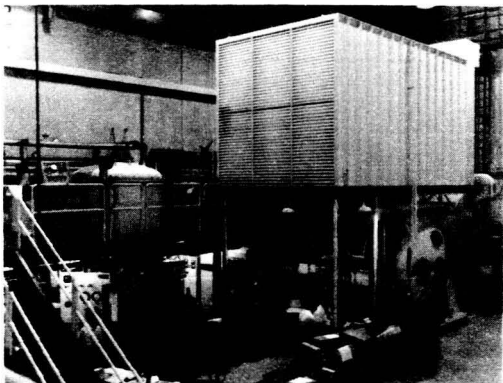


Figure 1. View of Test Facility

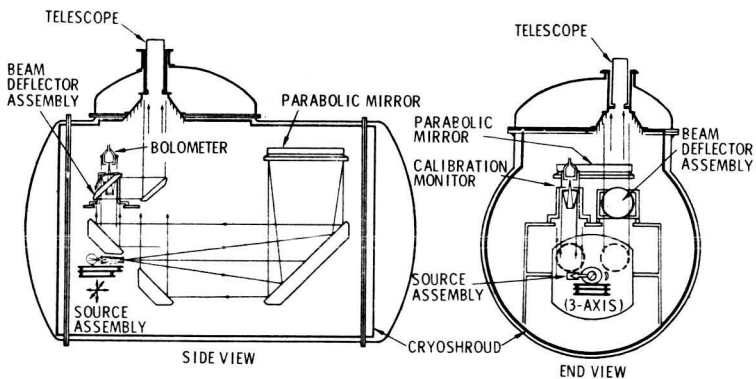


Figure 2. Schematic of ASET Facility

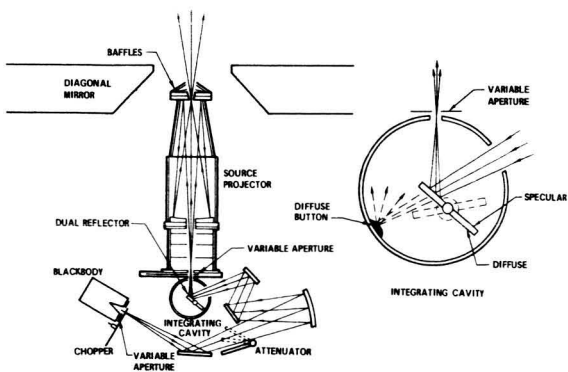


Figure 3. Standard Source Assembly

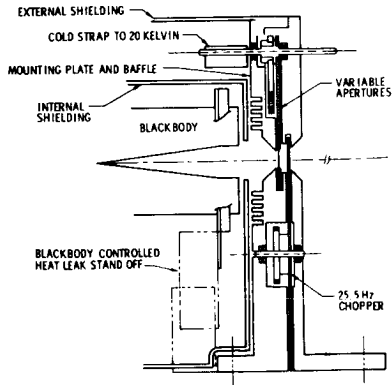


Figure 4. Blackbody Source Assembly

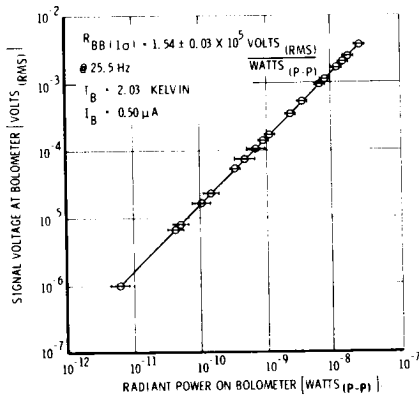
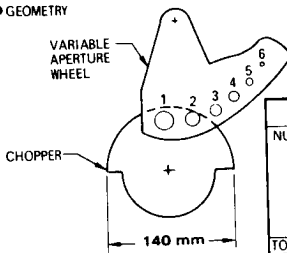


Figure 5. Bolometer Responsivity

● GEOMETRY



APERTURE DIAMETERS	
NUMBER	DIAM. MM
1	8.00
2	6.47
3	3.55
4	2.03
5	0.76
6	BLANK

TOLERANCE ± 0.003

● CHOPPING EFFICIENCY

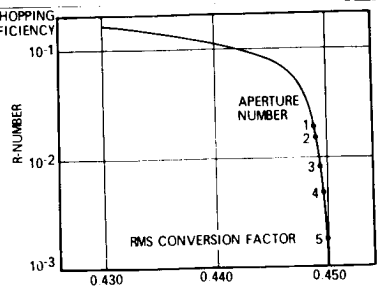
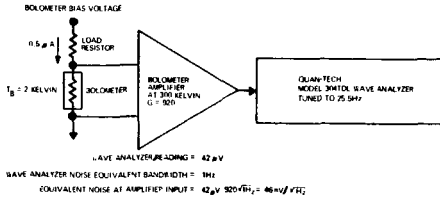


Figure 6. Source Chopper Temporal Variations

● MEASUREMENT CONFIGURATION & ANALYSIS



● NOISE CONTRIBUTORS

1. JOHNSON NOISE OF BOLOMETER ($\overline{v}_b = 5nV/\sqrt{Hz}$) AT 2 KELVIN
2. JOHNSON NOISE OF LOAD RESISTOR ($\overline{v}_{RL} = 22nV/\sqrt{Hz}$) AT 2 KELVIN
3. EXCESS CURRENT NOISE OF BOLOMETER ($\overline{i}_b = 3 \times 10^{-14} \text{ amp}/\sqrt{Hz}$) AT 2 KELVIN
4. AMPLIFIER CURRENT NOISE ($\overline{i}_a = 1 \times 10^{-14} \text{ amp}/\sqrt{Hz}$) AT 300 KELVIN
5. AMPLIFIER VOLTAGE NOISE ($\overline{v}_a = 8nV/\sqrt{Hz}$) AT 300 KELVIN

Figure 7. Noise Measurement & Analysis

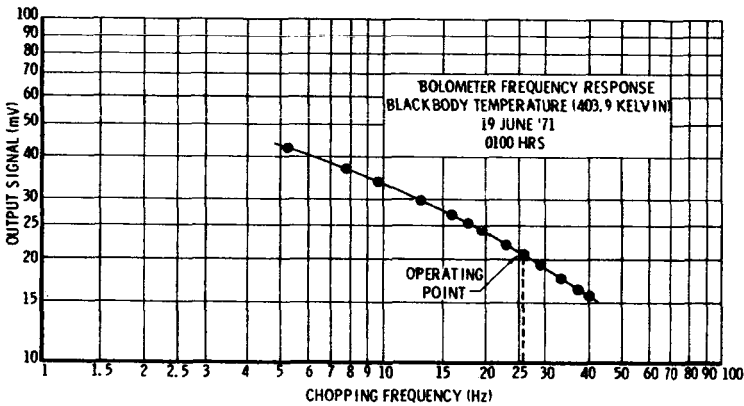


Figure 8. Bolometer Frequency Response

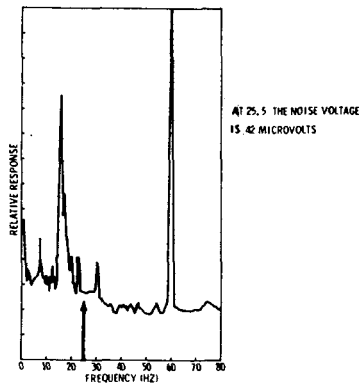


Figure 9. Bolometer Noise Spectrum

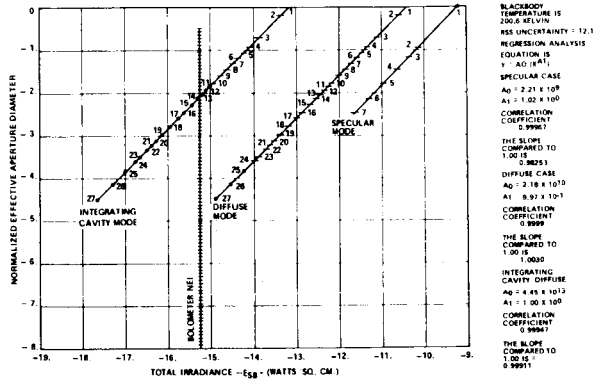


Figure 10. ASET Collimated Beam Total Irradiance, 200 Kelvin

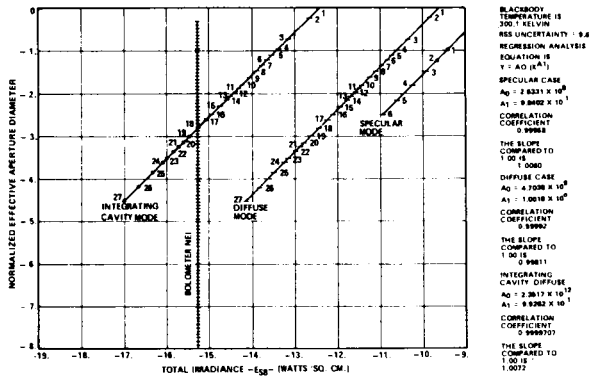


Figure 11. ASET Collimated Beam Total Irradiance, 300 Kelvin

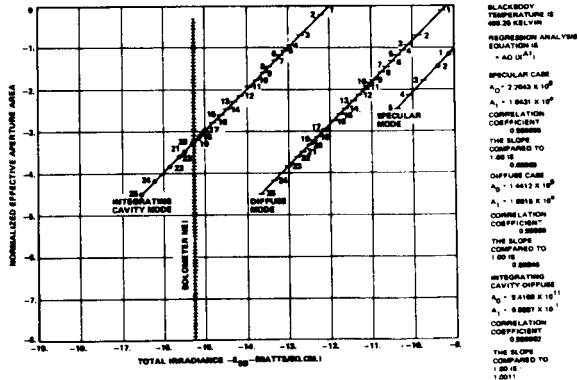


Figure 12. ASET Collimated Beam Total Irradiance, 400 Kelvin

SPECULAR CASE
200 KELVIN 300 KELVIN

- 1 - 0/5.00 0/2.0
- 2 - 0/2.0 0/1.5
- 3 - 0/1.5 0/1.1
- 4 - 0/1.1 0/0.75
- 5 - 0/0.75 0/0.50
- 6 - 0/0.50 0/0.34
- 7 - 0/0.34

IC APERTURE
ACTUAL DIMENSIONS

- 5.00 → 5.00
- 2.0 → 1.998
- 1.5 → 1.510
- 1.1 → 1.099
- 0.75 → 0.753
- 0.50 → 0.502
- 0.34 → 0.342

DIFFUSE CASE
200 KELVIN AND 300 KELVIN

- 1 - 0/5.00 15 - 0.47/0.50
- 2 - 0.47/5.00 16 - 0/0.34
- 3 - 3.56/5.00 17 - 2.03/1.1
- 4 - 0/2.0 0.47/0.34
- 5 - 0.47/2.0 18 - 3.56/0.50
- 6 - 0/1.5 19 - 2.03/0.75
- 7 - 2.03/5.00 0.76/2.0
- 8 - 0.47/1.5 20 - 3.56/0.34
- 9 - 0/1.1 21 - 0.76/1.51
- 10 - 0.47/1.1 22 - 2.03/0.50
- 11 - 3.56/2.0 23 - 0.76/1.1
- 12 - 0/0.75 24 - 2.03/0.34
- 13 - 0.47/0.75 25 - 0.76/0.75
- 14 - 2.03/2.0 26 - 0.76/0.50
- 27 - 0.76/0.34
- 0/0.5

INTEGRATING
CAVITY- DIFFUSE

ITEMS 1-27 ARE
THE SAME AS
FOR THE
DIFFUSE CASE

APERTURE DIAMETER, MM

Figure 13. Effective Aperture Code

SPECULAR CASE
400 KELVIN

- 1 - 0/1.5
- 2 - 0/1.1
- 3 - 0/0.75
- 4 - 0/0.50
- 5 - 0/0.34

DIFFUSE CASE
400 KELVIN

- 1 - 0.47/5.00 13 - 0.47/0.50
- 2 - 3.56/5.00 14 - 0/0.34
- 5.00
- 3 - 0/2.0 15 - 0.47/0.34 OR
- 2.03/1.1
- 4 - 0.47/2.0 16 - 3.56/0.50
- 5 - 0/1.5 OR 17 - 2.03/0.75
- 2.03/5.00 18 - 3.56/0.34
- 6 - 0.47/1.50 19 - 0.76/1.5
- 7 - 0/1.1 20 - 2.03/0.50
- 8 - 0.47/1.1 & 21 - 0.76/1.1
- 3.56/2.0 22 - 2.03/0.34
- 9 - 0/0.75 23 - 0.76/0.75
- 10 - 3.56/1.5 24 - 0.76/0.50
- 11 - 0.47/0.75 25 - 0.76/0.34
- 12 - 0/0.50 OR 2.03/2.0

INTEGRATING
CAVITY CASE
400 KELVIN

- 1 - 0/5.00 14 - 0/0.34
- 2 - 0.47/5.00 15 - 0.47/0.34
- 3 - 3.56/5.00 16 - 3.56/0.50
- 4 - 0/2.0 17 - 0.76/2.0
- 5 - 0.47/2.0 18 - 3.56/0.34
- 6 - 0/1.5 19 - 0.76/1.5
- 7 - 0.47/1.5 20 - 2.03/0.5
- 8 - 0/1.1 21 - 0.76/1.1
- 9 - 0.47/1.1 & 22 - 2.03/0.34
- 3.56/2.0 23 - 0.76/0.75
- 10 - 0/0.75 24 - 0.76/0.50
- 11 - 0.47/0.75 25 - 0.76/0.34
- 12 - 0/0.50
- 13 - 0.47/0.50

APERTURE DIAMETER, MM

Figure 13A. Effective Aperture Code, T = 400 Kelvin

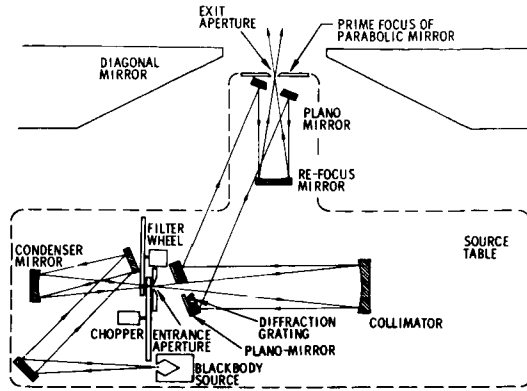


Figure 14. Monochromator Source

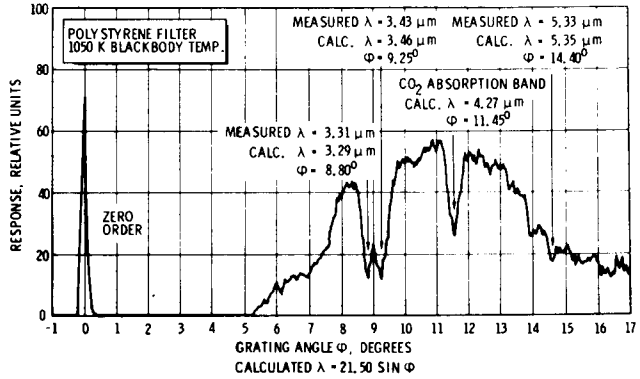


Figure 15. 80 Lines/MM Grating Calibration, Warm

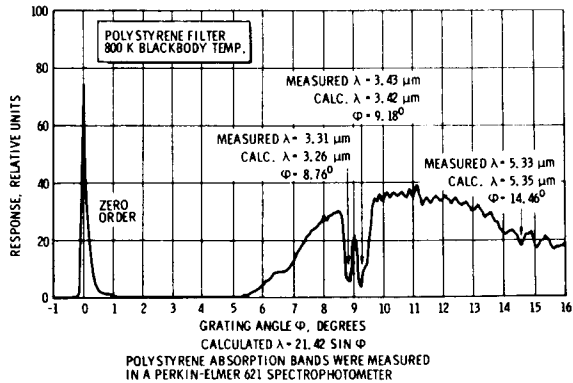


Figure 16. 80 Lines/MM Grating Calibration, Cold

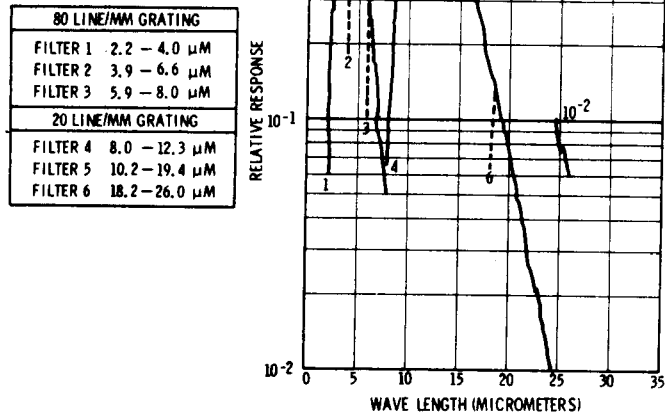


Figure 17. System Response of Monochromator

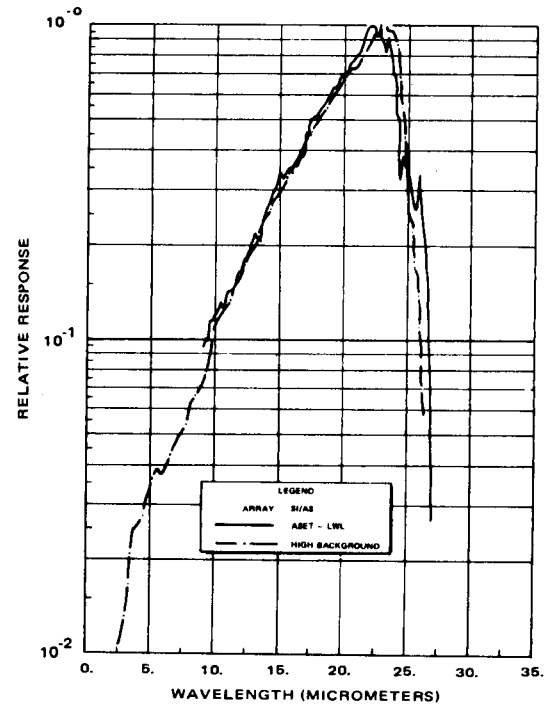


Figure 18. Spectral Response

APERTURE COMBINATIONS (mm)	SPECULAR MODE (VOLTS)			DIFFUSE MODE (VOLTS)		INTEGRATING CAVITY MODE (MILLIVOLTS)	
	17 MAY	30 MAY	10 OCT	17 MAY	30 MAY	17 MAY	30 MAY
8/5.88				6.55	6.65	10.4	10.3
8/2				0.760	0.765	1.21	1.2
8/1.5				0.447	0.440	0.680	0.69
8/1.1				0.243	0.245	0.355	0.36
8/0.75	1.64	1.65	1.65	0.106	0.106	0.165	0.160
8/0.50	0.7	0.7	0.7	0.047	0.047	0.075	0.075
8/0.34	0.335	0.335	--	0.022	0.022	0.034	0.035
PERCENT DIFFERENCE (WORST CASE)	≈ 0.6 PERCENT			≈ 0.9 PERCENT		≈ 3 PERCENT	

Table 1. Comparison of Voltage Data Taken On May 1972 With Data Taken On 30 May 1972 and 10 October 1972

UNCERTAINTIES IN BOLOMETER RESPONSIVITY CALIBRATION		UNCERTAINTIES IN BEAM IRRADIANCE CALIBRATION	
> 1 PERCENT	< 1 PERCENT	> 1 PERCENT	< 1 PERCENT
dT_{BBTBB} at 300°K = 6.7×10^2 and $dT = 5$ -degrees	dA_g/A_S = 4.44×10^5	dV_{SBN}/V_{SBN} = 2.0×10^2	dA_{TT}/A_{TT} = 1.0×10^3
$d\epsilon_{eff}/\epsilon_{eff}$ = 5.0×10^2	dA_D/A_D = 1.0×10^3	dG_E/G_E = 1.0×10^2	
dG_C/G_C = 1.0×10^2	$2\epsilon/S$ = 3×10^3		
dV_1/V_1 = 3.0×10^2	$d\epsilon/\epsilon$ = 6.1×10^4		

Table 2. Summary of RSS Uncertainties

MEASURED WAVELENGTH	ROOM TEMPERATURE, IN AIR		20 K, IN VACUUM	
	GRATING ANGLE	WAVELENGTH	GRATING ANGLE	WAVELENGTH
POLYSTYRENE 3.31 μm	8.80°	3.29 μm	8.76°	3.26 μm
POLYSTYRENE 3.43 μm	9.25°	3.46 μm	9.18°	3.42 μm
POLYSTYRENE 5.33 μm	4.40°	5.35 μm	14.46°	5.35 μm
CO ₂ ABSORPTION BAND 4.27 μm	11.45°	4.27 μm	NONE	

Table 3. 80 Lines/mm Grating Calibration

MEASURED WAVELENGTH	ROOM TEMPERATURE, IN AIR		20 K, IN VACUUM	
	GRATING ANGLE	WAVELENGTH	GRATING ANGLE	WAVELENGTH
POLYSTYRENE 13.33 μm	8.85°	13.32 μm	8.95°	13.33 μm
POLYSTYRENE 14.40 μm	9.60°	14.40 μm	9.60°	14.37 μm

Table 4. 20 Lines/mm Grating Calibration

INCREASE OF THE ABSORPTANCE OF A SHROUD FOR A THERMAL TEST FACILITY AND METHODS OF DETERMINATION

H. Nuss, J. Reimann, IABG, Laboratory of Space Simulation, D 8012 Ottobrunn, Germany

ABSTRACT

To reduce the large amount of reflected heat radiation by the shroud of the test facility measured during the thermal balance tests on the thermal model of the HELIOS Solar probe at high intensity (16 Solar constants) the testchamber was modified by installation of a shroud with a grooved surface. The paper describes the shroud surface (V-grooves) and the methods used for measuring and calculating the absorptance of the grooved surface.

1. Introduction

According to the mission of the HELIOS Solar probe with a perihelion of 0.25 AU thermal balance tests with simulated solar intensities of 16 S.C. were required. The tests with the thermal model of the HELIOS Solar probe equipped with a thermal canister for simulating intensities of 16 S.C. were carried out in a vacuum chamber with a cold shroud simulating vacuum and cold space environmental conditions respectively. Whereas the influence of the reflected heat radiation from the shroud surface to the thermal model could be neglected at 1 S.C. test conditions there was a considerable simulation error at 16 S.C. test conditions. This simulation error could not be considered with satisfactory accuracy in the mathematical model calculation and therefore it was decided to increase the absorptance of the cold shroud and in this way to reduce the amount of reflected heat energy.

The absorptance was increased by installation of a cold shroud with a grooved surface. (Fig.1 and 2) Published data(1)(2) show that an increase of the absorptance from $\alpha = 0.9$ for the coating to $\alpha = 0.97$ for the coated and V-grooved surface is possible. In this case the apex angle of the V-groove has to be less than 15 degrees. Such a surface was chosen for the modified shroud. (Fig.2)

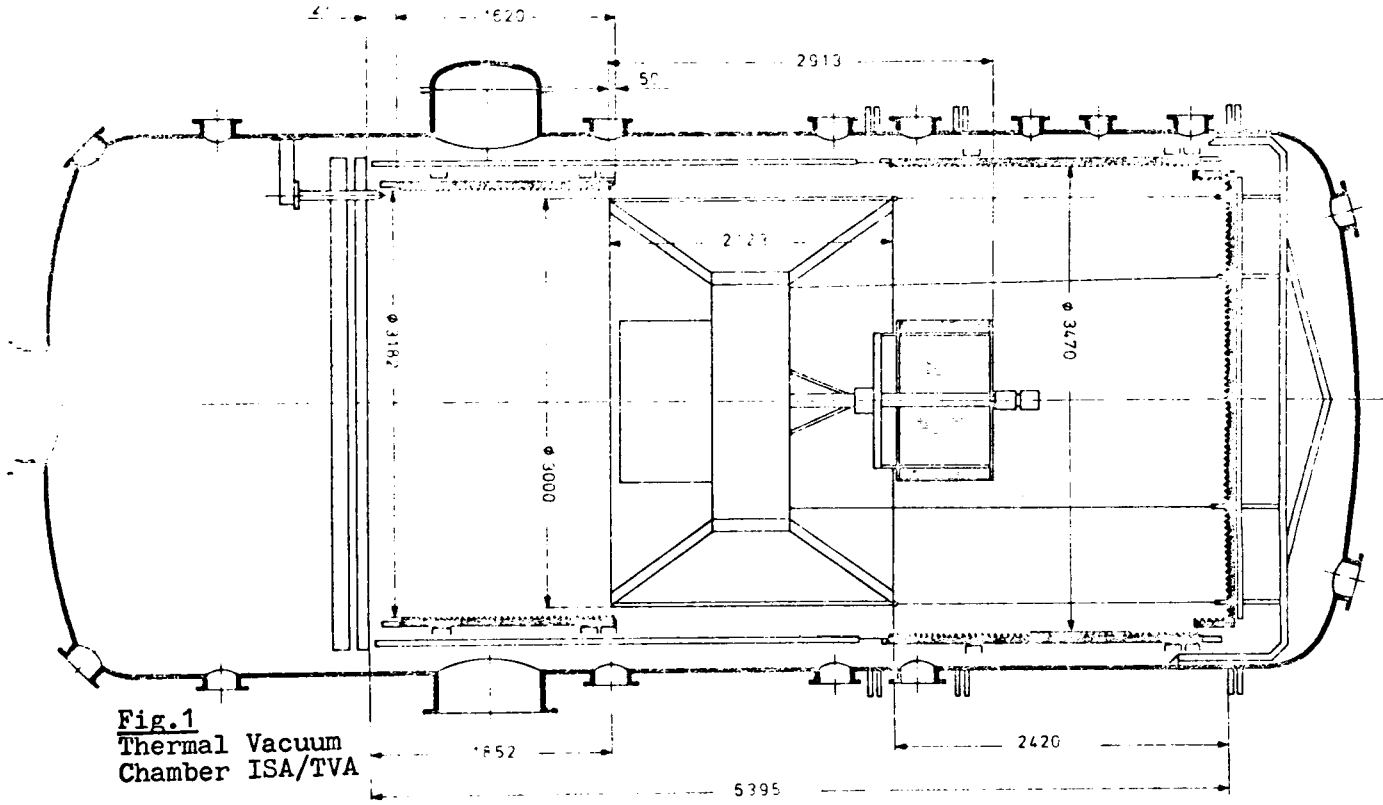
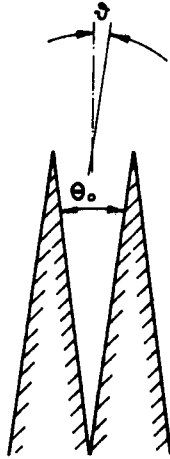
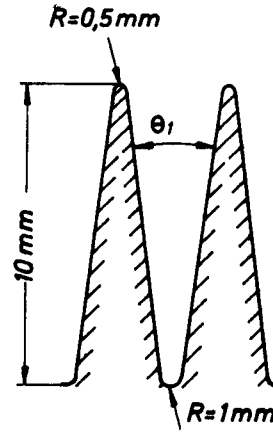


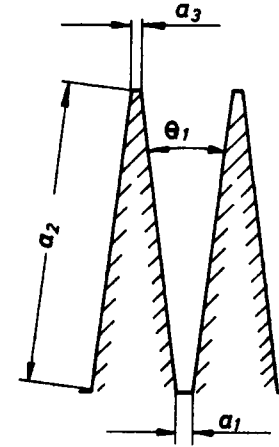
Fig.1
Thermal Vacuum Chamber ISA/TVA



1. Ideal profile
 $\theta_0 = 15^\circ$



2. Real profile
 $\theta_1 = 14^\circ$



3. Simplification
 of for calculation
 $\theta_1 = 14^\circ$
 $a_1 = 0.8 \text{ mm}$
 $a_2 = 10.1 \text{ mm}$
 $a_3 = 1.8 \text{ mm}$

Shroud surface with V-grooves

Fig. 2

The published data assume V-grooves with sharp edges (ideal grooves) and coating properties of a Lambert radiator. Practically it is not possible to realize these conditions. The V-grooves have rounded edges by reason of manufacturing and the used black paint (Black Velvet Coating 3MCo.) has not a Lambert distribution of radiation.

The aim of the measurements and calculations described in the following is the determination of the absorptance of the V-grooved surface coated with Black Velvet Coating 3M 401 C 10, the increase of the absorptance compared to a flat surface and the difference in absorptance between ideal and real grooved surfaces.

2. Determination of the absorptance of a grooved surface

For the determination of the absorptance three different measuring methods and a calculation procedure were used.

2.1 Measurements

2.1.1 Measurements of the emittance of samples with 90 mm diameter :

The emittance was measured by the PTB (Physikalisch Technische Bundesanstalt) according to a measuring and evaluation procedure developed by Lohrengel(3). This method compares the radiation density of the sample surface with that of a black body of equal temperature under vacuum conditions. The influence on the value of the emittance due to the temperature difference between the black body and the sample was investigated by the above mentioned method and the surface temperature was calculated by considering the radiation interactions of the sample with its environment.

With the above described method the total directional emittance for a flat sample and a grooved sample was measured for sample temperatures of -67°C and $+180^{\circ}\text{C}$ and with these results the total hemispherical emittance was calculated.

In Table 1 and 2 (4), (5) and Fig.3 the results are prepared :

Sample	Sample temperature	wavelength of radiation max.	ϵ_n	ϵ_H
Profile vertical	+180°C	6 μm	0.97±0.005	0.94±0.005
Profile horizont.	+180°C*	6 μm	0.97±0.005	0.93±0.005
flat surface	-67°C	14 μm	0.96±0.005	0.90±0.005
flat surface	+180°C	6 μm	0.96±0.005	0.90±0.005

ϵ_n :emittance in normal direction Table 1

ϵ_H :hemispherical emittance

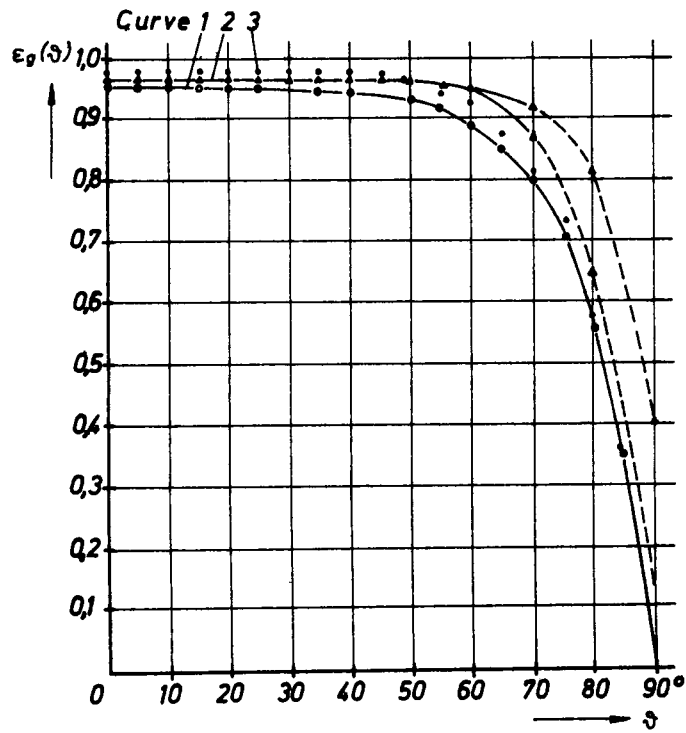
The emittance as a function of emission direction shows Table 2 and Fig.3 (ϑ is the inclination angle to the normal direction) :

inclination angle ϑ	flat sample $\epsilon_F(\vartheta)$	Profile vertical $\epsilon_g(\vartheta)$	Profile horizontal $\epsilon_g(\vartheta)$
0	0.96	0.97	0.97
30	0.95	0.97	0.97
50	0.94	0.97	0.97
60	0.90	0.96	0.96
70	0.80	0.92	0.88
80	0.58	0.82(extra pol.)	0.15(extra pol.)

Table 2

The hemispherical emittance ϵ_H (Table 1) is calculated from the results $\epsilon(\vartheta)$ according to the following equation :

$$\epsilon_H = 2 \int_0^{\pi/2} \epsilon(\vartheta) \sin\vartheta \cos\vartheta d\vartheta \quad (1)$$



- 1 Flat sample (s.2.1.1)
- 2 Grooved sample (s.2.1.1)
- 3 Grooved sample (s.2.1.3)

Fig. 3
Experimental results for the
Emittance $\epsilon_g(\delta)$
as a function of inclination
angle δ to normal direction

2.1.2 Measurement of the reflectance of heat radiation by a sample of 1m x 1m :

For the measurement of the reflectance of a sample 1m x 1m cooled by liquid nitrogen under vacuum conditions a special measuring equipment by the DFVLR (Institut für Raumsimulation) was developed (6).

The measuring equipment, by which the reflectance in an angle range of $\vartheta = -65^\circ$ to $\vartheta = +65^\circ$ can be measured, consists of a heated ring and a concentric sensor. The procedure is as follows :

- 1.) The calibration curve for the determination of the dependence of the temperature of the applied power for the sensor was measured.
- 2.) The influence of the radiated energy from the ring to the grooved sample and reflected to the sensor was investigated by measuring the sensor temperature and considering the power according to the calibration curve.
- 3.) The reflectance is proportional to the ratio of this power and the radiated energy.
- 4.) With the aid of the temperature of the sensor and the heater the reflectance was calculated and the temperature of isolating surfaces was considered.

Three test runs gave the following results :

Nr. of Test run	reflectance r according to 1.) - 3.)	reflectance r according to 4.)	Δr according to 4.)
1	0.031	0.017	± 0.008
2	0.030	0.017	± 0.008
3	0.028	0.015	± 0.007

Table 3

With the results of the table 3 for the reflectance the following values for the absorptance are calculated :

$$\alpha = 0.97 \pm 0.01 \quad (\text{according to 1.) - 3.})$$

$$\alpha = 0.98 \pm 0.01 \quad (\text{according to 4.})$$

2.1.3 Measurement of the directional reflectance for samples 20 mm x 20 mm (7):

The directional reflected radiation was measured for wavelengths of 2000 nm and 2500 nm with a Zeiss Spectralphotometer and a rotating sample holder installed in a Ulbricht sphere.

The directional reflectance was determined for inclination angles ν to the normal direction between 0° and 90° . The measurements were carried out for samples of flat and grooved surfaces. The spectral directional reflectance of the grooved samples was determined by a relative measuring method :

The ratio of the reflected intensity of the grooved and flat surfaces was measured and with the results measured by the above mentioned method 2.1.1 for the same surface the directional reflectance of the grooved surface was calculated. This is an approximation method and was especially used for measuring the possible change of the reflectance of the shroud after the thermal tests with the HELIOS thermal model.

Table 4 and Fig.3 shows the results for the grooved sample. The difference between vertical and horizontal profile was measured < 0.01 :

ν	grooved sample $\epsilon_g(\nu)$	
0	0.98	accuracy ± 0.02
30	0.98	
50	0.97	
60	0.94	
70	0.82	
80	0.59	

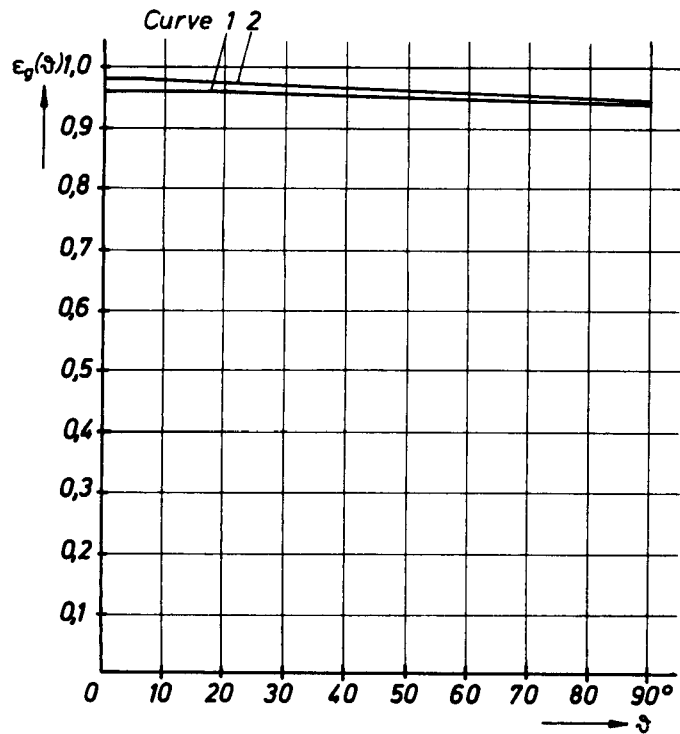
Table 4

The hemispherical emittance calculated according to equation (1) is :

$$\epsilon_{gH} = 0.93 \pm 0.02$$

2.2 Calculation

The calculation of the emittance of the surface with V-grooves is carried out based on a procedure developed by Daws (1). It is assumed that the laquer of the grooved surface behaves in the manner of a Lambert reflector to any incident radiant energy. As characteristic parameters for the radiation properties of



- 1 Real profile
- 2 Ideal profile

Fig. 4
Theoretical results for
the emittance $\epsilon_g(\vartheta)$ for
a grooved surface
described in Fig. 2

the grooved shroud the effective emittance $\epsilon_g(\nu)$ as a function of sighting angle ν and the mean effective emittance ϵ_{gH} over all sighting angles was calculated. The emittance $\epsilon_g(\nu)$ and ϵ_{gH} is calculated with the assumption of $\epsilon_F = 0.90$ for the coating (independent of ν) for the ideal and real profile (Fig. 2). The results are shown in table 5 and Fig. 4 :

	ϵ_{gn}	ϵ_{gH}
ideal profile $\epsilon_F = 0.90$	0.99	0.97
real profile $\epsilon_F = 0.90$	0.97	0.96

Table 5

The values for the hemispherical emittance ϵ_{gH} in table 5 are in good agreement with results calculated according to the formular of Treuenfels (9) for triangular grooves assuming also the coating is a diffuse reflector :

$$\epsilon_{gH} = \frac{\epsilon_F}{\epsilon_F + f_1(1 - \epsilon_F)} \quad (2)$$

$$f_1 = 1 - \frac{\pi - \theta_0}{4} \cos \frac{\theta_0}{2} \quad (3)$$

with $\theta_0 = 15^\circ$, $\epsilon_F = 0.90$ for the hemispherical emittance follows

$$\epsilon_{gH} = 0.97.$$

3. Summary of the results and conclusions

In table 6 the results for the emittance of the grooved surface in normal direction ϵ_{gn} and the hemispherical emittance ϵ_{gH} are described as a summary :

Measurement/ Calculation	ϵ_{gn}	ϵ_{gH}
PTB (S.2.1.1)	0.97±0.005	0.94±0.005
DFVLR(S.2.1.2)	0.98±0.01 0.97±0.01	for angle range -65° to +65°
IABG(Measurement S.2.1.3)	0.98±0.02	0.93±0.02
IABG(calculation S.2.2)		
real profile $\epsilon_F = 0.90$	0.97	0.96
ideal profile $\epsilon_F = 0.90$	0.99	0.97

Table 6

Considering all the described measuring and calculating procedures, their assumptions and accuracies the following values can be stated.

Emittance of a grooved surface (apex angle $\theta_0 = 15^\circ$) coated with Black Velvet 3 M 401 C 10 :

in normal direction $\epsilon_{gn} = 0.97$

hemispherical $\epsilon_{gH} = 0.94$

Literature

1. L.F. Daws :
The emissivity of a groove,
Brit.J.of Appl. Phys.Vol.5,
May 1954
2. E.M.Sparrow, R.D.Cess :
Radiation Heat Transfer, 1970
3. J.Lohrengel :
Diss. TH Aachen 1969
4. Protokoll PTB Nr.3.13 - 83 97/73 (profiliert)
5. Protokoll PTB Nr.3.13 - 83 97/73
6. W.Hallmann, H.P.Schmidt :
DFVLR, Institut für Raumsimulation
Bericht IB 353-73/19, March 1973
7. L.Krammer, H.Nuss :
IABG, Meßbericht TRW 11.02/23/34/73
8. P.Eysenbach, H.D. Keller :
IABG-Bericht 1973
9. E.W.Treuenfels :
J.Opt.Soc.Am.53,1162, 1963

**TESTING FOR THERMAL FATIGUE
FAILURES IN SOLAR ARRAYS**

G. J. Antonides, *Lockheed Missiles and Space Company,*
Sunnyvale, California

ABSTRACT

A temperature cycling test facility has been designed and constructed for the study of thermal stress and fatigue in solar arrays. Two bell jar type thermal vacuum chambers and their associated equipment and instrumentation provide close simulation of the space environment, automatic temperature cycling and data acquisition, and economical operation.

INTRODUCTION

The most severe environmental effect on a satellite solar array in long-term orbit is the thermal fatigue due to temperature cycling during the alternate sun/shade cycles. The severity also is increasing with the greater use of geosynchronous orbits where the temperature excursions are greater, and with the demands for longer orbit life and lower weight. Life testing of new solar panel designs for thermal fatigue thus has become a requirement for obtaining reliable power system performance when solar arrays are employed.

In order that testing for thermal stress and fatigue failures be meaningful, there must be close simulation of the space thermal environment, including:

- (1) high vacuum and a "cold space" shroud
- (2) the solar radiation intensity, uniformity and direction
- (3) the time periods associated with test module temperature transients

Lockheed Missiles and Space Company has built two thermal vacuum chambers specially designed for the temperature cycling of large numbers of multi-cell solar panel modules in an accurately simulated space environment and at low cost.

FACILITY DESCRIPTION

The facility presently includes two thermal vacuum chambers. These are stainless steel, bell jar type chambers having a test volume 24 inches in diameter by 42 inches high. Two 9-inch diameter quartz windows on one side of the bell jar permit irradiation of the solar array modules by a Spectrolab X-25 solar simulator

to test electrical output of the modules. Eight tungsten filament lamps are installed inside each chamber to provide uniform radiant energy for the temperature cycling during normal life testing. A liquid nitrogen cooled shroud completely surrounds the test volume and includes movable shutters for the quartz windows. At the center of the chamber there is a box, or "target", 7.5 inches square by 21 inches high on which test modules are mounted. The box rotates so that different sets of modules can be positioned in front of the windows, and it is cooled with liquid nitrogen to provide the "cold space" environment on the back side of the test specimens.

The vacuum system consists of a 400 liter per second differential ion pump on each chamber. Initial roughing is accomplished with a carbon vane mechanical pump and a two-stage sorption pump. The roughing equipment is contained in a portable cart which is connected as needed to either vacuum chamber.

A standard solar array module size was established with dimensions of approximately 3.5 inches by 5 inches. Thus a module might be, for example, an assembly of 12 2cm. by 4cm. solar cells. However, any module having a diagonal dimension of 9 inches or less can be tested when the solar simulator is to be used. Larger test articles also can be tested, and the rotatable box can be removed to permit testing of one or two panels up to 2 ft. by 3 ft.

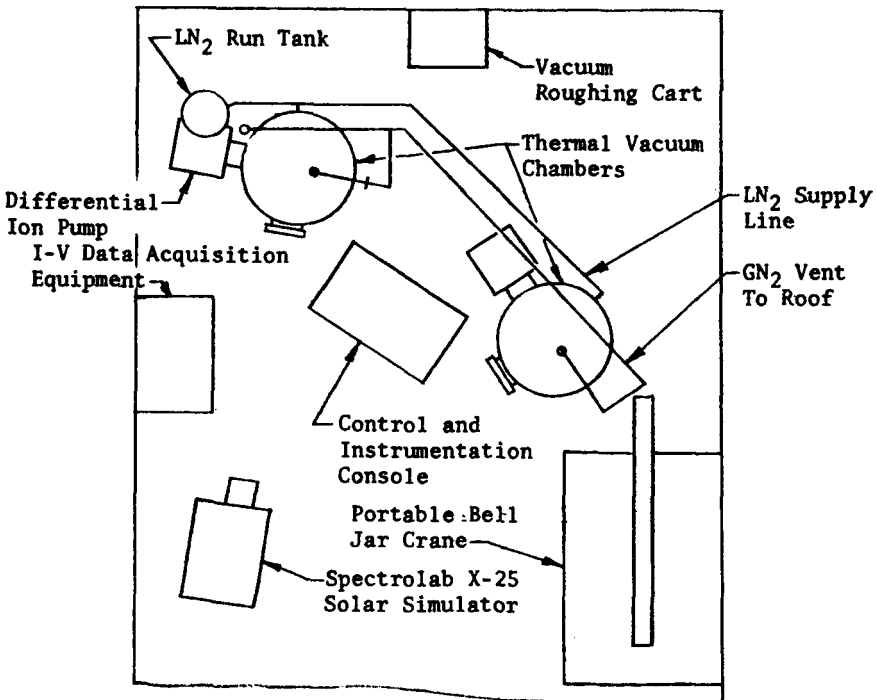


Fig. 1 - Thermal Cycling Facility Layout

FACILITY PERFORMANCE

The ion pumping, together with some cryopumping by the liquid nitrogen shroud system, yields a vacuum level below 10^{-7} torr when the chamber is clean and empty. Outgassing by the test articles will raise this pressure; however, the ion pump can maintain a chamber pressure of 6×10^{-5} torr with an air in-bleed of 8 micron liters per second and without liquid nitrogen in the shroud.

The chambers are designed to operate in the temperature range from -191°C to 300°C , and there is potential for lowering the minimum temperature several degrees. The interior tungsten filament lamps can direct from 0 to 4 solar constants of uniform radiant energy onto the test modules. Temperature cycles can be obtained by programming either the radiant energy intensity or module temperature vs. time. Two 40-channel digital recorders give both test module temperature and electrical output data. Complete, automatic data acquisition equipment is provided for round-the-clock, unattended facility operation.

A summary of test results to date will be presented.

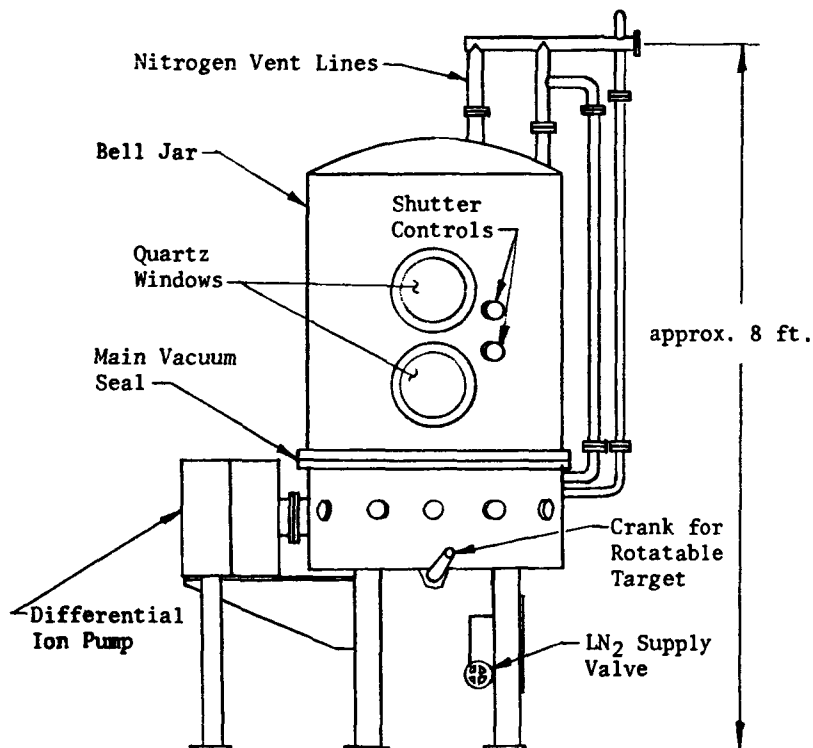


Fig. 2 - Thermal Vacuum Test Chamber

107 1-10241

PRECEDING PAGE BLANK NOT FILMED

Paper No. 10

A TEST FACILITY FOR 6000 HOUR LIFE TEST OF A 30 CM MERCURY ION THRUSTER

J. J. Caldwell, *Hughes Aircraft Company, Space Simulation
Laboratory, Space and Communications Group,
El Segundo, California*

Electrical propulsion engines for extended space missions require test periods comparable to the intended flight time in order to demonstrate satisfactory long-term performance. This is because the operation of these devices is typically optimized at some specific design point, and hence accelerated testing during a life test is not possible. The facility must provide an adequate environment for the thruster with maximum reliability at minimum initial and operating cost.

Some features of the test facility can be made to adequately simulate the ultimate space environment. Those which cannot must be controlled to the extent that damage to the thruster is prevented and thruster performance is not degraded or obscured.

In 6000 hours a 30 cm mercury ion thruster operating at 1.5 amperes ejects approximately 78 kg of propellant which will erode a significant amount of collector material. Accordingly, collector design must consider durability, contamination of the thruster or facility by erosion products, and dissipation of beam power. A frozen mercury collector was chosen because 1) erosion products are compatible with the thruster, 2) beam power is readily dissipated, and 3) eroded mercury which collects on shroud walls can be returned to the collector by warming the shrouds, thereby providing the required durability.

The thruster was mounted at the top of a vertical axis space chamber with the ion beam projecting downward 160 inches into a liquid nitrogen cooled collector which is 100 inches in diameter containing 2120 kg of mercury. Two cylindrical liquid nitrogen cooled shrouds are provided between thruster and collector to ensure that the ion beam can see only mercury covered surfaces.

Three view ports and two axis adjustable internal lighting have been provided to permit viewing and photographing of collector, shrouds, and thruster for assessing erosion, beam profile estimation, etc. Beam density distribution at two positions on the axis can be measured by the probes inserted through glands. Propellant and neutralizer mercury flow metering is accomplished by a weighing system.

The life test facility is provided with chamber operation, thruster operation, and personnel safety detection monitoring equipment which permits unattended operation. Any malfunction of the facility is indicated at a 24 hour guard station by a two digit number which identifies the difficulty and action required to correct the malfunction.

Thruster operating parameters are measured hourly by an automatic data collection system which may be locally or remotely interrogated for stored or real time data. A computer program for automatic operational parameter scanning and data acquisition is being implemented.

**COMPUTER SIMULATION OF TEMPERATURES ON THE
CENTAUR STANDARD SHROUD DURING HEATED
JETTISON TESTS**

Joseph A. Hemminger, *Lewis Research Center, Sandusky, Ohio*

ABSTRACT

In anticipation of a series of heated jettison tests to be conducted on the Centaur Standard Shroud at the NASA Plum Brook Station's Space Power Facility, a heating fixture was built to provide a simulation of the heating and environment encountered by the Centaur Standard Shroud during its ascent through the earth's atmosphere. A computer program was developed to provide a means of determining the overall temperature profile of a free-skin model of the Centaur Standard Shroud during the heating portion of the heated jettison tests. The program is unique in that it treats the energy contribution of each lamp on the heater to various points on the Centaur Standard Shroud surface. The analytic model was verified by adapting the computer program to the configuration of the hardware used in a series of Intermediate Scale Tests performed on a 2.4 meters by 2.4 meters section of the Centaur Standard Shroud corrugated structure. A comparison of some predicted versus experimental results from these tests is presented.

INTRODUCTION

A series of heated jettison tests on the Centaur Standard Shroud (CSS) is being planned for the fall of 1973 at the NASA Plum Brook Station's Space Power Facility (SPF). The CSS is to be heated during these tests using an infrared lamp heating fixture and in an air pressure environment of about 2700 newton/m² or 20 torr (equivalent to approximately 20,700 meters or 68,000 ft altitude). At the conclusion of the heating cycle, the heater halves are to be retracted and the CSS Super-Zip explosive seams and hinge spring system are to jettison the CSS halves into catchnets. During the jettison, high speed motion picture cameras will record the movements of the shroud.

One of the primary purposes for performing these tests at SPF is to provide data to be used in the verification of thermal and mechanical analytical models being developed at Lockheed Missiles and Space Company (LMSC), the designer and builder of

the CSS. The steps in the verification and use of these models are as follows: (1) Using the thermal data from the CSS tests, one analytical model will be developed and used to define the temperature distribution throughout the CSS structure. (2) The temperature distribution defined by the thermal model will be used in another model to define thermal stresses during the heating phase of the tests and subsequent motions of the CSS during jettison. Strain gauges, accelerometers, cameras, and other instrumentation will provide data for use in verifying this model. Some anticipated motion modes include a hot-dogging or banana effect (because of the unequally distributed thermal stresses) during heating of the CSS, and flapping and twisting motions during jettison. (3) Finally, these models will be used to reliably predict CSS motions during jettison with heating profiles encountered in other possible flight trajectories and to determine whether the CSS structure will impact any flight experimental package envelopes (such as the Mars Viking mission payload).

In support of the above program, test equipment designers determined that a means was required to predict what the actual heating profile would be on the CSS during these tests. A free-skin model of the CSS/heater system was incorporated into a computer program to carry out this function. The reasons for this choice can be summarized as follows: (1) The size of the CSS/heater system and the fact that the thermal response over the CSS surface varies continuously throughout the 4-minute test cycle makes the dimensions of the problem much too large to handle without the aid of a computer. (2) In designing the test configuration, it was necessary to provide a basically radiation simulation of the convection heating encountered during a flight trajectory. Because it is impossible to exactly simulate convection heating with a radiation heat source, it was desirable to provide the means to determine how much the actual temperature profile during the heated jettison tests would deviate from the anticipated trajectory heating profile. (3) End effects in the CSS/heater system were not taken into account in the heater design, except for providing reflectors to prevent radiation losses. It was therefore also desirable to know how much the temperatures at these points would vary from the design condition.

SCOPE OF THE PROBLEM

The scope of the problem can be seen from a brief consideration of test hardware, configuration, and requirements.

Centaur Standard Shroud

The overall dimensions (in inches) of the CSS is shown in figure 1. The thermal analysis is complicated by the existence of multiple surfaces (eight), different materials (aluminum and

and magnesium alloys), also indicated in figure 1. The skin is riveted to a frame consisting primarily of Z-shaped aluminum circumferential rings spaced at 38.1-centimeter intervals along the CSS axis. Additional structural elements include field joint rings at the various CSS surface intersections and the special Super-Zip explosive seams which split the CSS into two halves at jettison.

Centaur Standard Shroud Heater

The CSS heater, illustrated in figures 2 and 3, consists of an aluminum I-beam frame covered with a 0.305 centimeter polished and anodized aluminum reflector material. General Electric 1000-watt infrared quartz lamps (5910 on the full sized heater, 388 on the Intermediate Scale Tests' heater) are mounted on anodized bus bars attached to the reflector surfaces. The bus bars are mounted on the lamp side of the reflector surfaces to minimize potential arcing problems at the electrical penetrations of the reflector surfaces. The lamps are divided into 18 separate heating zones, 11 on the cylindrical section and seven on the conic sections of the heater. Each zone consists of two equally-sized and symmetrically-located halves. These heating zones run parallel to the CSS axis and are distributed circumferentially as shown in figures 4 and 5. Separate controllers provide power to the lamps in each heating zone.

Power Controllers

Power to the lamps in each heating zone originates from a three-phase, 416-volt supply and is varied using a specially designed Zee Power Control System. The signal from a thermocouple mounted on the Z-ring side of the shroud skin midway between Z-rings is used as one input to the power controller. The output from a rotating drum programmer device, on which the desired temperature response is scribed (a sample control temperature history is shown in fig. 6), is the other input to the power controller. The difference from these input signals is used to vary power by varying the portion of the a.c. voltage cycle, through the use of silicon-controlled-rectifiers (SCR's), during which current is provided to the lamps on the heater. The power history of each controller is recorded on the XDS 930 data acquisition computer and is necessary input for the temperature prediction program.

Control and Abort System

During the heating portion of the tests, a set of two thermocouples mounted adjacent to control thermocouples and another set in similar position in the second half of the control zone are monitored. The temperatures read from each of these pairs are compared with curve fits of the respective temperature control curves. These comparisons are performed in

the main component of the Test Control and Abort System, a PDP8E minicomputer. If the control temperature, as represented by a pair of thermocouples previously noted, deviates from the desired control temperature by predetermined limits, the test is automatically terminated. Both thermocouples in a pair must be out of limits in a half-zone before a test abort will occur.

Data Acquisition System

The same thermocouple pairs mounted in the Control and Abort System are also monitored, and compared with control temperature history curve fits, by the XDS930 computer used at SPF for data acquisition. Alarms are provided in this system again when both thermocouples in the monitored pairs deviate from their predetermined limits, allowing this system to be used for backup control and abort purposes.

Approximately 300 total temperatures, as well as signals from other instrumentation sources, are recorded by the XDS930 computer. The data from this instrumentation is available in engineering units soon after the completion of a test for test evaluation purposes.

Test Configuration and Requirements

The overall test configuration is shown in figures 2 and 3. The CSS/heater system is located in the 30.5-meters diameter by 36.6-meters high space simulation chamber at the Space Power Facility. The spacing between the heater reflector and the CSS outer surface is approximately 30.5 centimeters and the lamps are placed approximately 7.6 centimeters from the reflector surfaces.

A typical test heating cycle (based on time from liftoff to CSS jettison) is 280 seconds. The predicted trajectory temperature profile varies both circumferentially and axially over the CSS surface and with time. Typical circumferential and axial profiles are shown in figures 7 and 8. The actual heater design provided for a flat temperature distribution over each CSS section axially and over each half-zone circumferentially. The actual temperature distribution will be influenced by end effects between these heating areas. The circumferential location of the maximum temperature, which occurs on the windward side of the CSS during flight, will be skewed from the separation joint plane in the first heated jettison test (nominally by 32°) and aligned with it the second test, as illustrated in figure 9. The zone configuration for these tests is shown in figures 4 and 5.

METHOD OF APPROACH TO PROBLEM

During the original consideration of the problem of analyzing heater operation, a literature search was conducted in an attempt to find analytic tools that had already been developed which could be applied to the test configuration. No references were found concerning programs or documents which could function as the necessary analytic tools. The basic missing item concerned the treatment of heat output from individual lamps in a radiant heating system. This was considered to be a significant requirement because of the energy input discontinuities at surface intersections on the CSS (as illustrated in fig. 8) and was the primary consideration in the decision to develop a new computer program to handle the problem.

In reviewing the literature concerning radiant heater systems, the conceptual requirements for the program were defined. This resulted in a number of assumptions that were made to fit the anticipated test configuration. The thermal model used in the program was designed around these assumptions, which in summation include the following: (1) Because of the difficulty in analyzing the lamp filament and envelope as cylindrically-shaped heat sources, the decision was made to treat the 25.4-centimeters long filament/envelope combination as a string of ten-point sources. (2) The reflection of lamp radiation off the aluminum reflector sheets was treated as totally specular in nature. This permitted treatment of lamp reflections as an additional series of point sources, reduced in intensity by the amount of energy absorbed by the reflectors. (3) The reflector surfaces were treated as diffuse emitters and were treated as diffuse absorbers of radiation from low-temperature sources. (4) CSS surfaces, which are covered with a radiation-absorbing coating, were treated as both diffuse emitters and diffuse absorbers. (5) The CSS corrugated skin was treated as a single layer of material with an effective skin thickness. This approach produced consistent results in early LMSC development work. It also permitted future modifications by adding an appropriate nodal network to improve prediction results, if so desired. (6) The thermal model used is a free-skin model, that is, energy absorption by internal structural elements is not treated. This approach was used because the principal purpose of the program was to verify that the correct energy input distribution was being provided over the CSS. Comparison of predictions with early test data showed that the effect of structural elements on the CSS skin at points farthest removed from these structures was minimal and, therefore, the temperatures at these points were comparable to having a shroud with no internal structure. (7) Circumferential and axial heat conduction through the skin was treated as being negligible because of the comparatively low anticipated temperature differential per unit circumferential

length and because of the thin skin thickness. (8) Convection effects, which exist to a minor degree in the 2700 newtons per square meter test environment, were not included in the program. To do so would require a more extensive nodal system and does not appear to be required based on test results.

DESCRIPTION OF COMPUTER PROGRAM

The basic structure of the computer program consists of two primary parts. The first section of the program is setup to define the basic CSS/heater configuration. The coordinates of the centers of each lamp filament increment, and all of its reflections (including those in the end reflectors), are defined. These coordinates are used to calculate unit heat fluxes, similar in concept to geometric view factors, at various points on the CSS surface. These unit heat fluxes (in units of 1/inch²) are defined by the following equation:

$$F = \frac{(\cos \theta)}{4\pi} \times \frac{R_L \cos(\theta_L - \theta_S) - R_S + (Z_L - Z_S) \tan \theta}{\left[R_L^2 + R_S^2 - 2R_L R_S \cos(\theta_L - \theta_S) + (Z_L - Z_S)^2 \right]^{3/2}}$$

where R_L, θ_L, Z_L are lamp increment cylindrical coordinates

R_S, θ_S, Z_S are CSS point cylindrical coordinates

and θ is angle of a conic surface with its axis

These unit fluxes are summed for all lamp increments of a similar degree of reflection and multiplied by a factor representing the energy output per lamp filament increment length. This factor is based on the power being applied to all the lamps in a given heating zone. The resultant overall sum provides an incident heat flux from the lamps and reflections to the point being considered on the CSS, in units of Btu/sec-ft².

The second section of the program makes use of the incident heat flux at a CSS point determined in the first section. This section of the program defines an energy balance in the system. Radiation losses from the shroud to the reflector are calculated, based on local CSS and reflector temperatures. Incident lamp energy on the reflector surfaces is approximated based on the calculated incident heat flux on the CSS. Finally, net heat inputs to both the CSS and the reflector at a given CSS surface normal are calculated and are used to define the temperatures at these points, taking into account the thermal capacity of the skin per unit area.

In summary, the thermal model used in the program is three-dimensional from a radiation heat transfer viewpoint but only one-dimensional in considering CSS conduction through the skin. This free-skin model permits a fairly accurate representation of the actual thermal profile over the CSS surface. The program can be used to consider a large number of points over the CSS surface, thereby providing a temperature mapping, or can look at a limited number of points, such as thermocouple locations, and compare the predicted with experimental results.

VERIFICATION OF THE ANALYTIC MODELS

The computer program was adapted to the configuration of the hardware used in a series of Intermediate Scale Tests (IST's) performed at SPF. Temperatures were predicted on the corrugated skin panel used in these tests and were compared with the experimental data.

Centaur Standard Shroud Intermediate-Scale Tests Configuration

The configuration of the IST's was designed to as closely approximate the heated portion of the CSS heated jettison tests as was possible with the test hardware being used. The target heated test panel consisted of a 2.4-meters by 2.4-meters corrugated panel structure, in all respects similar to the hardware used on the upper portion of the cylindrical surface of the CSS. The panel was enlarged using sections of single-thickness aluminum, the thickness being equivalent to the effective thickness* of the corrugated skin as used in the thermal model. Enlarging the test panel area was required to make the heater of sufficient size to be able to test a single power controller at its full 360-kilowatt power capability. The same insulation used internally on the CSS covered the Z-ring side of the IST test panel, in order to minimize surface heat losses from that side of the panel.

The heater consisted of a similar cylindrical section as the CSS test panel, all hardware being the same as configured in the full-scale heater. Circumferentially, the heater included eight half zones. Because the heater was powered with only either one or two controllers, the lamp distribution varied circumferentially in order to obtain a circumferential temperature distribution.

Fifty-three test runs were performed on the CSS IST hardware. These tests were run in three air environments: (1) 101,300 newtons per square meter or normal atmospheric pressure;

*The effective skin thickness used in the design was incorrect, resulting in higher than anticipated temperatures on these "dummy" test panel sections.

(2) 2700 newtons per square meter, the anticipated full-scale test environment; and (3) 0.007 newtons per square meter, or hard vacuum. The lamps were powered with either a single controller supplying all eight heating zones or each of two controllers supplying four heating zones. The control temperature profiles consisted of either a typical LMSC flight trajectory temperature history, or a "square wave", which tested the controller at full power until the control temperature reached the plateau temperature.

Comparison of Predicted and Experimental Temperatures

The Intermediate-Scale Tests version of the computer program predicted temperatures at thermocouple locations and compared these predictions directly with experimental data. A sample of the results of this comparison is shown graphically in figure 10. Overall, comparing the experimental data with predicted results showed maximum deviations of the order of ± 17 degrees Celsius. This deviation usually peaked near the end of the 4-minute test cycle, which involved a temperature rise from ambient (21 degrees C) to temperatures of the order of 215 degrees Celsius on the CSS test panel.

Further studies are being made for conditions which might be influencing the temperature predictions. For example, one that has been discovered but which at the time of this writing has not been accounted for in the CSS IST model, concerns lamp power levels. The IST heater lamp configuration was such that the number of lamps could not be divided equally among the three-phase power source. The result was that individual lamp energy output varied somewhat in proportion to this load imbalance.

CONCLUSIONS

In general, it appears that the effectiveness of the thermal model used in the developed computer program has been proven in its adaptation to the CSS IST configuration. Efforts are continuing to improve the accuracy of the thermal model, prior to and during the actual heated jettison tests by: (1) increasing the number of nodes considered at a given area of the CSS, and (2) investigating the significance of heat transfer modes and paths other than those considered in the model.

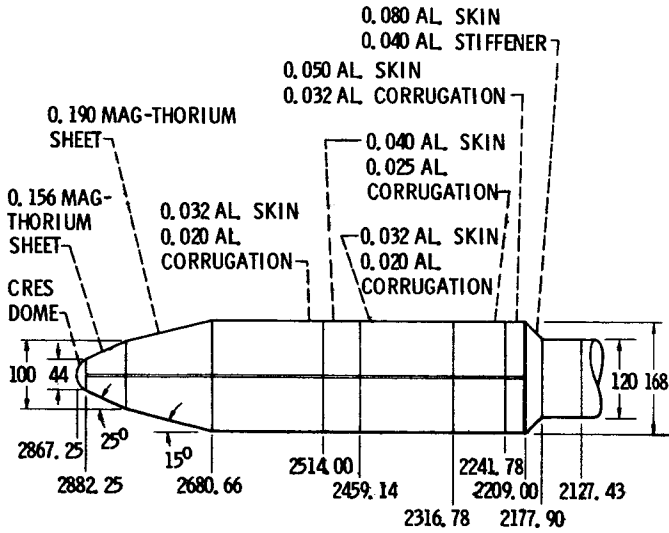


Figure 1 - Structural configuration.

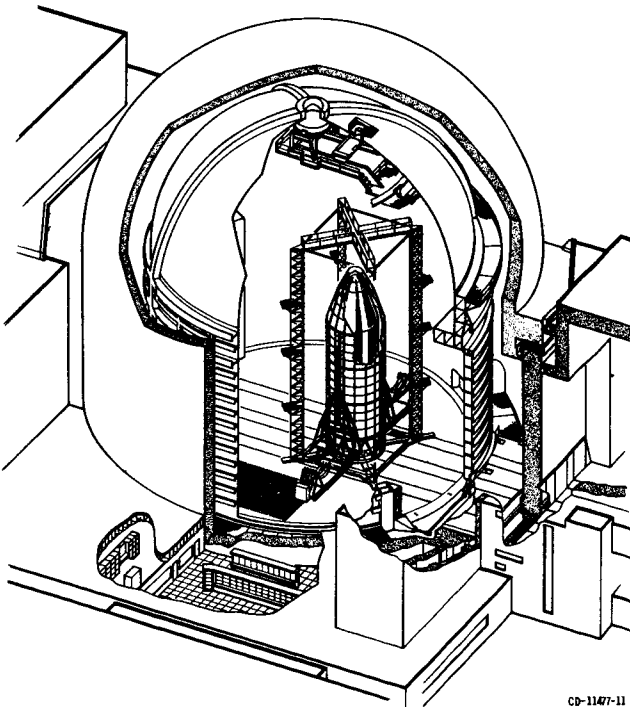


Figure 2 - Centaur standard shroud in space power facility.

CP-1147-11

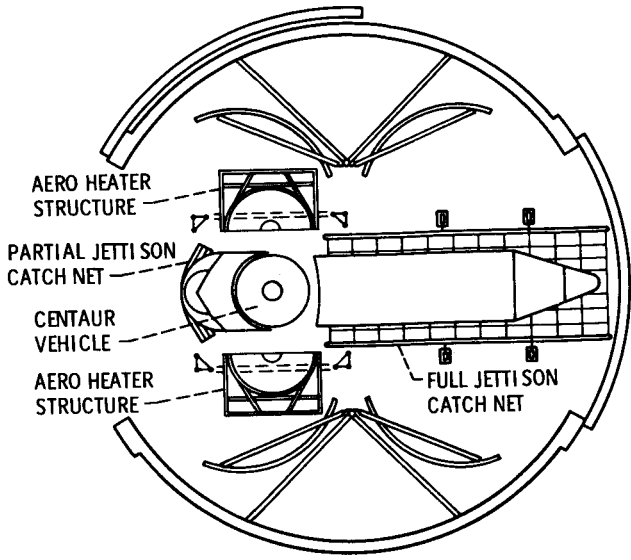


Figure 3 - Space power facility Centaur heated shroud jettison test.

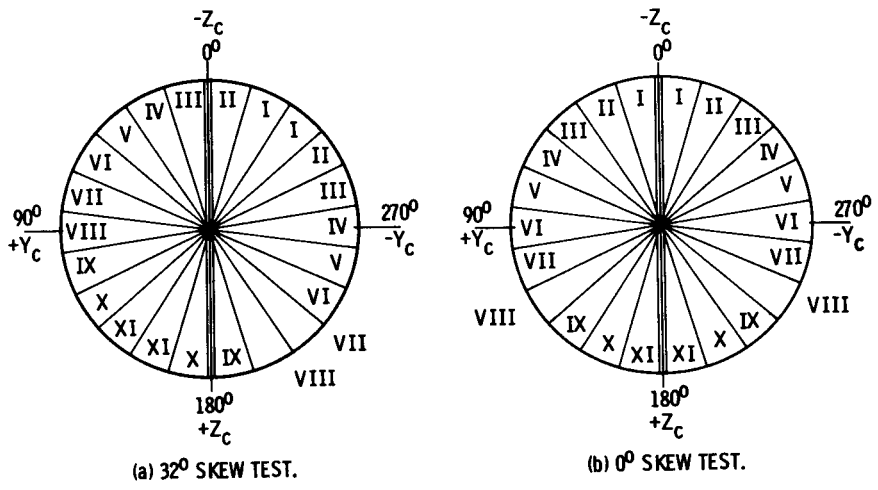


Figure 4 - CSS cylinder control zones.

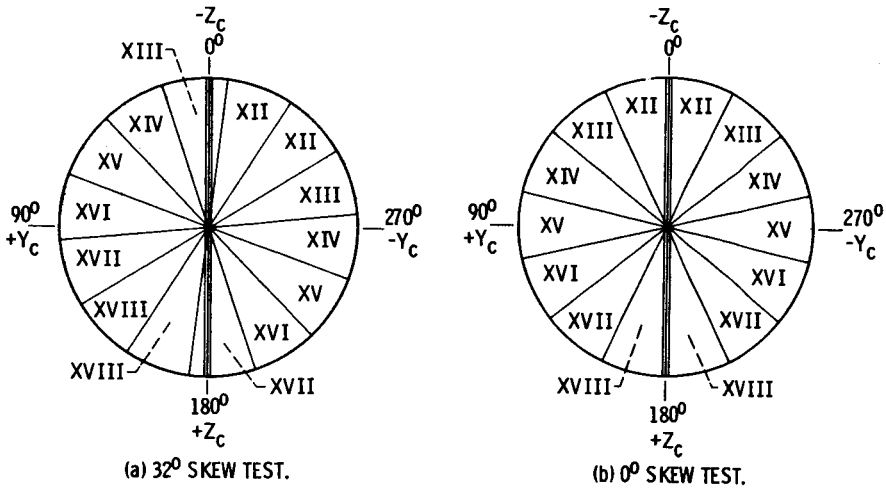


Figure 5. - CSS conic control zones.

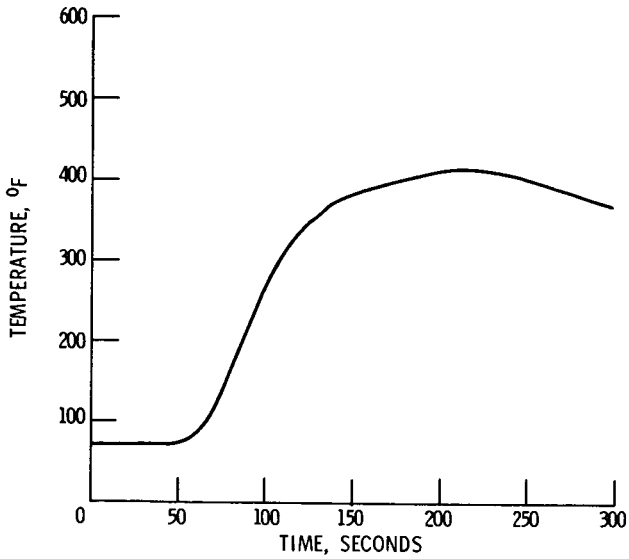


Figure 6. - CSS cylinder control zone 1 at leading edge (RH758B).

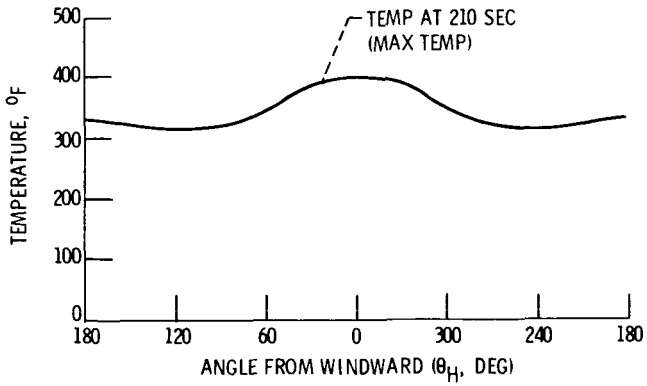


Figure 7. - Free skin circumferential shroud temperature distribution predictions for cylinder leading edge (RH758B).

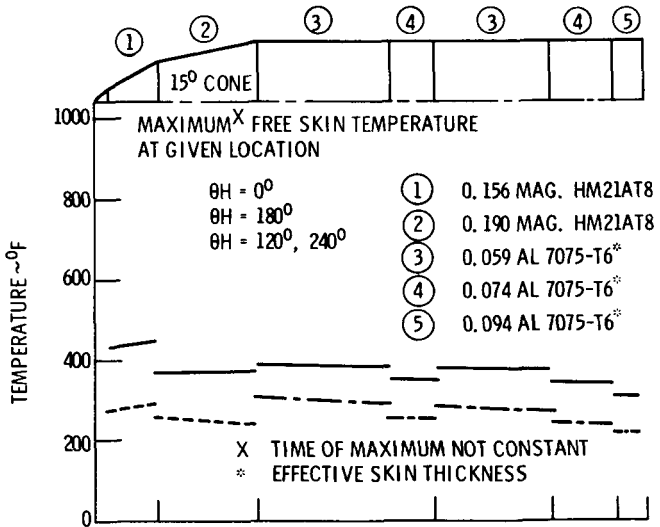
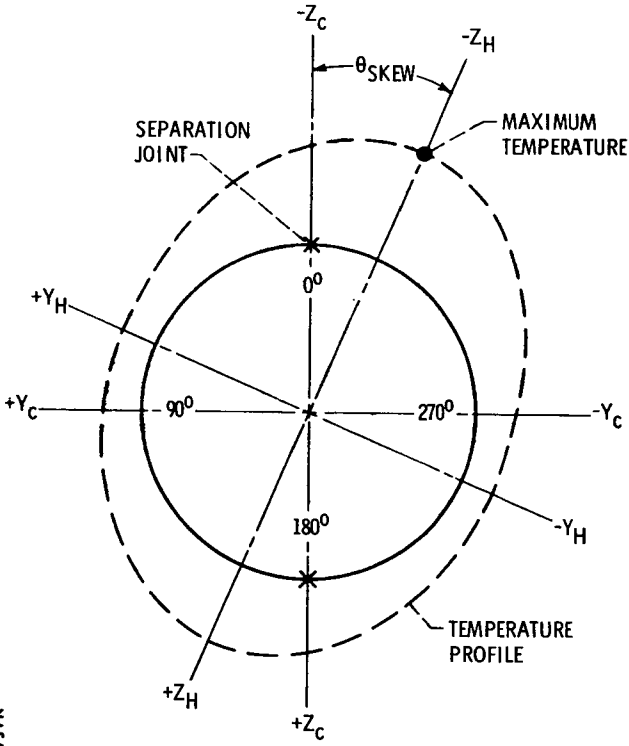


Figure 8. - Free skin axial shroud temperature distribution prediction (RH758B).



NASA-Lewis

Figure 9. - Skewed temperature distribution on cylinder.

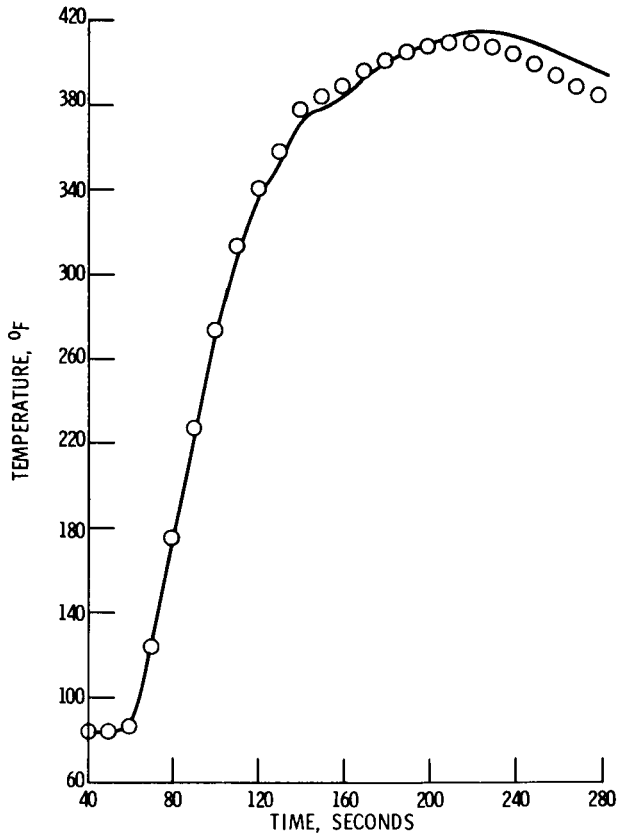


Figure 10. - CSS intermediate scale tests. Run, 41; thermocouple, 11; predicted temperature response and experimental data shown as functions of time.

**INFRARED SIMULATION AND THERMO-VACUUM FACILITY -
ISA/TVA**

H. J. Kurscheid, *Gesellschaft für Weltraumforschung mbH*
within DFVLR +)

ABSTRACTS

A test facility was designed in which the shroud temperature can be continuously varied between 100°K and 363°K by using gaseous nitrogen.

Introduction

The designation "Infrared Simulation and Thermo-Vacuum facility" is misleading, because the infrared radiation is in most cases not produced by the facility itself, but by devices designed specifically for each test specimen.

By the time the test requirements were specified, there remained little time available for preparation of the facility. An available vacuum chamber, previously used for the third stage of the ELDO II launcher, was modified by the addition of a shroud and a thermal system. The vacuum system was improved by the addition of oil-free high-vacuum pumps.

Test Facility Requirements

The HELIOS test requirements for the facility are tabulated in Fig. 2. Two different test methods had to be considered - heater tapes and canister - requiring an uneven heat flux distribution over the shroud. When heater tapes are used, with a shroud temperature of 100°K , the middle section must absorb 25 kw and the upper and lower sections 7.5 kw each. For economical reasons (lower L-N_2 consumption), the option of operating at room temperature that portion of the shroud adjacent to the canister has been provided for.

+) Deutsche Forschungs- und Versuchsanstalt für Luft- und Raumfahrt e.V., Porz-Wahn, Fed. Rep. Germany
(German Research and Experiment Agency for Aerospace Technology)

The thermal system was designed to allow thermo-vacuum testing from 203°K to 363°K, because no other facility for testing the full-size HELIOS models is available.

For economical reasons one single-phase thermal system using gaseous nitrogen was chosen instead of a two-phase system or one using two cooling fluids; it could be more quickly constructed. The system was built in 14 months - technical problems were reduced by using one refrigeration fluid.

A clean vacuum, less than 1×10^{-5} torr during heating of the test specimen, and as free as possible from hydrocarbons, must be guaranteed to protect the extremely sensitive HELIOS experiments.

F a c i l i t y S y s t e m s

Thermal System

The thermal system consists of two parallel circuits that can be independently controlled (Fig. 3). One circuit cools the middle shroud section and is capable of absorbing 25 kw at 100°K. The other circuit cools the top and bottom sections, capable of absorbing 7.5 kw each. This load distribution was chosen to accommodate the planned specimen mounting position, using the heater tape method mentioned previously.

The refrigeration fluid is gaseous nitrogen, circulated by a Roots blower. The heat of compression is mostly dissipated by the water-cooled blower jacket and the subsequent gas chiller. From there the gas passes through a large counter-flow heat exchanger, where it is cooled to about 109°K by the gas returning from the shroud. Next, in the injection cooling chamber, the gas is cooled to 95°K by a spray of liquid nitrogen. Before the gas reaches the shroud, it passes through an electric heater which is turned on for chamber warm-up or tests over room temperature. In the shroud the gas absorbs heat and is returned to the blower, after bleeding to atmosphere an amount equivalent to that injected. The efficiency of the single-phase system is mostly determined by the efficiency of the large heat exchanger, which allows the gas temperature to jump from 109°K to 285°K. In addition to the enthalpy of L-N₂ vaporization, the enthalpy difference between the temperature of vaporization and the temperature at which the gas leaves the system (285°K) contributes to the system efficiency. The high temperature of the gas input (285°K) allows the use of ordinary high-capacity Roots blowers. Also the relatively high friction losses associated with gas blowers can be dissipated by water cooling. Variation of the injection rate and turning on the heater allows adjustment of

the shroud temperature to any value between 100°K and 363°K .

To reach the required temperature of $100^{\circ}\text{K} \pm 7,5^{\circ}\text{K}$ under 40 kw load, 20,120 kg/h of gas must be circulated. This high flow rate requires large pipe cross-sections, achieved with special profiles (Fig. 4).

The top section of the shroud (chamber lid) is a double spiral using counterflow to achieve the most even temperature distribution. The cylindrical section is built up of rings with single or double feed according to load. Because of the vacuum pumps on the chamber floor, the floor shroud is constructed as a baffle to increase its conductivity.

The temperature control system is worth mentioning, because of its simplicity.

The gas temperature is maintained at the chosen value by a TIC regulator (1), which controls the injection rate.

The pressure difference between shroud input and output is held constant by a PIC regulator (2), which controls a by-pass (3).

To compensate for load variations in the 9 sections of the shroud, output valves for each section (4) can vary the flow. These valves are manually operated from the control room. A third regulator (5) maintains a constant pressure in the system by controlling the bleeder.

The Roots blowers are endangered at temperatures below 273°K . A by-pass (6) between blower output and input can be activated to raise the input temperature; this is only needed when shroud temperature is changed. At lower heat loads, the thermal system can be driven by one blower only (Fig. 3).

The control system is a compromise between automatic and manual operation. The operating point is set manually and held constant by the automatic regulators. The system is simple enough to be operated by two persons; experience has shown that the system is exceptionally trouble-free.

Vacuum System

The unmodified chamber already had a pump system consisting of two mechanical backing pumps and two oil diffusion pumps.

Two additional oil-free high vacuum pumps were installed because surface contamination, especially of the flight unit, is a great danger to the success of the HELIOS mission. They are: a titanium sublimation pump with a high pumping rate, and an ion getter pump which evacuates chiefly the noble gases.

In operation, the oil diffusion pumps are used for pre-

evacuation until a high vacuum is reached at which the titanium sublimation pump and the ion getter pump can function; at this point, the valves between the diffusion pumps and the chamber are closed, and the oil-free high-vacuum pumps take over.

The construction of the high vacuum system is shown in Fig. 6. Ten titanium melting crucibles, in which the metal is vaporized by electron bombardment, are located in the bottom flange of the chamber. The vaporized metal condenses onto the adjacent L-N₂-cooled pump surface. A pumping rate of about 200,000 l/sec is achieved at a pressure of less than 10^{-6} torr.

The ion getter pump consists of 28 elements with a pumping rate of 110 l/sec for each element.

The pumps are mounted on the chamber floor because there the operation is most effective.

Performance and Consumption Data

The operational costs are mostly due to consumption, chiefly if liquid nitrogen.

About 5000 kg of L-N₂ are required to cool the chamber from room temperature to 100°K. Steady operation at this temperature uses about 950 kg/h of L-N₂ at 4 kw heat load, and about 1450 kg/h at 40 kw load. At 203°K and 3 kw load the L-N₂ consumption is about 600 kg/h. To raise the temperature from 203°K to 363°K requires 2.5 hours.

The electrical energy consumption lies between 350 kw and 450 kw. At maximum heat load (40 kw), 20,120 kg/h of gas is circulated.

It is difficult to name a consumption figure for titanium sublimation pump because it is highly dependent upon the gas load. This load in turn is caused by leakage and outgasing from the shroud and the specimen; the order of magnitude of these quantities is difficult to establish. The maximum condensation rate is 14 grams per hour. Two kilograms of titanium are available in the ten melting crucibles, of which a maximum of 800 grams can be vaporized.

Specimen Handling

The configuration of the chamber requires that the test specimen be inserted from the top. For this purpose, the chamber lid with the upper shroud section is lifted. The specimen is installed with an adapter on a supporting framework (spider). This assembly is then lowered, using a lifting

device, onto the three mounting posts. After the specimen is in place, the lifting device is removed. The chamber has also been modified so that the specimen can be suspended therein (Fig. 7).

Operational Practice

The test facility has been operated for 1500 hours without problems, and the personnel training time was only a few days.

Test results show, however, that the shroud absorption coefficient of about 90 % is insufficient for tests on the HELIOS thermal model. The reasons for this, and the correctional steps taken, will be explained in a separate presentation.

Fig. 1
INFRARED-SIMULATION- AND THERMAL-VACUUM-FACILITY

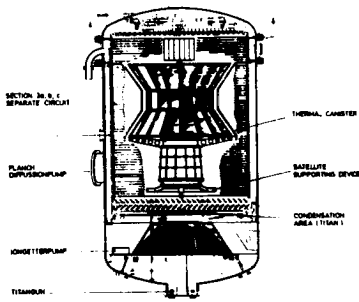


Fig. 4
ISA/TVA SHROUD ELEMENTS

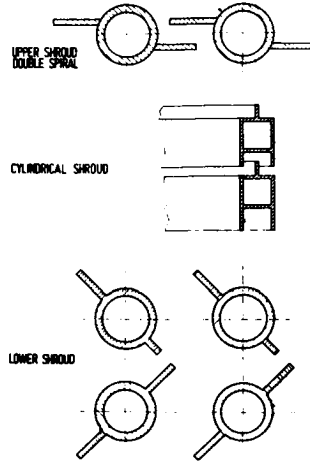


Fig. 2

HELIOS REQUIREMENTS FOR TEST FACILITY

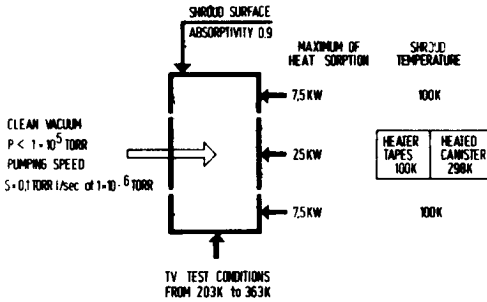


FIG 3 THERMAL SYSTEM

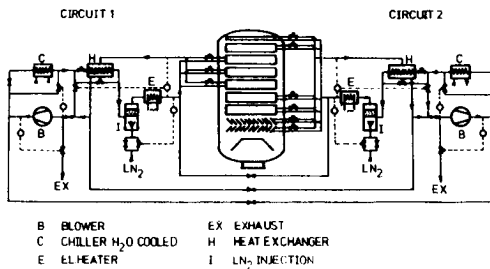


FIG. 5 ISA/TVA THERMAL SYSTEM CONTROL

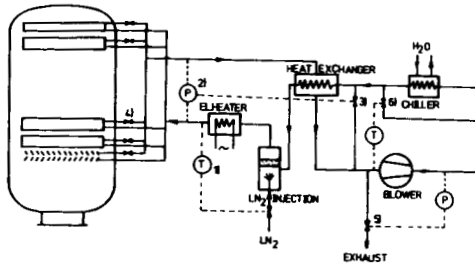
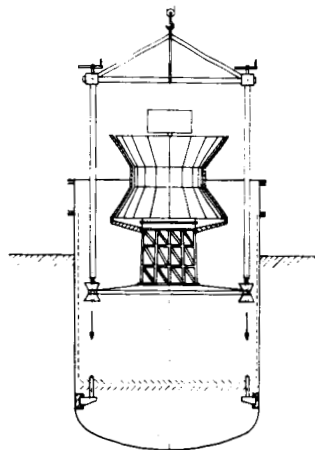
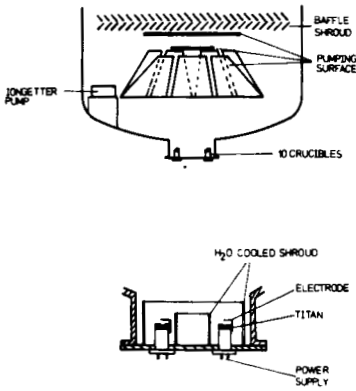


FIG. 7 HANDLING OF THE SPACECRAFT

FIG. 6 HIGH VACUUM SYSTEM



N74-10294

PRECEDING PAGE BLANK NOT FILMED

Paper No. 13

COMPARATIVE EVALUATION OF PREDICTED AND MEASURED PERFORMANCE OF A 68m³ TRUNCATED REVERBERANT NOISE CHAMBER

H. D. Cyphers, A. N. Munson and F. J. On; *Goddard Space Flight Center, Greenbelt, Maryland*

ABSTRACT

The performance of a medium size, truncated reverberation chamber is evaluated in detail. Chamber performance parameters are predicted, using classical acoustic theory, and compared with results from actual chamber measurements. Discrepancies are discussed in relation to several available empirical corrections developed by other researchers. Of more practical interest is the confirmation of a recent theory stating that the present rule of thumb for the ratio of specimen volume to test chamber volume, approximately ten percent, is overly conservative and can be increased by a factor of at least two and possibly three. Results and theoretical justification of these findings are presented.

INTRODUCTION

This paper details the results of an evaluation of the acoustic field produced within a new reverberation chamber constructed by the Structural Dynamics Branch at Goddard Space Flight Center. The chamber, with a total volume of 68m³ (2,400 ft.³), was constructed to provide a means of experimentally verifying the results of theoretical studies in the areas of noise field prediction and the effects of various sized test volumes on the acoustic field. In addition, the chamber is frequently used to test small scientific spacecraft and experiments.

At the completion of the empty evaluation and prior to beginning a series of tests using various test volume sizes, a requirement to acoustically test the German Helios spacecraft developed. This space-

craft, with an enclosed volume of approximately 14m^3 or 20% of the chamber volume, afforded an opportunity to obtain additional data on the effects of exceeding the 10:1 rule-of-thumb ratio for chamber to test volume. The results of this test are discussed in relation to the empty chamber performance.

The development of a criteria for acceptable performance of a room as a reverberant acoustic testing facility requires several considerations. For a given room design and acoustic driver, the first important consideration is the modal density (or the modal overlap index) of the room which indicates the frequency distribution of the acoustic modes in the room. The second consideration is the spatial variations in the sound pressure levels which indicate the degree of uniformity (or nonuniformity) of the sound field in the room. Other considerations are the maximum achievable sound pressure level and the spectra shaping capability of the reverberant room.

The performance of a well designed reverberation chamber depends strongly on the modal overlap index. In the frequency regime where the modal overlap index is very much less than one, the chamber acoustic field is usually unpredictable and the spatial variations are large. In the frequency regime where the modal overlap index is of the order unity or larger, the chamber acoustic field is well defined in a statistical sense and the spatial variations are relatively small. These considerations dictate the lowest usable frequency that the chamber can be used for reverberant acoustic testing.

Accordingly, several descriptors are commonly used to specify the performance of reverberation chambers. The most important of these are: the lowest usable test frequency and the ability to match the required spectra shapes and levels of vehicle specifications. In evaluating these characteristics, the following properties of the reverberation room were determined: reverberation time (or effective absorption), modal density (or modal overlap) and spatial variation of the sound pressure field. Each of these areas will be addressed in detail in the Test Results and Discussion section of this paper.

DESCRIPTION OF TEST FACILITY/SETUP

Figure 1 is an isometric view of the reverberation noise test facility. The chamber is rectangular in shape with two walls bisected in the vertical plane to conform to the space available. The practicability of this design was verified by a series of modal studies (Reference 1). The maximum orthogonal dimensions are in the ratio 1.00:0.79:0.63 suggested by Sepmeyer (Reference 2) for good chamber performance.

The acoustic excitation to the reverberant chamber is supplied by a 60 Hz exponential horn which can be driven by either a Noraircoustic Mark V (50 Kw) or a Ling EPT-94B (4 Kw) air modulated acoustic driver.

The control and data collection system consists of standard, laboratory-quality equipment. Spectrum shaping and control is done on a one-third octave basis in real time. A multi-channel microphone averager¹ is used to assure that the control signal is a good representation of the noise field.

All offline data analyses were done using the power spectral density, one-third octave band and coherence algorithms of the Goddard dynamic data-analysis computer program (DYVAN). This program is designed to handle sinusoidal-sweep, shock transient, or stationary random data.

In the experimental evaluation of the chamber performance descriptors, careful selection of microphone locations was required to accurately measure the acoustic field in the chamber. As the sound pressure levels in the chamber are higher nearer the walls, corners and edges than throughout the rest of the room, all microphones were placed at least $3/4\lambda$ away from the corners and edges of the chamber and at least $\lambda/4$ from the walls where λ is the wavelength of the lowest frequency of interest.

In addition to observing boundary conditions in locating microphones, the positions of the microphones relative to each other was selected, in the case of the empty chamber evaluation, to provide maximum

¹The use of multi-channel averaging control insures that the control sound pressure level will approach the average SPL over the test volume; i.e., the control SPL is centered within the inherent spatial variation of the chamber.

statistical independence (coherence approaching zero). This is desired in evaluating spatial variation of the noise field.

For the occupied chamber data, the microphone positions specified by the Helios test procedure were used. Boundary conditions were not satisfied as in the empty chamber evaluation due to the size of the spacecraft. Figure 2 shows the Helios spacecraft assembled in the chamber. Figure 3 shows the locations of the control and monitoring microphones.

The worst case coherence results, based on data from the empty and occupied chamber acoustic tests, are presented in Figure 4 to indicate the approximate degree of statistical independence of the microphone outputs actually achieved via the use of these microphone locations.

The theoretical plot of Figure 4 was computed from

$$C_{AB\Delta f} = \left[\frac{\sin \frac{2\pi}{c} fr}{\frac{2\pi}{c} fr} \right]^2 \quad (1)$$

where r is distance between microphone locations, f is center frequency and c is speed of sound. In practice it is reasonable to use this equation as a standard for determining the degree of statistical independence between microphone outputs.

TEST RESULTS AND DISCUSSION

The results of the study will be categorized in terms of specific properties of the acoustic field within the reverberation chamber. Each property will be discussed briefly from a theoretical standpoint; the predicted and measured results for the chamber will then be given along with a discussion of the method used and any unusual features of the data. The operational or performance characteristics of the reverberant acoustic facility, as derived from the measured properties, will then be summarized and discussed briefly from both a theoretical and applications point of view.

The necessity of obtaining chamber performance parameters during the actual Helios test limited the ability to measure all of the desired properties. The results of adding a 20% test volume will be

discussed under the section for which it was possible to obtain measured data.

The following properties of the room were determined: the reverberation time (or effective absorption), modal density (or modal overlap) and spatial variation. The most important operational characteristics from a user's standpoint are: the lowest usable frequency and the ability to match the required spectra shapes and levels of vehicle specifications.

Reverberation Time (Effective Absorption)

The reverberation time for a given frequency is the time required for the average sound pressure level, originally in a steady state, to decrease 60dB after the source has ceased. This decay is caused by absorption of the sound energy not only at the boundaries of a room, but also in the air itself.

The reverberation time is related to the total effective absorption of the reverberant room by Sabine's equation (Reference 3):

$$T_{60} = \frac{60V}{1.085c(a+4mV)}. \quad (2)$$

where T_{60} = reverberation time in seconds

V = volume of room in cubic meters

c = speed of sound in meters per second

a = number of metric absorption units in square meters

m = energy attenuation constant in meters
 $\times 10^{-1}$

The term, $a+4mV$, is the total effective absorption where a is the absorption at the boundaries (walls) and m is the energy attenuation constant in the transmitting medium.

In the chamber evaluated, predicted effective absorption losses were computed utilizing model

study data.

Figure 5 is a plot of the predicted and measured reverberation times. The times plotted are the average of three measurements taken at elevations of 1.50m (5 ft.), 3.04m (10 ft.) and 4.12m (13.5 ft.) on a vertical line through the center of the chamber. Also plotted are the predicted and actual effective absorption coefficients. The actual effective absorption was calculated from Equation 2.

The measured reverberation times possess some scatter and are sometimes multivalued below approximately 400 Hz. Above 400 Hz, the reverberation times decrease smoothly with increasing frequency. The scatter at the lower frequencies is due to expected sound pressure fluctuations in an enclosure of this size. Morse and Ingard (Reference 4) discuss in detail the reasons for the multiple slope and pressure fluctuation phenomena observed in some of the reverberation data.

Several means of exciting the chamber were tried to determine the effects of various types of excitation on the reverberation time. Figure 6 is a plot of reverberation times obtained using wide band white noise and discrete frequency excitation. As expected, the discrete frequency excitation values differ significantly, especially below 400 Hz, from random noise excitation because fewer standing waves are excited at a given time. The wide band white noise excitation (with the microphone response filtered on a one-third octave basis) agrees quite closely with the previous data. Although other experimenters seem to prefer one-third octave band excitations, wide band white noise excitation can provide representative data at considerably less effort and expense.

In the scaled model study (Reference 1), absorption coefficients were calculated from actual reverberation times for both the truncated and equivalent rectangular (dimensions equal to parallel dimensions of truncated chamber) model chambers. The absorption coefficients for the two configurations were approximately the same at all frequencies. Since the above data (Figure 5) show that the calculated absorption coefficient for the Goddard 68m³ chamber agrees with that predicted using the scaled model study results, it may be assumed that the reverber-

ation times will bear the same relationship as well. That is, the predicted reverberation time of the truncated chamber is approximately 85% of the reverberation time of an "equivalent" rectangular chamber in accordance with the dependency of the reverberation time on the volume to area ratio of the two chambers. No reverberation time data was obtained for the occupied chamber condition.

Modal Density, Sine Sweep Response, Modal Overlap

The frequency response of a reverberation room is characterized by a series of discrete resonant modes. For a simple, normal rectangular room, the lowest or first of these resonant modal frequencies occurs when one-half the acoustic wave length equals the longest dimension of the room. The second resonant frequency occurs when one-half the wavelength equals the next longest dimension of the room. An entire harmonic series containing integer multiples of the fundamental axial modes exists for each of the three room axes.

At frequencies higher than those of the fundamental axial modes, more complex modes appear. These include modes associated with four walls in which the standing waves are tangential to one pair of walls, and oblique modes, which involve the interaction of standing waves between all six walls.

The aim in reverberation chamber design is to achieve a sound field within the volume which is completely diffuse in all frequency ranges of interest. This implies that there are many modes uniformly spaced in frequency and that all angles of incidence of the sound are equally probable.

The modal frequencies of a rectangular chamber can be calculated from the characteristic equation given by (Reference 5)

$$f_{m,n,p} = \frac{c}{2} \left[\left(\frac{m}{L_x}\right)^2 + \left(\frac{n}{L_y}\right)^2 + \left(\frac{p}{L_z}\right)^2 \right]^{\frac{1}{2}} \quad (3)$$

where \underline{c} is the speed of sound in air (meters/second at 20°C) and L_x , L_y , and L_z are the room dimensions in meters, \underline{m} , \underline{n} and \underline{p} are mode numbers for the X, Y and Z modes respectively and take on the integer values 0, 1, 2, 3, ... etc.

Near the fundamental frequency of the room, the effective absorption coefficient is very dependent on the number of modes, thus contributing to the nonuniformity of sound level with frequency. As an approximation, Equation 3 was used in estimating the modal frequencies of the Goddard truncated chamber. The actual data indicate that many more modes are actually excited. Extensive computation of the modal frequencies of reverberation rooms using the classical Equation 3 is tedious unless handled by computers. It is generally more significant to know the approximate number of acoustic modes that might be excited within any given bandwidth Δf (i.e., the product of modal density and bandwidth).

Modal Density [n(f)]--Modal density is the frequency distribution of the acoustic modes (the number of modes per frequency bandwidth as the bandwidth approaches zero) in the room due to the excitation of the room by a sound source. It is largely dependent on the physical dimensions of the enclosure as well as the excitation frequency.

The asymptotic modal density of a rectangular reverberation room may be computed by Equation 4 which is derived from Equation 3 (Reference 6)

$$n(f) = \frac{4\pi f^2 V}{c^3} + \frac{\pi f A}{2c^2} + \frac{P}{8c} \quad (4)$$

where \underline{P} is the length of chamber wall intersections (total length of all chamber edges), \underline{V} is volume in cubic meters, \underline{A} is surface area in square meters, \underline{c} is velocity of sound in meters/second and \underline{f} is frequency. This equation has also been shown to be applicable to this particular truncated chamber shape (Reference 1). Accordingly, the number of resonant modes of the truncated chamber in each band of frequencies Δf may be computed by

$$N_{\Delta f}(f) = n(f) \Delta f = \left(\frac{4\pi f^2 V}{c^3} + \frac{\pi f A}{2c^2} + \frac{P}{8c} \right) \Delta f \quad (5)$$

where f is center frequency of the band.

Alternatively, the cumulative resonant frequency distribution (i.e., the integral of the modal density)

$$N(f) = \int_0^f n(f) df = \frac{4}{3} \frac{\pi f^3 V}{c^3} + \frac{\pi f^2 A}{4c^2} + \frac{Pf}{8c} \quad (6)$$

may be determined for comparison with a cumulative count of the sine sweep peaks obtained by counting the number of modes excited during a sinusoidal sweep survey of the chamber.

Sine Sweep Response--In making sine sweeps, the sweep rate and direction of sweep, up or down, can influence the number of resonances excited. A sweep rate of 2 minutes per octave gave good modal definition and repeatability when sweeping from either direction.

Figure 7 is a plot of the predicted modal density $[n(f)]$, predicted cumulative resonant frequency distribution $[N(f)]$ and the predicted and measured mode counts $(N_{\Delta f})$ for each one-third octave band in the chamber. The criterion used for counting the sine sweep response peaks required that the peak-to-valley ratio, on both sides of the peak, be 3dB or more in order that the peak be counted.

The results presented in Figure 7 indicate that, for the chamber under study, Equation 5 provides a conservative prediction of the number of modes on a one-third octave band basis. Above approximately 250 Hz the resonance peak count method greatly underestimates the number of modes that actually exist. This deviation from the predicted distribution is attributed to: (1) peaks that are missed in the counting procedure when the response peaks are closely spaced in frequency, and (2) many response modes occurring within the bandwidth of a single mode. In these cases, counting the response peaks does not yield an accurate measure of the

actual number of modal resonances (Reference 7). The first cause can be minimized by using a higher paper speed to expand the frequency scale.

Also shown on Figure 7 is the measured one-third-octave band mode counts of the occupied chamber. The number of modes is seen to be considerably lower than in the empty chamber condition. This is due primarily to the way the data was taken. The data was obtained by counting the peaks in a power spectral density plot of the microphone response using a 2 Hz analysis bandwidth. The peak to valley mode height criterion used during the empty chamber sine sweep evaluation was reduced to ± 1 dB to account for the averaging effect over the 2 Hz bandwidth. Because of the relatively broad analysis bandwidth used, this method of counting modes is very conservative. Based on a criteria of a minimum of 7 modes per one-third-octave bandwidth, the chamber is usable (considering only modal density) down to 200 Hz.

Modal Overlap (M)--The modal overlap index provides a measure of the diffuseness of the noise field in a well-designed reverberation room. It is defined as the number of adjacent modes which lie inside the 3dB bandwidth of a typical chamber modal resonance. Computationally, it is the product of the 3dB bandwidth $\Delta(f)$, and the average modal density, $n(f)$:

$$M(f) = \Delta(f) n(f) \quad (7)$$

where

$$\Delta(f) = 2.2/T_{60} \quad (8)$$

The 3dB bandwidth of a typical chamber modal resonance, $\Delta(f)$, is defined by the chamber resonant Q determined from the reverberation time. It will be recalled that one-third octave band noise excitation was used in this study to establish reverberation times. The modal density, $n(f)$, as shown in Figure 7, is the average modal density for the one-third octave band of interest with center frequency f .

The product of the 3dB bandwidth, $\Delta(f)$, and the average modal density, $n(f)$, assumed constant over the bandwidth used when counting the modes, yields a figure of merit in terms of modes per chamber resonant bandwidth. This term, together with the spatial variation of sound pressure levels in the chamber, provides a means of specifying the lowest usable frequency of the chamber. Selection of an appropriate value of $M(f)$ is considered further in the section on determining the lowest usable frequency. Figure 8 shows the predicted and measured values of modal overlap. Above 250 Hz it was necessary to use predicted values for the modal overlap due to the difficulty in measuring the modal density by the peak response count method.

The modal overlap was not computed for the occupied chamber because of the lack of measured reverberation data.

Spatial Variation (S)

The degree of spatial nonuniformity (commonly termed spatial variation) of the acoustic noise levels in the reverberant chamber was determined in terms of the standard deviation, S , of sound pressure level. The deviation was computed from a sufficiently large set of uncorrelated sound pressure levels measured at specified locations in the chamber with a specific noise excitation. In Figure 8, the predicted and measured results of spatial variation for the empty and occupied reverberant chamber are presented. The empty chamber modal overlap has also been plotted in this figure to facilitate the application of the criteria for determining the lowest usable frequency of the chamber.

The measured empty chamber spatial variation results were determined from a set of seventy-two sound pressure levels, L_i , measured at specified locations. In terms of standard deviation, S , the spatial variation was computed from

$$S = \left[\frac{n \sum_{i=1}^n L_i^2 - \left(\sum_{i=1}^n L_i \right)^2}{n(n-1)} \right]^{\frac{1}{2}} \quad (9)$$

where $n=72$ is the total number of measurements in the set. This determination was repeated for each one-third octave band and is independent of the mean level, (i.e., S would not change if the experiments were repeated at a different sound pressure level), as well as independent of time since the individual sample levels, L_i , were already time-averaged quantities computed via the DYVAN program.

The spatial variation data for the occupied chamber was calculated from the seven microphones ($n=7$) used for control and monitoring during the Helios test. The statistical independence of those microphones at these locations is illustrated in Figure 4. As noted previously, some of these microphones were located within inches of the spacecraft skin and thus were subject to some boundary effects.

The spatial variation data presented in Figure 8 for the empty chamber condition indicates a deviation of approximately 0.5dB between predicted and measured values at frequencies above 500 Hz corresponding to modal overlap indices greater than 1.8. Measured values of spatial variation exceed ± 3 dB at frequencies below 160 Hz.

The spatial variation for the occupied chamber yielded the same general shape as the empty chamber results. The noted irregularities were probably due to the boundary effects. In this case, the frequency above which the measured values of spatial variation exceed ± 3 dB has shifted upward less than one octave to approximately 260 Hz.

Lowest Usable Frequency (f_c)

The lowest usable frequency for a reverberation chamber (not to be confused with horn coupling cutoff frequency) is that frequency below which the sound field in the reverberation room ceases to have an acceptable level of spatial variation and diffuseness. This frequency may be affected by the size of the test specimen occupying the chamber.

Based on the criteria that for one-third octave band sound pressures, the lowest one-third band showing no more than ± 3 dB spatial variations and no less than one-third modal overlap index shall be

specified as the lowest acceptable test frequency, the data presented in Figure 8 thus indicate that the chamber is useful at frequencies above 160 Hz for test volumes less than 10 percent.

In the case of the chamber occupied by a test specimen of about 20%, the lowest usable frequency of the chamber cannot be established via the criteria on modal overlap index since the index cannot be determined without the use of reverberation times. Employing an equivalent criteria based on modal density consideration, together with the criteria on spatial variation, the lowest usable frequency for the 20% volume specimen occupied chamber case shifted to 260 Hz.

In terms of the modal overlap index M , known volume V in cubic meters and the reverberation time T_{60} in seconds for the mode in question, the lowest usable frequency may also be computed by:

$$f_c = \left[\frac{Mc^3 T_{60}}{8.8\pi V} \right]^{\frac{1}{2}} \quad (10)$$

The value for M corresponds to the minimum value of Modal Overlap Index ($1/3 < M < 3$) selected on the basis of an acceptable level of spatial variations of sound pressure levels within the chamber. Recall that M was based on the chamber resonant bandwidth. Equation 10 can be derived using the first term of Equations 5 and 7.

The underlying logic for establishing the above criteria on the basis of a modal density or modal overlap requirement is as follows: For qualification testing or design evaluation, it is frequently desirable to express the lowest usable frequency in terms of the number of modes required within the resonant bandwidth of a structure. The required modal density can be directly related to the anticipated Q of the test specimen and the average number of modes desired within the specimen's resonant band to give the proper response simulation by the following relationship:

$$n(f) \Delta f_r \approx \frac{4\pi V f_o^3}{C^3 Q} \geq \begin{array}{l} \text{minimum desired or specified} \\ \text{number of modes} \end{array} \quad (11)$$

where $\Delta f_r = f_o/Q$

f_o = fundamental structural mode frequency

Q = resonant amplification factor

Example: First establish the number of modes required within a resonant bandwidth of a structure. If a minimum of 7 is required, then the minimum structural resonant frequency, f_o , which can be excited satisfactorily can be determined. Using the following values in the equation:

$$V = 68m^3 \quad (2,400 \text{ ft.}^3)$$

$$C = 344m/\text{sec.} \quad (1,128 \text{ ft./sec.})$$

$$Q = 10 \quad (\text{expected maximum value})$$

f_o is calculated to be 150 Hz. For a resonant frequency of 150 Hz and an expected Q of 10 we have a resonant bandwidth of 15 Hz within which a minimum of seven chamber resonant modes are required. Figure 7 gives a plot of the actual number of modes, $n(f)$, at a given frequency for empty chamber conditions. Entering this graph at 150 Hz, one can expect to have at least 0.7 modes at this frequency. Multiplying the number of chamber modes (0.7) and the structural resonant bandwidth (15 Hz) yields 10.5 modes in the lowest frequency band of interest (Δf_r). Note that if this criteria is fulfilled at 150 Hz, it will be exceeded, on the average, above 150 Hz, since the modal density increases with frequency. Therefore, it appears reasonable to define a lower bound frequency for a reverberant room as the lowest frequency at which the room has the required modal density, provided the spatial variation requirement is not exceeded.

Spectra Shaping Capability

The ability of a generator/chamber configuration to reproduce a given noise spectra is one of the most important requirements to be satisfied by the designer. For the $68m^3$ chamber, the reproduci-

bility of noise spectra for three commonly used launch vehicles (Atlas Centaur, Improved Delta and Titan III-C) and for the acoustic noise portion of DOD Military Standard 810B was assessed. In all cases, the noise spectra was reproducible within $\pm 3\text{dB}$.

In testing the Helios to the Titan III-C spectrum, insignificant differences were observed between the four channel average of the empty chamber spectrum and the spectrum obtained with the Helios in the chamber. On the basis of these results, a test specimen volume of 20% of the chamber volume indicates negligible effect on the spectral shape as normally measured during acoustic tests. Wyle Laboratories has done some model study work in this area which supports these tentative conclusions (Reference 8).

Figure 9 is a plot taken from the Wyle study. This data was taken from a relatively small scale model with room dimensions ratios of 1:.82:.71. The plot shows the sound pressure levels measured in the chamber with various specimen sizes relative to sound pressure levels measured in the empty room. Superimposed on this plot are similar results from the Helios test.

The results from the GSFC full-sized chamber are more promising than was expected from the scale model data. The increasing difference in SPL between the occupied and empty chamber results, with increasing specimen size, at the low frequency end is primarily due to reduction in chamber volume caused by the specimen. An extended frequency scale employed in the model study to collect sine sweep test data shows that the longer average path lengths followed by the sound rays in passing around the specimen results in a general lowering of the individual resonances of the chamber. This lowering of the resonances has the effect of spreading the peaks out in the lower frequency range so that the chamber is even less usable at these low frequencies than when it is empty. This spreading out of the peaks was also demonstrated by the increase of spatial variation in Figure 8. Based on these results, the GSFC chamber occupied by a specimen having a volume of 20% of the chamber volume would not be considered to seriously degrade the chamber performance. Moreover, for specimens having sufficiently low resonant

magnification factors, a specimen as large as 50% of chamber volume possibly could be tested.

CONCLUSIONS

The purpose of this investigation was to obtain experimental data with which to verify the predicted performance of the truncated reverberation chamber and to assess the effect of various sized test volumes on chamber performance. From the results of the study, the following conclusions can be drawn:

1. The extremely close correlation obtained between predicted, model study, and measured data permit using existing theory to predict the chamber noise field and test item response with a high degree of confidence.
2. Test specimen volumes of up to 20% of the chamber volume are shown to have a negligible effect on the acoustic noise field when measured on an averaged one-third-octave basis. A closer examination on a narrow band statistical basis reveals only small changes which, when understood by the test engineer, give him a basis for justifying the testing of even larger test volumes of up to 50% of the chamber volume.
3. A simplified method of measuring reverberation time using broadband rather than the conventional narrow band noise excitation yielded, for all practical purposes, identical results.
4. All presently used and anticipated acoustic test specifications can be satisfactorily reproduced. The lowest usable frequency, assuming a maximum allowable spatial variation of $\pm 3.0\text{dB}$ is 160 Hz. For many tests, the chamber is adequate below this frequency. Data are presented for determining the degree of compromise necessary in chamber performance for operation at lower frequencies.
5. Maximum versatility in spectra shaping is obtained by using two air modulators. While the bulk of this evaluation was done using

the Noraircoustic Mark V generator, a limited amount was done using the lower powered Ling EPT-94B as a noise source. From extensive previous experience with the Ling source, the authors feel that this generator will provide superior shaping capability (at lower overall levels, 148dB maximum) on a one-third octave band basis over the range of 100-1,000 Hz.

Due to space limitations, considerable background data, theoretical justifications, and discussions on predicting overall and spectral sound pressure levels have been omitted in this paper. A NASA technical note covering these areas is presently being published.

REFERENCES

1. Scharton, T. D., Rentz, P. E., Lubman, D., and White, P. H., "Techniques for Improving the Low Frequency Performance of Small Reverberation Chambers." A report prepared for the National Aeronautics and Space Administration, NAS5-21003. California: Bolt, Beranek and Newman, Inc., (1970).
2. Sepmeyer, L. W., "Computer Frequency and Angular Distribution of the Normal Modes of Vibration in Rectangular Rooms," J. Acoust. Soc. Am. 37, 3, (1965).
3. Beranek, L. L., "Acoustics" McGraw-Hill Book Company, Inc., New York (1954).
4. Morse, P. M., and Ingard, K. U., "Theoretical Acoustics," McGraw-Hill Book Company, Inc., New York, Pg. 597, (1968).
5. Beranek, L. L., "Noise Reduction," McGraw-Hill Book Company, Inc., New York, Pg. 235, (1948).
6. Morse, P. M., "Vibration and Sound," McGraw-Hill Book Company, Inc., New York, Section 32 (1948).

7. Mills, J. F., "A Study of Reverberation Chamber Characteristics," Institute of Environmental Sciences, Proceedings, Fig. 10 (1967).
8. Cockburn, J. A., "Evaluation of Acoustic Testing Techniques for Spacecraft Systems." A report prepared for the National Aeronautics and Space Administration, NAS5-21203. Alabama: Wyle Laboratories (1971).

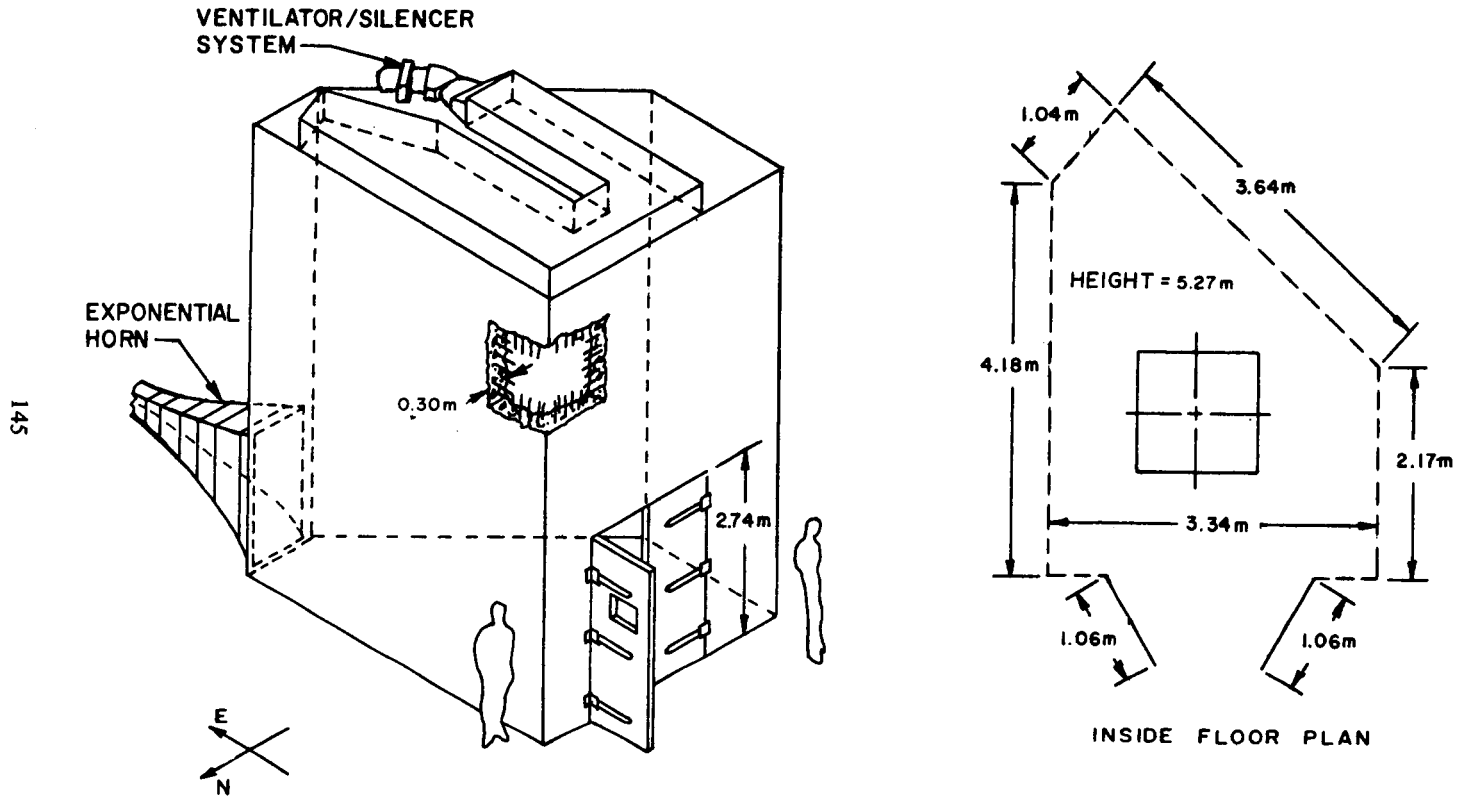


FIGURE 1. Goddard Reverberant Noise Chamber

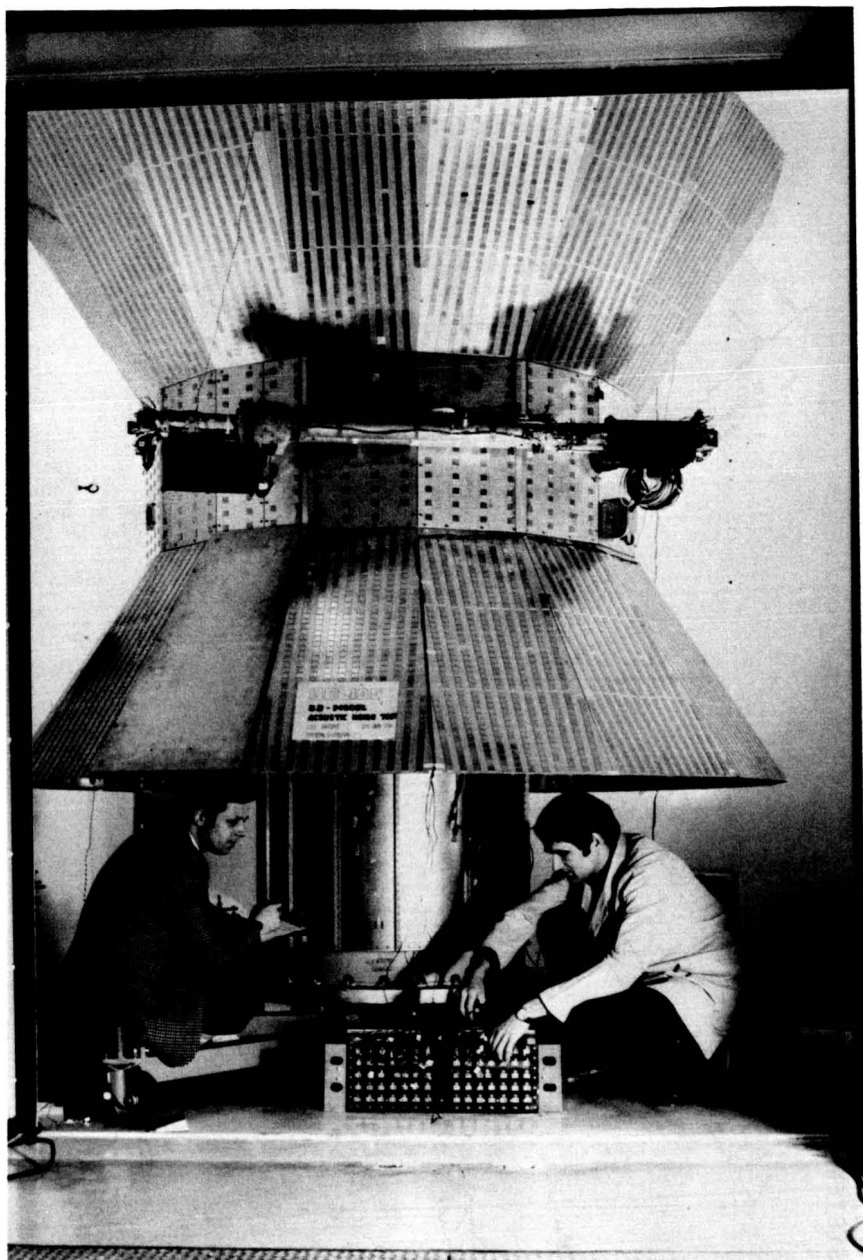


Figure 2. Helios Spacecraft Mounted in 68m^3 Chamber

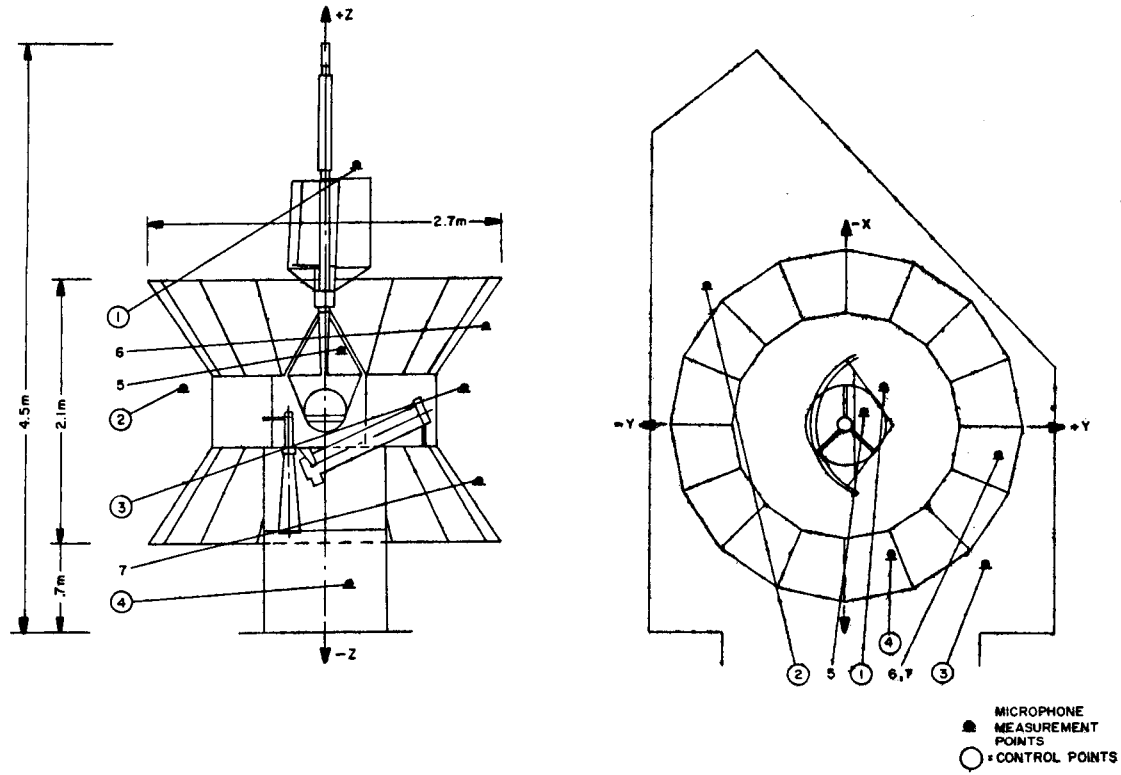


FIGURE 3. HELIOS SPACECRAFT SHOWING MICROPHONE LOCATIONS

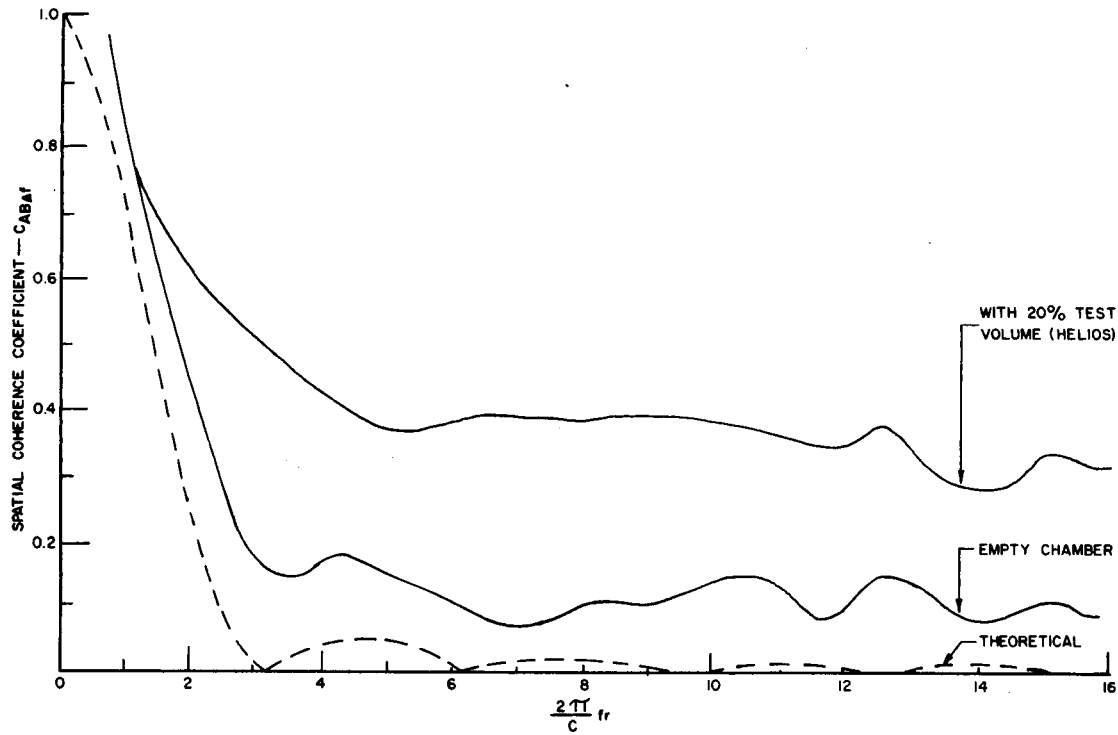


FIGURE 4. SPATIAL COHERENCE BETWEEN MEASURED 1/3 OCTAVE SOUND PRESSURES COMPARED TO THEORETICAL COHERENCE BETWEEN NARROW BAND DIFFUSE SOUND PRESSURES (f =CENTER FREQUENCY, r =DISTANCE BETWEEN POINTS, c =SPEED OF SOUND.)

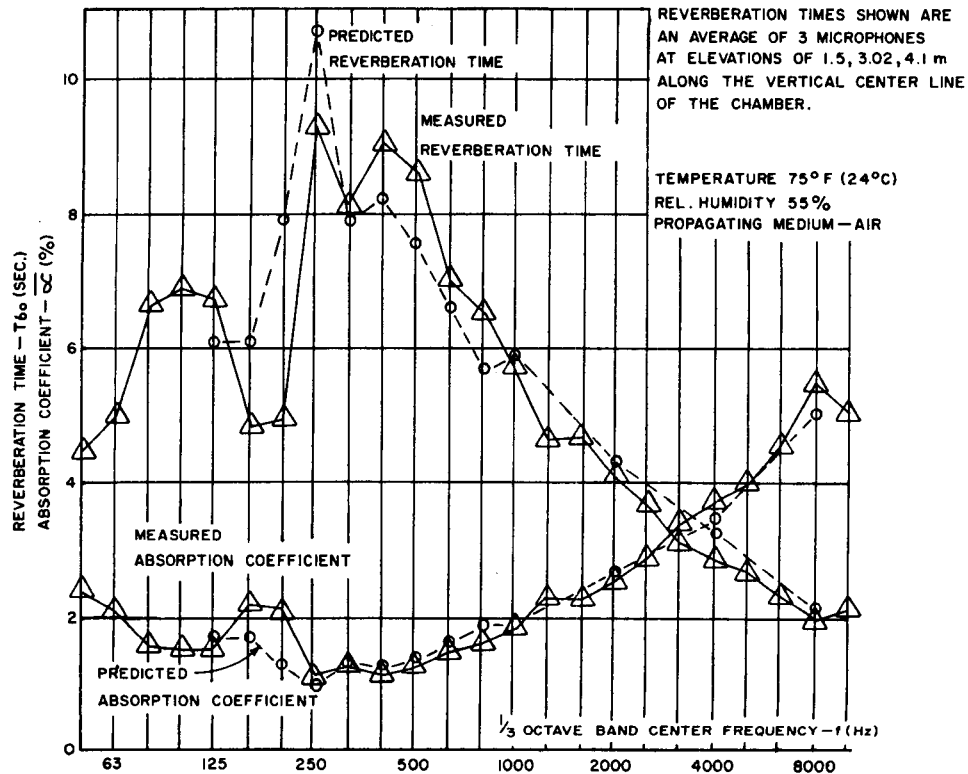


FIGURE 5. PREDICTED AND MEASURED REVERBERATION TIMES AND ABSORPTION COEFFICIENTS—EMPTY CHAMBER

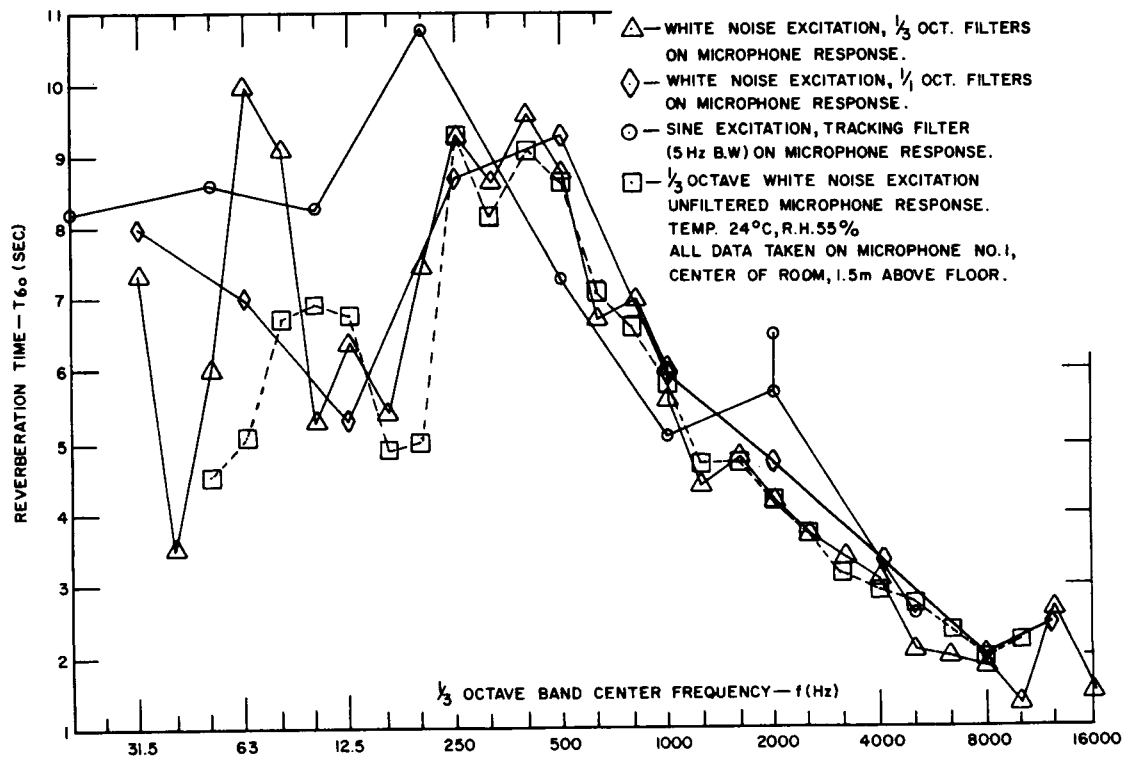


FIGURE 6. REVERBERATION TIMES USING VARIOUS TYPES OF EXCITATION — EMPTY CHAMBER

NUMBER OF MODES IN $\frac{1}{3}$ OCTAVE BAND - $N\Delta f$
 NUMBER OF MODES WITH RESONANT FREQUENCIES
 LESS THAN FREQUENCY $f - N\Delta f$

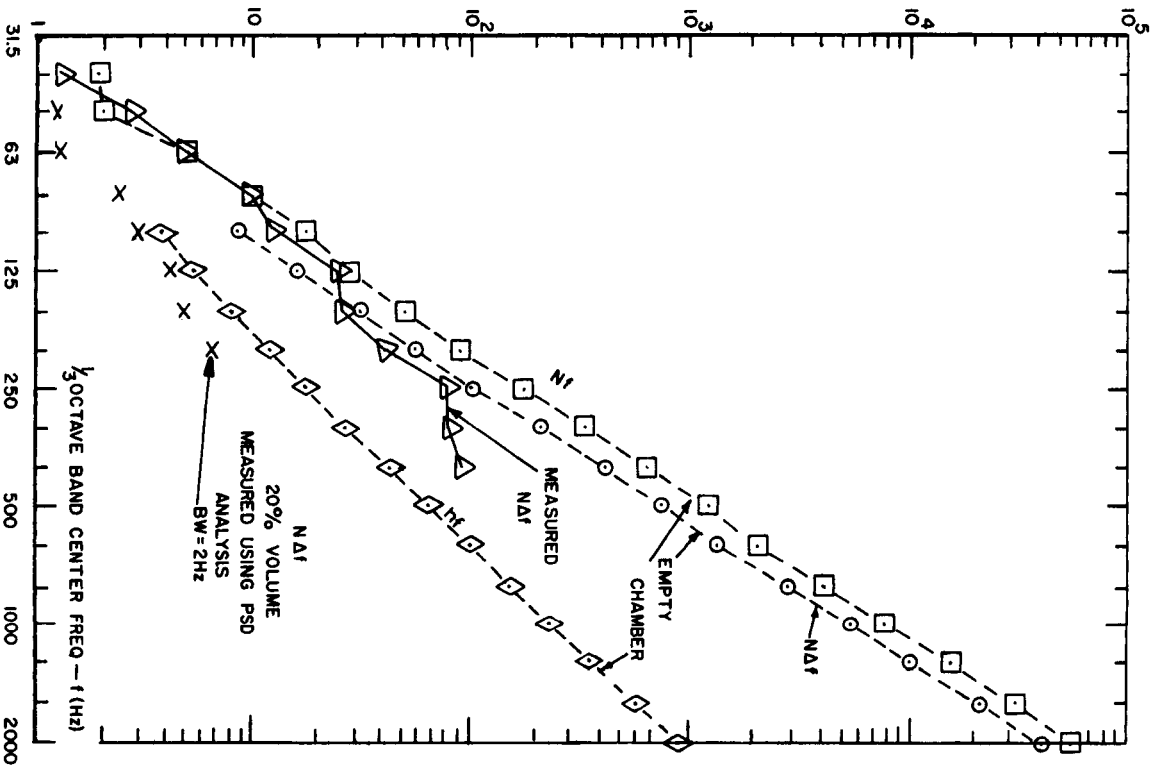


FIGURE 7. PREDICTED MODAL DENSITY (n_f), CUMULATIVE
 RESONANCE FREQUENCY (Nf), AND PREDICTED AND
 MEASURED MODE COUNTS ($N\Delta f$)

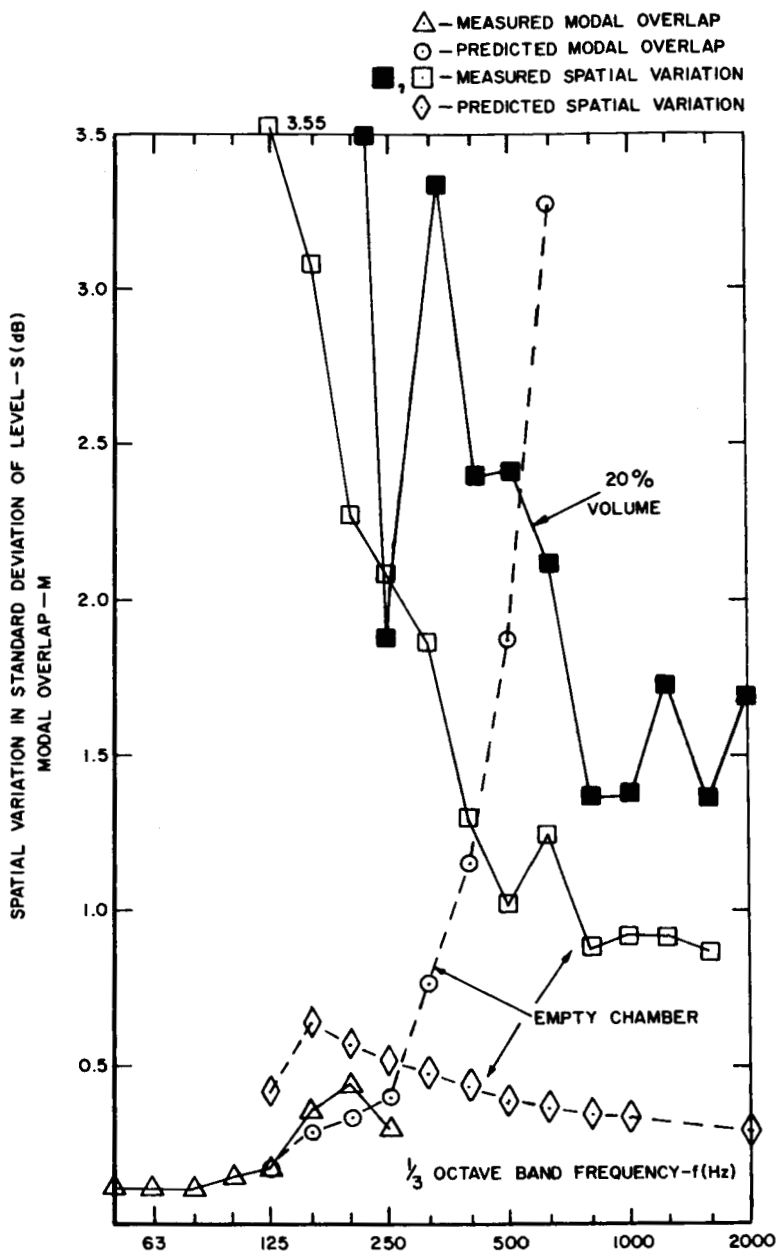


FIGURE 8. PREDICTED AND MEASURED MODAL OVERLAP AND SPATIAL VARIATION-EMPTY CHAMBER AND 20% VOLUME

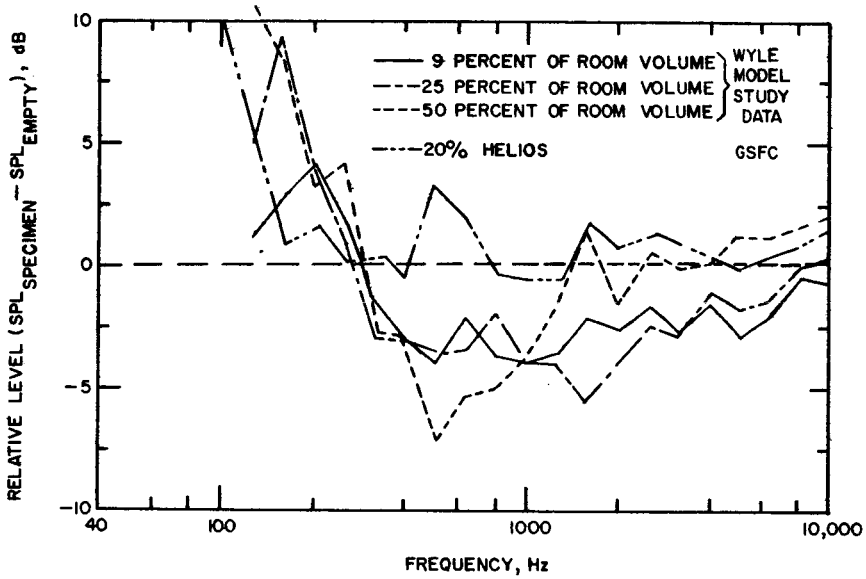


FIGURE 9. SOUND PRESSURE LEVELS MEASURED IN A REVERBERATION ROOM WITH VARIOUS SPECIMEN SIZES RELATIVE TO SOUND PRESSURE LEVELS MEASURED IN THE EMPTY ROOM.

PRECEDING PAGE BLANK NOT FILMED

Paper No. 14

DYNAMICS OF THE SKYLAB WASTE TANK SYSTEM

G. Rupprecht, *The Bendix Corporation, Denver, Colorado*

ABSTRACT

The waste tank venting system is a source of contamination for the Skylab space environment. Therefore the possibility for an assessment of the vapor flow rate under various conditions during and after liquid dumps is desirable. The dynamics of the Skylab waste tank venting system is discussed in terms of convenient subsystems. Some representative test results are reported and the experimental observations during a waste tank simulation test are connected with the mathematical model. During experimentation with CO₂ purges it was found that the sublimation rate of ice can be considerably changed by the presence of other gases.

INTRODUCTION

The Skylab waste tank is a continuous source of contamination of the space environment. For this reason it is important to know the rate of vapor flow which is expected under different circumstances. Of particular importance are the quasi steady state vapor flow rate and the time dependence of the flow rate during and after waste dumps.

The basic parameters which allow such prediction were collected during a simulation test of the Skylab waste tank performance at Martin Marietta's Denver facility. A model is conveniently developed by considering the total waste tank as an interplay between a number of subsystems which can be treated rather independently because their interaction with one another is either weak or can be readily described.

As an example the nonpropulsive vents of the waste tank can be treated as such a subsystem. Another example is the pile of ice, stored on the baffle of the waste tank. By virtue of its heat capacity it acts as a "temperature buffer" for additional liquid dumps. A buffer with negligible heat capacity is given by the considerable volume of the waste tank which acts as a "pressure buffer."

DESCRIPTION OF THE WASTE TANK

The waste tank which was used for simulation is a metal container with a total volume, $V=80,4 \text{ m}^3$ which is divided into three compartments as shown in figure 1. The compartments are separated by finely meshed screens which prevent solid particles $>1\mu\text{m}$ from passing. The top compartment has a volume $V_1=7.3 \text{ m}^3$ and contains a baffle fabricated of relatively thin plastic material. The baffle supports the ice pile which forms during liquid dumps through a nozzle situated at the top of the upper compartment and prevents the ice from coming into contact with the screen. As indicated in figure 1 the ice pile is partially enclosed by the baffle and for this reason the radiative heat transfer from the temperature controlled walls of the top compartment to the ice pile is partially attenuated by the baffle. The area of the screen is about $A=11 \text{ m}^2$. The middle compartment has about ten times the volume of the upper and lower compartment. The lower compartment is open to the outside of the waste tank by two pipes of length $L=34 \text{ cm}$ and inner diameter of $d=3.81 \text{ cm}$, corresponding to a cross sectional area of 11.4 cm^2 for each pipe.

In order to simulate space conditions the entire waste tank was placed into a still larger vacuum system of high pumping speed. Since the flow conductance of the wire screens is large compared to the combined conductance of the two venting pipes one finds usually only small pressure differences between the three waste tank compartments.

GENERAL RELATIONS AND IDENTIFICATION OF SUBSYSTEMS

Next the equations will be developed which govern the dynamic behavior of the waste tank. In figure 1 the pressure in the upper compartment of volume V_1 is P_1 , while the pressure in the remainder of the waste tank (volume V_2) is designated as P . The pressure difference across the top screen is

$$\Delta P = P_1 - P \quad (1)$$

It is caused by the wire screen of conductance $C(k_1)$ in $[\text{lsec}^{-1}]$. The symbol (k_1) is attached as a reminder that the screen conductance is a function of the composition of the gas which passes through the screen. With these notations the flow characteristics of the waste tank can be described by the following set of equations:

$$V_1 \dot{P}_1 = Q_{in} - C(k_1) \Delta P \quad (2)$$

$$V_2 \dot{P} = C(k_1) \Delta P - Q_{out}(k_2) \quad (3)$$

Q_{in} in equation 2 pertains to the incoming gas flow rate which is produced in the upper compartment either by the sublimation of the stored ice and/or by the dumping of gases or liquids through the inlet nozzle. Q_{in} therefore represents the generating system for the gas flow and can be singled out as a subsystem. Obviously Q_{in} depends upon a number of parameters such as the mass and spacial distribution of the stored ice on the baffle and the heat transfer from the surroundings to the ice pile. On the other hand, Q_{in} is for most practical purposes independent of the tank pressure P , with the exception of a strong pressure dependence in the vicinity of the triple point pressure.

Q_{out} pertains to the vapor flow rate through the two venting pipes which represent another subsystem. Q_{out} is mainly a function of the tank pressure P and this functional dependence will be intensively studied. The symbol (k_2) is to indicate that Q_{out} is a function of the gas composition. In a dynamic situation (k_1) can be different from (k_2) .

The total volume V of the waste tank can be regarded as a separate subsystem. The pressure P depends upon Q_{in} and Q_{out} in a simple manner. Addition of equations 2 and 3 and use of equation 1 leads to:

$$V_1 \dot{P}_1 + V_2 \dot{P}_2 = V \dot{P} [1 + (V_1/V) (\Delta \dot{P}/\dot{P})] \approx V \dot{P}$$

Therefore

$$V \dot{P} \approx Q_{in}(k_1) - Q_{out}(k_2) \quad (4)$$

In a quasi steady state condition:

$$Q_{in} = Q_{out} \quad (5)$$

Since the tank pressure P must build up through the contribution $(Q_{in} - Q_{out})$ as a function of time, the volume V of the waste tank acts as a "pressure buffer."

MEASUREMENT OF Q_{in}

Although the pressure drop across the screen is usually of little significance it can be used as a measure for the vapor flow rate Q_{in} . The passages through the screen are very small, of the order of $1 \mu m$ and as a consequence the vapor flow through the screen is molecular in nature as long as the tank pressure is below 20 torr. In the molecular flow regime the screen conductance C is independent of pressure and can be characterized by

$$C = g \cdot (T/M)^{1/2} \quad [l \text{sec}^{-1}] \quad (6)$$

g is a geometrical factor which depends upon the structure of the screen, T is the absolute temperature of the gas at the screen and M is the molar weight.

According to equation 2 one finds for a quasi steady state condition:

$$Q_{in} = C\Delta P \text{ [torr } \ell\text{sec}^{-1}] \quad (7)$$

By measuring the gas flow rate through the inlet nozzle with a flow meter and the pressure drop across the screen, the screen conductance can be determined experimentally. Such an experiment was carried out at room temperature with CO_2 and N_2 gas. The result is shown in figure 2 where ΔP in [mtorr] is plotted versus Q_{in} in [torr ℓsec^{-1}].

As expected a linear relationship results which is different for the two gases. One can note, that the straight lines representing the best fit to the experimental data do not cross the origin of the coordinate system as is required by equation 7. Either the pressure indicator for ΔP has a bias such that the measured value ΔP_m should be replaced by

$$\Delta P = \Delta P_m + \eta \text{ [torr]} \quad (8)$$

or the flow meter is biased and the measured value Q_m should be replaced by Q , where

$$Q = Q_m + \Delta Q \text{ [torr } \ell\text{sec}^{-1}] \quad (9)$$

or a combination of the two errors. Whatever the bias errors may be they do not impair the accuracy when the screen conductance is obtained from the slopes:

$$C = \frac{dQ}{d\Delta P} \quad (10)$$

With this procedure one obtains for room temperature the following values:

$$C(\text{CO}_2) = 2.33 \times 10^4 \text{ [}\ell\text{sec}^{-1}] \quad (11)$$

$$C(\text{N}_2) = 3.02 \times 10^4 \text{ [}\ell\text{sec}^{-1}]$$

Note that under equal conditions one should find according to equation 6

$$C(\text{CO}_2)/C(\text{N}_2) = [M(\text{N}_2)/M(\text{CO}_2)]^{1/2} = \left(\frac{28}{44}\right)^{1/2} = 0.796 \quad (13)$$

By comparison the experimental values from equation 11 and 12 yield

$$C(\text{CO}_2)/C(\text{N}_2) = 2.33 \times 10^4 / 3.02 \times 10^4 = 0.772$$

in satisfactory agreement with the theoretically expected value.

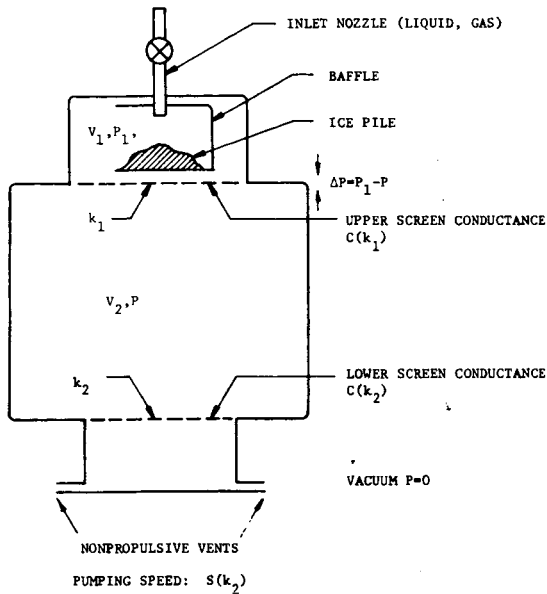


Figure 1. Schematic of the Waste Tank Configuration

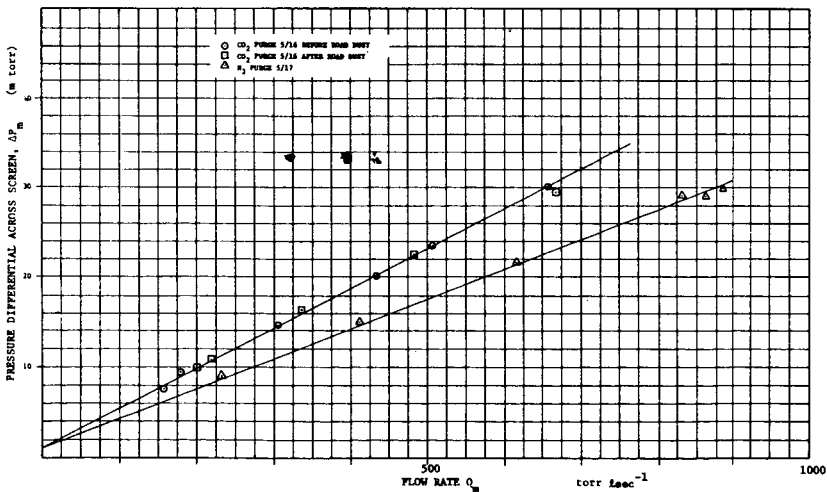


Figure 2. Pressure Differential Across Screen ΔP_m Versus Flow Rate, Q_m
 (ΔP_m , Q_m as Measured)

The error is 3 percent.

Using the most reliable experimental values at a temperature distribution closest to normal operational conditions one obtains from the data in figure 3 the following value:

$$C(\text{CO}_2) = 2.68 \times 10^4 \text{ [}\ell\text{sec}^{-1}\text{]}$$

and consequently

$$\begin{aligned} C(\text{H}_2\text{O}) &= 2.68 \times 10^4 \cdot (44/18)^{1/2} \\ &= 4.18 \times 10^4 \text{ }\ell\text{sec}^{-1} \end{aligned} \quad (15)$$

Through the calibration procedure of the screen conductance the easily measured quantity ΔP can be directly related to the vapor flow rate in the waste tank. The screen conductance can also be obtained for other gases and mixtures of gases.

Q_{out} AS A FUNCTION OF TANK PRESSURE

In this section the vapor flow rate through the combined action of the two nonpropulsive vents will be investigated as a function of the waste tank pressure P . It is assumed that a vacuum exists outside of the waste tank with an external pressure $P_{\text{ext}} < 10^{-6}$ torr.

When the pressure inside the tank equals the external pressure the flow rate is obviously zero. For $P < 10^{-3}$ torr the mean free path of the gas molecules is greater than the inside diameter of the pipes and one has a molecular flow. For $P > 10^{-3}$ torr the flow becomes laminar and viscous in character and the flow velocity at the end of the pipe is steadily increasing with increasing pressure. When the flow velocity reaches the Mach number $M=1$, a shock wave will reach the exit of the vent, at which point the maximum pumping speed for the vent has been reached. With increasing pressure only the density of the gas can increase and as a consequence the flow is "choked" and Q_{out} becomes proportional to the tank pressure P .

More quantitatively in the region of molecular and laminar flow one can approximate Q_{out} by the use of Knudsen's semiempirical formulation

$$Q_{\text{out}} = S_L(P) \cdot P \quad (16)$$

with

$$S_L(P) = \frac{D^3}{L} \left\{ 3.27 \times 10^{-2} \frac{PD}{\eta} + 7.62 \left(\frac{T}{M}\right)^{1/2} \frac{1 + 0.147 \left(\frac{T}{M}\right)^{1/2} \frac{PD}{2\eta}}{1 + 0.181 \left(\frac{T}{M}\right)^{1/2} \frac{PD}{2\eta}} \right\} \quad (17)$$

with the pumping speed for laminar flow, S_L , in $[\ell\text{sec}^{-1}]$, the inner pipe diameter D in $[\text{cm}]$, the length of the pipes L in $[\text{cm}]$, the viscosity η in $[\text{poise}]$, the molar weight M in $[\text{g/mole}]$, the absolute

temperature T in [°K] and the pressure P in [torr]. Inserting the values for water vapor one finds for the combined action of the two pipes approximately:

$$S_L(P) = 2.21 \times 10^3 P + 39 \text{ [}\ell\text{sec}^{-1}\text{]} \quad (18)$$

In general a theoretical calculation of the flow rate for Mach numbers close to unity is difficult to achieve. Gershman and Lannon, (Reference 1), subsequently referred to as (G&L) have carried out such calculations taking into account the friction loss near the duct entrance and the heat exchange of the flowing gas with the pipe walls. From their results one can conclude that an extrapolation of the flow rate to zero flow intercepts the pressure axis at about 0.2 torr. This result holds for water vapor as well as for nitrogen. The reason can be traced to the so-called "head loss," a pressure loss, which is caused by the friction of the flowing gas with the pipe walls. Since the flow rate must converge to zero for diminishing pressure the curve representing $Q_{out}(P)$ must end up at the origin of the coordinate system. The pressure region between 0.1 and 0.3 torr is of importance because the quasi steady state pressure is usually in this range. An accurate knowledge of the flow rate as a function of pressure yields therefore important information about the contamination contribution of the two nonpropulsive vents inbetween dumps.

We shall now use experimental data to determine $Q_{out}(P)$ explicitly. In figure 4 the pressure drop ΔP across the top screen under a steady state condition is plotted versus the tank pressure P during an admission of CO_2 gas. The data indicates that the flow is indeed choked. When the experimental values for ΔP are extrapolated to $\Delta P=0$ the pressure axis is intercepted at about 0.2 torr as predicted by (G&L) for N_2 and H_2O gas. Combining the results shown in figure 3 and 4 one obtains the bias free result

$$S(CO_2) = \frac{dQ}{dP} = \frac{dQ}{d\Delta P} \cdot \frac{d\Delta P}{dP} = C(CO_2) \cdot \frac{d\Delta P}{dP} = 331 \text{ [}\ell\text{sec}^{-1}\text{]} \quad (19)$$

During numerous water dumps P_m and ΔP_m have been registered. Therefore the time derivative of P_m , \dot{P}_m is also known. One has to allow, however, for the possibility that the measured values P_m and ΔP_m are offset by biases in the instruments as indicated by equation 8 and/or by

$$P = P_m + \eta \quad (20)$$

But one can notice that

Reference 1 Gershman and L. E. Cannon, Performance Analysis for the Skylab Waste Tank Nonpropulsive Vent System, Presented to SAE Aerospace Fluid Power and Control, Technology Meeting, San Francisco, California, 16 October 1972

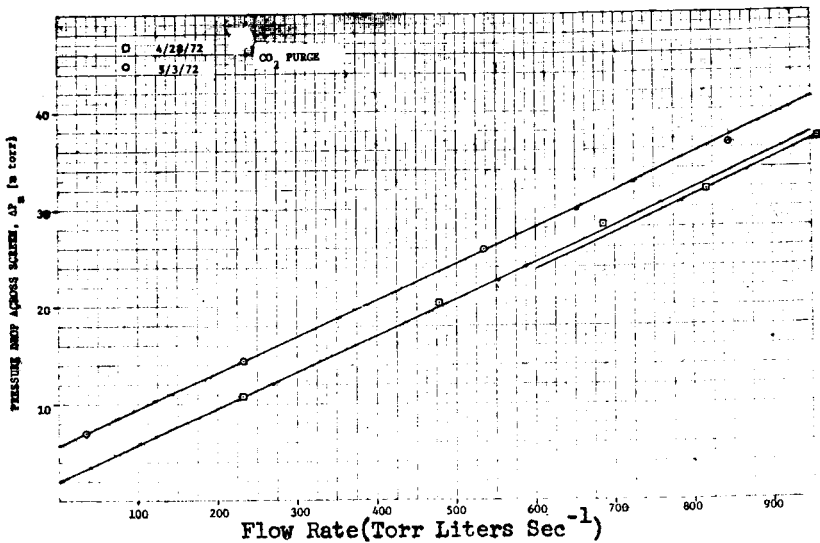


Figure 3. Determination of the Screen Conductance With CO₂ Gas

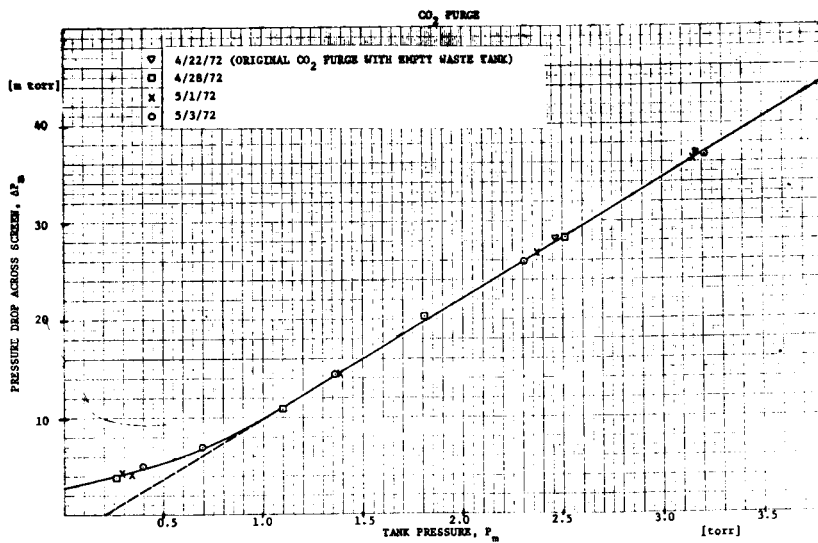


Figure 4. Relation Between Tank Pressure and Pressure Drop Across Screen

$$\dot{P}_m = \dot{P} \quad (21)$$

Using equation 3 one can calculate Q_{out} as

$$\begin{aligned} Q_m &= C(\Delta P + \eta) - V_2 \dot{P} \\ &= (C\Delta P - V_2 \dot{P}) + C\eta = Q_{out} + C\eta \end{aligned} \quad (22)$$

In table I data and resulting calculations are shown for a 8.3 lb condensate dump on 4/28/72. The result is plotted in figure 5. For pressures >0.6 torr the data yield

$$S(H_2O) = \frac{dQ_m}{dP} = \frac{dQ}{dP} = 455 \text{ [}\ell\text{sec}^{-1}\text{]} \quad (23)$$

a value which is free of bias error. For $P < 0.6$ torr the experimental points deviate from the linear relation. A great number of water dumps have been evaluated and show exactly the same behavior. It would serve no useful purpose to add more experimental points. One can, however, state that the behavior shown in figure 5 is highly reproducible. Figure 6 is a close-up of figure 5 exhibiting more distinctly the deviation of the data points at low pressure from a straight line. If the deviation is designated as δp a plot of $\log \delta p$ versus P_m shows an empirical relation for $\delta p(P_m)$ as shown in figure 7 which can best be expressed in the form

$$\delta p = \delta p_o \exp[-\alpha(P - \delta p_o + \delta p)] \quad (24)$$

where use has been made of the fact that the intercept of the linear extrapolation of Q_{out} crosses the P -axis at

$$\delta p_o = 0.2 \text{ [torr]} \quad (25)$$

The value for α is

$$\alpha = 1.68 \text{ [torr}^{-1}\text{]} \quad (26)$$

The dashed extrapolation of the curve connecting the experimental data in figure 6 is accomplished through the use of the dashed line in figure 7.

If one follows this procedure one can determine the instrumental biases ϵ and η . One finds

$$\begin{aligned} \epsilon &= -0.05 \text{ [torr]} \\ \eta &= 1.86 \text{ [m torr]} \end{aligned} \quad (27)$$

Using these corrections the two columns P and Q_{out} in table I have been calculated. The result is shown in figure 6.

Table I. Data and Evaluation of Event 4-5-13
8.3 Lb Condensate Dump on 4/28/72

P_m [torr]	ΔP_m [m torr]	$-\dot{P}$ [torr sec ⁻¹]	$-V_2\dot{P}$ [torr lsec ⁻¹]	CAP_m [torr lsec ⁻¹]	Q_m [torr lsec ⁻¹]	P [torr]	Q_{out} [torr lsec ⁻¹]
1.852	12.6	3.58×10^{-3}	261	526	787	1.802	709
1.750	12.1	3.46	252	506	758	1.700	680
1.573	11.4	2.67	195	477	672	1.523	594
1.309	10.2	1.84	134	427	561	1.259	483
1.209	9.8	1.55	113	410	523	1.159	445
1.125	9.3	1.32	96	390	486	1.075	408
1.020	8.4	1.00	73	352	425	0.970	347
0.864	7.8	0.72	52.5	326	378.5	0.814	300
0.721	6.26	0.44	32.1	263	295.1	0.671	217
0.616	5.49	0.25	18.2	229	247.2	0.566	169
0.558	5.13	0.16	11.7	215	226.7	0.508	149
0.514	4.83	0.12	8.8	202	210.8	0.464	133
0.410	3.87	0.10	7.3	162	169.3	0.360	91
0.359	3.54	0.07	5.1	148	153.1	0.309	75
0.327	3.35	0.02	1.5	140	141.5	0.277	64
0.280	3.11	-	-	130	130	0.230	52

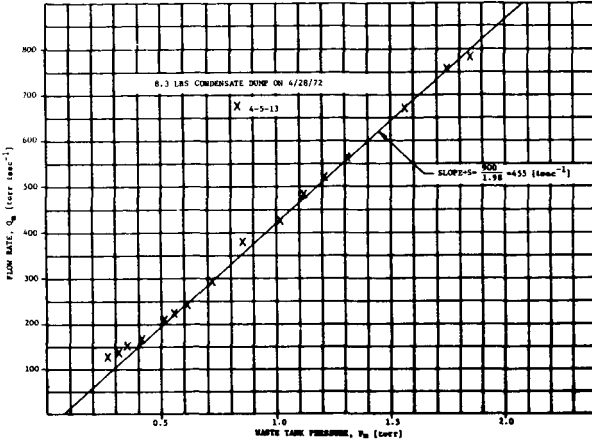


Figure 5. Determination of the Pumping Speed of the Waste Tank Venting System for Water Vapor

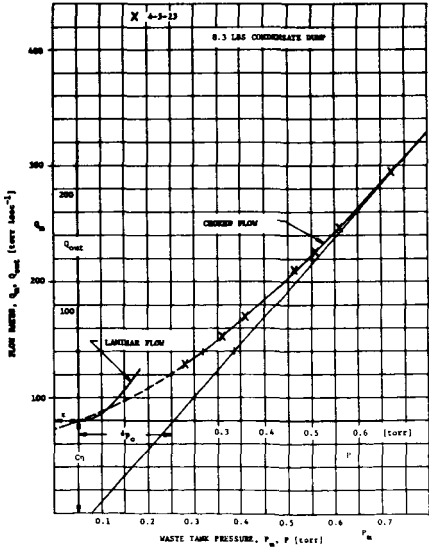


Figure 6. Flow Rate Vs Waste Tank Pressure for Water Vapor at Low Pressure

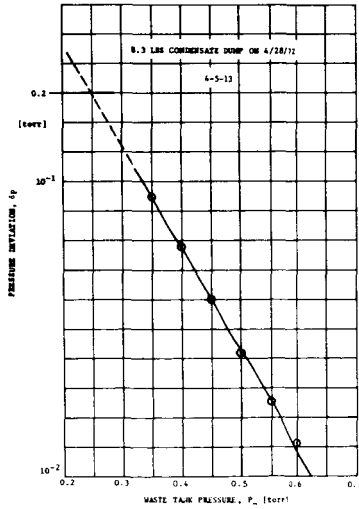


Figure 7. Pressure Deviation From Linearity as a Function of Waste Tank Pressure

It is worthwhile to note that (G&L) find theoretically for water vapor at temperatures of 5°C and 60°C respectively, the following values for the pumping speed.

$$S_{th} = 462 \text{ lsec}^{-1}$$

$$S_{th} = 454 \text{ lsec}^{-1}$$

The experimental value for S obtained during the waste tank simulation test is between the above mentioned values:

$$S_{exp} = 455 \text{ lsec}^{-1}$$

This agreement lends credibility also the value of the pressure loss $\delta p_o = 0.2$ torr.

In order to express Q_{out} in a mathematical formula one can use equation 24 to determine $\delta p(P)$ and subsequently calculate Q_{out} from

$$\begin{aligned} Q_{out} &= S[P - (\delta p_o - \delta p)] \\ &= \{S[1 - (\delta p_o - \delta p)/P]\}P = S_c(P) \cdot P \end{aligned} \quad (28)$$

Here $(\delta p_o - \delta p)$ is the pressure loss due to friction and $S_c(P)$ is the pumping speed for the two pipes for choked flow.

For the purpose of a comparison the flow rate for molecular and laminar flow as given in equation 18, is introduced into figure 6. Below 0.06 torr the flow rate for molecular and viscous flow is below the empirical extrapolated curve for choked flow. It is therefore reasonable to assume, that for pressures below the transition pressure $P_t = 0.06$ torr the flow rate is limited by the lower laminar flow rate. If this suggestion is accepted Q_{out} can be represented in the form:

$$Q_{out} = S(P)P \quad (29)$$

with

$$S(P) = S_L [1 - \int \delta(P - P_t) dP] + S_c \int \delta(P - P_t) dP \quad (30)$$

where the transition pressure P_t can be obtained from

$$S_L(P_t) = S_c(P_t) \quad (31)$$

One can check Q_{out} at low pressure by using the observation that in a quasi steady state condition the weight loss of the ice pile in the waste tank is about 6 lbs per day. It has been observed, that under these conditions the tank pressure is about 0.15 torr. According to figure 6 or equations 24 and 28 the corresponding value for Q_{out} is

$$Q(0.15) \approx 30 \text{ torr lsec}^{-1}$$

This flow rate corresponds to a weight loss over a 24 hour period of

$$\frac{30 \times 3600 \times 24 \times 18}{760 \times 22.4 \times 454} = 6 \text{ lbs}$$

in agreement with the directly measured weight loss of the ice pile.

DISCUSSION OF Q_{in}

The quantity Q_{in} has been identified as being characteristic for the subsystem which generates the gas flow. For a gas dump the behavior of the system is completely described by equations 2 and 3. Next we shall present the case of a liquid dump. To give an example how Q_{in} depends on different quantities, the variation of Q_{in} during the so-called "biocide dump" will be discussed. It entails the release of 57 lbs of slightly contaminated water at a rate of 2 lbs/min which is equivalent to a mass flow rate

$$\dot{m}_o = 15.1 \text{ [g sec}^{-1}\text{]} \quad (32)$$

From data taken during this event Q_{in} can be calculated from equation 2 as

$$Q_{in} = CAP + v_1 \dot{p} \quad (33)$$

The results are shown in figure 8 where Q_{in} is plotted as a function of the waste tank pressure. The data points are further characterized by the time (minutes:seconds) after the biocide dump was started. One should add, however, that the water flow through the nozzle did not start before (10:12).

One can assume that the main energy source for sublimation during the dump is the stream of water. By comparison other heat transfer mechanisms do not contribute to the sublimation rate Q_{in} to any appreciable extent. Due to its low heat capacity the presence of the baffle can also be neglected for our purposes. We make the further assumption that the temperature of the water upon entering the waste tank is 22°C and that the pressure is well below the pressure at the triple point (4.58 torr). Then one can estimate that about 16 percent of the total mass flow rate \dot{m}_o gives rise to a vapor flow rate Q_{in} (theory), while 84 percent of the water flow will be deposited as ice on the baffle with a temperature close to the freezing point. Therefore the mass flow rate, \dot{m}_s , of the sublimated water vapor is

$$\dot{m}_s = 0.16 \dot{m}_o = 2.42 \text{ [g sec}^{-1}\text{]} \quad (34)$$

which is equivalent to

$$Q_{in} \text{ (theory)} = 2.28 \times 10^3 \text{ [torr lsec}^{-1}\text{]} \quad (35)$$

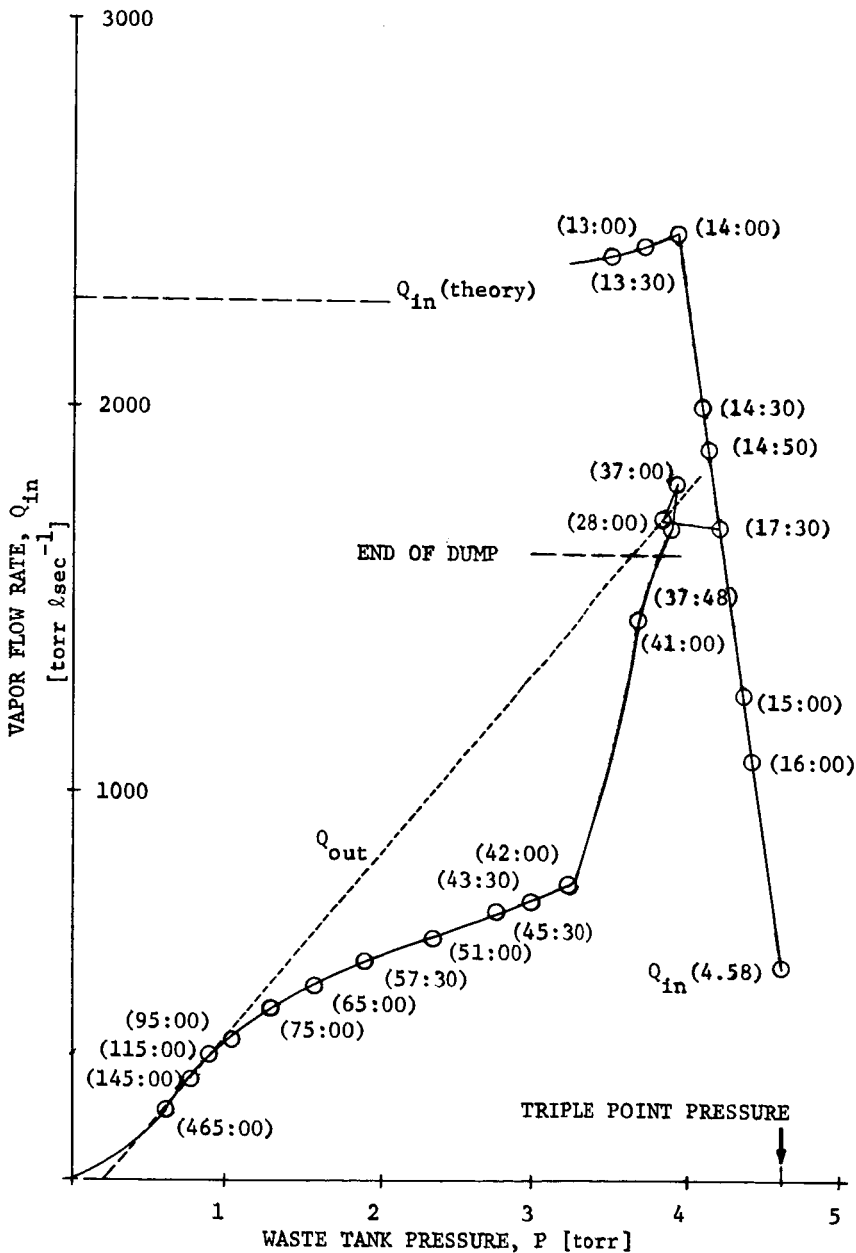


Figure 8. History of a Biocide Dump

which is shown as a dashed line in figure 8.

Q_{in} (theory) is in reasonable agreement with the experimental values observed at (13:00), (13:30) and (14:00).

After (14:00) a drastic decrease of Q_{in} is observed. This fast drop of Q_{in} has obviously to do with the fact that at this point the pressure in the waste tank has risen to a value where the sublimation rate of the dumped water is significantly reduced. This leads to the conclusion that not all of the dumped water will be frozen immediately and that water close to the freezing point will reach the ice pile.

A close look at the experimental points in figure 8 between (14:00) and (17:30) shows that these values can readily be connected by a straight line which, when extrapolated to the pressure $P_T=4.58$ torr at the triple point, yields

$$Q_{in} \approx 500 \text{ [torr } \ell \text{sec}^{-1}] \quad (36)$$

By comparison one can calculate Q_{in} which is expected at the triple point for a mass flow rate $\dot{m}_0 = 15.1 \text{ g sec}^{-1}$ and a water temperature of 22°C . One finds

$$Q_{in}(4.58) = 560 \text{ [torr } \ell \text{sec}^{-1}] \quad (37)$$

in reasonable agreement with the experimental value estimated above.

What is more interesting, however, is the constant rate of change for $Q_{in}(P)$ which is suggested by the straight line interpolation. One finds for the time interval (14:00) to (17:30)

$$\frac{dQ}{dP} \approx -2800 \text{ [}\ell \text{sec}^{-1}] = -2.8 \text{ [m}^3 \text{sec}^{-1}] \quad (38)$$

In order to connect this value with the theoretical expectation one can derive a relation between the equilibrium vapor pressure P_0 and the deviation δP from equilibrium in a steady state condition as a function of the pumping speed, S , the surface area of the source, A , the average thermal velocity of the water molecules, v_{av} , and the sticking coefficient, s (Reference 2). It is

$$\delta P = - \frac{SP}{Av_{av}} \cdot \frac{4}{s} \approx - \frac{Q_{in}}{Av_{av}} \cdot \frac{4}{s} \quad (39)$$

Therefore

$$\frac{dQ_{in}}{d\delta P} = \frac{dQ_{in}}{dP} = - \frac{1}{4} Av_{av} s \quad (40)$$

Reference 2 G. Rupprecht, "Steady State Solutions Concerning the Lox-Tank Venting System," Contract MC8-824000, December 1971

The average thermal velocity of water molecules at 0°C is $v_{av} = 615 \text{ msec}^{-1}$. Through the evaluation of photographs taken during the dump the surface area of the ice pile can be estimated to $A \approx 1 \text{ m}^2$. Therefore the sticking coefficient becomes:

$$s = -4 \left(\frac{dQ_{in}}{dP} \right) \cdot \frac{1}{Jv_{av}} = \frac{4 \times 2.8}{1 \times 615} = 1.8 \times 10^{-2} \quad (41)$$

Delaney et al., (Reference 3), have obtained the value $s = 1.44 \times 10^{-2}$ in the temperature range between -2°C and -13°C, while H. Patashnick and G. Rupprecht in a recent study found $s = 2 \times 10^{-2}$ for ice particles close to the triple point. Considering the uncertainty in the estimate of the surface area of the ice pile, the value obtained here fits well into the range of expected s values.

The straight line in figure 8 connecting the experimental value between (14:00) and (17:30) constitutes an upper limit for Q_{in} .

After some strong fluctuations on the part of Q_{in} the situation stabilizes and comes to a quasi steady state condition after (17:30) which lasts to the end of the dump at (37:48) when the water flow stops. During this time interval, the values for P and Q_{in} hover around 3.8 torr and 1700 torr lsec^{-1} , respectively. One can evaluate these values to calculate the pumping speed as

$$S = \frac{1700 \text{ torr lsec}^{-1}}{(3.8 - 0.2) \text{ torr}} = 472 \text{ lsec}^{-1} \quad (42)$$

a value which is slightly larger than the previously determined value for water vapor at lower pressures. See equation 23.

At the end of the dump at (37:48), Q_{in} drops again quite drastically and remains in a transient condition, ($Q_{in} < Q_{out}$).

What is changing in this time interval is the temperature of the ice pile which decreases from near freezing to about -32°C. This temperature change has been observed directly with a thermocouple underneath the ice pile. The sublimation energy during this transient time interval stems mainly from the ice pile which acts as a energy storage. In order to check this assumption a simple estimate can be carried out.

For about 4 minutes and 30 seconds, Q_{in} is close to the theoretical value of 2280 torr lsec^{-1} . During this time, 3.5 kg of ice are generated. In the following 24 minutes when ice and water are generated, one can define the fraction μ as

$$\mu = \frac{Q_{in}(\text{experiment})}{Q_{in}(\text{theory})} \approx \frac{1700}{2280} = 0.75 \quad (43)$$

Reference 3 L. F. Delaney & R. W. Houston & L. C. Eagleton, "The Rate of Vaporization of Water and Ice," Chemical Engineering Science, 1964, Vol. 19, Pg. 105-114

and calculate that under these circumstances the fraction of ice, i , and the fraction of water, w , which are produced. One finds

$$i = \frac{1}{L} \left\{ \mu \cdot \frac{(\Delta T + L)(\Delta T + H)}{\Delta T + L + H} - \Delta T \right\} = 0.52 \quad (44)$$

$$w = \frac{1}{L} (1 - \mu)(\Delta T + L) = 0.35 \quad (45)$$

H is the energy of sublimation in $[\text{cal g}^{-1}]$, L the latent heat in $[\text{cal g}^{-1}]$, $\Delta T \approx 32^\circ\text{K}$. At the end of the dump one has 14.5 kg of ice mixed with 7.4 kg of water at the freezing point which can deliver upon cooling the total energy of

$$E'_s = (21.9 \times 32 \times 0.49 + 7.4 \times 80) \text{kcal} = 935 \text{kcal} \quad (46)$$

On the other hand one can estimate the sublimation energy from Q_{in} during the time interval (38:00) to (80:00), assuming that by (80:00) the majority of the stored energy has been spent. Through integration one finds

$$E_s = \int_{(38:00)}^{(80:00)} Q_{in} dt \approx 1.62 \times 10^6 \text{ torr } \ell = 925 \text{ kcal} \quad (47)$$

A comparison between E_s and E'_s shows reasonable agreement between the two values and strongly suggests that the ice pile is indeed the essential source of sublimation energy. For this reason the temperature distributions of the surrounding is of negligible influence during and after the dump up to this point in time.

Later, however, as a quasi steady state condition is approached, the radiative heat transfer to the ice pile becomes important and to a lesser degree the heat transport due to the heat diffusion through the moving vapor. These problems concerning the quasi steady state condition a long time after the dump have been treated elsewhere (Reference 2).

Instead we shall report the observation of a phenomenon which was quite unexpected. It pertains to the influence of CO_2 gas on the sublimation rate of the ice pile, i.e., on Q_{in} . The original idea was to probe Q_{in} independently with a simple method which is insensitive to the bias of the instrumentation. For this purpose CO_2 gas was admitted through the nozzle until the pressure in the waste tank had risen to a certain level (≈ 1 torr). Then the gas was shut off. The assumption was that the ice pile would produce Q_{in} just as before the admission of CO_2 . The concentration of water vapor in the upper compartment would first become much greater than in the rest of the tank. Therefore (k_1) in equation 2 would be different from (k_2) in equation 3. With increasing time, however,

the CO_2 gas in the waste tank would be replaced entirely by water vapor and $(k_2) \rightarrow (k_1)$. The time it takes to replace the CO_2 gas by water vapor was thought to be a convenient measure of the sublimation rate of the ice pile, i.e., a measure of Q_{in} . It did not work out as planned, however.

The observation is reported in figure 9. Prior to time $t=0$, the pressure was held constant for a short while at $P_m \approx 1$ torr by admission of CO_2 at an appropriate flow rate. At the same time the pressure drop ΔP_m across the upper screen was constant at $\Delta P_m = 11.7$ mtorr. At $t=0$ the CO_2 gas flow is stopped. As a consequence ΔP_m drops immediately to about 2 mtorr; drops a bit more and rises to a constant level after 30 minutes. The pressure on the other hand decreases continually as is also shown in figure 9, to a constant level about 30 minutes later. The slight drop of ΔP_m in the first few minutes can be understood on the basis that $C(\text{H}_2\text{O}) < C(\text{CO}_2)$, and that it takes some time to clear the upper compartment of CO_2 gas. A rise of ΔP_m on the other hand is expected because $S(\text{H}_2\text{O}) > S(\text{CO}_2)$. The solution of equations 2 and 3 for the proper boundary conditions concerning (k_1) and (k_2) has been carried out for a sequential series of experiments considering Q_{in} as the unknown. The result of these calculations is shown in figure 10. After a dump of 10 lbs of condensate on top of an existing ice pile, Q_{in} is shown as a function of pressure. As the pressure has decreased to about 0.7 torr, CO_2 gas is added to bring the pressure up to about 1 torr. Then the CO_2 flow is shut off. Q_{in} is now supplied solely by the ice pile. While it was expected that Q_{in} would be unaffected by the presence of the CO_2 gas the experiment clearly shows a strong reduction of Q_{in} marked as Event #25. As time passes, Q_{in} recovers to its original value. In subsequent events, for lower H_2O pressure the effect of a CO_2 purge becomes even more pronounced. This observation shows that the presence of various gases and vapors may have a pronounced effect on the sublimation rate of the waste tank content and opens the possibility of influencing the contamination of the space environment. Of course, under these circumstances the use of CO_2 as a probe for Q_{in} had to be abandoned.

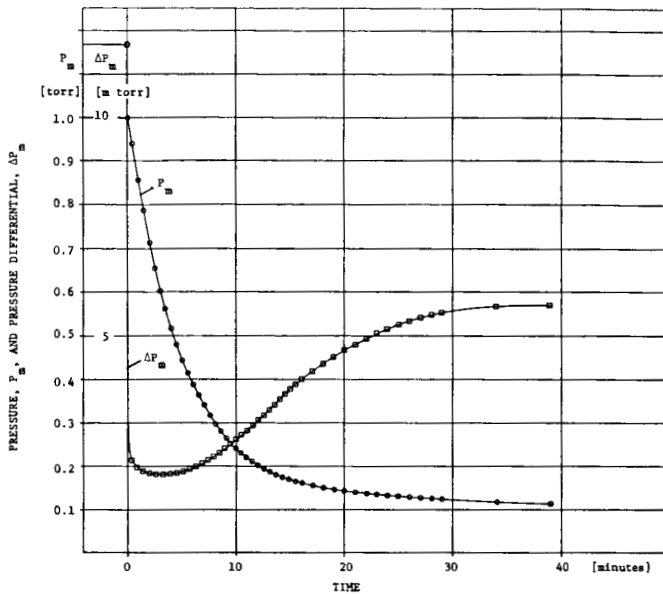


Figure 9. Time Dependence of the Tank Pressure, P_m , And of the Pressure Differential ΔP_m After a CO_2 Purge

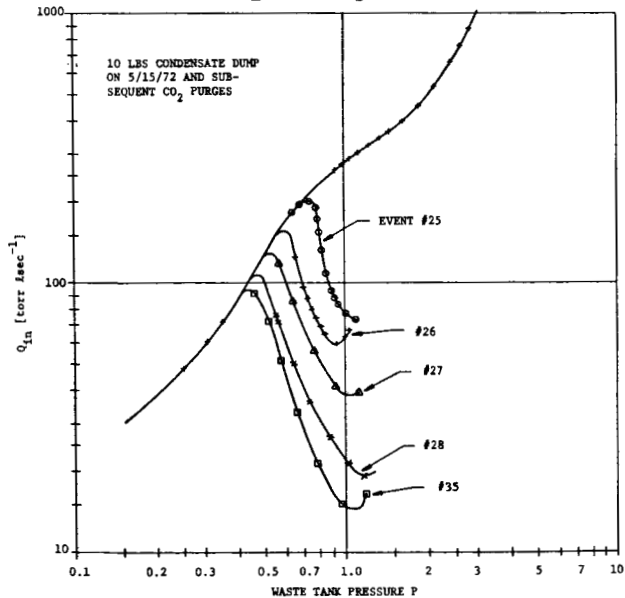


Figure 10. The Effect of CO_2 Gas on the Sublimation Rate of Ice

ACKNOWLEDGEMENT

The author likes to express his appreciation to Mr. E. B. Ress and Dr. R. Rantanen of the Martin Marietta Corporation in Denver for fruitful discussions, to NASA for contractual support and to Ms. Debra Strange and Mr. A. Spamer for helping with the data evaluation and the numerical calculations.

N74-102410

Paper No. 15

THERMAL SCALE MODELING OF A SPACECRAFT RADIATOR WITH COUPLED FORCED CONVECTION-CONDUCTION-RADIATION HEAT TRANSFER

Dr. David P. Colvin, *Becton Dickinson Research Center, Research Triangle Park, North Carolina*
Dr. Dupree Maples, *Louisiana State University, Baton Rouge, Louisiana*

ABSTRACT

A thermal model of a spacecraft radiator has been designed and tested at the National Aeronautics and Space Administration's Mississippi Test Facility. The unique feature of this model is that all three modes of heat transfer--forced convection, conduction, and radiation--are utilized simultaneously under steady-state conditions. A fluid is forced under pressure using similar flow conditions through both prototype and model which are suspended within a cryogenic vacuum chamber. Heat is transferred from the fluid to the tube's inside wall, which then conducts the energy to its outer surface where it is radiated to the surrounding shell that is maintained at a cryogenic temperature with liquid nitrogen. A high vacuum chamber at the facility is used to house the experiment. Both prototypes and models take the form of long tubes with thermocouples welded to the exterior surface to determine the effectiveness of the modeling criteria. Special precautions have been taken to isolate thermally the specimen and to establish a hydrodynamic boundary layer before specimen entry. The wall thickness of the models has been sized to permit both temperature and material preservation. The effects of physical size and fluid flow parameters on the modeling criteria for both low and high thermal conductivity materials are presented.

BACKGROUND

Measurement of temperature plays an important role in design and development of objects or systems which are exposed to hostile environments. An environment such as outer space with its high vacuum and low temperature may be simulated, for test purposes, with a cryogenic vacuum chamber. These space chambers are limited in size and may require extensive supporting facilities. For these and other reasons, use of scale models for test purposes has become expedient and sometimes necessary.

A thermal model may be defined as a model, different and usually smaller in size than its prototype, that will accurately predict the thermal behavior of its prototype under suitable conditions.

A radiator will be used to control the environment within the spacecraft during such extended missions as that proposed

for Skylab. These radiators will transfer heat energy from a fluid which has been circulated through the living quarters and electronic equipment. This energy will then be radiated in a controlled manner to deep space so that a suitable environment can be maintained within the spacecraft. Space radiators will be used on Skylab's Apollo Telescope Mount and the 14-foot-diameter Space Station Module. Future radiators such as those for a space Shuttle Vehicle may be extensive in size and could require elaborate test facilities.

In order to model thermally a given object or system accurately, the scale factors or ratios of model-to-prototype parameters must be determined. Thus, one may observe the behavior of the parameter of interest--for example, temperature--on the model; and by application of the scale factor, he may determine what the parameter would be in a corresponding location on the prototype or full-scale specimen.

The period of time during which the parameter of interest is observed is important for analysis purposes. Equilibrium conditions which may occur during long periods of space travel may be successfully modeled as steady-state conditions. Time periods during which parameters may vary, such as launch, mid-course correction, and reentry, involve transient conditions.

Thermal energy or heat is transferred due to a difference in temperature and depends upon the nature of the surrounding medium. Heat may be transferred by conduction through solids or fluids due to direct contact of mass. Convective heat transfer occurs between a fluid and a surface and depends upon the motion; e.g., velocity of the fluid relative to the surface. Free or natural convection involves fluid flow due to a density gradient whereas forced convection occurs when the fluid is forced to flow because of a difference in pressure. Radiation heat transfer or infrared electromagnetic radiation does not require an intermediary medium and becomes increasingly important with large temperature differences.

Previous work in thermal modeling has involved mainly steady-state conduction and conduction-radiation coupled systems such as may be found in the walls of an unmanned spacecraft during a long interplanetary voyage. Some investigations into transient modeling of these systems have also been accomplished. Convection-conduction-radiation coupled systems as encountered in fluid systems and manned spacecraft have only recently and partly been investigated. Steady state and transient analyses on a system of concentric cylinders with free convection within an annulus was completed in 1969; but, prior to this research, no work had been published on convection-conduction-radiation coupled systems involving forced convection.

The purpose of this research was to investigate the applicability of thermal modeling under steady-state conditions for a single material system involving forced convection from a flowing fluid in a tube, conduction through and down the tube, and radiation to a cryogenic vacuum environment.

Investigations into thermal modeling of spacecraft and their components began less than 10 years ago. Some of the studies included experimental programs, while others were theoretical. Numerical analysis has been frequently used to verify proposed modeling criteria. Most of the studies involved coupled conduction and radiation systems under steady-state and transient conditions. Jones [1] used the similitude method to reduce a set of simultaneous, first-order differential equations which described the thermal behavior of spacecraft to a group of 28 ratios that were required to remain constant. These ratios contained six independent sets. Rolling [2] used the similitude approach to develop the modeling criteria for space vehicles. Adkins [3] introduced a method of geometric scaling that allowed thermal modeling while preserving both material and temperature. He utilized similitude to develop modeling criteria for a thin-walled cylinder. Miller [4] investigated the application of thermal modeling to steady-state and transient conduction in cylindrical solid rods for both single and multiple material systems. Maples [5] was evidently the first to investigate thermal modeling with all three modes of heat transfer simultaneously. He analyzed the problem of free or natural convection in the annulus of a concentric cylinder system. The similitude approach was applied to the energy differential equation to obtain the modeling criteria. Both temperature and material preservation were employed, and the diameter was scaled as $D^* = L^2$. Thermal energy was conducted radially from a heater within the inner cylinder through the wall to dry air within the annulus. Following the free convection across the annulus, the heat was conducted through the outer cylinder and radiated to the cryogenic liner surrounding the inside of the vacuum chamber. MacGregor [6] at Boeing analyzed the limitations associated with thermal modeling. An understanding of errors resulting from uncertainties in the thermophysical properties, geometric dimensions, and the test environment was the primary objective of this study. Rolling, Murray, and Marshall [7] at Lockheed also discussed the limitations associated with thermal scale modeling at length. It was concluded that the problems regarding model construction, instrumentation, and materials selection become increasingly difficult at the smaller scale ratios. Temperature preservation was preferred over material preservation, and the use of both techniques simultaneously required geometric distortion of all components which could become difficult in most complex systems. Colvin and Maples [8] outlined the procedures for this experiment in April 1971 and presented preliminary data for one stainless steel model and prototype. Colvin [9] reported the complete results of this experiment in June 1971.

MODELING CRITERIA

Thermal modeling has been divided into two categories: temperature preservation and material preservation. Temperature

preservation required that temperatures at analogous locations on the prototype and model be equal. In some cases this may require that a different material be used for the model than for the prototype. Material preservation permits the use of the same material for both prototype and model, but predicts a scaled difference in temperature at analogous locations. Most researchers prefer to maintain thermal similitude between prototype and model, but it would also be desirable to use the same material for both objects. This combination of criteria has been used by Miller [4], Adkins [3], and Maples [5]; and appears to be satisfactory under certain circumstances. The restriction involves the use of a thin-wall approximation which may be acceptable depending upon the object being modeled. For the case of a thin-walled tube or chamber such as a spacecraft wall, this approximation may be used to develop certain modeling criteria.

Further, thermal modeling may be approached in two ways: dimensional analysis or similitude. Dimensional analysis requires knowledge of all parameters associated with the problem, but can lead to useful results. The similitude approach involves the use of the governing differential equations and boundary conditions and offers a distinct advantage to the inexperienced. Either method results in the same set of similarity parameters, but the similitude approach will be used here.

Before deriving the similarity parameters, the constraints imposed upon the problem will be discussed. The first restriction involved the use of homogenous and isotropic materials. The second required that there be perfect geometric similarity between prototype and model. Thirdly, the model and prototype must have the same uniform and constant surface characteristics. This was achieved by coating the surfaces of both the prototype and model with a highly absorptive flat black paint. The fourth requirement was that the radiant heat flux from the simulated environment was approximately zero. This approximation was achieved by using a cryogenic liner cooled to liquid nitrogen temperature to simulate the environment. It was also assumed that all energy radiated from the prototypes and models was absorbed by the cryogenic liner. The fifth restriction was that the properties of the prototype and model were constant and invariable during testing. Use of a small temperature range of approximately 30 F to 80 F insured this approximation. A sixth constraint was that heat transfer by convection and conduction external to the specimen was negligible. This criteria was satisfied by a vacuum environment, the suspension of the test element on nonconducting threads, and its connection to adjacent tubing with insulated fittings.

With these constraints it was decided to test a low and a high thermal conductivity material to verify the modeling criteria for the forced convection-conduction-radiation problem. A fluid at room temperature with a fully developed velocity boundary layer was introduced to a tubular specimen with a large length-to-diameter ratio. Heat was then transferred from the

water to the inner surface of the tube by forced convection. This energy was then transferred through the tube to its outer surface and along its length by conduction. Because the specimen tube was thermally insulated from its connecting members and surrounded by a vacuum environment, the only avenue remaining for heat transfer from the outer surface was radiation to the cryogenic liner. The specimen tube was allowed to achieve thermal equilibrium, thereby satisfying the steady-state criteria.

Similarity parameters were derived by Colvin and Maples [8] from the conduction equation for the temperature distribution in a pipe. The results of the modeling criteria may be summarized as

$$D^* = t_w^* = Nu^* = L^{*2} \quad (1)$$

and

$$T^* = \kappa^* = 1 \quad (2)$$

where Nu is the Nusselt number, κ is the tube's thermal conductivity, t_w is the wall thickness of the tubing, L is the length of the tube, and T is the surface temperature of the tube. Equation 2 implies both temperature and materials preservation. The * indicates a scaled quantity of model-to-prototype ratio.

TEST SPECIMENS

In order to verify the modeling criteria, a series of test models were fabricated of both high and low thermal conductivity materials. A 1.0-inch outside diameter (O.D.) type 304 stainless steel tube 48 inches in length was used as the prototype or full-size low thermal conductivity specimen. Three scale models were then fabricated from 0.75-inch O.D., 0.50-inch O.D., and 0.25-inch O.D. type 304 stainless steel tubing. Their scale lengths were 41.568 inches, 33.936 inches, and 24.000 inches, respectively. A 1.0-inch O.D. type 6061 aluminum tube 48 inches in length was used as the prototype high thermal conductivity specimen. Three scale models were also fabricated from 0.75-inch O.D., 0.50-inch O.D., and 0.25-inch O.D. type 6061 aluminum tubing to the same lengths as those of the stainless steel models.

The scale models were fabricated on a lathe by turning down the O.D. of the tube to the desired wall thickness based upon the modeling criteria given earlier and the average wall thickness of the 1.0-inch O.D. prototype. According to the criteria, the wall thickness scales as the diameter. Thus, the wall thickness of the 0.75-inch O.D. model must be 0.75 the wall thickness of the 1.0-inch O.D. prototype. Likewise, wall thickness of the 0.50-inch model must be 0.50 the wall thickness of the 1.0-inch O.D. specimen, and 0.25-inch O.D. model must have a wall thickness that is 0.25 the wall thickness of the 1.0-inch O.D. prototype. The outside diameter of the models was then turned down on a lathe to yield the desired wall thickness. A short lip of material was left to the original O.D. to facilitate machinability and allow connection of the model with common fittings

during testing. Because of the selection of nearest largest-size tubing, this lip was usually only 0.010 inch larger than the turned-down dimension and thus can be considered to contribute little, if any, thermal effect to the temperature measurement near the ends of the tubing.

In order to insulate thermally the specimen tube from the tubing before and after itself, nylon Swagelok unions were used as connections at each end. Teflon front ferrules were used in each fitting to achieve better sealing characteristics of the connection. Additionally, to insure a smooth flow within the tube at the leading end, a teflon insert was fitted within the nylon union and its inside diameter was matched to the inside diameter of the respective tubing.

It was then necessary to fabricate an entrance tube of proper length from the same stock as that of the test specimen so a desirable fluid flow profile or velocity boundary layer within the tube could be established before entry into the test specimen. The inside diameter of the entrance tube, front fitting, and test specimen were then the same; thus avoiding any discontinuities that could induce undesirable turbulence or mixing within the flowing fluid. The length of the entrance tube for the establishment of laminar flow is a function of both Reynolds number and tubing size according to the relation

$$L = \left(\frac{d}{20}\right) Re$$

where L was the required tube length, d was the tube diameter, and Re was the dimensionless Reynolds number.

The 1.0-inch O.D. tubing had an entrance tube length of 100 inches. The 0.75-inch O.D. entrance tube was 75 inches in length. Similarly, the 0.50-inch O.D. entrance tube was 50 inches long, while the 0.25-inch entrance tube was 25 inches in length. Plug gages were fabricated from brass or nylon rods and used to insure alignment.

It was necessary to attach thermocouples to the exterior surface of the specimen tube in order to determine thermal similarity between prototype and model. Fourteen 30-gage, copper-constantan thermocouples were fabricated and spot welded to each specimen tube at certain locations (Figure 1). Leads to each thermocouple were wrapped circumferentially around the specimen to minimize lead wire measurement error. The tubes were then spray painted with two thin coats of flat black paint (Velvet coating 101-C10 by 3M) to insure uniform and efficient radiative heat transfer. Thermocouple lead wires were then painted with a bright aluminum paint to a distance at least six inches from the tube to reduce lead wire radiation loss and subsequent measurement error.

EXPERIMENTAL APPARATUS

The experimental apparatus can be divided into eight basic

sections: the vacuum and cryogenic system, the tubular system, the instrumentation and recording system, the inlet temperature control system, the flow pressurization system, the flow evacuation system, the flow measuring and control system, and the flow collection system. A schematic diagram of the pressurization and flow systems is given in Figure 2.

Prototypes and models were fabricated for test inside a space simulation chamber that provided the necessary low temperature, high vacuum environment for accurate simulation of energy exchange between the tubes and their surroundings. A Murphy-Miller high altitude test chamber is a standard piece of test equipment located at the National Aeronautics and Space Administration's (NASA) Mississippi Test Facility. This chamber was constructed of carbon steel with an interior 48 inches in diameter, 60 inches long, and had a raised shelf four inches above the bottom. The chamber was evacuated through one end, and a full-width door across its opposite end provided easy access to the interior. Instrumentation feedthroughs in the chamber wall permitted direct connection to the 16 thermocouples; fluid feedthroughs introduced liquid nitrogen to the cryogenic liner. This liner was designed to fit within the chamber like a sleeve and simulate the low temperature environment of outer space. The liner shell was constructed of stainless steel with interior dimensions 54 inches long and 38 inches in diameter. The inner wall of the liner was coated with 3M Velvet Coating 101-C10 black paint to insure a surface with high and uniform values of emittance. The outer wall of the liner and the inner wall of the chamber were covered with aluminum foil to reduce the heat transfer between the two surfaces. The liner was supported on four adjustable legs to minimize heat conduction from the outer chamber wall to the liner. Installation of fitted covers to the liner wall reduced heat transfer through the chamber portholes. During operation the inner wall of the liner normally reached -290 F, while its outer wall read -275 F. The 100-gallon insulated dewars filled with liquid nitrogen supplied the cryogenic system.

The tubular system consisted of the specimen tube, its entrance tube, and the flex hoses used to connect the tubes to the other systems in this experiment. Flexible hoses used to connect the systems were made of stainless steel lined with teflon and had an inside diameter of 0.5 inches. The specimen tube under test was suspended horizontally from the top of the chamber liner on two thin nylon cords very long in comparison to their diameter to minimize conduction losses. A short fitting at the exit end of the tubing permitted a thermocouple measurement of the fluid temperature as it left the instrumented specimen tube. Here fluid flowed through a flexible hose insulated with radiation shielding made of 40 wraps of crinkled 0.001-inch aluminized mylar to the exit port on the chamber. A similar radiation shield was placed around the entrance tube between the chamber door and the front nylon coupling to the specimen tube.

Cajon Ultra-Torr fittings were used to vacuum seal entrance and exit tubes at the chamber flanges on the door and exit port. A thermocouple gland and stainless steel tee were attached to the front of the entrance tube to permit a fluid temperature measurement before the working fluid entered the specimen tube. A metal Swagelok union fitting with nylon ferrules at the front end of the entrance tube facilitated introduction of the plug gage into the tubes for alignment purposes. Fourteen 30-gage copper-constantan thermocouples were used to measure the temperature distribution along the specimen tube. Additionally, one was used to measure the temperature on the inside wall of the cryogenic liner, and another one was used to measure the exit fluid temperature as previously described. These 16 thermocouples were connected to 12-gage thermocouple lead wires with transition junctions where the larger thermocouple lead wire was inserted through the vacuum chamber wall by means of four vacuum feedthroughs. Outside the chamber, thermocouple lead wires were connected from the feedthroughs to an ice-bath reference junction and then to strip-chart recorders located in an adjacent recording room.

Constantan thermocouple lead wires were connected to copper wires, insulated with General Electric RTV silicone sealant at the reference junction, and placed inside an insulated dewar filled with a crushed ice and water mixture. A multipoint strip-chart recorder sampled each of 12 thermocouples for 10 seconds, amplified its signal through one common amplifier, and printed the appropriate thermocouple number at the temperature location on the continuously moving strip chart. These features permitted fast calibration, easy monitoring, and simple data reduction. Eight Bristol strip-chart recorders used in addition to the multipoint to record data such as tube temperatures, water temperature, liner temperature, helium ullage pressure, and water pressure. Strip-chart recorders were calibrated before each experiment with a Leeds and Northrup Type 8690 precision potentiometer.

Consisting of a heating chamber and an electronic temperature controller, the temperature control system was used to control the inlet fluid temperature to 75 ± 0.5 F. A source of pressurized gas, a pressure regulator, and a water reservoir made up the flow pressurization system. Because of its high insolubility in water, helium gas, stored in cylinders, was used to provide ullage pressure at the top of the reservoir; thus forcing the water through the bottom drain and a 10-micron filter, and into the temperature control system. An open-system arrangement was preferred to a closed system to maintain a constant and known water inlet temperature to the specimen tube within the vacuum chamber. Distilled water was used as the working fluid for this thermal modeling investigation. Eighty-two gallons were stored in a glass-lined water heater reservoir. The large capacity of this reservoir provided an adequate volume for a complete experiment, yet yielded a very slow change in head pressure due to the falling level of the water in the water

tank. This slow change in head pressure reduced the need for adjustment of the ullage pressure while awaiting stabilization of a steady-state temperature distribution down the specimen tube. A pressure regulating valve was used to control ullage pressure of a gaseous helium at 20 psig, and a pressure relief valve provided safety. A strain-gage type pressure transducer was used to sense ullage pressure.

To insure that no air was in the entrance and specimen tubes of the tubular system, water was forced to flow down to the entrance tube and up from the specimen tube inside the vacuum chamber. Moreover, a vacuum pump was used to evacuate the tubular system prior to water introduction and then to draw the water through the tubular system and into the fluid collection system. After valving off the flow measuring and collecting systems, this pump pulled a high vacuum on the tubular system at the exit tube and then drew the water from the water tank through the entrance and specimen tubes. A five-gallon, vacuum-transfer safety bottle prevented the introduction of water into the vacuum pump. A valve was used to close off this suction system when smooth and airless flow of water was obtained.

The effectiveness of this air-bleeding operation could be determined by comparing the two sets of thermocouples located the same distance down the specimen tube. One set in the middle of the tube was located at the top and bottom surfaces, while the other set near the exit end of the tube was located on the top and side surfaces. These two sets of thermocouples were used to indicate the peripheral heat flux about the tube and were invaluable in indicating the presence of entrapped air within the specimen tube.

It was important that similar flows be used in each tube so that the effectiveness of the modeling criteria could be studied. The Reynolds number, a dimensionless flow parameter, was selected as the criteria for flow similarity. For a given fluid and tube inside diameter (I.D.), the Reynolds number is related to the volume flow rate in gallons per minute or grams of water per minute. This fact provided a simple means of flow rate calibration. Water was collected in a beaker for one minute and weighed on a set of Ohaus Triple-beam laboratory balance scales accurate to 0.1 gram. Balance was calibrated against a set of certified standard weights. Timing was accomplished with a stopwatch whose accuracy was also certified.

The upstream or head pressure was held at 20.0 ± 0.05 psig by means of a Heise pressure measuring gage and a strain-gage type pressure transducer. The flow was then passed through a 10-inch Brooks rotameter modified to have a range capability of from 0.0003 to 0.04 gallons per minute of water. This was accomplished by using a rotameter that had a very low flow rate capability and shunting the rotameter with a fine micrometer needle valve. It should be pointed out that the calibration curves were used merely as a guide and that an on-line measurement of flow rate was made during each run of the experiments.

This insured an accuracy of flow rate measurement which exceeded the repeatability of the rotameter.

A 16-turn needle valve was used to control the flow and provided a sufficient fine adjustment to this critical parameter. The flow then passed through a tee that provided a choice of two paths, each of which could be shut off with a valve. One path was to the top of the two spherical storage containers of the flow collection system. The other path was to a height identical to that of the former path to the collection system and then to an open tube which permitted collection of the water in the beaker for a flow rate determination. The same height for each flex hose path was important to give the same back pressure during either the flow measurement or collection in the storage spheres.

The flow collection system consisted of two 40-gallon spherical tanks manifolded together to provide adequate storage for the water during an experiment. Water flowed into the top of each sphere rather than the bottom to provide a constant back pressure. Two tubes extended above the tanks provided venting of the displaced air.

Use of a closed collection reservoir system also permitted its pressurization to cycle the water back into the water tank at the conclusion of a day's run. Vent tubes were capped, the valve on the control system was closed, the helium pressurization system was connected to the collection system, and the resulting pressurization of the spherical tanks forced the water through the manifolded bottom of the spheres. From this point, the water flowed through a 40-micron filter and returned to the water tank reservoir.

RESULTS AND DISCUSSION

Experimental test data for the $\frac{1}{2}$ " stainless steel and $\frac{1}{2}$ " aluminum specimen tubes are shown in Figures 3 and 4. Although fluid inlet temperature to the entrance tube was held to 75 ± 0.5 F, the different lengths of entrance tube along with the different flow rates contributed to a varying degree of heat loss prior to fluid introduction to the specimen tube. Temperature measurement of fluid temperature at the specimen tube entrance was not possible without disturbing the established hydrodynamic boundary layer. Because of this variation it was necessary to normalize the data graphically to a consistent temperature of 65 F at thermocouple number 1 located at $z^* = 0.05$. The selection of this temperature required the least shift of fluid temperature at this location. The associated difference in thermal radiation is negligible. Results of this normalization are presented in Figures 5 through 6 for different Reynolds number and material as a function of tube diameter.

Comparison of the normalized data shows that the same temperature distribution down the tube occurs at $Re = 45$ for the 1.0-inch O.D. tube, $Re = 40$ for the 0.75-inch O.D. tube, $Re = 35$ for the 0.5-inch O.D. tube, and $Re = 25$ for the 0.25-inch

O.D. tube. Furthermore, the distributions and flow rates correspond well for both stainless steel and aluminum tubes. These results are shown in Figure 7, 8, and 9. The Reynolds numbers mentioned above gave a temperature difference less than 1 F for the stainless steel tubes and less than 2 F for the aluminum tubes. Consistency between both materials for the same Reynolds numbers was within 3 F. These temperature differences are also presented as percent error in terms of absolute temperature and percentage of total temperature difference down the tube in the Table 1 below.

TABLE 1
MODELING ERROR

Tube Combination	Temperature Difference	% Error Abs. Temp.	% Total Temp. Difference
Stainless Steel	1 F	0.196	5.88
Aluminum	2 F	0.392	11.75
S. Steel & Aluminum	3 F	0.588	17.65

The slight dispersion of data for the aluminum tubes is probably due to a larger conduction error resulting from the tube's higher thermal conductivity. Heat conduction is seen to be minimal at $z^* = 0.7$. Conduction error at this location is calculated to be 3.2% for the 1.0-inch O.D. tube and 6.45% for the 0.75-inch tube.

The thermal distribution around the cryogenic liner showed marked differences in temperature between the cylindrical shell and the uncooled end plates. Porthole and porthole covers, which were warmer than the surrounding shell, also contributed to the elevated temperature of the surroundings. The effect of this raised surroundings temperature introduced an error of 2.5% to the 1-inch O.D. tube radiating at 50 F.

Calculation of Grashof number requires the knowledge of temperature difference in the fluid at the top and bottom of the tube. This was not measured because of the disturbing effect of an instrument on the hydrodynamic boundary layer. Temperature differences between top and bottom on the exterior of the tube never exceeded 2 F, and an assumed $\Delta T = 1$ F across the fluid gave Grashof numbers ranging from $Gr = 7$ in the 0.24-inch O.D. tube at 40 F to $Gr = 8850$ in the 1.0-inch O.D. tube at 70 F. This range extends from the laminar into a region that is possible to have mixed flow (free and forced convection). Very little investigation has been made in this area, and no work could be found for mixed flow in horizontal tubes. It is difficult, however, to see where free convection can play a major role in the heat transfer within the tube.

Experimental verification of the modeling criteria for Nusselt number, $Nu^* = D^* = L^*2$ was not attempted since lack of fluid temperature data prevented the determination of h , the convective heat transfer coefficient. It may be pointed out, however, that $Nu^* = D^*$ requires that $h^* = 1$ for the same fluid.

The thermal entry length was calculated to range from $z = 1.6$ inches in the 0.25-inch O.D. tube at $Re = 25$ to $z = 12.8$

inches in the 1.0-inch O.D. tube at $Re = 45$.

The relationship between $Re^* = Re_m/Re_p$ and D^* may be determined from the experimental data presented in Figures 7, 8, and 9. Values for these parameters are given in Table 2 below.

TABLE 2
CALCULATION OF Re^* AND D^*

D_o (in.)	D_i (in.)	D_i^*	Re	Re^*
1.0	0.7629	1.0	45	1.0000
0.75	0.5625	0.73732	40	0.88889
0.50	0.3852	0.50492	35	0.77778
0.25	0.1913	0.25075	25	0.55556

These values are presented graphically in Figure 10.

A least-square curve fitting routine for a parabolic distribution was programmed on a computer. The resulting equation was found to be $Re^* = 0.29909 + 1.15314D^* - 0.45605D^{*2}$ over the range from $D^* = 0.25$ to $D^* = 1.0$. This resulting curve is also given in Figure 10. The overall estimated error was $-8.3 \pm 5.3\%$.

CONCLUSIONS AND RECOMMENDATIONS

Fluid flow rate was found to have a large effect upon thermal modeling, and its measurement at very low Reynolds numbers presented difficulties. With regard to Reynolds number criteria, no other investigations have been published in this area, therefore a comparison of results is not possible.

The experiment and its analysis was complex. In order to obtain a sufficient temperature distribution along the tube to allow thermal modeling, the flow rate had to be reduced to a point where the presence of mixed flow was possible. Complete thermal isolation of the specimen tube was impractical due to end connections which permitted some conduction error, particularly in the aluminum tubes. Fluid temperature measurements within the tube could not be made without disturbing the hydrodynamic boundary layer; hence, a complete analysis of convective heat transfer was not possible. The temperature distribution within the cryogenic liner was not close to being isothermal and low. This problem would have been minimized by fabrication of the cryogenic liner from a material with a high thermal conductivity such as brass or aluminum rather than stainless steel.

In spite of these problems it is felt that the investigation provided meaningful results which were previously unavailable and represents an initial inquiry into thermal modeling with three-mode heat transfer including forced convection.

Recommendations for further investigations include the study of mixed flow in a simulated space environment and its effect

upon thermal modeling with forced convection at higher flow rates, and further definition of the modeling criteria for the Reynolds number.

The study of mixed flow in a simulated space environment could be accomplished in a setup similar to the one used for this investigation. A thin-walled tube of low thermal conductivity could be thermally instrumented along its upper and lower surfaces and the temperature distributions could be studied for various tube orientations and flow rates.

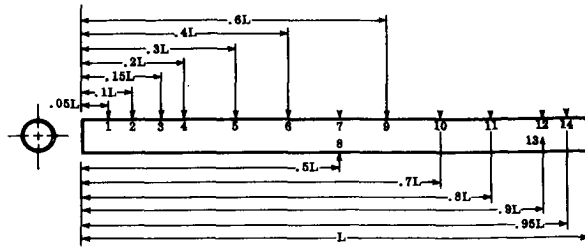
Thermal modeling with forced convection at higher flow rates may be possible by using higher inlet fluid temperature. Increased radiation heat transfer at higher temperatures may yield a sufficient temperature drop along the tube to permit modeling evaluation. Although tube length in experiment was limited to 48 inches by the chamber dimensions, the use of a coiled tube may provide an effective extended length.

The modeling criteria for Reynolds number should be evaluated under test conditions which preclude the possible effects of mixed flow. Conduction error can also be reduced by use of teflon union fittings or similar devices for connection of the specimen tube to the adjacent plumbing.

REFERENCES

1. Jones, B. P. "Thermal Similitude Studies." J. Spacecraft, 1 (4): 364-369, July-August 1964.
2. Rolling, R. E. "Results of Transient Thermal Modeling in a Simulated Space Environment." AIAA Thermophysics Specialist Conference, Monterey, California, Paper No. 65-659, September 1965.
3. Adkins, D. L. "Scaling of Transient Temperature Distributions of Simple Bodies in a Space Chamber." AIAA Thermophysics Specialist Conference, Monterey, California, Paper No. 65-660, September 1965.
4. Miller, P. L. "Thermal Modeling in a Simulated Space Environment." Ph.D. Dissertation, Oklahoma State University, July 1966.
5. Maples, Dago. "A Study of Spacecraft Temperature Prediction by Thermal Modeling." Ph.D. Dissertation, Oklahoma State University, November 1968.
6. MacGregor, R. K. "Limitations in Thermal Similitude." Boeing Report, Contract NAS8-21422, December 1969.
7. Rolling, R. E., D. O. Murray, and K. N. Marshall. "Limitations in Thermal Modeling." Lockheed Report, Contract NAS8-21153, December 1969.
8. Colvin, D. P. and Dupree Maples. "Thermal Scale Modeling of a Spacecraft Radiator with Coupled Convection-Conduction-Radiation Heat Transfer." Proceedings of the Institute of Environmental Sciences, page 428, 17th Annual Technical Meeting, Los Angeles, California, April 1971.
9. Colvin, D. P. "Thermal Scale Modeling of a Spacecraft Radiator with Coupled Forced Convection-Conduction-

Radiation Heat Transfer." Ph.D. Dissertation, Louisiana State University, June 1971.

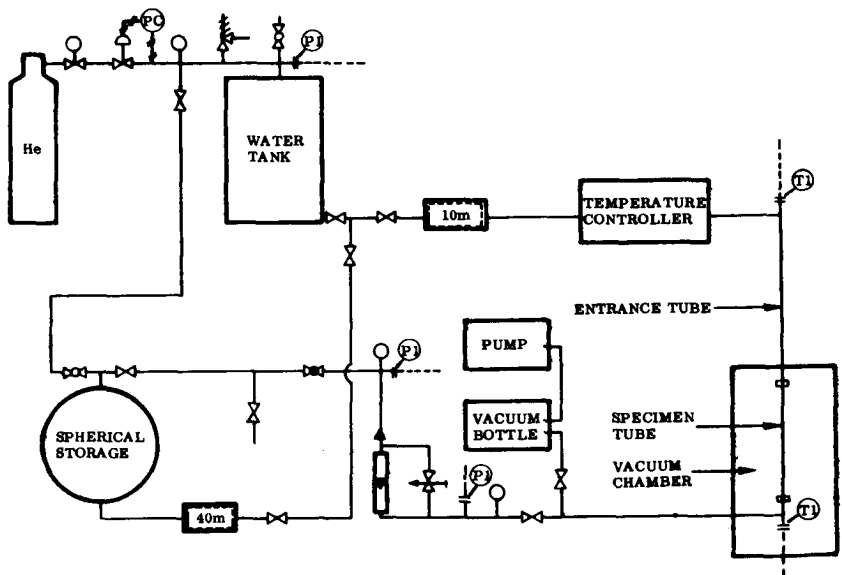


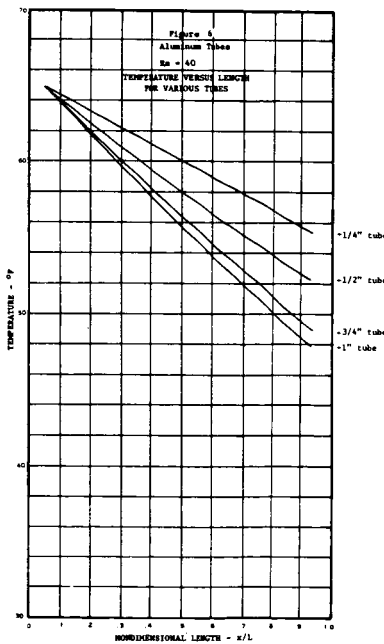
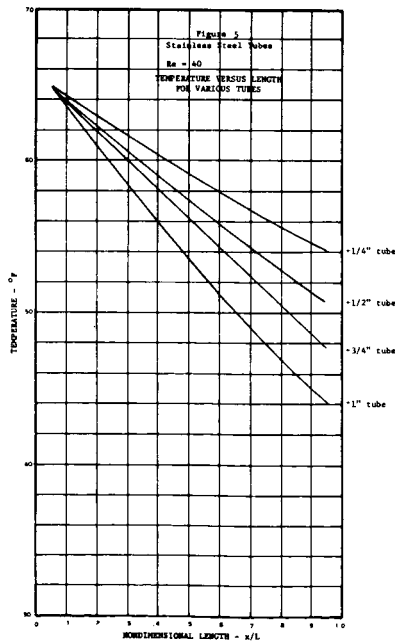
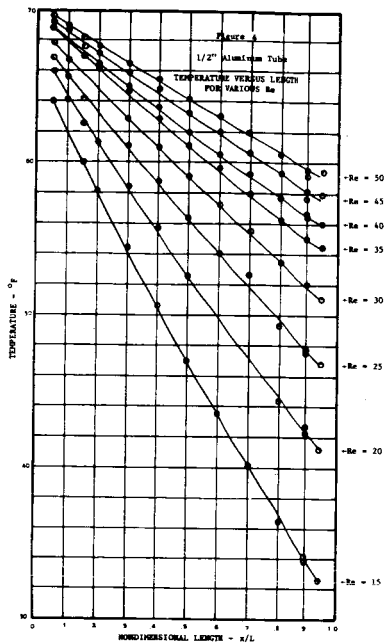
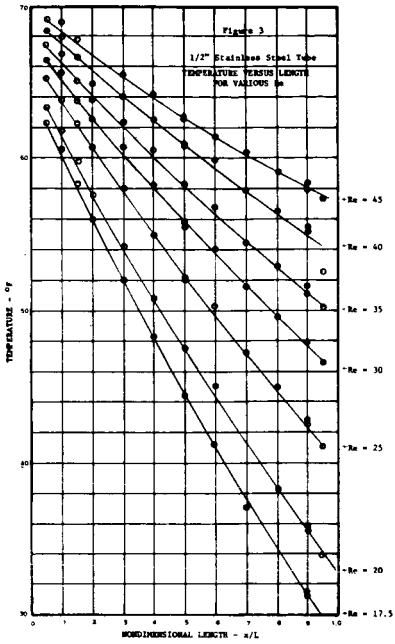
Thermocouple Number	TUBE LENGTH DIMENSION*													
	L	.05L	.10L	.15L	.2L	.3L	.4L	.5L	.6L	.7L	.8L	.9L	.95L	
Tube Diameter														
1.0	48.000	2.40	4.80	7.20	9.60	14.40	19.20	24.0	28.8	33.6	38.4	43.2	45.6	
.75	41.568	2.078	4.157	6.235	8.314	12.470	16.627	20.784	24.941	29.098	33.254	37.411	39.490	
.50	33.936	1.697	3.394	5.090	6.787	10.181	13.574	16.968	20.362	23.755	27.149	30.542	32.239	
.25	24.000	1.20	2.40	3.60	4.80	7.20	9.60	12.00	14.40	16.80	19.20	21.60	22.80	

* All dimensions are shown in inches.

Figure 1. THERMOCOUPLE LAYOUT ON SPECIMEN

Figure 2. PRESSURIZATION AND FLOW SYSTEMS SCHEMATIC DIAGRAM





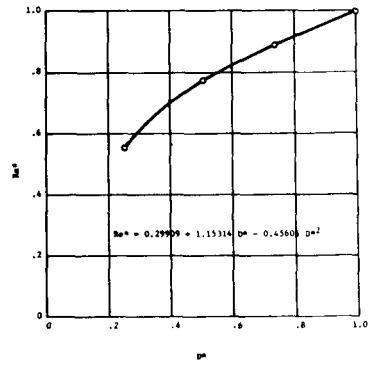
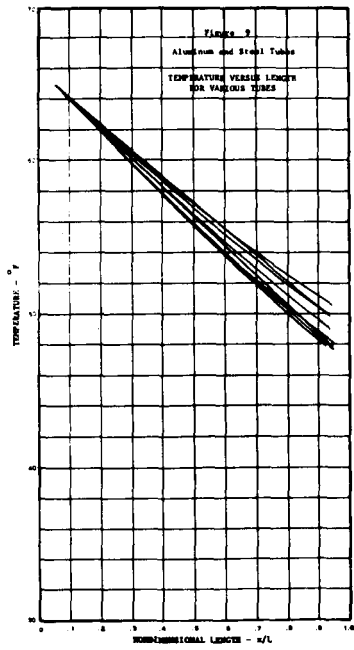
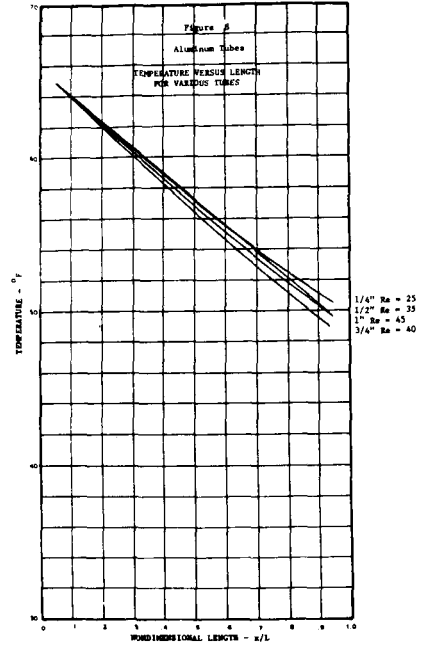
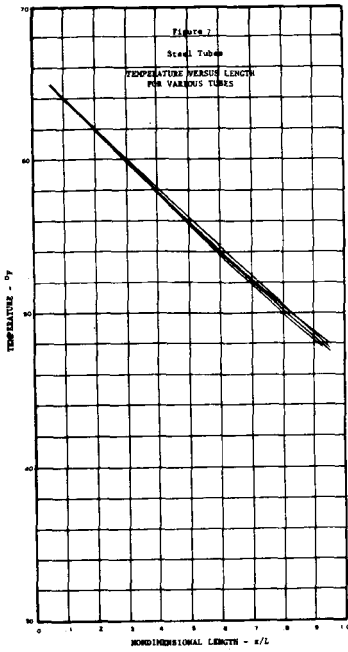


Figure 10. Graphical Relationship Between Be^* and D^*

SIMULATION OF MARTIAN EOLIAN PHENOMENA IN THE ATMOSPHERIC WIND TUNNEL

J. D. Iversen, *Iowa State University*; R. Greeley, *University of Santa Clara*; J. B. Pollack, *NASA, Ames Research Center*; and B. R. White, *Iowa State University*

ABSTRACT

Comparisons are made between the Mariner 9 photographs of wake streaks associated with craters on Mars, and experiments conducted in an atmospheric boundary layer wind tunnel. The appropriate modeling parameters are developed and discussed. The results of threshold speed experiments for a variety of particle densities and diameters are presented and used to predict threshold speeds on Mars.

The Atmospheric Wind Tunnel

Several wind tunnel installations have been constructed to investigate the effects of wind on sand and soil movement. The primary facility for studying the transport of sand by wind was that of Bagnold¹. Experiments conducted in his wind tunnel resulted in definitive curves and equations for threshold friction speed and mass transport of sand due to wind. Another facility used mostly for studying wind erosion of soil is described by Chepil and Woodruff². Other wind tunnels for the study of soil and sand transport by wind have been built^{3,4}. Since the atmosphere on Mars is much less dense than on Earth, facilities were proposed in which Martian dust storms could be simulated under reduced pressure^{5,6}. One wind tunnel was constructed and threshold speeds were determined at pressures as low as those on the surface of Mars⁷⁻⁹. Although an exact experimental determination of threshold speed should be performed in a low-density wind tunnel, deposition and flow patterns over surface features can be modeled to some extent in a normal atmospheric boundary-layer wind tunnel⁶, if close attention is paid to satisfying appropriate modeling parameters and to the wind tunnel boundary layer configuration.

The structure of the turbulent planetary boundary layer on earth has been studied extensively^{10,11}. Jensen¹² and others have observed that the lower portion of the planetary boundary layer (in a neutrally stratified atmosphere) follows the logarithmic law

$$\frac{u(z)}{u_*} = \frac{1}{k} \ln \frac{z}{z_0} \quad (1)$$

where u_* is the friction velocity and k is von Kármán's constant ($k \approx 0.4$). Jensen showed that for simulation of the atmospheric boundary layer, the roughness parameter for the wind-tunnel floor must scale with the roughness parameter in nature, i.e.,

$$\frac{z_{0M}}{z_0} = \frac{L_m}{L} \quad (2)$$

Most investigators have relied on the long test section to simulate the turbulent boundary layer profile so the model is immersed in the boundary layer^{13,14}. However, it is possible, although perhaps not as desirable, to produce thick boundary layers with the proper scaled velocity profiles in shorter test sections¹⁵⁻¹⁷. Effects due to a nonneutral atmosphere (stable or unstable) can be simulated to some extent by cooling or heating the tunnel floor¹³.

Modeling of Martian Eolian Phenomena

The deposition and erosion of fine particles blowing over a complex terrain presents a very intricate phenomenon to attempt to physically simulate on a smaller geometric scale. The erodibility of soil or sand is a complicated function of mean wind speed, frequency and intensity of gusts, and particle size distribution, density and shape, and topographic surface roughness. An optimum size occurs, for soil on earth, for which the threshold speed is a minimum. On Mars, the optimum particle size and threshold speeds are predicted to be larger¹⁸, mostly because of lower atmospheric density, although terminal speeds for like particles are predicted to be about the same as on earth⁵.

The list of important physical parameters in the eolian process includes:

- D_p particle diameter
- L major terrain feature length (such as crater diameter)
- l all other terrain feature lengths
- z_0 roughness length
- z'_0 roughness length in saltation
- h specified altitude for reference speed
- L^* Monin-Obhukov length (atmospheric stability parameter)
- λ ripple wavelength
- $U(h)$ reference wind velocity

U_F	particle terminal speed
u_*	friction speed
u_{*t}	threshold friction speed
ρ	atmospheric density
ρ_p	particle density
ν	kinematic viscosity
t	time (duration of phenomenon)
e	coefficient of restitution

These parameters can be arranged in the form of dimensionless similitude parameters.

1.	$\frac{D}{L}$	length ratio
2.	$U(h)/U_F$	reference to particle terminal speed ratio
3.	$[U(h)]^2/gL$	Froude number
4.	e	coefficient of restitution
5.	l/L	topographic geometric similarity
6.	z_o/L	roughness similitude
7.	z_o'/L	roughness similitude in saltation
8.	h/L	reference height similitude
9.	z_o/L^*	stability parameter
10.	λ/L	ripple length similitude
11.	U_F/U_{*t}	particle property similitude
12.	$U_{*t} D_p/\nu$	particle friction Reynolds number
13.	u_{*t}/u_{*t}	friction speed ratio
14.	ρ/ρ_p	density ratio
15.	$U(h)t/L$	time scale

The first four of these parameters have been suggested by Gerdel and Strom¹⁹ as the scaling parameters of primary im-

portance in modeling accumulation of wind-driven snow. Many of the other parameters are interrelated and so satisfaction of some of the parameters will result in automatic satisfaction of others. For example, the roughness height in saltation, z'_0 , has been assumed by different investigators to be proportional to particle diameter²⁰ (as is z_0 , if no nonerodible roughness elements are present¹), to ripple wavelength¹, or to be a function of particle terminal speed²¹ ($z'_0 \sim U_F^2/g$). Thus parameter number 7 is just a constant times number 1 in the first case and number 10 in the second case. In the third case, since¹

$$u_{*t} = A \sqrt{\frac{\rho_p g D_p}{\rho}}, \quad (3)$$

the parameter z'_0/L would be related to parameters 1, 11, and 14

$$\frac{z'_0}{L} \sim \frac{U_F^2}{gL} = A^2 \frac{\rho_p}{\rho} \left(\frac{D_p}{L}\right) \left(\frac{U_F}{u_{*t}}\right)^2 \quad (4)$$

Some of the listed modeling parameters may be combined by using the equation of motion for the particle. Since the flow pattern near a crater and in the crater wake is related to the crater diameter, the vertical equation of motion, for example, is made dimensionless by using the dimensionless variables $\bar{Z} = Z/D_c$ (where Z is the vertical displacement) and $\bar{t} = U(h)t/D_c$. The equation becomes

$$d^2\bar{Z}/d\bar{t}^2 = -3/4C_D \left(\frac{\rho D_c}{\rho_p D_p}\right) \bar{V}(\bar{W} - d\bar{Z}/d\bar{t}) - gD_c/U(h)^2 \quad (5)$$

where \bar{V} is the dimensionless relative speed and \bar{W} the dimensionless vertical air speed. Thus the dimensionless motion is a function of the three parameters $\rho D_c/\rho_p D_p$, $U(h)^2/gD_c$, and the particle Reynolds number.

Consider the modeling parameters:

1. $\rho D_c/\rho_p D_p$. By varying particle density and diameter and the crater diameter, this parameter can be varied from about 0.8 to 3. On Mars, this parameter would vary in value from about 1 for a 100 meter diameter crater to 100 for a 10 kilometer crater.
2. $U(h)/U_F$. Since the threshold friction speed u_* is proportional to the reference velocity $U(h)$, providing geometry (including roughness) is exactly modeled, the ratio of reference velocity $U(h)$ to terminal speed U_F will be modeled exactly if the ratio u_*/U_F is satisfied and if h/L is satisfied.
3. $[U(h)]^2/gL$. The Froude number cannot always be satisfied in the wind tunnel without having a tunnel speed far below threshold speed. It is desirable to make it as small as possible. Again since u_* is proportional to $u(h)$, this is equivalent to requiring a modeling

material with as small a threshold speed as possible. The value of this parameter varies from 10 to 150 in the wind tunnel, and from approximately 20 for a 100 meter diameter crater to 0.2 for a 10 kilometer crater.

4. e. The coefficient of restitution is satisfied if model and atmospheric materials have equivalent elastic properties.
5. h/L . Topographic features should be scaled exactly to satisfy this criterion. At large distances upstream from the region of interest, it is probably only necessary to have equivalent scaled aerodynamic roughness.
6. z_0/L . The aerodynamic roughness should, in general, be to scale¹². Except for those craters surrounded by large-scale ejecta or other rough surface features, this is probably small on Mars. If the corresponding model surface in the wind tunnel is too smooth, it may be necessary to distort this parameter in order to obtain a turbulent boundary layer. It is important at the same time, to insure that the ratio h/L be satisfied.
7. Z'_0/D_c . If the equivalent roughness height in saltation Z'_0 is proportional to particle diameter, this parameter obviously cannot be satisfied on the laboratory scale model, since such fine particles would have a very high threshold speed. Also, if introduced into the air stream, the particles would go into suspension and the saltation process would not occur. Calculations of saltation trajectory, however, show that the maximum height during saltation would be several times larger on Mars than on Earth, just as the saltation height on Earth is several times as large in air as it is in water. If the equivalent roughness Z'_0 is proportional to U_F^2/g , then z'_0/D_c is proportional to $\rho_p D_p / \rho D_c$, the inverse of the first parameter.
8. h/L . The reference height h at which the reference speed is measured should be located within the logarithmic portions of the wind tunnel and atmospheric boundary layers.
9. z_0/L^* . With a 'naturally' developed boundary layer in the wind tunnel, a boundary layer velocity profile is achieved which corresponds to a neutrally stratified atmosphere, for which the Monin-Obhukov length L^* is infinite and the ratio z_0/L^* is zero. A finite value of L^* is achieved in the wind tunnel by heating or cooling the floor to obtain unstable or stable stratification. Another way of obtaining a nonneutral velocity profile in the wind tunnel (but perhaps not correct modeling of turbulence characteristics) would be by means of shear fences, graded grids, or the like¹⁶.
10. λ/L . The relative ripple length may be related to

- z'_0/L and the same comments apply.
11. U_F/u_{*c} and 12. $u_{*c}D_p/\nu$. As will be shown later, for a given condition such as for a modeling particle of diameter corresponding to minimum threshold speed, these two parameters would have the same values as for minimum threshold speed material on Mars.
 13. u_*/u_{*c} . The manner in which particles are transported and, in particular, the amount of material which is moved is a function of this ratio. Thus, in order to keep u_* as small as possible because of the Froude number, the threshold friction speed of the particle should be small.
 14. $U(h)t/L$. The time scale in the wind tunnel is much shorter than the time necessary for pattern development on Mars since the characteristic time is the ratio of characteristic length L to reference velocity $U(h)$. The time necessary for pattern development on Mars can thus be predicted from wind tunnel tests.
 15. A Reynolds number $U(h)L/\nu$ may or may not be an important modeling parameter. For turbulent flows over sharp-edged features, the flow is relatively independent of Reynolds number. The critical model Reynolds number (above which effects are independent of Reynolds number) depends upon model shape. If the model is too streamlined so that the test Reynolds number is below the critical, the model may have to be distorted by roughening the surface, creating sharper edges, etc. in order to lower the critical Reynolds number. Snyder²² quotes critical Reynolds number for sharp-edged cubes of 11,000 and 79,000 for a hemisphere-cylinder. In the current tests, Reynolds numbers based on crater diameter were generally above these values for sharp-rimmed model craters.

The listed parameters are easier to satisfy or will come closer to satisfaction in the one atmosphere wind tunnel than in the low density tunnel. Thus, for modeling eolian features on Martian topography, the low density wind tunnel should not be used.

Threshold Speed Experiments

Two series of experiments have been initiated in atmospheric wind tunnels. The first series of tests is designed to gain additional fundamental knowledge about properties of saltating materials such as equivalent roughness height in saltation, ripple wavelength, and threshold friction speed. Results of tests for determining threshold friction speeds for a variety of particle sizes and densities are shown in Figs. 1 and 2. As Bagnold¹ discovered, an optimum particle size occurs for which threshold speed is a minimum, corresponding to a certain value of particle friction Reynolds number. The value of optimum diameter decreases as particle density increases with the

diameter ratio inversely proportional to the density ratio to the one-third power. The minimum threshold speed ratio should be directly proportional to the one-third power of the density ratio. Limited data in Figs. 1 and 2 comparing copper particles and glass spheres corroborate these trends.

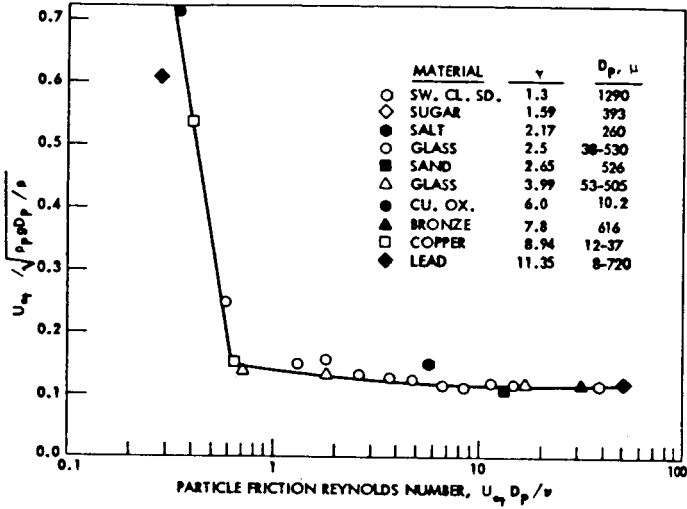


Fig. 1. Threshold speed parameter ratio vs particle friction Reynolds number.

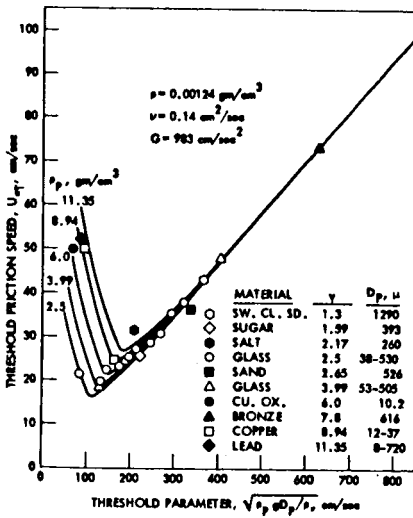


Fig. 2. Threshold friction speed vs threshold parameter.

In Fig. 1 the curve of Bagnold's parameter $A = u_{*t} / \sqrt{\rho_p g D_p / \rho}$ vs particle friction Reynolds number $B = u_{*t} D_p / \nu$ should be a universal curve as long as the surface over which the wind is blowing is composed only of the erodible particles in question. The solid lines in Fig. 2 are based on the single curve in Fig. 1. Part of the small scatter in the data could be attributed to particle shape.

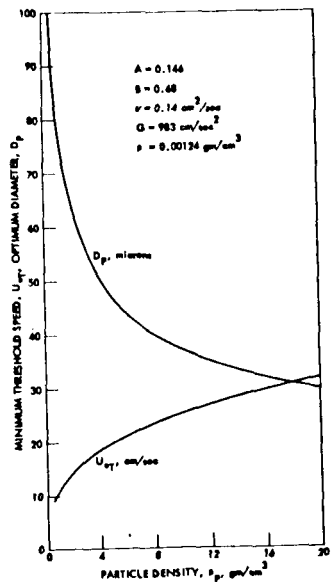
From the expressions for A and B the threshold friction speed u_{*t} and particle diameter D_p can be estimated for any values of density ratio, ρ / ρ_p , gravitational acceleration, g , and kinematic viscosity, ν , from Eqs. (1) and (2).

$$u_{*t} = A^{2/3} (\rho_p g \nu B / \rho)^{1/3} \quad (6)$$

$$D_p = (B \nu / A)^{2/3} (\rho / \rho_p g)^{1/3} \quad (7)$$

The point on the curve in Fig. 1 where the relatively sharp break occurs ($A = 0.146$ and $B = 0.68$) corresponds to the minimum threshold friction speed. For values typical of a one-atmosphere wind tunnel, the values of minimum u_{*t} and corresponding D_p were calculated for a range of values of particle density, using Eqs. (6) and (7). The results are shown in Fig. 3. If a modeling material is chosen to correspond to minimum threshold speed, then it is evident that if minimum diameter is desired, then the material should be of high density. However, materials of lighter density will result in somewhat lower minimum threshold speeds. Parameter number 1, for given values of A and B, is proportional to $(\rho / \rho_p)^{2/3}$. Thus, lighter materials will result in larger values of this parameter.

Fig. 3. Variation with density of particle diameter and threshold friction speed for minimum threshold speed.



The terminal speed to threshold friction speed ratio U_F/u_{*t} can be written as a function of A and terminal speed drag coefficient C_{DF} . However, C_{DF} is a function of $U_F D_p / \nu =$

$(U_F/u_{*t}) u_{*t} D_p / \nu = (U_F/u_{*t}) B$. Thus, for a given A and B corresponding to a particular point on the curve in Fig. 1, the ratio U_F/u_{*t} is uniquely determined and would have the same values on Mars as in the wind tunnel. It follows that

$$\frac{U_F}{u_{*t}} = \frac{2/A}{\sqrt{3C_{DF}}} \quad (8)$$

where $C_{DF} = C_{DF}(BU_F/u_{*t})$

Effect of Particle Lift on Threshold Speed

Although some investigators have ignored the effect of particle lift in attempting to predict threshold friction speed, the effect of lift is apparently important. Bagnold^{23,24} has stated that the initial upward acceleration of a particle (not struck by another particle) from the bed is due to a lift-force but that the lift force becomes very small shortly after the particle has lifted off the bed. The lift force is due to the very high mean velocity gradient very near the surface.

Experimental values of lift on hemispheres lying on a surface and immersed in a fluid were obtained by Chepil²⁵ and Einstein and El-Samni²⁶. In both cases the lift and drag forces were found to be of the same order of magnitude. However, the measurements of lift and drag in both cases were made at relatively high Reynolds number (diameters ranged from 1.27 cm to 6.86 cm in air and water), in fully turbulent flow, whereas the threshold values of u_* occur for values of particle friction Reynolds numbers in the laminar sublayer and transition ranges.

According to Schlichting²⁷, for a closely packed sand surface roughness, the surface is aerodynamically smooth if the particle friction Reynolds number, $u_* D_p / \nu$ is 5 or less, and a laminar sublayer exists adjacent to the surface. If the particle friction Reynolds number is greater than 70, the particles would be larger than a laminar sublayer if one could exist, and the boundary layer is fully turbulent. Between these values is a transition range in which the velocity profile is still a function of $u_* D_p / \nu$.

An effective lift coefficient at threshold was calculated from the data depicted in Figs. 1 and 2 with the use of a mean velocity profile equation valid throughout a turbulent boundary layer with a laminar sublayer as presented by Walz²⁸. This effective lift coefficient would include any packing factor or turbulence factor as used by Chepil²⁹. It is assumed (as did Chepil²⁹) that the lift acts at the center of the spherical particle and the drag acts at a distance of $D_p/6$ above the

sphere center, which is resting atop other spheres of the same diameter. Equating opposing moments due to lift, drag, and weight results in

$$u_{*t} = 0.3728 \sqrt{\frac{\rho_p g D_p}{\rho} \left[\frac{1}{1 + \frac{C_L}{9.6} \left(\frac{u}{u_*}\right)^2} \right]} \quad (9)$$

The substitution of Walz's velocity profile, evaluated at $z = D_p$, resulted in the value of lift coefficient shown as curve 1 in Fig. 4. For values of $u_* D_p / \nu$ greater than 5, curve 1 would not be expected to be valid, since Walz's equation implies an aerodynamically smooth surface. The lift coefficient was recalculated for the transition region (using Schlichting's velocity profile²⁴, his Fig. 20.21), shown as curve 2. His profile does not account for remnants of the laminar sublayer in the transition region, however, and would not be valid until $u_* D_p / \nu = 70$. Thus curve 3 is presented, an interpolated curve, which is

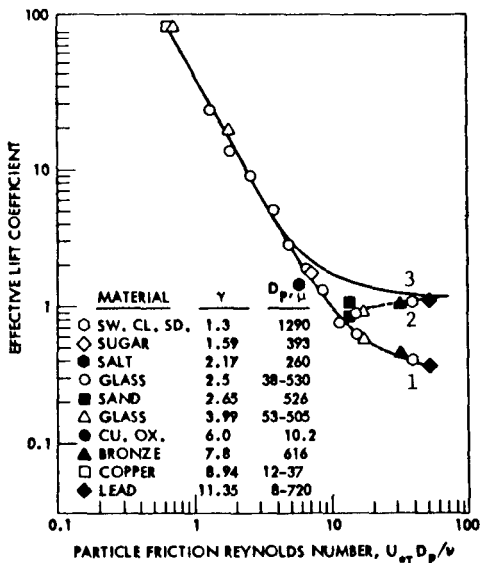


Fig. 4. Calculated effective lift coefficient at threshold.

probably closer to the actual value of effective lift coefficient.

As Bagnold²⁴ has recently pointed out, saltation can occur in purely laminar motion, so that saltation cannot be attributed to turbulence. Thus the assumption of a lift force, initiating saltation in the absence of the particle being struck by another, appears to be valid. The lift would be very small, however, as soon as the particle rises above the region of very high shear near the surface.

Whether or not the particle returns to the surface in a typical saltation trajectory, or becomes suspended due to fluid turbulence, depends upon the ratio of terminal speed to threshold friction speed, U_F/u_{*t} , and the friction speed to threshold ratio, u_*/u_{*t} . Since the vertical component of turbulent fluctuation is of the same order as u_* near the surface, if U_F/u_{*t} is near unity, then much of the material will be affected by turbulence at speeds very near threshold. Conversely, if U_F/u_{*t} is large, u_*/u_{*t} would also have to be large in order for turbulence to greatly affect particle motion. At minimum threshold speed, corresponding to $u_{*t} D_p/\nu \approx 0.68$, the ratio U_F/u_{*t} is 1.6. The ratio increases with $u_{*t} D_p/\nu$, and is 9.4 at $u_{*t} D_p/\nu = 10$, for example.

Effect of Nonrodible Roughness

From Fig. 4 it would appear the lift coefficient would change much less rapidly for Reynolds numbers greater than 70, and in fact, for fully turbulent flow, should be a function only of mean velocity gradient. This would also appear to be true from Fig. 1 where it is seen that Bagnold's coefficient A approaches a constant value for Reynolds numbers above 5 which implies a constant value of lift coefficient for Reynolds numbers greater than 70. Thus, for $u_{*t} z_0/\nu \geq 70/30$, if a reference velocity for computing lift coefficient of $u = \frac{u_*}{0.4} \ln\left(\frac{D_p}{z_0}\right)$ is chosen and if the lift coefficient is solved for by letting $A = 0.117$ (the limit value in Fig. 1) and $D_p/z_0 = 30$, an equation for u_{*t} as a function of D_p/z_0 results (for fully rough flow):

$$A = \frac{0.373}{\sqrt{\rho_p g D_p / \rho}} = \frac{0.373}{\sqrt{1 + 0.776[\ln(1 + D_p/z_0)]^2}} \quad (10)$$

For no nonrodible roughness, $D_p/z_0 = 30$ ($u_{*t} D_p/\nu \geq 70$), and $A = 0.117$. If large nonrodible roughness elements are present, then the equivalent roughness height z_0 becomes greater than $D_p/30$ and Bagnold's coefficient A increases according to Eq. (10).

It has been previously observed that nonrodible roughness elements do greatly increase the value of the coefficient². To test the validity of Eq. (10), values of threshold friction speed for several materials were determined for values of nonrodible equivalent roughness heights z_0 of 0.0104 cm and 0.338 cm. The results of the experiments are shown in Fig. 5. Although there is quite a bit of data scatter, the results seem to substantiate the form of Eq. (10). The letters NNR in Fig. 5 signify that no nonrodible roughness elements were present in those tests and that the ratio D_p/z_0 is 30 (or slightly higher in the transition range). Figure 6 shows the threshold friction speed as a function of particle diameter for one of the test materials (heavy glass spheres). The lower curve is derived from the curve of Fig. 1 and the other curves from Eq. (10). Again the trend of Eq. (10) seems to be substantiated by the experimental results.

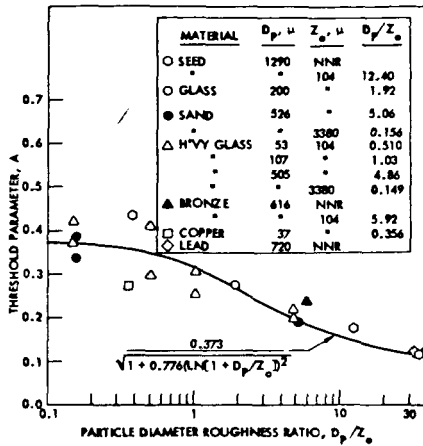


Fig. 5. Threshold speed parameter ratio vs ratio of particle diameter to nonerodible roughness height.

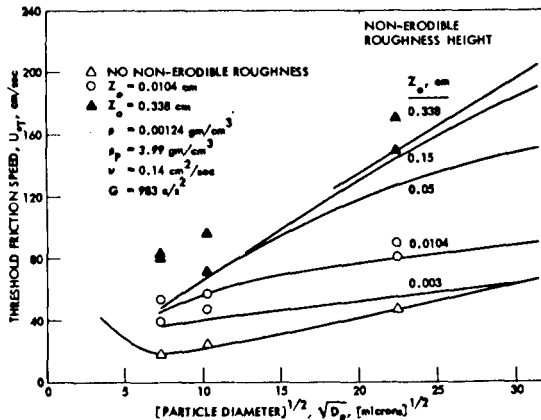


Fig. 6. Threshold friction speed as a function of particle diameter including effect of nonerodible roughness.

Predicted Threshold Speeds on Mars

With values of kinematic viscosity $\nu = 10.8 \text{ cm}^2/\text{sec}$, gravitational acceleration $g = 375 \text{ cm}/\text{sec}^2$, and atmospheric-to-particle density ratio of 4.21×10^{-6} , the curve of Fig. 1 was used to calculate threshold friction speeds on Mars, assuming that that curve also holds in the Martian atmosphere, with the use of Eqs. (6) and (7). Equation (10) was also used to calculate Martian values of threshold friction speed for several values of nonerodible roughness height z_0 . These calculations are presented in Fig. 7. The minimum threshold friction speed, for no nonerodible roughness, is about 240 cm/sec, corresponding to a particle diameter of about 305 microns.

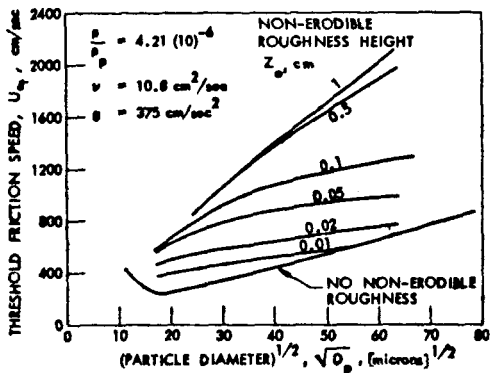


Fig. 7. Predicted threshold friction speed on Mars as a function of particle diameter.

The geostrophic wind at threshold, corresponding to the minimum value of threshold speed in Fig. 7 was calculated with the help of Csanady's drag coefficients for the diabatic Ekman layer³⁰, assuming that his results hold for the Martian atmosphere. For a latitude of 60° and an unstable atmosphere (Lettau number = 10^9), the minimum value of geostrophic wind is predicted to be 120 m/sec. The geostrophic winds at threshold would be slightly higher for a neutrally stratified atmosphere. It is apparent that very high winds are required for particle pick-up on the Martian surface. The corresponding minimum geostrophic wind at threshold on Earth would be on the order of 7.5 m/sec.

Modeling of Martian Eolian Features

The second series of tests concerns the modeling of eolian processes on Mars which have resulted in streaks emanating in a downstream direction from many of the craters. Figure 8 shows one of the Martian craters with the associated wake streak. The wind pattern over the crater would be similar to wind patterns observed over protuberances in boundary layers with small height to diameter ratios in laboratory scale tests on earth³¹⁻³³. A horseshoe vortex is wrapped around the leading edge of the crater with the trailing vortices emanating downstream from the crater sides. The tangential component of velocity in each trailing vortex is outward away from the wake centerline near the surface and inward above the vortex cores. The axial velocity components near the surface just behind the downstream crater rim are minimal on the wake centerline with maximum velocities on either side of the wake of greater magnitude than outside the wake. Further downstream the two maxima merge, and the maximum speed in the wake is then on the centerline.

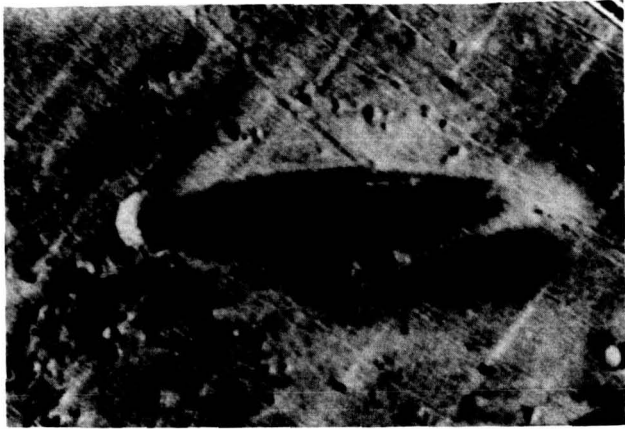


Fig. 8. Mariner-9 photograph - Mars crater with associated wake streak.

Figure 9 shows the results of a wind tunnel test over a model 30 cm diameter crater performed at a freestream speed of 675 cm/sec. Prior to the test, 393 micron diameter sugar particles were distributed evenly to a depth of 1 cm. The dark area in the crater wake represents the area cleared of particles because of the relatively high speed near the surface in the wake region. Except for the triangular area of material just downstream of the trailing rim, the cleared area bears a distinct resemblance to the Mariner 9 photo in Fig. 8. The values of the modeling parameters in this experiment were $U_{\infty}^2/gD_c = 15.41$, $U_F/u_{*c} = 10.10$, $U_{\infty}/U_{\infty c} = 0.995$, and $\rho D_c/\rho_p D_p = 0.644$.

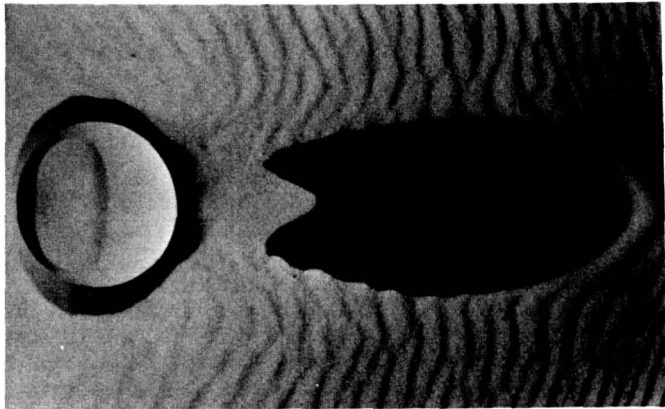


Fig. 9. Wind tunnel model crater with wake streak, $U_{\infty}^2/gD_c = 15.41$.

Another Mariner 9 photograph is shown in Fig. 10 with an apparent bi-lobate pattern in the crater wake, probably caused by the aforementioned two axial velocity maxima. The wind tunnel photograph in Fig. 11 depicts a very similar bi-lobate pattern, with clear area on either side of the wake and deposited material in the wake center. Prior to the test, no material was on the floor. Heavy glass spheres 107 micron average diameter were released from the tunnel ceiling upstream of the crater model. The modeling parameters were $U_{\infty}^2/gD_c = 6.6$, $U_F/u_{*t} = 3.5$, $U_{\infty}/U_{\infty t} = 0.673$, ($U_{\infty} = 441$ cm/sec), and $\rho D_c/\rho_p D_p = 0.739$.



Fig. 10. Mariner-9 photograph - Mars crater with bi-lobate pattern.

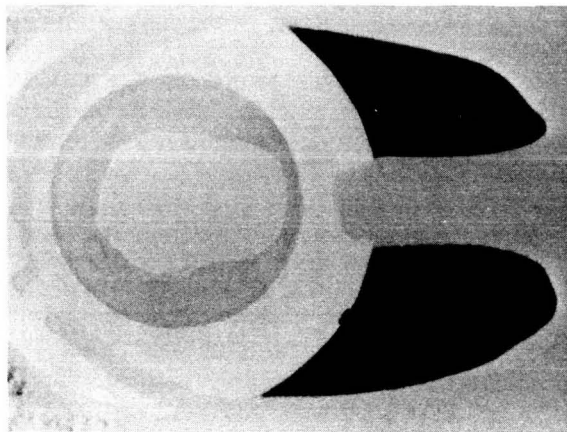


Fig. 11. Wind tunnel model crater with bi-lobate pattern, $U_{\infty}^2/gD_c = 6.6$.

Figure 12 illustrates the results of a wind tunnel test in which 12 micron diameter copper particles were placed inside a 30 cm crater and the floor was covered with 526 micron diameter sand. A very elongated bi-lobate pattern is observed in the crater wake due to a relatively higher crater rim height. Modeling parameters were $U_{\infty}^2/gD_c = 22.77$, $U_F/u_{*t} = 0.078$ and 14.30 for the copper and sand, respectively, $U_{\infty}/U_{\infty t} = 0.62$ and 0.86 , and $\rho_D/\rho_p D_p = 3.680$ and 0.283 . Similar patterns have been observed behind rocks in snow^{34,35}.

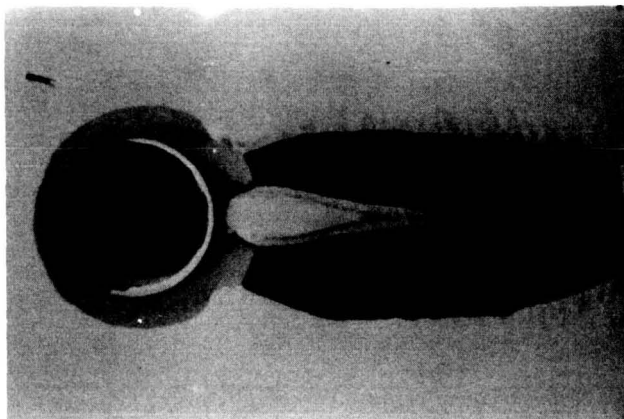


Fig. 12. Wind tunnel model crater with bi-lobate pattern, $U_{\infty}^2/gD_c = 22.77$.

The modeling parameters in the wind tunnel test pictured in Figs. 13 and 14 were $U_{\infty}^2/gD_c = 32.8$, $U_F/u_{*t} = 5.8$, $U_{\infty}/U_{\infty t} = 1.195$ ($U_{\infty} = 803$ cm/sec), and $\rho_D/\rho_p D_p = 0.525$. Again the bi-lobate pattern is very evident. As time passes, the central region of deposited material erodes away to leave a triangular region of material as shown in Fig. 14.



Fig. 13. Wind tunnel model crater with bi-lobate pattern, $U_{\infty}^2/gD_c = 32.8$.



Fig. 14. Wind tunnel model crater with triangular deposit region, later in same test as Fig. 13.

Another wind tunnel test in which 91 micron diameter glass spheres were redistributed one cm deep prior to the test is shown in Figs. 15 and 16. Evidence of higher wake velocity is shown here by the fact that the ripple wavelength is longer in the wake than outside. Modeling parameters were $U_\infty^2/gD_c = 5.8$, $U_F/u_{*t} = 2.4$, $U_\infty/u_{*t} = 0.773$ ($U_\infty = 413$ cm/sec), and $\rho D_c/\rho_p D_p = 1.599$.

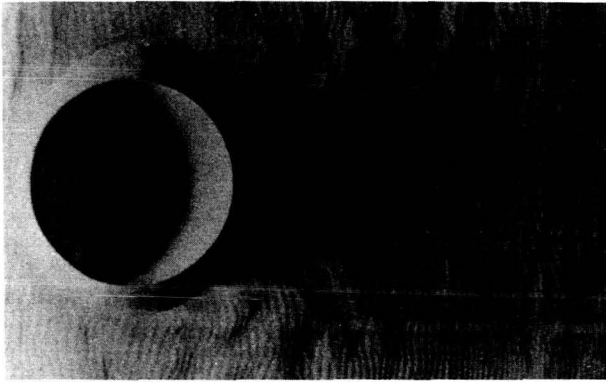


Fig. 15. Wind tunnel model crater showing longer ripple length in wake region, $U_\infty^2/gD_c = 5.8$.

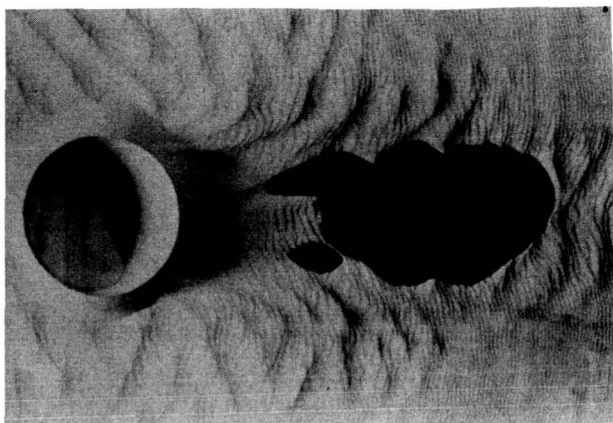


Fig. 16. Wind tunnel model crater, later in same test as Fig. 15.

Figure 17 illustrates the pattern developed for very small diameter particles. The particles are 38 micron diameter glass spheres and are too small to form the ordinary ripple formation¹. The modeling parameters are $U_{\infty}^2/gD_c = 17.85$, $U_F/u_{*t} = 0.49$, $U_{\infty}/U_{\infty t} = 1.036$ ($U_{\infty} = 484$ cm/sec), and $\rho D_c/\rho_p D_p = 2.606$.

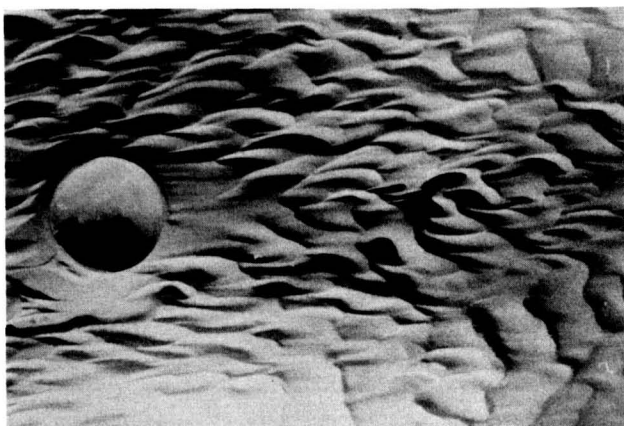


Fig. 17. Wind tunnel model crater, ripple pattern with very small particles, $U_{\infty}^2/gD_c = 11.88$.

Figure 18 and 19 compare Mariner 9 and wind tunnel photographs in which streamlines curving downstream off the edge of the crater rim can be seen by deposited material patterns in both pictures. Modeling parameters in the wind tunnel were $U_{\infty}^2/gD_c = 16.6$, $U_F/u_{*t} = 0.08$ (12 micron diameter copper particles), $U_{\infty}/U_{\infty t} = 0.53$ ($U_{\infty} = 700$ cm/sec), $\rho D_c/\rho_p D_p = 3.680$. In this test the modeling material was placed in the interior of the crater only prior to the test.



Fig. 18. Mariner 9 photograph — Mars crater with lateral curved streaks.

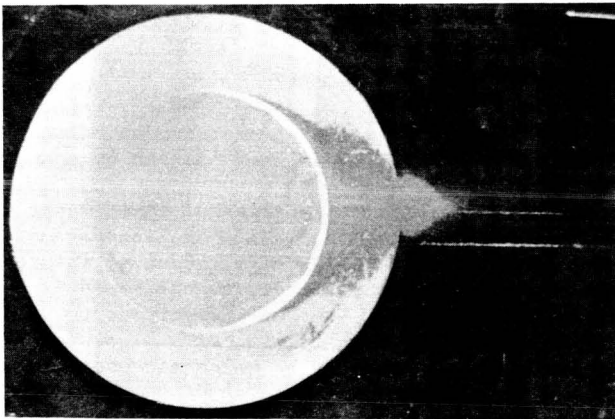


Fig. 19. Wind tunnel model crater with lateral streaks and triangular deposit, $U_{\infty}^2/gD_c = 16.6$.

Figure 20 illustrates a field test in which a natural snowstorm deposited material over a previously constructed crater (6 m diameter). Triangular deposit regions and cleared wake areas were observed after snowstorms in patterns very similar to the wind tunnel tests. The modeling parameters in this field test were estimated to be $U(h)^2/gD_c = 11$ (based on same relative height h/L in the wind tunnel), $U_F/u_{*c} = 5(\pm 3)$, $\rho D_c/\rho_p D_p \approx 30$, $U(h) = 2530$ cm/sec. In other snowstorms in which similar patterns were obtained, the value of the Froude number ranged down to 0.4.



Fig. 20. Snow deposits in vicinity of 6 meter diameter crater (at upper left).

Although not all modeling parameters can be satisfied in the wind tunnel, a great deal of information can be gained about the nature of the flow field and the resulting depositional and erosional features. A systematic series of experiments is currently underway, in which each of the major modeling parameters is varied independently, to determine its effect upon eolian features. This is done by varying crater diameter, tunnel speed, and modeling material. The results will not only enable us to determine effects of each similitude parameter, but will also assist greatly in later numerical experiments in which all modeling parameters can be satisfied.

Acknowledgment

This research was supported by NASA, Ames Research Center, California, and the Engineering Research Institute at Iowa State University.

References

1. Bagnold, R. A., The Physics of Blown Sand and Desert Dunes, Methuen, London, 1941.
2. Chepil, W. S., and N. P. Woodruff, "The Physics of Wind Erosion and Its Control," Advances in Agronomy, 15, 211-302, 1963.
3. Malina, F. J., "Recent Developments in the Dynamics of Wind-Erosion," Trans. American Geophysical Union, Pt. II, 262, 1941.
4. Ford, E. F., "The Transport of Sand by Wind," Trans. American Geophysical Union, 38, 171-174, 1957.
5. Chang, T. S., W. C. Lucas, and W. W. Youngblood, "Laboratory Simulation of the Mars Atmosphere, A Feasibility Study," NASA CR-61168, 1968.
6. Bidwell, J. M., "Notes on Martian Sandstorms," Martin Marietta Corp. Report 1610-68-34, 1965.
7. Adlon, G. L., R. K. Weinberger, and D. R. McClure, "Martian Sand and Dust Storm Simulation and Evaluation," NASA CR-66882, 1969.
8. Hertzler, R. G., "Particle Behavior in a Simulated Martian Environment," McDonnell Aircraft Corporation, Report E418, 1966.
9. Hertzler, R. G., "Behavior and Characteristics of Simulated Martian Sand and Dust Storms," McDonnell Aircraft Corporation, Report E720, 1966.
10. Lumley, J. L., and H. A. Panofsky, The Structure of Atmospheric Turbulence, Wiley, New York, 1964.
11. Plate, E. J., "Aerodynamic Characteristics of Atmospheric Boundary Layers," AEC Critical Review Series, 1971.
12. Jensen, M., "The Model-Law for Phenomena in Natural Wind," Ingeniøren, 2, 121, 1958.
13. Cermak, J. E., "Laboratory Simulation of the Atmospheric Boundary Layer," AIAA J., 9, 1746, 1971.
14. Davenport, A. G., and N. I. Symov, "The Application of the Boundary Layer Wind Tunnel to the Prediction of Wind Loading," In Wind Effects on Buildings and Structures, Vol. I, Univ. of Toronto Press, 1968.

15. Owen, P. R., and H. K. Zienkiewics, "The Production of Uniform Shear Flow in a Wind Tunnel," *J. Fluid Mechanics*, 2, 521, 1957.
16. Counihan, C., "An Improved Method of Simulating an Atmospheric Boundary Layer in a Wind Tunnel," *Atmospheric Environment*, 3, 197, 1969.
17. Sundaram, T. R., G. R. Ludwig, and G. T. Skinner, "Modeling of the Turbulence Structure of the Atmospheric Surface Layer," *AIAA J.*, p. 743-750, 10, 1972.
18. Sagan, C., and J. B. Pollack, "Windblown Dust on Mars," *Nature*, 223, 791-794, 1969.
19. Strom, G. H., and R. W. Gerdel, "Scale Simulation of a Blowing Snow Environment," *Proceedings, Institute Environmental Science*, 53, 53-63, 1961.
20. Zingg, A. W., "Wind-Tunnel Studies of the Movement of Sedimentary Material," *Proceedings of the Fifth Hydraulics Conference, Bull. 34, Univ. of Iowa Studies in Engineering*, 111-135, 1953.
21. Owen, P. R., "Saltation of Uniform Grains in Air," *J. Fluid Mechanics*, 20, Pt. 2, 225-242, 1964.
22. Snyder, W., "Similarity Criteria for the Application of Fluid Models to the Study of Air Pollution Meteorology," *Boundary Layer Meteorology*, 3, 113-134, 1972.
23. Bagnold, R., "The Flow of Cohesionless Grains in Fluids," *Philosophic Transactions of the Royal Society*, A, 249, 239-297, 1956.
24. Bagnold, R. A., "The Nature of Saltation and of 'Bed-Load' Transport in Water," *Proceedings of the Royal Society of London*, A, 332, 473-504, 1973.
25. Chepil, W. S., "The Use of Evenly Spaced Hemispheres to Evaluate Aerodynamic Forces on a Soil Surface," *Transactions American Geophysical Union*, 39, 397, 1958.
26. Einstein, H., and E. El-Samni, "Hydrodynamic Forces on a Rough Wall," *Reviews of Modern Physics*, 21, 520-524, 1949.
27. Schlichting, H., Boundary Layer Theory, McGraw-Hill, N.Y., 1968.
28. Walz, A., Boundary Layers of Flow and Temperature, MIT Press, Cambridge, Mass., 1969.

29. Chepil, W. S., "Equilibrium of Soil Grains at the Threshold of Movement by Wind," Soil Science Society Proceedings, 23, 422-428, 1959.
30. Csanady, G. T., "Geostrophic Drag, Heat and Mass Transfer Coefficients for the Diabatic Ekman Layer," J. Atmospheric Sciences, 29, 488-496, 1972.
31. Sedney, R., "A Survey of the Effects of Small Protuberances on Boundary-Layer Flows," AIAA J., 11, 782-792, 1973.
32. Gregory, N., and W. Walker, "The Effect on Transition of Isolated Surface Excrescences in the Boundary Layer," Great Britain, Aeronautical Research Council, Reports and Memoranda No. 2779, 1951.
33. Hunt, J. C. R., "The Effect of Single Buildings and Structures," Philosophical Transactions of the Royal Society of London, A, 269, 457-468, 1971.
34. Cornish, V., "On Snow-Waves and Snow-Drifts in Canada," The Geographical Journal, 20, 137-173, 1902.
35. Seligman, G., Snow Structure and Ski Fields, MacMillan, London, 1936.

PRECEDING PAGE BLANK NOT FILMED

Paper No. 17

SIMULATION OF SPACECRAFT INTERACTION WITH A
PARALLEL-STREAMING PLASMA

Anthony R. Martin and Richard N. Cox, *Department of Aeronautics,
The City University, St. John Street, London EC1V 4PB, England.*

ABSTRACT

An experimental study of the wakes produced by spacecraft moving in the ionosphere is reported. The work was done in an argon ion beam simulation facility which incorporated features enabling the production of a low background density of slow ions and an essentially parallel ion beam. The occurrence of these features, and their effect on the simulation validity in previous work is briefly reviewed. Stable variation of the divergence of the beam was possible and results are given of wake studies for a range of body size and potential in both parallel and divergent beams.

INTRODUCTION

The interaction of a conducting body, such as a spacecraft with the ionospheric plasma is a problem of great importance when considering such aspects as the drag on the body, the use of probes, radio frequency transmissions, radar detection, the excitation of plasma waves etc.

There are three ways in which the interaction can be studied. The first is by in situ measurements in space, using instruments which are carried by a spacecraft. In general, this method has so far yielded data which are difficult to interpret, and it is complicated and costly. Because of the complex nature of the interaction phenomenon, however, the complete answer to the problem will probably come from a future mission performed in the ionospheric regions of interest, and not from the two other methods, which must be regarded as complementary studies.

The second method is to numerically solve, using computer techniques, the equations (Vlasov and Poisson) which are normally used to describe the spacecraft - plasma interaction. This method is reasonably well established, but there is some controversy as to the significance and validity of assumptions (both physical and mathematical) used in the various theories; results have not been independently verified in detail, and extensive computation is both costly and time consuming.

The third method is laboratory simulation in which a stationary model is placed in an ion stream moving at velocities repre-

sentative of those found in the ionosphere. This method has been used extensively, but a review of the facilities used show that at least one of two effects limited the validity of the simulation. Either the background density of slow ions was a large percentage of the beam ions, or the ion streams were not generally parallel but diverged as they moved down the simulation chamber. The present work is mainly concerned with the correction of the latter defect in the simulation.

THE CAUSES OF BEAM DIVERGENCE

In the ionosphere below about 1200 km altitude the particle and vehicle velocities are such that the ion velocities, V_i are in general lower and the electron velocities, V_e , are in general higher than the spacecraft orbital velocity i.e.

$$V_i < V_s \ll V_e.$$

This flow condition is referred to as mesothermal. In the satellite frame of reference the ions are seen as impinging on the spacecraft at a velocity V_s , and as following straight, parallel trajectories with a small randomised component, V_i , superimposed. The ions can therefore be represented by a high velocity mono-energetic directed plasma stream and the electrons by a group of particles in equilibrium at the electron thermal temperature. This property suggests the use of ion beams directed past stationary models as a means of simulation.

However, it is found that in most plasma streams which have been accelerated in the laboratory a component of the ion velocity transverse to the streaming direction arises from the unequal deflection of the individual ions as they pass through the accelerator system.

The first estimate of the magnitude of this effect was made by Clayden and Hurdle (Ref.1) who considered the transverse motion of ions which pass through a series of parallel wires and are deflected unequally, the magnitude of the deflection depending upon the passage distance from a wire. From their analysis it was concluded that while the ion temperature in the axial direction was equivalent to $10^3 - 10^4$ °K, the values in the radial direction were nearer $5 \times 10^4 - 10^5$ °K.

The problem was also considered by Hester and Sonin (Ref.2) again by studying the unequal deflection of the ions, who estimated an effective ion thermal speed as

$$\bar{C}_i = \frac{8RU}{3\pi Z}$$

where R = source radius, U = ion flow speed and Z = distance downstream at which \bar{C}_i is being calculated. This represents an upper bound for the ion thermal speed but should give a good estimate when $Z \ll R$, i.e. $\bar{C}_i \ll U$

The importance of this directional distribution of the ions which leave the accelerator grid is because it is one of the two main factors that cause the ion stream to spread out with distance down the chamber. The other factor is the radial space-

charge field, which is minimised with the provision of adequate space-charge neutralisation in the beam chamber.

The magnitude of the divergence in the beam caused by these effects is usually indicated by calculating the divergence angle of the stream, θ . For a parallel beam $\theta = 0$. The common method of calculating θ is to determine the width of the number (or current) density profile of the beam at some constant fraction of its maximum value for a series of axial stations along the beam. These quantities can then be used to estimate the divergence angle and the degree of linearity in the ion trajectories.

THE EFFECTS OF SLOW BACKGROUND IONS

When an ion beam passes through a neutral gas then charge exchange processes occur, resulting in the fast moving beam ions giving their charge to the slow background neutral particles. The net result is the production of a beam of fast moving neutral atoms parallel to the main ion beam, and a background of slow moving ions. The fast neutrals should not influence the spacecraft/plasma interaction, because of the large mean free paths which the particles possess. However, the slow background ions have a much larger residence time in the beam chamber than the beam ions, and may perturb the electric field about the spacecraft and significantly influence the charged particle distributions.

The most important effect that these slow ions will have will be the partial filling of the ion-depleted regions in the wake behind a body, as the slow ions will not, in general, possess any preferred velocity vector. In addition the current collection due to ions which impinge upon the body will be much larger in the case where slow ions are present in appreciable numbers. Discrepancies of up to a factor of two between experiment and theory can be explained by assuming a slow ion component of only 1% (Ref.3).

The problem of charge exchange was again considered by Clayden and Hurdle (Ref.1), who showed that the slow ion population increased with both the ion flow speed and the neutral gas background pressure. The problem was also studied in detail by Sajben and Blumenthal (Ref.4), who derived expressions for a low estimate to the number of slow ions by using the hard sphere model to describe the collisions, and for a high estimate by assuming that the neutral atoms gained no momentum in a collision but lost an electron to ions passing within a certain distance.

REVIEW OF PREVIOUS SIMULATION FACILITIES

The situation in several ion beam facilities which have been used in the past for investigating the wake structure and the interaction problem is summarised in Table 1. The first column gives the facility location and references to its design and experimental work. The second column notes the background pressure

Table 1. Summary of Simulation Validity

FACILITY (References)	SLOW ION EFFECTS	BEAM DIVERGENCE EFFECTS
TRW-STL (5,6,7)	Pressure $\sim 2 \times 10^{-6}$ torr, any effects should be negligible, not specifically mentioned	$\theta \approx 3 - 4^\circ$, good value
RARDE (1,8)	$n_s/n_f \sim 0.1$, causing severe distortion of current collection results	Difficult to estimate due to lack of data, source-like
USSR (9,10)	pressure $\sim 4 \times 10^{-5}$ torr, probably a reasonable figure, not specifically mentioned	$\theta \approx 9^\circ$, moderate divergence
Caltech (4)	(a) 25.4 mm diameter source, $n_s/n_f \sim 1$, severe distortion (b) 300 mm diameter source, $n_s/n_f \sim 6$, very poor value	(a) $\theta \approx 17^\circ$, source-like, very divergent (b) "moderate divergence", probably essentially parallel
ESTEC (11,12)	Pressure $\sim 2-6 \times 10^{-4}$ torr, probably giving some distortion because of the large chamber used	$\theta \approx 11-14^\circ$, moderate divergence
MIT (2,13,14)	$n_s/n_f \sim 0.02$, good value	$\theta \approx 10^\circ$, moderate divergence
Marshall SFC (15,16)	Pressure $\sim 5 \times 10^{-6}$ torr, any effects should be negligible	$\theta \approx 6^\circ$, good value
ONERA (17,18,19,20)	$n_s/n_f \sim 0.05-0.2$, good to severe distortion	$\theta \approx 11^\circ$, moderate divergence

or the ratio of slow ions to fast beam ions, n_s/n_f . The third column lists values of the divergence angle, θ . More details can be found in Ref.21.

No attempts have been made to study the effects of a magnetic field on a spacecraft wake in ion beam facilities, but any effects will probably be negligible at spacecraft altitudes. In addition most of the facilities have used "cold" ions because the effects of random ion thermal motion are difficult to simulate. The thermal motion has the effect of smoothing out the features found in the wake, and of causing more rapid filling. Hence, this simulation defect (from which the present facility also suffers) is important. Hester and Sonin (Ref.2) attempted a partial simulation but the results were only preliminary and caution was urged in interpretation because the velocity distribution was not Maxwellian. The most promising results have been given in the ONERA facility (Ref.19) where transverse temperatures of 10, 700 and 1900 °K were given by inserting a negatively biased mesh between the source and the model position (following the suggestion of Ref.6).

It can be seen from Table 1 that no facility has fully satisfied the criteria for a parallel, fast ion stream. The two which best meet the requirements are those of TRW-STL and Marshall SFC, which should have a negligible slow ion population at the working pressures used, and had divergence of about $3-6^\circ$.

The next best facility was that at MIT, with good slow ion suppression but $\theta \approx 10^\circ$. The wake studies carried out in this facility give the most comprehensive set of data so far reported, and it is important to check the effects of divergence because of the fundamental nature of the results. The ONERA facility, although appearing as good as the MIT facility on paper, was usually worse under typical conditions due to the high background densities of slow ions found, a result of using a larger simulation chamber.

Therefore the situation can be summarised as follows. A simulation facility is needed in which the slow ions have been adequately suppressed, and in which the effect of divergence in the ion stream flowing past the model may be investigated by controlling this divergence by focussing and beam shaping techniques.

THE CITY UNIVERSITY FACILITY

With the aim of investigating wake structures in parallel and divergent ion streams the apparatus originally used by Clayden and Hurdle (Ref.1) has been acquired and modified. Apart from minor changes in the structural design of the ion source itself and the instrumentation used, modifications were made to reduce the effects of beam divergence and background ions. The necessary modifications were suggested by work on electron-bombardment ion engines. The similarity between the designs of simulation facilities and these engines has been noted many times.

The original single extraction mesh (0.075 mm diameter wire

spaced 0.175 mm) was replaced by a pair of matched grids (140 holes of 3 mm diameter, 55% open area, 1.5 mm spacing) in order to achieve easier focussing and control of the beam. Focussing is easier using grids rather than a mesh, but the voltages necessary to give the correct scaling of ion velocity in the beam are generally lower than optimum for good focussing. It was found that the voltages on the accelerator grid could be raised above that needed for velocity scaling and the ions, having been extracted, were then slowed down by a virtual decelerator plane in the plasma of the beam chamber. The plasma potential appeared quite sensitive to variations in accelerator and mesh potential (see below for discussion of mesh), and as the beam ion energy was essentially equal to the difference between the ion source plasma potential and the beam plasma potential, the velocity could be tailored within certain limits to correspond to the velocities typically found in the ionosphere.

The most important modification in the attempt to control the divergence, however, was the rewiring of the electrical circuits, as shown in Figure 1. The mesh which lines the beam chamber, providing an equipotential surface for the beam following extraction, was biased independently of the accelerator circuit in contrast to Ref.1. This meant that the backstreaming ratio

$$R = \frac{\text{net accelerating voltage}}{\text{total accelerating voltage}}$$

could be easily varied. In ion engines R must be less than about 0.9 to prevent electrons backstreaming from the beam into the engine, thus distorting the performance figures. In the present application this is not important and values of R greater than unity can be used.

The divergence of the beams, under various combinations of accelerator and mesh voltage, was measured by determining the half-width of the current-density profiles at some fixed fraction of the total current at several axial stations in the beam (usually 8-10 positions over some 150 mm). The results for 40eV and 100 eV argon beams are shown in Figure 2. These energies correspond to ion velocities of about 14 and 22 km/sec. Circular satellite velocities are about 7-8 km/sec for altitudes from 1200 km to 100 km. It can be seen from Figure 2 that the minimum divergence achieved is around one degree, and the ease of control of θ is evident. The minimum value of θ was found for values of R in the range 1.05 to 1.15 i.e. slight mesh over-voltages tending to "force" the ions back into paths parallel to the beam axis.

Stable operation of the beam was achieved, with and without neutralisation, over the range of R indicated. As the neutraliser current was decreased the electron density in the beam remained essentially constant and the electron temperature rose steadily. The plasma potential also varied, indicating sheath re-arrangement in order to provide particles striking the walls of the chamber with sufficient energy to cause neutralisation by secondary electron emission. Operation without neutralisation, however, tended to produce more plasma noise and non-Maxwellian

electron distributions in the discharge, and was avoided unless a large Debye length was required.

The ion density in the beam was found to be a linear function of the discharge current in the ion source, and the electron temperature was found to be essentially independent of the current. The density could be varied over a range of 10^{13} - 10^{15} m^{-3} .

In an attempt to reduce the slow ion density in the beam modifications were made to lower the attainable base pressure of the system without gas flow to about 5×10^{-6} torr, and to increase the propellant utilisation of the source. This term, a common parameter in ion engine studies, is the ratio of the extracted ion beam current to neutral mass flow rate into the source expressed in terms of an equivalent current. As higher utilizations are generally achieved in large diameter engines the extraction diameter was increased from 30 mm to 50 mm. The source was then run at the maximum extracted beam current which could be achieved at the relevant values of accelerating voltage and discharge current. This procedure was usually one of high discharge energy loss, which again is not important in the present context although it is of great concern in ion engine work. The aim of this modification is, of course, to reduce the neutral atom efflux through the acceleration plane and hence lower the background density in the beam and the probability of charge-exchange collisions.

The results of the slow-ion modifications are shown in Figure 3, where the ratio of the slow ions to the total ion density is shown as a function of pressure. The slow ion density can be measured in two ways (Ref.2), either by using to collect the ions a plate which can be shielded from direct impingement by the fast ions (as used in Ref.1 also), or by measuring the current to a probe in the region directly behind a model, where fast ions cannot penetrate. Both methods gave consistent results, and the data points in Figure 3 represent average values of n_s/n_t .

It can be seen that the value of n_s/n_t varies between about 0.02 to 0.07 over the operating pressure range of 7×10^{-5} to 3×10^{-4} torr. This is lower than the results of Clayden and Hurdle (Ref.1) and can be favourably compared with those of Hester and Sonin (Ref.2) which varied from 0.01 - 0.05. The requirement for an operating pressure an order of magnitude lower in the latter case arises from the larger size chamber in which the experiments were carried out (500 mm diameter and 1.2 m long, compared with 100 mm diameter and 0.5 long in the present case.)

Figure 4 shows the effect of the slow ion number density upon a radial profile at a constant axial distance downstream in the wake. This position is one in which a small peak is apparent in the centre of the ion-depleted region. At high pressure (7×10^{-4} torr) this peak is very prominent, but as the pressure is lowered the peak height decreases and the depleted region deepens, as a result of the decrease in the slow ion density. The shape of the wake remains essentially constant for pressures below about 10^{-4} torr, where the density of slow ions is about 3%, as shown in Figure 3.

DIVERGENCE EFFECTS IN NEAR WAKES

This section presents some results for the effects of stream divergence on the rear wake of a sphere which is moderately large with respect to the Debye length in the surrounding plasma i.e. the ratio of sphere radius to Debye length, $r_S/\lambda_D > 1$. A co-ordinate system which takes the centre of the body as its origin is used i.e. an axial distance $Z/r_S = 1.0$ represents the rear surface of the sphere, and is the nearest a probe can approach.

The wakes were mapped using spherical probes with a size much smaller than the body size to gain resolution. For a small negatively biased probe the ion current to the probe is proportional to the ion density and ion flow speed. As the flow speed was essentially constant in each wake a current profile at a fixed negative probe potential is equivalent to a number density profile (as noted in Ref.2).

Figure 5 shows the rear wake of a sphere with $r_S/\lambda_D = 4.5$ in a flow with a Mach number (based on the ion acoustic speed) $M = 6.5$, and a sphere potential $eV/kT_e = \phi_S = -2.35$. The results are traced directly from the recorder output and show the effects of the radial and axial non-uniformity of the ion stream. Wakes are shown in a 1° (parallel) beam and a 10° (divergent) beam. In both wakes common features can be seen. A region behind the body is depleted of ions, and the space-charge imbalance set up attracts ions which have passed the body into the wake to fill up this region. When the attracted ions fill the wake and reach the centreline a peak in ion density is found where the streams meet. These features are common in sphere wakes (e.g. Refs. 2, 16). However, a comparison of the parallel and divergent wakes also shows some differences. The wake filling occurs nearer the body in the parallel stream and the density peak develops earlier. Further downstream this peak is more sharply defined in the parallel case and can be seen at greater distances from the body.

The reasons for this can be visualised by considering the trajectories of the ions streaming past the body. The potential sheaths surrounding the body will be the same in each case, but the ions will possess a transverse component of velocity in the divergent stream. This will mean that fewer ions will be deflected into the wake by the body potential and the space-charge, and that those ions which are deflected will tend to cross the wake centreline further downstream.

Figure 6 shows the results for a sphere with $r_S/\lambda_D = 3.0$, $M = 5.4$ and $\phi_S = -3.8$, and for divergence angles of 1° , 10° and 20° . These two latter values are representative of the range of divergence angles generally found in previous work (see Table 1). Compared to the parallel case it can be seen that again the features in the wake appear later and are weaker in the divergent streams. Also the same trend is observed when the 10° and 20° beams are compared.

The sharper focussing of the downstream ion density peak in Figure 6, compared with the results of Figure 5 (specifically for

the parallel case where least distortion of the wake features occurs), is a result of both the larger negative body potential and the decrease of r_S/λ_D , both of which act to enhance the effect of ion attraction and focussing in the wake. The appearance of the density peak nearer the body is also a result of the stronger ion deflection caused by these changes.

CONCLUSIONS

Some preliminary results for wakes behind bodies in a plasma stream which simulates ionospheric satellite conditions have been presented. The facility combines the features of good slow ion suppression with an essentially parallel (1° divergence) ion stream, and thus fulfills simulation criteria more exactly than in previous work.

Near wake results for the case of a negatively biased sphere showed several differences between the features in parallel and divergent streams:

a) the filling of the ion depleted region of the wake directly behind the body, caused by potential focussing and space charge effects, occurs further downstream in a divergent wake, the exact distance depending upon the degree of divergence present.

b) ion density peaks formed on the centreline, due to the convergence of the ions attracted into the wake, are lower in number density, less sharply defined and decay into the ambient plasma sooner in a divergent wake.

The magnitude of these effects is dependent upon the divergence of the stream, i.e. the larger the divergence then the less rapid the wake filling and the more diffuse the density peaks.

Although the differences are not large relative to the overall scale of the wakes they are quite distinct and consistent in their behaviour, and previous results should be considered with this in mind. The divergence-related wake modifications do not influence the general physical picture of wake formation which is emerging (Refs.2,14) but should be taken into account in any attempt to give detailed agreement between actual space experiments or theoretical studies and laboratory simulations.

ACKNOWLEDGEMENTS

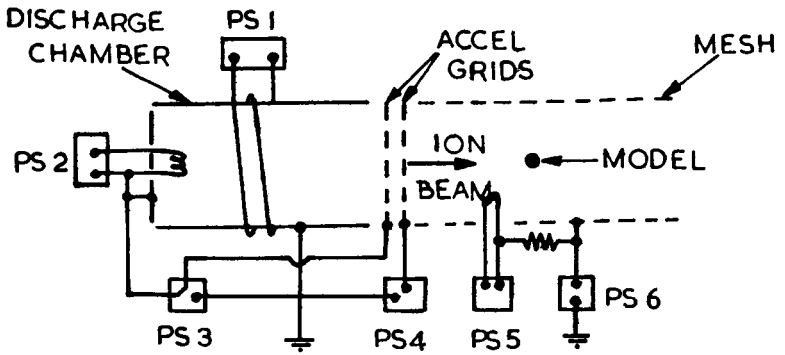
The authors would like to thank Chris Hurdle of R.A.R.D.E. for his interest in this work. The modifications were carried out by R.A. Valsler. This work was supported by the Department of Trade and Industry and the Science Research Council.

REFERENCES

1. Clayden, W.A. and Hurdle, C.V., Diagnosis of a plasma beam extracted from an electron-bombardment ion source, p.385 in Plasmas and Interactions of Electromagnetic Radiation with Plasmas and Flames, AGARD CP No.8, Vol.2., 1965.

2. Hester, S.D., and Sonin, A.A., A laboratory study of the wakes of artificial satellites, *A.I.A.A.J.*, 8, 1090 (1970).
3. Maslennikov, M.V., and Sigov, Yu. S., Rarefied plasma stream interaction with charged bodies of various forms, P.1671 in *Rarefied Gas Dynamics (6th.Symp.)*, L. Trilling and H.Y. Wachman (Eds.), Vol.2, Academic Press, New York and London, 1969.
4. Sajben, M., and Blumenthal, D.L., Experimental study of a rarefied plasma stream and its interaction with simple bodies, *A.I.A.A. Paper No.69-79*, 1969.
5. Hall, D.F., Kemp, R.F., and Sellen, J.M.Jr., Plasma-vehicle interaction in a plasma stream, *A.I.A.A.J.*, 2, 1032 (1964).
6. Hall, D.F., Kemp, R.F., and Sellen, J.M.Jr., Generation and characteristics of plasma wind tunnel streams, *A.I.A.A. J.*, 3, 1490 (1965).
7. Sellen, J.M.Jr., Bernstein, W., and Kemp, R.F., Generation and diagnosis of synthesised plasma streams, *Rev. Sci. Instr.*, 36, 316 (1965).
8. Clayden, W.A., and Hurdle, C.V., An experimental study of plasma-vehicle interaction, p.1717 in *Rarefield Gas Dynamics (5th.Symp.)*, C.L. Brundin (Ed.), Vol.2, Academic Press, New York and London, 1967.
9. Skvortsov, V.V., and Nosachev, L.V., The structure of the trail behind a spherical model in a stream of rarefied plasma, *Cosmic Research*, 6, 191 (1968).
10. Skvortsov, V.V., and Nosachev, L.V., Some results on disturbances introduced by extraneous bodies into a stream of rarefied plasma, *Cosmic Research*, 6, 718 (1968).
11. Agnello, V., A plasma-beam system for simulating the interaction of a spacecraft with the ionosphere, *ESRO SN-104 (ESTEC)* 1969.
12. Knott, K., and Pederson, A., Wake studies in an argon plasma beam, *ELDO/ESRO Scient. and Tech.Rev.*, 2, 499, (1970).
13. Hester, S.D., and Sonin, A.A., Some results from a laboratory study of satellite wake structure and probe response in collisionless plasma flows, p.1659 in *Rarefied Gas Dynamics (6th. Symp.)*, L.Trilling and H.Y. Wachman (Eds.), Vol.2, Academic Press, New York and London, 1969.
14. Hester, S.D., and Sonin, A.A., Laboratory study of the wakes of small cylinders under ionospheric satellite conditions, *Phys. Fl.*, 13, 641 (1970).
15. Stone, N.H., and Rehmann, W.K., The simulation of ionospheric conditions for space vehicles, *NASA TN D-5894*, August 1970.
16. Stone, N.H., Oran, W.A. and Samir, U., Collisionless plasma flow over a conducting sphere, *Planet. Space Sci.*, 20, 1787 (1972).
17. Pigache, D., A laboratory simulation of the ionospheric plasma, *A.I.A.A. Paper No. 71-608* (1971).
18. Fournier, G., Ecoulement de plasma sans collision autour d'un cylindre en vue d'applications aux sandes ionospheriques, *ONERA Publication No. 137* (1971).

19. Fournier, G., and Pigache, D., Transverse ion temperature in an ionospheric wind tunnel, *J. Appl. Phys.*, 43, 4548 (1972).
20. Charpenel, M., and Pigache, D., Simulation en laboratoire du plasma ionosphérique, ONERA Note Technique No.202 (1972).
21. Martin, A.R., Spacecraft-plasma interactions; Introduction and review of simulation validity, The City University, Research memorandum AERO 73/1, January 1973.



PS1 Magnetic field, 30V 10A PS4 Accelerator supply, 350V 150mA
 PS2 Filament supply, 12V 20A PS5 Neutraliser supply, 20V 10A
 PS3 Discharge voltage, 100V 2A PS6 Mesh bias, 300V 2A

Figure 1--Wiring diagram for the parallel-streaming facility.

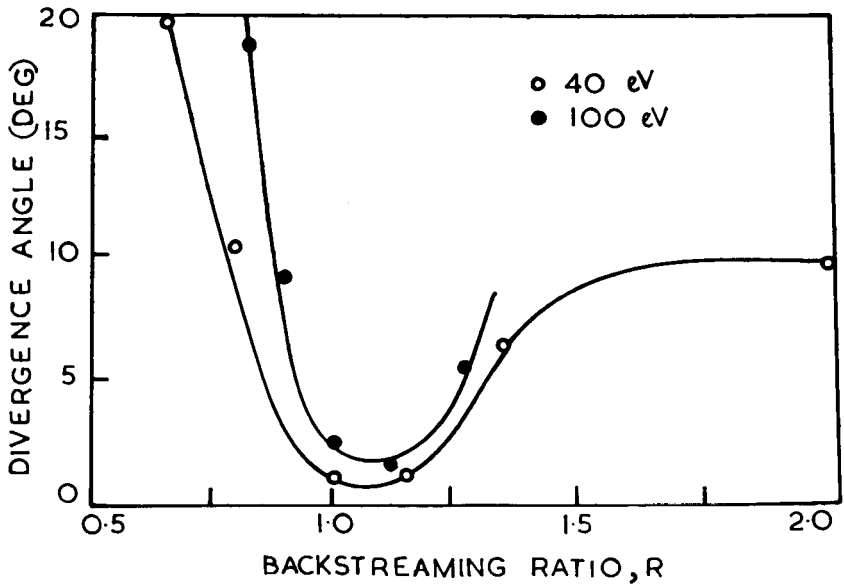


Figure 2--Divergence angle variation as a function of backstreaming ratio.

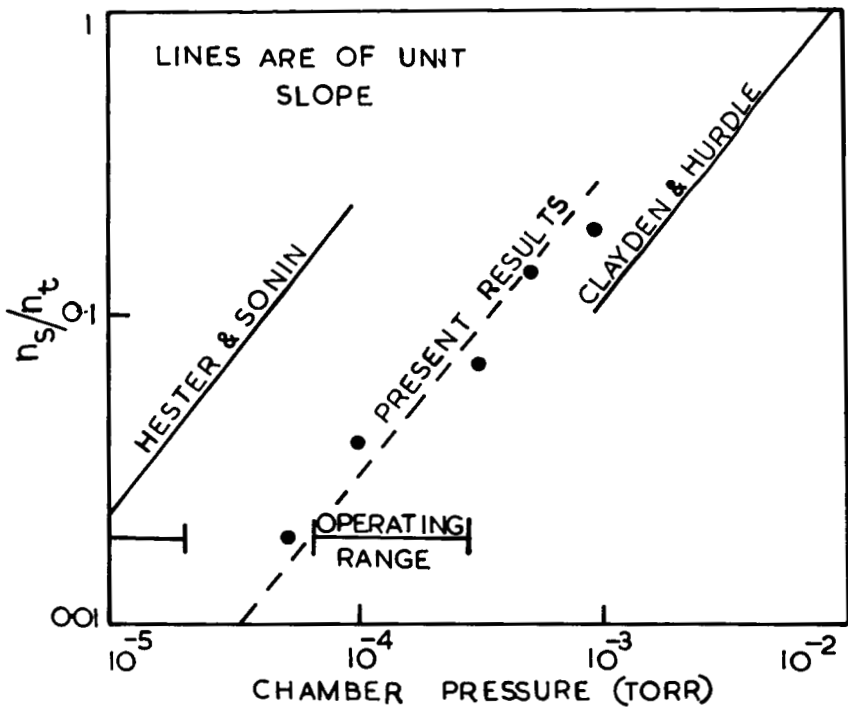


Figure 3--Variation of slow ion number density with chamber pressure.

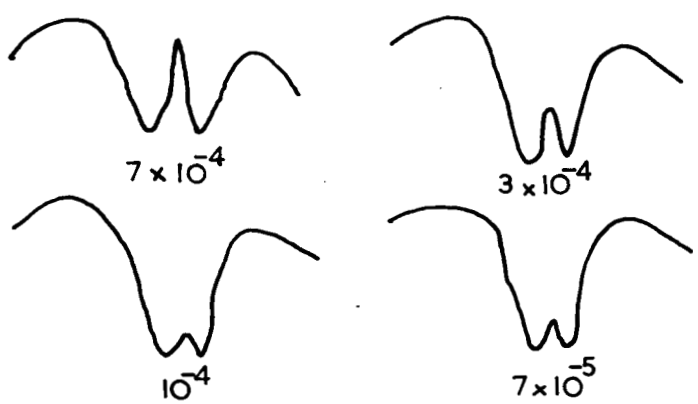


Figure 4--Effect of slow ion density on near wake shaping. (pressures in torr.)

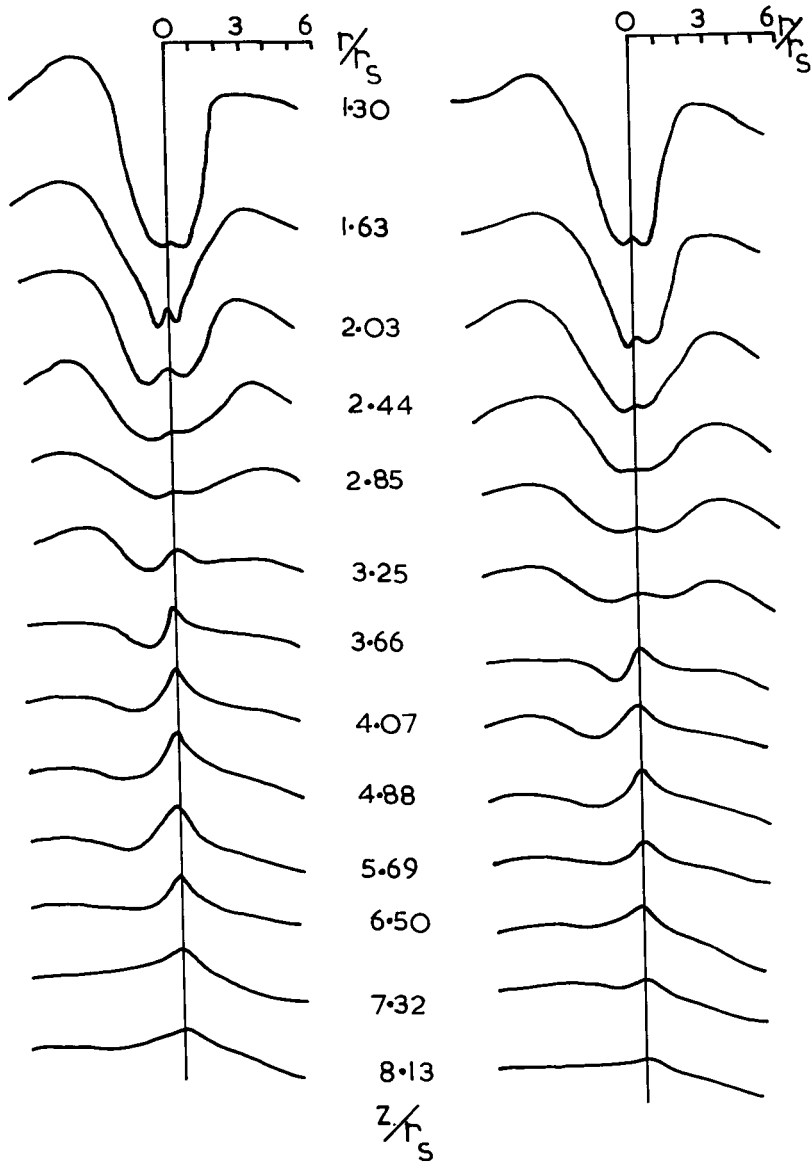


Figure 5--Near wake of a sphere $r_s/\lambda_D = 4.5$, $M = 6.5$, $\phi_s = -2.35$.
 Divergence $\theta = 1^\circ$ at left and 10° at right.

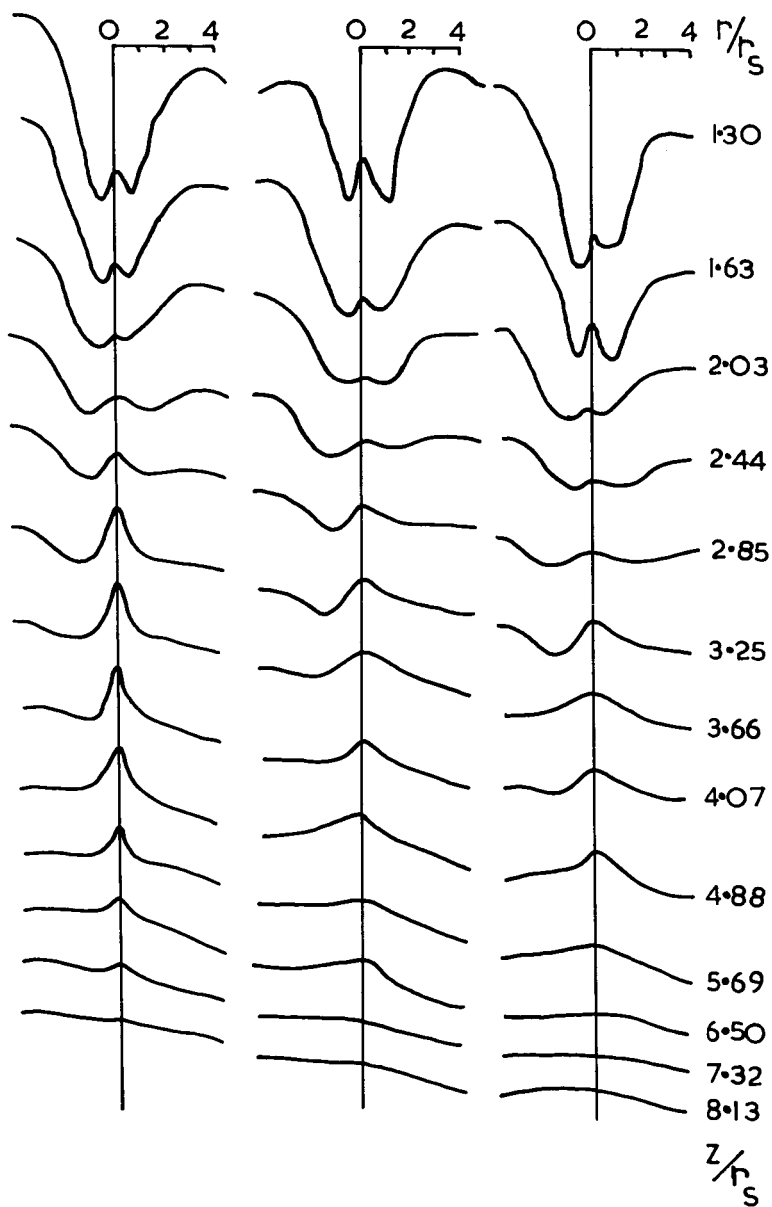


Figure 6--Near wake of a sphere $r_s/\lambda_D = 3.0$, $M = 5.4$, $\phi_s = -3.8$.
 Divergence $\theta = 1^\circ$ at left, 10° at centre and 20° at right.

N74-10249

PRECEDING PAGE BLANK NOT FILMED

Paper No. 18

SIMULATION AS A COMPUTER DESIGN AID

J. E. Weatherbee and D. S. Taylor, *Computer Sciences Corporation, Huntsville, Alabama*

B. C. Hodges, *Computation Laboratory, Marshall Space Flight Center, Huntsville, Alabama*

ABSTRACT

The use of simulation in evaluating hardware and software design concepts for the Automatically Reconfigurable Modular Multiprocessing System (ARMMS) is discussed. Two simulation models are described and results obtained from simulations conducted with these models were presented.

INTRODUCTION

Future space missions such as the earth-orbiting space station, astronomical space observatory and numerous outer-planet space probes will be measured in years instead of days. Long range missions of this type will place increased requirements on the onboard digital computing equipment, particularly in the areas of reliability and computing capacity. The use of third generation computing concepts such as micro-programming and multiprocessing for computational speed and fault tolerant computing concepts such as modular component design, redundancy, and system reconfigurability has made the design of future spaceborne computer systems no longer the relatively simple task it once was. The Marshall Space Flight Center, Huntsville, Alabama, is currently designing a complex avionics computer for use in the late 1970's to mid 1980's time frame. This system, the Automatically Reconfigurable Modular Multiprocessor System (ARMMS) (1), utilizes many of the above mentioned concepts previously not available for spaceborne systems. The ARMMS design goal is to meet the increased reliability and computing requirements of future spaceborne computer systems through a highly modular computer architecture which can be configured as a multiprocessor for maximum computing speed and as a duplex or triple modular redundant (TMR) system with standby spares for extremely high reliability. Moreover, the ARMMS will be dynamic in that it will be possible to alter its configuration, in real time, as required by various mission phases or events.

One problem encountered by the ARMMS design group was to determine an effective means for measuring the effect upon system performance of the various design concepts being considered. Since some of these features (e. g. , dynamic reconfiguration) are new not only to avionics computers, but to computer systems in general, there were no existing systems which could provide performance data relevant to the ARMMS design. This problem was resolved in part through the use of discrete event simulation, a technique which has gained general acceptance for use in the design and evaluation of computer systems. (2, 3)

Areas of interest for the application of simulation ranged from the instruction execution level to the simulation of the scheduling algorithms of the ARMMS executive system. Due to the high cost of computer time required to simulate all of these activities in a single model, two different models were developed; one which simulates the traffic between the central processing units (CPU's) and central memory (CM) as instructions are fetched and executed, and another which models the principal algorithms of the executive system required for resource allocation and task dispatching. This paper describes the two models and presents some results obtained from their application.

SYSTEM DESCRIPTION

The ARMMS design features a highly modular computer architecture which allows the system hardware to be configured according to the needs of individual tasks; highly critical tasks will be executed in triple modular redundant (TMR) or duplex mode while less critical tasks will be executed in simplex mode. Sufficient system components will be available to allow the concurrent execution of more than one task and to provide spare modules to replace certain critical system components in the case of failures. Thus the ARMMS executive must not only perform the functions required in a third generation multiprocessor system, but will also be charged with the tasks of system configuration control and response to component failures. A hardware/software complex, the Block Organizer and System Scheduler (BOSS), will perform these functions in ARMMS.

ARMMS Hardware

The ARMMS hardware configuration is illustrated in Figure 1. Upto four central processing units (CPU's) and four input/output processors (IOP's) will be active at any one time with up to sixteen logical memory modules available for program

instruction and data storage. A logical memory module consists of one, two, or three physical modules depending on whether the programs stored in the module are simplex, duplex, or TMR.

Upon execution of a computational task, one, two, or three CPU's will be assigned to process the task; again the number depends on the status of the task (simplex, duplex, TMR). If a task is critical enough to require redundant processing, multiple copies of the task will be stored in a logical memory module and the proper number of CPU's will execute the code in parallel with the results being compared or voted upon as they are transferred back to CM. Instructions fetched from CM are also compared or voted upon before execution. Four busses are provided for transferring addresses and data to memory and four different busses are provided for fetching instructions and data from memory. This bus structure is illustrated in Figure 2 which shows the ARMMS processor-memory interface. It is assumed that these memory modules contain plated wire components with access times of 300 ns and cycle times of 600 ns for read and 800-900 ns for write accesses to memory. The processors themselves are microprogrammable with a clock speed of 5 MHz. In order to match the memory and processor speeds, a bus speed of 10 MHz (twice the processor) is assumed.

Since the processors operate in a multiprocessing mode memory conflicts can occur. Whenever two processors require the same memory module, one will always have a higher priority. However, once one processor obtains entrance into the memory module, it cannot be preempted during that memory cycle time, even by a processor of a higher priority.

ARMMS Software

In order to provide a fast, reliable, executive, the logic in the ARMMS Control Executive System (ACES) is being kept as simple as possible. The task scheduling and facility allocation algorithms currently being considered for implementation are briefly described in the following paragraphs:

The following information about each task is required for task scheduling and resource allocation:

1. Task criticality (simplex, duplex, or TMR).
2. Task priority (the number of levels to be determined).
3. Task type (full processing, limited processing, I/O).
4. Task start time.

The resources required by a task will be determined by its criticality and type; full processing tasks require both CPU's and IOP's, limited processing tasks require only CPU's and I/O tasks require only IOP's. The number of CPU's and/or IOP's

allocated to a task is three for TMR, two for duplex and one for simplex with all the resources required by a task being assigned for the duration of its execution.

A fixed priority number is assigned to each task prior to an ARMMS mission and is used as a basis for all internal scheduling and resource allocation. Internal priority generation by ACES will be avoided if possible.

A limited processing task may be preempted during execution by a higher priority task if its preemption will yield sufficient resources to place the higher priority task in execution. Neither full processing tasks nor I/O tasks may be preempted once they begin execution because of the problems associated with the interruption of an I/O transmission.

Once ACES begins processing a task request, it cannot be interrupted or preempted by another task request regardless of the request type or the priority of the task issuing the request. Task requests originating while ACES is busy will be queued on a first-in-first-out basis. Tasks delayed due to insufficient system resources will be filed in the facilities queue on the basis of task priority.

The current ACES concept does not provide for the assigning of deadlines to tasks in order to assure execution within a certain time period. It will be the responsibility of the user to assign task priorities and task start times in such a way that task deadlines are met.

INSTRUCTION EXECUTION SIMULATION

One method that has been proposed to increase the ARMMS processor speed is to operate with an overlapped instruction fetch. It has been estimated that the additional hardware required to implement this feature is less than five percent of that which would be required for a non-overlapped processor. Instruction overlap is accomplished by allowing the processor to execute one instruction while the next instruction is being fetched from memory. Figure 3 illustrates how an instruction overlap is employed. It is apparent from this figure that the processor speed and the memory speed should be comparable in order to obtain the maximum benefit from instruction overlap. If one stream of the overlap is utilizing the processor (or memory), then the other stream is prohibited from utilizing that facility. The only exception to this rule is that the memory port becomes free at a point approximately equal to two-thirds of the memory cycle time, thus allowing the processor to transfer the next address to memory even though the memory module itself is still being utilized.

Instruction Execution Simulation Model

A simulation model which simulates the major activities involved in the execution of instructions by the ARMMS processors was developed to study the speed advantage offered by the instruction overlap features under different assumptions pertaining to the type and mix of instruction being executed, the degree of memory contention resulting from multiprocessing, the internal CPU and memory speeds, etc.

A simplified flowchart of the basic model logic is shown in Figure 4. This figure illustrates the primary and secondary paths for the overlap instruction streams. Not shown in this figure are the various queue blocks that prevent the two streams from both trying to utilize the same facility at the same time.

The model input parameters and output statistics are listed below:

Model Input Parameters

- I. System Description
 - A. Number of processors
 - B. Number of memory modules
 - C. Bus Speeds
 - D. Microprogram execution time
 - E. Memory characteristics
 1. Cycle time (read and write)
 2. Time that input port is released
 - F. Instruction overlap (yes/no)
- II. Software Input Characteristics
 - A. Task description
 1. Number of instructions
 2. Memory module where task is stored
 - B. Instruction description
 1. Decode time
 2. Flag if second operand is required
 3. Flag if jump type
 4. Flag if read into memory is required
 5. Execution time
 - C. Number of tasks to be executed
 - D. Relative distribution of instructions to be executed.

Model Output Statistics

- I. At the completion of each task
 - A. Task number
 - B. Memory module number
 - C. Instruction Overlap (yes/no)
 - D. Processor number
 - E. Total number of instructions executed

- F. Types and frequency of instructions executed
- G. Task start and end time
- H. Task execution time
- I. Minimum non-overlap task execution time
- J. Jump-caused aborts
- K. Memory and processor interference
- L. Average time (in percent) gained by utilizing instruction overlap (if overlap is used).

Note that the model input parameters permit a detailed description of the characteristics of individual instructions. For the purpose of evaluating the instruction overlap technique, only 15 instructions are described in this paper; Load, Store, Conditional Jump, Unconditional Jump, Compare, Add, Subtract, Multiply, Divide, Floating Point Add, Floating Point Subtract, Floating Point Multiply, Floating Point Divide, And/Or. While this is a relatively small number of instructions, it is felt that these 15 instructions would comprise approximately 95 percent of the instructions in a typical scientific program.

Simulation Results

Some typical simulation results are shown in Figures 5 and 6. The instructions used in these simulations were those mentioned in the preceding paragraph. Within each task the mix of instructions were distributed in a fashion which approximates the Gibson mix (4).

Figure 5 shows a direct comparison between an overlapped and non-overlapped instruction stream with various degrees of memory conflict. This figure illustrates that an overlap instruction stream is about 37 percent faster than a non-overlap instruction stream, if there is no memory contention. However, as more than one processor attempts to utilize the same memory module, any advantage of instruction overlap is quickly forfeited.

Figure 6 depicts the results of running 15 tasks (6254 instructions) in a multiprocessing mode on four processors, with and without instruction overlap. Nine memory modules were assumed, and some degree of memory conflict was experienced. As can be seen from this figure, the instruction overlap processors consistently finished their tasks ahead of the non-overlap processors. This means that, with the same speed of internal components, the overlap instruction processors appear to be over 30 percent faster than the non-overlap processors.

These results show that in general, the instruction overlap feature can be expected to yield a significant improvement in processor execution speed if a moderate amount of memory contention is experienced. Only under severe memory contention does the single instruction stream processor speed approach that of the processor with instruction overlap.

EXECUTIVE SYSTEM SIMULATION

A major factor to consider in evaluating the performance of a computer system is the degree to which performance is influenced by the system executive. This effect can often be measured in an existing system by using hardware and/or software monitors to gather statistics on variations in system performance induced by changes in executive parameters or algorithms. (5), (6). However, the problem of predicting the effect on performance of an executive for a system being designed requires that some other technique, such as simulation, be employed. A simulation model was developed to study the ARMMS performance under various assumptions pertaining to facility allocation procedures task priority schemes and the time required by the BOSS hardware to execute ACES, the software component of BOSS.

Executive Simulation Model

The major model components and the principal activities simulated are illustrated in Figure 7. When simulated time reaches a task start time, that task is created, its attributes are assigned values, and it is entered into the system where it places a request to be dispatched. When this request is acknowledged by ACES (either immediately or after waiting in the EXEC queue if another request is being processed), the dispatcher module determines whether:

1. Sufficient resources are available to place the task in execution;
2. Available resources plus resources obtained by preempting lower priority tasks will meet the task resource requirements; or
3. Neither 1. or 2. is true.

The time increment T required for the dispatcher to accomplish its function is calculated as a function of a number of input parameters and the next event (initiate task after 1. , preempt another task after 2. , place the task in the facilities queue and process the next ACES request after 3.) is scheduled at current time plus T .

If the dispatcher module determines that either 1. or 2. is true, ACES continues processing the current task until the initiation module places the task in execution, at which time the next ACES request will be honored. Once a task begins execution, it will be interrupted only if it is a preemptable task and is preempted by a higher priority task, in which case it is placed back in the facilities queue to await another dispatch. When a task completes execution, it requests that it be terminated by the terminator module; again the task request may be

queued if the executive is busy.

The principal inputs to the module are task attributes, the number of CPU's and IOP's in the system, and timing data used to determine how long the various ACES modules require to perform their functions. Random functions are used to produce the task inter-arrival pattern and to assign the task attributes. ACES timing data are based on the criticality and type of task being processed and reflect the number of instructions which must be executed to perform the ACES logic as well as the speed of the BOSS hardware executing ACES. Module output consists of utilization statistics for the CPU's, IOP's, and the major ACES modules and statistics showing the average time spent in the system for various classes of tasks.

Baseline Simulation

A baseline simulation was performed using instruction execution estimates for the ACES timing as shown in Table 1. Workload parameter values were based upon a mission analysis profile of space missions for which the ARMMS would be a suitable onboard data processing system. (1) Instruction execution estimates for ACES were obtained from flowcharts provided by the software designer.

A number of deductions concerning the match between the workload and the system as well as the relationship between system performance and ACES can be drawn from the baseline simulation statistics shown in Table 2. Note that the dispatcher module was active almost 40% of the time, a factor influenced by the average facility queue contents of more than 46. These results suggest that a more efficient or faster dispatcher design should be explored to accommodate large queues for facilities.

Figure 8 graphically displays the average time spent in the system, in excess of the average processing time, as a function of task priority, criticality and type. Note that TMR tasks of all types encountered the longest delays in the system with full processing tasks being delayed longer than either limited processing or I/O tasks.

It is clear from the Task State Statistics (average number of tasks in queue and average number of active tasks) that the baseline system is inadequate for the workload being imposed upon it. Based upon the average task inter-arrival time of two milliseconds and the average task execution time of five milliseconds, an average of approximately 2.5 active tasks must be maintained if the system is to accommodate the workload without queue build-ups; approximately 15 percent more than the 2.21 average maintained in the baseline simulation. The

average CPU and IOP utilization maintained in the baseline indicate that perhaps changing the ACES logic and/or speeding up ACES execution would provide an adequate system without having to increase system hardware. The following paragraphs discuss a series of simulations designed to investigate system performance improvement induced by such changes in ACES.

Other Simulation Results

Some results from five simulations are presented in Table 3 where they are ranked in order of improvement over the baseline simulation; improvement being measured as increase in the average number of active tasks (or alternatively, as the decrease in lapsed time for the simulation where lapsed time was measured from the time the first run entered the system to the time the last run terminated).

Run Priority Raised After 50 Milliseconds in System--In this simulation, a simple deadline scheme was implemented in which the priority of a task was incremented by ten if it had not been dispatched within 50 milliseconds of its entry into the system. The average number of active tasks rose to 2.34, approximately a six percent increase over the baseline, indicating that perhaps a more sophisticated deadline scheme would yield additional performance improvement. It was assumed that this deadline scheme could be implemented without any increase in ACES overhead, an assumption which might be unrealistic if a more sophisticated scheme were used.

All EXEC Times Equal Zero--The purpose of this simulation was to determine whether it was possible to speed up the executive to such an extent that the workload could be accommodated, a test accomplished by exercising a model option which sets all the executive timing parameters to zero. Results from this simulation show that, while system performance may possibly be improved up to 7.7 percent by making ACES faster, this technique alone will not give the performance improvement needed.

Priority a Function of Criticality--The graphs in Figure 8 show that among the various task types the longest delays are encountered by low priority TMR tasks. In this simulation, a priority scheme was implemented to see if special consideration to TMR tasks would not only alleviate this condition, but would increase overall system performance. Task priority in this simulation was given by

$$P = P' + 10 * C$$

where

P' is baseline priority

and

$C =$ 1 for simplex tasks
2 for duplex tasks
3 for TMR tasks

This priority scheme not only improved system performance by eight percent, but changed the task delay pattern to that shown in Figure 9. It is not surprising that with this priority scheme duplex tasks encounter the longest delays since a duplex task cannot be executed if a TMR task (now having the highest priority) is active but a simplex task can be executed.

Priority a Function of Criticality and EXEC Time Equal Zero--

This simulation combined the changes incorporated in the two previous simulations and showed an improvement in performance of approximately 13 percent, providing a system which was adequate for processing the given workload. Admittedly this simulation is unrealistic with respect to the zero executive assumption, but it indicates that perhaps an optimum scheduling strategy exists which, when combined with optimum executive code, will allow the baseline hardware configuration to process the baseline workload.

Five CPU's and Five IOP's--In this simulation, an additional CPU and IOP were added to the system hardware to yield a system which is more than adequate for the baseline workload (note average queue contents and facility utilization). It is interesting to note that even in this system, which has considerable slack resources, the pattern of delay by task type established in the baseline simulation still prevails, although the magnitudes of the delays are naturally smaller. This is illustrated in Figure 10 which shows that low priority TMR tasks, especially full processing TMR tasks, still have significant delays when compared to the other task types.

The results discussed in the preceding paragraphs led to the following conclusions and recommendations pertaining to the ACES design.

1. System performance is as sensitive to the ACES logic as to the execution time of ACES.
2. Full processing stream concept should be reviewed.
3. Some special consideration may be necessary when scheduling TMR tasks.

4. If large queue build-up is anticipated in an ARMMS mission, more efficient queue search logic than is currently planned should be implemented.
5. Some sort of dynamic priority assignment or task deadline scheme may be required to assure timely completion of critical tasks.

The ACES designer concurred with recommendations 2. and 4. , dropping the full processing stream concept from the ACES design and altering the queue search logic of the dispatcher to provide a more efficient and quicker method for finding the highest priority dispatchable task.

CONCLUSIONS

Simulation has proved to be an effective means for evaluating both hardware and software design concepts being considered for the Automatically Reconfigurable Modular Multiprocessor System (ARMMS). The instruction execution model demonstrated that implementing an instruction fetch overlap feature in the ARMMS processors could provide a significant improvement in processor speed. Results obtained with the ARMMS executive system simulation model identified areas in the system software where changes would improve overall system performance. These results would have been difficult to obtain without the use of simulation.

ACKNOWLEDGEMENT

The authors wish to acknowledge Dr. J. B. White (NASA-MSFC), the ARMMS project manager, for his cooperation and encouragement during the course of this work.

BIBLIOGRAPHY

1. Hughes Aircraft Company, Design of a Modular Digital Computer System, DRL4, Phase I Report, FR 72-11-450, April 15, 1972.
2. Proceedings of the ACM (SIGOPS) Workshop on System Performance Evaluation, Harvard University, April, 1971.
3. Proceedings of the ACM Symposium on the Simulation of Computer Systems, National Bureau of Standards, June, 1973.
4. Smith, J. M., "A Review and Comparison of Certain Methods of Computer Performance Evaluation", The Computer Bulletin, Vol. 11, 1968, pp. 13-18.

5. Bordsen, D. T. "UNIVAC 1108 Hardware Instrumentation System", ACM (SIGOPS) Workshop on System Performance Evaluation, Harvard University, April, 1971.
6. Schwetman, H. D., Jr., A Study of Resource Utilization and Performance Evaluation of Large-Scale Computer Systems, Technical Systems Note-12, Computation Center, University of Texas at Austin, July, 1970.

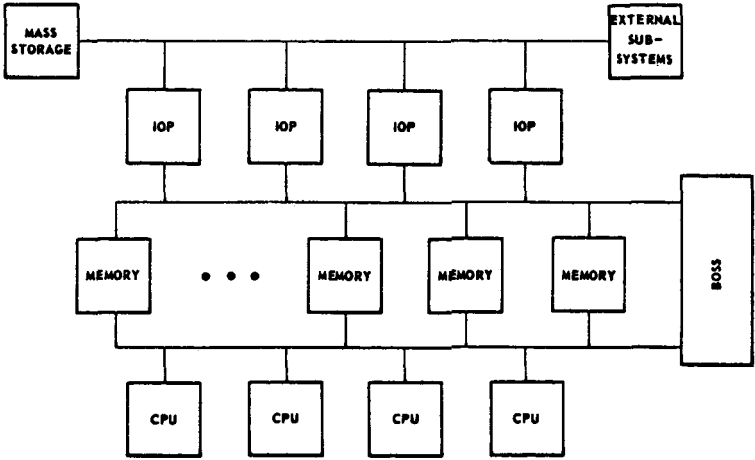


Fig. 1 - ARMMS Hardware Configuration

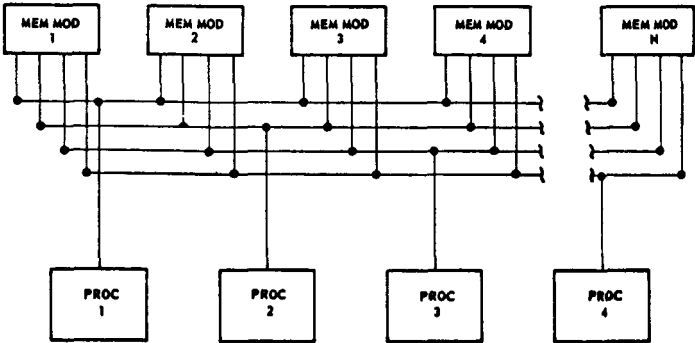


Fig. 2 - Processor-Memory Interface

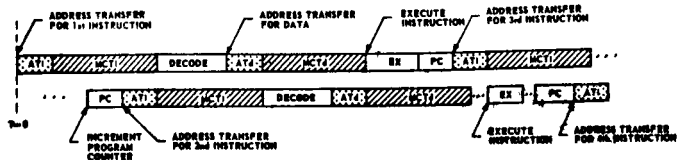


Fig. 3 - Instruction Overlap Concept

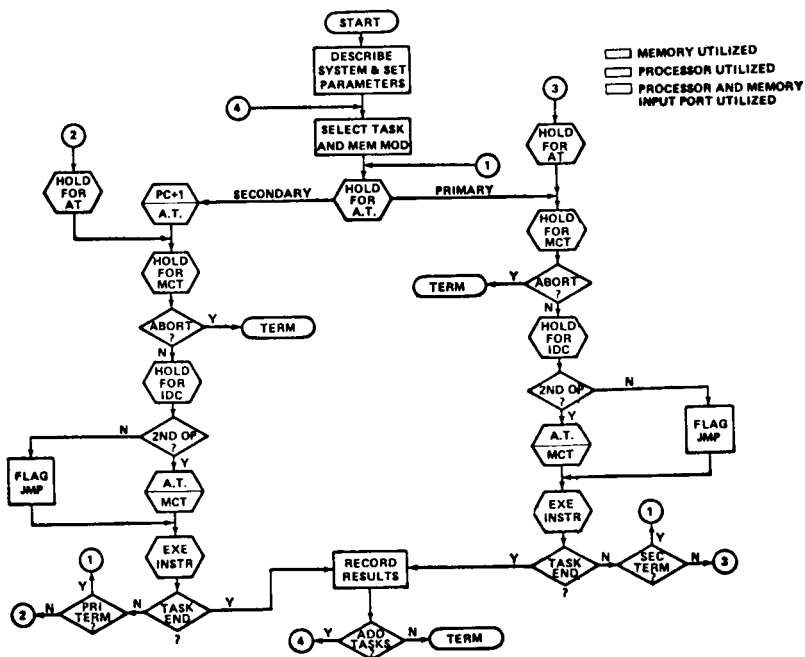


Fig. 4 - Instruction Overlap Simulation Model

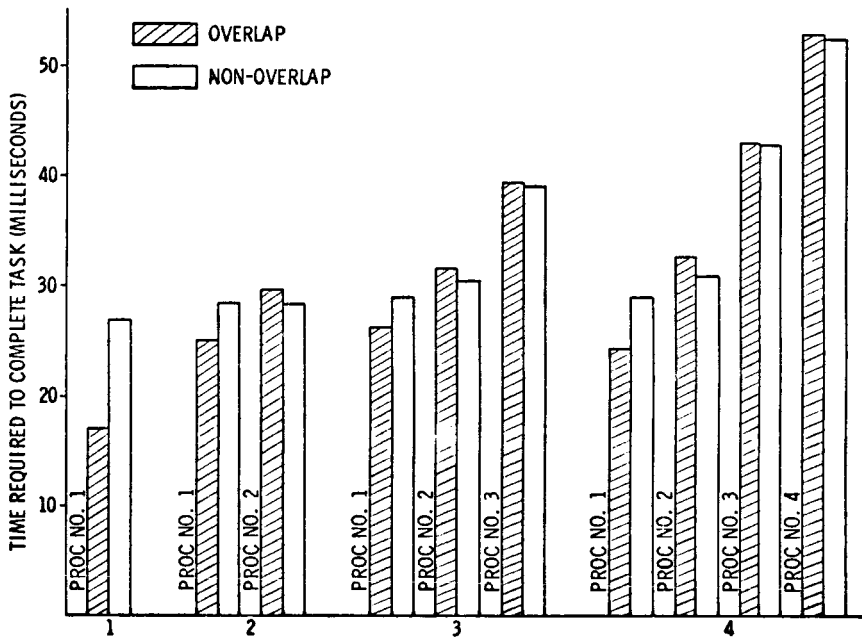


Fig. 5 - Number of Processors Contending for the Same Memory Module

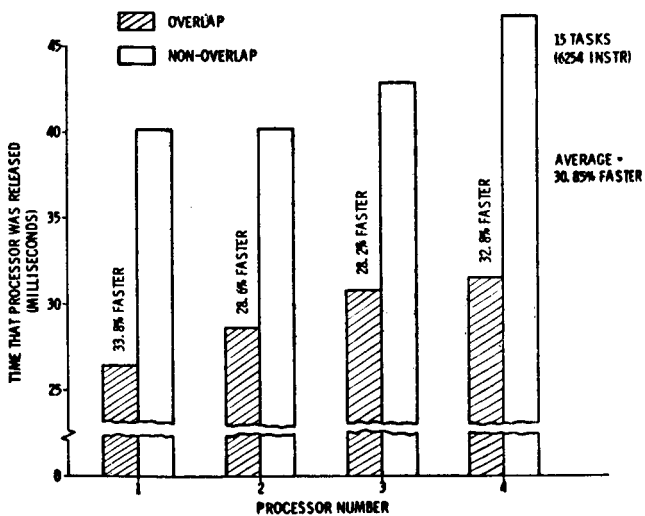


Fig. 6-

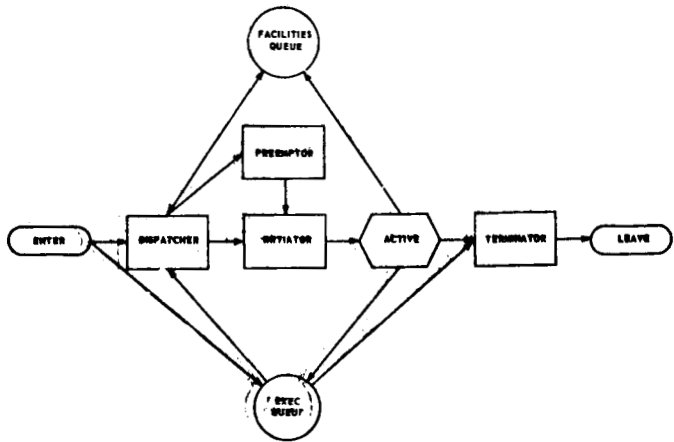


Fig. 7 – Simplified Simulator Logic

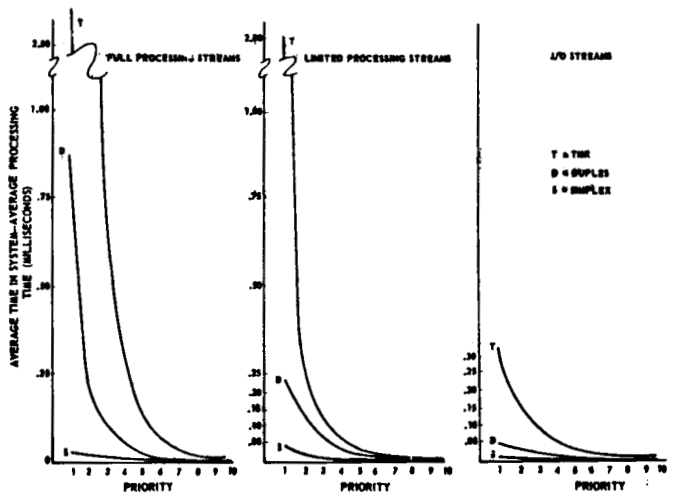


Fig. 8 – Task Wait Times for Baseline

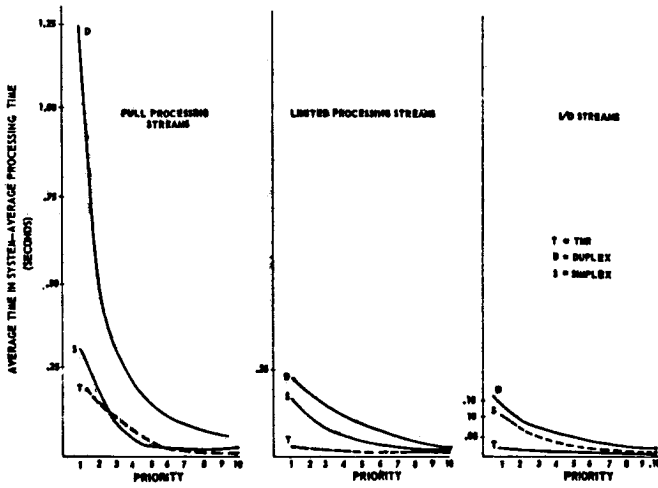


Fig. 9 - Task Wait Time with Priority Based on Criticality

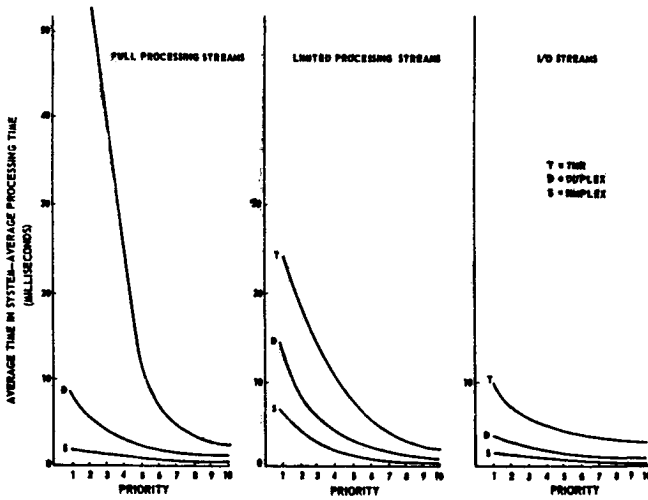


Fig. 10 - Task Wait Time with 5 CPU's and 5 IOP's

PARAMETER NAME	DESCRIPTION	INSTRUCTIONS REQUIRED
FCHK	TIME TO DETERMINE WHETHER FACILITIES ARE AVAILABLE	6
PCHK	TIME TO CHECK FOR POSSIBILITY OF PREEMPTION	6-4
TABS	TIME TO SEARCH FOR AVAILABLE CONFIGURATION	24-96
TABUP	TIME TO UPDATE TABLES AFTER FACILITY ACQUISITION	30
CNFIG	TIME TO ESTABLISH CONFIGURATION	5
MNPRI	TIME TO CALCULATE LOWEST PRIORITY TASK WHICH CAN PREEMPT	0-30
INITM	TIME TO INITIATE TASK (FIRST DISPATCH)	5
RELOD	TIME TO INITIATE TASK WHICH HAS BEEN PREEMPTED	30
TERM	TIME TO TERMINATE TASK	30-60
PRTM	TIME TO PREEMPT TASK	35-65

Table 1- Executive Timing Parameters

Facility Usage Statistics			
TYPE	NUMBER USERS	AVERAGE TIME/USE(MSEC)	AVERAGE UTILIZATION (%)
CPU	3649	3.773	76.0
IOP	2686	5.101	75.5

STATISTICS EXECUTIVE USAGE			
MODULE	NUMBER USERS	AVERAGE TIME/USE(μSEC)	AVERAGE UTILIZATION (%)
DISPATCHER	70,973	25	39.7
PREEMPTOR	410	130	1.4
INITIATOR	2,487	21	1.2
TERMINATOR	2,000	80	3.5

TASK STATE STATISTICS				
STATE	MAXIMUM CONTENTS	NUMBER ENTRIES	AVERAGE CONTENTS	AVERAGE TIME IN STATE (MSEC)
ACTIVE	6	2487	2.21	4.024
FACILITIES	132	68130	46.03	3.060
QUEUE				

Table 2 - Statistical Summary of Baseline Run

RUN DESCRIPTION	EXEC TIME (SECONDS)	LAPSED TIME (SECONDS)	CPU/IOP UTILIZATION (%)	AVG. NO. ACTIVE	AVG. NO. IN QUEUE
BASELINE	2.074	4.530	76.0/75.5	2.21	55.1
RUN PRIORITY RAISED AFTER 50 MILLISECONDS IN SYSTEM	1.541	4.275	79.2/78.6	2.34	29.7
ALL EXEC TIME EQUAL ZERO	.0	4.203	78.8/78.4	2.38	23.6
PRIORITY A FUNCTION OF CRITICALITY	1.957	4.196	80.7/80.3	2.39	36.0
PRIORITY A FUNCTION OF CRITICALITY AND EXEC TIME EQUAL ZERO	.0	4.006	82.7/82.3	2.50	9.6
5 CPU'S AND 5 IOP'S	.799	3.987	67.1/66.7	2.51	2.4

Table 3 -- Comparison of Simulator Run Statistics

PRECEDING PAGE BLANK NOT FILMED

Paper No. 19

DEVELOPMENT OF A STOCHASTIC SIMULATION MODEL
FOR PERFORMANCE EVALUATIONE. Gordon and P. G. Freese, *Aerojet ElectroSystems Company,*
Azusa, California

ABSTRACT

Simulation played a vital role in the evaluation of the performance of an extremely accurate attitude determination system before it was built and flight tested. This attitude determination system uses a high-sensitivity star sensor. The sensing element is an electron multiplier phototube which responds to incident radiation within a few nanoseconds. This system, with time constants dispersed over more than ten orders of magnitude, was simulated using a set of programs in which the effects derived from the shorter-time constant simulations are explicitly represented in the next model up. This paper describes the development of a representation of the stochastic effects in a manner usable for the models.

INTRODUCTION

Aerojet ElectroSystems Company has developed a high-accuracy attitude-determination system for space applications. The system contains a high-sensitivity star sensor and related electronics on board the spacecraft, producing data which is processed on the ground to accurately determine the attitude of the spacecraft. This paper addresses the development of simulation models used to demonstrate feasibility and evaluate the performance characteristics of the techniques being developed before the system was built and flight-tested. Since the development of the simulation paralleled the development of the hardware and software, early simulation results provided useful guidance for the detailed design.

The basic sensing element of the star sensor is an electron multiplier phototube. The response of the phototube to star signals is transmitted to a ground station for processing without significant loss in accuracy. In the ground data processing, the information received regarding star sightings is compared with

predictions based upon the accurately known star locations in celestial coordinates to determine the orientation of the spacecraft. The essential functions which must be performed by the attitude-determination system are summarized in the following subsections.

Functions Performed On Board the Spacecraft

The star sensor contains a sun shade, a sun sensor and shutter, an optical assembly, a reticle, a phototube, and electronics. The optical assembly collects and focuses the light from stars onto the surface of a reticle. The sun shade attenuates the stray reflections of sunlight within the optical assembly so that stars can easily be detected in the data generated when the sun is not close to the field of view of the optical assembly. The sun sensor provides a signal which causes the sun shutter to close when intense light from the sun can reach the phototube.

Only the light from stars whose focused images fall on a slit in the reticle interact with the light-sensitive cathode of the phototube. The probability that a photon will cause the photocathode to emit an electron is called the quantum efficiency and it is dependent upon the wavelength of the photon. The emitted electron is multiplied in the phototube by secondary emission each time an electron interacts with a dynode. The overall gain of the electron multiplication process in the phototube used is of the order of one million. Because of the rather short duration (tens of nanoseconds) of the anode pulse resulting from the electron multiplication process, a modest amount of additional signal gain in the star-sensor electronics is sufficient to produce a signal from a single emitted electron which is readily detected in the electronics and converted into a normalized output pulse. To simplify the terminology, each anode pulse due to an electron emission from the photocathode is called an event.

The number of normalized output pulses occurring in an interval (called a count cycle) of 140 microseconds duration is determined and the resulting count values are transmitted to the ground for processing. The system was designed based upon a star of sufficient intensity to cause events to occur at an average rate of two hundred thousand per second, i.e., one per five microseconds on the average. Because this average interval between events is long compared to the duration of typical anode pulses, it was possible to make performance and design analyses without getting bogged down by the complications resulting from the interactions in the electronics due to individual events. However, the system performance must be evaluated and

demonstrated over the full range of star intensities of interest. The brightest star, Sirius, was expected to yield an average rate sufficient to make the average time between events comparable to the anode pulse duration. Several planets are brighter than Sirius, yielding even lower average times between pulses.

The Model discussed in the following section was developed to simulate the consequences of the interactions between events in the star-sensor electronics. The initial purpose of this simulation model was to evaluate the possible need for higher frequency electronic components in the star-sensor electronics and in the pulse counter, and for refinements in the design to modify its response characteristics when exposed to the light from bright stars. Hence, this simulation was available and the results had been analyzed when the effort to develop an "end-to-end" simulation was initiated. It was clear that costs would be prohibitive if the "end-to-end" simulation included an explicit simulation of the individual events, even at the simplified level of representation used in the Nanosecond Regime Model. One simulation, which represented only one millisecond for the brightest star, had one hundred thousand events and consumed ten minutes of computer time. Fortunately, the single run at that intensity was sufficient to provide the information required for the analytical model of the Nanosecond Regime Model results.

Functions Performed in Ground Processing of the Data

The ground processing of the data starts with the receipt of the data telemetered from the spacecraft. The star-sensor data are separated from the rest of the data stream in a preprocessor which extracts candidate star sightings. The candidate star sightings are extracted from the data stream by the use of a threshold which is dependent upon the average background level.

The star candidates are transferred from the Preprocessor to the computer via a selector channel. The same data channel also contains timing information from which the time of each sighting can be calculated. Since most of the star candidates are background phenomena or dimmer stars not in the star catalog used for attitude determination, most of the candidates are rejected in the computer processing which edits the data. The edited, sighting-time data are the inputs to the Kalman filter which estimates the attitude of the spacecraft.

When the simulation effort described in this paper was initiated, a rudimentary version of the filter had been implemented and was undergoing preliminary development testing. For these tests, star sighting times were computed based upon

the star-sensor reticle geometry undergoing motions determined by a spacecraft dynamics simulator. The dynamics simulator represented both the motion of the center of mass of the spacecraft as well as the orientation variations typical of the attitude-control system.

Preliminary analyses of the requirements for the Performance Evaluation Simulation Model quickly led to the conclusion that the primary objective was the determination of how well the filter could follow realistic spacecraft motions. The details of the dynamics simulation were of secondary importance and there was no need to improve on the dynamics simulation available. The much more critical question was the effect of the rather complicated stochastic properties of the star sighting and background data on the dependability and accuracy of the spacecraft attitude determined by the filter. The attitude variations being estimated can be described in terms of time constants of the order of a minute superimposed upon longer-term alignment changes and orbital motion.

The full range of time constants which must be considered in the Performance Evaluation goes from phototube anode pulse durations of a few nanoseconds through the spacecraft attitude dynamics with time constants as long as hours. The development of the simulations which provided the needed results is covered in this report. Because the more slowly varying conditions cannot change significantly in the brief time span encompassed in the Nanosecond Regime Model runs, the model development effort did start with the Nanosecond Regime Model and developed summary relationships useful for the longer time scales.

NANOSECOND REGIME MODEL

There is a non-zero dispersion of secondary electron arrival times due to the variations in the paths the electrons travel and in the details of the electron multiplication process. The dispersion was reported as 10 nanoseconds in Reference 1, and it represents the minimum event duration (anode pulse width) physically possible. The non-zero capacitance in the phototube output wiring and limitations on the frequency response of the output electronics would tend to increase the effective pulse width. The general characteristics of the star-sensor electronics are such that when events are more than 200 nanoseconds apart, the circuitry can easily respond to each event separately. As the events get closer than the time required to handle one event, some of the events will be ignored. The baseline design is able to accept another event 100 nanoseconds after the

preceding event is accepted. One question which the Nanosecond Regime Model simulation addressed was the general signal-response characteristics of the baseline circuitry and the effect of exercising some of the design options available.

The logic of the simulation is summarized in Figure 1. IBM's General Purpose Simulation System (GPSS/360), described in Reference 2, was used; it is convenient for models which involve moderately complicated interactions between independent stochastic events. Generation of photons as the result of a Poisson process (characterized as a stochastic process with a constant expected number per unit time) is handled by a single GPSS generate block. The background caused by high-energy (cosmic) protons and (Van Allen) electrons can also be characterized by a Poisson process. Initially, the quantum efficiency of the phototube was modeled using the GPSS conditional transfer block where one minus the quantum efficiency was the probability that the processing of that photon would be terminated. The computer overhead involved in generating and terminating many simulated photons which were terminated without producing useful information was found to be significant. The simulation was more cost-effective when the generation rate corresponded to electrons emitted by the photocathode.

The counter tested in Block 6 is reset for 100 nanoseconds after acceptance of one anode pulse before it is ready to accept another anode pulse. As indicated in Figure 1, either source of pulses can set the counter. Then, pulses from either source cannot get through until the delay is completed. Blocks 2, 5, 10, 15, 20, and 25 are used to generate and output statistical information required for the analysis of the results without having any direct physical counterparts. The logic as shown is for the hypothetical case in which the anode pulse duration is zero. The effect of anode pulse duration was evaluated by adding logic in place of the termination Block 7 to allow for the possibility that the delay is completed after the anode pulse starts, but before the pulse ends.

In the simulation, the basic time interval used by GPSS as the clocktime increment was equal to 2 nanoseconds of system time. Therefore, the count-cycle duration was 70,000 clock times. Typically, five count cycles were simulated at each condition to provide an estimate of the standard deviation in addition to the mean value for each parameter calculated. For most of the simulations, the background expected count rate was one pulse per 20 microseconds. A few cases were run with background levels of five pulses per microsecond.

The effect of anode pulse duration determined by the simulation is presented in Figure 2. The number of events which do not produce normalized output pulses is indicated by the difference between the number of events (photons interacting with the photocathode and causing the emission of an electron) and the value from the response curve for the event-duration considered. For example, with an event duration of 10 nanoseconds, any event starting within the last 10 nanoseconds of the delay shown in Figure 1 would cause an output pulse when the delay is completed. A detailed analysis of the results demonstrated that the ratio of events to outputs, x/y , was equal to the sum of $x(X3/X6)$ and D , a function of the above probability, where $X3$ is the delay-interval duration, $X6$ is the count-cycle duration, and x is the expected number of events per count cycle. For values of x less than 2000 events per count cycle, it was found from the simulation results that

$$D = 1 - 5.5 cx$$

where c is the event duration expressed in milliseconds. Hence, the output count rate,

$$y = x / (1 + EC * x)$$

where EC is the electronics coefficient equal to $(X3/X6) - 5.5 c$.

The curves shown in Figure 2 are based upon the above relationship for values of x less than 2000 and the smoothed results for x greater than 2000.

At the very low event rates, the standard deviation of the output count rate from its expected value should have the square root relationship typical of Poisson processes. The results of simulations were consistent with the anticipated square root relationship until a maximum value of 15 was reached, thereafter decreasing to zero as the saturation effect indicated in Figure 2 was approached.

The most important result of the studies with the Nanosecond Regime Model was the demonstration that the delay interval duration, $X3$, had little effect on the amplitude resolution, i.e., ability to distinguish a relative change in the event rate for the star intensities of primary interest. This result supported the adequacy of the baseline design since the important performance parameters could not be significantly improved by any reasonable changes in frequency response characteristics in the star sensor electronics or in the output pulse counter.

Validation of the simulation involves consideration of debugging and verification of the computer program as well as the adequacy of the simulation model to represent the phenomena of interest. Debugging and verification of the computer program was expedited by the fact that the analyst was conversant with the simulation language so that the programming details were checked by both the analyst and the programmer. Further verification was provided by consistency of the results with simplified analyses for limiting cases. It was apparent that the simulation was a highly simplified model of the processes which occur in the star sensor and its electronics. It was anticipated that a more detailed model would be required to cover anode pulse amplitude variations and pulse shape variations. However, when the results demonstrated that pulse duration had little effect within the range of interest, it was obvious that the cost of developing an improved model was not commensurate with the very limited benefits.

The most important result from the perspective of the "end-to-end" simulation was the finding of a relatively simple relationship between event rate and expected output rate for the star intensity range of primary interest. This relationship could be used on a much slower time frame such as the Microsecond Regime Model.

MICROSECOND REGIME MODEL

The Nanosecond Regime Model is primarily concerned with the relationship between light intensity expressed in terms of the expected rate of electron emissions from the photocathode (events) and the statistical properties of the number of counts that would be output by the star sensor electronics per count cycle. The Microsecond Regime Model generates a stream of count values simulating the output from the star sensor. The expected event rate is the sum of the consequences of

1. Thermal or self-emission of electrons by the photocathode and first dynode
2. Interactions with cosmic rays and solar flare protons
3. Bremsstrahlung from trapped (Van Allen) electrons
4. Star signals used for attitude determination
5. Other star signals including unresolved star background
6. Sunlight scattered or reflected by attitude-control-jet effluent and space debris.

The actual number of pulses output by the electronics depends upon the expected event rate and the relationships derived

from the Nanosecond Regime Model. The operations within the Microsecond Regime Model can be partitioned into those involved in determining the expected event rate and those involved in determining the count value which will reach the ground station for processing. Longer-term considerations determine where in orbit the spacecraft is at each count cycle, and which portion of the celestial sphere is being scanned. The information is provided to the Microsecond Regime Model in terms of which stars are going to be sighted, the intensity of the signal received, and the time at which the star image impinges on each of the slits in the reticle.

Of the six sources of events, only the first one has stationary statistical properties. All that is required to represent the thermal emission of electrons by the photocathode is the specification of the expected emission rate. The high-energy-particle radiations are characterized in terms of two-level Poisson processes. The higher-level process is the arrival of high-energy particles, with a time between particles for the protons,

$$TNP = -SP \int_0^{\infty} e^{-x} x^{n-1} dx$$

where SP is the expected number of count cycles between particle arrivals and RU is a random number selected from a distribution uniform over the interval zero to one. Note that each time the symbol RU appears, a new sampling from the uniform distribution is selected by a pseudo-random-number generator. A similar expression applies for the time between high-energy electrons, TNE, based upon EP, the expected number of count cycles between electron arrivals.

Although the expected rates of arrival of high-energy particles do exhibit variations with time, the time constants for solar flares and trapped electrons are on the order of hours. The value of SP and EP could have been left unchanged throughout a simulation run. For increased generality, a gradual change in these expected times between particle arrivals was provided by the FORTRAN expression

$$SP = SP(1.0 + PO*MDT)$$

applied whenever a star sighting is processed, where MDT is the number of count cycles since the last star sighting and PO is the relative increase in the expected time between expected particle arrivals per count cycle. A similar expression applies for EP within the parameter EO in place of PO.

Each arriving particle activates a portion of the star sensor near the photocathode, causing a prompt emission of photons followed by a decaying rate of emission as the activated material returns to its normal state (see Reference 3). The expected contributions to the event rates, RP, and due to protons, due to electrons RE, are time varying. The model used is based upon an exponential decay, with a time constant set by an input parameter. It was assumed that, within each count cycle, the variation was small enough so that the average expected rate could be used without worrying about second-order effects due to variations in the expected rate from the average within the count cycle. The exponential decay is computationally convenient since all that is required is a multiplication of the expected event-rate contribution for one count cycle (e.g., RP) by a factor, DP, which is one minus the decay effect, to determine the expected contribution for the next count cycle if no new particles arrive. It was assumed that the initial responses (PN and PE, respectively) due to a newly arrived particle were the same for all particles of a given type. However, that was later changed to an initial contribution selected from an exponential distribution,

$$\Delta RP = -PN \ln RU$$

or

$$\Delta RE = -EN \ln RU$$

to allow for the energy variation of the particles when it was found that this variation had a significant effect. The effect of scattered sunlight is represented by an exponentially increasing background contribution until a plateau is reached, followed by an exponential decay.

FORTTRAN is the language used for the Microsecond Regime Model and all of the subsequent models. FORTRAN was selected since GPSS would have been inconvenient for the star signal representation. One complication arose when very low expected rates were simulated. Since the expected contribution is decreased by applying the factor for decay, when the expected particle arrival rate was much less than one per one hundred count cycles, the expected contribution could get smaller than the smallest positive number normally represented by floating point 10^{-78} , producing underflows and consequent diagnostic messages.

The star-sighting-time information was generated by a companion model. This model used a simulation of the dynamics of the spacecraft and the attitude control system to select the stars to be sighted, and when they will be sighted, from the

Smithsonian Astrophysical Observatory (SAO) catalog available on magnetic tape. This companion model is outside of the scope of the simulation described. It includes provision for representing alignment changes between the star sensor and the rest of the spacecraft, as well as the reticle slit geometry including deviations from nominal. In the processing of each star signal to be used for attitude determination, the Microsecond Regime Model determines the relationship between computed sighting time and computed count-cycle start times. The portion of the star signal expected to occur in each of the count cycles containing the star signal depends upon this relationship as well as the image quality of the optics. The possibility of overlapping star signals is handled by having the allocations and sighting times for the next two star sightings available.

Background contributions are made by stars which are too dim to be handled on an individual basis, plus intermediate brightness stars which do require individual representation. Initially, the intermediate stars were obtained by carrying the SAO catalog two visual magnitude values beyond that of the stars used for attitude determination. This extension of the star catalog consumed more computer time than desired, and the simplified representation of pseudo-random intermediate brightness stars was added, based on the assumption that the image spot size is zero. The interval between intermediate brightness stars, TND, was determined from an exponential distribution in the same manner as that used for particles.

The contributions of dim and intermediate brightness stars were varied, with a portion of the celestial sphere being scanned to allow for the nonuniform distribution of stars. For the dim stars, the expected contribution was varied; for the intermediate brightness stars, the expected interval between stars was varied.

The expected event rate in any count cycle was the sum of the expected values for each of the sources. Except when the count cycle contained the signal from a bright star, the expected output count was determined by applying the nonlinearity relationship derived from the Nanosecond Regime Model. With bright stars, the rate of variation in intensity within a count cycle could be significant and the correction for nonlinearity was adjusted for the rapid variation. A random variation sampled from a normal distribution, with standard deviation equal to the square root of the expected value, was added to represent the stochastic variation effect from the Nanosecond Regime Model. If the expected value was more than 225, the standard deviation used was 15. This deviation was used to approximate the complicated behavior of the standard deviation when the events

frequently interfered with each other in the star-sensor electronics.

Telemetry transmission errors cause the data value received to be uncorrelated with the value sent. The occurrence of these errors was represented by a Poisson process, with time between errors equal to $-TE \ln R$ RU, where TE is the expected number of count cycle between error. The value in error is equal to $4095 * RU$ to represent a randomly selected 12-bit value.

MILLISECOND REGIME MODEL

The Millisecond Regime Model differed from the Microsecond Regime Model only in the omission of the background which was not in the neighborhood of a star used for attitude determination. The output desired from the model was the stream of data that the preprocessor would select as star candidates, based upon exceeding the threshold applied. Thus, false outputs were added to represent threshold exceedances due to background sources.

The representation of star signals and telemetry errors was the same as the Microsecond Regime Model. The representation of the effect of particle radiation was also the same after the first count cycle contributions from electron and proton radiation. The primary difference between the Millisecond Regime Model and the Microsecond Regime Model is the absence of the previous history, since the count cycles between star signals were not simulated. This omission is computationally important because less than 1 percent of the count cycles have contributions from star signals used for attitude determination.

Results for background radiation obtained from simulations made using the Microsecond Regime Model were analyzed to determine the distribution of peak expected contributions. This peak represents the last particle arrival prior to the star signal. The model then applies a decay for the elapsed time selected from an exponential distribution between the peak value determined and the first count cycle containing the star signal.

The possibility that the star signal would not exceed the threshold applied by the preprocessor was represented by applying a threshold equal to the expected background value, plus a random variation representative of the measured average background determined by the preprocessor, plus an increment applied within the preprocessor.

LONGER-TERM MODELS

The above models were the primary sources of data used for testing the Preprocessor and for testing the software developed to process the data telemetered from the spacecraft. Other studies (including the effort developing the Kalman filter implementation) for determining attitude used only small portions of the data processing software. Therefore, these studies had to be provided with inputs equivalent to those which the attitude determination portion of the computer program under development would use.

The Millisecond Regime Model provides sets of count values representing the signals from star sightings and noise, whereas the Kalman filter used for attitude determination actually receives sighting times of identified stars. The editing of the data to reject background noise exceeding the threshold applied, and to identify the star signal, is performed by logic preceding the filter. The filter handled only sighting times for identified stars. A Second Regime Model was developed based upon results from Microsecond Regime Model and Millisecond Regime Model simulations. Logic was added to calculate the sighting time that the program would determine from the count values provided. Mean and standard deviations were determined over a range of background conditions and star intensities.

For studies of boresight techniques used to evaluate the alignment between the primary sensor and the satellite reference frame defined by the attitude determination process, the more important time constants are on the order of hours. Thus, it is uneconomical to base the simulations on individual star sightings. Instead, the statistical characteristics of deviations from the "known" attitude that was simulated were determined from analyses of the results of the Second Regime Model studies. These statistical variations were the basis for the boresight studies.

REFERENCES

1. Charles Susskind, The Encyclopedia of Electronics, New York: Reinhold Publishing Corporation, 1962.
2. General Purpose Simulation System/360, IBM Applications Program H20-0326-0 Introductory User's Manual, IBM Technical Publications Department, White Plains, New York, 1967.
3. Dressler, K. and Spitzer, L., Jr., "Photomultiplier Tube Pulses Induced by Gamma Rays," Review of Scientific Instruments, Vol. 38 (1967), pp. 436-438.

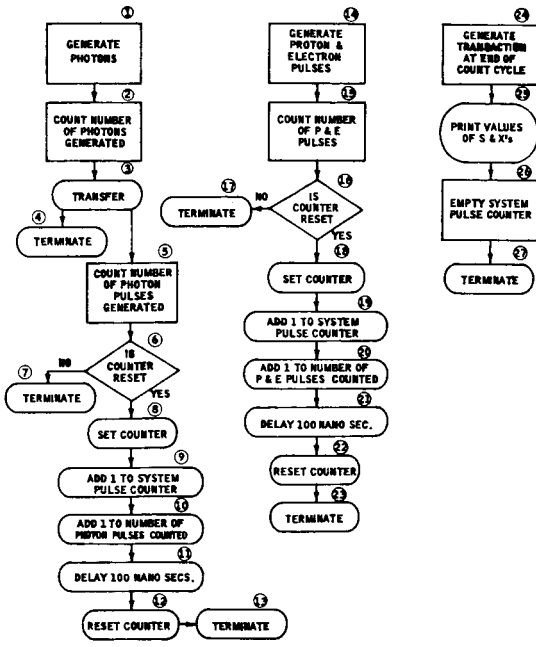


Fig. 1—Nanosecond Regime Model logic

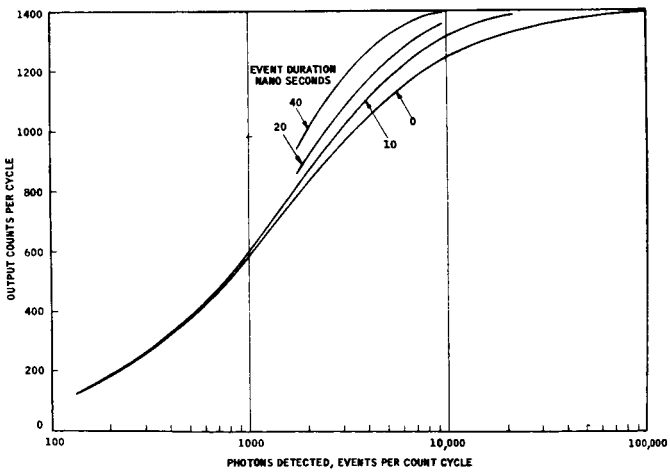


Fig. 2—Effect of event duration

N74-10251

PRECEDING PAGE BLANK NOT FILMED

Page No. 20

CONTAMINATION CONTROL IN SPACE SIMULATION CHAMBERS

B. C. Moore, R. G. Camarillo, L. C. Kvinge, *McDonnell Douglas
Astronautics Company, Huntington Beach, California*

ABSTRACT

Protection of sensitive vehicle surfaces during space simulation tests requires that the chamber be clean. Various methods of cleaning are considered. Cleaning is a progressive process; the methods must be altered as cleanliness improves. If an inappropriate method is used, varnish residues may form. Experience with vacuum outgassing a 39 ft. diameter space chamber is reviewed. It is shown that acceptably low contamination rates may be achieved with the present state-of-the art. Possible future developments are discussed, including the use of fluorocarbon pump oil, and cleaning with atomic oxygen.

INTRODUCTION

The customers of a space simulation laboratory are frequently concerned that their space vehicles may be damaged by contamination during test (References 1 and 2). For example, the reflectivity of optical components, and the absorptance/emittance characteristics of thermal coatings can be significantly changed by material deposited during tests.

Warm material under vacuum can be transferred to the vehicle in a direct line of sight. During normal operation the cold shroud condenses and holds any material, thus preventing contamination; however, some small warm surfaces may be present: e.g., infrared arrays, ionization gage filaments, or observation windows. Also, during the chamber-pumpdown shroud-cooling operation, and during the inverse warmup and backfill operation, it is possible to transfer contaminants. It should be noted that significant transfer from one part of the space vehicle to another may also take place (References 3 and 4).

Another way for material to be deposited in the space vehicle is through abnormal operations or accidents in the roughing or diffusion pumps. These can cause massive backstreaming, even though no measurable backstreaming is usually observed during normal operation (Reference 5). Although the risk of these accidents is very low, the potential damage must be considered.

The operator of a space simulation facility is, of course, responsive to the needs of his customers. He must not only operate the facility to minimize any contamination, but also must present convincing evidence that contamination flux levels are acceptable. In addition, parts of the facility such as solar optics may be damaged by films of contaminant. Thus, the customer and the operator have a strong mutual interest in reducing contaminant flux.

Space chamber operations differ significantly from those of conventional vacuum chambers. Installation of a space vehicle is a complex mechanical operation. It creates a certain background of contamination, no matter how clean the chamber. The amount and constituents of this installation contamination is an interesting subject for further study. Another difference from conventional vacuum chamber operations lies in the relative unimportance of total vacuum level and of the common outgassing constituents - H_2O , N_2 , etc. On the other hand, there is always great concern about specific contaminants, such as pump oils, or materials from previous spacecraft.

Many approaches are used to safeguard the space vehicle. Critical areas are shielded with remotely actuated covers. A purge of clean gas may protect the vehicle; timing of purge shutoff and shroud cooldown is optimized to avoid any unprotected interval. However, to supplement these methods of protection, it is important that the chamber be clean, that the flux of contaminating molecules be acceptably low, and that the risk of contamination be acceptable even if worst-case mishaps occur.

This paper discusses the steps that may be taken by the facility operator to minimize contamination flux levels and the risks of contamination. It is desirable for the plan to be flexible enough to provide either adequate cleanliness at minimum cost, or to reach extreme cleanliness with extra operations.

The generalized approaches to cleaning a space chamber are listed in Table 1. These are arbitrarily divided into basic methods, which are those immediately available to most facilities and improved methods, which usually cannot be implemented without some special effort.

Table 1
CLEANING METHODS

BASIC METHODS - immediately available at most facilities

Washing - Sweep, Brush, Vacuum

- Water, Steam, Detergent
- Solvents

Vacuum Outgassing - Vacuum Soak

- Transient Flow Outgassing
- Transient Flow Outgassing with gas purge
- Molecular Flow Outgassing
- Elevated Temperature, with any of above

IMPROVED METHODS - usually require special effort to implement

Energized Surface - Shock, Vibration, Gas Jets

- Heating - RF Pulses
- Laser

Energized Molecules - Electron Bombardment

- Ion Bombardment
- UV Radiation - Solar Beam
- Chemical Reaction - Atomic Oxygen

Preventive Methods - Perfluoroalkyl Polyether Fluid -
Diffusion and Mechanical Pumps

- Porous Metal Screens over Pumps
- Material and Operation Selection

BASIC METHODS OF REMOVING CONTAMINANTS - WASHING AND VACUUM OUTGASSING

WASHING

Washing is necessary if large quantities of contaminant are present. Vacuum outgassing a dirty chamber has been found to leave on the wall a powdery residue, which rubs off and stains clothes; this residue could be expected to be carried to a space vehicle during installation operations. Contaminants can also be converted into varnish-like polymer films by ultraviolet (solar) radiation or electron bombardment (Reference 6), or even by hot surfaces as low in temperature as 300°C. (Reference 7). Cleanup is a progressive process that must start with a relatively clean chamber.

Relative merits of washing methods will not be discussed here. However, there is an interesting question as to the amount of contaminant that can be tolerated without washing before proceeding with vacuum outgassing. Just how dirty can the chamber be before washing is required? It would appear that quantitative guidelines could be established; however, the authors are not aware of any work on this point.

VACUUM OUTGASSING

In these methods, the contaminants are allowed to evaporate from the chamber surfaces into some level of vacuum. The vacuum serves to reduce the recondensation rate of contaminants so that the effective evaporation rate increases as compared to atmospheric pressure (Reference 8). The operation may be at room temperature, or accelerated by heating.

One problem to be considered is the risk of spreading localized contaminants throughout the chamber, especially into small passages behind shrouds and shields. This problem is more serious with low-vapor-pressure materials such as diffusion pump oils. This is another reason for carefully washing the chamber before outgassing. Although no general solutions to the problem are offered here, a number of specific small passages have been analyzed. In all these cases, it was determined that outgassing would reduce contaminant levels.

Variations of vacuum outgassing include vacuum soak, outgassing at transition flow conditions (with and without gas purge), and outgassing at molecular flow conditions.

Vacuum Soak

The simplest outgassing method is a vacuum soak. The chamber is roughed down, sealed, and left with pumps off. The advantages of this method are primarily economic: labor, equipment operation costs, and material use are all zero during the soak. The soak can be over a weekend, or for longer periods: the MDAC 39-ft-diameter chamber (S-1) was once soaked for

nine months, with excellent results, judging by the speed of subsequent pumpdowns.

Soaking does not produce the most rapid cleanup, however, it is surprisingly effective. In S-1 a nominal monolayer (10^{14} molecules/cm²) over all internal surfaces, when desorbed into the internal volume would raise the pressure by 4.6×10^{-7} torr. Many contaminants have vapor pressures substantially greater than this figure, so that they move towards an equilibrium where most of the material is in the gas phase. Even low-vapor-pressure materials, such as diffusion pump oils (typically 10^{-9} to 10^{-10} torr) tend to diffuse out into the residual gas atmosphere (typically 1 to 100 microns, although a GN₂ backfill in the mm range may also be used). The cleanup progress can be checked periodically by bleeding a sample through an external mass spectrometer through a heated pipe. If appropriate, the residual gas may be pumped off occasionally.

Outgassing at Transition Flow

In this method, the roughing pumps are used to continually remove residual gas, thus reducing reabsorption of outgassed molecules, and speeding the cleanup. The penalty is some increased cost, for although these pumps may usually be left operating unattended, there is a cost involved in power and maintenance. An additional consideration is the possibility of backstreaming. This problem may be handled by careful trapping in the roughing line, or by a gas purge.

The gas purge might also be considered as a method of outgassing in itself. As discussed above, evaporants from low-vapor-pressure materials may be contained in a gas atmosphere, thus accelerating the net removal process as long as the mean free path remains large. One possible way to ensure gas flow sweeping behind shrouds and shields is to periodically vary the purge pressure over wide (10:1) limits. This would avoid high concentrations of contaminants in the small passage atmosphere. A problem to monitor with these methods is that the gas purge itself may introduce contaminants which limit the ultimate cleanliness.

A still faster variation of roughing pump outgassing is the addition of cryogenic panels within the chamber. These condense and concentrate contaminants for later removal by washing.

These transition flow methods are low in cost and effective in cleanup. For the very low-vapor-pressure contaminants, they appear to offer the most rapid cleanup, reducing the number of desorptions before pumping. The ultimate cleanliness may not be of quite as high a level as achieved with molecular flow outgassing. (The gas purge not only may introduce contaminants, but also interferes with their measurement.) Considering the contaminants introduced during installation of the test vehicle however, the net result may be the same.

Molecular Flow Outgassing

This method is similar to transition flow outgassing in continually removing contaminants. However, it uses a lower vacuum level and a different flow regime with different pumping speeds. Qualitatively, an outgassed molecule no longer diffuses out into surrounding gas, where there is a relatively high probability of being swept away. Instead, it travels directly to some other surface, where it recondenses.

In considering molecular flow, the concept of pumping fraction is useful. How many times must a molecule be desorbed before it is pumped? What is the probability of being pumped for an average desorption? For the typical space chamber this probability is very small, usually much less than 0.01. This means that the molecular flux within the chamber is essentially uniform over all surfaces - the reduction in flux near the pumps is negligible. This uniformity allows the pumping fractions to be calculated directly from the geometry: the effective area of the pump divided by total surface area.

Another useful concept is the Uniform Flux Theorem (Reference 9). Despite temperature differences of surfaces within the chamber, the molecular flux remains uniform. This means that heating only part of the surface (for example the shroud) simply concentrates material on the cool surfaces (in this example the chamber wall).

IMPROVED METHODS - ENERGIZING SURFACE, ENERGIZING MOLECULE, AND PREVENTIVE

Improved methods of cleanup are arbitrarily defined as those which require additional cost to implement. These methods are conceptually divided into three groups: methods which energize the surfaces, those which energize the contaminant molecules directly, and preventive methods.

Surfaces may be energized by shock and vibration; or by heating, as with pulsed radio frequency energy or lasers. Molecules may be directly energized by electron or ion bombardment, or ultraviolet radiation, or by chemical action, as with atomic oxygen. Preventive methods limit the amount and type of contaminant through selection of pump fluids, materials, and operations within the chamber.

Many of these accelerated methods are potentially harmful to painted or optical surfaces. However, some of them appear to be useful for specific limited applications.

SURFACE ENERGIZING METHODS - Shock, Vibration, and Gas Jets

It is commonly observed that mechanical shocks or vibration applied to a chamber will produce bursts of gas. However, tests showed only 20 percent particle removal by a 1,000-g, 1-msec shock of a particular surface under vacuum. (Reference 10.)

Gas jets, particularly after extended vacuum soak, were capable of removing up to 50 percent of the particles. These processes appear to be difficult to implement on a large scale. They do have some potential as a supplement to other methods. For example, a gas purge after extended vacuum soak might remove particles.

Heating

Short (microsecond) pulses of radio frequency energy have been used to heat thin (1 micron) layers at a surface to extreme temperatures (1,000°C) without heating the bulk material. (Reference 11.) Pulsed lasers have also been used to clean and erode surfaces by heating thin layers. (References 12 and 13.) Application of these methods to large areas presents difficulties in uniform heating. The maximum usable temperature is also limited by paint characteristics, reducing the potential effectiveness of these methods.

MOLECULE ENERGIZING METHODS - Electron Bombardment

Surfaces flooded by electrons release gas. This technique is widely used in the fabrication of vacuum tubes and in outgassing ionization gages. Equipment for this method is especially simple. Tungsten filaments are installed within the chamber. They are heated by adjustable currents and biased by adjustable voltages. The initial cleanup uses low voltages and currents to avoid arcing in the outgassed vapor. As the cleanup progresses, maximum available power is gradually applied. (Reference 14.) The electrons released from the filaments are drawn to the wall. On impact, they release secondary electrons, which tend to provide uniform flooding of all surfaces.

Two problems exist with application of this method to space chambers. Many contaminants will leave polymer films when electron bombarded; these could dull mirrors, or increase LN_2 consumption of shroud. Mayer has shown these films will form with electron energies as low as 6 volts. (Reference 15.) Painted surfaces may be damaged by electrons and, as insulators, may be difficult to bombard uniformly. However, there is at least the possibility that bombardment with low-energy electrons might be effective in removing contamination without damaging painted surfaces.

A very promising application is cleanup behind shrouds where there is usually no paint. This could be especially beneficial because contaminants tend to concentrate on the cool surfaces, as previously discussed.

Ion Bombardment

Surfaces bombarded by ions are eroded. This technique is widely used for cleaning substrates and for sputtering getter

material in ion pumps. Its use is recommended only for rugged, unpainted surfaces, because it is so destructive. Possible applications are for areas such as diffusion pump elbows and roughing line entrances.

Application is straightforward and only slightly more complex than electron bombardment. A simple approach is to use a combined static magnetic and electric field, as in ion pumps and magnetron gages. Radio frequency plasma is also common. Many geometries are available to fit specific situations. However, coverage is usually far from uniform, and contaminating deposits are often formed.

Ultraviolet Radiation

Ultraviolet radiation may directly energize a molecule; which may then either outgass, leaving the surface, or polymerize into a film. This method is attractive if a large solar beam is readily available. Rotating mirrors could illuminate most of the inner chamber surfaces. This method does degrade paints, but much more gradually than ion bombardment. A major problem is defining the level of contamination where formation of polymer films would be acceptable.

Chemical Action

Atomic oxygen rapidly combines with many materials. It is widely used in "dry ash" machines. It has been successfully used to remove polymer residues from mirrors (Reference 16.) Atomic oxygen from an RF plasma restored optical surfaces to their original properties by a rapid non-destructive oxidation of the polymer film. The test mirrors were cleaned within a 10-min time span, at a vacuum of 0.5 torr. Atomic oxygen also has been found to tend to restore white thermal coatings damaged by proton and ultraviolet radiation (Reference 17).

Application of this method to large space chambers presents interesting development problems. A low-temperature oxygen plasma may be generated by radio frequency, or by electron beam excitation. This plasma could be directed to flow over chamber surfaces, especially over solar optics. Other chemical reactions, such as with hydrogen, might also be used. Hazards in the use of these activated chemicals should be carefully considered.

PREVENTIVE METHODS

Pump Fluid

A new fluid for diffusion pumps and mechanical pumps (References 18, 19, and 20) offers the possibility of acceptable backstreaming incidents. The perfluoroalkyl polyether molecules do not adhere to surfaces and are easily removed. In addition,

they break up into completely volatile products when bombarded, leaving no residue.

This fluid requires more evaluation, but offers a potential solution to the serious problem of accidental backstreaming.

Porous Metal Screens

Porous metal screens have been suggested as a means of avoiding backstreaming during accidental repressurization. Milleron (Reference 21) used a 1/16 inch thick stainless steel screen with 150 micron passages to isolate a diffusion pump. He found that the white vapor cloud formed by rapid repressurization was visually eliminated. However, quantitative measurements of backstreaming were not made. Screens could be used over both rough and diffusion pumps.

Material and Operation Selection

Lubricants for moving parts and for O-ring vacuum seals might be perfluoroalkyl polyether, similar to the pump fluid above. Electrical wiring might be insulated with ceramic; aluminum wire with aluminized oxide insulation is available. Test buildup operations can be arranged to minimize the work to be done in the chamber, and the time required for installation.

EVALUATION OF BASIC METHODS

What is the amount of contaminant a space vehicle will receive during a test, if the basic methods of cleanup are used to prepare the chamber? There is, of course, no simple general answer to this question. Yet, if we answer it as best we can, it will be helpful in considering the development of accelerated methods. Recent experience with the cleanup of S-1 leads to a tentative answer.

S-1 is a 39-ft. diameter spherical chamber at the MDAC Huntington Beach Facility. It is roughed by mechanical pumps and blowers through the diffusion pumps. LN₂ cooled elbows (but no valves) separate the diffusion pumps from the chamber. On completion of a test series last fall (1972), the chamber was dirty, oily to the touch. It had been 3-1/2 years since the last major cleanup. During that time, 25 tests were conducted in 75 pumpdowns and 152 days under vacuum.

The cleanup procedure was a series of molecular flow outgassings. Prior to the first pumpdown, the chamber floor only was swept and wiped. The outgassing was done on weekends and holidays, while buildup for the next test continued during working days. Approximately 700 hours under vacuum were accumulated in seven pumpdowns. These included four consecutive weekends and one 10-day Christmas holiday. The last pumpdown followed a month of buildup, and installation of considerable

equipment, including a 190-ft² earth simulator, freshly painted with 3M Black Velvet 101C10. Various combinations of shroud and building temperatures were used. (Figure 1.)

A number of interesting results emerged from this work. First, a residue of dry powder was left on the chamber surfaces. Despite the low outgassing, it later was necessary to wash this off.

The total pressures showed a substantial and cumulative improvement. (Figure 1.) The last pumpdown was especially surprising; even after a month of buildup and the large new outgassing surfaces, the improvement continued.

Most specific mass spectrometer (ms) peaks showed a rapid cleanup. One of the slowest was an unidentified material at AMU 350 (Figure 2). Note the dramatic response of this material to shroud heating. It finally disappeared below the threshold for good (10^{-13} torr for this particular instrument). Extrapolating the pressure decay transient, the present level must be much less than 1 monolayer/year.

(All mass spectrometer measurements presented are estimates based on nitrogen equivalent pressure. The ms viewed the center of S-1. The nature of the measurement is illustrated in Figure 3.)

Diffusion pump oil, DC-704 (AMU 199) cleaned up more rapidly than expected but showed some tendency to return on succeeding pumpdowns. It also is now below threshold. (Figure 4.)

Roughing pump oil, AMU 55 and 57, cleaned up very rapidly but was the only material that continued to return. (Figure 5.) A gas purge for use during diffusion pump shutdown and LN₂ baffle warmup is being installed. It is expected that this oil will also disappear below the threshold.

What do these results mean in terms of the original question, i.e., how much contaminant will a space vehicle receive? Pumpdown to 1 torr takes two hours in S-1; by this time, the shrouds may be cooled, ending contamination. During these two hours some part of the contaminant outgassing could reach the vehicle through turbulent flow. Conservatively, assume this fraction to be 1/10. If a specific contaminant is known to be outgassing at less than 1 monolayer/year, then during pumpdown less than 2.3×10^{-5} monolayers would be deposited on the vehicle. A similar amount might deposit during backfill. The total amount would be less than 10^{-4} monolayers for the particular contaminant.

This present limit is primarily one of measurement. If improved measurements could lead to assurance that the contamination rates were less than 1 monolayer/century, then the result would be less than 10^{-6} monolayer. This appears to be an achievable goal.

The major contamination thus is expected to be that resulting from the installation of the particular vehicle.

SUMMARY

It has been experimentally demonstrated that the flux rates of various specific contaminants in a large (39 ft. diameter) space simulation chamber can be reduced to levels of less than 1 monolayer/year, with the cryogenic shrouds at room temperature. This corresponds to a vehicle contamination of less than 10^{-4} monolayers during the pumpdown-cooldown and warmup-backfill operations of a typical space simulation test. The cleaning procedures used were confined to washing and vacuum outgassing.

Figure 1
**TOTAL PRESSURE
TRANSIENTS**

S-1 CHAMBER - 39-FT DIA
SHROUD TEMPERATURE:
HEAT ON = 90°F
HEAT OFF = 45 TO 70°F
DATES INDICATE START
OF PUMPDOWN

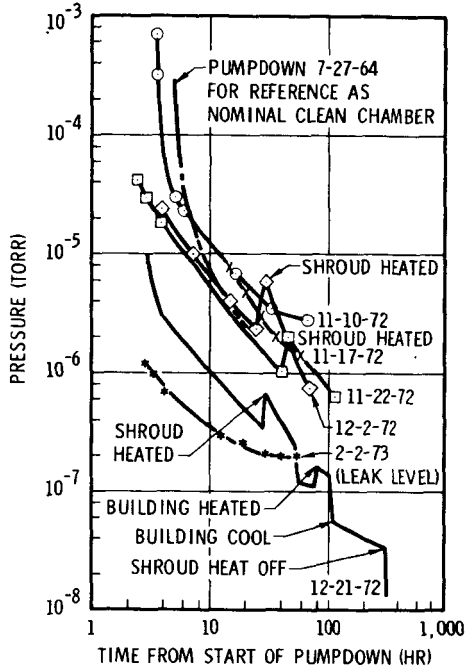
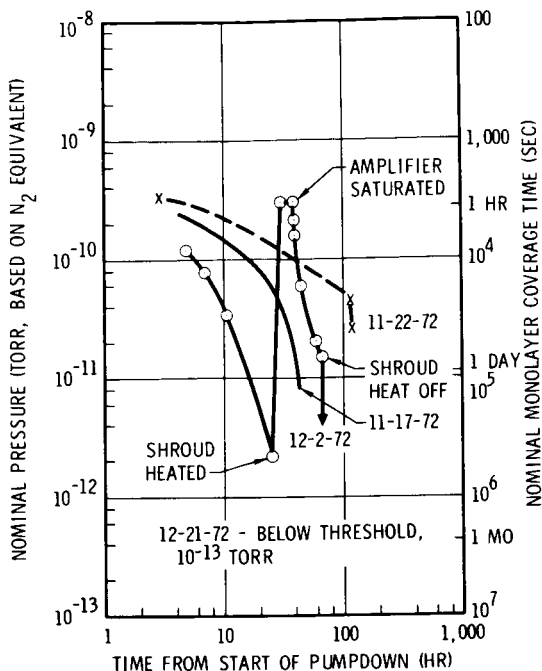


Figure 2
PARTIAL PRESSURE
TRANSIENT -
AMU 350 -
UNIDENTIFIED

S-1 CHAMBER - 39-FT DIA
 SHROUD TEMPERATURE:
 HEAT ON = 90°F
 HEAT OFF = 45 TO 70°F
 DATES INDICATE START
 OF PUMPDOWN



PUMPDOWN 2-3-73

T = 40 HR

20 AMP/TORR N_2 EQUIVALENT

TWO SCANS AT DIFFERENT GAINS SUPERIMPOSED

AMU 55 AND 57 ROUGHING PUMP OIL

OTHER PEAKS FROM FRESH PAINT AND/OR HEATER TAPE OUTGASSING

Figure 3
MASS SPECTROMETER SCAN

S-1 CHAMBER

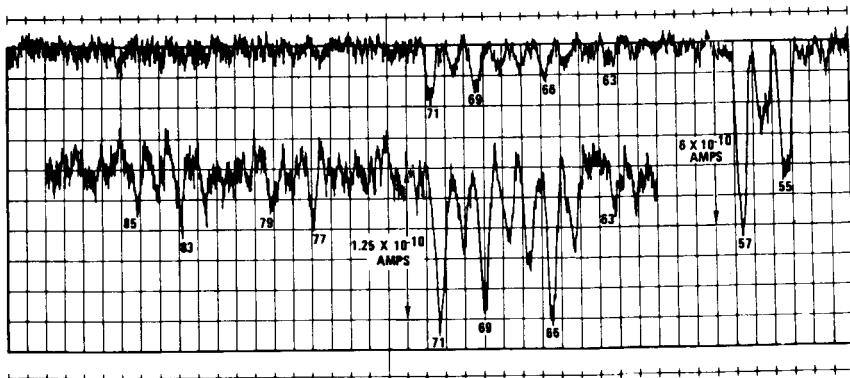


Figure 4

**PARTIAL PRESSURE
TRANSIENT -
AMU 199 - DC 704**

S-1 CHAMBER 39-FT DIA
SHROUD TEMPERATURE:
HEAT ON = 90°F
HEAT OFF = 45 TO 70°F
DATES INDICATE START
OF PUMPDOWN

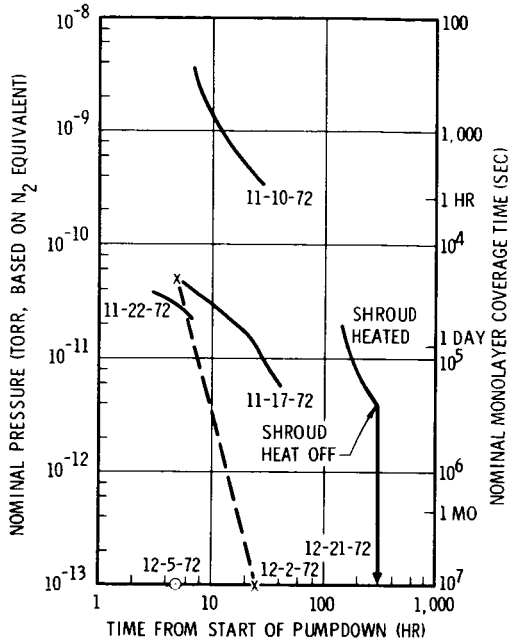
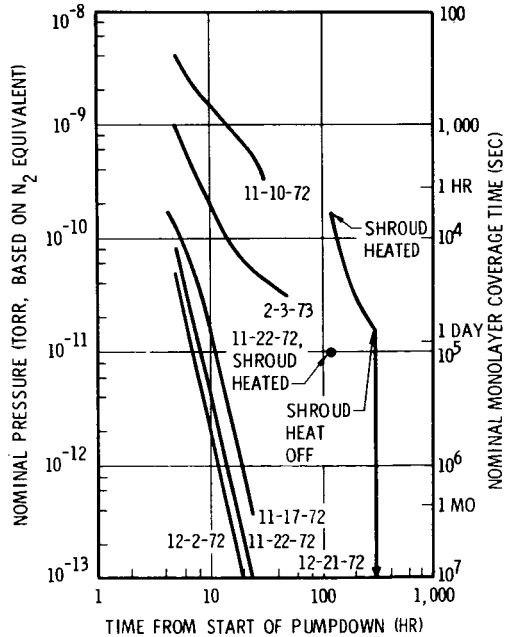


Figure 5

**PARTIAL PRESSURE
TRANSIENT - AMU 57 -
ROUGHING PUMP OIL**

S-1 CHAMBER - 39-FT DIA
SHROUD TEMPERATURE
HEAT ON = 90°F
HEAT OFF = 45 TO 70°F
DATES INDICATE START
OF PUMPDOWN



REFERENCES

1. James T. Visentine, John W. Ogden, Melvin L. Ritter, Charles F. Smith, "Preparation, Verification, and Operational Control of Large Space-Environment-Simulation Chamber for Contamination Sensitive Tests." Proceedings of the Sixth Space Simulation Conference, p. 361 NASA SP-298, 1972.
2. Philip W. Tashbar, Daniel B. Nisen, W. Walding Moore, Jr., "V-3 Contamination Test in the Manned Spacecraft Center's Vacuum Chamber-A." Proceedings of the Sixth Space Simulation Conference, p. 389 NASA SP-298, 1972.
3. Dr. John J. Scialdone, "Predicting Spacecraft Self-Contamination in Space and in Test Chamber." Proceedings of the 6th Space Simulation Conference, p. 349 NASA SP-298, 1972.
4. T. Baurer, M. H. Bortner, I. M. Pikus, A. M. Cooper, "External Spacecraft Contamination Modeling and Countermeasures." Proceedings of the Fifth Space Simulation Conference, p. 79 NBS SP-337, 1970.
5. J. C. Goldsmith, E. R. Nelson, "Molecular Contamination in Environmental Testing at Goddard Space Flight Center." Proceedings of the Fifth Space Simulation Conference, p. 1 NBS SP-336, 1970.
6. L. Holland, "Review of Some Recent Vacuum Studies." Vacuum, v. 20, p. 175, 1970.
7. C. Burch, "Some Experiments on Vacuum Distillation," Royal Society London Proc. Series A, V. 123, p. 271-287, 1929.
8. J. H. de Boer, "The Dynamical Character of Adsorption." Clarendon Press, Oxford, 1953.
9. B. C. Moore, "Measurement of Vacuum in Non-uniform Temperature Environments," Journal of Vacuum Science & Technology, 1, p. 10-16, 1964.
10. D. L. Enlow, "Contamination Studies in a Space Simulated Environment." Proceedings of the Fifth Space Simulation Conference, p. 51 NBS SP-336, 1970.
11. K. I. Lobacher, V. A. Shiskin, USSR Patent No. 263, 752, appl. 17 Jan 1968, Abstract Vacuum, 21, 287, 1971.
12. S. M. Bedair, H. P. Smith, Jr., "Atomically Clean Surfaces by Pulsed Laser Bombardment," J. Appl. Phys., 40, 4776-81, 1969.

13. L. P. Levine, J. F. Ready and E. Bernal G, "Laser Bombardment Effects on Vacuum Surfaces," Research/Development Dec. 1965, p. 56-59.
14. R. E. Clausing, "Release of Gases from Surfaces by Energetic Electrons," (paper presented at the Eleventh National Vacuum Symposium, Chicago, Illinois, Sept. 30-Oct. 2, 1964).
15. L. Mayer, "Photocontrol of Growth Rate of Thin Polymer Films Formed by Electron Bombardment," J. Applied Physics, 34, 2088-2093.
16. R. E. Gillette, J. R. Hoilahan, G. L. Carlson, "Restoration of Optical Properties of Surfaces by Radio Frequency-Excited Oxygen," J. Vac. Sci. & Tech., 7, 534-537, 1970.
17. R. E. Gillette and W. D. Beverly, "Restoration of Degraded Spacecraft Surfaces Using Reactive Gas Plasmas," AIAA Paper No. 71-463, AIAA 6th Thermal Physics Conference, Tullahoma, Tenn., April 26-28, 1971.
18. M. A. Baker, L. Holland, L. Laurenson, "The Use of Perfluoroalkyl Polyether Fluids in Vacuum Pumps," Vacuum, v. 21, p. 479-81, 1971 (Oct).
19. L. Holland, "The Use of Perfluoroalkyl Polyether Lubricants in Mechanically Driven Vacuum Pumps," Vacuum, v. 22, p. 234 1972 (June).
20. L. Holland, L. Laurenson, P. W. Baker, "The Use of Perfluoropolyether Fluids in Vapour Stream Pumps," Vacuum, 22, p. 315-319, August 1972.
21. N. Millerson, "Porous Metal Isolation Traps and Cryosorbents in Vacuum Technique," 1965 Transactions of the Third International Vacuum Congress, v. 2, p. 189-192. H. Adams editor, Pergamon Press, NY, 1967.

N74-10752

PRECEDING PAGE BLANK NOT FILMED

Paper No. 21

**SPACE SIMULATION ULTIMATE PRESSURE LOWERED
TWO DECADES BY REMOVAL OF DIFFUSION PUMP
OIL CONTAMINANTS DURING OPERATION**

Alvin E. Buggele, *Lewis Research Center, Cleveland, Ohio*

ABSTRACT

The complex problem why large space simulation chambers do not realize the true ultimate vacuum was investigated. Some contaminating factors affecting diffusion pump performance have been identified and some advances in vacuum/distillation/fractionation technology have been achieved which resulted in a two decade or more lower ultimate pressure. Data are presented to show the overall or individual contaminating effect of commonly used phthalate ester plasticizers of 390 to 530 molecular weight (M.W.) on diffusion pump performance. Methods for removing contaminants from diffusion pump silicone oil during operation and reclaiming contaminated oil by high vacuum molecular distillation are described.

SUMMARY

Identification of contamination problems associated with space simulation test programs, their overall or individual effect on diffusion pump performance and its rapid deterioration on silicone diffusion pump fluids were studied. Diffusion pump performance as measured in terms of ultimate vacuum, shall be compared between identically contaminated oils in diffusion pumps with or without self-purification capabilities.

A series of experimental scale model glass diffusion pump vacuum systems evolved which investigated certain physical properties associated with evaporative surface behavior phenomena versus ultimate realizable vacuum. This research indicates that contaminants divide into light-end and heavy-end constituents inside the diffusion pump. Boiler fluid separation-purification design innovations successfully remove the heavy-end fractions from the evaporative surface by skimming-bleed methods and light-end fractions by vacuum distilling/bleeding action at temperatures of approximately 130° C in the foreline. These diffusion pump innovations, which are discussed and illustrated, resulted in a two decade or more lower ultimate pressure.

Documentation reveals the progressive improvement in molecular

release rate corresponding with the increase in diffusion pump performance and resultant lower ultimate pressure. This documentation consists of infrared thermovision polaroid pictures, slow and high speed movies, and 35mm slide photographs of the diffusion pump boiler evaporative surface and jet assembly molecular flow patterns.

Other significant results revealed were:

a. Contamination in the pump fluid limit the efficiency of diffusion pumps by 100 to 1000 times as indicated in terms of ultimate vacuum obtained.

b. Contaminants, commonly found in large vacuum chambers, that adversely affect silicone oil diffusion pump performance were identified as phthalate ester plasticizers. These plasticizers are utilized in cable insulation jackets, alkyd paints, electronic components, etc.

c. Contaminated (silicone) diffusion pump fluid can be successfully reprocessed by a triple cut (two light-end and one heavy-end) high vacuum centrifugal molecular distillation method. Reclaiming process nets an approximate 75±5% yield of oil capable of achieving an ultimate vacuum close to that of new DC-705 oil.

d. The effect of specific or mixtures of various phthalate plasticizer contaminants on performance of diffusion pumps were measured. Of all the plasticizers studied di-isooctyl phthalate (DIO P) (390 molecular weight, M.W.) had the most deteriorating effect on DC-705. Di-isodecyl phthalate (DIDP) (446 M.W.) di-octyl phthalate/di-2-ethylhexyl phthalate (DOP/DEHP) (390 M.W.), and di-tridecyl phthalate (DTDP) (530 M.W.) all achieved nearly the same ultimate vacuum. Higher molecular weight contaminants (such as 530 M.W. for DTPP) in DC-705 does not guarantee a lower ultimate pressure.

INTRODUCTION

Large space simulation chambers are not presently capable of realizing their true ultimate vacuum because of contamination limiting the efficiency of their diffusion pumps. Present diffusion pumps are not totally suitable for self-purification; that is capable of removing or preventing contamination of the pump fluid. Since a rapid degradation in pump performance occurs when exposed to sources of outgassing contaminants associated with space simulation test programs, a study of the fundamental performance limiting causes was initiated with the following objectives:

a. Identify contaminants commonly found in large vacuum chamber that adversely affect silicone oil diffusion pump performance.

b. Measure the effect of various contaminants on performance of diffusion pumps.

c. Develop means of removing contaminants from oil by vacuum distillation during diffusion pump operation.

BACKGROUND THEORY AND DEVELOPMENT

Overall Problem Background--While performing initial Brayton Power System testing in the 800 000 cu ft (22.7×10^6 liter) SPF test chamber, accumulations of condensable volatiles were observed on the 100 ft (30.5 m) diameter floor in 1969. NASA, Kennedy Space Center (KSC) Analytical Laboratory analyzed these condensables by a combination of column and gas chromatography, infrared, emission and mass spectroscopy. Samples were found to consist primarily of phthalate esters, an aromatic amine plus smaller amounts of a hydrocarbon oil and silicone oil.

During 1970 and 1971 while conducting Skylab Payload Shroud Jettison tests at a simulated altitude of 300 000 ft (3.3×10^{-4} Torr) the DC-705 diffusion pump oil became contaminated due to the large outgassing load, see Figure 1. A complete oil change costing \$30 000 was implemented. The magnitude of the diffusion pump oil contamination problem was revealed by the 1.5 decade loss in performance of new DC-705 after twenty-five operational hours of Skylab Shroud testing.

In order to thoroughly understand the outgassing contamination problem, associated with large space simulation test programs, a materials inventory search was undertaken to establish which compounds of those presently being used were the most volatile. Thirty-nine major materials were used in quantities ranging from 1580 kg (3500 lb) to 4.54 kg (10 lb) in conjunction with the Brayton and Skylab test programs. Those materials that are formulated with plasticizers, found in the analyses of eight DC-705 oil samples, shall be listed and described.

Background Information Relative to Contamination of Vapor Pumps--Diffusion pumps commonly called inverted condensation pumps or vapor pumps are dynamic equilibrium systems. These pumps are dependent on the respective vapor pressure-molecular weight-temperature interrelationships associated with a mixture of working fluid constituents. As such, diffusion pumps are stills, a commonly known fact.

For years many have been recommending that clean pump fluids generate the best ultimate vacuums.⁶⁻¹⁰ Huntress does state that less than one part per million of certain types of volatile contaminants was shown to alter seriously the effective vapor pressure of the working fluid. Removing contaminants though, has not been easy. Cryo trapping them on baffles is not a complete corrective measure since eventually saturation occurs causing vacuum system pressure spikes and contamination of the test article. Also upon baffle warmup, condensed contaminants may drip back into the pump fluid. Since occasional diffusion pump boiler eruptions, sometimes called burps, have been considered undesirable from a backstreaming standpoint, it has been the practice to minimize or eliminate vigorous boiling evaporative surfaces by design.¹⁰

Other contamination related factors are: large outgassing test hardware in large space simulation chambers which are difficult and expensive to clean; diffusion pump oil is too costly to be periodically replaced or repeatedly reprocessed when quickly contaminated; and elaborate baffle systems too expensive to purchase and/or operate. A logical course of action was to investigate methods to increase the self-cleaning, self-purification-separation capabilities of our present diffusion pumps (stills).

Background Distillation Information--The art of distillation was practiced before the Christian era by the Egyptian temple priests. However, molecular distillation is relatively new. In the early 1950's, Hickman found while working with pot stills that when liquids are permitted to evaporate rapidly without restriction into a high vacuum environment their surfaces often separate into two zones of widely different appearance and properties.^{6,7} One, which is in rapid self-motion called "WORKING" and the other, which is acquiescent and photographically highly reflective called "TORPID." An evaporative surface exhibiting a dual working/torpid behavior pattern or patterns was called "SCHIZOID." Torpidity, a floatation phenomena, is believed to be due to traces of impurities that block the surface during rapid evaporation.

Development Approach--The self-cleaning 1×10^{-6} SPF scale model glass vacuum system was designed to meet the following objectives:

- a. Understand the fundamental phenomena of torpidity and its effect on achieving ultimate vacuum or maximum pump speed.
- b. Determine methods and operating parameters for preventing torpidity or removing a torpid evaporative surface condition in order to generate a 100% working surface.
- c. Determine percent of contaminants inducing torpidity and/or its related ultimate vacuum limiting effects.
- d. Determine methods and operating parameters for removing light-end contaminants in the forearm.
- e. Determine methods and operating parameters for removing heavy-end contaminants from the boiler fluid.

Supporting Keys to Self-Cleansing Design--

- a. The concepts of torpid/schizoid/working evaporative surfaces. Torpidity as a surface phenomena subject to removal by surface skimming resulting in a schizoid evaporative surface.
- b. Existence of multiple groups of contaminant by spectroscopy analyses. Heavy-end contaminants grouping at approximately 700 M.W., and light-ends peaking at approximately 300 M.W. established the necessity for a triple cut molecular distillation process. Nearly two to three

times the quantity of light-ends exist than the quantity that exists of heavy-ends.

c. The final key was within normal vacuum fractionation distillation ranges.^{11,12} Hickman's early condensation pump designs, all use the alembic concept of liquid-vapor equilibrium in the vertical stage. Acute observation revealed that when the alembics fill up, the heavier volatile constituents overflow back into the pump boiler and are never fully discharged.

APPARATUS AND PROCEDURE DISCUSSION

Analysis Apparatus--The following equipment was utilized to study the material outgassing contamination problem:

- a. Computerized digilab FTS-20 infrared-fourier transform spectrometer (at KSC)
- b. RMU GL Hitachi mass spectrometer and 900 Perkin-Elmer gas chromatograph linked with a 6201 Varian data system (at GSFC)
- c. Q-250 residual gas analyzer (RGA) (at LeRC)
- d. Individual 502 Water Associates liquid chromatographs (at KSC and GSFC)
- e. Gas chromatography mass spectroscopy units (at KSC, GSFC, and LeRC)
- f. AGA thermovision (at LeRC)
- g. Quartz crystal microbalance (at GSFC and LeRC)
- i. Environment control-instrumentation systems (at LeRC)
- j. SPF - 1×10^{-6} scale model glass vacuum systems (at LeRC): G-4, modified G-4, 1st generation self-cleansing and 2nd generation self-cleansing

Standard Diffusion Pump Oil Performance Test Setup-- A single stage glass diffusion pump (designated a G-4) having a rated pump speed of 4 liters/sec was used for all oil performance comparison tests, see Figure 3. The G-4 vapor pump has long been used by the pump fluid and vacuum system manufacturers for comparing performance of various pump fluids. The prime reasons for using glass were the control over material contaminating factors plus the benefit of visually observing the operational phases of the vapor pump.

Molecular Distillation, Silicone Oil, Reprocessing Setup--Conventional methods for reclaiming contaminated pump oil are relatively ineffective or expensive. A new method was developed for reclaiming contaminated vacuum diffusion pump oil by high vacuum molecular distillation processes.³ A high vacuum centrifugal molecular still was utilized to centrifugally separate volatile contaminant/component compounds from the oil at their individual respective evaporation temperatures. Preheated dis-

tilland feedstock is metered onto a heated rotating evaporator disk where separation occurs. The light end contaminant vapors are condensed on the cool inner surface of the bell jar. The pure oil and heavy end compounds are not vaporized and are spun off the rotating disk by centrifugal force, caught in a water-cooled gutter and collected as a residue. Final cut distillation is performed in a similar manner except that the pure oil is vaporized, condensed, and recovered as a distillate with the heavy end contaminants being separated as a residue. See Figure 2 for reprocessing setup.

Acceptance criteria of molecular distilled-reprocessed DC-705 is attainment of a 5×10^{-6} Torr ultimate vacuum within 4 hr using the G-4 pump oil performance setup. Failure to meet the acceptance criteria indicates the residual existence of additional light-end contaminants, which necessitates another light-end cut distillation. A high vacuum molecular wiped-film type still may also be used successfully. For additional theory relative to molecular distillation see Burrows⁴ and Watt⁵.

More extensive information on the reprocessing set up, including equipment description, molecular still operating philosophy, distillation processing and G-4 solvent cleaning preparations plus operation procedures may be obtained from the Technology Utilization Officer at NASA/LeRC regarding Reference 3.

Second Generation Self-Cleansing 1×10^{-6} SPF-Scale Model Glass Vacuum System--A three jet glass diffusion pump, having approximately the same size boiler and resultant evaporative surface as the (G-4) single stage diffusion pump, was constructed to study the effects of inserting phthalate plasticizers and other contaminants directly into the pump fluid or into the chamber during pump operation (see Fig. 4(a)). The necessary removal of and identification of these volatile contaminating constituents are required in order to prevent the rapid deterioration of the pump fluid and the resultant reduced pump efficiency. See Figure 4(b) for self-cleansing (purification-separation) design innovation details.

Since the second generation self-cleansing 1×10^{-6} scale model apparatus generates ultra pure pump fluid with resultant lower ultimate chamber pressures, these innovations shall be described. Follow-on foreline vacuum distillation designs have been fabricated which should further improve the separation capability of contaminants in pump fluid, see Figure 4(c). Because these designs have not generated sufficient performance data to allow comparison as of this writing no further discussion will be included.

The design solution unfolded as a merger of the three interrelationships: (1) surface skimming heavy-ends, (2) periodically draining different light-end fractions until the foreline temperature when heated externally stays stabilized at a maximum of about 130° C, and (3) obtain-

ment of a 100% working evaporative surface indicated by a 5° to 7° C boiler vapor-liquid temperature difference. Optimum performance was achieved with a boiler fluid level being 5mm±1mm in depth. Any one of the three concepts by itself or paired with another will not allow achievement of the optimum pump efficiency condition possible with a continuous 100% working evaporative surface. Analyses showed the pump boiler fluid improves to a purity of 99.8% or better when the evaporative surface exhibits a continuous 100% working condition. The critical point in the ratio of contaminant to pure liquid versus lowest realizable ultimate pressure is still uncertain. This is primarily due to the existing noise levels in the spectroscopy analysis system.

Foreline Purification--In the forearms of Figure 4(b) and (c), a distillation process occurs in which mixtures of soluble liquids, carried along by the pumps throughout, are separated by evaporation and condensation, whereby the condensed part becomes richer in the most volatile constituents. This condensate, high in percentage of contaminant, is periodically drained into a vessel of slightly lower pressure while the diffusion pump is operating. If this high volatile condensate, or reflux is allowed to return to the diffusion pump boiler the volatile constituents are vaporized, move up the Christmas tree and are discharged out the respective jets to be condensed on the cooler wall of the diffusion pumps barrel. Both pure fluid and contaminated fluid molecules follow similar paths. The primary distinction between the two types of vapor or condensates being the dwell time each exists on the diffusion pump barrel wall surface. More volatile molecules for a specific temperature and pressure tend to break the polar and dispersion bond forces and thus become free to "backstream" (also known as, "reverse fractionation") back up into the chamber. Other less volatile constituents are carried as reflux up into the forearm of the diffusion pump where reverse fractionation again occurs.

Surface Skimming--Means were built into the self-cleansing pump to remove impurities from the evaporative surface. (See Figs. 4(a) and (b)). DC-705 silicone diffusion pump oil is a discrete phenylmethyl siloxane species and is chemically a pentaphenyltrimethyltrisiloxane having a molecular weight of 546. Thus being basically a pentamer, by hypothesis, when the oil becomes contaminated and cracks it may become a trimer and/or a heptamer. This was essentially proven by analyses, identification of 700 M.W. group peaks, and the heavy-end molecular distillation cut. Skimming the evaporative surface, analyzing the sample and discovering small quantities of phthalate esters proves the validity of the hypothesis.

RESULTS AND DISCUSSION

Contaminating Compounds Affecting DC-705

An inventory search of 99% of the SPF materials utilized for the Brayton and Skylab Space Simulation Test Programs revealed thirty-nine different components. Only those materials that were found to be volatile compounds (extensive outgassing materials) are included with their respective analyses in Table I(a).

Standardized outgassing tests, to determine the percent weight-lost and percent of volatile condensable materials (VCM), was performed by exposing a material sample to a 1×10^{-6} Torr pressure at 125° C for 24 hr or more.¹³ Making up the percent of weight losses are noncondensables (true gases), and hot vaporous condensables (VCM) which are deposited on a 23° C surface. Differential thermal analysis (DTA) performed at Kennedy Space Center (KSC) subjected a similar sample to progressively higher temperatures at a 10^{-4} Torr environment while measuring the decreasing weight. Comparing outgassing and DTA test results for typical volatile cable insulations sample 5(a) and 6(a), 5(b) and 6(b) revealed a close correlation between the two methods. Per DTA, volatile materials that were subjected to 3000 hr of a 10^{-5} to 10^{-4} Torr vacuum had nearly the same weight loss (90 to 97%) as did those samples that were never exposed to vacuum.

Comparing alkyd paint samples 2(c) and 4(b) and 2(a) and 3(a) outgassing weight loss or percent VCM data revealed a greater difference in outgassing rates, 55 to 150% for nearly 3000 vacuum hours difference. Nearly the same outgassing rate of 88% existed for the relative short time of 600 hr difference in vacuum exposure. Per Reference 13, one percent total outgassing and 0.1 percent volatile condensables should be the outer limits on material acceptable for spacecraft use, especially for long-term missions.

Identification of Worst Outgassing Materials and Compounds

As previously specified, all materials listed in Table I(a) were found to contain volatile compounds and as a result would be unsuitable for deep-space missions by violating the foregoing outgassing acceptance criteria. However practical considerations in operating large space simulation chambers and conducting large test programs is always a compromise between schedule and availability of materials. Such was the case with Belden's #8404 two conductor or four conductor shielded cable. The manufacturer states it is 25% plasticized with di-isodecyl phthalate (DIDP) 446 M. W.. Test results indicate it was the worst offender in the chamber, followed by polyvinylchloride (PVC), neoprene, alkyd oil paints, etc. Independent KSC/GSFC chemical analyses and

References 14 to 16 reveal the existence of phthalate esters, carbonaceous materials, aromatic amine, antioxidant, organic salt, and to a lesser degree nonphthalate type ester resin in the material samples listed in Table I(a).

The foregoing contaminants were also detected in analyses of various DC-705 oil samples listed in Table I(b) and (c).

Effect of Various Contaminants on Performance of Diffusion Pumps and DC-705 Silicone Oil

Various Aged Oil Performance Comparisons--The G-4 single stage glass diffusion pump system illustrated in Figure 3 was primarily used as an oil performance-calibration-evaluation-device. The rapid deterioration of silicone pump fluid in an environment that is filled with (high outgassing) materials is illustrated by Figure 5. New DC-705 in a typical G-4, 4 hr test consistently achieves an ultimate vacuum of 1×10^{-6} Torr. New DC-705 after being exposed to a high outgassing environment for 25 hr in conjunction with performing Skylab Payload Shroud Jettison Test No. 3, achieved only 4.8×10^{-5} Torr for a resultant performance loss of nearly fifty times. Significant was the 0.3 decade performance gain of 339 hr old oil to approximately 2×10^{-5} Torr. Interest in the 0.1 decade pressure fluctuation at the 4 hr point of the standard G-4 performance test lead to confirming the repeatability and/or the extent of such fluctuations in pressure. Since any changes in ultimate pressure are indications of changes in pump efficiency, which is directly correlatable to pump speed, the approach of improving the self-cleansing capability of the diffusion pump as a still was embarked upon.

After 943.5 hr of operation another oil sample was drawn from a 48-in. pump and its performance checked. This 943.5 hr old oil for all practical purposes was identical to 3000 hr oil in performance. However, color was slightly lighter for 943 hr oil. As previously described in the foregoing theory discussion, the G-4 now was operating at a higher equilibrium pressure, limited by the reverse fractionation rate of the contaminated pump oil which in effect is dependant on the total number of contaminants, their respective quantities, and their respective vapor temperatures and pressures.

Contaminant Effect on Oil Performance--Study of individual plasticizers, their effect when mixed into new DC-705 at various percentages and the resultant effect on ultimate vacuum are revealed in Figure 6. Three milliliters (ml) of di-isooctyl phthalate (DIOP) into 60 ml of new DC-705 for a total of 4.78% contaminant achieved an ultimate vacuum of 2.2×10^{-5} Torr. However, 5 ml of DIOP into 60 ml DC-705, 7.7% total contaminant mixture achieved only a 2.3×10^{-4} Torr ultimate vacuum representing a 100 times loss in efficiency. The 0.1 decade fluctuation was ob-

served to be associated this time with the filling of the top alembics in the vertical portion of the G-4 glass diffusion pump, and the following reduction in ultimate vacuum pressure rise corresponded to the spill over of contaminant concentrated fluid from these top alembics. Thus the logical solution was to remove the fluid from these top alembics periodically which was accomplished in a modified G-4 diffusion pump. The other phthalate plasticizer contaminant runs with new DC-705 followed the general increase in pressure trend with corresponding increase in percentages of DIOP contaminant. However, in this paper only the data associated with 7.7% of the following contaminant mixtures were included for di-isodecyl phthalate (DIDP), di-octyl phthalate/di-2-ethylhexyl phthalate (DOP/DEHP), and di-tridecyl phthalate (DTDP). Surprising was the slightly higher ultimate pressure obtained with DTDP (M.W. 530) contrary to the expectation that higher molecular weight contaminant would affect the DC-705 mixture the least. Evidently additional study is required in this area.

Reclaiming Contaminated Vacuum Diffusion Pump Oil

Molecular Distillation Reprocessing Results--The triple cut distillation process, utilizing either a high vacuum centrifugal molecular still or a high vacuum molecular wiped-film type still, successfully reclaimed 3000 hr old DC-705 oil.³ Contaminated oil that was once considered worthless was recovered yielding 71.5% (335 kg reclaimed from 469 kg) resulting in a \$34 700 annual savings. The 4 hr G-4 acceptance performance test achieved 2×10^{-4} Torr for contaminated 3000 hr oil versus 1.65×10^{-6} Torr for triple cut reprocessed oil.

Molecular Distillation Reprocessing Other Silicone Fluids--The molecular still operating philosophy and distillation process/procedures and parameters would be similar for contaminated DC-704 tetramethyltetraphenyltrisiloxane. However, distillation temperatures would be slightly reduced because of its lower molecular weight of 484.

Philosophy of Reprocessing by Molecular Distillation--DC-705 oil is chemically a pentaphenyltrimethyltrisiloxane having a molecular weight 546. As the oil becomes contaminated and/or cracks, an unknown amount may be a trimer and/or heptamer. Volatile constituents are separated from the pure DC-705 oil by pre-cut distillation where light-end contaminants such as phthalate esters (common cable insulation plasticizers) ranging between 100 and 400 M.W. are removed as a distillate and heavy-end contaminants with molecular weight about 700 being removed as a residue during final cut distillation.

Economic Limitations of Molecular Distillation Reprocessing--Using high vacuum centrifugal molecular distillation as an occasional method

of reclaiming a high priced fluid such as DC-705 or DC-704 is certainly economical. A CMS-15A single molecular still reprocessed the contaminated SPF oil in about one week at a continuous 4 gal/hr rate per each distillation cut. However, if the diffusion pump oil deteriorates as rapidly as experienced at SPF, (see Fig. 5) the necessity of repeated oil changes and reprocessing becomes impractical because of the hinderance to the test program. A solution to this problem would be a totally self-cleansing diffusion pump.

Second Generation Self-Cleansing 1×10^{-6} SPF-Scale Model Glass Vacuum System

Figures 7(a) to (c) are the product of one continuous test lasting 40 days with the 1×10^{-6} SPF-scale model self-cleansing vacuum system. Figure 7(d) data was obtained with the same test apparatus. The same 65 cm (2.5 in.) diam by 8mm thick sodium chloride (NaCl) single crystal specially polished was used for all comparison tests shown in Figure 7. Because the discussion of critical interrelated parameters are time correlated and effected by specific events, letters and/or numerals are utilized designating significant data. Numbers assigned to top-chamber pressure or boiler fluid depth parameters designate a specific serialized photographic condition, for typical corresponding slide, movie frame, thermovision monitor movie frame and polaroid picture of a torpid/schizoid/working surface (see Fig. 8).

Figure 7(a) Phase I, New DC-705 Oil Performance Test Data, Increased Purification of New DC-705 Nets 1.5 Decade--The second generation vacuum system incorporating contamination removal technology was initially charged with 55 ml of new DC-705 oil (see Fig. 4(a) and (b)). After three days of operation the upper ion gage in the 1×10^{-6} scale chamber was indicating a consistant 5×10^{-5} Torr pressure. Point "A" on the fourth day reveals the effect of putting on all ion gages and slowly increasing the foreline heater up to full rated capacity (35 W). A 100% working surface as previously defined existed 10% of the time. The effect of removing approximately 6 ml of light-end (L. E.) fractions in the foreline, 2 ml (L. E.) from each drain line, revealed a 60° F increase in foreline temperature almost instantly, along with a correspondingly 0.6 decade lower chamber pressure. Also an increasing trend in boiler vapor and liquid temperature was observed. After a night in this configuration the variation in boiler vapor and liquid temperatures were diminishing. The 100% working surface periods were now increased in duration and in frequency to 25% of the time.

On the fifth day, the initial effect of removing approximately 7 ml of heavy-end (H. E.) fractions from the boiler evaporative surface, was to increase the 100% working surface periods to 50% of the time and to sta-

bilize the boiler vapor and liquid temperatures. Only a slight reduction in chamber pressure resulted.

On the sixth day, three additional milliliters of L. E. were removed from the top alembic of the foreline. As experienced on the fourth day, foreline temperature increased to 275° F, boiler vapor rose to 435° F, while boiler liquid temperature reached 455° F, and the jet molecular release rate was visully observed to intensify resulting in a decreasing trend in ultimate chamber pressure. The 400 W heater input to the boiler was reduced at point "B."

Data points "C," "D" and "E" are associated with establishing the optimum boiler heater input for best diffusion pump performance corresponding to the lowest chamber pressure. Chamber pressure now ranged between 7×10^{-7} and 2×10^{-6} Torr from the 10th day to the 12th day while evaporative surface was working 75% of the time.

On the 12th day, with the boiler's evaporative surface behavior described as 100% working 75% of the time, foreline temperature stabilized at about 250° F, boiler vapor temperature was stable within 405° to 420° F, and boiler liquid temperature varied from 430° to 440° F. The only limitation remaining was the achievement of a continuous 100% working evaporative surface. Thus addition 4 ml of L. E. fractions were removed in 2 ml steps within an hour from the top alembic in the foreline. This reduced the boiler fluid depth to approximately 4mm when this alembic again became full within 20 to 22 min. These removal of minute quantities of unknown L. E. fractions achieved a continuous 100% working evaporative surface behavior pattern for the first time. Further removal of 2 ml of L. E. from the top alembic resulted in a decrease in ultimate chamber vacuum (See movie take #31). Foreline temperature reduced by 25° to 250° F, however, fluctuations in boiler vapor and liquid temperature were for all practical purposes nonexistent. Both parameters were near their all time weighted average maximum point, respectively 425° and 442° F. The boiler fluid depth was now about 3mm for 75% of the evaporative surface area, but due to vapor recoil action, 20 to 30% of the boiler bottom was bare, except for what appeared as a minute molecular film layer. This layer was surmised to be left or caused by the ever moving-vigorous boiling evaporative surface. See photograph No. 21 for an equivalent visual illustration. Point "F" indicates where 10 ml of new DC-705 was directly added to the diffusion pump boiler at a slow insertion rate of 1 ml/min causing a small rise in chamber pressure. The foregoing addition of new DC-705 into the boiler brought the fluid level back up to approximately 7mm. However since the chamber pressure rose approximately 0.5 decade to 5×10^{-6} Torr, and the boiler evaporative surface was again 100% working 75% of the time, the remaining L. E. and H. E. contaminants in new DC-705 was suspect. Upon removing 2 ml of L. E. and approximately 0.5 ml of H.E. chamber pressure decreased to between 1×10^{-6} to 2.5×10^{-6} Torr.

Since it is very difficult to measure a highly dynamic liquid depth and/or determine the exact amount being removed through relatively long glass tubulation, the accuracy on all fluid depth and volume measurements is $\pm 1\text{mm}/\pm 1\text{ ml}$ respectively.

Figure 7(b) Phase II, New DC-705 Performance Test Data, Effect of Plasticizer Contaminants Added into Ultra Pure DC-705 and Their Removal

With the detail self-cleansing operational philosophy established, the following data Figures 7(b) to (d) will be described in a more comprehensive manner, utilizing data points or significant occurrences.

(Event "I") Inserting 4 ml of a phthalate ester mixture containing 2 ml of DIOP, 2 ml DIDP, and 2 ml of DOP/DEHP directly into the highly purified DC-705 diffusion pump boiler after Phase I testing resulted in chamber and foreline pressure increase of 1000 to 10 000 times.

(Event "II") Stabilization of chamber pressure occurred at 7×10^{-4} Torr. Removing 4 ml of L. E. from the top alembic of the foreline obtained the expected improvement in chamber pressure. Chamber pressure was 1.2 to 1.5 decade lower (2.5×10^{-5} Torr) within one hour.

(Event "III") Inserting the remaining 2 ml of phthalate ester contaminant mixture slowly (at a less than 1 ml/min) directly into the boiler duplicated the pressure parameter fluctuation previously. Ten ml of new DC-705 was added so not to deplete the boiler supply during the pending cleansing period. When 2 ml of L. E. fractions were removed twice within a 30 min period, the chamber pressure was reduced three decades within 1 hr, from 3×10^{-3} to 2.5×10^{-6} Torr. The following morning, 15 hr later 8.5×10^{-7} Torr was achieved.

No improvement in chamber pressure occurred until the 1×10^{-6} SPF scale model glass chamber was baked out on the 17th day at 230° F whereupon a 0.25 decade improvement was achieved to 7×10^{-7} Torr. Configuration of the boiler's evaporative surface was 100% working 99% of the time. This behavior pattern was maintained for over three days.

(Event "IV") Lowering the 1×10^{-6} scale test chambers baffle temperature to -10° F in order to study its effect on ultimate chamber pressure were inconclusive. Six days later (26th day of operation) the baffle temperature was reduced to -55° F without an expected corresponding change in chamber pressure. Chamber pressure now was $2-5 \times 10^{-6}$ Torr, up 0.5 decade.

(Event "V") Surmising the existence of light-ends, 1 ml of L. E. was removed from the top foreline alembic with the immediate increase in pump efficiency indicated by a 0.5 decade decrease in chamber pressure to 7×10^{-7} to 1×10^{-6} Torr. After a 16 hr period of chamber bakeout at 180° F, the lowest ultimate chamber pressure of 5×10^{-7} Torr was observed.

Figure 7(c) - Phase III, New DC-705 Performance Test Data, Effect of Plasticizer Contaminants Added into Chamber, Their Removal with Cold and Warm Baffles

(Event "VI") Inserting 4 ml of phthalate ester mixture containing 2 ml of DIOP, 2 ml DIDP, and 2 ml of DOP/DEHP slowly into the ultra clean test chamber resulted in the expected chamber and foreline pressure increases of 1000 to 10,000 times. Chamber baffle temperature was -55° F.

(Event "VII") Sixteen hours later the chamber pressure was 1.5 to 2×10^{-6} Torr. The bottom of the test chamber revealed condensed plasticizer contaminant. A chamber bakeout at 220° to 280° F was initiated in an attempt to vaporize the newly added plasticizers. An immediate 1.2 decade chamber pressure rise occurred. With the chamber heated to its hottest bakeout temperature (220° to 280° F), two additional milliliters of the phthalate mixture was inserted into the top of the chamber. Chamber pressure increased from the 1×10^{-5} Torr range to 3×10^{-3} Torr range. The chamber baffle was allowed to warm up to 20° F in order to render it ineffective in protecting the highly purified DC-705 in the diffusion pumps. The outgassing load created by the vaporizing plasticizers on the heated chamber walls started to affect the pumps efficiency until chamber pressure stabilized out at $1.5-3 \times 10^{-5}$ Torr. This was a crude simulation of the outgassing from heated (heavily plasticized) cables.

On the 31st day, upon removing 3 ml of L. E. from the top alembic in the foreline, the typical expected improvement process started immediately again. However, due to a power outage in the SPF vacuum technology laboratory sometime that night a discontinuity in the data exists.

(Event "VIII") As the DC-705 pump fluid purity became reinstated, the chamber pressure returned to its prior levels of 6×10^{-7} Torr with a corresponding foreline temperature of 265° F indicating a high molecular throughput. The chamber baffle temperature was -25° F. Warming up the chamber baffle to ambient after the diffusion pump is ultra pure did result in a slight chamber pressure rise of approximately 0.5 decade. Evidently the vast majority of deteriorating contaminants were removed by the self-cleansing process of this diffusion pump vacuum system.

Figure 7(d) - Five Year Old Michigan State Cyclotron DC-705 Oil Performance Test Data with the 1×10^{-6} SPF-Scale Model Self-Cleansing Pump

Even though the typical torpid/schizoid/working surface behavior patterns have been repeatedly duplicated with various DC-705 contamination modes, discussion of the photographic/thermovision/movie documentation has been purposely deferred to this section. The test sample was

DC-705 previously exposed to an average gamma dose rate of 25 milliroentgen (MR)/hr for 5 yr while operating in the vacuum diffusion pump system of the Michigan State University Cyclotron. It had a photographic distinction being discolored by use to a dark brown color. This oil achieved a 2.5×10^{-5} Torr ultimate vacuum in the standard G-4 oil performance test, (see Fig. 5). This oil always was handled with the best of vacuum practices; that is back filling the vacuum system with dry gaseous nitrogen (GN_2) upon diving the cyclotron to atmospheric pressure, never thermally shocking it to atmospheric environmental contaminants, etc.

Figure 7(d) shows after a day of operation that the ultimate test chamber vacuum obtained was 5×10^{-5} Torr. A corresponding chamber baffle temperature of -40° F did not appear to limit the deteriorating effect or reverse fraction of light-end contaminants. For a comparison of boiler evaporative surface behavior patterns as a function of generated ultimate chamber pressure, see Figure 8.

Photograph No. 15, taken at a chamber pressure of 2×10^{-4} Torr, reveals a schizoid pattern of many working holes typical of the silicone pump fluids. A broken light source similar to Hickman's was utilized to high light the evaporative surface.⁶ The movie film which is a dynamic documentary portion of this research contains the actual thermovision visual record. The thermovision camera essentially thermally maps what its viewing by utilizing the isotherm markers.¹⁷ The NaCl lense affixed to the boiler allows 90% transmittance between the wave lengths of 0.2 to 13 microns. A typical thermovision polaroid picture of a torpid/schizoid/working evaporative surface with numerous individual working holes is shown next to photograph No. 15.

The other typical thermovision polaroid picture just below reveals a single working hole in a torpid surface. The evaporative surface horizon in the diffusion pump boiler is easily identified. Significant is the localized eruption of molecules being released from the working hole, well into the pump boiler vapor cavity. This thermovision photograph confirms what Hickman described in References 6 and 7, associated with working valleys of different depth. The deepest part of the working valley emits the most vapor. Molecular release is greatest from these areas since the evaporative surface is always changing, the size and shape of the working holes are also changing relative to existence, location, growth, movement, etc.

Two photographs both labeled No. 16 were taken within a few seconds of each other. One taken at a rising chamber pressure of 5 to 10×10^{-5} Torr portrays primarily a torpid surface generating a 0.5 decade higher chamber pressure. The other, a 100% working evaporative surface having an improved chamber pressure of 5×10^{-5} Torr. The evidence of increased molecular flow is everywhere in this photograph; inside the

Christmas tree, at the rim of the individual jets, molecular buildup on the barrel surface, in the foreline, etc.

Marked increase in pump-performance was apparent as soon as light-end and heavy-end contaminants began to be removed from the pump fluid. Within 8 hrs from the start of cleansing-separation-purification processing a 50 times increase in pump performance was achieved as indicated by a 1.5 decade lower chamber pressure varying between 1×10^{-6} to 5×10^{-6} Torr. After the second day of total operation, first full day of contaminant pump fluid cleansing activity, an ultimate chamber pressure varying between 8×10^{-7} to 1×10^{-6} Torr was obtained. The corresponding boiler evaporative surface behavior associated with this pump efficiency was 100% working 90% of the time. The fluid color was still dark brown.

After the first seven(7) days of system operation, the ultimate chamber vacuum fluctuated between 5×10^{-7} and 1×10^{-6} Torr with a corresponding improved evaporative surface now being 100% working 99% of the time. All other critical operating parameters were similar to those of the previous tests. Points "A" and "B" confirmed the interdependancy between all critical parameters and minute changes in chamber baffle temperature. This is evident when even at nominal baffle temperatures of -40 to -15° F. Significant were the occasional higher isolated pressure rise spikes caused by the total 100% working surface startups, as noted in points "B₁" and "B₂".

Point "C" shows again that further increase in pump efficiency (decrease in chamber pressure) can be expected as long as there are some light-ends available for removal, regardless of the chamber baffle temperature fluctuations.

Point "D" indicates achievement of a continuous 100% working evaporative surface. Point "E" shows the effect of changing the air cooling flow/distribution in the SPF Vacuum Technology Laboratory and/or the change increase in diffusion pump heater voltage.

Point "F" is noteworthy in that the color of the boiler fluid changed from dark brown to light yellow overnight after the heater voltage was increased approx. one volt. Expected effect of putting additional ion gages on is also shown. See photographs No. 19 for further evidence of increase in molecular flow throughout the entire pump when evaporative surface is continuously 100% working.

An investigation into the effectiveness of the chamber baffle at 5×10^{-7} Torr vacuum range was undertaken. The effect of the first major baffle temperature warmup cycle to 40° F on all critical parameters are indicated by event "I". Respective baffle temperature warmup cycles are revealed by events "II", "III", "IV", "V", and "VI". As Huntress⁹ implied, and the foregoing results confirm, if fluid vapor pressure is maintained at its lowest absolute value (10^{-10} Torr for DC-705) corresponding to an ultra high purity condition, many hours of vapor-free testing are provided with no more than a watercooled baffle. This could pro-

vide a significant operational cost reduction to large space simulation facilities.

Photograph No. 21 reveals the violent-dynamics of a continuous 100% working evaporative surface. Note, the partially bare boiler bottom, the vapor recoil action, the gobs of liquid actually carried along with the high molecular release rate from the boiler fluid, and the heavy buildup of molecules/liquid formations throughout all portions of the diffusion pump assembly.

Events "VII" and "VIII" reveal the criticality of the proper amount of boiler heater input in order to successfully maintain a continuous 100% working evaporative surface with its associated increase in optimum diffusion pump efficiency.

SUMMARY OF RESULTS AND CONCLUDING REMARKS

1. Torpidity, a menace to high vacuum pot stills but not considered at present a serious factor in the vapor pumps, is a definite factor in reducing the pumps efficiency by factors of 100 times. The scale model (self-cleansing) glass diffusion pump data showed 100% working evaporative surfaces produce ultimate pressures 100 to 1000 times lower than those of torpid evaporative surfaces. It is surmised that torpidity is the result of an increased surface tension phenomena caused by impurities collecting on the evaporative surface, acting as a barrier limiting the molecular release rate.

2. Where no specific chemical has previously been known which will confer torpidity when added to a nontorpid liquid, 1×10^{-6} SPF-scale model test data showed that phthalate esters, namely DIOP and/or DIDP, added directly into the boiler fluid or vacuum system chamber caused a nontorpid surface to become partially schizoid (100% working 50% of the time) with a corresponding increase in pressure of three decades. Analyses of light-end and heavy-end fractions separated from contaminated (torpid/schizoid producing) DC-705 silicone oil detected phthalate ester plasticizers.

3. Where further increases in specific pumping speed have not been considered likely, the scale model (self-cleansing) glass diffusion pump, incorporating contamination removal technology innovations, consistently produced ultimate pressures that were for new DC-705 oil, 1.5 decade lower; for 5 yr old DC-705, over 2 decades lower; and for new DC-705 oil intentionally contaminated with phthalate esters, nearly 3 decades lower. Diffusion pump innovations were successfully tested allowing removal of contaminants from pump oil during operation. Vacuum distillation removal of light-end fraction contaminants and boiler bleed removal of heavy-ends from the evaporative surface resulted in a 2 decade or more lower ultimate pressure.

4. When self-purification of the intentionally contaminated diffusion pump oil was not allowed, no significant improvement in ultimate vacuum

was achieved after continuous operation in excess of one month, thereby indicating the necessity of removing these phthalate esters.

5. The color of DC-705 is not indicative of purity or capability for obtaining maximum molecular release conditions from an evaporative surface, since similar ultimate vacuum levels and conditions were realized with a dark brown color oil as with a lighter color oil.

6. A water baffle at ambient temperature may be all that is required for a high efficiency diffusion pump, provided the boiler fluid is maintained at an ultra high purity condition (fluid vapor pressure kept at its lowest absolute value - 10^{-10} Torr for DC-705) by vacuum systems incorporating contaminate removal technology innovations.

7. Contaminants, commonly found in large vacuum chambers, that adversely affected silicone oil diffusion pump performance were identified as phthalate ester plasticizers. These plasticizers are utilized in cable insulation jackets, alkyd paints, electronic components, etc. Those having the most deteriorating effect on DC-705 being: DOP 390 M.W., DTDP 530 M.W., DIDP 446 M.W., and DOP/DEHP 390 M.W., respectively.

8. Contaminated DC-705 diffusion pump oil can be successfully reprocessed by high vacuum molecular distillation with an approx. 75% yield and capable of achieving an ultimate vacuum close to that of new DC-705 oil.

9. Further study to improve the purification-separation concepts described, methods of measuring changes in molecular release rates, and spectroscopy fingerprints identifying contaminating constituents and related physical properties on the evaporative surface is warranted.

ACKNOWLEDGMENTS

W. R. Carman and L. Underhill, KSC, Analytical Lab. Div.; F. Gross and J. Colony, GSFC, Material Eng. Br.; V. R. Lalli, LeRC, Power Electronics Br.; R. K. Lohwater, Bendix Corp.; K. Hickman, Rochester Institute of Technology.

REFERENCES

1. Fenn, David B.; Deyo, James N.; Miller, Thomas J.; and Vernon, Richard W.: Experimental Performance of a 2-15 Kilowatt Brayton Power System in the Space Power Facility Using Krypton. NASA TM X-52750, 1970.
2. Daye, Charles J.: Skylab Payload Shroud Jettison Tests. NASA TN D-6913, 1972.
3. Buggele, Alvin E.; and Lohwater, Robert K.: Improved Method for Reclaiming Vacuum Diffusion Pump Oil. NASA Tech Brief B72-10511, August 1972.

4. Burrows, G.: *Molecular Distillation*. Oxford University Press, Amen House, (London) 1960.
5. Watt, Peter R.: *Molecular Stills*. Reinhold Publishing Corp., 1963.
6. Hickman, Kenneth: *Torpid Phenomena and Pump Oils*. *Jour. of Vacuum Science and Technology*, Vol. 9, No. 2, Jan./Feb. 1972, pp. 960-976.
7. Hickman, K.; Maa, J. R.; Harris, P. J.; and Davidhazy, A.: *The Effects of Surface Properties of Water on Evaporation and Condensation*. R&D Progress Rept. No. 585, Rochester Institute of Technology, for Office of Saline Water, U.S. Dept. of the Interior, Grant No. 14-01-0001-2119, Dec. 1970.
8. Huntress, Arnold R.: *Clean Diffusion Pump Fluids, How They Stay That Way*. Dow Corning Corp. (Presented Amer. Vac. Soc. Symposium - Abstract 1966, unpublished).
9. Huntress, Arnold R., and Schmock, Walter R.: *A Direct Analytical Method for Measuring the Condition of Diffusion Pump Fluids*. Dow Corning Corp. (Presented Amer. Vac. Soc. Symposium - Abstract 1965, unpublished).
10. Hablani, M. H.; and Maliakal, J. C.: *Advances in Diffusion Pump Technology*, *Jour. of Vacuum Science and Technology*, Vol. 10, No. 1, Jan./Feb. 1973, pp. 58-64.
11. Krell, Erich; and Lumb, E. C.: *Handbook of Laboratory Distillation*, Elsevier Publishing Co., 1963.
12. Perry, E. S.; and Weissberger, A.: *Distillation: Technique of Organic Chemistry*. Vol. IV, Interscience Publishers, 1965.
13. Fisher, Aaron; and Mermelstein, Benjamin: *GSFC Micro-volatile Condensable Materials System for Polymer Outgassing Studies*. NASA GSFC X-735-69-471, 1969.
14. Gross, Frederick C.; and Colony, Joe A.: *An Etiological Study of Phthalate Self-Contamination of Spacecraft and Contamination from Their Earthly Environs*. NASA TN D-6903, 1972.
15. Winspear, George G. (editor): *The Vanderbilt Rubber Handbook*. R. T. Vanderbilt Co., Inc., 1968.
16. *Infrared Spectroscopy Committee, Chicago Society for Paint Technology: Infrared Spectroscopy - It's Use in the Coating Industry*. Federation of Societies for Paint Technology, 1969.
17. Borg, Sven. Bertil.; *Thermal Imaging with Real Time Picture Presentation*. *Applied Optics*, Vol. 7, Sept. 1968, pp. 1697-1703.

TABLE I - SOME EPF TEST SUPPORT MATERIALS ASSOCIATED WITH DC-105 OIL CONTAMINATION PROBLEM

(a) Volatile (Outgassing) Materials and Their Analyses							
Material description type	Manufacturer	Total quantity exposed, lb	Length of time exposed to vacuum, hrs	GFC outgassing test results ⁽¹⁾		KFC DTA test results 25°-240° to 360° C.	General information provided by manufacturer or by KFC analyses
				wt. loss, %	VCM, %		
Cable							
Sample #84 FM40 3C or 4C shielded cable	Belden	18 000	0	----	----	62.6	Approximately 50% PVC resin, 25% DEDP
Sample #84 FM40 2L or 4L shielded cable	Belden	18 000	3000	13.9	9.9	59	Approximately 50% PVC resin, 25% DEDP
Sample #84 #282 EG-38C/U shielded coax	Belden Consolidated	1 000	0	----	----	21	Nitrile modified PVC (no phthalate ester plasticizers used) in Geon #720
Sample #84 #282 EG-38C/U shielded coax	Belden Consolidated	1 000	3000	2.9	1.2	30	Nitrile modified PVC (no phthalate ester plasticizers used) in Geon #720
Neoprene	Dupont			3.01-7.98	1.9-6.14	33.6	Nitrile modified PVC (no phthalate ester plasticizers used) in Geon #720
						(15°-300°) C	
#16 Avg. 3C 80 cable	Cavel Cable Co.	2 500	3000	-----	-----	-----	Neoprene type rubber with high aromatic amine antioxidant level. Inner layer - a nitril rubber (polybutadiene)
2.4 in. B-ring seal	Irving B. Moore	496	3000	-----	-----	-----	PVC resin with phthalate ester plasticizer and carbonate and silica filler for samples #17, and #18, and #21 outer jacket only. #21 Mylar type
380 MCM cable (sample #)	Parasitic Cable	750	3063	-----	-----	37	Terephthalate ester wrap with polyethylene conductor insulation Gray alkyl oil paint typical
Samples #17, #18, and #21 #19 Avg., #12 Avg., and #18 Avg., single conductor or shielded cable	Cavel, Apex, and Belden or Ray Chem	3648, 3000, 40, 3000, and 10 000	and 40				PVC resin with phthalate ester plasticizer and carbonate and silica filler for samples #17, and #18, and #21 outer jacket only. #21 Mylar type Terephthalate ester wrap with polyethylene conductor insulation Gray alkyl oil paint typical
Polar crane		300 m ²					
Paint samples							
2(a) green ⁽²⁾	P. H. Hols	68	6 g ⁽³⁾	2.0 ⁽⁴⁾	-----	-----	Phthalic anhydride, M. W. 148.1 (approx. 24%), alkyl binder, titanium oxide and traces of DC-105
2(b) red primer under gray ⁽³⁾	Bushnell & Sherman Williams	68	2 g ⁽⁴⁾	0.4 ⁽⁴⁾	-----	-----	Phthalate type (diethyl phthalate, M. W. 218), alkyl binder, talc, silica
2(c) gray paint ⁽¹⁾	General Electric	68	6 g ⁽³⁾	2.0 ⁽⁴⁾	-----	-----	A nonphthalate ester alkyl, carbonate, sulfate, titanium oxide, traces of DC-105
2(d) green ⁽²⁾	P. H. H Tractor Drive Hose	68	6 g ⁽³⁾	1.5 ⁽⁴⁾	-----	-----	Ratio of 665 hr to 85 hr outgassing rates is 89%, ratio of 965 hr to 85 hr VCM rate is 19%
4(a) light gray ⁽³⁾	G. E. control cable door	3065	2.6 ⁽⁴⁾	0.6 ⁽⁴⁾	-----	-----	Ratio of 3065 hr to 85 hr outgassing rates is 95%, ratio of 3065 hr to 85 hr VCM rate is over 190% due to silicone oil being absorbed with time
4(b) dark gray ⁽¹⁾	G. E. control cable door	3065	4.6 ⁽⁴⁾	1.1 ⁽⁴⁾	-----	-----	Ratio of 3065 hr to 85 hr outgassing rates is 191%, ratio of 3065 hr to 85 hr VCM rate is 85%
4(c) black	Mercury vapor light	3065	1.7	0.4	-----	-----	No data given
Sample #38 Catch Net, structure paint	Unknown	3 000 m ²	68	-----	-----	-----	Phthalate type alkyl binder, organic salt (iron salt, probably also oxide) and traces of DC-105 oil
(b) Contaminated - Reprocessed Oil Analyses ⁽⁵⁾							
Sample No.	DC-106 (New Curing) Oil Sample Description	Color	Analyses using infrared spectrophotometric techniques at KFC				
41	3046 hr old, 10% percent distillation of light-end contaminants	clear white	Detected a phthalate-type ester or alkyl				
42	3040 hr old, 80% final cut distillation of heavy-end contaminants	dark brown	Detected a phthalate-type ester alkyl, a polyethylene resin				
44	3040 hr old EPF DC-105	brown	Some phthalate ester detected, carbonaceous material showing carbonyl character and silicone character, probably a degradation of reaction product				
(c) 1-10 ⁻⁸ Scale Model Contaminated Oil Analyses							
II	2-7-73 Contaminated DC-106 oil samples (taken post-insertion of 6 ml mixture of phthalate plasticizers - 2 ml DEDP, 2 ml DOP, 2 ml DOP DENP directly into boiler fluid)(color, clear white)						
	Sample #8 - Light-end fractions from (boiler): color, pure white; 18.4% phthalate ester content						
VIII	2-19-73 Contaminated DC-106 oil samples (taken post-insertion of 6 ml mixture of phthalate plasticizers - 2 ml DEDP, 2 ml DOP & 2 ml DOP DENP directly into top of chamber)(color, clear white)						
	Sample #4 - Post test residual boiler fluid - color, pure white; 0.7% phthalate ester content ⁽⁶⁾						
	Sample #4 - Post test light end fractions from (boiler); color, pure white; 67% phthalate ester content						
VIII	4-18-73 Post test Michigan State cyclotron 9 yr old DC-106 oil samples (color, dark brown):						
	Sample #1 - Light end fractions from (boiler); color, clear white; 1.2% phthalate ester content						
	Sample #2 - Blurred heavy ends from evaporative surface; color, deep yellow; 0.77% phthalate ester content ⁽⁶⁾						

⁽¹⁾One percent is the least quantity detectable with any certainty, due to instrument system noise and no assurance that curve goes to zero

⁽²⁾A FT-20 infrared Fourier transform spectrometer was used to determine the phthalate ester content of the DC-106 silicone oil samples

⁽³⁾Perkin Palmer spectrophotometer.

⁽⁴⁾Statistical sources.

⁽⁵⁾Statistical sources.

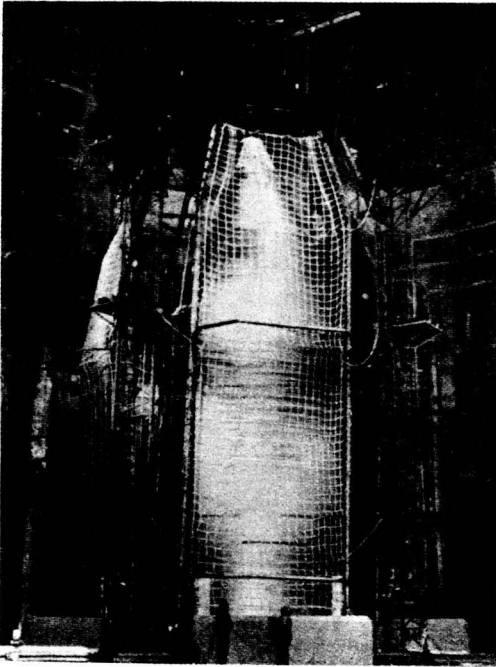


Figure 1. - Skylab payload shroud jettison test setup in SPF chamber.

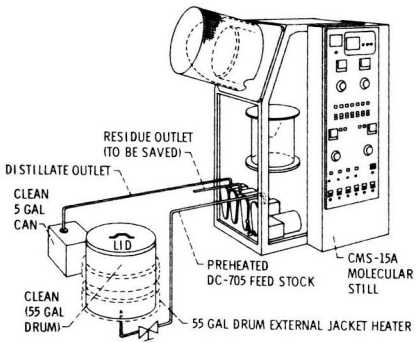


Figure 2. - Typical DC-705 reprocessing setup.

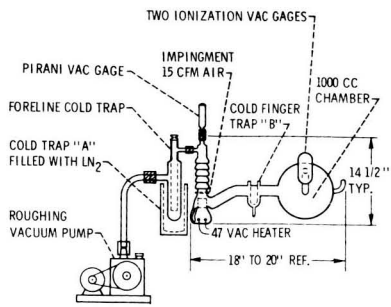
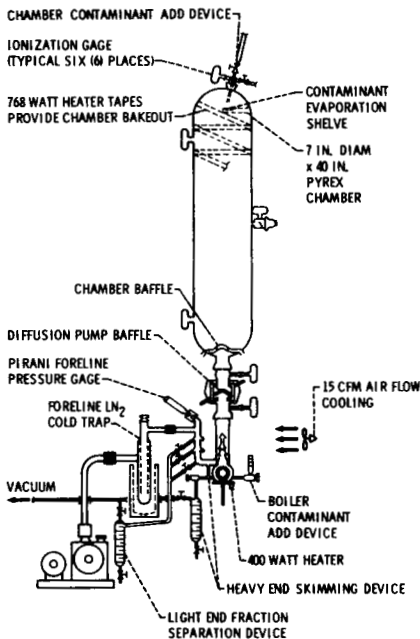
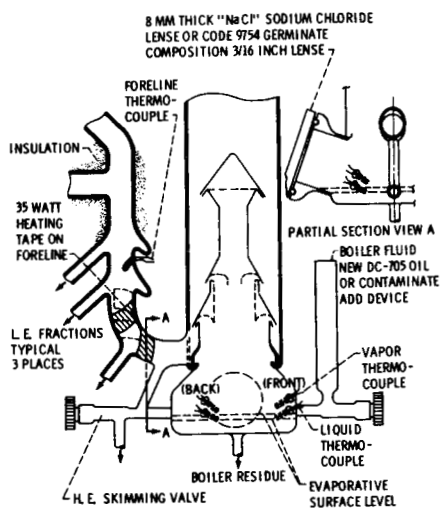


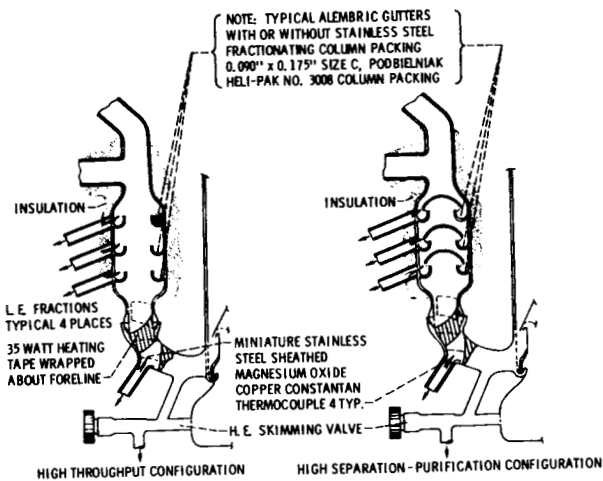
Figure 3. - Typical DC-705 oil performance evaluation setup.



(a) 1×10^{-6} SPF SCALE MODEL GLASS 2ND GENERATION VACUUM SYSTEM INCORPORATING CONTAMINATION REMOVAL TECHNOLOGY.



(b) EXPOSED VIEW OF 1×10^{-6} SPF SCALE MODEL GLASS 2ND GENERATION DIFFUSION PUMP INCORPORATING CONTAMINATION REMOVAL TECHNOLOGY.



(c) PARTIAL EXPOSED VIEW OF 1×10^{-6} SPF SCALE MODEL GLASS 2ND GENERATION DIFFUSION PUMP INCORPORATING CONTAMINATION REMOVAL TECHNOLOGY.

Figure 4

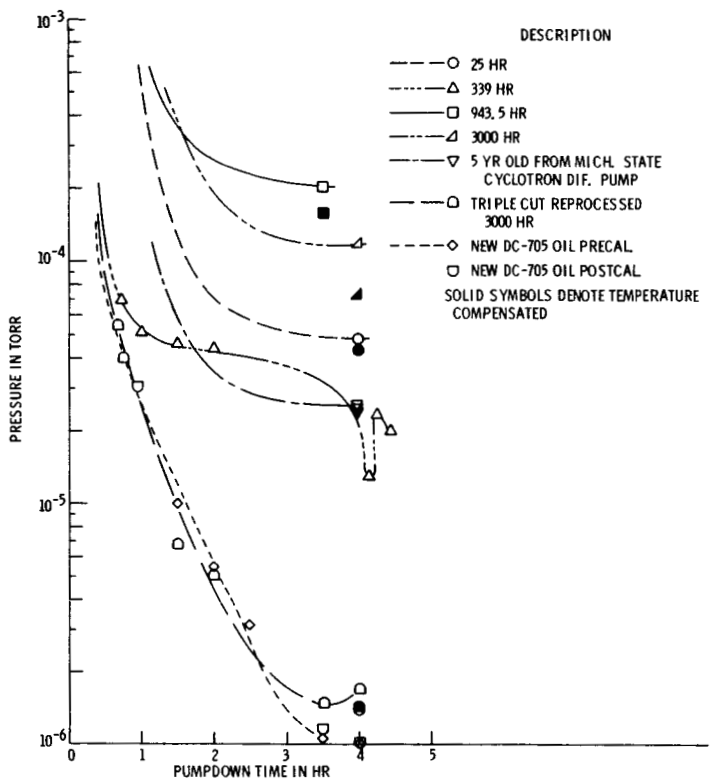


Figure 5. - Performance of DC-705 oil compared with new and reprocessed oil utilizing a (G-4) single stage glass diffusion pump.

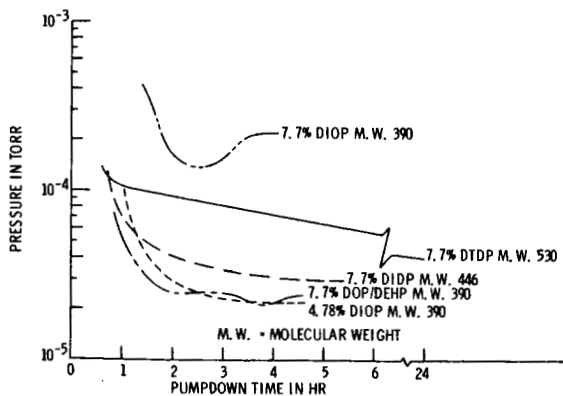


Figure 6. - Diffusion pump performance of DC-705 oil with various contaminants utilizing a (G-4) single stage glass diffusion pump.

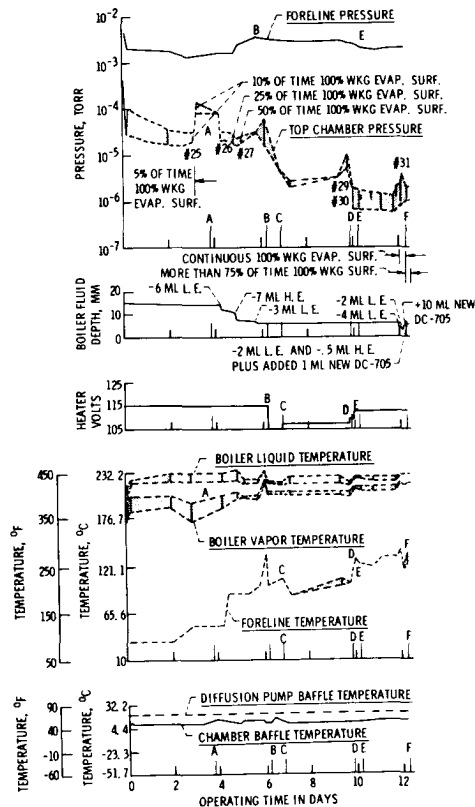


Figure 7(a). - Phase I, new DC-705 performance test data, increased purification of new DC-705 nets 1.5 decade.

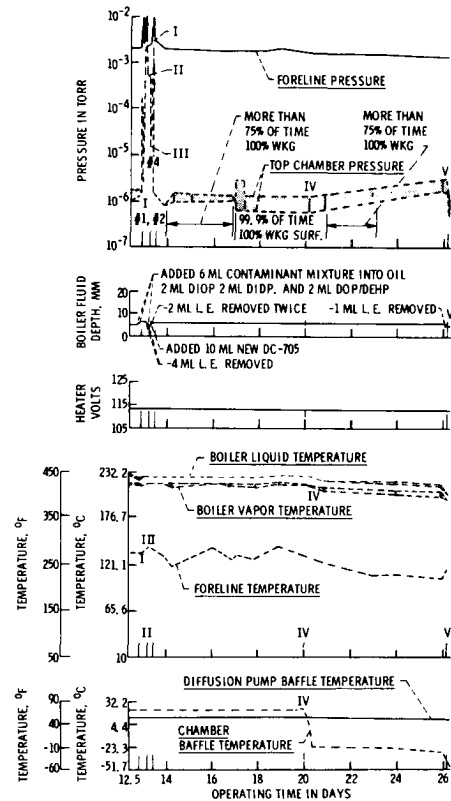


Figure 7(b). - Phase II, new DC-705 performance test data, plasticizer contaminants added into ultra pure DC-705 and their removal.

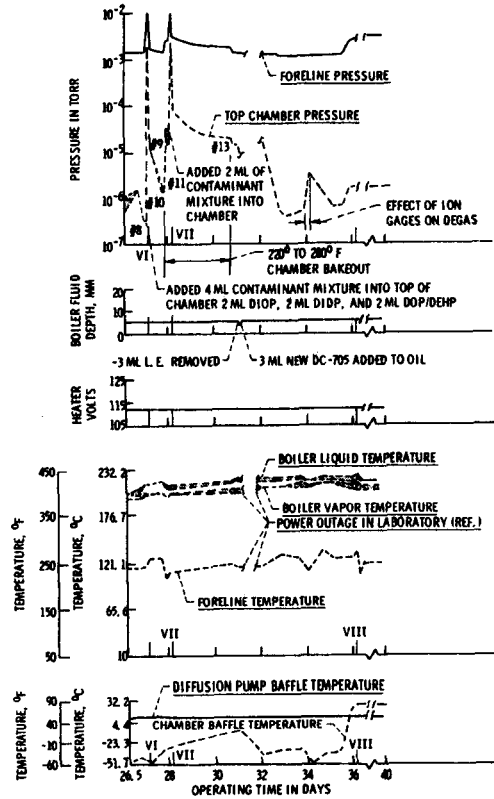


Figure 7(c). - Phase III, new DC-705 performance test data, plasticizer contaminants added into chamber and their removal with cold and warm baffles

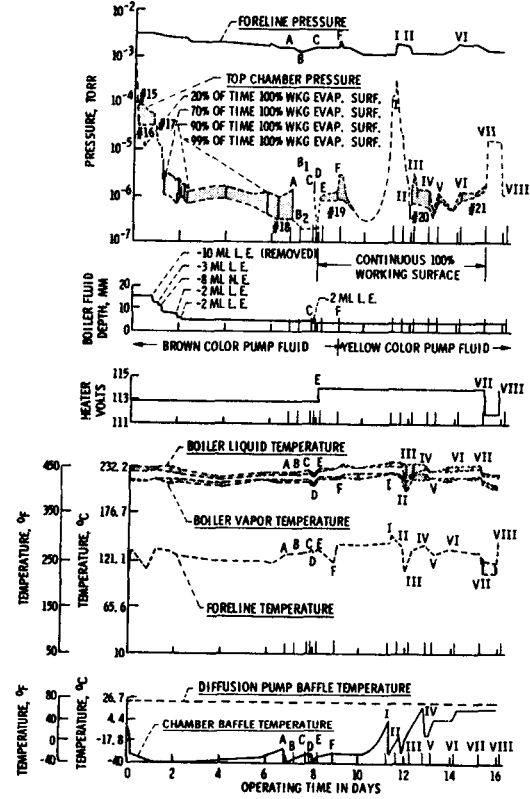
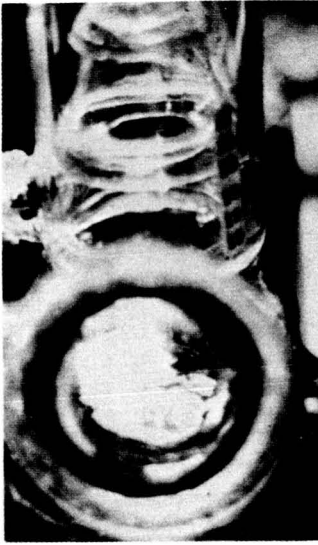
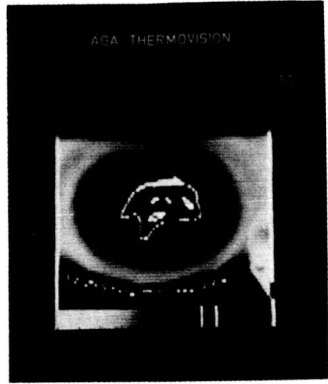


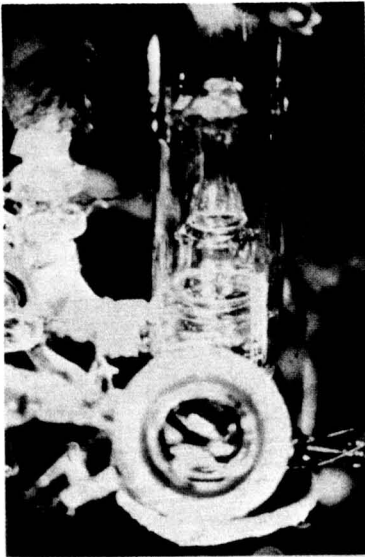
Figure 7(d). - 5 year old Michigan State cyclotron DC-705 oil performance test data with the 1x10⁻⁶ SPF scale model self-cleansing pump.



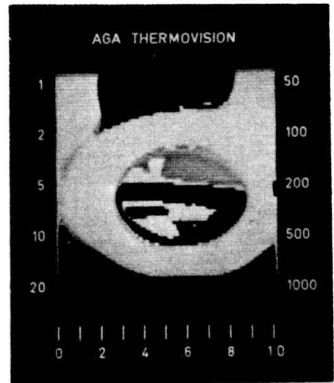
TORPID/SCHIZOID WORKING EVAPORATIVE SURFACE, VACUUM 2×10^{-4} TORR AT TOP OF CHAMBER. (PHOTOGRAPH # 15).



TYPICAL THERMOVISION MONITOR POLAROID PICTURE OF A TORPID/SCHIZOID/WORKING EVAPORATIVE SURFACE.



TORPID/SCHIZOID WORKING EVAPORATIVE SURFACE, VACUUM 10×10^{-2} TORR AT TOP OF CHAMBER. (PHOTOGRAPH # 16).

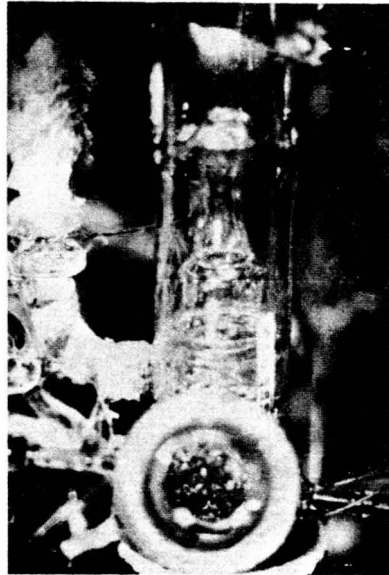


TYPICAL THERMOVISION MONITOR POLAROID PICTURE OF VAPOR BEING RELEASED FROM A WORKING HOLE.

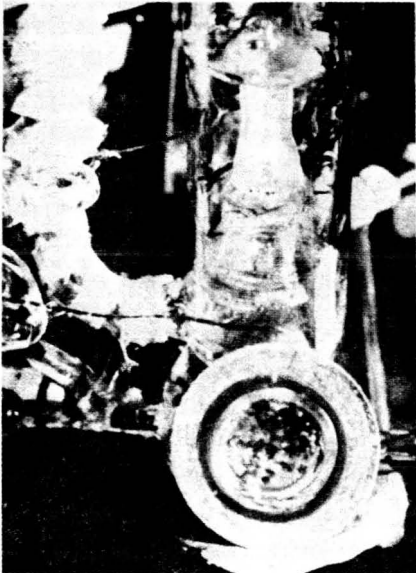
Figure 8. - Typical corresponding slide, thermovision/polaroid picture of a torpid/schizoid/working surface.



100 PERCENT WORKING EVAPORATIVE SURFACE (CONTINUOUS). VACUUM AT TOP OF CHAMBER 1.5×10^{-9} TORR, BAFFLE TEMPERATURE 70° F AT PUMP AND -25° F AT CHAMBER. (PHOTOGRAPH # 19)



100 PERCENT WORKING EVAPORATIVE SURFACE (APPROXIMATELY 20 PERCENT OF TIME), VACUUM AT TOP OF CHAMBER 5×10^{-9} TORR. (PHOTOGRAPH # 16)



100 PERCENT WORKING EVAPORATIVE SURFACE (CONTINUOUS) SAME CONDITIONS AS ABOVE BUT SURFACE APPEARS MORE DYNAMIC. (PHOTOGRAPH # 19)



100 PERCENT CONTINUOUS WORKING EVAPORATIVE SURFACE, VACUUM AT TOP OF CHAMBER 1×10^0 TORR, 20 TO 30 PERCENT OF BOILER BOTTOM APPEAR BARE DUE TO VAPOR RECOIL ACTION. (PHOTOGRAPH 21)

Figure 8. - Concluded.

PRECEDING PAGE BLANK NOT FILMED

Paper No. 22

**MULTI GAS CRYOPUMPING EXPERIMENTS IN A LIQUID
HELIUM COOLED SPACE SIMULATION FACILITY**

J. F. Cassidy, *NASA Lewis Research Center*

Paper not submitted in time for this publication.

Paper No. 23

**REAL-TIME, MULTIPROGRAMMABLE COMPUTER OPERATING
SYSTEM FOR SPACE SIMULATION FACILITY AND TEST CONTROL**

*N. T. Selvey, McDonnell Douglas Astronautics Company,
Huntington Beach, California*

ABSTRACT

The McDonnell Douglas Astronautics Company Engineering Laboratories have initiated an automation program to provide computer control of major space simulation facilities, test specimen operation and control, and special interactive monitor and control for complex facility/test operations.

Automation of the laboratory was initiated to provide increased technical capability; to provide accurate, reliable and uniform system performance; to provide continuous monitoring of critical parameters concurrently with test operations; and to reduce the manpower required to support test and facility operations. Another influencing factor in the decision to automate was the trend in space simulation testing toward long-duration test programs, some of which in this facility have run continuously up to 90 days.

Ground rules established for implementation of automated computer control included:

1. System must be planned with modular flexibility to allow controlled growth of both software and hardware.
2. The computer system must be capable of real-time control of multiple facility and/or test programs running simultaneously.
3. Retain independent, manual operating mode with hard-wired fail-safe protection of facilities.
4. Utilize existing equipment where possible for economic reasons while maintaining overall technical objectives.
5. Automated facilities must be capable of complete unattended operation for extended periods of time.

A Digital Equipment Corporation, PDP-15/40 computer was selected for the laboratory automation effort. The basic computer configuration included 32K of core, 500K words of disk storage, dual DEC tape units, paper tape reader and punch, line printer, card reader, and two teletypes. Software provided by the computer manufacturer included a real-time system executive for multi-task scheduling and control, I/O supervision and queuing, and on-line interactive system communication.

Engineering laboratory personnel established priority interrupt assignments, defined and installed multi-program memory partitions, and developed a memory-to-disk swapping technique. The swapping technique was developed to allow a task running in a particular memory partition to be swapped to the disk to allow a second higher priority task to run in that partition. The low priority task image is saved on the disk in a manner that allows it to be returned to a memory partition and continued from the point of interruption.

Two existing data systems, a 700 channel low-speed unit and a 64 channel high-speed device, were modified and interfaced to the computer. Digital inputs are handled by remote status monitoring devices and output commands by remote digital control units. The remote status monitors are sized at 48 channels each and the digital control units provide a total of 88 output commands. These units are located at use points throughout the laboratory and are interfaced to the computer via a master device controller. The device controller will accommodate up to 16 units each of status and control.

A cathode ray tube display was added to the system configuration to provide on-line, test monitoring and control. The display is a portable device which can be situated at the various chambers for remote on-line test support.

Implementation of the automation project was initiated in February 1972. Accomplishments to date include installation of the computer and associated system hardware; device controllers; and the interfacing of data systems, remote status monitors, digital control output units, and CRT display. System software has been completed along with common software programs such as data reduction and various operating sub-routines.

Automation of two 20°K Dense Gas Helium Refrigeration Systems has been completed. The 39-Foot space simulation chamber and an associated 300KW LN₂ subcooler system are near completion. Work has started on an 8 x 8 Ft ultra-high vacuum chamber, 50KW LN₂ subcooler and an "Advanced Sensor Evaluation and Test" facility.

This paper describes the development and implementation of a laboratory test and facility automation program. Computer hardware and software, data systems, digital control, status monitoring, interface hardware and facility modifications are described by detailing a typical automated control application.

Paper No. 24

**EXPERIENCES IN BRINGING ON-LINE A LARGE
SELECTIVELY PUMPED THERMAL VACUUM SPACE
SIMULATION CHAMBER**

E. K. Beck, Sr., A. A. Edwards, Sr., *Lockheed Missiles
and Space Company*

Paper not submitted in time for this publication.

PRECEDING PAGE BLANK NOT FILMED

Paper No. 25

A METHOD FOR PREDICTING BLAST WAVE OVERPRESSURE
PRODUCED BY RUPTURE OF A GAS STORAGE VESSELP. W. Garrison, *McDonnell Douglas Astronautics Company*

ABSTRACT

A method, based on a hydrodynamic solution to the spherical shock problem, is developed to predict blast wave overpressure. Generalized curves are presented that permit the application of this technique to a wide range of pressure vessel sizes and pressures. Safety analyses of high pressure system failures are normally based on scaled explosive data (TNT scaling). An evaluation of available experimental data indicates that the hydrodynamic model provides a better approximation of blast overpressures generated when a pressure vessel ruptures.

NOMENCLATURE

A	ACOUSTIC VELOCITY	ft/sec
E	ENERGY	ft-lb _f
K	SPECIFIC HEAT RATIO	
M	MACH NUMBER	
P	PRESSURE	psfa
ΔP	STATIC OVERPRESSURE	psi
R	RANGE	ft
R _o	SPHERE RADIUS	ft
t	TIME	sec
V	VOLUME	ft ³

SUBSCRIPTS

i	INITIAL CONDITIONS
f	FINAL CONDITIONS
1	PRESHOCK CONDITIONS
4	INITIAL "DRIVER" CONDITIONS; i.e., INITIAL VESSEL CONDITIONS

INTRODUCTION

Gas storage vessels constitute a potential safety hazard to facilities and personnel. In order to establish safety requirements for the operation of these systems, it is necessary to predict the damage that might be sustained in the event of a system failure. In such an analysis, unjustified conservatism can result in costly constraints on test operations while the failure to recognize the full damage potential of a system can result in unnecessary risk.

Two basic damage mechanisms exist in any explosion. There is damage produced by the resultant shock wave and shrapnel damage caused by fragments of the pressure vessel. The scope of this paper will be limited to the shock wave and specifically to overpressure of the primary shock

wave. A complete damage analysis requires consideration of blast wave impulse and positive phase duration as well as the natural and harmonic frequencies of the structure. Normally, this depth of analysis is not justified and incident overpressure in conjunction with established damage threshold data, Table I, is sufficient to establish safety criteria.

TABLE I
BLAST DAMAGE DATA

Type of Damage	Side-On Overpressure	Reference
Window Breakage (Lower Limit)	0.2	11
Structural Damage (Lower Limit)	0.4	11
Plaster Cracking	0.54	11
Eardrum Rupture	2.5	9
Lung Damage	6.0	9

TNT SCALING

The characteristics of the blast wave produced by the sudden release of a high pressure gas can be approximated by considering the blast produced by an "equivalent" amount of TNT. Expansion of a high pressure gas represents the release of energy. The magnitude of this energy is not only a function of initial and final pressures but is also a function of the thermodynamic path of the process. For a quasi-static expansion,

$$E = \int_{V_i}^{V_f} p dv \quad (1)$$

If an isentropic expansion of a calorically perfect gas is assumed, the available energy may be expressed:

$$E = \frac{V_i p_i}{K-1} \left[1 - \frac{p_i}{p_f} \frac{1-K}{K} \right] \quad (2)$$

In Figure 1 is presented the energy density (E/V) associated with the expansion of a gas from some initial pressure to a final pressure of one atmosphere. This energy can be expressed in terms of an equivalent weight of TNT (W_{TNT}). For this purpose, 1.0 lbm of TNT (Symmetrical Trinitrotoluene) is assumed to generate 1.425×10^6 ft-lb of energy.

Experimental TNT overpressure data are presented in Figure 2 for free air and surface bursts. The higher overpressures exhibited by the latter are the result of interactions between the incident shock wave and the ground. The effect of such interactions is to increase the apparent yield of the explosion. A completely unyielding surface, one that absorbs no energy from the explosion, effectively doubles the apparent yield by concentrating the released energy into a single hemisphere. Typical apparent yield factors range from 1.5 to 2.0 (Ref. 7).

The characteristics of a blast wave are unchanged if the scales of length and time by which they are measured are changed by the same factor as the dimension of the explosive charge. Therefore, two explosions which differ only in energy release will exhibit identical blast wave intensities at

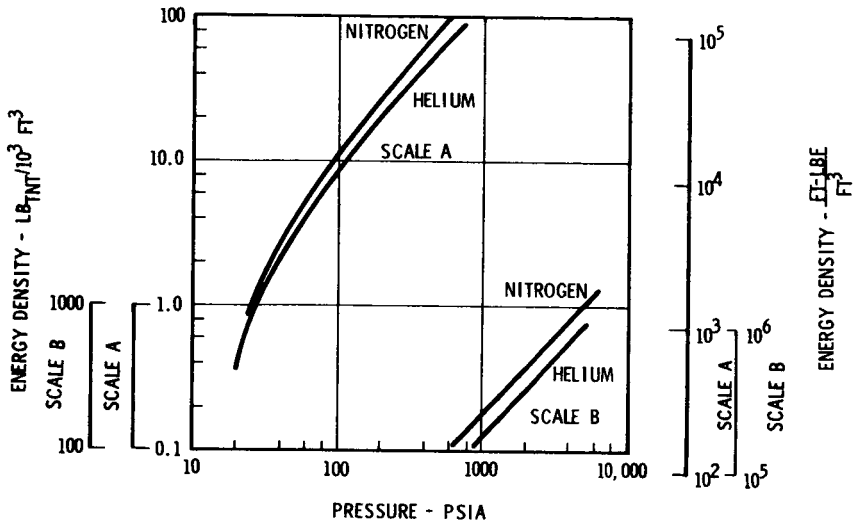


Figure 1. Pressure Vessel Energy

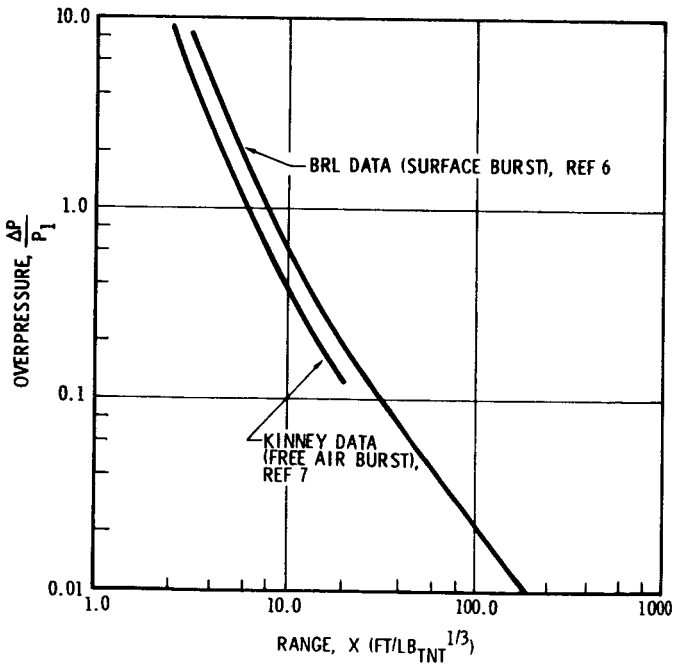


Figure 2. Overpressure Versus Scaled Distance for TNT

distances which are proportional to the cube root of the respective energy yields. This is expressed in terms of a range parameter, X, defined:

$$X = R/(W_{TNT})^{1/3} \quad (3)$$

TNT scaling permits the application of the data in Figure 2 to a wide range of explosive yields.

There is some question about the "equivalency" of a high explosive blast and the blast produced by the rupture of a pressure vessel. In a high explosive blast, a region of high pressure, high temperature gas is rapidly generated and subsequently expands into the surrounding environment. It is unlikely that the thermodynamic path followed by this process is the same as that followed by the "cold" gas of the latter case.

CHARACTERISTICS OF THE SPHERICAL SHOCK WAVE

The rapid release of a gas at an initial pressure in excess of atmospheric pressure is characterized by the formation of a spherical shock wave which propagates into the surrounding medium. As in the one dimensional problem, a centered expansion wave simultaneously propagates into the high pressure region. Unlike the one dimensional problem, a left facing secondary shock wave originates from the tail of the expansion wave, reflects from the origin as a right facing shock wave, and subsequently trails behind the primary shock wave, (Figure 3). The study will be confined to the primary shock wave which is of major concern in damage analysis.

There is an important difference between the one dimensional problem as characterized by the shock tube and the spherical shock problem. The former exhibits a constant shock intensity and the latter a rapid decay of shock intensity with distance. This decay is the result of the three-dimensionality of the spherical flow. The evolution of a spherical shock wave is illustrated in Figure 4. Here, a quantity of gas at a pressure in excess of atmospheric pressure is allowed to

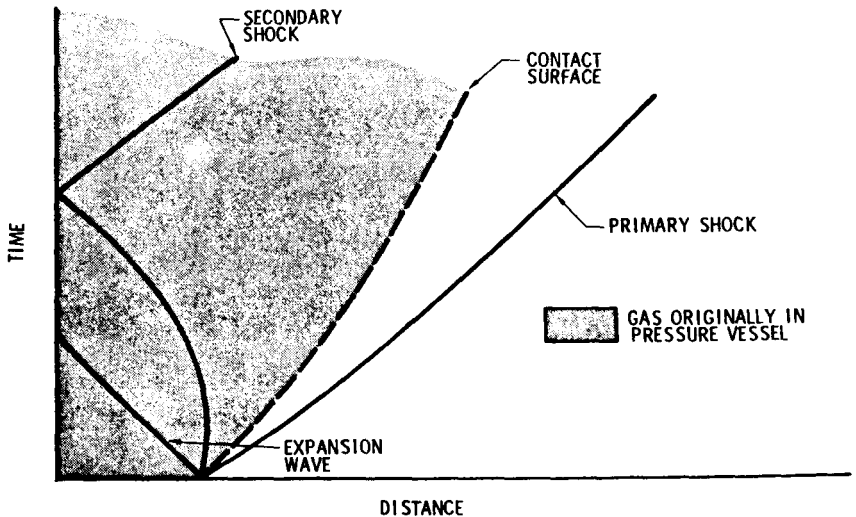


Figure 3. Space-Time Plot for Spherical Shock Wave

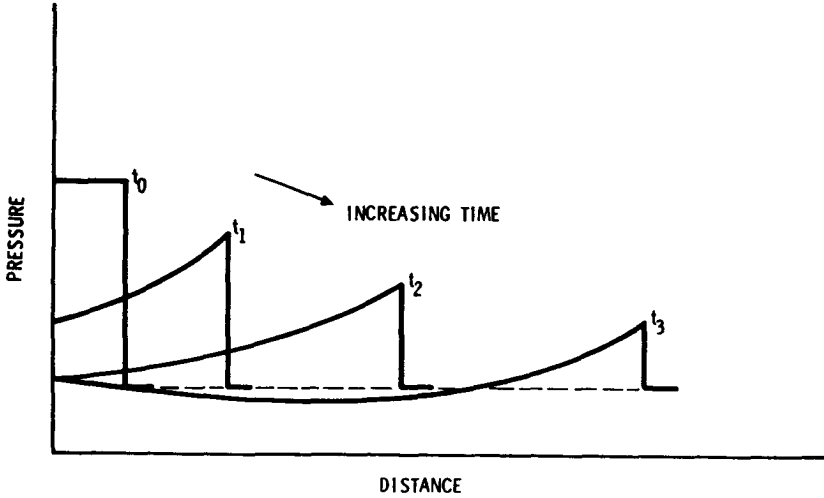


Figure 4. Overpressure Versus Distance

expand into the surrounding environment. The pressure disturbance is characterized by positive pressure discontinuity followed by a negative pressure phase of considerably less magnitude. The pressure history at a fixed station is depicted in Figure 5.

Along a streamline, a spherical shock is locally indistinguishable from a one dimensional normal shock such that jump conditions can be computed from the Rankine-Hugoniot relation.

$$\frac{\Delta P}{P_1} = \frac{2K_1(M^2 - 1)}{K_1 + 1} \quad (4)$$

Equation (4) gives the increase in static pressure across the shock front (overpressure) as a function of shock mach number.

HYDRODYNAMIC MODEL

A mathematical description of the spherical blast wave requires the solution of the full set of nonlinear partial differential equations representing conservation of mass, momentum and energy. Similarity solutions were first obtained for the hypothetical point source explosion by Von Neumann and Taylor. Brode (Ref. 3 and 4) developed a numerical solution to the finite source explosion based on the numerical integration of a set of finite difference equations for a specific set of initial and boundary conditions. Witham later developed an approximate set of differential equations which describe the relationship between shock strength and area for a shock wave moving through a channel with a varying cross-sectional area. Friedman's (Ref. 5)

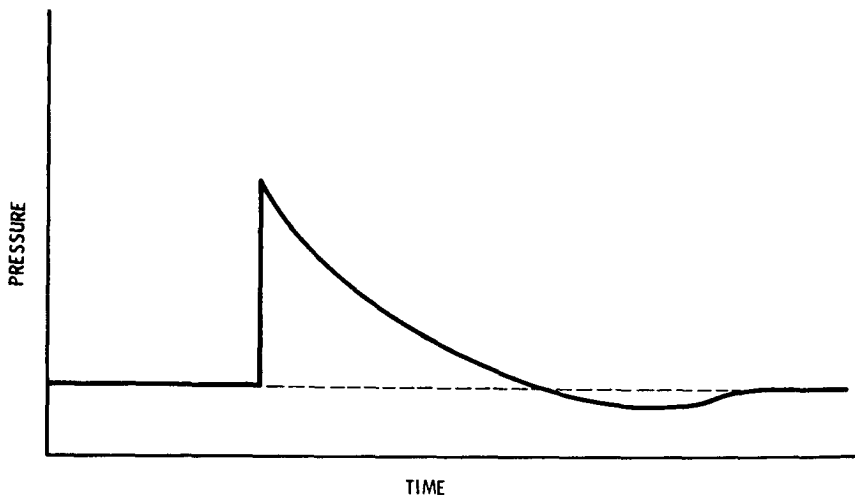


Figure 5. Overpressure at a Fixed Station

successful integration of these equations lead to the following closed form solution for the finite source problem:

$$\left(\frac{R^2}{R_0}\right) \frac{(Y-Z)^2}{M} [(K-1)^{1/2} Y + (2K)^{1/2} Z] (2K/(K-1))^{1/2} Y^{2/K} \cdot \text{EXP}(2K-2)^{-1/2} \text{SIN}^{-1} \left[\frac{2Y^2 - (K-1)Z^2}{(K+1)^2 M^2} \right] = \text{CONSTANT} \quad (5)$$

$$Y^2 = 2KM^2 - K + 1$$

$$Z^2 = (K-1)M^2 + 2$$

Given the initial position and magnitude of the shock wave, equation (5) can be used to describe the subsequent shock history. These initial conditions can be obtained from the one-dimensional shock tube equation.

$$\frac{P_4}{P_1} \left[1 - \frac{A_1}{A_4} \frac{K_4 - 1}{K_1 + 1} \left(M - \frac{1}{M} \right) \right]^{2K_4/(K_4-1)} = \frac{2K_1 M^2 - K_1 + 1}{K_1 + 1} \quad (6)$$

Equation (6) is presented graphically in Figure 6 for nitrogen and helium drivers (Region 4). In this equation, Region (4) refers to conditions in the unruptured pressure vessel and Region (1) refers to the external environment into which the shock propagates. From this equation, the

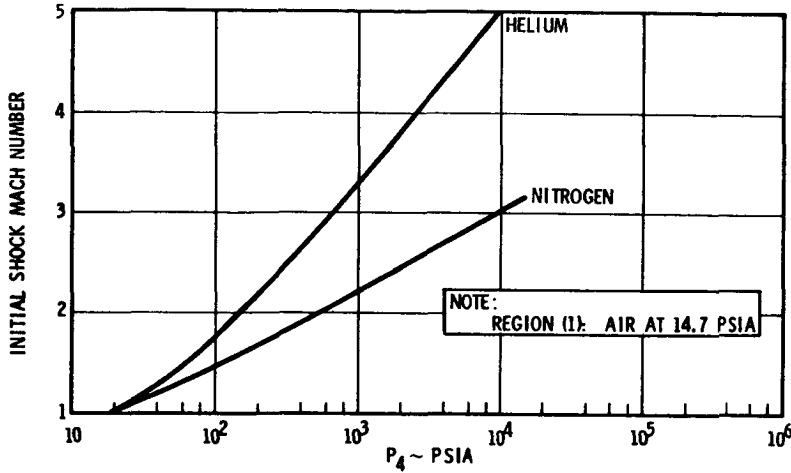


Figure 6. Initial Shock Intensity Versus Burst Pressure

initial mach number at $R/R_0 = 1$ can be computed and the constant of integration in equation (5) can be evaluated. Once the mach number at a given station is established, equation (4) can be employed to compute the corresponding overpressure. Solutions to equations (4) through (6) are presented in Figures 7 and 8 for helium and nitrogen drivers (Region 4). In both cases, the Region (1) medium is assumed to be air at one atmosphere.

It should be emphasized that the Friedman-Witham solution is approximate and does not take into account the weakening effects of disturbances which originate in the flow field behind the shock wave. Brode's numerical solution does account for these effects and differs only slightly from the approximate theory in its description of the initial motion of the shock wave. The effects of such disturbances can become more pronounced at distances far removed from the blast. Care should be exercised, therefore, in applying the model at ranges significantly beyond those verified by data.

EXPERIMENTAL DATA

Experimental data from four sources are summarized in Table II. Boyer's data (Ref. 1 and 2) are based on small glass spheres which were pressurized (326 psia and 400 psia) with air and ruptured in a one atmosphere (air) environment. Kornegay's experiments (Ref. 8) also utilize small glass spheres. These spheres were filled with air at approximately one atmosphere and ruptured in a low pressure chamber at 2.0 and 5.0 torr. The Pittman data (Ref. 10) are based on the burst tests of five full scale pressure vessels. Burst pressures ranged from 640 to 8145 psia. The Altas data (Ref. 9) are included to demonstrate the application of the two blast models to a large scale pressure vessel. These data were obtained from the explosive failure of a full scale missile pressurized to 49.7 psia with nitrogen.

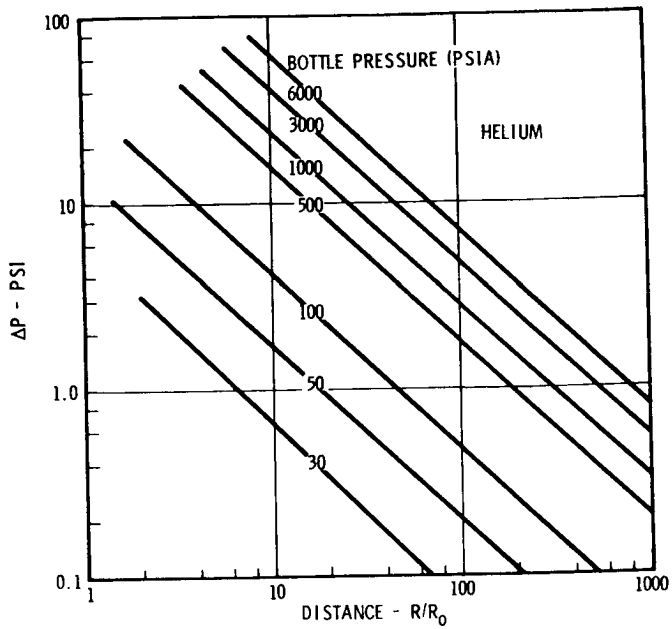


Figure 7. Blast Wave Overpressure for Bottle Rupture - Friedman Witham Model

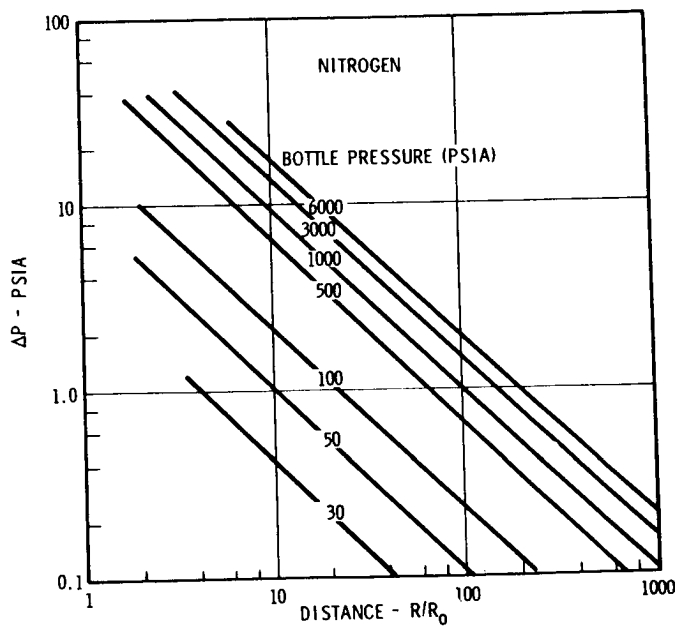


Figure 8. Blast Wave Overpressure for Bottle Rupture - Friedman-Witham Model

TABLE II
EXPERIMENTAL DATA

Source	Run	Volume (ft ³)	R ₀ (ft)	Gas	P ₄ /P ₁	P ₄ (psia)	E (lbs TNT)
Atlas (Ref. 9)		4050.0	9.89	N ₂	3.38	49.7	14.9
Boyer (Ref. 1 & 2)	a	2.27 X 10 ⁻³	0.0815	Air	22.2	326	1.1 X 10 ⁻⁴
	b	2.27 X 10 ⁻³	0.0815	Air	27.2	400	1.4 X 10 ⁻⁴
Kornegay (Ref. 8)	a	1.37 X 10 ⁻⁴	0.032	Air	425	16.4	1.78 X 10 ⁻⁴
	b	1.37 X 10 ⁻⁴	0.032	Air	130	12.6	4.97 X 10 ⁻⁵
Pittman (Ref. 10)	a	1.34	0.684	N ₂	43.5	640	0.143
	b	1.68	0.738	N ₂	41.8	615	0.171
	c	0.235	0.383	N ₂	545	8015	0.397
	d	6.0	1.127	N ₂	545	8015	10.14
	e	6.0	1.127	N ₂	554	8145	10.3

Calculations based on TNT scaling and the hydrodynamic model have been made for initial conditions corresponding to the experimental data. In each case, lower overpressures are predicted with the hydrodynamic model than with TNT scaling for the initial stages of the blast wave. For the TNT model, decay is more rapid as the shock propagates outward. At distances removed from the origin, overpressures are predicted with the hydrodynamic model that exceed those indicated by TNT scaling.

In applying the hydrodynamic solution to non-spherical pressure vessels, it has been assumed that the blast wave assumes the characteristics of wave produced by a spherical vessel of the same volume at some distance from ground zero.

No attempt has been made to account for the kinetic energy associated with the fragments of the pressure vessel produced by the explosion. This represents a reduction in the energy associated with the blast wave but is a quantity that cannot easily be established. Based on Schlieren records (Ref. 1), Boyer estimates that 16 percent of the total energy is found in the kinetic energy of the fragments. It appears likely that the percent of the total energy that is transferred to the fragments is not constant but is a function of the failure mechanism, tank geometry, and tank material. In this report, the conservative approach will be taken, i.e., it will be assumed that all the energy is involved in the blast wave. The uncertainty associated with this variable may be responsible for some of the scatter observed in the experimental data presented.

Blast wave interaction with the ground plane must be taken into account for the Pittman and Atlas data (Ref. 9 and 10). For these cases, the BRL surface burst data (Figure 2, Ref. 6) is used

for TNT scaling. The hydrodynamic model does not account for interactions between the blast wave and the ground plane. Therefore, an apparent yield factor must be established to account for this effect. During the Pittman test, a series of known TNT charges were exploded to evaluate the interaction coefficient. From these data, a coefficient of 1.5 was determined. This apparent yield factor was used in conjunction with the hydrodynamic model for both the Pittman and Atlas calculations. The effective pressure vessel volume for these tests is 1.5 times the actual volume. The range scale computed by the hydrodynamic model (free air burst) is increased by a factor of $(1.5)^{1/3}$ to account for the ground effect.

Figures 9 through 15 present data from these four sources and corresponding predictions based on TNT scaling and the hydrodynamic model. The Atlas data (Figure 9) falls in a region where the two models are indistinguishable and provide no information concerning the relative merit of the two models. It does, however, demonstrate that overpressure prediction techniques under investigation can provide a reasonable approximation of blast wave overpressure for a large volume (4050 ft³), low pressure (49.7 psia) tank rupture.

Boyer's data (Figures 10 and 11) were taken in the region where the hydrodynamic solution exceeds the TNT model. These data fall below the TNT prediction. Insufficient data were taken to provide any information concerning the relationship between overpressure and range.

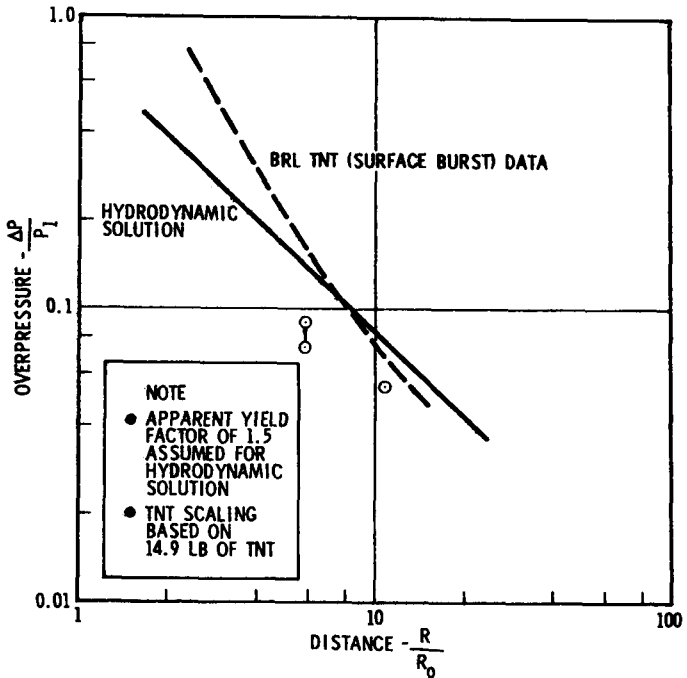


Figure 9. Atlas Data

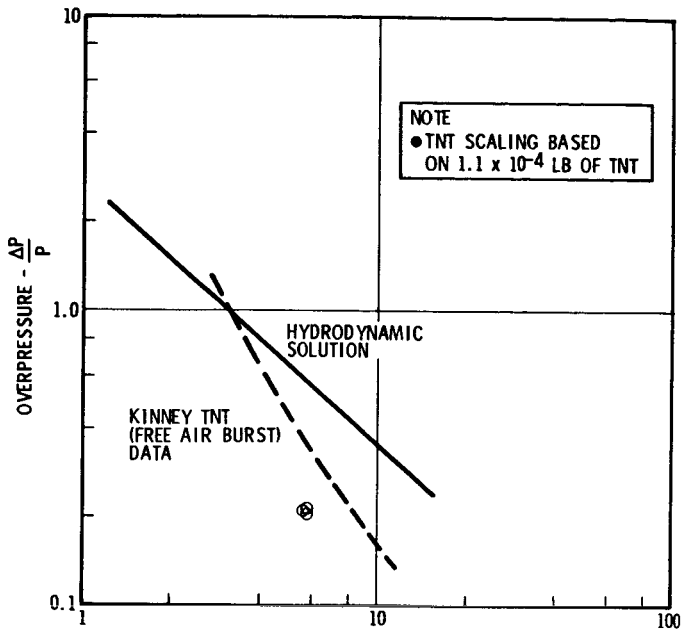


Figure 10. Boyer Data - Run (A)

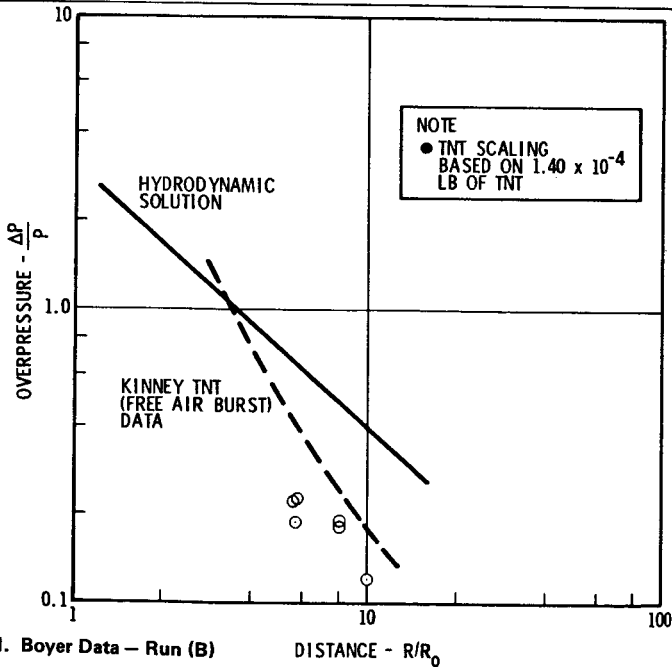


Figure 11. Boyer Data - Run (B)

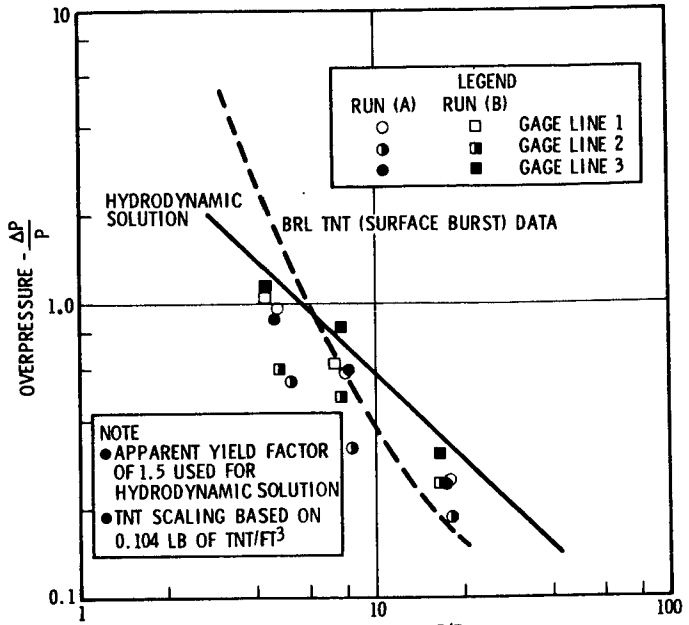


Figure 12. Pittman Data - Run (A) and (B) DISTANCE - R/R_0

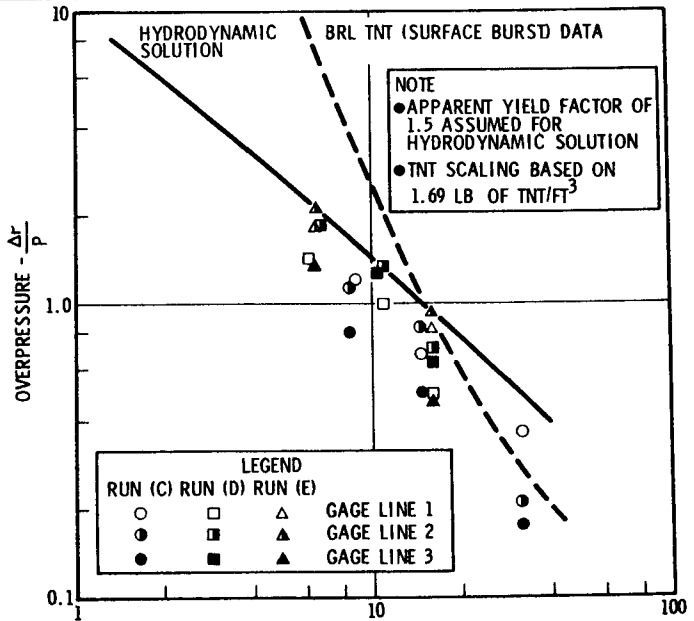


Figure 13. Pittman Data - Runs (C) - (E) DISTANCE - R/R_0

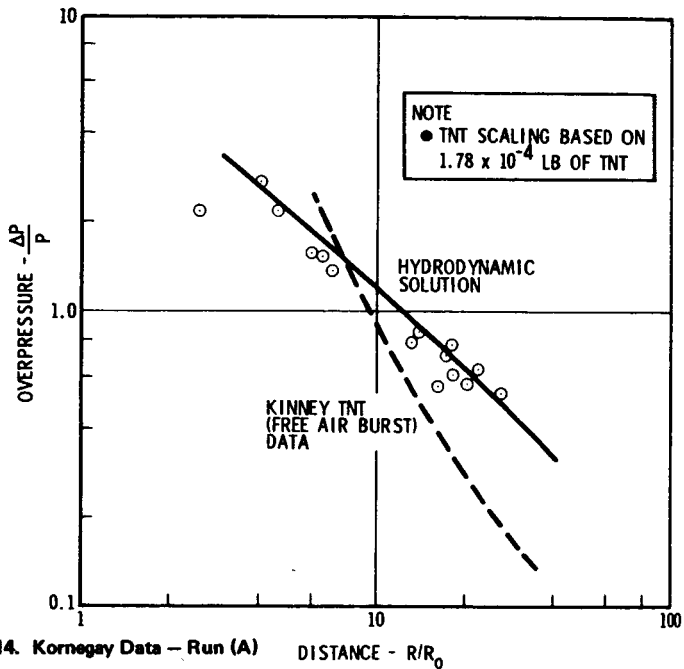


Figure 14. Korngay Data - Run (A)

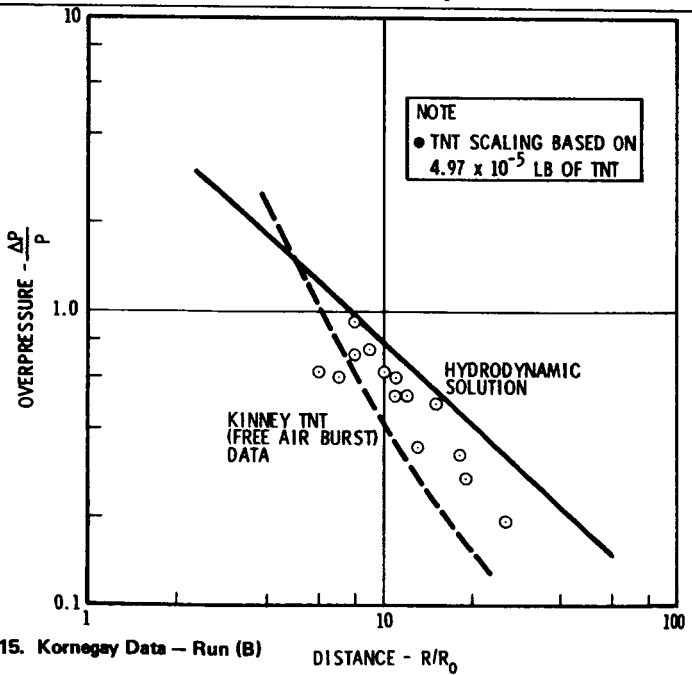


Figure 15. Korngay Data - Run (B)

Two of Pittman's tests (Figure 12) were conducted at burst pressures (640 psia and 615 psia) not significantly different from those of the Boyer test (326 psia and 400 psia). Pittman's data, taken in this same region (R/R_0), fall above the level predicted by TNT scaling. Pittman's data taken near the origin are significantly less than that predicted by TNT scaling and agrees well with the hydrodynamic model. Pittman's three tests conducted at approximately 8000 psia (Figure 13) follow the same trend and provide a large number of data points which support the lower overpressure predicted by the hydrodynamic model for stations near the origin. Pittman's data were taken along three equally spaced radial lines extending from the center of the pressure vessel. Different overpressures were measured along different gage lines. A lack of symmetry in the shock front is indicated. This asymmetry is most likely a result of the asymmetric failure of the pressure vessel.

Kornegay's experiments, Figure 14 and 15 were conducted at moderate pressure ratios ($P_4/P_1 = 130$ and 425). These data agree quite well with the magnitude and slope predicted by the hydrodynamic model.

CONCLUSION

This analysis indicates that the TNT scaling technique does not adequately describe the pressure vessel burst problem. Overpressures predicted by this method are unrealistically high for stations near the pressure vessel and too low for stations far removed. The hydrodynamic solution (Friedman-Witham) provides a better correlation with available data in both regions.

Overpressure is directly related to damage potential in an accidental rupture of a pressure vessel. If the region of interest is near the blast, the proposed method, Figures 7 and 8, may permit some relaxation of constraints placed on test operations by conventional blast analysis (TNT scaling). At distances removed from the blast, the hydrodynamic model will assure that the full potential of the blast wave is taken into account. The hydrodynamic solution (Friedman-Witham) presented in this report is approximate and may be overly conservative at distance significantly beyond those empirically verified.

REFERENCES

1. D. W. Boyer, H. L. Brode, I. I. Glass, and J. G. Hall. Blast from a Pressurized Sphere. University of Toronto Institute of Aerophysics, Report No. 48, January 1958.
2. D. W. Boyer. An Experimental Study of the Explosion Generated by a Pressurized Sphere. *Journal of Fluid Mechanics*, August 16, 1960.
3. H. L. Brode. Numerical Solution of a Spherical Blast Wave. Report No. P-452, The Rand Corporation, Santa Monica, California, November 10, 1953.
4. H. L. Brode. The Blast from a Sphere of High Pressure Gas. Report No. P-582, The Rand Corporation, Santa Monica, California, January 27, 1955.
5. M. P. Friedman. A Simplified Analysis of Spherical and Cylindrical Blast Waves. *Journal of Fluid Mechanics*, Volume II, 1961.
6. C. N. Kingery and B. F. Pannill. Peak Overpressure vs. Scaled Distance for TNT Surface Bursts (Hemispherical Charges). BRL Memorandum Report No. 1518, Ballistic Research Laboratories, Aberdeen Proving Grounds, Maryland, April 1964.
7. G. F. Kinney. Explosive Shocks in Air. The MacMillan Company, New York, 1963.
8. W. M. Kornegay. Production and Propagation of Spherical Shock Waves at Low Ambient Pressures. Technical Report 375, Massachusetts Institute of Technology, Lincoln Laboratory, Lexington, Massachusetts, January 26, 1965.
9. H. Moskowitz. Blast Effects Resulting from Fragmentation of an Atlas Missile. AIAA Paper No. 65-195, AIAA/NASA Flight Testing Conference, Huntsville, Alabama, February 15-17, 1965.
10. J. F. Pittman. Blast and Fragment Hazards from Bursting High Pressure Tank. Report No. NOL-TR-72-102, May 17, 1972.
11. Criterion For Locating SIVB Testing Facilities at SACTO, Douglas SM42365, September 1962.

N74-10254

PRECEDING PAGE BLANK NOT FILMED

Paper No. 26

LEAK TESTING OF HIGH PRESSURE OXYGEN AND NITROGEN TANK SYSTEMS FOR THE SKYLAB AIRLOCK*

R. A. Dutton, G. L. Adlon and R. K. Weinberger,
McDonnell Aircraft Company, St. Louis, Missouri
R. G. Morris, Jr., *McDonnell Douglas Astronautics*
Company, Eastern Division, St. Louis, Missouri

ABSTRACT

An existing Propulsion Test facility was modified for use as a leak test facility for acceptance testing of the 3000 psig oxygen and nitrogen gas storage tank systems used on the Skylab Airlock U-1 and U-2 Vehicles. Leak rates in the range of 10^{-2} to 10^{-5} standard cc/sec of helium were measured remotely from an explosion containment test cell. Selection of the test site was based on consideration of techniques, equipment, potential test hazards, leak measurement methods, and the availability of existing applicable equipment from prior test programs. Facility design, operating experience, and test results are discussed.

INTRODUCTION

The life support atmosphere of the Skylab Orbital Workshop is supplied by six oxygen and six nitrogen tank assemblies mounted on the Airlock. Each tank is pressurized to 3000 psig with gas prior to launch. The maximum allowable equivalent helium leak rate at 3000 psig for each tank assembly, including its valve package, is 10^{-2} standard cc/sec.

Although the tanks themselves were leak checked by their suppliers prior to delivery to MDC, additional hydrostatic and leak testing was required after installation of the valve packages and associated pressure transducers at MDC. The tanks were received at MDAC-E and the valve package attached by brazing. The brazed joint connection was designed to permit replacement of a defective valve package without danger of damaging the tank or valve package. The leak test program was designed to assure that the entire tank assembly, including its valve package, was ready for installation on the Airlock vehicle without the necessity for subsequent leak checking.

*This paper is related to work performed under NASA Contract NAS 9-6555.

Although numerous smaller high pressure tanks had been pressure and leak tested in previous programs, none of them presented as much damage potential in the event of tank or valve package failure. Therefore, special precautions were taken to reduce the risk of harm to personnel and facilities.

TEST SPECIMEN DESCRIPTION AND SAFETY CONSIDERATIONS

The oxygen tanks are constructed with a 321 stainless steel liner reinforced by a filament wound fiberglass-epoxy shell bonded to the liner. The nominal external dimensions are 45 in. diameter and 90 in. long. Minimum internal volume is 57 ft³. The tank assembly weight does not exceed 2500 pounds. Nitrogen tanks are fabricated from titanium hemispheres welded together at their circumference. The nominal external diameter of each spherical nitrogen tank is 41 in., and the minimum internal volume is 19.28 ft³; tank assembly weight did not exceed 393 pounds. The tanks and their control valve packages were hydrostatically tested, prior to leak measurement, with Freon PCA (Precision Cleaning Agent) to 1.50 times the 3000 psig working pressure (or approximately 4500 psig). The nitrogen tank design pressure considerations were 3000 psig working, 5000 psig proof, and 6660 psig burst at 70°F. The oxygen tank assembly design pressure considerations were 4500 psig working, 7530 psig proof and 10,000 psig burst.

Freon PCA was used for three reasons: (1) to avoid potential tank weakening which can occur if, for example, methyl alcohol is used to hydrostatically test titanium tanks at high pressure, (2) to avoid potential corrosion problems of valve packages when water is used, and (3) to permit thorough removal of the hydrostatic test fluid after testing. The nitrogen tanks have an operating temperature range of -20 to 160°F. The oxygen tanks have a similar temperature restriction but with an additional requirement to avoid temperature changes in the liner of 1°F per minute or more, which might cause debonding of the tank liner from its reinforcing filament wound fiberglass-epoxy reinforcement.

An initial examination of the potential hazards of leak testing large high pressure tanks revealed that it would be unwise to conduct the work in a conventional building. The types of tanks to be tested had exhibited excellent safety records in previous programs and the likelihood of tank rupture was considered very slight. However, tank rupture due to flaws, human error, or any other cause could produce catastrophic results in a conventional laboratory. For example, calculations indicated that the 19.28 ft³ nitrogen tank at 3000 psig contained potential energy equivalent to 14.0 pounds of TNT. The 57 ft³ oxygen tank at 3000 psig contained the energy of approximately 41.0 pounds of TNT, although, due to the type of tank construction, the energy might be released at a slightly less explosive rate.

The need to perform the leak tests in a remote safe facility became evident. A high pressure fuel test facility with a 7 ft diameter vacuum chamber became available from another program. The chamber was located in a test cell designed for explosion containment. Cell operations could be monitored and controlled from an adjacent control room. A study showed that the facility could be modified economically within the available schedule time.

The test cell chosen had been designed to withstand an internal pressure 225 psi above normal atmospheric pressure without rupturing the walls and without forcing the doors open. Calculations indicated the possibility that in the event of a tank failure, shrapnel could acquire enough energy to damage but not penetrate the foot-thick cell walls which were constructed of concrete with two independent grids of 1-1/4 in. diameter steel rods on 9 in. centers. The cell doors, made of steel I-beams with welded steel facing plates and filled with concrete, were secured with massive locking plates at their top and bottom. Part of the control cell was separated from the test cell by two reinforced concrete walls, one on each side of an access hallway. The most conservative calculations indicated the possibility that impact of large pieces of shrapnel with the inside surface of the test cell wall might cause spalling of concrete from the opposite side of the wall. Therefore, a barrier of sand bags was erected parallel to the single wall separating a portion of the test cell from the control cell.

SURVEY OF LEAK TEST METHODS

Various ways were considered to measure leak rates of the tank systems. The chamber rate of pressure rise method with the chamber vacuum pump operating was found to be too insensitive and unsteady to measure 10^{-2} standard cc/sec of gas leakage over any reasonable time span. Chamber leakage, chamber outgassing, test article outgassing, chamber temperature changes, and tank system temperature changes (principally heating during the filling process) would have obscured the measurement of the small allowable leakage.

Comparison of tank leakage into a chamber with leakage from a reference manometer was found to be theoretically sensitive enough, but would have been subject to some of the same uncertainties as for the chamber rate of rise method. In both cases, the source of the gas could not be determined to be actual tank system leakage instead of a combination of leakage and outgassing.

A variation of the chamber rate of pressure rise was considered in which the chamber would be evacuated and then sealed off from its pump. Its rate of rise due to leakage, outgassing, etc., would be measured and plotted as a function of time. Then the tank system would be pressurized and the new chamber rate of pressure rise would be plotted. The difference in the slopes of the curves would be interpreted as tank system leakage. This

method would not distinguish accurately between actual tank leakage and outgassing due to tank heating.

Various techniques of bagging the tank system to collect helium leaking from the tank system were considered, but were found to be too insensitive and uncertain for good quantitative results. Helium permeation through the bag and helium nonuniformities within the bag would have been difficult to determine.

A technique was considered in which the tank system would be enclosed within an inner chamber containing its own ion gauge. The inner chamber would be within a conventional space chamber with its ion gauge. The inner chamber would have a gas inleak system and a solenoid valve between the inner and outer chambers. During initial evacuation the solenoid valve would be open to equalize pressures in both chambers; then the solenoid valve would be closed. During a leak test, the rate of rise of the inner chamber relative to the outer chamber would be a measure of the tank system leakage. A measured flow of gas from the inleak system would be used for reference purposes to calibrate the leak rate.

A somewhat similar system using two ion gauges in series, with a passage of known conductance between them, could be used to measure the gas flow from a test article in the inner chamber to the outer chamber. This principle is used in calibrating ultrahigh vacuum gauges by extrapolation of the response of two standard gauges operating within their normal ranges.

All of the methods mentioned above in this section have various drawbacks, particularly the inability to distinguish between true tank system leakage and gas flow from other sources such as outgassing of tank and chamber materials.

The method selected for the leak test program was that of placing the tank system in a vacuum chamber, pressurizing the tank with a mixture of 10% helium and 90% nitrogen, and then measuring the helium leaking into the chamber.

A further description of various leak detection methods used in the Space Systems Laboratory at MDC has been presented elsewhere.¹

FACILITY DESIGN REQUIREMENTS AND ASSEMBLY

A portion of the propulsion test facility which was available for modification for leak testing is shown in plan view in Figure 1. The 7 ft diameter vacuum chamber in Cell 8, normally evacuated only by the mechanical pumps and blowers in the adjacent vacuum system room, was modified to provide high vacuum and leak measurement capability.

The tank system specifications required that each tank, including valve package and pressure and temperature transducers, have an equivalent helium leak rate no greater than 10^{-2} standard cc/sec. With the concurrence of the Airlock Project, a mixture of helium and nitrogen was chosen for leak testing; this was considered acceptable provided that the total gas pressure was 3000 psig and that proper allowance was made for the ratio of helium to nitrogen. Since actual leakage through passages of fixed

geometry was of interest, and since permeation due to diffusion was not a factor for the test articles, a gas mixture was considered to give results substantially as accurate as could be obtained with pure helium. The accuracy and reliability were of primary concern and were established by calibration prior to the test of each tank system. In order to obtain leak rate measurements greater than and less than the allowable maximum of 10^{-2} standard cc/sec, the leak measurement system was designed to measure from less than 10^{-5} to 10^{-2} standard cc/sec equivalent leakage of 100 percent helium. The actual gas mixture used was 10% helium and 90% nitrogen; thus, the leak detector response was an order of magnitude less than it would have been with pure helium. The system was calibrated with a 10^{-3} standard cc/sec leak using 100% helium. Thus the system could be adjusted to measure the maximum allowable leak without encountering detector saturation problems. The system background level was also determined and taken into account to provide for full-range calibration.

The modified system is shown schematically in Figure 2. A 32-in. diameter oil diffusion pump and its associated water-cooled elbow and liquid-nitrogen cooled anti-backstreaming baffle, reclaimed from another deactivated chamber, were added to provide chamber pressures in the 10^{-5} to 10^{-6} torr range. DC-704 silicone pump fluid was used in the diffusion pump. A 130-cfm mechanical pump was used to back the diffusion pump during initial chamber evacuation and during leak detection measurements when the total gas flow from the chamber exceeded the throughput capability of the leak detector. Remote-controlled motorized valves were added to permit the leak detector to share as much as possible of the gas load from the chamber for maximum sensitivity. The original leak detector installation involved separating an NCR series 925-50 leak detector into its modular components. These components included a sensing section (cold trap, diffusion pump, ionizer, collector, etc.), which was installed in the test cell, and a control and instrumentation electronics section, which was installed in the control room. The leak detector was backed by a 15 cfm foreline pump in the test cell. To provide additional protection of the leak detector from contamination, an external liquid nitrogen cold trap was installed between it and the chamber system foreline. All system controls requiring operation during the test were located in the control room or non-hazardous areas for safety.

The liquid nitrogen system which serviced the facility cold traps is shown schematically in Figure 3. The internal cold trap inside the leak detector was filled manually prior to pressurization of a tank system and did not require refilling during a normal test. The other cold traps were kept filled automatically by remote-controlled liquid level sensors.

The helium and nitrogen gas pressurization system is shown in Figure 4. This system permitted the tank system to be pressurized to 300 psig with helium from gas cylinders and to the

full 3000 psig test pressure by the addition of gaseous nitrogen produced by vaporization of high pressure liquid nitrogen.

The vacuum chamber and leak detector combination was provided with a positive means to accurately calibrate the response of the entire system to known helium flow rates. This calibration was in addition to the normal leak detector tuneup and calibration procedures, and was based on fundamental primary standards. The calibration system is shown schematically in Figure 5. Later, in the test program, a second independently operated Veeco helium mass spectrometer leak detector was added to the system to verify the results obtained with the original leak detector and to act as a spare in case of instrument malfunction. The system calibrator located on the chamber was used to calibrate both leak detectors simultaneously.

Prior to the first tank system leak test, the facility was checked out to see that all equipment functioned as planned, and training sessions were conducted to familiarize test personnel with equipment and procedures. A detailed operating test procedure was prepared which included normal operations, emergency procedures, safety precautions, checkoff lists, etc.

TEST OPERATIONS

Prior to a test run, the calibration of all instrumentation was certified as up to date and the proper functioning of the test equipment was verified.

Installation of an oxygen tank system is shown in Figure 6. A transportation dolly was used to bring the tank to the chamber; the tank then was raised to the chamber level and the dolly rails were aligned with mating rails inside the chamber. Installation of a nitrogen tank system is shown in Figure 7. The quilted fiberglass blanket on the nitrogen tank was removed prior to leak testing. The nitrogen tank valve package with pressure transducers is mounted on the front boss of the tank.

Thermocouples were taped to the nitrogen tank to provide additional information during the pressurization and depressurization process. Temperature sensors were attached to the oxygen tank during assembly by the manufacturer.

After installation of a tank system in the chamber, all gas lines inside the chamber were checked for leaks, using a sniffer probe attached to a leak detector. Prior to "sniffing", the lines were pressurized first to 2000 psig with helium, and the pressure was increased to 3000 psig with nitrogen. These tests were conducted with the tank system manual fill valve closed to avoid pressurizing the tank. If no leaks were detected, the chamber was closed and evacuated. The chamber was evacuated with the auxiliary pumping system which consisted of two 500-cfm mechanical pumps and two Roots-type blowers. Approximately twenty minutes were required to attain 5×10^{-2} torr in the chamber.

Next the diffusion pump elbow was cooled with water and the anti-backstreaming baffle in the 32-in. diameter ducting above the diffusion pump was cooled with liquid nitrogen from a 500-gallon insulated trailer. Another 500-gallon trailer supplied a liquid-to-gas converter to produce the 3000-psig gaseous nitrogen necessary to pressurize the tank systems being tested.

When chamber pressure reached 5×10^{-5} torr, or less, the auxiliary pumping system was closed off and the 130 cfm pump, in conjunction with the 32-in. diffusion pump was used for system calibration and leakage measurement. Next the leak detectors were tuned individually with their helium sensitivity calibrators.

The chamber leak calibration system, shown in an earlier sketch (see Figure 5), was used to permit a calibrated flow of helium to enter the chamber. The motorized valves between the chamber foreline, the NRC leak detector inlet, and the 130-cfm backing pump were adjusted to provide a steady high response on both leak detectors. At least three calibration runs were made to assure calibration stability. The leak calibration system used a Veeco pinched tube to regulate the helium flow to 3×10^{-3} scc/sec. The value was verified each time with the inclined manometer.

After system calibration, the tank system was slowly pressurized to 300 psig with helium then increased in 500 psig steps to a maximum of 3000 psig with nitrogen. The 3000 psig pressure was maintained for at least one hour to permit pressure and temperature stabilization to occur and to ensure reliable leak rate measurements.

One of the test requirements was to measure tank fill valve seat leakage with the tank at 3000 psig, after the one-hour stabilization period. No suitable remote procedure was devised for this, since the valve had to be closed manually and the torque measured during closing. Hence, with the approval of safety personnel, the chamber was backfilled to ambient pressure, and the required test personnel entered the test cell to connect a bubble burette to a vent valve outside the chamber. Personnel left the area while the leakage gas, if any, was being collected. The maximum allowable leakage past the valve seat was 13.7 standard cc/hr. At this time, a quick helium sniffer test was performed to locate any leaks which might have been indicated by the tank system leak test described previously.

After the high pressure test was completed, tank pressure was reduced to 435 psig and the flow rate of gas through the tank system vent valve was measured with a flowmeter. The minimum allowable flow rate was 15.1 standard cfm. The tank gas pressure was then reduced to 100 psig, and a sample of gas collected for analysis of any trace of Freon PCA which might have been left in from the hydrostatic testing which preceded the gas leak test. The tank system was then removed from the chamber for return to the Airlock assembly areas. The tank systems exhibiting any anomalies were refurbished and retested until all specification requirements were met.

TEST RESULTS

For the U-1 Skylab Airlock Vehicle, six nitrogen and six oxygen tank assemblies were tested. Likewise, for the U-2 Vehicle, six nitrogen and six oxygen tanks were tested. Some of the leakage tests disclosed anomalies, causing rework and retesting. However, all successfully met specification requirements before being delivered for assembly into their respective vehicles. A summary of tank assembly test results is presented in Table 1.

The facility functioned satisfactorily from the first tank system leak test in May 1971 to the most recent test in March 1973.

SUMMARY

An existing propulsion test facility was modified for use as a leak test facility for acceptance testing of the 3000 psig oxygen and nitrogen gas storage tank systems used on the Skylab Airlock U-1 and U-2 Vehicles. Quantitative leak rates in the range of 10^{-2} to 10^{-5} standard cc/sec of helium were measured remotely from an explosion containment test cell. The program, which covered the period of May 1971 through March 1973, was successful in testing all 13 nitrogen and all 13 oxygen tank assemblies to assure that they are flight ready.

REFERENCES

- ¹ McKinney, H. F., "Practical Applications of Leak Detection Methods," the Journal of Vacuum Science and Technology, Vol. 6, No. 6, Nov/Dec, pages 958-964.

ACKNOWLEDGEMENTS

The authors wish to thank Mr. Paul L. Melgaard for his assistance on high-pressure test safety calculations and Mr. George L. Dowdy for his help in organizing Launch Operations ground support equipment and procedures which were essential to the test program.

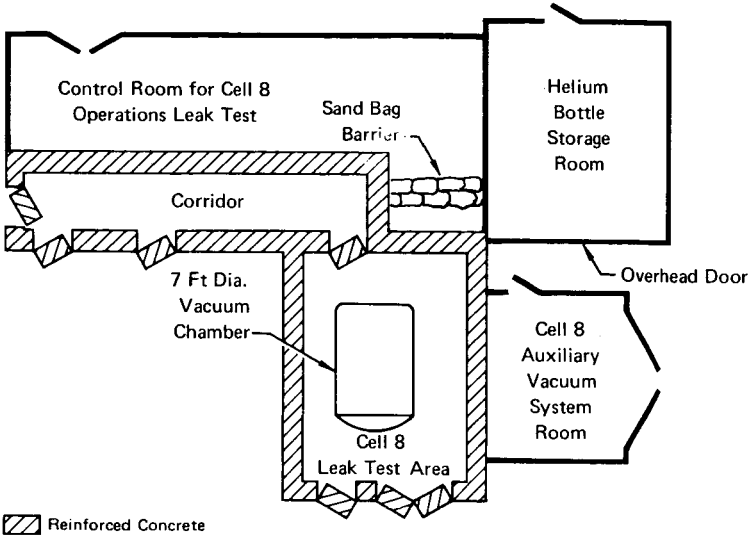


Figure 1 - Leak Test Facility

GP73-3324-1

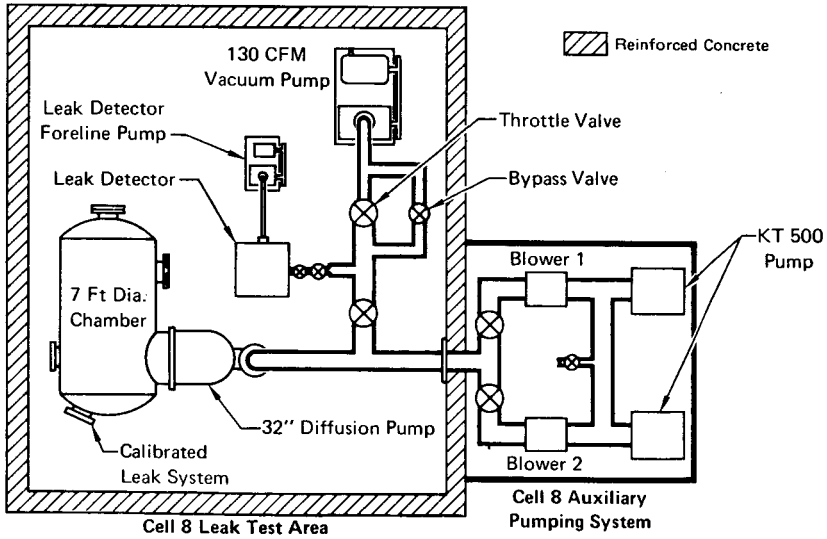


Figure 2 - Seven Foot Diameter Vacuum Chamber System Modified to Provide High Vacuum and Leak Measurement Capability

GP73-3324-2

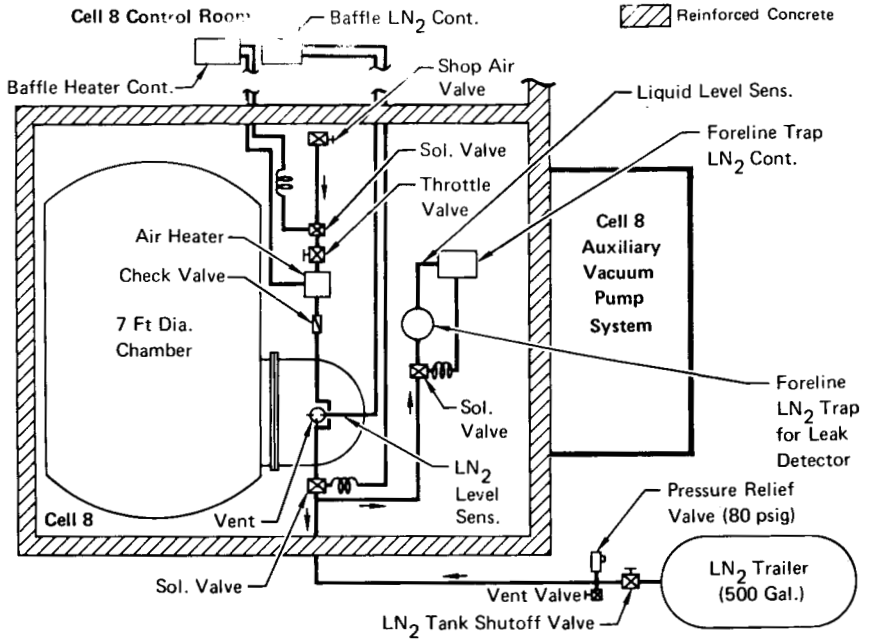


Figure 3 - Seven Foot Diameter Vacuum Chamber Liquid Nitrogen System GP73 3324 3

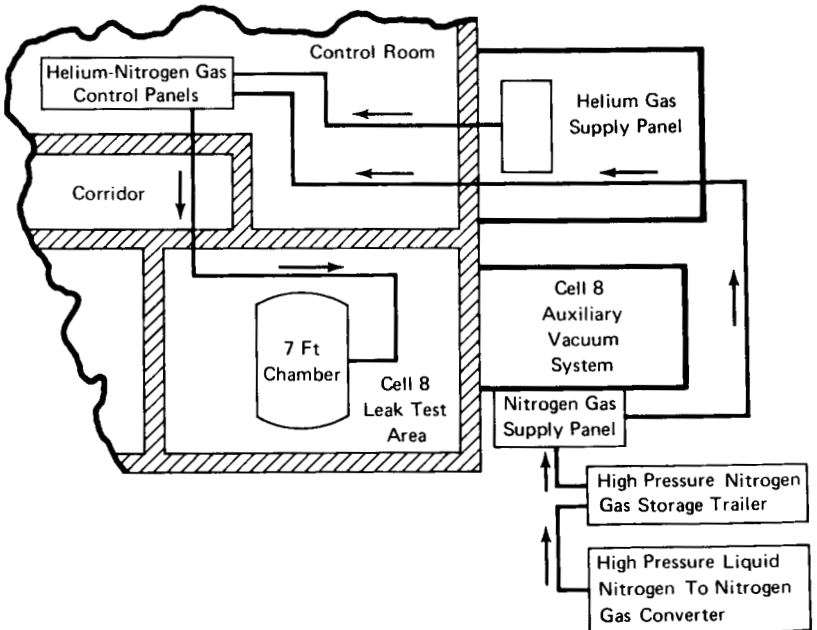


Figure 4 - N₂-He Gas Pressurization System GP73 3324 4

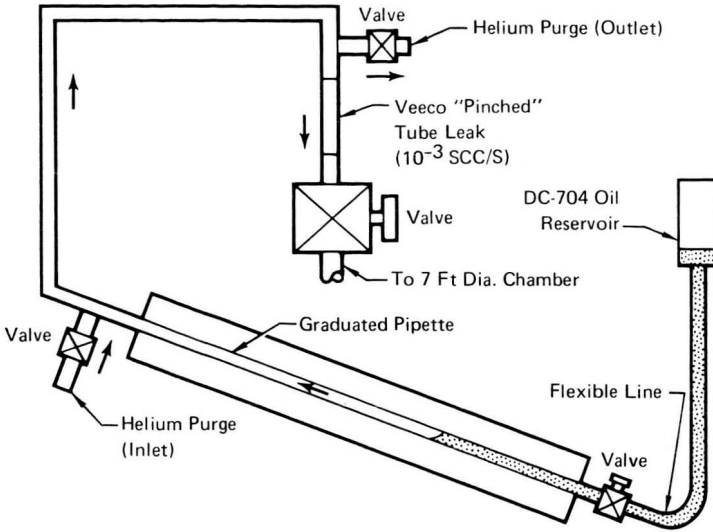


Figure 5 - Chamber Leak Calibration System

GP73-3324-5

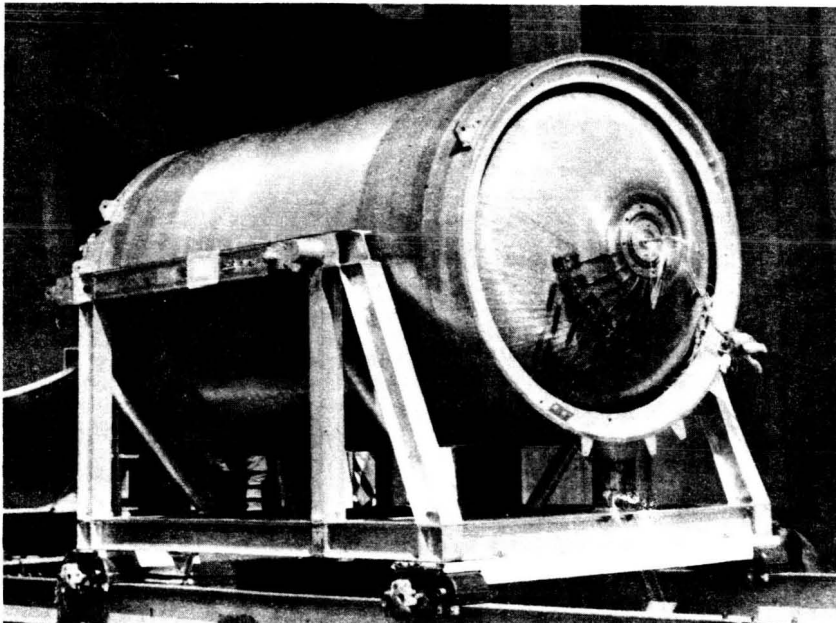


Figure 6 - Oxygen Tank System in Position in Front of 7 Foot Chamber of Cell 8

GP73-3324-6

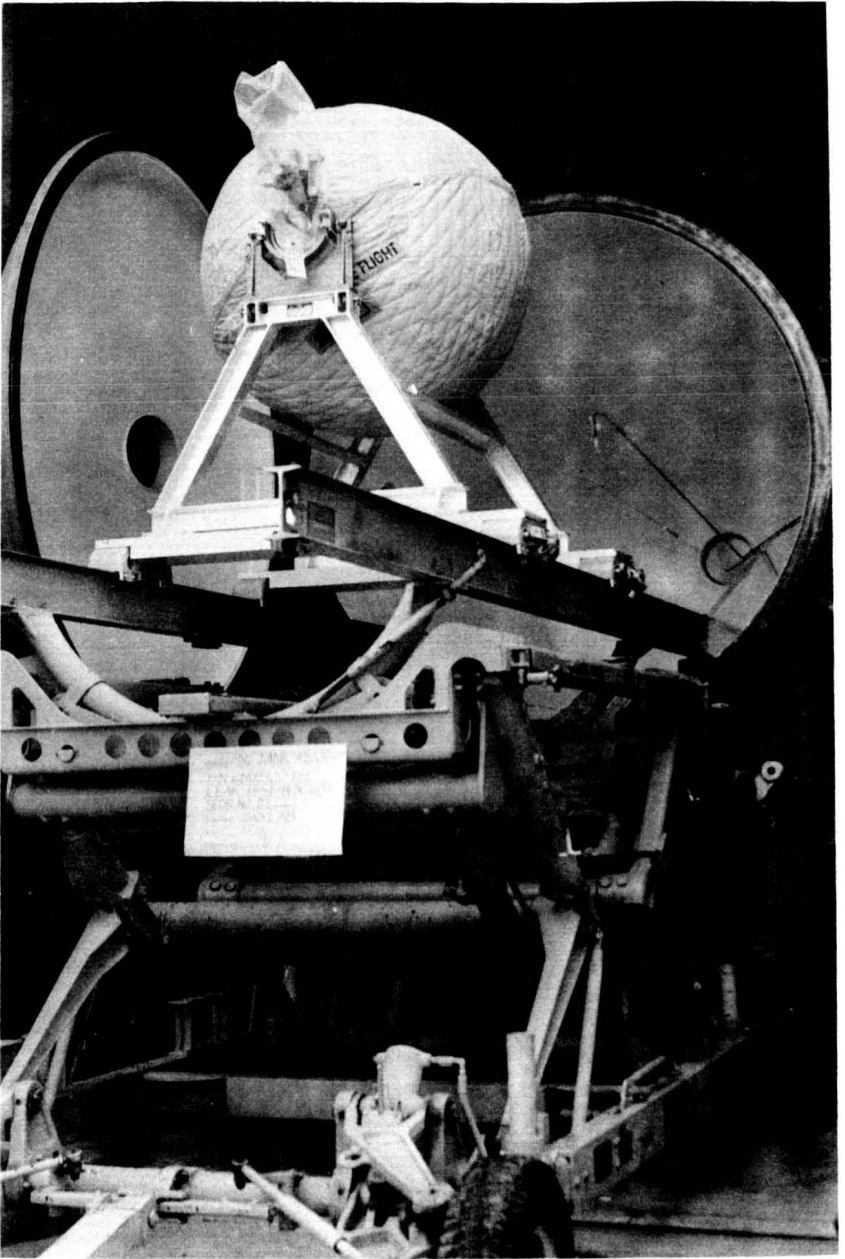


Figure 7 - Nitrogen Tank Prior to Installation in Vacuum Chamber
Quilted Fiberglass Blanket was Removed Before Leak Testing

GP73-3324-7

Table 1 - O₂ - N₂ Tank Test Data

Vehicle	S/N	MDC P/N	Type of Tank	Test No.	MRR	Test Date	Assembly Leak Rate SCC/Sec (10% H _e)	Fill Valve Seat Leakage SCC/HR 10% He, 90% N ₂	Vent Valve Flow Rate SCF/MIN 10% He, 90% N ₂
				Test Chamber Pressure					
U-1	0003	61A830248	N ₂	1/Vac 2/Amb	A51AE8	5-5-71 6-8-71	3.54 x 10 ⁻⁴ (Not Req'd)	0.0 4.2 (N ₂ Only)	26.6 (Not Req'd)
U-1	0012	61A830248	N ₂	1/Vac	None	5-7-71	<2.63 x 10 ⁻⁶	0.0	23.0
U-1	0010	61A830248	N ₂	1/Vac 2/Vac	A51AE18	5-11-71 6-10-71	3.83 x 10 ⁻⁴ 6.0 x 10 ⁻⁶	3.2 5.2	19.3 20.0
U-1	0011	61A830248	N ₂	1/Vac	None	5-13-71	3.07 x 10 ⁻⁵	3.2	22.5
U-1	0007	61A830248	N ₂	1/Vac	None	5-18-71	3.56 x 10 ⁻⁵	2.4	24.8
U-1	0002	61A830248	N ₂	1/Vac 2/Amb 3/Vac	None A61AE14 None	6-4-71 6-7-71 7-9-71	1.23 x 10 ⁻⁴ 1.08 x 10 ⁻⁴ <1.09 x 10 ⁻⁶	4.0 Not Meas. 4.0	16.8 Not Meas. 19.1
U-1	P001	61A830243	O ₂	1/Vac	None	9-22-71	1.68 x 10 ⁻⁴	0.0	17.9
U-1	P006	61A830243	O ₂	1/Vac 2/Amb 3/Vac	A31AE33 New Valve Stem	9-29-71 10-7-71 3-31-71	1.6 x 10 ⁻⁴ (Not Req'd)	0.2 0.076	20.0 (Not Req'd)
U-1	P003	61A830243	O ₂	1/Vac 2/Vac		10-4-71 4-12-72	1.62 x 10 ⁻⁴ 8.72 x 10 ⁻⁶ 2.037 x 10 ⁻⁵	11.2 0.0 7.2	> 15.1 20.02 30.0
U-1	P005	61A830243	O ₂	1/Vac 2/Vac 3/Vac	None A42AE17 None	10-22-71 4-20-72 6-8-72	9.80 x 10 ⁻⁴ 1.209 x 10 ⁻³ 3.11 x 10 ⁻⁵	0.0 7.20 12.4	15.1 > 30.0 > 15.1
U-1	P004	61A830243	O ₂	1/Vac	None	10-28-71	<2.3 x 10 ⁻⁵	0.0	20.0
U-1	P002	61A830243	O ₂	1/Vac	None	11-30-71	<1.464 x 10 ⁻⁴	0.0	> 15.1
U-2	0009	61A830248	N ₂	1/Vac	None	11-2-71	2.88 x 10 ⁻⁴	2.1	19.4
U-2	0005	61A830248	N ₂	1/Vac 2/Vac	None None	12-8-71 12-8-71	1.602 x 10 ⁻³ 2.904 x 10 ⁻⁵	Not Meas. 0.0	Not Meas. > 15.1
U-2	0008	61A830248	N ₂	1/Vac	None	12-15-71	1.017 x 10 ⁻⁴	3.0	> 15.1
U-2	0013	61A830248	N ₂	1/Vac	None	1-26-72	1.293 x 10 ⁻⁴	8.4	> 15.1
U-2	P007	61A830243	O ₂	1/Vac	None	2-15-72	1.02 x 10 ⁻⁵	7.2	> 15.1
U-2	P008	61A830243	O ₂	1/Vac	None	2-17-72	4.665 x 10 ⁻⁶	12.0	> 15.1
U-2	0014	61A830248	N ₂	1/Vac	None	3-22-72	8.59 x 10 ⁻⁵	0.0	> 26.0
U-2	0004	61A830248	N ₂	1/Vac	None	4-27-72	2.7 x 10 ⁻⁵	4.0	> 15.1
U-2	P009	61A830243	O ₂	1/Vac	None	5-10-72	7.79 x 10 ⁻⁶	11.6	> 15.1
U-2	P010	61A830243	O ₂	1/Vac	None	5-18-72	1.11 x 10 ⁻⁴	12.0	> 30.0
U-2 U-1	0006	61A830248	N ₂	1/Vac	None	6-29-72	2.215 x 10 ⁻⁵	6.6	> 30.0
U-2	P011	61A830243	O ₂	1/Vac	None	7-6-72	2.38 x 10 ⁻⁵	13.2	> 30.0
U-2	P012	61A830243	O ₂	1/Vac	None	8-8-72	7.67 x 10 ⁻⁶	0.8	> 15.1
U-1 U-2	P013	61A830243	O ₂	1/Vac 2/Vac	A13AE12	1-19-73 3-20-73	1.91 x 10 ⁻⁵ 6.6 x 10 ⁻⁴	1.0 10.8	> 15.1 > 15.1

GP73-3324-8

Paper No. 27

**THERMOELECTRICALLY-COOLED QUARTZ CRYSTAL
MICROBALANCE***

D. McKeown and W. E. Corbin, Jr., *Faraday Laboratories Inc.,
La Jolla, California*
R. J. Naumann, *Marshall Space Flight Center, Huntsville, Alabama*

ABSTRACT

A quartz crystal microbalance is of limited value in monitoring surface contamination on satellites or in space simulation chambers because it operates several degrees above ambient temperatures. The amount of contamination adsorbed on a surface is highly temperature dependent and the higher temperature of the microbalance will significantly reduce the amount of contamination it adsorbs. Generally, a quartz crystal microbalance will indicate a lower level of contamination than the amount that is actually present. To overcome this problem, a thermoelectrically-cooled quartz crystal microbalance has been developed to monitor surface contamination as a function of temperature.

INTRODUCTION

The use of a quartz crystal microbalance (QCM) is a well established method for weighing thin films of solid materials, down to a fraction of an Angstrom, that are deposited¹ or removed² from a surface. Solid films couple strongly into the oscillating QCM and its frequency change is proportional to the mass loading. Direct application of a QCM to monitor a wide range of contamination in space simulation chambers has proven to be a more difficult task because a QCM operates several degrees above ambient temperatures. Gaseous contamination in equilibrium with solid materials in the chamber is not readily adsorbed on a QCM because of its higher temperatures. Contradictory results are often obtained where a passive optical system shows contamination while a QCM operating nearby indicates little is present.

As the study of surface contamination becomes more funda-

* This work supported under NASA Contracts NAS8-27879 and NAS5-11163

mental in nature, a QCM specifically designed to monitor contamination is needed. Not only must the heat generated by the QCM be removed, but a convenient method found to automatically control its operating temperature, so that, surface contamination studies can be made over temperature extremes common to spacecraft. To permit in-situ reflectivity measurements, the crystals should be optically polished. With these objectives in mind, a thermoelectrically-cooled quartz crystal microbalance has been developed for monitoring contamination on optical surfaces as a function of temperature.

QCM LIMITATIONS

A QCM is an active quartz crystal oscillator and power dissipation raises its temperature several degrees above the ambient. Because the amount of contamination adsorbed on a surface is highly temperature dependent, a passive surface at ambient temperature will adsorb a number of contamination monolayers until it reaches an equilibrium with sources in the chamber while a QCM will adsorb a smaller number because of the different equilibrium condition. In some cases, a heavily driven QCM will operate about 10°C above ambient. At this elevated temperature no measureable amount of contamination will be observed.

The amount of contamination adsorbed on a surface is dependent on the residence time, τ , of the contamination molecules³.

$$\tau = \tau_0 \exp(\Delta E/RT)$$

where τ_0 is the vibrational period of the contamination lattice, ΔE the desorption activation energy, R the gas constant and T the absolute temperature. Griffith⁴ has shown that the desorption rate of contamination with desorption activation energies of less than 25,000 cal/g mol (oil and epoxies) is highly dependent on temperature. A 10°C temperature rise can result in nearly a ten fold increase in the desorption rate. Use of a QCM to monitor contamination will consistently give lower readings than the actual level present because of its higher temperature.

The strong effect of temperature on the adsorption and desorption of contamination is shown in Fig. 1. Here long-term OGO-6 measurements are shown correlating QCM contamination loading to the eclipse period of the satellite. As has been previously reported, the primary source of contamination on the satellite was the solar panels baking out in the sun⁵.

OGO-6 was inserted into a polar orbit with its orbit plane normal to the earth-sun line. This orbit was chosen so that the satellite would be in full sunlight for the maximum period after launch. During the four week period after launch, the amount of contamination adsorbed onto the QCM steadily increased until the first week in July when it abruptly decreased and finally in August the QCM showed a net loss of contamination and became a contamination source. By correlating the eclipse periods of the satellite to the QCM measurements, the reason for the fluctuation in the contamination adsorption and desorption rates became apparent.

In full sunlight the temperature of the solar panels was 72°C and a wide range of high and low volatile contamination outgassed from the panels onto the QCM. During maximum eclipse, when OGO-6 was in the earth shadow 30% of the time, the average temperature of the solar panels dropped to 60°C and the contamination flux from the panels decreased significantly. The QCM lost contamination during the eclipse period because the lower flux rate from the panels did not balance out contamination desorbing from the QCM. The QCM desorbed contamination into space and onto adjacent surfaces that were at a lower temperature than the QCM.

Although the QCM indicated a loss of contamination during eclipse, contamination was present. Reber's Neutral Mass Spectrometer, located next to the QCM, showed that a strong flux of contamination continued to outgas from the panels.

THERMOELECTRICALLY-COOLED QCM

In order to conduct contamination experiments as a function of temperature, a new instrument called a thermoelectrically-cooled QCM (TQCM) was developed. A thermoelectric device was picked to control temperature because it offers several advantages over other methods. It uses only a series of solid-state bismuth telluride junctions, through which electrical current is passed, to pump heat to or from a load by the Peltier effect. It is small in size and can be remotely operated with a signal pair of electrical leads. It has no moving parts and is highly reliable. There are no requirements for pumping a refrigerant or for supplying a coolant, such as, liquid nitrogen. These features result in greatly reduced operating and maintenance costs in controlling the temperature of a QCM with a thermoelectric device.

The design of the TQCM has been previously reported⁶ and only its operation will be described here. The TQCM instru-

mentation operating under ambient conditions is shown in Fig. 2. The TQCM Controller operates on 115 Vac, 60 Hz at 0.25 A and provides the various voltage outputs to operate the crystal oscillators, temperature bridge, thermoelectric device and readouts of temperature and frequency.

The TQCM Electronics, Heat Sink, and Sensor are shown in Fig. 3. The TQCM uses a two-stage thermoelectric device to automatically control the sensor crystal temperature between -50°C and $+100^{\circ}\text{C}$ to $\pm 1^{\circ}\text{C}$ in vacuum. For operation over this range, the heat sink temperature is to be maintained below $+40^{\circ}\text{C}$. No problem will be encountered in maintaining the heat sink below $+40^{\circ}\text{C}$ by mounting it on a 0.6 cm thick metal bracket. Heat generated by the TQCM is readily dissipated by the bracket at ambient room temperatures.

The TQCM has been designed with an extended temperature bridge circuit and reserve power and will reach a lower temperature limit of -59°C if its heat sink is maintained below $+25^{\circ}\text{C}$. To maintain a $+25^{\circ}\text{C}$ temperature, the heat sink is to be mounted on a 1.2 cm thick metal bracket capable of removing a maximum 2.8 W when the TQCM is at -59°C . The TQCM cool-down time in vacuum is shown in Fig. 4.

The TQCM operating temperature is set by positioning the thumb wheel switch on the Controller. A 3 1/2 digit panel meter is provided in the Controller for direct readout of temperature.

A temperature output is provided for remote readout or recording. The TQCM temperature sensor is a precision platinum resistance thermometer linear to 0.5%. At 100°C the voltage output is 1.00 Vdc. At -59°C the voltage output is -0.59 Vdc. The TQCM operating temperature in $^{\circ}\text{C}$ equals 100 times the voltage output of the Controller.

A matched pair of precision 10-MHz quartz crystals is used to measure mass loading. The crystals are designated as a sensor and reference crystal. The crystals are optically-polished and plated with Al. The sensor crystal is coated with magnesium fluoride for in-situ reflectivity measurements while contamination is collecting on its surface. The crystals can be changed by unloosening two set screws in the TQCM Sensor.

The output frequency of the TQCM is the beat frequency between the two oscillating crystals. The beat frequency effectively eliminates frequency changes caused by ambient temperature variations. By carefully matching sets of crystals in vacuum, frequency change with temperature of less than ± 50 Hz between -59°C and $+100^{\circ}\text{C}$ is attained. Because only the sensor crystal sees the contamination flux, the TQCM output frequency will increase with mass loading. The crystal sensor is optically pol-

ished and full plated on one side. This technique produces a more active crystal whose mass sensitivity is greater by about 20% than semi-polished crystals. The TQCM mass sensitivity, m , is

$$m = 3.5 \times 10^{-9} \text{ g/cm}^2 \text{ Hz}$$

A frequency output is provided in the TQCM Controller to measure the frequency change of the crystal sensor produced by mass loading. Frequency is measured by a counter, such as, a Hewlett Packard Model HP5321B.

The TQCM can be set at any particular temperature over its operating range. If the TQCM is set at ambient, the heat generated in the oscillating crystal will be removed so that contamination loading to passive optical systems can be monitored. By increasing temperature to about +100°C the crystal can be cleaned. By periodically dropping the temperature of the TQCM in fixed steps, the amount of surface contamination for different equilibrium temperatures can be determined and the background level of contamination in a space simulation chamber monitored with time.

The TQCM can be used to generate a calibrated contamination flux so that the contamination sticking coefficients of surfaces can be measured. A TQCM calibrated source is generated as follows. Contamination from an uncalibrated source is directed at a TQCM cooled to -50°C. Contamination is allowed to freeze out on the TQCM. The uncalibrated source is then turned off and the vacuum system allowed to pump down. The TQCM now becomes the calibrated source by simply raising its temperature so that the contamination will desorb at the desired rate. By monitoring the TQCM frequency increase with time, the contamination mass flow rate can be accurately determined.

The TQCM can also be used to calibrate the mass loading of viscous films on the quartz crystal sensor that do not couple well into the oscillating mass of the crystal. As a contamination film grows to several hundred monolayers, its top layers will slip relative to the oscillating crystal. The simple relationship between mass loading and frequency change will not hold true. Calibration is achieved by dropping the sensor temperature to freeze the contamination and provide rigid mass coupling to the crystal.

CONTAMINATION MEASUREMENTS

Studies of background contamination in a vacuum chamber

were made to show the capability of the TQCM to measure surface contamination under equilibrium conditions. A 150 l/sec Vac-Ion pump was used to evacuate the chamber to the 10^{-9} Torr range. Just prior to the measurements, the chamber was contaminated with Welsh Duo-Seal roughing pump oil that raised its pressure into the 10^{-7} Torr range.

The net mass gain or loss for an aluminum surface from the adsorption and desorption of background contamination present in the chamber at 7×10^{-7} Torr is shown in Fig. 5. Below -30°C adsorption predominated and contamination collected on the surface. Above -30°C desorption predominated. The break in the curve at about -10°C where the rate of desorption increased abruptly is significant.

The break shows a phase change occurring in the contamination from a solid to a liquid. The phase change caused a large increase in its vapor pressure and the higher desorption rate. We were unable to make a measurement at $+20^{\circ}\text{C}$ because the desorption rate became so large that by the time the surface reached $+20^{\circ}\text{C}$ the contamination was nearly completely desorbed.

Fig. 6 shows the desorption rate of roughing pump oil as a function of the number of monolayers on the surface for a contamination background pressure of 4×10^{-7} Torr. When the number of contamination layers reaches 200, the increase in the desorption rate starts to level off indicating the bulk properties of the oil predominate and the properties of the surface have little effect on the desorption. At 0°C the leveling off of the desorption rate is quite evident.

The desorption rate decreases rapidly as the number of layers present is reduced because of the higher bonding energy holding contamination layers near to the surface. The higher bonding energy results from contamination molecules filling cracks and crevices in the polycrystalline aluminum surface.

The number of monolayers of contamination on a surface in equilibrium with the contamination on the walls of the vacuum chamber as a function of temperature is shown in Fig. 7. The ambient temperature of the chamber was 23°C . The measurements were made by raising the TQCM temperature to $+80^{\circ}\text{C}$ to bake off surface contamination and then dropping its temperature to -50°C to adsorb a film of contamination. The TQCM temperature was then increased to a particular equilibrium temperature shown in the figure to determine the number of contamination monolayers. From the figure it can be seen that there was always oil contamination on the surface even at 4×10^{-7} Torr for temperatures below $+30^{\circ}\text{C}$. It would have been impossible to make the measurements with a QCM because there are no net

mass changes at equilibrium.

CONCLUSIONS

Most contamination is adsorbed on a surface in the gaseous or liquid state and the adsorption rate is highly temperature dependent. A QCM is of limited value in monitoring contamination because it operates several degrees above ambient temperatures and does not readily adsorb contamination. For accurate measurements, a temperature controlled QCM should be used.

If a QCM is used to monitor contamination, measurements should be made from a directed source. The source temperature should be much higher than the QCM operating temperature to insure that the contamination sticking coefficient is greater than zero.

REFERENCES

1. Sauerbrey, G., "Application of Quartz Resonators for Weighing Thin Films and for Microweighing", *Zeitschrift fur Physik*, 155 206-222 (1959).
2. McKeown, D., "New Method for Measuring Sputtering in the Region Near Threshold", General Dynamics Convair Report ERR-AN-001, San Diego, Calif. (1959).
3. Vacuum Technology and Space Simulation, NASA SP-105, National Aeronautics and Space Administration, Washington, D.C.
4. Griffith, J.S., "Some Tests for Increase in Friction of Mechanisms of the Mariner Mars 1969 Spacecraft in the JPL Molsink Space Simulation Chamber", Proceedings of 4th Space Simulation Conference, AIAA/ASTM/IES, Los Angeles, Calif. (1969).
5. McKeown, D. and W.E. Corbin, Jr., "Space Measurements of the Contamination of Surfaces by OGO-6 Outgassing and Their Cleaning by Sputtering and Desorption", Space Simulation, NBS Special Publication 336, pp 113-127 (1970).
6. "Thermoelectrically-Cooled Quartz Crystal Microbalance", Operational Data, Faraday Laboratories Report FAR-73-101, La Jolla, Calif. (1973).

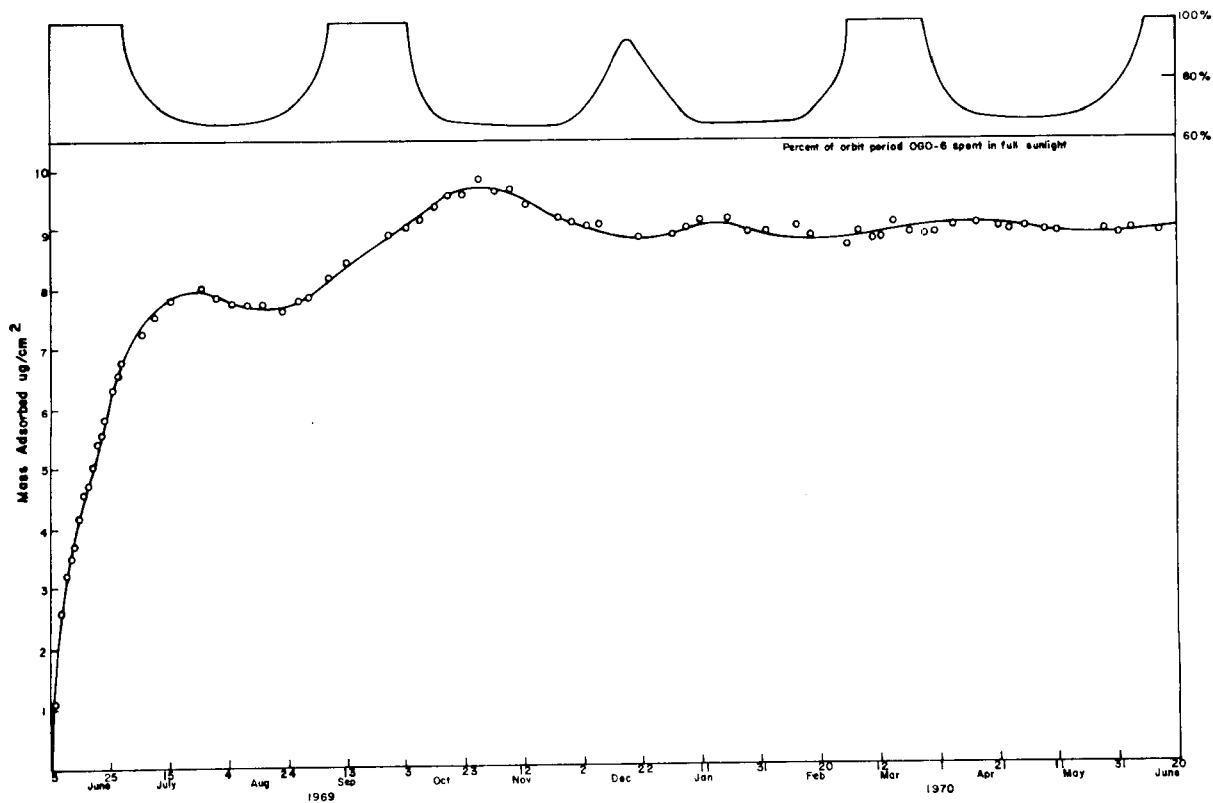


Fig. 1 Long-term OGO-6 surface contamination measurements correlated to the eclipse periods of the satellite

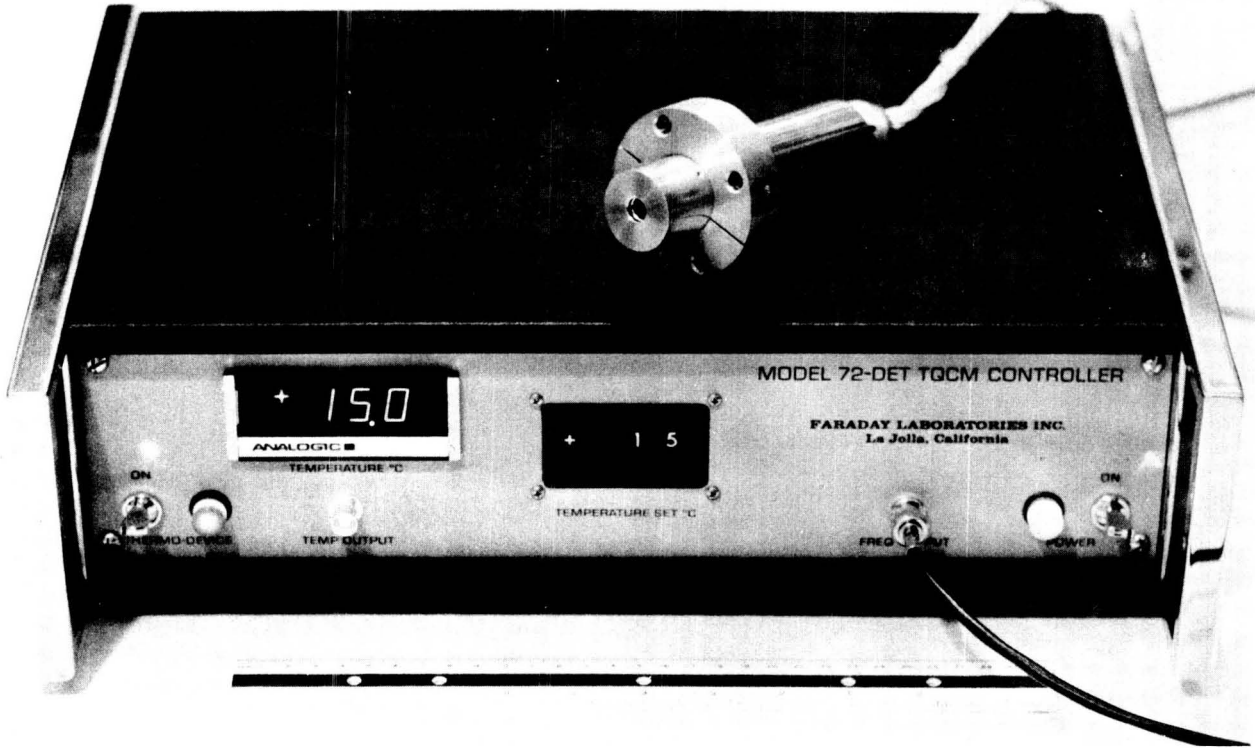


Fig. 2 TQCM Operating at +15°C under Ambient Conditions

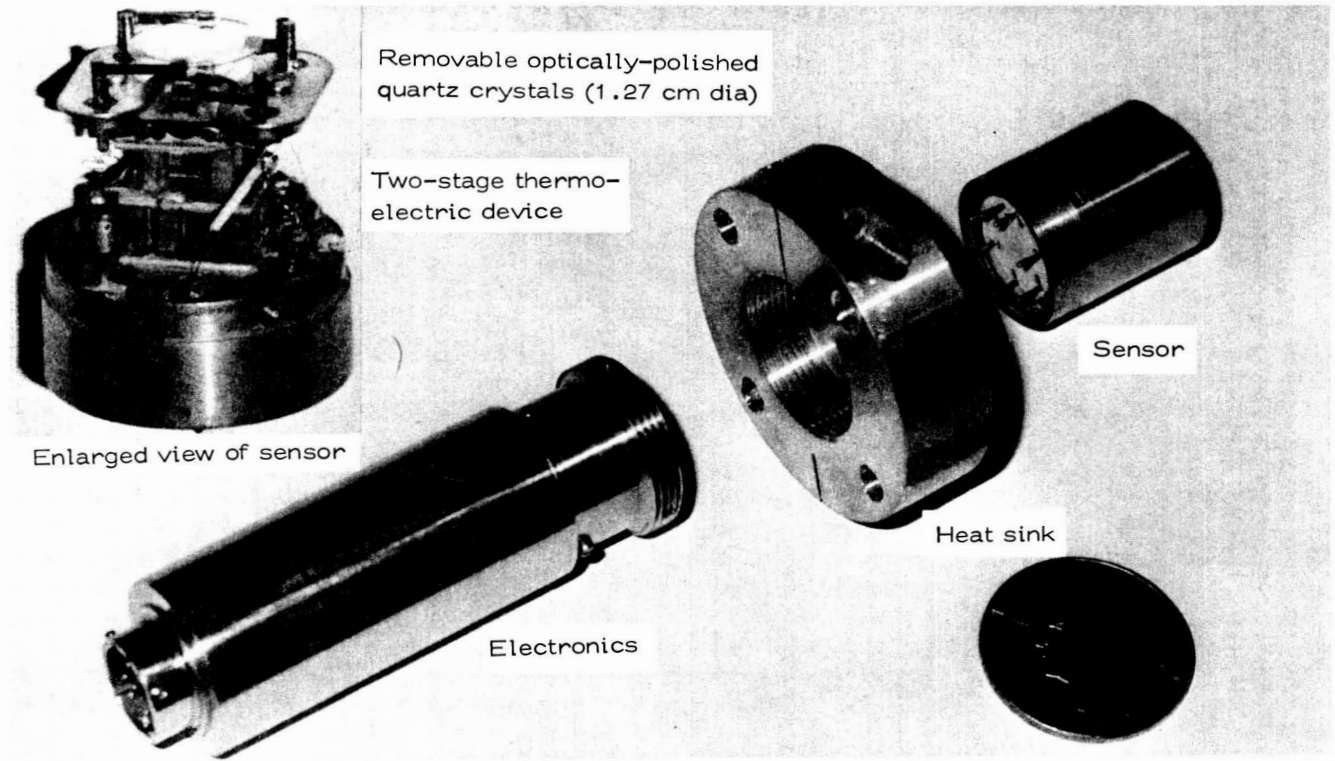


Fig. 3 TQCM Electronics, Heat Sink and Sensor

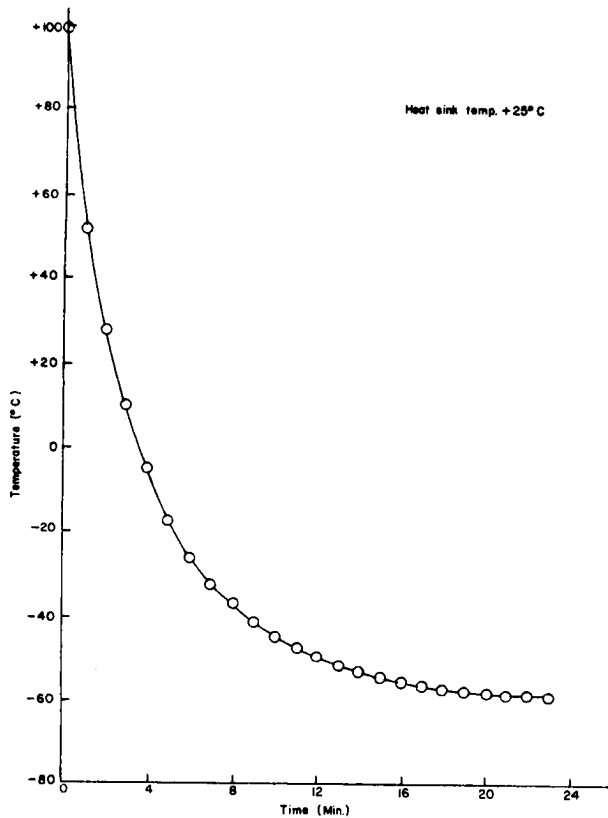


Fig.4 TQCM cool-down time in vacuum from +100°C to -59°C

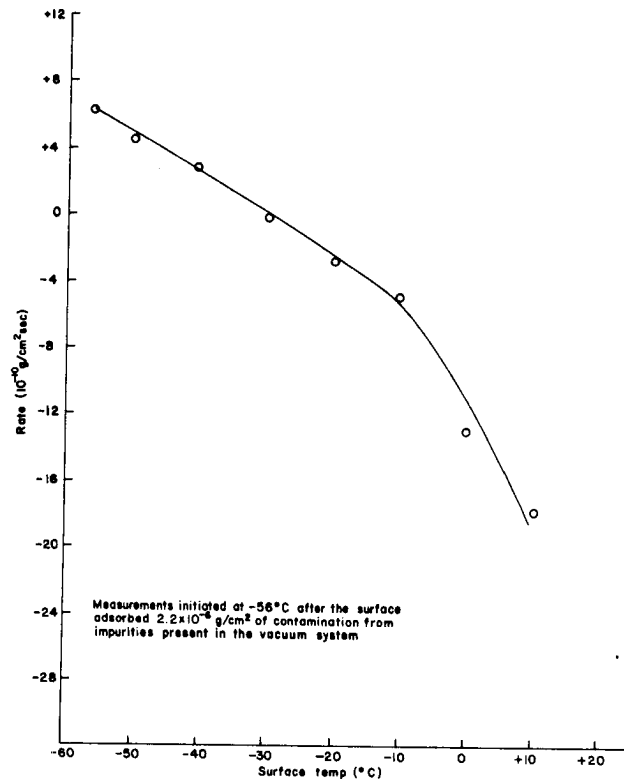


Fig.5 Contamination adsorption and desorption rates for an Al surface with temperature in a 7×10^{-7} Torr vacuum

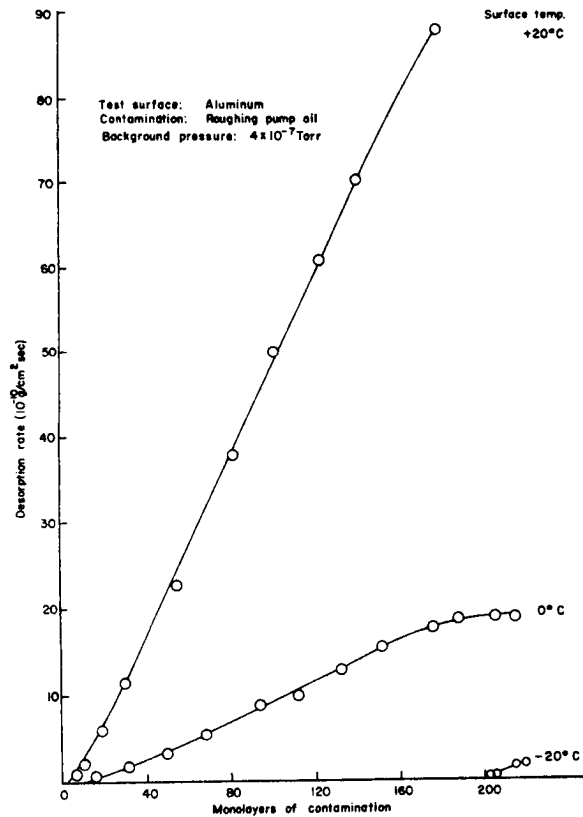


Fig. 6 Contamination desorption rate as a function of monolayers on the surface

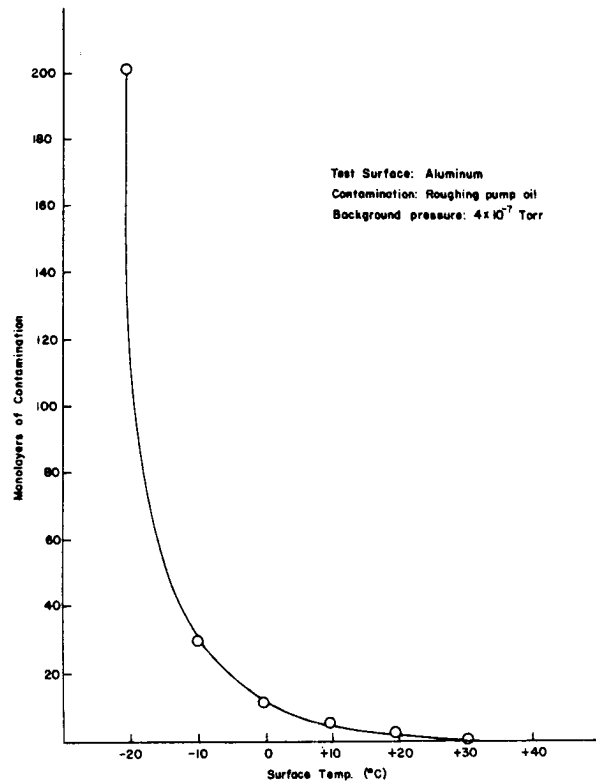


Fig. 7 Number of contamination monolayers on a surface at equilibrium

N71-15251c

DEVELOPMENT OF A MINIATURE CRYOGENIC QCM FOR LOW TEMPERATURE CONTAMINATION MEASUREMENT

D. A. Wallace, Celesco Industries Inc., Costa Mesa, California

INTRODUCTION

A need exists in contamination monitoring for a mass monitor which is small in size, has monolayer coverage detectability, is capable of operation to liquid Helium temperature and dissipates a minimum amount of power. As an example, the testing of cryogenically cooled telescopes for scattering effects produced by condensed contaminant on optical surfaces could use such a QCM in a correlation of contaminant mass to system degradation. Development of a Quartz Crystal Monitor (QCM) for such an application involves consideration of the effect of crystal size and crystal temperature on the all important parameters: crystal mass sensitivity and maximum mass accumulation range. A considerable body of data exists on these parameters at 25°C and to a lesser extent to near liquid Nitrogen temperatures, but very little data is available at liquid Helium temperature. Additionally, low power dissipation electronics must be developed which not only operate at liquid Helium temperature but which also have "start up" capability after an extended cold soak.

This paper describes the development of a miniature QCM shown in Figure 1 that meets the above needs. The mass sensitivity and the mass detectability are considered analytically and the crystal temperature coefficient and the mass range are shown experimentally to be comparable to larger QCM's operated at ambient (25°C) temperature.

SIZE EFFECT ON CRYSTAL PERFORMANCE

Mass Sensitivity

In crystals vibrating in thickness shear mode, changes in frequency are directly related to changes in the plate thickness.

$$\frac{\Delta f}{f} = \frac{\Delta t}{t}$$

f = crystal resonant frequency
t = crystal thickness

For a crystal placed in a free molecular flux field, (\dot{m}/A), the change in material thickness on the crystal with time is,

$$\frac{\Delta t}{\Delta \tau} = \frac{\Delta m}{\rho_m A_e \Delta \tau} = \frac{\dot{m}/A}{\rho_m} \quad \begin{array}{l} \rho_m = \text{deposited mass density} \\ A_e = \text{active crystal area or} \\ \text{electrode area} \end{array}$$

Since the thickness change is a function only of the unit mass flux and the mass density, the material thickness increases at the same rate regardless of the crystal size in a given flow field and thus the frequency shift rate is the same. The mass sensitivity relationship for crystals in thickness shear vibration is,

$$\frac{\Delta m}{A} = - \frac{\rho_m \left(\frac{V_{tr}}{2} \right)^2}{f^2} \quad \begin{array}{l} V_{tr} = \text{transverse wave} \\ \text{velocity in plate} \end{array}$$

Therefore for the 10 MHz crystals used in this QCM development, the theoretical sensitivity is,

$$S = 4.43 \times 10^{-9} \frac{\rho_m}{\rho_q} \text{ gm/cm}^2 \text{-Hz} \quad \begin{array}{l} \rho_q = \text{quartz density} \\ = 2.65 \text{ gm/cc} \end{array}$$

The criteria used in selecting the crystal frequency was monolayer detectability. If, for instance, nitrogen is the condensing gas of interest, monolayer surface coverage represents 8.1×10^{14} molecules/cm² or 3.77×10^{-8} gm/cm² as calculated by the density method. The density of solid nitrogen condensed from the gaseous state has been shown experimentally (Reference 1) to be 0.9 gm/cc. Therefore 10 MHz crystal sensitivity for solid nitrogen is,

$$S_{N_2} = 1.5 \times 10^{-9} \text{ gm/cm}^2 \text{-Hz}$$

The monolayer is 3.75 \AA thick and,

$$\Delta f / \text{monolayer } N_2 = \frac{3.77 \times 10^{-8}}{1.5 \times 10^{-9}} = 25.3 \text{ Hz}$$

Thus partial nitrogen monolayer coverage is easily measurable with 10 MHz crystals.

Mass Detectability

Unlike the condensate thickness relationship, the quantity or mass of condensate collected per unit time varies directly as the electrode area. Thus for the same frequency shift, i. e., for the same condensate thickness increase, a

smaller actual mass of condensate is collected as the crystal electrode decreases in size.

$$\Delta m = \frac{\Delta f t \rho_m A_e}{f}$$

The minimum mass detectable by a crystal for a given minimum resolvable frequency shift will consequently be quantitatively less for crystals with the smallest electrodes.

In the case of a 1/2" diameter crystal with a 1/4" diameter electrode, the mass required for a one hertz frequency shift is 1.4×10^{-9} grams for mass density 2.65 gm/cc condensate whereas for a 1/4" diameter crystal with 0.14" diameter electrode, the value is 4.4×10^{-10} grams.

Mass Accumulation

Thickness shear mode crystals are usually chosen for QCM work since the elastic damping of the deposited material is minimized in this type of vibration. As deposition increases however, a thickness is reached which does provide losses greater than the circuit driving power and vibration ceases. There are indications that this loss is a direct function of thickness rather than total mass on the crystal in which case the maximum mass accumulation will be independent of the crystal size and depend solely on the Q of the oscillator circuit and the damping properties of the deposited material. Since crystal Q is related to the plate diameter to thickness ratio and thickness is specified for a desired frequency, smaller crystals tend to have lower Q's. Therefore, there may be a tendency to reduced collectible material thickness before oscillation ceases. This important parameter was investigated experimentally and the results discussed in a later section.

LOW TEMPERATURE OPERATION

Determination of mass deposition by observing crystal frequency shifts implies either the elimination or the complete understanding of all other crystal stress producing and thus frequency shift producing parameters. These other parameters include equilibrium temperature coefficient, crystal mechanical mount and incident thermal radiation.

The primary source of frequency change in the crystal other than mass deposition is the change produced by crystal temperature change. The temperature coefficient for various crystallographic cuts has been studied extensively and is generally known for the temperatures of interest (Figure 2). Ideally, crystal cuts are chosen for a desired temperature operating range with zero temperature coefficient. The

cancellation of the temperature effect is greatly improved if two crystals of the same cut are placed in the same temperature environment (one crystal shielded from mass flux) and the beat frequency of the two crystals measured. In this way, despite changes in the temperature coefficient with temperature the beat frequency will be essentially unaffected. In practice, exact cancellation is difficult to achieve over large temperature variations; however, the several decade reduction in temperature induced frequency shifts obtainable with careful crystal selection greatly improves mass measurement.

In this study two temperature ranges were of interest; one at temperatures below 40°K and the other from 100 to 200°K.

The selection of crystals for the very low temperature range, i. e., temperature less than 40°K, was based upon the National Bureau of Standards study of crystals at low temperature (Reference 2). This NBS study used 5 MHz crystals; however, the crystallographic cut should control the temperature coefficient and on the basis of the NBS data a cut of 40°28' was chosen. The temperature coefficient is very nearly constant from LN₂ temperature down to liquid helium temperature as shown in Figure 3. Unfortunately the NBS reference presents data just slightly in excess of LN₂ temperature and in this region most of the crystal cuts shown, including the 40°28' cut, exhibit radical slope changes and reversals in their temperature coefficients.

This is not considered to be a limitation on the usefulness of the crystal since in applications requiring less than 40°K temperature, wide temperature variations are rarely encountered and simply means another crystal cut must be chosen for other applications at higher temperatures.

One common class of earth orbiting satellite experiences temperature excursions in the 100°K to 200°K temperature range. Therefore a crystal cut of 37°03' was chosen for testing since this cut minimizes the overall temperature induced frequency shift in this region as shown in Figure 3.

The crystals used were 1/4" in diameter with 0.14" diameter electrodes. Vacuum deposited aluminum was used as the electrode material for all crystals in order to minimize thermal irradiance induced effects.

In order to avoid mounting stresses caused by differential contraction during temperature changes, the crystals were mounted on three stainless steel springs which also acted as electrical leads.

Crystals at 10 MHz fundamental frequency were used to obtain high sensitivity. Capacitance problems make long leads at this frequency undesirable; therefore, a hybrid chip with sensing crystal oscillator, reference crystal oscillator and a frequency mixer was developed which could be located immediately adjacent to the crystals. In this location,

ever, the hybrid chip must dissipate a minimum amount of power for two reasons: first, the dissipated power may raise the crystal temperature above the condensation temperature of the gas of interest; and secondly, an unacceptably high heat load may be imposed upon the refrigeration system. Low heat dissipation means, however, minimal hybrid chip temperature rise; thus the transistors, etc., must operate at near liquid helium temperature. One compensating factor is the fact that the Q of the crystal increases as the temperature decreases, partially offsetting the drop in output of other components. The hybrid chip developed for this unit dissipates approximately 25 milliwatts with 5 volt input voltage. Its performance over a wide temperature range is reported later.

TEST PROGRAM

The complete QCM was mounted on a copper button at the cryotip of an AIRCO Model LT-3-110 Liquid Transfer Cryo-Tip Refrigerator. The temperature at the base of the QCM as well as the cryotip temperature was sensed by Chromel vs Gold-0.07 at. % iron thermocouples and measured by a HP 419A micro-voltmeter with LN₂ reference junction. The QCM beat frequency output was measured by a HP 5245L frequency counter and recorded on a HP 5050B printer. The beat frequency wave shape was monitored continuously on a Tektronix 453 oscilloscope to observe any erratic behavior.

The initial test was performed on a QCM with 37⁰⁰³¹ crystals, intended for the 100°K to 200°K region therefore liquid nitrogen was used as the coolant. Test results are shown in Figure 4, Run 1. The QCM was operated in the cooldown phase at 5 volt input to the oscillators. The observed frequency shift with temperature from 300°K to 80°K of 206 Hz shows an excellent crystal match since a single crystal frequency excursion is 8400Hz in the same temperature range (Figure 3). The effect of input voltage on hybrid chip operation was tested at LN₂ temperature and indicated some frequency dependence on the voltage. The QCM was operated during the warming cycle with 7 volt power until a temperature of 134°K was reached at which time the voltage was dropped to 5 volts.

During the cooling cycle, a very small air leak was permitted to deposit condensibles on the cryotip. These condensibles did not affect QCM performance since the mount shielded the crystals from direct impingement of the air until condensibles could deposit on the colder cryotip. During the warming cycle, however, the cryotip is purposely heated by an integral resistance element resulting in tip temperatures higher than the crystal temperature and the transfer of condensibles from the cryotip to the QCM. As indicated in Figure 4, this process resulted in a frequency change of 190, 530 Hz without noticeable beat frequency wave shape distortion. Thus the small crystal is capable of operation with a mass accumulation that results in

a frequency shift of 2% of its fundamental frequency. The first of the mass accumulations shown in the data is probably CO₂ and the second, H₂O based on vapor pressure considerations although gas specie identification measurements were not taken.

The second test of the same QCM was performed with liquid helium cooling. The QCM was operated at 12 volts during cooling and during most of the warming cycle. The test cell was maintained at a high vacuum and no mass accumulation was noted during warmup.

The third test involved the crystals intended for very low temperature operation with a crystal cut of 40°28'. The test data is shown in Figure 5. During cooling, 12 volt power was supplied and 5 volts used throughout the warmup. Mass was again allowed to accumulate on the crystal during warmup to illustrate mass loading capability. Some frequency dependence on voltage was shown by the crystals at low temperature as indicated by differences in the 5 volt and 12 volt curves. However, below 20°K where these crystals will find their major usefulness, there is very good agreement. A comparison of the QCM two-crystal beat frequency variation with temperature compared to the NBS single crystal data is shown on Figure 6. The two crystals chosen at random for this experimental set apparently have nearly identical temperature characteristics in the 36°K to 78°K range but exhibit some deviation from 36°K to 5°K. From Figure 6, it is observed that the total temperature induced frequency change from 78°K to 5°K is less than the frequency change represented by a single monolayer of condensed nitrogen. Therefore, this QCM can measure mass changes comparable to partial monolayer coverage with minimal concern for temperature effects particularly if the QCM is held at a fixed temperature, e. g. 10°K.

CONCLUSIONS

Crystal mass sensitivity has been shown to be uninfluenced by crystal size and crystal mass detectability increases with decreasing electrode size. The mass accumulation range on the small crystals used in this program is in excess of 2% of the fundamental frequency which is equivalent to accumulations on crystals with twice the diameter.

The crystal cuts chosen for the two temperature ranges of interest performed as expected with excellent temperature coefficient cancellation down to 5°K.

The miniature cryogenic QCM thus has attributes which should result in partial monolayer measurement at liquid helium temperatures.

ACKNOWLEDGMENTS

Mr. D. Bergquist assisted in performing the experiments and his dedicated efforts are gratefully acknowledged.

REFERENCES

1. Experimental Investigations of Solid Nitrogen Formed by Cryopumping - K. W. Rogers
NASA CR-553
2. Investigation of Stability of Quartz Resonators at Low Temperatures - F. P. Phelps, R. D. Goodwin, and A. H. Morgan. National Bureau of Standards Report 5021

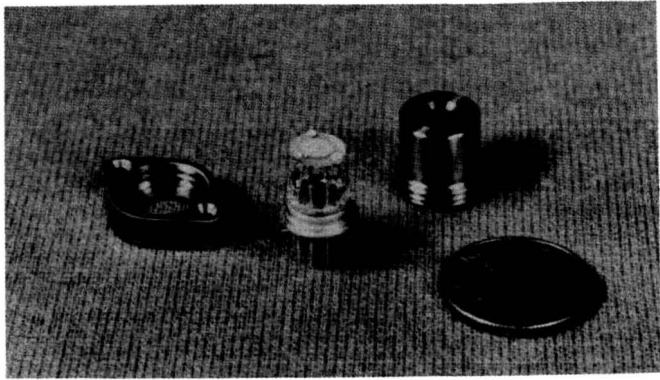


Figure 1—Miniature, Cryogenic QCM

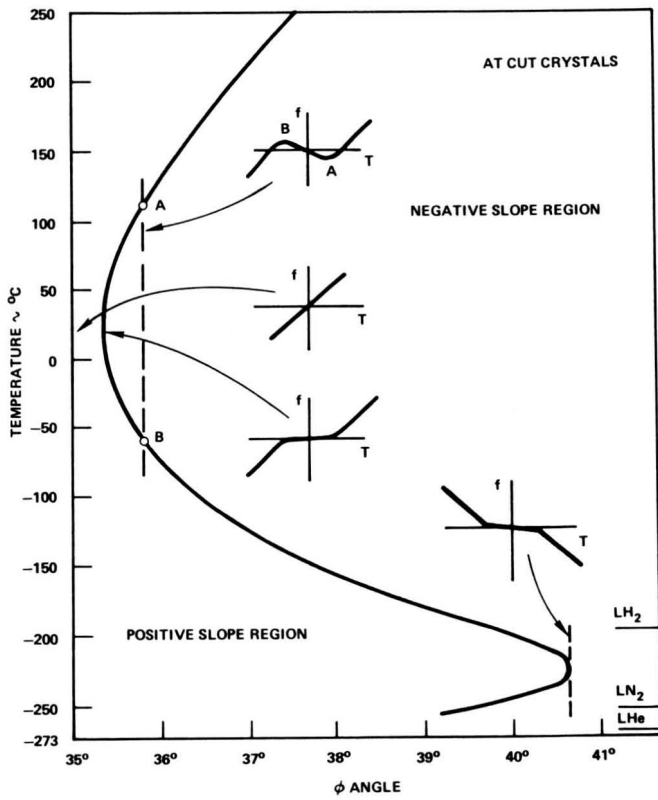


Figure 2—Temperature of Zero Temperature Coefficient of Frequency vs ϕ

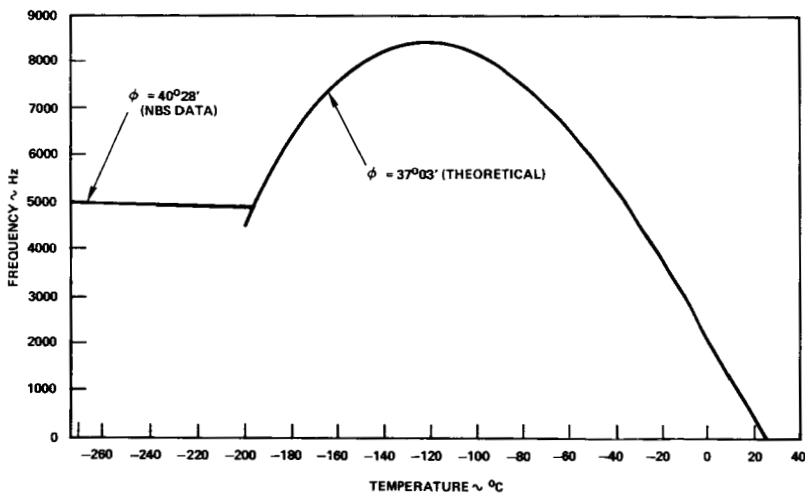


Figure 3—Temperature Coefficients for $\phi = 37^{\circ}03'$ and $\phi = 40^{\circ}28'$ Crystals

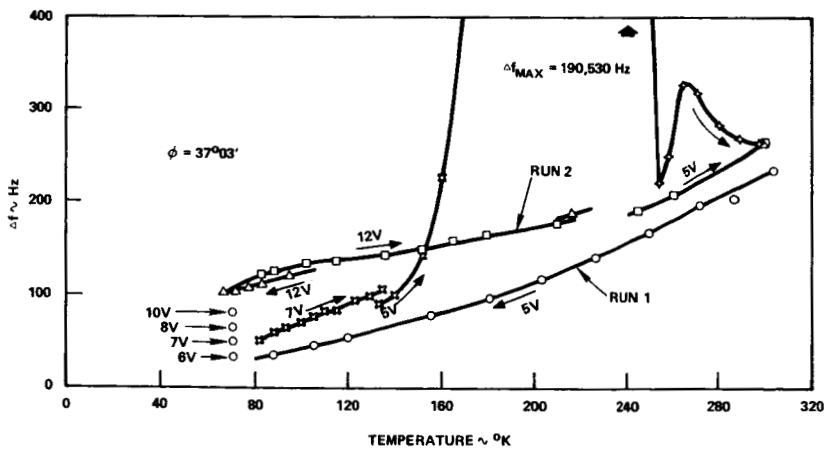


Figure 4—Temperature Coefficient and Mass Accumulation Test of $\phi = 37^{\circ}03'$ Crystal

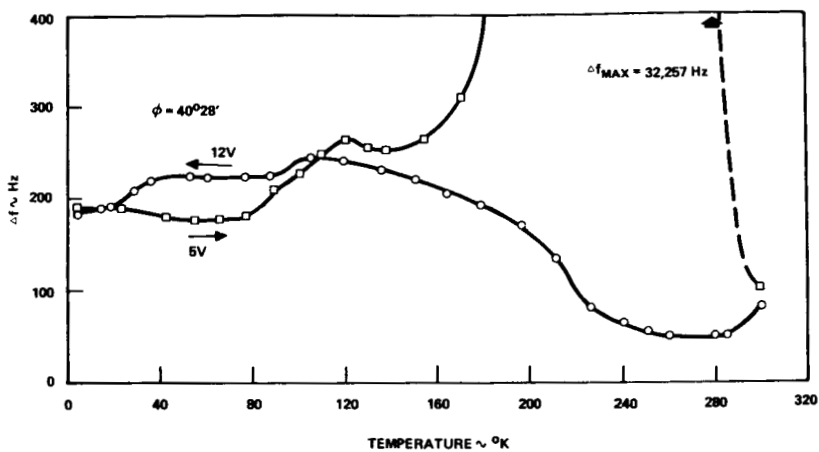


Figure 5—Temperature Coefficient and Mass Accumulation Test of $\phi = 40^{\circ}28'$ Crystal

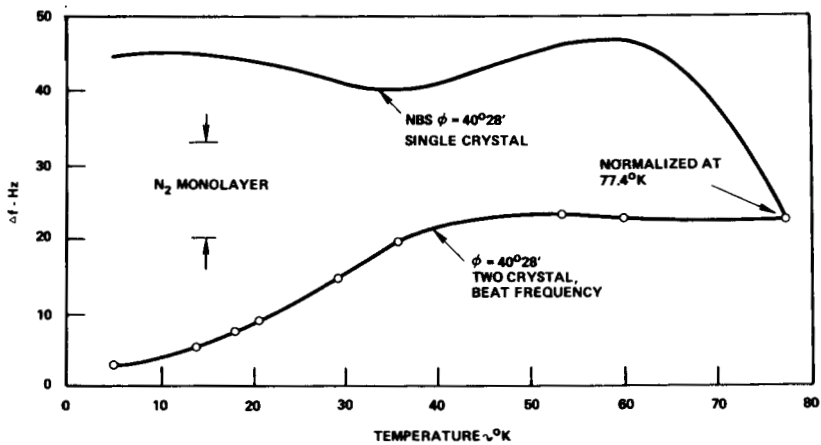


Figure 6—QCM Two Crystal Beat Frequency and NBS Single Crystal Frequency at Low Temperature

N74-107

Paper No. 29

TRANSIENT FREQUENCY EFFECTS IN PIEZOELECTRIC QUARTZ CRYSTALS CAUSED BY INCIDENT THERMAL RADIATION

D. A. Wallace, *Celesco Industries Inc., Costa Mesa, California*

ABSTRACT

An analytical and experimental program examined step function and cyclic thermal irradiance of piezoelectric crystals. Metal crystal electrodes with different α/ϵ ratios as well as dielectric over-coated electrodes were tested.

INTRODUCTION

Quartz Crystal Microbalances (QCM's) are widely used to measure small mass changes resulting from condensible efflux depositing upon a piezoelectric crystal. The condensing mass results in a predictable crystal vibrational frequency change which has been treated theoretically and experimentally by various investigators. To relate crystal frequency changes to mass changes, however, other potential frequency effecting phenomena must be considered. The relationship between crystal frequency and equilibrium quartz crystal temperature has been thoroughly studied for various crystallographic cuts and over a broad temperature range. With a full understanding of this frequency-equilibrium temperature relationship, QCM's can be produced with essentially zero beat frequency change with temperature by using two crystals with matched temperature characteristics and exposing only one crystal to mass flux.

An important frequency change producing parameter which has been inadequately studied, however, is transient or steady state incident thermal radiation. QCM's positioned on spacecraft so as to be exposed to solar radiation and thin film monitors subjected to IR heating by evaporative sources are examples of QCM's in this incident radiation environment. This study considered various theoretical thermal models for the prediction of heat flow through the quartz plate and the resultant stress producing thermal gradients which could result in frequency shifts completely independent of any equilibrium temperature effects. An experimental program provided input information for the thermal modeling and verification of the analytical predictions.

Analytic Study

Using the case of constant heat flux suddenly applied at the surface of a plate at equilibrium, the heat pulse within the

plate produced by sudden exposure to solar radiant flux can be analyzed.

The solution for the temperature variation within the plate with sudden constant heat flux applied to one side of the plate and with radiative heat rejection from the other plate surface is found in Reference 1.

Evaluating the eigen functions for the quartz crystal case indicates a high thermal conductivity through the plate compared to the heat rejected by radiation from the back surface of the plate. The calculated time for the heat pulse to pass through the crystal is much less than one second.

In the case of the crystals being studied, a metallic electrode is deposited onto a piezoelectric quartz crystal with a diameter ratio (d_e/d_q) of approximately one-half. The metal electrode is absorptive to the irradiation, however the quartz has a high transmittance or in practice is shielded from the radiant flux.

In actuality then the crystal case is much closer to the case of a hollow cylinder with suddenly applied heat at the inner diameter (Figure 1) since the heat absorbed by the metal electrode passes very quickly through the quartz and then proceeds to flow radially throughout the plate --the crystal thickness to diameter ratio being 1/80.

The plate diffusivity (α) controls the time required to reach steady state temperature gradient in the plate.

$$\alpha = \frac{k}{\rho c_p} = 8.3 \times 10^{-3} \text{ cm}^2/\text{sec at } 25^\circ\text{C}$$

Therefore, for the typical one-half inch diameter crystal with a one-quarter inch diameter electrode the transient heat flow parameter is

$$\frac{\alpha \tau}{l^2} = 0.09$$

A unity value of $\alpha \tau / l^2$ indicates steady state has approximately been reached. Therefore, approximately 10 seconds are required to establish a steady state temperature gradient in the crystal. Once this gradient is established the bulk temperature of the quartz rises at a rate dependent upon its specific heat but with the initial gradient superimposed upon it.

It has been established experimentally that radial thermal gradients with heat flow from the center of the crystal to the periphery result in plate stresses that produce increases in frequency. Imposing a radiant heat flux onto the crystal thus invariably will initially result in a frequency rise which is dependent upon the heat actually absorbed by the plate and the quartz thermal diffusivity. The transient which follows this initial frequency increase is controlled by the equilibrium temperature coefficient of the crystal and the thermal resistance of the conductive joint through which heat must leave the

quartz plate.

Figure 2 illustrates this behavior for radiant flux to a crystal operating in a temperature region of negative equilibrium temperature coefficient. If the crystal is essentially insulated, i. e. very poor joint conductivity, the initial frequency rise may eventually be more than compensated by a drop in frequency resulting from bulk plate temperature rise. As the thermal joint conductance increases the bulk plate temperature is prevented from rising as high and thus the compensating drop in frequency is lessened. Likewise, a reduced temperature coefficient due to either a changed crystallographic cut or to operation in a more favorable temperature range, will reduce the secondary frequency drop. Discontinuance of the radiant flux results in a drop in frequency of the same magnitude as the radial gradient induced rise with subsequent plate cooling.

The effect of the equilibrium temperature coefficient on transient response is shown for various temperatures in Figure 3. In this figure, case 1 corresponds to the high negative temperature coefficient condition just discussed and case 2 illustrates the effect of decreased temperature coefficient as the turnover point is approached. In case 3, the radial gradient induced frequency rise and the bulk temperature induced frequency increase are complementary.

EXPERIMENTAL PARAMETERS

The parameters chosen for general verification of the thermal model were:

1. Heat absorbed by crystal. The α/ϵ ratio of the electrode was varied by use of both vapor deposited gold and aluminum electrodes as well as aluminum electrodes with a 8000Å overcoating of SiO_x .
2. Heat rejected by crystal. The crystals were mounted in supportive rings which provided varying degrees of thermal conductance for heat transfer from the crystal. Crystals were peripherally mounted using RTV 118, and RTV 566 approximately 0.002" thick, as well as a spring loaded mechanical mount with four helical springs providing 300 grams of force on the crystal edge which was seated on a #16 polished gold plated stainless steel ring. All three of these mounting techniques have been previously flight qualified.
3. Equilibrium temperature coefficient. Crystals with 10 MHz fundamental frequency and two different crystallographic crystal cuts were used ($\phi_1 = 35^\circ 18'$, $\phi_2 = 37^\circ 03'$) to obtain widely differing temperature coefficients at a particular temperature.
4. Cyclic heat input. The effect of a 6 rpm rotation into and out of a one solar constant irradiance was also examined.

TEST SETUP

The test program was conducted in Celesco Industries'

three foot diameter by four foot long diffusion pumped vacuum chamber. The test setup within the chamber is shown in Figure 4. The crystals under test, were supported from a temperature controlled heat sink which facilitated testing at various temperatures.

The crystals were surrounded by liquid nitrogen cooled surfaces essentially eliminating background radiation to the unit. The crystal mount and shield are shown in Figure 5. The test crystal oscillator/mixer electronics and reference crystal were positioned below the test rig in a constant temperature environment to avoid extraneous temperature effects.

The simulated solar irradiance was provided by a GE 500 watt, 3400°K color temperature photo spot lamp projected into the radiation shielded crystals by a liquid nitrogen cooled front surface mirror. Simulation of the solar flux during 6 rpm rotation cycle was provided by a shaped aluminum plate which rotated through the field of the lamp as illustrated in Figure 6. The transient frequency effects produced by the photo spot lamp are comparable to effects produced by true solar spectrum flux as discussed in Appendix A.

The crystal frequency was displayed on a Model 3735A HP frequency counter, and analoged and recorded on a Model 7100B Mosely strip chart recorder. A thermistor attached to the ring of the crystal was used to monitor the crystal mount temperature.

A Hy-Cal Engineering Hy-Therm Pyrheliometer Model P-8400-B-050120 was used as the basic heat flux calibration gage. The Hy-Cal calibration was based upon one solar constant of 1398 watts/m² rather than the newly accepted 1353 watts/m². To this extent the data will be conservative.

TEST PROCEDURE

All tests were performed at pressures below 10⁻⁶ torr. The crystals were exposed to two separate intervals of continuous one solar constant irradiance and a period of 6 rpm cyclic irradiance at 0.5, 1, and 1.5 solar constants. The lower limit of test temperature varied with the crystal mount configuration. Previous steady state testing indicated stress producing phase changes for RTV 118 at -65°C, RTV 566 at -110°C and no noticeable change to -196°C for the spring mount. The RTV 118 mount was thus tested only to -50°C, the RTV 566 to -80°C and the spring mount to -140°C to avoid any extraneous mount induced effects.

TEST RESULTS

The transient response of the various test configurations, as a function of temperature is shown in Figure 7 and the quasi-steady state frequency shift (measured after the initial transient) in Figure 8.

Generally the frequency transient behavior was as described in the analysis section i. e. initial frequency rise followed by a temperature coefficient or thermal joint conductivity controlled increase or decrease in frequency.

Crystal Mount Parameter

As indicated in Figures 7 and 8 the spring mount resulted in a more nearly insulated crystal mount with the temperature coefficient becoming the controlling parameter as the crystal was able to change bulk temperature readily. Thus at 25°C with a large negative temperature coefficient (aluminum electrode crystals) the initial increase is quickly reversed by a frequency decrease induced by the rising crystal bulk temperature frequency. The same crystal ($Al + SiO_x$) mounted on RTV 566 recovered only fractionally from the initial rise indicating higher thermal conductivity through the mounting material. At temperatures below the turn-over point, the positive temperature coefficient resulted in a large additive frequency increment to the initial rise in the spring mount whereas a much lower rise would be expected with the RTV 566 with its higher thermal conductivity. This assumption is supported by the slope of the RTV 566 data.

The importance of joint thermal conductivity is illustrated also by the difference in frequency shift between the gold electrode RTV 566 and the RTV 118 mount. The evidently lower conductivity of the RTV 118 may be influenced by the lack of gold plating on these particular crystal mounting rings and thus lower heat transfer from the RTV 118 joint to the eventual heat sink. However, on an area basis it appears that the RTV must be the main contributor to poor heat conduction.

Absorptance Parameter

The gold electrode crystals have a higher absorptance than aluminum for the photo spot's radiation spectrum as discussed in Appendix A and therefore the initial frequency shift is higher as shown in Figures 7 and 8. However, the slope of the gold electrode crystal's temperature coefficient curve is so small compared to that of the aluminum electrode crystal ($\sim 1/14$ at 25°C and -50°C) that very little effect of the bulk plate temperature change is observed. As discussed in Appendix A, the radiation source used in this test produces frequency transients on the aluminum electrode crystals which should clearly match transients produced by actual solar radiation, however, considerably larger transient effects are expected for gold electrodes in solar radiation (Figure 10). Reference 2 reports 200 Hz frequency shifts for crystals and mounts identical to the gold RTV 118 configuration reported here for several QCM's on Skylab.

The SiO_x coated crystals experience greater frequency shifts than the uncoated crystals at all temperatures indicating a higher absorptivity than the base metal electrode. If the SiO_x has the same absorption characteristics as SiO , the increased

absorptivity is apparent from the data of Figure 10. Additionally, the SiO_x is applied by evaporation resulting in a porous coating with mass density of only one-half the bulk density of fused silica. Reference 3 indicates higher absorptance does result from highly anisotropic layers.

The general nature of the cyclic (6 rpm) thermal radiation induced transients is shown in Figure 3 at several different temperature coefficient conditions. Since at the simulated 6 rpm the crystal is only exposed to a sine function of one solar constant irradiance for five seconds per cycle and the radial gradient induced frequency rise time is ten seconds, a general "chopping" of the steady flux transient is expected and is confirmed by Figure 9. In this graph the amplitude of the frequency variation is shown as well as the cycle's displacement from the zero radiation ($\Delta f = 0$) frequency.

CONCLUSIONS

In order to minimize frequency transients due to solar irradiance, QCM crystals should have the following characteristics:

1. Metal electrode material should have low absorptance for solar radiation. Aluminum in this case being superior to gold.
2. SiO_x overcoatings on crystals increase frequency shifts and therefore should be avoided if possible.
3. High thermal conductivity of the crystal to mounting ring joint will reduce frequency shifts.
4. Cyclic rotation in and out of the solar irradiance will reduce the frequency shift amplitude if the rotation period is shorter than approximately ten seconds.

REFERENCES

1. Conduction of Heat in Solids - H. S. Carslaw and J. C. Jaeger, Clarendon Press.
2. Quartz Crystal Microbalance Contamination Monitors on Skylab - A Quick-look Analysis, R. Naumann, W. Moore, D. Nisen, W. Russell and P. Tashbar. NASA MSFC, June 8, 1973.
3. Effects of Surfaces on the Intrinsic Radiation Properties of Dielectrics - J. C. Klein, Symposium on Thermal Radiation of Solids NASA SP-55.
4. Ultraviolet Radiation, Koller, Wiley Press.

ACKNOWLEDGEMENTS

Mr. D. Bergquist spent many hours performing diligently these tests as well as assisting in the analysis. Mr. K. Rogers provided as usual many helpful suggestions in the heat transfer analysis.

APPENDIX A

THE PHOTO SPOT LAMP AS A SOLAR IRRADIANCE SIMULATOR

The argument for the validity of a 'solar simulator' test using any type of lamp source hinges not upon how well the lamp reproduces the solar spectrum but rather on how well the effects of radiation of a solar spectral nature impinging upon surfaces of interest are duplicated by a lamp of a different spectral character.

In the present test a GE 500 watt, 3400°K color temperature photo spot lamp was used to produce one solar constant (1398 watts/m²) of irradiance at the test station. To produce this irradiance level the lamp was operated at only 58 volts. Reference 4 indicates reduction to one-third filament temperature would be expected for this reduction from the 110 volt rated voltage. The peak irradiance thus should be reduced from approximately 1 micrometer wavelength to 2.5 micrometers by Wien's displacement law. Measurements with a Jarrell Ash Monochromator did not verify this prediction. This instrument has reduced sensitivity in the near IR region, however no spectral differences were measurable for the two lamp voltage settings. The most that can be said then is that blackbody radiation at between 1000°K and 3400°K is incident on the crystals. This is not to say that either blackbody spectral radiance curve fully describes the radiation emitted by the lamp. The lamp's glass envelope has a 2.7 micrometer cutoff on the IR side of the curve as seen in Figure 10, thus only wavelengths less than 2.7 micrometer are emitted by the lamp.

The materials to be considered in this test are aluminum and gold vacuum deposited on 3μ grit polished natural quartz and silicon dioxide vacuum deposited to a 8000Å thickness over the aluminum. In the case of vacuum deposited aluminum films, Figure 10 indicates a relatively small change in reflectance as the spectrum shifts from solar to the near IR. Transient thermal effects in aluminum coated quartz plates irradiated with the Photo Spot lamp should be very nearly the same then as the effects produced by true solar radiation. Very nearly the same amount of heat energy will enter the plate for the same irradiation level. This is not true for gold electrodes. Even if the lamp temperature is on the high side (3000°K) only a fraction of the energy is at wavelengths less than .5 micrometers where gold has a high absorptance (Figure 10). Solar radiation on the other hand is peaking in this region. Test results on gold electrodes using this lamp thus can be used on a comparative basis only.

The Si₂O₂ is actually deposited as a Si₂O_x which has slightly higher absorptance in the Photo Spot spectrum as previously discussed and somewhat larger absorptance in the UV portion of solar spectrum which is missing in Photo Spot lamp.

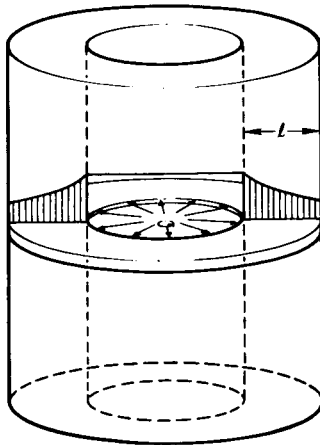


Fig. 1—Hollow Cylinder Heat Transfer Model

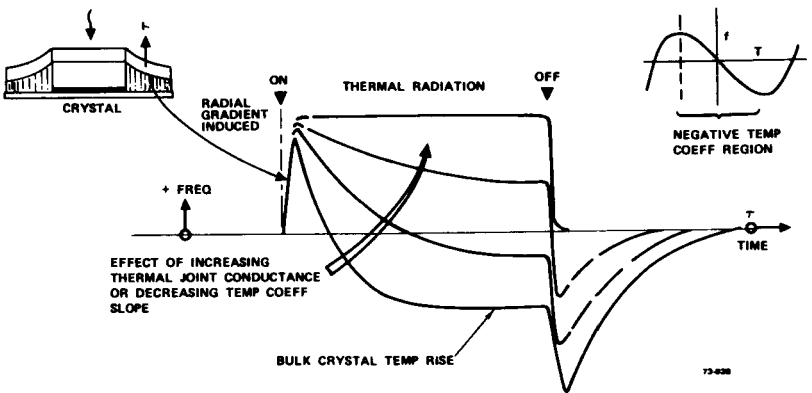


Fig. 2—Crystal Transient Response for Negative Equilibrium Temperature Coefficient

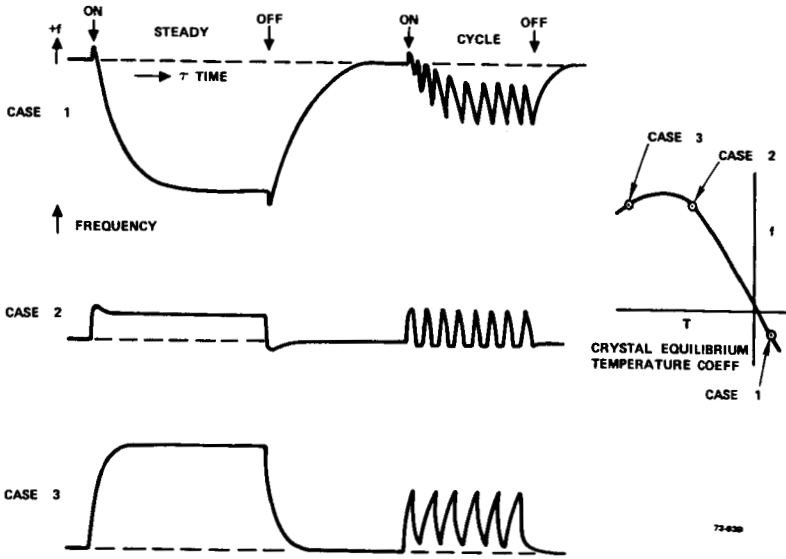


Fig. 3—Transient Frequency Response as a Function of Temperature Coefficient

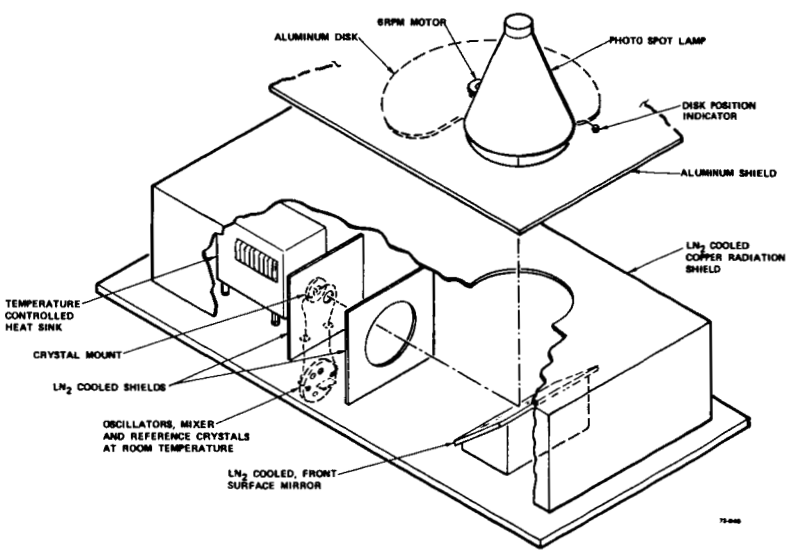
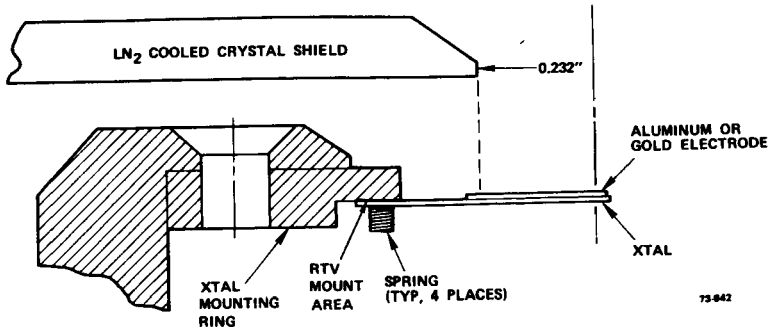
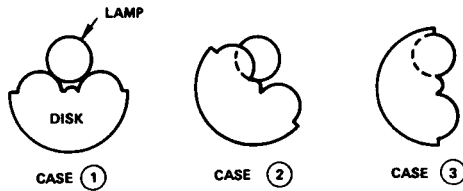
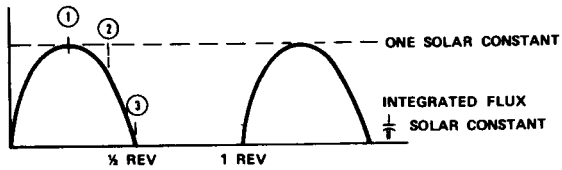
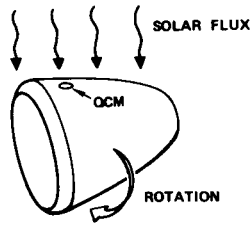


Fig. 4—Test Setup



73-842

Fig. 5—Aperture for Crystal Irradiance



73-841

Fig. 6—Rotation Simulation

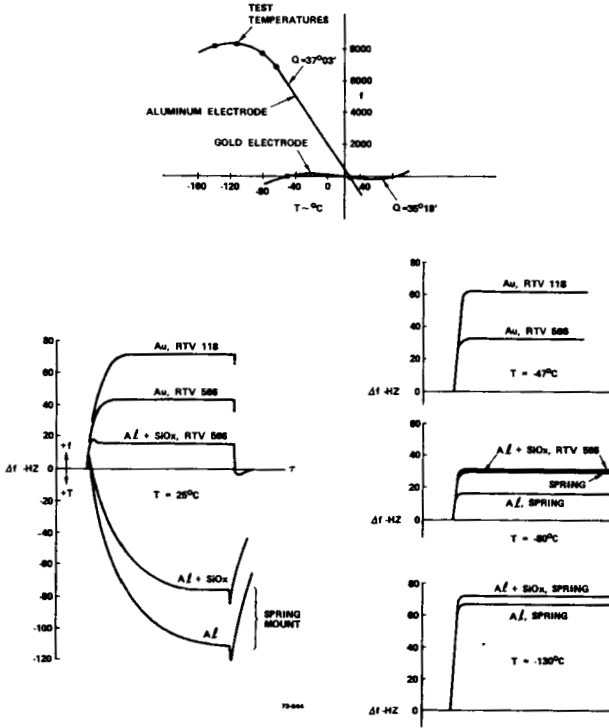


Fig. 7—Crystal Frequency Response to Irradiance at Various Temperatures

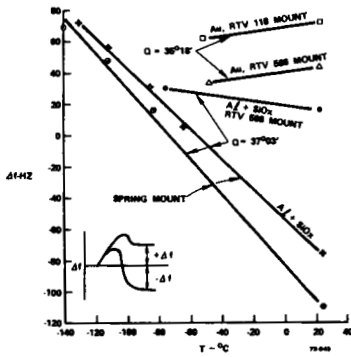


Fig. 8—Effect of Electrode Material and Mount Configuration on Transient Amplitude

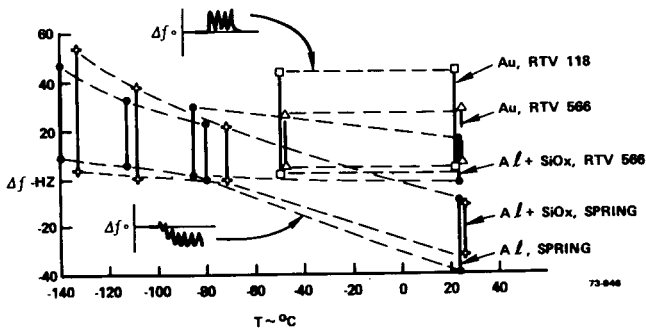


Fig. 9—Effect of Simulated 6rpm Rotation on Transient Amplitude

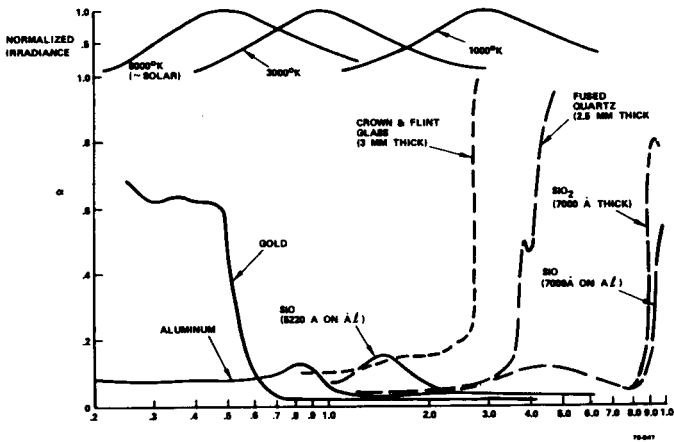


Fig. 10—Wavelength λ Micrometers

Paper No. 30

PHOTOGRAPHIC MEASUREMENT OF PARTICULATE SURFACE CONTAMINATION

O. Hamberg, *The Aerospace Corporation, El Segundo, Calif.*

ABSTRACT

The particulate surface cleanliness of spacecraft is important to the proper functioning of certain spacecraft devices. This report reviews the limitations of some surface contamination measurements currently used, and shows how an approach based on the use of macrophotography has some inherent advantages over the usual methods for field measurement of assembled spacecraft. These advantages are that no contact with sensitive surfaces is required, the measurement is direct, and a permanent record is provided. The results of an experiment which compares particle visibility and sizing using 4X macrophotography with 37X photomicrography are provided. These results, based on the use of available equipment, indicated that macrophotography with non-optimized equipment provided reasonable accuracy down to 16 microns and that further refinement might allow the measurement of smaller particle sizes.

INTRODUCTION

Increasingly rigorous requirements for the control of particulate contamination of orbiting scientific payloads have made the study of spacecraft particulate surface contamination on the ground an important part of several programs. This is based on the consideration that many of these spacecraft contain devices which are sensitive to particles in their field of view and on their surface. The methods currently used to measure surface particulate contamination are generally not suitable for in situ examination of most assembled spacecraft since they require intimate contact of fluids or equipment with sensitive surfaces and are generally indirect. Therefore, the use of photographic measurement techniques which require no intimate contact, are direct, and provide a permanent record, were evaluated.

BACKGROUND

The reasons for concern about particulate contamination and current methods used to measure surface cleanliness were

explored with the following results.

Particulate Contamination Problems

As an example, based on Ref. 1, the star Canopus was used as a roll reference by the Surveyor, Lunar Orbiter and Mariner spacecraft. A consistent problem that plagued some of the spacecraft, particularly the 1964 Mariner, was that roll signal transients occurred frequently, occasionally causing loss of Canopus lock. Analysis and tests of possible mechanisms that could cause this behavior led to the conclusion that small dust particles were being released from the spacecraft by some means and were drifting through the star sensor field of view. Sunlight scattered from the particles then appeared as illumination equivalent to that from a bright star causing a roll error transient while the sensor was locked on Canopus. It was theorized that a 25-micron translucent dust particle with a diffuse scattering coefficient of 0.4 would appear as bright as Canopus at a distance of 66 cm from the star sensors. Large numbers of dust particles of this size and larger are collected on exposed surfaces even in the controlled environment of the spacecraft assembly area. It was considered plausible that minor vibrations or shock events could release particles from the spacecraft surface.

For spacecraft where the mapping of the celestial sphere and other items are of interest, the effect of dust particles is not a loss of lock-on as with the Mariner spacecraft. However, particulates in the field of view can appear as false targets that will degrade accuracy of the data returned. Cleanliness requirements called out in specifications are becoming more stringent. Several earlier programs stipulated requirements simply as "no visible particles," and recently the trend is toward the imposition of quantitative cleanliness requirements with attempts to impose levels as low as MIL-STD-1246 Class 10. The various classes of standards are shown in Figure 1.

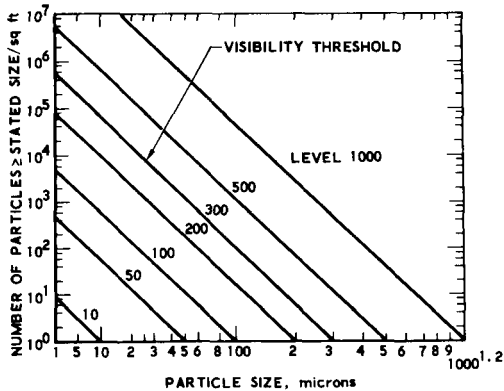


Fig. 1. Surface cleanliness standard

Particulate Contamination Measurement Methods

A literature survey was conducted to determine the applicability of current methods of measuring surface cleanliness of assembled spacecraft to this stringent accuracy.

Indirect Measurements. One of the most popular types of surface particulate measurements²⁻⁷ is conducted by flushing portions of the surface with a cleaning solution, collecting the solution, and then filtering particles from the solution by using a membrane filter of 0.45- to 1.2-micron pore size. The collected particles on the filter are then counted and sized under a microscope of 45 to 100X magnification. This test then indicates surface cleanliness assuming that the majority of particles collected were removed by the flushing operation and represent the particulate contamination degree of the surface.

The total filterable solids test⁸ obtains particles in the same manner as the previous method, except instead of counting and sizing the particles under a microscope, the weight of the particles is obtained by using a sensitive weighing system. The wipe test⁷ is carried out by wiping clean filter paper across the surface of concern. The count and size of distribution of the particles lodged on the filter paper is again measured by microscopic examination. The vacuum cleaning test⁷ is conducted by vacuuming applicable portions, collecting the vacuumed particles on a 100-mesh screen and observing the screen with a 10-power magnifying glass. If any significant amount of particles are on the screen, the screen is flushed with an appropriate service fluid and the particles are filtered from the fluid by a membrane filter followed by microscopic examination for size and count.

Witness plates consisting of flat surfaces of various compositions and colors have been used in some applications. These plates are placed in strategic locations and are microscopically examined as indicators of particle fallout in the vicinity of sensitive surfaces. Aside from problems of accessibility, no assurance can be provided that these plates are truly representative of the surfaces of concern and are located in the proper areas. Nevertheless, if accessibility for removal of the plates is feasible as late as possible in the launch operation cycle, this method of ground contamination measurement has advantages over other methods since the sensitive spacecraft surfaces do not have to be contacted.

The previous methods provide indirect measurements of surface contamination. For the flushing and wiping methods, the particles from relatively large surfaces are concentrated on smaller collecting devices and thereby allow the examination of less area by high power microscopy. Although this allows the detection of particles less than 1 micron in size, the accuracy is questionable since it depends on the unknown particle removal or collection efficiency and reproducibility of the devices used. Also, with the exception of the witness plate method, the methods are usually impractical for use on assembled spacecraft in the field

since direct contact of the spacecraft or fluid is required. In most applications the spacecraft contractors would not allow such operations because of potential damage to the spacecraft or sensitive surfaces.

Direct Measurements. The only direct surface examination of assembled spacecraft presently performed is a visual inspection⁷ utilizing white or ultraviolet light. The visual inspection without magnification is relatively qualitative, dependent on the acuity of the inspector's vision. Under optimum conditions, the human eye can detect particles > 25 to 50 microns. It has been approximated that roughly 1000 particles > 50 microns on a surface, equivalent to MIL-STD-1246A Class 300, are required to allow a general impression of visible contamination since it is unlikely that the eye can focus on a few scattered particles in the visible size range. The ultraviolet light inspection would reveal only particles that fluoresce under ultraviolet radiation and is mainly used to detect surface films such as hydrocarbons.

A 10-power magnifying glass has been used to allow the detection of relatively small particles of high contrast (~5 microns); however, the time to count and size particles in this manner is considered excessive, no record is provided, and it is judged not suitable for field use.

New Developments in Measurement. Among new developments under investigation are a sonic velocity vacuum probe especially designed for the collection of particles down to 1 micron by Sandia Corporation⁹, quartz crystal microbalances (QCM) under development by Celesco Industries and various other corporations¹⁰, and a photometer developed by SAAB-Scandia of Sweden¹¹. These devices are subject to a considerable number of problems such as the vacuum probe that must have direct contact with the surface under consideration, which is not allowable on many spacecraft. The QCM will measure small changes in the mass of deposits on a crystal surface. However, they must be coated with an adhesive to bind particles to the surface. Otherwise, the microbalance will only measure the impulse of impacting particles. The recording and interpretation of such data is more complex than for adhesive coated microbalances. Also, the small size of a QCM requires that many be used to obtain statistically meaningful sampling areas. The SAAB photometer measures changes of specular reflectance due to particles, does not provide a measure of particle count or size, and requires the use of witness plates as opposed to direct measurements.

Because of this lack of suitable methods to measure the surface cleanliness of spacecraft in the field, an experimental program using photographic techniques was initiated.

APPROACH

Consideration was given to the use of photographic techniques

because it would allow a direct measurement of surface particulate contamination, provide a record of the degree of cleanliness, would not require physical contact with sensitive and vulnerable surfaces, and could potentially be performed in a short time period. All of these factors were judged of importance in obtaining field measurements.

Particle measurement using conventional photomicrographic techniques is a well established art^{12, 13}, but generally requires specimens that can be placed under a microscope. After precise adjustments, magnification up to 350X can be relatively easily photographed. For direct examination of spacecraft surface contamination it was believed impractical to utilize photomicrography for several reasons. The field of view decreases rapidly as the magnification power increases. Drinker and Hatch¹⁴ have indicated that a statistically meaningful sample requires the capture of at least 100 particles. Using this as a basis, the number of 35-mm photographs that would be required at various magnifications and cleanliness levels is shown in Table 1.

Table 1. Number photographs versus magnification power

<u>Item</u>		<u>35-mm Photographs/100 Particles</u>			
<u>Lens Mag. Powers</u>	<u>1X</u>	<u>4X</u>	<u>10X</u>	<u>40X</u>	
<u>MIL-STD-1246A</u>					
Class 500	< 1	< 1	< 1	4	
Class 300	< 1	< 1	3	37	
Class 100	3	37	230	3,640	
Class 50	23	364	2,300	36,400	
Class 10	1,150	18,200	115,000	1,820,000	
Field of View (sq mm)	870	55	8.7	0.55	

It can be seen that at high magnification powers and low contamination levels extremely large numbers of photographs are required to capture 100 particles. From a practical standpoint the author assumed that approximately 37 photographs of 35-mm size are the upper limit of the number of photographs that can reasonably be analyzed within a practical time period. For this reason, based on Table 1, if contamination levels considerably below MIL-STD-1246A Class 300 (the visible contamination threshold) are to be measured, magnification powers exceeding approximately 6X would be impractical. This would theoretically allow measurements of cleanliness levels somewhat better than MIL-STD-1246A Class 100. This degree of magnification falls within the limits of macrophotography and led to its selection.

Other considerations leading to the elimination of photomicrography as a candidate were the field conditions under which the photographs are taken. These require a relative insensitivity

to small vibrations and thus a large depth of field is desirable. Because of irregular surfaces on the spacecraft, it is also desirable to have the viewing lens as far as possible from the surface under examination. Both conditions present difficulties at high magnifications since the depth of field and the working distance decreases with magnification power.

References 15 and 16 describe initial attempts to perform macrophotographic surface contamination studies on spacecraft STP 70-1 and 71-2 where particles in the 50- to 100-micron range were of concern. During these measurements it was noted that relatively little knowledge was available on the smallest size particle that could practically be measured on a spacecraft by macrophotographic means.

THEORY

Before embarking on experiments, an evaluation of some of the photographic parameters was conducted to determine the theoretical variables that might influence the particle measurement accuracy obtainable.

Diffraction Limit¹⁷

Photographic objective lenses have an ultimate physical limit in their ability to transmit an accurate image of point sources of light to the image plane. This is the diffraction limit of the objective. Although the reflection of light from particles is not a true representation of a point source of light, the diffraction limit of lenses enters into the consideration of variables that affect the image transmitted by the photographic objective.

Diffraction is a phenomenon which occurs whenever an aperture is placed in a light beam in such a way as to limit its diameter. In an optimally corrected photographic lens the spreading of the light caused by the aperture stop is manifested in the image plane by the appearance of the Airy disk, a circularly symmetric distribution of the light from a point source consisting of a bright spot with a system or rings of much weaker intensity around it. About 84 percent of the energy from the point is contained in the central disk. The diameter of the central disk is generally the only one considered and is defined by

$$d = 2.44\lambda F (1+M) \quad (1)$$

where

- d = the central Airy disk diameter, microns
- λ = the light wavelength (~ 0.55 microns for visible light)
- F = the lens f number
- M = the magnification

The image produced by a photographic objective of point sources or objects such as particles approaching point sources is thus enlarged. The apparent size of a magnified point source in

the image plane is defined by

$$d_a = d/M \quad (2)$$

where d_a = the apparent diameter of a point source and M = magnification.

It can be expected that particles smaller than the apparent diameter produced by the Airy disk will thus appear at least as large as the apparent diameter and probably somewhat larger since they are not point sources, even if a perfect lens system is used. Table 2 shows the relationship between selected f numbers of a perfect lens and the apparent diameter of a point source for selected magnifications.

Table 2. Apparent diameter of point sources*

Objective f - number	Apparent diameter on image plane, microns				
	Magnification	1X	2X	4 X	8X
1		2.7	2.0	1.68	1.5
1.4		3.8	2.8	2.3	2.1
2		5.4	4.0	3.4	3.0
2.8		7.5	5.6	4.7	4.2
4		10.7	8.0	6.7	6.0
5.6		13.7	11.2	9.4	8.5
8		21.5	16.0	13.4	12.0

*These data are for high contrast conditions

Although some cameras have minimum f numbers between 1 and 1.4, photographers generally use f numbers approximately three stops above the minimum f number to obtain good definition (resolution) with a reasonable small image of a point source (Airy disk). This is done because ordinary commercial grade lenses are not diffraction limited at small f numbers due to residual aberrations. By stopping the lens down with an internal diaphragm these aberrations are reduced and the lens more nearly approaches its diffraction limit.

With objectives specifically designed for macrophotography, it is possible to operate at the minimum f number with good resolution since lenses are manufactured to produce minimum aberrations even when the aperture is wide open. In general, such lenses have minimum f numbers between 2 and 4. A high quality macrophotographic lens was not available at The Aerospace Corporation and it was necessary to use a lens with a minimum f number of 3.5 which was not designed for macrophotography. For good resolution this lens was stopped to $f/8$. Per Table 2, the diffraction limit of such a lens would be 13.4 microns at the 4X magnification. This size can thus be predicted to be the diffraction limited size particle image seen through the lens, regardless of the actual size of the object.

Lens Contrast Modulation and Film Emulsion Spread

A photographic lens modulates the contrast between the object photographed and the background so that the image seen by the film has less and less contrast as the object becomes smaller¹⁸. The ability of the film emulsion to capture the image transmitted by the lens is related to the emulsion sensitivity¹⁹. The sensitivity of an emulsion to give good definition and to reproduce fine detail is limited by its microstructure at the exposure stage and after development. If an infinitesimally small point or narrow line image could fall on an emulsion layer, it would diffuse the light into a broadened point or line of an intensity that would diminish toward zero at the borders²⁰. The amount of spread is a function of the type of film used with greater spread for high speed than for lower speed films, such as microfilm as indicated in Figure 2.

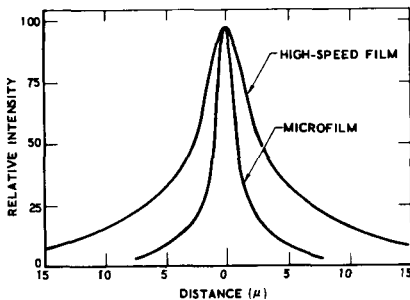


Fig. 2. Spread function of film

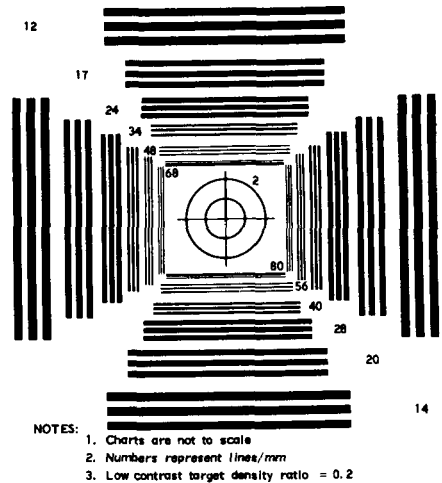


Fig. 3. High-contrast resolution test chart, density ratio = 1.4

This shows that slow, fine grain emulsions theoretically provide better and more accurate definition than high speed, coarse grain emulsions. For this reason two types of films were used for the experiment; a relatively fast Panatomic X film and a relatively slow High Contrast Copy film.

Lens/Film Resolution Thresholds

Subjects consisting of various contrast resolution targets are photographed using an identical lens with different types of film to determine resolution of the lens/film combination.

Figure 3 is a high contrast NBS target²¹ where contrast is a measure of the ratio of densities of the dark lines and the background. Density ratio is defined as follows¹⁹:

$$D = \log (I_{\max} / I_{\min}) \quad (3)$$

where D = density ratio, I_{\max} = the luminous intensity of the lines-candles, and I_{\min} = the luminous intensity of the background-candles.

The relative performance of the films used can be measured by determining the number of lines per mm that are distinguishable as separate and distinct lines on the negative (resolution).

Figure 4 shows the performance of two different speed films using such a test¹⁹. The curves labeled high and low contrast object represent the contrast modulation caused by the camera lens which decreases the object contrast in the image plane from its highest value when the lines are far apart to lower values as the line spacing decreases. The curves labeled high speed and high contrast film threshold represent the implicit threshold resolution values of the films which allow higher resolutions as the object contrast increases. The intersections of the film threshold curves with the lens contrast modulation curves are the resolution thresholds of the lens/film combinations as depicted on Figure 4. Note that the slower speed high contrast film has a considerably higher resolution threshold than the high speed film. While tests using bar type subjects are not representative of tests on point-type subjects, a similar resolution relationship exists for point subjects.

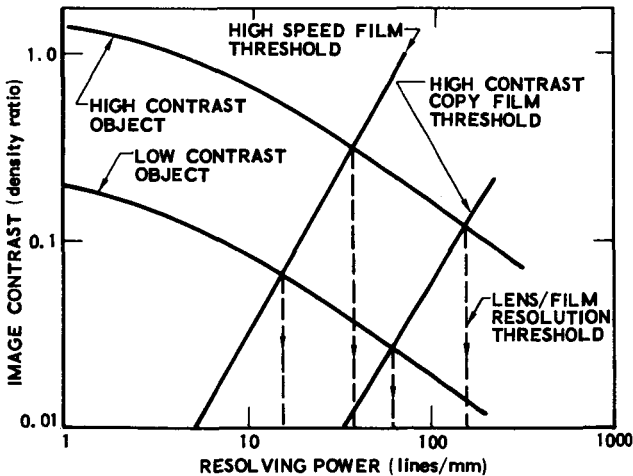


Fig. 4. Typical lens/film resolution thresholds

The diffusion of a point of light by both lens diffraction and emulsion spread is such that maximum intensity exists at the center and less intensity at the edges. As a result it can be expected that the contrast between the background at the image decreases at the edges so that the emulsion does not reproduce the complete size of the image. There is thus a compensating mechanism for diffraction and point spread enlargement which depends on emulsion sensitivity to contrast. It can be expected that as a photographic negative is processed to an enlarged print, further contrast reduction occurs and a given point image will appear smaller. Illustrations used in this report are enlarged prints of negatives. They are thus not necessarily true representations of the data. The negatives themselves were used to collect the actual data on particle count and size.

The illumination of the surface is an additional variable that must be considered. Decreasing intensity can be compensated for by increasing aperture opening or exposure times. The angle of illumination is important in the ability to distinguish between particles and surface roughness and also influences the sizing accuracy.

EXPERIMENTAL PROCEDURE

The basic experiment was designed to obtain 37X photomicrographs of certain areas of the artificially contaminated specimen for use as a baseline, followed by macrophotographs of the identical areas under varying magnifications and types of illuminations using a relatively high speed and slow speed film. The results would then be compared to determine the degree of contamination visible on the macrophotograph relative to the 37X photomicrograph baseline.

Prior to initiation of the primary experiment, the development of experimental specimens, particle sizing and counting techniques, plus photomicrographic and macrophotographic techniques was required. There was no attempt made to optimize on an absolute basis. The development of the technique was confined to the most practical usage of equipment available.

Specimen Preparation

The test specimen used for the experiment consisted of a 1/8-in. thick aluminum plate measuring 1 x 1 in., painted with white acrylic paint, and gridded with 2 x 2 mm grids as shown in Figure 5. The surface roughness was not measured. It is approximated that maximum irregularities in the paint projected 10 microns above the general surface.

The fly ash used to contaminate the specimen consisted of particles with a relatively wide size distribution, ranging from submicron to in excess of 100 microns. The substances contained within fly ash provide a wide range of colors from almost pure carbon black to white aluminum oxide, and almost colorless silica particles. This substance thus presented a good cross

section of potential surface contaminants with varying contrasts against a white background.

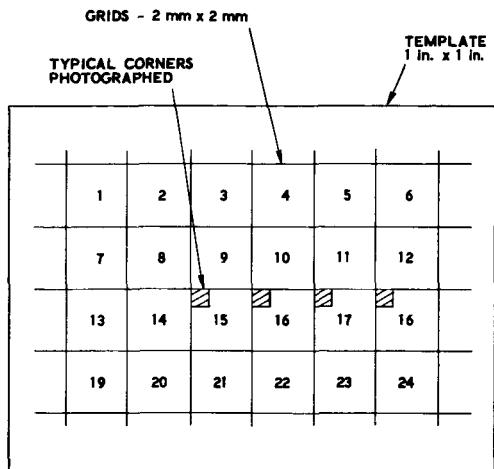


Fig. 5. Test specimen

The sample was artificially contaminated by mixing a relatively small amount of fly ash with solution consisting of 95 percent isopropyl alcohol and 5 percent by volume of liquid soap. The fly ash contained within the alcohol-soap solution was stirred and spread over the surface of the specimen until a relatively homogeneous amount of fly ash seemed to be covering the grids as observed by direct microscopic examination. After the alcohol evaporated, the fly ash remained on the surface to be used as the artificial contaminant. An initial attempt to utilize freon (MIL-C-81302A Type II) to suspend the fly ash was not successful since the fly ash did not stay in suspension long enough and coagulated quite rapidly. The alcohol-soap solution showed minimum coagulation of particles and good homogeneity of surface coverage by microscopic examination.

After the artificial contamination was accomplished, the sample was kept in a closed container to protect it from further contamination. It was only removed from the container when photographs were taken. Repeated examination indicated no apparent change in contamination as a result of these short exposure times.

Counting and Sizing Techniques

Photomicrographs. Photomicrography using 37X magnification was selected since it allowed the measurement of 1-micron particles with reasonable accuracy. The measurements were performed by projecting the negatives onto a white paper screen measuring 70 x 85 cm at a projection magnification of 30X for a

total magnification of 1110X. The projector was a Society for Visual Education Model 49 500-watt, 35-mm film strip projector and was equipped with a 5-in. focal length, $f/3.5$ coated lens. At the 1110X magnification a 1-micron particle would measure slightly above 1 mm and was easily visible. The outlines of the particles on the screen were traced, the paper screen removed, and the traced particle sizes measured using a metric ruler graduated in millimeters. It is estimated that the accuracy of measurement using this method was $\pm 1/2$ mm, equivalent to approximately $\pm 1/2$ micron at the 1100X total magnification. The number of particles was determined by simply counting the particles traced. A tabulation of size and count was then made by totaling the number of particles within specific size ranges.

Macrophotographs. For the 1X, 2X, 4X and 6X macrophotographs similar sizing, counting and tabulation techniques were used. Table 3 shows the sizing accuracies estimated for the various macrophotographic magnification powers used.

Table 3. Sizing accuracies

<u>Photo Magnification</u>	<u>Screen Magnification at 30X Projection</u>	<u>Sizing Accuracy, Microns</u>
6X	180X	± 3
4X	120X	± 4
2X	60X	± 8
1X	30X	± 16

Photomicrographic Technique Development

The test specimen was placed under a Leitz Ortholux microscope with a 35-mm Leica camera attachment, and 35-mm photomicrographs at 37X magnification, using Kodak Panatomic X film, were taken of the upper left hand corner of each of the 24 grids. The field of view covered by each photograph was approximately 0.6 sq mm. The initial photographs were taken with conventional microscopic illumination using a light in an almost vertical angle position. Upon completion of this phase, the illumination angle was changed to ~ 30 -deg angle from the horizontal and photomicrographs were taken with this oblique illumination. Standard methods were used to develop the Panatomic X film.

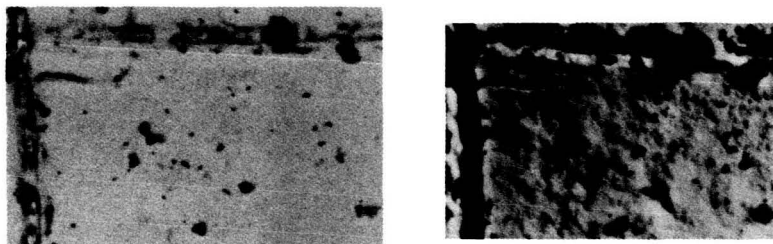
It was found that the obliquely lighted photomicrographs allowed distinguishment between particles and shadows and also indicated the roughness of the white painted background. Figure 6 shows an example of a vertically and obliquely lighted 37X photomicrograph of grid no. 4 on Figure 5.

By comparing the vertically and obliquely lighted photomicrographs, it was concluded that a large number of the spots appearing on the vertically lighted photomicrographs were not particles but were reflections created by the roughness of the background. As an example, on grid no. 4 the vertical lighting

led to a count of 72 spots, whereas the oblique lighting only revealed 34 true particles. It thus appeared that vertically lighted photomicrographs of rough surfaces were not suitable for analysis and that oblique lighting would be required.

Vertical lighting

Single oblique lighting



37X photo, 1.6X print, and 60X total enlargements

Fig. 6. Vertical vs. oblique lighting 37X photomicrographs

Macrophotographic Technique Development

Equipment. The macrophotographic equipment consisted of a Leica M2 camera fitted with a 135-mm $f/4.5$ Hektor lens for 1X magnifications and a 50-mm, $f/3.5$ Elmar lens for 2X, 4X and 6X magnifications. These were the best lenses available to the author at The Aerospace Corporation and procurement of more optimum equipment was not within the scope of this study. It is reasonable to postulate that some modern macro lenses could have been more effective.

The camera was equipped with a Visoflex II reflex housing and extension bellows were inserted between the lens and camera body for reproduction scales up to 4X. For 6X magnifications extension tubes were inserted between the lens and camera body since the available bellows could not extend far enough. Illumination was produced by Colortran Multi-6, 650-watt quartz lights and photographs were taken at a variety of angles. It was decided to use three illumination angles for the macrophotographs; approximately perpendicular to the surface, single oblique at approximately 30 deg to the surface, and two diametrically opposite oblique lights at 30 deg to the surface. Figure 7 shows the vertically lighted photographic set-up used for the macrophotograph at 1X magnification.

Quartz lamps were used since field conditions required explosion-proof equipment. All pictures were taken at $f/8$ and the exposure time was varied in accordance with the degree of magnification.

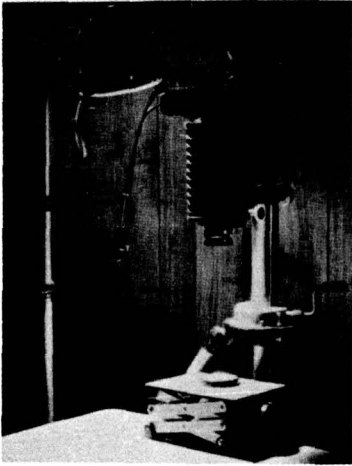


Fig. 7. Vertically lighted photographic set-up

Illumination, Exposure and Projection. Experiments were conducted on illumination and exposure techniques. Also, the variation in particle visibility with magnification power was tested to determine the most practical magnification with the available equipment. Photographs at 1X, 2X, 4X and 6X magnifications of the identical specimen areas were taken using illumination at oblique and vertical angles. Optimum exposure for each picture was obtained by using three different exposure times at a constant f/8 aperture. The technique provided approximately equal density negatives. It was concluded that at magnifications up to 6X vertical lighting would be best for close-up photographs since it allowed more accurate sizing.

The particle visibility at various photographic and projection magnification powers was tested by analyzing identical portions of the template using photographs taken at various magnifications and projecting each at 60X, 30X and 15X magnifications. The 30X projection magnification was selected as the best compromise. Table 4 shows the results in condensed form for 30X projection magnification.

Table 4. Macrophotographic particle distributions

Size, Microns	No. of Particles at Photographic Magnification Powers			
	6X	4X	2X	1X
≥ 2	--	--	--	--
≥ 10	--	--	--	--
≥ 12	65	--	--	--
≥ 16	62	61	--	--
≥ 20	51	54	--	--
≥ 25	38	29	30	12
≥ 32	21	23	25	9
≥ 46	12	13	15	9

It can be noted that relatively small differences exist between the 6X and 4X size and count distributions, but that at photographic magnifications below 4X major changes in particle visibility occur. For this reason 4X was selected as the most practical macrophotographic magnification power.

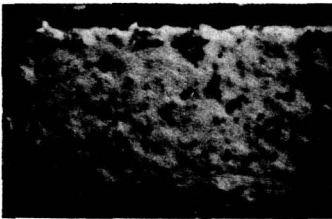
PRIMARY EXPERIMENT

The basic experiment, using the techniques developed, was performed by comparing 4X macrophotographs with 37X photomicrographs of identical areas on the test specimen, using Panatomic X and High Contrast Copy film.

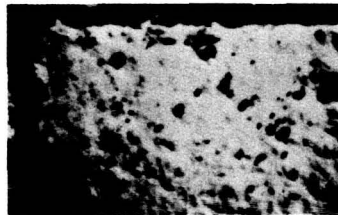
37X Photomicrographs

In order to limit the number of photographs required to obtain statistically meaningful data, the artificially contaminated sample was examined under a microscope and it was estimated that four 37X photomicrographs would capture approximately 200 particles. Figure 8 shows an example of a 37X photomicrograph using Panatomic X film and also shows the same area for High Contrast Copy film. The results of particle size and count analysis derived from 37X photomicrographs are shown in Table 5 for the two types of film used.

Panatomic X film



High contrast copy film



37X photo, 1.6X print, and 60X total enlargements

Fig. 8. 37X photomicrographs, grid no. 17

It can be noted that the High Contrast Copy film provided considerably better visibility at particle sizes less than 12 microns.

4X Macrophotographs

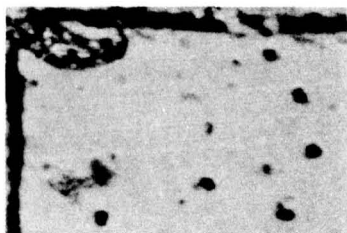
The fly ash contaminated template was photographed at 4X magnification using vertical illumination with both Panatomic X film and High Contrast Copy film and the same areas previously photomicrographed at 37X were examined and compared for particle count and size.

Table 5. 37X photomicrographic particle distributions

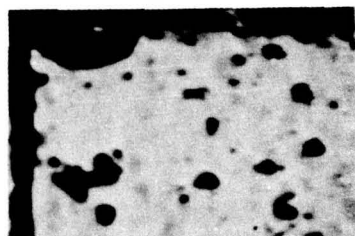
Size, microns	Film	
	Panatomic X	High Contrast Copy
	Number of Particles/1.5 sq mm \geq Stated Size	
≥ 2	170	234
≥ 6	168	207
≥ 12	114	117
≥ 20	55	58
≥ 32	20	18
≥ 46	5	5
≥ 64	4	3
≥ 90	2	1

As an example, Figure 9 shows the upper left hand corner of grid no. 15 photographed with Panatomic X film and High Contrast Copy film. These pictures are enlarged to a total of 60X for purposes of illustration only. The actual enlargements for sizing and counting were 120X.

Panatomic X film



High contrast copy film



4X photo, 15X print, and 60X total enlargements

Fig. 9. 4X macrophotographs, grid no. 15

The results of the macrophotographic count and size distribution as compared to the High Contrast photomicrograph count and size previously described are provided in Table 6.

It can be noted that the smallest particle size visible on the macrophotographs was 16 microns for both films. The total number of particles visible on the macrophotographs was 25 and 31 percent, respectively, for the Panatomic X and High Contrast Copy films as compared to those visible on the photomicrographs. It can also be noted that relatively poor particle count correlation exists at sizes 16 microns and above between the macrophotographs and the photomicrographs.

Table 6. Macrophotographic vs. photomicrographic particle distribution

<u>Film</u>	Panatomic X		High Contrast Copy
<u>Magnification</u>	4X	4X	37X
<u>Size, microns</u>	<u>No. of Particles/1.5 sq mm \geq Stated Size</u>		
≥ 2	--	--	234
≥ 4	--	--	232
≥ 6	--	--	207
≥ 12	--	--	117
≥ 16	58	73	81
≥ 20	55	71	58
≥ 32	39	37	18
≥ 46	7	11	5
≥ 64	3	6	3
≥ 90	1	3	1

DISCUSSION

An explanation for the lack of correlation was sought by comparing the sizes measured on the macrophotographs with the size of identical particles measured on the photomicrographs. This was done by measuring the position of the particles relative to the template grid lines using a rectangular coordinate system. Each particle was then numbered and a particle by particle comparison of size was made on the four grid portions examined. The results are shown on Figure 10 for Panatomic X film and on Figure 11 for High Contrast film by plotting the sizes of particles obtained from macrophotographs against the size of the identical particle from photomicrographs. Note that for both films most of the macrophotographic sized particles appear larger than the photomicrographed particles since a majority of points are above the equal size 45-deg lines drawn on both figures. The reason for the point spread can most likely be explained by photographic considerations discussed in the section on theory, such as lens diffraction, emulsion spread, contrast modulation, etc. The constant f/8 number used for the macrophotography produces a diffraction limited size of approximately 13.4 microns as shown in Table 2. When coupled with the point spread induced by the film, it is not unreasonable to expect a minimum apparent size of 16 microns, although the actual size of a few particles captured by the macrophotographs was as small as 6 microns. It is assumed that these were especially high contrast particles. The apparent smaller than actual size particles (below the equal size line) is probably due to the low contrast of certain particles and the contrast modulation of the lens which would reduce the size of the image as compared to the subject.

Figure 12 shows the cumulative particle count and size distributions, with curves A and B representing the particle count and size distribution for photomicrographs, using High Contrast

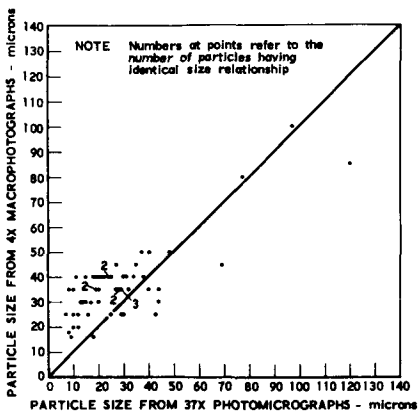


Fig. 10. Particle Size, Panatomic X film

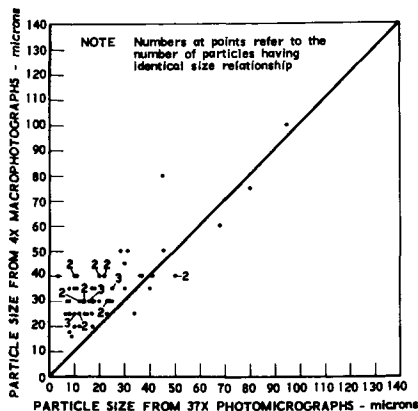


Fig. 11. Particle Size, High Contrast Copy film

Copy film and Panatomic X film, respectively. Curves C and D represent the particles captured and counted on macrophotographs, but located and sized on the photomicrographs. Curves E and F represent the particles captured, counted and sized on macrophotographs.

It can be seen that curves C and D merge with curves A and B at approximately 32 microns. This indicates that good correlation of count and size would have been obtained at this size if the true particle size had been measurable on the macrophotographs.

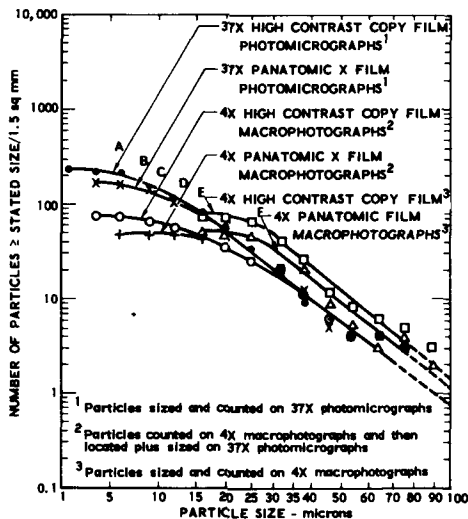


Fig. 12. Cumulative Experimental Results

A comparison of curves E and F with curves A and B showed that the apparent particle count at a given size on the macrophotographs started to exceed the count on the photomicrographs at 20 microns for Panatomic X film and 16 microns for High Contrast Copy film. The macrophotographs thus indicated a higher than actual contamination degree at sizes above these values.

Although the accuracy and particle visibility obtained with macrophotography was not as high as desired, the experiment indicated that this method is usable for field surface contamination measurements where a degree of measurement above the "no visible" surface contamination is desired. Also, it provides direct measurements, requires no contact with surfaces and provides a permanent record. It should be noted that the cleanliness of the environment surrounding the surfaces must be closely controlled after photographic accessibility is no longer feasible to assure that the measured cleanliness is retained.

Conclusions

Based on the experiments conducted and the equipment used, it is concluded that field contamination measurement by 35-mm, 4X macrophotography provides conservative results within reasonable limits for sizing and counting particles ≥ 16 microns. It is also concluded that adoption of the technique described by these experiments can realize the inherent advantages of photographic measurement of (1) no direct contact between the measuring equipment and the surface undergoing measurement is necessary, (2) a direct measurement is obtained, and (3) a permanent record is provided. The experiments provided sufficiently encouraging results to warrant further exploration with more optimized equipment.

Recommendations

For the technique described, it is recommended that 560-watt quartz light illumination perpendicular to the surface be used and that a slow speed film such as High Contrast Copy film be employed with a minimum of 5 exposures per measurement. For sizing and counting particles from the macrophotographic negatives obtained, a 30X projection is recommended.

Future work by other investigators should consider the feasibility of using more modern optical equipment and techniques which are more specifically related to macrophotographic procedures in order to enhance the results that may be obtainable. A partial listing of potential refinements is provided.

Optics. In place of the infinity corrected Triplet Elmar lens, use lenses specifically designed for macro-optics such as a 55-mm f/2 Ultra-Micro Nikkor lens used in reverse position.

Photographic System. Match the types of surfaces to be examined, field conditions, lens, film, filtering, illumination, and film processing for optimum results.

Particle Measurement. Consider the adaptation of automatic image analysis techniques to measure particle quantities and sizes in place of the laborious manual techniques used. Such techniques could probably reduce the time for analysis by an order of magnitude.

Advanced Techniques. Consider the use of stereo photography and color film as means of enhancing performance.

ACKNOWLEDGMENTS

The writer wishes to acknowledge the valuable contributions made by the following: Mr. Craig Smith who supervised some of the tests and participated in the analysis; Mr. Theodore Carrington who performed the photography; and Mr. James Richardson who acted as advisor on photomicrography.

REFERENCES

1. Goss, W. C., "The Mariner Spacecraft Star Sensors," Applied Optics, 9 (5), May 1970.
2. "Procedure for the Determination of Particulate Contamination of Hydraulic Fluids by the Particle Count Method," SAE-ARP-598.
3. "Measuring and Counting Particulate Contamination on Surfaces," ASTM-F-24.
4. "Microscopic Sizing and Counting Particles from Aerospace Fluids on Membrane Filters," ASTM-D-2390.
5. "Processing Aerospace Liquid Samples for Particulate Analysis Using Membrane Filters," ASTM-D-2391.
6. "Sampling Aerospace Fluids from Components," ASTM-D-2429.
7. "Cleaning and Inspection Procedures for Ballistic Missile Systems," Air Force T. O. 42C-1-11, 1 April 1969.
8. "Procedure for the Determination of Particulate Contamination in Hydraulic Fluids by the Control Filter Gravimetric Procedure," SAE-ARP-785.
9. Dugan, V. L., "Principles of Operation of the Vacuum Probe Microbiological Sampler," Sandia Laboratories, 5C-RR-67-688, Aug. 1967.
10. Chuan, R. L., "Particulate Contaminant Measurement by Quartz Crystal Microbalances," ASTM/IES/AIAA Space Simulation Conference, 14-16 Sept. 1970.

11. Lindahl, B. O., "A New Method for Determination of Surface Contaminants Caused by Particle Fallout," Contamination Control Laboratories, Levonia, Michigan.
12. McCrone, Walter C., et al, The Particle Atlas, Ann Arbor Science Publishers, Inc., Ann Arbor, Michigan, 1967.
13. Schenk, R. and G. Kistler, Photomicrography, Franklin Publishing Co., Englewood, New Jersey, 1963.
14. Drinker, P. and T. Hatch, Industrial Dust, McGraw-Hill Book Co., Inc., New York, 1954.
15. Smith, C. R., "Contamination Analysis of Space Vehicle SESP 70-1," Aerospace Report No. TOR-0172(2701-04)-1, 20 July 1971.
16. Smith, C. R., "Cleanliness Analysis of Space Vehicle STP 71-2," Aerospace Report No. TOR-0172(2164-01)-1, 15 April 1972 (Unpublished).
17. Brown, F. M., et al, Photographic Systems for Engineers, Society of Photographic Scientists and Engineers, Washington, D. C., 1969.
18. Back, Frank G., "A New Production Unit for Optical MTF Recording," SPIE Seminar Proceedings, 13, 1968.
19. Brock, G. C., et al, Photographic Considerations for Aerospace, Itek Corporation, Lexington, Mass., 1965.
20. Kingslake, R., Applied Optics and Optical Engineering, Academic Press, New York, 1965.
21. "Method for Determining the Resolving Power of Photographic Lenses," U. S. Government Printing Office, NBS Circular 533, Washington, D. C., 1953.

PRECEDING PAGE BLANK NOT FILMED

Paper No. 31

**MEASUREMENT OF CONDENSATE FILM CONTAMINATION
ON CRITICAL SURFACES BY CHARGED PARTICLE
EXCITED X-RAY FLUORESCENCE**W. P. Saylor, *General Electric Company, Valley Forge, Pa.*

ABSTRACT

A unique technique was developed by the General Electric Co. for the determination of trace quantities of a hydrocarbon film contaminant on critical surfaces by a charged particle excited x-ray fluorescence method. The method was successfully employed for constructing an instrument to be used to measure condensate contaminants deposited on optical and thermal control surfaces of the Nimbus 5 spacecraft after environmental testing. Data is presented showing the measured thicknesses of hydrocarbon film condensed during the environmental testing period. Measurements were also used to establish the effective removal of these contaminant films. As an extension of this technology, modifications of the device are presently being made for application of in-situ contamination monitoring during thermal-vacuum environmental testing of a spacecraft.

INTRODUCTION

Contamination of critical spacecraft surfaces and its corresponding effect upon spacecraft performance has long been of mutual concern to both NASA and the General Electric Co. Spacecraft subsystems and experiment malfunctions and failures experienced during both environmental system test activity and actual flight performance, which have been determined to be directly attributable to contamination, have emphasized the need to determine, control, and maintain the cleanliness of critical surfaces.

Hydrocarbon film contamination of less than 1000A° in thickness on critical optical and/or thermal control surfaces can be produced as a result of outgassing by-products. These thin films are frequently not visible to the eye and cause no reasonable changes to the original sensor optical characteristics. In space, however, exposure of these surfaces to short wavelength UV or low energy ionizing radiation can cause coloration of these thin films resulting in deleterious changes to original sensors performance. A large part of this hydrocarbon contamination may well be deposited during ground handling operations. In order to minimize or eliminate these contamination problems it became necessary to institute a system to detect thin organic film contaminants to insure operational integrity of the critical component prior to launch. In addition, the detection system will also be used to establish contaminant origin, if possible, as well as to insure effective removal of the contaminant by an established cleaning procedure.

Measurement Technique

The method by which condensate film thicknesses are to be measured is by a unique X-ray fluorescence technique. X-ray fluorescence is used quite extensively in industry for trace elemental analysis. The sensitivity of the method is such that elemental concentration of less than 10 nanograms can easily be detected. The method is nondestructive, insensitive to the geometry or stoichiometry of the polymer films and is not susceptible to environmental effects. In addition, instrumentation for the method is relatively simple and can be made small in size and easily portable.

The principle by which the measurement technique operates is based on detecting the carbon characteristic x-rays (280 ev) generated by alpha-particle induced fluorescence of the hydrocarbon contaminant film on a given substrate. Alpha-particles are well suited for exciting the thin hydrocarbon film in that they have low penetrating powers, yet produce high fluorescent X-ray yields for low atomic number target elements.^(1,2) Perhaps, the most important feature is the fact that little or no bremsstrahlung continuum x-radiation is generated in the slowing processes of the alpha-particles resulting in low background counting rates which aids in the systems overall sensitivity. Figure 1 shows the basic layout. A low level radioisotopic source of polonium emits alpha particles. These particles bombard the inorganic substrate. If there is a thin layer of carbon bearing contaminate deposited on the substrate, characteristic x-rays due to carbon (44 Å) are generated. These x-rays are sensed in a x-ray sensor which converts them into electronic pulses. The electronic pulses are amplified and counted for a fixed time interval, typically 10 - 100 seconds. The number of counts is then directly proportional to the number of carbon atoms deposited and hence directly proportional to the thickness of the contaminated layer. The sensitivity of the method is derived as follows: The total number of output counts detected in a channel corresponding to A atoms of an element in a thin sample is given by,

$$N = An \sigma \omega K (\Omega/4\pi) \epsilon$$

where n is the total number of alpha particles per cm², σ the cross section for ionization for the shell in question, ω the fluorescence field, K the relative transition probability for the particular x-ray peak, used in the measurement, Ω the solid angle subtended by the detector and ϵ the efficiency of the detector. One can now substitute numerical values for all these factors to compute an order-of-magnitude value of sensitivity for a given amount of condensate on a substrate surface.

Sample Thickness Computation

For a 100-angstrom-thick layer of a typical hydrocarbon contaminate

such as dioctyl phthalate, the total number of carbon atoms A equals 2.92×10^{17} . The cross section $\sigma = 2 \times 10^5$ (Reference 3) Barns, $\omega = 1.2 \times 10^{-3}$ (Reference 4) and $K = 1$. The factor $\Omega/4\pi$ is equal to 2×10^{-2} for good geometry. Detector efficiency is assumed at 20-percent. A 10 mC alpha source is used which results in a flux of 1.45×10^7 alphas - cm^{-2} - sec^{-1} . For a measuring period of 100 seconds the total intensity N is then $= (2.92 \times 10^{17})(2 \times 10^{-19})(1.2 \times 10^{-3})(1)(2 \times 10^{-2})(0.2)(1.45 \times 10^7)(10^2)$ or $N = 406$ counts. The predicted accuracy, as limited by statistical variations (3σ limits), is then 100 ± 15 angstroms. The minimum detectable thickness will be limited by instrumental background and counting rate statistics.

Constructional Parameters of The Sensor

Figure 2 shows a schematic of the contamination sensor head construction. A standard 5 millicurie polonium - 210 alpha-particle source(5) is used to bombard the interested substrate. If a condensate film is present, the carbon-K X-rays generated by excitation with the alpha-particles are isolated and detected by a thin-window P-10 gas flow proportional counter. The proportional counter is of standard construction except for the entrance window. The entrance window was constructed of aluminized polypropylene stretched to a thickness of one micron. This yielded a detection efficiency for carbon-K X-rays of 50%. A 5 micron thick stretched polypropylene filter was used to help isolate the carbon-K X-rays in the presence of a oxygen and nitrogen generated x-ray background. The alpha-source is so shielded such that the proportional counter cannot see the source directly. The entire region surrounding the alpha source, proportional counter and surface being analyzed is bathed in a helium atmosphere. The helium atmosphere is required to overcome the extremely short mean free path of the carbon-K X-rays in air.

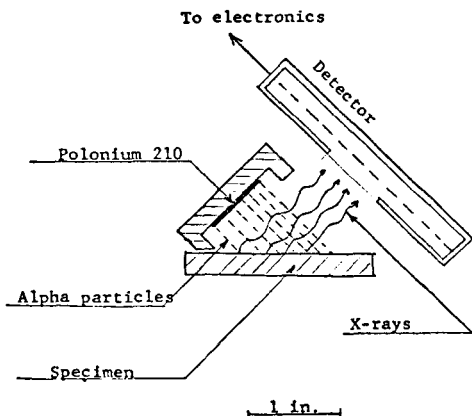


Figure 1, Basic Layout of Sensor System

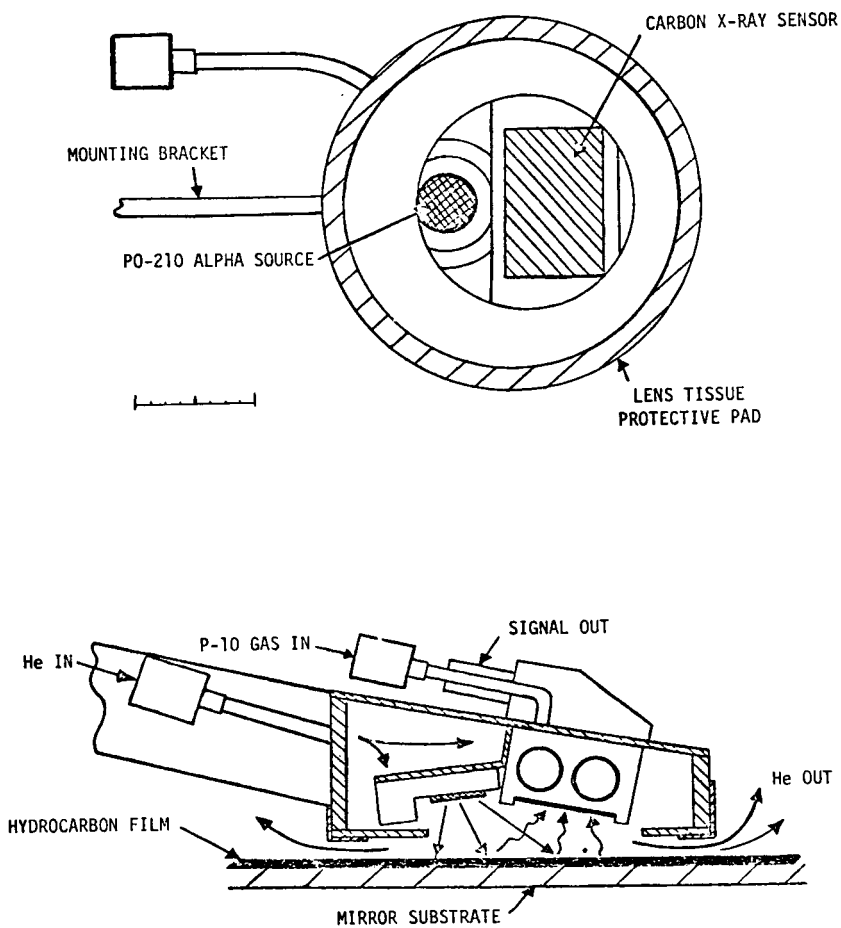


Figure 2, Schematic Diagram of the Contamination Sensor

The carbon-K x-rays detected by the sensor are isolated by a combination of the 5 micron polypropylene filter and energy discrimination in the proportional counter. A preamplifier is used to amplify the pulses from the proportional counter and drive the signal cable to the remainder of the processing electronics located remotely. The proportional counter is operated in the pulse counting mode, and coupled with the high gain of the unit makes the system insensitive to variations in electronic gain and power supply voltage drift. The constructed sensor has a sensitivity that lies in the hydrocarbon film thickness range of 50 to 10,000Å, and the device can detect a hydrocarbon film of less than 100Å in thickness in a response time of 100 seconds as established through calibration. Figure 3 shows a photograph of the constructed contamination monitor sensor head.

Calibration of sensor

Thin polymer films of "formvar" ranging in thickness from 200 to 2000Å were created for use as hydrocarbon film thickness calibration of the contamination sensor. The formvar films were made by dissolving 2 grams of formvar powder in 100 ml of ethylene dichloride solvent. One or more drops of the solution, depending on the film thickness desired, were then spread on a large tray of water and allowed to dry. The resulting film was then picked off the water surface by an aluminum wire screen substrate. The thickness of each of the formvar films used for calibrating were measured by x-ray transmission techniques. The mesh supported thin polymer films were placed directly in front of an x-ray sensor. The monochromatic x-ray line used for the measurement was that of nitrogen-K α at 31.68Å. The line was generated by alpha-particle x-ray fluorescence excitation of pure nitrogen gas at atmospheric pressure. The x-ray line intensity was measured with and without the thin formvar films present in front of the sensor. The intensity ratio then is proportional to the film thickness. Table I gives the measured results of the calibration films x-ray transmissions at 31.68Å.

TABLE I
Measured Film Transmissions

No. 1	Aluminum support mesh only	19540 C/100 sec.	
No. 2	Mesh plus thin formvar film 1	18550	95%
No. 3	Mesh plus thin formvar film 2	17020	87%
No. 4	Mesh plus thin formvar film 3	14462	74%
No. 5	Mesh plus polypropylene film 4	1804	8.6%
No. 6	Mesh plus 1 mil thick polypropylene 5	140	Background

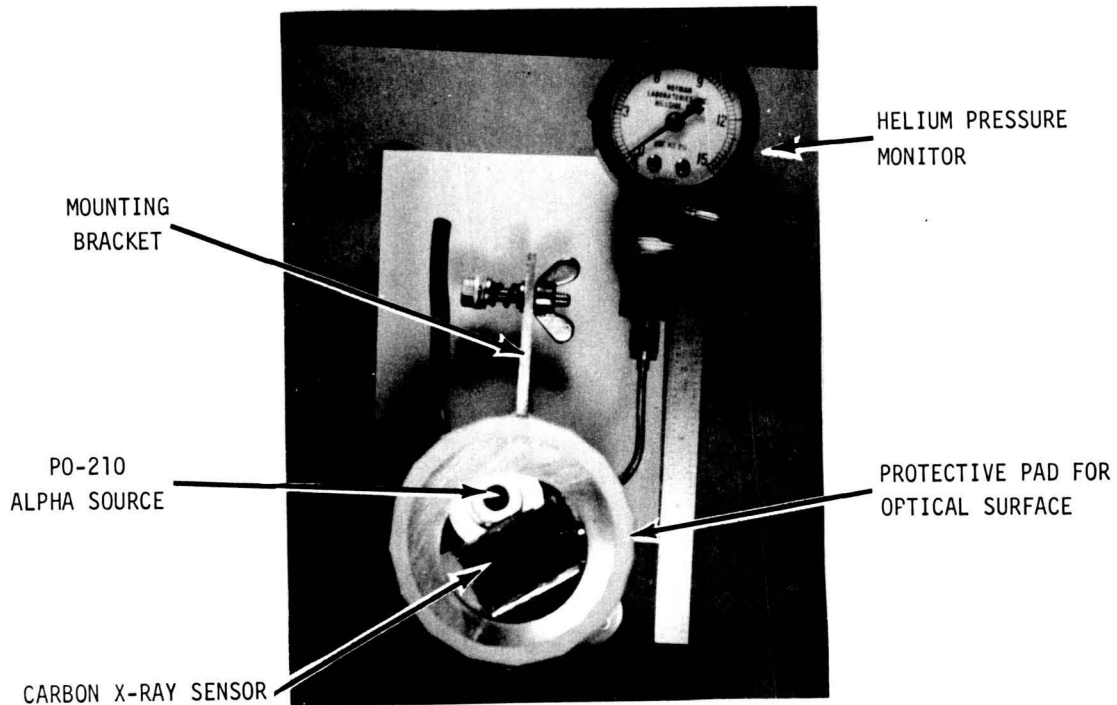


Figure 3, Photograph of Contamination Monitor Sensor Head

The instrumental background is created by the x-ray sensor itself. The x-ray sensor unfortunately has a very poor low energy x-ray resolution and therefore cannot completely isolate the carbon x-ray energy. The sensor retains a degree of sensitivity to those elements that comprise the mirror itself, such as oxygen, silicon, nickel, beryllium or gold. It is this detected x-ray counting rate to these mirror elements that gives the instrumental background rate. This background, however, is reproducible, stable and is such as not to interfere with the organic film measurements as shown by the measurements of Figure 4.

The mass per unit area of the polymer films is equal to the natural logarithm of the intensity transmission divided by the mass absorption coefficient of the materials for the measuring x-ray wavelength. The mass absorption coefficients for formvar at 31.68\AA is $19300\text{ cm}^2/\text{gm}^6$ and that for polypropylene is $21700\text{ cm}^2/\text{gm}^6$. Based on these values of mass absorption coefficient and measured x-ray transmissions, the formvar films thicknesses are as follows; No. 2 - 250\AA , No. 3 - 700\AA , No. 4 - 1600\AA and the polypropylene film No. 5 - 11300\AA . The alpha-particle excited carbon -K α x-ray count ratio from each of the calibrated films was then measured, both for the case of an unbacked film and with the film coating a glass microscope slide substrate. The results are plotted in the form of a calibration curve in Figure 4. The minimum detectable contamination film thickness is determined by the 3σ statistical variations in the instrumental background counting rate. From Figure 4 the background counting rate was 34,000 counts/100 seconds, which yields a 3σ limit of ± 600 counts/ 100 seconds. Again from Figure 4, a hydrocarbon film of about 50\AA in thickness will give an increase in the background counting rate of about 1000 counts/100 seconds and is therefore fully detectable.

The chemical structure of formvar is $(\text{C}_5\text{H}_7\text{O}_2)_x$ or about 35% carbon by atom density. Polypropylene is $(\text{CH}_2)_x$ or about 33% carbon by atom density. These films then are believed to be fairly representative in terms of behavior to those condensed hydrocarbon contaminants on cold mirror surfaces.

Contamination Measurements of the Critical Surface on the Nimbus 5 Spacecraft

The contamination sensor was developed expressly to be used as a monitor for maintaining quality control of cleanliness for the Temperature Humidity Infrared Radiometer (THIR) scan mirror and the thermal control surface of the Electrically Scanning Microwave Radiometer (ESMR) on the Nimbus 5 spacecraft, successfully launched in December 1972.

Contamination Measurements of the THIR Scan Mirror

Figure 5 shows a photograph of the contamination sensor,

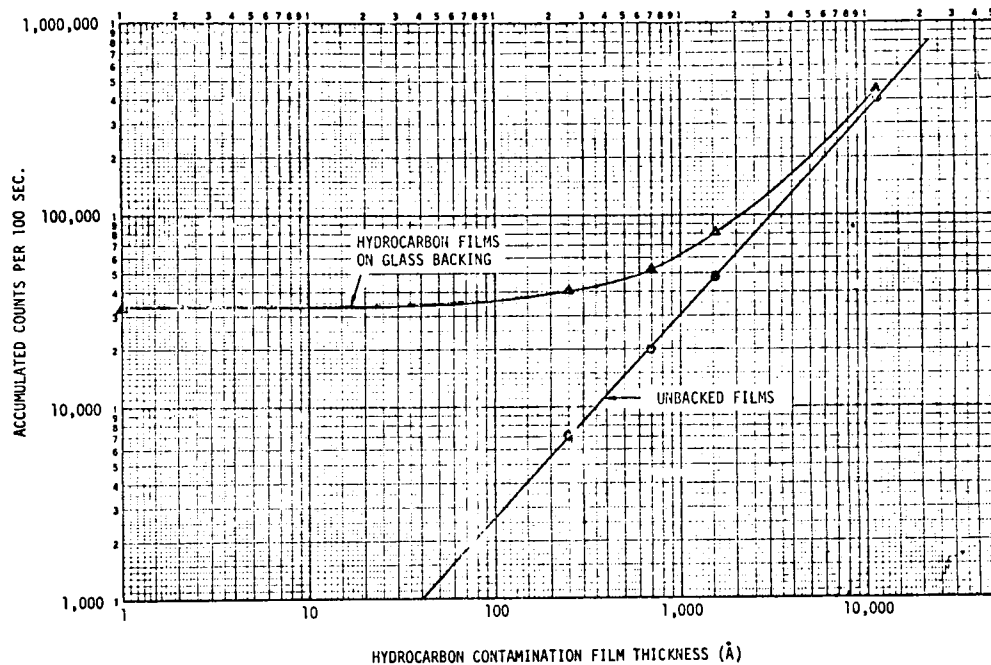


Figure 4, Contamination Sensor Calibration Curve
 (Hydrocarbon Film Thickness As A Function of Sensor Count Rate Based On Films
 Of 35% Carbon By Atomic Density)

mounted tripod and processing electronics. The tripod on which the sensor head is mounted provides three degrees of motion such that the sensor head can be carefully and accurately positioned to the surface to be examined assuring full protection to the critical surface. In addition, a lense tissue covered pad is provided on the sensor head to protect the mirror surface from a accidental contact with the sensor head. The necessary processing electronics consists of a high voltage power supply to energize the x-ray sensor, a pre-amp and amplifier, single-channel pulse height analyzer and pulse counter. Figure 6 and 7 are photographs of the contamination sensor being positioned to the scan mirror of the THIR experiment on the Nimbus E spacecraft for contamination measurements. Measurements were taken on four areas of the scan mirror, the center, left of center, right of center, and below center or bottom section of scan mirror. Measurements were made before cleaning, after cleaning and after cleaning a second time. The results are shown in Table II.

The results show that there was about a 10% difference in the counting rates before and after cleaning the THIR scan mirror, indicating hydrocarbon contamination was removed from the mirror surface. Measurements after a second cleaning showed no further changes to the counting rate level, indicating either all contamination was removed, or all that could be removed by the particular cleaning procedure used. The cleaning procedure used consisted of wiping the mirror with a pre-extracted lens tissue soaked in acetone followed by a second wiping of the mirror using a pre-extracted lens tissue soaked in isopropyl alcohol. Assuming the mirror contamination to be similar chemically to those films used for sensor calibration, then referring to Figure 4, a 4000 to 6000 counts/100 second rate corresponds to a contaminant film of about 200A° in thickness was removed from the THIR scan mirror surface. Figure 8 shows the pulse height energy spectrum obtained with the contamination monitor before and after cleaning of the THIR scan mirror.

Contamination Measurements of the Gold Kapton Thermal Control Surface of the ESMR

Measurements were taken on the gold Kapton tape covering the two main support areas of the ESMR. Two areas were measured on each support area. No additional cleaning of these surfaces were undertaken. The results are shown in Table III.

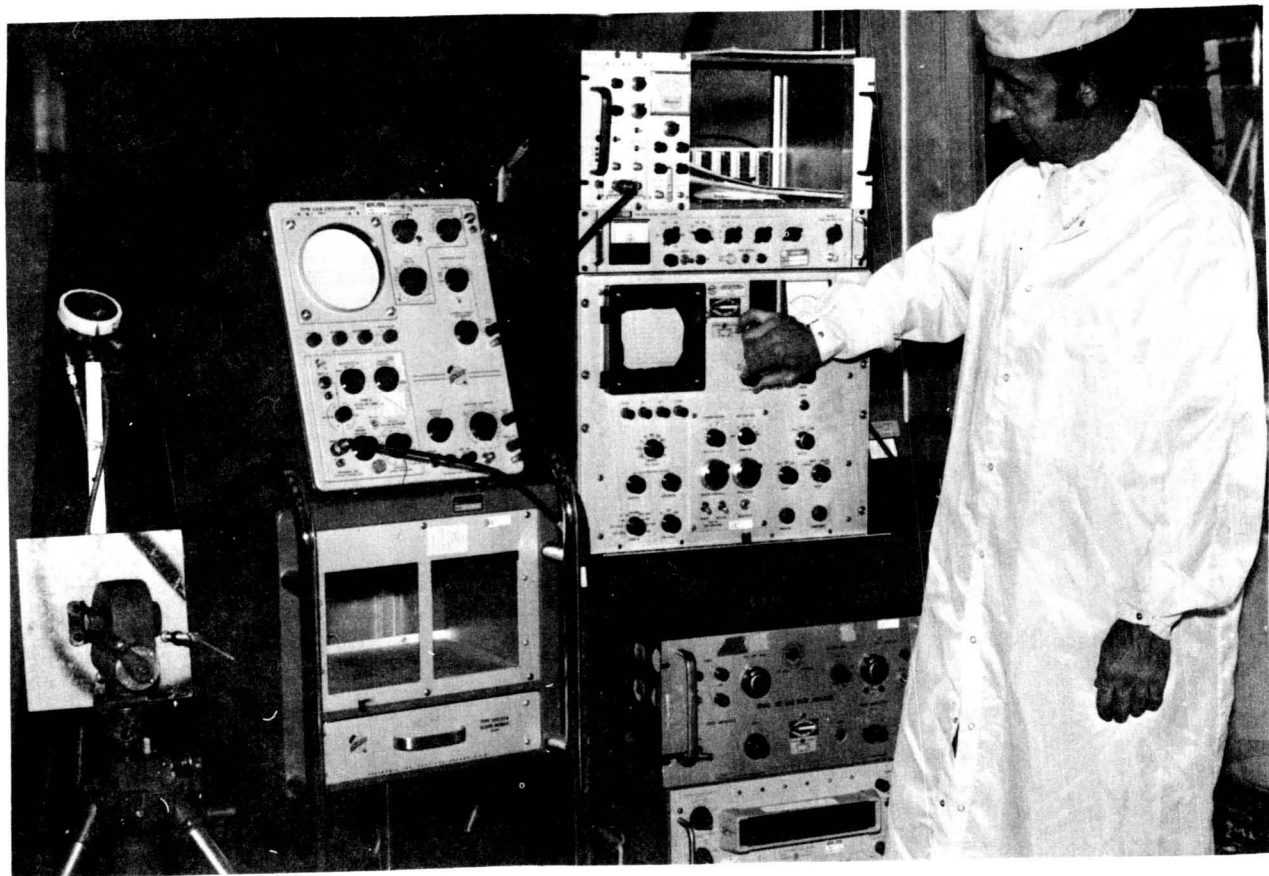


Figure 5, Photograph of the Contamination Sensor, Mounting Tripod and Processing Electronics



Figure 6, Photograph of Contamination Sensor Being Positioned to the Scan Mirror of the THIR Experiment on the Nimbus E Spacecraft

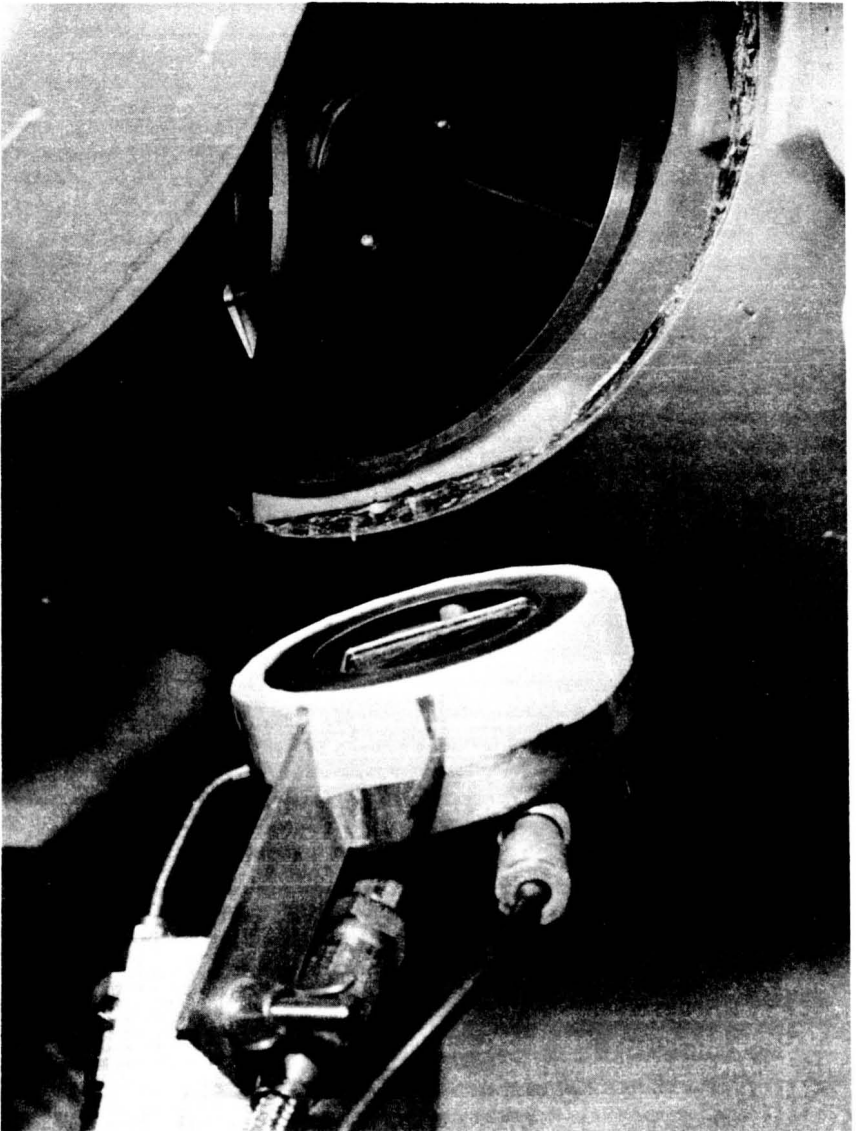


Figure 7, Close-up of Contamination Sensor

Table II

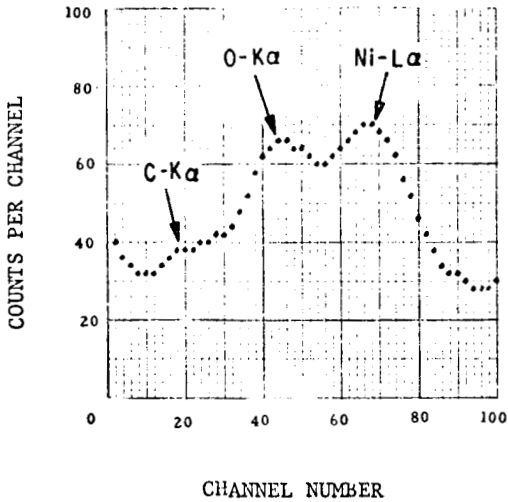
Measured X-Ray Counting Rate From THIR Scan Mirror
(Counts per 100 seconds)

<u>Section</u>	<u>Before Cleaning</u>	<u>After Cleaning</u>	<u>Difference</u>	<u>After 2nd Cleaning</u>	<u>Difference</u>
Center	49893	45395	4498		
Left Center	48726	43971	4755		
Right Center	49266	44987	4279		
Below Center	50897	44832	6065	44921	00

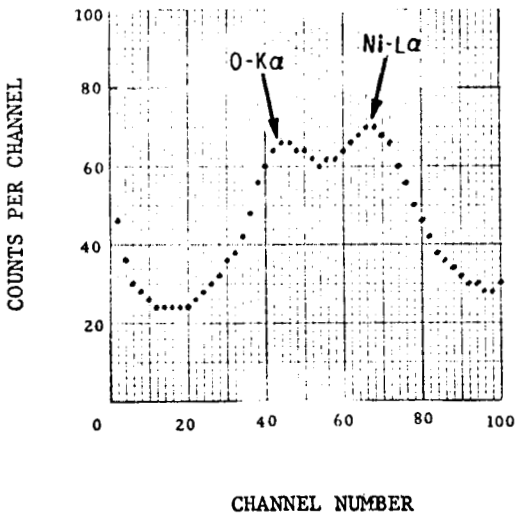
Table III

Measured X-Ray Counting Rates From the Gold Kapton on the ESMR
(Counts per 100 seconds)

Left ESMR Support Area (looking at ESMR)	top section	33938
	bottom section	35211
Right ESMR Support Area	top section	36730
	bottom section	34284
Fresh Sample of Gold Tape		33840
Fresh Sample with <u>one</u> finger print stamped		43910
Fresh sample with finger print removed with isopropyl alcohol and cotton swab		34240



The Energy Distribution of X-Rays Emitted From The THIR Mirror When Excited by Alpha-Particles, Before Cleaning. (The oxygen and nickel x-rays lines are generated from the composition of the THIR mirror itself).



The Energy Distribution of X-Rays Emitted From The THIR Mirror After Cleaning. (Note the disappearance of the carbon x-rays from the condensed contamination.)

Figure 8, Pulse Height Energy Spectrums Obtained From Examination of The THIR Mirror With The Contamination Monitor

A fresh sample of the gold Kapton tape was used to establish the baseline counting rate of a "clean" gold Kapton surface for comparison. The results, using the fresh sample as a basis of comparison, shows that there are some areas on the ESMR support structure that have retained a degree of contamination. Referring to Figure 4, these areas of contamination measured about 100\AA in thickness. As a further indication of the sensor sensitivity, a single finger print was placed on the fresh gold tape sample used as a reference and measured. The results (Table III) showed a 30% increase in the x-ray counting rate establishing extreme sensitivity even to a single finger print. The finger print was then "cleaned" from the gold tape sample. The measured results showed that the x-ray counting rate returned to the original level within the experimental error. The results also show just how effective a particular cleaning technique is or can be in removing condensed contamination from a particular surface.

In order to determine and maintain the cleanliness of a critical surface using the x-ray fluorescence contamination monitor, the baseline x-ray counting rate of the surface should be established prior to its subjection to any possible contamination. Measurement of the surface before and after exposure to a possible contaminating environment will then permit comparison to the baseline rate and enable quick detection of contaminants. Upon contamination and cleaning of the surface via an established cleaning procedure, the measurement technique can be re-employed to ascertain that the contaminant has been totally removed.

Thermal Vacuum Contamination In-Situ Measurement

In conjunction with the Nimbus F and ERTS B Contamination Programs, it was proposed to expand the existing thermal-vacuum contamination measurement capability to include two identical instruments known as the X-Ray Fluorescence Contamination Monitors modified for vacuum operation.

Contamination measurements within the thermal-vacuum chamber in the past had been limited to data taken from witness mirrors and from quartz crystal microbalance monitors. Witness mirrors provide information only after termination of the test. The quartz crystal microbalance (QCM) is very effective in measuring film thicknesses of metals and some inorganics in the range from 100\AA to above $10,000\text{\AA}$. However, experience at GE, using QCM's as polymer contaminant crystal monitors for thermal vacuum testing of the Nimbus 5 spacecraft, show that the devices were only effective when polymer films exceeded some 500\AA in thickness and when their temperature was maintained very constant. Another drawback in using the QCM technique is that condensate thickness is measured on the crystal surface, per se, and the sticking coefficient between the outgassed species and the QCM might be quite different from the condenser surface under investigation.

The X-Ray Fluorescence Contamination Monitor has the capability of monitoring absolute levels of contamination on a true optical surface and because of its digital nature, is free of environmental problems inherent in the quartz crystal monitor.

It was originally intended to design the Fluorescence Monitor so that it could measure the contamination level on a critical surface of the spacecraft (experiment). Because of mechanical, safety, and other considerations, the design was dropped, and it is proposed to fabricate and use the Fluorescence Monitor as a replacement for the quartz crystal monitor, i.e., to measure contamination levels in the proximity of the spacecraft experiments and critical thermal control surfaces.

Instrument Description

The sensor head of the In situ X-Ray Fluorescence Contamination Monitor consists of a thin window proportional counter and an alpha-particle source. The source is a 0.375 inch disk of polonium 210 of 5 millicurie strength located in the center of the proportional counter window. The counter window consists of a 9-micron thick polypropylene aluminized films supported by a 75% transmitting aluminum wire mesh. The diameter of the window is 2 inches. The detected carbon X-rays are isolated by energy discrimination in the proportional counter. An integrated circuit preamplifier is used to amplify the pulses from the counter which are delivered outside the vacuum system to the remainder of the processing electronics.

The mechanical design of the instrument is presented in Figure 9. The witness mirror is rotated from the open position ninety degrees to accurately position the mirror beneath the sensor head for condensate contamination film measurement. Upon completion of the measurement, the mirror will be rotated to the open position for the continuation of contaminate collection.

The witness mirror will also be equipped with a heater and thermocouple to provide the capability of setting collector temperature to levels other than that of LN_2 .

A secondary witness mirror is also provided which is not exposed to the contaminate environment. This secondary witness mirror is used to establish and maintain the background baseline count rate. This mirror is measured when the primary mirror is in the open position.

Experimental Check-Out of the X-Ray Sensor

On April 20, 1973 an experiment was initiated to establish that the proposed x-ray sensor for the Vacuum X-Ray Fluorescence Contamination Monitor would not only survive the vacuum environment, but also remain operational throughout a typical thermal vacuum test period of between 250 and 400 hours continuously.

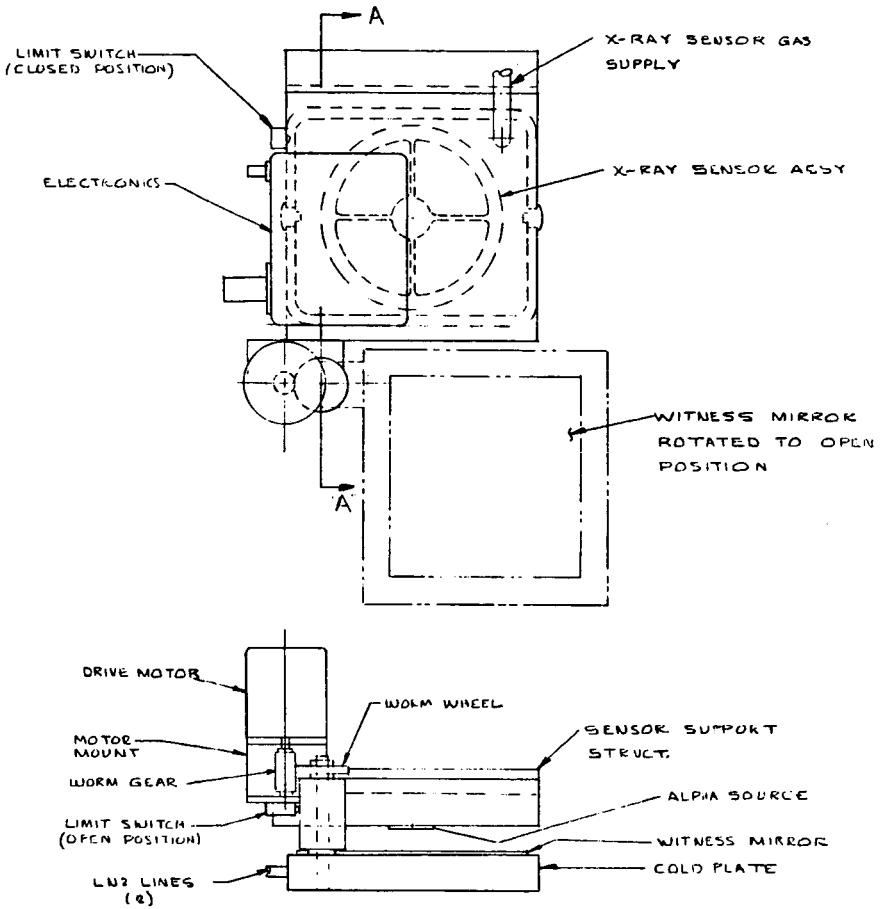


Figure 9, Mechanical Design Of The Vacuum X-Ray Fluorescence Contamination Monitor

The system performance criteria was based on maintaining system gain to within 50% and pulse-height energy resolution to within $\pm 20\%$ of the original values before vacuum testing as established with a test source.

The proportional counter used, although not identical in geometry and construction as the unit proposed, is adequately representative of the design. The counter consists of sealed metal cylinder with an epoxyed thin x-ray entrance window. The window consists of a 9-micron thick polypolyene film supported by a 75% transmitting aluminum wire mesh. A 50 microcurie Iron 55 radioisotope x-ray source was used to simulate the x-ray flux to the sensor. The entire system was placed in a Materials Engineering vacuum chamber and maintained continuously at a pressure below 10^{-6} torr. The sensor performed satisfactorily with gain increase of 30% and no measurable change to the pulse-height resolution for a period of more than 1100 hours.

Based on this experiment then, one should expect reasonable success for the actual vacuum units when they are completed. The thermal vacuum tests for the Nimbus F spacecraft are scheduled for early 1974.

CONCLUSION

It has been shown experimentally through calibration of actual thin hydrocarbon films that the charged particle excited x-ray fluorescence contamination sensor is an extremely sensitive device for determining minute quantities of a condensed hydrocarbon surface contaminant on optical or thermal control surfaces.

The sensor itself is relatively inexpensive, reliable, accurate and relatively easy to use. It is small in size and requires no "special" electronic equipment. The device is non-destructive and non-interfering with the surface being investigated and it provides relatively quick detection of contamination. (A typical contamination measurement of a mirror surface such as the THIR scan mirror takes only an hour to an hour and a half, including the set-up time.) The sensor is stable and poses no radiation hazard to personnel or equipment. In addition, selected elements that make up the contaminating film can also be identified if desired, these include, beside carbon; oxygen, nitrogen, fluorine, sulphur, silicon, etc. The device however, does require operation either in a vacuum or a helium atmosphere.

In all the x-ray fluorescence contamination sensor makes a useful monitor for the detection and measurement of environmental contamination on critical surfaces either remotely or in-situ for the establishment and preservation of cleanliness.

REFERENCES

1. A. A. Sterk, X-Ray Analysis of Thin Film by Positive Ion Bombardment, Norelco Reporter, 14, 3-4, 99, July-December, 1967.
2. W. P. Saylor, Measurement of Thin Oxide Surface Film Thicknesses and Atomic Densities By The Analysis of Positive Ion Excited Soft X-Ray Spectra, Advances in X-Ray Analysis, 12 Plenum Press, N.Y., 1969.
3. J. A. Kaiwer, et al, Trace Element Analysis by Observation of Characteristic X-Rays, Amer. Phy. Soc. Meeting, Washington, D.C., April 25, 1972.
4. J. R. Russ, X-Ray and Electron Probe Analysis, ASTM-STP 485, 1971, p.219.
5. Model 204 Spot Static Eliminator. 3M Co. (Nuclear Products) St. Paul, Minn.
6. B. L. Henke, et al, X-Ray Absorption in The 2 to 2000° Region, Norelco Reporter, 14, 3-4, 127, July-December, 1967.

PRECEDING PAGE BLANK NOT FILMED

Paper No. 32

EVALUATION OF RADIOISOTOPE TRACER AND ACTIVATION ANALYSIS TECHNIQUES FOR CONTAMINATION MONITORING IN SPACE ENVIRONMENT SIMULATION CHAMBERS*

J. B. Smathers, W. E. Kuykendall, Jr., R. E. Wright, Jr. and
J. R. Marshall, *Texas A&M University, College Station, Texas*

ABSTRACT

The use of radioisotope tracer and activation analysis techniques in the determination of space simulation chamber contaminant levels was evaluated in a theoretical study. Each procedure was evaluated based on its sensitivity, ability to identify specific contaminants, speed of analysis, suitability for real-time operation, radiological safety and cost of implementation. Of the many techniques considered, only alpha particle range variation with mass density of chamber atmosphere, indicated a sensitivity, 1.9×10^{-10} g/cm², competitive with methods presently in use.

INTRODUCTION

The objective of this study was to determine the feasibility of several nuclear analytical techniques for the identification and measurement of very small quantities of contaminants in space environment simulation chambers at NASA Manned Spacecraft Center. This project was carried out in two phases: Phase I being directed toward the use of radioactive isotope techniques while Phase II was concerned with the use of activation analysis. The merits of a given technique are evaluated on the basis of measurement sensitivity, ability to identify specific contaminants, speed of analysis, suitability for real-time operation either in-chamber or on-site near the chamber, radiological safety and cost of implementation.

PRESENT METHOD SENSITIVITIES

For purposes of comparison the maximum sensitivity as quoted in the literature for methods presently in use was chosen as the design objective. For the Contamination Control Units (CCU) system (1) and for the Quartz Crystal Microbalance (QCM) system (2) this limit is 10^{-9} g/cm². This design basis sensitivity is somewhat artificial as the typical contamination levels during chamber tests have been reported to be 1×10^{-7} g/cm²(3).

*Research sponsored by LBJ Space Center, NASA Contract NAS9-12586.

RADIOISOTOPE TAGGING

General--Two methods were considered for tagging the suspect molecules with a radioactive atom; isotopic exchange with a high specific activity isotope and transmutation by neutron irradiation. The former requires a high specific activity source of the element of interest to be mixed with the suspect agent and chemical exchange between radioactive and non-radioactive atoms to occur. This is generally performed with small quantities of materials and the extent of tagging which occurs varies greatly among compounds. The latter technique is essentially that of producing a radioisotope by neutron activation, the amount produced depending on the neutron flux intensity and the time of irradiation. One problem with this technique is that of radiation damage to the molecular structure of the compound thus changing its chemical properties. Obviously an irradiation time must be chosen which is a compromise between sufficient activity and minimum radiation damage.

Major Composition Elements--The majority of the suspect agents can be described as hydrocarbons many of which incorporate silicon in their structure. In the calculations which follow Dow Corning 704 vacuum oil, DC 704, was considered as a typical agent. For tagging of carbon or hydrogen only isotopic exchange is feasible and the radioisotopes ^{14}C and ^3H were considered respectively. As both isotopes decay by low energy beta emission and have rather long half lives, several constraints are imposed on the detector system and by radiological safety considerations on the usage of the method. The isotopic tag was calculated based on exposure of one gram of the suspect agent with the source and achieving a specific activity of 1 millicurie/gm (4). This small amount was then distributed throughout the total suspect agent volume and a final molecular tagging efficiency of $7 \times 10^{-8}\%$ was assumed.

The silicon tag was obtained by the neutron activation technique which for the purposes of these calculations assumed the following: neutron flux of 5×10^{12} n/cm²/sec, one hour irradiation, DC 704 oil with three silicon atoms per molecule, and incorporation of the radioactive agent in the vacuum system one hour after the end of irradiation. The tagging process converts stable silicon-30 to ^{31}Si which has a 2.6 hour decay half life.

The detector system considered had to be able to measure the low energy betas, 18 KeV, emitted by ^3H as well as the higher energy radiation emitted. Among the systems considered were high pressure gas detectors, avalanche detectors, scintillation detectors and semiconductor detectors. The optimum system design was exhibited by a large surface area, radiantly-cooled plastic scintillator which had the desirable properties of no detector window absorption, large sensitive volume, and minimal

expense.

The resulting analysis yielded the following detectable amounts of DC 704:

$$\begin{aligned}^{14}\text{C tag} & - 1.3 \times 10^{-4} \text{ g/cm}^2 \\ ^3\text{H tag} & - 2.7 \times 10^{-7} \text{ g/cm}^2 \\ ^{31}\text{Si tag} & - 2.7 \times 10^{-5} \text{ g/cm}^2\end{aligned}$$

Obviously the ^{14}C and ^{31}Si tag sensitivities are inadequate and the ^3H tag is marginal at best. The radiological safety complications posed by the 12.33 year half life (5) of the ^3H would probably negate its use. However if the tagging efficiency could be increased by a factor of 100, the sensitivity is correspondingly lowered to $2.7 \times 10^{-9} \text{ g/cm}^3$ which becomes competitive with other techniques.

Minor Composition Element--Analysis of several oil samples indicated the presence of trace amounts of sodium (Na) and bromine (Br). Following the procedure outlined for the silicon tagging, the detectable limits for various oils were calculated based on transmutation of the Br and Na impurities into a radioactive tag. The values calculated for the detectable limits were in the range of $3 \times 10^{-3} \text{ g/cm}^2$ for Na and $3 \times 10^{-4} \text{ g/cm}^2$ for Br. Thus the use of the trace impurities as a tagging procedure was quite unacceptable.

NON-RADIOACTIVE ISOTOPE TECHNIQUES

Consideration was also given to using stable isotopes, namely carbon-13 and deuterium as a means of tagging a particular oil followed by a subsequent analysis by Nuclear Magnetic Resonance (NMR) or Mass Spectrometry. The rather large sample size required, 1 to 10 mg, and the percentage tag required in order to obtain sufficient sensitivity precluded further consideration of this approach.

CHARGED PARTICLE RANGE

General--The monoenergetic nature of heavy charged particle emission and the single valued limited magnitude nature of subsequent range led to the consideration of this method for gross contamination monitoring. The general design for the system consisted of a source with two tubes extending out from it, a variable absorber, and two detector systems placed one each at the ends of the two long tubes, opposite the source (Figure 1). Both detectors are movable and track evenly. One tube is open to the atmosphere of the chamber, whereas, the other tube, filled with clean air, is sealed and a check valve-bellows system for pressure equalization with the chamber. With the detectors positioned at the point of maximum variation of range

with incremental absorber thickness, the difference in count rates between the two detector systems allows determination of contamination in the chamber.

Fission Fragment Range--The consideration of fission fragments violates the previously assumed monoenergetic property however these high mass, high energy charged particles have a very short range. A typical curve of intensity, $I(X)$, vs range, X , and $dI(X)/dX$ vs X are given in Figure 2. The range value used for the calculation was that which resulted in the steepest slope of dI/dX i.e. ~ 0.97 of X_{MAX} . Assuming a counting precision of 0.1%, a detection sensitivity of 2.3×10^{-6} g/cm² resulted.

Alpha Range--The typical intensity vs range characteristics for alpha particles are illustrated in Figure 3. The only significant difference between this analysis and the previous one for fission fragments is the larger values of dI/dX obtained due to the monoenergetic nature of the particles. This results in a detection limit of 1.9×10^{-10} g/cm² which is quite competitive with existing techniques of impurity analysis.

The method is particularly unique in that it actually measures total mass between the detector and the source, thus responding to condensable and non-condensable contaminants. Assuming a ten meter long tube, values as low as 2×10^{-13} g/cm³ could possibly be detected.

SUMMARY OF ISOTOPE MEASUREMENTS

Of the isotopic methods surveyed in this analysis, only that of variation of alpha particle range with mass of the absorber is shown to have the sensitivity required to be truly competitive with the existing methods. The pertinent information on each technique considered is reviewed in Table 1.

NEUTRON ACTIVATION ANALYSIS

General--The feasibility of using neutron activation analysis to identify and locate sources of contamination in the NASA space environmental simulation chambers was also investigated. Several activation analysis alternatives were studied on the basis of technical feasibility, expected performance and cost. Efforts were directed primarily at the detection of several oils, greases, and paint which were suspected as likely contaminants. Charged particle and high-energy photon activation analysis techniques were not considered due to the high cost of particle accelerators and the lack of detailed experimental data on which to base sensitivity estimates.

The basic approach using neutron activation analysis involved detecting a specific element or set of elements whose presence in a sample uniquely identified a given contaminant

and whose concentration in a sample is directly proportional to the amount of that contaminant present. Since activation analysis is an elemental method, not capable of determining compounds or molecular structure, this approach requires that the elemental composition of each possible contaminant contain a unique set of elements suitable for neutron activation analysis. This unique "fingerprint" characteristic may be an inherent property of the material or may be the result of a process in which certain suitable elements are placed into the compound for use as "tag" elements.

This investigation focused on the following six materials commonly used in the space environmental simulation chamber and which were thought to be likely contaminants:

Dow Corning 705
Dow Corning 11
Sun Vis 706
3-M Black Velvet Paint
Houghton Safe 1020
Houghton Safe 1055

Basic Description of the Method--Neutron activation analysis can be generally described as having three basic steps:

1. sample activation
2. sample cooling
3. gamma ray spectrometry

Sample activation consists of irradiating a material with a flux of neutrons to produce radioisotopes by means of nuclear transmutation. Sample cooling is an optional step which may be used to allow undesirable short lived radioisotopes to decay to an acceptable activity level before attempting to measure the activities of the elements of interest. After suitable cooling period, gamma ray spectrometry is used to measure the energies and intensities of the various gamma rays emitted by the activated material. Using the spectral data, a comparison can be made between the spectra from an unknown sample and those from a known standard to provide identification of elemental constituents and a determination of the elemental concentrations. Under optimum conditions with high neutron flux densities, over half of the naturally occurring elements can be detected in quantities below one microgram (6).

Activation Analysis of Potential Contaminants--Samples of the six potential contaminants were evaluated on the basis of their elemental composition to determine their suitability for detection and identification using neutron activation. The major elements comprising these materials include carbon, hydrogen, oxygen, silicon and phosphorus, none of which activate appreciably with thermal neutrons and only silicon, oxygen and phosphorus activate well with fast neutrons. Fast neutron activation analysis was considered as a possible technique but rejected due to lack of a

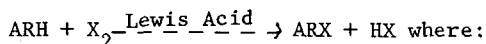
practical means of producing very high fluxes of fast neutrons required for sub-microgram measurement sensitivities. Since their major elements could not be used for "fingerprinting" the potential contaminants, analyses were carried out on samples of these materials to determine if minor or trace elements suitable for thermal neutron activation were present. Analyses were performed with a nuclear reactor which produces a usable thermal neutron flux of 5×10^{12} n/cm²/sec. Gamma ray spectrometry was accomplished with a Ge(Li) detector and a 4096 channel pulse height analyzer. Results of these analyses, shown on Table 2 revealed no "fingerprint" elements in these samples which would be sufficiently reliable and unambiguous for use in contaminant identification. While several samples showed possible unique trace element patterns, such as hafnium in Houghton Safe 1020 and tungsten in Sun Vis 706, the low concentrations (sub-ppm) make detection of microgram amounts of samples virtually impossible by neutron activation analysis.

Inactive Tracers--When a material is inherently free of suitable "fingerprint" elements, it is sometimes possible to label or tag the material with an element or set of elements which can be measured with good sensitivity and specificity. This method of inactive or stable tracers offers many of the advantages of radioactive tracers while avoiding the radiological safety and radioactive contamination problems. Tagged materials would be used in the chamber in place of usual materials. Samples of contaminants would then be collected in the test chamber and analyzed by neutron activation to determine the identity and amount of each tag element present.

The sensitivity of this procedure for detecting small quantities of a tag element depends upon the element's activation cross section as well as the energy and intensity of the irradiating neutron flux. Reactor thermal neutron activation analysis provides a median detection limit of approximately 10^{-8} grams (6) whereas 14 MeV NAA provides a median detection limit in the range of 10^{-3} to 10^{-4} grams using a state-of-the-art Cockcroft-Walton type neutron generator (flux of approximately 2×10^8 n/cm²/sec). It is obvious that for thermal neutron activation, elements with the best sensitivity (Eu, Dy, Mn, etc.) would be desirable for use as tags, however, a further requirement is that the tag element be chemically suitable for inclusion in the compound being labeled.

In view of this chemical compatibility requirement, a brief study was undertaken to determine the practicality and reliability of an elemental tagging system. In reference to the chemical makeup of the expected contaminant materials, a typical electrophilic aromatic substitution process (halogenation) was chosen for the tagging mechanics. The elements best suited for this tagging procedure and trace activation analysis are chlorine and bromine. The halogenation is expected to take place on the phenyl radical common to the proposed DC-11, DC-705, HS-1055,

and HS-1120 contamination materials. The general equation for this reaction is:



AR = phenyl radical

X₂ = Cl₂ or Br₂

Lewis Acid - FeCl₃, AlCl₃, etc.

Measurement Sensitivity--A primary measure of the effectiveness of a neutron activation analysis system for contaminant detection is the sensitivity with which tag elements can be determined under given conditions of sample acquisition, irradiation, and counting. A large number of variables must be considered in estimating measurement sensitivity, some of which are set by system design and others determined by the physical properties of the materials in the sample. The more important factors which influence system measurement sensitivity are:

1. Size of collected sample
2. Activation properties of tag element and other constituents in sample
3. Available neutron flux density
4. Irradiation time
5. Half-life of activation product
6. Delay between irradiation and counting
7. Detector background
8. Energy resolution of counting system

In order to assess the feasibility of using bromine, chlorine and iodine as tag elements to be detected by a neutron activation analysis system located in or near the chamber, a set of "best case" conditions were assumed and detection limits calculated. First, detection limits for elemental Br, Cl and I were calculated based upon a one hour irradiation with a thermal neutron flux of 1.25×10^9 n/cm²/sec and counted with a 3 in. x 3 in. NaI(Tl) detector. Further assumptions which were made to determine "best case" performance are as follows:

1. Tag element is uniformly distributed in the contaminant material.
2. Only one contamination source is responsible for the tagged material deposited on the 3 inch diameter collection disk.
3. Tag element does not disassociate from the contaminant materials.
4. Average contaminant deposition is approximately 10^{-6} gm/cm².
5. A non-activable collection medium is used in lieu of presently used pyrex plate.

Assumptions one through three above are "best case" con-

ditions with respect to the measurement of trace element tags in chamber contaminant samples. To assure that the first three assumptions are valid would require further research beyond the scope of this project; however, it should be pointed out that variations in any one of these would significantly degrade the overall effectiveness of the tagging approach. Assumption number three (stability of tag element in the contaminant materials) is probably the most uncertain of all. The effects of extreme temperatures and high vacuum could cause the release of tag elements from the labeled material thus defeating the method. A quantitative evaluation of this factor would require extensive testing of various tagged contaminants under conditions equivalent to those present in the test chamber.

Four Irradiation Alternatives for Neutron Activation Analysis--Four alternatives for a NAA system and their important characteristics are summarized in Table 3.

The on-line monitoring system proposed a shielded isotopic neutron source, sample changer, and a NaI(Tl) gamma ray spectrometer to be located inside NASA Chamber A. The major advantage of this type system is its ability to offer hourly real-time analysis during chamber operation. A major consideration in this approach would be the effect of hostile environmental conditions (ie. 125°C and 10^{-6} Torr vacuum) inside the chamber during operation. Precautions must be taken to seal the shield assembly to prevent outgassing from the hydrogenous source shield.

The second alternative, a variation of the previous approach, involves the use of a subcritical multiplier system which employs a centrally located neutron source in a $^{233}\text{U}\text{-H}_2\text{O}$ or $^{235}\text{U}\text{-H}_2\text{O}$ solution. Such a system, as suggested by Currie, McCrosson and Parks (7), could enhance the neutron flux by factors of 6.4 and 4.8 respectively. However, to achieve these useful flux enhancement factors the assembly must be operated so near criticality that safety procedures and regulations may preclude practical application of this approach. Due to the complexity and size of this system, it would most likely be located outside the chamber, offering only daily analysis.

The third alternative, using a 14 MeV neutron generator as the source of neutrons was found to be unfeasible due to insufficient sensitivity.

The last technique proposed involved using the nuclear reactor at Texas A&M University. Although the return time analysis would be several days, the available thermal neutron flux of 4.3×10^{12} n/cm²/sec offers the best sensitivity and reliability for contaminant identification.

Summary of Neutron Activation Approach--While neutron activation analysis is well known as a highly sensitive trace analytical technique, it must also be recognized that ultimate sensitivities are achievable only under favorable conditions. This study has shown that conditions are very unfavorable for the on-site

detection and identification of microgram quantities of space environmental chamber contaminants by neutron activation analysis techniques. Factors supporting this conclusion are given below:

Lack of inherent contaminant "fingerprint":

Contaminant materials studied are composed of elements which do not have suitable properties for neutron activation. Experimental results indicated no unique neutron activation products useful for contaminant identification.

Contaminant tagging stability: Evaluation of chemical stability of proposed tagged compounds under high vacuum and temperature conditions would be required.

Neutron source replacement cost: Cf-252 (2.6 year half-life) would require periodic replenishment at an average annual cost of approximately 20 to 25% of the original source cost.

Reliability factor: Under "best case" conditions, the expected performance of the in-chamber system can be rated only marginal. Since the probability of achieving "best case" conditions in actual test operations is unlikely, the in-chamber system would not be a reliable solution.

REFERENCES

- (1) "High Vacuum Technology, Testing and Measurement Meeting, Compilation of Papers", (NASA) Aug. 1966, N66-35906 through N66-35936.
- (2) "Monomolecular Contamination of Optical Surfaces", Shapiro, H, Hanyok, J., Vacuum, 18:11 (Sept. 68).
- (3) "Preparation, Verification, and Operational Control of a Large Space-Environment-Simulation Chamber for Contamination Sensitive Tests", MSC-05237, NASA MSC, November, 1971.
- (4) Personal Communication, Mr. Alan Petty, New England Nuclear Corp.
- (5) Chart of The Nuclides, 10th Edition, Knolls Atomic Power Laboratory, Naval Reactors Branch, USAEC.
- (6) "Experimental Reactor Thermal Neutron Activation Sensitivities," Yule, H. P., Anal. Chem., Vol. 37, No. 1 (1965), pp 129-132.
- (7) "Neutron Sources and Applications", Proceedings of the American Nuclear Society, National Topical Meeting, CONF-710402 (Vol. 1) August 1971.

Table 1 - Summary of Isotopic Techniques

Method	Detection Limit g/cm ²	Advantages	Deficiencies
¹⁴ C	1.3 x 10 ⁻⁴	Operational over complete system, allows selective testing of suspected agents on an individual basis.	Long half life radioactive contamination of chamber, tag may not follow more volatile fraction of compound.
³ H tag	2.7 x 10 ⁻⁷	Operational over complete system, allows selective testing of suspected agents on an individual basis.	Long half life radioactive contamination of chamber, tag may not follow more volatile fraction of compound.
Na tag	1.7 x 10 ⁻³	Selective tagging of some specific agents, operational over complete cycle.	Tag may not follow more volatile fraction of compound.
Br tag	2.9 x 10 ⁻⁴		
³¹ Si tag	2.7 x 10 ⁻³	Selective tagging of some specific agents, operational over complete cycle, also short half life isotope.	Severe time constraint on use of method, possible radiation damage to compound.
Alpha Range	1.9 x 10 ⁻¹⁰	Fully operational over complete cycle, detects both condensable and non-condensable agents, system can be made very directional.	Size problems, sensitivity very directional dependent, new system never used before for this purpose.
Fission Product Range	2.3 x 10 ⁻⁶	Same as alpha range.	Same as alpha range, also possible radioactive contamination problem.

Table 2 - Elemental Analysis of Suspected Contaminants¹

Sample Element	Concentrations in ppm					
	Sun Vis 706	DC 705	DC 11	3m PT.II	HS 1020	HS 1055
Al ²	25.0	537.0	1400.00	---	108.0	123.0
Br	0.49	0.52	---	39.0	5.0	1.8
Cl	28.0	15.0	35.0	52,000.0	118.0	313.0
Cu	2.8	0.32	13.0	0.64	1.2	0.47
I	1.9	---	---	---	---	---
La	---	0.08	---	---	---	0.06
Mn	---	---	0.90	---	---	---
Na	43.0	25.0	1106.0	20.0	50.0	25.0
V	0.19	---	0.63	---	---	---
W	0.11	---	---	---	---	---
Zn	168	---	2.4	2.7	1.3	---
Co	---	---	0.2	0.16	---	0.09
Hf	---	---	---	---	0.39	---

¹Analyses performed using instrumental neutron activation
²Al data not corrected for Si interference due to $^{28}\text{Si}(n,p)^{28}\text{Al}$.

Table 3 - Summary of Irradiation System Characteristics

Technique	Initial Cost Analysis	Analysis Speed	Obtainable Thermal Neutron Flux ¹ (n/cm ² -sec)	Measurement Sensitivity
On-line ²⁵² Cf System (In-chamber)	\$525,000 ³	Hourly	1.25 x 10 ⁹	Poor
²⁵² Cf and Multiplier System ² (On-site)	\$200,000 ^{3,4}	Daily	1.52 x 10 ⁹	Fair
14 MeV Generator (On-site)	\$ 25,000	Daily	4.0 x 10 ⁷	Very Poor
Reactor at Texas A&M University	\$600 min. ⁵	Several Days	4.3 x 10 ¹²	Good

- (1) Uniform flux over 3 inch diameter disk.
- (2) 5-3 mg sources with a 4 times multiplier.
- (3) Based on 10 dollars per microgram.
- (4) Cost of multiplier approximately \$50,000.
- (5) \$300/day for reactor time plus \$30/sample for analysis. Minimum 10 samples.

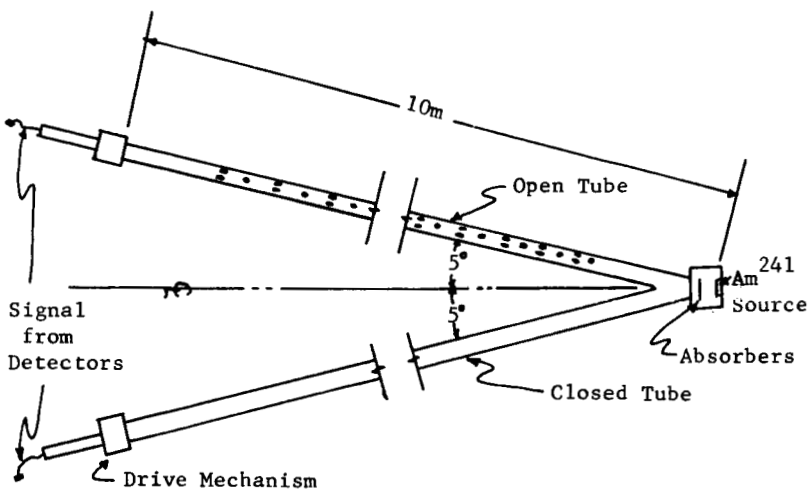


Figure 1 - Charged Particle Range Equipment Layout.

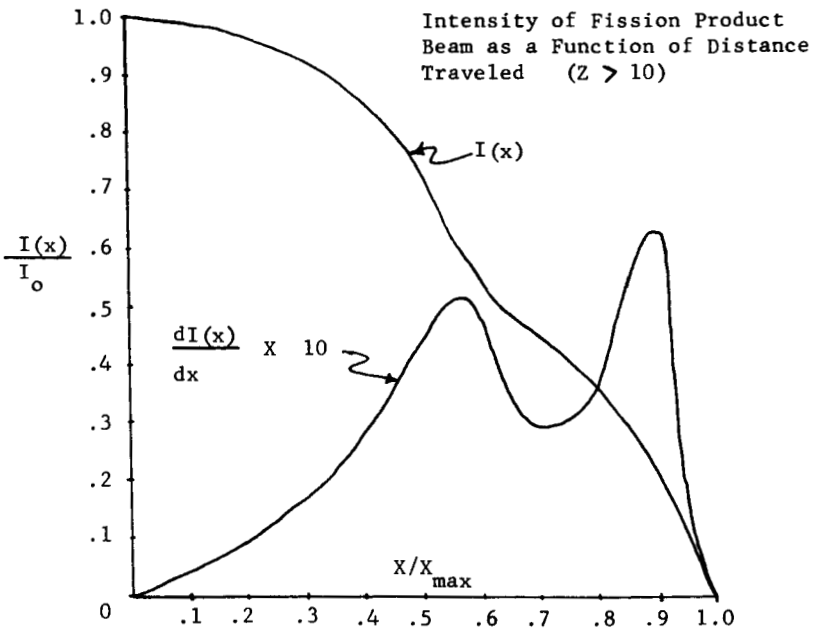


Figure 2 - Fission Product Range Characteristics.

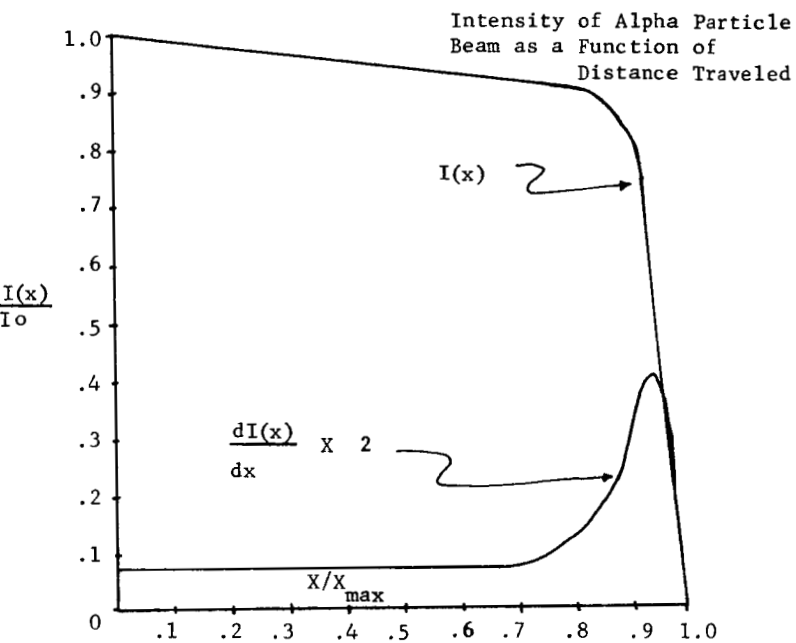


Figure 3 - Alpha Range Characteristics.

N74-10261

PRECEDING PAGE BLANK NOT FILMED

Paper No. 33

OUTGASSING TESTS IN SUPPORT OF
A PROPOSED ASTM SPECIFICATION

John J. Park, Richard S. Marriott, William A. Campbell, Jr., and Charles L. Staugaitis, *Goddard Space Flight Center, Greenbelt, Maryland*

ABSTRACT

The data gathered from three different laboratories by the technique of determining the weight loss in vacuum at 125°C and of collecting the volatile condensable materials at 25°C in vacuum is presented. Two sets of eight commercial samples were tested as was one commercial material prepared to help resolve some variations in results.

A preliminary outgassing specification has been submitted to Committee E-21 on Space Simulation via E. N. Borson for critique and revisions, and it now has gone through two revisions. A data gathering round robin type of measurement was started with the participation of laboratories at Jet Propulsion Laboratory (JPL), Pasadena, California and at European Space Research and Technology Centre (ESTEC), headquartered in Holland, though the apparatus is located near Madrid, Spain. A group of eight commercial materials were distributed to the three laboratories from Goddard Space Flight Center (GSFC) and a second group of eight materials were distributed from ESTEC. Each laboratory conducted the outgassing tests in similar equipment reproduced from that developed at Stanford Research Institute.

Stanford Research Institute personnel, under Contract No. 950745 from JPL during the period from June 1964 to August 1967, developed the technique of determining the percent total weight loss and the percent volatile condensable materials. The primary objective of that program was "to assist the Jet Propulsion Laboratory in the selection of polymeric materials to be used in the construction of spacecraft" (Reference). The technique consisted of subjecting micro-gram quantities of materials to a simulated spacecraft environment as a means of rapid screening of these materials.

Ref. *Polymers for Spacecraft Applications* by R. F. Muraca & J. S. Whittick, Final Report, JPL Contract 950745, p. 1, 9/15/67.

The Apparatus

The particular apparatus devised consisted of a solid copper bar in which was machined twelve sample chambers. Each sample chamber is 15.8 mm (0.625") diameter, 11 mm (7/16") deep and tapering to a 6 mm (0.250") diameter exit port. The back of the sample chamber is removable for inserting the sample and closure is made with a solid copper cover; the exit port is the opening through which volatiles escape. The copper bar is heated to 125°C by means of resistance heaters brazed to the bar. A minimum of two thermocouples are attached to each heater bar, for controlling and recording temperatures.

Opposite the exit port of the individual sample chamber is a collector plate cooled to 25°C for the condensation of those volatile materials which will condense. The gases exit from the sample chamber, passing through a hole in a separator plate which is compartmented to prevent cross-contamination, and to the cooled collector plate. The distance from the exit port to the front surface of the collector plate is approximately 12 mm (0.475 inches). The collector plate is usually metallic with a plated surface, or it may be a salt-flat for use in obtaining infrared spectra. The condenser plate is maintained at 25°C and, with good thermal contact with the back of the metallic collector plate or with the back of a metallic device holding the salt flat, the collector plates are also at 25°C.

Test Method

Various polymeric materials, such as potting compounds, adhesives, and paints can be tested for outgassing. The sample should be prepared in the same manner as they will be used. The solid potting compounds should be cut into small pieces on the order of 3 to 6 mm (1/8" to 1/4") on a side. Adhesives, usually applied in thickness of 0.07 to 0.12 mm (0.003 to 0.005 in.) with only the edges exposed, should be applied between preweighed pieces of aluminum foil for curing, which can then be cut or folded to fit into the sample boat. Paints may be applied to a polyethylene or Teflon sheet from which the paint could be stripped.

The discardable sample boat is made of aluminum foil pressed into shape and degreased, cleaned, and dried. The sample, of between 200 and 300 milligrams, is placed into a pre-weighed boat and then preconditioned for 24 hours in a 50% relative humidity (RH) chamber. The starting weight of the sample is obtained after the 50% RH conditioning. The collector plate is also cleaned and dried before being weighed. Sample

boats and collector plates and loaded into their respective heating and cooling bars following weighing.

The vacuum system is capable of being evacuated into the 10^{-6} torr range in about 45 minutes. The heaters raise the temperature of the sample bar to $125^{\circ} \pm 2^{\circ}\text{C}$ in a 60-minute period. The collector bar is maintained at $25^{\circ} \pm 2^{\circ}\text{C}$ by utilizing a thermal exchanger; two thermocouples attached to each cooling bar indicate the cooling bar temperature and its variation. The heating at 125°C is continued for 24 hours after which the heater current is turned off and dry nitrogen let in to cool the bar rapidly. Within two hours the heater bar should have cooled to 50°C , at which time the bell-jar is raised. Samples and collector plates are transferred to dessicators immediately and all are weighed beginning within one-half hour.

Calculations are made, utilizing the starting weights of the boat and the sample and the final weight of the sample and boat, to provide the percentage of Total Weight Loss (TWL). In a similar manner the percentage of volatile condensable materials (VCM) can be calculated as a percentage of the sample starting weight from the weight gained by the individual collector plate.

One additional step may be taken, that of identifying the major compounds in the condensable materials. The use of a salt-flat as a collector permits direct transfer of the salt-flat to the spectrophotometer. Alternately, by washing or dissolving the condensables from the metal collector plate into a clean beaker the solution can then be applied to a separate salt-flat for spectroscopy.

Round Robin I

The eight materials sent from GSFC included a Mylar film often used at JPL as a standard. The other materials consisted of potting compounds 3 mm ($1/8''$) thick and also one paint as a film. The potting compounds were mixed and cured at GSFC by a technician experienced in working with such polymeric materials. One-third of each material was sent to the other two laboratories with the hope that all tests could be begun in the same week. The shipments to California and to Europe were by air freight, and it was presumed that there was little effect on the samples due to changing temperatures and atmospheric pressures.

The results of the first tests are presented in Table I. These do not show the expected uniformity of results but they do show some peculiarities.

TABLE I

RESULTS OF ROUND ROBIN, IA

MATERIAL	TWL Average			VCM Average		
	GSFC	ESTEC	JPL	GSFC	ESTEC	JPL
I. Chemglaze Z-306	0.953	0.91	-	0.007	0.009	-
II. D. C. 93-500	0.068	0.054	0.15	0.000	0*	0
III. Epon 828/Versamid 125	0.370	1.18	2.07	0.004	0.010	0
IV. Epon 828/Versamid 125 post cured	0.426	1.31	2.11	0.001	0.009	0
V. Epon 828/Versamid 125 with glass bubbles	0.375	1.06	2.05	0.001	0.007	0
VI. GE RTV-11	1.701	1.75	1.60	0.371	0.116	0.36
VII. Mylar A Film	0.191	-	0.47	0.002	-	0
IX. Solithane 113/ C113-300	0.222	0.26	0.40	0.004	0.009	0

*0 in the VCM column indicates a weight loss by the collector plate

The Epon 828/Versamid 125 samples gave confusing results. These three sets of samples, one with a room temperature cure, the second with a heat cure, and the third having glass bubbles mixed in, were prepared by the same person, one experienced in mixing polymeric compounds. He prepared thin samples of 125 mm (5-inch) diameter and cut large sections to be sent to our three test laboratories. Assuming that there was random selection of the large pieces sent to each laboratory, the results show a wide, but consistent disparity:

Total Weight Loss, Epon 828/Versamid 125

	GSFC	JPL	ESTEC
No Heat	0.38%	2.07%	1.22%
	0.36	2.06	1.44
	0.38	-	1.18
Heated	0.41	2.10	1.31
	0.43	2.11	1.39
	0.44	-	1.23
With Bubbles	0.36	2.03	1.07
	0.37	2.06	1.08
	0.40	-	1.02

Note that all GSFC samples are low, JPL's are high and ESTEC's are in the middle.

The group of samples received from ESTEC included potting compounds, films, paints on aluminum foil, and mixtures. The results are presented in Table II. The data for the paints on aluminum foil were calculated on the basis of 0.0044 gm/cm² of foil; this assumes that the density of the foil and the dimensions of the foil with the paint were known accurately. However, it is recognized that this type of sample is less desirable than a solid piece of material, as the results show.

TABLE II
RESULTS OF ROUND ROBIN, IB

MATERIAL	TWL (Average)			VCM (Average)		
	GSFC	ESTEC	JPL	GSFC	ESTEC	JPL
I. BLS 203	0.741	1.10	1.09	0*	0	0
II. Glassofix 802	4.290	6.78	5.27	0	0	0
III. Kynel 5505	1.487	2.51	2.94	0	0	0
IV. Mylar A Film	0.255	-	0.40	0	-	0
V. Rilsan	0.948	0.99	0.87	0.013	0.018	0
VI. Sellotape 8002	0.895	1.03	1.62	0.223	0.099	0.29
VII. Silcoset 101	1.588	1.57	1.26	0.250	0.071	0.18
VIII. Technoflon	0.433	0.45	0.45	0	0	0

*0 in the VCM column indicates a weight loss by the collector plate.

With the variations in results from these first two groups of samples, a third run was made utilizing the remaining sample materials, including those from both GSFC and ESTEC. These results are in Table III.

It is recognized that the differences within the samples and differences between the laboratories could not be controlled. However, the samples must be considered as samples which might be sent from a contractor who desires data on the suitability of the material for spacecraft use. For this reason, the use of screening criteria are most helpful in selecting materials known to be low in outgassing. The differences in testing techniques between the three laboratories are also of interest.

TABLE III
RESULTS OF ROUND ROBIN, II

MATERIAL	TWL Average		VCM Average	
	GSFC	JPL	GSFC	JPL
I. BSL 203	0.736	0.96	0.026	0.01
II. Epon 828/Versamid 125	0.673	1.52	0.040	0.03
III. Epon 828/Versamid 125 Post cured	0.672	1.32	0.053	0.04
IV. Epon 828/Versamid 125 with glass bubbles	0.564	1.31	0.049	0.02
V. GE RTV-11	1.745	1.58	0.422	0.28
VI. Kynel 5505	1.199	1.49	0.016	0.02
VII. Rilsan	0.741	0.62	0.059	0.03
VIII. Silcoset 101	1.543	0.98	0.231	0.27

A review of information gathered from these three laboratories brought out certain differences between the techniques utilized at the laboratories. These differences included the material of the collector plate, the use of 50% RH or of 65% RH in conditioning the samples, and the existence of a negative weight gain by the collector plate in some instances. These differences may be summarized as follows:

Known Variations

- (a) The surface of the collector plate is different at the three locations, GSFC uses a chromium-plated collector. ESTEC uses a solid salt-flat collector, and JPL uses a solid copper collector.
- (b) GSFC and JPL condition the samples in 50% RH but ESTEC uses a 65% RH atmosphere, each for a 24-hour period.
- (c) At ESTEC, the temperature of the sample was found to be 115°C. They planned to increase the temperature to the 125°C level.
- (e) At GSFC, the observations that condensation occurs on the separator plate and that the collector plate may show a loss or gain in "blank" runs indicate that further refinements in the system are necessary.

In addition, certain questions were raised with regard to the length of time of RH conditioning, the variability within samples,

and the effect of sample size, whether as many small pieces or one large piece.

The question of length of RH conditioning was raised because of the scheduling of the GSFC's weekly tests and the recent change to having some U. S. national holidays on a Monday. In this connection, GSFC carried out tests using longer than 24 hours in the RH chamber. Duplicate samples were used, one being in the RH chamber 96 hours from Friday until Tuesday, the other being in the chamber for the 24 hours from Monday to Tuesday. Twenty-three samples of the 92-hour RH were higher in weight loss and seventeen of the 24-hour RH were higher, the samples showing the large weight loss differences due to the different times of preconditioning were very high in TWL. For example, a sample of 3M 1157 tape with a polyester adhesive had a TWL of 6.08% with a 24-hour preconditioning and a TWL of 6.45% with a 96-hour preconditioning, or a difference of 0.37%. Seven samples showed no TWL difference, ten of fifteen with the 24-hour preconditioning, and twelve of nineteen with the 96-hour conditioning showed TWL differences of 0.10% or less. It appears that the time of 50% RH preconditioning has no significant effect on TWL.

The effect of sample dimensions was also investigated, utilizing the Epon 828/Versamid 125 samples mentioned above. In the rerun of these samples, the GSFC samples in the second run were cut into many small pieces about 1.5 mm on a side (about 1/16" x 1/16" x 1/16") as opposed to the samples in the first tests which were a single piece weighing about 200 milligrams.

TWL, Epon 828/Versamid 125
Particle Size

	GSFC (small pieces)	GSFC (one piece)
No Heat	0.69	0.38
	0.66	0.36
	0.67	0.38
Heated	0.67	0.41
	0.69	0.43
	0.67	0.44
Bubbles	0.55	0.36
	0.55	0.37
	0.59	0.40

Note that the data are higher for small pieces. As a first assumption, it appears that size has a significant effect.

To check this further, a fresh sample of Epon 828/Versamid 125, 50/50 parts by weight, room temperature cured was prepared and tested. The results are as follows:

Sample Dimensions, Epon 828/Versamid 125

Total Sample > 300 milligrams

14 pieces 1.5mm x 1.5mm x 2.2mm (1/16" x 1/16" x 3/32")
TWL = 0.38, 0.37, 0.36

1 piece 6mm x 9mm x 3mm (1/4" x 3/8" x 1/8")
TWL - 0.19, 0.18, 0.23

It appears that these results demonstrate, particularly for Epon 828, that the dimension of the sample has an effect upon the weight loss. As expected, the volatile condensable material (VCM) results are also higher, the total VCM being higher for the higher TWL.

In considering the variabilities in the materials themselves, it was realized that separate mixtures of two component polymers had a built-in inconsistency because of the human element in mixing. In order to reduce the variables, it was decided that a one-component sample, DC 3140 which is available from a tube, should be tested, prepared the same day each week for a number of weeks, cured the same length of time, and tested during the next week's run. In addition, the location of the samples in the heater bar was changed, moving the samples to different locations, with a fourth location for the determination of the "blank."

Two results were noted. The VCM data were unuseable because of an unknown amount of condensate upon the separator plate instead of solely on the collector. Though all of the VCM data were greater than 0.34%, the GSFC system must be modified to collect "all" of the condensables.

TABLE IV
DC 3140

Sample	Location	TWL	Avg. of 3	VCM	Avg. of 3
A	1	1.080		0.341	
A	2	1.150	1.126	0.363	0.352
A	3	1.149		0.352	
B	1	0.928		0.347	
B	2	0.928	0.951	0.356	0.369
B	3	0.997		0.404	
C	1	1.003		0.373	
C	2	0.984	1.011	0.357	0.367

TABLE IV(continued)

Sample	Location	TWL	Avg. of 3	VCM	Avg. of 3
C	3	1.047		0.371	
D	5	1.063		0.370	
D	6	1.069	1.076	0.383	0.374
D	7	1.097		0.368	
E	9	1.039		0.356	
E	10	1.051	1.042	0.374	0.369
E	11	1.036		0.376	
F	13	1.169		0.397	
F	14	1.222	1.204	0.463	0.436
F	15	1.221		0.448	
G	17	1.096		0.459	
G	18	1.116	1.119	0.495	0.488
G	19	1.146		0.511	
H	21	1.094		0.431	
H	22	1.109	1.104	0.415	0.420
H	23	1.108		0.414	

Second Round Robin

as a result of the preceding tests, another series of tests was proposed with the three laboratories. This series of tests was intended to provide some answers to the questions previously raised. Specifically, the aim of this second round robin was to evaluate the role of collector plate material and the influence of humidity (RH) conditioning. GSFC uses a chrome-plated collector plate in contrast to the salt flat employed by ESTEC, and JPL uses a Cu plate. Thus, the question of surface energy and attendant sticking coefficient arises relative to VCM deposition. In addition, GSFC and JPL condition samples at 50% RH while ESTEC performs this treatment at 65% RH. Whether this difference in RH conditioning is really significant in the final analysis has not yet been established.

The sample chosen was a Stycast 1090SI with the 24LV catalyst. It was mixed at GSFC as a thin layer about 1.5mm (1/16") thick; after curing, the slab was cut into small cubes of approximately 1.5mm (1/16") dimensions. The samples were distributed as many such pieces, mixed and randomly selected, and requiring ten or more such pieces for each outgassing sample.

The results from this series of tests are presented in Table V.

TABLE V
Stycast 1090SI/24LV

Laboratory	RH	Specimens	Avg. %		Avg. % VCM
			TWL	Collector	
GSFC	50	7	2.186	Cr	0.084
	50	7	1.988	Cu	0.069
	50	7	2.216	Salt-flat	0.131
	65	7	1.934	Cr	0.079
ESTEC	50	7	2.087	Cr	0.078
	65	7	2.21	Cr	0.067
	65	9	2.189	Salt-flat	0.120
JPL	50	7	2.83	Salt-flat	-
	50	7	2.77	Cu	0.156

The lack of data for the JPL salt-flat data is due to the fact that the fragility of the salt-flat resulted in five of the seven collectors being chipped in handling, resulting in weight differences.

The above results were treated statistically, along with the samples of the one-component RTV 3140. Treating each laboratory's data separately, the results are in Table VI. In these calculations the mean, $\hat{\mu}$, and the standard deviation $\hat{\sigma}$, were calculated, using the formulation

$$\hat{\sigma}^2 = \sum_{L=1}^n \frac{(X_i - \bar{\mu})^2}{n - 1}$$

The percent 2σ was also calculated to present an indication of the comparative consistency of the results from each laboratory.

The information from ESTEC on the use of the salt-flat collector should be clarified. By adhering a thermocouple to the front of the NaCl collector, which is about 5mm thick, the temperature of the cooling bar and of the collector could be determined. The cooling bar had to be cooled to about 10°C in order to get the front of the NaCl collector to 25°C . Also, when the cooling bar was held at 25°C , the front of the collector was at about 31°C . The data above from ESTEC show that the average VCM with the NaCl collector at 25°C was 0.120%, and was 0.033% when the NaCl collector was at 31°C .

TABLE VI

GSFC Sample	n	TWL $\hat{\mu}$	$\hat{\sigma}$	%2 σ	Collector	$\hat{\mu}$	VCM $\hat{\sigma}$	%2 σ
RTV 3140	24	1.079	0.0779	15.6	Cr	0.397	0.048	24.0
Stycast-65%	7	1.934	0.049	5.0	Cr	0.079	0.015	38.0
Stycast-50%	7	1.988	0.074	7.4	Cu	0.069	0.008	23.0
Stycast-50%	7	2.190	0.059	5.4	Cr	0.084	0.021	48.0
Stycast-50%	7	2.216	0.059	5.2	NaCl	0.131	0.024	37.0
ESTEC								
Stycast-65%	9	2.189	0.087	7.95	NaCl	0.120	0.068	113.0
Stycast-65%	7	2.210	0.092	8.3	Cr	0.067	0.020	60.0
Stycast-50%	7	2.087	0.067	6.4	Cr(3)	0.078	0.015	39.0
					NaCl(4)*	0.033	0.018	110.0
JPL								
Stycast-50%	7	2.83	0.054	3.8	-	-	-	-
Stycast-50%	7	2.77	0.029	2.1	Cu	0.156	0.018	23.0

*NaCl flat was known to be above 25°C.

The wide discrepancies in the %2 σ column from each laboratory is unexpected. The lowest value was 23.0% using a copper collector for the Stycast sample while the greatest deviation was in the 100% range using a salt-flat collector. The consistency in the TWL values is much better, with the percent 2 σ ranging from 2.1% to 9.6% for the Stycast samples.

One other possibility as a collecting surface was that of a gold-plated collector which arises from data generated at Lockheed Missiles and Space Company. This laboratory was sent a quantity of the Stycast which was tested by the VCM apparatus and also by a modified thermogravimetric balance. Their results following a 24-hour 50% RH equilibration were as follows:

Method	TWL, %	VCM, %
VCM Device	2.20	0.25
VCM Device	2.19	0.24
VCM Device	2.14	0.24
Thermal Gravimetric Device		
a 12mmx3mm($\frac{1}{2}$ "x1/8")piece	1.39	0.23
Many Small Cubes	2.03	0.26

The most interesting information is the uniformity of the VCM results by different techniques. In order to verify these results, gold-plated collectors were used at GSFC and compared with chromium-plated collectors. The results were as follows:

Sample Position	TWL, %	Collector	VCM, %
#1	2.307	Cr	0.063
#2	2.203	Cr	0.065
#3	2.260	Cr	0.070
#4	2.400	Au	0.091
#5	2.332	Au	0.086
#6	2.226	Au	0.080

These results do not verify the higher VCM obtained at Lockheed, nor do they answer any questions.

As a result of these tests, it is apparent that certain additional testing must be done. The collector material must be standardized, though the handling problems with the salt-flat and the thermal conductivity of the salt-flat indicate the preference for a metallic collector. As a consequence, tests on the use of the gold-plated collector and the use of a roughened versus smooth chromium-plated collector are being done. In addition, means to avoid deposition of material on the separator plate by better collimation of the condensables or by enlarging the hole in the separator plate are being investigated. It is noteworthy that those materials having VCM greater than the desirable maximum of 0.10% will also have visually detectable condensation on the separator plate; the use of the RTV 3140 which had at least 0.397% VCM only points out that the material on the separator plate would make the VCM even greater than 0.397%. In a similar manner, the use of six decimal places in weighing and the calculation to 0.001% is too sensitive when one considers the variability in the one-component RTV 3140 which had a mean of 1.079% in TWL and had 15.6% 2σ variation. One might have expected better consistency in a material which does not require the addition of a catalyst or the mixing together of components. The present results have helped to point out where certain improvements should be made.

N74-10262

A SHROUDED FLOW ARC AIR HEATER FOR SIMULATION OF A 250 MEGAWATT PLASMA JET HEATER

J. C. Beachler and W. A. Kachel, *AF Flight Dynamics Laboratory,
Wright-Patterson Air Force Base, Ohio*

ABSTRACT

A 50 Lbm/sec shrouded flow arc air heater producing the pressure field and centerline temperature of a 250 MW plasma jet heater has been developed for reentry missile nose tip testing.

INTRODUCTION

The requirement for higher performance ballistic reentry vehicles has placed greatly increased demands on thermal protection techniques. One of the primary tools for screening and developing improved heat protection methods and materials has been the high pressure - high temperature arc plasma jet. These facilities normally employ a supersonic ($M = 1.5$ to 2.0) high stagnation pressure air plasma flow to duplicate the pressure and heating rates experienced in flight. However, the power required for uniform test flows large enough for full scale model tests is in excess of 200 megawatts to the gas which is far greater than present arc heater capabilities.

Since the cost of large power supplies is discouraging and a long heater development cycle would be required, other means were investigated by AFFDL for producing or simulating the large arc heated flows required. The goal of this effort was to develop an arc air heater from the AFFDL 50 MW unit which would provide simulation of a 250 megawatt plasma jet heater.

Development Procedure

The Air Force Flight Dynamics Laboratory's 50 Megawatt RENT (Re-Entry Nose Tip) Arc Heater (Reference 1) represented a large stride toward this goal by extending powers from the 10 megawatt level to 50 megawatts at pressures of 125 atmospheres and total temperatures of 14,000 °R. This heater, shown schematically in Figure 1, produced 1.11 inch diameter Mach 1.8 test jets with model stagnation pressures up to 100 atmospheres. Although this capability has proven most useful for sub-scale testing, it still falls short of the power levels required for full scale models in uniformly heated arc jets.

The approach taken in this effort was suggested by J. P. Doyle (Reference 2) and by tests in the peaked heating rate profiles shown in Figure 2 from Reference 1. These tests showed that for low angles of attack ($\alpha = 0$ to 6°) on axisymmetric bodies the stagnation point and body heating rates were governed by the hot core flow when the model was centered in the test jet. This led to the possibility that large high-power uniformly-heated test flows might be simulated for most axisymmetric missile nose tip tests by surrounding a much smaller arc jet with a large cold air shroud flow if a uniform pressure field in the test region could be maintained. The approach

which during these tests was to introduce a large (up to 45 lbm/sec) cold air flow into the 50 Megawatt RENT Arc Heater just ahead of its sonic throat as shown in Figure 3, and to size and configure the throat to pass the cold and hot air flows simultaneously without mixing. This cold shroud air was injected subsonically with a large tangential component to generate a large stabilizing radial pressure gradient in the turbulent shear layer which divides the hot core and cold shroud flow to inhibit mixing of the two flows.

Shrouded Arc Heater Performance

A series of tests were conducted over a wide range of mass ratios (i.e. $\frac{\dot{m}_{\text{shroud}}}{\dot{m}_{\text{hot flow}}}$).

Figure 4 shows the performance of the shrouded arc heater versus the standard RENT heater at the nozzle design mass ratio of 8:1 and an arc current of 2600 amps. This condition produced an effective throat size of $d^* = .900$ inches for the hot core with the design shroud throat diameter of 1.60 inches. Performance of the shrouded heater is nearly identical with the standard heater at the design point.

A series of "off-design" tests with mass ratios from 3.5 to 9.5 produced the effective hot core throat sizes shown in Figure 5 with the 1.60 inch nozzle at $P_0 = 100$ atmospheres and an arc current of 2600 amps. These effective throat diameters were determined by the method of Reference 3. Typical arc heater operating characteristics at mass ratios (M.R.) of 4, 6 and 8 are shown in Figure 6. No difficulty was experienced in operating the shrouded heater over a wide range of mass ratios and pressures with the 1.60 inch throat.

Typical test section profiles at the 2.125 inch nozzle exit diameter are shown in Figure 7 from Reference 4 for M.R. = 5.95. A centerline total enthalpy of 6320 BTU/lbm was calculated from heating and pressure measurements using the method of Reference 5. The pressure field at the exit appears to duplicate that of a uniformly heated 1200 psi jet.

Considering heaters of the same efficiency and defining the following for the conditions of Figure 7:

$$\text{Shrouded Arc Heater Power} = P_{s_{\text{arc}}} \approx 35 \text{ Megawatts}$$

$$\begin{aligned} \text{Shroud Factor} = F_s &= \frac{\text{shrouded throat area}}{\text{unshrouded throat area}} \\ &= \left(\frac{1.6}{.9} \right)^2 = 3.160 \end{aligned}$$

$$\begin{aligned} \text{Unshrouded Flow Enthalpy Peaking Factor} = F_p &= \frac{H_o \text{ centerline}}{H_o \text{ average}} \\ \text{(From Reference 1)} & \approx 2.0 \end{aligned}$$

$$\begin{aligned} \text{Flared Nozzle Factor} = F_f &= \frac{\text{flared nozzle exit area}}{\text{non-flared nozzle exit area}} \\ \text{(For an undisturbed test flow - See Reference 6)} &= 1.160 \end{aligned}$$

We see that the arc heater power required to produce an equivalent uniform jet is:

$$\begin{aligned} P_{\text{equivalent}} &= P_{s_{\text{arc}}} \times F_s \times F_p \times F_f \\ &= 35 \text{ MW} \times 3.16 \times 2.0 \times 1.160 \\ &= 256 \text{ Megawatts} \end{aligned}$$

Comparison of the measured heating and pressure profiles in Figure 7 indicate that the shrouded arc heater operating at 35 Megawatts effectively duplicates the pressure field and centerline total enthalpy of a 250 Megawatt arc heater producing a uniform jet.

Summary and Future Plans

The AFFDL Shrouded Flow Arc Heater with a peaked enthalpy profile and flared nozzle has successfully duplicated the pressure field and centerline temperatures of a 250 Megawatt uniformly heated arc heater operating at 108 atmospheres total pressure.

Basic operating characteristics of the unshrouded arc heater may be maintained if the shrouded heater nozzle throat is sized to accommodate the normal hot flow plus the cold shroud flow. Also, a wide range of "off-design" mass flow ratio conditions may be run with no significant heater operating difficulties. The lower mass ratios gave the maximum heater voltage, hot core mass flow, and model heating rates with little or no degradation of the test jet pressure field or hot core size.

The Shroud Flow Arc Heater is a novel method of meeting the extremely large test flow requirements for full scale ground tests of missile heat protection systems, representing a considerable economy over the power required for a uniformly heated arc jet.

Future plans include development of larger higher pressure shroud flow systems for the AFFDL RENT Facility.

REFERENCES

1. Beachler, J. C., "Operating Characteristics of the Air Force Flight Dynamics Laboratory Re-Entry Nose Tip (RENT) Facility", Proceedings of ASTM/IES/AIAA 6th Space Simulation Conference, September 1970.
2. Doyle, J. P., Private Communication , April 1971.
3. Winovich, W., "On the Equilibrium Sonic-Flow Method for Evaluating Electric-Arc Air-Heater Performance", NASA TN D-2132, March 1964.
4. Brown-Edwards, E. G., Preliminary Calibration Data , September 1972.
5. Fay, J. A., and Riddell, F. R., "Theory of Stagnation Point Heat Transfer in Dissociated Air", Journal of Aeronautical Sciences, Volume 25, Nr 2, February 1958.
6. Huber, Franz J. A. and Van Kuren, James T., "Flared Nozzle for Testing Missile Nose Tips in the AFFDL 50 MW Re-Entry Nose Tip Facility", Paper Presented at 35th Semi-Annual Meeting of Supersonic Tunnel Association.

454

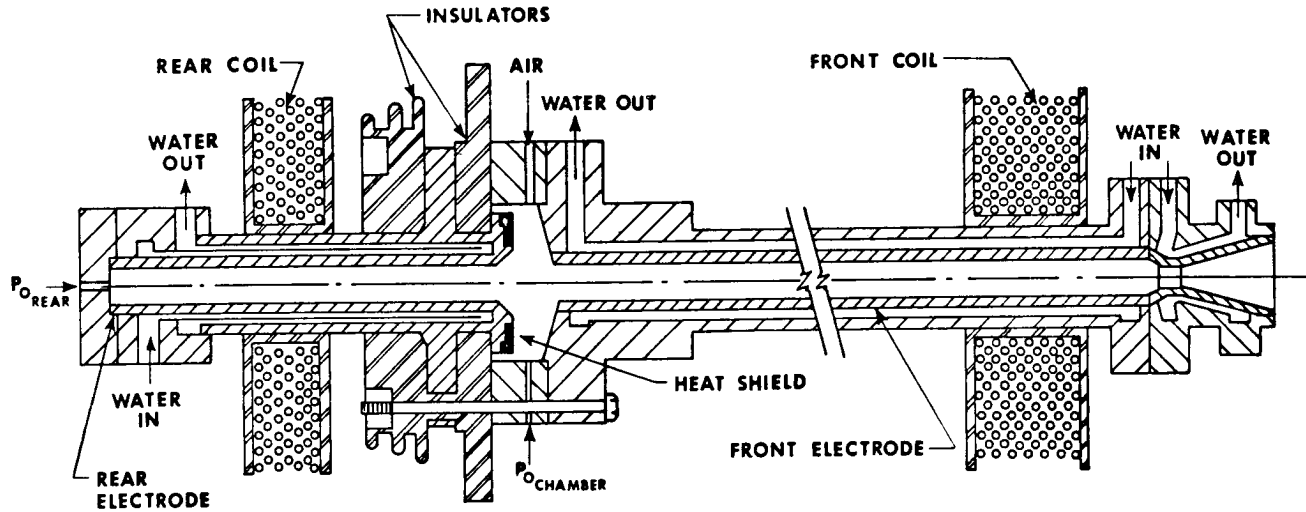


FIGURE 1. 50MW RENT ARC HEATER SCHEMATIC

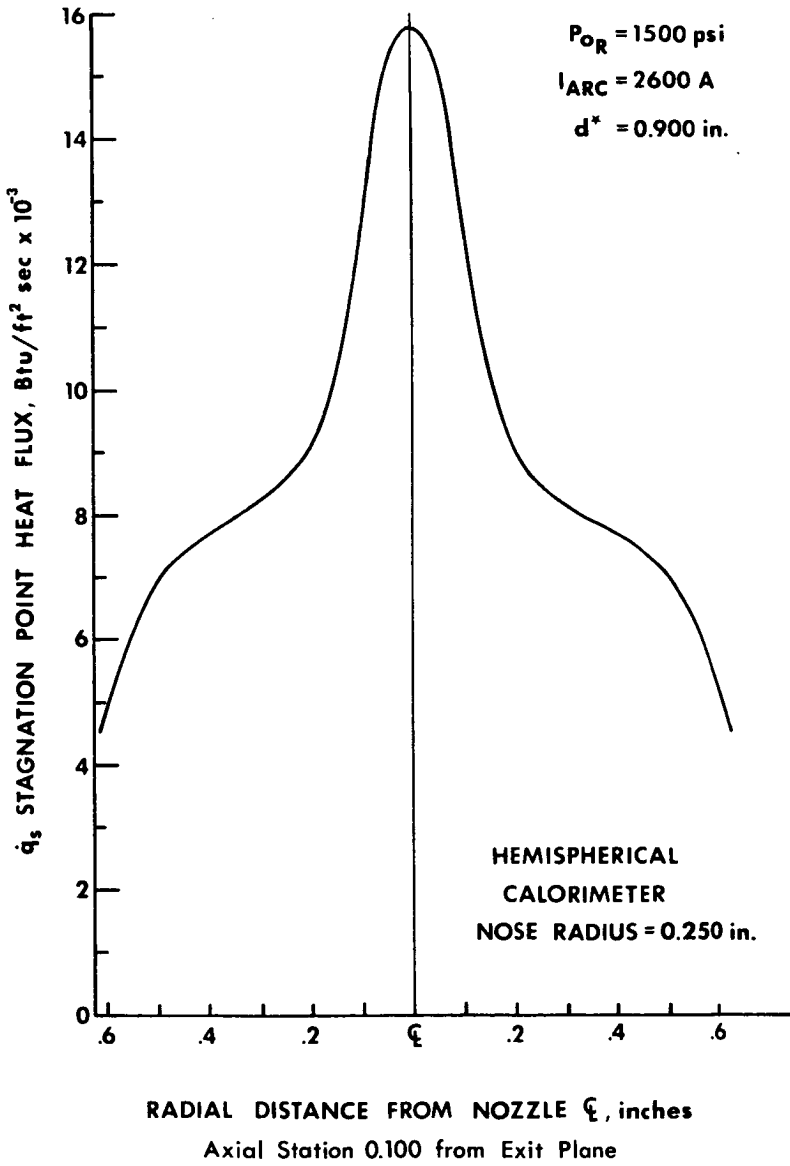


FIGURE 2. HEAT FLUX PROFILE
 OF CONTOURED RENT NOZZLE
 WITH STANDARD ARC HEATER

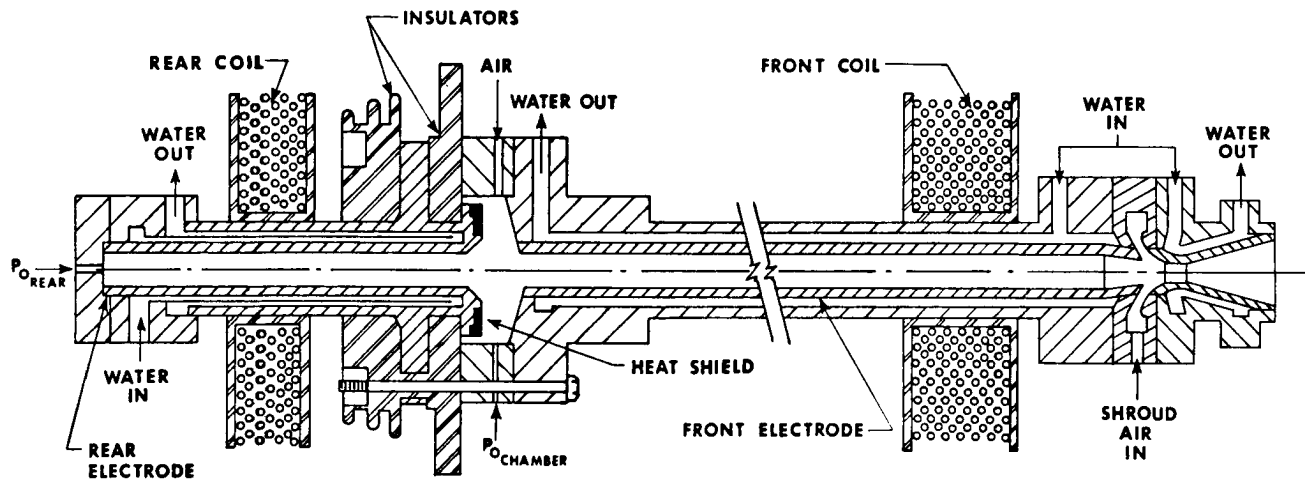


FIGURE 3. SHROUDED FLOW ARC HEATER

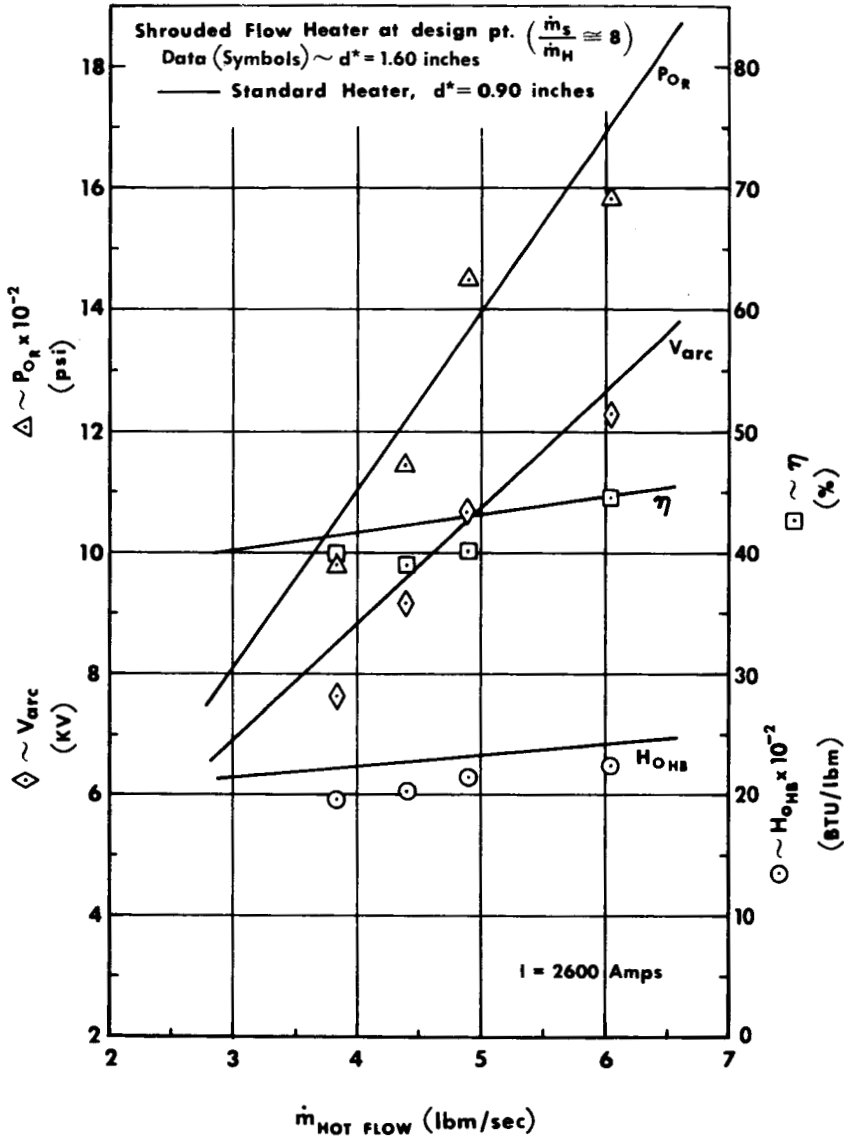


FIGURE 4. ARC HEATER OPERATING CHARACTERISTICS
 STANDARD AND SHROUDED FLOW

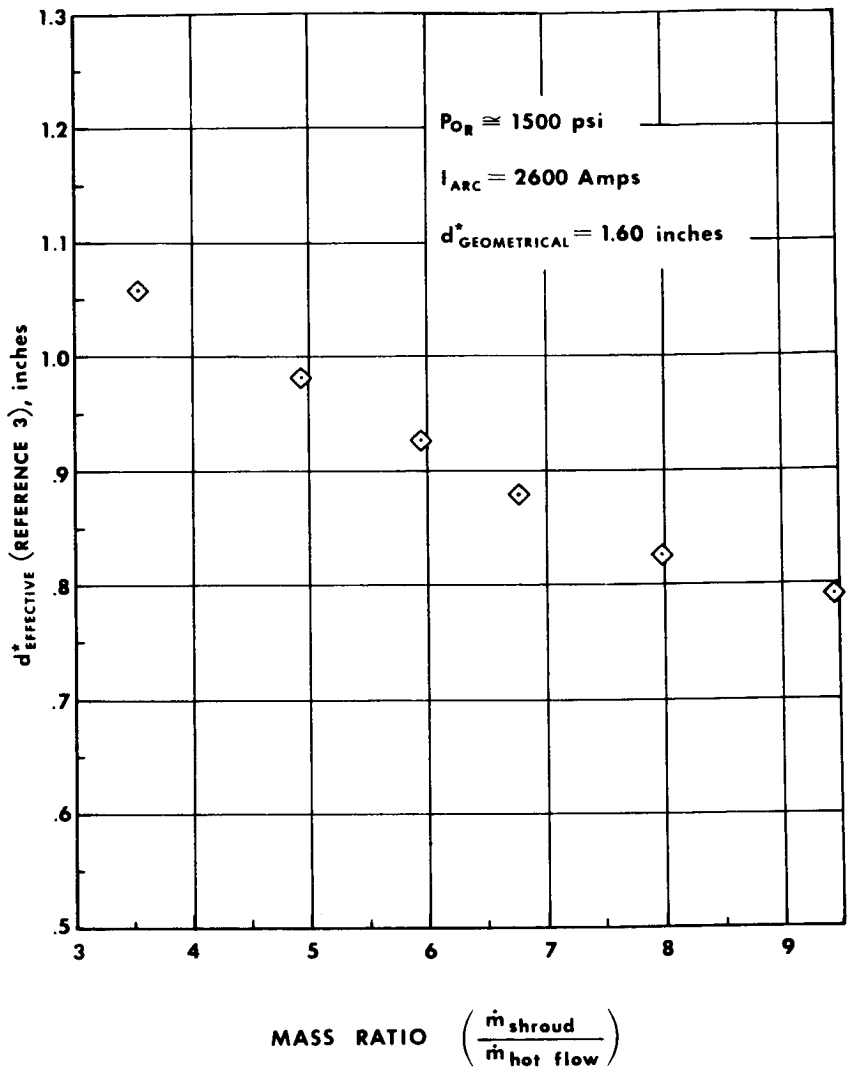


FIGURE 5. EFFECTIVE HOT FLOW THROAT SIZE (d_{EFF}^*) FOR VARIOUS MASS RATIOS IN SHROUDED ARC HEATER

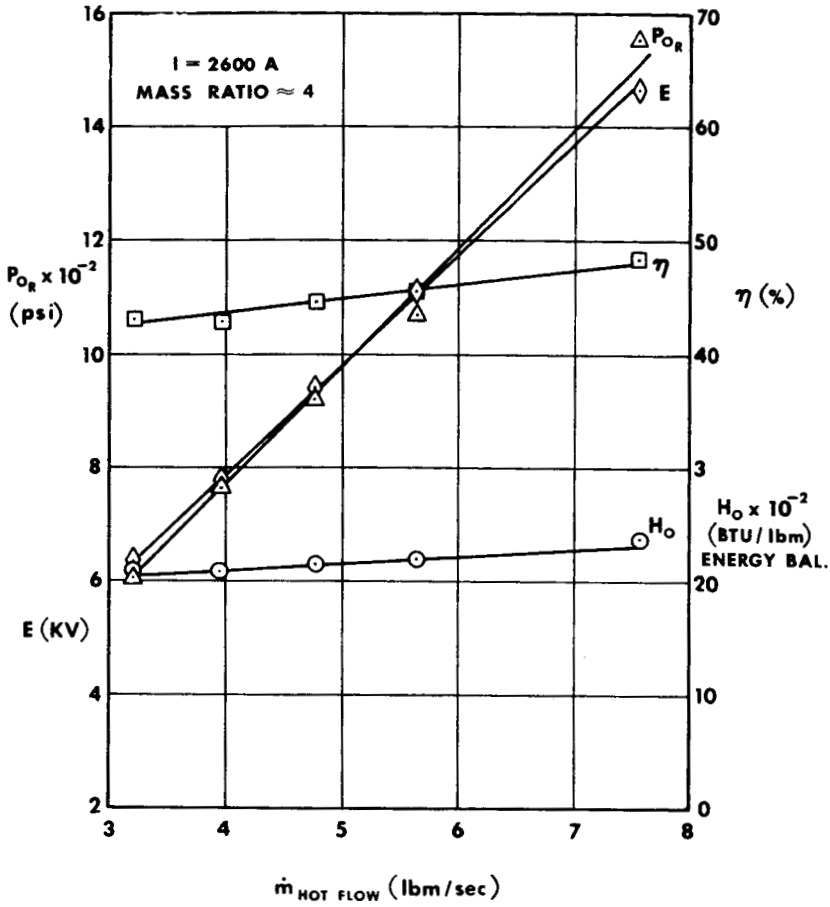


FIGURE 6a. SHROUD FLOW ARC HEATER OPERATING CHARACTERISTICS FOR CONSTANT MASS RATIO

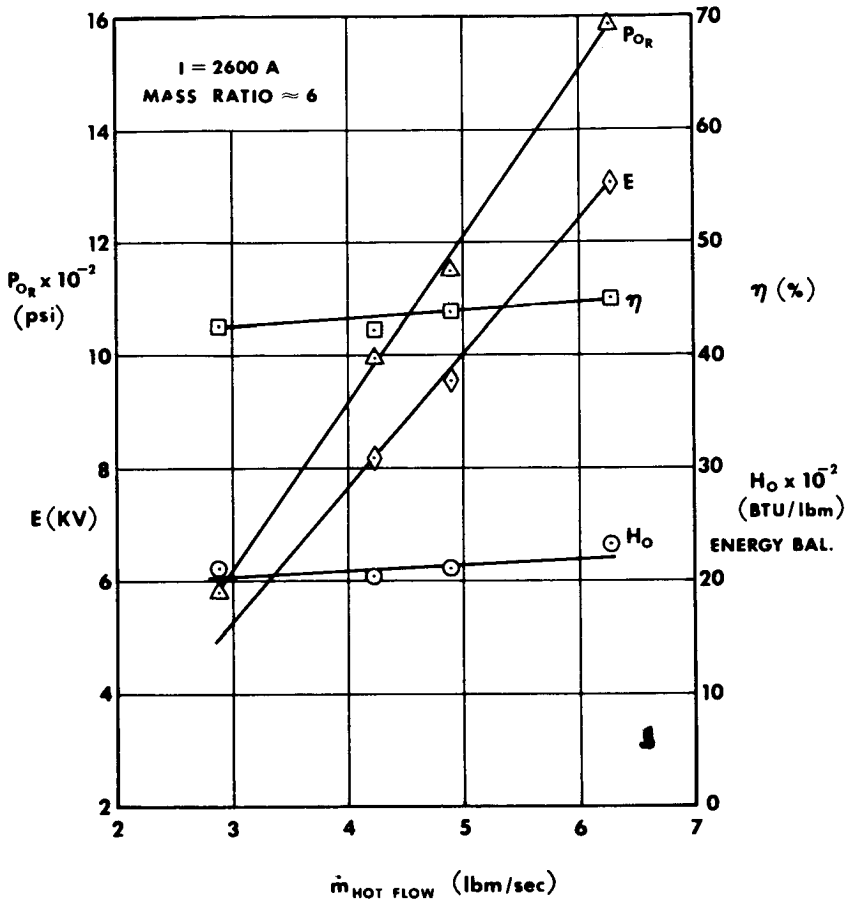


FIGURE 6b. SHROUD FLOW ARC HEATER OPERATING CHARACTERISTICS FOR CONSTANT MASS RATIO

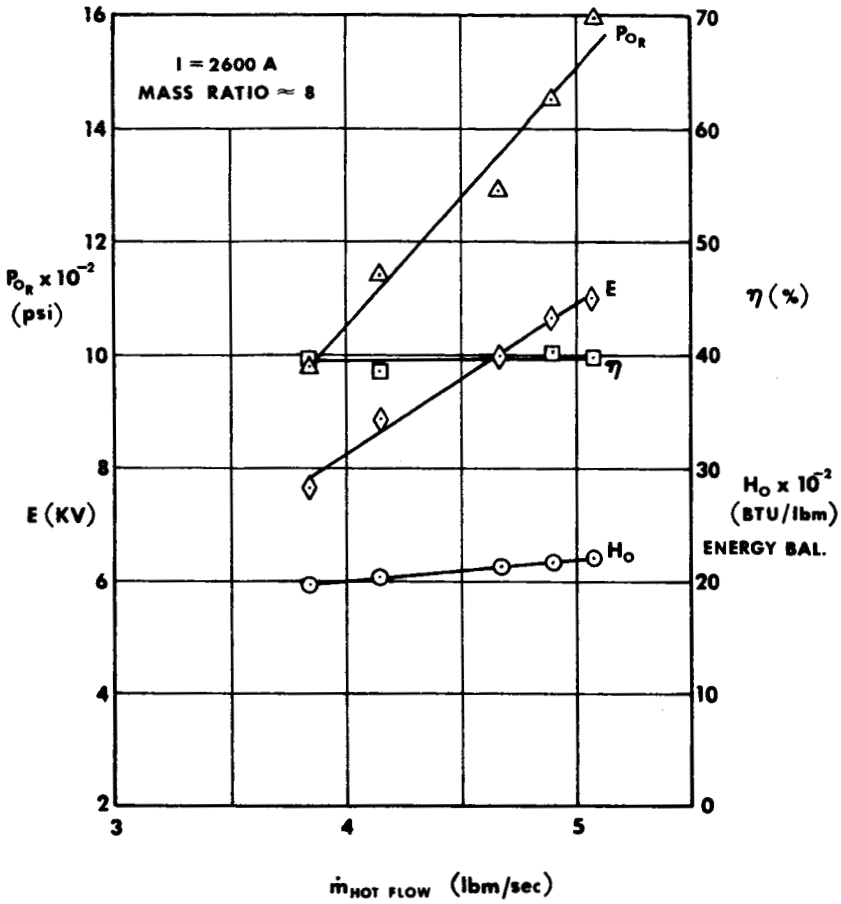


FIGURE 6c. SHROUD FLOW ARC HEATER OPERATING CHARACTERISTICS FOR CONSTANT MASS RATIO

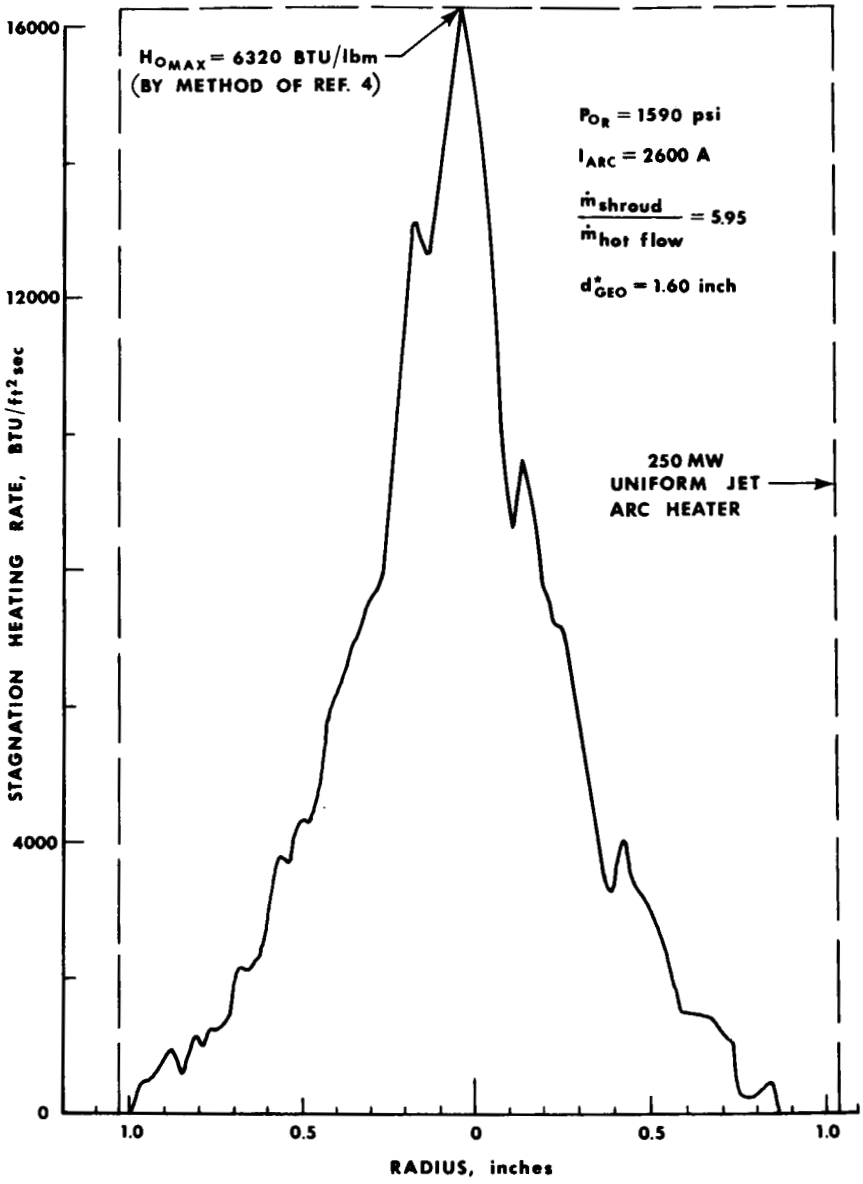


FIGURE 7a. RADIAL HEAT FLUX PROFILE FOR SHROUDED FLOW
 ARC HEATER WITH 2.125 INCH EXIT DIA. NOZZLE

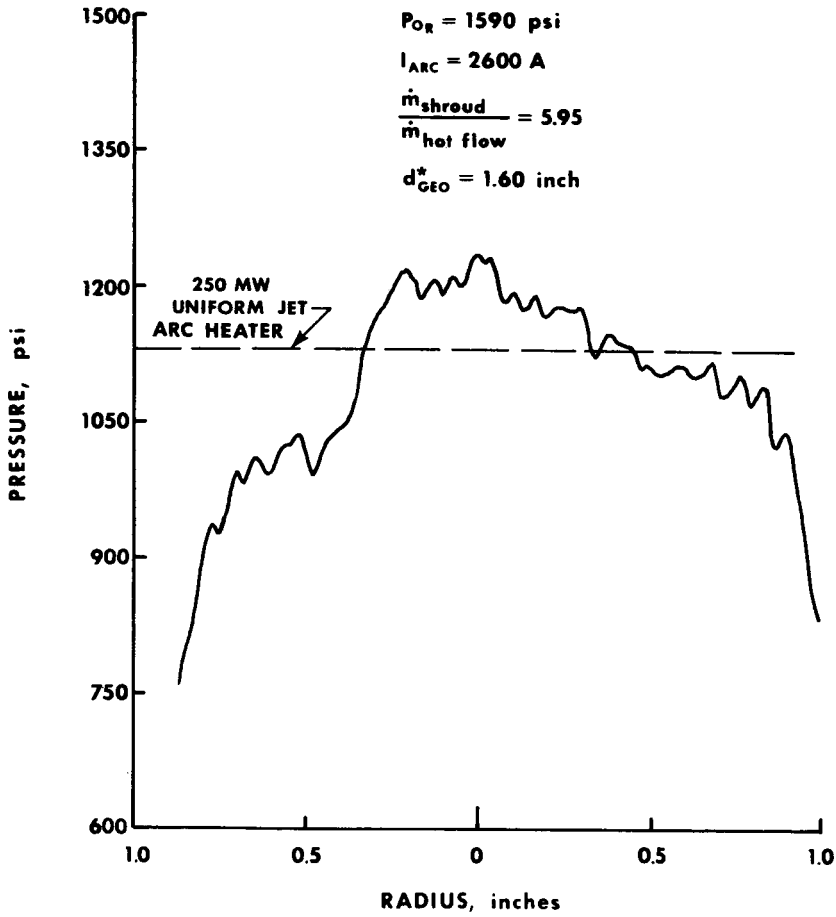


FIGURE 7b. RADIAL PRESSURE PROFILES AT $X = 0.1''$ FOR SHROUDED FLOW ARC HEATER WITH 2.125 INCH EXIT DIA. NOZZLE

Paper No. 35

THE ABLATION PERFORMANCE OF FOAMS IN A LOW HEAT FLUX

D. H. Smith and D. R. Hender, *McDonnell Douglas
Aeronautics Company, Huntington Beach, California*

ABSTRACT

Tests of ablation performance of low-density, polyurethane-based foams have been conducted in a low-heat-flux plasma-arc environment. It is shown that fire-retardant chemicals included in the foam have a significant effect in reducing surface recession, and that these materials are attractive candidates for ablative cryogenic insulation systems.

INTRODUCTION

A wide range of future space missions will employ large cryogenic tanks, either as payloads or as launch stages, which will require an insulation system that must not only minimize ground-hold boiloff and propellant quality degradation but also resist the surface erosion caused by aerodynamic heating. Conventional procedures usually dictate the screening of numerous proven ablators for their ability to adhere to cryogenic surfaces. In this study, however, materials with proven cryogenic insulation capabilities were modified to enhance their ablative performance.

The materials investigated are shown in Table 1 and included the Saturn S-II polyurethane spray-foam material, BX-250; two pour foams, BX-251 and CPR-421; a one dimensionally reinforced foam (Z-direction fibers), BX-251-1D; and the MDAC-W "filled" foams, XF-2 through XF-7, which are essentially different-density versions of a polyurethane pour foam to which various amounts of fire-retardant chemicals have been added.

ABLATION TESTS

The tests were conducted at the McDonnell Douglas Research Laboratories (MDRL) Plasma Arc Tunnel (PAT) Facility (Figure 1) in St. Louis, Mo. The aerodynamic heating environments expected during ascent flight encompass heating rates ranging from near zero to 6 Btu/ft² sec. Since this heating level could not be attained in the conventional stagnation or splash mode of material exposure, it was necessary to consider

Table 1 Materials Tested

Foam	Density	Component Weight Percent			
		Polyurethane Foam	$\text{NH}_4\text{HBO}_4\text{O}_7 \cdot 3\text{H}_2\text{O}$	$(\text{NH}_4)_2\text{HPO}_4$	Other
BX-250	2.6	100			
BX-251	1.7	100			
BX-251 - 1D	3.0	80			20-Nylon Thread
XF-1	1.9	100			
XF-2	3.3	72	14	14	
XF-3	4.6	72	14	14	
XF-4	8.0	72	14	14	
XF-5	3.5	84	8	8	
XF-6	4.5	84	8	8	
XF-7	3.5	84		16	
CPR-421	2.0	Proprietary Foam (CPR Div., Upjohn Co.) Polyurethane Base			

WD 2196

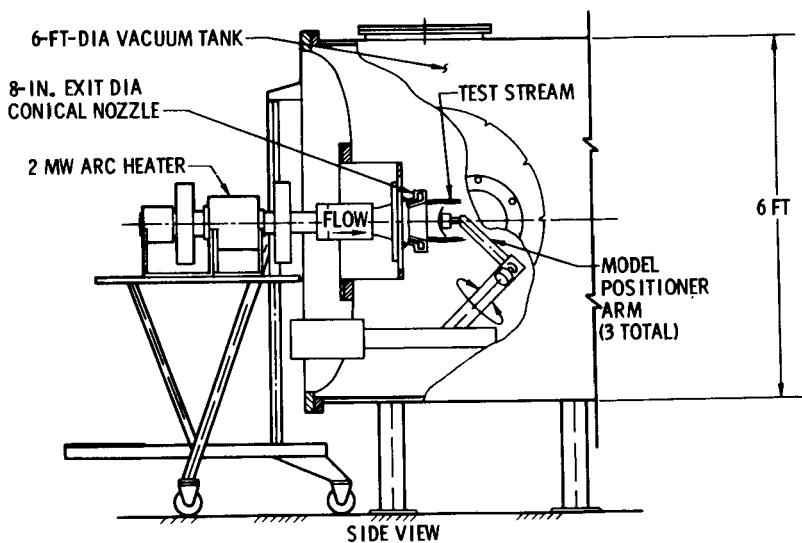


Fig. 1—Schematic of McDonnell Douglas plasma arc tunnel

Table 2 Pressure and Heating Rate Distribution
as a Function of Surface Position*

	Pressure (torr)					Heating Rate (Btu/ft ² sec)				
	1	2	3	4	5	1	2	3	4	5
Right Calorimeter (Flush)	0.52	0.49	--	0.43	0.40	2.2	2.2		1.5	1.6
Left Calorimeter (Flush)	--	--	--	--	--	2.1	1.9		1.4	1.7
Stagnation Line				9.44					23.3	
Right Calorimeter (Flush)	0.54	0.53	--	0.46	0.43	2.1	2.0	2.1	1.4	-
Left Calorimeter (1/16 in. recessed)	--	--	--	--	--	1.8	1.6	1.6	1.0	1.4
Stagnation Line				9.33					24.0	
Right Calorimeter (Flush)	0.53	0.53	--	0.44	0.44	2.1	2.1	2.1	1.4	1.6
Left Calorimeter (1/8 in. recessed)	--	--	--	--	--	1.8	1.5	1.5	1.1	1.4
Stagnation Line				9.35					24.9	

*See Fig. 1 for location of sensors 1 through 5.

During later tests, a calibration plate was made up with seven copper-slug calorimeters in the direction of the flow to provide more definition of the streamwise heating gradients as well as the effect of smaller recessed increments. Unfortunately, the results were inconclusive since the changes in arc conditions from run to run and deviations in the measurement of calorimeter slopes overshadowed any other trends.

Instrumentation of the material samples consisted of three chromel-alumel thermocouples per sample. Two were located at the sample-backup structure interface on the centerline, and one was at the geometric center of the ablative material (Figure 3).

Supplemental surface-temperature information was obtained from a TD-17 optical pyrometer, sighted on the right-side sample surface 1/2 in. downstream of the leading edge and on the centerline. The pyrometer was sighted through a calcium fluoride window with 92-percent transmission in the 1.7-to 2.6-micron range, with the pyrometer emittance set to 1.0.

Table 3 summarizes the test foams and their performance. Since most of the materials ablated smoothly and uniformly, recession- and heating-rate data are only given for the model's trailing edge, farthest from the influence of the step formed

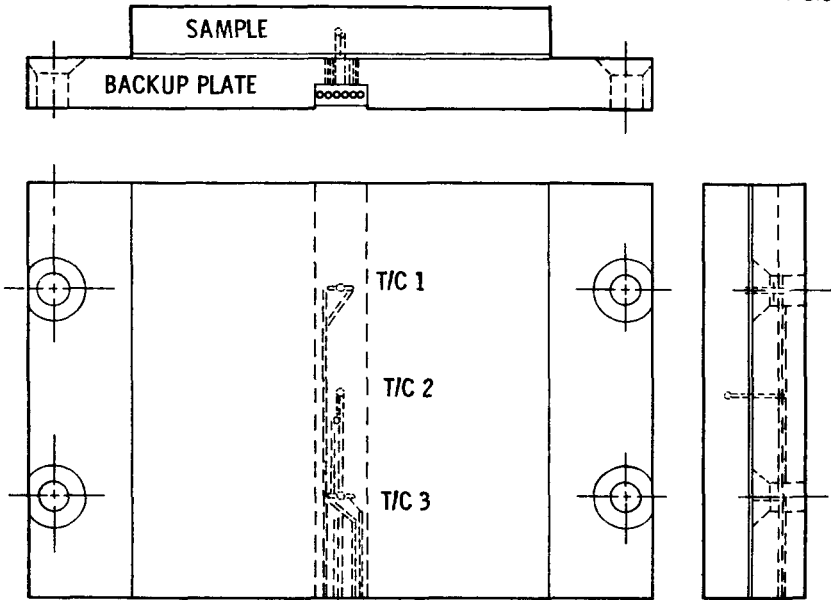


Fig. 3—Ablation sample and backup plate

when the model's front edge recedes below the holder's surface. Back-face temperature rise reflects the response of the aft-most thermocouple (No. 3). All data are averaged for both models on each side of the holder.

The basic polyurethane foams--BX-250, BX-251, XF-1, and CPR-421--showed a moderate resistance to low-level heating rates, and performed better than expected. In applications where the surface radiation equilibrium temperature reaches 600 to 700°F for short periods of time, the resultant ablation can be incorporated in the overall cryogenic insulation thickness requirements. For higher heating-rate environments, however, the performance deteriorates rapidly, and it would be advantageous to consider other material formulations. The XF series of ablative foams (XF-2 through XF-7) show a significant improvement in ablation resistance over the basic polyurethane foams. Where aerodynamic heating rates exceed acceptable limits for the basic foams, these materials offer an ideal alternative, combining good cryogenic insulation qualities with moderate ablative performance.

ANALYTICAL MODELING

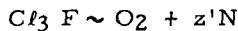
The ablation of a number of these materials was calculated using the CHAMP charring ablator program (Reference 2)

Table 3 Ablation Test Program Summary

Foam	Heat Rate (Btu/ft ² sec)	Enthalpy [†] (Btu/lbm)	Duration (sec)	Surface Recession (in.)	Backface Temperature Rise (°F)	Peak Pyrometer Reading (°F)	Weight Loss (%)
BX-250	1.50	2,150	120	0.11	118	660	81
BX-250	1.43*	2,050	140	0.146	100		
BX-250	2.32	3,050	60	0.168	105		
BX-250	3.26	3,300	16	0.172	150		
BX-251	1.50	2,000	65	0.12	95	545	69
BX-251-1D	1.60	2,050	280	0.05**	412	660	
CPR-421	1.65	2,340	342	0.098***	160	705	
XF-1	1.85	2,150	69	0.10	97	612	81
XF-2	1.60	2,100	425	0.07	130	585	
XF-3	1.70	2,050	425	0.06	160	600	72
XF-3	3.55	3,290	200	0.026	120		
XF-3	6.35	4,670	185	0.062	480		
XF-4	1.80	2,050	425	0.02	175	585	35
XF-5	1.80	2,650	425	0.066	610		
XF-5	3.60	3,590	44	0.084			
XF-6	1.60	2,350	425	0.028	80	592	
XF-6	4.45	3,620	168	0.090	103	950	
XF-6	6.35	4,525	180	0.119	450		
XF-7	1.70	2,340	429	0.144	170	645	

*Higher aero shear
 **Material receded between threads
 ***Large areas in center of specimen totally eroded
 †Bulk enthalpy. Recovery enthalpy is approximately 85% of this value.

parametrically to determine steady-state ablation rates caused by diffusion-controlled oxidation modified by blowing, with equilibrium boundary layer chemistry plus rate-controlled pyrolysis and surface oxidation. An empirical chemical formula, $C_w H_x O_y N_z$, was determined for the virgin and charred forms of each material studied, based on data from thermo-gravimetric analysis (TGA) and knowledge of the chemical constituents. It was assumed that all foams had cells filled with Freon 11 (CFC13) foaming agent, and the empirical formula was modified to account for this, assuming that the halogen molecules could be treated as effectively as a mixture of oxygen and nitrogen:



where z' was determined so that the equation balances in mass.

The borate and phosphate salts indicated for many of the foams listed in Table 1 are fire-retardant chemicals added to the foams to improve their ablation performance. For foams containing these salts, the empirical formula was further modified to account for the products of the salts' thermal decomposition. It was assumed that the final reduction products would be B_2O_3 that would remain in the material as a solid, and P_4O_6 that would be driven off as a gas. The fraction of residue seen in the TGA data on these salts agrees well with those calculated under these assumptions.

Five types of foams were modeled using these techniques: BX-250, BX-251, XF-3, XF-6, and a polyurethane foam with 7-percent KBF_4 , described in Reference 3. Good agreement was obtained with the data of Reference 3, and with the BX-250 and BX-251 data for heat fluxes below 2 $\text{Btu}/\text{ft}^2\text{sec}$. However, where the heating exceeded this, the ablation performance of BX-250 and BX-251 rapidly diverged from the thermochemical predictions. Figure 4 presents a summary of the nondimensionalized ablation rates scaled from side-aspect movies of the BX-250 and BX-251 tests along with the thermochemical curve.

WD 2186

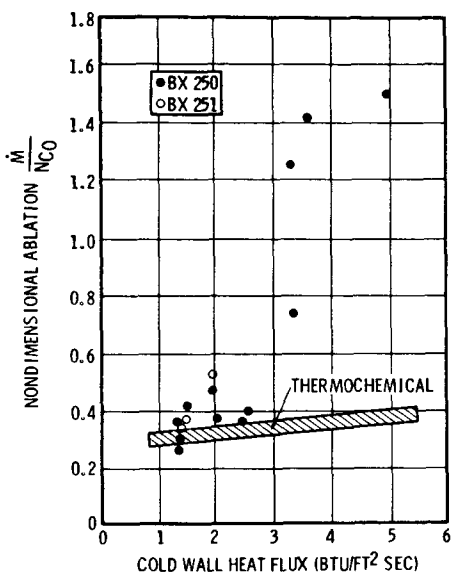
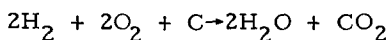


Fig. 4—BX-250 and BX-251 ablation summary

In this series of analyses, it was found that, analytically, oxidation is bistable at the temperatures and pressures of these tests. Equilibrium chemistry predicts that either of the following reactions is possible:



The SCREEN reaction-rate chemistry program (Reference 4) predicts that the second reaction would dominate in a mixture of molecular hydrogen, oxygen, nitrogen, and atomic carbon; however, it also predicts that a mixture of the products of the first reaction would revert extremely slowly

toward the products of the second. Obviously, to obtain realistic ablation rate predictions it is essential to select the proper reaction, since ablation rates are much higher with the second reaction because most of the carbon must come from the removal of surface material. Figure 5 shows the predicted non-dimensional ablation rates for both oxidation modes. The predictions shown in Figure 4, and the correlation with the results of Reference 3, represent recession predicted with the second oxidation reaction.

WD 2196

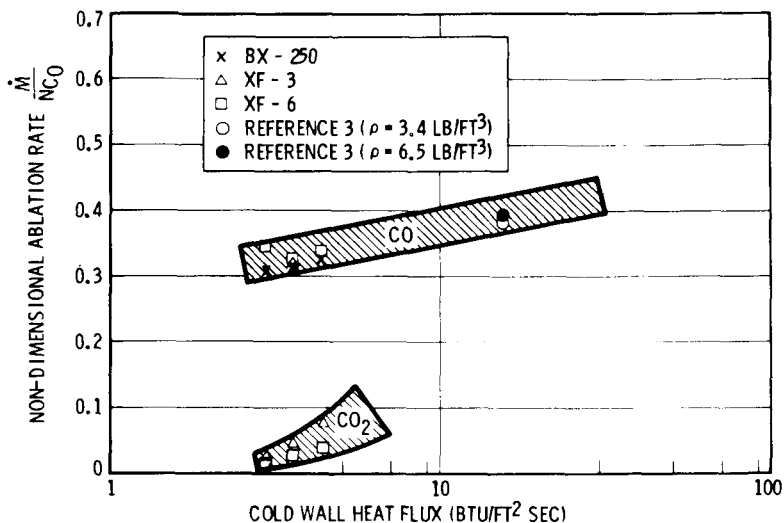


Fig. 5—Thermochemical steady-state ablation predictions

Ablation of foams with salts generally differs considerably from that of BX-250 and BX-251. Initially, their recession rate seems to be about the same as for the plain foams, but, it drops much lower after 15 to 20 sec. Post-test inspection of the samples shows that the foams with added salts form a soft porous char with a delicate crusty surface, while the plain foams do not. It is not clear why this char formation affects ablation rates; however, it was noted that the recession rates predicted using the first oxidation reaction match quite well those seen in the latter phase of the tests, as shown in Figure 6. Apparently, as the carbon in the char is removed by oxidation, the salt residue remains on the surface and changes the character of the surface chemical reactions after ablation reaches some critical depth. It is felt that the significant additive causing this is boron, both because a pair of samples containing only the phosphate (XF-7) was tested and performed quite poorly, and because the foams

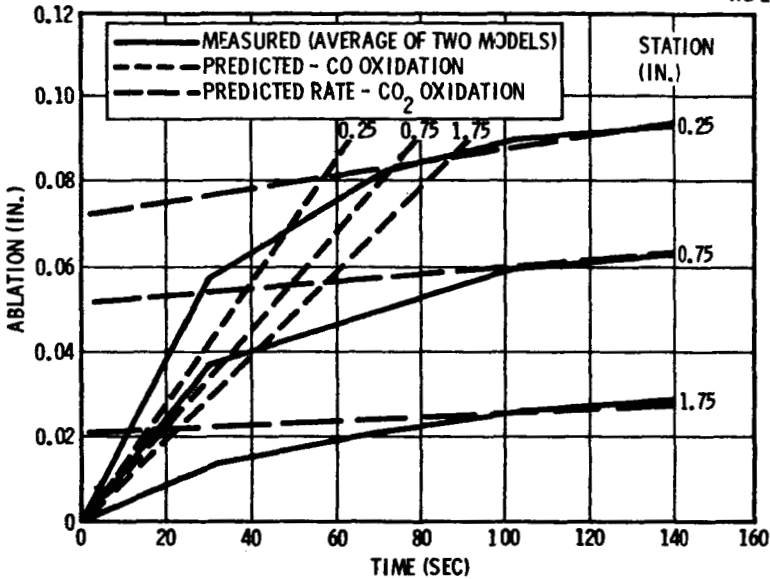


Fig. 6—Predicted and measured ablation for XF-6 (run 3629)

of Reference 3 also contain a boron compound. This critical ablation depth can be fairly well correlated by an equation of the form of the Arrhenius equation, as shown in Figure 7, using the radiation equilibrium surface temperature and the concentration of boron in the material:

$$\Delta S_{\text{critical}} = \frac{1}{\rho_{\text{boron}}} A e^{-\frac{B}{T_e}}$$

CONCLUSIONS

Foams appear to be very attractive ablation materials for low-heat-flux applications. Standard polyurethane foams tested have good ablation resistance for heat fluxes below 2 Btu/ft²sec, while modified foams have demonstrated ablation resistance many times better. Figure 8 shows the regimes of applicability of both types. With their low density and conductivity, and ablation rates as low or lower than most denser ablators, foams are attractive candidates for many ablative protection roles, especially where cryogenic insulation is required.

ACKNOWLEDGMENT

This work was sponsored by the McDonnell Douglas Astronautics Company and performed under Independent Research and Development.

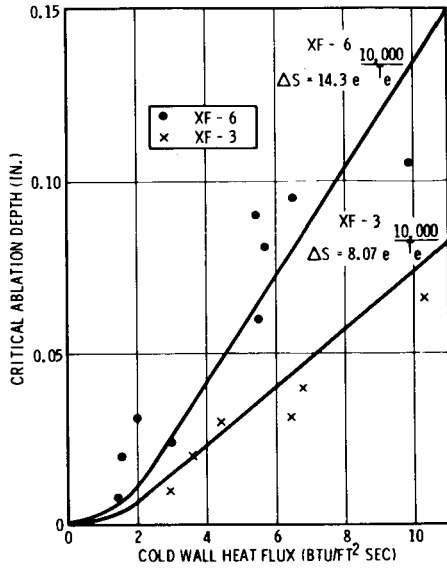


Fig. 7—Critical ablation depth for modified foams

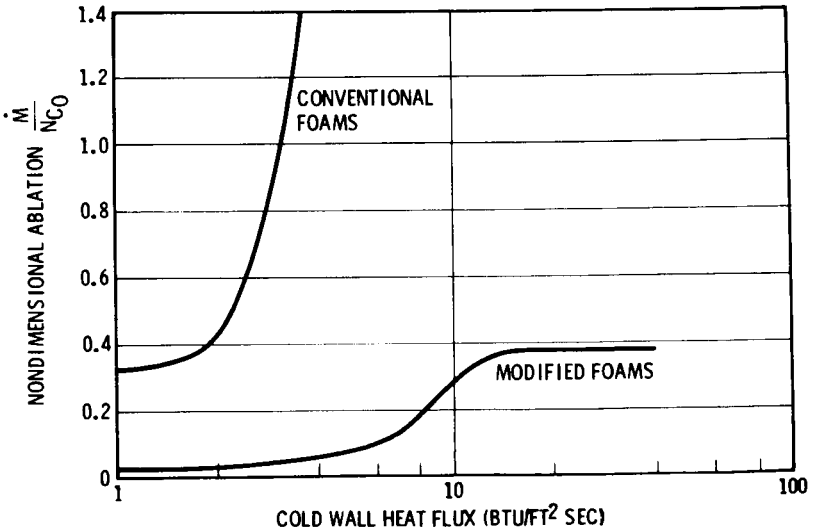


Fig. 8—Foams' ablation regimes

SYMBOLS

A	Empirical coefficient	$\frac{\text{in.} \cdot \text{lb}}{\text{ft}^3}$
B	Empirical coefficient	°R
\dot{M}	Mass loss rate	$\frac{\text{lb}}{\text{ft}^2 \text{ sec}}$
N_{CO}	Non-blowing enthalpy heat transfer coefficient	$\frac{\text{lb}}{\text{ft}^2 \text{ sec}}$
T_e	Radiation equilibrium temperature for a black surface	°R
ρ	Material density	$\frac{\text{lb}}{\text{ft}^3}$

REFERENCES

1. Nestler, D. E., et al. Heat Transfer to Steps and Cavities in Hypersonic Turbulent Flow. AIAA Paper No. 68-673, June 1968.
2. Arne, C. L. Charring Ablator Multiphase Processes Computer Program. Douglas Report SM-49310, July 1966.
3. Pope, R. B., S. R. Riccitiello, and H. E. Goldstein. Ablative Thermal Protection at Low Heating Rates. Materials Journal, SAMPE Quarterly, Vol. I, No. 1.
4. Frey, H. M. and G. R. Nickerson. A Computer Program for the Screening of Chemically Reacting Gas Mixtures. Dynamic Science Report No. TR-141-1-CS, February 1970.

474-10264

**SPACE SHUTTLE ENTRY ENVIRONMENT
TESTING TECHNIQUES**

E. L. Mulcahy and R. R. Rogers, *LTV Aerospace Corp.,
Dallas, Texas*

ABSTRACT

Testing techniques have been developed for simulating the high temperature portion of the entry environment which have been applied to testing large Space Shuttle leading edge structural segments. The test techniques involve the use of arrays of graphite heating elements which radiate heat to the test articles.

INTRODUCTION

Development of materials for the Space Shuttle leading edge structure requires new testing techniques which can be used to evaluate the performance of these materials in their specific operating environments. The type of materials being addressed in this paper are the non-metallic composites which are baselined for use on the Shuttle wing leading edge, nose cap, and belly panels. Figure 1 identifies the location of the special leading edge materials on a proposed Space Shuttle configuration. A close view of a typical wing segment of the leading edge is shown in Figure 2. Other shapes of segments will be used on the belly and nose portions of the Shuttle vehicle.

These materials will be exposed to temperatures up to 3000^oF in an oxidizing environment during entry of the Space Shuttle vehicle from earth orbit. The standard test technique which was used for baseline evaluation of small specimens was plasma arc exposure. The plasma arc provides a relatively good simulation of the entry environment when considering the desired entry gas temperature, composition, pressure and enthalpy but generally have a severe limitation in the size and geometry of specimen that can be tested. For example the largest plasma arc specimens (with a few exceptions) that were tested in LTV's development work were simple 3" diameter discs using a 10 megawatt plasma arc facility at Johnson Space Center. Because of the specimen size limitation, new test equipment was designed to test a wider variety of specimen

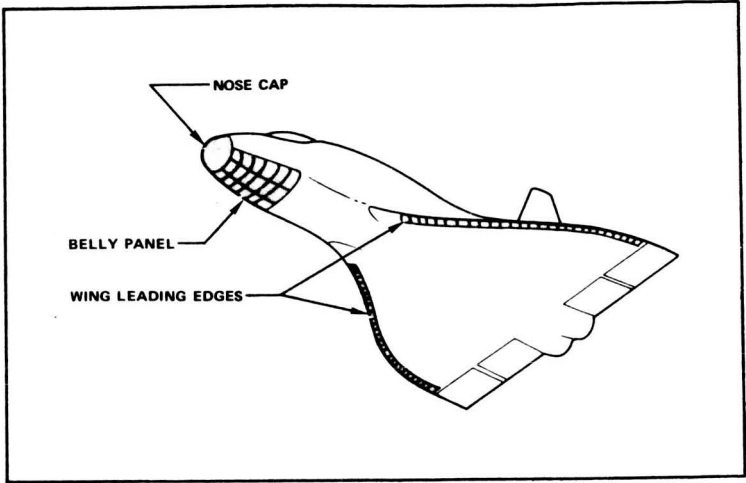


Fig. 1 - Location of Leading Edge Materials on Proposed Space Shuttle Configuration

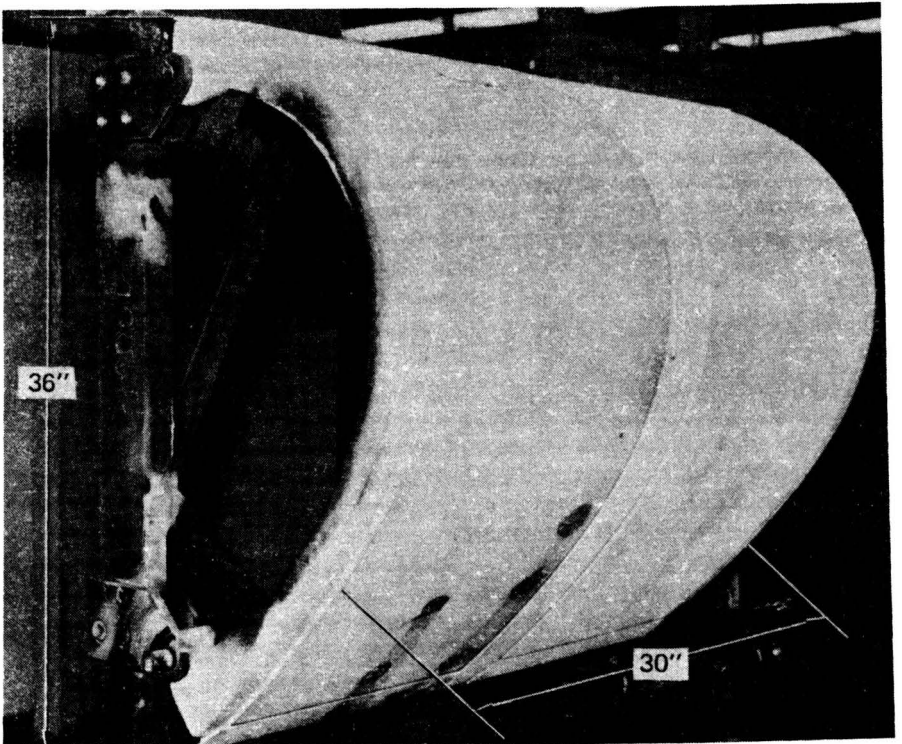


Fig. 2 - Shuttle Wing Leading Edge Test Article

sizes and geometries.

Two categories of test specimens were required by the materials development specialists at LTV. The first category was a large batch of physical property specimens (tensile, compression and flexure) from which statistical data could be obtained for correlation to the number of exposures to a simulated entry environment. Typical shapes of this type of specimen are shown in Figure 3. The second category of specimens were full size leading edge segments similar to that shown in Figure 2.

The entry environmental parameters are shown in Figures 4 through 9. The work being reported in this paper involves the exposure of test specimens to the temperature and atmosphere environmental parameters illustrated in Figure 6, 8 and 9. A considerable amount of work has been done in other areas of testing but is not being reported in this paper. The effects of temperature and an oxidizing atmosphere on the leading edge material were considered the most critical aspect of the leading edge design.

HARDWARE APPROACH

It was decided to expose batches of physical property specimens to the combined oxidation temperature environment and restrict the full scale testing to the temperature environment in an inert atmosphere. Another ground rule was that the physical property specimen would be exposed to at least 100 cycles of the combined environment. Each cycle was designed to simulate one entry mission. During the course of 100 combined environment cycles a statistical sampling of flexure, tensile and compression specimens was removed from the heating fixture every 20 cycles. These specimens were to be tested to failure in order to evaluate physical property degradation as a function of the number of mission cycles.

Two test setups were planned. The first setup was to satisfy the multicycle combined environment requirement for small specimens and the second setup was to provide the entry temperature environment for a full scale test article segment.

HARDWARE DESIGN

For the combined environment test a fixture was designed as shown schematically in Figure 10 consisting of a vacuum

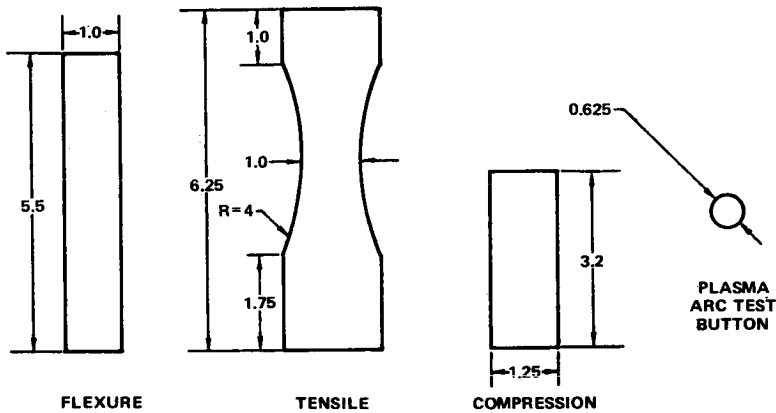


Fig. 3 - Physical Property Test Specimens

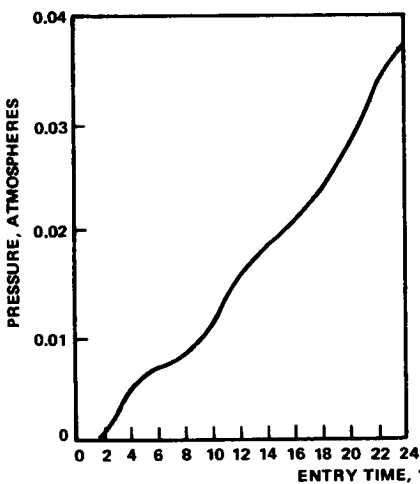


Fig. 4 - Stagnation Pressure

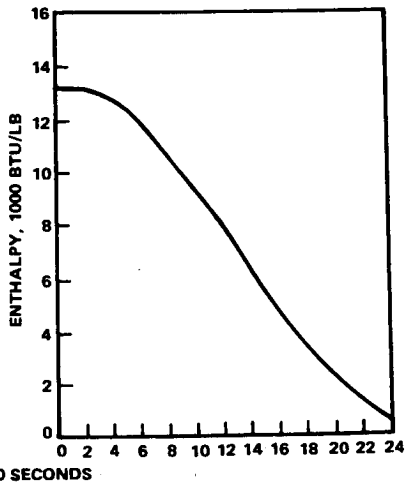


Fig. 5 - Total Enthalpy

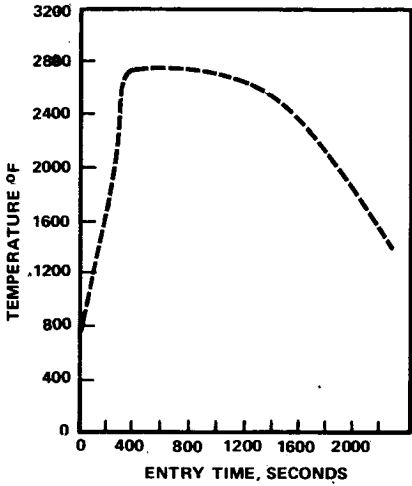


Fig. 6 - Leading Edge Temperature

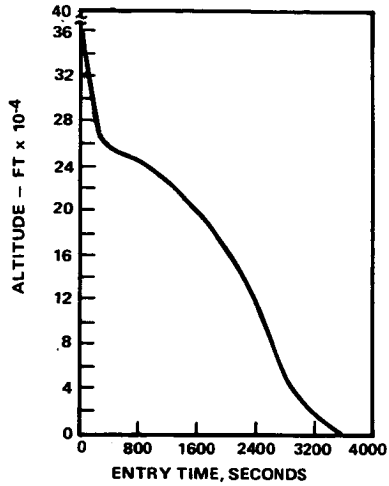


Fig. 7 - Mission Altitude

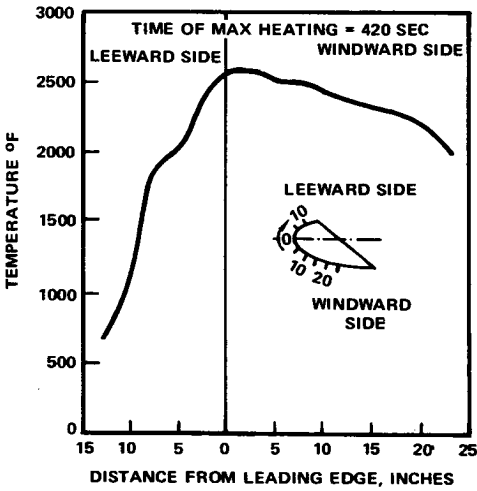


Fig. 8 - Temperature Distribution Around a Leading Edge Segment

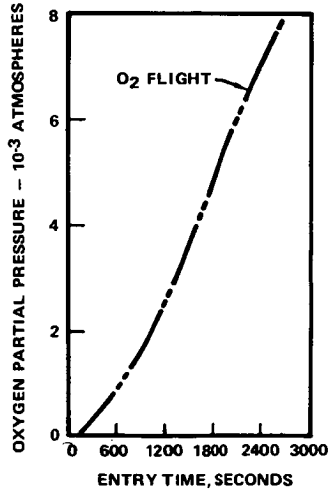


Fig. 9 - Oxygen Partial Pressure

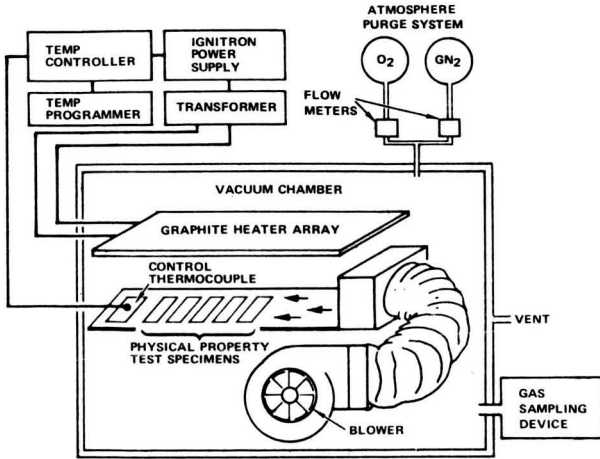


Fig. 10 – Diagram of Combined Environment Test Equipment

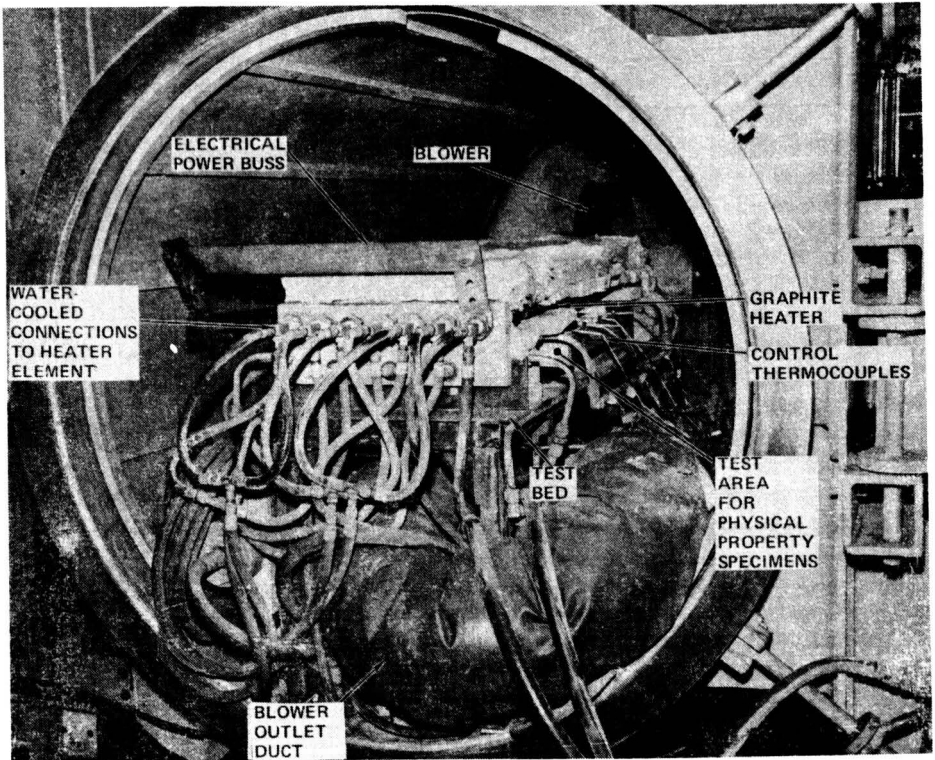


Fig. 11 – Combined Environment Test Chamber

chamber, radiant heater array, power supplies, gas circulating system, and a gas purging system. Figure 11 is a photograph of the actual setup. The vacuum chamber was 4 feet in diameter by 8 feet long with necessary ports and feedthroughs for power, cooling water, gas, and instrumentation. The heater elements were machined from graphite rods into a configuration as shown in Figure 12. A common heater element design was selected for use on both the combined environment and the temperature environment test fixtures. For the combined environment fixture, seven heater elements were connected in series to the output of a 150 KW, 120 volt secondary single phase transformer. This arrangement provided a test area of approximately two square feet in which up to 75 specimens could be exposed at one time. A threaded water cooled aluminum electrode was designed which attached to the end of each heater element. Copper bus bars were used as both electrical power connectors and structural supports to join the heater elements. Tungsten-5% Rhenium/Tungsten-26% Rhenium thermocouple assemblies were used as temperature sensors for the temperature control arrangement shown in Figure 10. The temperature programmer provided the temperature profile shown in Figure 16. Additional thermocouples were located in various specimens throughout the test area.

In order to test the full scale leading edge segment shown in Figure 2, a test fixture was designed as shown schematically in Figure 13. The fixture consisted of a vacuum chamber, radiant heater array and a power supply system. The LTV Space Environment Simulator chamber, which is 12 feet in diameter, was used for the vacuum chamber. The graphite heating elements described above were assembled in a contoured manner as shown in Figure 14.

The heating elements were divided into four zones which could be individually controlled in order to produce the temperature gradients shown in Figure 8.

Figure 15 is a photograph of the actual setup showing the leading edge segment partially raised out of the insulated heating array assembly. The total assembly is shown mounted inside the vacuum chamber. Thermocouple assemblies can be seen attached to the various surfaces of the leading edge segment. A steel mounting fixture, which simulated the structural interface between the leading edge and the Shuttle wing, was provided onto which the segment was attached with pin connections at six locations. One of the attachment points can be seen in Figure 15. The heater array was powered by use of four individually controlled power circuits as illustrated in Figure 13.

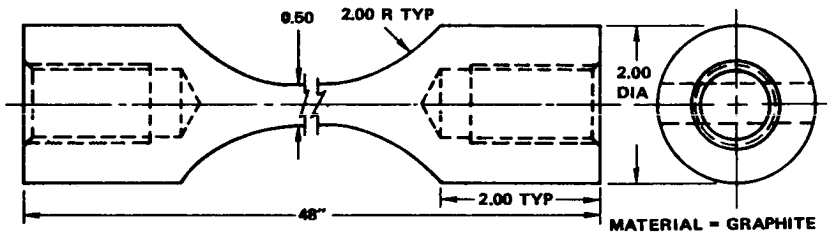


Fig. 12 - Graphite Heating Element

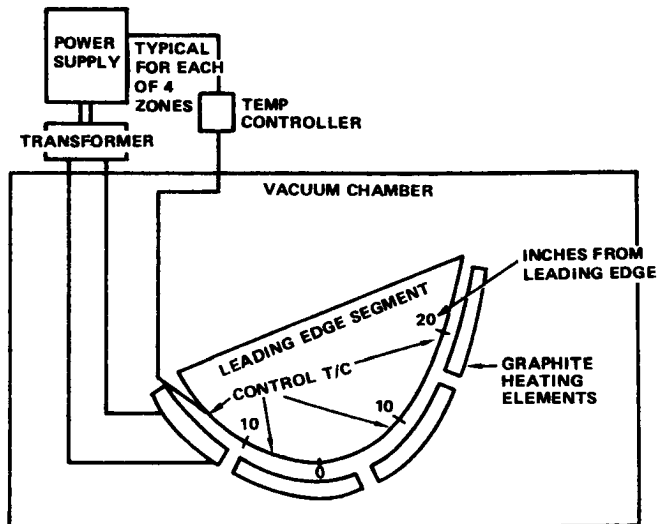


Fig. 13 - Full Scale Test Arrangement

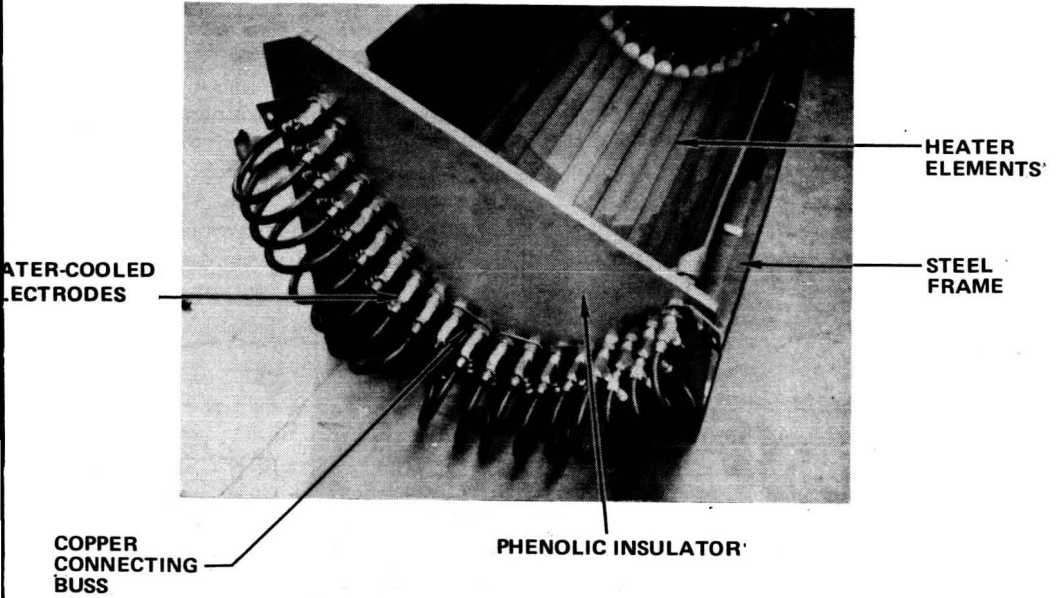


Fig. 14 - High Temperature Entry Test Fixture

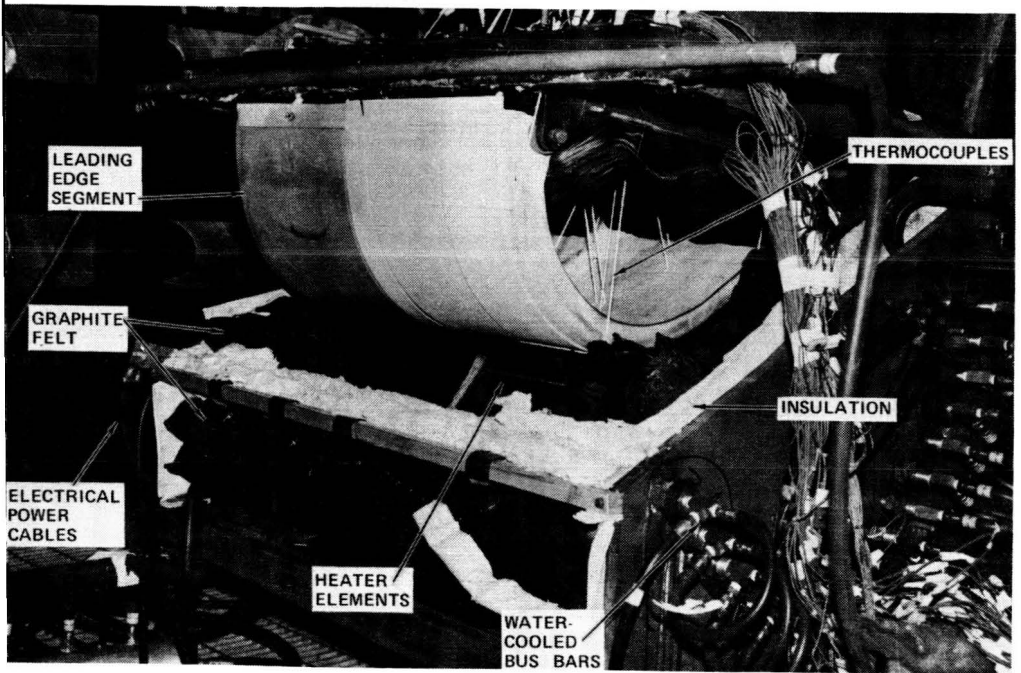


Fig. 15 - High Temperature Entry Test Set Up

The gas purge system provided a 3 psig mixture of nitrogen and oxygen simulating an average oxygen partial pressure level which would occur during the high temperature portion of the entry environment. The blower and duct arrangement provided a continual circulation of the chamber atmosphere across the exposed face of the specimens at a velocity of approximately twenty feet per second. The oxygen partial pressure was monitored by periodically drawing samples from the chamber and measuring the oxygen content on a gas chromatograph.

TEST PROCEDURE AND RESULTS

The combined environment test fixture was calibrated for temperature by conducting trial runs and measuring the temperature of sample test specimens with thermocouples. The desired oxidizing rate for a given temperature cycle was established as that rate which would cause a specimen weight loss comparable to the rate which would occur during exposure to a specimen button to a plasma arc simulation of the entry environment. The combined environment oxidation rate was determined experimentally through trial runs. The heating area was then loaded with an assortment of physical property specimens. A total of 100 entry cycles were performed. The average temperature versus time and oxygen partial pressure versus time data are shown in Figure 16.

For the full scale temperature environment test the leading edge segment shown in Figure 15 was exposed to an entry temperature profile in an inert atmosphere at a chamber pressure of 10 torr. The resulting temperature data are shown on Figures 17 and 18.

CONCLUSIONS

The above described tests represented a first step toward developing techniques for testing large space vehicle structures in a high temperature entry environment. They were not accomplished without difficulty and considerable improvements need to be made in order to achieve reliable and repeatable test results.

By far the most difficult task was to design the combined oxidation-high temperature test fixture. The selection of oxidation resistant insulations, specimen holding materials and heating elements for long duration testing is quite limited.

Development efforts are continuing to improve upon the testing techniques from both the standpoint of the quality of the test environment and the size of articles that can be handled.

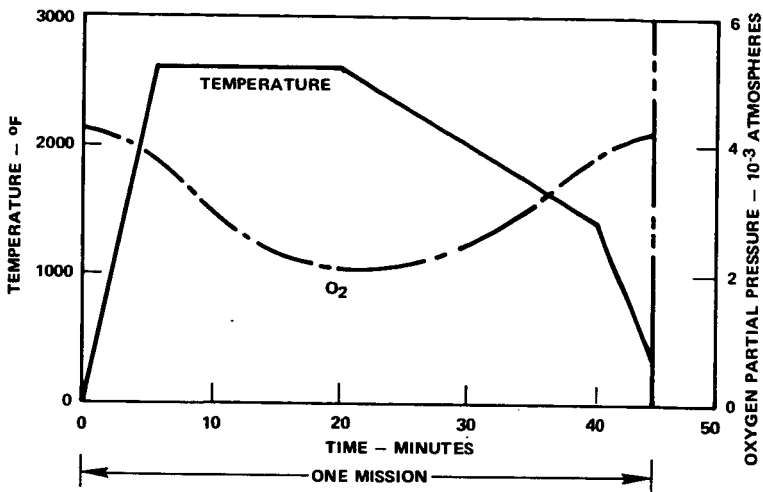


Fig. 16 - Thermal/Oxidation Test Environment

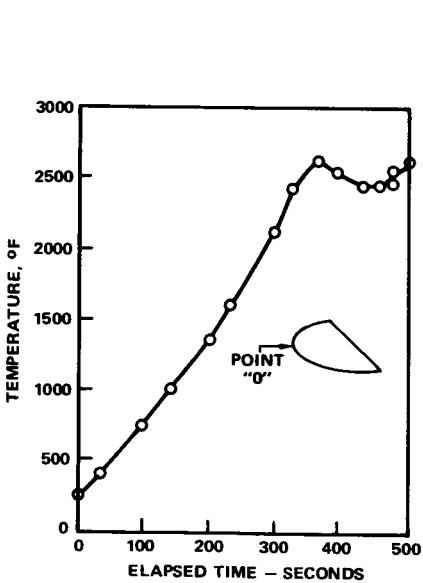


Fig. 17 - Actual Test Temperature at Point "0"

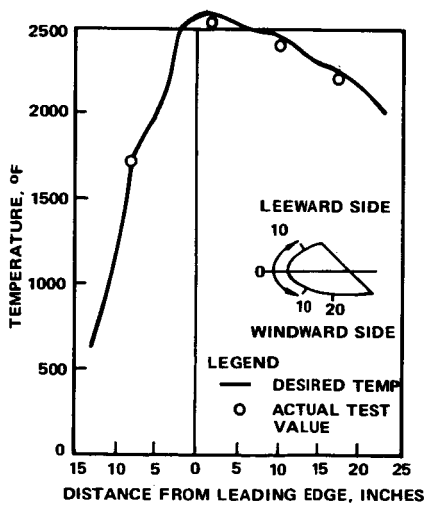


Fig. 18 - Actual Temperature Distribution Around Leading Edge

PRECEDING PAGE BLANK NOT FILMED

Paper No. 37

RESPONSE OF CANDIDATE METALLIC SPACE SHUTTLE MATERIALS
TO SIMULATED REENTRY ENVIRONMENTSI. M. Grinberg, E. S. Bartlett, R. G. Luce, *Battelle-Columbus
Laboratories, Columbus, Ohio*

ABSTRACT

Coated columbium alloys were evaluated in an experimental program to determine their degradation and reuse capability for the thermal protection system of the space shuttle. Intentionally defected specimens were thermally cycled in either an arc-heated wind tunnel or static furnace environment. The relative effect of the environmental exposures on defect growth, mechanical properties, and surface emittance degradation was determined. Techniques used to characterize the arc-heated wind tunnel environment and to determine the thermal response of the specimens during the exposures are described.

INTRODUCTION

During the early stages of the space shuttle program, coated columbium alloys were investigated as to their ability to provide reradiative thermal protection for those portions of the shuttle vehicle which would attain maximum temperatures of approximately 1590 K during reentry. Of concern in this regard was the effect of coating defects on the system's oxidation resistance and mechanical performance, considering the requirement of 100 flight and reentry missions. Also of interest was the possible surface degradation that could occur due to the reuse missions which could require significant refurbishment of the oxidation-protective, high-emittance coating.

A program was undertaken for NASA Marshall Space Flight Center to develop data on the degradation and reuse capability of coated columbium alloy systems for the space shuttle and to establish defect tolerances, failure modes, and methods of assurance of the integrity of these material systems. Both dynamic, hypersonic shear, reduced-air-pressure, and static, reduced-air-pressure furnace environments were used to expose the materials to simulated reentry thermal profiles. This provided for a comparison of the relative degradation of the specimens resulting from the dynamic and static environments. Detailed flaw growth and mechanical property effects studies were conducted, the results of which are summarized herein. Details of hyperthermal arc-heated wind-tunnel experiments are also presented, with

particular attention given to the techniques used to characterize the environment and measure the specimen surface temperature response during the wind-tunnel exposures.

APPARATUS

Arc-Heated Wind Tunnel Facility

The arc-heated wind-tunnel exposures were conducted in the Battelle-Columbus Aerothermal Research Facility. The facility consists of two separate wind-tunnel legs each of which includes a continuous-flow arc heater, a conical convergent-divergent nozzle, a free-jet test cabin, and a conical convergent-divergent diffuser. The arc-heated gas from either leg exhausts into a common heat exchanger and then to the pressure recovery system which consists of a five-stage steam ejector system. Electrical power for both legs is supplied by a 1.5 mw rectifier substation controlled by a saturable reactor. A schematic layout of the facility is shown in Figure 1.

For these exposures, the nontoxic leg was used with the high-enthalpy arc heater. This arc heater is of a modular design with a segmented column, gas stabilization of the arc column, and separate injection of oxygen and nitrogen. The conical nozzle used has a 2.54 cm diameter throat and a 12.7 cm exit diameter. Test-cabin pressure was maintained at a desired level, consistent with the 12.7 cm exit diameter nozzle and the heater stagnation pressure, by varying the amount of secondary air that was bled into the cabin.

Specimens

The test specimens used for the exposures were nominally 7.6 x 1.9 x 0.05 cm in length, width, and thickness, respectively, with additional length provided for two tabs at each end. The tabs were bent at a nominal radius of 0.05 cm. This configuration permitted mounting of the specimens in the model holder by the insertion of pins into supporting blocks through small holes in the end tabs on the specimens. Six specimens were exposed simultaneously by mounting three specimens on each of two silicide-coated molybdenum blocks which were positioned and held in the water-cooled model holder. Figure 2 shows the molybdenum blocks in the model holder. The pins on the leading edge of the front and rear blocks can be seen in Figure 2. The majority of the block material was machined out in order to reduce the heat conduction losses to the supporting water-cooled structure. Fibrous zirconia thermal insulation was placed in the wells to further reduce heat losses from the specimens.

In order to obtain approximately the same heat flux level on the front and rear specimens, the orientation of the front and rear block relative to the model holder surface could be adjusted

during the exposure. In practice, the angle of attack of the rear block and specimens was set slightly higher than the front block to account for the flat plate heat flux decay with distance from the leading edge. Although the surface discontinuity between front and rear specimens gave rise to a shock wave at their intersection, it was found that the conditions for a major portion of the rear specimens were approximately the same as those for the front specimens. The slight difference in the local Mach numbers between the front and rear specimens is unimportant in terms of material performance.

Model Holder

The specimens and blocks were mounted in a water-cooled model holder 1.9 cm thick, through which passages were machined for water cooling. A photograph of the model holder is shown in Figure 2. The major components of the model holder consist of a flat plate with a 0.31 cm nose radius, an instrumentation block for mounting of the spring-loaded thermocouples, and a housing to shield the instrumentation. Overall dimensions of the model holder are 26 cm long (air-flow direction) and 13.9 cm wide. A cutout having nominal dimensions of 15.7 cm long and 5.9 cm wide was provided in the holder for the specimens and block. The cutout was centered with respect to the width of the holder and extended from 8.9 cm (14 nose diameters) to 24.7 cm from the leading edge of the holder. This location relative to the leading edge was selected in order to reduce pressure and heat flux gradients to a minimum consistent with specimen and nozzle size. The angle of attack of the water-cooled holder was set at approximately 18 degrees with respect to the arc-heated air flow direction.

Instrumentation

Thermocouples, infrared pyrometry, infrared photography, and time-lapse panchromatic photography were used to determine the response of the specimens during plasma arc exposures. Accurate determination of the specimen temperatures was necessary for correlation of the mechanical property data with exposure and for comparison of the effects of the dynamic and static environments on oxidation and mechanical property measurements. A spring-loaded, Pt/Pt-10 Rh thermocouple was used to determine the back-face temperature of each coated columbium specimen during exposure. Thermocouples protruding through holes in the bottom of each support block can be seen in Figure 2. Two infrared-radiation (IR) pyrometers were used during the wind-tunnel exposures to measure the surface temperature of the specimens. The pyrometers are manufactured by Ircon, Inc., and operate in the spectral range of 2.0 to 2.6 μm . Infrared photographs were taken during the nominal peak-temperature-exposure portion of the cyclic exposures to determine the temperature gradients over the entire surface area of the specimens. Black-and-white infrared

film was used with an 87 C filter over the camera lens. This combination of film and filter limits the radiation detection to a relatively narrow wavelength interval, 0.85 to 0.90 μm . An electrically driven, remote-controlled, Hasselblad camera (70 mm) and a 35 mm Cannon camera were used to obtain these photographs. Time-lapse photographs of the specimens were taken during the exposures to determine the rate of defect growth. A remote-controlled Hasselblad camera was used for these pictures.

Facility instrumentation was also provided to characterize the arc-heater performance. This included arc-heater stagnation pressure, voltage, current, coolant water-flow rate and temperature rise, and gas mass-flow rate. Also, the specimen surface/environmental conditions were measured using instrumented, water-cooled blocks that fit into the water-cooled model holder. These blocks had provisions for surface pressure taps and water-cooled heat flux calorimeters.

The specimen temperatures and arc-heater operating conditions were recorded on the facility's digital data-acquisition system. Since the exposure times per cycle were on the order of one-half hour, data reduction and permanent recordings were made on-line. A complete set of data was printed on the TTY about every 20 seconds. Also, continuous monitoring of the arc-heater conditions and selective data were provided visually on a CRT display.

EXPERIMENTAL PROCEDURES

Columbium Alloy Materials

Three coated columbium alloys were evaluated in thin-sheet form. Substrates were the commercial columbium alloys Cb752 (Cb-10W-2.5Zr), C129Y (Cb-10W-10Hf-0.01Y), and FS85 (Cb-27Ta-10W-0.8Zr). Both Cb752 and FS85 were coated with 80 μm of the commercial oxidation-protective silicide coating R512E (Si-20Cr-20Fe, slurry-fusion process), and C129Y was coated with 80 μm commercial VH109, also a fused slurry silicide. All specimen surfaces were coated. For the application of coated columbium alloys to space shuttle TPS, knowledge of environmental effects upon structural performance is critical. Furthermore, a low, but significant frequency of occurrence of defects in the protective coatings is expected. The response of properties to oxidation/contamination effects at the sites of coating defects represents the "worst case" analysis for coated columbium alloys. For this reason, most specimens were treated to introduce intentional defects by electrical-discharge machining holes (0.1 and 1 mm in diameter) through the coatings. These penetrated about 20 μm into the columbium alloy substrate to insure total coating penetration.

Evaluation of Defect Growth

The rate of growth of defects provides one measure of degradation of structural properties. Substrate metal that is lost through oxidation can no longer support structural loads. Also, for columbium alloys, diffusion of oxygen into the metal matrix embrittles some of the metal surrounding the defect such that it loses some of its load-bearing capability.

Visible defect growth was measured in several ways. Time-lapse photographs taken during aerothermal exposures provided a direct measure of defect growth for many specimens. Radiographs of exposed specimens were inspected to determine the amount that selective substrate oxidation affected undercutting of the coating. Defect growth rates determined by time-lapse photography and before-and-after measurements were adjusted for undercutting on a pro rata basis. In addition, metallographic sections were prepared through the centers of defect sites. From these, metal surface recession (equivalent to 1/2 the defect growth) and depth of hardening of substrate material surrounding the defect via oxygen influx (an indicator of depth of embrittlement) were measured. Measurements were converted to the appropriate rates by factoring according to total time at the maximum exposure temperature for each intentional coating defect site.

Specimen Thermal Characterization

Spring-loaded, 28-gauge, backface thermocouples were used to obtain a continuous record of temperature for one location per specimen. To avoid reactions of the thermocouple material with the specimen's disilicide coating, a 25 μm -thick, 0.3-cm square, platinum foil was attached to the coated columbium using a thin application of Sauereisen No. 8 Electrotemp refractory cement. This was found experimentally to be reasonably compatible with both R512E and VH109 coatings under nominal thermal conditions. The spring-loaded device forced contact of the thermocouple bead against the platinum foil cemented to the underside of the specimen. Chemical compatibility experiments were conducted to determine possible effects of the cement and foil on the thermocouple output at elevated temperature. No deleterious effects were obtained.

Two infrared pyrometers were used during the arc-heated wind-tunnel exposures. One of the pyrometers (control pyrometer) was fixed and sighted on the middle specimen in the front row, approximately in the center of the specimen, and was used for control of the arc heater during the heatup and cooldown portions of the cycles. The second pyrometer (scanning pyrometer) was used to obtain data on the surface temperature profile of the specimens. This pyrometer was mounted on a remote-controlled traversing mechanism which permitted the pyrometer to scan over the specimens during the exposures. In this manner, it was

possible to obtain one or more complete scans in the side-to-side and flow directions. The voltage output of a positioning potentiometer (which indicated the precise pyrometer scan location) was recorded simultaneously with the pyrometer output voltage. The pyrometer scan speed was adjusted to a maximum compatible with the response characteristics of the pyrometer. The pyrometer temperature-voltage calibration tabulations were experimentally corrected for arc radiation reflected from the specimen surface at operating conditions identical to those used during the specimen exposures. Also, because the pyrometers were mounted on top of the test cabin, it was necessary to correct the signals for radiation attenuation due to the test cabin window. This was accomplished experimentally by measuring the change obtained in pyrometer signal with and without the window as a function of source temperature.

Infrared photography was used to obtain periodic total specimen area records of the surface temperature distribution. Several exposure durations and f-stops were used depending on the specimen surface temperature. The cameras were mounted on top of the test cabin and were sighted on the specimens through the test-cabin window. Calibration of the infrared film was accomplished using a technique similar to that described by Pollack and Hickel.⁽¹⁾ In this calibration, the density of the film is uniquely related to the source or specimen brightness temperature. In essence, the procedure consists of three key elements: (1) a calculated relationship between the surface temperature and the relative radiant energy, which results in a master distribution curve (MTD curve); (2) an experimentally determined relationship between film density and the relative film exposure energy, which results in a film response curve (FR curve); and (3) a calibration point which is a known temperature on the specimen surface that can be associated with a corresponding film density. The first two elements are independently determined and are associated with each other by the temperature-density calibration point. Calibrations were performed for both the 70 mm and 35 mm infrared films. Details of the calibration procedures can be found in References (2) and (3).

A representative black-and-white infrared photograph obtained during the arc-heated wind-tunnel exposures is shown in the bottom photograph of Figure 3. Light regions represent hotter areas, and dark regions are indicative of cooler areas. Contours of the specimen surface temperature were generated using infrared positive transparencies and the temperature-film density calibration. This detailed contour mapping was useful in that specimen temperatures at the various defect sites could be obtained simultaneously with considerable accuracy. Specimen surface temperature contours were also obtained by color-enhancing the black-and-white infrared photograph. A color-enhanced (black-and-white in the publication) picture of the black-and-white infrared photograph in Figure 3 (bottom) is shown as the

top photograph in Figure 3. Each color represents a photographic density interval considered to be a region of constant temperature (in the publication, these colors appear as various shades of gray). The temperature range represented by each of the eight colors in Figure 3 is approximately 20 K. A finer increment in temperature can be achieved by selecting a finer density interval on the Data-Color System. This would result in a greater number of constant density intervals for the density range of the photograph.

During the arc-heated wind-tunnel exposures, apparent emittance variations were noted from cycle to cycle on multicycle runs by comparing the output of the control pyrometer with the temperature obtained from the backface thermocouple as cycling progressed. Apparent emittance changes were also observed by considering the arc heater power level (enthalpy) required to maintain a fixed nominal specimen temperature from cycle to cycle.

Environment Thermal Characterization

The arc-heated air environment was characterized to define free-stream and local surface conditions. Characterizations were obtained for the arc-heater operating conditions used during the exposures of the columbium alloy specimens. A summary of the environment characterization data is given in Tables 1 and 2.

The free-stream Mach number was calculated for the 12.7 cm exit diameter nozzle using a chemically reacting nozzle flow program based on the analytic technique developed by Lordi, et al⁽⁴⁾, for nonequilibrium expansions of reacting gas mixtures. Also, a laminar boundary layer program based on the Cohen and Reshotko⁽⁵⁾ solution with heat transfer and arbitrary pressure gradient was used. The arc-heater reservoir pressure was measured experimentally using a pressure transducer and the gas total enthalpy was determined using the energy balance technique.

Surface shear stresses were calculated using a technique described by Harney and Petrie⁽⁶⁾. In this procedure, the flow-field equations are formulated in a manner that brings out their explicit dependence on gas thermodynamic and transport properties with minimal dependence on Mach number. The skin-friction coefficient is expressed in terms of surface and free-stream flow properties. Numerical values for the free-stream flow properties were obtained from the solution of the nonequilibrium nozzle flow expansion. Surface pressures and heat-transfer rates were measured experimentally using water-cooled copper blocks which fit into the spaces occupied by the specimens and molybdenum blocks that were used during the material exposures. Both front and rear calorimeter blocks had three pressure taps and two heat flux calorimeters to determine the axial pressure and heat-transfer rate distributions. An average pressure representative of the

front and rear water-cooled blocks were within 0.01 kN/m^2 of each other, with variations of less than $\pm 0.37 \text{ kN/m}^2$ on the front and rear blocks.

A summary of the measured heat-transfer rates for the two nominal operating conditions is shown in Table 2 along with heat-transfer rates calculated using two separate correlation techniques. It can be seen that there is good agreement between the measured and calculated heat-transfer rates.

The nominal simulated time-temperature reentry profiling condition used in dynamically cycling the columbium alloy specimens is as follows:

- (1) Heat specimens to 1061 K in approximately 2 minutes
- (2) Hold at 1061 K for 5 minutes
- (3) Heat to 1561 K or 1644 K, depending on nominal temperature level desired, in approximately 2 minutes
- (4) Hold at nominal temperature level 1561 K or 1644 K for 15 minutes
- (5) Cool to approximately 977 K in approximately 6 minutes
- (6) Repeat (1) through (5) for desired number of exposure cycles.

EXPERIMENTAL RESULTS

Temperature Determination

A typical comparison of all three methods used for determining the specimen surface temperatures (thermocouples, infrared pyrometry, and infrared photography) is shown in Figure 4 for a representative exposure. In this figure, the specimen surface temperature is plotted as a function of distance across the specimens. Also shown are the temperatures indicated by two of the spring-loaded thermocouples. It can be seen that there is good agreement among the temperature-measuring techniques with a maximum difference of approximately 22 K occurring between temperatures obtained from the pyrometer and photographic techniques. This maximum difference is representative of those obtained from similar comparisons of other arc-heated wind-tunnel runs.

Specimen Surface Emittance

The general appearance of the coated columbium alloy specimens was different for the static furnace and arc-heated wind-tunnel exposures. Specimens exposed to the furnace environment developed oxides, the colors of which depended primarily on the coating, and to a lesser extent, upon the substrate. For example, specimens coated with VH109 developed a greenish-brown color,

R512E/Cb752 specimens oxidized to an orange-brown color, and R512E/FS85 oxidized to a reddish-brown color. In contrast, these coating/substrate combinations exhibited fine-textured, cream-colored or white oxide coatings when exposed to the arc-heated wind-tunnel environment.

Apparent emittance variations noted from cycle to cycle on the basis of the arc-heater power level required to maintain the nominal specimen temperature are shown in Figure 5 (circular symbols). It can be seen that there is a relatively large decrease in apparent emittance from the first to the third exposure cycle, with relatively little change occurring in subsequent cycles. Also shown in Figure 5 are apparent emittance changes obtained by comparing the output of the control pyrometer with the temperature indicated by the corresponding backface thermocouple (square symbols). Although this correlation does not yield as rapid an apparent decrease in emittance within the first three cycles, the trend of the data is quite similar and toward decreasing emittance with increasing number of exposures cycles. Both correlation techniques indicate similar emittance values after 8 to 10 exposure cycles.

Apparent changes in specimen emittance can also be illustrated by considering the pyrometer output signal and the indicated thermocouple temperature during the cooldown portion of the cycle. The changes in emittance for the 10-cycle run are shown in Figure 6. The symbols represent the pyrometer output signal and thermocouple temperature at corresponding times. Lines of constant emittance are also shown. It can be seen that there is an apparent decrease in specimen emissivity during the multicycle exposures. The decrease is roughly the same as is obtained by considering the nominal maximum-temperature portion of the cycles as was illustrated in Figure 5. Pyrometer output-temperature data are not shown for the fourth cycle since this cycle was terminated early during the cooldown (specimen temperature of approximately 1476 K).

In contrast with these apparent emittance changes resulting from the arc-heated wind-tunnel exposures, there was little, if any, change in specimen surface emittance noted for those specimens exposed in the furnace environments.

Defect Growth

The maximum intended temperature for the initial exposure series of arc-heated wind-tunnel exposures was 1644 K. Under these high-mass-flow conditions, unexpectedly rapid growth of several intentional coating defects was observed in only one simulated reentry cycle. Figure 7 shows the appearance of a group of six specimens following a 15-minute exposure at 1644 K, nominal. The unlettered specimen is included to illustrate specimen appearance before exposure for comparison. Each

specimen contained one 0.1-mm defect (barely visible in its orientation at the left of the "before" specimen) located forward relative to the flow, and two 1-mm defects, located "center" and "aft". Several of the individual defects in the figure show obvious growth. Also apparent is "wash" from oxidation product effluent swept from the defects by the hypersonic flow. Analysis of temperatures at individual defect sites for several such exposure runs allowed correlations between local exposure temperature and defect growth rates as shown in Figure 8. Neither defect type, location, nor coating type influenced the onset of rapid growth independently from temperature. Substrate composition, however, did have some influence. At exposure temperatures less than about 1620 K, defect growth resulting from the oxidation of any of the columbium alloy substrates was well controlled, and occurred at a rate on the order of $1 \mu\text{m}/\text{min}$. As the exposure temperature at defect sites exceeded about 1625 K, defect growth rates increased precipitously for the C129Y and Cb752 alloy substrates, and rates as great as $0.5 \text{ mm}/\text{min}$ of exposure were observed. The FS85 alloy substrate was not nearly so sensitive to aerothermal degradation, as rapid defect growth was not observed even at temperatures as great as 1690 K.

Ambient-pressure furnace oxidation tests of coated-plus-defected Cb752 and C129Y showed that a temperature of at least 1705 K was needed to initiate similar rapid-defect-growth under static conditions. This is about 80 K greater than the threshold temperature under hypersonic shear conditions.

Rapid defect growth under either static or dynamic conditions is associated with melting of columbium oxide. The resulting catastrophic oxidation occurs so rapidly that embrittlement of the remaining metal by solid-state oxygen diffusion is not of much consequence. Figure 9 shows a defect which had grown from an initial size of 0.01 cm to about 0.33 cm in one wind-tunnel exposure cycle. By comparison, the visible contamination front has advanced to a depth of only about 0.01 cm from the oxide-metal interface.

During arc-heated, wind-tunnel exposures at a nominal peak temperature of 1560 K, no growth of small defects was observed in up to 10 simulated reentry cycles. After the first two or three cycles, a buff-colored oxide resulting from oxidation of the coating covered the specimens so that small defects were no longer visible. Figure 10 shows a group of six specimens of coated FS85 after five wind-tunnel exposure cycles. Each contains a small, 0.1-mm coating defect in the center, but these are not visible because of coating oxide overgrowth. The larger, 0.1-cm defects (in other specimens) were readily visible, but grew slowly, so that after ten wind-tunnel-simulated reentry cycles, they had grown to only about 0.13 cm in diameter. Under these lower temperature conditions, actual loss of metal to oxidation is minor in relation to property degradation resulting from oxygen

contamination. Figure 11 shows, in metallographic cross-section, the negligible growth of a small defect after 100 furnace exposure cycles, and also the substantial spread of contamination in the columbium alloy substrate. (The coating spalling and cracking occurred when the specimen was manhandled after exposure.)

Mechanical Property Effects

Numerous tensile, creep, fatigue, and bend tests were conducted on the coated-plus-defected columbium alloy specimens before and after both arc-heated wind-tunnel and static (furnace) exposures at temperatures of not greater than 1590 K. The intent was to establish differences in property degradation attributable to exposure mode. Although all materials experienced some degradation due to the "worst-case" exposures, there was no difference in the amount of degradation experienced under dynamic versus static exposure conditions.

In brief summary, contamination associated with the small, nongrowing defects had only relatively minor effects on mechanical properties. No gross degradation in useful structural properties was observed.

At large defect sites, degradation assumed more macroscopic proportions. It was found that the Cb752 and C129Y substrates were much more severely degraded than was the FS85 substrate. For example, the fracture strength of contaminated material surrounding large defects was noticeably decreased following as few as 3 or 4 exposure cycles for Cb752 and especially C129Y, but the associated strength in FS85 remained stable throughout at least 10 exposure cycles as shown in Figure 12. Some specimens of C129Y and Cb752 failed by catastrophic and total brittle fracture in tensile tests. Specimens of FS85 always failed "safely" by ductile shear. In high-cycle fatigue tests, the life of coated Cb752 at a stress level of about 275 MN/m^2 was reduced from about one million cycles to essentially zero cycles by the presence of contamination surrounding large defects following five exposure cycles. In contrast, no degradation was observed in comparison tests of coated, defected, and exposed FS85.

CONCLUSIONS

The following conclusions are valid in the context of the considered use of coated columbium alloys for which this evaluation was designed, namely, space shuttle orbiter thermal protection system hardware:

- Under conditions of hypersonic flow, rapid growth of defects in some coated columbium alloys occurs at temperatures above 1620 K. This is lower by about 80 K than the temperature required for similar growth rates under static oxidation conditions. In general, columbium

alloys should not be used in hypersonic, oxidizing environments at temperatures greater than 1620 K.

- At temperatures less than 1620 K, mechanical property stability of coated columbium alloys is not influenced by environmental flow dynamics at reasonably high levels of oxidation potential.
- For potential service at 1620 K, small coating defects are well tolerated by columbium alloys. Large coating defects can result in serious degradation in mechanical properties. Of the alloys studied, Cb752 and C129Y were seriously degraded; FS85 was not.
- Apparent degradation in coating/substrate emittance of coated columbium alloys occurs under multicycle hypersonic shear exposure conditions. Similar changes in surface emittance are not observed in furnace exposure conditions.

REFERENCES

- (1) Pollack, F. G. and Hickel, R. O., "Surface Temperature Mapping with Infrared Photographic Pyrometry for Turbine Cooling Investigations", NASA TND-5179, January, 1969.
- (2) Bartlett, E. S., et al, "Degradation and Reuse of Radiative-Thermal-Protection-System Materials for the Space Shuttle", Final Report to NASA-Marshall Space Flight Center, Contract No. NAS 8-26205, August 26, 1972.
- (3) Kistler, C. W., et al, "Evaluation of Nonmetallic Thermal Protection Materials for the Manned Space Shuttle", Volume V, Final Report to NASA-Manned Spacecraft Center, Contract NAS 9-10853, June 1, 1972.
- (4) Lordi, J. A., et al, "Computer Program for the Numerical Solution of Nonequilibrium Expansions of Reacting Gas Mixtures", NASA CR-472 (1965), 120 pp.
- (5) Cohen, C. B. and Reshotko, E., "The Compressible Laminar Boundary Layer with Heat Transfer and Arbitrary Pressure Gradient", NACA Report 1294 (1956), 16 pp.
- (6) Harney, D. J. and Petrie, S. L., "Hypersonic Surface Pressure and Heat Transfer on Slender Bodies in Variable Composition and Nonequilibrium Atmospheres", AFFDL-TR-70-31 (April, 1970), 42 pp.

TABLE 1. ENVIRONMENTAL CONDITIONS FOR COLOMBIUM ALLOY EXPOSURES

Specimen Type	Surface Temperature, K	Free Stream Mach Number	Heater Reservoir Pressure, kJ/m^2	Gas Total Enthalpy, kJ/kg	Average Surface Pressure, kJ/m^2	Average Surface Shear Stress, N/m^2	
						Front Specimens	Rear Specimens
Coated columbium alloy	1561	4.5	102-132	10.9-13.4	1.7	82	106
Coated columbium alloy	1644	4.3	112-132	13.4-16.0	2.1	87	116

TABLE 2. COMPARISON OF MEASURED AND CALCULATED HEAT TRANSFER RATES FOR COATED COLOMBIUM ALLOY WIND TUNNEL EXPOSURES

Nominal Specimen Surface Temperature K	Calorimeter Location Distance from Specimen Leading Edge, cm	Measured Cold Wall Heat Flux W/m^2	Calculated Cold Wall Heat Flux, W/m^2		Measured Cold Wall Heat Flux Corrected to Nominal Specimen Temperature W/m^2	
			(a)	(b)		
1644	2.29	60.4×10^4 51.3×10^4	Front Specimen		43.0×10^4 37.4×10^4	
			61.7×10^4	51.0×10^4		
	5.33	51.2×10^4 44.5×10^4	Rear Specimen		37.4×10^4 31.7×10^4	
			52.9×10^4	42.6×10^4		
	1561	2.29	38.2×10^4 33.5×10^4	Front Specimen		27.5×10^4 24.0×10^4
				37.4×10^4	33.2×10^4	
5.33		38.0×10^4 34.6×10^4	Rear Specimen		27.3×10^4 25.0×10^4	
			31.5×10^4	28.0×10^4		

(a) Method from Harney, D. J. and Petrie, S. L., "Hypersonic Surface Pressure and Heat Transfer on Slender Bodies in Variable Composition and Nonequilibrium Atmospheres", AFFDL-TR-31 (April, 1970), 42 pp.

(b) Method from Hankey, W. L., Jr., et al., "Design Procedures for Computing Aerodynamic Heating at Hypersonic Speeds", WADC-TR-59-610 (June, 1960), 157 pp.

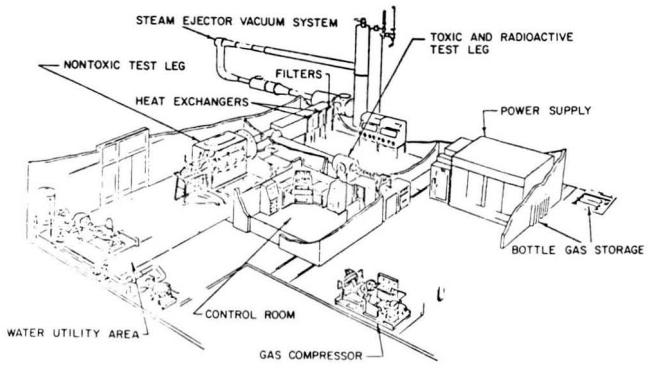


FIGURE 1. SCHEMATIC OF AEROTHERMAL RESEARCH FACILITY

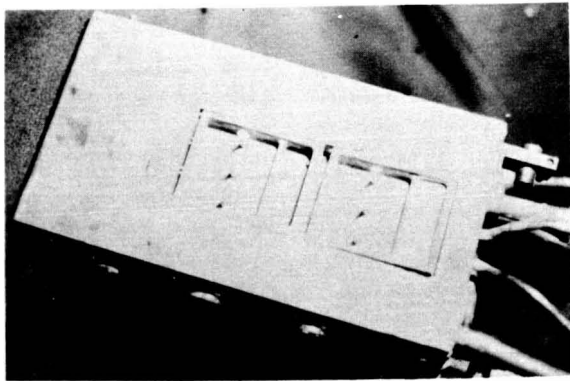


FIGURE 2. PHOTOGRAPH OF SPECIMEN MODEL HOLDER



FIGURE 3. BLACK AND WHITE (BOTTOM) AND COLOR ENHANCED (TOP) INFRARED PHOTOGRAPH (AIR FLOW FROM LEFT TO RIGHT)

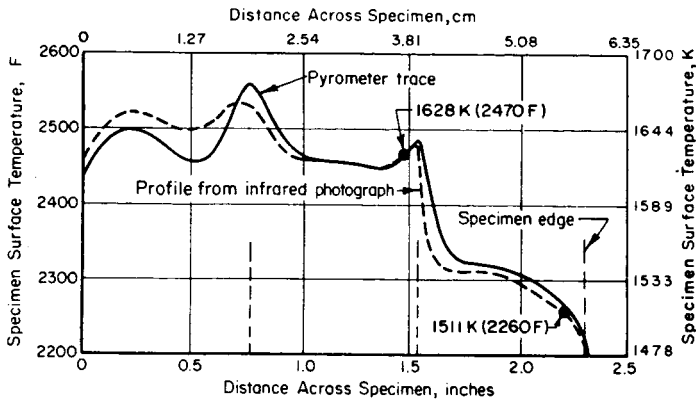


FIGURE 4. COMPARISON OF PYROMETER TEMPERATURE AND INFRARED PHOTOGRAPHIC TEMPERATURE DISTRIBUTION DATA

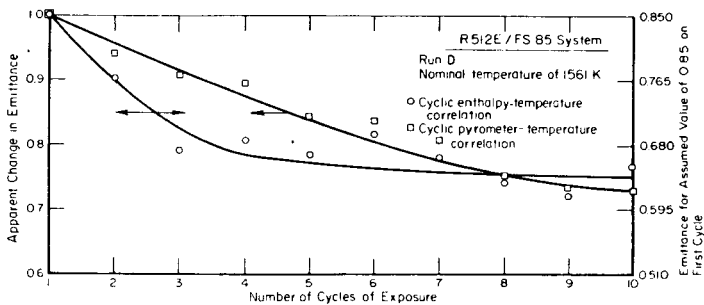


FIGURE 5. VARIATION IN EMITTANCE OF COATED COLUMBIUM ALLOY DURING MULTICYCLE WIND TUNNEL EXPOSURE.

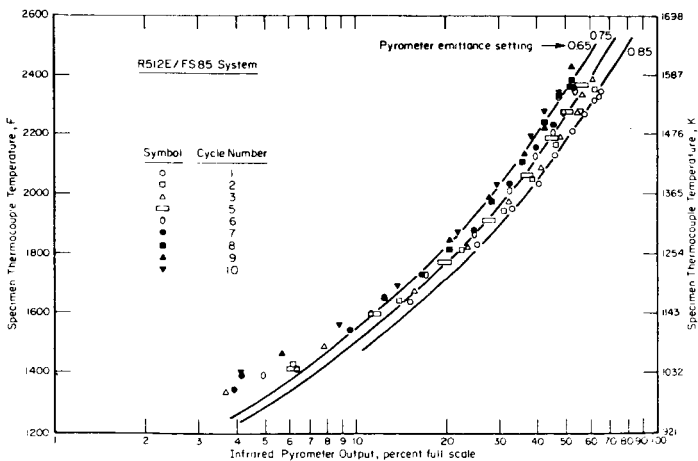


FIGURE 6. CHANGE IN EMITTANCE OF COATED COLUMBIUM DURING COOL-DOWN PORTION OF MULTICYCLE WIND TUNNEL EXPOSURE

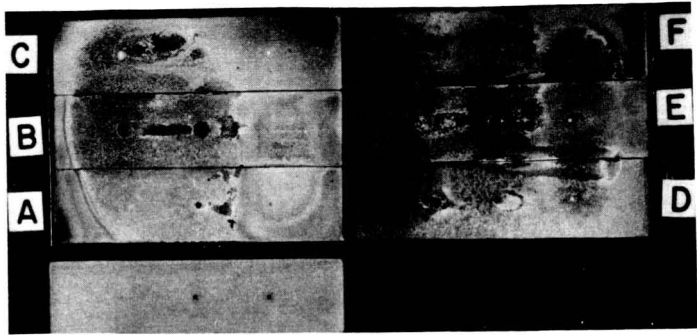


FIGURE 7. SPECIMENS FOLLOWING ONE REENTRY CYCLE AT 1644 K.

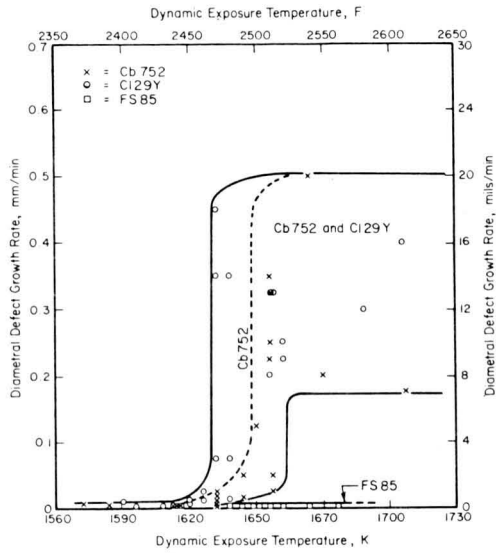


FIGURE 8. DEPENDENCE OF DEFECT GROWTH RATES ON TEMPERATURE.

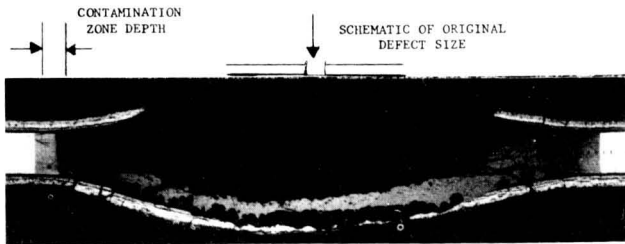


FIGURE 9. DEFECT GROWTH; ONE WIND TUNNEL EXPOSURE CYCLE AT 1644 K. (25X)

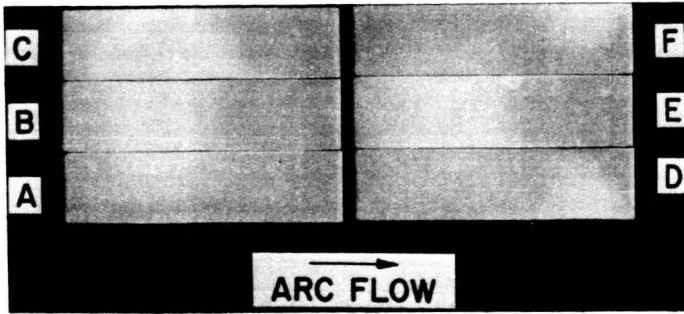


FIGURE 10. SPECIMENS FOLLOWING FIVE WIND TUNNEL CYCLES AT 1560 K.

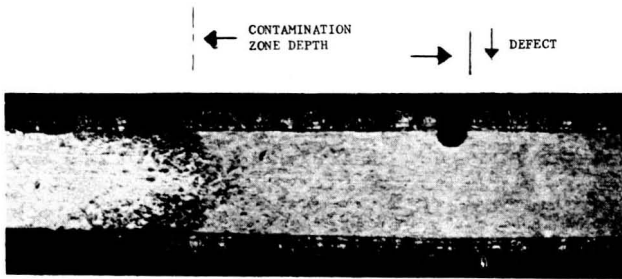


FIGURE 11. SMALL STABLE DEFECT FOLLOWING 100 FURNACE EXPOSURE CYCLES. (42X)

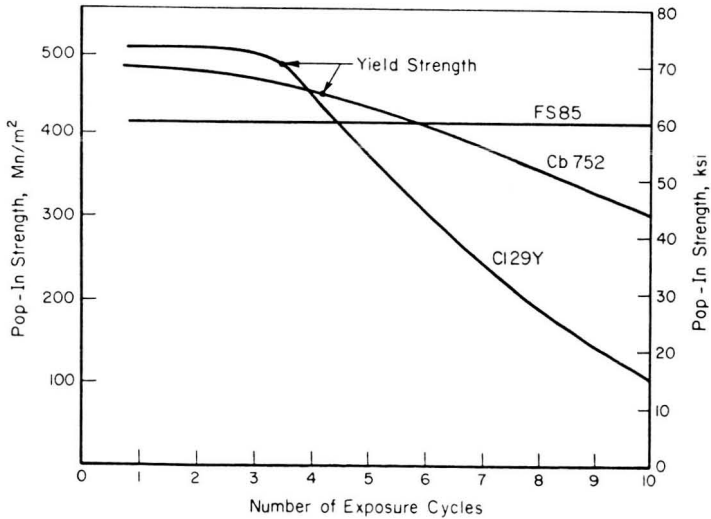


FIGURE 12. DEGRADATION IN FRACTURE STRENGTH OF CONTAMINATED COLUMBIUM ALLOYS ASSOCIATED WITH LARGE COATING DEFECTS.

NTM-10769

PRECEDING PAGE BLANK NOT FILMED

Paper No. 38

TESTING OF SPACE SHUTTLE THERMAL PROTECTION SYSTEM PANELS UNDER SIMULATED REENTRY THERMOACOUSTIC CONDITIONS

Carl E. Rucker and Robert E. Grandle, *NASA Langley Research Center, Hampton, Virginia*

ABSTRACT

The advantages of maintaining a real-time computerized thermoacoustic testing system are demonstrated by results from space shuttle thermal protection system tests of Rene 41 and composite material panels.

INTRODUCTION

The mission profile and reuse of the space shuttle vehicle impose a severe acoustic fatigue problem for the design of the Thermal Protection System (TPS) for the orbiter. The orbiter TPS panel systems must withstand 100 flights and launch acoustics above 159 dB. Testing with high temperature and acoustic loading is required to qualify new materials and design configurations for the extreme environments which include orbiter reentry temperatures from 480° C to 1350° C. This testing must include detailed measurements of TPS panel behavior so that design changes required by development test or flight experience can be carried out systematically while maintaining minimum weight.

The Langley Research Center approach to the thermoacoustic fatigue problem is to test large "complete" structures and to simulate the environments (thermal and acoustic) as nearly as possible. Under this approach the theories or computations required to extrapolate from test conditions to service conditions are minimized as compared to approaches using more simplified environments such as equivalent-block loadings. The details of test control and data measurements are both highly controlled and extensively supervised under real-time executive computer control allowing maximum man/machine interaction.

The capabilities of Langley Research Center's new thermoacoustic fatigue apparatus for space shuttle thermal protection system (TPS) panel testing were presented in Reference 1. The purpose of establishing the thermoacoustic test capability was to develop and demonstrate workable test techniques which could be

used in order to proof test TPS panels and provide diagnostic tools for the designer to "troubleshoot" his design in a complete, timely manner and to graphically illustrate to him during the test how his panel is performing.

Tests have been done in the LRC facility on two basic TPS panel system concepts, referred to as metallic and RSI (reusable surface insulation) panels. Both the metallic and RSI panels share the common characteristic of being composed of materials on which there is relatively little materials data and use experience. The designs are complex consisting of corrugated plates with elaborate standoffs and closure fairings to allow thermal expansion or a substructure to which is affixed a ceramic tile material by a heat-sensitive adhesive. The early LRC designed Rene 41 metallic TPS panel was used for two purposes: (1) to provide data on the behavior of a candidate metallic panel and (2) for developing the software, troubleshooting the hardware, and establishing the test methods which are described in this paper.

Data from actual tests of the metallic and RSI TPS panel are presented in this paper to demonstrate the effectiveness of the data systems employed and to illustrate how these methods may be used as diagnostic tools. Strain-gage response data and thermocouple data are included to illustrate damping effects of panel insulation, thermal profiles, and the effects of excitation level on panel response.

THERMOACOUSTIC FATIGUE TEST SPECIMENS

The TPS not only carries loads generated by the environment such as gravity loads, wind loads, engine noise and thermal and vibration inputs caused by passage through the atmosphere but also must withstand normal maintenance abuse. Since the TPS protects the entire vehicle from heat loads, it is a big factor in the vehicle weight and thus its weight must be minimized. Requirements for lightweight structures rule out drastic over-design to meet acoustic requirements. Thermal loads in the range of 480° C to 1350° C during reentry dictate the use of exotic materials and complicated designs for the TPS. Descriptions of the expected TPS vibration and acoustic environments are included in papers by Schock (2) and Jones (3). Selection of the final vehicle configuration has fixed the expected maximum noise level in the range 159 to 168 dB rms overall. Several test TPS panels were selected by LRC as a part of the research program in support of the space shuttle development. The test panels were fabricated from a variety of exotic materials and

represented a range of designs. Two of these designs are described here and test results for these TPS panels are presented in this paper.

Metallic TPS

The installation of the Rene 41 TPS panel in the LRC thermoacoustic fatigue facility is shown in Figure 1. The panel is supported by longitudinal steel facility mounting beams which are attached to the six vertical stainless-steel hat section stringers shown in Figure 1. The insulation package which covers the rear of the panel is attached to a wire mesh screen and is held in place by the standoff/hat section interface which is a bolted joint. The panel was fabricated from 0.04 cm thickness Rene 41, 1.486 m long by 1.072 m wide plate and was supported by four transverse standoff systems and 14 individual standoffs across the center of the plate as shown in Figure 2. The standoffs were of sufficient height to allow installation of a 7.6-cm-thickness fiber-type insulation package. This panel was a very

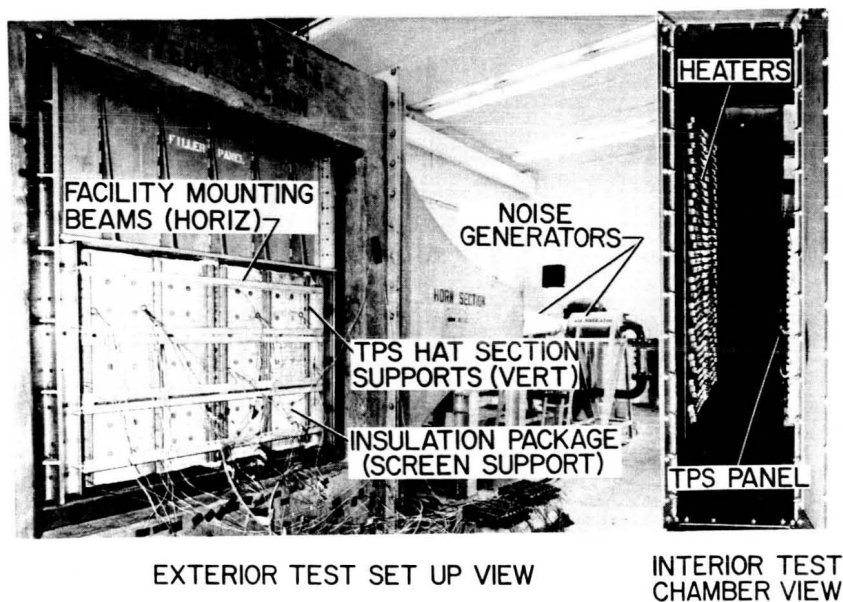


Fig. 1—(left) Test setup for a Rene 41 TPS panel showing facility and TPS support members and rear view of insulation package. (right) Interior test chamber view showing heaters and TPS panel.

early LRC design described in papers by Dixon and Shore (4), and Dowell (5) and Stein, et al. (6).

RSI TPS

The RSI concept tested consists of graphite-epoxy laminate installed on a glass-phenolic honeycomb core panel and supported on aluminum extrusions along its sides. The 1.9-cm-thickness subpanel was protected with a 1.52-cm-thickness RSI composed of mullite ($3\text{Al}_2 \cdot 2\text{SiO}_2$) fibers with ceramic fillers and binders and was glazed with an external vitreous coating. The RSI tiles are bonded to the subpanel with an elastomeric adhesive. The elastic modulus of the vitreous coating was 0.37 times that for aluminum and the RSI has a modulus only 0.0018 that of aluminum. The test article consists of one 66-cm-wide by 76-cm-long TPS panel and partial panels at each end to bring the total length to 1.07 m.

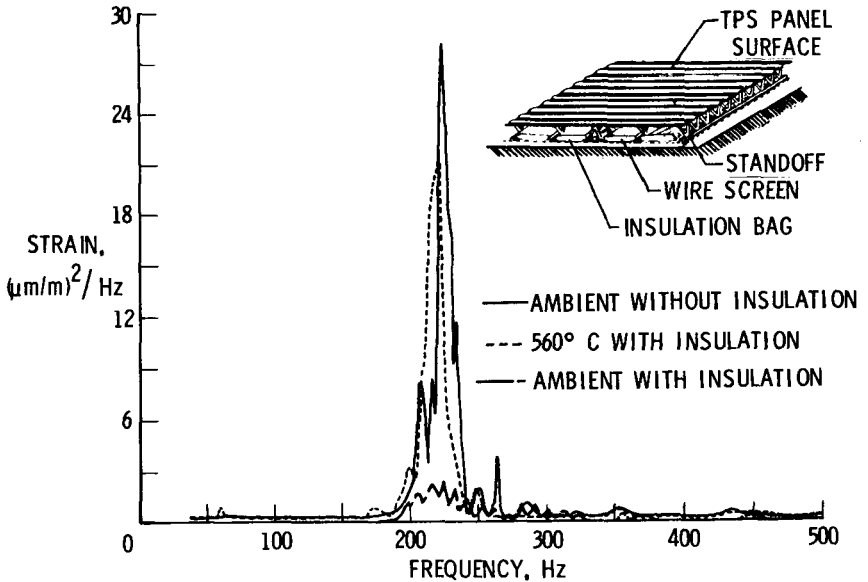


Fig. 2—Linear mean square spectral analysis using strain response data from 560° C and ambient temperature tests of a Rene 41 TPS panel shown in inset, which demonstrate the damping effects of insulation and further effects of thermoacoustic excitation at 145 dB.

TEST PROCEDURE

The basic test conditions for these tests are described in Reference 1. The major elements of the test program which demand emphasis for the purpose of this paper are the following:

1. Extensive data must be taken rapidly to determine modal response and correlation with theory or previous work and yet avoid damage to the panel and instrumentation.
2. Extensive thermal data must be gathered quickly in order to evaluate heating distributions so they can be altered during the test if necessary and over heating may be avoided.
3. Mission cycles during failure testing must be simulated in order to best represent service conditions and prevent both over and under testing due to test technique.

Metallic TPS

This panel was tested at ambient and 560° C for both response and mission simulation conditions. The panel was rated for 816° C and was used in the development of the computer software controlling the mission cycling since there was no danger of over heating the panel. Response tests were of very short duration at 145 dB rms overall continuing for approximately 5 minutes to allow analog tape recording to data. Digital data acquisition required less than 1 minute of testing time. Mission cycles were defined as 30 minutes at continuous acoustic loading and at the beginning of the cycle the panel was heated for approximately 18 minutes. The panel was held at its maximum temperature for about 9 minutes and was heated and cooled at a controlled rate as shown in Figure 3 (curve A). During 86 cycles at 150 dB overall rms and nine cycles at 158 dB overall rms, the panel was inspected visually at least once each five cycles in order to detect failure. During the nine cycles at 158 dB the temperature dropped to 510° C due to increased airflow at the higher noise levels.

RSI TPS

The test sequence for this panel was similar for testing of the open section corrugation TPS, but greater care was required in heating the panel. The adhesive which bonds the RSI to the subpanel is rated for only 177° C and therefore when temperatures in excess of 177° C are applied they must be time limited. The time lag through the insulation must be evaluated in order to peak the temperatures at the bond line appropriately

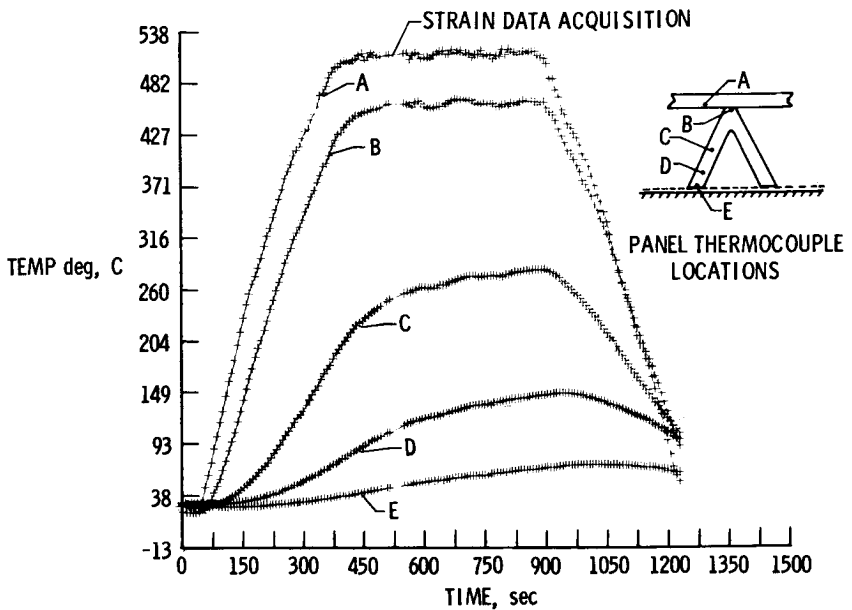


Fig. 3—Demonstration of thermal time history and strain acquisition capabilities by presentation of five of 32 sequentially logged thermocouples and indication of time during which 15,000 points for each of 18 strain gages were digitized for a Rene 41 TPS panel. Thermocouple locations on standoff are shown in inset.

and avoid over or under testing of the panel. Since the insulation on this panel was not removable, subpanel response was not evaluated separately. Tests reported herein included only ambient temperature response tests.

TEST INSTRUMENTATION

Each of these TPS panels was extensively instrumented with strain gages and in addition the RSI panel was instrumented with nine accelerometers. One of the reasons for the metallic panel test was to evaluate strain gages and establish effective instrumentation systems. Chromel alumel thermocouples were used extensively in order to monitor the temperature and a selected thermocouple channel was used as a feedback element during mission cycle to establish test control through the digital computer.

Metallic TPS

This panel was instrumented with 18 strain gages and 32 thermocouples. Seven strain gages were located on the longitudinal center line of the panel. Adjacent to the transverse panel center line in the upstream bay, six gages were located on the bay center line and five gages were located on the center line of the corresponding downstream bay (upstream is used to indicate the position nearest the noise source) including one each on the panel longitudinal center line. The strain gages were distributed in representative locations to allow interpretation of mode shape through cross spectral density analysis where signal quality is good and panel response is regular (i.e., where symmetry of response is maintained and corresponding panel segments respond similarly). Eight thermocouples were installed on the longitudinal panel center line, 11 thermocouples were an integral part of free filament strain gages, nine thermocouples were located on two standoffs (arrangement is shown in Fig. 3 for one standoff) and four thermocouples were embedded in the insulation package. The 0.95-cm-length welded strain-gage response is analyzed to provide the data in Figure 2 and was located on the panel longitudinal center line, 9 cm from the upstream rivet line of second bay downstream (54.5 cm from the upstream edge).

RSI TPS

Thirty-eight strain gages and 27 thermocouples were installed by the manufacturer of this TPS. Eleven thermocouples are constructed as an integral part of the high temperature free filament strain gages. Twenty-seven of the gages used on this panel are conventional foil gages as the adhesive's limitations required the remaining structure to be below 177° C. Instrumentation is installed at four depths in the panel: (1) the RSI surface, (2) the bond line, (3) the honeycomb panel backface, and (4) the face of the aluminum extrusion to which the panel is attached. Most of the instruments on the RSI surface (strain and temperature) failed during the first test sequence due to poor adhesion of the gage to the RSI's vitreous coating. Nine accelerometers are also bonded to the back face of this panel and are located at the intersection of lines which divide the basic TPS panel into nine equal 19-cm squares. The accelerometers are low mass piezoelectric devices. Data from these devices were used in conjunction with microphone measurements at the corresponding spatial locations to determine the transfer functions of

the panel (i.e., the input/output relationship of the acoustic field and the panel vibration response).

DATA ACQUISITION

Basic data acquisition capabilities are described in Reference 1; however, changes made after July 1972 have added considerably to the speed and flexibility of the system. Spectrum analysis and plotting as shown in the figures can be accomplished in less than 3 minutes. The number of possible input/output interfaces was increased from 32 to 45. Increased capability was achieved by adding a 32K word memory computer to the system.

Figure 3 illustrates data obtained during computer control of the experiment and data acquisition. Figure 3 shows five of 32 thermocouple measurements that were taken each 7 seconds by the computer system and stored for later plotting as shown. There are a number of switch options including tabulation of the temperature data on a teletype during the test. One thermocouple is designated as control and in this test an exterior thermocouple such as "A" in Figure 3 is used to increase and decrease the temperature 2.2°C per second in order to simulate reentry. Acquisition of strain-gage data took place during the gap in temperature measurements which can be seen in each of the profiles in Figure 3 (+ symbols on plot indicate temperature measurement). During the gap shown in Figure 3, dynamic strain-gage data were digitized for a total of 15,000 measurements for each of 18 strain gages (30 transducers including microphones and accelerometers were digitized in earlier runs). Digitization of the 270,000 points required only 6 seconds with other elements of the program accounting for the additional time. Analysis of the strain-gage data was accomplished by a second program used after testing of the panel was complete. The new computer improved the speed of the analysis program by a factor of 4 or greater making it feasible to do on-line corrections using the analysis as a feedback element.

TEST RESULTS

The tests discussed in this paper marked the first time thermoacoustic tests had been run on structures of this size and complexity with both thermal and force inputs, the test adjustment taking place under real-time computer control. Results to date demonstrate that automated control of thermoacoustic tests are both practical and efficient. A lack of analytical results for

the complex structures presented here prevented maximum use of these real-time test results which can be powerful design tools where the designer can interact directly to make immediate interpretations of the test results to optimize testing.

Metallic TPS

The results of a welded gage response along the panel longitudinal center line is expressed as strain in dimensionless amplitude squared per unit bandwidth versus frequency in Hz in Figure 2. Three panel conditions are compared in Figure 2. It can be seen from Figure 2 that addition of the insulation reduces the acoustic response of the panel considerably. During later thermoacoustic excitation, however, Figure 2 shows the effects of previous insulation damping almost entirely eliminated. All three curves are for the same nominal 145-dB rms overall random noise whose spectrum is similar to that presented in Reference 1.

The panel in Figure 4 is labeled to show the temperature distribution across the plate. The upstream and lower edges of the panel are slightly cooler due to adjacent steel members used as facility supports which act as heat sinks. The aluminum filler panel on the upper edge (see Fig. 1) stabilizes in temperature more rapidly while the downstream edge benefits from air heated across the panel and a narrow aluminum filler/support member. The panel which is about 60 cm from the heaters is heated to temperatures about 80° C higher when no air is flowing.

When response testing was concluded this TPS was subjected to a simulated mission where a 150-dB random noise excitation was maintained for 30 minutes, and during that time the thermal profile illustrated in Figure 3, curve A, was applied. Figure 3 shows the temperatures measured on the panel and a standoff in the center of the panel. It can be seen that the time from the beginning of heating until the termination of heating was about 1200 seconds. The upper surface of the insulation blanket was approximately at the elevation of point C on Figure 3 and the maximum temperature of this side of the insulation was 253° C. The back-side temperature of the insulation package was 28° C at peak heating. The thermal data were used to control the thermal loading and to evaluate the performance of the insulation package.

The change of the TPS response as a function of time during mission cycling is illustrated in Figure 5. Figure 5 is a spectrum level plot of strain in dB versus frequency in Hertz for cycles number 2 and 86. The sound level was raised to 158 dB

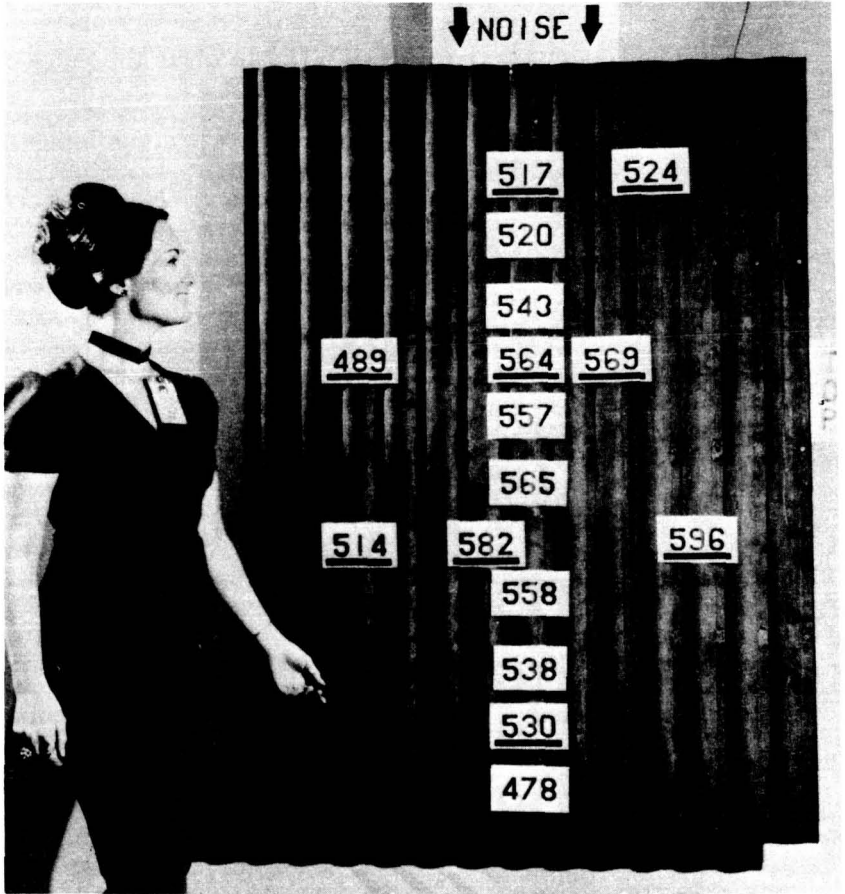


Fig. 4—Heat distribution on a Rene 41 TPS panel as recorded during test and printed on teleprinter. Temperatures in $^{\circ}\text{C}$ are centered on thermocouple locations. Numerals underlined indicate thermocouples which were on the lower surface of the panel as shown.

and heating correspondingly reduced to 510°C on the 87th cycle and panel failure as pictured on Figure 6 was detected after the 95th cycle. Figure 5 shows that the overall strain response has increased in the region from 50 to 150 Hz and also from 300 to 500 Hz and also shows a downward shift in the resonant frequencies.

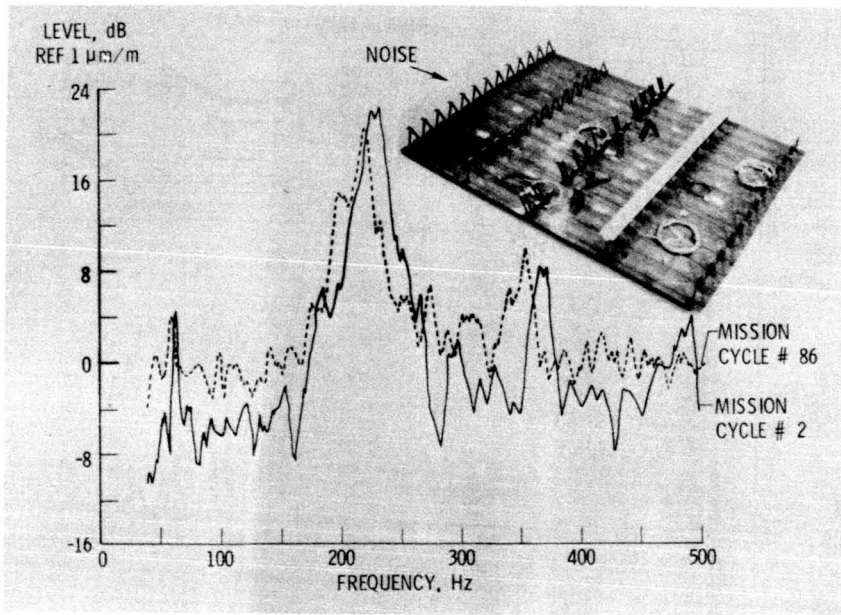


Fig. 5—Illustration of the change in strain response of the Rene 41 TPS panel between the second mission cycle and the 86th mission cycle during combined 150 dB random noise and 560° C heating. After nine additional cycles at 158 dB random noise and 510° C heating, the panel failed as shown in inset.

The inspection of this panel for failure was difficult and only visual inspection was used. Most failures (except for the popped rivet which was recognized) could not have been detected without disturbing the insulation or disassembly of components.

It is probable that failure occurred by the 86th cycle. If a standoff had broken off and "rattled around" it could be expected to build up the high-frequency content of the response much as is shown by the buildup of energy in the 300- to 500-Hz range in Figure 5. When as many standoffs had broken as were finally detected there should also be a buildup in the low-frequency end due to the plate randomly "floating around" much as we see in the 50- to 150-Hz range in Figure 5. These effects, of course, cannot be verified for this test but one can readily see from this illustration how knowledge of these differences during a test might benefit the test conductor.

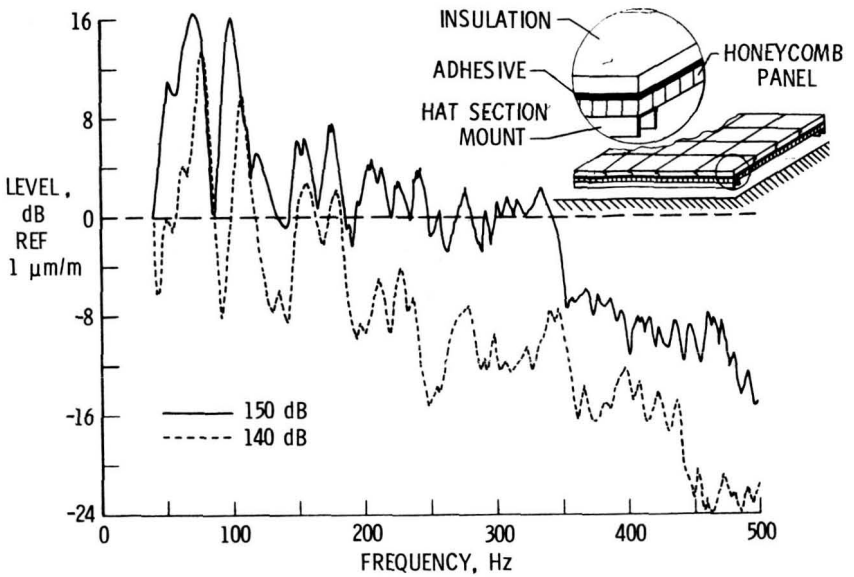


Fig. 6—Demonstration of log amplitude plot of strain spectrum level with linear frequency scale using strain response data from a reusable surface insulated graphite/epoxy honeycomb panel shown in inset.

RSI TPS

Results of ambient temperature tests of the RSI panel at acoustic excitation levels of 140 dB rms overall and 150 dB rms overall are shown in Figure 6. Figure 6 data are spectrum level plots of strain in dB versus frequency in Hz for a centrally located strain gage located between the RSI bond line and attached to the subpanel surface. A sketch of the RSI panel is shown in the insert of Figure 6.

The two peaks in Figure 6 near 100 Hz shift down in frequency slightly and become wider when the acoustic load is increased from 140 dB to 150 dB. The broadening peaks indicate an increase in damping. The acoustic loading has increased by a factor of 3.16 and the overall rms strain increased from 10.84 to 23.32 $\mu\text{m}/\text{m}$. It is perhaps important to note that a pseudo-random noise generator is used as the signal generator and that the details of the spectrum do not change significantly in the range of 40 to 500 Hz. When the level is increased from 140 dB

to 150 dB these results indicate nonlinear behavior of the RSI panel. Thermal profiles similar to those in Figure 3 were recorded for this panel but are not shown. Thermal loading was minimized to prevent bond-line damage and as an illustration of control problems, a 120-second duration heat pulse peaked at the bond line about 120 seconds after heating of the panel surface was terminated.

Instrumentation Performance

Welded strain gages were found to be particularly good from the standpoint of signal quality and endurance. The primary disadvantages of welded gages were their cost and stiffening effects of their stainless-steel cabling where this is a problem. Free filament gages installed with aluminum oxide were also used with good experience and there were few failures of the gages themselves but wiring endurance was poor.

During tests of the metallic TPS system the welded strain gages endured the environments of high temperature and acoustics extremely well. Only two welded gages have been failed during testing and these failed during the 87th cycle of the single corrugation TPS. The difficulty with the free filament gages is not so much the gages themselves as the wiring of these gages. More than half of the free filament gages were failed after 30 minutes of combined environments and 90 percent of the gages were failed by the 86th cycle of the single corrugation TPS. Thermocouple life was only slightly better than that for strain gages but a variety of types were not evaluated.

Materials Performance

The Rene 41 material was not heated to its design temperature of 816° C short-term use but combined environments were adequate for failure. The Rene 41 standoff system failed extensively as shown in Figure 5. The upstream row of standoffs failed prior to failure of the individual standoffs in the center. A "popped" rivet head at the center line was the first observed failure but abrasion of the upstream standoff caused by rubbing against the insulation support screen indicated failure began in the upstream standoff. Under the testing ground rules established for the single corrugation panel inspection at the mount/standoff interface was not possible due to the presence of the insulation. Early detection would not have been likely without frequent disassembly of the panel.

The RSI tests have not progressed into mission cycling at this writing but virtually all strain gages that were attached to the vitreous coating on the panel surface have delaminated possibly due to a silicone residue on the coating.

CONCLUSIONS

A thermoacoustic fatigue facility of the type used for experiments described in this paper is an extremely useful tool for use in the design process and for proof testing TPS structures. It is shown that computerized test control and real-time data acquisition are important in evaluation of complex structures of the type described in these tests.

The metallic TPS tests represented a unique step forward in the state of the art of thermoacoustic testing as it represented the first time structures of this size were subjected to combined environments under such detailed computer control and in which strain and thermal data were so extensively and efficiently obtained and analyzed. A number of phenomenological illustrations were presented as evidence of this capability including the effects of damping in reducing panel response during initial response tests caused by insulating the panel. It was shown how thermal loading was carefully controlled and how profiles are easily compiled for comparisons. The need for rapid data evaluation was demonstrated by showing the changes in response between mission cycle number 2 and mission cycle number 86. Buildup of the high-frequency response between 300 to 500 Hz which may have been indicative of standoff failure and the resulting vibration of the cantilevered strut was pointed out. The later buildup of response between 50 to 150 Hz may have been indicative of increased motion of the "unsupported" plate. The decline in frequency of the primary modes are supportive of the previous interpretations. The rapid analysis capability that is now a part of our capability would have been a potentially useful tool in detecting early failure of the TPS panel, which in these tests was failed extensively.

The RSI TPS data presented for excitation levels of 140 dB and 150 dB represent only initial data from continuing thermoacoustic tests. An increase in damping of the two lowest frequency primary response peaks due to increased loading is illustrated from these early tests on the RSI structure.

REFERENCES

1. Rucker, C. E., and Grandle, R. E.: Thermoacoustic Fatigue Testing Facility for Space Shuttle Thermal Protection System Panels. Presented at 1972 Symposium on Fatigue at Elevated Temperatures, Storrs, Conn., June 18-23, 1972, STP 520.
2. Schock, R. W.: Vibration Environment. Space Transportation Systems Technology Symposium, Vol. II - Dynamics and Aeroelasticity, NASA TM X-52876, July 1970, pp. 273-284.
3. Jones, J. H.: Acoustic Environment Characteristics of the Space Shuttle. Space Transportation Systems Technology Symposium, Vol. II - Dynamics and Aeroelasticity, NASA TM X-52876, July 1970, pp. 285-300.
4. Dixon, S. C., and Shore, C. P.: State of the Art for Panel Flutter as Applied to Space Shuttle Heat Shields. Space Transportation Systems Technology Symposium, Vol. II - Dynamics and Aeroelasticity, NASA TM X-52876, July 1970, pp. 199-221.
5. Dowell, E. H.: Theoretical Panel Vibration and Flutter Studies Relevant to Space Shuttle. AIAA/ASME/SAE 13th Structures, Structural Dynamics, and Materials Conference, April 1972, AIAA Paper No. 72-350.
6. Stein, B. A., Bohan, H. L., and Rummel, D. R.: An Assessment of Radiative Metallic Thermal Protection Systems for Space Shuttle. NASA Space Technology Conference, Dynamics and Aeroelasticity, Structures and Materials, NASA TM X-2570, July 1972, pp. 267-302.

PRECEDING PAGE BLANK NOT FILMED

Paper No. 39

SIMULATION OF THREE-DIMENSIONAL COOLANT
FLOW WITHIN TRANSPIRATION NOSETIPS*J. R. Schuster and G. E. Seay, *McDonnell Douglas
Astronautics, Huntington Beach, California*

ABSTRACT

Steady-state equations are presented to describe coolant mass and energy transfer within transpiration noisetips. The energy model, which assumes thermal equilibrium between the coolant and matrix, is justified on the basis of pore size. An iterative computational technique is given which can be applied to the finite-difference equivalents of the steady-state equations, causing a relaxation in the pressure and enthalpy fields to satisfy the boundary conditions. To maintain stability, the calculations must be damped. The final results show isothermal approximations to be substantially in error for high- and low-pressure reentry conditions.

NOMENCLATURE

- A = Interfacial area between nodes, ft^2
 C_p = Specific heat, $\text{Btu}/\text{lb}_m\text{-}^\circ\text{R}$
D = Diameter, ft
E = Energy flow into or out of a node, Btu/sec
 \dot{e} = Energy flux defined by Equation (26), $\text{Btu}/\text{ft}^2\text{-sec}$
f = Function defined by Equation (25)
 g_c = Conversion factor, $32.17 \text{ lb}_m\text{-ft}/\text{lb}_f\text{-sec}^2$
H = Fluid enthalpy, Btu/lb_m
h = Heat-transfer coefficient, $\text{Btu}/\text{ft}^2\text{-sec-}^\circ\text{R}$
J = Conversion factor, $778 \text{ ft-lb}_f/\text{Btu}$

*This work was supported by McDonnell Douglas independent research and development funds.

- K = Porous matrix permeability, ft^2
 k = Conductivity, $\text{Btu}/\text{ft}\cdot\text{sec}\cdot^\circ\text{R}$
 L = Length measurement in direction of mass flow, ft
 M = Mass flow into or out of a node, lb_m/sec
 \dot{m} = Effective fluid mass flux based on matrix cross section, $\text{lb}_m/\text{ft}^2\cdot\text{sec}$
 N = Number of pores per unit matrix cross section, ft^{-2}
 P = Pressure, lb_f/ft^2
 \dot{Q} = Conduction heat flux, $\text{Btu}/\text{ft}^2\cdot\text{sec}$
 R = Porous matrix heat flow parameter defined by Equation (22), $\text{Btu}/\text{sec}\cdot^\circ\text{R}$
 T = Temperature, $^\circ\text{R}$
 v = Effective fluid velocity based on matrix cross section, ft/sec
 W = Porous matrix fluid flow parameter defined by Equation (18), sec/ft
 y = Distance from outer surface of porous matrix, ft
 α = Porous matrix viscous pressure drop constant, ft^{-2}
 β = Porous matrix inertial pressure drop constant, ft^{-1}
 Γ = Porous matrix tortuosity for heat conduction, dimensionless
 γ = Porous matrix void fraction, dimensionless
 μ = Fluid viscosity, $\text{lb}_m/\text{ft}\cdot\text{sec}$
 ρ = Fluid density, lb_m/ft^3
 $\bar{\sigma}$ = Elemental surface area normal vector, ft^2

Subscripts

- e = Effective value
 c = Value for coolant

- in = Into a node
- o = Storage value
- out = Out of a node
- pore = Value for pore within the porous matrix
- s = Value for porous matrix parent material
- surf = Outer surface value
- 0, 1, 2, 3, 4, 5, 6 = Nodal subscripts defined by Figure 5

INTRODUCTION

The design of a transpiration-cooled nosetip, represented in the cross section in Figure 1, is predicated upon delivering coolant to the nosetip surface at a rate sufficient to dissipate thermal energy from aerodynamic heating. From this standpoint, ideal coolant flux at the surface varies greatly with location; it can be complicated by aerodynamic boundary-layer transition and angle of attack. For reentry vehicle application, it is desirable to minimize wastage of coolant, i. e., no excess coolant flux should be delivered to any portion of the nosetip surface. However, this is difficult to accomplish in view of the severe pressure gradient that can exist over the nosetip surface at high stagnation pressures. The pressure gradient acting over the surface is transmitted to the isotropic porous material of the nosetip, and when superimposed on the internal radial pressure field, it can cause significant bending of coolant streamlines between the inner and outer surfaces of the nosetip. To define coolant distribution accurately at the outer surface, three-dimensional porous flow calculations must be done because of the surface pressure gradient, coupled with the irregular shape of the nosetip inner surface and the effects of angle of attack.

LITERATURE REVIEW

The traditional approach to analyzing incompressible steady flow through porous media has been to assume the process is dominated by viscous effects and that effective fluid velocity averaged over a typical cross section is proportional to the pressure gradient and a material property called permeability. The resulting relationship, Equation (1), is sometimes referred to as the Darcy⁽¹⁾ equation.

$$-\frac{dP}{dL} = \frac{\mu}{Kg_c} v \quad (1)$$

To better match experimental data, Green and Duwez⁽²⁾ modified the Darcy equation by adding terms to account for inertial or nonviscous effects within the porous flow:

$$-\frac{dP}{dL} = \frac{(\alpha\mu + \beta\rho v) v}{g_c} \quad (2)$$

where α is the viscous pressure drop constant (the inverse of the material permeability) and β is the inertial pressure drop constant of the material. In order to characterize a specific porous material, both α and β should be evaluated experimentally, as they strongly depend on such factors as material porosity and pore shape and size.

Equation (2) can be extended to multidimensional flow in isotropic porous media provided the acceleration due to flow curvature is neglected.

$$-\nabla P = \frac{(\alpha\mu + \beta\rho|v|) \bar{v}}{g_c} \quad (3)$$

Considering only viscous pressure drop, Schneider and Maurer⁽³⁾ utilized Equation (3) to obtain analytic solutions for the flow of coolant through a hemispherical, transpiration-cooled shell subjected to a Newtonian surface-pressure distribution. They found that with streamline curvature, there is a tendency toward coolant starvation in the stagnation region, and that one-dimensional calculations are inadequate.

In order to study other shapes besides concentric hemispheres and to include inertial effects, Timmer and Dirling⁽⁴⁾ treated the axisymmetric porous nosetip flow problem by approximating the quantity $(\alpha\mu + \beta\rho|v|)$ as a constant for the porous region, thus reducing Equation (3) to Laplace's equation.

$$\nabla^2 P = 0 \quad (4)$$

By assuming symmetry in a plane normal to the nosetip axis, the question becomes an interior Dirichlet problem, and for a given set of boundary conditions, may be solved numerically using the method of Hess⁽⁵⁾. If an analytic external pressure distribution such as modified Newtonian is assumed for the outer surface, then the linearity of Laplace's equation permits the decoupling of the complex numerical calculations from the physical boundary conditions. The physical solution is then represented by summation of three separate sets of simple artificial boundary conditions.

Gold et al.⁽⁶⁾ examined the nosetip porous flow problem for angle of attack. They reduced the flow to Laplace's equation by ignoring inertial effects and approximating the surface-pressure distribution as an analytic function of the meridian angle and the pressures on windward, yaw, and leeward meridians. They utilized nondimensional graphical data for fixed angles of attack to determine coolant distributions.

Although the previous porous flow analyses for transpiration nosetips are useful, they have several drawbacks:

1. Conservation of coolant mass is ignored inside the porous matrix.
2. Inertial effects are either approximated or ignored.
3. The nosetip analysis is restricted by the assumption of symmetry.
4. The external pressure profiles must be described as simple analytic functions.
5. The analyses assume constant coolant properties; i. e., isothermal flow.

Curry and Cox⁽⁷⁾ developed a set of complex equations for the transient flow of a compressible gas through porous media with heat transfer. They solved some two-dimensional low-heating cases numerically. Although their method is general, the numerical techniques are extremely difficult to extend to three dimensions (for angle of attack).

This paper describes and demonstrates an analytical model and numeric technique that does not have the shortcomings of some of the previous work. The analysis

1. Is general with regard to geometry and boundary conditions.
2. Permits porous media heat transfer.
3. Is steady-state.
4. Is three-dimensional.

It is currently in use as an analytical and design tool for the development of transpiration-cooled nosetips.

ANALYSIS

The object of this analysis is to provide a steady-state solution for coolant distribution on the outer surface of a

transpiration-cooled nosetip. Because typical operating conditions may involve high stagnation pressures, the final numerical relationships should provide for variable real-fluid properties in terms of local temperature and pressure. Therefore, it is necessary to solve for the temperature distribution as well as the pressure distribution throughout the porous matrix.

Basic Equations

The basic equation for porous-flow pressure drop is a minor modification of Equation (3):

$$-g_c \nabla P = (\alpha\mu + \beta\dot{m}) \frac{\bar{m}}{\rho} \quad (5)$$

where the velocity vector has been replaced by the mass flux vector, \bar{m} .

In addition, there is the steady-state continuity equation

$$\oint_s (\bar{m}) \cdot d\bar{\sigma} = 0 \quad (6)$$

and the steady-state porous-flow energy equation

$$-k_e \nabla^2 T - (\nabla k_e) \cdot (\nabla T) + \nabla \cdot (H\bar{m}) = 0 \quad (7)$$

The local effective thermal conductivity is that of the coolant-infiltrated matrix, and is determined by the following equation

$$k_e = \gamma k_c + (1-\Gamma)(1-\gamma) k_s \quad (8)$$

where

k_c = the local coolant conductivity

k_s = local conductivity of porous matrix parent material

γ = void fraction of porous matrix

Γ = porous matrix tortuosity

Assessment of Thermal Equilibrium

Equation (7) assumes that the fluid within a pore and the surrounding pore material are in thermal equilibrium. This assumption can be examined by the following approximations. Figure 2 presents an idealized one-dimensional flow through a matrix composed of circular pores. Assuming thermal equilibrium and uniform conductivity, Equation (7) reduces to

$$\dot{Q} = -k_e \frac{dT}{dy} = \dot{m}(H_c - H_{c,o}) \quad (9)$$

where $H_{c,o}$ is the coolant storage enthalpy.

Examining the energy exchange within the pores, a balance yields

$$-\dot{m} C_{p_c} \frac{dT}{dy} = N \pi D_{\text{pore}} \dot{Q}_{\text{pore}} \quad (10)$$

while the pore density per unit area is

$$N = \frac{4\gamma}{\pi D_{\text{pore}}^2} \quad (11)$$

Within a pore, the porous matrix-to-coolant temperature differential is

$$T_s - T_c = \frac{\dot{Q}_{\text{pore}}}{h_{\text{pore}}} \quad (12)$$

Assuming purely laminar flow within a pore, the pore heat-transfer coefficient is

$$h_{\text{pore}} = \frac{4 k_c}{D_{\text{pore}}} \quad (13)$$

Combining Equations (9) through (13), the porous matrix-to-coolant temperature differential is

$$T_s - T_c = 0.0625 D_{\text{pore}}^2 \dot{m}^2 \frac{C_{p_c}}{\gamma k_c k_e} (H_c - H_{c,o}) \quad (14)$$

Approximating $(H_c - H_{c,o})$ as $C_{p_c} (T - T_{c,o})$, Equation (9) can be integrated and combined with Equation (14) to yield the local temperature differential in terms of the total enthalpy rise of the coolant at the surface (a function of the surface pressure) and the distance from the surface.

$$T_s - T_c = 0.0625 D_{\text{pore}}^2 \dot{m}^2 \frac{C_{p_c}}{\gamma k_c k_e} (H_{c, \text{surf}} - H_{c,o}) \exp\left(-\frac{\dot{m} C_{p_c}}{k_e} y\right) \quad (15)$$

Equation (15) indicates that the maximum temperature differential will occur at the surface where the coolant enthalpy is a maximum, and that the differential will decrease in exponential fashion below the surface.

As transpiration nosetip materials consist of sintered metallic powders of various particle sizes, it is necessary to characterize the pore distribution in order to assess the degree of thermal inequilibrium. Figure 3 presents a pore size distribution, based on mercury-intrusion porosimeter tests, for a typical sintered stainless-steel nosetip material with a porosity of 20.3 percent. The median pore size is 2.7 microns. For a typical mass flux of liquid water of 20 $\text{lb}_m/\text{ft}^2\text{-sec}$ at a surface pressure of 200 atm, saturated liquid conditions on the surface result in a porous matrix-to-coolant temperature differential of 50°F. This decreases to 5°F 0.002 in. below the surface. It can be readily seen that thermal equilibrium is a good assumption for coolant flow within the porous matrix.

Viscous Dissipation

If a liquid coolant is caused to flow through a nosetip by an imposed pressure differential, the coolant temperature will rise because frictional shear forces transform the flow work done on the coolant into thermal energy (i.e., viscous dissipation). If the coolant flow is assumed to be adiabatic, the local temperature of the incompressible fluid in the porous matrix is

$$T_c = T_{c,o} + \frac{P_{c,o} - P_c}{\rho C_{p_c} J} \quad (16)$$

where J is the mechanical equivalent of heat. For water, this temperature change amounts to about 3°F for each 1,000-psi differential in pressure. In reality, the flow process is not adiabatic, the coolant is not incompressible, and some kinetic energy is imparted to the coolant. However, for water, the latter two effects are negligible. Additionally, if the flow rate is high enough to negate the effect of heat conduction along coolant flow vectors within the porous matrix, as indicated by Equation (9), then the assumption of adiabatic flow is appropriate. Since liquid viscosity is usually a strong function of temperature, viscous dissipation can have a significant effect on coolant pressure drop and flow distribution.

FINITE-DIFFERENCE MODELING

The porous transpiration nosetip is segmented radially, axially, and circumferentially so as to form a nodal network, as illustrated in Figure 4. The interfacial areas bordering nodes and the distances between centroids of adjacent nodes are evaluated and utilized in conjunction with Equations (5) through (7) to determine pressures and temperatures at node centroids and the mass and energy flow either into or out of each nodal face. To satisfy Equation (6), the interfacial areas between nodes are corrected for nonorthogonality by multiplying them by the unit vector dot product between the normal to the face and the line connecting the centroids of the adjacent nodes. Due to symmetry about the plane passing through the windward and leeward meridians, only half the nosetip need be analyzed. Using the numbering system of Figure 5, the finite-difference, Cartesian equivalent of Equation (5) is

$$\begin{aligned} \dot{m}_{0,4} &= g_c W_{0,4} (P_0 - P_4) \\ \dot{m}_{0,5} &= g_c W_{0,5} (P_0 - P_5) \\ \dot{m}_{0,6} &= g_c W_{0,6} (P_0 - P_6) \end{aligned} \quad (17)$$

where

$$W_{0,4} = \frac{2}{L_{0,4} \left[\frac{\alpha\mu_0 + \beta\dot{m}_0}{\rho_0} + \frac{\alpha\mu_4 + \beta\dot{m}_4}{\rho_4} \right]}$$

$$W_{0,5} = \frac{2}{L_{0,5} \left[\frac{\alpha\mu_0 + \beta\dot{m}_0}{\rho_0} + \frac{\alpha\mu_5 + \beta\dot{m}_5}{\rho_5} \right]} \quad (18)$$

$$W_{0,6} = \frac{2}{L_{0,6} \left[\frac{\alpha\mu_0 + \beta\dot{m}_0}{\rho_0} + \frac{\alpha\mu_6 + \beta\dot{m}_6}{\rho_6} \right]}$$

The equivalent of Equation (6) is

$$\begin{aligned} \dot{m}_{1,0} A_{1,0} + \dot{m}_{2,0} A_{2,0} + \dot{m}_{3,0} A_{3,0} &= M_{in} \\ &= M_{out} = \dot{m}_{0,4} A_{0,4} + \dot{m}_{0,5} A_{0,5} + \dot{m}_{0,6} A_{0,6} \end{aligned} \quad (19)$$

Substituting Equation (17) into Equation (19) and rearranging,

$$P_0 = \frac{\frac{M_{in}}{g_c} + [W_{0,4} A_{0,4} P_4 + W_{0,5} A_{0,5} P_5 + W_{0,6} A_{0,6} P_6]}{[W_{0,4} A_{0,4} + W_{0,5} A_{0,5} + W_{0,6} A_{0,6}]} \quad (20)$$

Equation (20) presents a relationship for the nodal pressure in terms of the net mass flow-in from three adjacent nodes and the pressures in and geometric relationships with the other three adjacent nodes.

The energy relationship, Equation (7), becomes

$$\begin{aligned} E_{in} &= \dot{m}_{1,0} H_1 A_{1,0} + \dot{m}_{2,0} H_2 A_{2,0} + \dot{m}_{3,0} H_3 A_{3,0} \\ &\quad + R_{1,0} (T_1 - T_0) + R_{2,0} (T_2 - T_0) + R_{3,0} (T_3 - T_0) \\ &= E_{out} = \dot{m}_{0,4} H_0 A_{0,4} + \dot{m}_{0,5} H_0 A_{0,5} + \dot{m}_{0,6} H_0 A_{0,6} \\ &\quad + R_{0,4} (T_0 - T_4) + R_{0,5} (T_0 - T_5) + R_{0,6} (T_0 - T_6) \end{aligned} \quad (21)$$

where

$$R_{0,4} = 0.5 \frac{A_{0,4}}{L_{0,4}} (k_{e_0} + k_{e_4})$$

$$R_{0,5} = 0.5 \frac{A_{0,5}}{L_{0,5}} (k_{e_0} + k_{e_5}) \quad (22)$$

$$R_{0,6} = 0.5 \frac{A_{0,6}}{L_{0,6}} (k_{e_0} + k_{e_6})$$

Equation (21) can be rearranged to two forms:

$$T_0 = \left(E_{in} - \dot{m}_{0,4} H_0 A_{0,4} - \dot{m}_{0,5} H_0 A_{0,5} - \dot{m}_{0,6} H_0 A_{0,6} + R_{0,4} T_4 + R_{0,5} T_5 + R_{0,6} T_6 \right) / (R_{0,4} + R_{0,5} + R_{0,6}) \quad (23)$$

or

$$H_0 = \frac{E_{in} - R_{0,4}(T_0 - T_4) - R_{0,5}(T_0 - T_5) - R_{0,6}(T_0 - T_6)}{\dot{m}_{0,4} A_{0,4} + \dot{m}_{0,5} A_{0,5} + \dot{m}_{0,6} A_{0,6}} \quad (24)$$

where

$$H_0 = f(T_0, P_0) \quad (25)$$

Equation (24) is used in the present analysis as it provides greater stability in the numerical solution.

The Cartesian energy fluxes are

$$\dot{e}_{0,4} = \dot{m}_{0,4} H_0 + \frac{R_{0,4}}{A_{0,4}} (T_0 - T_4)$$

$$\dot{e}_{0,5} = \dot{m}_{0,5} H_0 + \frac{R_{0,5}}{A_{0,5}} (T_0 - T_5)$$

$$\dot{e}_{0,6} = \dot{m}_{0,6} H_0 + \frac{R_{0,6}}{A_{0,6}} (T_0 - T_6) \quad (26)$$

Boundary Conditions

As the inner and outer surfaces of the nosetip are represented by dummy nodes, essentially any prescribed distributions of pressure, mass flux, temperature, or heat flux can be simulated. Practical cases involve the following set of conditions:

1. Specified constant pressure over the inner surface of the nosetip.
2. Specified constant coolant-supply temperature (permits heat conduction at the inner surface of the nosetip).
3. Specified pressure distribution over the outer surface of the nosetip.
4. Local saturation temperature over the outer surface corresponding to the prescribed pressure distribution.

The fourth boundary condition is justified for liquids because the surface shear encountered during reentry drastically reduces the coolant flow within the surface film by causing liquid to be stripped from the film and entrained in the gaseous boundary layer.⁽⁸⁾ In proportion, this reduces the film thickness, and allows the porous matrix surface to approach the local vaporization temperature of the coolant. This interpretation is supported by recent experimental data indicating surface temperature essentially equal to the vaporization temperature in regions covered by a liquid film.

Iteration Technique

Initial estimates of the pressure, mass flux, and temperature and energy flux distributions are made within the nodal matrix representing the nosetip. The mass and energy flow from the nosetip cavity into the innermost node bordering the nosetip axis of symmetry and centered on the windward meridian is then calculated utilizing Equations (17) and (26). This provides an updated value for mass flow into that node; therefore, an updated nodal pressure and temperature can be calculated using Equations (20) and (24). With the updated pressure and temperature, Equations (17) and (26) can then be utilized to evaluate updated mass fluxes and energy fluxes from that node into the three adjacent nodes in the outward radial direction,

the downstream axial direction, and the circumferential direction toward the leeward meridian.

This technique is then applied to successive nodes radially and outward until the surface is reached, whereupon a transfer is made to the innermost node in the adjacent row in the downstream axial direction. After a pass has been made through the row of nodes furthest downstream, a transfer is then made to the adjacent bank of nodes in the circumferential direction and the sequence is repeated.

The basis for the technique is that the fixed temperature and pressure boundary conditions cause a relaxation in the matrix internal pressure and enthalpy and temperature distributions until conservation of coolant mass and energy is achieved. Convergence is obtained when each nodal pressure and enthalpy varies by less than a specified percentage from the value on the previous pass through the network; i. e., for the i^{th} iteration, $(P_{0,i} - P_{0,i-1})/(P_{0,i-1}) < \text{convergence margin}$ and $(H_{0,i} - H_{0,i-1})/(H_{0,i-1}) < \text{convergence margin}$.

To maintain a uniform progression from the initialized distributions to the final solution, the calculations must be damped by weighting the updated nodal pressure and enthalpy as determined by Equations (20) and (24) with the values on the previous pass; i. e.,

$$P_{0,i} = \text{damping factor} \times P_{0,\text{calculated}} \\ + (1.0 - \text{damping factor}) \times P_{0,i-1}$$

and (27)

$$H_{0,i} = \text{damping factor} \times H_{0,\text{calculated}} \\ + (1.0 - \text{damping factor}) \times P_{0,i-1}$$

where a decreasing damping factor results in increased damping.

If the damping is inadequate, oscillations result in the internal pressure and enthalpy fields, either slowing convergence or causing the calculations to become unstable. The amount of damping required appears to increase with both the number of nodes in the mesh representing the nosetip and the

variation between the initially estimated and final pressure and enthalpy distributions. Subsequent numerical results that will be shown utilize one-dimensional estimates for the initial distributions. It has also been determined that as the amount of damping and number of nodes in the mesh increase, the convergence margin must be decreased to maintain accuracy.

RESULTS

For the nosetip contour shown in Figure 1, with a radius of 1.0 in., a series of calculations was performed to determine the material permeability that most efficiently distributed the coolant around the nosetip surface. The optimum permeability was found to be 5.45×10^{-11} in.². Utilizing this permeability and some typical reentry conditions, studies and comparisons were made utilizing a computerized model of the analyses. Surface pressure distributions were obtained from a method-of-characteristics solution of the inviscid shock layer.

Critical Parameter Requirements

Isothermal porous flow and 0-deg angle of attack were selected in order to study the damping and convergence requirements and the relative accuracy obtained by varying the fineness of the nosetip mesh. Figure 6 gives an approximate indication of the amount of damping required to obtain convergence as a function of mesh dimensions. Above the curve, the calculations tend to go unstable. As the curve is approached from below, the oscillations take longer to damp out. Rapid convergence is usually obtained with the damping factor set about 10 percent below the critical value.

Since one-dimensional relationships are used to establish the initial estimates of pressure and enthalpy field, other nosetip geometries that are not proportional may require damping other than that shown in Figure 1. However, the trend with increasing mesh fineness should hold. Multiplying the total number of nodes by circumferentially segmenting the nosetip to simulate angle of attack seems to have little or no effect on the damping requirement. The radial and axial mesh fineness are the primary factors.

Figure 7 illustrates the effect of convergence margin on the accuracy of the calculated coolant distribution. Generally, as the fineness of the mesh increases, the convergence margin must decrease in order to maintain accuracy. The convergence margin must also decrease with decreasing damping factor. For the 5 by 25 mesh and 0.3 damping factor of Figure 7, the solution has nearly converged for a margin of 0.0182. Convergence is complete at 0.005, although requiring twice the number of iterations.

Figure 8 illustrates the effect of the mesh dimensions on the predicted coolant distribution. The nosetip geometry and multidimensional flow are handled adequately by even a very coarse mesh. It should be noted, however, that these solutions ignore temperature effects. Due to the coupling between the pressure and temperature fields through fluid viscosity, fine partitioning in the radial direction is desired for accuracy.

Angle-of-Attack Effects

Figure 9 presents the coolant distribution at the nosetip surface for 20-deg angle of attack at high stagnation pressure. As is evident, there is substantial cross flow from the windward meridian toward the leeward meridian. It is clear that axisymmetric analyses using only the windward meridian pressure distribution would provide misleading results.

Figure 10 presents windward meridian coolant distribution for various angles of attack. The turbulent heating distribution on a hemisphere usually peaks around 30 deg from the stagnation point. In view of the altered coolant distribution at high angle of attack, substantial increases in coolant supply pressure will be required to provide adequate coolant flux as the heating profile shifts over the nosetip surface.

Comparison with Two-Dimensional Approximation

Figure 11 presents a comparison of the results obtained at two pressure levels using the present method with the method of Timmer and Dirling, (4) who approximated inertial effects and truncated their flow distribution at the tangency point. At the high-pressure, high-flow condition, the present solution is consistently lower. This is because Timmer and Dirling approximated the quantity $(\alpha\mu + \beta\rho\nu)$ as a constant in their solution by setting the velocity component equal to the average coolant velocity at the nosetip outer surface. This underestimates inertial effects, thus providing higher fluxes. The Timmer and Dirling solution also does not have the upward trend at the tangency point. This is due to the truncated solution. The solution at the lower pressure level appears to agree fairly well.

Temperature Effects

The results presented are for isothermal porous flow using the supply temperature of the coolant. Figure 12 shows how isothermal results compare with solutions coupling the porous flow enthalpy and pressure fields while accounting for heat conduction and viscous dissipation, and the partially coupled solution allowing only for viscous dissipation in the coolant.

At the high-pressure level, the isothermal solution provides slightly lower fluxes while the viscous dissipation approximation

agrees very well with the completely coupled solution. The reason for the good agreement is that the high coolant flux causes steep temperature gradients near the outer surface, essentially isolating the main portion of the porous flow from substantial heat conduction. The viscous dissipation solution predicts even slightly higher flows in the stagnation region, although this is due to greater streamline curvature for the fully coupled solution.

For the lower pressure level, the fully coupled solution provides substantially higher coolant fluxes than the isothermal or viscous dissipation approximations. This is because heat conduction has a greater effect on in-depth temperatures in the porous flow; as indicated by Equation (9), the temperature gradient along the porous flow vector should be proportional to coolant flux. The isothermal and viscous dissipation solutions coincide almost exactly, as very little flow work is done on the coolant.

Therefore, if accurate porous flow estimates are required over a wide range of reentry conditions, the fully coupled solution which accounts for both heat conduction and viscous dissipation through the porous flow energy equation should be utilized.

CONCLUSIONS

The conclusions are:

1. A fully coupled three-dimensional porous flow solution can be obtained by simultaneously solving the pressure drop, mass continuity, and energy continuity equations in finite-difference form using iteration to relax the pressure and enthalpy fields.
2. The small pore size of typical porous material permits an energy model based on thermal equilibrium between the material and the coolant.
3. Damping is required to maintain stability in the computational procedure.
4. As the fineness of the noisetip mesh increases, the required amount of damping also increases.
5. Very coarse meshes can provide good accuracy, particularly for conditions where heat conduction is of secondary importance.
6. For high coolant fluxes, the importance of heat conduction is small and viscous dissipation dominates thermal effects on coolant distribution.

7. For low coolant fluxes, the importance of viscous dissipation is small and heat conduction dominates thermal effects on coolant distribution.

REFERENCES

1. Darcy, H., Les Fontaines Publiques de la Ville de Dijon, 1856.
2. Green, L., Jr., and P. Duwez, "Fluid Flow Through Porous Metals," Journal of Applied Mechanics, March 1951, pp. 39-45.
3. Schneider, P. J., and R. E. Maurer, "Coolant Starvation in a Transpiration-Cooled Hemispherical Shell," Journal of Spacecraft and Rockets, Vol. 5, No. 6, June 1968, pp. 751-752.
4. Timmer, H. G. and R. B. Dirling, Jr., "An Approximate Solution for the Flow of a Fluid Through a Porous Solid," AIAA Journal, Vol. 7, No. 2, Feb. 1969, pp. 371-372.
5. Hess, J. L., Extension of the Douglas Newmann Program for Axisymmetric Bodies to Include the Calculation of Potential, Nonuniform Cross Flow, Added Mass, and Conductor Problems, Report No. LB31765, Sept. 1, 1964, Douglas Aircraft Company.
6. Gold, H., R. E. Mascola, and P. C. Smith, Flow Characteristics of Porous Media and Surface Liquid Film Interactions, AIAA Paper No. 70-152, AIAA 8th Aerospace Sciences Meeting, New York, N. Y., Jan. 1970.
7. Curry, D. M., and J. E. Cox, Transient, Compressible Heat and Mass Transfer in Porous Media Using the Strongly Implicit Iteration Procedure, AIAA Paper No. 72-23, AIAA 10th Aerospace Sciences Meeting, San Diego, Calif., Jan. 1972.
8. Schuster, J. R., "Mass Loss From Thin Liquid-Surface Films Exposed to Re-Entry Heating and Shear," Journal of Spacecraft and Rockets, Vol. 9, No. 4, April 1972, pp. 271-276.



Figure 1. Typical Transpiration-Cooled Nosetip

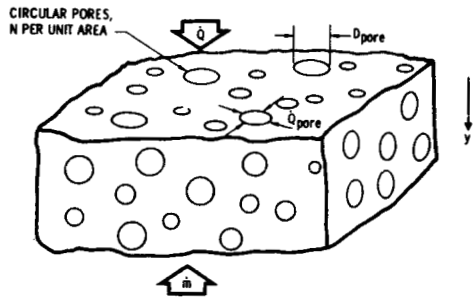


Figure 2. Idealized Porous Flow

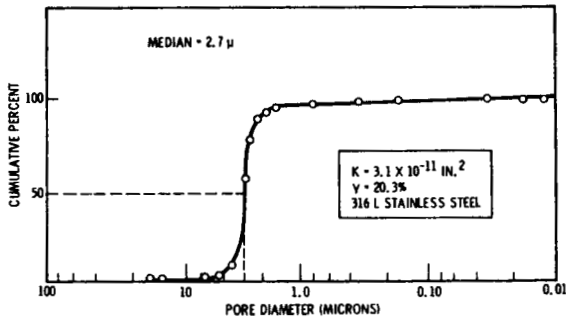


Figure 3. Typical Pore Size Distribution

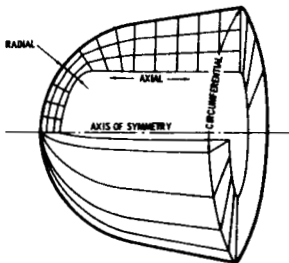


Figure 4. Nosetip Nodal Representation

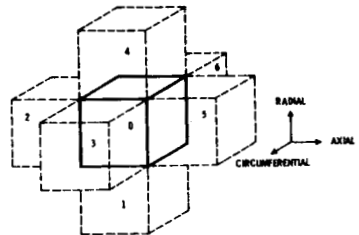


Figure 5. Nodal Matrix Numbering System

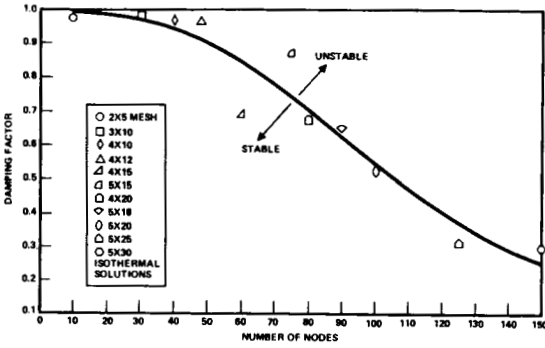


Figure 6. Damping Requirement for Convergence

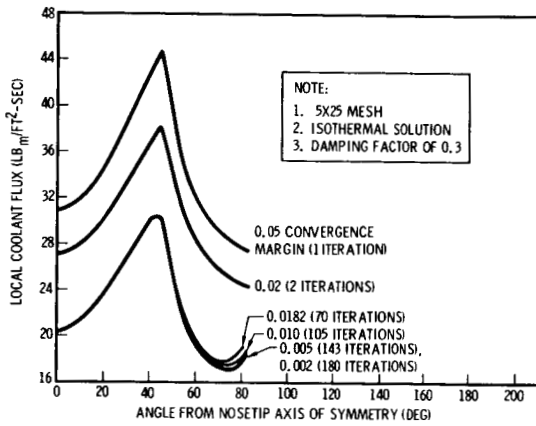


Figure 7. Effect of Nodal Convergence on Accuracy

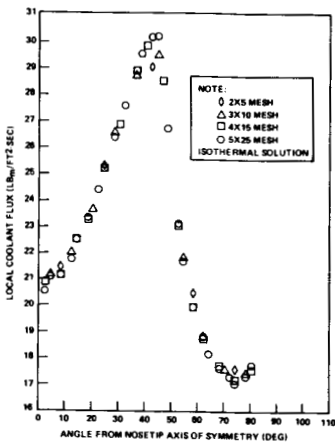


Figure 8. Effect of Mesh Fineness on Calculated Coolant Distribution

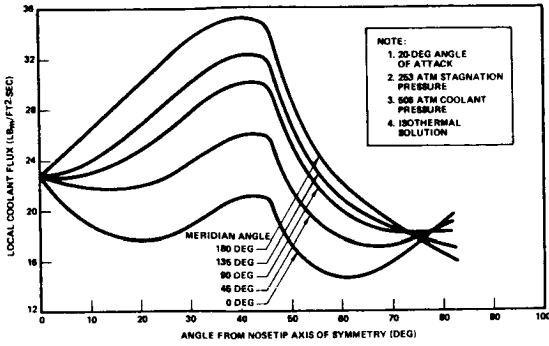


Figure 9. Nosedip Coolant Distribution at Angle of Attack

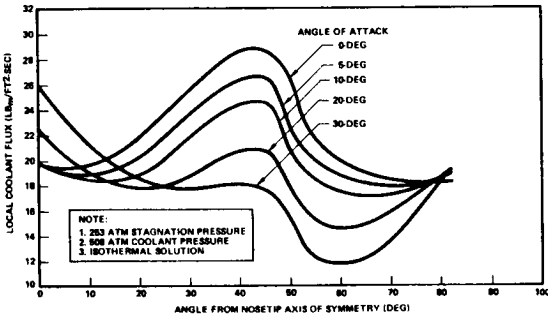


Figure 10. Effect of Angle of Attack on Windward Meridian Coolant Distribution

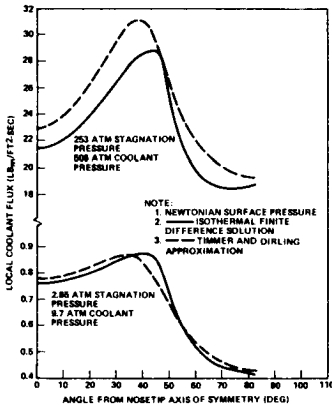


Figure 11. Comparison of Coolant Distributions

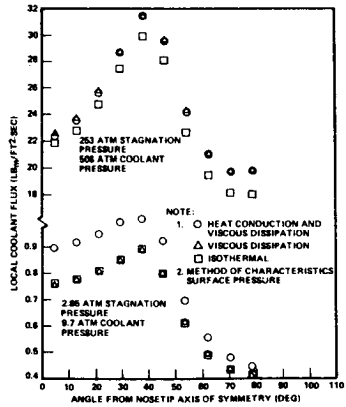


Figure 12. Effects of Energy Coupling on Coolant Flow Distribution

NTY-10268

Paper No. 40

INVESTIGATION OF CRITICAL DEFECTS IN ABLATIVE HEAT SHIELD SYSTEMS

C. C. Miller and W. D. Rummel, *Martin Marietta Aerospace, Denver, Colorado*

ABSTRACT

An experimental program was conducted under NASA Contract NAS1-10289 to determine the effects of fabrication-induced defects on the performance of ablative heat shield materials. Critical defects were identified and methods of their detection during inspection were established. Steps to streamline the fabrication and inspection processes were then postulated in order to lower the mass production costs of these material composites in the event that they were to be used on a Space Shuttle Orbiter.

INTRODUCTION

Ablative materials have been proven as heat shields in space flight. Because reliable, low cost heat shield materials are required for Space Shuttle vehicles, ablators are now considered to be confident backup candidates to the current baseline shuttle thermal protection system. Prime considerations in this application are: mission function, producibility and inspectability. We have recently completed a program for NASA-Langley Research Center (Contract NAS1-10289¹) on the study of the effects of anomalies in elastomeric ablative materials. This work is the basis for data presented in this paper.

Our study of the effects of ablator anomalies was divided into five tasks:

- Task I Identification, nondestructive evaluation and characterization of potentially critical defects;
- Task II Application of nondestructive evaluation techniques to ablative panels which had been fabricated by four different manufacturing processes;
- Task III Evaluation of various fabrication-induced defects on ablator performance in a simulated space shuttle reentry environment;
- Task IV Characterization of various fabrication-induced defects on Space Shuttle environments prior to reentry;

Task V Updating current state-of-the-art nondestructive evaluation techniques for ablative heat shield certification.

The overall objectives of this approach were to establish quantitative engineering acceptance criteria and low cost production and assurance methods based on performance requirements. Since ablator materials function in both active and passive performance, our study involved both physical and physical-chemical properties evaluation.

GROUND RULES (TASK I)

In establishing the basis for our study involving the effects of fabrication flaws, it was necessary to select from the many aspects of missions, vehicle locations, environments, possible defects and design configurations a baseline approach which could be adequately investigated within the scope of this program. In addition, a proper definition of the performance expected was vital in that it created guidelines against which the reactions could be measured.

Definition of Criticality

A critical defect was established as a perturbation of the ablative system that affected critical properties to the extent that the system did not meet basic performance requirements. In particular, these depended on the deterioration of the composites structural and/or thermal capabilities due to flaws. Flaws introduced at one point in the material's history could fully develop to a critical defect later in the sequence of the mission environments and thereby affect performance in a phase such as reentry.

Investigation Point

Thermal protection requirements were based on the bottom centerline region of a Shuttle Orbiter on a logistic resupply mission.

Origin of Flaws

All variances were assumed to be introduced before completion of the panel assembly. Furthermore, assuming the raw materials meet specific acceptance criteria, the majority of flaws were initiated during the subcomponent fabrication or final assembly.

Assembly Configurations

The heat shield assembly construction used in the first half of this effort consisted of a full depth phenolic-glass honeycomb filled with an elastomeric ablator (MG-36) and bonded to a fiberglass backface sheet, see Figure 1. A honeycomb subpanel TPS

design was selected for the second half of the studies. In addition, the ablative fill was altered to a mixture identified as SS-41, see Figure 2. These changes were enacted as a result of Task I, II and III evaluations to: (1) provide support for the ablator in the presence of positive and negative normal airloads, (2) establish a more reproducible baseline material composite, and (3) introduce some latitude to the materials and combinations considered.

INITIAL CAUSE AND EFFECT TESTING (TASK III)

Using the MG-36 design, flaw-characterized specimens were investigated. The procedure involved the determination of the reactions of defects in a reentry heating environment immediately after fabrication, except for two wedge panels which were exposed to other environments before and after heating. An ancillary phase investigated the mechanical properties of defective samples over a range of temperatures. Simultaneous studies involving production and assurance methods evaluation were also initiated. The latter are discussed later.

Reactions to Entry Heating Only

Cylinders of ablator material MG-36, with defects, were exposed to end splash heating in the MMA Plasma Arc Facility. These were machined from large billets in the form of 5-in. diameter, 2-in. thick slugs.

Defects--The 68 slug specimens concentrated individually on variances in density (15 to 18 pcf), poor priming of the filler's honeycomb reinforcement (off B-staging, overloading), internal voids (up to 25% of the volume), formulation (fiber substitution and omission), overcuring, and undercuring.

Entry Heating Exposure and Results--Steady state cold wall heating rates (\dot{q}_{cw}) of 23 or 55 BTU/ft²-sec (at stream enthalpies (H_r) of 3800 or 6400 BTU/lb) were exposed in the plasma arc facility for 1200 or 900 seconds, respectively. The following observations were noted: (1) low density was not critical with respect to excessive backface temperature until it dropped to about 80% of the nominal density, (2) an excess amount of the ablator core wet-coat resin created a maximum backface temperature violation because of an increase in net thermal conductance through the material, and (3) voids initiated in the ablator at fabrication were not critical until they reduced the net density of the medium to the 80% value. Omission of silica fibers was not found to be critical. Also, large variations in cure temperature, pressure and time did not appear to be critical in this test set.

Reactions to Entire Mission Spectrum

Two panels (8 x 16 x 2-in.) were investigated to initially evaluate TPS response to a typical sequence of Shuttle environments. One panel was defect-free while the other had a variety of defects located about the panel planform.

Defects--The flaws incorporated were as follows: all the defects examined in the first entry heating set, plus inclusions, non-homogeneity, surface voids, undercut core, crushed core, face sheet disbond from the ablator, and face sheet delaminations.

Exposures--Those entry and non-entry environments which were believed to be the most likely to precipitate critical defects from manufacturing flaws during their period of influence were simulated individually on the panels. The environments were, in order: ascent acoustics (up to 154 db), hot/cold vacuum (+300°F (72 hour) and -320°F (48 hour) at 10^{-5} torr), entry heating (panel inclined at 20 degrees, \dot{q}_{cw} (avg) = 18 BTU/ft²-sec, $H = 11,700$ BTU/lb, for 1,000 seconds), and descent acoustics (154 db max for 4 minutes).

Observations--No significant degradation of the test panel appearances or performances was noted until after the entry heating exposure. There, local areas of unsupported char cracked into a random pattern, with little difference noted between the regions of crushed core and undercut core. Char retention elsewhere was not noticeably affected by these localized core defects or by the surface discontinuities created by ablator material removal. A facility failure destroyed the control panel at about the midpoint in the run; no adverse conditions were noted in the undestroyed fragments. The descent acoustics spectrum, subsequently imposed on the defect panel, created additional char losses in the areas of crushed core and new failures in the regions of undercut core and undercured material.

Mechanical Properties Evaluation

Tensile tests of representative coupons of control and defective ablator billets were conducted at temperatures ranging from -150°F to 300°F to ascertain any notable changes in physical properties which could affect the performance of the material. The specimens were conventional 7-in., necked-down configurations.

Defects--The potential defects included in this strength investigation involved wet-coat variations, density variations, altered cures, and material omissions.

Observations--Ultimate tensile strengths decreased for wet-coat variations, off densities, and altered cures. The same was true for ultimate elongation percentages. The data also indicated the

absence of any increase in tensile modulus for any of the flaws.

FINAL CAUSE AND EFFECT TESTING (TASK IV)

This task concentrated on the determination of the criticality of manufacturing flaws in ablative thermal protection systems relative to many environments and influences. It would have been desirable that all conceivable manufacturing variations be tested in all possible environments throughout the service life of a Shuttle ablative TPS. However, the matrix of potential environment-flaw combinations had to be reduced to a practical program which hopefully encompassed the significantly critical items.

As previously explained, this portion of the program had the ablator fill material change from MG-36 to SS-41 and the substrate from a single sheet to a honeycomb subpanel. The 27 composite panels used were 22 x 17.5 x 2-in. prior to subsequent subdivision for the later tests.

Defects

There were ten basic flaw characteristics examined in the final phase, with two variations of each. (The balance of the panels (7) were controls.) Several of the defects selected were among those previously examined. The new flaws, also utilizing two panels each were: horizontal delaminations just below the surface, high filler moisture contents, broken honeycomb ribbons and broken honeycomb nodes. A summary is presented in Figure 3.

Environments

Several additional environments and progressive quality inspections were added to the list of operations performed on investigation panels. The complete sequence associated with each wave of panels (with a wave consisting of a group of eight) is graphically illustrated in Figure 4.

All three waves were exposed to a single 24-hour, 98% relative humidity cycle at 140⁰F. They then received an average over-all ascent acoustic excitation of 163 db for one minute. This was followed by uniaxial flexure (in the weak direction) such that the strain on the outer face of the ablator was the equivalent of 1/2%. Thermal vacuum cycling followed, with one extended period (40 hours) at +200⁰F and five cycles between room temperature and -150⁰F, all at 10⁻⁵ torr.

The panels were then subdivided, with the major portion (8 x 12-in.) converting to an inclined specimen for entry heating simulation (at 20 degrees) in our Plasma Arc Facility. Seven beams per panel were machined (8 x 4-in.) for failure testing (in the unpyrolyzed state) in four-point flexural assemblies.

The latter beams were cut along either the strong or the weak panel ribbon direction.

The nominal plasma arc conditions were: $\dot{q}_{cw} = 13 \text{ BTU/ft}^2\text{-sec}$, $H_r = 8550 \text{ BTU/lb}$, time = 1100 seconds, and static pressure of 15 torr. These exposures were followed by descent acoustic environments (151 overall db level for two minutes). Centerline sectioning of each specimen was the final operation, terminating in visual examinations of the ultimate influences of the flaws.

Observations

A complete reiteration of the data and rationales utilized to highlight the critical defects finally designated is beyond the scope of this presentation¹. Figure 5 summarizes all the adverse comments made with respect to the intentional flaw, the defect symptoms noted, and the environments in which they were detected.

Based on the limits of this study, therefore, it would appear that the fabrication flaws which must be avoided focus on: ablator undercuring and overcuring, ablator low density, improper B-staging of the reinforcement honeycomb core's wet-coat priming, and any form of undercut or crushed core. These flaws have, in this study, displayed adverse combinations of excessive backface temperature, internal char fracturing, surface deterioration, and material losses. The crucial period begins at entry and continues to the safe return of the vehicle.

PRODUCTION AND ASSURANCE METHODS EVALUATION

Quality Assurance Orientation

Initial work with the baseline MG-36 material consisted of the evaluation of fabrication process variations and evaluation of potential nondestructive evaluation methods. The baseline process consisted of bonding a fiberglass backface sheet to the honeycomb core, packing the ablator from the open cell side, during the billet and mechanical machining of the excess "head" material to a constant thickness. Numerous evaluation methods were investigated.

X-radiography was determined to be sensitive to honeycomb core anomalies, bulk density variations, voids and contamination. A critical reaction to honeycomb "wet coat" and resin component composition was identified. This sensitivity overshadowed all other effects, thus limiting the usefulness of the technique.

Neutron Radiography was affected by honeycomb core anomalies, bulk density variations, voids and contamination. It was less sensitive than x-radiography to wet coat and resin variations

and was also less influenced by other anomalies.

Radiographic Image Processing provided additional discrimination and quantitative readout of x-ray images. The technique extended the potential for radiographic techniques but was influenced by the same phenomena which is inherent to the radiographic processes.

Indentation Hardness (Shore A) was sensitive to ablator cure, density and moisture content, with cure demonstrating the greatest indications. The technique was somewhat variable. Variations were attributed to resin-rich areas near the honeycomb cell wall and to the large indentation produced.

Microwave examinations reacted to ablator thickness, moisture content, resin content, density, cure, packing variations and wet coat variations. Its sensitivity to a number of anomalies made identification of a critical defect difficult.

Thermal (Infrared) scanner techniques were influenced by voids and density variations but were less sensitive than x-radiography.

Sonic and Ultrasonic techniques could determine unbonds and debonds from the facesheet side but could not penetrate the ablator material.

Holographic Interferometry provided some detection of voids and unbonds, but results were difficult to repeat.

These nondestructive evaluation techniques were applied to characterize test specimens used in Task III assessment of defect criticality in a simulated space shuttle reentry environment.

Fabrication Process Evaluation (Task II)

X-radiography, indentation hardness and sonic techniques were selected for Task II evaluation of panels produced by four different processes. These processes were specified to result in identical end item panels. Nondestructive evaluation demonstrated variations in both processes and materials. Dissection of a section of each panel verified nondestructive evaluation results. This effort resulted in a change in both the material and the fabrication process to the SS-41 designation for the remainder of the program. Changes included slight composition variation, a change in wet coat from a silicone to a phenolic resin, a change to packing the ablator mix in honeycomb which was open from both sides, curing in billet form and secondarily bonding to a honeycomb substrate support panel. These changes considerably improved producibility and inspectability.

Assurance Methods Refinement (Task V)

X-ray, indentation hardness, ultrasonic and holographic techniques were selected to characterize the SS-41 ablator material and for further refinement.

X-radiometric Gaging parameters were determined for monitor of variations in ablator density. One-half pound per cubic foot changes in ablator density were determined at energies ranging from 65 to 75 kilovolts. Separate calibration curves were necessary for each ablator thickness. X-ray (or gamma ray) gaging was determined to be applicable to production of the SS-41 material and could be automated for low cost production control.

X-ray evaluation for soundness was also determined to be applicable to the SS-41 material and could be automated. In-motion radiographic techniques using both film and electronic monitoring were evaluated. A penetrometer sensitivity of approximately 30% was determined for monitor by electronic (video) techniques. Video image analysis was determined to be feasible to direct, automatic readout of the resultant image for voids and density variations.

Indentation Hardness was monitored by a modified Shore "D" durometer. Modifications consisted of changing the indenter foot to a flat disc configuration and reducing the spring load on the indenter. These modifications enabled monitoring of the resilience of the ablator without variations due to crushing. No permanent mark was made in the ablator by the indenter. Greater consistence of measurements was obtained by this technique, but it was more sensitive to changes in panel thickness than was the Shore A unit used in previous evaluation. The modification was concluded to be useful due to greater consistency of results and elimination of the indenter mark.

Sonic/Ultrasonic evaluation of secondary bonding of the ablator to its subpanel was made using a sonic resonator (Model 101C). Unbond and debonds larger than one inch in diameter were detected from the subpanel side. Considerable variation in resonance response was experienced within a panel and successive evaluations of panels after environmental exposure. Known unbonds and debonds were consistently detected but variations in instrument response made inspection difficult. Sample panels were dissected and the variations were concluded to be due to differential absorption of the adhesive into the ablator material. Variations after environmental exposures were attributed to changes in modulus due to cure and/or absorbed moisture changes. Further refinement would be necessary for application of the sonic technique to full scale production.

Holographic evaluation results were negative on the SS-41 material. Loss in sensitivity was attributed to the increase in material permeability which prevented vacuum stressing of the material.

X-ray, Shore A and Shore D modified indentation hardness and sonic resonator methods were applied to evaluation and monitor of Task IV panels after various exposures. All techniques were determined to be applicable and meaningful in evaluating critical defects identified.

CONCLUSIONS

From this program we conclude that:

1. Elastomeric ablators are "very forgiving materials." No catastrophic defects analogous to cracks in metals were identified. Critical defects, i.e., defects which result in out-of-tolerance performance, are the result of out-of-tolerance variations in fabrication.
2. Critical defects identified were: a) ablator undercure and overcure; b) low ablator density; c) poor bonding of the ablator to the honeycomb support; d) undercut or damaged honeycomb core; e) large internal voids.
3. State-of-the-art inspection methods will detect all critical defects identified with the exception of poor bonding to the honeycomb core. Bonding is readily assured by process control.
4. Elastomeric ablators are proven heat shield materials and could be applicable to space shuttle missions for primary or for "off-the-shelf" backup utilization in leading edge or total surface vehicle protection with incorporation of future streamlining of production and inspection methods.

REFERENCES

1. Miller, C. C. and Rummel, W. D., "Study of Critical Defects in Ablative Heat Shield Systems for the Space Shuttle," NASA CR Document to be published, 1973.
2. Thompson, R. L., Rummel, W. D., and Driver, W. E., "Study of Critical Defects in Ablative Heat Shield Systems for the Space Shuttle, Tasks I, II and III", NASA CR-2010, April, 1972.

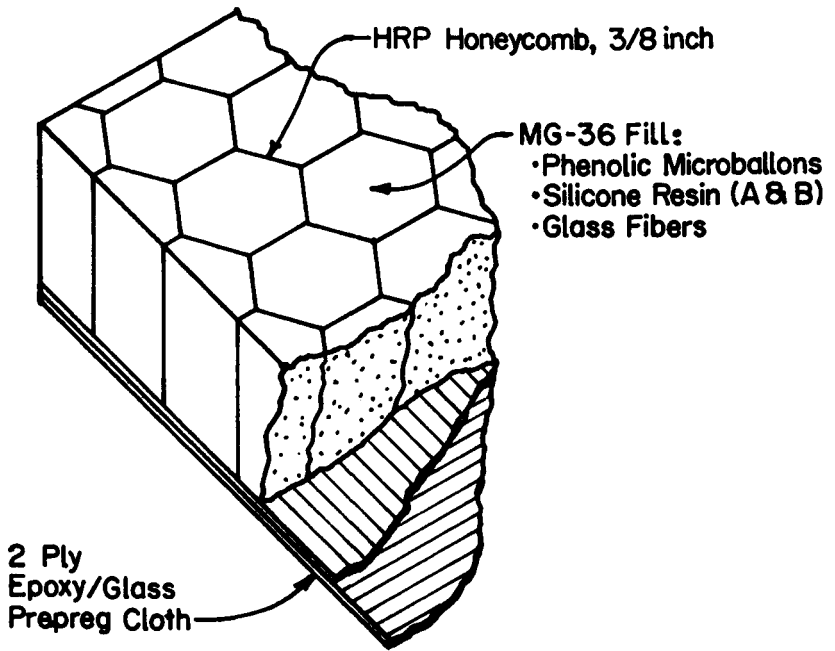


Figure 1 - Baseline Configuration - MG-36

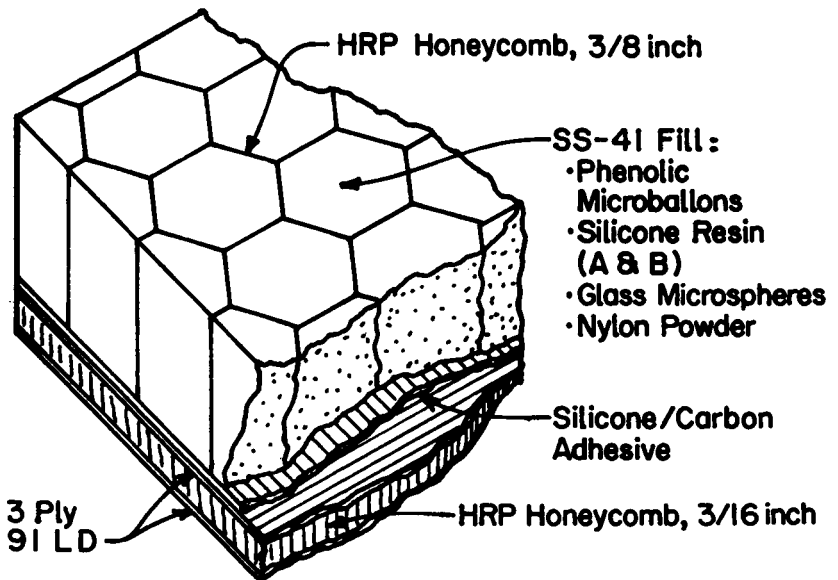


Figure 2 - Baseline Configuration - SS-41

Defects	Normal	Variances		Units
		A	B	
Undercure, Overcure	250	150	350	°F
Net Density Variances	16	15	17	pcf
Filler Moisture Contents	0	5	10	%
Undermixing	45	15	30	Min.
Weak Bond to Honeycomb	45 minutes at 150°F	90 minutes	250°F	In.
Horizontal Cracks in Fill	0	.25	.50	In.
Undercut Core	0	.10	.20	In.
Disbonds from Subpanel	0	1.0	1.5	--
Broken Node Bonds	0	Center	Edge	--
Broken Ribbons	0	Center	Edge	--

Figure 3 - Defects Description, Final Testing

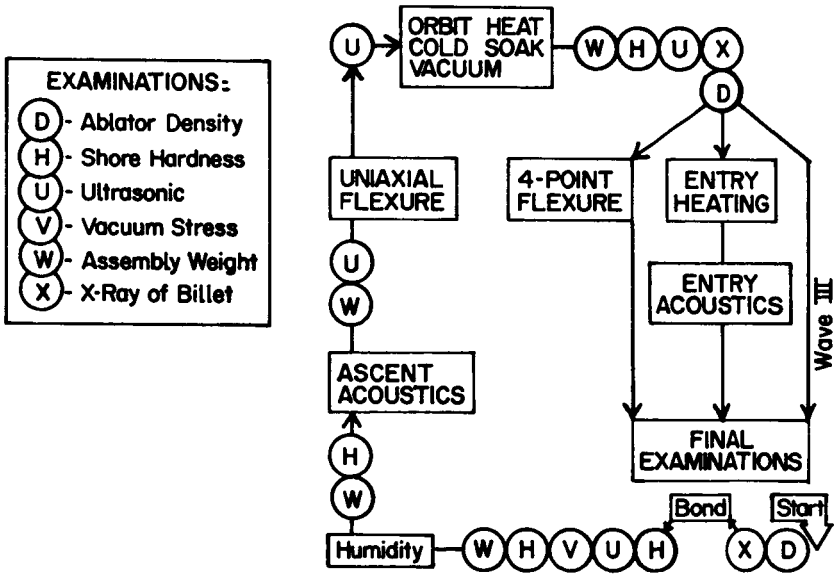


Figure 4 - Sequence of Environments and Examinations, Final Testing

Environment / Defect Stage	Cure		Density		Wet Basics		Under Mix		B-Staging		H. Cracks		Undercut Core		Dis-Bonds		Nodes		Ribbons	
	A	B	A	B	A	B	A	B	A	B	A	B	A	B	A	B	A	B	A	B
Humidity																				
Ascent Acoustics																				
Uniaxial Flexure																				
Thermal Vacuum			P7							P5										
Four Point Flexure	P1 P2		P1	P2	P2	P2	P1	P1	P2	P1	P2	P2	P1	P1						
Reentry Heating		E1								E3			E2 E3	E2 E3						
Descent Acoustics	E2 E6					E6			E6	E2 E3			E2 E3	E2 E3						
Cross Sectioning	E5	E5	E5 E7							E5	E7									

CRITICAL DEFECTS

Pre-Entry

P1 Low Strength
 P2 High Modulus
 P5 Fill Separation
 P7 Material Shrinkage

Entry

E1 High Backface Temperature
 E2 Material Losses
 E3 Surface Roughening
 E5 Internal Char Cracking
 E6 Loose Cell Surfaces
 E7 Deep Pyrolysis

▲ Definite
 △ Possible

Figure 5 - Summary of Critical Comments on Defects

N74-10267

**PROPERTIES OF A CLOSED PORE INSULATION
THERMAL PROTECTION SYSTEM***

A. Tobin, C. Feldman, M. Russak, and J. Reichman,
*Research Department, Grumman Aerospace Corporation,
Bethpage, New York 11714*

ABSTRACT

The need to develop a 100 mission reusable external thermal protection system for the Space Shuttle Orbiter has led to the development of a unique closed-cell glass ceramic foam insulation derived from sintering fly ash cenospheres in the presence of a high emittance binder. The outstanding characteristics of this material are: (1) rigidity, (2) water repellant structure, (3) high emittance, (4) machinability, (5) outstanding mechanical properties, and (6) good thermal shock resistance. Detailed design integration studies have led to the construction and testing of scaled-up heat shield panels which have survived re-entry cycling in Areas 1 and 2 of the Shuttle.

The need to develop a 100 mission reusable thermal protection system for the Space Shuttle Orbiter has led to the investigation of lightweight, refractory ceramic insulation materials. Recent activities have shown that promising low density silica fibrous insulations require complex brittle coatings to provide a water repellant, erosion resistant, high emitting surface because the substrate materials have low strength and readily absorb moisture.

To overcome these inherent problems associated with fibrous materials a unique closed-cell glass-ceramic foam insulation material (CPI = closed pore insulation) was developed from sintering low cost hollow alumino-silicate glass microspheres (obtained from fly ash residues) with high emittance binders. The outstanding characteristics of this material are: (1) rigidity, (2) water repellancy, (3) high emittance, (4) machinability, (5) superior mechanical properties when

*This work was partially sponsored by the NASA Langley Research Center under Contract No. NAS1-10713 and the Johnson Spacecraft Center under Contract No. NAS9-12781.

compared to rigidized fibrous insulations, and (6) good thermal shock resistance.

The processing variables are closely related to the mechanism of the foam formation. An optimum firing rate was necessary to form the closed cell structure since the forces of expansion of the residual gas entrapped within each cenosphere are balanced by the forces of contraction due to the sintering, viscous flow of the glassy shell, and atmospheric pressure. Final cell sizes are related to the temperature, time, and cobalt oxide additive. Increasing temperature and cobalt level led to increasing pore size (Fig. 1) and decreased softening point of the glass.

X-ray data indicated the presence of mullite, cobalt aluminate, and a residual glass phase. Tables 1 and 2 lists the principal thermo-physical properties of CPI tiles.

TABLE 1 TYPICAL PHYSICAL PROPERTIES OF CPI - 4% CoO

Microstructure	Network of Closed Cells
Color	Brown-Blue
Density (Kg/m ³)	640-720
Wt % Water Absorption	0.5-4
Average Pore Size	80 μ m
Available Sizes (cm)	20 x 20 x 2.5
Available Shapes	Flat Tile
Machinability	Machinable Ceramic Within 0.005 cm Tolerance

TABLE 2 CHEMICAL & THERMAL PROPERTIES OF CPI - 4% CoO

Chemistry	Al ₂ O ₃ , SiO ₂ , CoO, Fe ₂ O ₃ , TiO ₂
Chemical Stability	Inert to Most Reagents
Thermal Expansion	5.4 x 10 ⁻⁶ /K
Thermal Stability	No Disruptive Internal Changes on Cycling
Softening Point of CPI Glass	1310K
Emissivity (Uncoated)	0.63 - .65
Emissivity (Coated)	.82 - .88

Thermal expansion increased with cobalt additions due to the increasing concentration of cobalt aluminate in the glass. Total normal emissivity increased with cobalt additions over the range of temperatures investigated (RT-1500K). Emissivity

of CPI tiles was relatively independent of temperature. Increasing cobalt additions appeared to reduce the thermal conductivity of the foam at elevated temperatures. This may be due to the increased radiation absorption contribution of the cobalt ion in the glass. Theoretical calculations have shown that the radiation scattering and absorption component of the thermal conductivity are of the same magnitude (Ref. 1). This is in contrast to fibers where the scattering component dominates. In addition, solid conduction through the foam makes a substantial contribution to the total thermal conductivity.

Differential thermal analysis has shown no physical or chemical changes occurring over the range of temperatures investigated (RT-1700K).

To assess the possibility of employing these foams in a mechanical attachment scheme, a detailed characterization of the mechanical properties of CPI materials -- including elastic modulus tension, compression, flexure and shear at room and elevated temperatures -- was undertaken (Refs. 2 and 3). Figures 2 through 5 illustrate the general trends. Increasing cobalt oxide levels caused a reduction in the softening point of the glass, resulting in corresponding large decreases in elastic modulus and strength above 1135K with large increases in ductility. In fact, a large strain rate dependence of the strength was noted above 1175K. No significant degradation of strength properties was observed after 20 hrs of exposure in vacuum to 1380K. It should be noted that the strengths reported are one to two orders of magnitude higher than those reported for RSI materials. It was noted that CPI-4 had overall significantly superior mechanical properties than CPI-8 and CPI-12 for similar bulk densities (Fig. 6). This may be due to the finer and more uniform pore size of CPI-4 leading to a smaller probability of finding a critical flaw that will propagate to failure.

The significantly higher strength of CPI over conventional RSI materials is related to the continuous network of cell walls which can support a much larger load than a structure which is held together only at fiber intersections.

To assess the elevated temperature creep characteristics of CPI materials, a flexural creep apparatus was constructed which allowed measurements of the deflection of a flexural bar with varying continuous loads applied along its length. The deflections were recorded photographically while the specimens remained in the furnace. Creep deflections depended strongly on temperature, time and cobalt level; the lower cobalt level being the most creep resistant (Fig. 7). This is consistent with

the relationship between creep and glass viscosity

$$(\epsilon \sim \eta \sim A e^{-E/kT}).$$

In order to assess the ability of CPI materials to resist simulated re-entry heating, a radiant heat lamp and a plasma arc jet (Refs. 2 and 4) were employed. The radiant heat lamps were programmed to simulate the Area 1, Area 2, and Area 2P shuttle heating profile (Fig. 8). CPI plates of varying thickness (backed by low density fibrous insulation to simulate the correct heat transfer conditions) were tested (Ref. 2). The following observations were made: (1) the maximum thickness above which thermal stress cracks were observed was 1.25 cm; (2) CPI plates have withstood 920K temperature drops across their thickness without thermal stress failure; (3) a slight buckling of CPI plates occurred at higher cobalt levels and at higher temperatures during thermal cycling; (4) the effect disappeared at below 1275K for CPI-12, 1360K for CPI-8, and 1530K for CPI-4; (5) 1.25 cm plates of CPI-4 withstood 25 cycles of Area 2P re-entry exposure with no observable changes; (6) no observable degradation of thermal or mechanical properties of CPI-8 and CPI-12 was found after 25 cycles of re-entry exposure; (7) plasma arc jet tests of CPI materials have shown a slight discoloration of the surface possible due to cobalt evaporation from the surface.

Simulated salt spray exposure tests were conducted on 2.54 cm diameter CPI-4 disc samples, which had a cobalt rich surface layer (Ref. 5). A fine sea water mist was sprayed on the samples and dried to leave a salt residue. A sprayed and a control (unsprayed) sample were then cycled in an electric furnace to simulated area 2P re-entry heating. The test sample was re-sprayed after each cycle. As cycling progressed, a glazing effect was noted on the surface of the test specimen. This was evidenced by a deformation of the surface pore structure and was attributed to the fluxing effect of the alkali element present in salt mist deposited on the sample. After 20 cycles, several hairline surface cracks was observed, which accounted for an increase in water absorption of the sample from approximately 2.7% to 6.8%. Electron microprobe analysis indicated an increase in alkali concentration in the crack vicinity. The effect of this increased alkali level was to locally increase the thermal expansion of the CPI, in turn lowering the material's thermal shock resistance, giving rise to fine surface microcracking. Microprobe studies across the interface region near the crack showed an increase in sodium concentration, thus accounting for a higher local expansion area in the crack vicinity.

Rain erosion tests on CPI tiles were conducted at AFML-Bell Aerospace Rain Erosion Test Facility (Ref. 6). Angles of attack varied from 10° - 40° . Rain velocities varied from $32-64 \times 10^4$ m/hr for periods of up to 1 hr. Erosion weight losses were dependent on angle of attack and rain velocity; however, loss of surface material did not result in the destruction of the tile or loss in water proofness due to the monolithic nature of CPI (Ref. 7).

As the thermal shock resistance and the higher density of CPI became a major design constraint, it became clear that a "composite" type heat shield would be required in which the CPI surface was backed by a lower density efficient fibrous high temperature insulation, which was appropriately packaged. Such a design then reduces thermal shock by reducing the temperature gradients through the CPI and consequently reduces weight. Two basic variations evolved from these concepts: (1) a mechanically fastened heat shield (Fig. 9) and (2) a bonded heat shield (Fig. 10).

In Fig. 9 a CPI tile is supported on 4 superalloy studs which are "bonded" into the tile using a CPI washer-retainer. The studs fit into a sliding bushing, whose motion accommodates the thermal and mechanical stresses acting on the tile during launch and re-entry. A bag of lightweight insulation fits under the CPI tiles which are pierced by the superalloy studs and is mechanically fastened to the primary structure. This design features a fail-safe capability along with increased ease of inspection, replacement and removal. In the second concept (Fig. 10), a thin plate 0.25 cm of CPI is bonded on to a rigidized block of insulation (Kaowool or mullite) whose sides are packaged in a thin superalloy foil. This concept is analogous to the RSI concept except that the CPI provides a thicker, more rugged and durable surface, while the foil packaging around the sides simplifies routine inspection to examination of the surface.

These concepts have been tested using scaled-up models in the radiant heat lamp facility in Area 1, Area 2, and Area 2P. Results indicate that more detailed design is required at the attachment points as excessive oxidation of the metallic parts during cycling prevented the freedom of motion of the CPI tile, causing a local buildup of stresses at the support points. This resulted in a slight buckling of the CPI tile.

For the bonded concepts it was found that the rigidized fibrous materials (Kaowool and mullite) did not possess the required thermal shock resistance in themselves to survive the Area 2 and Area 2P re-entry cycling. Failure in the fibrous

insulation occurred at points of maximum thermal stress during re-entry heating. Further work is needed to improve the thermal shock performance of the rigidized fibers.

References

1. Tobin, A., Feldman, C., Russak, M. and Reichman, J., "Development of a Closed Pore Insulation Material," NASA Contract CR-2254, 1972.
2. Varisco, A., Tobin, A., Harris, H. G., "Development and Design Applications of a Closed Pore External Thermal Protection System," NASA Contract NAS 9-12781 (1972).
3. Feldman, C., and Russak, M., "Further Characterization of a Closed Pore Insulating Material," NASA Langley Contract Extension NAS 1-10713 (1973), CR-11295.
4. Geschwind, G., Hershaft, A., Hoff, M. and Jenkins, R., "Environmental Testing of Closed Pore Insulation-I-Arc Jet Testing," Grumman Research Memorandum RM-565 (1973).
5. Feldman, C., and Russak, M., "Environmental Testing of Closed Pore Insulation-II-Salt Spray Testing," Grumman Research Memorandum RM-570 (1973).
6. Wahl, N., "Rain Erosion Characteristics of Thermal Protection System Materials at Subsonic Velocities," AFML-TR-72-145 (1972).
7. Russak, M., "Environmental Testing of Closed Pore Insulation-III-Rain Erosion," Grumman Research Memorandum RM-573.

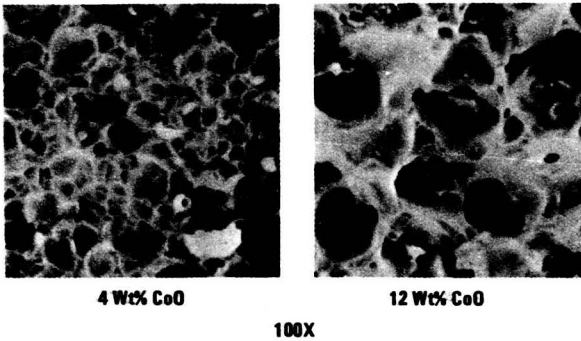


Fig. 1 SEM Photographs of Sintered Cenosphere Bodies Fired at 1650K for 1 Hour

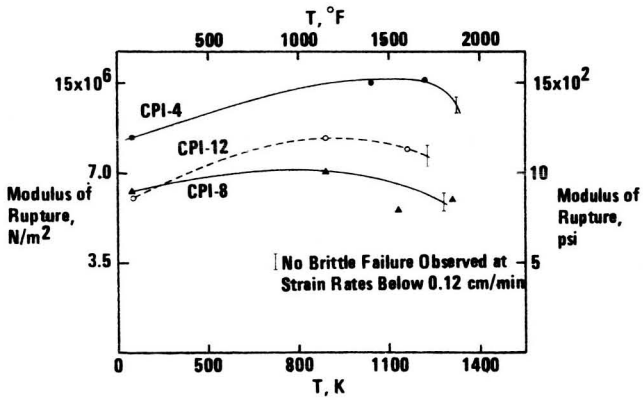


Fig. 2 Elastic Modulus vs Temperature for Three CPI Materials

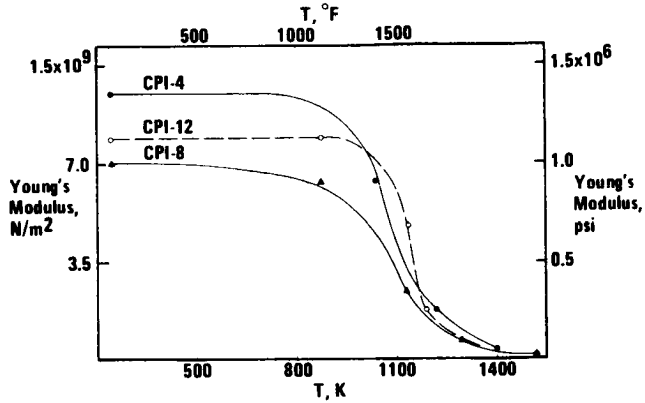


Fig. 3 Modulus of Rupture (Flexure) vs Temperature for Three CPI Compositions

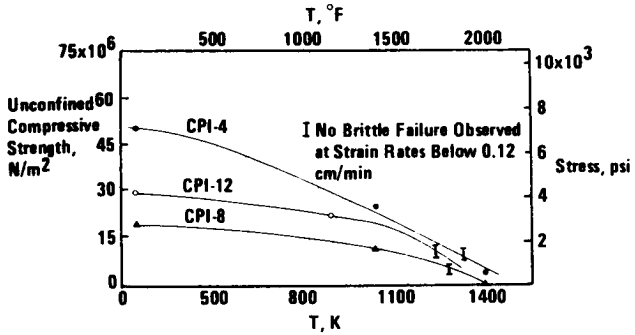


Fig. 4 Compressive Strength vs Temperature for Three CPI Compositions

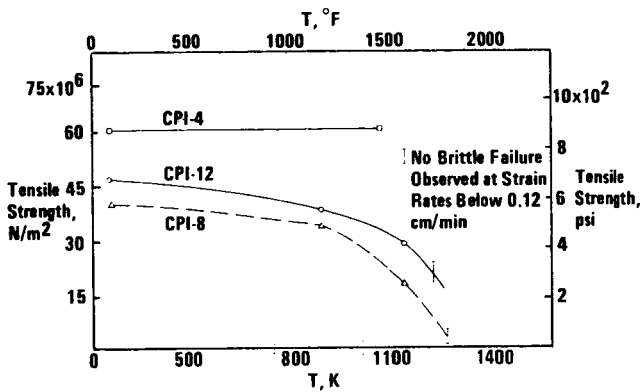


Fig. 5 Tension Strength vs Temperature for Three CPI Compositions

COMPARISON OF ROOM TEMPERATURE MECHANICAL PROPERTIES OF CPI MATERIALS

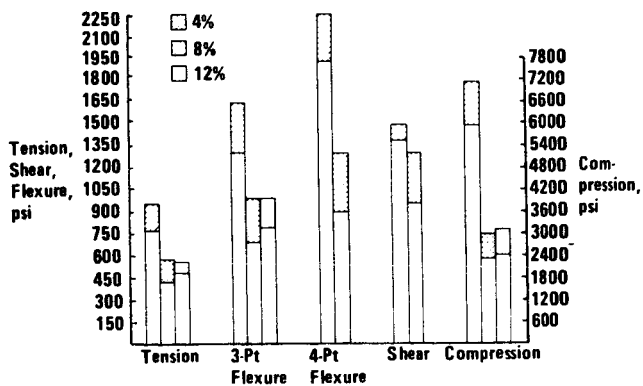


Fig. 6 Comparison of Room Temperature Mechanical Properties of CPI Materials

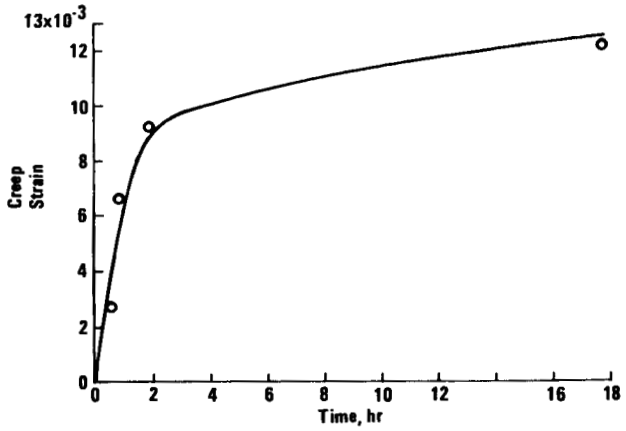


Fig. 7 Flexural Creep Strain vs Time for CPI-8 at 1800°F

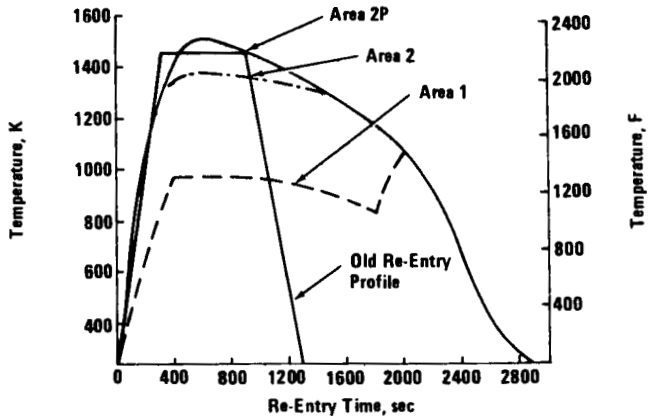


Fig. 8 Modified Re-Entry Thermal Profile

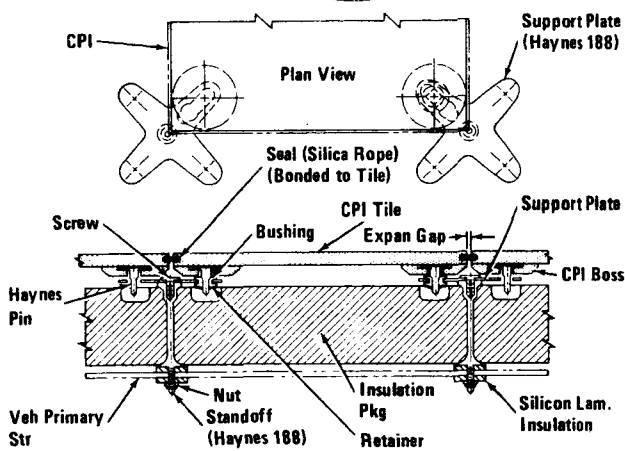


Fig. 9 CPI/Mechanically Supported

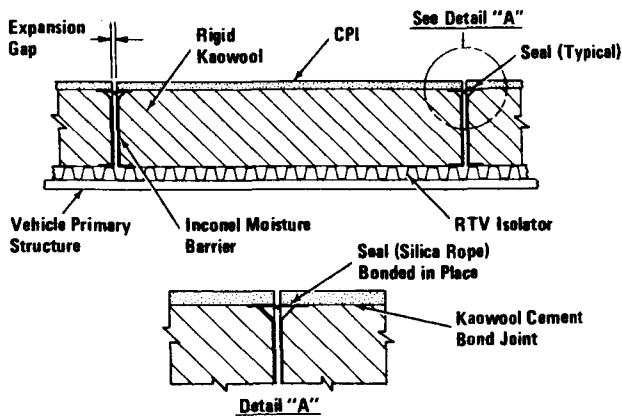


Fig. 10 CPI/Kaowool Bonded Concept

NTM-10270

PRECEDING PAGE BLANK NOT FILMED

Paper No. 42

ABLATIVE HEAT SHIELD DESIGN FOR SPACE SHUTTLE

R. W. Seiferth, *Martin Marietta Aerospace, Denver, Colorado*

Information in this paper resulted from work conducted under NASA Contract NAS1-11592.

ABSTRACT

Ablator heat shield configuration optimization studies were conducted for the Orbiter. Ablator and RSI trajectories for design studies were shaped to take advantage of the low conductance of ceramic RSI and high temperature capability of ablators. Comparative weights were established for the RSI system and for direct bond and mechanically attached ablator systems. Ablator system costs were determined for fabrication, installation and refurbishment. Cost penalties were assigned for payload weight penalties, if any. The direct bond ablator is lowest in weight and cost. A mechanically attached ablator using a magnesium subpanel is highly competitive for both weight and cost.

INTRODUCTION

Ablators are a well-established system of thermal protection having been employed on vehicles such as Apollo, Gemini, Viking, X-15, Titan, PRIME and others. The need for ablator refurbishment following each flight is a drawback of this thermal protection system and has led NASA and industry into the development of reusable ceramics (RSI). The RSI system of thermal protection has been baselined for use on the Shuttle Orbiter.

Much work needs to be done to qualify the RSI for space shuttle application and, to quote E. S. Love from the Tenth Von Karman Lecture, "Ablators offer a confident fall-back solution (temporary) for both leading edges and large surface areas, should development of the baseline approaches lag."

In the past, ablator systems have been bonded directly onto the structures they are designed to protect. While this approach is both low in weight and cost effective, it has the drawback for the Shuttle Orbiter of taking up critical turn-around time for refurbishment between flights, and during refurbishment creates a problem of debris and dust control.

The purpose of this program was to investigate Shuttle Orbiter TPS design concepts utilizing available state-of-the-art ablators. An end objective of the program was to obtain ablator TPS weight and cost estimates based on detailed, verified heat shield designs. RSI cost estimates were not part of this program. Direct bond ablator and RSI designs were prepared for weight comparison purposes. The bulk of the effort has dealt with methods of mechanically attaching prepared ablator panels onto the Orbiter. Radiant heat tests were conducted to verify the design concepts.

The program was divided into five tasks:

- Task 1 - Design Criteria;
- Task 2 - Flight Environment;
- Task 3 - Heat Shield Designs;
- Task 4 - Design Verification;
- Task 5 - Weight and Cost Analysis.

DESIGN CRITERIA (TASK 1)

Design criteria was prepared in order to develop valid heat shield configurations for the total environment from prelaunch through reentry and landing. Criteria was prepared for the trajectory definition and for the thermal and stress analysis.

Factors of Safety

Safety factors on loads and pressures for prelaunch through deorbit are based on engineering practice developed for boosters and spacecraft and for entry and atmospheric flight, and are those commonly used in the design of aircraft.

FACTORS OF SAFETY			
Location	Ultimate Design Condition	Ultimate or Design Factor of Safety (X)	Limit Load or Nominal Heating Load
Total Orbiter	Through Orbit	1.4	Limit Load
Total Orbiter	Entry	1.5	Limit Load
Leading Edges and Lower Forward Surfaces	Ascent and Entry	1.15	Nominal Heating Load
Lower Surfaces Aft		1.25	
Upper Surfaces		1.50	

Backface (Structural) Temperature Limits

Ablator Bond Line	500°F
Maximum Structural Temperatures	
At Start of Entry	100°F
At Completion of Entry	350°F

Ablator Strain Limits

Ablators are low strength (< 70 psi at room temperature) and low modulus (< 3,000 psi at room temperature) materials in the virgin form with unspecific mechanical properties after charring. The following induced strain limits have been developed for the Viking program:

	<u>Virgin</u>	<u>Charred</u>
Tension Strain (in./in.)	1.0%	0.6%
Compression Strain (in./in.)	1.0%	1.0%

Strength Analysis

The ablation material shall not be considered load carrying but shall be included in thermal and mechanical deflection analysis to determine the strain in the ablation material. The sub-panel shall be capable of carrying design loads without the ablator, and without exceeding the following surface waviness deflection criteria:

H = 0.0125L Limit	L = Panel Wave Length;
	H = Maximum Deflection (wave height)

FLIGHT ENVIRONMENT (TASK 2)

Orbiter flight environments were defined for the boost, orbit and entry conditions. Airloads and thermal histories were established including interference heating during ascent. Heating load distributions accounted for the variances in time at which transition from laminar to turbulent flow occurs. Flow transition near the fuselage nose and wing leading edge occurs several hundred seconds following peak heating. Transition from laminar flow was considered to occur when

$$\frac{Re_{\theta}}{M_L \left(\frac{Re_L}{X} \right)^{0.2}} = 10$$

where: Re_{θ} = local Reynold's number based on momentum thickness
 M_L = local Mach number
 Re_L/X = local unit Reynold's number

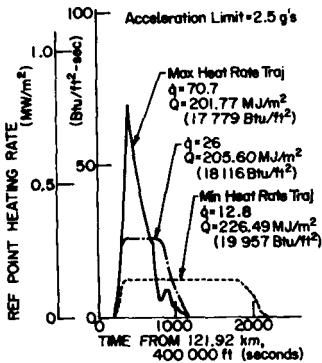
Fully turbulent flow was assumed to occur at a location twice the length of the transition onset length.

The Orbiter heating load distributions were normalized to reference point selected as 50 feet aft of the fuselage nose on bottom centerline.

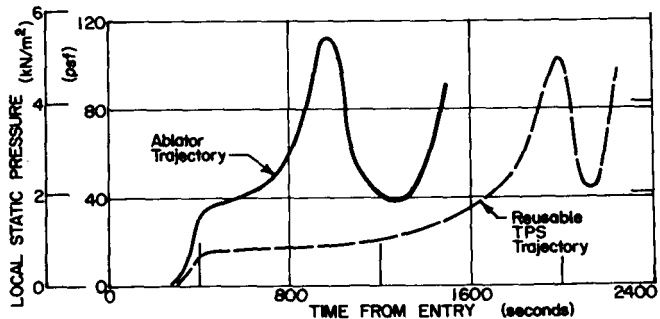
Trajectory Shaping

Design entry trajectories were established for the ablator TPS and the RSI TPS. The ablator trajectory was shaped to take advantage of ablator's high heating rate capability. The maximum heat rate trajectory within the acceleration limit of 2.5 g's yields a $\dot{q} = 70.7$ BTU/ft²-sec at the reference point. With a thermal design factor of safety of 1.15, the design heat rate equals 81.3 BTU/ft²-sec. Since SLA-561 ablator is limited to a maximum heating rate of 60 BTU/ft²-sec, the entire lower surface of the Orbiter would require the higher densities of ESA-3560HF

and ESA 5500. Reducing the entry angle and heating rate to 26 BTU/ft²-sec at the reference point permits use of low density SLA-561 over 98% of the Orbiter surface area. The $\dot{q} = 26$ BTU/ft²-sec at the reference point was therefore designated as the ablator design trajectory. The RSI trajectory was shaped to take advantage of the ceramic TPS low thermal conductivity for total heat insulation. By reducing entry angle to the skip-out limit, heat rate is minimized and total heat maximized resulting in an efficient RSI TPS design. Local static pressure histories were prepared for the Orbiter for ascent and entry. These pressures are used for the ablator subpanel design.

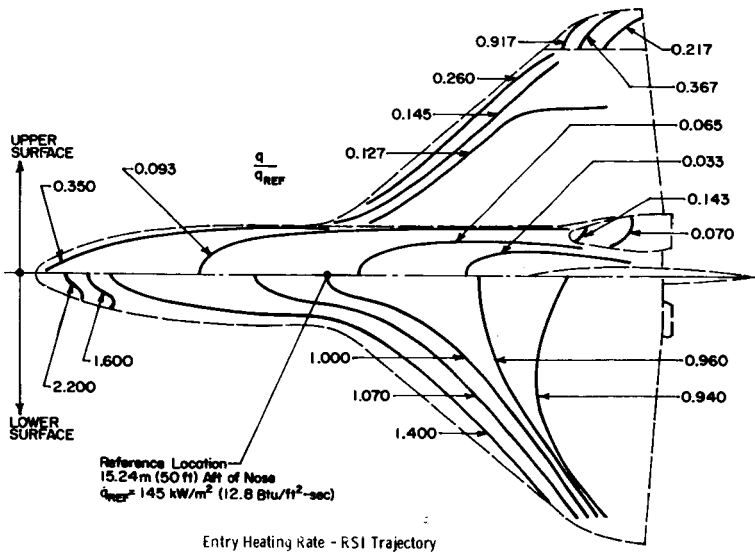
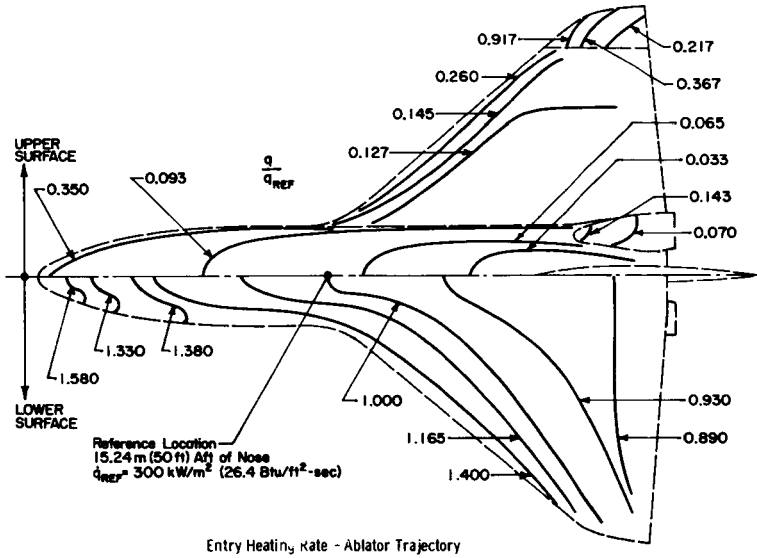


Trajectory Shaping



Entry Local Static Pressure History at Body Lower Centerline Reference Location

Heating Rate Distributions--Heating rate distributions normalized to the reference point at the lower fuselage centerline 50 feet aft of the fuselage nose were prepared for the ablator and RSI trajectories.



HEAT SHIELD DESIGNS (TASK 3)

The contractual program investigated eight locations on the Orbiter to establish heat shield configurations, weights and costs. This paper will concern itself with one location--the reference point, 50 feet aft of the fuselage nose on the lower surface centerline.

The baseline method of ablator attachment was considered to be the direct bond. Alternate configurations investigated were:

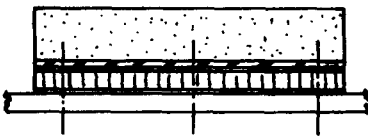
1. Ablator bonded to a subpanel plate and mechanically attached directly to the Orbiter structure;
2. Ablator bonded to a subpanel honeycomb panel and mechanically attached directly to the Orbiter structure;
3. Ablator bonded to a subpanel honeycomb panel and mechanically attached through standoff fittings to the Orbiter structure.



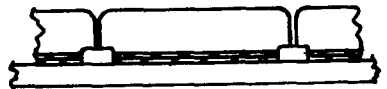
Plate Subpanel
Aluminum 2024-T81
Lockalloy
Magnesium HM-21A



Ablator Direct Bond
Baseline



Honeycomb Subpanel
Aluminum 2024-T81
Magnesium HM-21A
Graphite Polyimide



RSI Direct Bond
Through Strain Isolator



Honeycomb Standoff Subpanel
Aluminum 2024-T81
Graphite Polyimide

Each configuration was examined for 5, 10, 15 and 20 inch attachment spacing for weight and cost optimization. In addition, four materials of construction for the subpanel were studied: aluminum 2024-T81, Lockalloy, magnesium HM-21A, and graphite polyimide.

Thermal Analysis

Thermal analysis for ablator sizing was carried out with the Martin Thermochemical Ablation Program (TCAP III). Data input to this program includes trajectory data; i.e., velocity, altitude, heating rate, recovery enthalpy; thermophysical properties for the ablator material and backup structure materials; ablation kinetics; and geometry of the model being analyzed. Analysis results include time-temperature distributions throughout the model and a time-density profile through the ablative material.

Analysis for sizing the RSI material and for developing backup structure modeling techniques was carried out with the Martin Three Dimensional Heat Transfer program. Data input and analysis results are similar to TCAP III with the exception that no considerations are made for an ablation process. Both programs allow for variations of conductivity with pressure as well as temperature.

Ablator thickness design charts were prepared for the ablator trajectory assuming an entry start temperature of 100°F and limiting the maximum structural temperature after entry to 350°F.

Given $\dot{q}/\dot{q}_{ref} = Q/Q_{ref}$, using the heating rate distribution charts

and computing $\sum_i^n t \rho C_p$, the ablator thickness can be determined for any point on the Orbiter surface. $\sum_i^n t \rho C_p$ is the total heat capacity of the local Orbiter structure, the subpanel and the ablator bond line.

EXAMPLE: At the reference point, determine ablator thickness for an aluminum subpanel, $t = .031$

Orbiter Structure, .103 aluminum $\rho = 0.100$; $C_p = .225$

Ablator Bond, .030 RTV $\rho = 0.054$; $C_p = .300$

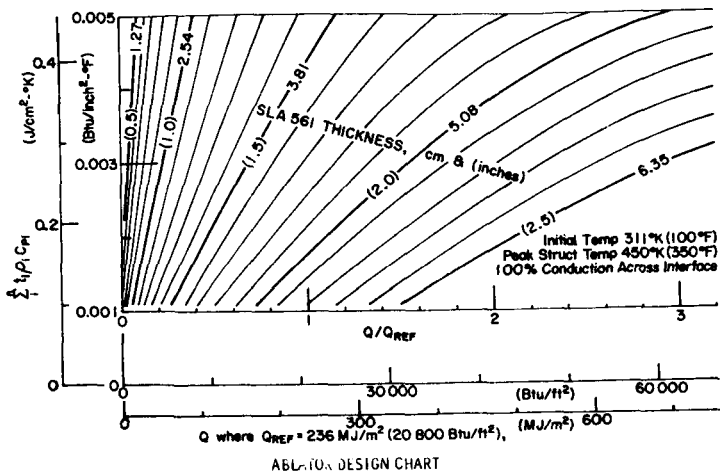
Subpanel, .031 aluminum $\rho = 0.100$; $C_p = .225$

$$\sum_i^n t \rho C_p = (.103)(.100)(.225) + (.030)(.054)(.300) \\ + (.031)(.100)(.225) = .00351$$

Enter the design chart with $\sum_i^n t \rho C_p = .00351$ and $Q/Q_{ref} = 1$ and read Thickness SLA-561 = 1.63 in.

Stress Analysis

The plate and honeycomb subpanels are designed by local aerodynamic airloads. Orbiter structural strains are isolated from



the subpanels by using a mechanical fastener in an oversized hole. The strains and deflections of the subpanels must be limited to prevent induced strains in the ablator from exceeding 1% and to limit surface waviness to less than 0.0125 times the attachment spacing. Subpanel overall dimensions are limited by handling capabilities. A 42 inch by 42 inch panel size was selected for this program. Since total heat shield weight and cost optimizes with small attachment spacing (less than 10 inches), the analytical methods for internal loads predictions were selected from "Theory of Plates and Shells" by Timoshenko, and Woinowski-Krieger, "Bending of Plates Supported by Rows of Equidistant Columns."

Allowable Loadings--The subpanel plates are checked for thickness limitations to meet deflection requirements and moment limitations to meet ablator strain limits. Both of these are a function of support spacing.

$$\text{Deflection Limit} \leq 0.0125 \ell$$

$$\text{From Timoshenko deflection} = \frac{.00581 q \ell^4}{D}$$

$$\text{Combining and simplifying, } t \geq .0062 \ell$$

$$\text{Ablator Strain Limit} \leq 1\% \text{ (during ascent)}$$

$$\epsilon = \frac{\text{Moment} (1 - \mu^2) (\bar{y})}{EI}$$

where \bar{y} is distribution from neutral axis of plate to ablator surface and I is for plate only.

$$\text{Allowable moment} = \frac{(0.01)EI}{(1 - \mu^2)(\bar{y})} \quad \text{with } \epsilon = 0.01$$

Honeycomb subpanels must also be checked for face wrinkling and intracell buckling.

$$\text{Face wrinkling moment} = (0.33) \left[(E_c)(E_f)(t_{\text{core}}) \right]^{1/2} (t_{\text{face}})^{3/2}$$

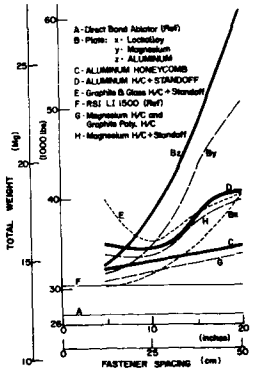
Example Heat Shield Configurations at Reference Point

l	Direct Attached Aluminum Plate 2024-T81			Direct Attached Aluminum Honeycomb 2024-T81				Standoff Aluminum Honeycomb 2024-T81			
	Subpnl. Thick-ness	Abl. Thick.	Crit. For	Face Thick.	Core Height	Abl. Thick.	Crit. For	Face Thick.	Core Height	Abl. Thick.	Crit. For
5	.031	1.74	∅	.005	.030	1.86	MIB	.005	.180	1.50	MIB
10	.062	1.64	∅	.005	.190	1.86	MIB	.007	.480	1.47	MAS
15	.148	1.51	MAS	.006	.300	1.85	MIB	.009	.900	1.44	MFW
20	.228	1.41	MAS	.007	.420	1.82	MAS	.014	.990	1.41	MAS

∅ Deflection
 MAS Ablator Strain Moment
 MIB Intracell Buckling Moment
 MFW Face Wrinkling Moment

Total Heat Shield Configuration Weights

Using the method illustrated for the reference point, heat shield configurations were determined for other materials and locations on the Orbiter and the total heat shield weights plotted against fastener support spacing.



TPS Attachment Configuration on Weight vs Fastener Spacing

DESIGN VERIFICATION (TASK 4)

A test program was conducted to evaluate the mechanically attached heat shield concept. The aluminum subpanel system at 10 inch fastener spacing was selected as being representative of most of the direct mechanically attached configurations. Testing was performed in three parts.

VERIFICATION TEST PROGRAM		
Test	Specimen	Objective
Ablator Panel Open Gap	SLA-561 Ablator on Aluminum Subpanel, 10 inch Fastener Spacing. Size: 22 in. x 44 in.; Gap Size: 0.070 in.	Verify: 1. Open Gap Concept 2. Fastener Design 3. Temperature Distribution in Fastener Cavity
Gap Sealer	Fiberfrax Rope, 1/4 inch diameter; Fiberfrax Blanket	Determine resiliency in thermal environment.
Ablator Panel Sealed Gap	SLA-561 Ablator on Aluminum Subpanel, 10 inch Fastener Spacing. Size: 22 in. x 44 in.; 0.80 inch Fiberfrax Blanket Sealer	Verify: 1. Sealed Gap Concept 2. Fastener Design 3. Temperature Distribution in Fastener Cavity

Open Gap Test--Ablator panels can be installed with a limited width gap at the joint between adjacent panels (1/8 inch for 42 inch x 42 inch panels). Due to the thermal coefficient of expansion of the ablator, the gap closes with increasing temperature limiting aerodynamic heating at the bottom of the gap. The entry heating pulse was simulated using radiant heat lamps. Although heating was not uniform, some gap closure with acceptable temperature limits at bottom of gap was noted. The attaching fasteners tended to bind, inhibiting free thermal motion of the subpanel. Temperature in the fastener cavity in the ablator was not excessive.

Gap Sealer Tests--Candidate materials were tested in ovens under deformation at elevated temperatures. Springback or recovery of deformation following temperature reduction was measured. Five percent to ten percent springback was desired following heating. Only the Fiberfrax blanket compressed normal to fiber direction was satisfactory.

Sealed Gap Test--Ablator panels can be installed with a sealer in the joint between adjacent panels. During ascent heating the gap closes partially, then opens while in orbit, closing again at entry. The selected sealer was Fiberfrax blanket, which is resilient enough to take these thermal cycles. The test panel was exposed to ascent and entry heating using radiant heat lamps. The sealer did not perform satisfactorily since temperatures were higher in the bottom of the gap than under the ablator. Fiberfrax blanket is stratified and the thermal conductivity is therefore transversely isotropic with the low values across the gap and the high values parallel to the gap.

WEIGHT AND COST ANALYSIS (TASK 5)

This program has developed design concepts and weight data for several competing methods for ablator attachment to the Orbiter structure. It remains only to select the best attachment system on a weight and cost basis. Competing heat shield weights were converted to costs and added to operational costs to establish the total program costs. The ablator configuration choice on the basis of minimum program costs thus includes the effect of heat shield weight.

Payload Weight Penalties

To aid in the optimum ablator heat shield selection, an ablator heat shield was assumed for the first five years or 151 flights of Shuttle operations--1979 through 1983. The payloads planned for that period were identified from the "Preliminary Traffic Model for the Space Shuttle", November 9, 1972 by MSFC. Each of the competing heat shield design weights was compared to the payloads of the traffic model and payload weight penalties, if any were determined. To ascribe a dollar value to these weight penalties, a cost per pound to orbit was derived. All program costs were apportioned against all the payload weight. A DDT&E cost of \$5,150M was apportioned to 445 flights for a cost per flight of \$11.57M or \$1,747.5M for the first 151 flights. Added to this is an operational cost of \$10.5M per flight or \$1,585.5M for the first 151 flights. The total cost for the first five years of 151 flights is \$3,333M. The first 151 flights carry a total of 4.56M lbs of payload. Dividing \$3,333M by 4.56M lbs yields a cost per pound to orbit of \$731/lb. This does not include the costs of the payloads themselves.

The payload weight penalties for each of the competing ablator systems was multiplied by this cost per pound to orbit of \$731/lb and added to the operational costs of each ablator system to establish a total program cost. The RSI heat shield weight was used as a baseline to establish payload weight penalties. In many cases, the full payload weight capability of the Orbiter was not utilized due to volume constraints. This reduced payload was utilized in establishing payload weight penalties. For example:

THREE MISSIONS OF THE 1981 PERIOD			
Flight Number	15	18	20
Payload Capability	65,000	45,000	45,000
Actual Payload	-20,150	-17,100	-37,450
Unused Capability	44,850	27,900	7,650
RSI Heat Shield	30,240	30,240	30,240
Available Heat Shield Weight	75,090	58,140	37,890
Ablator Direct Attached by Aluminum Plate at 15"	-48,782	-48,782	-48,782
Payload Weight Penalty	0	0	-10,892
Payload Penalty Cost at \$731/lb	0	0	\$7.96M

All the payload penalties for all flights were added resulting in \$364M cost penalties for the aluminum subpanel with 15 inch spacing.

Operational Costs--Operational costs are the fabrication, refurbishment and quality assurance tasks incurred during the 151 flight program. These costs include:

- Ablator slab raw materials and fabrication including scrappage (this accounts for 3/4 of the operational cost);
- Subpanel raw materials and assembly costs, including scrappage;
- Assembly of ablator slab to the subpanel;
- Installation of ablator panel assembly--tools and labor;
- Removal of used ablator panels--tools and labor;
- Repair materials and labor due to damage from handling during packing, shipping, storage and installation;
- Bond line inspection;
- Mechanical fastener inspection;
- Subpanel fabrication inspection;
- Refurbishment cleanliness inspection;
- Inspection for damage following ablator installation;

• Inspection of repaired areas.

The total operations costs show the direct bond heat shield and the aluminum and magnesium subpanel mechanically attached heat shields to be very competitive with the 10 inch spacing subpanels having the lowest cost primarily due to the reduction in ablative materials required and lower installation costs due to smaller numbers of fasteners.

Total Program Costs--The inclusion of the heat shield weight as a payload weight penalty costs has a direct effect on determining the optimum heat shield selection. The direct bond system has the lowest total program cost followed closely by the magnesium and aluminum subpanel plate systems at 5 inch fastener spacing. The low operational cost magnesium and aluminum subpanels at 10 inch spacing are prohibitively heavy as is shown by the \$34.9M and \$76.9M payload weight penalties. For the direct bond system, the effect of dust and debris and turn-around time was not evaluated.

Considering these items qualitatively, the slightly higher cost, direct attached magnesium and aluminum plate systems at 5 inch fastener spacing are attractive alternates. The selection of mechanically attached heat shields must be made prior to Orbiter CDR to permit inclusion of anchor nuts into the basic design. The addition of this fastener hardware following the original engineering release becomes increasingly difficult and at the point where Orbiter hardware has been fabricated without heat shield anchor nuts, adding them becomes prohibitive.

OPERATIONAL COSTS (\$M) - FIVE YEARS - 151 FLIGHTS								
Configuration		Ablator Slab	Sub-Panel	Panel Ass'y	Install. and Removal	Repair	Qual. Assur.	Total
Subpanel	Fastener Spacing							
Direct Bond	N. A.	125.7	-	-	27.9	4.4	6.8	164.8
Aluminum Plate	5 inches	120.7	1.2	8.7	21.9	6.6	9.2	168.3
Magnesium Plate		122.1	1.8	8.7	22.4	6.8	10.0	173.8
Lockalloy Plate		120.7	31.1	10.4	25.6	6.8	10.6	205.2
Aluminum Honeycomb		124.9	8.7	8.7	25.7	7.0	12.1	187.1
Magnesium Honeycomb		121.8	12.2	8.7	28.1	6.9	13.0	190.7
Graphite Composite Honeycomb		122.3	15.0	8.7	25.7	6.8	12.0	190.5
Aluminum Plate		10 inches	117.2	1.1	8.5	15.2	6.2	6.5
Magnesium Plate	116.2		1.9	8.5	16.7	6.2	7.1	156.6
Lockalloy Plate	116.3		49.1	10.2	17.9	6.3	7.7	207.5
Aluminum Honeycomb	124.9		7.8	8.5	18.0	6.7	9.0	174.9
Magnesium Honeycomb	121.8		12.0	8.5	19.4	6.6	9.6	177.9
Graphite Composite Honeycomb	122.3		17.2	8.5	18.0	6.6	9.1	181.7

TOTAL PROGRAM COSTS (\$M) - FIVE YEARS - 151 FLIGHTS					
Configuration		Heat Shield Weight (lbs)	Payload Weight Penalty	Operational Costs	Total Program Costs
Subpanel	Fastener Spacing				
Direct Bond	N.A.	27,199	0	164.8	164.8
Aluminum Plate	5 inches	32,577	10.6	168.3	178.9
Magnesium Plate		31,602	3.6	173.8	177.4
Lockalloy Plate		30,092	0	205.2	205.2
Aluminum Honeycomb		32,158	7.3	187.1	194.4
Magnesium Honeycomb		30,882	0.5	190.7	191.2
Graphite Composite Honeycomb		30,994	0.6	190.5	191.1
Aluminum Plate		10 inches	37,803	76.9	154.7
Magnesium Plate	34,738		34.9	156.6	191.5
Lockalloy Plate	31,549		3.3	207.5	210.8
Aluminum Honeycomb	32,749		12.0	174.9	186.9
Magnesium Honeycomb	31,811		5.0	177.9	182.9
Graphite Composite Honeycomb	31,772		4.7	181.7	186.4

DISCUSSION OF PROGRAM RESULTS

Based on heat shield weight alone, the first six lowest weight ablator systems are ranked:

- Direct Bond 27,199 lbs
- Lockalloy Subpanel at 5 inches 30,092 lbs
- Magnesium Honeycomb at 5 inches 30,882 lbs
- Graphite Composite Honeycomb at 5 inches . 30,994 lbs
- Lockalloy Subpanel at 10 inches 31,549 lbs
- Magnesium Plate at 5 inches 31,602 lbs

Based on total program costs, the first six ablator systems are ranked:

- Direct Bond \$164.8M
- Magnesium Plate at 5 inches \$177.4M
- Aluminum Plate at 5 inches \$178.9M
- Magnesium Honeycomb at 10 inches \$182.9M
- Graphite Composite Honeycomb at 10 inches . . \$186.4M
- Aluminum Honeycomb at 10 inches \$186.9M

The only repeaters in both lists are the direct bond and the magnesium plate subpanel at 5 inch attachment spacing.

While the direct bond ablator has the lowest heat shield weight and program cost, the concerns with dust control and minimization of turn-around time during the refurbishment period makes the second alternate attractive. Magnesium HM-21A subpanel at 5 inch fastener spacing is less than 5% heavier than the base-lined RSI and only 8% higher in total program cost than the direct bond heat shield.

The decision of interim ablator usage should be made prior to Orbiter CDR to permit incorporation of ablator subpanel fastener hardware into the Orbiter structure. A late decision for interim ablator usage will make ablator heat shield attachment other than direct bond progressively more difficult and expensive.

Paper No. 43

**EVOLVEMENT OF A SPRAYABLE ABLATOR FOR
THERMAL/CRYOGENIC APPLICATIONS**

J. W. Maccalous, *Martin Marietta Aerospace, Denver, Colorado*

ABSTRACT

This paper presents the sequential development of an elastomeric based ablative material which is contained in an all sprayable heat shield system-- primer, adhesive interlock, sprayable ablator and protective coating. Application methodology is compared with previously evolved systems for programs such as PRIME (single cell injection), X-15 (spray) and Viking (multi-cell mold) and cost deltas discussed. Methods of "in-process" controls and critical parameters will be discussed as will a comparison of room temperature versus oven curing ablative systems.

Pertinent physical property data obtained at elevated, room and cryogenic temperatures will be presented including density, tensile, strain, bond tension, hardness, and so forth. As this testing is currently in progress, data is not given here, but will be included in the finalized paper. Qualitative testing of test articles up to ten feet in diameter at LH_2 temperatures will be discussed and results presented.

PRECEDING PAGE BLANK NOT FILMED

Paper No. 44

A STUDY OF ABLATOR PRODUCIBILITY AND
REFURBISHMENT METHODS

William E. King, Jr., *Martin Marietta Aerospace,*
Denver Division, Denver, Colorado

ABSTRACT

This paper describes a study of fabrication, installation, and removal methods for ablative thermal protection systems that was conducted using a lifting-body space vehicle airframe as a full-size demonstration test bed for prototype hardware.

INTRODUCTION

The Space Shuttle Orbiter must withstand surface temperatures during ascent and entry that can exceed 3000°F in some areas. Ablative heat shields are potential backup candidates for protecting the spacecraft's metal structure from this environment, but with the repeated use of the Shuttle vehicle, the unit cost of ablators must be reduced to make them competitive with other systems. These efforts have been concentrated on reducing fabrication costs and simplifying replacement. Previous studies have shown that although the lightest installation method is direct bonding, where the ablator is bonded directly to the orbiter structure, refurbishment time and costs for this approach are excessive. Accordingly, the goals of this study were to improve the producibility of the basic ablator, to develop more efficient refurbishment methods for the direct bonded system, and to determine the effects of these improvements on the cost of the Space Shuttle program.

APPROACH

The Martin Marietta SLA-561 ablator was selected as the baseline material for this study since it has been fully characterized on the Viking program and is a suitable material for Shuttle application. This system consists of an elastomeric silicone ablator supported in a glass-phenolic honeycomb core matrix and bonded to the vehicle structure.

The large size of the Shuttle vehicle precludes the use of conventional ablator application methods, such as those used on PRIME and Viking. In these programs, the core was bonded to the vehicle using high-temperature adhesive and the entire vehicle was placed in a vacuum bag and cured in an oven under vacuum pressures. After curing, the core was hand-filled with the

uncured ablator mix and the vehicle was again placed in a vacuum bag and cured in an oven under vacuum pressures. Then the excess was hand-machined until the proper ablator thickness was obtained. In contrast, the only practical approach for Shuttle is to apply the ablator in segments (such as prefabricated and cured panels of the proper thickness) using room-temperature-curing adhesives that require very low pressures. This approach has been demonstrated to be satisfactory in terms of thermostructural reliability during development of the Viking heat shield, as well as on other IR&D programs. Using this approach as a baseline, we established a program to study and improve the producibility of the basic SLA-561 ablator, develop more efficient refurbishment methods, and determine the effects on the cost of the Space Shuttle program.

In an effort to conduct meaningful ablator fabrication and refurbishment demonstrations, the Martin Marietta SV-5J (X-24 configuration) lifting body vehicle (Fig. 1) was used as a representative flight vehicle structure. Three ablative panels with compound curvature (totalling 22.5 sq ft) were fabricated and installed on the vehicle, and fabrication costs were generated and projected to the Shuttle program.

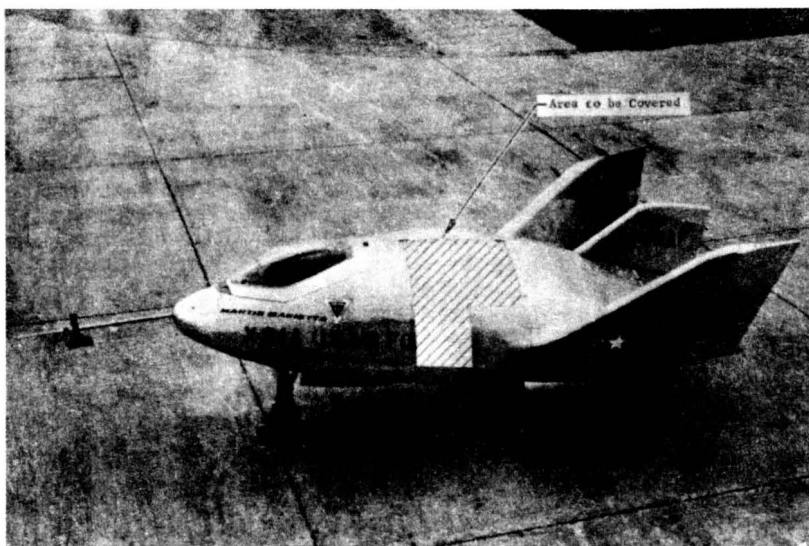


Fig. 1 SV-5J Area to Be Covered

FABRICATION

All previous methods for packing honeycomb core had relied on high localized pressure to force ablative material into the cells. Rivet guns and multiple autoclave pressure cycles were generally used in an effort to load the panels to the desired

density. Combinations of hand packing and auxiliary pressure always resulted in severe lateral and in-depth density gradients because of the poor flow characteristics of the material. However, even with these methods the typical density gradients were approximately 3 lb/ft^3 (pcf) through the thickness of a 2-in. panel, and over 1 pcf across the surface. In addition, voids occurred throughout the material and were difficult to control.

To overcome this situation, we developed a method that reverses the procedure and vibrates the core into the prepacked ablator mix while controlling the density gradients to within ± 0.5 pcf. A vibration assembly, consisting of four compression springs mounted between a fixed plate and a floating plate, with an air-driven vibrator motor (16,000 rpm) attached to it, was mounted in a Dake bearing press and held with tension springs (Fig. 2). Panels up to 13 in. by 13 in. by $2\frac{1}{2}$ in. thick were fabricated by placing uncured molds of ablator material into the press and pressing the vibrating core into it. Checks on the first few panels formed in this manner indicated that the density at the center of the thickness was greater than that at the top and bottom surfaces due to the material being compacted from both sides. Subsequent trials indicated that packing the panels from both sides prevented this gradient. This was accomplished by partially packing the mold frame, vibrating the core into it, inverting the packed core and frame, partially loading a second mold frame, and pressing the partially filled core into it. After loading the panel with ablator, the assembly was vacuum-bagged and cured in an oven under a vacuum pressure of 15 in. of Hg. Our experiments indicated that a 65%/35% ratio produced density gradients within ± 0.5 pcf.

The panels planned for installation demonstrations on the SV-5J vehicle were approximately 29 in. by 48 in. by $1\frac{1}{2}$ in., which required increasing the area of the prototype vibration press by approximately four times. A vibration assembly consisting of four subassemblies, each similar in size and construction to the one previously described, was made and mounted in a 36-in. by 48-in. platen press (Fig. 3 and 4). Panels large enough to be installed on the SV-5J were successfully vibration-packed using this assembly (see Fig. 5).

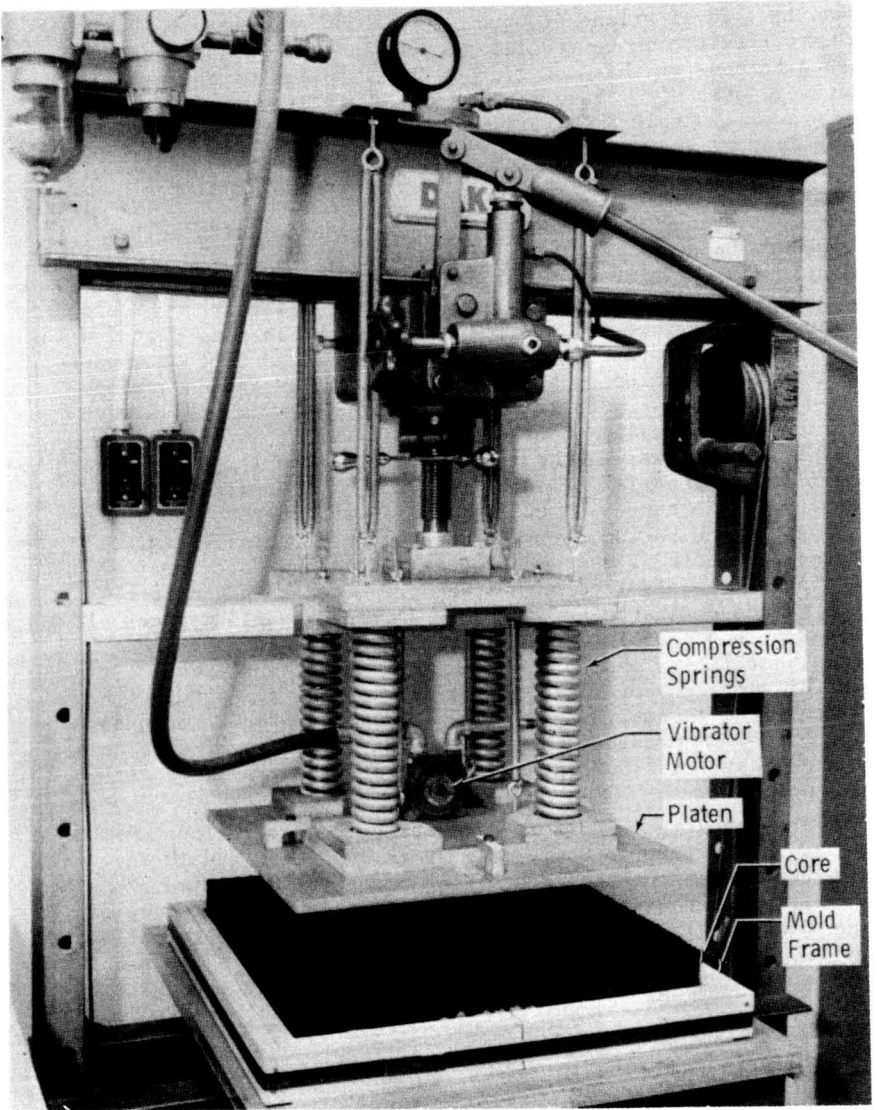


Fig. 2 Dake Vibrator Press

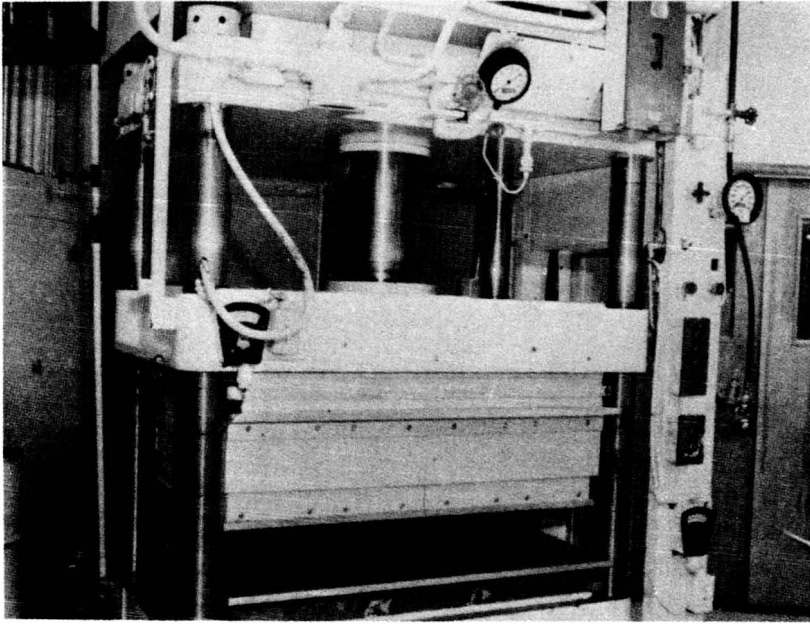


Fig. 3 Enlarged Press Assembly (36 in. x 48 in.)

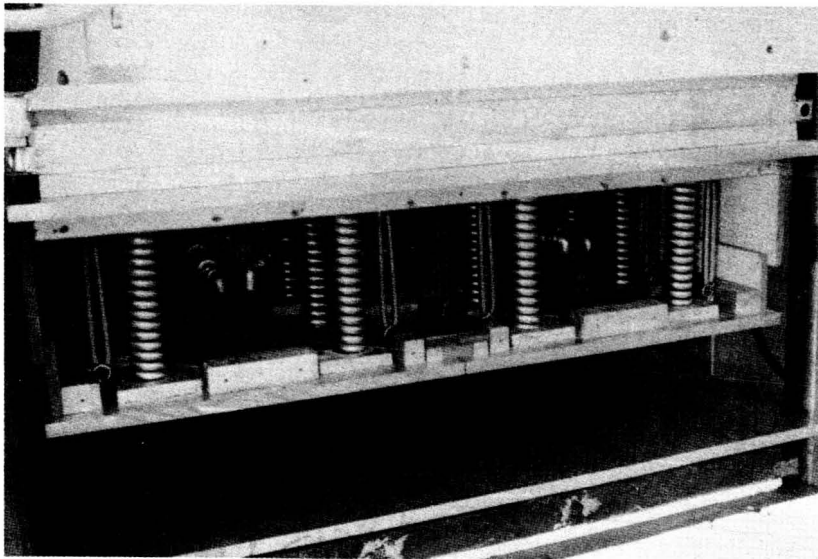


Fig. 4 Press Assembly with Acoustic Insulation Panel Removed

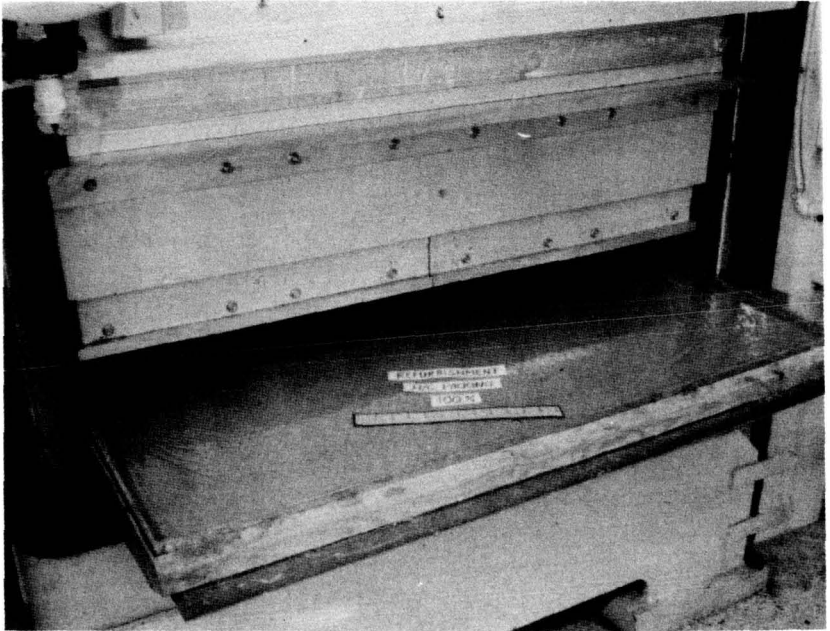


Fig. 5 Completed Panel after Filling the Remaining 35%

REFURBISHMENT

The reuse capability of the Shuttle requires that the ablator be removed and replaced after each flight at a reasonable cost. This aspect of the requirement is unique to the Shuttle since all ablator applications to date have been for single exposures. To match the surface contours of the SV-5J vehicle, splashes (laminated sheets of fiberglass, molded in place against the vehicle surface) were taken in selected areas. These splashes were then used to make the vacuum-forming and trim tools used in fabricating the ablator panels, as well as the pressure-bag restraining fixtures used to apply the ablator to the vehicle (see Fig. 6 and 7).

The ablative panels were fabricated by cutting the core to the proper thickness, vibration-packing the core into the ablator, placing the flat, uncured panel on the vacuum forming tool and forcing it to take the shape of the tool, and vacuum-bagging and curing the panel in an oven. After being cured the panel was hand-machined to remove the excess head material down to the pre-sized core, and then trimmed to size. At this point, the panels were ready for installation on the vehicle. Figures 8 through 12 show the major steps in the panel fabrication sequence after the core has been vibration-packed.

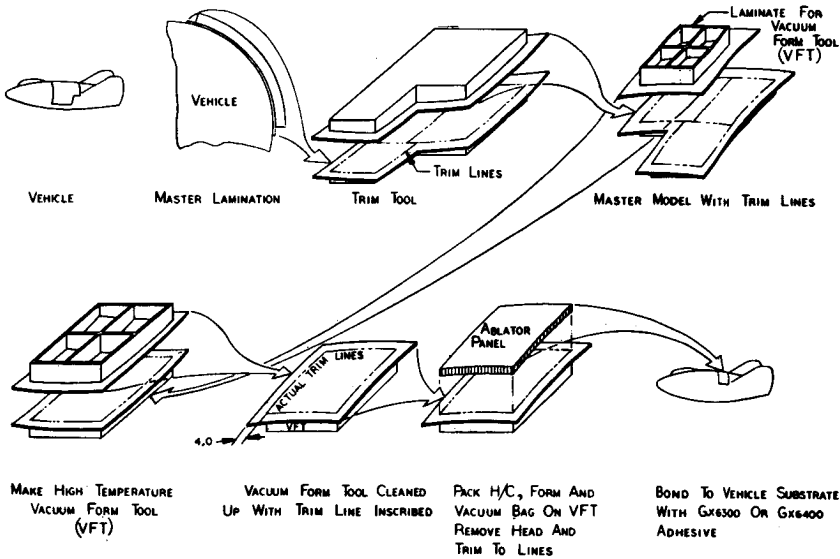


Fig. 6 Tooling Technology for Refurbishment

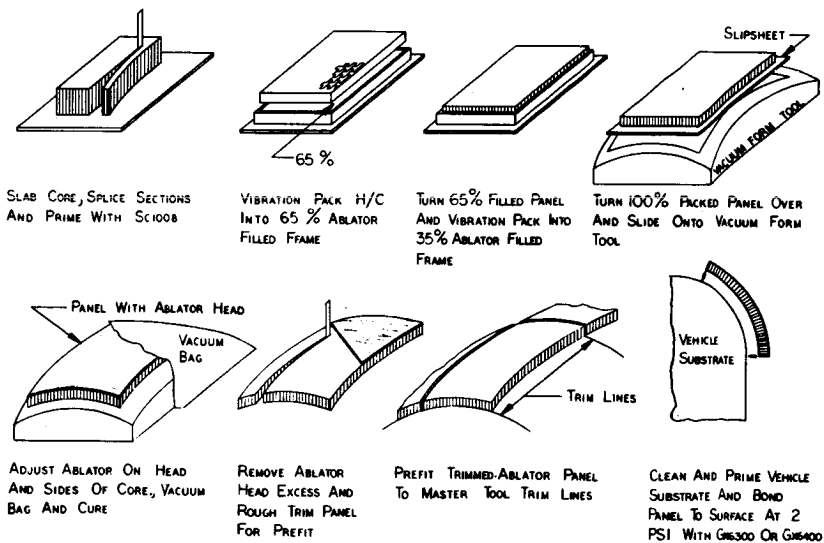


Fig. 7 Ablator Panel Fabrication Technology

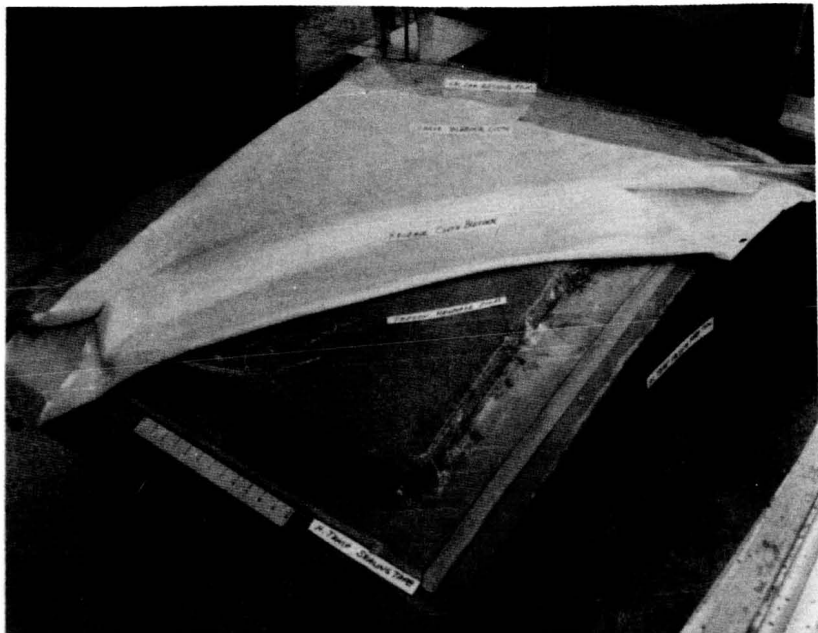


Fig. 8 Vacuum Bag Installation

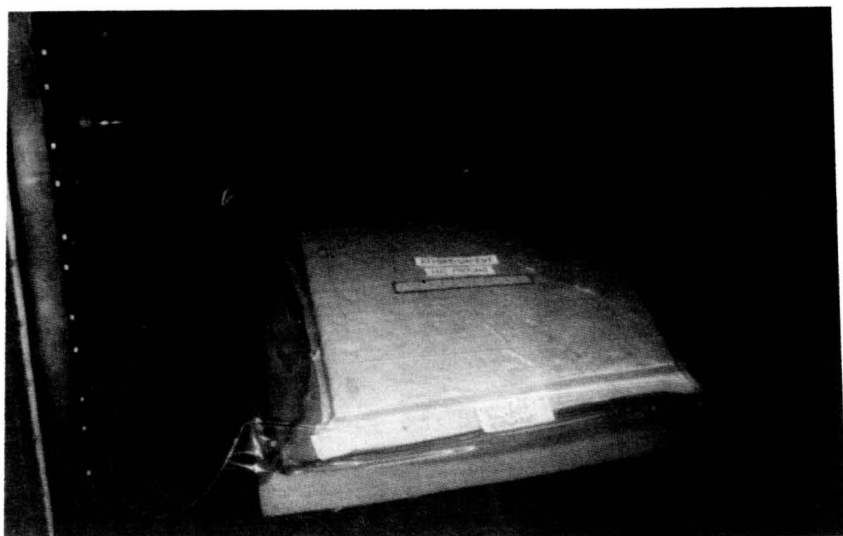


Fig. 9 Panel Being Cured in Autoclave

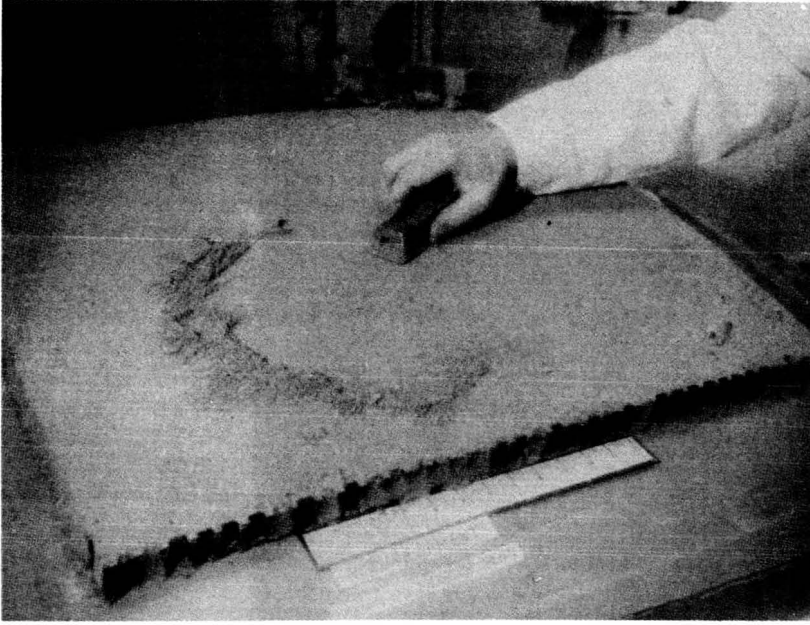


Fig. 10 Head Being Removed

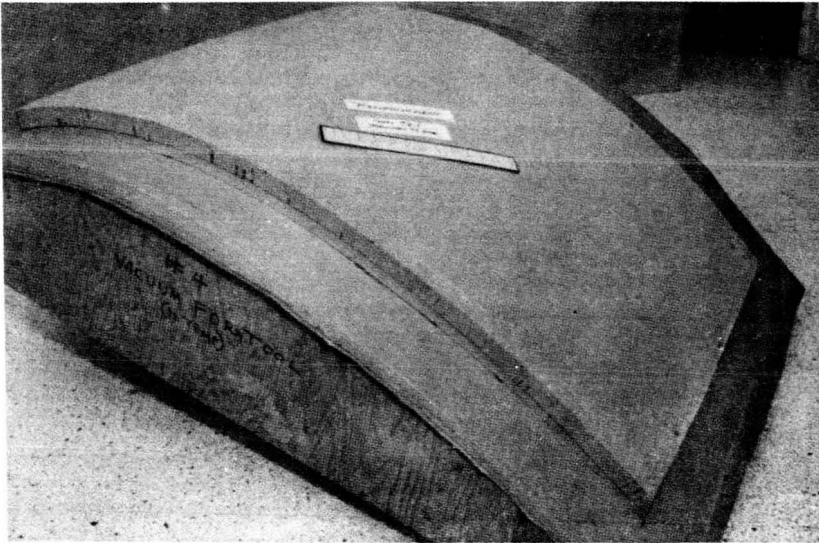


Fig. 11 Finished Panel

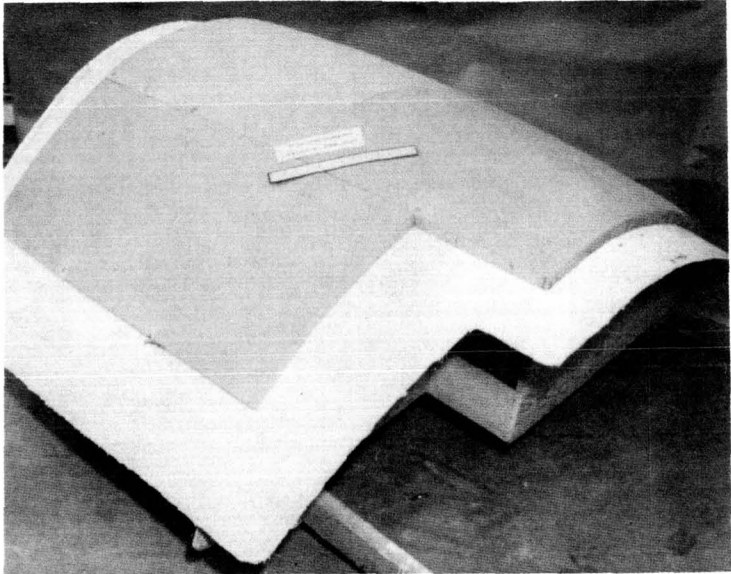


Fig. 12 Panels on Prefit Tool

The procedures just described were, of necessity, laboratory in nature and more time-consuming than would be anticipated on a production basis. In a production program the vehicle and TPS tooling would probably be made to matched master contours to ensure a proper fit and the ablator fabrication operations would be oriented toward automated procedures. The extent of this master tooling and automation would depend primarily on the number of vehicles that would require refurbishment. The higher the number of refurbishment cycles required, the more extensive the tooling could be to reduce the unit cost.

Installing the panels presented a challenge due to the size of the vehicle and the requirement that the refurbishment must be accomplished at the launch site within the short turnaround time specified for the Shuttle. Even if it were practical to place the entire vehicle in an oven to cure the adhesive used in attaching the ablative panels, this method would be precluded by the existence of on-board systems that could not survive this type of environment. As a result we decided to install the panels using a room-temperature-curing silicone RTV adhesive that requires very low pressures (1 to 2 psi) to obtain satisfactory adhesion.

The next problem was that of applying pressure on the panels until the adhesive had cured. The use of pressure plates mounted on the launch stand, or mounted to some other fixture that surrounds the vehicle, is impractical for several reasons. Since so many panels (approximately 1200), pressure plates, and load cells

of one kind or another are required to completely cover the vehicle, service personnel required to work on other subsystems would be denied access to the vehicle while the thermal protection system was being refurbished. Second, this approach would also require that the vehicle be refurbished in one particular area where the pressure plate fixtures were located. Finally, a very complicated system of pressure plates and load cells would be required to completely cover the vehicle. To circumvent this type of cumbersome system, two approaches were used during this demonstration.

The first approach was to bolt pressure plates to the vehicle to restrain a pressure bag that was located between the ablator panel and the plate. When the bag was pressurized, the loads were reacted by the vehicle surface through the attaching bolts, thereby applying pressure on the ablative panel. This pressure (2.0 psi) was held for 1.0 hr while the adhesive cured, after which the plates and bag were removed from the vehicle (see Fig. 13). The access holes through the ablator were then filled with a trowelable mixture of SLA-561 ablator and allowed to cure at room temperature.

Note that this method involves pressure plates and bags for each panel with a different size, shape, and contour, and requires a study of the vehicle to determine how many common pressure plates and bags are needed.

The second method of installing the panels was the vacuum bag technique. Adhesive was trowelled on both surfaces and rolled to obtain a smooth, even coat. After applying the adhesive, the panel was positioned on the vehicle. Holding devices were not required since the panels were temporarily held in place by the adhesive, even when positioned on the bottom surface of the vehicle. A vacuum bleeder cloth and Vac-Pac bagging film, which had been fitted with a suction tube, were then placed over the panel and sealed around the edges with caulking (Fig. 14), and the assembly was evacuated using a portable vacuum pump. Vacuum pressure was maintained at 2 psi for 1 hr. (Double-backed, pressure-sensitive tape was used when bagging over adjacent ablator-covered areas to ensure adhesion of the bag and minimize leakage). After the adhesive cured, the vacuum bag was removed from the vehicle. When all the panels had been installed, the gaps between them were filled with a trowelable mixture of RTV silicone resin and filler, and allowed to cure.

The gaps were filled using a pneumatic gun (Fig. 15) equipped with a special thin nozzle that extruded the mixture into the gaps. To check the adequacy of the bond, 3/4-in.-diameter plugs were cut into the ablator at four places on each of the three panels, tension plates were bonded to the plugs, and a force gauge was attached. A load was applied by pulling on the gauge until failure occurred (Fig. 16). In each case the ablator failed just above the bond line, which is indicative of a satisfactory bond.

The next step in the refurbishment procedure was to remove the ablator from the vehicle and prepare it for reinstallation. To make the demonstration more realistic, a 2-ft by 4-ft portion of the ablator-covered area was charred using an acetylene torch.

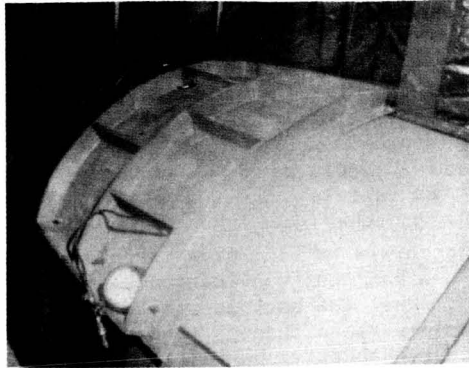


Fig. 13 Pressure Being Applied

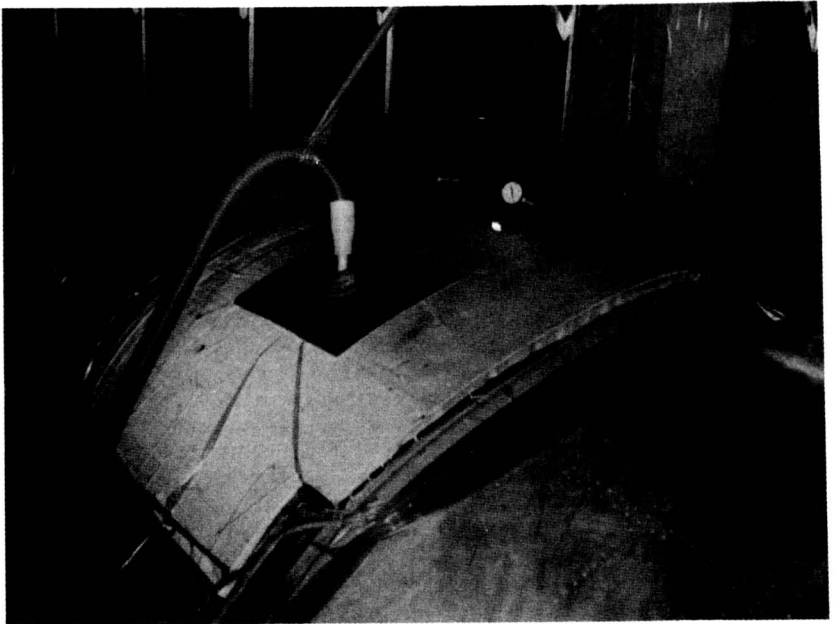


Fig. 14 Vacuum Pressure Being Applied



Fig. 15 Gap Filling

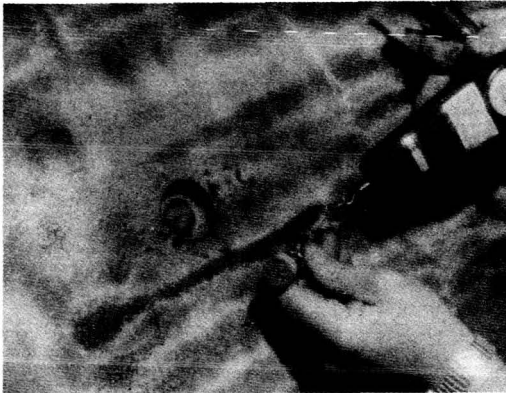


Fig. 16 Test Plug Being Removed

The standard procedure projected for the Space Shuttle involves using a rotary plane (Fig. 17) to remove the ablator in approximately 1/2-in. steps to within approximately 1/4-in. of the vehicle surface (Fig. 18); the final 1/4-in. must be removed by hand using plastic scrapers to avoid damage to the vehicle. This method is time-consuming and creates a considerable amount of dust and debris that may contaminate the vehicle. Consequently, one goal of this study was to develop a method of removing the ablator in chunks, rather than minute particles or shavings, and do it in considerably less time than with the rotary plane method.

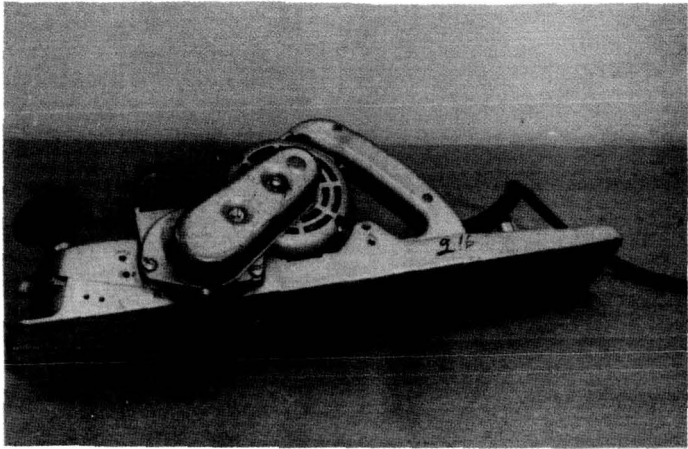


Fig. 17 Rotary Plane

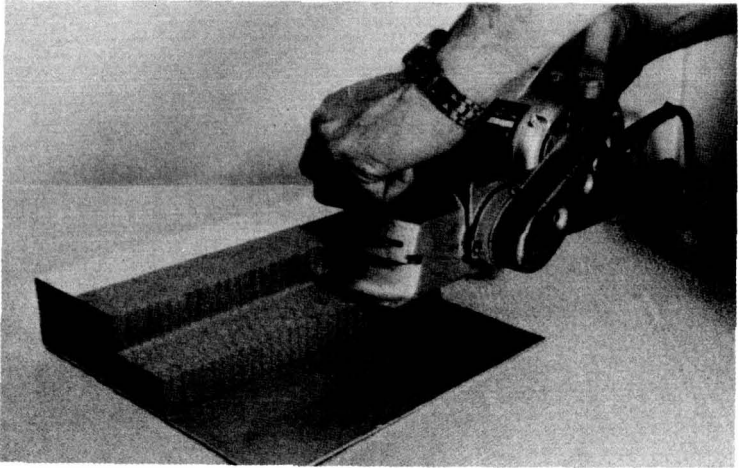


Fig. 18 Ablator Being Removed Using Rotary Plane

Several methods were tried before a successful method was actually developed. This method uses a device that slices the ablator along a line normal to the skin while a trailing wedge shears the ablator at the bond line (Fig. 19). The cutting force is applied by placing the wedge in a pneumatically driven rivet gun that is positioned and guided by the operator. Experiments indicated that strips $1\frac{1}{4}$ to 2 in. wide could be stripped off with considerable ease (Fig. 20).

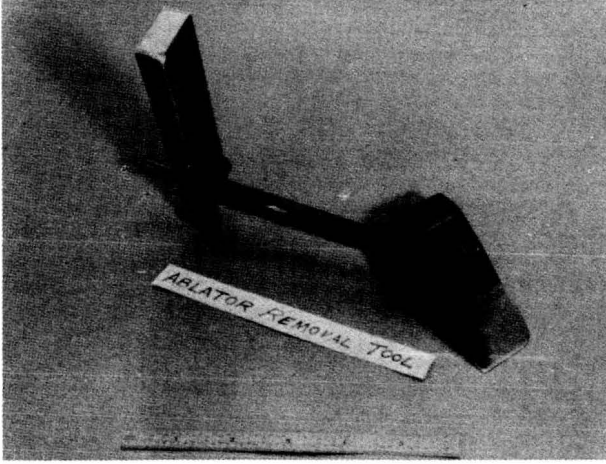


Fig. 19 Ablator Removal Tool

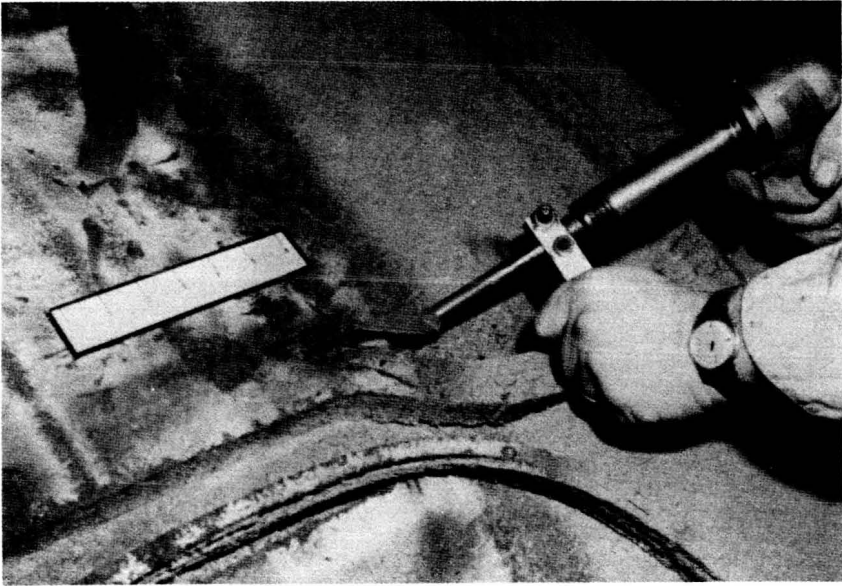


Fig. 20 Strip Being Removed

The slicing portion of the chisel is designed with a cutting edge that slopes away from the skin to reduce the risk of damaging the skin. The lower surface of the wedge portion of the chisel is flat and covered with hard plastic (cloth-reinforced epoxy) to further minimize the risk of damage. Demonstrations have shown that although the flat surface of the wedge bounces along the skin line, no damage occurs: since the breaking action of the ablator occurs above the bond line, the skin is somewhat protected by the adhesive during the removal cycle.

At this point in the demonstration study we realized that a local area of ablator must be removed before the wedge can be used since its success depends on sideways displacement of the material being removed. To do this, we designed a "U"-shaped scooping chisel (Fig. 21) to operate with the pneumatic rivet gun. To remove the ablator, a channel is first cut along the entire length of the section to be removed (Fig. 22). Another cut, 90° to the first one, is then made along the entire length of the section to be removed. This results in an "L"-shaped channel (Fig. 23) that allows ablator to be removed with the wedge chisel.

Although the scope of this program was limited to prototype development, our efforts indicated that further improvements could be obtained in several areas. First, the chisel/wedge and rivet gun could be combined into one compact unit. Various materials, such as tungsten carbide tips, could also be investigated. Next, vacuum attachments could be included to collect the small amount of minute particles generated during the removal cycle. Lazy-arm supports could also be used to reduce operator fatigue. Finally, the procedure could be automated by using tracking devices, such as those employed in the "skate" machining technique.

At this point, the demonstration on the SV-5J vehicle was carried out using the methods previously described (Fig. 24). Two complete cycles were performed; i.e., initial installation, one removal and replacement cycle, and final removal. The adhesive was removed by using plastic scrapers to remove the bulk of the residual ablator and adhesive, and the remainder was solvent-cleaned with heptane.

To demonstrate the ability to install a panel in an overhead position, one flat panel, 20 in. by 44 in., was installed on the lower left-hand flap using the vacuum-bag method (Fig. 25). No new problems were created due to the overhead position and we concluded that the one application was sufficient to demonstrate that this could be done.



Fig. 21 "U"-Channel Starter Tool

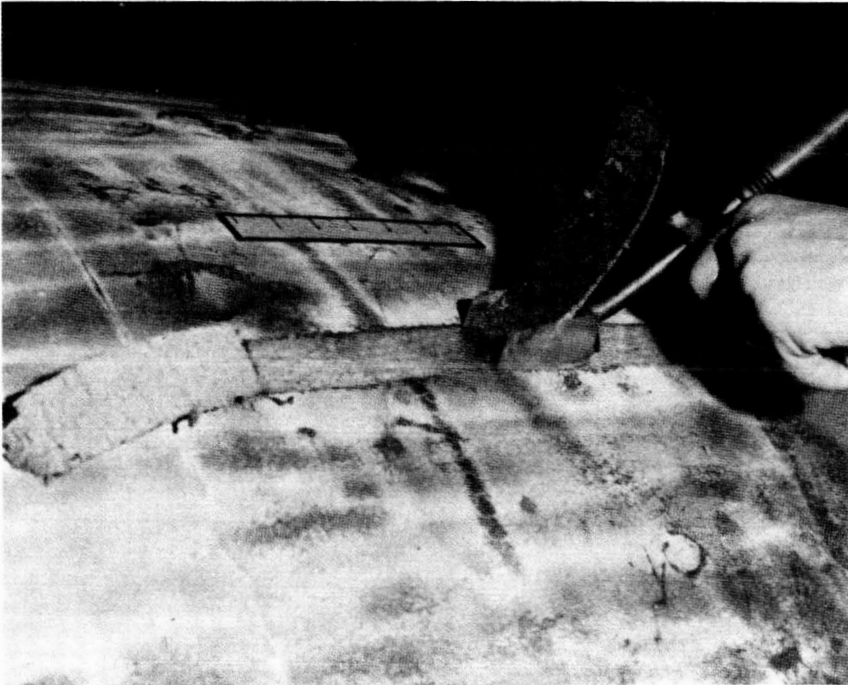


Fig. 22 Starter Strip Being Removed

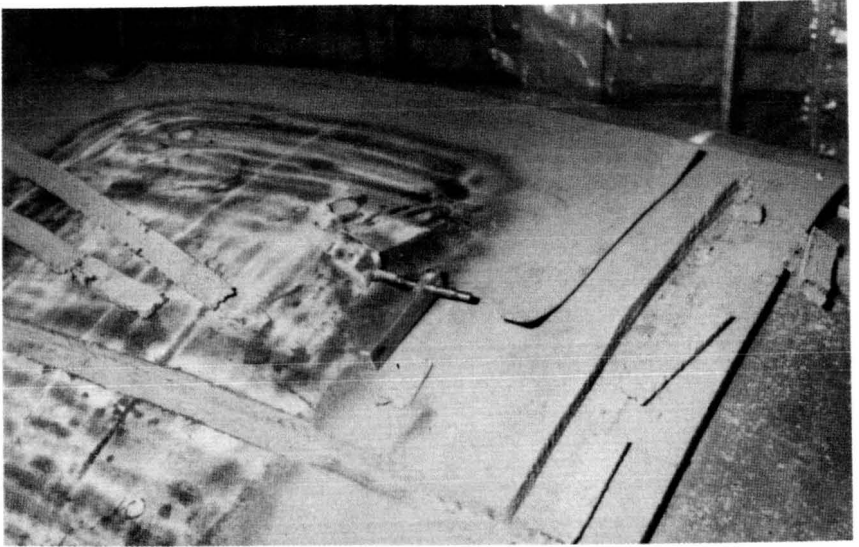


Fig. 23 Starter Strip Removed

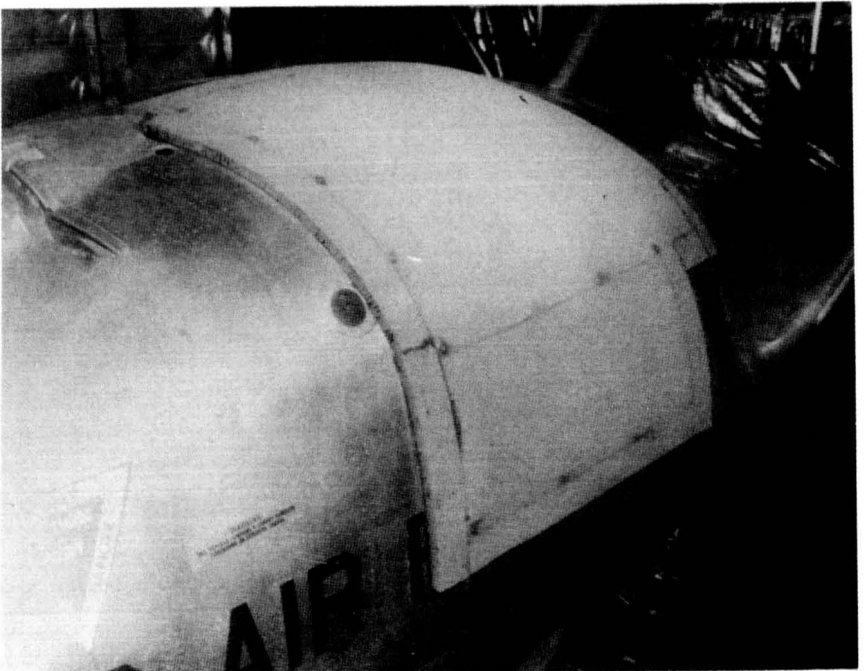


Fig. 24 SV-5J with Ablator Installed

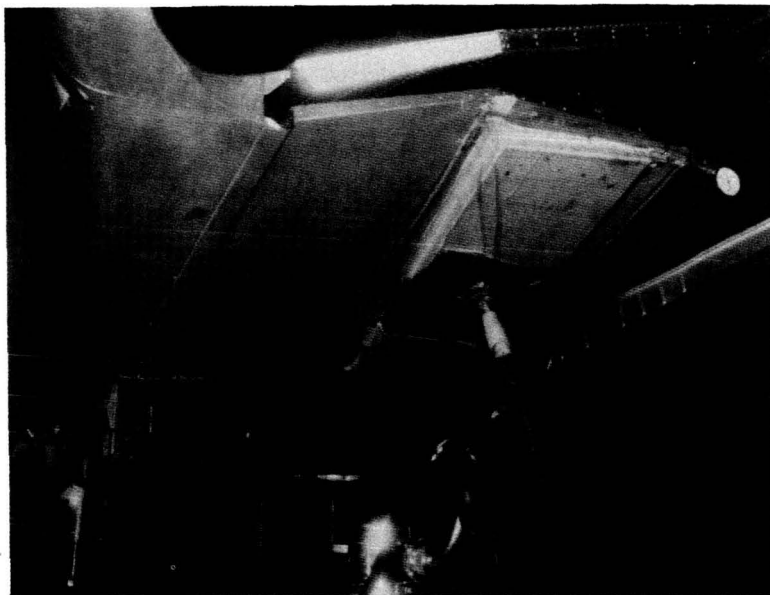


Fig. 25 Installing Panel Upside Down

COST STUDY

During the study, costs were obtained for each element of the total operation. Comparisons were made between the different methods, and the least costly methods were extrapolated for the Shuttle vehicle to obtain program operational costs, excluding DDT&E. The results of the cost analysis showed that the vacuum-bag method was by far the cheapest of the installation methods considered. Costs for this method are summarized in Table 1.

Table 1 Operational Costs for Directly Bonded Ablator (SLA 561)

ACTIVITY	PER FLIGHT	1973 DOLLARS*	
		PER SQUARE FOOT	439 FLIGHTS
PANEL FABRICATION	\$714K	\$71.40	\$313.4M
INSTALLATION	\$ 83K	\$ 8.30	\$ 36.3M
REMOVAL	\$ 47K	\$ 4.70	\$ 20.6M
TPS OPERATIONAL COST	\$844K	\$84.40	\$370.3M

*Costs apply to acreage areas only (10,000 sq ft per vehicle), and do not include profit or fee. Comparative figures are based on vacuum-bag installation. All costs are based on 439 flights and assume an 87% learning curve.

CONCLUSIONS

A new and unique method of fabricating, installing, and removing ablators for a space vehicle has been demonstrated in this program, and is within the realm of practical application. Some of the specific conclusions drawn from this study are as follows:

- Flat panels can successfully be shaped to fit the contours of a representative flight vehicle.
- Ablative panels can successfully be installed using pressure panels or a vacuum bag.
- The methods described in this paper can be used to remove and replace ablative panels at lower cost than previous methods.
- Besides being less expensive, these techniques also produce considerably less dust and debris.
- Ablative panels can be removed and replaced without disturbing adjacent panels.
- Further studies are required to develop nondestructive evaluation methods. The best solution at this time appears to be process control.
- Tooling should be further developed to improve efficiency and dust collection.

Specific application of an ablator on any space vehicle is contingent on its useful service life, since the ablator must be refurbished after each flight. Ablative systems are generally economical only for space vehicles where exposures to the thermal cycle are limited. Comparisons must still be made with reusable systems to determine where the ablative system ceases to be economical.

ACKNOWLEDGMENTS

The author would like to express his appreciation to the following colleagues for their significant contributions to this study: J. W. MacCalous, Chief, Plastics Laboratory; B. Burke, Plastics Laboratory, SV-5J demonstration test; R. Kromrey, Plastics Laboratory, vibration core-packing development.

**THE STUDY OF MOLECULAR CONTAMINATION KINETICS
USING ELLIPSOMETRY**

T. H. Allen, *McDonnell Aircraft Company, St. Louis, Mo.*

ABSTRACT

The study of molecular surface contaminants presents many problems because of their minimal thickness and tenuous nature. This problem has been approached by the use of ellipsometry to make real time, in-situ measurements on these surface contaminants. The materials are deposited in the form of uniform films ranging in thickness from 2 to 30 nm using a vapor effusion source. Measurements have been made on DC 704 and DC 705 diffusion pump oils and the condensible outgassing products from silicon rubber. The results of these measurements and their use in determining the vapor pressure and sticking coefficients will be discussed.

Paper No. 46

**USE OF ELLIPSOMETRY FOR THE QUANTITATIVE
DETECTION OF CONTAMINANTS ON SECOND
SURFACE MIRRORS**

Leon Dormant, *Chemistry and Physics Laboratory,
The Aerospace Corporation, El Segundo, California*

ABSTRACT

While ellipsometry is the preferred technique for the quantitative detection of contaminant films (in the 10-1000 Å range) on second-surface-mirrors (SSM), experimental difficulties arise when using SSM as presently manufactured. We have designed two alternatives -usable in witness plate arrangement- both of which allow ellipsometric determination while retaining the surface and reflective properties of SSM. Examples in which ± 5% accuracy were obtained are described.

PRECEDING PAGE BLANK NOT FILMED

Paper No. 47

DEVELOPMENT OF TECHNIQUES FOR ADVANCED OPTICAL
CONTAMINATION MEASUREMENT WITH INTERNAL
REFLECTION SPECTROSCOPY

J. D. Hayes, *Physicist, Teledyne-Brown Engineering, Huntsville, Alabama;*
R. G. Richmond, *Aerospace Technologist, Research and Development
Section, NASA-Johnson Space Center, Houston, Texas;* N. E. Chatterton,
*Manager, Research Department, Teledyne-Brown Engineering,
Huntsville, Alabama*

ABSTRACT

A program has been undertaken at the National Aeronautics and Space Administration (NASA) - Johnson Space Center (JSC) to develop and evaluate diagnostic instrumentation for the measurement of molecular contamination in space simulation chambers. This paper describes a technique of monitoring volatile contaminants in a large space simulation chamber using internal reflectance spectroscopy. The analytical phase included: (1) parameter effects determination (film thickness, sample absorption, refractive index variation, chemical reactions, film homogeneity, polarization, etc.), (2) thin film/thick film/bulk sample optimization analysis, (3) optical properties of candidate internal reflectance element (IRE) materials, (4) IRE design considerations, and (5) potential system range and sensitivity. Three IRE's were fabricated. Experimental results of IRE infrared spectra for six potential contaminants are reported.

INTRODUCTION

Increased complexity of space-vehicle designs and experiments have resulted in significantly more stringent cleanliness requirements for space-environment testing and simulation facilities. Although some vehicles and experiments are relatively insensitive to contamination, many spacecraft contain systems and components that are ultrasensitive to contamination (particularly molecular contamination, as from backstreaming of vacuum-pump oils, outgassed paints, and epoxies).

A program has been undertaken at the National Aeronautics and Space Administration (NASA)-Johnson Space Center (JSC) to: (1) define, control, and reduce contamination levels in their space-environment simulation facilities, and (2) minimize these levels within the test-environment requirements. This program logically includes development and evaluation of diagnostic instrumentation. This paper describes the feasibility of monitoring volatile contaminants in a large space simulation chamber using internal reflectance spectroscopy (IRS) techniques.

IRS has been used for several years to identify qualitatively minute quantities of organic compounds. The feasibility of this method for thick film measurements has been widely demonstrated. The feasibility for very thin films, however, has been shown only for a few selected compounds.

This study was directed primarily at determining feasibility of using IRS techniques for identifying, both qualitatively and quantitatively, six specific components known or suspected of contaminating surfaces tested in the space simulation chamber A at the JSC. In performing this study, the method of approach was: (1) to optimize sensitivity and measurement precision, (2) to select internal reflection elements that would not be sensitive to small experimental parameter variations that complicate the analysis, but yet could theoretically detect samples several monolayers thick, and (3) to develop procedures and provide data necessary for correcting the spectra of thick samples with rapidly varying (with wavelength) refractive indices.

The effort was divided into analytical and experimental phases. The analytical phase included: (1) a determination of the effects of several parameters (film thickness, sample absorption, refractive index variation, chemical reactions, film homogeneity, polarization, etc.), (2) an optimization analysis for thin films versus thick films versus bulk samples, (3) determination of optical and physical properties of candidate internal reflectance element (IRE) materials, (4) IRE design considerations, and (5) potential range and sensitivity of an assembled system.

Theoretical Considerations

The optical properties of absorbing media may be described quantitatively by the complex refractive index, $N = n + ik$, where n , the real part of the refractive index, is defined as the ratio of the velocity of light in vacuum, c , to the phase velocity, v ,

in the dielectric of a plane electromagnetic wave having constant amplitude along a wave front,

$$n = c/v . \quad (1)$$

The imaginary part of the complex refractive index, k , often called the extinction coefficient, describes the damping of the wave as it traverses the absorbing medium, and is defined by the relation

$$E = E_0 \exp\left(-\frac{2\pi kz}{\lambda}\right) \quad (2)$$

where

- z - coordinate in the direction of propagation
- E_0 - amplitude of the electromagnetic wave at $z = 0$
- E - amplitude at z
- λ - wavelength of the electromagnetic wave in vacuum.

The theory of reflection and transmission of light by thin films has been discussed in many texts. Expressions for the reflectance, R , at a given wavelength are obtained by the application of boundary conditions to Maxwell's equations for a plane electromagnetic wave incident on the boundary between two media.

When a plane wave falls onto a boundary between two homogeneous media of different optical properties, it is split into two waves, a transmitted wave proceeding into the second medium and a reflected wave propagated back into the first medium. The existence of these two waves can be demonstrated from the boundary conditions, since it is easily seen that these conditions cannot be satisfied without postulating both the transmitted and the reflected wave. The transmitted beam is refracted according to Snell's law:

$$n_1 \sin \theta = n_2 \sin \phi \quad (3)$$

where

- n_1 - the refractive index in medium 1
- n_2 - the refractive index in medium 2
- θ - the angle of incidence in medium 1
- ϕ - the angle of refraction in medium 2.

For the reflected beam, the angle of reflection is equal to the angle of incidence. The reflected amplitudes for unit incident amplitudes for light with

the electric field vector perpendicular and parallel to the plane of incidence, respectively, are given by Fresnel's equations,

$$R_{\perp} = \frac{n_1 \cos \theta - n_2 \cos \phi}{n_1 \cos \theta + n_2 \cos \phi} \quad (4)$$

$$R_{\parallel} = \frac{n_2 \cos \theta - n_1 \cos \phi}{n_2 \cos \theta + n_1 \cos \phi} \quad (5)$$

For internal reflection, i.e., when the light approaches the interface from the denser medium, both R_{\perp} and R_{\parallel} become 100 percent at the critical angle θ_c , given by

$$\theta_c = \sin^{-1} \left(\frac{n_2}{n_1} \right) = \sin^{-1} n_{21} \quad (6)$$

where $n_{21} = n_2/n_1$. (Ref. 1).

It can be shown from Maxwell's equations that standing waves are established normal to a totally reflecting surface because of the superposition of the incoming and reflected waves (ref. 2). For total internal reflection, there is a sinusoidal variation of the electric field amplitude with distance from the surface in the denser medium. By selecting the proper angle of incidence, it is possible to locate the antinode (the electric field maximum) at the surface and thus obtain the most efficient energy transfer across the interface. An evanescent wave exists in the rarer medium whose electric field amplitude decays exponentially with distance from the surface (see fig. 1). Consequently, one can define a depth of penetration, d_p (ref. 2) as the distance required for the electric field, E , to fall to $1/e$ of its d_p value at the surface, E_0 , i.e.,

$$E = E_0 \exp(-z/d_p) \quad (7)$$

The depth of penetration is given by

$$d_p = \frac{\lambda}{2\pi} \cdot \left(\sin^2 \theta - n_{21}^2 \right)^{-\frac{1}{2}} \quad (8)$$

When the actual material thickness, d , is much less than d_p , the effective thickness d_e is given by the thin film formula (ref. 1)

$$d_e = \frac{n_{21} E_0^2 d}{\cos \theta} \quad (9)$$

while for $d \gg d_p$, d_e is given by the bulk material formula

$$d_e = \frac{n_{21} E_0^2 d_p}{2 \cos \theta} \quad (10)$$

When d_e is comparable to d_p , equations 9 and 10 are not valid, one must use:

$$d_e = \left(\frac{n_{21}}{\cos \theta} \right) \cdot \left(\frac{E_0^2 d_p}{2} \right) \cdot [1 - \exp(-2d/d_p)] \quad (11)$$

When the rarer medium is absorbing, the critical angle is not sharply defined and the reflectivity curves become less steep in this region. The absorption loss is quite large near the critical angle, is greater for parallel polarization than it is for perpendicular polarization, and decreases with increasing angle of incidence.

This behavior is the basis for attenuated total reflectance (ATR) spectroscopy, since the internal reflection, particularly in the vicinity of the critical angle, may be extremely sensitive to changes in the absorption coefficient.

The above equations indicate that four factors influence the strength of coupling of the evanescent wave with the absorbing medium. These four factors are the depth of penetration, d_p , the electric field strength at the interface, E_0 , the sampling area and the refractive index matching.

The great advantage of ATR spectroscopy is that because of a reflectance of 1 for nonabsorbing media, many reflections can be utilized without reflection losses. Hence, small absorption losses for weakly absorbing films can be multiplied many times without a simultaneous increase in "noise" due to substrate reflection inefficiencies.

IRE Design Considerations

The design of an IRE for real-time contamination detection and identification considered several trade-offs, the first of which was between maximum detection sensitivity and contaminant identification. The strongest absorption bands for most materials are

found in the vacuum ultraviolet spectral region between 1200 Å and 2200 Å. Although the gross identifying features characteristic of certain groups of contaminants may be inferred from the recorded spectra in this region, unique identification of single components is difficult and analysis of multicomponent samples is virtually impossible. In addition, materials which are sufficiently transparent in the vacuum ultraviolet have very low refractive indices, which vary rapidly in this spectral region. For the contaminants considered, the sample refractive index exceeds that of the candidate IRE materials. Although the use of thin-film samples may have circumvented this problem, the rapid variation of both the IRE material and the sample refractive indices with incident wavelength also significantly complicates the analysis of spectra in this region.

In the vacuum ultraviolet region, the peak absorption coefficient is not much different than the peak values in the infrared, however, the ultraviolet spectra are more ambiguous than the infrared spectra. In the infrared spectral region, unique identification of individual components is relatively easy and multicomponent analysis is often not much more difficult.

Three element designs were selected for element fabrication based on the analytical results. These included a 46-reflection KRS-5 element for operation at 30 degrees, a 26-reflection germanium element for operation at 35 degrees, and a 26-reflection germanium element for operation at 40 degrees in conjunction with KRS-5 plates as the third optical medium.

Of the many factors affecting ATR spectra (e.g., sample and IRE refractive index variation, chemical reactions of the IRE with atmospheric constituents or with the sample, degree of film homogeneity, incident light polarization, and the degree of collimation) the greatest factor is film thickness.

It may be shown that for any sample thickness, d , the maximum interaction possible is $E_0^2 d$. However, as the actual thickness of the sample is increased, the total interaction will be increased, but may not reach the maximum possible for that particular thickness. As d becomes greater than $0.1 d_p$, the interaction becomes dependent on wavelength, since d_p is wavelength-dependent. If an interaction efficiency, IE , is defined by

$$IE = \frac{d_p}{2d} \cdot [1 - \exp(-2d/d_p)] \quad (12)$$

the wavelength dependence of the interaction can be calculated and plotted as interaction efficiency versus wavelength for various actual film thicknesses, independent of the various other affecting parameters. Although the effect can be shown as a function of d_p/d , it is more relevant to the purposes of this study to plot IE versus wavelength.

Figures 2, 3, and 4 show the variation of IE with wavelength for film thicknesses of 0.01 micrometer (100 Å), 0.1 micrometer (1000 Å), and 1 micrometer (10,000 Å), for IRE materials with refractive indices of 4.00 (Ge), 2.37 (KRS-5), and 1.98 (AgCl) respectively. These curves can be used to select a maximum film thickness for a particular IRE material such that the wavelength distortion of the absorption bands will be negligible, or alternatively to correct for such distortion, assuming the film thickness is known.

Table 1 summarizes the pertinent optical physical properties of the materials for the infrared spectral region. For the region 2 to 20 micrometers, the materials with most appeal are cesium bromide ($N = 1.65$), silver bromide ($N = 2.3$), and germanium ($N = 4.0$). Cesium bromide has a high solubility in water (124 g/100 g H_2O) and is quite soft. Silver chloride is extremely soft and must be handled and cleaned carefully to avoid surface finish destruction. Silver bromide has low solubility, but is extremely soft. Potassium bromide transmits to about 18 micrometers, but has high solubility. Potassium fluoride and potassium iodide have extended transmission ranges but also are highly soluble. Practically all of the alkali halides have useful optical properties in the infrared spectral region, but almost all are highly soluble and deteriorate in atmospheres with relative humidity greater than 35 percent (ref. 3).

TABLE I.- OPTICAL AND PHYSICAL PROPERTIES
OF INFRARED IRE MATERIALS

Wavelength (μ m)	Refractive index				
	CsBr	Si	Ge	KRS-5 25° C	AgCl 23.9° C
0.5	1.71				2.0965
1.0	1.677			2.4462	2.0224
2.0	1.672	3.4534	4.1066	2.3950	2.0062
3.0	1.669	3.4320	4.0452	2.3857	2.0023
4.0	1.668	3.4253	4.0246	2.3820	1.9998
5.0	1.667	3.4223	4.0152	2.3798	1.9975
6.0	1.666	3.4202	4.0100	2.3780	1.9948
7.0	1.665	3.4189	4.0071	2.3763	1.9919
8.0	1.664	3.4184	4.0048	2.3745	1.9885
9.0	1.663	3.4181	4.0038	2.3727	1.9846
10.0	1.662	3.4179	4.0032	2.3707	1.9803
11.0	1.661	3.4176	4.0028	2.3685	1.9756
12.0	1.659	3.4176	4.0024	2.3662	1.9703
13.0	1.658	3.4176	4.0021	2.3637	1.9644
14.0	1.657	3.4176	4.0015	2.3610	1.9581
15.0	1.655	3.4176	4.0014	2.3581	1.9511
16.0	1.653		4.0012	2.3550	1.9436
17.0	1.651			2.3517	1.9354
18.0	1.648			2.3482	1.9266
19.0	1.646			2.3445	1.9171
20.0	1.644			2.3406	1.9069
21.0	1.641			2.3364	
22.0	1.638			2.3321	
23.0	1.635			2.3275	
24.0	1.632			2.3226	
25.0	1.628			2.3176	
26.0	1.625			2.3123	
27.0	1.621			2.3068	
28.0	1.617			2.3010	
29.0	1.614			2.2950	
30.0	1.609			2.2887	

Experimental Results

The spectral response of each of the individual contaminants (Dow Corning DC705, Sun vis 706, Houghto Saf 1120, 3M "Black Velvet" paint - 2 components) for several contaminant thickness using the different IRE's was measured using the experimental geometry shown in figure 5. Several methods of depositing the contaminants were attempted. The most desirable method was to outgas or heat to volatility the contaminant in a vacuum chamber and then deposit the contaminant on the IRE while monitoring the thickness of the deposit with a quartz crystal microbalance (QCM) located adjacent to the IRE. For this experiment, however, the sticking coefficient of the contaminant/IRE interface was determined to be much greater than that of the contaminant/QCM interface. In addition, the QCM exhibited a self-cleaning process when operated during the deposition. The contaminants were successfully applied directly to the IRE from standard acetone and carbon tetrachloride solutions.

A known quantity of the desired solution was dispersed on each reflecting face of the IRE and the solvent allowed to evaporate before the spectra were recorded. The thickness of the deposited film was calculated from the quantity of solution dispersed and the area of the IRE face, assuming a film of uniform thickness. The mass of contaminant deposited was checked by depositing an equal quantity of contaminant on a QCM crystal and measuring the frequency shift after solvent evaporation.

Figures 6 through 12 show ATR spectra of the individual contaminants of interest as measured with a 45-degree KRS-5 IRE, in conjunction with a Beckman filter wheel monochromator and a highly convergent (half-angle approximately 20 degrees) incident radiation beam. The incident radiation was unpolarized. For all the measurements except for the mixtures, the 3M Black Velvet coating components were measured separately and after the carbon pigment had been removed from the component. This was done because the Black Velvet coating is an epoxy coating that would ruin the IRE's if allowed to cure. The spectra in figures 6 through 12 are for films approximately 0.6 microns thick on each face of the IRE.

Typical individual spectra of the contaminants on the 35-degree germanium and on the 30-degree KRS-5 IRE's are shown in figures 13 through 18. These spectra were recorded using a McPherson Model 218 grating monochromator with 2-millimeter entrance and exit slits, and converging incident radiation beam of 5-degree half-angle, with the incident radiation

polarized parallel to the plane of incidence of the internal reflections. The films for these spectra were approximately 0.2 micrometer thick. In general, the spectra taken with the latter IRE's show higher resolution and greater sensitivity than do those taken with the 45-degree KRS-5 IRE in a highly convergent radiation beam.

Spectra of DC-704 and Sun vis 706 were recorded for three different film thicknesses and are shown in figures 19 through 22. The thinnest films shown are approximately 220 Å thick while the thickest films are approximately 2 micrometers thick. Spectra were also recorded (fig. 23), for some films approximately 20 Å thick, although these spectra are not very clean due to a high level of noise in the detector.

Figure 19 shows spectra of three films of DC-704 on the 30-degree KRS-5. As can be seen, both the 175 Å film and the 1750 Å film are quite adequate for identification, with little or no spectral distortion. However, the 1.75-micrometer film shows almost total absorption for wavelengths greater than 7 micrometers and thus would not be useful for spectral identification. It should be recalled, however, that the 30-degree KRS-5 IRE was designed for thin films primarily and this effect was anticipated. The 35-degree germanium IRE, on the other hand, was designed for thick films as well as for thin films. Figure 20 shows DC-704 spectra on the 35-degree germanium IRE. Note that the 35-degree germanium IRE is not quite as sensitive as the 30-degree KRS-5 IRE (compare the 240 Å curve with the 175 Å curve on KRS-5) but that the spectra for the thick film (2.4 micrometers) is still very clean and undistorted for the 35-degree germanium IRE.

The same type behavior is demonstrated for Sun vis 706. Figure 21 shows Sun vis 706 on the 30-degree KRS-5 IRE and figure 22 shows Sun vis 706 on the 35-degree germanium IRE. Again the 30-degree KRS-5 IRE shows distortion for the thickest film while the 35-degree germanium IRE exhibits no spectral distortion.

A mixture of 0.2 percent DC-705, 0.2 percent Sun vis 706, 0.2 percent Houghto Saf 1120, and 0.4 percent 3M Black Velvet was prepared and spectra recorded using the 45-degree KRS-5, and the 30-degree KRS-5 IRE's, as before. These spectra are shown in figures 24, and 25. Film thickness on the 45-degree KRS-5 IRE was approximately 0.4 micrometer, while that for the other spectrum was approximately 0.2 micrometer. The improved detail for the 30-degree KRS-5 over the standard 45-degree KRS-5 IRE is readily apparent. The Houghto Saf 1120 contaminant had so many strong

absorption bands that the spectra was difficult to analyze quantitatively.

Conclusions

The experimental results verified the analytical predictions and demonstrated the feasibility of using ATR techniques to detect and identify their contaminant deposits. This work has shown that it is possible to identify contaminants with deposits as thin as 20 Å from infrared ATR spectra obtained with a 30 degree, 46-reflection KRS-5 element using radiation polarized parallel to the plane of incidence. It has also demonstrated that thick film or bulk spectra can be obtained undistorted by using a 35-degree, 26-reflection germanium element.

The quantitative analysis of a complex spectrum of a multicomponent mixture yielded the concentrations of the individual components with an accuracy of ± 50 percent for the worst masked bands and ± 10 percent for the most easily interpretable bands. This example demonstrates the feasibility of quantitative multicomponent mixture analysis. Had the Houghto-Saf 1120, a material with very strong bands across the entire spectral range, been omitted from the mixture, an overall accuracy of ± 10 percent could probably have been obtained.

The proposed 40-degree germanium/KRS-5 combination did not perform as well as anticipated, due primarily to the difficulty of maintaining optical contact between the germanium and the KRS-5 with a contaminant present. Also, the KRS-5 is extremely soft and deforms easily so that maintaining the uniform optical contact necessary is impractical.

The 35-degree, 26-reflection germanium element showed high sensitivity with thin films (although not as high as that of the 30-degree KRS-5) and displayed no special distortion with thick films or bulk spectra. In addition, the germanium is easily cleaned and is very hard, making it ideal for use in all applications except those demanding the highest sensitivity.

REFERENCES

1. Harrick, N. J., Internal Reflection Spectroscopy, Interscience Publishers, New York, 1967
2. Born, M., and E. Wolf, Principles of Optics, Second Edition, MacMillan, New York, pp. 277-281, 1964
3. Harshaw Optical Crystals, Harshaw Chemical Company, 1967

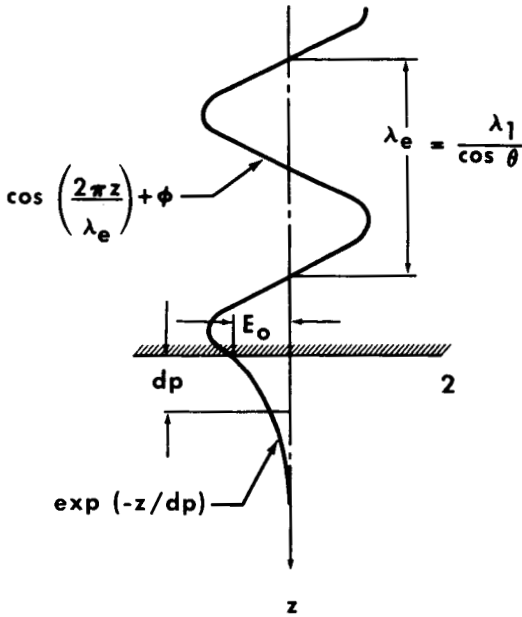


Fig. 1 - Standing wave amplitudes established near a totally reflecting interface (ref. 1)

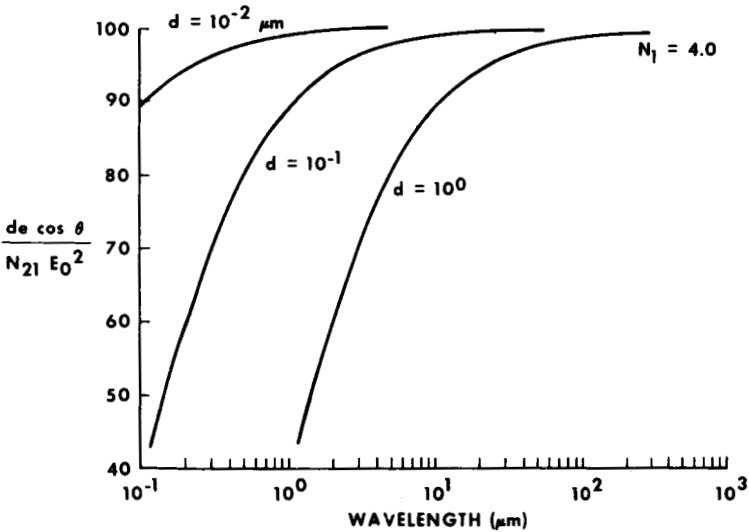


Fig. 2 - Variation of interaction efficiency with wavelength for germanium IRE

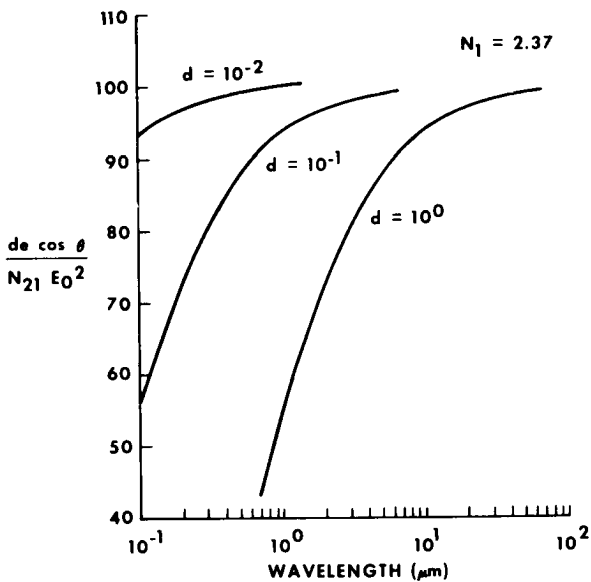


Fig. 3 - Interaction efficiency as a function of wavelength for KRS-5 IRE

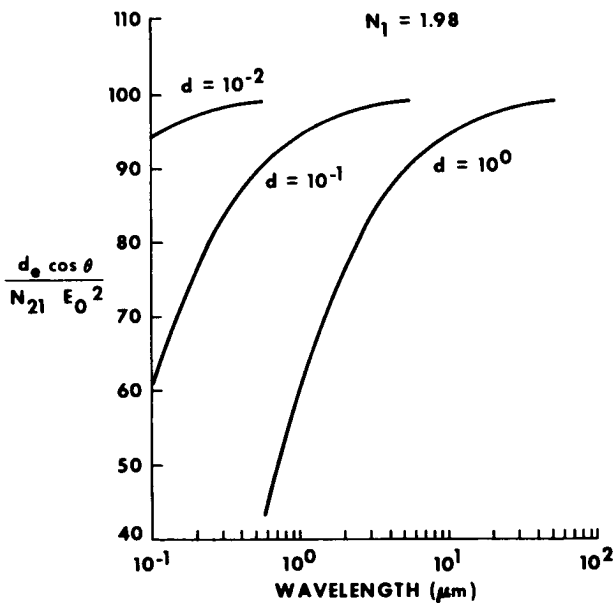


Fig. 4 - Variation of interaction efficiency with wavelength for AgCl IRE

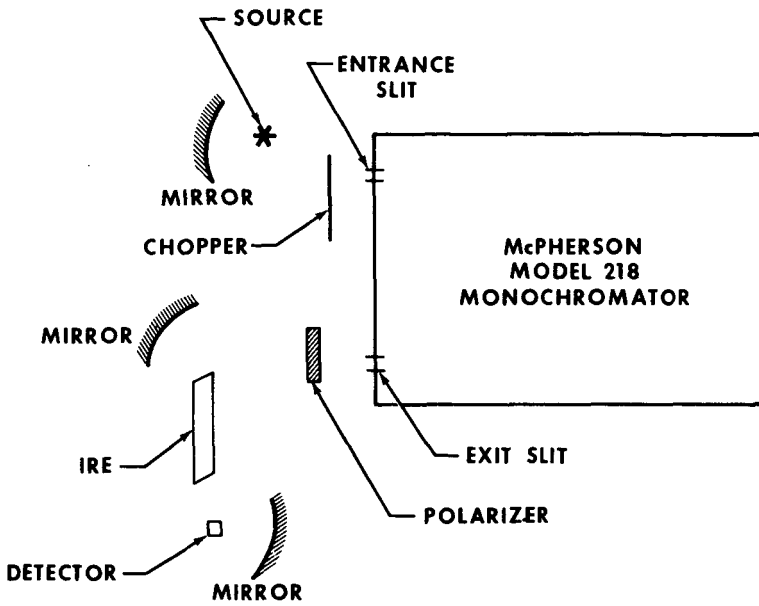


Fig. 5 - Optical schematic of experimental apparatus

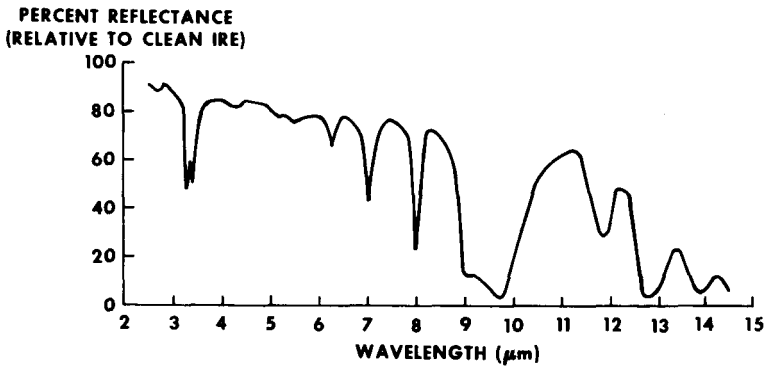


Fig. 6 - DC-704 on 45-degree KRS-5 IRE

PERCENT REFLECTANCE
(RELATIVE TO CLEAN IRE)

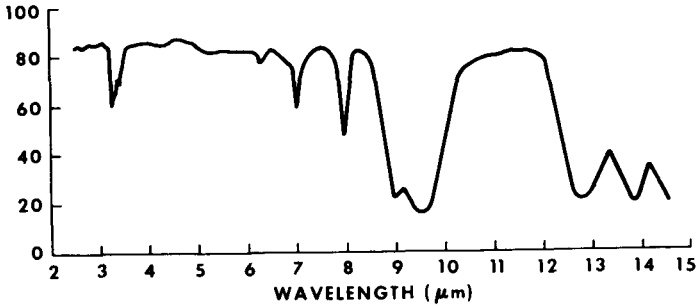


Fig. 7 - DC-705 on 45-degree KRS-5 IRE

PERCENT REFLECTANCE
(RELATIVE TO CLEAN IRE)

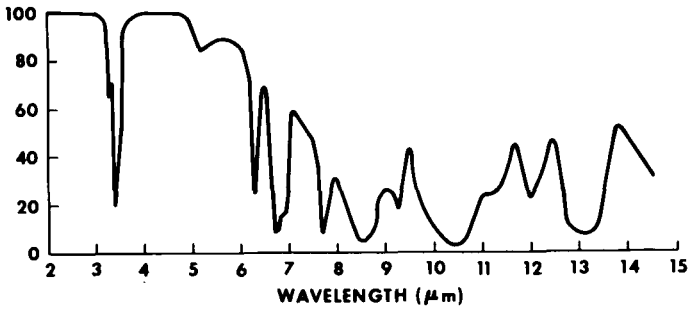


Fig. 8 - Houghto SAF 1120 on 45-degree KRS-5 IRE

PERCENT
REFLECTANCE
(RELATIVE TO
CLEAN IRE)

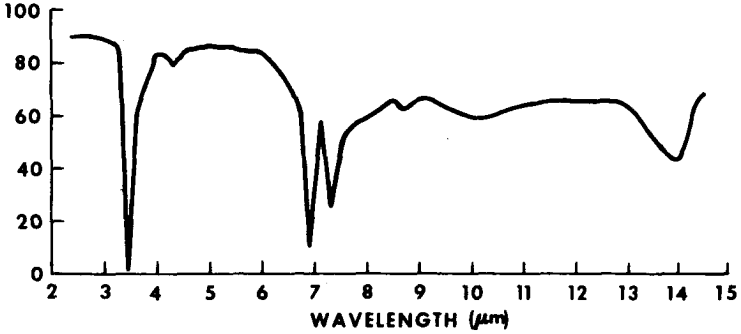


Fig. 9 - Sun vis 706 on 45-degree KRS-5 IRE

PERCENT
REFLECTANCE
(RELATIVE TO
CLEAN IRE)

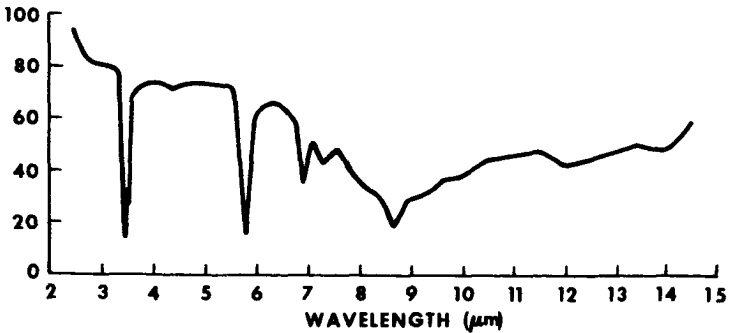


Fig. 10 - 3M black velvet 401-C10 (component I)
on 45-degree KRS-5 IRE

PERCENT
REFLECTANCE
(RELATIVE TO
CLEAN IRE)

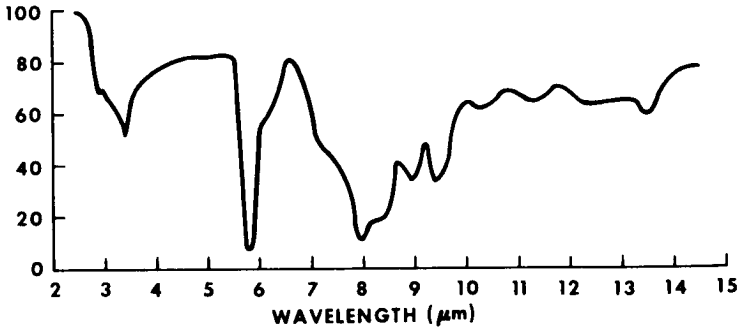


Fig. 11 - 3M black velvet 401 series (component II)
on 45-degree KRS-5 IRE

PERCENT
REFLECTANCE
(RELATIVE TO
CLEAN IRE)

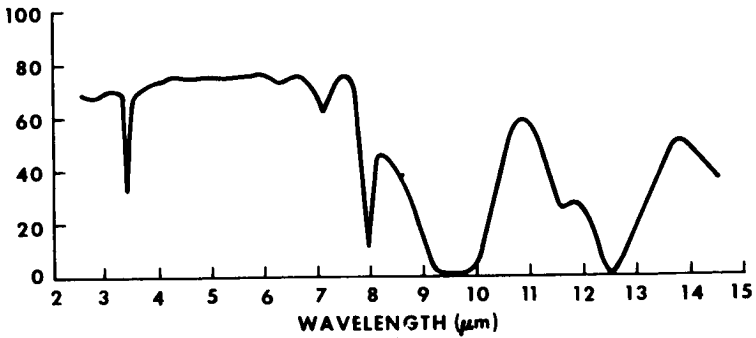


Fig. 12 - DC-11 on 45-degree KRS-5 IRE

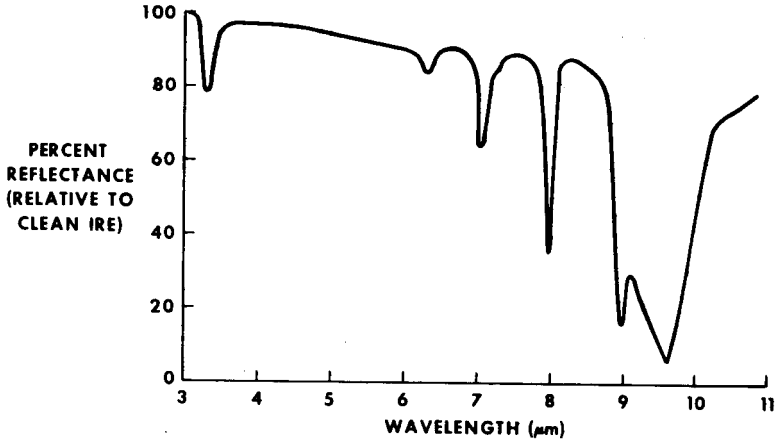


Fig. 13 - DC-704 on 35-degree germanium IRE

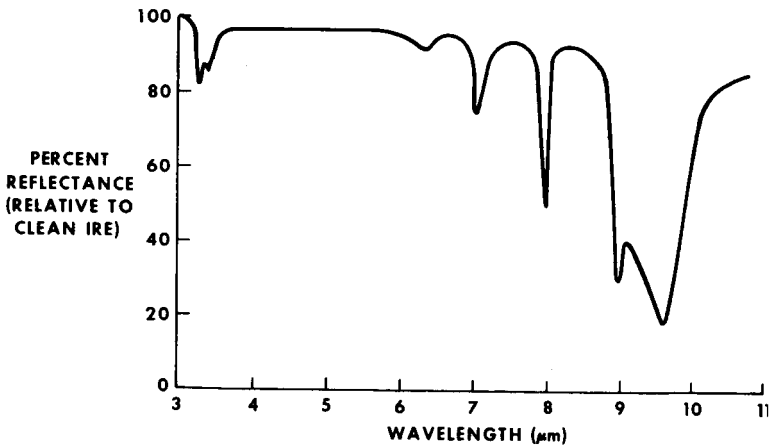


Fig. 14 - DC-705 on 35-degree germanium IRE

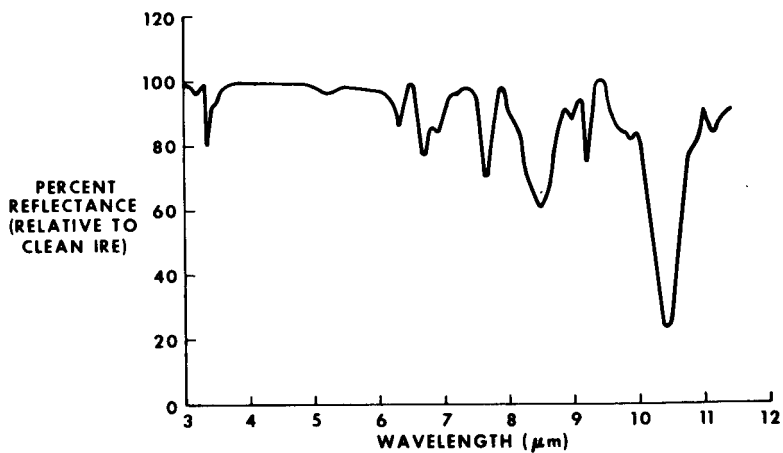


Fig. 15 - Houghto SAF 1120 on 35-degree germanium IRE

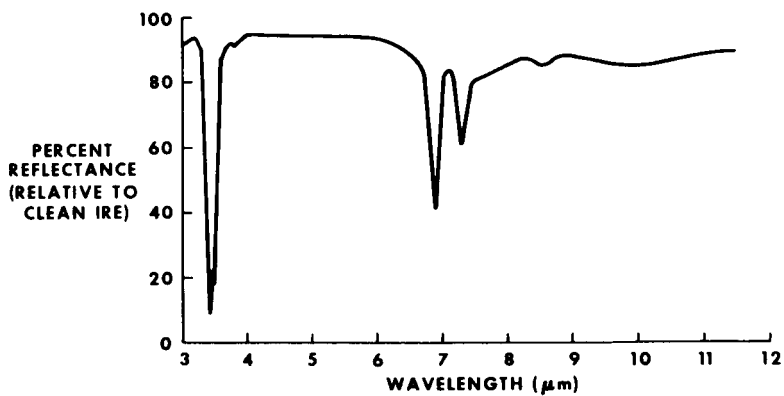


Fig. 16 - Sun vis 706 on 35-degree germanium IRE

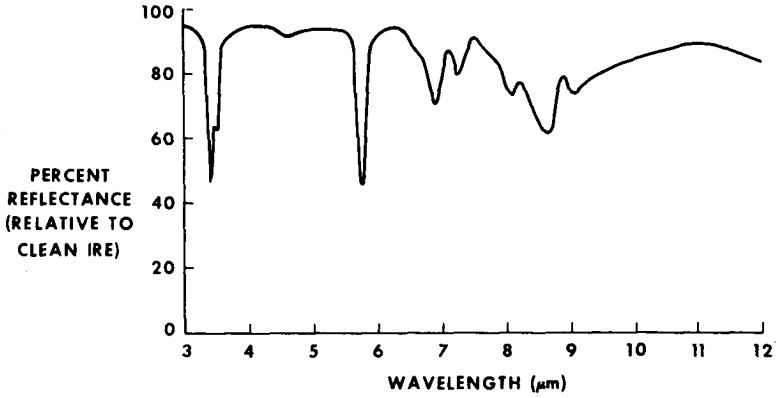


Fig. 17 - 3M black velvet coating 401-C10 (component I) on 35-degree germanium IRE

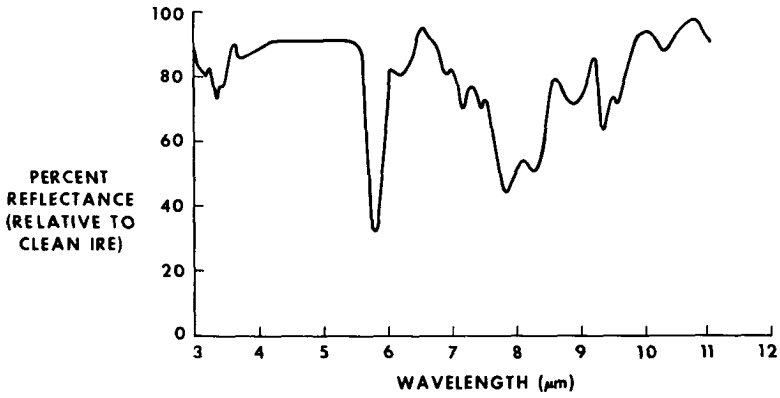


Fig. 18 - 3M black velvet coating 401 series (component II) on 35-degree germanium IRE

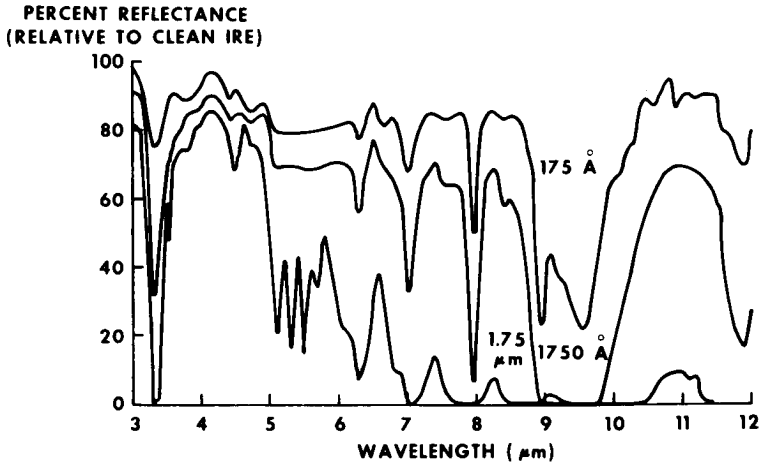


Fig. 19 - Three films of DC-704 on 30-degree KRS-5 IRE

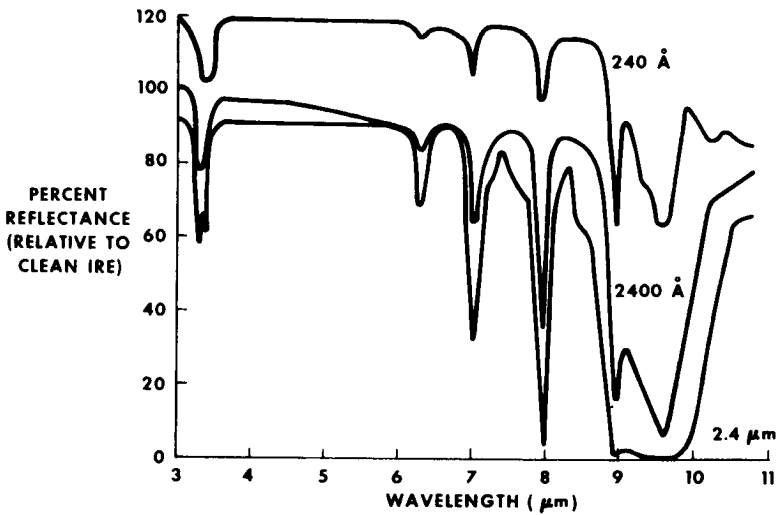


Fig. 20 - Three films of DC-704 on 35-degree germanium IRE

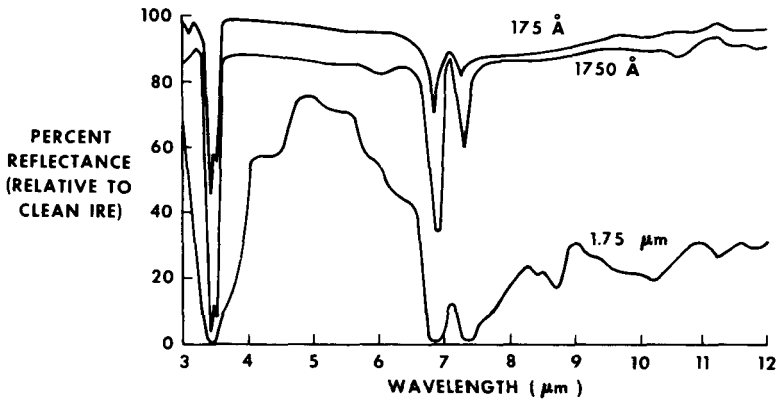


Fig. 21 - Three films of sun vis 706 on 30-degree KRS-5 IRE

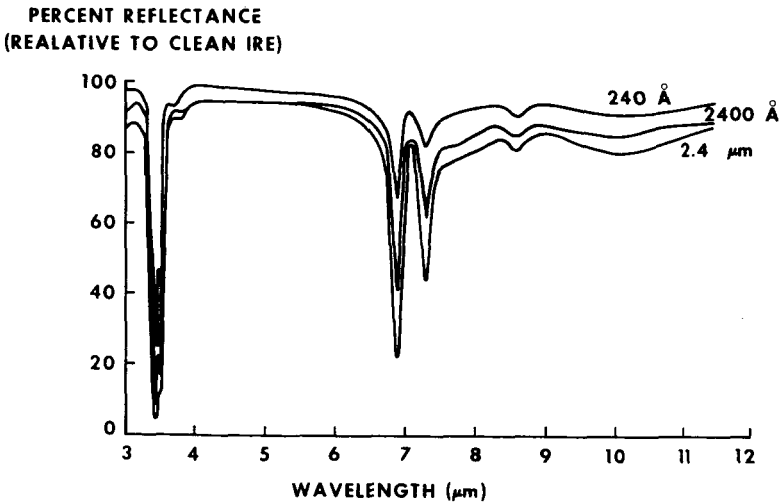


Fig. 22 - Three films of sun vis 706 on 35-degree germanium IRE

PERCENT REFLECTANCE
(RELATIVE TO CLEAN IRE)

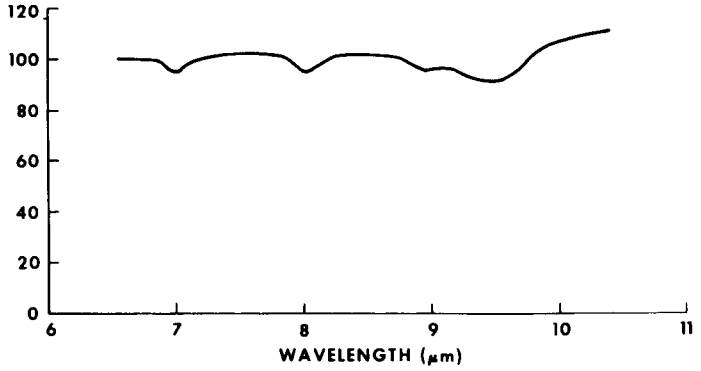


Fig. 23 - 20 A film of DC-705 on 30-degree KRS-5 IRE

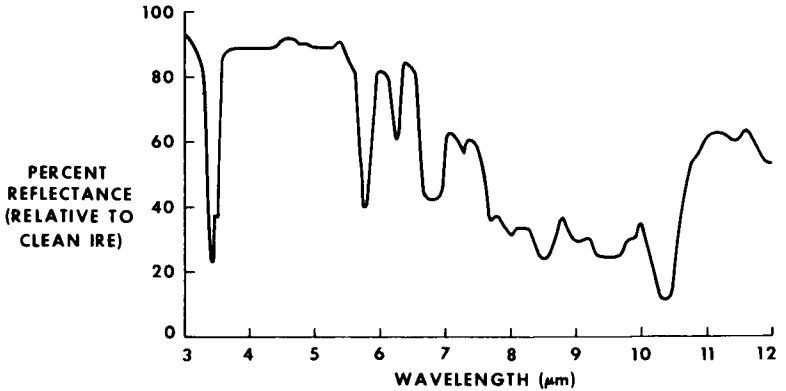


Fig. 24 - Mixture of sun vis 706, Houghto SAF 1120, DC-705, and 3M black velvet on 45-degree KRS-5 IRE

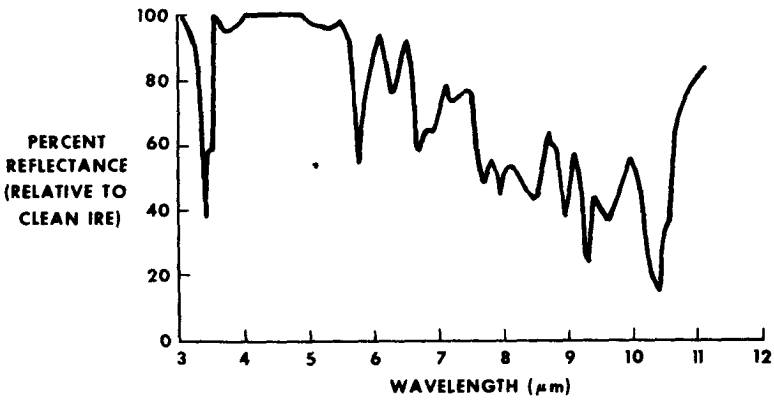


Fig. 25 - Mixture of sun vis 706, Houghto SAF 1120, DC-705, and 3M black velvet on 30-degree KRS-5 IRE

Paper No. 48

CONTAMINATION EFFECTS OF TITANIUM SUBLIMATION-PUMPED SYSTEMS ON OPTICAL SURFACES

J. T. Visentine and R. G. Richmond, *Aerospace Technologist, Research and Development Section, NASA-Johnson Space Center, Houston, Texas*

ABSTRACT

Previous studies have indicated that ultra-clean vacua can be produced when titanium sublimation pumps are used in conjunction with getter-ion pumps. Experiments are described in which the degrees of cleanliness of a typical titanium sublimation pumped system were monitored by measuring the effects of surface contamination on the reflectance of evaporated vacuum ultra-violet mirrors. Results are presented which indicate that severe reflectance losses occurred when startup of a getter-ion pump was initiated at too high a chamber pressure. Significant reflectance losses also occurred as a result of titanium sublimation pump operation. These data are reviewed and recommendations for improved system performance are presented.

PRECEDING PAGE BLANK NOT FILMED

Paper No. 49

THE VACUUM-ULTRAVIOLET DEGRADATION OF
SALT-SPRAY-CONTAMINATED THERMAL
CONTROL COATINGS*

J. E. Gilligan, *IIT Research Institute, Chicago, Ill., and*
H. M. King, *NASA-Marshall Space Flight Center,*
Huntsville, Ala.

ABSTRACT

An experimental program in which salt-spray-exposed coatings have been irradiated is described and discussed.

INTRODUCTION

In this paper we will describe the nature of, and the results and conclusions reached in a study to determine the effects of a coastal (seashore) environment, Cape Kennedy, Florida, on the solar absorptance values of S-13G samples. A major objective of the study was to assess the benefit (in terms of reduced optical degradation) obtained by rinsing and/or by scrubbing these exposed samples. Several other coatings of interest, though not salt-exposed, were also irradiated in the program. The specimens were irradiated in two (2) space simulation tests, IRIF Tests I-56 and I-57. In each irradiation test there were three (3) S-13G specimens that had been "salt-air" exposed for 6 weeks at beach level near high tide (designated "BL"). and three (3) S-13G specimens that had been "salt-air" exposed for 4 weeks at an approximate height of 150 ft on the Mobile Service Stand (designated "MSS")--both at the Saturn Launch Facility at Cape Kennedy. Other specimens in the tests included Cat-A-Lac White and A-429M (in I-57 only) and other S-13G (control) specimens. This work was performed under NASA Contract NAS8-28765; H.M. King was the NASA project monitor.

EXPERIMENTAL CONDITIONS

A series of three MSS and of three BL samples were prepared for IRIF Test I-56 and for IRIF Test I-57. One of each series of three samples was set aside without any cleaning or other treatment, and was further designated "control". A second sample of each series was given a light rinse, simulating the cleaning action which would be expected if a vehicle on a launch pad were hosed down to remove loose dirt and contamination; these samples were further designated "rinsed". The third sample was vigorously scrubbed with detergent and water to simulate the effect of a vehicle scrub-down, with the further designation "scrubbed".

Reflectance spectra of all samples were recorded in the wavelength range 325-2600 nm. During both irradiation tests, the equivalent solar ultraviolet irradiation rate was maintained at five (5) suns (solar equivalents). Sample temperature in test I-56 was maintained at +45°F; and in test I-57, at +153°F. The pressure during irradiation was well below 1×10^{-7} torr in both tests.

RESULTS

The solar absorptance values are given in Table 1. The uncleaned ("control") and "rinsed" samples all evidence the accumulation of salt on their surfaces; note the high initial value of α_s . The degradation rates of salt-contaminated S-13G^s specimens compared to those of uncontaminated ("standard") S-13G specimens are approximately the same. In short, salt-contamination affects only the initial properties of S-13G, not its photostability. Additionally, the "rinsed" samples

TABLE 1A
 SOLAR ABSORPTANCE VALUES, IRIF TEST I-56

Sample Description	Exposure, ESH			Air	
	Initial	415	1100	3085	Bleach
MSS Series*					
S-13G-Control	0.270	0.273	0.286	0.307	0.306
S-13G-Rinsed	0.252	0.257	0.273	0.304	0.301
S-13G- Scrubbed	0.225	0.226	0.237	0.267	0.252
BL Series**					
S-13G-Control	0.293	0.289	0.303	0.340	0.333
S-13G-Rinsed	0.293	0.296	0.315	0.341	0.337
S-13G-Scrubbed	0.229	0.229	0.238	0.246	0.237
S-13G-Standard (Batch C-389)	0.197	0.198	0.201	0.244	0.222
Porcelain Enamel (HAC)	0.263	0.279	0.293	0.306	0.296
Al Mirror (Control)	0.298	0.302	0.309	0.314	0.313
Cat-A-Lac White	0.294	0.442	0.513	0.614	0.572
Cat-A-Lac White	0.306	0.415	0.506	0.634	0.567
S-13G; Batch C-392 (Standard)	0.197	0.203	0.210	0.220	0.218

TABLE 1B
SOLAR ABSORPTANCE VALUES - IRIF TEST I-57

Sample Description	Exposure, ESH					Air	
	Initial	120	480	1032	1540	2010	Bleach
MSS Series							
S-13G, Control	0.245	0.272	0.302	0.317	0.319	0.332	0.312
S-13G, Rinsed	0.331	0.352	0.386	0.396	0.397	0.410	0.376
S-13G, Scrubbed	0.225	0.238	0.265	0.276	0.278	0.288	0.254
BL Series							
S-13G, Control	0.284	0.314	0.340	0.355	0.362	0.377	
S-13G, Rinsed	0.302	0.335	0.345	0.368	0.372	0.390	
S-13G, Scrubbed	0.215	0.248	0.261	0.273	0.282	0.297	
S-13G-Standard (Batch C-389)	0.190	0.221	0.235	0.249	0.253	0.262	0.246
Porcelain Enamel (HAC)	0.291	0.323	0.335	0.342	0.346	0.354	
Al Mirror (Control)	0.335	0.339	0.343	0.344	0.347	0.358	
A-429M (Batch C-406), 250°F/ 15 hr	0.211	0.213	0.223	0.224	0.227	0.232	
A-429M (Batch C-406), 250°F/ 15 hr	0.212	0.210	0.222	0.225	0.236	0.234	0.225
A-429M (Batch C-406), 350°F/ 4 hr	0.260	0.262	0.271	0.273	0.283	0.299	0.255

*Exposed at approximately 150 feet up on the Mobile Service Stand at Cape Kennedy.

**Exposed on the beach at high tide level at Cape Kennedy.

†A-429M is a paint using S-13G pigment in an IITRI-modified Owens-Illinois 650 "glass" resin.

appear not only to possess higher initial α_s values, but also to degrade slightly more than the "control" samples.

The overall results of these tests show that the degradation of salt-spray exposed samples is decreased by vigorous scrubbing, but essentially unaffected by rinsing or no cleaning at all. The "scrubbed" samples in I-56 degraded even less than unexposed ("standard") S-13G samples, presumably because the scrubbing action removes excess curing agent from the surface. Irradiation at high temperatures, however, minimizes this curing agent effect - probably because excess curing agent is removed by high temperature also. Consequently, no significant benefit will accrue as a result of cleaning S-13G surfaces that have been exposed to a seashore environment, unless they are vigorously scrubbed.

As expected, higher temperatures increase the initial rate of solar absorptance degradation; however, after the initial rapid rate, the degradation rate apparently diminishes to a level approaching the room temperature rate. The general trends of the high temperature test, nevertheless, parallel those of I-56, with the total degradation, of course, being greater. An analysis of the spectral reflectance data from I-57 shows that the effect of temperature (153°F vs 45°F) outweighs the effects of initial cleanliness; the beneficial effect of scrubbing is not, therefore, as evident. Degradation appears to depend to some extent on the initial reflectance; the higher the initial reflectance, the greater the total degradation. In both tests the initial α_s values of the "scrubbed" samples, even though lower than those of the "control" or of the rinsed samples, are not as low as those of

unexposed ("standard") S-13G samples.

The extraordinary stability of the A-429M paint systems stands out very plainly among all the test data. Although this paint system has yet to be optimized with respect to PVC, thickness, curing conditions, primers, etc., it has consistently exhibited excellent stability. In tests at room temperature the degradation of A-429M has never exceeded 0.01 in 2000 ESH.

The Cat-A-Lac White coatings sustained extensive optical damage in I-56; α_s values more than doubled, nominally from 0.29 to 0.62, in 3085 ESH. Since this amount of degradation occurred at room temperature, this coating system was not tested in the high temperature irradiation test.

The high initial solar absorptance values of A-429M result from non-optimum paint film thicknesses; nevertheless, its optical performance in ultraviolet exposure tests shows it to be superior to any coating system thus far tested. Cat-A-Lac White, in contrast, represents a clearly inferior choice.

CONCLUSIONS

From the perspective of the thermal control researcher, the results obtained point up once again the need to protect critical thermal control surfaces prior to launch. Thermal control surfaces are indeed optical surfaces and they must be effectively protected from the influences of harmful environments during the entirety of their pre-launch life. The principle involved is simple: an ounce of prevention is worth a pound of cure. The data presented here strongly re-inforce this principle. Accordingly, we must re-assert the need for process engineering, quality control and other organizations responsible for establishing the criteria and procedures for protection to specify and assure that the optical properties of critical surfaces will not be compromised by unnecessary exposure to deleterious environments.

We have seen also that even vigorous scrubbing of salt-spray exposed S-13G samples, even though it reduces the degradation substantially, does not restore the original (design) optical properties. These results, we feel, can be extended to any porous or semi-porous coating, - e.g. any coating based on a silicone rubber. Since there are no study results which indicate the contrary, we feel strongly that pre-launch protection, particularly in the case of long term storage at a coastal launch site, is mandatory for all thermal control surfaces - not just the white coatings.

The observation that salt contamination evidently affects the initial optical properties of S-13G more than it effects subsequent performance is significant in several respects, and merits some discussion. First,

this effect is not entirely unexpected or difficult to understand; the salt deposit is essentially inorganic and relatively inert. The important point, however, is that this effect should not be presumed to be operative in the case of other contaminants on S-13G or in the case of salt contamination on other coatings. Second, the loss of initial reflectance as a result of salt contamination can be substantial (as much as 0.09 $\text{in}(\rho_s)$), making it even more important to protect critical thermal control surfaces. It should be noted that the appearance of the exposed S-13G samples did not betray any evidence of contamination - with the exception of one sample. Hence, salt contamination will in most instances remain invisible to the unaided eye. In fact, the inability to detect contamination of any kind by visual inspection seems to be more the rule than the exception. Finally, we should emphasize that the type of protection afforded "stored" surfaces should be carefully considered. Many of the so-called "strippable" protective coatings, though satisfactory for short term use, tend to "age" and to leave degradable residues after periods of approximately 4-6 weeks. Plastic sheets, unless they are unplasticized, may transfer plasticizer to the "protected" surface. The protection problem thus involves insuring that the protecting system itself does not contribute to the contamination threat.

N74-10274

paper No. 50

THE FAR ULTRAVIOLET PHOTOLYSIS OF POLYMETHYLPHENYLSILOXANE FILMS ON QUARTZ SUBSTRATES

P. D. Fleischauer and L. Tolentino, *The Aerospace Corporation, El Segundo, California*

ABSTRACT

Siloxane films containing phenyl and methyl substituents in different proportions were irradiated with ultraviolet light in the wavelength region 147-229 nm. This far ultraviolet irradiation produced increased equivalent solar absorptance α_s of the films. The measured increases depend on the thicknesses and the composition of the films and on the wavelength of incident radiation.

INTRODUCTION

The optical properties of second surface mirrors and other critical surfaces on spacecraft can be degraded significantly as a result of the formation of thin contaminant films on the surfaces. Mechanisms of contamination include improper cleaning before launch, condensation of volatile materials from other locations, and migration of adhesives and other materials near the critical surfaces. A critical aspect of thin film contamination is the susceptibility of the contaminants to damage by solar radiation and, in particular, by far ultraviolet (FUV) radiation. In space vacuum, this radiation can cause chemical reactions that change an initially transparent film into a partially absorbing one. This degradation, increase in α_s of the mirror contaminant system, will depend on the amount of solar UV that is absorbed by the film (i. e., on the film thickness and on the wavelength dependent absorption coefficient), the chemical composition of the film, and possibly the temperature of the film during the irradiation.

The chemical composition and thickness of contaminant films on various critical surfaces depend on the sources of the contaminants and the proximity of the sources to the important surfaces. Silicone materials are used extensively in adhesives (e. g., RTV-566, 615) and in binders for paints (S 13 G); they constitute a major source of potential contaminants. We have chosen three different siloxane polymers that are probable contaminants from these sources and have investigated their optical properties as a function of FUV irradiation.

In this paper, we report on the FUV-induced changes in α_s of contaminant films as a function of siloxane composition, film thickness, temperature, and wavelength of exciting radiation. The results show that the FUV induces near UV and visible absorption in the films. This induced absorption, increased α_s , reaches a saturation value that increases with increases in film thickness and in the ratio of phenyl to methyl substituents in the siloxane. The amount of induced absorption is independent of the sample temperature during irradiation. Excitation wavelengths longer than ~ 230 nm are quite ineffective in causing changes in α_s for these films.

One of the original objectives of this study was to determine the thicknesses of contaminant films on optical surfaces that can be tolerated for various space missions. It may be concluded from our results that the answer to this question depends dramatically on the composition of the contaminant (i.e., whether or not it contains phenyl substituents). For example, a 1000 Å thick film of polydiphenylmethylsiloxane¹ would exhibit a saturation increase in α_s of ~ 0.015 after only ~ 500 hr of solar UV irradiation, whereas a similar treatment of a 1000 Å film of polymethylsiloxane would result in a $\Delta\alpha_s$ of only ~ 0.002 at saturation.

EXPERIMENTAL

Deposition of Contaminants

Thin films of siloxane contaminants on quartz substrates (Industrial grade 7940) were prepared by first dissolving the siloxane in an appropriate solvent, usually xylene, and then applying a known volume of the solution to the substrate with a micropipet. After evaporation of the solvent, film thicknesses were determined ellipsometrically.² The films form with a small ring around the edge of the substrate and a uniform region in the center portion where all measurements are made. Typically, the ellipsometer results gave thicknesses from one-half to two-thirds of the values estimated from the solution concentration and volume and the substrate surface area.

Irradiation Facility

The facility used for the irradiation of thin films and blank quartz slides consists of an all glass and metal, low-temperature Dewar, vacuum chamber for simultaneously maintaining two samples at a vacuum of $\leq 10^{-6}$ Torr and at temperatures from -196°C to above room temperature. The vacuum is maintained by pumping through a molecular sieve trap cooled to -196°C , and there are no O ring or other type seals that could produce any outgassing within the vacuum chamber. An Al_2O_3 window in the chamber permits irradiation of samples with 147, 163.3, 184.9, and 229 nm radiation. Calibration of these various lamps showed

the photon flux incident on the samples to be between 10^{14} and 10^{15} photons $\text{cm}^{-2}\text{sec}^{-1}$. The entire sample chamber can be removed from the vacuum system, while both temperature and vacuum conditions are maintained, for the measurement of transmission spectra of both the sample and the blank in the wavelength region of 200-800 nm with a Cary Model 15 Spectrophotometer. Irradiations of blank samples demonstrated that the chamber is contaminant free.

RESULTS

Changes in solar absorptance $\Delta\alpha_s$ were determined relative to blanks that had no films by measuring the visible-UV transmission spectrum before and after irradiation and then using a computer calculation to correlate these changes to the α_s of second surface mirrors.³ Two methods were used to correct the measured absorbance change in the sample for color center formation in the quartz substrates. The first involved estimating the fraction of the exciting (184.9 nm) light that is absorbed by the film, subtracting this fraction from the incident light flux to determine the change due to the quartz, and then correcting the total absorbance change for that due to quartz color center formation. The estimation of this "inner filter" effect was done by reference to the extent of formation of the 650 nm color center in the sample and blank quartz.³ The contaminants did not absorb any light at 650 nm either before or after irradiation.

The second method involved warming the sample and blank to room temperature after irradiation at -100°C and then remeasuring the transmission spectra. This annealing process bleached the quartz absorptions such that the contaminant FUV-induced absorption could be determined by simple subtraction of the blank (reflectance loss) from the sample. Both procedures agreed to within 10% of the α_s determination, indicating that the warming step had little or no effect on the contaminant absorption.

The results of these irradiation experiments are shown in Figures 1-3. Figure 1 shows the FUV-induced absorption spectrum of a 2000 Å thick film of polydiphenylmethylsiloxane after different times of irradiation. As was the case for all of the irradiations, the sample was maintained in a clean vacuum chamber at pressures of $\leq 10^{-6}$ Torr for both irradiation and spectral measurements. In this experiment, the temperature of the sample was controlled at -100°C during the irradiations.

The initial spectrum shows a very small amount of absorption of the near UV and visible wavelengths, the spectral region that is important for the second surface mirrors. The FUV-induced absorption is composed of a tail from a FUV peak that extends out into the visible with a shoulder at ~ 260 nm. As shown in Figures 1 and 2, this induced absorption increases rapidly during the first few hours of irradiation, but then the rate of increase

slows until a saturation value of α_s is obtained. The magnitude of $\Delta\alpha_s$ at saturation is very nearly proportional to the thickness of the contaminant film.

Figure 3 shows that the changes in α_s also depend on the composition of the irradiated contaminant. For example, the material with a 4:1 ratio of phenyl to methyl groups on the siloxane backbone has a larger α_s at saturation than the 2:1 material, which is, in turn, larger than the polymethylsiloxane (no phenyl groups). The differences between the first two, phenyl containing, materials are due to the extension of the induced absorption in the 4:1 material farther into the visible spectrum, even though the UV absorption at ~ 260 nm is not quite as intense as for the 2:1 siloxane.

In the case of the polymethyl material, the decreased $\Delta\alpha_s$ appears to be due to a decrease in the total amount of degradation and not just to a slower rate of approach to saturation. Unfortunately, for this material only one of the laboratory irradiation sources corresponds, in wavelength, to a feature in the initial absorption spectrum. For the phenyl containing materials, the simulation wavelengths are in the region of absorption maxima, whereas for the polymethyl material, only the 147 nm source was absorbed to a large extent by the contaminant film.

The temperature of the sample (contaminant) during irradiation has little effect on the changes in α_s . Films of 2:1 phenyl to methyl material were irradiated at -100° and 25°C for equivalent times. The results are included in Figure 3. Since no temperature effect was observed, many of the reported experiments were conducted at room temperature for convenience and in order to eliminate complications due to quartz substrate color center formation.

DISCUSSION AND CONCLUSIONS

From the results of these irradiation experiments it is apparent that the combination of thin siloxane contaminant films on critical optical surfaces, such as second surface mirrors, and FUV solar irradiation can cause severe degradation of the optical properties of the mirrors. This degradation is made manifest by an increase in the solar absorption constant α_s of the contaminant/mirror system. It is particularly critical if the contaminant contains phenyl substituents on the siloxane chain.

A film of a given thickness will reach a limiting or saturation value of α_s that will be a function of the film thickness, its composition, and the wavelength of the exciting radiation. The saturation α_s will not depend on the temperature of the contaminant during the exposure to the damaging radiation. Films that are $\sim 500 \text{ \AA}$ thick can cause significant problems; they can have saturation α_s values of ~ 0.005 . However, the real difficulty would

be encountered if contaminants were continuously deposited on the mirror surface during a mission. Such continuous deposition must be limited such that film thicknesses do not exceed the critical values described in Figures 2 and 3.

It is also apparent from these results that normal solar simulation experiments that utilize high-pressure xenon lamps would not produce the degradation produced by these shorter wavelengths. Specifically, when a 2000 Å film of polydiphenylmethylsiloxane was irradiated with radiation at 229 nm, no measurable effect on α_s was observed (Figure 2). The reasons for this large decrease in effect are: (1) the contaminant does not absorb a significant amount of 230 nm radiation and (2) the quantum yield for degradation is apparently much less for the lower energy radiation.

In certain space applications, such as in RTV adhesives, silicones that contain a high percentage of phenyl substitution have been used to provide certain desirable properties such as increased flexibility at low temperatures, increased resistance to particulate radiation, and potentially lower outgassing rates. The results of our experiments demonstrate that the effects of FUV solar radiation on the solar absorptance of potential contaminants must also be considered in choosing the proper materials for specific objectives. A film of polymethylsiloxane exhibits a factor of 5 times less α_s degradation than an equivalent thickness of 4:1 phenyl to methyl siloxane. An alternative view is that for a given tolerable degradation in α_s , a polymethylsiloxane film five times the thickness of a phenylmethyl film can be accommodated. Therefore, the advantages derived from phenyl substitution must exceed the factor of 5 loss in FUV radiation stability.

Finally, it must be recognized that these results represent the degradation of relatively pure samples of potential contaminants on critical spacecraft surfaces. Although impurity analyses were not performed, these candidate materials are almost certainly "cleaner" than actual contaminants. Consequently, the degradation reported, the changes in α_s , represents "best possible" conditions in terms of the simulation of flight experience.

REFERENCES

1. We refer to diphenylmethylsiloxane and tetraphenylmethylsiloxane. These materials are siloxanes with monomer units containing phenyl and methyl substituents in 2:1 and 4:1 ratios, respectively.
2. L. M. Dormant, to be presented at 7th AIAA-NASA/ASTM/IES Space Simulation Conference, Los Angeles, 12-14 November 1973.

3. H. K. A. Kan and L. H. Rachal, "Radiation-Induced Coloration in High-Purity Silica," to be published.

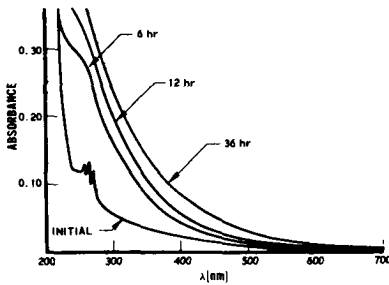


Fig. 1—Spectral changes for 184.9 nm irradiation of 2000 Å film of polydiphenylmethylsiloxane

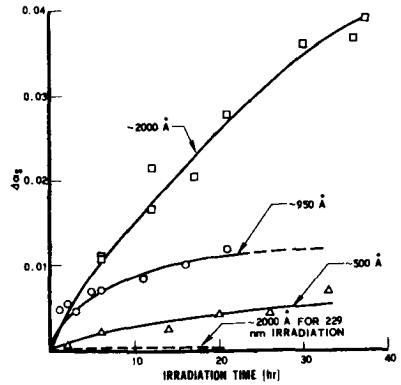


Fig. 2—FUV induced changes in α_S of polydiphenylmethylsiloxane films at different thicknesses. 184.9 nm irradiation

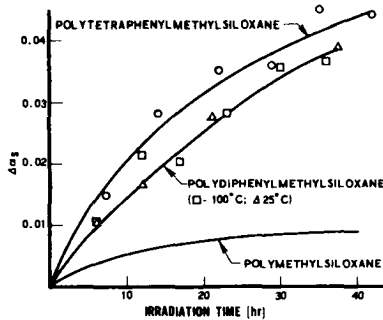


Fig. 3—FUV induced changes in α_S of different siloxane films. 184.9 nm irradiation; all samples 2000 Å thick

SKYLAB PLUME CONTAMINATION EXPERIMENTS

R. L. Bowman, E. W. Spisz, R. D. Sommers, and J. R. Jack,
NASA Lewis Research Center, Cleveland, Ohio

ABSTRACT

Continuing research is being conducted in the Lewis Research Center Environmental Simulator Facility to determine the effects of exposure to various rocket exhaust plumes on various spacecraft optics and critical surfaces (refs. 1, 2, 3, 4, and 5). Recently a series of tests were conducted to determine the effects of contamination on typical Skylab surfaces due to the exhaust plume of a five-pound MMH/N₂O₄ thruster similar to that to be used during docking and undocking maneuvers. Degradation of Skylab solar cells, white thermal control coatings, and several popular transmitting and reflecting materials was measured.

The bipropellant engine using MMH as fuel and N₂O₄ as an oxidant was fired in a pulse mode (14 msec ON, 100 msec OFF in a series of 25 pulses) for a total firing time of 75.5 seconds. At the same time a carbon arc was used to provide solar simulation (44.1 equivalent sun hours) and a deuterium lamp was used to provide 7.3 equivalent sun hours of ultraviolet radiation. Complete data will be presented on the combined effects of exposure to the thruster plume, solar and ultraviolet simulation on solar cells, S13G white thermal control coatings, and several transmitting and reflecting materials. Also data from a "covered sample experiment" and quartz crystal microbalances which were used to determine space simulator contamination effects will be discussed.

The effect of the combined exposures on the maximum power output of a quartz-covered silicon solar cell typical of those to be used on Skylab was determined from the current voltage characteristics measured in situ during periods of solar simulation. A decrease of about 6 percent in maximum power was found for this solar cell. An additional decrease of this amount may become troublesome if all of the radiation damage expected is obtained for these solar cells.

The solar absorptance (α_s) and thermal emittance (ϵ) of a S13G white thermal control coating were measured. Increases of 45 to 73 percent in α_s and decreases of 13 to 18 percent in ϵ were found due to the combined exposure to the ultraviolet radiation and rocket exhaust plume. This yields a possible increase in α_s/ϵ of two with an associated temperature increase of approximately 100 degrees which could be

very detrimental.

Spectral transmittance and reflectance measurements were made in air to determine the effect of the combined exposure of samples of fused silica, front surface mirrors, and KRS-5. A significant change in the short wavelength transmittance was obtained. Not only was significant degradation in transmittance obtained but the short wavelength cut-off was changed from 0.18 to 0.20 μm . Similar spectral transmittance data from 0.2 to 2.5 μm and spectral reflectance data from 0.35 to 2.5 μm will be presented.

REFERENCES

1. Cassidy, J. F.: Space Simulation Experiments on Reaction Control System Thruster Plumes. Paper 72-1071, AIAA, November 1972.
2. Jack, J. R.; Spisz, E. W.; and Cassidy, J. F.: The Effect of Rocket Plume Contamination on the Optical Properties of Transmitting and Reflecting Materials. Paper 72-56, AIAA, January 1972.
3. Spisz, E. W.; Bowman, R. L.; and Jack, J. R.: Effects of a Bipropellant Thruster Plume on Spacecraft Materials and Optical Components. Presented at the 7th JANNAF Plume Technology Conference, Redstone Arsenal, Alabama, April 3-5, 1973. NASA TM X-68212, March 1973.
4. Bowman, R. L.; Spisz, E. W.; and Jack, J. R.: Effects of Contamination on the Optical Properties of Transmitting and Reflecting Materials Exposed to a MMH/N₂O₄ Rocket Exhaust. Paper presented at the 7th JANNAF Plume Technology Conference, Redstone Arsenal, Alabama, April 3-5, 1973. NASA TM X-68204, March 1973.
5. Sommers, P. D.; and Raquet, C. A.: Effect of Thruster Pulse Length and Thruster Exhaust Damage of S13G White Coatings. Presented at the 7th JANNAF Plume Technology Conference, Redstone Arsenal, Alabama, April 3-5, 1973. NASA TM X-68213, March 1973.

HIGH INTENSITY SOLAR SIMULATION TEST FOR STRUCTURE PARTS AND EXPERIMENTS FOR THE HELIOS SOLAR PROBE

P. Kleber, *Space Simulation Institute of DFVLR, 505 Porz-Wahn*
F. R. Germany

ABSTRACT

The entire HELIOS solar probe cannot be tested with the intensity of 16 solar constants corresponding to 0.25 AU mission. Therefore critical parts of the solar probe have been tested in an especially built solar simulation test facility in the Space Simulation Institute of the DFVLR. The requirements of the structure and experiment engineers and physicists were changed from one test specimen to the other. After a brief description of the solar simulation system, the different requirements and their technical solution will be discussed. This includes the possibilities of flash illumination corresponding to the spin rate of HELIOS, as well as the background for the test article.

1. INTRODUCTION

The mission of solar probe HELIOS leads to an approach to the Sun that up to now was never reached by a flight object launched from the Earth. By this fact requirements of the thermal household as well as of structural parts of the probe and experiments must be met which were so far unknown in space research. These requirements necessitate a detailed examination of critical parts in tests by a very close adaptation to the real conditions. Increased consideration must in this connection be given to the subsystem tests.

In order to be able to conduct such subsystem tests, the German Ministry for Science and Technology assigned the task to the Space Simulation Institute of the DFVLR to develop a High Intensity Solar Simulation unit, the main components of which are briefly described in the following. [1]

2. Brief description of plant

2.1. High Intensity Solar Simulator

In the left half of picture 1 the opened solar simulator is visible. We have to deal with an on-axis system with divergent beam. As a light source we use a water cooled 20 KW

Xenon lamp the main mirror of which reflects the light vertically downwards. A diverting mirror under 45° versus the horizontal line directs the beam into the exit window of the solar simulator. This exit window consists of a lenticular lens system comprising 2×19 lenses. Between the folding mirror and the lenticular lens system an attenuator and a douser are fixed with the aid of which each desired irradiance can be adjusted continuously between 0.8 and 16 solar constants. The spectral adaptation to the Johnson curve is carried out by an optical filter between the two lens systems (system manufacturer: Messrs. Spectrolab).

The radiation cone has the shape of a hexagon with an inner circle of 300 mm diameter in the so-called reference plane, that is the area which is situated vertically to the radiation axis in the axis of the motion gear, which will be described later. The deviation of the local intensity from the mean value of the mentioned area is smaller than $\pm 5\%$, the time constancy of the irradiance is better than $\pm 1.5\%$.

The virtual light source for determining the irradiance in the direction of the radiation is placed at a distance of 1835 mm in front of the reference plane. (Picture 2)

2.2. Vacuum and Shroud System

As vacuum chamber a plant is used which was originally constructed for a carbon arc solar simulator with 1 SC and in which certain modification had been carried out with respect to the shroud. The usable volume in the interior of the shroud has a diameter of 900 mm and is 1400 mm long. The plant can be baked out up to 200°C . The vacuum system with an oil diffusion pump has a capacity of 2000 l/sec. The ultimate vacuum of the plant in the CDE-test is lower than 10^{-8} torr, measured with an open ionisation manometer tube inside the shroud.

2.3. Motion Gear and Data Acquisition Plant

As already mentioned before, there is a one-axis motion gear in the reference area, the rotation axis of which is vertical to the radiation axis of the solar simulator. With the aid of this motion gear, rotations of the test specimen with 0 - 10 rpm can be carried out. The transmission of the measurement values is completed via a harness which reduces the angle of rotation of the test specimen to 720° . The registration and evaluation of the data is conducted - depending on the requirements - by one of the data acquisition systems which are available in the Institute, which, however, are not described in detail in this paper.

2.4. Use of the 2.5 m Thermal Vacuum Chamber for High Intensity Tests

For completion purposes it must be mentioned that besides the high intensity test facility, the Institute includes also a space simulation facility, the cold wall of which has a diameter of 2.5 m and its cylindrical length is 5 m. As solar simulator a divergent system comprising ten 6.5 KW Xenon lamps is in use. All 10 radiation cones enter through a window of 500 mm diameter into the chamber. The complete cover of the cones is reached in the reference area with 1300 mm diameter. A partial overlapping of the cones is available in front of the reference area. By approaching the test specimen to the entrance window it is thus possible to produce for instance 11 solar constants on a diameter of 300 mm at a uniformity of better than $\pm 5\%$. This facility was also used for thermal tests at the start of the HELIOS project and for test specimens with too large dimensions.

3. Conducting of the Test

3.1. Types of Test

With reference to the test specimen, 4 types of tests can be distinguished:

- IR-heater calibration
- Thermal balance tests
- Components qualification tests
- Experiment sensor tests

3.1.1. IR-Heater Calibration Tests

For verifying the thermal household of the total system, IR-tests are conducted according to the canister method. For this purpose the probe's surfaces which are exposed to solar radiation are surrounded by a canister which has IR radiators. These IR radiators convey the same energy to the probe which it receives during rotation on its orbit from the Sun. At the experiment openings, however, difficulties arise, as the surfaces do not more correspond to the closed shape of the main body. For this reason special heaters must be mounted at these places which need separate calibration. For this purpose the experiment opening is first loaded by various irradiances. The resulting temperature at various points of the opening or of the experiment are then measured. Thereupon the IR heater is mounted in front of the area and the heating load is found which is necessary to obtain the same temperature as before with simulated solar radiation and identical background.

3.1.2. Thermal Balance Test

The temperature resulting from heat conductance and radiation exchange is found by this conventional test method. Usually the thermal household of the experiment is controlled within the solar simulation tests with the thermal model of the spacecraft. As high intensity solar simulation tests of the entire spacecraft cannot be carried out as described before, in this case the thermal household of the experiment must be tested for each experiment separately. The background of the experiment must be simulated by an especially designed temperature controlled box. Our experiences have proved that a good radiation exchange of the box with the shroud of the simulation facility at simultaneous counter heating with soldered on electrical heaters leads to easily controllable results.

As the solar simulator is constructed as a divergent system, care must be taken when assembling the experiment that the rotation axis of the motion gear passes through the area to be tested, so that the maximum intensity is not greatly exceeded during the rotation of the test specimen.

The sides of the boom experiments E2A and E4A which are constantly turned away from the Sun, are equipped with radiators which serve as reflection sides. During the first tests with these experiments it had been tried out to avoid a lateral incidence of the divergent ray in the radiator areas by mounting screens. These tests, however, did not give the expected result. On suggestion of our Institute thereupon LN₂-cooled screens adapted in their shape to the test specimen, were built in the chamber, which screens ensure a complete shadowing of the radiator areas without making special changes for the test.

3.1.3. Components Qualification and Experiment Sensor Tests

The purpose of these tests is to investigate the influences of flashes of high intensity on active components, as for instance solar cells, experiment windows and open sensors; these flashes are caused by the spin rate of the solar probe. By simulation of the thermal level, the background temperature of the component to be investigated is reproduced by suitable measures. Also for this purpose the method of radiation exchange with the shroud at simultaneous counter heating of the mounting support, as previously described, has given satisfactory results. The actual physical influence by the light impulses is superimposed by the processes resulting from the equilibrium temperature of the component. (Picture 3)

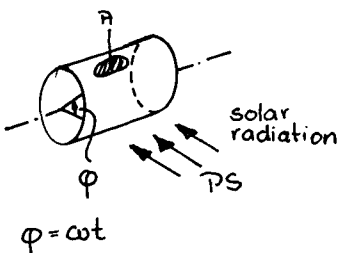
Only after completion of the plant, the experimentors expressed their request for simulating the light impulses. For dimension reasons it was not possible to integrate suitable devices between the solar simulator and the vacuum chamber. A corresponding mounting in the solar simulator itself had to be excluded as it would have interfered with the internal GN_2 -cooling. The only solution of the problem was therefore the mounting of shutters inside the vacuum chamber. To achieve this, two methods could be applied which were both investigated by experiments.

- Pendulum with shutter, cycle operation via electromagnet;
- rotating sector disc.

A third method using a rotating "Venetian blind" had to be dropped, as a reduction of the intensity would have resulted when the Venetian blind was open from about 3 to 5 %. For reasons of operation security the rotating disc was preferred to the pendulum method.

For the use of the sector disc the following marginal conditions are valid: [2]

1. The energy radiated to the experiment opening corresponds to the total energy of each revolution of the solar probe.
2. The maximum radiated intensity corresponds to the intensity in the perihelion, or the distance to be examined resp.



$$\dot{Q}_{\text{orb}} = \frac{PSA \int_{-\pi/2}^{+\pi/2} \cos \varphi d\varphi}{\int_0^{2\pi} d\varphi} = \frac{PSA}{\pi}$$

$$\dot{Q}_{\text{orb}} = \dot{Q}_{\text{sim}} = T \frac{PSA}{\pi} = t PSA$$

consequently:

(1)

$$\frac{T}{t} = \tilde{\omega}$$

with

$$T = \frac{2\tilde{\omega}}{\omega_3}$$

and

$$t = \frac{\mathcal{D}}{\omega_3}$$

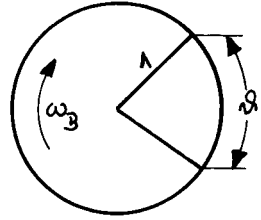
follows

(2)

$$\frac{T}{t} = \frac{2\tilde{\omega}}{\mathcal{D}}$$

with (2) in (1)

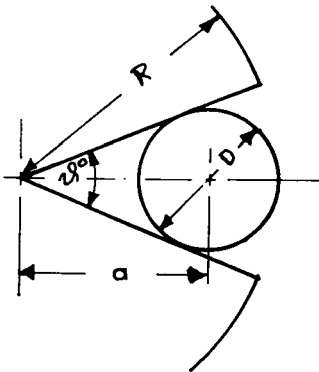
$$\widehat{\mathcal{D}} = 2 \hat{=} 114.8^\circ$$



For the dimension of the sector disc, under the condition that the total area of the experiment has to be irradiated, the following results:

$$R = a + \frac{D}{2}$$

$$\text{with } \sin \frac{\mathcal{D}}{2} = \frac{D}{2a}$$



$$D = \frac{2R}{1 + \frac{1}{\sin \frac{\mathcal{D}}{2}}} = \frac{2R}{1 + \frac{1}{\sin \frac{\mathcal{D}}{4} \cdot 360^\circ}}$$

$$\text{with } \widehat{\mathcal{D}} = 2$$

$$D \approx 0.9 R$$

In conjunction with the usable diameter of the shroud, these conditions cause a limitation of the test specimen for light impulse measurements to maximum 270 mm diameter, which, however, cannot be utilized fully for construction reasons.

With this test method various tests are conducted by the Institute. As an example, the following tests are mentioned: tests to prove the stability of parylen foils of 1.3μ thickness which are vaporized on both sides by 0.1μ Al; the output of solar cells, the background noise of semiconductor detectors, and similar tests.

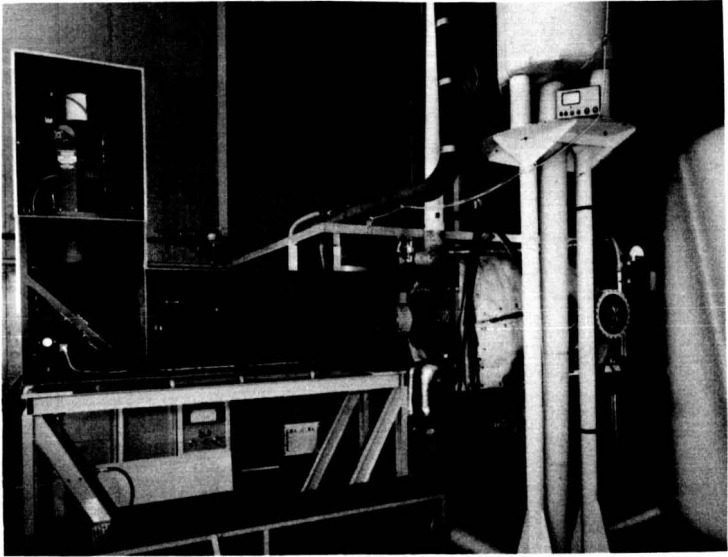
SUMMARY

By its extreme requirements - especially with respect to thermal conditions - solar probe HELIOS demands efforts of the engineers involved in its development, as no other space experiment before has ever asked for. The scientists and technicians responsible for ground tests must find ways which harmonize technical requirements and commercial possibilities.

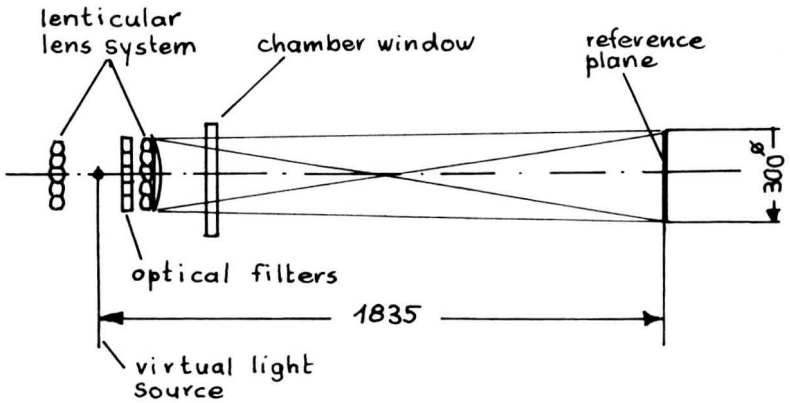
Some examples out of the various test tasks demonstrate which requirements have to be met, and which solutions our Institute has found. We hope to have thus contributed somewhat to the development of space simulation.

BIBLIOGRAPHY

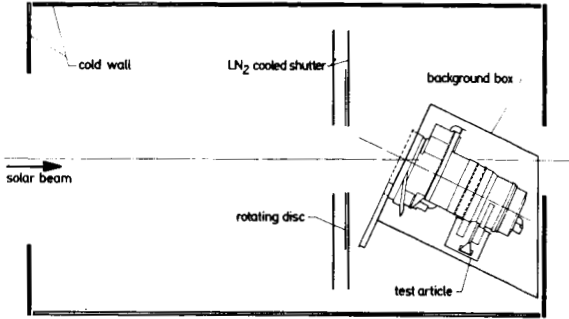
- 1 Nöhle, R. Kurzbeschreibung der Hochintensitäts-Komponententestanlage HISS,
DFVLR IB 020-72/5
- 2 Hallmann, W. und Schmidt, H.P.
Einflüsse der Reversionsparameter bei einem Weltraumsimulationstest auf die Temperaturverteilung eines spinstabilisierten Hohlzylinders,
Raumfahrtforschung vol. 1/71, p. 9 - 18.



Picture 1: Overall view of the high intensity solar simulation test facility (the housing of the solar simulator is open)



Picture 2: Beam of the solar simulator between lenticular lens system and reference plane



Picture 3: Typical setup for test of an experiment for the HELIOS solar probe with light impulses (experiment EOB)

PRECEDING PAGE BLANK NOT FILMED

Paper No. 53

DEVELOPMENT OF A HEATER POST AND SPOTLIGHT
ARRAY FOR THERMAL VACUUM TESTING OF THE
INTELSAT IV COMMUNICATIONS SATELLITE

Lloyd A. Nelson and Milton B. Levine, *Hughes Aircraft Company,
El Segundo, California*

ABSTRACT

A thermal simulation system developed to provide a reliable thermally acceptable simulation of orbital solar radiation for space simulation testing of a spinning spacecraft is discussed. The thermal system consists of a high intensity IR lamp array which provides radiant energy to the spinning solar panel section, as well as a spotlight array which maintains proper temperatures on the despun antenna farm.

INTRODUCTION

A thermal simulation system was developed at Hughes Aircraft Company to provide boundary thermal conditioning during acceptance testing of production communications satellites in a space simulation chamber. The thermal system was to provide a thermal flux simulation of solar radiation incident on the spacecraft during the various seasonal sun angles to be experienced during its orbital mission. The requirement evolved as a result of the spacecraft being too large to be oriented normal to the chamber solar simulator.

A test program concept was generated, wherein empirical data from an initial solar thermal vacuum test on the prototype spacecraft conducted in a larger off-site space simulation chamber was used to program the thermal simulation system to be utilized for more economical on-site acceptance testing of production spacecraft.

The environmental spin fixture utilized to spin (at a nominal 60 rpm) and cantilever the 8' diameter by 16' high spacecraft horizontally in the larger off-site chamber with a top solar simulator, was modified to spin the spacecraft in a vertical orientation during acceptance testing in the smaller chamber (15' diameter by 36' high with a top solar simulator).

SPACECRAFT DESCRIPTION

The spacecraft to be tested was the Intelsat IV Communications Satellite, constructed for Intelsat by an international

team headed by Hughes Aircraft Company, which was also responsible for testing of the integrated spacecraft. The spacecraft as shown in Figure 1 consists of a cylindrical solar cell array spinning at a nominal 60 revolutions per minute topped by the "antenna farm", a de-spun array of communication antennas. The cylindrical solar cell array consists of top and bottom solar panels separated by the "belly band" which contains earth and sun sensors and position and orientation rockets. The spacecraft is covered by a sun shield at the top and a thermal barrier at the bottom to protect the interior electronics. The antenna farm consists of two large spot beam antennas as well as one telemetry and command, and four global coverage antennas.

DESIGN GOALS

The design objective of the development program was to provide the mechanism for subjecting the Intelsat IV flight spacecraft to a realistic thermal simulation at orbital conditions (long term dwell phases and eclipse transients) during flight acceptance thermal vacuum testing. Thermal analyses and data from a previous solar thermal vacuum test on the prototype spacecraft were to be used to control the thermal environment. Since the number of thermal sensors on the spacecraft would be limited, the thermal system would be required to give a uniform thermal input over areas of similar geometry and surface characteristics to achieve maximum control with the minimum amount of sensors.

The thermal simulation system would be required to simulate the changes in thermal inputs due to sun angle variations from summer to winter solstice as the spacecraft was to be placed in a synchronous equatorial orbit. Since the spacecraft would be passing through the earth's shadow (in orbit) where the solar heating would drop to zero in four minutes, the thermal simulation system would also be required to cool rapidly to simulate this cut-off of thermal flux experienced by the spacecraft when the sun was eclipsed by the earth.

A major constraint on the thermal system design was minimization of stray thermal radiation which was not incident on the spacecraft surfaces, as it would have to be absorbed by the liquid nitrogen cooled shrouds which provide the simulated cold-black space environment within the space simulation chamber. Additional thermal energy falling on the shrouds would result in higher consumption of liquid nitrogen, which could become costly due to the anticipated number of tests required for the production spacecraft. An efficient thermal simulation system was required to meet this goal.

Thermal simulation to the spinning spacecraft was to be supplied by a "heater post." The heater post concept shown in Figure 2 uses a relatively intense thermal energy source at one

location on the circumference of the spinning satellite. The rotation of the spacecraft distributes the thermal energy around its entire circumference, just as the true solar flux in space is distributed around the spinning spacecraft in orbit. The use of a compact high energy source of low thermal capacity that could drop rapidly in heat flux intensity was required to provide eclipse simulation.

HEATER POST

The heater post for heating the spinning portions of the spacecraft was to consist of tubular quartz-envelope tungsten filament IR lamps with gold ceramic reflectors. Banks of five and ten-inch long quartz lamps were used. The lamp and reflector assemblies were mounted on a liquid nitrogen cooled structure for dimensional stability and to provide rapid cooling during eclipse simulation. The lamps were arranged in banks of three with a common control for the three lamps which were wired in parallel so that in case one lamp failed, power to the other two lamps could be increased. Each bank overlapped the next bank of lamps so that the lamp filaments were effectively continuous along the solar panel to provide uniform thermal flux in the axial direction.

The IR lamp and reflector assemblies were installed close to the spinning spacecraft to cut down stray thermal radiation and to provide good zone definition for thermal control. The lamps were mounted four inches from the solar panel and the lighted filaments extended two inches above and below the ends of the solar panel. The arrangement of three parallel filaments exhibited an installed power rating of 3.6 KW per linear foot. With lamp efficiency estimated at 75% and with a solar panel lamp absorptance of 0.85, the power that would be absorbed on each 54 inch long solar panel with all the lamps at full power would be 9.3 KW. Since only 5.4 KW of absorbed power would be required to simulate maximum solar heating in orbit there would be sufficient reserve capacity.

In addition to the cylindrical array of solar cells, the spacecraft had conical and flat sunshields on top and an aft thermal barrier on the bottom, all of which required simulation of the anticipated orbital solar heating. Solar heating of these areas varies considerably with sun angle. The heat post with the IR lamps was extended across the top of the spacecraft between the antennas and the sunshield to provide solar simulation to the sunshield area. A separate section of heat post with IR lamps was fitted between the aft thermal barrier and the spin fixture to provide solar simulation to the aft area of the spacecraft.

The conical sunshield was heated by eight 10-inch quartz

lamps. The lamps were mounted 2 inches from the sunshield on the liquid nitrogen cooled structure. The power that would be absorbed by the sunshields with all the lamps at full power would be 1.1 KW for the conical sunshield and 0.75 KW for the disc sunshield. Since only 0.8 KW of absorbed power would be required by the conical sunshield and 0.5 KW by the disc sunshield in orbit, this would be sufficient reserve capacity.

The aft barrier heater post envelope was constrained within the annular clearance between the spin fixture and the spacecraft. The aft barrier was heated by six 10-inch quartz lamps and six 5-inch quartz lamps. These lamps were mounted as close as two inches and as far as eight inches from the aft barrier. The power that would be absorbed by the aft barrier with all the lamps at full power would be 7.5 KW. Since only 3.1 KW of absorbed power would be required, the aft barrier heater would also have sufficient reserve capacity.

SPOTLIGHT ARRAY

Thermal simulation at the despun antenna farm required special attention. IR lamps could not be located close to the antennas as the antennas would be spun up during part of the test. Only a small portion of the energy from lamps mounted at a distance would be incident on the antennas due to poor collimation exhibited by the IR lamp and reflector assemblies.

An alternative to the tubular quartz lamp array was necessary. A commercial TV and movie spotlight which uses a 1000 watt quartz-iodide lamp with a tungsten filament was chosen.

The spotlight which required significant rework to render it vacuum compatible is shown in Figure 3. The spotlight array was primarily designed to provide sufficient thermal energy to the antenna farm components to ensure temperatures within survival limits. However, the array would also provide some adjustable temperature control of the antenna farm components and provide thermal energy to the despun "hard hat" on the center of the sunshield without affecting the thermal control of the spinning sunshield by the heater post.

In order to meet the aforementioned objectives, the spotlight array as shown in Figure 4 was designed with six spotlights in a planar array aimed at the various antenna farm components; one spotlight on the bicone antenna, two spotlights on the earth horns, two spotlights on the center of the spot beam antennas, and one spotlight on the mast. In addition, three spotlights were aimed at the despun sunshield hard hat at an angle of 45° . The spotlights would be run at reduced power as the available thermal flux from the spotlights was higher than required. Redundancy in case of spotlight failure would be provided by stray energy from the other spotlights in the array. Although

a spotlight failure would preclude positive thermal control of that particular component, there would still be sufficient energy to maintain temperatures within survival limits.

ECLIPSE PERFORMANCE

Eclipse performance of the system, that is the rate at which the thermal flux from the system would drop off when the power was turned off, was of primary interest. Transient thermal analysis of the IR lamp and spotlight assemblies indicated that the flux would drop off as rapidly as the drop off of thermal flux the spacecraft would experience when it entered the earth's shadow.

Tests were run on the IR lamps and spotlights to obtain empirical data and to qualify the components for space chamber operation. The IR lamp and spotlight cool-down performance curves at various power levels are shown in Figure 5, where they are also compared with the anticipated spacecraft orbital eclipse transient. As the experimentally determined flux transient is steeper than the orbital transient, a realistic simulation was anticipated.

The thermal simulation system was calibrated by mapping with radiometers to determine flux incident on the various spacecraft surfaces. These thermal flux values were used in determining the initial power settings for the IR lamps and spotlights. The thermal simulation system installation is shown in Figures 6 & 7.

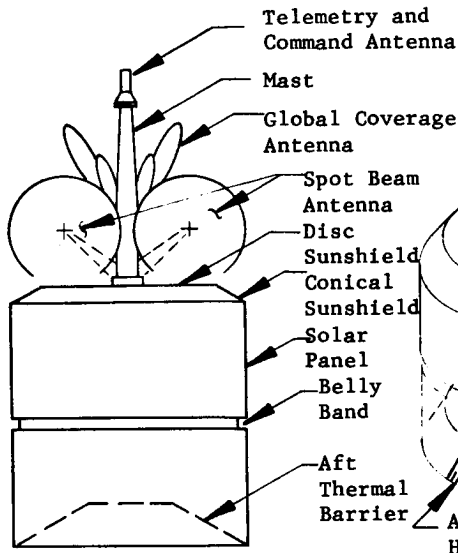
The heater post and spotlight array were installed in the space simulation chamber and subjected to a quick vacuum shakedown test. After the test, the spacecraft was installed on the spin fixture and the first thermal vacuum test of the production Intelsat IV spacecraft commenced.

CONCLUSION

The heat post and spotlight array successfully met the design requirements during the initial test and the first production spacecraft was tested without problems. The heat post and spotlight array provided proper simulation throughout the range of simulated seasonal sun angles and also realistically simulated the heat flux transient anticipated during eclipse phases when the spacecraft entered the earth's shadow.

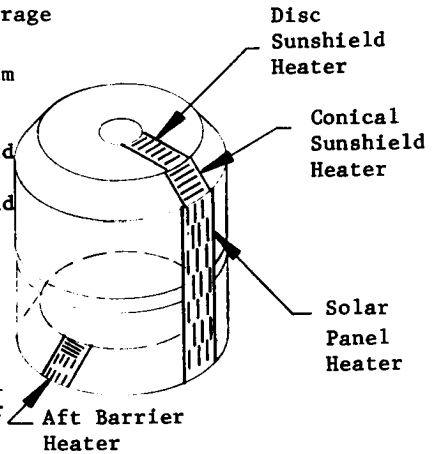
- - - - -

This paper is based upon work performed under the sponsorship of the International Telecommunications Satellite Organization "Intelsat". Any views expressed are not necessarily those of Intelsat.



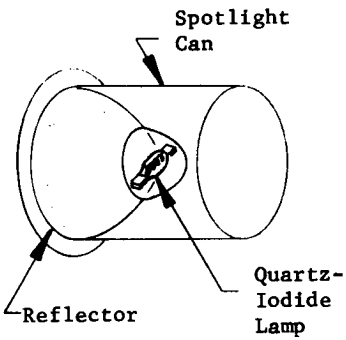
Intelsat IV Spacecraft

FIGURE 1



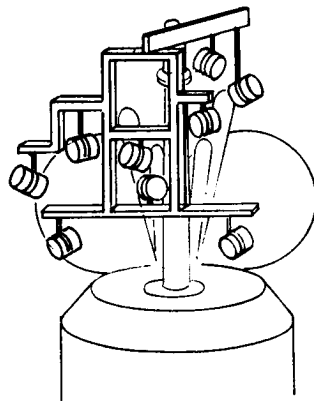
Heater Post Configuration

FIGURE 2



Quartz-Iodide Spotlight

FIGURE 3



Spotlight Array

FIGURE 4

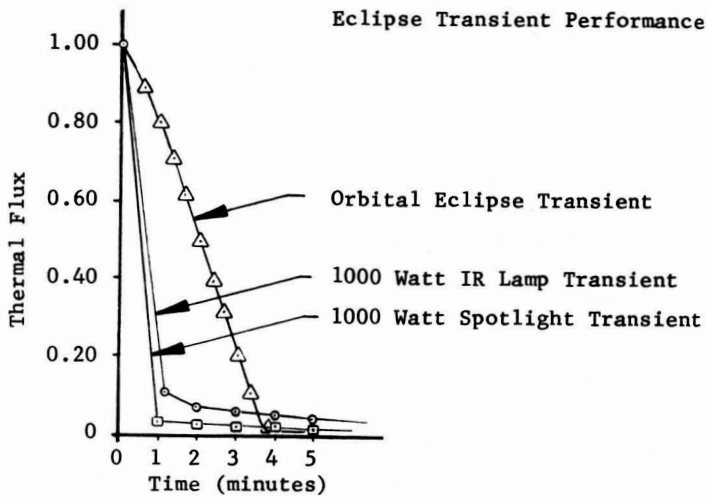
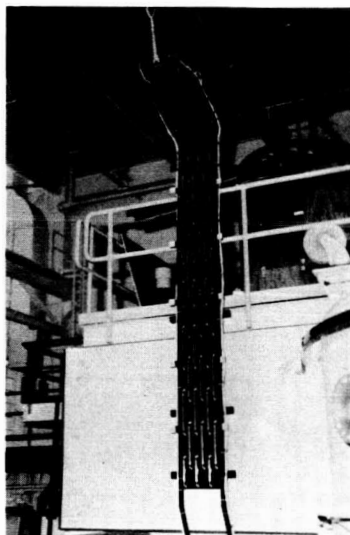


FIGURE 5



Aft Thermal Barrier Heater

FIGURE 6



Solar Panel & Sunshield Heater

FIGURE 7

PRECEDING PAGE BLANK NOT FILMED

Paper No. 54

**SOLAR PROBE HELIOS, MISSION REQUIREMENTS AND
APPLIED SPACE SIMULATION TECHNIQUES**

Dr. H. Schütz and R. A. Karsten, *Gesellschaft für Weltraumfor-
schung mbH within DFVLR +)*

ABSTRACTS

The HELIOS Mission with maximum irradiation up to 16 S.C. requires special simulation techniques. The different simulation techniques and their realisation are described.

1. Introduction

The HELIOS A and B missions will be the first Deep Space Missions to attempt investigation of the sun's environment at, respectively, 0.3 and 0.25 Astronomical Units (AU). Since our knowledge of the sun's environment is only approximate, the specifications for Space Simulation must be based on assumptions.

Furthermore, it is not yet possible, for a full-size HELIOS model, to simulate the sun's radiation at the closest approaches of, respectively, 11 and 16 Solar Constants (SC). One is forced to use diverse simulation techniques in the attempt to attain maximum reliability in the spacecraft at minimum cost. The following text describes the newly constructed and/or modified facilities, test methods, and results.

2. The HELIOS Mission

Seven years ago, President L.B. Johnson and Chancellor L. Erhard agreed to proceed with a joint bilateral project for the research of interplanetary space. The "Memorandum of Understanding" between the U.S. and Germany was signed in mid-1969 (1); the development contract for the HELIOS probe was awarded to industry at the start of 1970.

+) Deutsche Forschungs- und Versuchsanstalt für Luft- und Raumfahrt e.V., Porz-Wahn, Fed. Rep. Germany
(German Research and Experiment Agency for Aerospace Technology)

The launching of the probe, with a Titan III-D rocket, is planned for September 1974.

The first probe will be injected into an orbit in the plane of the ecliptic with the perihelion at 0.3 AU (1 AU = about 150 million kilometers), and will return to the aphelion at 1.0 AU in about 180 days (Fig. 1). If the first mission is successful, and the transmitted data indicates that a closer approach with this probe seems possible, a second probe will be launched 15 months after the first, with a perihelion of 0.25 AU. The periods of closest approach, occurring 90, 270, and 450 days after launch, will doubtless be most important. The solar radiation intensity, according to the inverse square law, will peak at 11 and 16 SC, respectively (Fig. 2), equivalent to 22.5 kw/m^2 at closest approach. Clearly, this can cause unusual thermal problems to arise - just consider the absolutely necessary ports for experiments and telemetry, the external attachments such as antennas, as well as the solar cells on the probe's surface.

The participation of several countries in the scientific aspects of the program underlines its international significance. The USA, Italy, and Australia are each supplying one experiment. The rest of the total of 11 experiments comes from Germany. The experiments will perform measurements ranging from electric and magnetic fields over a wide spectrum, to mass spectrometry and analysis of the zodiacal light.

3. The HELIOS Solar Probe

Since realistic simulation techniques are necessarily determined by the complexity of the specimen, a short description of the probe is in order.

Detailed information can be found in the references (2, 3, 4, 5). The 320 kg probe is spin stabilized and shaped somewhat like a spool of thread 2.8 meters in diameter and 2.1 meters high. For protection against heat, the middle section is super-insulated, however, this insulation layer must be breached for necessary ports and appendages. An active temperature control system using louvers (6) is situated over and under the cylindrical middle section; this system must protect not only against over-heating at closest approach, where the radiation intensity is 11 or 16 SC, but against the cold of outer space, where the intensity is only 1 SC. The solar cells are installed on the two diverging cones attached to the middle section. In order to reduce the temperature, about half the area of the solar cells panels is covered with second surface mirrors. In addition to the thermal problems caused by the ports in the middle section, when the louvers are open at close approach the high-gain antenna reflector reflects sunlight and radiates heat (due to its own high temperature) into the probe compartment. An overall picture of the several measures for controlling

the thermal balance over the necessary temperature range is provided in Fig. 4. The measures reduce the over 100 kw of solar energy which strikes the probe to a residual of 500 w, to be dissipated by passive radiators and active louvers.

4. Environmental Problems

The intensity of evenly distributed radiation from a point source is inversely proportional to the square of the distance from that source. Using this ideal law the intensity can be calculated as a function of the known intensity at earth. This applies also to electromagnetic radiation and uncharged particles. The accuracy of the predicted solar flux will be influenced by uncertainties in the final achieved orbit and the accuracy of the solar constant. The different types of radiations, influenced even at great distances by the sun's wide-ranging electric and magnetic fields, are not well known - to measure them close to the sun is the aim of the HELIOS mission. The degradation effects of charged particles can only be estimated. The severest degradation and contamination (for example, outgasing from organic materials such as adhesives, and condensation of these gases on cooler parts) are expected at closest approach due to the strong ultraviolet radiation and temperatures up to 180°C on the solar panels (7, 8). Furthermore an inadequate simulation in the test facility can change these effects. For this reason, certain test facilities have been so constructed that contamination from the facility itself is held to an absolute minimum.

5. Test Philosophy and Sequence

In order to achieve maximum stability over the range of temperatures expected, it is necessary first to select or develop materials to withstand the extreme conditions, and to test them to exact specifications. At many facilities, especially at Goddard Space Flight Center (GSFC) at Washington, materials and components have been subjected to tests for absorption and emission (α, ϵ), outgasing, and heat conductivity at various temperatures - also under bombardment with charged particles. The following remarks will concentrate on thermal resp. solar simulation.

A space simulation facility, in which a full-size HELIOS model could be tested with 11 or 16 SC, is not available. The construction of such a facility for this special case is not feasible because of cost and time, not to mention development risk. Clearly, several compromises must be made. Step by step, the critical areas were isolated in which maximum of quality and reliability with minimum effort could be achieved. Logistic problems resulting in higher costs arose - for example, tests

in the U.S.A. with all necessary ground support equipment.

Since true solar simulation for the full-size model was not possible, it was agreed to test critical materials and components at full intensity. For this purpose a U.S. solar simulator was ordered with the capability to produce 15 SC with a 30 cm beam diameter, filtered, and with high collimation. Also, in the Institut für Raumsimulation (DFVLR), a small chamber was modified by the addition of a motion simulator and an improved shroud. Uncertainty existed about the validity of extrapolation to 11 or 16 SC from tests at 1 to 2 SC (in 1970) or at 1 to 5 SC (later), because different heat transfers are superposed (thermal radiation prop. T₄, conductivity prop. ΔT) and the coefficients still have a certain temperature-dependence. In order to clarify and confirm the possibilities for extrapolation, a relatively simple 48-node small-scale model was constructed and tested at 1, 2, 7 and 11 SC. In these tests the temperatures obtained at 1 and 2 SC were mathematically extrapolated to 7 and 11 SC and compared with measured values (9, 10). These tests served also to provide practical experience in high-intensity measurements. The first test, in the IABG ⁺) simulation chamber, uncovered systematic errors that, during the second test in the DFVLR chamber, could be eliminated by a more precise determination of the chamber-influences.

The results of these tests increased our confidence in the validity of extrapolation. However, the model was very much simplified and small (30 cm in diameter), hence the gained information limited. Besides component-tests solar simulation tests at natural size of HELIOS were envisaged in U.S.-chambers. The functional thermal/vacuum testing of the spacecraft (soak tests) and the thermal balance tests at the expected high and low orbit temperatures were performed in a German chamber under simplified simulation conditions. The flow plan for thermal testing is shown in Fig. 5. First, materials (e.g. solar panels and surface layers) and components (e.g. experiments exposed to space) are tested under spectrally-matched high-intensity radiation in the DFVLR component test facility. Next, complete sections, as well as the thermal model (TM), of HELIOS are tested in a modified vacuum chamber at IABG with simple infrared heating, without solar simulation and motion simulator (11). Final testing of the TM and prototype (P) is accomplished in the 25 ft chamber at JPL in Pasadena under high intensity (5.4 SC at 11 ft beam diameter). Problems which arise in the course of testing (e.g. high-gain antenna reflector) can be studied and corrected by repeating previous tests in smaller facilities.

⁺) Industrieranlagen-Betriebsgesellschaft mbH, Ottobrunn/München
(Industrial Testing Corporation)

6. Summary of Simulation Methods

The possible simulation methods are listed in Fig. 6.

- o Solar simulation, e.g. an "off-axis" system using xenon lamps, allows the generation of collimated, spectrally-matched sunlight. Because of the enormous power required such facilities are expensive as investment and in operation. None exists capable of meeting HELIOS mission requirements.
- o Tube lamps, e.g. xenon low-pressure or tungsten lamps. The spectrum of tungsten lamps varies with the power, and cannot be matched to the sun's. It is difficult to achieve the correct energy distribution along the spin axis.
- o Simulation of the absorbed energy with heater tapes imbedded in the surface is often used for satellites near earth (1 SC); but for the high temperatures of HELIOS, this method is problematic. Since the heater tapes should not be left in the flight unit, the surface-panels have to be changed after the test.
- o A heated canister to warm the spacecraft to the expected surface temperatures is the simplest method. However, a realistic irradiation of the ports is not possible. Also, re-contamination due to outgasing from hot spots condensing on to cooler parts can occur in the small (3 cm) gap between the canister and the spacecraft.

The thermal testing in three stages has turned out to be practical, although temperature deviations between tests in different facilities have been recorded. These inconsistencies have been largely resolved by facility improvements (e.g. of infrared absorption) and reduction of disturbing influences (e.g. test adapter). As a result of the tests, a series of improvements on the spacecraft, especially on apertures and antenna reflector, were found necessary. Details of the tests and facilities are the subject of other presentations and will not be discussed here. This presentation is intended to provide an overall survey and to explain the relationship between the various tests designed to solve the critical thermal problems involved in the challenging HELIOS mission. Although the final results can only be demonstrated by the actual flight-data, the test program allows high hopes that the essential problems can be mastered.

In closing, the authors acknowledge the technical support of various organisations, especially Goddard Space Flight Center, Washington, but also Ames Research Center, San Francisco, and Jet Propulsion Laboratory, Pasadena.

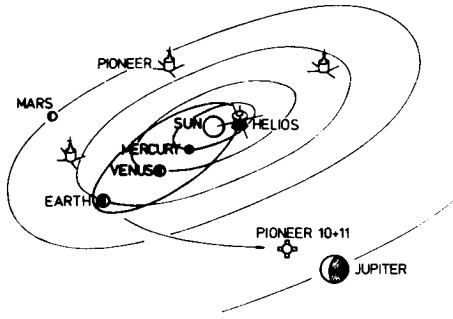


Figure 1

- HELIOS MISSION 0.25 AU -

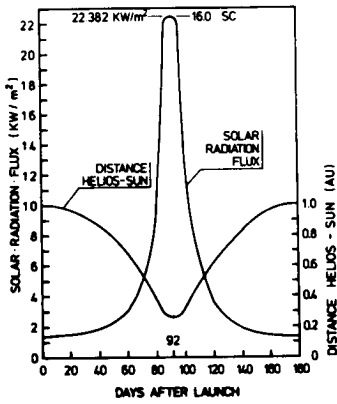


Figure 2

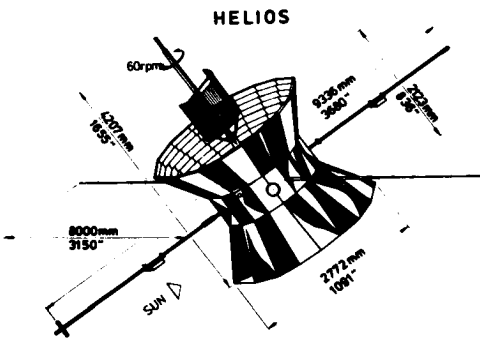


Figure 3

THERMAL BALANCE OF HELIOS AT 16 SC

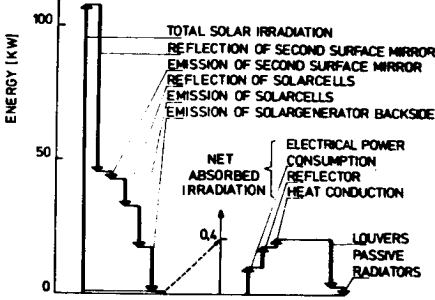


Figure 4

**FLOWDIAGRAM OF THERMAL BALANCE TESTS
- DEVELOPMENT AND QUALIFICATION -**

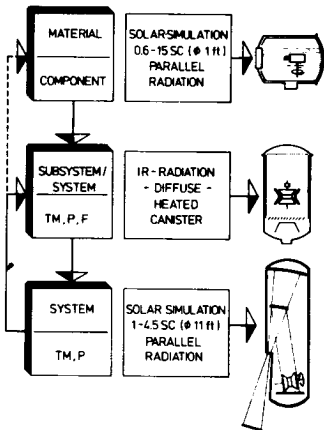


Figure 5

SIMULATION METHODS FOR TESTING THE SPACECRAFT

	TYP	CHARACTERISTICS	REMARKS
	SOLAR SIMULATION	COLLUMATED RADIATION SPECTRAL MATCHED	EXPENSIVE HIGH INTENSITY NOT AVAILABLE
	TUBE - LAMPS TUNGSTEN, XENON CYLINDRICAL ARRANGED	RADIATION DIFFUSE NOT SPECTRAL MATCHED	HEAT FLUX ALONG SPINAXIS DIFFERENT
	HEATER TAPES	TAPES IMBEDDED IN SURFACE	ELECTRICAL ENERGY EQUALS ABSORBED SOLAR FLUX
	HEATED CANISTER	SURFACE TEMPERATURE OF SPACECRAFT ADJUSTED TO CALCULATED ORBIT TEMPERATURE	RADIATION PROBLEMS ON APERTURES

Figure 6

R e f e r e n c e s

- (1) HELIOS Program Mission Definition Group Report. NASA - BMwF, April 1969
- (2) Gilbert Ousley, GSFC and Ants Kutzer: GfW HELIOS-Cooperative Solar Probe. Ninth Symposium on Space Technology and Science, Tokyo, Japan May 17, 1971
- (3) Friedrich Unz: Solar Probe HELIOS. XXI International Astronautical Congress, October 5, 1970, Konstanz
- (4) Friedrich Unz: The Development Phase of Solar Probe HELIOS. 23. International Astronautical Congress, October 1972, Vienna
- (5) Friedrich Unz: Development and Application of New Technology for the Sunprobe HELIOS. October 1973, Baku, UdSSR
- (6) W. Lorenz: Über die Entwicklung des Wärmekontrollsystems der Sonnensonde HELIOS. 5.DGLR-Jahrestagung, Berlin, Oktober 1972
- (7) W. Wilkens: Kontaminationsprobleme bei Raumflugkörpern. Raumfahrtforschung, Heft 4/72
- (8) H. Hörster/H. Köstlin und W. Schäfer/L.Ludwig Preuss: Untersuchung des optischen und wärmetechnischen Verhaltens von Oberflächen-Beschichtungen für die HELIOS-Sonde. Raumfahrtforschung, Heft 3/72
- (9) W. Schwarzott: HELIOS Phase "C" Extrapolation von Temperaturfeldern. Bericht Dornier System, DS-41/70, September 1970
- (10) H.P. Schmidt, K. Kramp, H.J.P. Genzel: Extrapolation von Temperaturfeldern. DFVLR-Institut für Raumsimulation & Dornier System - GfW 009-020/71 H (Internal Report)
- (11) J. Gülpen, W. Lorenz: Infrared Test Techniques Developed for the HELIOS Spacecraft. Seminar on "Structural and Thermal Tests, their Evolution and Present Trends", ESRO/ESTEC, December 1972.

N74-10278

THE DESIGN AND OPERATION OF AN INFRARED SIMULATOR FOR TESTING OF THE SHUTTLE RADIATOR SYSTEM

Douglas J. Skinner, *Northrop Services* and Jack E. Breiby,
NASA Johnson Space Center, Houston, Texas

ABSTRACT

An infrared simulation system was designed and installed in chamber A of the NASA Johnson Space Center in support of the development of the Space Shuttle Modular Radiator System. Various types of simulator designs were considered for conditioning of the test article during thermal-vacuum testing. This paper discusses the design and operation of fluid controlled panels to simulate the incident infrared flux which would be experienced by the Space Shuttle radiators during earth orbit. The thermal capabilities of the simulator are presented together with the reasons for the selection of this type of system.

INTRODUCTION

A series of tests were conducted in the Space Environment Simulation Laboratory chamber "A" at the NASA Johnson Space Center to determine parametric thermal performance of a candidate modular radiator system proposed for the space shuttle. The conventional heat sink and solar simulation systems of the chamber could not be used for these tests because of the size of the radiator system, and the requirement for simulating different heat loads simultaneously for various combinations of the eight radiator panels comprising the array. The major requirements for thermal simulation were as follows:

- o Heat flux simulation had to be provided by individually controlled modules for each of the eight radiators.
- o The infrared (IR) flux absorbed by each radiator had to be uniform and individually controllable in the range 20 to 150 Btu/ft² hr at an accuracy of 5 Btu/ft² hr.

- o The average flux actually obtained from the IR simulator had to be within ± 10 percent of the desired flux level.
- o For cold soak conditions a flux level of approximately 5 Btu/ft² hr had to be provided.
- o The accuracy of the actual flux had to be known within ± 5 Btu/ft² hr.
- o The flux at any point on each radiator had to be within ± 10 percent of the average flux for that specific radiator.
- o The original test plan outlined a series of steady state conditions within the flux range; orbital profile simulation was not required. However, requirements for dynamic orbital simulation were subsequently identified and these requirements were also accommodated by the system design described below.

DESIGN

IR Simulator System Selection

An extensive design study was conducted where several simulator concepts were evaluated to provide the above thermal simulation requirements. Among these were electrical strip heaters, quartz lamps, and fluid panels. Strip heaters of thin nichrome were available from a previous test program and could be assembled to provide individually controlled zones. The main disadvantage of this design was that some sort of rotatable or retractable mechanism had to be provided for each panel to meet the cold soak and low flux profile requirements due to excessive blockage of the chamber cold wall. Quartz lamps were not selected primarily due to the difficulty in providing the absorbed flux uniformity on the large 6- by 12-foot test articles. In addition an infrared simulator designed with quartz lamps or strip heaters would require full chamber cold walls during the testing. The initial cost of the fluid panels was high, but the relatively simple thermal analysis and accuracy of providing known flux levels on a real-time basis more than offset the initial higher cost. The fluid panels had the additional advantage of being cold soaked rapidly with LN₂, eliminating the slow cooling by radiation to the chamber cold sink. The thermal simulation system that was selected was a set of eight individually controlled fluid conditioned panels. The overall rectangular

dimensions of the panels were the same as the test article radiators, 6- by 12-feet. Each simulator panel was installed directly below a test radiator (see fig. 1). The majority of the testing was conducted by enclosing the test radiator and the simulator panels in radiation shields, thereby eliminating the need for full chamber cold walls. Each panel had two independent flow systems, one for Freon-11 and a second for gaseous or liquid nitrogen. The Freon-11 was used to provide controlled flux levels between 20 and 150 Btu/ft² hr, and the LN₂ was used for the 5 Btu/ft² hr condition. Controlled fluxes between 5 and 20 Btu/ft² hr could not be obtained due to the -168° F freezing temperature of Freon-11. The Freon-11 heating system had the capability of both manual or closed loop computer control. The hot gaseous nitrogen system was used primarily to warm the panels from LN₂ temperature to above -130° F at which point the Freon-11 system could again be used. In addition it served as a backup for simulation of higher flux levels if problems occurred with the Freon-11 system. Eight identical systems were installed with a unitized control console and a common Freon-11 reservoir.

Thermal Considerations

The fluid panels were designed to have a maximum of 5° F drop from the inlet to the outlet manifolds and a 3° F differential between the fluid channel centerlines when the panel conditioning was provided by Freon-11. The thermal calculations were based on the assumption that the heat transfer from the fluid is exchanged with the panel at the welded joints (see following section, "Mechanical"). The 8-inch Freon-11 channel spacing was based on the calculations that the heat exchanged by the panel is from the midpoint between the fluid channels to an element and must pass through the element to the liquid. When view factors and emittances are considered the average temperature differentials between the Freon-11 channels was calculated to be 3° F and 15° F between the LN₂ channels. The Freon-11 flow rate calculated for a maximum of 5° F temperature differential along the tube was based on an heat exchange between the radiator and simulator panel of 150 Btu/ft² hr. Using a panel size of 6- by 12-feet and the specific heat of Freon-11 being 0.21 Btu/lb °F, the minimum Freon flow required was 10,300 lb/hr or 14 gal/min.

In order to provide a surface with a high emissivity, the simulator panel surface on the opposite side of the tubing was coated with

approximately 3 mils of 3M 410C Nextel black matte paint. A special coating procedure was required to withstand the temperature extremes (-320° F to +130° F) that would be encountered during the testing. The aluminum surface was first abraded with sandpaper and then washed with Freon MF. After drying, a coating of 3M 901-P1 primer was applied and the 3M 410C paint followed within a few minutes by spraying. The large panels were cured at 250° F for 24 hours by flowing steam through the tubes. This coating did not deteriorate even after several hundred hours of thermal-vacuum testing and also provided as high as 216 Btu/ft² hr flux levels (under limited radiator temperature conditions) without exceeding the maximum Freon-11 system operating pressures.

The incident flux level as a function of the simulator panel temperature is presented in figure 2. Also shown is the approximate flux absorbed by the radiator (emittance 0.85). During actual testing the simulator panel temperatures had to be adjusted to compensate for the reflected energy between the panel and the radiator.

Mechanical

The preceding thermal considerations resulted in the mechanical design illustrated in figure 3 and figure 4. An aluminum plate 0.187 inches thick was chosen to provide the conductive path, with the Freon tubes spaced on eight-inch centers. One-inch square tubing was selected for the flow paths. Staggered full fillet welds were used to attach the tubing to the plate, which also provided a good conductive path to the plate. Attached at every second tube was another of the same size to form a separate GN₂/LN₂ flow path. Placing one tube on the other also increased the moment of inertia so that the panel was stiff enough to be supported at only two places with no noticeable sag. The 1-inch tubes were welded to 1-1/4-inch square tube manifolds on each end. The manifolds were sized to provide equal flow in each of the fluid channels.

Simple aluminum angle tables were used to support the test radiator-simulator panel assembly (see fig. 1). Isolation brackets were built which supported the shuttle radiators a uniform 6 inches above the thermal simulator panels. The whole assembly was wrapped with radiation shielding and operated without the necessity of cooling the entire chamber to LN₂ temperature for some test modes. For certain test modes, the radiation shields were also placed at an angle and

used with full LN₂ cold walls to simulate blockage by the shuttle cargo bay doors.

The radiator and simulator panel pairs were arranged in the chamber as shown in figure 5. This panel arrangement provided a close simulation of the Shuttle cargo bay door plumbing installation. Aluminum tubing (6061-T6) of 1-1/4-inch diameter was used for the Freon-11 and the GN₂/LN₂ plumbing. All in chamber lines were welded and helium leak-checked prior to the installation of two layers of aluminized Kapton insulation.

Heat Supply

To supply the heat output of 10,800 Btu/hr a power rate of 3.2 kilowatts was required. The mass of the panel, interconnecting plumbing and fluid was calculated to be approximately 600 pounds. Assuming an average specific heat of 0.22 Btu/lb °F, the transient power constant was 2.3 KW min/°F. A 9 KW Calrod heater (22 watts/in²) and a 5 horsepower, 50 psi centrifugal pump was installed for the Freon-11 circulating system. Assuming about 1/4 of the motor power going into the fluid, approximately 10 kilowatts of heat was available. This provided a transient of 3° F/min rise in the system temperature.

Heat Rejection

Cooling of the Freon-11 was accomplished by using a Freon/LN₂ heat exchanger. The cooling requirements for average steady-state conditions were 10,800 Btu/hr for heat input from the test radiators, plus pump cooling, heat leaks in the lines, and some trim heat to ensure computer control. This gave an approximate fixed heat load of 18,000 Btu/hr. The cooling required during transient conditions was about 40,000 Btu/hr. The total maximum cooling load was 58,000 Btu/hr.

The Freon/LN₂ heat exchanger was sized to provide the cooling with an LN₂ flow of approximately 1 gallon per minute.

Freon Fluid System

The temperature of the simulator panels was controlled by its own independent fluid system; a schematic illustrating the major components is illustrated in figure 6. A single Freon storage tank supplied the Freon-11 to the zones. A separate Freon drain tank and transfer system (not shown in the figure) was used to drain the system prior to initiating LN₂ to the

panels. The independent circulating and control system for each panel provided flexibility in controlling the panel temperatures at different levels. An alternate approach which was considered and rejected consisted of a central large capacity pumping system with the necessary controls to blend the hot and cold fluid streams. This system could not provide the required flexibility without the complexity of an elaborate control system. A 20 gpm, 50 psig discharge pressure centrifugal pump with standard controls was used to circulate the temperature controlled Freon-11 through the panels. A 60 psig blanket pressure was maintained on the storage tank to provide sufficient net positive suction head for the high temperature operation. Aluminum tubing 1-1/4 inch in diameter was used for the liquid flow paths. The Freon-11 temperature was controlled with a 9 kw Calrod heater and a 100,000 Btu/hr, LN₂ /Freon heat exchanger. A needle metering valve was modified for cryogenic application and was used for manual control of the LN₂ to the heat exchanger. The electrical heater could be controlled manually or by automatic computer control in increments of approximately 145 watts. During most operations the system was set to always require some trim heat since the final temperature control of the panel was maintained by the facility computer.

Computer Control

The 9 kw heaters were controlled by a facility computer. The software computer program used previously for an electrical IR simulator was modified to permit either open- or closed-loop control of the heater to provide a predetermined simulator panel temperature. The software package provided considerable flexibility through real-time input options which included the following:

- o Selection of open or closed-loop control.
- o Selection of the time interval between power control signal updates.
- o Definition of thermocouples to be averaged for closed-loop temperature control.
- o Selection of primary and secondary control modes and cathode-ray tube display of the average panel temperatures.

The power controllers were silicon-controlled rectifiers capable of producing a 117-volt rectified

alternating current. The computer program generated a 6-bit binary power input signal to each control which resulted in a heater control of approximately 145 watt increments.

The IR simulator control sensors were copper/constantan thermocouples, which were installed on the tube side of the panel. The distribution of the thermocouples on the simulator panels is shown in figure 4. (The location dimensions are in inches.) A coded measurement numbering system was incorporated, the second digit of the number is the simulator panel number, while the last two digits are the thermocouple number.

The control program read the desired average panel temperature and compared this value to the actual temperature for the current update interval. The program then corrected the command to the power controllers to cause the measured temperature to approach the desired value. The control system options enabled the thermal engineer to provide the precise thermal simulation required for the specific test mode and to make real-time corrections as required. A comparison of the desired and actual flux profiles is shown in figure 7.

LN₂/GN₂ System

The unitized control console (see fig. 8) with the valving, flow and pressure indicators provided controlled closed-loop and single-pass LN₂ flow from the facility system into the panels. Alternate valving provided heated GN₂ through the same piping. Each loop was independent of the others except for the common facility supply. The heated gas was used primarily to bring the panel temperature above the freezing point of Freon before reloading the Freon loop. The heated GN₂ was also used as a redundant system for flux levels up to about 130 Btu/ft² hr.

Thermal Calculation Technique

A mathematical model of the radiator-simulator panel assembly was derived by assigning 12 thermal nodes to the radiator, one node to the IR simulator panel and four nodes to the radiation shields enclosing the perimeter of the assembly (see fig. 9). Based on these nodes view factors were calculated. A desktop calculator was programed using these view factors, the emissivity of both the radiator and the IR simulator panels, and the node temperatures to calculate the average absorbed flux and that absorbed by each node. Pretest predicted radiator temperatures

were entered and iterative panel temperatures were tried until one was selected which would provide the desired absorbed radiator flux. During the test phase the measured radiator and panel temperatures were used to calculate the actual absorbed flux into the radiator. After some testing the thermal engineers became familiar with the system operation, and the number of radiator nodes were reduced from twelve to four without any loss of accuracy in the calculations. For final data analysis of the absorbed flux, only one node was used. Selected thermocouples were used to meld the flux distribution into an accurate average.

SYSTEM OPERATION

The first series of tests were conducted with the radiator and simulator panels completely enclosed by radiation shields. (See fig. 1.) The radiation shields were multilayer super-insulation blankets. This configuration provided insulation on one side of the radiator simulating operation in the "single-sided" radiation mode. For the "two-sided" radiation test configuration the blankets were removed so that the top side of the radiators would reject heat to the chamber cold walls. A third series of tests were conducted by positioning the blankets at an angle above the radiator. This configuration simulated "two-sided" radiation with some blockage by the Shuttle cargo bay doors. Initially the theoretical radiator temperature patterns were used to determine the simulator panel temperatures for the desired flux level. The thermal simulation using these values provided a flux level that was approximately 5 percent high. Between test series the emittance of the test radiator coating was measured and was found to be higher than had been expected. The calculator program was corrected for the new emittance value and the simulated flux levels agreed with the analytical predictions. The fluid system had been initially designed to the requirement for steady-state levels of IR simulation. After the system was fabricated, simulation of dynamic orbital profiles were requested. When this was first attempted, Freon-11 was left in the panels and was frozen by the LN₂ while attempting simulation of the cold side of the orbit. In order to initiate Freon-11 flow again for the warmer environment simulation, hot GN₂ was introduced in the LN₂/GN₂ manifold in an attempt to thaw the frozen Freon-11. Nonuniform heating of the Freon-11 channels caused expansion of the liquid between frozen sections resulting in excessive pressure build-up and the subsequent rupture of the Freon-11 manifold. This problem

was solved during subsequent testing by draining the Freon-11 loop before introducing LN_2 .

The calculator programs developed for this test proved to be indispensable for determining panel set-point temperatures and for quick-data reduction to verify that proper flux levels were being provided. The IR system met all the original design requirements plus the added requirement for orbital cycles. It also was used to provide fluxes as high as 175 Btu/ft^2 hr. Coincidentally, the thermal mass of the system was such that the heating and cooling rates very closely met the 90-minute earth orbital profile. The system was not originally designed for this requirement. The closed loop computer control of the heater proved especially effective during steady state flux conditions. It allowed the test engineer to maintain the final fluid temperature control after the initial approximate manual setting was made at the control console.

Figure 10 illustrates a typical case of providing both steady state and orbital cycle flux profiles. This graph was generated by a computer program available at JSC which calculated the average flux levels from the test data tapes and provided both tabulated data and graph plots.

Figure 11 shows a plot of the same time period for a different Shuttle radiator where the flux level was controlled by the GN_2/LN_2 loop after the Freon control loop had failed. Note the close similarity with figure 9 which demonstrated the back-up capability of the GN_2/LN_2 system.

A typical radiator flux level trace is presented in figure 7. These data show the desired absorbed steady state and cyclic flux levels compared to the actual flux levels. The slopes and the steady state drift were well within the design requirements indicating the excellent performance of the IR simulation system.

CONCLUSIONS

The fluid controlled IR simulation system was a good choice for this application because of the flexibility in providing desired flux levels over a wide range on a real-time basis. The system response time was very good in that a single zone could be changed from cold soak LN_2 temperatures to controlled warmer environment simulation with the Freon-11 loop in approximately 30 minutes. Approximately 2 hours were required for this sequence for all eight panels. The time required to change all eight panels from a

controlled flux level using the Freon loop to stable LN₂ temperatures was approximately 90 minutes.

The programed desk calculator was an essential aid to the thermal engineer in determining the panel temperatures necessary to provide the absorbed infrared flux by the radiators. The data could be analyzed during the actual test sequence and rapid real-time adjustments could be made as required to provide the exact flux level. The simulator system exceeded the design requirements in all cases and in addition provided orbital flux simulation.

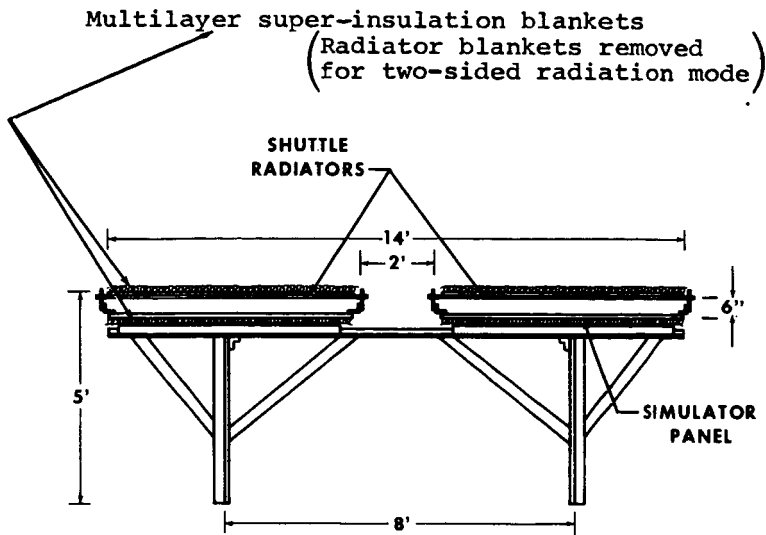


Fig. 1 - End-View of typical radiator-simulator pair installation

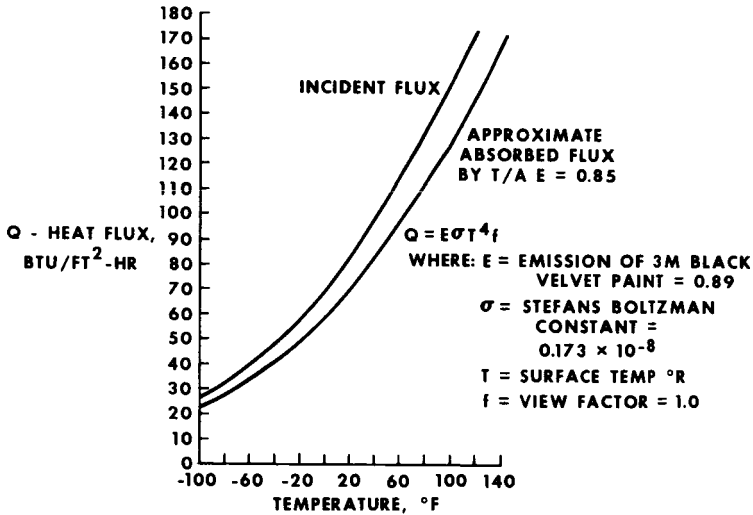


Fig. 2 - Simulator panel flux as a function of temperature

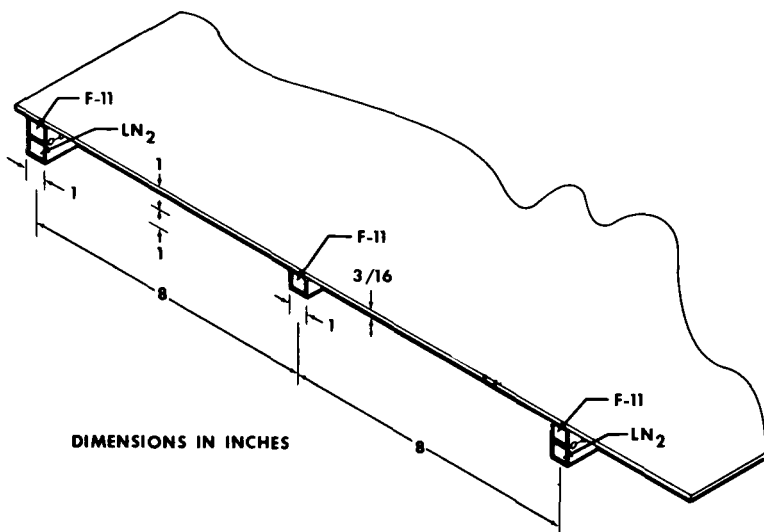


Fig. 3 - IR simulator panel fluid tube spacing

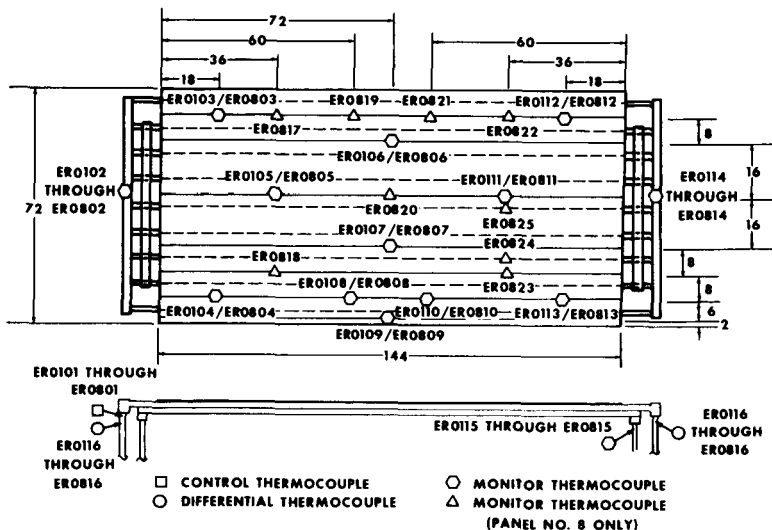


Fig. 4 - Piping and thermocouple distribution on simulator panel

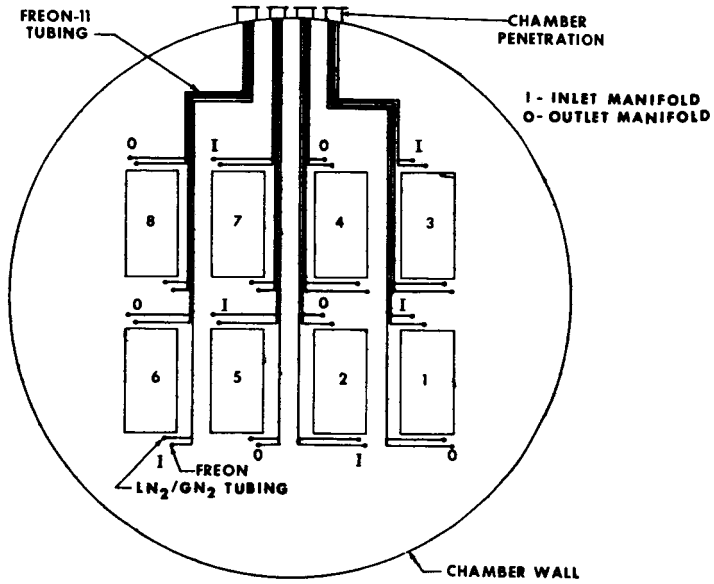


Fig. 5 - Chamber A installation of radiator/simulator pairs

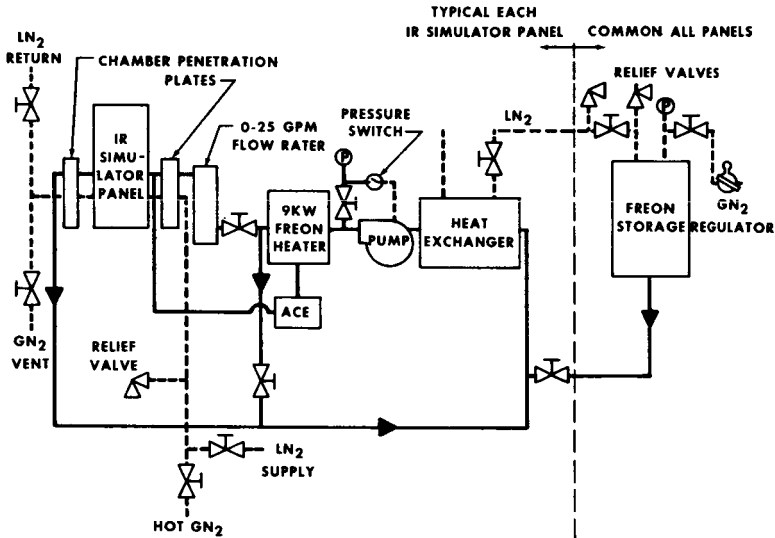


Fig. 6 - Schematic of individual fluid control system

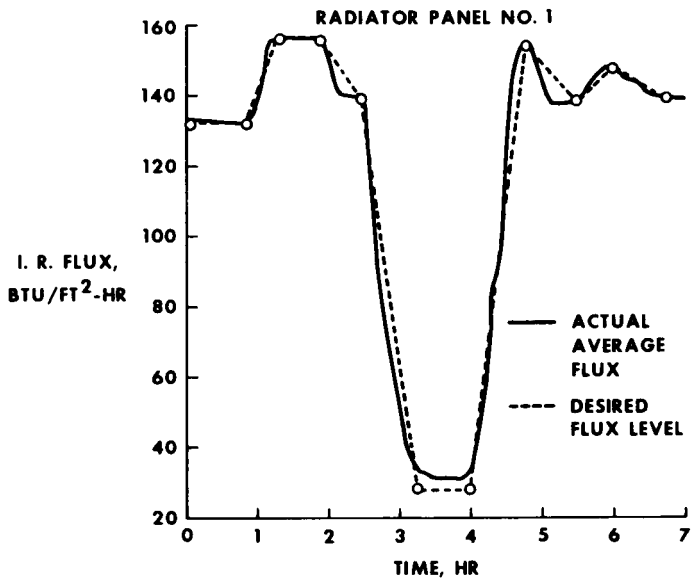


Fig. 7 - Typical simulator performance compared with desired profile

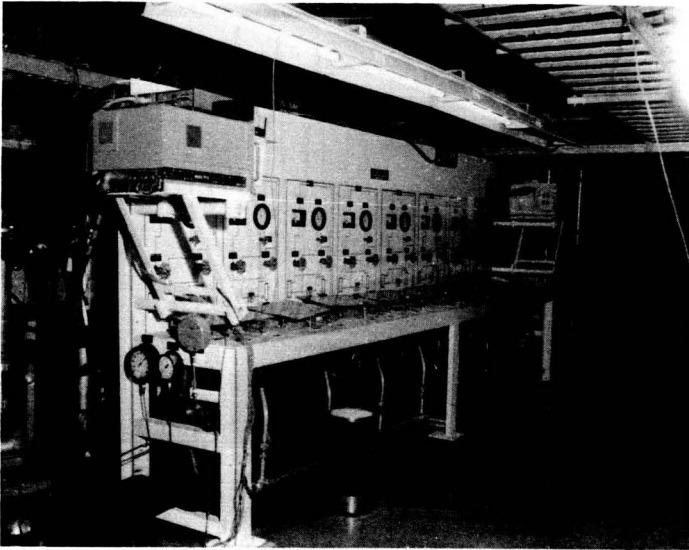


Fig. 8 - Unitized fluid control console

NODE IDENTIFICATIONS

- 1 TO 12 RADIATOR PANEL
- 13 IR SIMULATOR
- 14 TO 17 INSULATION

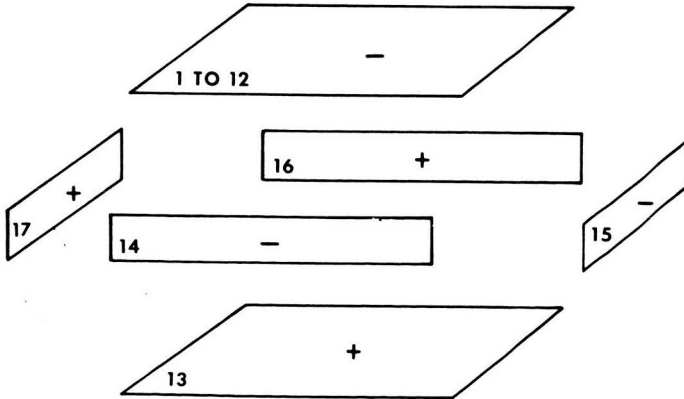
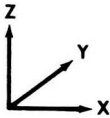


Fig. 9 - Mathematical model of radiator/simulator installation

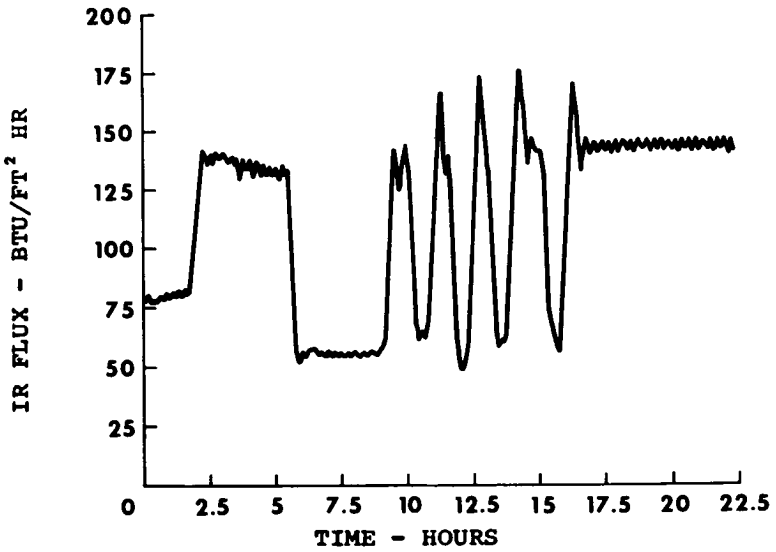


Fig. 10 - Simulator performance with Freon-11 operation

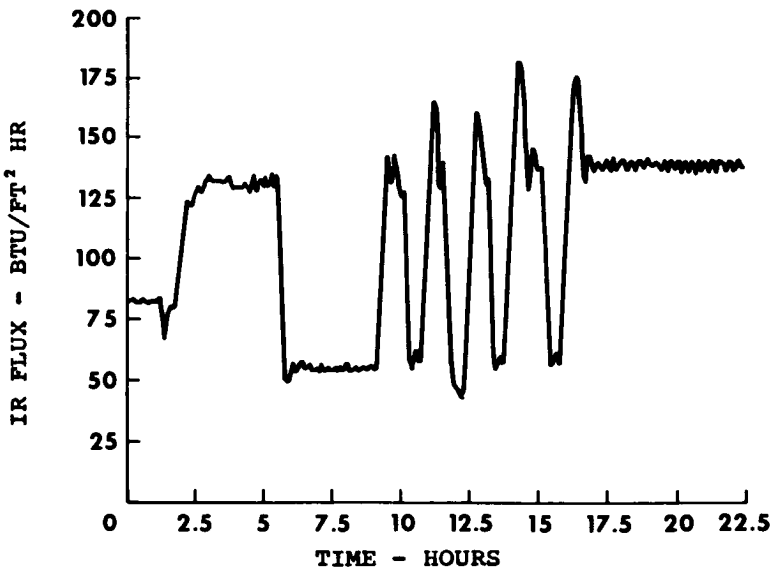


Fig. 11 - Simulator performance with GN₂/IN₂ operation

N74-10279

Paper No. 56

METHOD AND RESULTS OF INFRARED TESTING OF THE HELIOS SOLAR PROBE

J. Guelpen and W. Lorenz,
ERNO Raumfahrttechnik GmbH, Bremen, Germany

ABSTRACT

The infrared test technique developed to test the HELIOS solar probe at intensities equivalent to up to 16 Solar-Constants is described. The principle of this technique and the design of a test facility derived from it are discussed. The particular application of this technique to the measurement of heat input into a solar irradiated aperture is presented. Test results are compared to solar simulation test results.

INTRODUCTION

The HELIOS solar probe is a spin stabilized spacecraft, which consists basically of a centerbody containing all the equipment and most experiments, a heat shield which protects the centerbody from the environment, and two conical solar arrays (see Fig. 1).

This spacecraft will approach the sun to 0.25 Astro-nomic Units (1 AU = distance earth - sun) and will pass through solar irradiation intensities up to 22,4 kW/m² or 16 Solar Constants (S.C.) which have never been encountered by a spacecraft before. It is obvious that the thermal design of this spacecraft should be verified by the most realistic space simulation tests possible.

The simulation of solar radiation by Xenon arc lamps has some slight inaccuracies as there are several deviations from solar radiation characteristics, e.g.

- collimation of rays,
- local intensity distribution,
- spectral intensity distribution,
- transient variations in local or spectral distribution.

Nevertheless, the Xenon arc lamp has become the standard source for solar simulation and has proven to be highly accurate in most cases.

Unfortunately, there is no solar simulator available, which can provide 16 solar constants on a spacecraft of this size.

Therefore, there was no alternative but to simulate the solar heat input by infrared radiation.

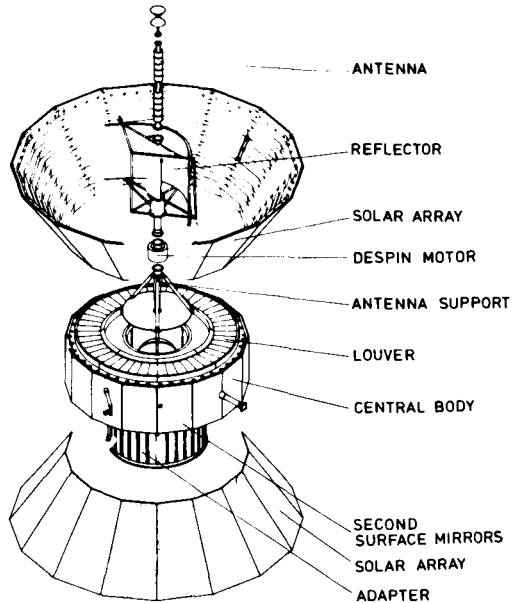


Fig. 1 HELIOS spacecraft

HELIOS INFRARED TEST TECHNIQUE

A heat balance of the HELIOS spacecraft shows that a very high amount of energy - 100 kW - is radiated onto the spacecraft (Fig. 2). Due to the particular design most of this energy is, however, directly reflected and emitted from the irradiated surfaces.

Only about 15 kW are conducted through the structure of the spacecraft - mainly through the solar panels - and emitted from other surfaces. From these figures it is readily apparent that an infrared test technique should try to simulate only the net heat flux through the spacecraft in order to reduce problems of power supply and energy transport in the space simulation chamber.

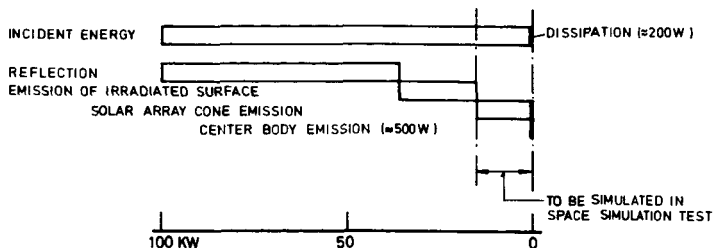


Fig. 2 HELIOS heat balance

Principle

Each thermal test technique should try to base its validity on as few assumptions and uncertainties as possible and, if uncertainties are unavoidable, their magnitude should be easily assessable and limited.

Therefore, the HELIOS infrared test technique is coupled as close as possible by means of tests and measurements to the Xenon arc lamp solar simulation. Use of complicated mathematical computer models and other sophisticated analytical means to establish the validity of the HELIOS infrared test technique are avoided. The reason for this is obvious: The validity of thermal test results should be completely independent of mathematical computer models of the spacecraft as the primary purpose of spacecraft thermal testing is to establish valid mathematical computer models by improving these due to test results.

The HELIOS thermal test technique is characterized by 3 steps which are described in the following.

Step 1: Determination of absorbed solar radiation incident to outer spacecraft surfaces.

The absorbed solar radiation is defined by

$$Q_{\text{abs}} = a_s \cdot I_s \cdot e_s \cdot A, \quad (1)$$

where

a_s is the solar absorptance of the surface for the particular solar light incident angle,

I_s is the solar intensity,

e_s is the cosine of the incident angle φ in the range

$0 \leq \varphi \leq \frac{\pi}{2}$ ($e_s = 0$ for $\varphi \geq \frac{\pi}{2}$, of course) and

A is the area of the absorbing surface.

A sample of the surface, for which the absorbed solar radiation shall be determined, is equipped with a thin heater skin just below the surface coating, as it is shown in an example in figure 3. The heater skin shall have a low thermal resistance and the thermal contact resistance between heater skin and substrate on the one side and heater skin and surface coating on the other side shall be kept low too by use of adequate adhesive material, because electrical heating in the heater skin instead of simulated solar irradiation shall not essentially disturb the formation of lateral and longitudinal thermal gradients in the sample. The heater skin is designed to generate the heat quite uniformly over its total area.

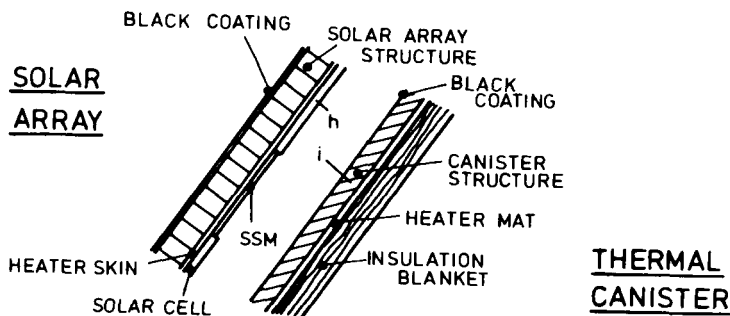


Fig. 3 Solar array infrared test set-up

Under simulated space conditions the sample is irradiated by simulated solar light with an intensity I_s and experiences equilibrium temperatures $T_{h1}, T_{h2} \dots$ at different locations 1, 2 a.s.o. Then the simulated solar light beam is switched off and the heater skin is heated by an electrical power Q_h which is regulated such that the sample experiences the same temperatures $T_{h1}, T_{h2} \dots$ at the same locations as before. The absorbed heat Q_{abs} is determined by the electrical power Q_h .

$$Q_{abs} = Q_h \quad (2)$$

The solar radiation, of course, is only uniformly absorbed by the sample area, if the absorptance a_s and the cosine factor e_s is uniform for the entire sample area.

However, under certain circumstances as are valid for the HELIOS solar arrays, for instance, the method of determining the absorbed heat as described above holds for surfaces with non-uniform α_s and e_s too. This will be discussed later.

Step 2: Calibration of infrared heater.

Simulated solar heating or electrical heating now is replaced by infrared heating. The infrared heater may be designed as shown in figure 3. However, the essential requirements are that the infrared heater emits the heat without local intensity variations and that the thermal conductance within the infrared heater along the surface is sufficiently low. The reason for the last requirement is discussed later.

The infrared heater is electrically heated with a heater power Q_i such that the irradiated sample exhibits the same temperatures T_{h1} , T_{h2} at the same locations as in step 1. The net heat transfer Q_{net} between infrared heater and sample is equal to the difference between absorbed and emitted heat and is described by the equation

$$Q_{net} = \alpha_s \cdot I_s \cdot e_s \cdot A - \epsilon_h \cdot A \cdot \sigma T_h^4 \quad (3)$$

where

ϵ_h is the emittance of the sample surfaces and
 σ is the Stefan-Boltzmann constant.

When the heat loss of the infrared heater through gaps between heater and sample is standardized by defining a fixed distance between both surfaces and/or avoiding heat losses from both surfaces by covering the circumferential gaps with highly reflective foil, the calibration of the infrared heater in form of a functional dependency

$$I_s = f(Q_i) \quad (4)$$

can be established.

In case that there is suspicion that the thermal background environment of the infrared heater or the conductance of the infrared heater superinsulation may vary from test case to test case, it might even be better to establish a functional dependency

$$I_s = f(T_i^4) \quad (5)$$

as a calibration curve.

Step 3: Performance of thermal test.

The performance of the thermal test now can take place. The original irradiated surface, of course, is not equipped with a heater skin, but otherwise identical to the sample. The simulated solar intensity is controlled by using the calibration curves, eq. (4) or eq. (5).

Extension of Infrared Test Technique Applicability

For constantly rotating surfaces neither obviously e_s nor usually a_s is constant. The absorptance a_s usually is dependent on the incident angle. However, for rotating surfaces irradiated by solar light the described infrared heating technique can be applied too, if the angular velocity and/or the thermal capacity of the surface are high enough such that transient temperature variations during one revolution are negligible.

Furthermore, the method is applicable for surfaces with a coating pattern containing elements of different absorptances a_s provided that the surface substrate has a sufficiently high thermal conductance which allows only negligibly small temperature differences between the surface elements of different absorptance, or provided that not microscopical but only macroscopical temperature distribution is of interest.

An example for a rotating surface with a coating pattern of non-uniform absorptance is the HELIOS solar array. This array is a rotating conical surface with a pattern of solar cells, second surface mirrors (= optical solar reflectors) and gaps between cells and mirrors with different absorptances.

A further extension of the infrared test technique is possible for irradiated sensor apertures, which really cannot be called "surfaces" anymore, as they usually mainly consist of funnels. Here another parameter - the temperature level of the spacecraft interior - is influencing the net heat input to the "surface" and, therefore, complicates the infrared test technique. The availability of an applicable test technique in this case, however, is very important for HELIOS, as the heat absorbed by sensor apertures is of essential magnitude for solar probes.

Theoretical Basis of Sensor Aperture Infrared Heaters

In order to determine the heat input to apertures a special aperture test body for each of the sensor apertures has been built. An aperture test body consists of the aperture part (e.g. funnel) of the sensor, a heat shield part surrounding the sensor, a black heater plate, which exclusively has radiative heat exchange with the aperture part, and a surrounding superinsulation, in which only the sensor

aperture and a radiator area of the heater plate remains uncovered. The heater plate is black, as it represents the interior of the solar probe; it is used to sense the net heat input via sensor aperture into the probe interior. An example of an aperture test body is shown in figure 4 and the principle of an aperture test body with aperture infrared heater is shown in figure 5.

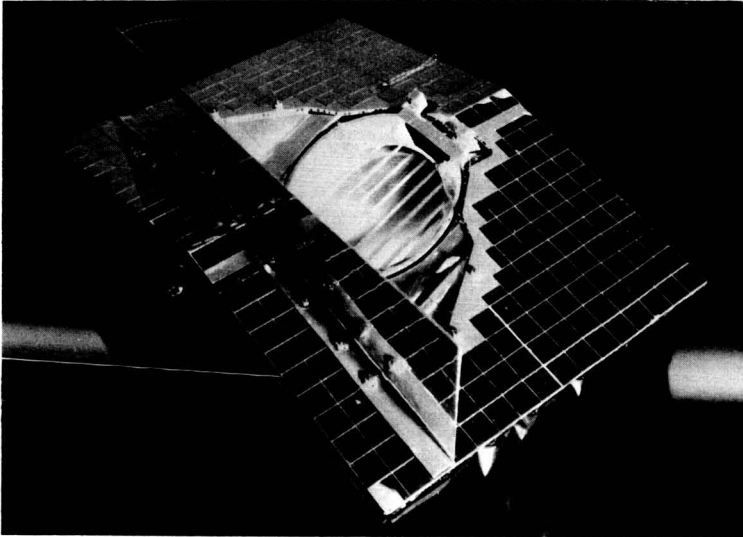


Fig. 4 Aperture test model

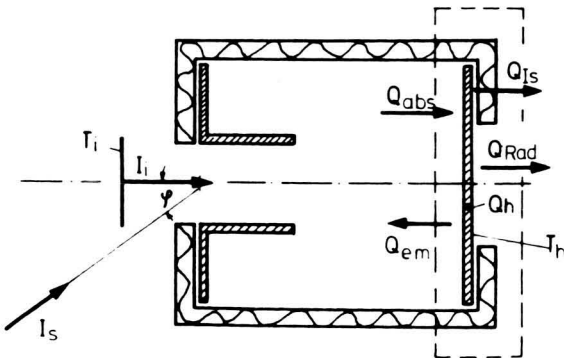


Fig. 5 Principle of aperture test body

As far as not yet defined earlier, the meaning of the designations shown in figure 5 is the following:

- Q_{em} : Heat emitted by heater plate
- Q_{IS} : Heat loss of heater plate across superinsulation
- Q_{Rad} : Heat emitted by radiator area of heater plate
- I_i : Intensity of infrared heater

Generally a thermal balance holds:

$$Q_{abs} - Q_{em} - Q_{IS} - Q_{Rad} + Q_h = 0 \quad (6)$$

For solar irradiation (I_s, φ) equation (6) by adding the parameters in brackets can be more fully written by

$$Q_{abs}(I_s, \varphi, T_h) - Q_{em}(T_h) - Q_{IS}(T_h) - Q_{Rad}(T_h) + Q_h(I_s, \varphi, T_h) = 0 \quad (7)$$

For irradiation by an infrared heater correspondingly holds:

$$Q_{abs}(I_i, T_h) - Q_{em}(T_h) - Q_{IS}(T_h) - Q_{Rad}(T_h) + Q_h(I_i, T_h) = 0 \quad (8)$$

Without irradiation ($I_s=0, I_i=0$ respectively)

eq. (7) and (8) reduce to

$$Q_{abs}(I=0, T_h) - Q_{em}(T_h) - Q_{IS}(T_h) - Q_{Rad}(T_h) + Q_h(I=0, T_h) = 0 \quad (9)$$

If the heater plate in case without irradiation is heated to the same temperature T_h as in case with irradiation (I_s, φ, I_i respectively) from eq. (7), (8) and (9) can be derived that

$$Q_{abs}(I_s, \varphi, T_h) - Q_{abs}(I=0, T_h) = Q_h(I=0, T_h) - Q_h(I_s, \varphi, T_h) \quad (10)$$

or

$$Q_{abs}(I_i, T_h) - Q_{abs}(I=0, T_h) = Q_h(I=0, T_h) - Q_h(I_i, T_h) \quad (11)$$

respectively.

As the heat irradiated to sensor apertures is independent of heater plate temperature T_h , it can be concluded that the differences in absorbed heat and the differences of heater powers, respectively, are essentially independent of T_h . This was proven by tests and can be expressed by the following equations:

$$\Delta Q_h(I_s, \varphi) = Q_h(I=0, T_h) - Q_h(I_s, \varphi, T_h), \quad (12)$$

$$\Delta Q_h(I_i) = Q_h(I=0, T_h) - Q_h(I_i, T_h) \quad . \quad (13)$$

Furthermore, in tests the expected proportionality between heater power difference and intensity was proven, which can be expressed by

$$\Delta Q_h(I_s, \varphi) = C_{1s}(\varphi) \cdot I_s \quad (14)$$

and

$$\Delta Q_h(I_i) = C_{1i} I_i \quad , \quad (15)$$

with $C_{1s}(\varphi)$ and C_{1i} being proportional constants.

In general the net heat input to a sensor aperture is

$$Q_{net} = Q_{abs} - Q_{em} \quad . \quad (16)$$

Using eq. (10), (11), (12) and (13) equation (14) can be written in the forms

$$Q_{net}(I_s, \varphi, T_h) = \Delta Q_h(I_s, \varphi) + Q_{net}(I=0, T_h) \quad (17)$$

and

$$Q_{net}(I_i, T_h) = \Delta Q_h(I_i) + Q_{net}(I=0, T_h) \quad (18)$$

respectively.

Corresponding to eq. (9) the net heat input in case without irradiation ($I=0$) can be determined by

$$Q_{net}(I=0, T_h) = Q_{Is}(T_h) + Q_{Rad}(T_h) - Q_h(I=0, T_h) \quad (19)$$

with

$$Q_{Is}(T_h) = \epsilon_{Iseff} \cdot A_{Is} \cdot \sigma T_h^4 \quad (20)$$

and

$$Q_{Rad}(T_h) = \epsilon_{Rad} \cdot A_{Rad} \cdot \sigma T_h^4 \quad , \quad (21)$$

where

ϵ_{Iseff} , ϵ_{Rad} are the quite accurately known effective emittances of the insulation and the heater plate radiator, respectively, and

A_{I_s} , A_{Rad} are the areas of the insulation and the radiator, respectively.

$Q_{net}(I=0, T_h)$ is always negative. It is obvious that $Q_{net}(I=0, T_h)$ is only dependent on T_h . In fact, tests showed the expected result that $Q_{net}(I=0, T_h)$ is essentially proportional to T_h^4 . The functional dependency

$$Q_{net}(I=0, T_h) = -C_2 \cdot T_h^4, \quad (22)$$

with C_2 being a proportional constant, can be easily determined by testing the aperture test body without irradiation.

With eq. (14), (15) and (22) the eq. (17) and (18) are rearranged to

$$Q_{net}(I_s, \varphi, T_h) = C_{1s}(\varphi) \cdot I_s - C_2 \cdot T_h^4 \quad (23)$$

and

$$Q_{net}(I_i, T_h) = C_{1i} \cdot I_i - C_2 T_h^4. \quad (24)$$

Based on the described theory the calibration of the infrared heater is done now in a quite simple manner:

The infrared heater, characterized by I_i or T_i^4 , respectively, is irradiating exactly the same heat input as a simulated solar radiation, characterized by I_s and φ , into the sensor aperture, if for identical heater plate temperature the heater powers $Q_h(I_i, T_h)$ and $Q_h(I_s, \varphi, T_h)$ or $\Delta Q_h(I_i)$ and $\Delta Q_h(I_s, \varphi)$, respectively, are of equal magnitude.

By few measurements a correlation between solar irradiation (I_s, φ) and infrared radiation (T_i^4) can be established and, in principle, is shown in figure 6.

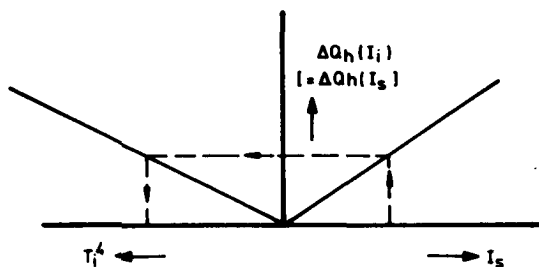


Fig. 6 Functional dependency between solar intensity I_s and infrared heater temperature T_i^4 with infrared heater power difference $\Delta Q_h(I_i)$ as coupling parameter

The evaluated constants C_1 and C_2 can be used as input data for the mathematical model of the probe. If for a sensor aperture node C_1 is used at the place where usually $a_s \cdot e_s \cdot A$ is introduced and C_2 is used at the place where usually $\epsilon_h \cdot e_h \cdot \text{Space} \cdot A \cdot \sigma$ is introduced, the net heat input to the sensor aperture is taken into account correctly, inspite of $C_1 \cdot I_s$ not being identical to the absorbed heat Q_{abs} and $C_2 \cdot T_h^4$ not being identical to the emitted heat Q_{em} . In fact, from eq. (10) to (18) is derived that

$$C_1 \cdot I_s = Q_{abs}(I_s, \varphi, T_h) - Q_{abs}(I=0, T_h) \quad (25)$$

and

$$C_2 \cdot T_h^4 = Q_{em}(T_h) - Q_{abs}(I=0, T_h) \quad (26)$$

It is a specific advantage of the described method that the net heat input to sensor apertures can be determined in the same way without modifying the method, if the aperture funnels for sensor design reasons are covered by special foils or grids, etc.

Adaptation of the Aperture Heater Method to the Spinning Probe

Actually the HELIOS probe is spinning with an angular velocity of 60 r.p.m. and, therefore, the incident angle φ varies rapidly. Provided that the rotation of the probe is sufficiently rapid, such that the sensor temperature remains essentially time independent - which actually is the case for 60 r.p.m. angular velocity - the mean, during one revolution experienced heat input $\bar{Q}_{net}(I_s, T_h)$ corresponding to eq. (17) is

$$\bar{Q}_{net}(I_s, T_h) = \overline{\Delta Q_h}(I_s) + Q_{net}(I=0, T_h) \quad (27)$$

with

$$\overline{\Delta Q_h}(I_s) = \frac{1}{2\pi} \int_0^{2\pi} Q_h(I_s, \varphi) d\varphi \quad (28)$$

The experimental evaluation of the integral $\overline{\Delta Q_h}(I_s)$ usually requires a considerable testing effort as the aperture test body has to be mounted in a vacuum chamber on a spin table and the lines for temperature measurement and power supply have to be led across slip rings.

The effort, however, can be reduced if the integral is approximated by a sum. In this case ΔQ_h can be measured for some constant incident angles φ_{n_1} and φ_{n_2} , with

$$\varphi_{n_1} = n_1 \cdot \frac{\pi}{2N} \quad , \quad n_1 = 0, 1, 2, \dots, N \quad (29)$$

and

$$\varphi_{n_2} = n_2 \cdot \frac{\pi}{2N} \quad , \quad n_2 = -1, -2, \dots, -N \quad , \quad (30)$$

and, based upon this, $\overline{\Delta Q}_h(I_S)$ can sufficiently accurately be determined by

$$\overline{\Delta Q}_h(I_S) = \frac{1}{N+1} \sum_{n_1=0}^N \Delta Q_h(I_S, \varphi_{n_1}) + \frac{1}{N} \sum_{n_2=-1}^{-N} \Delta Q_h(I_S, \varphi_{n_2}) \quad (31)$$

In most cases tests for incident angles $\varphi_{n_1=N}$ and $\varphi_{n_2=-N}$ needed not to be performed, as for geometrical reasons

$$\Delta Q_h(I_S, \varphi_{n_1=N}) = \Delta Q_h(I_S, \varphi_{n_2=-N}) = 0$$

was obvious.

Moreover tests for all incident angles φ_n could be cancelled, if for symmetry reasons apparently

$$\Delta Q_h(I_S, \varphi_{n_1}) = \Delta Q_h(I_S, \varphi_{n_2=-n_1})$$

held.

Thus the number of these steady state temperature tests could be kept within reasonable limits.

SPECIFIC VALUE OF HELIOS INFRARED TEST TECHNIQUE

Somewhat paradoxically, the specific value of the HELIOS infrared test technique is based on the fact that in most cases Step 1 of the sequence has not to be carried out, because the absorptances of the surface are fairly accurately (tolerance: $\pm 0,02$) known from measurements of small samples and, therefore, the absorbed radiation Q_{abs} can be determined due to eq. (1).

In fact for HELIOS the costly and in many cases - because of the lack of sufficiently powerful Xenon arc solar simulators for high intensities - impossible solar simulation tests of Step 1 could be avoided for all surfaces except for the sensor apertures.

For the cylindrical heat shield section covered by second surface mirrors and nearly ideally insulated from the probe central body even Step 1 and Step 2 needed not to be performed. In this case the temperature of the heat shields was only dependent on the solar absorptance and the emittance of the heat shield surface and, as these data very accurately could be determined by spectral measurements on small samples, the heat shield temperature could easily and accurately be calculated. The corresponding infrared heater section during Step 3 just had to be heated such that the calculated heat shield temperature was met.

A further essential advantage of the described infrared testing principle is the fact that all macroscopic temperature gradients along the spacecraft surfaces are generated without any additional effort just as they are generated under real solar irradiation. Although the heat generation within an infrared heater section is exactly uniformly distributed and, therefore, net heat flux from infrared heater to surface is uniform over the total surface area, the infrared heaters under discussion not necessarily will be isothermal. They, of course, do adjust their temperature distribution to gradients within the irradiated surfaces. This, by the way, is the reason why infrared heaters of the described kind should have an as low as possible thermal conductance in surface direction.

DESIGN ITEMS

The Thermal Canister consists of a thin aluminium sheet structure with heater foils glued to the outside of the sheets. The space-viewing side is coated with a high emissivity paint in order to enhance radiative heat exchange with the spacecraft (Fig. 7).

Following equation (2) the net heat transfer between canister and spacecraft and consequently the heat to be generated per unit area in the canister depends on the thermo-optical properties of the spacecraft section irradiated. In this respect HELIOS is divided into three main sections: the upper solar array, the center body, and the lower solar array. Thus the canister is divided into three corresponding sections which are thermally insulated from each other by fibreglass stand-offs and by mirror foils. In the centerbody section special heaters are incorporated for the experiment apertures in the heat shield.

The three sections and each of the aperture heaters can be separately electrically controlled. The installed power is 9,8 kW in each solar array section and 2 kW in the centerbody section. Because the thermal canister is to be used for the prototype and flight spacecraft the heaters are supplied with stabilized dc voltage (max. 200 V), and the heater mats are designed to generate a sufficiently low electro-magnetic

field in order not to disturb the spacecraft operation during testing.

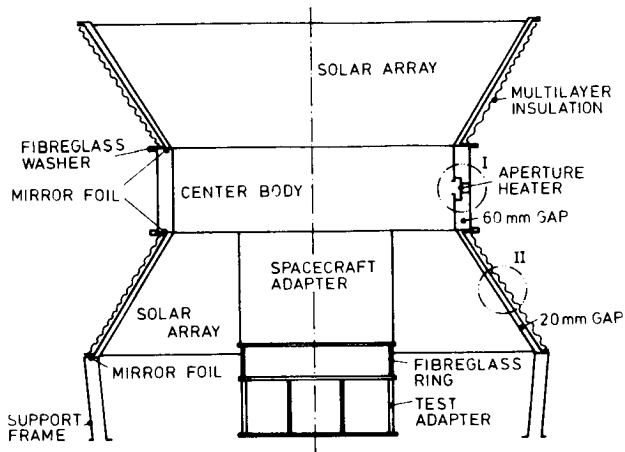


Fig. 7 Thermal Canister design

In order to reduce the heater power needed, the solar array sections are covered by multilayer insulation blankets on the outside. The centerbody section has a bare outside with an emissivity adjusted so that the coupling of the heat shield to the cold shroud of the test chamber is sufficient to cool the heat shield to the 1 AU conditions low temperatures (Fig. 8).

The canister is mounted on studs around the spacecraft without direct conductive contact to the spacecraft skin. For mounting purposes it is divided into two halves in axial direction.

Special Design Problems

For the simulation of the net heat flux to the solar arrays at 16 S.C. the canister has to be heated to 230 °C. For the non-metallic materials and components involved this presented many problems which in most cases could only be solved by tests and special developments. MINCO Products Inc. produced a special type of thermofoil heater out of Kapton which has the required power per unit area and temperature resistivity. The heaters are glued to the structure by Bloomingdale FM 150-2u adhesive which has to be cured at 150 °C under vacuum pressure. Midland Industries Sicon 8 x 906 black paint was found to have the required emissivity, temperature stability and low outgassing characteristics.

For the experiment aperture heaters which reach 350°C the problems were even more severe. The heaters used here are Philips Thermocoax wires which are hard-soldered into a stainless steel plate. The high emissivity surface is achieved by an anorganic paint (IIT's IITRI-Z 93), the mirror foils reducing heat exchange with the surrounding heat shield are Kapton foils aluminized on both sides (Fig. 9).



Fig. 8 HELIOS Thermal Canister

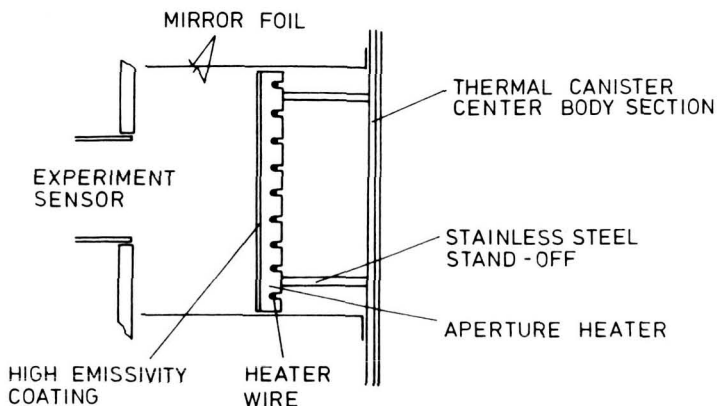


Fig. 9 Aperture heater design

COMPARISON OF THERMAL CANISTER AND SOLAR SIMULATION TESTS

Since the validity of the infrared test technique is of some importance to the success of the HELIOS mission, the thermal canister test results are verified in the thermal model test program by solar simulation tests at the highest possible intensities. The solar simulation tests have been performed at 0.9 S.C., 4.5 S.C. and 7.4 S.C. with the complete model in a Xenon arc light beam (Fig. 10).

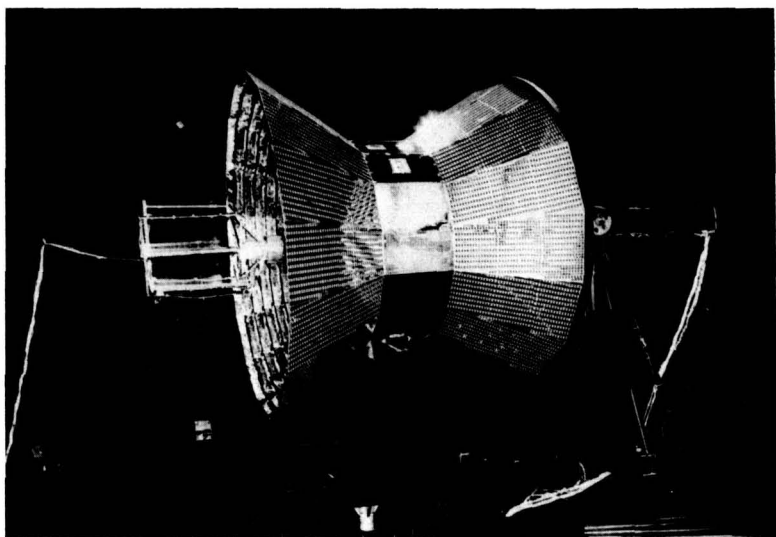


Fig. 10 HELIOS solar simulation test

In Fig. 11 the temperatures of the solar array and heat shield as measured in solar simulation tests and in canister tests are displayed. The temperatures of the solar arrays and the heat shield measured during both kinds of tests are in good agreement for the three solar intensities mentioned. For the 7.4 S.C. solar simulation test the temperature of the outer end of the lower solar array is considerably lower than the temperature of this part for the corresponding canister test, because at this intensity the solar light beam diameter was not big enough to cover this part of the spacecraft too.

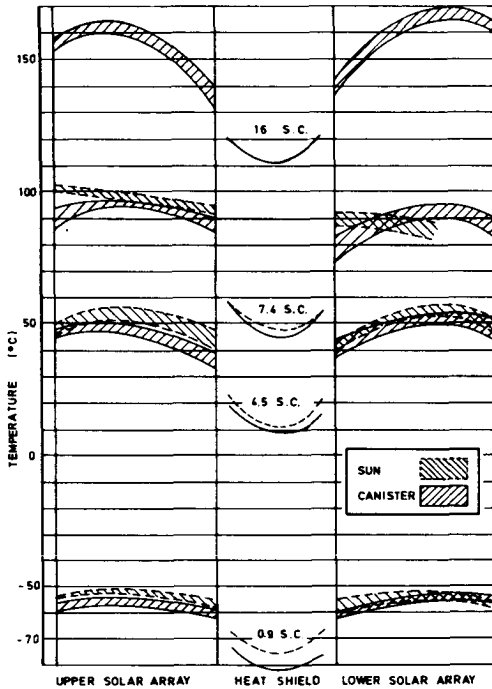


Fig. 11 HELIOS spacecraft skin test temperatures

Fig. 12 gives an analysis of the temperature difference between both kinds of tests at 0.9 S.C. and 7.4 S.C. for internal components based on measurements of about 170 sensors.

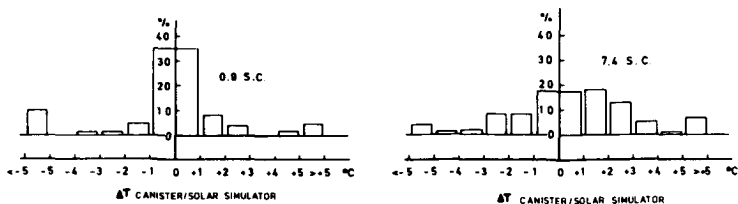


Fig. 12 Temperature difference between canister and solar simulation test of internal components at 0.9 S.C. and 7.4 S.C.

Apparently the agreement of internal component temperatures for both kinds of tests is good, too. The few differences of ± 5 °C or more are due to a change in dissipation in one compartment of the centerbody between canister and solar simulation test. A detailed evaluation of the solar simulation test also verifies the aperture heat input determination. The analytical model which takes the aperture test results into account duplicates the solar simulation test temperatures for the experiments with apertures.

CONCLUSION

The tests performed indicate that the infrared test technique developed for the HELIOS spacecraft gives identical results as solar simulation tests at low and medium intensities. Therefore, the extrapolation to the highest intensity of the mission seems to be valid.

It is the conviction of the authors that the described infrared heater technique can be advantageously applied in practically all cases, in which either the required simulated solar intensity or the required magnitude of illuminated area (or both) cannot be fulfilled by existing or available Xenon arc lamp solar simulation sources.

N74-10250

Paper No. 57

LARGE SOLAR BEAM TESTING AT PLANET MERCURY AND GREATER INTENSITIES IN THE JPL 25-FT SPACE SIMULATOR

John W. Harrell, *Jet Propulsion Laboratory, Pasadena, California*

ABSTRACT

Minor modifications to the off-axis solar simulation system in the JPL 25-Ft Space Simulator have been made which allow testing at very high solar intensities over reasonably large test areas. Tests have been conducted on Mariner and Helios class spacecraft at intensities up to 7.4 solar constants with anticipation of Helios testing in early 1974 at 11 solar constants. The optical components required for these high energy solar beams can be installed or removed quickly which enhances the versatility of the facility and permits high facility utilization.

INTRODUCTION

The JPL 25-Ft Space Simulator has been in operation for solar, thermal, vacuum testing since 1962 when the first planetary mission outside earth orbit was flown. Such programs as Ranger, Surveyor, Mariner Venus, Mariner Mars, Mariner Venus/Mercury, and Viking have been tested in the simulator as well as several non-JPL projects.

The facility was originally fitted with a cassegranian solar simulator utilizing 133, 2.5KW mercury xenon compact arc lamps. This system was replaced in 1965 with an off-axis optical arrangement (Fig. 1) which uses as an energy source an array of 37, 20KW xenon arc lamps (Fig. 2). The energy from these lamps which are housed in 27-inch ellipsoidal water cooled collectors passes through a 19-channel optical mixer (Fig. 3) or integrating lens unit. From the mixer the energy is projected through the penetration window onto a 23-foot collimating mirror (Fig. 4) in the top of the chamber and reflected back down into the test volume. This off-axis system is capable of producing solar intensities in excess of that at the planet Venus over a 15-foot diameter area.

High Solar Intensity Test Requirements

In order to meet the interplanetary mission objectives set forth by NASA, it was necessary to further develop the facility

*This paper presents the results of one phase of research carried out at the Jet Propulsion Laboratory, California Institute of Technology, under Contract No. NAS 7-100, sponsored by the National Aeronautics and Space Administration.

capabilities to allow testing of Mariner class spacecraft at solar intensity levels in excess of that at the planet Mercury (4.8 earth constants).

With the anticipation of a Mariner Venus/Mercury (MVM73) mission to be launched in 1973, an expansion of the capabilities of the solar simulator was initiated. Because of the nature of the off-axis solar simulation system, the optical path inside the chamber had only to be intercepted at a lower elevation to concentrate the energy into a smaller but more intense solar beam. Consequently, the modification (Reference 1) did not require major changes to the system, but instead required the addition of some replaceable optical components. It was decided to provide quick-change capabilities between the existing beams required for Viking orbiter testing and the higher intensity beams needed for MVM73 (Fig. 5).

Solar System Modifications

The solar source array was not changed. Present lamp power can be increased from 20 to 25KW (limited by existing 25KW D.C. power supplies).

Two new optical mixers were built (Fig. 6) with ample water cooling to permit high energy transmission without distortion of the lens supports. One mixer was built with the proper lens arrangement to provide a 9-foot diameter beam in excess of 6.5 solar constants. The second mixer provides an 11-foot diameter beam at an excess of 4.8 solar constants.

A new 15-foot diameter collimating mirror (Fig. 7) was built and installed upon a removable support system below the existing 23-foot diameter collimator. The 15-foot mirror has a spherical curvature and is structurally similar to the 23-foot mirror.

Versatility of System

The versatility of the off-axis solar simulator is apparent in view of the variety of solar beams and intensity levels available as described in Table 1.

CURRENT AND PROJECTED SOLAR
SIMULATOR PERFORMANCE

Mixer and Beam Diameter (Feet)	Number of Lamps Available	Solar Intensity (SC) Lamps Operated at 20KW		Solar Intensity (SC) Lamps Operated at 25KW	
		Sustained, with 25% Margin	Maximum Power No Margin	Sustained, with 25% Margin	Maximum Power No Margin
SSB-15	37	1.9	2.5	2.3	2.9
SSB-15.5	37	2.2	3.0	2.8	3.5
SSB-18.5	37	1.6	2.1	2.0	2.5
SSC-9	37	7.7	10.2	9.6	12.0
SSC-11	37	4.7	6.2	5.8	7.3
SSB-8	7	1.4	1.7	1.7	2.2

1 Solar Constant = 126 w/ft²

TABLE 1

High Energy Test Programs

In June 1972 the MVM73 Thermal Control Model (TCM) (Fig. 9) was tested at JPL using the 9-foot diameter beam. The total operating time for the solar simulator was 576 hours at intensities from 1 solar constant to 4.8 solar constants (intensity at planet Mercury). At the highest levels operated, a margin of 25% or more was reserved for lamp degradation or failure. In July 1973, the MVM73 flight spacecraft was tested at 1, 2 and 4.8 solar constants.

The second mixer which produces an 11-foot diameter beam was built to accommodate the Helios spacecraft being built by the West German Government. It is a spin stabilized solar probe designed to fly to within 0.3 AU (Fig. 10). Its mission requirements call for testing at 11 solar constants in an 11-foot diameter beam. The Helios TCM was tested at JPL in February 1973, at intensities up to 7.4 solar constants. A test of the prototype vehicle is scheduled for April 1974 at 11 solar constants using the 9-foot diameter beam, which will necessarily but tolerably be a compromise in beam size.

System Limitations

It has been noted during high intensity test programs that the chamber penetration window temperature has become the limiting factor in further performance increases. The high intensity levels cause very high center-to-edge temperature differences. The outer edge temperature was measured using thermocouples, while the center of the window was monitored with a vacuum rated infrared radiometer. The temperature of the center of the window has attained a level of 1000° F, while the edge temperature remained at 150° F. The hoop stress produced by this gradient combined with the atmospheric pressure load has significantly reduced the safety factor such that restrictions have been placed on high power operations.

Window Contamination

It has been observed that surface contamination of the vacuum side of the penetration window is a major contributor to the measured temperature. After cleaning the window (hand polishing with cerium oxide), a reduction of as much as 200° F can be realized. This indicates that the infrared radiometer, which looks only at the surface of the window, may be measuring the effect of the contamination instead of a temperature related to the calculated internal temperature of the quartz. There may be many sources of this contamination. Diffusion pump oil, the test item, cabling, etc. Since all of these sources cannot be eliminated, procedures for monitoring window temperature and cleaning have been established for high intensity testing.

A quantity of inconsistent data collected during high intensity testing indicates that spacecraft configurations also affect the window temperature. Further studies will be required to determine the nature and significance of this effect (see Fig. 8 and Fig. 9).

Ozone Hazards

During the course of performing solar beam mapping with the chamber open, excessive levels of ozone were observed at intensities above 1 solar constant. Consideration must be given to both personnel safety and collimator mirror degradation when exposed to ozone levels above 0.25 ppm. The solar source array and the beam path external to the chamber are protected with appropriate filters which remove the ozone. Ozone levels in the building can be monitored as a protection for personnel and hardware.

SUMMARY

Recent modifications to the JPL 25-Ft Space Simulator have greatly enhanced the capability for solar simulation testing for interplanetary missions. Tests have been conducted at intensities up to 7.4 solar constants. A new penetration window which will absorb less energy than the current window, thereby reducing its operating temperature, will be installed towards the end of 1973. The facility will then be capable of performing extended tests at solar intensities up to 12 solar constants over reasonably large test areas. Highly uniform beams ($\pm 5\%$) are available with adequate collimation ($\pm 1^\circ$ to $\pm 2^\circ$, depending on choice of collimators) to simulate solar effects on complicated spacecraft configurations.

REFERENCE

1. Morgan, N. R. "The 7.63-Meter Space Simulator Modification" JPL TM 33-639, To Be Released.

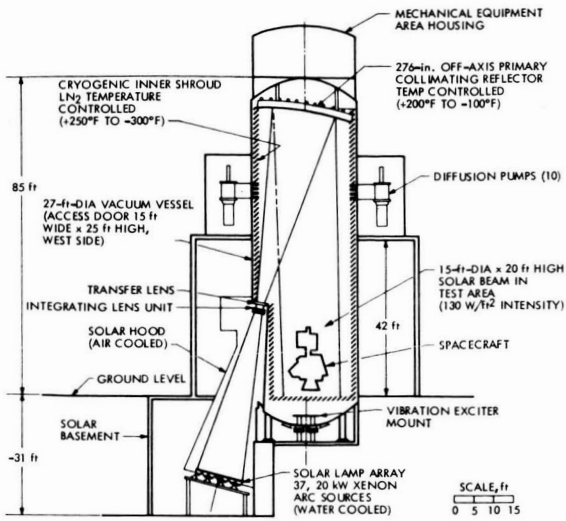


Fig. 1. JPL 25-ft space simulator

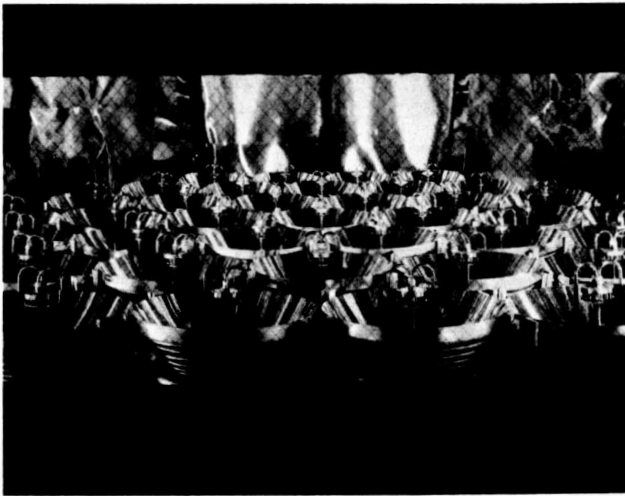


Fig. 2. Typical lamp and collector arrangement

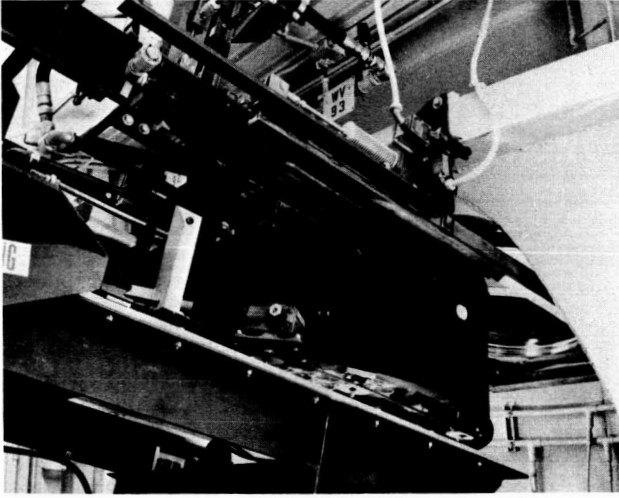


Fig. 3. Mixer lens and carriage



Fig. 4. JPL 23-ft mirror

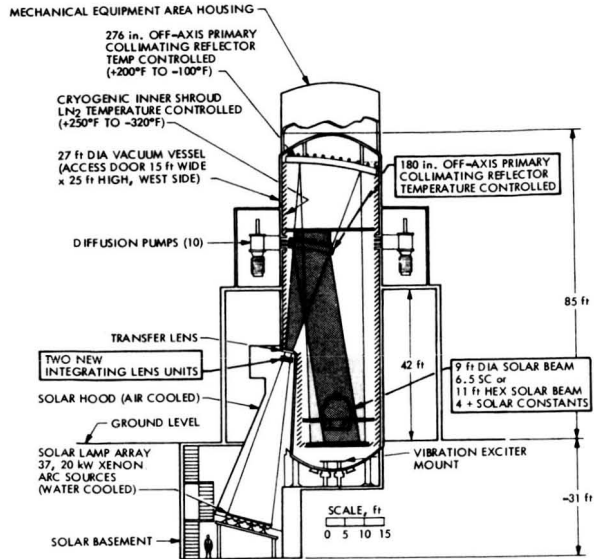


Fig. 5. JPL 25-ft space simulator cross section

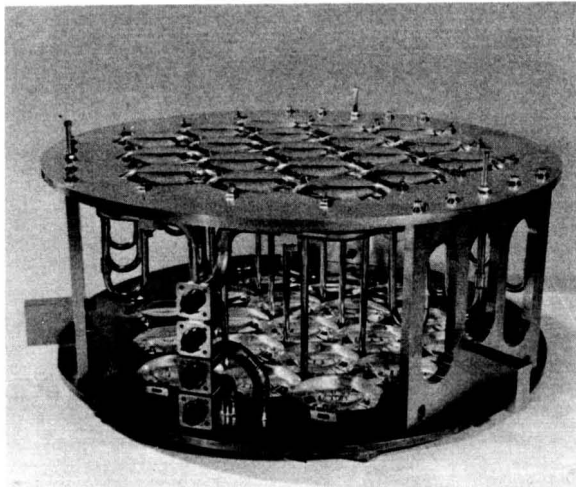


Fig. 6. Optical mixer

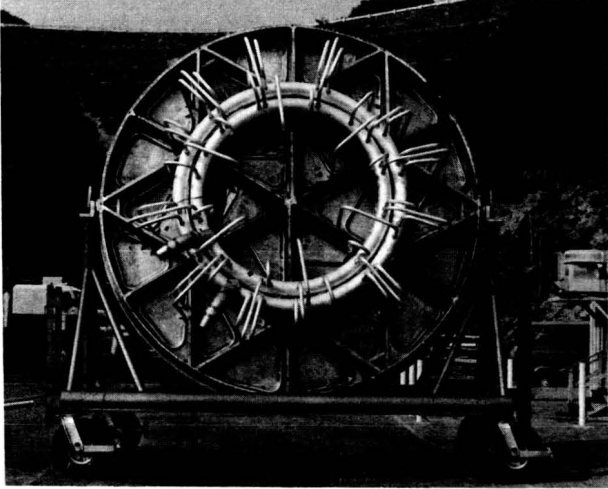


Fig. 7. JPL 15-ft collimator

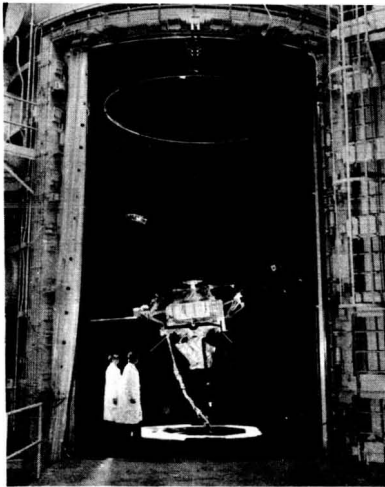


Fig. 8. MVM '73 thermal control model



Fig. 9. Helios thermal control model

Paper No. 58

SURVEY OF SOLAR SIMULATION FACILITIES

T. L. Hershey, *Spectrolab Division of Textron;*
A. Lunde, *the Boeing Company*

Paper not submitted in time for this publication.

Paper No. 59

PLUME MASS FLOW AND DAMAGE DISTRIBUTIONS
FOR AN MMH/N₂O₄ RCS THRUSTER

E. W. Spisz, R. L. Bowman, J. R. Jack, *NASA Lewis
Research Center, Cleveland, Ohio*

SUMMARY/ABSTRACT

The problems and concerns regarding contamination of spacecraft systems and components is well recognized. For example, SKYLAB, because of its many critical surfaces, sophisticated optical components and extended mission duration is particularly susceptible to contamination effects. Of the many possible sources of contamination which may occur, that due to the exhaust products from RCS thrusters is least understood and may present one of the more serious threats. The exhaust products from the earth storable propellants tend to "stick" to even high temperature surfaces and to "stay" for long periods of time. Furthermore, there is much uncertainty as to the extent of the plume flow field and the physical and chemical dynamics of the exhaust products.

Quantitative data defining the plume flow field and, more importantly, the resulting damage to various surfaces and components is very limited. The paucity of data is due primarily to the experimental difficulties encountered in the rigorous simulation of the environment surrounding a firing thruster and the sophisticated instrumentation that is required to obtain useful data. The Lewis Research Center, which has a large liquid helium cryopumped space facility that can provide the proper space simulation for a firing thruster, has been engaged in a continuing program to obtain experimental data on the contamination aspects of RCS thrusters. Data obtained using a 5-pound thrust, bi-propellant (MMH/N₂O₄) rocket engine as the contaminating source will be presented for the two most recent experiments from this facility.

Experiment 1 was primarily a study of the degradation in the transmittance of quartz samples that were located at various angles around the perimeter of the thruster. The samples were 1-inch diameter fused quartz which were mounted at the engine centerline elevation and approximately 50 cm from the nozzle exit plane. The thruster was fired in a pulse-mode with 50 msec ON-time and 100 msec OFF-time. A total of 62 seconds exposure was accumulated during the course of the experiment.

Experiment 2 was a more complex simulation experiment that was performed to compare damage effects on various surfaces and materials with the plume mass flow distribution as determined by quartz crystal measuring devices (QCM's). The

thruster used in Experiment 2 was identical to that used in Experiment 1, except that the pulse mode of firing was changed to 14 msec ON-time. The total firing exposure time accumulated for experiment 2 was 72 seconds.

The damage data obtained during the two experiments show a trend of increasing damage with decreasing wavelength and a decreasing effect as the angle between the sample location and the nozzle axis increases. Very significant changes in transmittance are measured for wavelengths below $0.25\mu\text{m}$ even for off-axis angles up to 90° .

The plume mass flow distribution around the engine as measured by the QCM's also shows a decreasing trend as the off-axis angle increases. Again, significant mass flow values were measured for off-axis angle of 90° . These QCM measurements substantiate the damage measurements at the large angles and indicate that significant mass flow and subsequent damage can occur in regions of the spacecraft which initially may be thought to be unaffected by the thruster plume.

Preliminary results indicate that a correlation between measured monochromatic transmittance damage and the measured plume flow distribution can be made if the transmittance changes are presented in terms of an optical density, which through Beer's Law and various idealized assumptions, can be related to an effective contaminant layer thickness and thereby related to plume mass flow distribution and sticking coefficients. The comparisons which have been obtained to date are encouraging. It is believed that with further refinement, it will be possible to improve the correlation and develop a useful technique which can be applied to contamination prediction.

**DETERMINATION OF HIGH-VELOCITY WATER-VAPOR PLUME
PROFILES IN A THERMAL-VACUUM ENVIRONMENT**

J. T. Visentine, *Aerospace Technologist, Research and Development
Section, and H. K. F. Ehlers, Head, Research and Development
Section, NASA-Johnson Space Center, Houston, Texas*

ABSTRACT

A test program was conducted in chamber A at the NASA-Johnson Space Center to investigate operational characteristics of candidate evaporative heat exchangers (sublimator and flash evaporator) for use on future spacecraft. These devices were evaluated in a thermal-vacuum environment using supersonic nozzle, plugged nozzle, and sonic orifice configurations. Sensors used to perform backstreaming and flow field measurements are discussed. Locations chosen for these sensors are reviewed. Results are presented which indicate that (1) flow field property predictions and measurements are in substantial agreement for both the supersonic nozzle and sonic orifice configurations, (2) evaporator pulsed operation and sublimator steady flow operation yield essentially the same contamination potential for a given average mass flow rate, and (3) supersonic and plugged nozzles offer a significant reduction in backstreaming and subsequent impingement of water vapor on spacecraft scientific payloads.

N74-10781

PRECEDING PAGE BLANK NOT FILMED

Paper No. 61

OUTGASSING MEASUREMENTS OF A THERMAL BLANKET AND A SPACE CHAMBER USING QUARTZ CRYSTAL MICROBALANCES

J. J. Scialdone and R. Kruger, *Goddard Space Flight Center, Greenbelt, Maryland*

ABSTRACT

The outgassing characteristics of an ERTS-type thermal blanket used as an insulation shell for the attitude control system of a spacecraft were investigated. A test conducted in a vacuum chamber established the thermal blanket's outgassing rate, the nature and mechanism of the outgassing, and determined its rate of deposition on surfaces at different temperatures. The test established a method for measuring outgassing and the temperature and the duration for such outgassing. For about 60 hours the blanket was degassed. The measurements of the quantities and the identification of the material were obtained as follows: (1) accretions on quartz crystal microbalances (QCM) held at -120 and -10° C; (2) mass spectrometer analyses of the gases in the chamber; (3) analysis of the condensates on a cold finger at -196° C by infrared spectroscopy and gas-chromatography/mass-spectrometry; (4) identification of the vapor pressures of the accreted materials by temperature cycling of the QCMs. In 60 hours, the blanket outgassed a total of about 0.1 g of material that included hydrocarbon oxides, phtalates and tetrabutoxyethylene. One tenth of this material appeared to have vapor pressures varying from 2×10^{-8} torr at -50° C to 3×10^{-7} torr at -1° C. The surface at -10° C collected about 7.5×10^{-6} g/cm² of this material during the duration of the test.

INTRODUCTION

The vacuum chamber test described had as its overall objective the study of the outgassing of an ERTS thermal blanket. The removal or reduction of outgassing from the blanket is important because the outgassed products can condense or be adsorbed on critical surfaces of the spacecraft. When this occurs, the optical and thermal properties of these surfaces can degrade.

More specifically, the objectives of this study were to determine the quantity of outgassed material, its accretion rate at various surface temperatures, its chemical nature, and its outgassing mechanisms. Implicit in the test was the development of the method of measuring the outgassing, the temperatures to be used, the duration of the test, the instrumentation, and the instrument locations.

BLANKET AND TEST FACILITY DESCRIPTION

The ERTS-type blanket consisted of about 30 layers of mylar that were crinkled and aluminized on both sides (polyethylene terephthalate and 99 percent pure aluminum) and sandwiched by supports consisting of glass cloth and Epon 815 (on epoxy catalyzed by triethylene tetramine). These supports were painted with D-4D alkyd silicone paint and held together with nylon thread and polyamide buttons. The blanket's generally trapezoidal shape had a surface estimated at about 8500 cm² on each side.

For the test, the blanket was suspended vertically inside the Test and Evaluation Facility No. 240 vacuum chamber. This chamber has a nominal working volume of 0.6 m³. It is pumped by a 66-1/s mechanical pump and by a 5300-1/s diffusion pump. Provisions for heating to 100° C and cooling to liquid nitrogen (LN₂) temperature of the Cat-A-Lac flat, black, painted shroud are provided. The pressure measurements are made with alphanatron and ion gages. Measurements of pressure and temperature are transmitted to a central data collection station on 12 channels at 100-s intervals. An LN₂ cooled "finger" is used to collect condensable materials. The pumping speed of the chamber under molecular flow conditions is approximately 1000 l/s.

OUTGASSING, MASS DEPOSITION, AND MASS SPECTRA ANALYSIS INSTRUMENTATION

Two quartz crystal microbalances (QCMs), a quadrupole mass spectrometer, and an LN₂ cooled finger comprised the instrumentation. Of the two microbalances, one was operated at -120° C and measured the total outgassing. The other was operated at -10° C, a slightly lower temperature than sensitive spacecraft surfaces would experience in orbit, hence a conservative indication of contamination. The LN₂ cold finger provided a cumulative record of the condensable outgassing for the duration of the test. Washings from the cold finger provided the material for infrared radiometry and gas chromatographic/mass spectrometer analysis of the condensate. The quadrupole mass analyzer was suspended in the chamber in the same region as the microbalances and provided real-time analyses.

QUARTZ CRYSTAL MICROBALANCES

The microbalances consisted of two piezoelectric quartz crystals of the same cut and dimensions. They were matched to have the same resonant frequency and same temperature response. The two crystals of the unit, maintained at the same temperature, were excited by electric charges to vibrate at resonance during operation. When one of the crystals was shielded from the gas flux while the other crystal accreted

mass, a beat frequency was established between the two. The beat frequency Δf is related to the mass accretion Δm by the relation¹

$$\Delta f = - f_0 \frac{\Delta m}{\rho t A} = - c_f \frac{\Delta m}{A} \quad (\text{Hz}) \quad (1)$$

The crystals used in these tests had an f_0 of 10^7 Hz, a thickness $t = 1.7 \times 10^{-2}$ cm, an area $A = 0.2 \text{ cm}^2$, and a density $\rho = 2.65 \text{ g/cm}^3$. Therefore, their sensitivity factor c_f , was $2.22 \times 10^8 \text{ Hz cm}^2 \text{ g}^{-1}$. Deviation from the linear relation would occur when Δf becomes too large. In the tests, Δf was never allowed to exceed 10^5 Hz so that the deviation was always less than

$$D = \frac{2 \Delta f f_0}{f_0^2} = 2\%$$

This was accomplished by warming the QCM and therefore unloading the crystal when the Δf reached a value of approximately 70 to 80×10^3 Hz. After unloading, the crystal was returned to -120° C , and the accumulation continued.

The conductance of the port leading to the vibrating surface of the crystal operating at -120° C was calculated to be 1.86 l/s for air at 25° C . The other crystal unit operating at -10° C had focusing lenses at the entrance. Its conductance for the same gas conditions was 1.13 l/s .

TEST PROCEDURES

The chamber was evacuated to a pressure of 10^{-5} torr or lower, while the chamber walls and the blanket were held at the ambient temperature. The customary pumping procedures were followed. At this pressure, the temperatures of the shroud and blanket were raised to $+60^\circ \text{ C}$, refrigerant was admitted to the -10° C crystal, and LN_2 was directed to the -120° C microbalance and the cold finger. A rapid rate of mass accretion (due mostly to water) was normally noted and it became necessary to unload the crystal within a relatively short period. This prevented the deviation from linearity of the mass-frequency relation of the crystal or the complete loss of oscillation. This unloading, however, became less frequent as the condensable gases in the chamber were depleted and the outgassing was reduced. The unloading was accomplished in a manner that allowed the retention of a certain amount of condensed mass on the crystal. Previous tests had established that, upon unloading the crystal, a rapid drop of frequency would be followed by a slow drop. This indicated that a material or materials with a low vapor pressure at the temperature of crystal unloading had been accreted together with more volatile materials. Accordingly, in these

tests the unloading was accomplished by increasing the temperature to -55°C from -120°C . At this temperature, the vapor pressure of water is about 10^{-2} torr, and, in an environment where the partial pressure of water was at least two orders of magnitude lower than 10^{-2} , the water on the crystal evaporated within a short period of time. The time at which this evaporation was accomplished was obvious from the frequency rate of change. When evaporation of the volatile material was complete, the frequency changed slowly. In the warming periods of these tests, an increase in pressure in the chamber resulted from the release of condensed gases on piping and other surfaces of the QCM. The normal accretion on the crystal was resumed by cooling the crystal to the test temperature of -120°C . This cycle lasted from 15 to 20 minutes during which time outgassing from materials continued, but the recorded data were complicated by the fact that crystal temperature effects obscured mass information. However, the accretion which would have occurred during these unloading periods was estimated by matching the slopes of the frequency curve before and after the crystal unloading.

THE QCM MEASUREMENT OF OUTGASSING

The crystal microbalance at -120°C registered the accumulation of molecules that impinged and remained on the sensing surface. This amount, however, was less than the total quantity emitted by the blanket and chamber because most of the gases were removed by the chamber pumping system and by other cold surfaces in the chamber. Further, the QCM had a conductance limiting passage to the crystal. The mass balance can be expressed as throughput. Restating the above,

$$Q = Q_p + Q_1 + Q_2 = (S_p + S_1 + S_2) P$$

where Q_p and S_p are the throughput and speed of the pumping system and cold surfaces in the chamber other than the QCM; Q_1 and S_1 are the throughput and pumping speed of the -120°C microbalance unit; Q_2 and S_2 are those of the -10°C microbalance in the chamber; and P is the isotropic pressure in the chamber. The values of the pumping speeds have already been indicated: $S_p = 1000$ l/s, $S_1 = 1.86$, and $S_2 = 1.13$ l/s. The pressure P can be obtained in terms of the throughput at the surface of the -120°C crystal, as $P = S_x P_x / S_1$ where P_x and S_x are the pressure and surface speed at the crystal. Inserting these values in the mass balance equation, changing to mass, and noting that the mass on the crystal as shown in Equation 1, is

$$\Delta m = \rho S_x P_x dt = \frac{\Delta f A}{C_f}$$

one obtains

$$W = \rho Q dt = \left(\frac{S_p + S_1 + S_2}{S_1} \right) \rho S_x P_x dt = (536) \frac{\Delta f A}{C_f}$$

$$= 4.82 \times 10^{-7} \Delta f \quad (\text{g}) \quad (2)$$

where $S_p + S_1 + S_2/S_1 = 536$, the constant that accounts for the unit restriction and for other pumping systems in the chamber. The total outgassing of condensables on a -120°C surface, expressed in grams, is therefore the change in frequency of the -120°C crystal times the constant (536).

THE QCM MEASUREMENT OF ACCRETION ON -10°C SURFACE

The -10°C unit had been designed for measurements of beaming effects and had been provided with focusing lenses. The mass registered by this unit was therefore less than it would have been with an unrestricted passage. To account for this lower mass, one can reason as follows. The pumping speed of the crystal microbalance passage leading to the vibrating crystal was calculated to be $S_2 = 1.13 \text{ l/s}$ for air at 25°C . The crystal pumping speed² was $S_x = 11.6 \times 0.2 \text{ l/s}$ for a 0.2 cm^2 area and for the same gas conditions. The correction factor to be applied to this unit to account for the flow restriction was then $S_x/S_2 = 2.05$. The mass W , which would be registered by the unobstructed unit, is

$$W = (\rho S_x P_x dt) \frac{S_x}{S_2} = 2.05 \frac{A \Delta f}{C_f} = 1.84 \times 10^{-9} \Delta f \quad (\text{g}) \quad (3)$$

The mass per unit area is

$$\frac{W}{A} = \frac{1.84 \times 10^{-9}}{0.2} \Delta f = 9.23 \times 10^{-9} \Delta f \quad (\text{g/cm}^2) \quad (4)$$

The above relationships do not account for the effect of the chamber pumping speed, and, this QCM measured the accretion corresponding to the actual gas conditions in the chamber.

OUTGASSING OF THE 3- BY 3-FOOT CHAMBER

In advance of the degassing of the blanket, measurements of the empty chamber outgassing were carried out. The chamber was evacuated to a pressure of about 10^{-7} torr, and its walls were held at $+60^\circ \text{C}$. Following the procedure described above, the two microbalances were brought to -10°C and -120°C . No accretion was

measured throughout the test on -10°C . The -120°C unit required unloading several times to prevent excessive accretion. However, the unloadings to -55°C temperatures and return to -120°C were performed mainly to establish the amount of low vapor pressure materials on the crystal. The test was carried out for about 26 hours. It was terminated when it appeared that the rate of accretion on the crystal was minimal. The accretion expressed as mass versus time, due to chamber outgassing, is shown in Figures 1 and 2. Figure 1 shows the total accumulation on the crystal and Figure 2 shows the amount of the total that did not evaporate rapidly at -55°C . The amount in grams is obtained as the product of the frequency and the constant derived previously. For a 24 hour outgassing, these were $7.5 \times 10^{-2}\text{ g}$ total outgassing of which $1.68 \times 10^{-3}\text{ g}$ are of the heavy molecular weight material. The rates of degassing as a function of time are shown in Figure 3. These rates were obtained from Figures 1 and 2, and they reveal considerable information about the chamber outgassing. The slope of the total degassing is -1 . This is representative of the simultaneous surface desorption of several materials when each has a different heat of desorption³. The low vapor pressure material outgassing showed an initial slope of about $-1/2$ for the first 6 or 7 hours followed by what appears to be a -1 slope. The initial slope is characteristic of processes of a diffusional nature. Therefore, this material consisted mostly of molecules of diffusional origin for the first 6 or 7 hours and then mostly of molecules from surface desorption. After several hours the surface desorption is still present, and this could imply that the material of desorption origin was tightly bound to the surface such as in a chemisorbed state. On the other hand, the surface desorption was the predominant outgassing, as shown by the total rate curve. The curve plots show that the total outgassing decreased from an initial $4 \times 10^{-6}\text{ g/s}$ to an order of magnitude lower in about 10 hours. In 100 hours of pumping, the magnitude would be another decade lower. The low vapor pressure material outgassing rate was initially about $1/10$ of the total, that is, approximately $5.5 \times 10^{-8}\text{ g/s}$. It became about $1/2$ of the total rate after about 10 hours. In about 35 hours of pumping, its magnitude was about $1/10$ of the initial rate (or about $1/100$ of the total rate). These times are predicated on $+60^{\circ}\text{C}$ surfaces. An estimate of corresponding times for other outgassing temperatures is given later. In regard to the nature of the gases, the periodic mass spectrometric analyses and the cold finger analysis at the end of the test indicated that the gas was mostly water with traces of phthalates and hydrocarbons.

BLANKET OUTGASSING

Mass accretions on the -120°C microbalance due to blanket outgassing are also shown in Figures 1 and 2. Figure 1 pertains to total outgassing and Figure 2 to the portion of the total outgassing that consisted of materials having a lower vapor pressure at -55°C . The net accretion due to the blanket (obtained by subtracting the results of the empty chamber test from those including the blanket) are shown in these figures. Figure 1 shows that the blanket lost material at a rapid rate during the initial hours of the test. The rate decreased steadily after that, and when between 24 and 36 hours, it appeared to become constant. A tendency toward a decrease in rate appeared to develop after 56 hours of degassing. However, this is not apparent from the curve and could not be established with certainty because data from the empty chamber was not available for times beyond 26 hours. The plots in Figure 2 show the material, originating from the blanket and chamber, that remained on the crystal when it was brought to a temperature of -55°C . The relative magnitude and slopes of the curve with respect to that found for the empty chamber indicate that the material was definitively of blanket origin.

For convenience, Table 1 indicates the cumulative losses at discrete times.

Table 1
Blanket Weight Loss

Time (hr)	Total Weight Loss (g)	Material Loss with Low Vapor Pressure at -55°C (g)
12	6.07×10^{-2}	6.15×10^{-3}
24	7.61×10^{-2}	7.76×10^{-3}
36	8.58×10^{-2}	8.77×10^{-3}
48	9.44×10^{-2}	9.56×10^{-3}
60	$\sim 1.05 \times 10^{-1}$	$\sim 1.03 \times 10^{-2}$

As shown, most of the material losses occurred during the first 12 hours of degassing. Additional losses after this time were of diminishing magnitudes.

The outgassing rates are shown as a function of time in Figure 4. The rates decreased an order of magnitude in about 15 hours. Thirty to 40 hours after initial degassing, the rate became almost constant, with a value of about $2.5 \times 10^{-7}\text{g/s}$. The total outgassing rate appeared

to approach an inverse proportionality to the square root of the time. This is characteristic of diffusion processes. The deviation from this process may be due to the inclusion of surface desorption. The constant rate approached at the end of 30 to 40 hours could have been caused by material sublimation or by a constant leak such as one which could be produced by the slow venting of the volumes between mylar layers. On the other hand, the low vapor pressure material rate appeared to follow a diffusional process ($t^{-1/2}$) during the first 6 or 7 hours, followed by a t^{-1} process that is characteristic of surface desorption of a combination of several materials. The outgassing rate of heavy materials became constant with a value of about 1.8×10^{-8} g/s at about the same time that the total outgassing approached a constant. The conclusions for long term degassing should be moderated by the fact that data for the empty chamber after 26 hours were extrapolated.

The plots of Figures 1 and 2 are typical of the weight loss curves obtained from the outgassing of organic materials. Outgassing during the initial hours typically consists of physically adsorbed gases, evaporation of certain additives and unreacted fragments, and the evaporation of low molecular weight components of the material itself. The physically adsorbed gases consist mainly of water. Additives and fragments, consisting of stabilizers, plasticizers, solvents, and unreacted varieties, diffuse to the surface before their evaporation takes place. The evaporation of the material will consist of the loss of all its molecular components.

During the described testing the outgassing curve of the blanket included a certain amount of gas trapped between the layers of mylar. This outgassing should occur at a constant rate for a short period of time. The combination of all these outgassing mechanisms would appear as has been shown by the test, that is, an exponential curve followed by a quasi-constant rate weight loss.

DEPOSITION OF BLANKET OUTGASSED MATERIAL ON -10° C SURFACES

The outgassed material that accumulated on a -10° C surface as provided by the microbalance, is shown in Figure 5. This temperature was chosen to represent the lowest temperature that could exist at some critical surface of the spacecraft while in orbit. The temperature chosen was conservative because the spacecraft should not experience temperatures lower than -4° C. The figure does not show accumulation for the empty chamber test because the crystal did not show changes accountable to mass accretion during that test. The curve shows that one half of the total deposit occurred within the first 2 hours of the test. In contrast, Figure 1 shows that one-third of the total outgassing occurred during the same period. The accretion on the surface of the crystal held at -10° C was 6.25×10^{-6} g/cm² after 24 hours and about

$7.6 \times 10^{-6} \text{g/cm}^2$ after 60 hours.

The rate of accretion on a unit surface is shown in Figure 6. The rate decayed more rapidly after 10 to 12 hours and became less than $1 \times 10^{-11} \text{g/cm}^2 \cdot \text{s}$ after 30 hours. It should be understood that the accretions obtained here are predicated on the conditions existing in the chamber and would not be the same under other conditions. An external surface of the spacecraft in orbit at -10°C could be exposed to lower partial pressures of the contaminating gases and accretion might not occur. On the other hand, a surface at this temperature in an enclosure or exposed directly to the same flux would accrete this amount for the duration of the outgassing. In regard to the material accreted on the crystal, one can consider the following. The saturated vapor pressure of water at -10°C is a few torr. Water vapor condensation on this surface could not occur unless its partial pressure was quite high, that is, greater than the saturated vapor pressure. The accretion must be attributed to materials with low saturated vapor pressure at -10°C . The accretion in 12 hours corresponding to $5.25 \times 10^{-6} \text{g}$ could consist of about 20 monolayer for a material assumed to have a molecular weight of 300 grams. The quantities of the materials accreted during the entire test were small, and a determination of the nature of the material or materials was impossible on the actual microbalance sensing surface.

EFFECT OF TEMPERATURE ON OUTGASSING RATES

A crude estimate of the effect of temperature on the rate of outgassing, and the time to accomplish a certain degree of degassing of the blanket or chamber can be obtained as follows. If one assumes that the degassing proceeds according to a first order reaction rate law, then the time for degassing is $t = Ke^{A/T}$ for a temperature T , where K and A are constants for the reaction⁴. Therefore, assuming that the process of degassing in the present test was completed in 24 hours with a temperature of 60°C , the time to obtain the same condition at other temperatures would be roughly as follows:

Temperature (C)	20°	60°	80°	100°
Time (hrs)	37	24	20	17

This indicates that at the ambient temperature of 20°C , the degree of degassing accomplished in this test, would be obtained in 37 hours rather than in 24 hours.

IDENTIFICATION OF OUTGASSED MATERIALS

Throughout the tests, the chamber gases were monitored with a quadrupole mass analyzer and by a cold finger that provided samples for infrared spectrometry and gas chromatography/mass spectrometry analysis.

The residual gas analyzer provided an identification of the blanket contributed molecules by comparing scans made during the empty chamber test and the test including the blanket. Three peaks at $m/e = 77$, 105, and 122 stood out as blanket contributed molecules. These are shown as a function of time in Figure 7. These fragments per se are insufficient to identify the materials. Further considerations indicated that they are probably hydrocarbon oxides. No amines were present, which eliminated nylon and glass cloth as contaminants.

Gas chromatography/mass spectrometry identified phthalates and tetrabutoxyethylene. The phthalates are so commonly found in these tests as to be practically omnipresent. The tetrabutoxyethylene is often used to cause paint to flow and may have originated from the D-4D paint used on the blanket. In conclusion, it is difficult to ascribe these molecules to particular materials from the conditions found in these tests. It can be stated, however, that most peak heights are decreased by at least one decade within the first 24 hours of pumping. Total decreases after 72 hours rarely exceed two decades without any indication that further decreases would result beyond that time. This behavior is also shown in Figure 7.

At the conclusion of the test period, an attempt was made to obtain vapor pressure data for the materials deposited on the -120°C microbalance. The microbalance showed that a sublimation rate of 1×10^{-9} $\text{g}/\text{cm}^2/\text{s}$ existed when its temperature was raised to -50°C . This would correspond to a material having a saturated vapor pressure of about 2×10^{-8} torr if one assumes that the material has a molecular weight of about 300 g. After material from the cold finger had been allowed to sublime and deposit on the microbalance, the rate of sublimation at -21°C was 2×10^{-8} $\text{g}/\text{cm}^2.\text{s}$ which corresponded to a vapor pressure of 3×10^{-7} for the same molecular weight assumption. This rate, however, was not constant but decreased rapidly after the initial rate. Subsequent warming to -1°C resulted in a sublimation at about the same rate experienced at -21°C . A return to a lower temperature of -12°C indicated a rate corresponding to a vapor pressure of 3×10^{-8} torr.

The fact that at -21°C the pressure is higher than at -12°C infers that at least two materials had condensed on the crystal. Also, the rapid drop in rate at -21°C indicated that one of the materials was sublimed during that period. A resume of the above experience is shown in Table 2.

Table 2
The Behavior of Materials A and B

Test Sequence	Temperature (°C)	Material A		Material B	
		ϕ (g/cm ⁻² · s ⁻¹)	P _s (tofr)	ϕ	P _s
1	-50	1×10^{-9}	2×10^{-8}		
2	-21	2×10^{-8}	3×10^{-7}		
3	- 1			2×10^{-8}	3×10^{-7}
4	-12			1×10^{-9}	3×10^{-8}

COMPARISON OF BLANKET AND CHAMBER DEGASSING

A comparison of the empty chamber and blanket weight losses and rates of weight losses are shown in Table 3.

Table 3
Comparison of Blanket and Chamber Degassing

	Blanket		Empty Chamber	
	Total	L. V. Press. Mat.	Total	L. V. Press. Mat.
Total Wt. Losses	From Fig 1	From Fig 2	From Fig 1	From Fig 2
After 24 hr	7.61×10^{-2} g	7.76×10^{-3} g	6.84×10^{-2} g	1.68×10^{-3} g
After 60 hr	1.06×10^{-1} g	1.03×10^{-2} g	—	—
Rates of Weight Losses	From Fig 4	From Fig 4	From Fig 3	From Fig 3
After 1 hr	3.8×10^{-6} g/s	3×10^{-7} g/s	4.2×10^{-6} g/s	5.4×10^{-8} g/s
After 24 hr	2.7×10^{-7} g/s	2.5×10^{-8} g/s	1.6×10^{-7} g/s	7.5×10^{-9} g/s
After 40 hr	2.5×10^{-7} g/s	1.8×10^{-8} g/s	—	—

Table 3 shows that the total weight losses of the blanket and the empty chamber were of the same order of magnitude after 24 hours of pumping. The rates of total weight losses were also about the same during the first 24 hours of pumping. After that period, the blanket total outgassing rate remained constant. The rates of the low vapor pressure materials were an order of magnitude lower for the empty

chamber than those of the blanket during the 24 hours in which comparison is possible. The fact that the total outgassing was of the same order of magnitude suggests that the outgassing in both cases was mostly from surface desorption and that the loss of heavy materials does not appreciably change the total outgassing values.

In regard to the nature of the outgassing, the slope of the total outgassing rate of the chamber shows it to be produced by surface desorption of several different molecules. On the other hand, the heavy molecular weight material was produced by a diffusion process during the initial 6 or 7 hours followed by a process resembling surface desorption. The outgassing from the blanket appeared to be a combination of surface desorption and diffusion during most of the time during which outgassing rates decayed. The constant rate shown to occur after 35 to 40 hours may be the result of sublimation of some material. The heavy material degassing resembled an initial diffusion process followed by surface desorption after six or seven hours. Its rate became constant after 40 to 45 hours. Other data from the chamber degassing were: (1) the outgassing rate decreased from 4×10^{-6} g/s to 4×10^{-7} g/s in 10 hours and it would decay another order of magnitude after approximately 100 hours and (2) the low vapor pressure material outgassing rate decayed from 5.5×10^{-8} g/s to 5.5×10^{-9} g/s in approximately 30 to 35 hours. These rates are based on a 60°C wall temperature. At other temperatures, longer or shorter times would be needed to accomplish the same outgassing. Estimates of required times have been indicated previously. The outgassed material was mostly water with traces of phthalates and hydrocarbons. Of course, traces of other materials will be found in these tests, depending on the previous history and uses of the chamber.

CONCLUSIONS AND SUMMARY

Crystal microbalances can be employed to provide accurate measurements of evaporation and sublimation phenomena in a vacuum chamber. They can also provide, by appropriate variations of their temperatures, a means of identifying materials with different saturated vapor pressures.

The described test on the outgassing at 60°C of an ERTS blanket has indicated that

- The blanket lost about 1×10^{-1} g of material in 60 hours of vacuum exposure. Of this amount, about one-tenth consisted of heavy molecular weight materials with vapor pressures varying from 2×10^{-8} torr at -50°C to 3×10^{-7} torr at -1°C .

- The rate of outgassing after 45 hours was about 2.5×10^{-7} g/s and appeared to remain constant.
- Gas chromatography/mass spectrometry and infrared radiometry indicated that in addition to ambient gases, the outgassing included traces of hydrocarbon oxides, phthalates, and tetrabutoxyethylene. Hydrocarbon oxides are frequently found when organic materials are present. The origin of phthalates cannot be defined but are often found in tests of spacecraft hardware. The tetrabutoxyethylene probably originated from a flow agent used in D-4D blanket paint.

On the accretion of the above outgassing on a -10° C surface, the microbalance showed that

- Accumulation occurred on this surface at a rate of 1×10^{-10} g/cm² · s for 2 or 3 hours. This rate decayed to about 1×10^{-11} g/cm² · s after 35 hours and continued to diminish very slowly.
- The total accretion was 7.5×10^{-6} g/cm² in 60 hours.
- The materials accreted appear to be deposits of a combination of materials having vapor pressures from 1×10^{-8} to 10^{-7} torr in the range of temperatures -50 to -1° C.

The following are comments on the blanket outgassing and its deposition on critical surfaces.

- In about 40 hours the accelerated test at 60° C accomplished the removal of surface adsorbed molecules and some sublimation of low and high molecular weight fractions of the blanket material.
- A portion of the surface desorbed molecules will be reacquired by the blanket when this is re-exposed to ambient conditions.

A portion of the diffusing and subliming molecules of the blanket has been removed by this test. The return of the blanket to a vacuum environment would resume the outgassing of subliming materials, and the desorption of surface reacquired molecules. The venting of gas trapped between mylar layers will also reoccur. The rate of material

sublimation will be a function of the material temperature.

The time to reach steady-state outgassing at +20° C will be almost double the time noted here.

For a spacecraft in orbit, at about ambient temperature, bulk accretion of blanket outgassing on a critical surface at -4° C will probably not occur for the following reasons.

- The rate of sublimation in space will be smaller than in this test because the material will be at a temperature less than +60° C. A larger dispersion of the contaminant will exist (the chamber simulates the dispersion at about 2- to 300-km altitude) while the spacecraft orbits at about 900 km. As a result of this, the flux required for accretion on the -4° C surface will not be available. However, accretion could occur if the surface is directly exposed to or is in the path of such a flux.

Some of the results of the outgassing of this particular chamber at +60° C are the following.

- The initial outgassing rate was 4×10^{-6} g/s. It is reduced to 4×10^{-7} g/s in about 10 hours, and it appears that another order of magnitude drop would be obtained in about 100 hours.
- The outgassing is of surface origin, and most of it can be removed in 24 hours at this temperature.
- The portion of the outgassing consisting of heavy molecular weight materials had an initial rate of 5×10^{-8} g/s. It comes off at a high rate during the first 7 or 8 hours of degassing and becomes less than 1×10^{-8} after 18 hours.
- It is estimated that the above events would occur in about double the indicated time at an outgassing temperature of +20° C but 30 percent less time for an outgassing at +100° C.

As expected, phthalates and hydrocarbons were components of the outgassing. The quantities of these components and others are predicated on the previous history of the chamber.

REFERENCES

1. K. H. Behrndt. "Long Term Operations of Crystal Oscillators in Thin Film Deposition." *Journal of Vacuum Science and Technology*. 8. No. 5. Sept - Oct 1971. pp. 622-626
2. A. E. Barrington. *High Vacuum Engineering*. Prentice-Hall Inc. 1963. p. 55
3. P. A. Redhead, J. P. Hobson, and E. V. Kornelsen. *The Physical Basis of Ultrahigh Vacuum*. Chapman and Hall Ltd. London. 1968. p. 104
4. D. J. Santeler, D. H. Holkeboer, D. W. Jones, and F. Pagano. "Vacuum Technology and Space Simulation." NASA-SP-105. 1966. p. 186

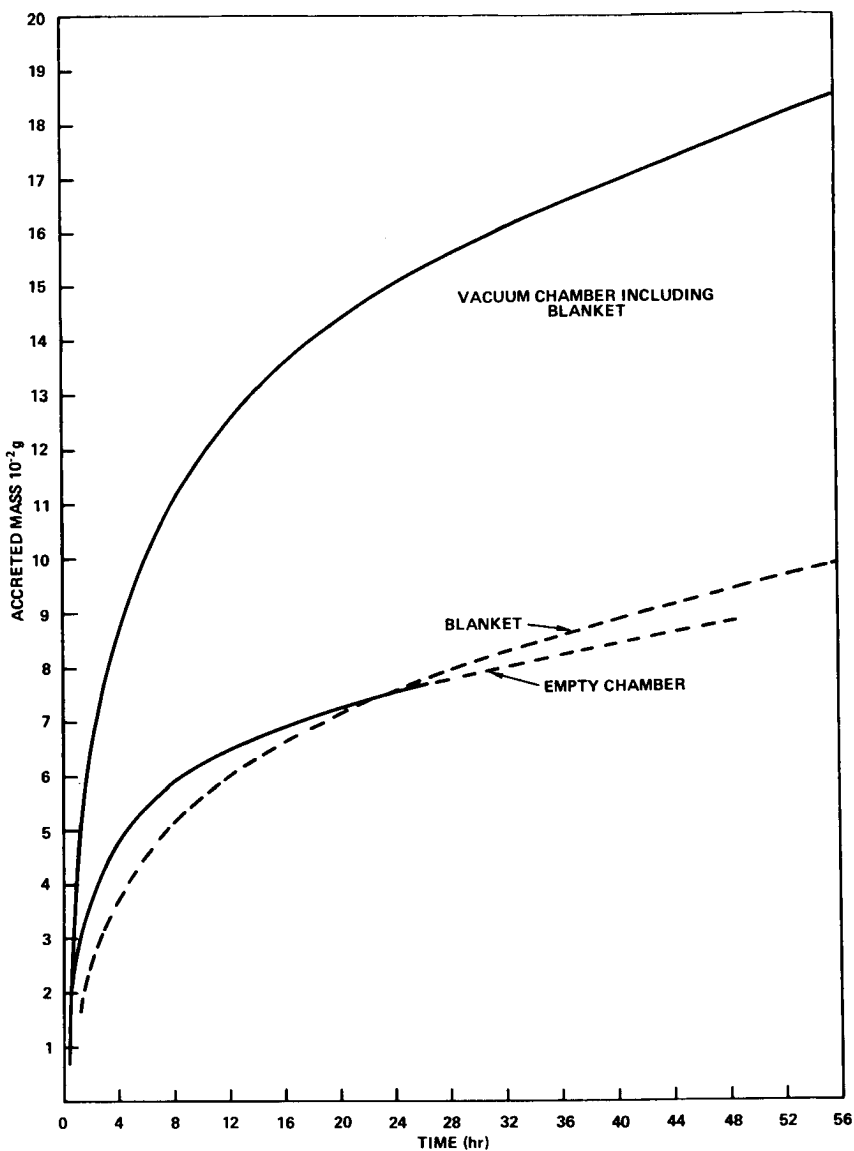


Figure 1. Total outgassing material accreted on -120°C surface.

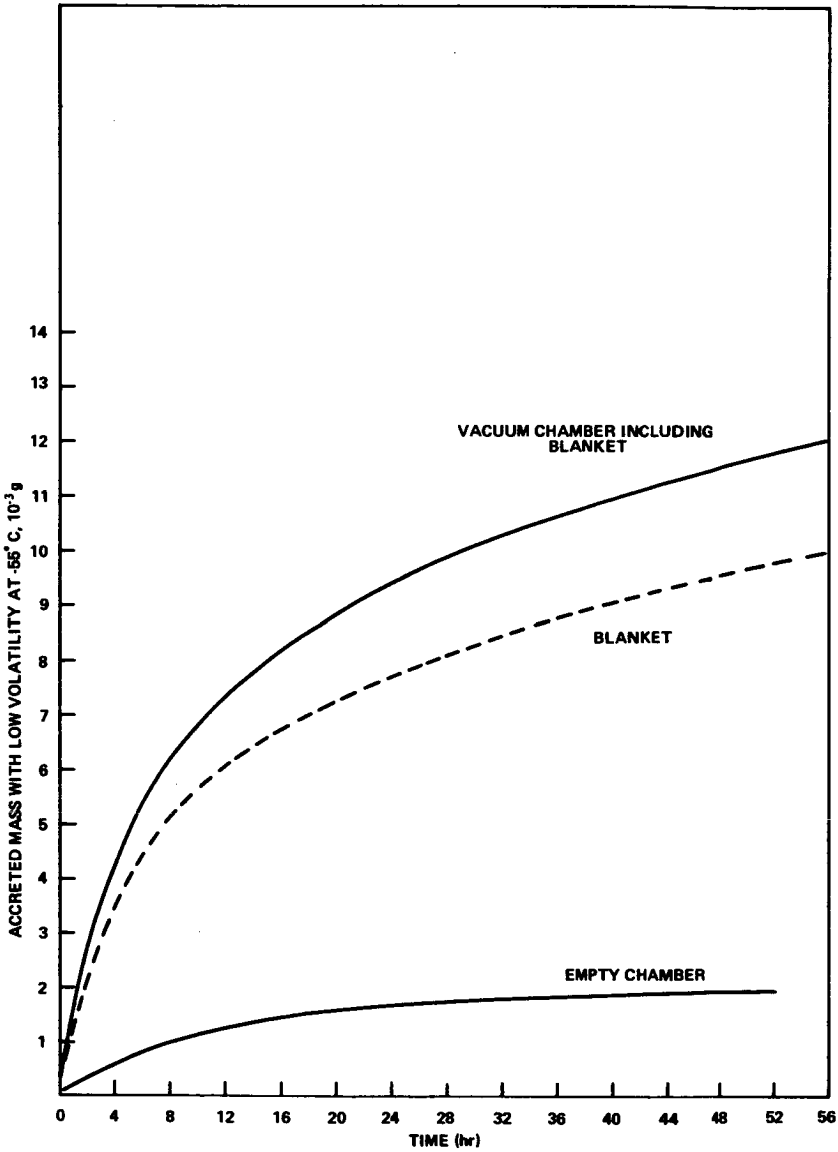


Figure 2. Accreted outgassing with low volatility at -55°C .

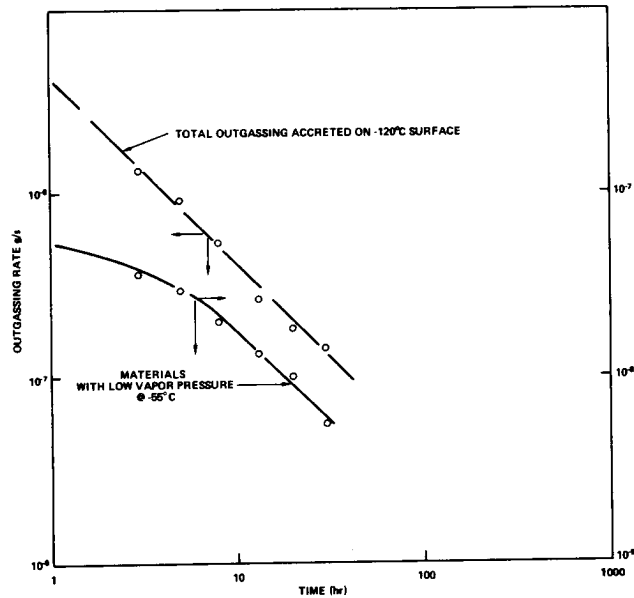


Figure 3. Outgassing rate of 3-by 3-ft chamber No. 240 at 60° C.

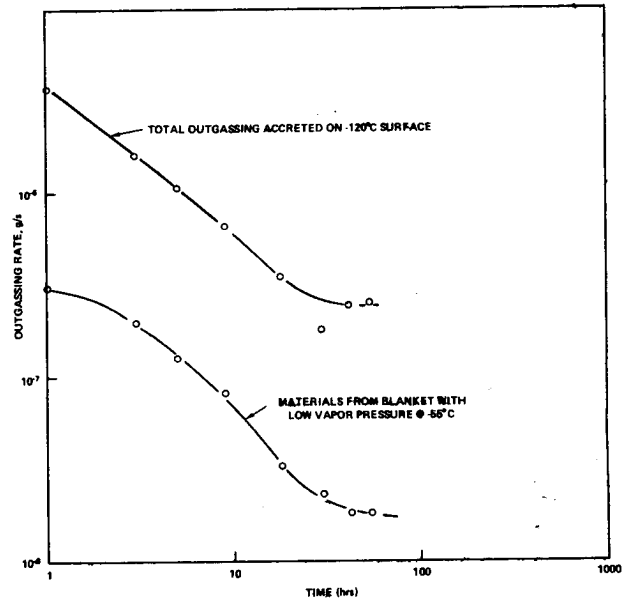


Figure 4. Outgassing rate of blanket at 60° C.

747

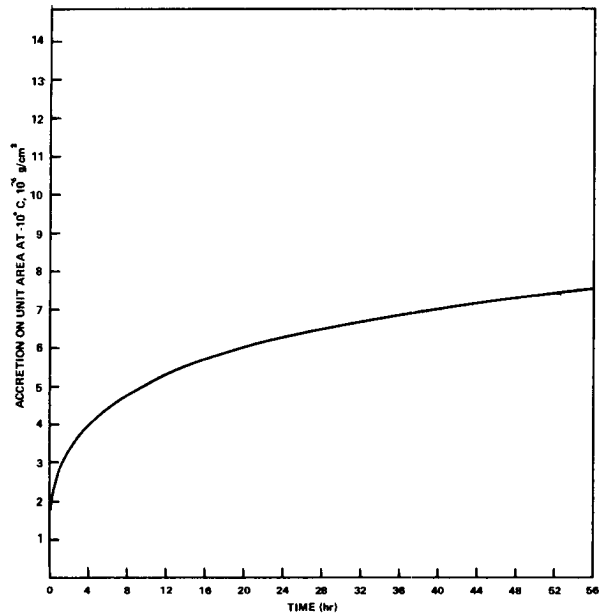


Figure 5. Blanket outgassing accreted on unit area at -10°C .

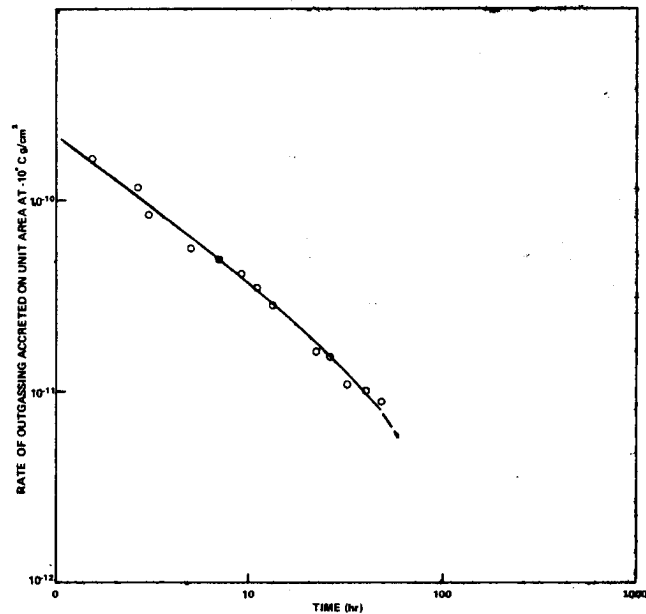


Figure 6. Rate of blanket outgassing accreted on unit area at -10°C .

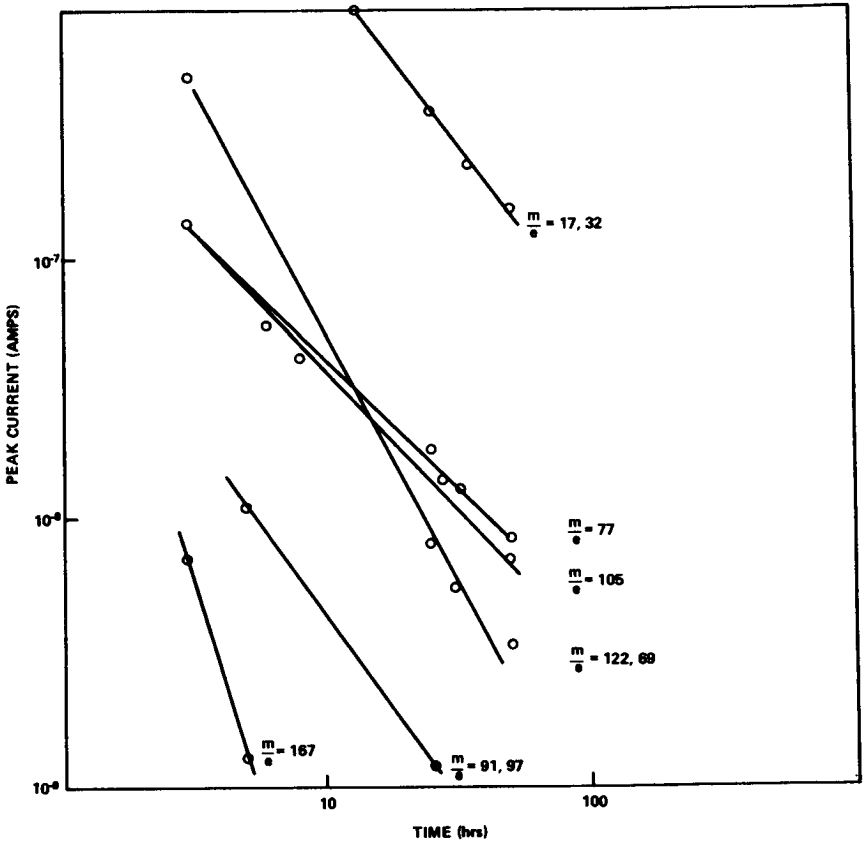


Figure 7. Sample mass spectrometer peak current readings.

N701 107282

**MOLECULAR DENSITY DETERMINATION OF WATER VAPOR
IN A 10^{-4} TO 10^{-2} TORR VACUUM ENVIRONMENT BY
ULTRAVIOLET ABSORPTION**

R. G. Richmond, and J. T. Visentine, *Aerospace Technologist,
Research and Development Section, NASA-Johnson Space Center,
Houston, Texas*

ABSTRACT

A new sensor has been developed for water vapor molecular density measurement in NASA's space environment simulation chambers at the Johnson Space Center. Its intended use is to obtain measurements in the exit planes of supersonic nozzles without disturbing the plume flow field in the chamber. A laboratory version of the sensor has been built and tested in a static pressure environment to determine its sensitivity. Water vapor absorption cross sections were determined in the molecular density range 10^{13} to 10^{15} molecules/cm³ (3.1×10^{-4} to 3.1×10^{-2} torr, respectively). The results show the sensor is extremely sensitive in detecting water vapor, and that its useful measurement range exceeds 10^{15} molecules/cm³. Design features of the sensor are reviewed and the results of the test program are discussed.

INTRODUCTION

A test program has been initiated in chamber A at the National Aeronautics and Space Administration (NASA)-Johnson Space Center (JSC) to investigate operational characteristics of supersonic nozzles for directing and controlling water vapor. These nozzles will be tested in a simulated space environment and evaluated to determine how efficiently they concentrate and direct water from spacecraft evaporative heat sinks.

To aid in nozzle performance evaluation, a water vapor molecular density sensor was developed and tested at the JSC. This sensor was designed to measure molecular densities at the nozzle exit plane without disturbing the plume flow field in the vacuum chamber.

This paper describes the effort required to develop a sensor for water vapor molecular density

measurement, and calibrate the sensor over the molecular density range 10^{13} to 10^{15} molecules/cm³.

Sensor Description

The sensor consists of a sealed hydrogen lamp, a magnesium fluoride (MgF₂) lens, and a nitrous oxide (NO)-filled ionization chamber. The lamp is filled with hydrogen gas at a pressure of 8 torr. The clear aperture of 8 mm. is covered with a 1-mm.-thick Mg F₂ window. The detectors are NO-filled ionization chambers with windows of Mg F₂ and apertures of 0.53 mm. The ionization chambers are operated at 50 VDC in the saturation region with unity gain.

The radiation from the source is collected by a 3.75-cm. Mg F₂ lens with a focal length of 7.6 cm. The source-to-detector distance is 10.1 cm. This array yields a 1000-percent increase in detector output over that without the lens.

The Mg F₂ lamp and detector windows eliminate any radiation of wavelengths shorter than 1150 Angstroms, and the NO gas ionization upper limit occurs at approximately 1350 Angstroms. Hence, the bandwidth of the system is about 200 Angstroms, and the useful wavelength range is from 1150 to 1350 Angstroms.

Theoretical Considerations

Water vapor has been found to be highly absorbing in the wavelength range 1150 to 1350 Angstroms. The maximum absorption cross section over this range is reported to be in excess of 20 megabarns (1 mb = 10^{-18} cm², ref. 1). The measurement of absorption cross section is based on the Lambert-Beer law (ref. 2):

$$I_{\lambda} = I_0 \exp(-\sigma_{\lambda} nL) \quad (1)$$

where I_0 is the incident radiation flux of wavelength λ ; I_{λ} is the flux transmitted through the absorbing gas; σ_{λ} is the absorption cross section; n is the molecular density of the absorbing gas; and L is the absorption path length.

The Lambert-Beer law is valid only for truly monochromatic radiation of infinitely narrow bandpass. However, previous studies have shown that if the

absorption cross section does not vary or is a slowly varying function of the wavelength over a given bandpass, an effective cross section can be measured for this bandpass (ref. 3).

When the semilog plot of $\log_{10}(I_0/I_\lambda)$ versus the molecular density, n , is a straight line, the absorbing medium is said to follow the Lambert-Beer law. However, if the sensor bandwidth is greater than the line width of the discrete structure, the linearity relation does not hold, and a "pressure effect" is observed. In this situation, a working curve for the sensor must be constructed over the nonlinear portion of the curve to obtain useful measurements (ref. 3).

Experimental Procedure

Calibration of the water-vapor molecular-density sensor was accomplished in a small (1-meter diameter, 1.5-meter length) vacuum chamber. This chamber was capable of attaining pressures in the 10^{-7} torr range using two 4100 liter/sec oil diffusion pumps. A millitorr gage was used to determine the pressure and, hence, the molecular density of the absorbing gas. An ionization gage was installed near the millitorr gage to measure the background pressure before the diffusion pump gate valves were closed and water vapor was admitted into the chamber. After the background pressure had stabilized around 1×10^{-6} torr, a heated inlet tube was used to introduce water vapor into the chamber. The water vapor pressure was controlled in the range 3.1×10^{-4} to 3.1×10^{-2} torr at the sensor using a variable orifice valve. Inlet tube pressure and temperature were monitored outside the chamber. The test setup and sensor configuration are shown in figure. 1.

The molecular density at the sensor was determined from the relation (ref. 4):

$$p = nkT \quad (2)$$

where p is the pressure in torr measured by the millitorr gage, n is the molecular density of the absorbing gas in molecules/cm³, k is the Boltzmann constant, and T is the gas temperature in °K.

Experimental Results

To calibrate the sensor and determine its sensitivity (measurement range), a plot of absorbance vs water vapor molecular density was obtained as a working curve over the range 10^{13} - 10^{15} molecules/cm³ (3.1×10^{-4} to 3.1×10^{-2} torr, respectively).. This

working curve is shown in figure 2. As indicated in this figure, the absorbance exhibits nonlinear behavior for increasing molecular densities and varies between 0.004 and 0.63 (99.1 and 23.4 percent transmittance respectively). This result was expected since the sensor bandwidth (1150 to 1350 Angstroms) is greater than the line width of the discrete structure of the hydrogen spectrum produced by the radiation source.

The sensor accurately measures absorbances as high as 1.0 (10 percent transmittance). At a molecular density of 10^{15} molecules/cm³, the measured absorbance was 0.63. Hence, this test result indicates the molecular density range of the sensor exceeds 10^{15} molecules/cm³.

The effective absorption cross section for each point shown in figure 2 was calculated and plotted as a function of molecular density. This curve is presented in figure 3. As indicated by this curve, the absorption cross section varies between 23 and 58 megabarns over the molecular density range 1×10^{13} to 1×10^{15} molecules/cm³.

An interesting aspect of this curve is that it rises rapidly, reaches a peak at a molecular density of 8×10^{13} molecules/cm³ (2.5×10^{-3} torr), and then falls off rapidly. By the time the molecular density has increased to 1×10^{15} molecules/cm³ (3.1×10^{-2} torr) the absorption cross section has decreased from 58 to 25, which represents a $\Delta\sigma/\sigma$ loss of 57 percent.

CONCLUSIONS

Absorption measurement in the wavelength range 1150 to 1350 Angstroms is an extremely sensitive technique for water vapor molecular density determination. The useful measurement range for the sensor tested was determined to be from approximately 1×10^{13} molecules/cm³ (3.1×10^{-4} torr) to densities in excess of 1×10^{15} molecules/cm³ (3.1×10^{-2} torr). The absorption cross section, which establishes the limits of the sensor's sensitivity, was found to be dependent on molecular density.

Values calculated for the absorption cross section agree well with values reported in the literature. The sensor was found to have the highest absorption cross section (58 megabarns) at a molecular density of 8×10^{13} molecules/cm³ (2.5×10^{-3} torr). Additional tests will be performed on the sensor to determine the upper limit of the molecular density measurement range.

REFERENCES

1. J. A. R. Sampson and J. A. Myer, "Absorption Cross Sections of Minor Constituents in Planetary Atmospheres from 1050 to 2100 A," Technical Report Contract No. NASA-1726, November 1969.
2. IBID.
3. Conley, Robert T., Infrared Spectroscopy, Allyn and Bacon, Inc., Boston, Mass., copyright 1966, pp 207-209.
4. Dushman, Saul, Scientific Foundations of Vacuum Technique, John Wiley and Sons, Inc., New York, N. Y., copyright 1962, p2.

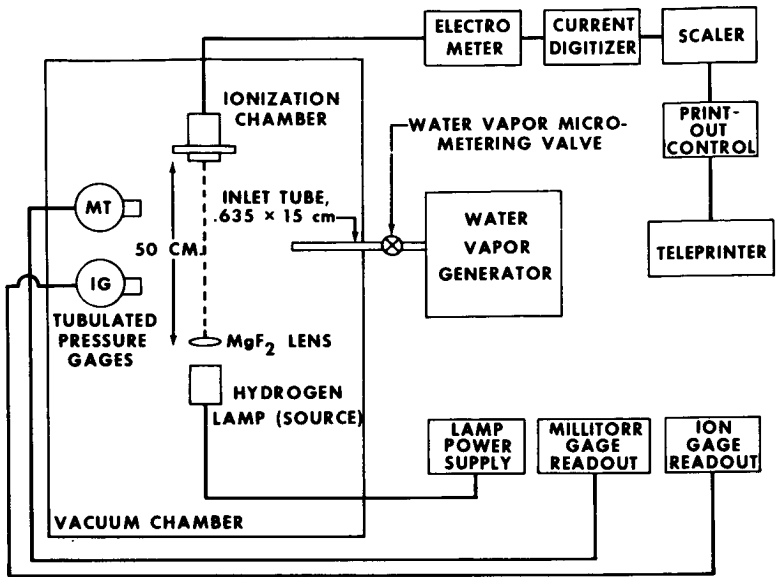


Fig. 1 - Test setup block diagram

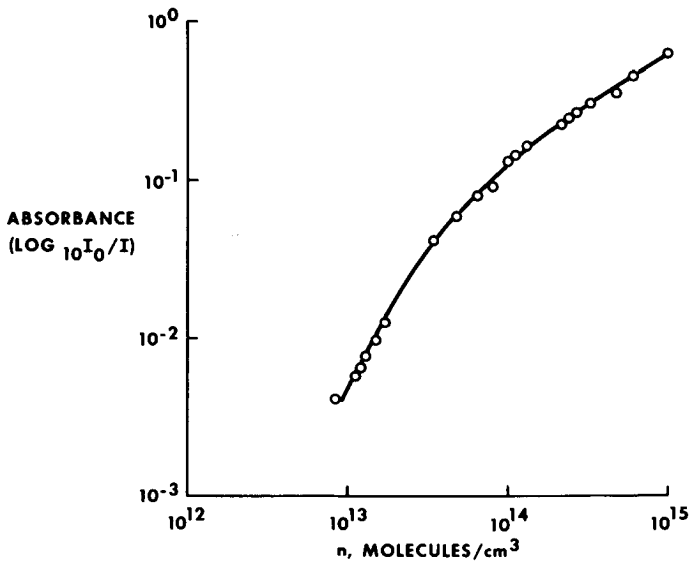


Fig. 2 - Absorbance as a function of water vapor molecular density

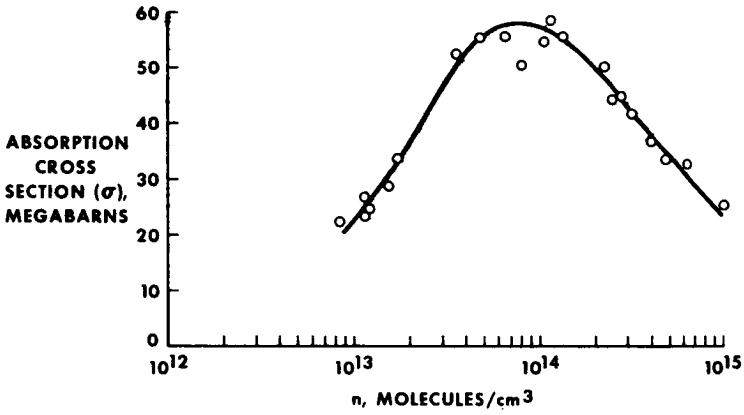


Fig. 3 - Absorption cross section as a function of water vapor molecular density

PRECEDING PAGE BLANK NOT FILMED

Paper No. 63

MATHEMATICAL MODEL OF MOLECULAR FLOW IN THE
NASA-JSC THERMAL-VACUUM CHAMBER A

A. L. Lee and S. J. Robertson, *Lockheed Missiles and Space Co., Huntsville, Alabama*; Horst K. F. Ehlers, *NASA-Johnson Space Center, Houston, Texas*

ABSTRACT

A new computer program has been developed for the math modeling of molecular flux inside a typical large thermal-vacuum chamber. It can be applied in four general areas: prediction, evaluation and improvement of the chamber performance; prediction of contamination migration; location of sources of leaks and outgassing; and design of new thermal-vacuum chambers.

INTRODUCTION

Thermal-vacuum chambers of various capacities installed at National Aeronautics and Space Administration (NASA) centers are extensively used for space simulation testing. One of the major concerns of such testing is the maintaining of required environmental conditions, specifically the preventing of the contamination of the most sensitive test article components with undesirable molecules released by materials such as outgassing paints, vacuum pump oils, etc. The ability to identify and locate in-chamber gas leaks and sources of contamination is of prime importance so that they may be controlled or removed. Current practices in fulfilling this need at NASA-Johnson Space Center's (JSC) thermal-vacuum chamber A involve the use of directional molecular flow sensors, referred to as the Directional Gas Flow Measurement (DGFM) system¹. The accuracy of the DGFM system has been restricted when gas or contamination sources are located behind the liquid nitrogen (LN₂) cooled shroud, below the chamber floor, or when other chamber structures are located between source and sensor. In addition, the sensor cannot always be positioned at locations where the need for molecular flux measurements is greatest (e.g., near the spacecraft).

There appears to be a need for some theoretical model that relates molecular flux rates and gas or

contamination sources in order to solve these and other problems that are normally encountered in thermal-vacuum testing; and, as a result, help reduce the cost in the performance of these tests. A truly analytical model exists so far only for space environment simulation chambers and test articles of ideal spherical symmetry and concentric arrangement. This model usually helps in making gross estimates of molecular flow rates in most chambers; it does not provide sufficiently accurate data to meet the actual requirements arising from practical thermal-vacuum testing. This is true even for chambers of "spherical" design.

Mathematical modeling based on more realistic chamber and test article configuration appears to allow reasonable and adequate prediction and extrapolation of molecular flux during testing.

A new Monte Carlo computer program was developed for the mathematical simulation of molecular flux inside a typical thermal-vacuum chamber, such as chamber A at NASA-JSC. This program constitutes a new approach in developing a tool that may be used to accomplish any of the following tasks:

1. Assisting in interpreting the readings of a molecular flux sensor in order to locate and identify gas leaks and contamination sources.
2. Predicting the molecular flow rates in specific locations depending on test configuration (contaminant migration).
3. Predicting and evaluating the adequacy of space vacuum simulation and test environment condition, specifically with respect to level of contamination.
4. Predicting the effect of abnormal test article and chamber conditions (aid in troubleshooting).
5. Predicting and evaluating the effects of chamber modifications and configuration on test objectives. (test planning)
6. Aiding in the design of new vacuum chambers.

The program therefore permits the study and evaluation of specific test configurations before any hardware is produced thereby eliminating possible costly configuration changes after hardware is manufactured.

This paper describes characteristic features of the mathematical model developed by Lockheed Missiles & Space Company, Inc., (LMSC) on contract to NASA-JSC and some specific application cases.

MATHEMATICAL MODEL

The mathematical approach taken in developing the molecular flow model involves variations of the Monte Carlo method. During the course of the model development, it became apparent that a complete modeling of the entire chamber geometry, using the classical Monte Carlo technique, would require an unreasonable amount of computer time and, in some cases, would be unproductive. The reasons for this will be made clear in the following discussion. The approach taken, therefore, was directed toward developing a model which would provide the optimum combination of utility and computer usage economy.

Consider the schematic of the chamber A geometry shown in figure 1. The leak detector sensors have been located within the main chamber area near the interior surface of the LN₂ shroud. Molecular flow originating from a source located within the main chamber will reach the sensors by direct flight, providing there are no intervening obstacles, and by indirect flight after undergoing collisions with the chamber interior surfaces and other molecules. Molecular flow originating behind the LN₂ shroud will undergo a large number of collisions behind the shroud before eventually escaping into the main chamber area through one of the gaps or openings in the shroud. Finally, molecular flow originating within the lower dome area, and particularly within the plenum chamber, will undergo an enormous number of collisions before eventually migrating into the main chamber. In fact, it can be shown that the flow in the plenum chamber becomes randomized to the point that the location of the source becomes irrelevant to the molecular flow distribution. This means that it would be impossible to determine the source location by measuring molecular flow characteristics at a point outside of the plenum chamber.

The nature of the Monte Carlo method is such that each collision that each molecule undergoes represents calculations that have to be made and, hence, computer time usage. With the large number of sample molecules that must be generated to achieve statistical accuracy, a prodigious amount of computer time can be required for a single run.

One of the primary purposes of the mathematical model is to calculate the molecular flow rate at the DGFM sensor location. To accomplish this by the classical Monte Carlo method, the geometry of the sensor must be modeled, and the number of sample molecules that eventually enter the sensor are counted. Since the sensor diameter is of the order of an inch while

the chamber diameter is of the order of 60 feet, the probability of a single sample molecule entering the sensor is, for all practical purposes, infinitesimal. The number of sample molecules required for a molecular flow rate calculation, therefore, would approach infinity. A compromise can be made by utilizing a larger diameter sensor in the mathematical model. This would, in effect, average the calculated flow rate over a larger area and would still require a large sample size to achieve statistical accuracy. The method finally selected eliminates the need for large sensor diameters and actually calculates the flow rate at a point using a combination of Monte Carlo and view factor concepts. Compared to the classical Monte Carlo technique, this method is extremely economical from a computer usage standpoint and, in most cases, is a great deal more accurate. This method is designated the ray tracing technique and is described in the following paragraphs.

Ray Tracing Technique

The ray tracing technique is based on the fact that for molecules traveling directly from a source to a point, the molecular flux can be calculated directly from a simple view factor relationship without a need for counting sample molecules. This concept is extended to include scattering from other molecules and from walls by utilizing certain Monte Carlo principles. Consider the hypothetical molecular flow configuration shown in figure 2. The molecular flux, q_1 , at the sensor location, due to molecules streaming directly from the source, is given by the following equation:

$$q_1 = \frac{\dot{m}_0 \cos \alpha_1 \cos \gamma_1}{\pi r_{a-c}^2} \exp(-r_{a-c}/\lambda) \quad (1)$$

where \dot{m}_0 is the source strength, r_{a-c} is the distance between source and sensor, λ is the mean free path, and α_1 and γ_1 are given in figure 2. The source is assumed to emit in a cosine law distribution. The exponential factor accounts for attenuation due to intermolecular collisions.

For molecules arriving indirectly at the sensor location after undergoing collisions, a variation of the Monte Carlo technique is used. First, a representative sample of molecular trajectories is selected randomly according to a cosine distribution, and each

of these trajectories is traced to a point of intersection with a wall. Each of these sample trajectories is considered to represent a flow rate of \dot{m}_0/N , where N is the number of trajectories in the sample. For each of these trajectories, an amount $(\dot{m}_0/N)[1 - \exp(-r_{a-b}/\lambda)]$ will be scattered from the beam by intermolecular collisions. The remaining $(\dot{m}_0/N) \exp(-r_{a-b}/\lambda)$ will reach the point of intersection with the wall where a fraction C , the capture coefficient, will remain stuck to the wall. The remaining fraction $(1-C)$ will be scattered in a cosine distribution. Those molecules attenuated from the beam by intermolecular collisions are represented by a new source of strength $(\dot{m}_0/N_0)[1 - \exp(-r_{a-b}/\lambda)]$ located at a point on the trajectory at a distance from the original source. If $\lambda > r_{a-b}$, these scattered molecules are neglected. This new source emits in a cosine distribution in the direction of the trajectory. The molecules that reach the point of intersection with the wall are represented by a new source of strength $(1-C)(\dot{m}_0/N_0)\exp(-r_{a-b}/\lambda)$ at the point of intersection, again with a cosine distribution. These new sources will contribute to the flux at the sensor location according to

$$q_2 = (1-C) \frac{\dot{m}_0}{N_0} \exp(-r_{a-b}/\lambda) \frac{\cos\beta \cos\gamma_2}{\pi r_{b-c}^2} \exp(-r_{b-c}/\lambda) + \frac{\dot{m}_0}{N_0} \left[1 - \exp(-r_{a-b}/\lambda)\right] \frac{\cos\delta \cos\gamma_3}{\pi r_{d-c}^2} \exp(-r_{d-c}/\lambda) \quad (2)$$

This procedure may be repeated as many times as accuracy requires or economy permits, so that the total flux q at the sensor location is given by

$$q = q_1 + \sum_{i=1}^{N_0} q_{2_i} + \sum_{i=1}^{N_0} \sum_{j=1}^{N_0} q_{3_{ij}} + \dots \quad (3)$$

In practice, it is unnecessary to go beyond the second wall collision (q_3), since additional collisions merely serve to randomize the molecular flow into the background pressure. The results presented in a later section were obtained using values of N_0 around 250 for the first collision and values of N_1 around 25 for the second collision. This represents a considerable

gain in economy over the classical Monte Carlo approach, which usually requires a sample size of from 10,000 to 100,000 to achieve even moderate accuracy. In addition to the gain in economy, the statistical fluctuations associated with Monte Carlo calculations are practically eliminated.

Modeling of Sensor

Another gain in economy is achieved by computing a directional distribution of molecular flux at the sensor location. From this directional distribution, the molecular flux can be determined for any direction that the sensor might be oriented. This allows a single computer run to develop data which would otherwise have required several runs. In the results presented in a later section, a single run simulates both horizontal and vertical scans of the DGFMS sensors.

The directional distribution is obtained by dividing the vertical and horizontal angles (latitudinal and longitudinal) into increments, and each contribution, q_{ij} , to molecular flux at the sensor location is determined to correspond to one of these increments, where i and j refer to vertical and horizontal angle increments. The molecular flux, q_{lm} , corresponding to a particular sensor direction is then obtained from

$$q_{l,m} = \sum_{ij} q'_{ij} \cos \theta_{ij;lm} \quad (4)$$

where $\theta_{ij;lm}$ is the angle between the sensor direction and the increment ij , and the summation is made over angular increments within the field of view of the sensor.

Classical Monte Carlo

In a previous section it was pointed out that molecular flow originating in the lower dome region would undergo a large number of collisions before eventually migrating into the main chamber area where it could be detected by the DGFMS sensors. For this reason it was decided to treat this region separately from the main chamber. Because of the large number of wall collisions, and the fact that a sensor simulation was not required, the classical Monte Carlo approach was used to calculate molecular flow characteristics in this region. In this approach, a representative sample of molecular trajectories is selected randomly from a cosine distribution at the source location, and

each trajectory is traced until it leaves the system. The molecular flux at some point of interest, such as the diffuser grid between the lower dome and main chamber, can be calculated by counting the number of molecules that intersect a unit area of surface.

Chamber Geometry Simulation

The overall chamber geometry was simulated in separate sections, primarily depending on the mathematical approach being utilized.

Main Chamber: The main chamber, including helium panels, LN_2 shroud, LN_2 panel, test article and sensors, was included in one program with molecular flow being treated using the ray-tracing technique. The geometry simulated in this program is shown in figure 3. The dimensions of the chamber and the locations of the source and sensor were made arbitrary. The program can handle one source and 2 sensor locations during one run. The test article geometry is arbitrary to the extent that it can be constructed of combinations of cylinders, spheres, cones, disks and plane quadrilaterals. The locations and dimensions of these subshapes are made arbitrary to allow the simulation of complex test article geometry.

Plenum Chamber: Flow in the plenum chamber was calculated using the classical Monte Carlo technique with the geometry simulated as shown in figure 4. The program calculates the flow from a source and records the distribution of collisions around the chamber wall. This program was developed primarily to demonstrate the fact that the large number of wall collisions effectively randomizes the flow into a background pressure and to calculate the flow of migrating contamination in and out of the plenum chamber.

Repressurization Plenum: Flow in the repressurization plenum was modeled by the classical Monte Carlo technique using the geometry in figures 4 and 5. The repressurization diffuser duct was not included because the time and effort required to model the complex geometry did not appear to be justified by the impact of the duct's presence on the molecular flow distribution. Test calculations made without the duct indicate that, except for sources located inside the duct, the flow tends to become randomized to a large extent on all sides of the duct, so that the duct's influence on the flow is essentially nullified.

The computer program is set up to first compute the transmission probability for flow through the channel formed by the trays under the main chamber floor, and then through the diffuser grid. After this

transmission probability is computed, the molecular flux along the diffuser grid surface is calculated as a function of angular position around the chamber. The results of this computation can be used as inputs to the main chamber program.

Solar Simulators: In the main chamber program, the solar simulators are treated as solid plates without gaps. The reason for this is that the gaps are considered to be negligibly small compared to the principal openings in the LN₂ shroud. A separate program, based on the classical Monte Carlo technique, was developed to simulate molecular flow from a source behind the solar simulator. The individual lamps are represented as circular disks set off from the wall on the same plane. The diameter of the circles are made arbitrary and allowed to overlap to simulate varying gap sizes.

Diffusion Pump Ports: A separate program, based on the classical Monte Carlo technique, was developed to trace the backstream flow from the diffusion pump ports as well as the molecules that were pumped by diffusion pumps. The pump ports are located behind the LN₂ shroud. In order to trace the molecular flow between the LN₂ shroud and the chamber wall, additional structural features and cooling surfaces have to be considered. These include the cylindrical shield at the door, LN₂ cooled baffles over each manlock and LN₂ cooled surfaces on and around manlocks and around the side sun simulator. The result of this program tabulates the quantities of the molecules which are deposited on certain surfaces, pumped by diffusion pumps, and which escape into the test area.

APPLICATIONS

The math model can be applied in three general areas: evaluation and improvement of the chamber performance; prediction of contaminant migration; and, location of sources of leaks and outgassing.

The performance of a thermal-vacuum chamber can be rated by its selfcontamination factor, Z , which is defined as the ratio of the number of molecules returning to the test vehicle surface to the number of molecules leaving the vehicle surface. A low value for Z represents a good space simulation. The Z factor depends primarily on the capture coefficients of chamber surfaces and the relative values of the test vehicle and the thermal-vacuum chamber. However, the location of cold surfaces and the direction of outgas flux affect the value of Z also. The Z factor and the average capture coefficient of the chamber are calculated at the same time. Capture coeffi-

cient, C_{av} , is defined as the fraction of molecules being captured by the cooled wall at its first encounter. C_{av} , like Z , is also dependent on local capture coefficients, location of cold surfaces and direction of flow.

Table 1 shows the results of a simulation using the Apollo command and service module (2TV-1) as the test vehicle. C_1 and C_2 are the capture coefficients for the LN_2 -cooled and He-cooled panels, respectively.

TABLE I

Case	C_1	C_2	Z	C_{av}
1	0.00	0.01	0.668	0.026
2	0.85	0.97	0.016	0.848
3	0.20	0.95	0.118	0.362
4	0.20	0.95	0.168	0.304
5	0.10	0.90	0.166	0.250
6	0.10	0.90	0.142	0.396
7	0.10	0.90	0.112	0.408
8	0.10	0.90	0.150	0.224
9	0.10	0.90	0.138	0.246
10	0.10	0.90	0.1418	0.3048

Cases 1 through 4 simulates the uniform outgassing of the test vehicle by putting a uniformly emitting point source at the center of the vehicle geometry. Cases 1 and 2 compare very favorably with previously calculated results (Ehlers, 1970)², where Z was 0.70 and 0.003 for zero pumping and LN_2 coldwall pumping, respectively. Cases 3 and 4 are under identical conditions except that in case 4 half of the He panels are shut off. Each of the "off" panels alternate with "on" panels. Note the corresponding increase in Z and reduced C_{av} value. Cases 5 through 8 simulate the conditions in which gas is released on the side of the rotating vehicle at 90 degree intervals. When the source is facing the large door or the side sun cut-out, the local average capture coefficient is markedly reduced due to the reduced area covered by the He panel. This effect is clearly shown in the increased values of Z in cases 5 and 8. Case 9 simulates the outgassing for a point located on the command module surface. Case 10 is the accumulated average for cases 5 through 9.

The movement of contaminants can be traced either from one partition of the chamber to another or from the source to the surfaces within the same partition.

Table 2 tabulates the results of contaminant back-streaming from diffusion pump ports on the same level. CPP is the diffusion pump port capture probability.

The coordinates of sources are normalized by the chamber radius. Equivalent capture coefficients for noncondensable gases due to pumping at the diffusion pump ports can also be calculated for the cutouts on the LN₂ shroud. The simulation is made by treating the LN₂ shroud cutout as an area source, and counting the fraction of molecules pumped by the diffusion pumps. A calculation shows that the equivalent capture coefficients for manlock cutouts 1, 2, and 3 are 0.013, 0.04, and 0.0956, respectively.

In order to calculate the migration of gas molecules from one subchamber to another, the conductivity is calculated for the passage between the repressurization plenum and main chamber. The result is plotted versus the capture coefficient of the repressurization diffuser in figure 6. An example of the molecular distribution over the repressurization diffuser when a source is located beneath is shown in figure 7. This distribution can be detected by the sensors in the chamber.

When a leak or contamination source is to be located, the position of the sensor itself is very important. When the source is in the field of view of the sensor, there is an unambiguous peak in the direction of the source. When the source is obscure, either behind the test vehicle or behind the LN₂ panels, the reading would show more than one peak which may depict the shadow of the vehicle or the cutouts on the panel. A source was placed at a DF port (-.809,.588,1.29) for example. Two sensors were placed behind LN₂ shroud, and two were inside the shroud. The locations of sensors and source and relevant features of the chamber are shown in figure 8. The simulated reading of sensor ① showed a strong flux from side sun cutout. The horizontal reading is shown in figure 9. Sensor ② readings were generally lower in magnitude. The peak pointed to the direction of manlocks. Interpreting the readings of sensors ① and ② it is logical to conclude that a source was behind the LN₂ shroud at the location probably closer to side sun cutout than to manlock cutouts. The sensors ③ and ④ behind the LN₂ shroud showed peaks pointing directly to the source location.

TABLE 2

 Location of Source (-.951,-.309,1.29) (-1.0,0,1.29) (-.951,.309,1.29) (-.809,.588,1.29)

Total Condensed (%)	92.0	92.6	92.2	90.8
Due to C1	0.6	0.4	0.6	1.0
Due to C2	91.4	92.2	91.6	89.8
On Manlock Dr. 1	0.2	0.0	0.2	0.0
On Manlock Dr. 2	2.0	1.4	0.6	0.0
On Manlock Dr. 3	0.8	0.4	0.0	0.0
On Side Sun				
Cooled Area	0.0	0.0	1.4	3.0
On Conic Top	0.8	1.4	1.0	1.0
On Baffle Over				
Manlock 1	0.0	0.2	0.2	0.2
On Baffle Over				
Manlock 2	0.8	0.4	0.4	0.2
On Baffle Over				
Manlock 3	0.4	0.2	0.2	0.0
Escaped Through				
Side Sun Cutcut	0.4	0.8	2.0	4.8
Floor Grid	0.0	0.0	0.2	0.2
Manlock 1	0.0	0.0	0.0	0.0
Manlock 2	4.4	0.4	0.4	0.0
Manlock 3	0.0	0.2	0.0	0.0
Pumped by				
Diffusion Pump	3.2	6.0	5.0	4.2

 C1 = 0.01, C2 = 0.50, CPP = 0.95

CONCLUSIONS

The mathematical model is a powerful tool in the design, improvement and day-to-day operation of a thermal-vacuum chamber. Simulations of new configurations can easily be run with the model before costly hardware is manufactured.

The effectiveness of the space simulation can be determined by its Z factor. The values of Z and the average capture coefficient, hence the overall pumping speed, can be improved by relocating the He panels and the diffusion pumps used, adding more pumping capability, shielding hot spots, etc. Because of the numerous parameters involved, the mathematical model is the most logical way to determine the optimum configuration. On the other hand, adverse effects can be predicted when new surfaces, such as IR heaters, are introduced into the chamber.

Contamination has always been a matter of concern in thermal-vacuum testing. The main concern is the migration path and distribution at specific locations. If the movement of contaminating molecules can be traced, it might be possible to control the contaminant flow. The model would provide a useful tool in this respect.

The usefulness of the model is very broad, limited only by the user's imagination. The model is programmed specifically for the NASA-JSC chamber A. The geometric flexibility inherent in the model, however, allows its use in a variety of chambers.

REFERENCE

1. Ehlers, H. K. F., "Directional Molecular Flow Analysis and Leak Detection With a Rotatable Gas Analyzer in a Large Space Simulation Chamber," NASA SP-298, pp 789-795.
2. Ehlers, H. K. F., "Pressure Measurements and Gas-Flow Analysis in Chambers A and B During Thermal-Vacuum Tests of Spacecraft 2TV-1 and LTA-8," J. Spacecraft and Rockets, Vol. 7, No. 4, April 1970.

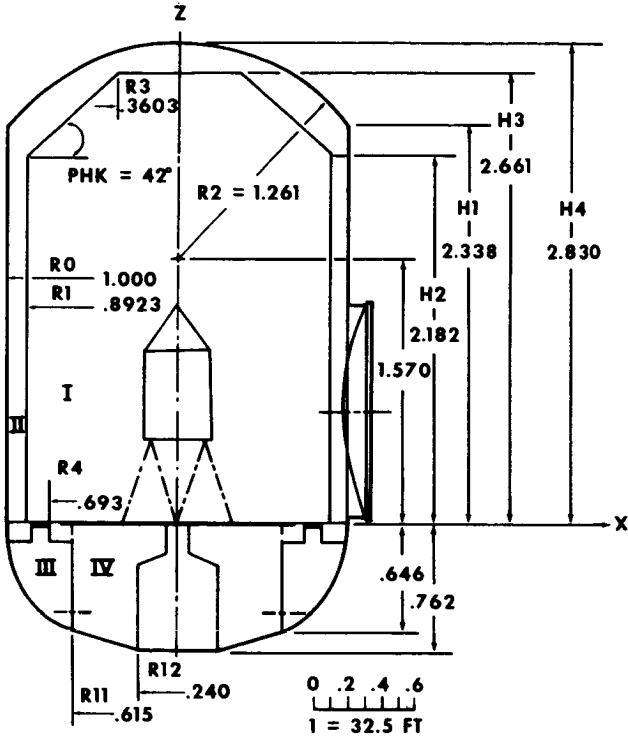


Fig. 1 - Schematic of Chamber "A" model

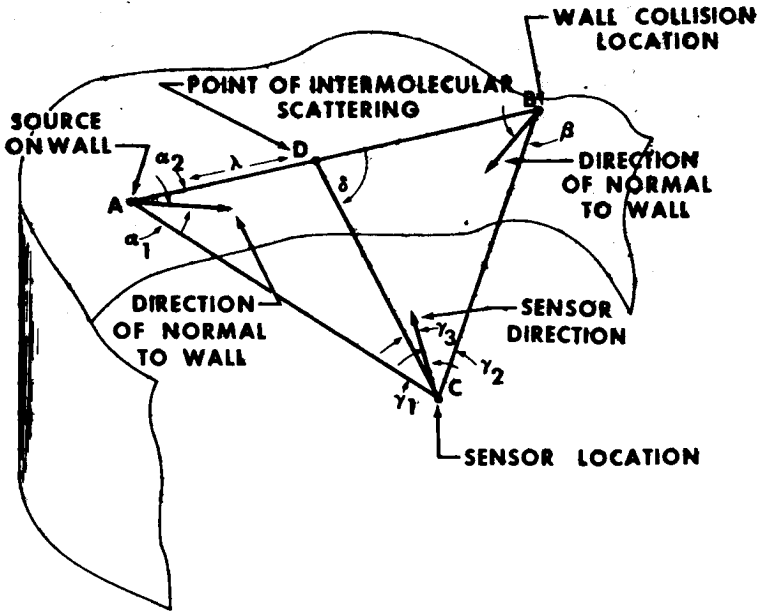


Fig. 2 - Illustration of ray-tracing technique

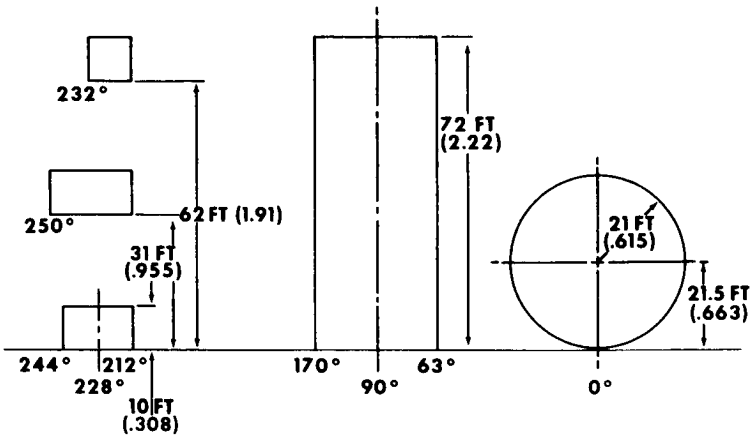


Fig. 3 - Developed view of LN₂ shroud openings (R1 = 29')
(normalized quantities in parentheses)

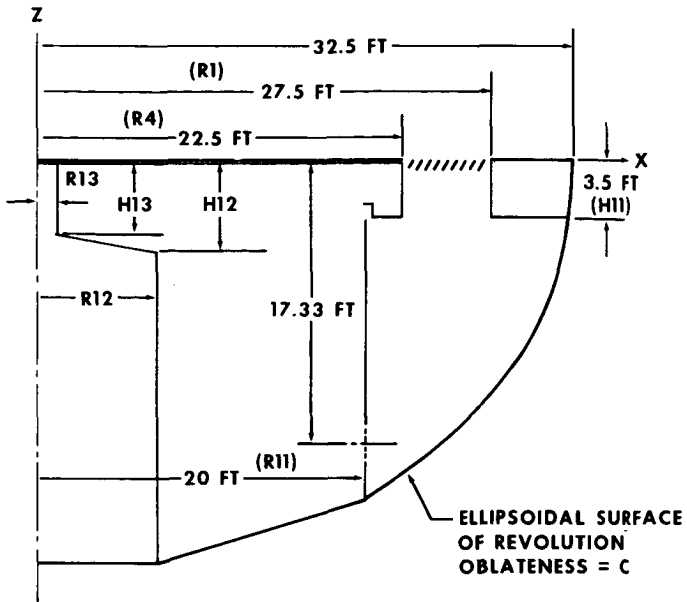


Fig. 4 - Geometry of repressurization plenum

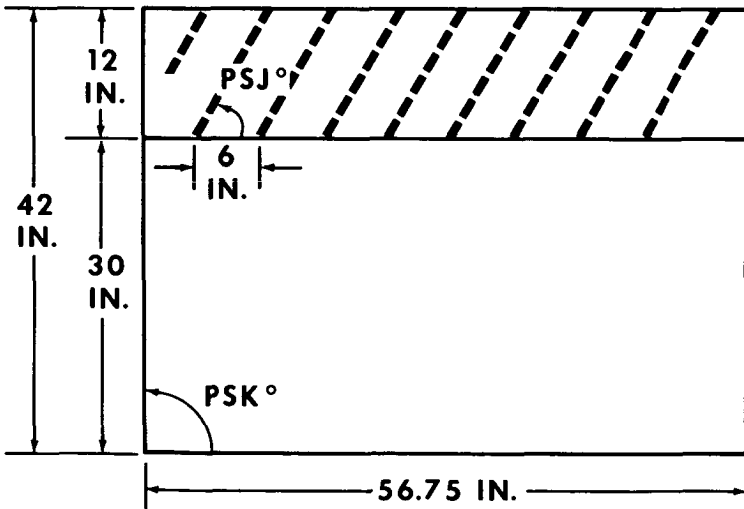


Fig. 5 - Model of passage from repressurization plenum to main test area

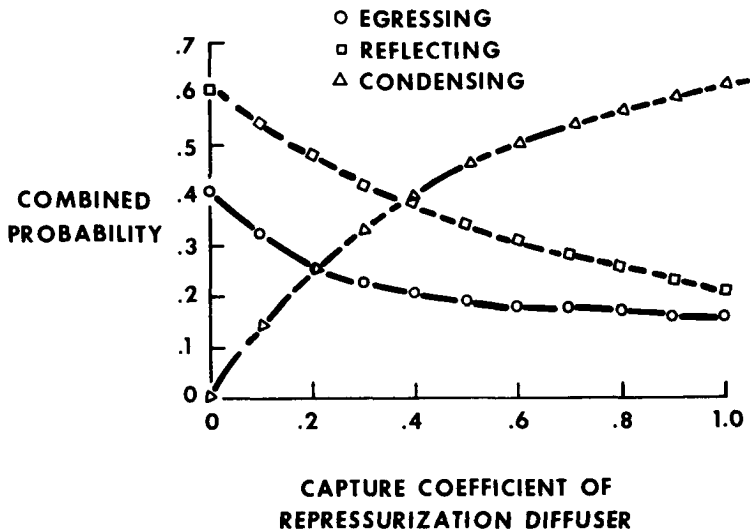


Fig. 6 - Probabilities of transmission, reflection and adsorption of the passage between repressurization plenum and main chamber

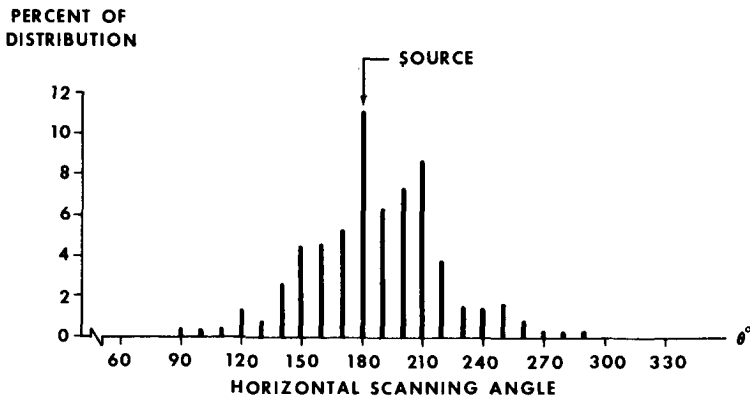


Fig. 7 - Molecular distribution over repressurization diffuser with a source underneath at $\theta = 180$ degrees

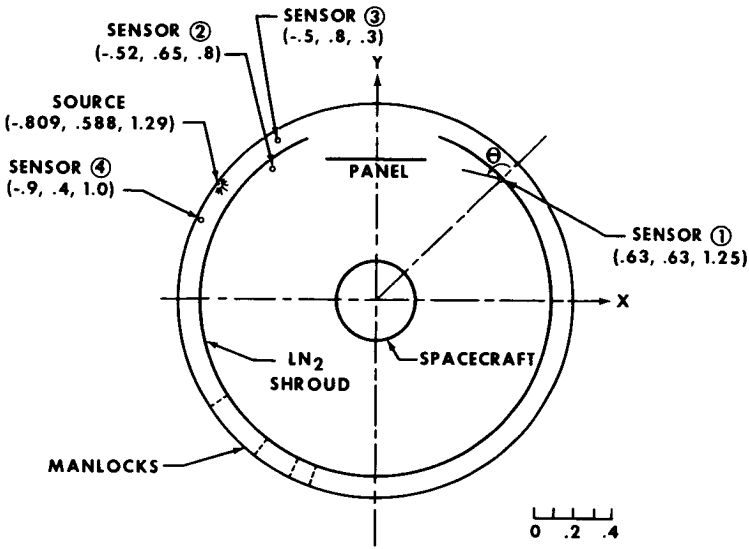


Fig. 8 - Schematic of chamber layout

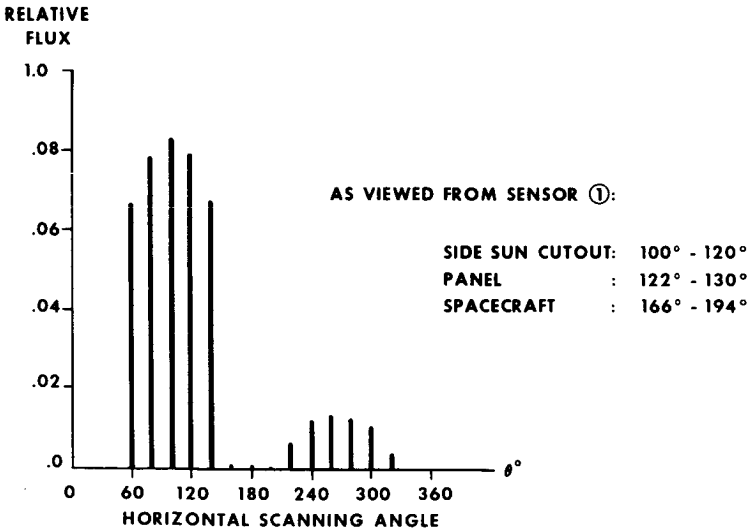


Fig. 9 - Horizontal scanning of sensor ① over source at (-.809, .588, 1.29)

N74-10259

PRECEDING PAGE BLANK NOT FILMED

Paper No. 64

A UNIQUE HIGH INTENSITY SOLAR SIMULATION SYSTEM

Leo Romanowski, Jr. and Ignatius N. Serafino, *Northrop Services, Inc.,
Goddard Space Flight Center, Greenbelt, Maryland*

ABSTRACT

This simulator is unique in that it is capable of producing intensities up to 16.0 solar constants (25 solar constants without spectral filters) and closely simulates the solar spectrum over a 12 inch diameter area. The paper describes the simulator and discusses the capabilities, calibration, operational experiences, data collection, and safety considerations associated with this simulator.

INTRODUCTION

Within the past decade an increase in sun orbited missions has emphasized the need for more sophisticated solar simulation techniques. An example is the Helios spacecraft which must fly within 28 million miles (.3AU) of the sun. During its 18 month mission, it will experience solar intensities varying from one to eleven solar constants. A simulator capable of exceeding these intensities recently passed NASA acceptance tests at Goddard Space Flight Center.

This High Intensity Solar Simulator is interfaced with either of two adjacent thermal-vacuum chambers. It is presently being utilized in the environmental testing of several Helios experiments in material degradation and thermal balance studies.

This report describes the unique simulator, its various systems and modes of operation, and discusses its application in a major thermal-vacuum testing program.

DESCRIPTION

The High Intensity Solar Simulator consists of six modular components interrelated as shown in Figure 1 and described as follows:

1. Source Box

The source box shown in Figure 2 is a large rectangular box 170 inches long, 44 inches high and 31 inches wide. It is constructed of steel, weighs 1800 pounds and houses the components of the optical train as shown in Figure 3. It also serves as an environmental envelope to control the damaging effects of excessive heat, ultra-violet radiation, and ozone resulting from the operation of the xenon arc lamp. The sealed enclosure also protects the optics from the dust and moisture contained in normal room atmosphere. Two systems are provided for circulating water through separate plumbing networks within the enclosure. A flow of GN_2 is also maintained within the box so that the ultra-violet radiation will not produce ozone. Two access panels provide openings into the enclosure for servicing components of the system. Electrical, water and GN_2 connections are located near the bottom of the rear panel. In addition to housing the negative lens, attenuators, and douser the enclosure provides an attachment area for the source module and transfer optics. The following is a description of the negative lens, attenuators, and douser.

a. Negative Lens

The negative lens as shown in Figure 4, is a concave quartz lens 13 inches in diameter. It is factory aligned and installed on an adjustable mounting plate. Surrounding the lens are coils of copper tubing circulating water for cooling the assembly which serves as the lens holder and energy absorber. Plumbing disconnects are provided so that the negative lens assembly and mounting plate can be removed from the source box. To ensure proper alignment when replacing the lens assembly, the mounting plate must be indexed with the source box support framing and

all shims must be positioned at each of the four anchoring points exactly as they were removed.

b. Attenuators

Two attenuators are mounted within the source box to provide a means of changing the beam intensity. Each attenuator can be positioned "in" or "out" of the beam by means of pneumatic cylinders which are actuated by switches located on the control console. The two units are interlocked so that only one can be positioned in the beam at a time. Each is cooled by de-mineralized water which is circulated through copper tubing welded to its frame. Attenuator #1 which is also fan-cooled, is so constructed to provide variable attenuation to reduce the final intensity by 68 to 99 percent. This is accomplished by closing the wedge-shaped spaces with the adjustable vanes of the attenuator as shown in Figure 5. The adjustable vanes are driven by a small electric motor in response to the electrical signal controlled by the attenuator transmission knob located on the control console. As shown in Figure 6, attenuator #2 is a grid-like light baffle with no moving parts; it reduces the beam intensity by a fixed percentage of 34% of the total beam output. Both attenuators can be positioned "out" of the beam to permit full unobstructed light transmission when required. Neither attenuator changes the spectral quality of the beam.

c. Douser

The douser, Figure 7, provides a method of shutting off the beam transmission completely without turning off the lamp. It is an optically dense metal plate, cooled by circulating de-mineralized water. An air-operated control cylinder positions the douser "in" or "out" of the light beam in response to the electrical signals from the control switches on the control console.

2. Source Module

The source module as shown in Figure 8 is the light source for the simulator. The source module is removable from the basic enclosure and consists of several individual components. The major components are:

- a. 32KW short arc xenon lamp
- b. Automatic lamp starter
- c. 100 cfm blower for circulating GN_2
- d. Aconic collector
- e. Lamp adjustment mechanism
- f. Energy absorber

The source module is mounted on a flat circular plate, machined and drilled to fit into an opening at the rear of the source box. A special RFI sealing gasket is installed between the source module and source box. Electrical and water connections for the source module are located on the circular mounting plate. A removable box-like insulated metal cover is attached to the rear of the source module to protect the operator from high voltages.

3. Transfer Optics

The transfer optics module is mounted at an opening in the front panel of the source box. The optical components of the transfer optics include a quartz plano-convex tipping lens, a field lens assembly, spectral filters and a projection lens assembly as shown in Figure 9. The light beam transmitted thru the source box is centered on the field lens by the tipping lens. Nineteen pairs of biconvex lens of the field and projection lens assemblies divide the light beam into nineteen separate beams each of which covers the target area, thus integrating the various portions of the beam. The spectral content of the simulated solar energy is maintained by placement of the spectral filters in each of the individually projected beams. The transfer optics assembly is cooled by two blowers that circulate ambient air.

4. Coolant Conditioning Unit

The coolant conditioning unit is installed at a selected location on the laboratory floor best suited to serve the simulator at either of its operating locations. The compact, cabinet-mounted module supplies de-mineralized filtered water for cooling the modular components of the simulator. The CCU contains a circulation pump, filters, de-mineralizers, storage tank and heat exchanger. Sensors in the internal plumbing system and associated electrical circuitry provide protection against high temperature, high and low pressure and low supply of the processed cooling water.

5. Power Supply

The power supply as shown in Figure 10 is installed next to the CCU. This unit supplies and controls the direct current electrical power required to operate the lamp within the range of 11 to 32KW. The automatic control circuit maintains the lamp output stable throughout the operational range. This control is obtained by either a light-sensing system or current-regulating circuit. Commercial power, 480 V.A.C., 3 phase, is rectified to direct current for lamp power. The control circuit uses 115 V.A.C., 1 phase commercial power. The power supply is cooled by the processed water supplied by the coolant conditioning unit; it is operated from the control console. The unit weighs 1300 pounds, excluding cables, and is 60 inches high, 24 inches wide and 26 inches deep.

6. Control Console

The control console is a compact, cabinet-mounted module that provides operating controls, performance monitoring instruments and performance display indicators for the simulator. The unit is 48 inches high, 30 inches wide and 32 inches deep and is installed on the laboratory floor next to the power supply. The three basic components of the control console are: the Module Controller, Auxiliary Module Controller and a twelve point strip recorder. The monitoring instruments provide the operator with critical data such as lamp intensity, power and system temperatures. The

display indicators show the status of the operational equipment in addition to displaying any malfunctions of the system. Interlock circuits, combined with the performance display indicators also aid in the diagnosis and location of the system failures.

The simulator is equipped with many interlocks that will turn off the lamp if there is a malfunction. Most of the interlocks are thermal and the temperatures can be observed on a strip chart recorder as they approach the cut-off limit. However, interlocks such as high current, low water flow and low GN₂ flow do not give the operator any previous warning and turn off the simulator immediately. This could be detrimental to the experiment if the cause of the failure cannot be determined in a short period of time.

CAPABILITIES

The projection distance is 74 inches from the front surface of the transfer optics package and the light beam produces a target of hexagonal shape that measures 12 inches across the flats.

The beam intensity is variable from 1 to 16 solar constants with spectral filters in place. If the filters are removed an intensity of 25 solar constants can be obtained. Due to test schedules the authors have not had experience with intensity levels greater than 16.0 solar constants.

The beam uniformity over the target area was $\pm 2.5\%$ as measured during acceptance tests at Goddard with a total irradiance sensor at an intensity level of 1.0 solar constant. At 16.0 solar constants the uniformity measurement was $\pm 2.3\%$.

Irradiance stability as measured with a solar cell at an intensity of 16.0 solar constants was 1.8% R.M.S. over a period of 100 seconds. The long term stability over a 48 hour period was $\pm 3.9\%$.

During the acceptance test the beam subtense angle was measured to be ± 3.0 degrees which meets the specification.

CALIBRATION OF THE SIMULATOR

Before each test the lamp is adjusted in relation to the aconic collector to minimize the non-uniformity. Because the uniformity has a negligible variance up to 16 solar constants, the simulator is frequently calibrated only at 1.0 solar constant.

This calibration is performed by directing the light beam into a 10' x 11' x 6' black interior calibration booth, where intensity measurements are taken by either of two methods. One method involves taking approximately 50 radiometer readings $1\frac{1}{2}$ inches apart by manually moving a 1 inch diameter sensor over the 12 inch hexagonal pattern which is projected onto a water-cooled, black, copper plate. The other method incorporates a multi-solar-cell X-Y scanner which is computer-interfaced to generate intensity profiles as shown in Figure 11.

OPERATIONAL EXPERIENCE

The High Intensity Solar Simulator has been in use at Goddard Space Flight Center since May, 1972. Since that time there have been 450 hours of operation on the simulator. As previously mentioned the simulator has been operated at intensity levels from 1.0 solar constant to 16.0 solar constants.

The power required to obtain 1.0 solar constant has been averaging 12.9KW. Due to the design features of the system the lowest power level obtainable is 11.5KW. So, to achieve 1.0 solar constant attenuator #1 or #2 must be inserted into the beam.

To obtain 16.0 solar constants the power has been approximately 25.0KW. This power level is required when utilizing a new collector and a new lamp. However, the present collector and lamp with approximately 200 hours of operation time requires approximately 28.5KW to obtain the 16.0 solar constants.

There are two modes of control for the simulator, current and light. When operating in the current mode the power is controlled at a value that is proportional

to the setting of the intensity control potentiometer. When the simulator is operated in this mode for a long period of time the intensity level may decrease due to the degradation of optical components. However, with an intensity monitoring device such as a radiometer at the target plane, the power level can be increased as the intensity decreases by manually resetting the control potentiometer. This mode of operation is preferred when the simulator is operated for a short period of time. It has also been determined that this mode is more stable than the light mode.

There are two methods in which one may operate the simulator in the light mode, internal and external. In the internal mode, there is a light sensor mounted in the source box where it receives light from the source module. The signal from this sensor which is fed into the control circuit is proportional to the setting of the intensity control potentiometer. In the external mode, a light sensor is located at the target plane. This signal which is also fed back to the control circuit will change the power if there is a change in intensity.

When operating the High Intensity Simulator at any intensity level the cooling conditioning unit is capable of cooling the components within a safe limit. As can be seen in Table 1 there is no drastic change in temperature as the intensity level increases. Since the most critical component is the lamp, the water temperature in and out of the lamp is monitored very closely.

During the acceptance test, the spectral irradiance was measured. To make these measurements at 16 solar constants, a quartz beam splitter was used to reflect approximately 10% of the light into the Perkin-Elmer spectrometer. The spectrum was scanned at several points in the target plane, 74" from the transfer optics and the results are shown in Table 2. The spectrum is within specification limits in all but five of the 14 wavelength bands.

OPERATIONAL REQUIREMENTS

One man per shift is normally required for monitoring the performance of the simulator during a routine test. These tests average about 15 hours of continuous lamp on-time with a facility engineer overseeing the operation and interfacing the simulator with the thermal vacuum chamber to meet the required solar intensities. The engineer is also responsible for calibrating and aligning the simulator, directing maintenance and the training of personnel.

An operational check is performed before each test and requires about 16 manhours to complete. It covers such items as a functional check of each module in the system, alignment with the calibration booth, check and adjustment of beam size, intensity and uniformity at each of the required test levels. However, if any optical component such as the lamp or collector have been replaced approximately 32 manhours must be spent to realign and calibrate the simulator.

To effectively operate the simulator five utilities must be available: they are, additional cooling water (other than the de-mineralized water), 115 VAC and 480 VAC, GN₂ and air.

DATA COLLECTION

The central data collection system continuously monitors the High Intensity Solar Simulator and prints out a listing every 100 seconds. This data which is accumulated in each 8 hour shift is printed in a summary report as shown in Table 3a. The critical parameters of the simulator are listed here.

Table 3b is an Accumulation Report for the lamp, collector, and filter. The time, kilowatt hours and starts are accumulated until there is a failure or a replacement of the component. When this occurs the data for that part is shifted into a Replacement Report as seen in Table 3c.

Table 3d is a plot of the number of starts (S), and kilowatt hours (P) vs. time. This data is accumulative. The scale for each parameter automatically changes whenever the new data exceeds the previous limit.

SAFETY CONSIDERATIONS

Probably the greatest personnel hazard associated with the High Intensity Solar Simulator is the explosive potential of the 32KW short arc xenon lamp. Serious damage to both personnel and equipment can result from flying fragments of glass upon failure of the quartz envelope. Therefore, the wearing of proper safety gear such as a helmet with face shield, gloves and apron is mandatory when handling or even observing the xenon lamp. Fortunately, an explosion which might occur with the lamp mounted in the source module, whether operating or not, will be confined and will not involve personal injury unless the access panels are removed.

In addition to these explosive dangers, there are hazards dependent on the operation only. They are radiation, chemical, and electrical. The simulator emits radiation with wavelengths from $.2\mu\text{m}$ in the ultraviolet to about $2.5\mu\text{m}$ in the infrared. However, the ultraviolet radiation is the most harmful to the eyes and skin. The reflected U.V. is potentially more hazardous than the direct U.V. due to ignorance and carelessness on viewing these reflections. Permanent damage to unprotected eyes could result with extended exposure but the most frequent injury is an irritating inflammation of the mucous membrane which covers the eyeball. This condition is caused by U.V. wavelengths below $.32\mu\text{m}$ and is not directly detected until a few hours after exposure. Dark sun glasses or goggles made of glass with side shields easily eliminate this persistent hazard for operating personnel.

A potential chemical hazard is the ozone formed by exposing oxygen in the air to ultraviolet light. This strongly oxidizing gas attacks metal and rubber rapidly and will cause discomfort to individuals in the form of headaches and dryness of throat, nose and

eyes even at low concentrations. Fortunately, the problem can be reduced by introducing gaseous nitrogen into the simulator to displace the ambient air present, thus minimizing generation of ozone. Concentrations of .02 PPM have been recorded at the source module when the simulator was operated at the maximum of 16 solar constants. This concentration offers little danger since exposure levels up to .06 PPM are safe for any two consecutive hourly measurements.

Electrical precautions are noteworthy because the ignition voltages are as high as 70KV and contact with them can be lethal. A large residual charge also remains in the power supply capacitors long after shut-down. Consequently, the grounding of this charge is necessary before attempting any maintenance.

CONCLUSION

Solar irradiation is being routinely simulated from 1.0 to 16.0 solar constants over a one foot diameter target area for the testing of spacecraft equipment for near sun missions. Although this simulator, manufactured by Spectrolab, Textron Inc., adequately meets the present needs for high intensity solar simulation at Goddard Space Flight Center, it has the potential for increased utilization. The purchase of a different transfer optics system would increase the pattern size and using 20KW lamps would decrease the operating costs (wherever lower intensities are required).

REFERENCES:

1. "Operation and Service Manual," Spectrolab-A Division of Textron, Inc., Sylmar, California, April 1972.
2. "High Intensity Solar Simulator Operating Procedure," R. Lange, Northrop Services, Inc., Goddard Space Flight Center, May 1973.
3. "Acceptance Test Report - High Intensity Solar Simulator," I. Serafino, D. Orbock Northrop Services, Inc., Goddard Space Flight Center, August 1972.

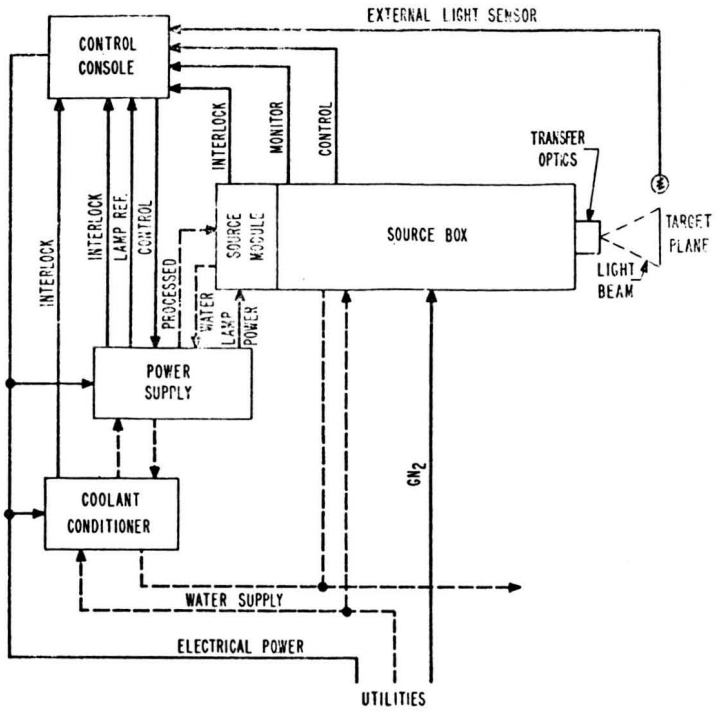


Fig.1 Solar Simulator Block Diagram

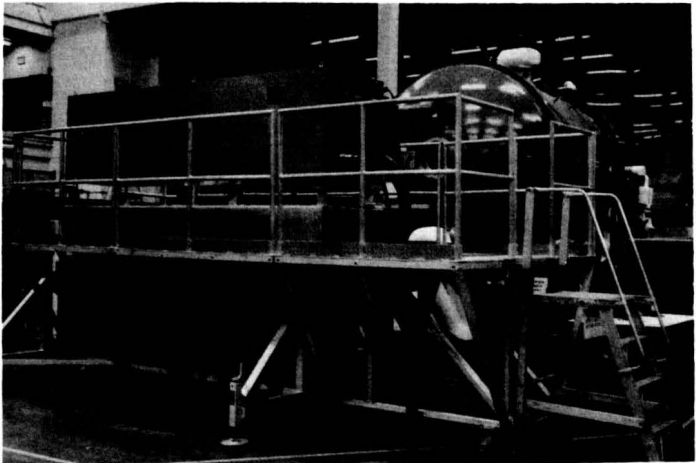


Fig. 2 High Intensity Solar Simulator

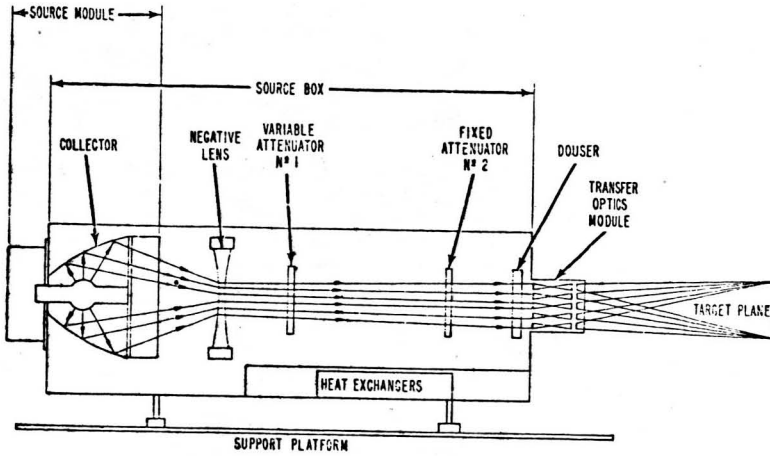


Fig. 3 Source Box Schematic

Fig. 4
Negative Lens

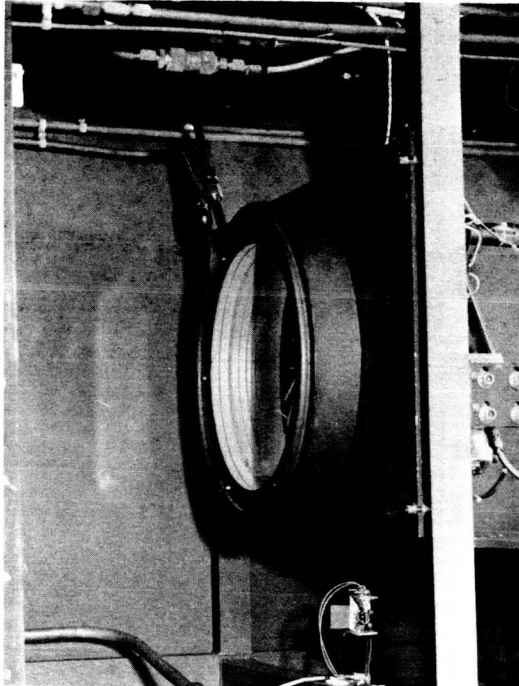


Fig. 5
Attenuator #1

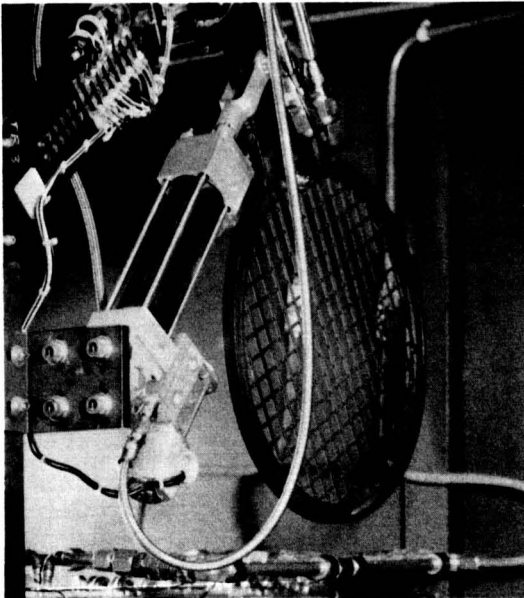
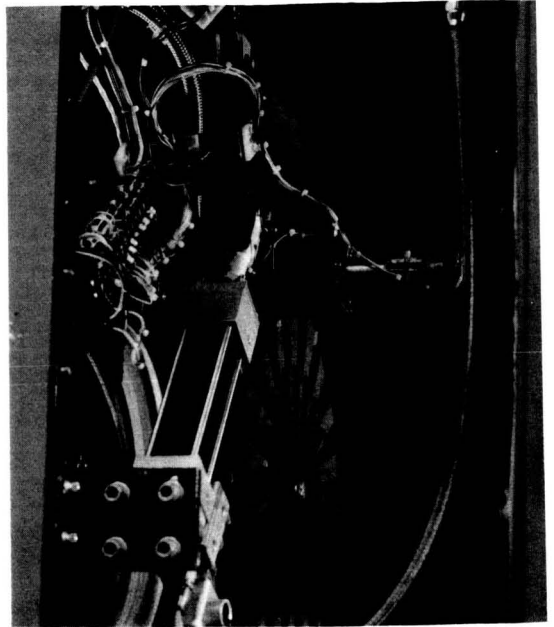


Fig. 6
Attenuator #2

Fig. 7
Douser

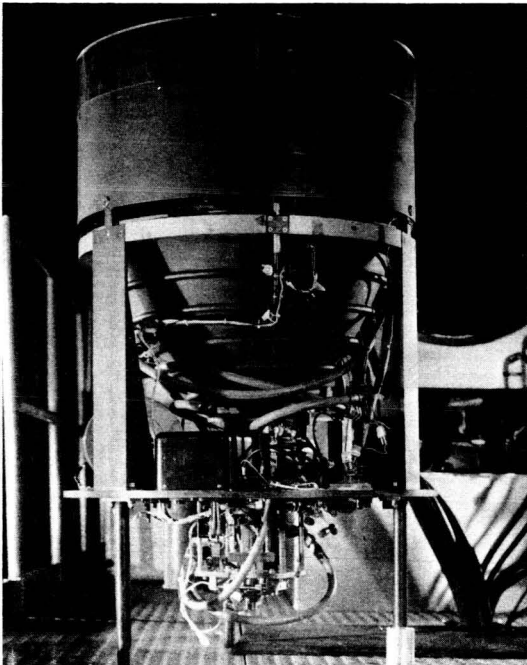
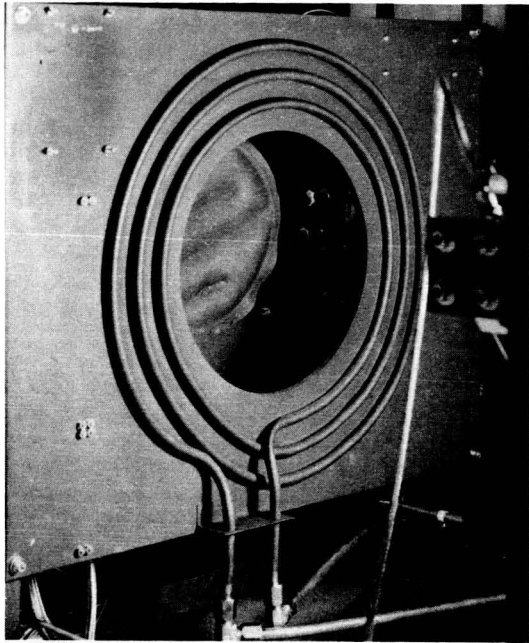


Fig. 8
Source Module

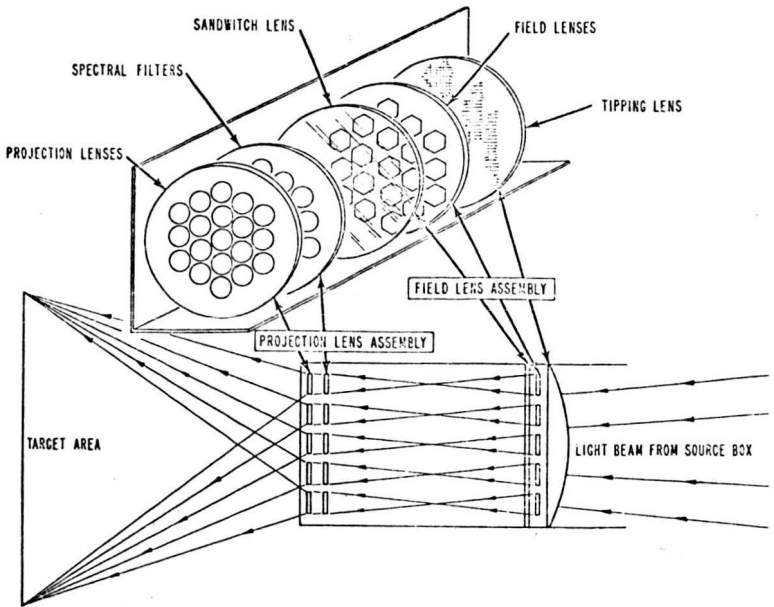


Fig. 9 Transfer Optics Schematic

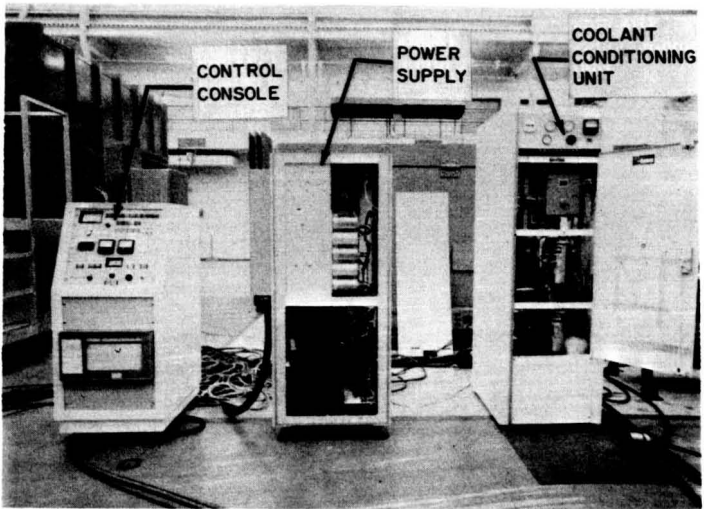


Fig. 10 Component Layout

Table 1

COMPONENT TEMPERATURES

Intensity S.C.	PWR KW	Dousser	Filter	Power Supply H ₂ O Out	Collector	Anode H ₂ O Out	Cathode H ₂ O Out	Atten. #1	Atten. #2
1.0 *	14.1	41	32	34	41	40	38	42	40
5 **	13.9	40	31	34	41	40	38	39	42
7	12.7	39	32	33	39	38	37	40	38
11	20.3	46	30	37	47	46	43	46	46
16	27.4	54	35	41	56	54	47	56	55

NOTE: All Temperatures °C

- * Attenuator #1 in the beam
- ** Attenuator #2 in the beam

Table 2

SPECTRAL IRRADIANCE

(WAVEBAND) (MICRONS)	ENERGY (mw/cm ²)				ENERGY (PERCENT)				OUT OF SPEC.	
	SPEC.	BEAM POSITION			BEAM POSITION			AVG.		SPEC.
		I	II	IV	I	II	IV			
.25 - .35	5.89	5.24	5.24	5.16	-11.0	-11.0	-12.4	-11.5	40	-
.35 - .40	5.69	5.28	5.44	5.24	- 7.2	- 4.4	- 7.9	- 6.5	25	-
.40 - .45	8.68	8.53	8.80	8.29	- 1.7	1.4	- 4.5	- 1.6	10	-
.45 - .50	10.09	8.44	8.76	8.45	-16.4	-13.2	-16.3	-15.3	10	-5.3
.50 - .60	17.70	17.49	17.99	17.83	- 1.2	1.6	0.7	0.4	10	-
.60 - .70	15.15	15.40	15.87	16.21	1.7	4.8	7.0	4.5	10	-
.70 - .80	12.37	13.84	13.80	14.18	11.9	11.6	14.6	12.7	10	+2.7
.80 - .90	9.93	12.20	12.06	12.31	22.9	21.5	24.0	22.8	15	+7.8
.90 - 1.00	8.28	10.72	10.96	11.11	29.5	32.4	34.2	32.0	15	+17.0
1.0 - 1.2	12.06	12.34	12.31	12.40	2.3	2.1	2.8	2.4	20	-
1.2 - 1.5	11.14	9.05	8.73	8.73	-18.8	-21.6	-21.6	-20.7	20	-0.7
1.5 - 1.8	6.70	5.78	5.45	5.49	-13.7	-18.7	-18.1	-16.8	20	-
1.8 - 2.2	4.38	3.78	3.32	3.49	-13.7	-24.2	-20.3	-19.4	30	-
2.2 - 2.5	1.98	1.89	1.29	1.14	-4.5	-34.9	-42.4	-27.3	30	-

Table 3a

MI-INTENSITY SOLAR SIMULATOR

FACILITY 216

8 HOUR REPORT

LSDT	DATE	SHIFT	ON TIME	KWATT		KWATT		LT DG	DOUSER	FILTR	PS H2O	COLLECT	CATHODE		ANODE		ATTEN1	ATTEN2
				STARTS	AG POW	MA POW	H2O IN						H2O OUT					
8410	1/10/73	1	5.21	2	12	11	-0.010	45.0	34.8	38.9	45.8	44.7	42.5	45.0	44.5	42.7	44.7	44.5
8416	2/ 1/73	1	6.31	1	12	13	-0.039	43.0	35.3	36.9	43.9	42.8	40.4	44.9	42.7	44.7	44.5	44.5
8428	2/ 5/73	1	7.53	1	18	19	-0.008	44.5	39.8	39.9	44.5	50.2	48.0	44.5	49.3	48.4	48.4	48.4
8431	2/ 6/73	1	3.11	1	19	26	-0.008	55.9	44.7	43.7	58.3	54.9	49.9	58.6	55.8	55.8	55.8	55.8
8437	2/ 8/73	1A	0	0	0	0	0	0	0	0	0	0	0	0	0	0	0	0
8437	2/ 8/73	1B	.25	1	20	22	-0.007	48.6	28.3	38.7	48.7	47.6	43.8	37.7	47.6	47.6	47.6	47.6
8439	2/ 8/73	3	1.14	1	15	28	+0.02	55.6	39.8	42.9	53.3	53.3	48.4	43.6	53.7	48.4	53.7	53.7
8440	2/ 9/73	1	3.39	1	11	13	+0.03	45.3	39.8	36.6	43.4	42.7	40.4	41.6	45.1	40.4	45.1	45.1
8441	2/ 9/73	2	2.74	3	17	28	+0.01	59.1	46.5	45.8	59.0	57.1	52.2	54.1	58.0	54.1	58.0	58.0
8442	2/10/73	3	4.64	2	23	27	+0.01	57.3	35.6	44.5	58.2	56.0	51.0	56.3	57.1	56.0	57.1	57.1
8443	2/10/73	1	5.77	0	26	27	+0.00	59.1	48.6	45.9	58.8	56.8	52.3	56.7	58.1	56.8	58.1	58.1
8443	2/11/73	3	5.03	1	12	12	+0.02	41.1	32.7	35.2	41.5	41.0	38.7	42.5	40.7	42.5	40.7	40.7
8446	2/11/73	1	6.50	0	12	12	+0.02	41.1	32.7	35.2	41.5	41.0	38.7	42.5	40.7	42.5	40.7	40.7
8452	2/13/73	1	2.03	1	12	16	+0.03	42.7	30.9	35.4	43.0	42.2	39.3	41.5	45.1	42.2	45.1	45.1
8453	2/13/73	2	1.01	1	11	12	+0.03	39.8	29.3	34.2	40.1	39.6	37.4	40.5	42.0	39.6	42.0	42.0
8456	2/14/73	1	1.14	1	17	27	+0.01	50.9	30.9	39.4	51.5	49.4	45.0	43.4	50.3	49.4	50.3	50.3
8477	2/24/73	2	4.23	1	11	12	+0.06	39.4	30.1	33.6	39.8	39.3	37.1	41.1	41.0	41.1	41.0	41.0
8478	2/25/73	3	8.03	0	21	30	+0.03	55.2	54.1	42.3	56.0	54.9	52.5	55.9	55.5	54.9	55.5	55.5
8479	2/25/73	1	8.01	0	26	27	+0.03	55.2	54.1	42.3	56.1	53.7	48.6	54.7	54.9	53.7	54.9	54.9
8480	2/25/73	2	7.94	0	18	19	+0.06	45.5	44.4	36.8	46.2	45.0	43.6	47.2	45.9	46.2	45.9	45.9
8554	3/29/73	1	.23	1	13	20	+0.02	40.4	25.2	33.5	40.1	39.3	36.8	32.9	43.9	39.3	43.9	43.9
8577	3/30/73	1	2.54	1	16	27	-0.140	54.2	33.8	40.3	53.9	50.6	45.9	46.1	52.3	50.6	46.1	52.3
8580	4/ 2/73	1	1.84	1	17	22	-0.340	46.9	33.2	37.2	46.1	44.6	40.9	43.7	45.8	44.6	43.7	45.8
8583	4/ 3/73	1	1.89	1	15	20	-0.137	49.1	32.9	38.4	50.4	48.5	44.2	44.9	49.9	48.5	44.9	49.9
8587	4/ 4/73	2	1.04	2	11	11	-0.041	37.3	27.8	34.5	37.7	36.8	35.1	37.3	37.1	37.3	37.1	37.1
8598	4/ 5/73	3	3.27	1	14	18	-0.176	43.3	29.0	35.9	44.9	43.3	39.3	41.0	44.7	43.3	41.0	44.7

793

Table 3b

MI-INTENSITY SOLAR SIMULATOR

FACILITY 216

TOTAL ACCUMULATION REPORT

COMPONENT	SERIAL NO.	DATE INSTALLED	TOTAL ON TIME HRS.	TOTAL KILOWATT HOURS	TOTAL STARTS
LAMP	700A-5	2/ 7/73	225.8	4216.8	45
COLLECTOR	20151/02	2/ 7/73	225.8	4216.8	
FILTER		6/ 6/72	223.6	4196.8	

Table 3c

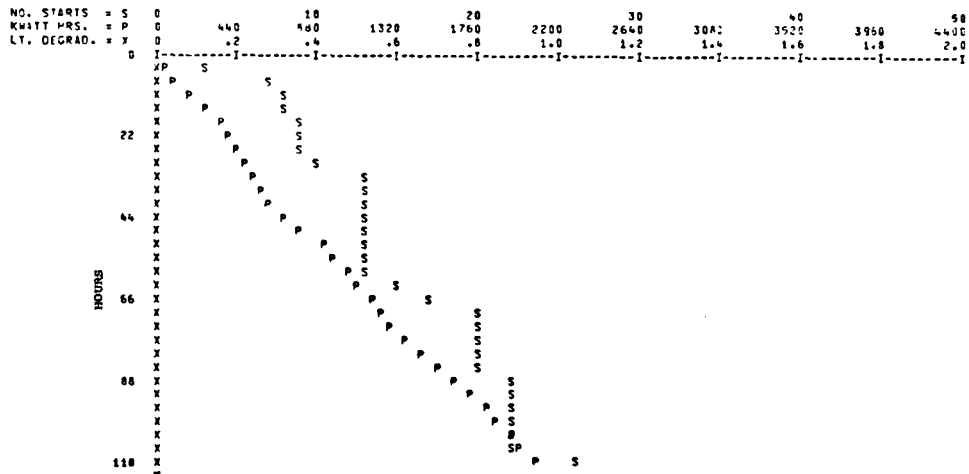
MI-INTENSITY SOLAR SIMULATOR

FACILITY 218

COMPONENT	REPLACEMENT REPORT		REPLACED	ON TIME HRS.	KILOWATT HRS.	STARTS	REMARKS
	SERIAL NO.	INSTALLED					
LAMP	700A-1	11/17/72	2/ 7/73	22.2	336.6	5	LAMP EXPLODED
COLLECTOR	3747/01	6/ 6/72	2/ 7/73	22.2	336.6		LAMP EXPLODED

NOTE: The simulator was operated an additional 100 hours prior to the use of this program.

Table 3d



NTM-10285

Paper No. 65

**SOLAR IMAGE, CORONA AND RADIATION
SIMULATIONS FOR THE APOLLO TELESCOPE
MOUNT DISPLAYS OF THE SKYLAB SIMULATOR**

Anibal J. da Silva, *Johnson Space Center, Houston, Texas,*
George Gause and Robert J. Nobilini, *Aero Service Corporation,*
Philadelphia, Pennsylvania

ABSTRACT

An objective of the Skylab Simulator is to train crews to point the solar telescopes of the Apollo Telescope Mount and to recognize, select and record solar activity of scientific interest. The simulator utilizes Hydrogen-alpha photography and correlated simulations of predicted emissions from regions of the solar spectrum, much of which is not detectable from earth, as data sources for the displays of the simulator's control and display panel. Analog servoes with digital feedback enables precision pointing at selected solar features viewed on the visual displays. This paper is about the development and utilization of solar activity simulations from a visual aspect.

INTRODUCTION

The Skylab Orbital Assembly was launched in May of 1973 and is manned by a thoroughly prepared crew. This preparation was obtained through exhaustive academic and procedural training at several locations using various devices, including the Skylab Simulator. Many different types of experiments are being conducted aboard the Skylab spacecraft which pertain to earth resources, to the functions of the spacecraft and to the effects of space on man. Astronomical experiments using the ATM (Apollo Telescope Mount) are being performed in the visible, the near and far ultraviolet and in the soft and hard X-ray regions of the sun. The ATM is the first manned orbiting solar observatory.

Simulation of the ATM in the Skylab Simulator enabled the training of the astronauts in pointing the solar telescopes properly and in coalignment procedures between experiments, as well as in the exercise of judgment in the selection of features of scientific interest. The purpose of the solar experiments is, in part, the collection of data which may establish spatial and temporal correlation between solar activity at different wavelengths and bandwidths, both on and off disc. Because of the sparsity of correlated data, the simulations had to be based upon the scientific knowledge and judgment of the Principal Investigators and their colleagues. As more knowledge was gained it was put into immediate use in the production of more authentic solar image simula-

tions.

This discussion concerns itself with the ATM simulation design philosophy from a visual aspect and with the production of highly accurate films depicting the sun in H-alpha (Hydrogen-Alpha), in simulated XUV (Extreme Ultra Violet), in simulated X-ray and with the production of precision slides showing solar corona simulations and white light solar discs. Radio noise and simulated radiations are also mentioned to illustrate the extent of simulated correlation.

BACKGROUND

Along with digital readouts for X-ray and ultraviolet, and the History Plotter for X-ray and radio noise, the visual displays for the ATM consists of two television monitors and one X-ray cathode ray tube. The television monitors provide independently selectable solar video scenes in H-alpha, XUV, white light corona and XUV slit, that is, white light solar disc with XUV slit. There are two H-alpha telescopes operating at the same frequency and bandwidth. The zoom ratio of the televised optical leg of each telescope is 5:1. However, the maximum video field of view for H-alpha 1 is only 22 arc minutes while that of H-alpha 2 is 35 arc minutes. Since the diameter of the sun as viewed from earth subtends about 32.1 arc minutes the entire sun cannot be seen in H-alpha 1. The video fields of view in XUV, white light corona and XUV slit are 60 arc minutes, 1.5 to 4.5 solar radii and three arc minutes, respectively. The field displayed on the X-ray cathode ray tube is a 48 by 48 arc minute matrix.

HYDROGEN-ALPHA

Solar radiation is mostly characteristic of hydrogen because of the abundance of this element on the sun. H-alpha, the 6562.8 Angstrom light emission arising from transitions between the second and third electron orbits of the hydrogen atom, is especially strong and only slightly attenuated by the atmosphere of the earth. For this reason, the sun may be viewed in H-alpha from earth (Figure 1a). The narrow band H-alpha filters reveal finely structured detail of the chromosphere of the sun. Readily observable solar features are sunspots, plages, flares, and filaments. The image quality of the sun in H-alpha as viewed from earth is dependent upon the "seeing" conditions. Since the H-alpha telescope in the ATM cluster is operated above the atmosphere of the earth the seeing exceeds that viewed from earth.

One of the purposes of these telescopes during the Skylab mission is to identify solar features which can be examined with other telescopes operating in the UV and X-ray regions of the solar spectrum. Another purpose is to enable precise positioning of instruments coaligned with H-alpha, particularly instruments with narrow fields of view, such as the S055A UV Polychromator Spectroheliometer experiment and the S082B XUV Spectrograph experiment, both of which rely upon the H-alpha 1 video display

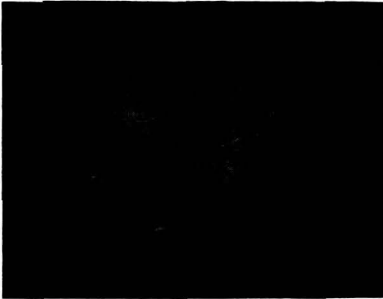


Figure 1a The Sun in H-alpha



Figure 1b Big Bear Telescope

for guidance. The H-alpha 2 display is used as a backup pointing system. In addition, photographs taken with the H-alpha 1 film camera will be used after each mission to correlate the emissions recorded by the other instruments with the features recognized in H-alpha because previous earth-based H-alpha experience provides an excellent datum for the other experiments.

H-ALPHA SIMULATION

The H-alpha system on a whole had to meet more difficult requirements so H-alpha will be discussed in some detail. Much of what is about to be said about the H-alpha simulation design philosophy applies also to the other systems. The function of the H-alpha displays in the Skylab Simulator is the same as that in the spacecraft. For this reason the emphasis has been placed upon obtaining good quality imagery of the sun in H-alpha with as complete a complement of solar phenomena as obtainable. Basically, the system utilizes 35-mm film in an electro-optical projection system. The projected image is viewed by a television camera and displayed at the ATM console. The rationale for this approach was arrived at after considerable study.

Rationale

Most of the available H-alpha imagery was recorded on film. Some had been collected on video tape because video recordings have the advantage of an order of magnitude greater dynamic range than film. However, to utilize video tapes in H-alpha simulation would require too complex a design concept - this is especially so because of the zoom in/zoom out requirement at the control and display panel. After due consideration, real time simulation of computer generated H-alpha imagery was judged to be beyond the current state of the art. Thus it was clear that the best choice

would be to use H-alpha photography as the data source. To confirm the feasibility of an approach utilizing film as the image source, a vidicon telecine chain with zoom capability was bread-boarded early in 1969 by Mr. Ralph Payne of Johnson Space Center prior to the writing of specifications. It demonstrated the practicability of this concept. Interestingly, although film was not specified as the image storage medium, all respondents to the request for proposals proposed only this medium.

Photography

Existing H-alpha photography was deficient for simulation use in several respects: unreliable frame-to-frame image registry, truncated solar discs, variable exposures, low resolution, short duration sequences and low frame rates. But even with good registry, whole solar discs, uniform exposures, specified resolution and sufficiently long sequences, none of the available solar patrol films contained sun images in H-alpha at the same band-pass as that of the spacecraft telescopes.

Because of these deficiencies, the successful offerer, the Link Division of Singer-General Precision, Inc., purchased an 8.6 inch Boller and Chivens solar vacuum telescope with the same bandpass at H-alpha as the ATM telescopes. It was especially fabricated and equipped with an Acme 35-mm camera for the H-alpha data collection. It is installed on the side of an existing larger telescope at the Big Bear Solar Observatory of the California Institute of Technology (Figure 1b), under the direction of Dr. Zirin. The optical quality of the system at H-alpha was demonstrated to have a modulation transfer of 65 percent at the specified spatial frequency of two arc seconds. An automatic exposure system compensates for changes in the sun's luminance and a photoelectric guider system maintains the telescope at sun-center even when the main spar is off center. The camera film is Kodak Type S0-392 Solar Patrol Film.

To ensure precise film positioning, the camera, 35-mm printer and 35-mm projector, each uses similar pin register systems precise to three ten thousands of an inch, which together with the control of film perforation pitch to five ten thousandths of an inch on the negative and positive star base films, assures excellent image placement.

Initial filming sequences were taken at one frame per ten seconds during quiet periods and one frame per second during flare activity. This provided the crews with an undesired flare onset cue which was eliminated in subsequent sequences by going to a constant rate of one frame per five seconds.

Monitoring positive prints are made from the negatives to less stringent quality standards than those required for the simulation prints. These monitoring prints are reviewed for the selection of four-hour training sessions of reasonably consistent image quality and containing activity of interest to the Observing Program Instructors, who are the representatives of the Principal Investigators. Once a selection is made a script print is

laid out for correlating X-ray and XUV films to H-alpha. A simulation quality H-alpha print reel on Kodak Type 2430 film is then produced for the image projection system of the simulator.

Sensitometry

Sensitometry is now discussed because of its relative importance. The intensity range of the sun's chromosphere in H-alpha is relatively short thus making tonal differences difficult to distinguish. The negative film is processed to a gamma of three to expand this range thereby enhancing subtle differences in the solar activity. The range is further expanded by processing the positive print to a gamma of one and a half, resulting in a product gamma of four and a half. The product gamma is the gamma of the negative times the gamma of the positive, where gamma is the ratio of density to the logarithm of intensity, or more practically, the ratio of density to the logarithm of exposure. Efforts were made to place all areas of concern on the straight line portion of the H&D (Hurter and Driffield) curves to take full advantage of the linear film responses (Figures 2a and 2b). The required product gamma was arrived at experimentally since the film input requirement is dependent upon the electro-optical equipment of the simulator.

H&D CURVES FOR THE H-ALPHA CAMERA AND DUPLICATE FILMS

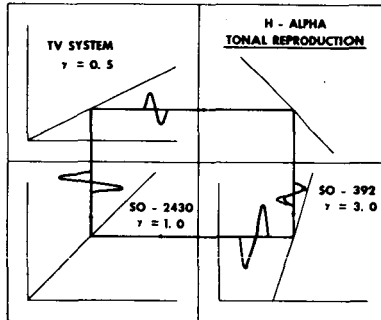
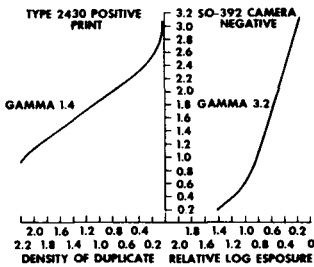


Figure 2a H&D Curves

Figure 2b H-alpha Tonal Reproduction

Image Evaluation

The capability of a system to resolve fine detail can be predicted with some certainty even without taking all variables into consideration. By using a spatial frequency of 58 lp/mm representative of a 2 arc second image resolution throughout, the MTF (Modulation Transfer Factor) may be computed by way of contrast ratio once the MTF of the telescope, the camera film, the printer and the print film is known. The telescope optical system was designed to yield an optical transfer factor of 57 percent. Utilizing a sinusoidal MTF pattern of varying spatial

frequency including the required 58 lp/mm, the camera negatives were experimentally found to have an amplitude of 40 percent and in like manner the print film was found to have an amplitude of 75 percent. With a test target of 1000:1 contrast ratio the printing MTF was found to be 97 percent. With these values, H-alpha positive print image resolution capability can then be predicted.

By operating on the straight line portion of the H&D curves density is equal to the product of gamma times the logarithm of exposure:

$$D = \gamma \log E .$$

The maximum less minimum density difference is proportional to the logarithm of the ratio of maximum to minimum exposure:

$$D_{\max} - D_{\min} \propto \log E_{\max} / E_{\min} .$$

This ratio is the contrast ratio of the exposure:

$$C_e = E_{\max} / E_{\min} .$$

Also, transmittance of a recorded image is inversely proportional to the antilogarithm of density,

$$T \propto 1 / \log^{-1} D ,$$

and thus the contrast ratio of the image is equal to the ratio of maximum to minimum transmittance:

$$C_i = T_{\max} / T_{\min} .$$

The modulation of the image is equal to the ratio of the difference to the sum of the maximum and minimum transmittance:

$$M = (T_{\max} - T_{\min}) / (T_{\max} + T_{\min}) .$$

Knowing this, contrast ratio in terms of modulation and vice versa can be determined.

From the preceeding, it can be shown that the logarithm of the contrast ratio of the recorded image is equal to the product of gamma times the logarithm of the contrast ratio of the exposure:

$$\log C_i = \gamma \log C_e ,$$

or

$$C_i = C_e^\gamma .$$

Remembering from above that the required product gamma was found experimentally, once the gamma of the camera film is determined the gamma of the print film is controlled to give the desired

product gamma:

$$\gamma_p = \gamma_d / \gamma_c .$$

Now then, the exposure modulation is the product of the modulation of the telescope times that of the camera film:

$$M_e = M_t M_c .$$

The contrast ratio of the camera film exposure is equal to the ratio of one plus exposure modulation to one minus exposure modulation:

$$C_e = (1 + M_e) / (1 - M_e) .$$

The contrast ratio of the camera film image is equal to the contrast ratio of the camera film exposure to the predetermined gamma power:

$$C_i = C_e^{\gamma_c} .$$

The modulation of the camera film image is then equal to the ratio of the image contrast ratio minus one to image contrast ratio plus one:

$$M_i = (C_i - 1) / (C_i + 1) .$$

The product of this modulation times the modulation of the print film times the modulation of the printer is the modulation of the exposure of the print film:

$$M_e = M_i M_r M_p .$$

The contrast ratio of the print film exposure is then calculated:

$$C_e = (1 + M_e) / (1 - M_e) .$$

The film is developed to the controlled gamma to obtain the contrast ratio of the print image:

$$C_i = C_e^{\gamma_p} .$$

The modulation of the print image can then be calculated using this contrast ratio:

$$M_i = (C_i - 1) / (C_i + 1) .$$

Image Generation System

Now we can discuss the H-alpha image generation system through to the video displays. The raster format and scan rates

are the same as in the spacecraft as is the simulated television downlink to Mission Control Center. A single H-alpha image centered in the film gate is projected through a dual optical system mounted upon a granite optical bench onto the photocathodes of two vidicon cameras. The image is optically split into H-alpha 1 and H-alpha 2 and, to ensure precise tracking, the X-Y excursion and roll capabilities are common to both images. Movable reticles are provided in each optical leg. Analog servoes with digital feedback enables precision pointing at selected solar features viewed on the visual displays. The table on which the lens is mounted is driven in X and Y translation by a lead-screw drive in a linear relation of inches of travel to image excursion in arc minutes.

A transformation program determines the image translation associated with the H-alpha scene by computing the direction cosines of the line of sight to the center of the sun in the frame of reference associated with the image and scales it to meet the requirements of the image translation servoes (Direction cosines differ for each experiment because of misalignments relative to the ATM canister). Small angle approximations are used in defining the transformations between experiment and canister frames of reference. Direction cosines of the canister are evaluated by the attitude control system. Another transformation program generates drive signals to the roll prisms by using canister frame components of the solar spin axis.

The response and resolution capabilities of the system is sufficient to display the effects of pointing accuracies, experiment misalignment and cluster vehicle jitter in compliance with pointing control requirements. The display system X-Y servo resolution for all servoes is as tabulated with monitor fields of view in arc minutes, monitor resolution in arc seconds per element, servo resolution in arc seconds per bit, servo excursion in inches and servo word in bits:

<u>Exp.</u>	<u>Mon.FOV</u>	<u>Mon.Res.</u>	<u>Servo Res.</u>	<u>Servo Exc.</u>	<u>Servo Word</u>
H-alpha 1	22 to 4.4	0.31	0.30	0.8063	14
H-alpha 2	35 to 7	0.47	0.30	0.8063	14
X-Ray	48	3.36	1.52	0.7150	12
WLC	144.45	10.11	6.08	0.8087	11
XUV Slit	3.0	0.21	0.17	0.7171	14
XUV Mon.	60	4.2	2.74	0.9381	11

Conveniently, the servo excursion for H-alpha can be and is deliberately limited when the solar scene leaves the video field of view and is replaced by a dark scene. This approach is also used on the other displays with the exception of the white light coronagraph display.

In the typical servo a variable bit word representing desired position is the input to an arithmetic processor which determines the difference between the actual shaft position as an output from a 14-bit shaft encoder and the position provided by

the computer. This difference is weighted and transferred to D/A converters. The difference consists of 8 linear bits, overflow and a sine bit. The overflow bit drives the servo amplifier at maximum rate by applying 28 volts to the servo motor. The linear bits cause a variable rate to be applied to the motor. An auxiliary circuit processes the sine bit to determine servo rotation direction.

S055A UV SCANNING POLYCHROMATOR SPECTROHELIOMETER

This instrument is used for photometric UV observations of the solar atmosphere near and above active and quiet regions on the solar disc. The experiment is operated in one of two modes. In the Mirror Raster Mode the primary telescope mirror is rastered in two axes to cover a region five arc minutes by five arc minutes, while the spectrometer grating remains stationary. This provides telemetry data for reconstruction of monochromatic ultraviolet spectroheliograms of the solar region. Up to seven simultaneous spectroheliograms of different wavelengths may be reconstructed through use of any of seven detectors. In the Grating Scan Mode the telescope mirror remains fixed on a five arc second by five arc second feature of interest while the grating is rotated to scan the entire operating spectrum past one of the photomultiplier detectors. The crew may select the mode of operation, spectral line (or lines) to be observed and detector (or detectors) to employ.

S055A SIMULATION

The solar UV intensity is simulated by software data describing a solar disc with nominal background intensity and circular areas of desired size, location and intensity superimposed on the disc. There is a separate solar model for each training sequence derived by tracing outlines of simulated S082B XUV active regions displayed on the simulator's television monitor. From each tracing a three dimensional software model is programmed. In addition, the size and intensity of three selected areas vary as a function of time. Selected spectral lines are programmed in the simulator, which together with randomly generated spectral line simulations make up the desired spectral scanning region. The crew views a digital readout of simulated Detector No. 1 or Detector No. 3 outputs on the Intensity Data Display. For training in collaboration with the flight controllers, these simulations are transmitted as simulated telemetry from the Skylab Simulator, as is data from the other experiment and spacecraft simulations.

S056 EXTREME UV AND X-RAY TELESCOPE

S056 is comprised of two individual and independently operated instruments. An X-Ray Telescope provides filtergrams on film of the solar image in five bandwidths from 5 to 33 Ang-

stroms. The other instrument, an X-Ray Event Analyzer, consists of a Beryllium-window and an Aluminum-window proportional counter subsystem. Each proportional counter produces outputs proportional to the intensity of the detected energy. Pulse-height analyzers sort these outputs into six energy levels in one channel and four energy levels in the other. These data are then available for telemetry or display on the counters or the History Plotter of the control and display panel of the ATM.

S056 SIMULATION

There is no visual simulation of the X-Ray Telescope except for selected filter, frames remaining and other such indicators typical of all experiment simulations necessary for training in procedures.

The source data for the X-Ray Event Analyzer is the Solrad 9 X-Ray Memory Data (Figure 3a) from the Naval Research Laboratory for the time period of the selected training session. Solrad 9

SOLRAD X-RAY DATA

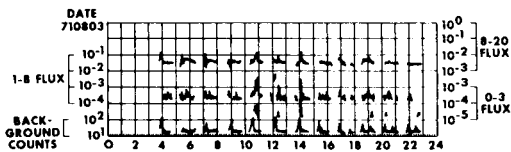


Figure 3a Solrad 9 X-Ray Memory Data

data is processed as Aluminum and Beryllium counts logarithmically and utilized as pulse-height analyzer output simulations. These data are stored and released throughout the training session to Monitor Counters 2 and 3, simulated telemetry and to the History Plotter. Initially, the simulated intensity was increased as a function of location to account for the South Atlantic Anomaly, but this effect was found to be trivial so its simulation was discontinued.

RADIO NOISE BURST MONITOR

A C-Band Radio Noise Burst Monitoring System aboard the spacecraft is capable of receiving solar electromagnetic radiation in the 5 GHz frequency range and indicating the radiation's relative intensity. The outputs from the RNBM (Radio Noise Burst Monitor) drive the History Plotter, the RNBM meter and the flare detector.

RNBM SIMULATION

Solar radio noise data at 6 cm are collected as daily sequen-

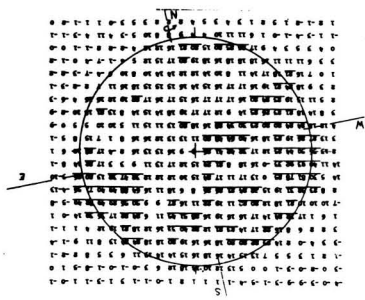
ces, processed and stored by NOAA at Boulder, Colorado, on magnetic tapes. These tapes are processed at JSC through a modified existing SPAN data reduction program to output IBM compatible data tapes. Sequences temporally correlated with the training sessions selected are stored on magnetic disc and utilized throughout the session as a function of time.

S054 X-RAY SPECTROGRAPHIC TELESCOPE

This instrument, which is sensitive to wavelengths between 3 and 60 Angstroms, produces high resolution images that are photographically recorded. As an aid to the crew in aligning the telescope a real-time X-Ray Image display is provided. An X-ray image of the sun is formed on a thin scintillator and coupled to an image dissector tube by a fibre optic faceplate to convert it to a photon image. The photocathode of the Image Dissector converts the photon image into an electron image. This image is scanned sequentially point-by-point over a 48 by 48 arc minute matrix during a one second scan time. The output is a string of variable height pulses proportional to intensity which is gated through and to the Image Intensity Counter for display as a three-digit readout. The intensity output is converted to an analog signal to intensity modulate the X-Ray Image display trace. A Photomultiplier System detects X-rays which are produced as a series of pulses for high energy X-rays and a dc signal for low energy X-rays. The former is processed through an eight-level pulse height analyzer and telemetered to earth while the latter is routed to the flare detection system and the automatic camera exposure duration control.

S054 SIMULATION

Large positive H-alpha transparencies are made containing the basic H-alpha background and active flare regions during a particular training sequence. Solrad 9 (Figure 3a) data is used to provide flare onset cues which, along with the H-alpha monitor-



(Shown North Up)

Figure 3b Stanford Radio Map

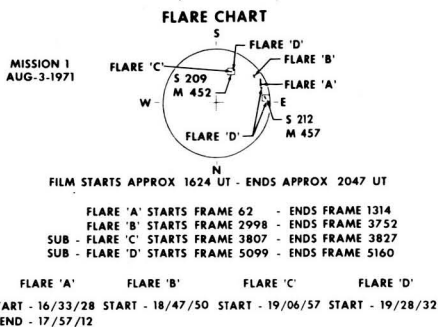


Figure 3c Flare Chart

ing print, is used to prepare a script coordinating X-ray flare activity with the selected sequence. A spectroheliogram (Figure 3b) within the same period is used to compile a coarse contour map of brightness levels on an overlay. From analyzed H-alpha pictures, fine intensity contour maps are prepared on other overlays. Individually categorized stencils are prepared for each contour. Using H-alpha basic background picture and spectroheliogram stencils a negative X-ray artwork is rendered and the artwork is photographed as a positive image. In like fashion artwork is rendered and photographed for each active flare and for significant changes in location and shape of flares. The basic X-ray positive transparency is photographed for the entire sequence to produce a session length negative film. The taking film is then exposed again, but this time for each selected flare scene (Figure 3c) at the time and for a duration determined by the script. During this dual exposure, intensity is varied for flare animation. From the X-ray master negative made with accurately positioned imagery, a simulation quality positive print (Figure 4a)



Figure 4a X-Ray Simulation

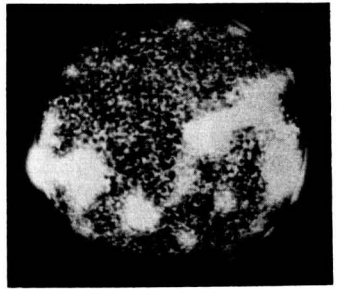


Figure 4b XUV Simulation

reel is produced for use in the simulator's electro-optical chain. The projected image produces a video image at a slow scan rate of 48 lines per second. This output is digitized and used as though it were an image dissector output to produce a 48 by 48 arc minute matrix of simulated X-ray image on the X-Ray Image display.

Solrad 9 (Figure 3a) data is scaled and stored on disc for each training session and released as a function of time. After processing and provided with random noise the output drives the Image Intensity Counter, simulated telemetry and the Photomultiplier Counter as an antilogarithmic function of intensity. The South Atlantic Anomaly was found to affect only the Photomultiplier output. The simulation has been altered to create this condition. The intensity versus photomultiplier curves provided by Dr. Zombeck, former Senior Scientist at American Science & Engineering, Inc., were approximated as a logarithmic relationship. The short dynamic range of film did not permit use of the X-ray simulation graphics as an Image Intensity Counter display source. The point-by-point correlation with the X-Ray Image display was

not considered essential for effective training before the first manned mission. During the mission it was generally found that there wasn't much to be seen on the X-Ray Image display although the Image Intensity Counter indicated that the system was working.

S082B XUV MONITOR AND SPECTROGRAPH

An XUV Monitor telescope rigidly attached to the Spectrograph telescope is used to observe the video image of the full solar disc in the 170 to 550 Angstrom range. This is done through conversion of the XUV image to white light and viewing it with a low-light level television camera. Its purpose is to produce real-time video pictures of the sun extending beyond the limb into the corona and to point the Spectrograph to features of interest. A seven-position sensitivity control permits camera sensitivity reduction in the event excessive input illumination is experienced by the camera. In the event of saturation a grid discharge switch is used to restore the camera to normal. An integrate switch increases camera sensitivity by gating target sweep off. When the integrate switch is released the camera output is the first single frame of information flashed onto the display monitor. It is only used when there is insufficient illumination for the camera. Picture intensity increases with the duration of time that the switch is held down. The Spectrograph, which includes an imaging system, is used to photographically record line spectra of small selected areas on and off disc and across the limb using a 2 by 60 arc second slit in two overlapping wavelengths extending from 970 to 3940 Angstroms. A Pointing Reference Subsystem in the same housing views the image of the sun which is formed at the spectrograph entrance slit by the primary mirror with an image dissector tube video camera. This subsystem generates either a video image in white light of the 3 arc minute area presented to the slit or a signal representative of limb to fiducial (the origin of reference) mark distance.

S082B SIMULATION

A simulated 304 Angstrom negative is produced by using a calcium K-line photograph combined with texture screens and utilizing photographic masking, exposure and development techniques. The basic XUV positive transparency is produced by combining modified X-ray negatives with the simulated 304 Angstrom negative. For flare scenes, XUV overlays, artwork and positive transparencies are produced in the same way that the X-ray flare scenes were made. The final XUV master negative is also produced by using the multiple exposure technique. A simulation quality positive print (Figure 4b) reel is produced for use in the electro-optical chain of the simulator. The displayed video field is 60 arc minutes. The grid discharge and integrate controls operate the same as in the real world. The sensitivity control is simulated by adjusting the gain and the pedestal of the video signal in opposite directions through a D/A converter.

Full white light solar disc photographs are taken every half hour during H-alpha photography at the Big Bear Solar Observatory (Figure 1b) with a Hasselblad camera mounted on the spar to the right of the H-alpha telescope. Hourly photographs of the white light sun for selected sequences are used to produce precision glass slides. During processing care is taken to enhance limb detail using dodging and bleaching techniques. In the absence of suitable white light solar disc photographs, simulations are produced from H-alpha photography by the Aero Service Corporation. Machined slide holders provide positional registry to an accuracy of one ten thousandths of an inch in a precision two by two inch dual carousel slide projector. An optical system is used to project a 3-arc minute segment of the white light solar disc image from the projector onto the television camera faceplate.

S052 WHITE LIGHT CORONAGRAPH EXPERIMENT

This instrument is an externally occulted WLC (White Light Coronagraph) designed to photograph the solar corona in the visible region with a field of view of 1.5 to 6 solar radii. A television camera similar to that of the XUV Monitor experiment enables visual observation of the corona as an aid in determining opportune times for photography, for monitoring particulate contamination surrounding the ATM and in providing ATM pointing capability backup. The video field of view is 1.5 to 4.5 solar radii. To prevent damage to the video camera from direct sunlight, a mirror which routes the image to the television camera reroutes it to the film camera instead when pointing angles exceed five arc minutes off sun center. A pointing error sensor system detects the external occulting disk location on the objective lens aperture. Its output is to present pointing error information thus providing an inflight fine pointing capability. An internal occulting disk provides internal alignment capability for the coronagraph.

S052 SIMULATION

Generally one corona simulation is provided for each training session selected. A few corona simulations are provided with additional slides depicting static simulations of the corona with contaminants and with transients or the effects of transients in the corona scene.

To determine what the corona should look like for any specific day an indepth study of the sun is made for a period covering thirteen days before and after the selected day. H-alpha photographs and K-coronameter plots (Figure 5a) for each of those days are studied. A sketch of the sun is prepared showing the location of sun spots and filaments for the selected day and where they would appear during the preceding and succeeding days. A three-dimensional model (Figure 5b) is constructed based upon plots for the thirteen days under study. The K-coronameter data

are intensity plots taken around the sun at one and a half solar radii. From this study an accurate sketch of a solar corona for the selected day is compiled and submitted to the Principal Investigator, Dr. MacQueen, at the High Altitude Observatory, for

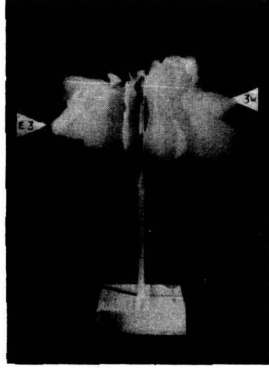
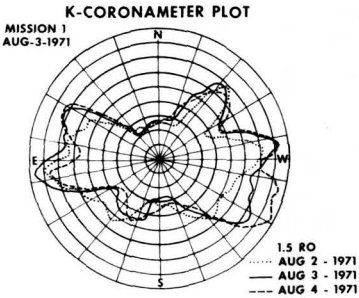


Figure 5a K-Coronameter Plot

Figure 5b K-Coronameter Model

evaluation. If necessary, suitable changes are made and artwork of the simulated corona is rendered as a negative image. Overlays and double exposure techniques are used to provide transient and contaminant effects.

A positive photograph of the final rendition (Figure 5c) is also submitted to the Principal Investigator and colleagues for

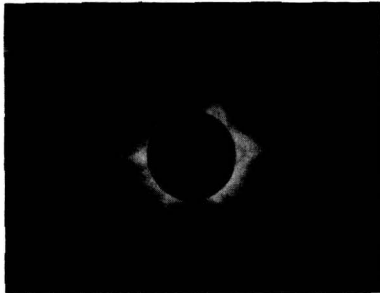


Figure 5c Corona Simulation

comments and approval. A properly scaled and positioned positive image on a precision slide is prepared for use in the electro-optical system of the simulator. It also uses a precision dual carousel slide projector. However, this system differs from the other in that the corona is projected onto a screen in the optical path which is then viewed by a standard television camera.

In addition, this system utilizes a separate optical leg to project auxiliary lighting into the main optical path. This is to simulate scattered light brightening at the edge of an occulting disc with pylon, as would be caused by pointing the canister off sun center.

Whenever the canister is pointed more than five arc minutes off sun center or when an aperture door open command is given, video is removed from the display monitor as though the scene were rerouted to the film camera instead of to the television camera. In the event of simulated malfunction, camera tube damage is simulated by displaying a white screen.

CONCLUDING REMARKS

The correlation of simulated emissions to earth-based H-alpha photography were in effect predictions of the anticipated correlation. Confidence was high that the correlation would hold particularly because the Observing Program Instructors had been using the simulator to develop observing programs for the Skylab missions. In general, the simulated correlation proved to be a reasonable assumption. The high fidelity simulations provided to the crews resulted in a high transfer of learning from the simulator to the spacecraft.

N74-10284

A NOVEL 20 KW SOLAR SIMULATOR DESIGNED FOR AIR POLLUTION RESEARCH

J. H. Beauchene, *Aerospace Controls Corporation, Gardena, Calif.*,
P. J. Bekowies, J. M. McAfee, A. M. Winer, L. Zafonte, and
J. N. Pitts, Jr., *Statewide Air Pollution Research Center, University of California, Riverside, Calif.*

ABSTRACT

An atmospheric chamber facility for the study of photochemical air pollution at ambient pollutant concentrations has been established at the Statewide Air Pollution Research Center of the University of California, Riverside.* The facility consists of two environmental chambers and a 20 KW solar simulator. This paper describes the properties and detailed performance characteristics of the solar simulator, including beam intensity, spectrum, uniformity and collimation. The simulator was designed to the special requirements of the SAPRC facility, and subsequently built and tested by the Aerospace Controls Corporation.

I. INTRODUCTION

Investigations of the photochemistry of polluted atmospheres have been conducted in a variety of "smog chambers" in various laboratories in the United States during the past 20 years. The great majority of these chambers utilized UV blacklamps, or other conventional lighting systems, as a source of photolysing radiation. Studies conducted in such chambers have been criticized with regard to the lack of authenticity of both the spectral distribution and the intensity of radiation employed relative to that found in the troposphere.¹

Thus, a major design consideration in establishing a new environmental chamber facility was to improve the quality of simulation of solar radiation with respect to previous studies. To this end the technology developed for aerospace solar simulation has been applied to the design and construction of a specialized solar simulator to be used specifically to investigate photochemical reactions in simulated, as well as ambient polluted urban atmospheres, and in simulated polluted stratospheric air masses. This goal necessarily imposed conditions and requirements different than those usually encountered in aerospace

* The chamber facility described in this paper was constructed under Grant No. 5-067-1 from the Air Resources Board of the State of California.

applications of solar simulation. We here describe in detail the design and performance characteristics of the resulting 20 KW system which is currently in operation at the Statewide Air Pollution Research Center (SAPRC) of the University of California at Riverside, California.

II. BASIC CONSIDERATIONS IN THE SYSTEM DESIGN

The SAPRC laboratory houses two smog chambers, both having an approximate volume of 200 cubic feet. One chamber is of conventional "box-like" design with Pyrex walls supported by a metal frame. The second chamber is an evacuable, thermostatted, cylindrical vessel with an inside diameter of 52 inches and a length of 156 inches. Arrays of 16 fused silica panes (13 inches on a side) form the end windows of the evacuable chamber. The SAPRC solar simulator was designed for use primarily with the cylindrical evacuable chamber but it can also be employed with the glass chamber.

The dimensions of the evacuable chamber and the nature of the photochemical air pollution research to be conducted imposed constraints on several properties of the solar simulator beam. For example, it was deemed important to minimize irradiation of the walls of the chamber (constituting 84% of the total surface area) so as to reduce the contribution of light-initiated heterogeneous reactions to the gas-phase photochemistry being investigated. Since at the same time a minimum dark volume was desired, a high degree of beam collimation and a small solar subtense angle were dictated. In addition, at least one solar constant irradiance level in the photochemically important region from 250 - 500 nanometers, as measured by chemical actinometry in the chamber volume (and not just in the area of the cross section of the simulator beam), was a third stringent design requirement. An adjunct to this objective was that good spectral match to the solar spectrum be obtained in the actinic region defined above. Finally, although reasonable beam uniformity and stability were required, the long irradiation times involved in the research (5 - 10 hours) permitted less stringent requirements to be placed on these characteristics than is the case for most aerospace applications.

III. OPTICAL DESIGN

A diagram of the simulator optical design is shown in Figure 1. The M.E.C.^C (Maximum Efficiency Contour) collector collects and projects the lamp output, via a 45° flat, onto the optical integrator. The integrator, in turn, projects the beam onto the spherical secondary mirror of a modified Gregorian collimating system with a parabolic primary. The surface of the secondary mirror contains the plane of superposition of the integrator channels. This uniform plane is imaged at the test plane (162 inches from the secondary) via the parabolic colli-

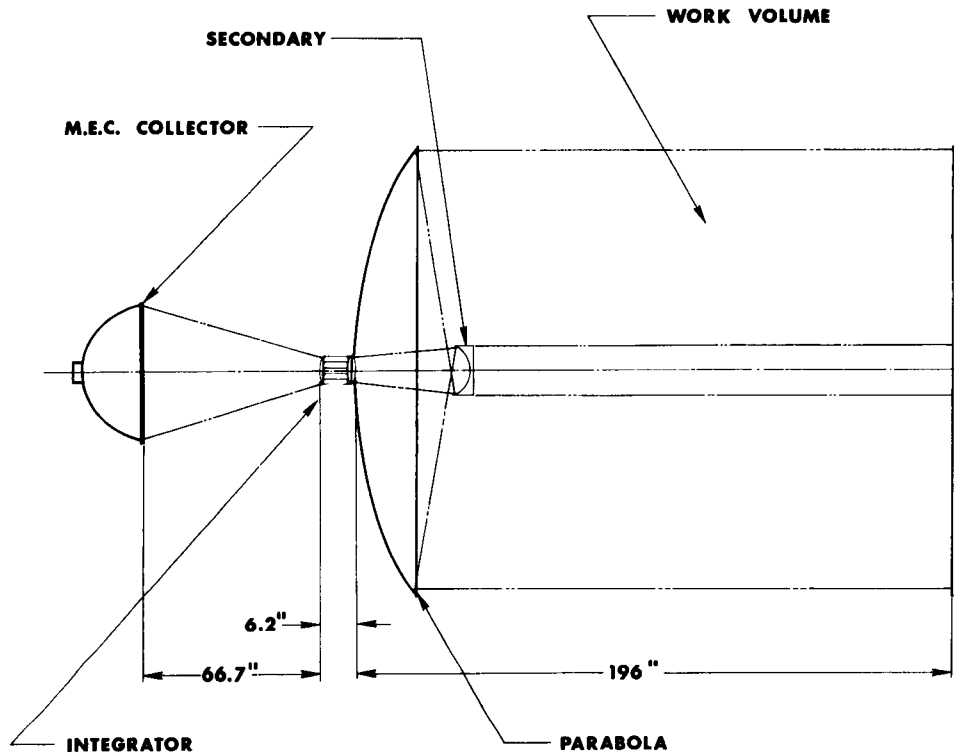


Figure 1 Optical Diagram

mator.

A spectral filter is located at the input side of the optical integrator. Its function is to remove some of the energy in the near infrared portion of the spectrum, thereby improving the systems spectral qualities.

The refractive elements of the system are fabricated from U.V. grade fused silica.² The reflective surfaces are all aluminized for peak reflectivity at 300 nanometers. The collector and folding mirror are not overcoated. The collimating optics are overcoated with magnesium fluoride for peak reflectivity at 300 nanometers.

In the following sections more detailed descriptions of the components of the simulator optical system are given.

A. Lamp and Collector

The lamp is a 20 KW compact arc lamp with water cooled anode and cathode.³ It is of the J.I.S. (Joint Industry Standard) configuration with a 12 mm cold arc gap and fused quartz envelope.⁴ This type of lamp typically converts about 50 percent of its electrical input to radiant output.

The M.E.C.^C collector is shown in Figure 2.⁵ The collector is machined from an aluminum forging and plated with electroless nickel. It was then ground and polished to a high optical finish and aluminized. Cooling coils are attached as shown to remove the heat load absorbed from the lamp. The collector is water cooled in series with the xenon lamp.

B. Trichroic Spectral Filter

The spectral filter coating is deposited on a fused silica substrate. The coating generally has a high transmission value for most of solar spectral range (see Figure 3). The peak reflectance of the coating occurs in the near infrared between 800 and 900 nanometers. This type of filter is called "trichroic" since it exhibits a resonant increase in reflectivity at one third the primary rejection wavelength.

This coating design is a compromise from what would typically be used in an aerospace spectral match application. The primary wavelength was purposely shifted to shorter wavelengths so that the resonant high reflectivity band would fall entirely below 300 nanometers. Since the important photochemical reactions occurring in the polluted troposphere are initiated in the 300 to 450 nanometer region, it was felt that maintaining a good continuum of radiation in this region must take precedence over an ideal spectral match in the visible and IR regions.

The energy absorption of the coating is very small, being on the order of 0.2 to 0.4%. The energy is either very highly transmitted or reflected. It is for this reason, and the fact that the coating materials are very stable, that the filter can be inserted at such a high intensity area at the input of the

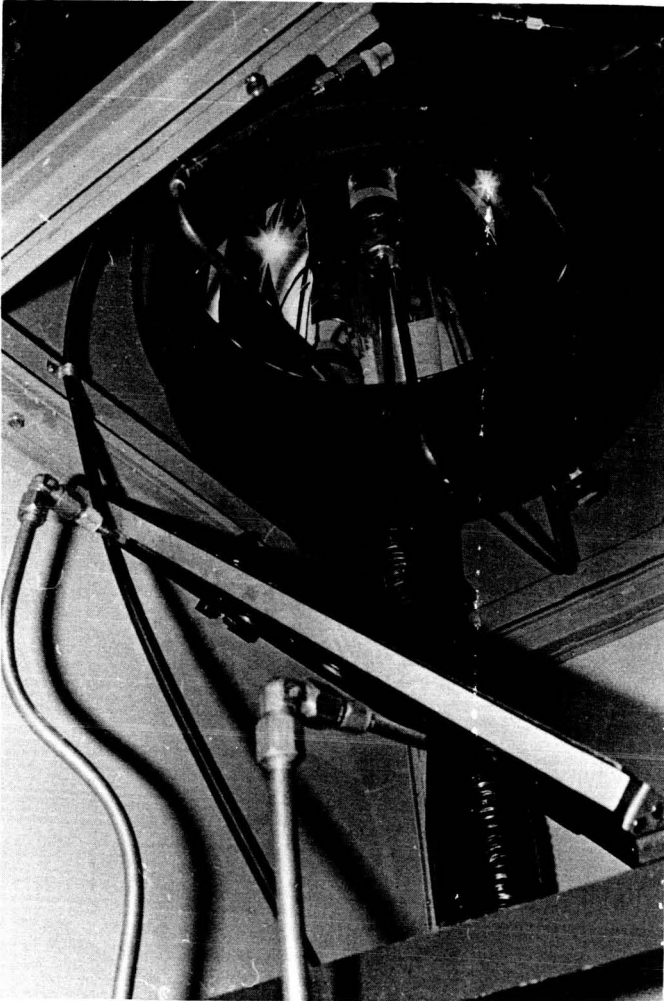


Figure 2
M.E.C. Collector and
Lampholder Assembly

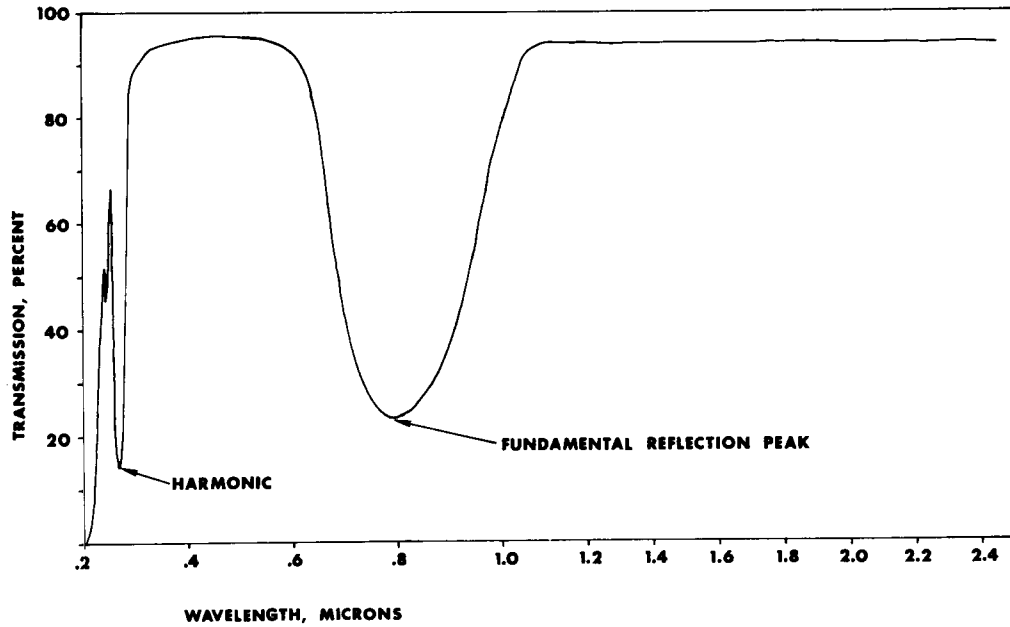


Figure 3
Transmission Curve of
Trichroic Filter

integrator.

C. Absorptive Filters

The system has the necessary bracketry and spill tray to allow for insertion of a large variety of additional absorption cells which may be required to modify the spectrum during the research programs. These include solution absorption filters (i.e. aqueous solutions of metal salts) and interference bandpass and cutoff filters.

D. Optical Integrator

The optical integrator consists of 34 round cylindrical lenses with an input and output lens. The function of the integrator is to separate the beam coming in from the collector into separate channels each of which projects onto the secondary mirror. The output lens causes the channels to superimpose at the secondary mirror. The superimposed images are re-imaged at the test plane.

There is a large intensity gradient at the input of the integrator. Each channel of the integrator relays to the test area, an image of the portion of the gradient which is incident at its input end. Since an opposing channel will have a nearly opposite gradient the two channels will approximately cancel each others intensity gradients. When this effect is summed up over all of the channels, the result is a highly uniform test area.

E. Collimating System

The modified Gregorian collimating system uses a spherical secondary mirror and a parabolic primary reflector to image the output of the integrator at infinity and place the test plane image at a distance of 162 inches from the secondary mirror.

The spherical mirror is a water-cooled, metal mirror fabricated in a manner similar to the collector.

The parabolic primary mirror is a 25.6 inch focal length searchlight mirror made of electroformed copper approximately 3/16 inch thick. Its optical surface is rhodium plated, aluminized and overcoated with magnesium fluoride. The mirror was originally fabricated for a military searchlight. The use of this mirror and its searchlight mounting drum effected a major cost savings with only a small penalty in uniformity.

The use of an on-axis collimating system causes a dark shadow in the center of the beam due to the secondary mirror. No attempt was made to fill in the hole in the center of the beam due to its small area (~4%) relative to the overall area of the beam. The hole is 10 inches diameter at the entrance to the chamber and about 4.5 inches diameter at the chamber exit window.

IV. MECHANICAL DESIGN

The mechanical construction of the 20 KW solar simulator is shown in Figure 4. The housing structure is welded from square steel structural tubing. The water cooling system including the reservoir, pump and heat exchanger are all inside the lamphouse. The system has a kinematically designed lampholder assembly to allow precise adjustments for optical alignment. The system has a water-cooled, manually-operated douser and an air cooling system which draws its air supply through a filter from the laboratory area. The air is used to cool the lamp and provide a mass air flow through the system. The lamphouse exhausts through a duct to the outside of the laboratory at approximately 400 CFM. The area between the collimator drum and the evacuable chamber is sealed off from the laboratory by a flexible shroud. There is a blower which circulates air through the collimation unit. Its exhaust is into the simulator air intake.

The system is equipped with jacks for leveling and castors for mobility. The nominal working beam height is 48 inches from the floor to the centerline of the beam. The system is self-contained except for the power supplies which are mounted remotely.

V. ELECTRICAL DESIGN

All of the operating controls are located on the control and diagnostic panels which in turn are located on the lamphouse. The panel for facilities hookup of water and power is located on the side opposite the control panel. The diagnostic panel displays the condition of the safety interlocks each of which has the ability to shut down the system if a fault occurs. The interlocked functions are: lamp cooling water flow; facility water flow; douser water flow; lamp air flow; and lamphouse doors.

In addition there is a non-displayed interlock in the power supplies to protect them from excessively high temperatures due to overload.

The control circuit and all power mains are fused for protection.

There are two 15 KW power supplies operated in parallel from a single set of duplex controls on the control panel.⁶ The power supplies are equipped with current ripple filters to limit the RMS current ripple to 2% maximum. The power supplies share the load equally at all times and have a continuous power rating of 30 KW at any current level up to 700 amps.

The power supplies are equipped with special weather shields and are placed outdoors to conserve laboratory space.

The interconnecting cables to the lamphouse are 65 feet long. The power supply open circuit voltage is approximately 100 VDC to facilitate easy starting of the lamp. The power supplies operate from a power-factor corrected source of 208 VAC, 3 phase, 60 Hz.

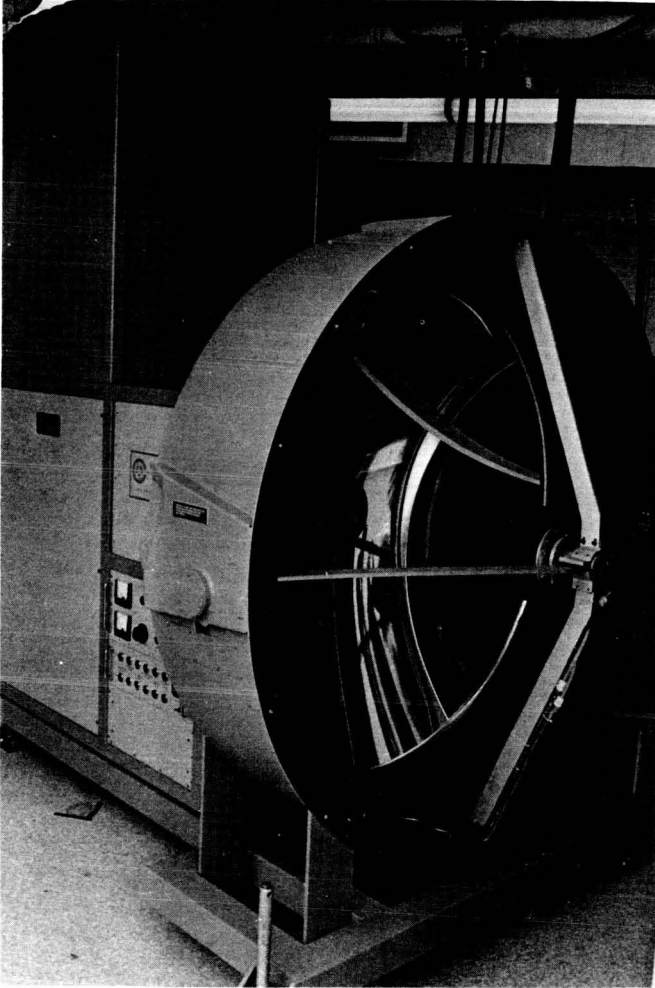


Figure 4
20KW Solar Simulator

The lamp ignitor is a forced-convection cooled unit with 1000 AMP current rating. The unit produces up to 50,000 volts AC to break down the arc gap and start current flowing in the lamp.

VI. OPERATIONAL SAFETY

The system has several red warning signs to alert personnel in the simulator area to the hazards of high pressure lamp explosion, ultraviolet burns and the danger of looking back into the system or at the arc without eye protection.

The ozone generated by the system is drawn out of the lamp-house by an exhaust fan which maintains the system at a negative internal pressure. The ozone is discharged outside the laboratory.

When the system bay doors are closed for operation, the lamp presents no explosion problem since the lamphouse will contain any lamp explosion. Personnel making adjustments to the system while the lamp is on are required to wear protective clothing.

When the lamp is to be removed a special tool is used to hold the lamp while its mounting screws are being removed. This tool minimizes the exposure time for the person removing the lamp. Again, protective clothing is required.

VII. PERFORMANCE

The system was performance tested after installation at the SAPRC laboratory. The following is a synopsis of those tests.

A. Total Irradiance

The intensity of the beam was measured using a radiometer with a blackened receiver for flat spectral response.⁷ The irradiance intensity was measured at 4 points at a radius of 11 inches and 4 points at a radius of 16 inches. The mean value of these measurements was accepted as the intensity level. The simulator produced 1.0 solar constants⁸ at a lamp input power of 16 KW. The intensity at 20 KW lamp input power was 1.32 solar constants.⁸ All intensity tests were made with the removable trichroic spectral filter in place.

B. Irradiance Uniformity

The irradiance uniformity was measured with the same detector as used for measuring total irradiance of the simulator. The detector was placed at various radii from 6 inches to 23 inches. A total of 48 readings were taken and the uniformity of irradiance was determined to be $\pm 10.4\%$. There is a dark hole in the center of the beam which is 4 1/2 inches diameter at the nominal test plane.

C. Solar Subtense Angle

The solar subtense angle was measured with a sextant at the nominal test plane. The solar subtense angle is $\pm 1^{\circ} 6'$ at a point near the beam center and $\pm 1^{\circ} 9'$ at a point near the edge.

D. Beam Douser

The system is equipped with a beam douser to occult the beam. The douser is water cooled and absorbs the heat load projected from the lamp and collector assembly onto the integrator. It can absorb the heat load continuously at lamp powers in excess of 20 KW.

In the photochemistry investigation for which the simulator is being employed, it is quite important to have the capacity to shutter the beam by means of the douser until complete warm-up of the system occurs. As Demerjian, Kerr and Calvert have pointed out, for conventional chambers in which it is not possible to shutter the irradiation system until full light intensity is achieved initial reaction rates will show an induction period which will be due largely to an artifact related to the lamp warm-up characteristics.¹

E. Spectral Irradiance

The spectral irradiance of the beam was measured with a Carl Zeiss spectroradiometer.⁹ The spectroradiometer has been modified for solar simulator measurements by ACC. The incident radiation is reflected from a magnesium oxide diffuser into the entrance slit of the monochromator. The diffuser is first positioned to look at the unknown source and a reading is taken. The diffuser is then rotated 90° to look at a reference source and another reading is taken. The reference source is a 1000 watt, quartz halogen lamp whose calibration is NBS traceable. The readings are then compared to determine the spectral irradiance of the unknown source.

The spectrum of the beam was measured with and without the trichroic spectral filter and the resultant measurements are as shown in Figure 5.

VIII. CONCLUSION

The solar simulator system described above is now in routine operation in the environmental chamber laboratory of the State-wide Air Pollution Research Center. It is commonly employed for six-hour irradiations of either synthetic smog mixtures or ambient Riverside air. Plans are underway to equip the simulator power control with a clock drive which will permit simulation of the diurnal variation in solar intensity in the atmosphere. This refinement would be difficult to achieve readily in chambers with conventional irradiation sources and to our knowledge has not

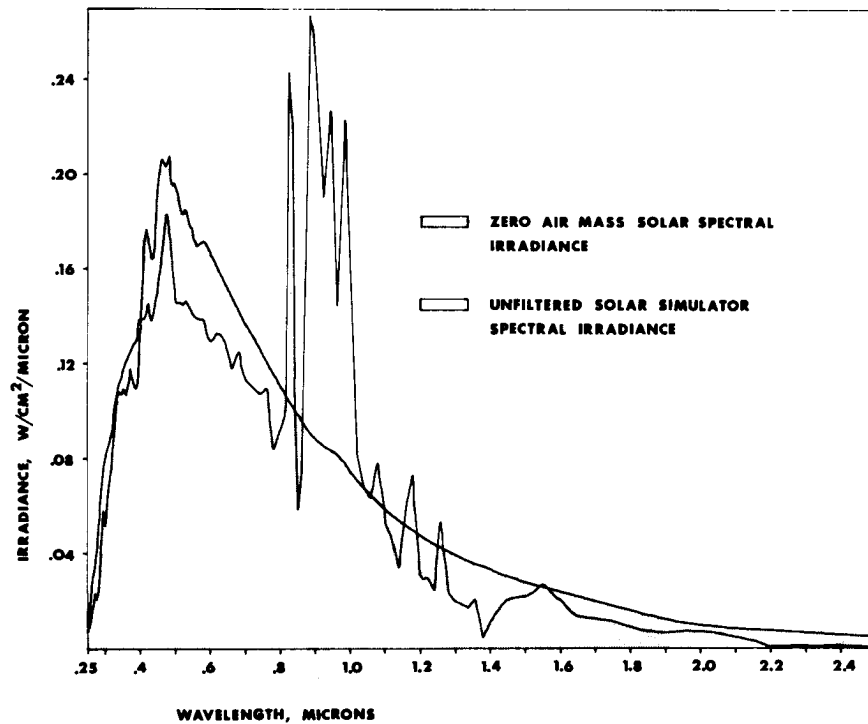


Figure 5a
Unfiltered Solar Simulator
Spectral Irradiance

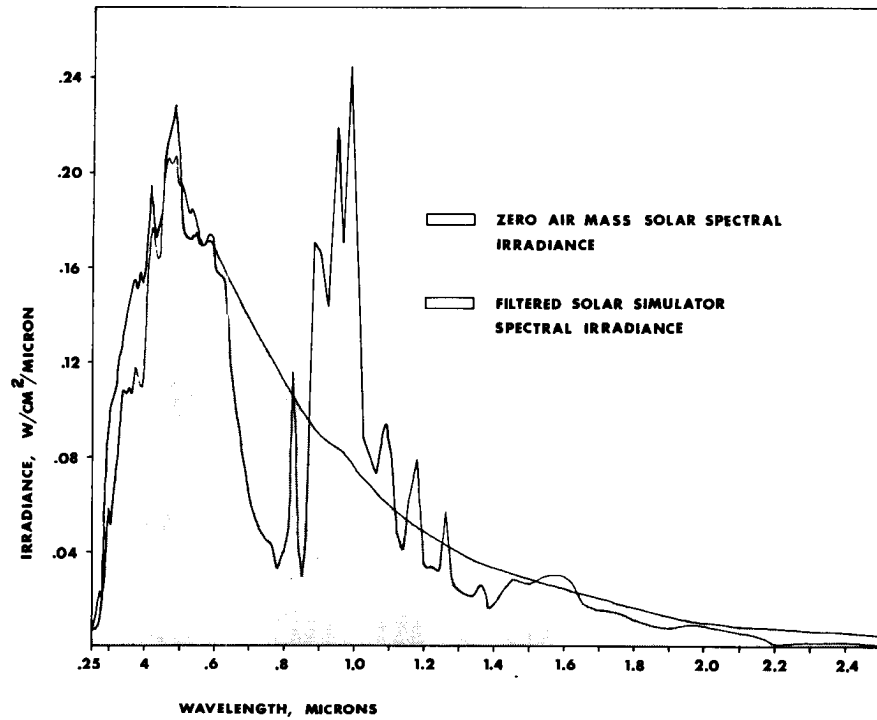


Figure 5b
Filtered Solar Simulator
Spectral Irradiance

been employed in previous smog chamber studies.

Although the primary research goal of the chamber facility is to investigate the photochemistry of the polluted troposphere, temperature and pressure control in the evacuable chamber permits simulating the earth's atmosphere to stratospheric altitudes. Since the evacuable chamber is also equipped with high-grade quartz windows, which are 90% transmitting down to wavelengths as short as 220 nanometers, good spectral and intensity simulation of photolysing radiation at upper altitudes is possible. The abundance of energy below 300 nanometers produced by the 20 KW system will permit such upper altitude studies to be conducted in the evacuable chamber.

Finally, although it is not presently anticipated that experiments will be carried out at intensities in excess of one solar constant, greater intensity can be obtained, if necessary, by use of a reflector outside the far end of the evacuable chamber which results in a two-pass configuration. The simulator can also be operated with a 25 KW xenon lamp if still greater intensity is required.

Acknowledgments

We gratefully acknowledge grants from the California State Air Resources Board and the National Science Foundation for the design and construction of the 20 KW solar simulator.

References

1. K. L. Demerjian, J. A. Kerr, and J. G. Calvert, Advan. Environ. Sci. Technol., J. N. Pitts, Jr. and R. L. Metcalf, eds., John Wiley & Sons, 4, pp. 1, (1973).
2. UV-grade Fused Silica, Corning #7940, Corning Glass Works, Corning, New York; Suprasil II, Amersil, Inc., Hillside, New Jersey.
3. O. E. Lienhard, "Xenon Compact Arc Lamps with Liquid Cooled Electrodes," presented at the National Conference, Illuminating Engineering Society, Miami, Florida, August 1964.
4. Hanovia Lamp Division, Conrad Precision Industries, Newark, New Jersey.
5. L. F. Polak, "High Efficiency Collectors for High Energy Radiant Sources," presented at I.E.S. Conference 1966, San Diego, California.
6. Power supplies: Miller Electric Mfg. Co., Appleton, Wisconsin.
7. Radiometer: Hy-Cal Engineering Model P8400, Santa Fe Springs, California.

8. M. P. Thekaekara, NASA Goddard Space Flight Center, "Proposed New Engineering Standard for the Solar Constant and Zero Air Mass Solar Spectral Irradiance," presented at I.E.S. Conference, 1970, Boston, Mass.
9. Carl Zeiss PMQII Spectroradiometer, Germany (modified for solar simulation measurements by ACC).

PRECEDING PAGE BLANK NOT FILMED

Paper No. 67

A NOVEL FACILITY FOR RADIANT HEAT TRANSFER EXPERIMENTS

J. Metzger, *RESO, General Electric Co, King of Prussia, Pa.*

ABSTRACT

In order to perform a special experiment in radiant heat transfer a unique facility was designed and built. The fundamental design parameters included the capability for achieving rapid initial temperature rise and for establishing effective maximum temperature as high as possible for continuous operation. In this presentation, the design procedures and operation of the facility are discussed. A particular experiment measuring the emittance of a titanium alloy is summarized to exemplify one application of the facility and finally, the versatility of the equipment is pointed out in discussing other potential areas of applicability.

INTRODUCTION

The particular requirements of a special radiant heat transfer experiment led to the design and utilization of a responsive and versatile test facility. The unit evolved is shown in Figure 1. Based on the requirements of the experiment, an initial rate of rise in temperature of 700° per second and a nominal maximum temperature of 1700°R were selected as design criteria for the radiant source. The rapid rise in temperature was obtained by applying the combustive heat provided by an oxy-acetylene flame to a metallic radiator with minimal heat capacity. The radiator, a thin walled metallic cylinder, was mounted on a rotating platform in order to distribute the heating as uniformly as possible. The acetylene flame issued from 34 individual jets spaced along each of four columnar manifolds, washing the length of the cylinder. The design permitted the columnar manifolds to swivel, controlling the absolute level of the temperature at which the cylinder equilibrated.

Among the experiments for which the facility was employed was one in which the total emittances of various metal radiators in cylindrical form were determined. The temperature of each metal cylinder was recorded by two thermocouples affixed to its surface and the thermal flux density emitted was measured by a calorimeter placed close to the interior wall of the cylinder.

One cylinder was constructed from a titanium alloy. The characteristic emittance varied from 0.4 to 0.6, indicating some sensitivity to temperature, and suggesting a slight progressive variation at an approximately steady temperature.

In addition to the experiment involving the imposition of a controlled temperature profile on the radiative source, quite a number of other experiments can be performed in the oxy-acetylene facility. One of these, the measurement of total emittance, is described in this presentation. As with the several other studies performed in this facility, the experiment yielded useful information. Additional applications for which the facility might be used are reviewed.

DESIGN CRITERIA

The radiant facility was created to simulate with reasonable fidelity, variable temperature profiles. The principal restriction on the profiles was the establishment of moderately high temperature levels in a brief period of time. A design objective was established which sought to achieve an initial rate of rise in temperature of $700^{\circ}\text{F}/\text{sec}$. The nominal value of the maximum operating temperature of the facility was identified as a second design criterion. While the highest possible value was desirable, the design value had to consider the high temperature structural capabilities of the radiating cylinder. A conservative value of 1700°R was selected. The two elementary criteria are shown in Figure 2.

Having established design objectives, the actual design procedures involved first an estimation of the heat transfer mechanisms involved, to ascertain the quantity of heat required to achieve them. Thereafter, the combustion of acetylene was reviewed to determine that the process would indeed provide the necessary heat at adequate rates. When the technique appeared to satisfy the criteria the quantities of oxygen and acetylene required were used as the bases upon which the physical design was developed. The design provided a system for distributing the combusting acetylene and incorporated a system of target rotation to approximate uniformity of heating on the surface of target cylinder. In addition to satisfying requirements of the original experiment, mechanical design attempted to maximize versatility in the operation of the facility.

THERMAL DESIGN

To determine, ultimately, the quantities of oxygen and acetylene required to achieve the projected performance of the facility, the demands of the various mechanisms consuming the thermal energy generated were examined. These include

- Heat capacity of the cylindrical radiator
- Natural convection
- External radiation
- Internal radiant exchange

It is obvious that the relative contributions of the various factors will be time dependent. The net effect of all the factors taken as a function of time constitute the thermal demand of the system, which must be satisfied by the combustion of the acetylene.

The first step in treating with the contributing thermal process was to prepare design curves of the individual processes. Since the heat capacity of the cylindrical radiator appeared to be the most significant mechanism initially, it was examined first. The cylinder was to be made of metal. A titanium alloy was one material selected. Preliminary sizing requirements fixed the cylinder at twelve inches in diameter and three feet in height. To minimize the thermal capacity, a wall thickness of 10 mils was assumed. Using the appropriate properties from Table 1, the effective heat transfer rates necessary to sustain specified temperature rise rates were computed using the calorimetric equation.

$$\dot{q} = \rho C_p s \frac{\Delta T}{\Delta t} \quad (1)$$

The design graph (Figure 3) indicates the quantities of heat necessary to produce specified increases in temperature per unit time. The data reflect the sensitivity of the relationship to variable specific heat.

Another mechanism which utilizes the input energy is thermal radiation. It was assumed that the combusting acetylene contributed a negligibly small thermal radiation input into the cylinder. Most of the heat transfer entered through convection. However, as higher temperatures were attained by the metal cylinder, increasingly large amounts of thermal energy were lost through reradiation. Using the Stefan Boltzmann equation, the energy reradiated per square foot of surface area can be calculated parametrically. The equation.

$$\dot{q} = 5.0c \left[\left(\frac{T_w}{1800} \right)^4 - \left(\frac{T_a}{1800} \right)^4 \right] \quad (2)$$

was evaluated for emissivities of 1.0, 0.8, and 0.6. The numerical results are illustrated as design curves in Figure 4.

Along with the foregoing modes of heat transfer, a convective loss in the system was expected. Although the metal cylinder was designed to rotate the speed is minimal. Therefore, to a first approximation, the heat transfer was treated as free convection. The system was represented as a vertical wall. According to Fishenden and Saunders (Reference 1), the heat transfer coefficient correlates as follows:

$$h' = 0.28 (\theta/l)^{1/4} \quad (3)$$

for laminar flow and

$$h' = 0.30 (\theta)^{1/4} \quad (4)$$

for turbulent flow. Turbulence is defined to exist for flows in which the product of the Grashof Number and Prandtl number exceeds 10^8 , numerically. The rate of heat transfer is then given by:

$$\dot{q} = \frac{h' \theta}{3600} \quad (5)$$

The Grashof Number was obtained at an average film temperature

$$T_f = \frac{T_w - T_a}{2} \quad (6)$$

and is given by

$$N_{gr} = \frac{g \theta \frac{1}{2} \theta^3}{\nu} \quad (7)$$

Taking advantage of the fact that for a gas, θ is proportional to $1/T$, the product of Grashof and Prandtl numbers were calculated for a range of representative average film temperatures. It was determined that for the conditions of operation of the cylinder, the flow was, according to the above criterion, predominantly turbulent (i.e., $N_{gr} N_{pr} > 10^8$). Consequently, the film coefficient and the consequent rates of heat transfer were based on equation (4). The values of the rate of heat transfer for a representative range of temperatures are presented in the form of a working design curve. (Figure 5).

Having compiled data assessing the potential contributions of the various modes of heat transfer, it is appropriate to estimate the contributions of each and establish a time dependent profile of heat transfer. At the initial application of heat (time zero), the titanium is at ambient temperature. Hence, both radiant and convective heat transfer will be zero. Therefore, initially all of the heat transferred will be consumed in satisfying the heat capacity of the titanium. To assess the subsequent behavior, it is convenient to define a coefficient of heat transfer at time zero. A family of coefficients for arbitrary temperature differences is shown in Figure 6. The design point has been indicated. It may be noted that the design rate of heat transfer, 40 Btu/sec ft², exceeds the 25.2 Btu/sec ft² that is demanded by the titanium as depicted in Figure 3. It is inherently impossible for the transfer of heat to proceed with an efficiency of 100%, a condition implicit in the evaluation of the heat capacity requirements of titanium. Therefore, the rate of heat transfer

selected as an objective exceeded the ideal, implying an assumed efficiency of approximately 60%. Since, as is summarized in Table 2, typical flame temperatures of combusting acetylene exceed 4500°R, at time zero, the initial difference in temperature between the combusting gas and that of the cylinder metal will be at least 4000°R. Assuming this difference, the coefficient of heat transfer to the cold wall used for initial design was 0.01 Btu/sec ft² °F. This value is based on the elementary definition of the heat transfer coefficient. In furnace analysis, the rate of heat transfer between combustion gases and the charge in a furnace is represented by a formula of the form:

$$\dot{q} = h (\Delta T)^y \quad (8)$$

Empiric treatments have provided for variations in the performance of the combusting environment by introducing to Newton's expression a variable exponent for the temperature difference. However, according to Thring, (Reference 2), the exponent is in most cases unity, and in all cases, near to unity. Hence, the simpler assumption is consistent with furnace practice.

The combined heat transfer was assessed by determining first the changes in temperature of the metal of the cylinder as a function of time, due to heat storage. This was treated incrementally using arbitrary, small temperature rises. The new driving difference in temperature was then applied to each subsequent calculation. Each incremental temperature rise was calculated from that preceeding it, using the equations

$$t_n = \frac{(\rho C_p S)_n (T_{n+1} - T_n)}{h (T_s - T_n)} \quad (9)$$

which evaluates an incremental time associated with the assigned temperature rise, $(T_{n+1} - T_n)$, of the cylinder, and

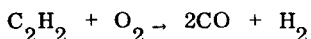
$$\dot{q}_{n+1} = h(T_s - T_{n+1}) \frac{T_m - T_{n+1}}{T_m - T_n} \quad (10)$$

which provides the data necessary to continue with the next incremental evaluation. The procedure iterates using each incremental value. The numerical values obtained are presented in Table 3. The table indicates a theoretical time rate of rise of 1190°/sec can be expected initially, although the rate declines very rapidly.

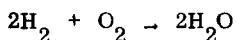
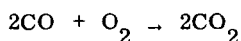
The time profile defined by the foregoing analysis was employed to approximate the thermal demand required by the other modes of heat transfer. Utilizing the appropriate design curves, values for both radiant and convective heat transfer rates were obtained for the incremental times previously calculated. The values are given in Table 4. Radiant exchange, assuming an emissivity of 0.6 was charged to both faces, although the subsequent test programs were performed under different conditions. Convec-

tive heat transfer rates were increased three fold to compensate for possible enhancement of heat transfer due to the rotation of the cylinder. A compilation of the data from Table 4 is presented graphically in Figure 7. The information must be interpreted for application to the operating facility. An incident heat transfer rate of 40 BTU/sec ft², were it to be achieved, would be more than adequate to satisfy the first criterion. However, the primary purpose of the design based on 40 BTU/sec ft², as previously stated, was to protect against unanticipated losses and the inefficiency of the system.

A natural consequence of establishing a specific design rate of heat transfer is to determine the quantities of fuel and oxygen which will be required to maintain such a rate. Commercial applications, of which the facility design made use, employ the principals, acetylene and oxygen, in a combustion process that departs from the stoichiometric reaction (Reference 3). Combustion is controlled to occur in two steps. Pure oxygen is supplied in equal volume with the acetylene. The initial oxidation process involves these volumes.



The products created are further oxidizable. These combine with oxygen from the air to produce the stoichiometric end products.



In this system, 40% of the required oxygen is supplied in pure form. The remaining 60% is supplied from the surrounding air. Thus only 15 volumes of air are needed to complete the combustion process. The two step process was chosen as most suited to the facility because it provides an additional measure of control over the thermal environment by adjusting the oxygen-acetylene mixture. A one-to-one mixture of oxygen and acetylene yields a "neutral" flame. An excess of acetylene yields the reducing environment, while an excess of oxygen will produce the oxidizing flame. In actual application it proved convenient to use the neutral flame mode of operation.

The one to one mixture of fuel and oxygen, together with the supplementary air produce the operating flame. Based on visual observation of an oxy-acetylene flame it was estimated that a single jet, although dispersed over a larger area, provided the nominal heat transfer rate over an area one inch in extent. Consequently, for a 36" multijet column, there were 34 jets located on one inch centers. Four columns were specified. For the rotating cylinder, each column contributed a proportionate share of heating. The total surface area of the cylinder was 9.42 ft² and the maximum heat transfer conservatively estimated to satisfy the design criteria was 40 Btu/sec ft². Since the

heating value of acetylene is 20,000 Btu/lb, (See Table 2) the mass flow needed to satisfy the rate of heat transfer is calculated from

$$\dot{q} = \frac{h_v (\dot{w})}{A} \quad (11)$$

Upon rearranging,

$$\dot{w} = \frac{40 (9.42)}{20 \times 10^3}$$

$$\dot{w} = 18.84 \times 10^{-3} \text{ lb/sec}$$

A like amount of oxygen is used in the combustion as conventionally provided; therefore, the total mass flow will be 37.7×10^{-3} lb/sec. Since there are 136 orifices, from each will issue 27.7×10^{-5} lb/sec of mixed gases. There remains the problem of sizing the orifices. Since the gas mixture is variant from gases commonly tabulated, the properties have been separately assessed. Since commercial mixing ratios were to be used in the facility nozzle calculations were based on equal volumes of acetylene and oxygen being emitted from the nozzles. Using the individual gas properties, the properties of a mixture were assigned according to the data in Table 5. The data were given in Reference 4. Note that the gas constant R differs from that employed in the nozzle calculations (R_u) by the gravity acceleration constant. The properties are representative of gases at 540°R. These values were used in the subsequent flow calculations. To better define flow rate, a choked flow was assumed. Each orifice was designed to provide fixed mass flow rates above the critical pressure. The flow rate is calculated with the equation (Reference 5).

$$\dot{w} = \frac{144 p_o}{R_u T_a} \left(1 + \frac{\gamma - 1}{2} \right)^{-1/(\gamma - 1)} \sqrt{\frac{2\gamma R_u T_a}{\gamma + 1}} \text{ gA} \quad (12)$$

Using the properties of the gas mixture, the mass flow per unit area was obtained allowing for the orifice efficiency of flow. The nozzle size of each of the 136 of the jets was determined to be 0.005 inches. Since this was a value impractical to realize because of manufacturing costs, an arbitrary diameter of 0.020 was specified for manufacture. It was realized that the increase in diameter would result in a significant increase in gas consumption and would very likely degrade facility performance.

MECHANICAL DESIGN

The mechanical design of the radiant heat transfer facility had two objectives. The first was to provide a system which satisfied the design criteria and adequately met the requirements of the original test program. The second objective went further. It attempted to incorporate features which made the system more adaptable and more versatile. Adaptability was required to resolve on-site developmental problems and versatility was desired to make the facility useful for investigations beyond the initial one.

The basic structure and salient features of the facility are illustrated by the cutaway view (Figure 8). The outer flanged housing supports and protects the drive motor. The flanged column inside is the base for a fixed platform on which target specimens are mounted. Supported on the column through roller bearings is a large flat plate topped with insulation which rotates freely, driven through a system of gears by the electric motor. The radiating cylinder mounts atop the rotating top plate. The outer edge of the plate is supported on rollers mounted atop the flanged housing. A large diameter slip ring assembly was mounted to the underside of the driven gear and permitted thermocouple data to be transmitted from the rotating metal cylinder to stationary brushes. Model instrumentation lines were brought down the interior of the central column. Four supportive brackets with bushings each received a shaft onto which mounted a horizontal bracket structure. A clevis joined the columnar torch heat to the end of this bracket, and a turnbuckle assembly restrained the two parts in relative positions one to another. Conventional oxy-acetylene torch equipment was purchased to supply the facility torch heads. The normal torch head was removed and the handle, with mixing equipment and valving retained, was brazed to each columnar torch head. The 34 jets were screw fitted into the column and sealed with silicone O-rings. A band of copper tubing looped around each header to provide water cooling.

Although not shown, each shaft passing through the supportive brackets on the periphery of the flanged housing was equipped with a sprocket, and all the sprockets were joined by a sprocket chain. Thus rotation of one torch head resulted in the united rotation of all. Movements were produced by manual control.

Sizing the facility was dictated principally by the requirements of the original test program. The metal cylinder serving as radiator was sized to accommodate the test specimen and the number of jets in the columns were fixed as soon as their interval was established. As already noted, flow rates and thermal parameters consistent with the physical geometry of the housing were determined. The thermal calculations merely indicated that for the size proposed, the energy requirements apparently were attainable.

The features providing flexibility were numerous. Several are enumerated to emphasize their advantages.

1. The gear system was designed to accept any of seven pairs of gears to provide variations in speed of cylinder rotation. Although only one was used, they offer opportunities to investigate in detail the effect of varied convection flow characteristics.
2. Orifices were threaded individually into the torch heads. Modification of orifice sizes was possible with little difficulty. Obviously, there are limits in size which could not be exceeded, however.
3. The use of turnbuckles proved very helpful. They not only restrained the columnar torch heads in their proper position but they also provide a relative fine control on changes in the alignment of them.
4. The ability to align the columnar torch heads on either side of the vertical anticipated one problem which required alleviation. When in the vertical position, the jets tended to produce a temperature gradient on the cylinder from top to bottom. The cylinder ran hotter at the top. By retracting the top of each column so that it was inclined outward at an angle of six degrees, a remarkably gradient - free vertical profile was observed on the cylinder.
5. The radiating cylinder was very simple to replace. Any formable sheet metal could be rolled and spot welded to produce a replacement cylinder. In some cases (aluminum for example) special consideration of the maximum operating temperature must be given.
6. The water cooling lines affixed to the torch head columns were installed to reduce the possibility of preignition of the oxygen-acetylene mixture in the headers. They were apparently successful; no incident of flash back was experienced.

The facility was furnished oxygen and acetylene from a bank of bottles organized in independent groups to supply each of four sets of inlet hoses leading to the mixing manifolds brazed to the columns. The gas system manifolded three bottles of acetylene and two of oxygen to supply each column (Figure 9). Individual torch columns could be ignited, adjusted, and even calibrated independently.

PERFORMANCE

The initial test for the complete system involved varying the temperature after achieving the nominal maximum value. The variation was obtained by manually swiveling the torch headers to vary impingement of the combustion gases. Guidance for such manipulation was provided by the responses of an IRCON two color pyrometer. In order to make more determinate the temperatures reported by the pyrometer, the outer surface of the cylinder was

blackened. Acetylene soot was deposited by applying the torches. Obviously, a black radiating surface on the outside lowered the effective maximum temperature attainable, but permitted more meaningful control of transient temperatures. Nevertheless, the detailed data obtained during the initial period of heating (Figure 10) indicate the mean heating rate exceeded the design value over the first two seconds. Indeed, the experimental data are not only self consistent, but demonstrate a relatively close approach to design was achieved. The complete test profile is shown in Figure 11. Upon observing the temperature to reach 1700° initially, the torch heads were swiveled to an off-center position resulting in the recorded decline. The variations of the cylinder temperature profile are indicative of the sensitivity of the cylinder in response to changes in the input heating.

EMITTANCE EXPERIMENT

The facility may be employed for a variety of experiments. One which has been performed investigated the emittance characteristic of a titanium alloy. In the original experiment involving the titanium alloy radiating cylinder, an emittance of 0.6 reported in the literature was employed. During subsequent tests of the emittances of various materials, it was convenient to make a measurement endeavoring to verify independently the value reported. The radiating cylinder itself became the test specimen. However, unlike the original cylinder, the ones used in this study were only six inches high. In order to minimize possible convection effects a close fitting cover was installed atop the fixed platform of the facility which effectively closed the upper end of the cylinder. Schematically, the system is shown in Figure 12. The specimen was inserted in a recessed base ring to raise it and more fully utilize the surface of the cylinder. Two thermocouples were welded into the inside of the test cylinder to monitor the specimen temperature. Signals were transmitted through the slip rings installed on the facility to the recording instrument.

Inside the test cylinder a second heavy walled cylinder of steel supported a commercially available thermal flux detecting calorimeter in a hole midway down the length of the cylinder. The gauge, calibrated with a radiant source, was furnished with a coating of ϵ_2 0.825 emittance, and had a capability of up to 10 Btu/sec ft². Basically, it was a Gardon gauge, which functions by generating a calibrated electrical output resulting from the temperature gradient between a constantan foil and a copper heat sink as shown in Figure 13. In the instrument employed, the heat sink is kept at constant temperature by water cooling.

During the test, the acquired data consisted of the temperature of the titanium cylinder and the flux absorbed on the face of the Gardon gauge. The data obtained from the two thermocouples on the cylinder was averaged. The thermal flux to which the Gardon gauge responded was based on the calibration of the electrical output provided by the manufacturer. The two sets of

data are coplotted in Figure 14 as a function of time. The test duration was 125 seconds in an effort to establish complete thermal equilibrium.

The rotating cylinder and the fixed one with the calorimeter mounted flush with its surface were less than $\frac{1}{4}$ " apart in the region of the gauge. Although the two surfaces are close together it was estimated that of the convective heating developed along the surface of the rotating cylinder, very little was transferred to the massive heat sink and the water cooled gauge it contained. Hence, the entire measured response of the gauge was attributed to thermal radiation.

The experimental data were reduced by using the Stefan-Boltzmann equation rearranged to solve for an effective emittance

$$\epsilon = \frac{2.1 \times 10^{12} \dot{q}}{T_1^4 - T_2^4} \quad (13)$$

The value obtained is, of course, comprised of two components: the geometry of the system and the actual emittances of the surfaces involved in the exchange. Two interpretations of the geometry were considered. The one case assumed the two surfaces to be parallel plates. The other treated the exchange as that between an infinite plane and a small element of area, representing the gauge. Both provide a geometric factor of essentially unity, according to Reference 6. Therefore, the primary effect will be that of the two emittances. Of the two, that of the calorimeter surface ($\epsilon = 0.825$) is known. The other, that of the titanium alloy cylinder is unknown. The two are related as follows: for the parallel plates:

$$F_e = \frac{1}{1/\epsilon_1 + 1/\epsilon_2 - 1} \quad (14)$$

And for the plane and planar element:

$$F_e = \epsilon_1 \epsilon_2 \quad (15)$$

For arbitrary emittances on the detector the corresponding values of the cylinder were plotted for all values of the effective emittance measured, (Figure 15). As can be seen, the divergence between the two methods of treatment is not large, even at the mid-range of values. Using the experimental data and evaluating them in accord with the two models illustrated in Figure 15, two possible values of emittance were obtained both have been plotted along with the unadjusted effective emittance, in Figure 16. Taking the solutions to represent extreme in the evaluation of the cylinder emittance, the error is approximately $\pm 6\%$ over most of the time of the test. Note that as the experiment progressed, there was evidence of a gradual increase in the emittance. The

final average value of 0.58 is consistent with the reported value employed in the design of the original experiment. The trend to increase in emissivity suggests that continued heating affects the radiation characteristics of the surface progressively.

POTENTIAL APPLICATIONS

The versatility of the oxy-acetylene facility, coupled with the simplicity of the equipment makes possible a variety of useful experiments. Consider the opportunities to use the variable flux capability. For any of a variety of metallic radiators, the response of complex target specimens can be studied. The "time constant" for the response of a multiple radiation barrier can be determined, as well as its net effectiveness in the steady state.

The variation of the emissive power of materials subject to change because of the thermal environment can be examined in both the transient and the steady states. Furthermore, the radiant behavior of composites consisting of substrate and overlay may be explored.

For very precise experiments, the exact contributions of the convective heat transfer mode must be determined, but accepting that as achievable, data may be acquired regarding radiant interchange factors for a variety of geometries, and additional high temperature emittance data can be obtained by the same general method as described for the titanium alloy. Obviously steady state values can be derived at each of a series of selected temperatures. Note that the titanium data were acquired at a temperature in excess of 2000°R. Obviously, the existing system has a capability to establish temperatures levels greater than the original design temperature.

CLOSURE

The oxy-acetylene radiant heat transfer facility was designed to perform a specific experiment. The design procedure and features have been discussed. As it developed, the concept which evolved resulted in a facility of great versatility. Various additional experiments were performed, one of which has been described briefly. That experiment used the facility to obtain a measure of the emittance of a titanium alloy at a specific level of temperature. As has been briefly summarized, other experiments in radiant heat transfer are possible. The capabilities of the facility far exceed those originally required and many additional experiments can be performed using the superior capabilities.

REFERENCES:

1. An Introduction to Heat Transfer, M. Fishenden, O. A. Saunders, Oxford University Press, London 1950.
2. The Science of Flames and Furnaces, M. W. Thring, Second Edition, John Wiley and Sons, 1962.
3. The Oxy-Acetylene Handbook, A Manual on Oxy-Acetylene Welding and Cutting Procedure, Linde Air Products Co., 1943.
4. Thermodynamics, Virgil M. Faires, Applied Thermodynamics Third Edition, Mac Millan Co., 1957.
5. Engineering Supersonic Aerodynamics E. A. Bonney, McGraw Hill Co., Inc., 1950.
6. Engineering Heat Transfer, S. T. Hsu, D. Fan Nostrand Co., 1963.
7. Handbook of Chemistry, "Lange, Editor, 8th Edition, Handbook Publishers, Inc. 1952.

TABLE 1 - PROPERTIES OF TITANIUM ALLOY
(Ti - 6Al - 4V)

T °R	500	1000	1500	2000	2500
ρ , lb/ft ³			277		
C _p	.140	.167	.216	.283 e	.351 e
k	5.4	7.6	10.0	12.6 e	15.2 e
e	0.6 (mean value)				

Values of C_p and k from Reference 4 e: extrapolated

TABLE 2 - THERMAL PROPERTIES OF ACETYLENE

Heating Value	1350 Btu/ft ³ , 21449 Btu/lb	
	<u>IN AIR</u>	<u>IN OXYGEN</u>
Flame Temperatures	2325°C	2927°C
	2598°K	3200°K
	4676°R	5760°R
	4216°F	5300°F

Data From Reference 7

TABLE 3 - SUMMARY OF TRANSIENT HEAT TRANSFER, ALL MODES

HEAT TRANSFER BTU/FT ² SEC	Time, Sec.	.101	.283	.448	.759	1.059	1.680	2.480	4.730
	Temp., °R	660	840	960	1140	1260	1440	1560	1740
	°F	200	380	500	680	800	980	1100	1280
\dot{q}_{Cp}		40.0	34.8	27.4	22.8	16.4	12.5	6.95	3.61
\dot{q}_{rr}		.07/.14	.15/.30	.22/.44	.40/.80	.62/1.24	1.20/2.40	1.70/3.40	2.55/5.10
\dot{q}_{conv}		.06/.18	.22/.66	.32/.96	.50/1.50	.62/1.86	.82/2.44	.96/2.88	1.18/3.54
$\Sigma \dot{q}$		40.32	35.76	28.80	24.10	19.50	17.36	13.23	12.25

TABLE 4 - TRANSIENT HEAT TRANSFER FOR HEAT CAPACITY

n	T _n °R (T _{init})	\dot{q} Btu/sec ft ²	T _{av} °R	C _p s	T/ t °R/sec	T _{final} °R	t sec	T °R (new)*	$\frac{T_m - T_n + 1}{T_m - T_n = 1}$
1	540	40.0	600	0.0336	1190	660	0.101	3880	0.895
2	660	34.8	750	0.0353	990	840	0.182	3700	0.750
3	840	27.4	900	0.0373	730	960	0.165	3580	0.637
4	960	22.8	1050	0.0391	580	1140	0.311	3400	0.482
5	1140	16.4	1200	0.0410	400	1260	0.300	3280	0.380
6	1260	12.5	1350	0.0428	290	1440	0.621	3100	0.224
7	1440	6.95	1500	0.0447	150	1560	0.800	2980	0.121
8	1560	3.61	1650	0.0465	80	1740	2.250	2800	-----

*Initial Value of T = 4000°R

Tabular Solutions for Equations 8 and 9

TABLE 5 PROPERTIES OF COMBUSTION GASES

	<u>C₂H₂</u>	<u>O₂</u>	<u>MIXTURE</u>
MOL. Wt.	26.02	32	29.01
SPECIFIC HEAT	.409	.2193	.324
SPEC. HEAT RATIO	1.23	1.394	1.321
GAS CONSTANT, R	48.25	58.8	53.27

FROM REFERENCE 4

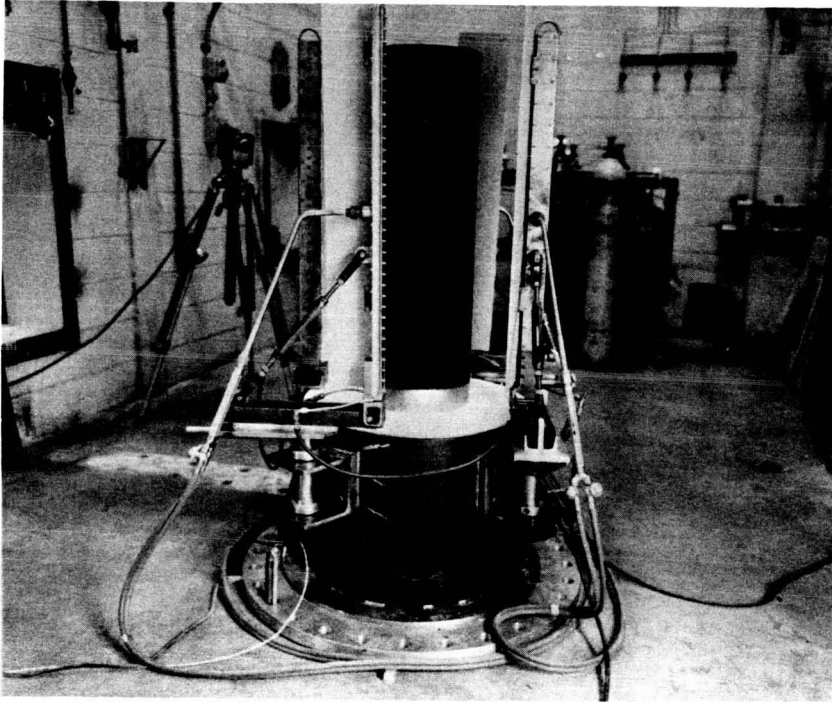


Fig. 1 General View of Oxy-Acetylene Facility

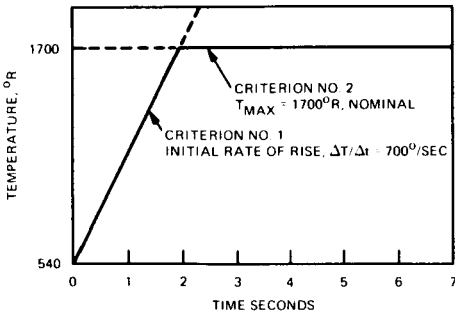


Fig. 2 Design Criteria

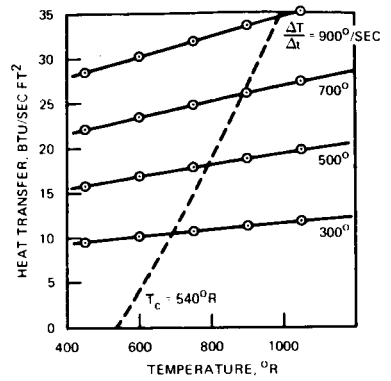


Fig. 3 Heat Transfer Rates for Given ΔT Rates

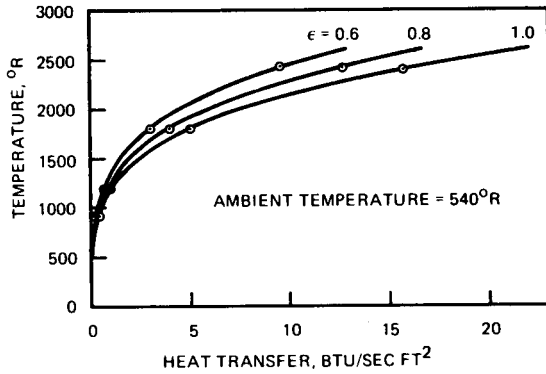


Fig. 4 Radiant Heat Transfer Losses

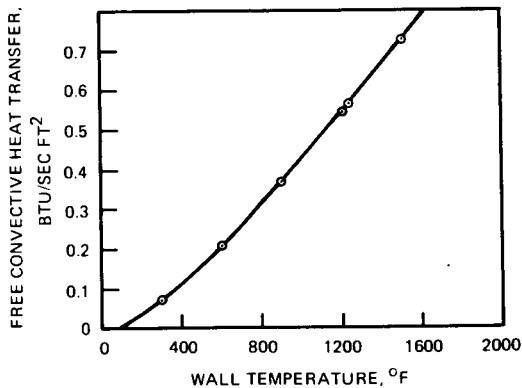


Fig. 5 Heat Transfer by Free Convection

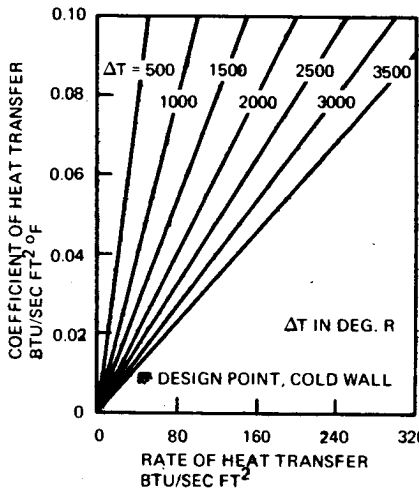


Fig. 6 Coefficients of Heat Transfer

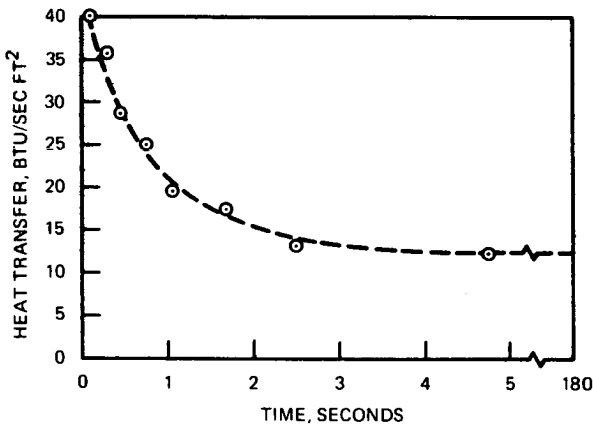


Fig. 7 Summary of Transient Heat Transfer

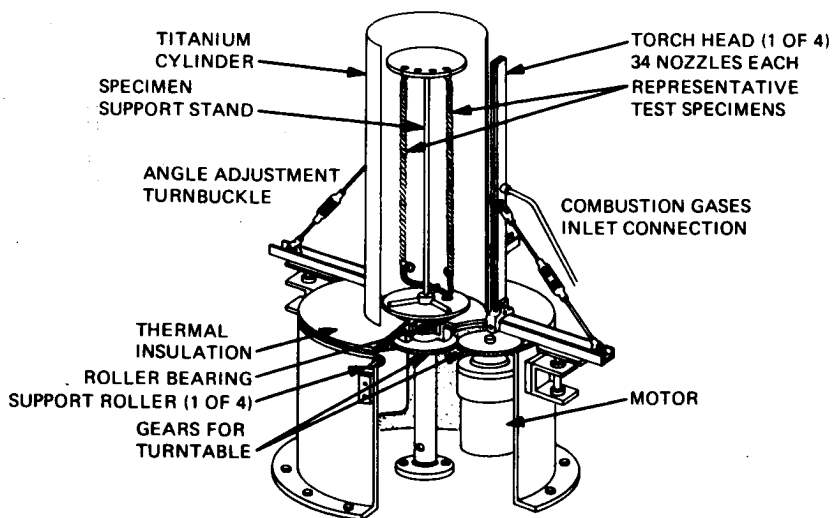


Fig. 8 Cut Away View of Radiant Test Facility

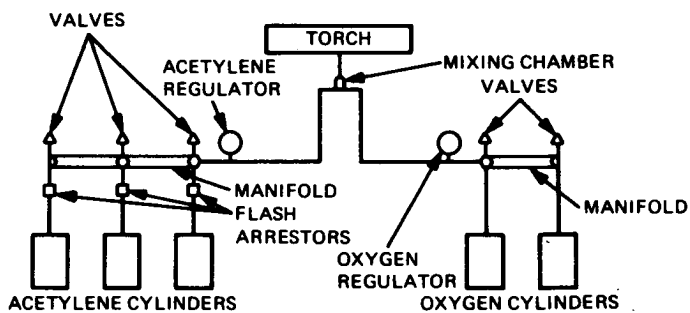


Fig. 9 Schematic of Gas Manifold System

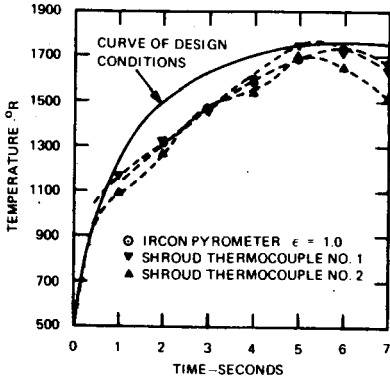


Fig. 10 Initial Temperature Profile

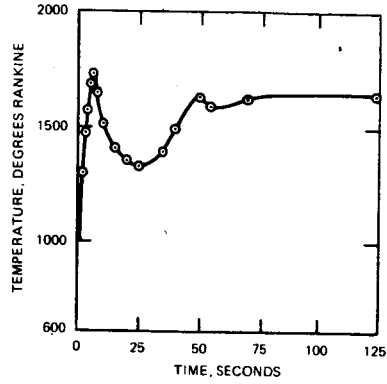


Fig. 11 Surface Temperature History of Cylinder

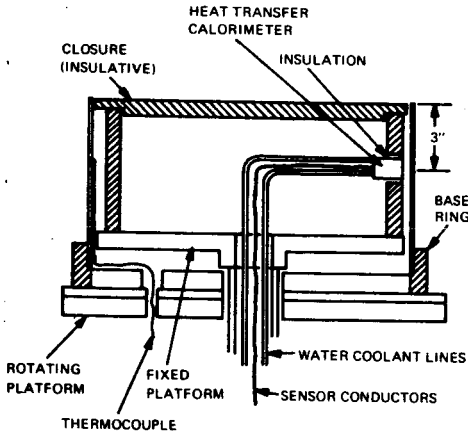


Fig. 12 Emittance Test Arrangement

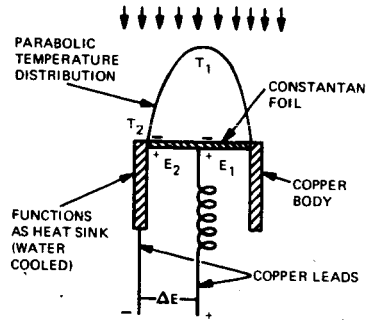


Fig. 13 Gardon Gauge Operation

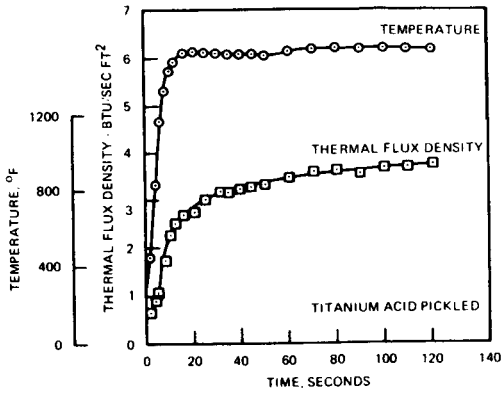


Fig. 14 Measured Response Data-Emittance Experiment

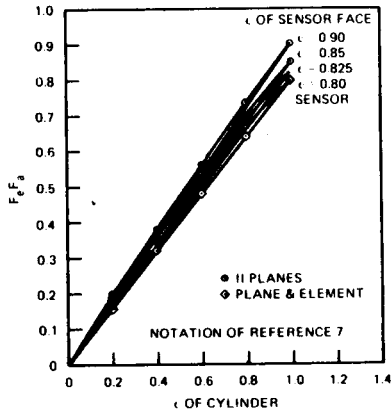


Fig. 15 Emittance Configuration Factors

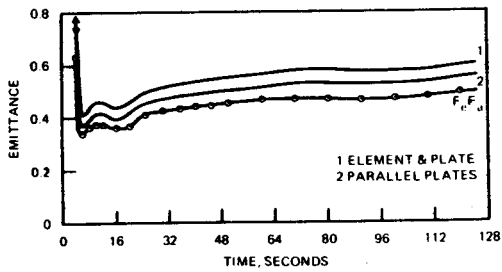


Fig. 16 Emittance-Titanium Alloy

N74-10255

A VERSATILE INSTRUMENT FOR THERMAL RADIATION MEASUREMENT

Calvin M. Wolff, *Scientist, Northrop Services, Inc.,
Houston, Texas*

ABSTRACT

A radiometer has been designed, fabricated, and tested which is rugged, versatile, and highly reliable for measurement of real or simulated solar radiation in an ambient or vacuum environment, and for measurement of total hemispherical infrared radiation in a vacuum. This radiometer may be considered as an all purpose radiometer for space environment simulation and testing.

INTRODUCTION

There are a number of types of radiometers used in solar simulation that employ a variety of sensing principles. Photoelectric, photoemissive, and photoconductive instruments have an extremely fast response time and are very sensitive; however, they are spectrally selective. Thermal devices such as thermopiles and bolometers have a relatively slow response time (one second time constant or greater), are very delicate, and are of low sensitivity (5 to 15 millivolts per solar constant). Also, thermal devices are spectrally nonselective, which permits them to be used in solar simulation measurements and the uncertainties caused by spectral nonuniformity may be eliminated. Where spectral uniformity is assured, photon-activated devices, generally solar cells, are used. Another advantage of photon-activated devices is that their sensitivity does not vary with atmospheric pressure (from vacuum to one atmosphere), and they do not respond to thermal radiation (when selected for response in the solar spectral range). An additional problem with photon-activated sensors is that they must be calibrated against a standard whose spectrum is the same as that to be measured.

The closest device to qualifying as a hybrid of the photon and thermal sensors is the thermodielectric sensor. In this sensor a slight change in temperature of a black surface absorbing light causes a change in

dielectric constant, which is detected when the sensor is in a capacitance bridge circuit. This type sensor is sensitive, spectrally nonselective and quite fast in response time.

However, it is delicate and temperature sensitive and has not been used (to the author's knowledge) in solar simulation measurement. One of the manufacturers does not recommend it for use in solar simulation measurement.

Space environment simulation has the additional requirement of nonselective measurement of infrared radiation (3 to 100 microns wavelength) that is incident from any variety of geometries within a hemisphere of view as well as measurement of solar and/or infrared energy absorbed by a given surface material (e.g., thermal control coating).

A thermal-type sensor has been designed, fabricated, developed, and tested. This sensor is more sensitive and faster to respond than most other thermal sensors and can be used for measuring infrared and absorbed irradiance, and incident solar irradiance.

DESCRIPTION

The instrument consists of two semicircular Boelter-Schmidt type sensors mounted adjacent to each other on a cylindrical aluminum block (fig. 1). The sensors are painted with a black matte finish, and two output leads from each sensor extended from the block. A thermocouple is mounted in the block along its center line and near the face of the sensors. The instrument can be mounted on a cylindrical heater Bezel (fig. 2) of the same diameter as the radiometer. The heater Bezel contains two independent thermostated heaters that control at approximately $90^{\circ} \pm 5^{\circ}$ F. Two sets of 110-volt leads come from the heater Bezel, which weighs about 3 ounces.

The Boelter-Schmidt type sensors were selected for this radiometer because they are very rugged and measure heat transfer, regardless of mode (absorbed, emitted, conduction, convection). The versatility of the radiometer is due to its configuration and the data reduction technique used to determine the heat transferred into the sensor by each mode, or a selected combination of modes. The sensors may be considered as elements in a thermal circuit in which heat flow is measured by the temperature differential across them, just as current flow is measured by the voltage differential across a low-value resistor.

IRRADIANCE MEASUREMENTS IN THE SOLAR SPECTRAL RANGE

For measuring irradiance only in the solar spectral range (0.2 to 3.5 microns wavelength), the radiometer is outfitted with a half-silvered quartz window (fig. 3) that is similar to the window used in a split disc bolometer commonly used in solar simulation practice. The window is circular, one-half is clear with the other half bearing a vacuum deposited aluminum coating. The window is mounted on the radiometer so that the aluminum is used as a second surface reflector. The aluminum is coated over with black matte paint, so both sensors view a surface of high emittance (the quartz is also very high emittance). In this configuration, the sensor covered with the second surface mirror receives radiation only from the quartz, whereas the sensor viewing through the clear quartz receives transmitted radiation as well as that emitted by the quartz. If the negative electrical outputs of the two radiometers are tied together, and the positive output of the mirrored sensor is connected to the negative terminal of a millivoltmeter, and the positive lead of the unmirrored sensor to the positive terminal, the radiometer will measure the net transmitted radiation through the window only, being a single compensated radiometer. A stand-off ring must be employed to keep the quartz window from contacting the sensor surfaces. A ventilation hole must be provided for gas pressure between the window and the sensor to be the same as that of the environment. The window mounting device must be designed so that pressure on the radiometer body is avoided (as applied with a set screw). A slight distortion of the body may cause a sensor to detach from the body. Finally, the window must be very carefully aligned over the sensors so that the mirror edge is exactly over the line separating the two semicircular sensors.

MEASUREMENT OF TOTAL INCIDENT IRRADIANCE

Total solar and infrared incident irradiance can be measured by either sensor when no window is employed. The signal received is proportional to the net heat transferred through the sensor. To determine the incident irradiance on the sensor the quantity σT_R^4 must be added to the net transfer value (T_R = radiometer temperature, σ = Stefan-Boltzmann constant). An emissive value is not necessary because assuming the black matte coating is a "gray" surface, absorptivity is the same as emissivity. If the radiometer is calibrated for incident irradiance, no adjustment in the amount of calculated emitted irradiance is necessary.

MEASUREMENT OF NET ENERGY TRANSFERRED THROUGH A SURFACE

If the radiometer is coated with a particular gray or nongray material and is employed without a window, the signal generated by the radiometer is proportional to the net heat transferred through that surface at the temperature of the radiometer. The sensitivity factor (calibration) of the radiometer in heat per unit area per unit time per millivolt is adjusted by dividing that value by the hemispherical emittance of the black matte coating on the radiometer present when the radiometer was calibrated. The best method of calibrating the windowless radiometer is to place it in a vacuum chamber outfitted with a black matte liquid nitrogen cooled shroud. The radiometer should be mounted on an aluminum or copper block having water or water-glycol solution flowing through at a minimum rate of 0.2 gallons per minute. The water temperature should be controlled by a suitable circulating bath. The output of the radiometer when viewing the cold environment at a pressure of less than 10^{-5} torr is proportional to the heat emitted to the environment, less a small amount of heat received. The sensor sensitivity can be determined according to the following equation:

$$\text{millivolts output (mv)} = \frac{\sigma T_r^4 - \sigma T_w^4}{S}$$

where σ = Stefan-Boltzmann constant,
 0.173×10^{-8} btu/ft² - hr °R⁴

S = radiometer sensitivity for
incident radiation

T_w = shroud (wall) temperature - °R

T_r = radiometer temperature - °R

This calibration is a single point absolute calibration for hemispherical infrared radiation viewed in a vacuum. To convert the calibration to net heat transferred through the radiometer, the value S is divided by the hemispherical emittance of the black matte surface, which is approximately 0.89.

MEASUREMENT OF SOLAR ABSORPTANCE AND EMITTANCE OF AN UNKNOWN SURFACE

If a sufficiently thin (0.005-inch or less) layer of a surface coating is applied on one sensor surface

and the other sensor left black, the emittance can be determined as follows:

$$\text{Emittance } [\epsilon] = \frac{\text{mv. coated sensor}}{\text{mv. black sensor}} \times \frac{\text{sen. coated sensor}}{\text{sen. black sensor}}$$

x emittance of black surface

If the windowless radiometer, in a vacuum chamber at less than 10^{-3} torr atmosphere views radiation from a solar simulator of good spectral quality, the solar absorptance of the unknown surface is determined as follows:

$$\text{Absorptance } [\alpha] = \frac{\text{mv. coated sensor}}{\text{mv. black sensor}} \times \frac{\text{sen. coated sensor}}{\text{sen. black sensor}}$$

x solar absorptance of black surface

CHARACTERISTICS AND PERFORMANCE

The physical and performance characteristics of the radiometer are as follows:

Diameter	1.5 inches
Depth	1.0 inches
Weight with window (without heater)	100 grams
Coating on sensors	3M Nextel 410C black
Range	0 to 3 solar constants
Sensitivity, with window	26 millivolts/solar constant
Time constant of response	0.5 seconds
Sensitivity air/ sensitivity vacuum	0.98
Drift in signal at one solar constant, window- ed configuration, tem- perature range -50° F to $+92^{\circ}$ F	1.0 percent
Linearity	$\pm 1/2$ percent within 0-3 solar constant range
Operating temperature range	-50 to 150° F
Drift in signal, radio- meter at room tempera- ture exposed to one solar constant, from 30 seconds after initial exposure to 2 hours later	0.3 percent

The light weight of the radiometer and ability to include all necessary controls and output information in a small single unit with a 10-wire cable make it very amenable for use in remote and fragile configurations. The high sensitivity and fast response permit its use in scanning systems. Since the ratio of sensitivity in air to that in vacuum is close to unity, only a single initial determination of this ratio is required for the radiometer. Other radiometers used in space environment testing have sensitivity ratios that are considerably less than unity and must be frequently checked for variation in that ratio. The low signal drift is due to the compensated configuration, which eliminates the signal due to window heating. Window heating of noncompensated solar measuring radiometers give errors of approximately 8 to 10 percent as the windows slowly heat on solar exposure to an equilibrium temperature.

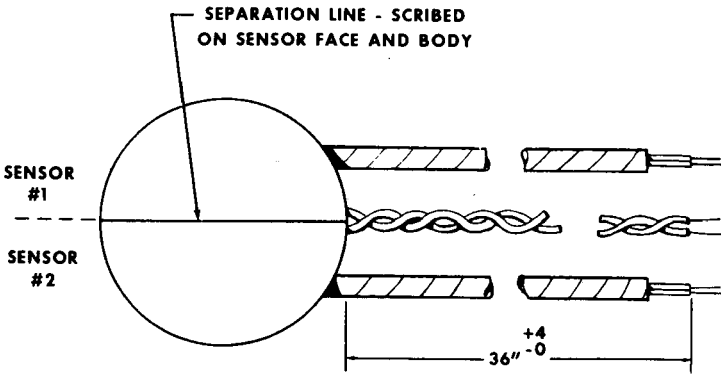


Fig. 1 - Basic two sensor instrument

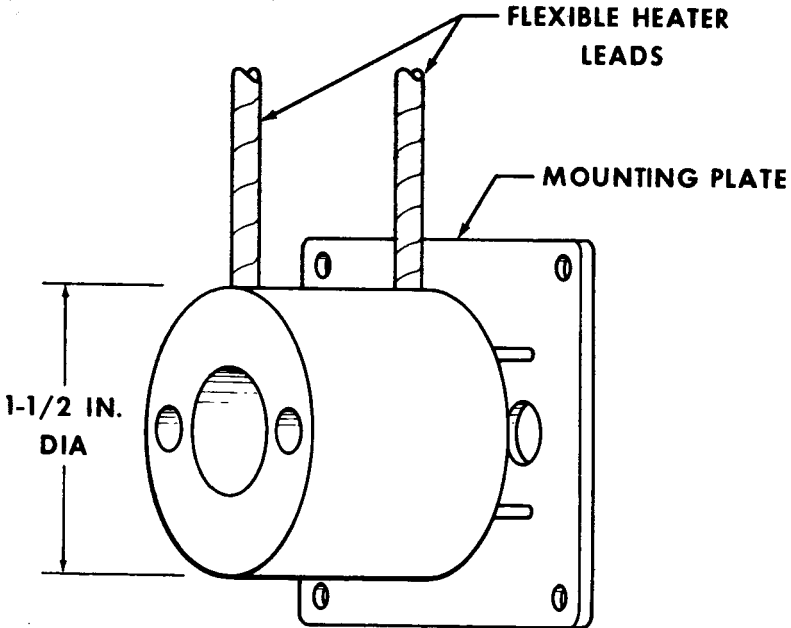


Fig. 2 - Heater Bezel

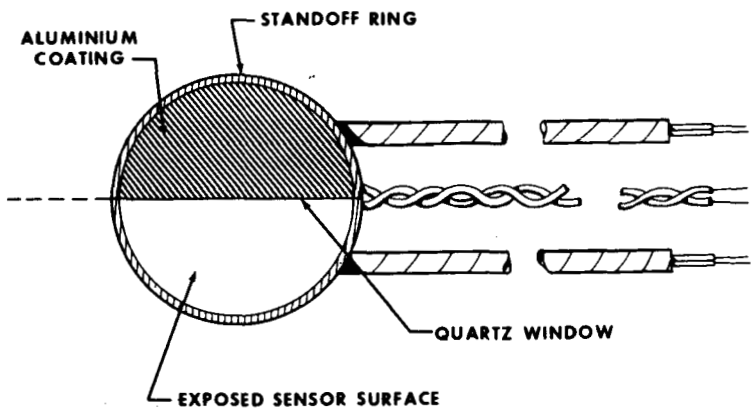


Fig. 3 - Configuration for solar measurement

**IMPROVED SPATIAL UNIFORMITY OF BEAM-PLANE
INTERACTION BY MEANS OF INVERSE RASTERING**Charles G. Miller, *Jet Propulsion Laboratory, Pasadena, Calif.****ABSTRACT**

An analysis is presented that shows the desirability and feasibility of conducting irradiations of large test objects by beams of penetrating radiation, by the method of moving the test object back-and-forth through the beam, rather than by sweeping the beam across the object. An extension of this method of inverse rastering allows the generation of composite beams with any desired intensity-vs-energy spectrum, obviating the need to determine equivalent damage factors for every energy in the spectrum.

INTRODUCTION

The study of the effects of penetrating nuclear radiation, particularly protons and electrons, on spacecraft-related parts, has been done in the past by allowing beams of these particles to emerge from an accelerator and fall upon the test objects. Test objects exposed to beams of radiation receive uniform exposure on all areas only when the beam is well collimated. If the beam is spread out with a large angular divergence, as needed for extended test objects, the uniformity of exposure suffers. If a collimated beam is rastered across a (large) extended object, the uniformity of exposure still suffers because of aberrations introduced into the beam when it is deviated farther and farther off axis in the rastering process.

Such off-axis aberrations are particularly important when using the high energy beams from accelerators, such as beams of electrons over one MeV and beams of protons over 20 MeV, both of which are needed to simulate planetary radiation belt radiations.

Present practice consists of spreading the beam to a small angular divergence, typically 4 or 5 degrees half-angle, which

*This paper presents the results of one phase of research carried out at the Jet Propulsion Laboratory, California Institute of Technology, under Contract No. NAS 7-100, sponsored by the National Aeronautics and Space Administration.

gives a field of 8- to 10-inch diameter at 60 inches working distance from the end of the accelerator beam exit window. The field is then mapped, and the most uniform 4-inch by 6-inch section is used for test irradiations. The tests must then be conducted exposing one 4-inch by 6-inch board at a time. For a representative test involving 25 such boards, there are required 25 separate irradiations, leading to an expensive--in terms of man-hours--test.

METHOD OF APPROACH

To avoid the need for irradiating test boards one at a time, which requires shutting down and starting up before and after each change, the present method has been developed which permits completion of such tests in two, or at most three exposures. Furthermore, the method reduces the importance of uniform beam pattern so that a wider variety of accelerators becomes useful for tests.

This method is a variant of rastering, which is a widely used method of covering a large target with a small beam. Rastering involves relative motion between a small beam and a large target to give complete, although not simultaneous, coverage of the target. There is thus time-sharing of the beam. Because the characteristics of the beam change due to aberrations introduced when the beam is magnetically deviated farther and farther off-axis in a rastering process, simple sawtooth time-sharing drive of the beam does not give acceptable uniformity of exposure over the whole target area. An improved method consists of moving the individual boards through a matching, apertured-beam field, so as to superpose all parts of the beam on all parts of the test boards, and thus average out spatial variation in beam intensity. This is, of course, the equivalent of holding the test boards fixed in space, and moving the beam back-and-forth across all parts of the test board. The advantage of moving the test boards is that the beam profile and beam intensity distribution do not change, since the beam does not leave the fixed beam-optic axis along the centerline of the system.

An example of the application of such inverse rastering would consist of the exposure of 12 test boards ganged in a three-wide by four-high array on a 24-inch by 24-inch support; (see Figure 1). A moving beam, to raster the 12 boards, would have to cover a field of 18 inches by 18 inches with a half-angle of $\arctan(9/60) = 8.5^\circ$, assuming a practical quadrupole-to-exposure plane distance of 60 inches. Such wide angle uniformity cannot be achieved with simple quadrupole magnetic lenses. However, if the test boards are moved past a small, fixed beam spot, say of 5 by 6 inches, such difficulties disappear. In use, a simple X-Y scanner with 24-inch by 24-inch motion could be adapted with a minimum of effort to carry the array of test boards back-and-forth through an apertured beam field.

CALCULATIONS AND RESULTS

The most useful and stable beam distribution that has been achieved in past proton exposures at Crocker Radiation Laboratory is shown in Figure 2. This meets the uniformity requirements needed for tests, but the restricted size of the beam requires exposing the test boards one by one, as had been discussed. If the test boards are drawn across this field pattern repeatedly, from left to right, starting as shown in Figure 3, and being raised an infinitesimal amount in the Y direction for each pass, the integrated exposure on every part of the test board would be precisely uniform no matter how greatly the distribution of intensity on the fixed particle field varied.

Since we cannot, in practice, conduct an irradiation using an infinite number of passes, it is necessary to see how satisfactory is a system using a small, finite number of passes per board. An examination of Figure 2 shows that the horizontal sweeps of the beam by a segment of the test board delivers decreasing values of fluence as the sweeps take place at increasing Y-values of the proton field. Assuming, as is evident from Figure 2 that successive, horizontal sweeps of short segments of the proton field give successively smaller proton fluences as the sweeps increase their Y-value, we can schematically plot the proton flux in relation to the Y-location, as in Figure 4A where ϕ is the value of the proton flux rate, p^+/cm^2 sec per unit of Y-distance, and ranges from a maximum of a, when $y = 0$ to a minimum of b when $y = y_0$, y_0 being the height of the proton fixed field which is equal to the height of the test board. In general, the contour C which gives the value of ϕ for any chosen value of Y will be irregular. For the situation shown in Figure 2, the value of ϕ will decrease generally as shown in Figure 4A from the value a to the value b.

To make the problem tractable, let us assume that a $y-\phi$ diagram can be represented as in Figure 4B where the value of ϕ decreases uniformly from a to b. If a test board were simply exposed to the field, having a $y-\phi$ relation as shown, the bottom strip of the board would have a proton fluence of a, the top strip of the board would have a proton fluence of b, and the average exposure would be $(a + b)/2$. The percentage variation from the average of the top strip is $100((a - b)/(a + b))$. If, as might be required by a Test Plan, the maximum variation in fluence across the test board must be less than $\pm 30\%$, then $((a - b)/(a + b)) = < 0.30$ and $a \leq 1.86 b$ for a stationary board exposure to be within $\pm 30\%$. If the test boards are swept through the beam in the X-direction, stepping Δy between steps, i.e., with an overlap $\Delta y/h_2$ or h_1/h_2 (see Figure 5) between steps, the uniformity increases markedly as shown in Table I.

TABLE I									
Ratio of Maximum Fluence-to-Minimum Fluence On Any Location On Test Board									
No. of Passes:		1	1.33	2	3	4	5	6	
Equiv. Amt. of Overlap:		0%	33%	50%	66%	75%	80%	87%	
Ratio a:b	}	∞	∞	4.00	3.00	2.00	1.67	1.50	1.40
		3:1	3.00	2.80	1.60	1.40	1.28	1.22	1.18
		2:1	2.00	2.50	1.40	1.25	1.18	1.14	1.12
		1.5:1	1.50	2.28	1.22	1.14	1.10	1.08	1.07

The analytical development is quite straightforward, but rather lengthy. If Table I be translated to resultant maximum deviation from the average fluence delivered to a test board, we find the values given in Table II.

TABLE II									
Percent Variation of Fluence, \pm Percent from Average									
No. of Passes:		1	1.33	2	3	4	5	6	
Equiv. Amt. of Overlap:		0%	33%	50%	66%	75%	80%	87%	
Ratio a:b	}	∞	100	60	50	33.3	25	20	16.67
		3:1	50	47.5	25	16.6	12.5	10	8.33
		2:1	33	43.0	16.67	11.1	8.33	6.67	5.56
		1.5:1	20	39.2	10	6.5	5	4	3.33

It seems practical to allow the ratio a/b to vary by 3:1, and use three passes/board which will give a field flatness of $\pm 16-2/3\%$. A larger number of passes/board while possible, does not bring down the percentage variation very rapidly (see Figure 6).

The foregoing discussion leading to Table II represents a worst-case situation based on a uniform $y-\phi$ distribution, as shown in Figure 4B. If we were to select the beam so as to have

more symmetry about a y traverse near the center of the apertured field, i.e., with a hot spot in the center of the apertured field, we should expect a y- ϕ diagram, as sketched in Figure 4C. In such a case, the percentage variation, similar to the values derived for Table II, would depend on the relation between the number of passes (relative size of the Δy step in exposure sweep) and the ratio a/b, the values in Table II representing the worst-case percentages, so that uniformity would, in every case, be better than the values shown in Table II.

SPECIAL FEATURES AND OPPORTUNITIES

Generating Spectral Intensity Matched Beam Instead of Monoenergetic Equivalent Beam

It has not, in the past, been practical to do any but monoenergetic electron or proton beam exposures, even though what we wish to simulate in the laboratory is the actual penetrating radiation flux which has a well known intensity-vs-energy spectrum (see Figure 7, adapted from Reference 1). The use of a monoenergetic beam requires the Test Plan to have an equivalent damage function for each energy band in the spectrum. The equivalent damage function will vary for different types of test objects (e.g., npn and pnp transistor damage functions response will require different equivalents). Since such damage equivalences are not known with sufficient precision, monoenergetic testing is less realistic, less satisfactory, and more costly than a matched energy spectrum-vs-intensity beam for testing.

It has always been possible to produce a variety of proton or electron energies in the form of abutting or overlapping parallel sub-beams from an original single high energy beam by the method of placing a number of absorbers that act as energy degraders, side by side across the beam. Without relative motion of the beam and test area, however, each **area** of the test object would receive a different distribution of the several energy ranges produced by the absorbers. With the use of inverse rastering, it becomes practical and straightforward to superpose all parts of the various energy sub-beams on every part of the test object, thus allowing any desired intensity-vs-energy spectrum distribution to be used for testing purposes.

The construction of a graduated absorber-set across the fixed beam aperture is shown in Figure 8. Such an absorber-set, when placed in front of the high energy proton beam, will give rise to sub-beams of energy dependent on the depth d of the absorbing material. The relative contribution of each sub-beam will be proportional to the width w of each absorber strip. The two factors, w and d, can be adjusted independently to allow any desired spectrum to be simulated in a finite, reasonable number of steps.

Some Possible Undesirable Consequences of Raster Exposure

The use of any rastering technique gives rise to high peak-to-average flux rates during the irradiation, since the beam is irradiating any given location only a small fraction of the total time of exposure. Under some circumstances, a high peak-to-average exposure may be undesirable.

A further point that must be taken into account is that every test exposure by means of high energy radiation is accompanied by an induced flux of undesired, secondary radiation, e.g., neutrons and bremsstrahlung, caused by the interaction of the primary beam with the experimental environment. An irreducible minimum of contaminant radiation, even in non-rastered exposures, is that due to the interaction of primary beams with mounting hardware, and with the air in the vicinity of the test object. Figure 9 shows some neutron production efficiencies as a function of primary proton energy and atomic number. We note that for 12 boards ganged on an X-Y transport, as shown in Figure 10, a complete exposure, with repeated passes through the beam, would keep each board in the vicinity of the "target area", and exposed to the contaminating radiation for a length of time equal to 30 times the stationary board exposure time. The 30 X factor arises from the ratio of the total area shown in Figure 10, including overtravel to the area of the beam at the test plane, here taken as 6 inches x 5 inches to agree with one test board. The factor of 30 could possibly be reduced to a factor of 18 by the use of a one-inch wide by five-inch high fixed field, instead of the 6-inch wide x 5-inch high fixed field, when exposing the test boards. This could eliminate almost all of the overtravel area on the right and left sides of the arrangements shown in Figure 10. For tests of current interest, increases by a factor of 18 to 30 in contaminant secondary radiations would not compromise test results. Future tests which may require lower contamination levels can be accommodated if more attention is paid to the experimental arrangements. For example, less massive or lower atomic number materials in the mounting hardware, or replacement of the ambient air by helium gas or by vacuum environment will decrease the amount of secondary radiation markedly.

SUMMARY AND CONCLUSIONS

Uniform exposure of an extended test plane by a beam of penetrating nuclear radiation can be accomplished by a method of inverse rastering in which the workpiece moves, and the beam remains constant in direction. Methods to ensure that the beam remains stable in position and in time are described in the literature (Ref. 2).

The amount of exposure experienced by any area on the test plane as it is systematically moved back-and-forth across a fixed direction beam is found by numerical integration of the flux-time

product for each point on the test plane field, as the test plane is rastered in the X-direction and advanced in the Y-direction with respect to the fixed beam. It is shown that for a non-uniform beam of intensity ratio 3:1 top to bottom, only two passes through the beam will reduce the test object variation to $\pm 25\%$ from the average. For a non-uniform beam of 100:1 intensity ratio, top to bottom, only four passes (through one beam height) will reduce the test object variation to $\pm 25\%$ from the average. Uniform exposure can result from the use of even exceedingly non-uniform beams as long as the beam does not vary with time.

The method of inverse rastering allows the generation of a composite, time-shared beam with any desired intensity-vs-energy spectrum. Such a beam can be used for testing purposes, avoiding the need to determine equivalent damage factors for each energy in the spectrum.

REFERENCES

1. Parker, R. H. "Effects of Electrons and Protons on Science Instruments," in 'Proceedings of the Jupiter Radiation Belt Workshop,' TM-33-543. JPL July 1972, p. 173.

See also Divita, E. "Impact of Jovian Radiation Environmental Hazard on Spacecraft and Mission Development Design," Ibid, pp. 189, 190.
2. Peterson, D. G. "Proton Beam Positioning System with Computer Control," Nuclear Instruments and Methods, 104, 451 (1972). Note especially refs. 1-12 in this citation.

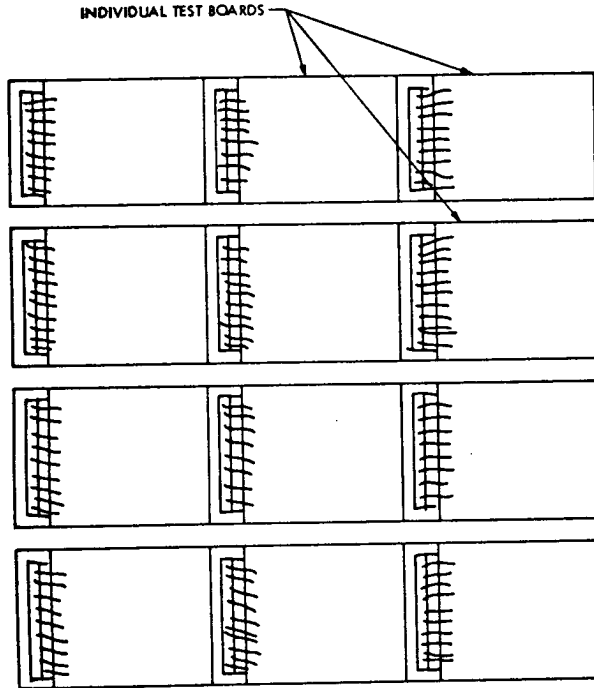


FIG. 1 Arrangement of assembly of test boards. Assembly to be moved as a group past fixed particle beam.

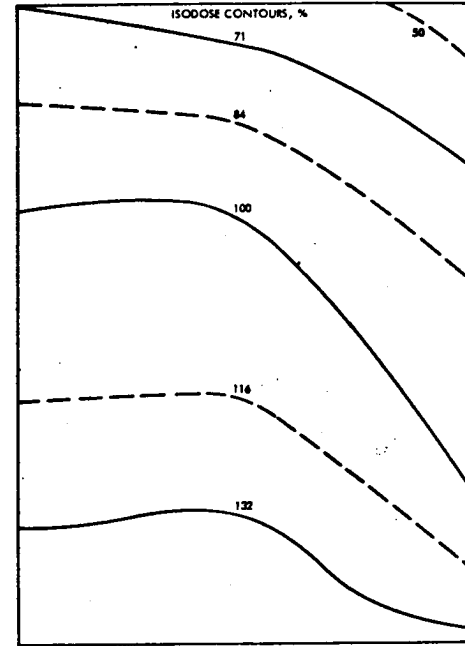


FIG. 2 Isodose contours showing variation of intensity in proton beam at target plane.

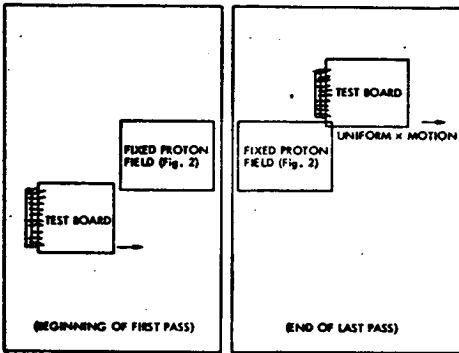


FIG. 3

Inverse rastering. Test board moves back-and-forth in x-direction, advancing in fixed increments between x-sweeps.

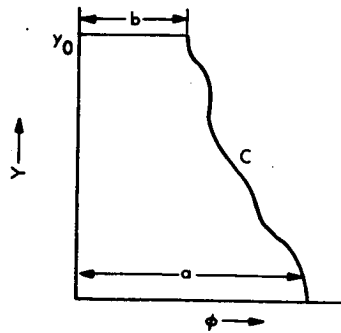


FIG.4A

Integrated value of fluence falling on differential element of area $y \cdot x$, as element of area is drawn at uniform time rate across fixed beam field of Fig.2, for every value of y .

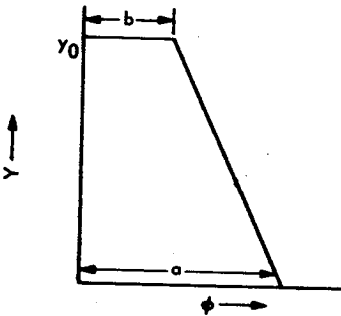


FIG. 4B

Straight-line approximation to contour C shown in Fig. 4A.

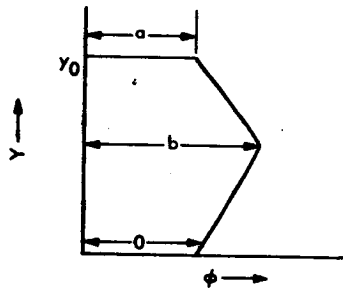
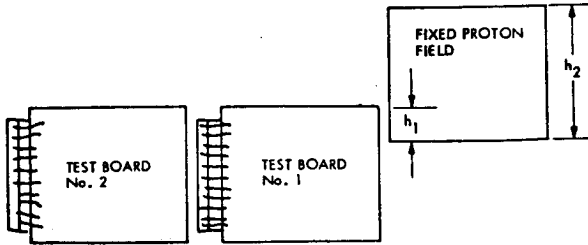


FIG. 4C

Straight-line approximation to contour when maximum ϕ is at an intermediate value of y rather than at an extremum of y .



OVERLAP = h_1 / h_2

NUMBER OF PASSES TO COVER ALL PARTS OF A TEST BOARD: $(1/\text{OVERLAP}) = (h_2/h_1)$

FIG. 5 - Nomenclature for 'overlap' ($=h_1/h_2$), and "height" ($=h_2$).

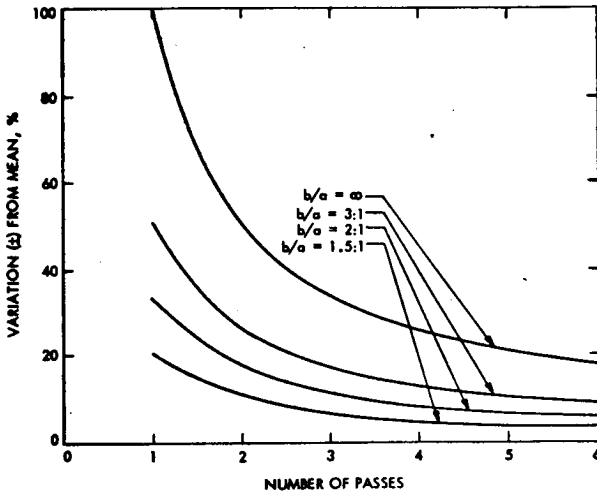


FIG. 6 - Uniformity of exposure of test board as a result of inverse rastering. Percentage variation from mean exposure in relation to number of passes, for various ratios of maximum ϕ : minimum ϕ as in Fig. 4A

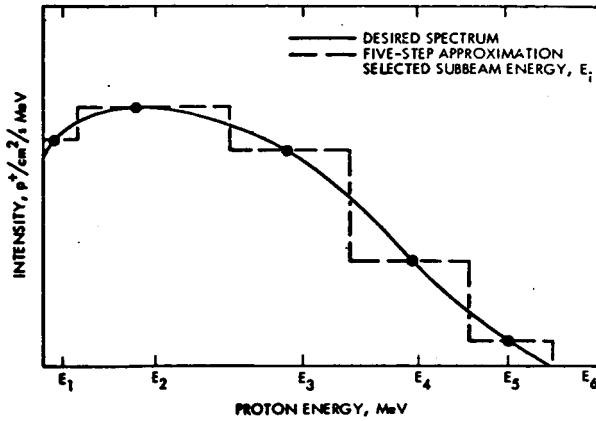


FIG. 7 - Intensity-vs-energy distribution for planetary trapped radiation (schematic) and 5-step approximation to distribution.

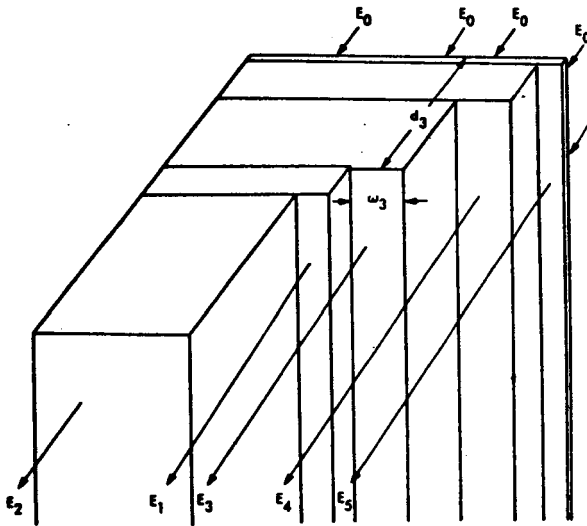


FIG. 8 - Construction of stepped energy-degrader to generate 5 sub-beams of energy E_1, E_2, \dots, E_5 from original beam of energy E_0 .

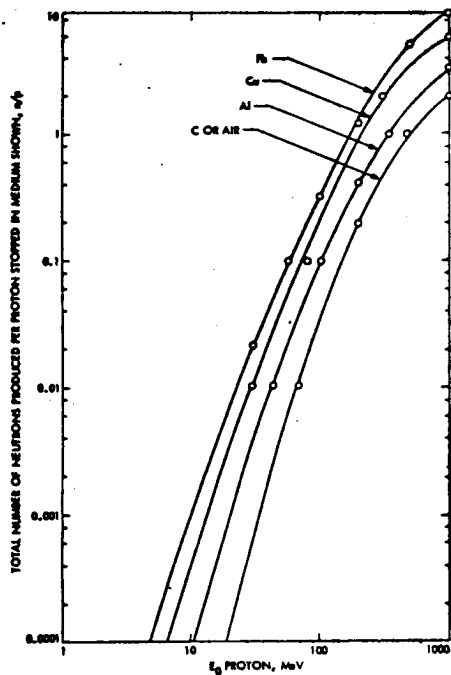


FIG. 9

Total neutron production efficiencies, n/p , for various energies of incident protons on varying atomic number targets.

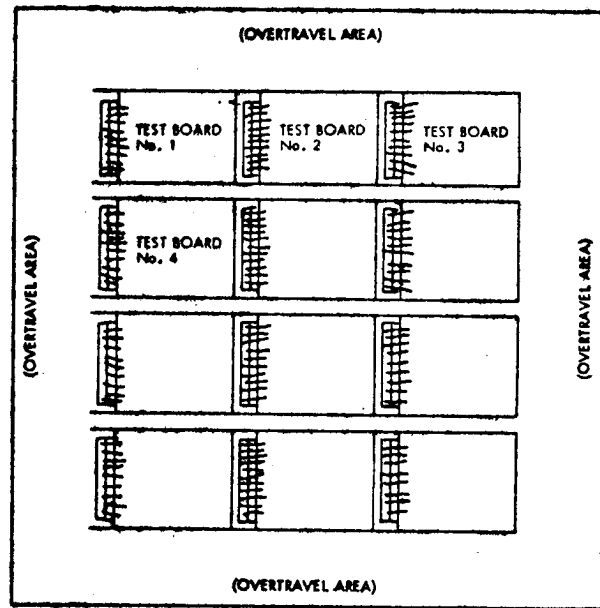


FIG. 10

Configuration, showing required overtravel area for inverse rastering of 4 x 3 board array, when fixed beam is same size as any one test board.

N74-10290

AN ABSOLUTE TOTAL RADIATION RADIOMETER FOR MEASURING A WIDE RANGE OF IRRADIANCES IN SPACE SIMULATORS

J. M. Kendall, Sr., *Jet Propulsion Laboratory, Pasadena, California*

INTRODUCTION

The Jet Propulsion Laboratory has developed a radiometer designated MK IV which is especially suited for use in space chambers for measuring a wide range of simulated solar irradiances during tests of spacecraft. The radiometer is now in use in several space chambers in both USA and in Europe. The MK IV is a further development of the radiometers described in references 1 and 2.

The MK IV radiometer has an absolute accuracy of $\pm 0.5\%$ and is self-calibrating. On this account it is not necessary to compare the MK IV with any other standards, since it itself can very well serve as a primary standard. It has uniform responses over the entire spectrum, uv, visible, and on into the far ir. Furthermore, measurements can be made with the stated accuracy of 0.5% throughout a range of irradiances of about 0.1 KW/M² up to 42 KW/M² (30 solar constants). The radiometer performs equally well in the environment of the space chamber under high vacuum with LN₂ chilled shrouds, or in normal room environment at 25°C and 1 atmosphere pressure. It is generally used without a window on the radiometer. Of course, should it be desired to use a window, it is then necessary to make the necessary allowances for the effect of the window on the response.

DESCRIPTION OF THE RADIOMETER

Figure 1 is a photograph of the radiometer, and Figure 2 is a sketch showing the cross section. The most essential part of the radiometer is the internally blackened cavity which constitutes a small blackbody. Thermally connecting the cavity to the main body of the radiometer is a thermal resistor, which conducts heat produced in the cavity to the main body, whose temperature is held constant either by water of constant temperature flowing through the tubular coil around the main body, or else by the controlled electrical heating of the main body. The temperature drop across the thermal resistor (measured by a thermopile), serves as a measure of heat flux through the thermal resistor of the heat produced by the incoming irradiance, or produced by the calibrating electrical heater built into the cavity. When the current and voltage fed to the calibrating heater are accurately measured, this heater produces heat which is accurately equiva-

lent to that produced by incoming irradiance so that, together with the thermopile response, a means is available for obtaining an accurate calibration of the radiometer without making a comparison to any other standard. This is why the MK IV can itself be considered as a primary standard.

An electronic control unit has also been developed. With the built-in DVM, it gives a continuous readout in absolute values in selectable units of the irradiance being measured.

The radiometer is generally used without any window, which (except under special circumstances) can cause complications in interpreting measurement results.

The overall dimensions of the MK IV radiometer are 2 inches (51 mm) in diameter, and 3 inches (75 mm) long. The area of the aperture is very nearly 1 cm². The radiometer weighs 0.9 Kg.

CHARACTERISTICS

Basically, the accuracy of the radiometer depends on:

1. Area of the aperture.
2. Electrical measurements of current and voltage to the calibration heater.
3. Effective absorptance of the cavity.

Measurements of area of the aperture, and measurements of current voltage are straightforward and present no difficulties. The effective absorptance of the cavity has been calculated. The black coating used inside the cavity has an absorptance of about 0.98, but the cavity enhancement of the absorptivity brings the overall effective absorptance up to 0.998. Since an allowance can easily be made for the 0.2% lack of perfect blackness, there is essentially no loss of accuracy from this cause.

With everything considered, measurements by the radiometer are within 0.5% of true values. This statement has been verified by using the radiometer to make an experimental determination of the Stefan-Boltzmann constant. (See Ref. 2). The value found was within 0.3% of the theoretical value of the Stefan-Boltzmann constant. This circumstance gives an indication of the accuracy of the MK IV.

Over the range of irradiances of 0.1 KW/M² to 42 KW/M², the MK IV is within 1.5% of being perfectly linear. This deviation can easily be measured by calibrating the radiometer at various levels throughout this range. The effect of this small non-linearity can easily be allowed for in measurements, so that the non-linearity does not introduce error.

When the temperature of the main body of the radiometer is held constant at some standardized value, the calibration of the radiometer remains constant. If the temperature is not held constant, then the radiometer sensitivity increases with increasing temperature through the variation of sensitivity of the chromel constantan thermocouples making up the thermopile. For example, if the water temperature varies 3°C from the standardized value, the calibration constant of the radiometer is changed about 0.25%.

The $1/e$ time constant of the radiometer is between 7 and 8 seconds for a step change in irradiance. If the step change is large, like zero up to 1 solar constant from either irradiance or from calibration heating, then stabilization to 0.1% is attained after one minute.

RESPONSE IN DEPENDENCE ON VIEW LIMITING

Radiometers are frequently provided with view limiters, and the MK IV is no exception. However, the MK IV can be used without a view limiter, or on the other hand, it can be view limited to as small an acceptance angle as desired. For use in space chamber, it is generally desirable not to view limit the radiometer too much. The radiometer should at least be capable of viewing the mirror in the space chamber, and certainly must have an acceptance angle which is considerably wider than the angles due to lack of collimation and divergence of the beam.

Figure 3 shows three different responses of the MK IV with three different amounts of view limiting and Figure 4 shows how the angle ϕ is to be taken. Curve 1 shows the angular response with no view limiting (so called 180° setup). Curve 2 is with the normal view limiting used in the JPL space chamber. In this case the viewing angle is about 80° . Curve 3 shows a response with a view limiter giving about 40° . It is to be noted that even the 180° arrangement has considerable directivity. In other words, such a radiometer has by far most of its response in the general direction in which it is aimed. It sees very little to the sides, and, of course, nothing in the opposite direction. A more restricted view limiting simply accentuates the directivity, resulting in less response to off-axis irradiances.

For space chamber work, any degree of view limiting from 180° down to 40° (see Figure 3) apparently can give satisfactory results. In other words, the degree of view limiting above a certain value is not very critical.

Generally, as shown in Figure 5, the radiometer is mounted in the space chamber with its axis aimed at the simulated solar source, and it is located enough ahead of the spacecraft under test so that the radiometer will not "see" any of the spacecraft. Then irradiances from the LN_2 cooled shrouds on the sides and below or behind (if in a horizontal space chamber) the spacecraft, as well as any "hot spots" in the chamber will not enter into the measurement by the radiometer. Fortunately, in a properly designed space chamber, the magnitude of these effects is quite small, of the order of a couple milliwatts/cm². Hence, only a rather crude estimation of their magnitude is usually sufficient for making an allowance for these effects. On the surfaces of the spacecraft facing the simulated solar source, no correction to the irradiance measurement is made, since it is assumed that the radiometer has measured the sum total of irradiances from the simulated solar source and from stray effects from the mirror, and the neighboring areas.

TARE

When no irradiance is applied to a radiometer, one would expect the radiometer would give a zero indication. As anyone who has made measurements with radiometers well knows, zero applied input seldom gives zero indication. In other words, with zero applied irradiance, there is a definite indication of input. This anomalous indication is frequently referred to as tare. If tare is not correctly taken into account, a serious degradation to the measurement accuracy can result. Hence, tare phenomena are very important and deserve to be carefully considered.

Tare does not usually represent an imperfection in the radiometer, for tare can, and usually does occur, with every type of radiometer, except certain special conditions. With a total radiation radiometer, tare generally is observed when the temperature of the radiometer differs from the temperature of the surrounding environment. As long as the radiometer and environment are above absolute zero temperature (0°K), infra-red radiation to which the radiometer responds is very much present. The environment emits ir some of which finds its way into the aperture of the radiometer, and at the same time the radiometer is itself radiating ir. If, for example, the radiometer is at a different temperature than the environment, the radiometer will probably absorb a different amount than it is emitting, and hence will indicate a "tare" reading. If the radiometer is warmer than the environment, it will be emitting more radiation than it is receiving and will then indicate a negative tare. For the special case that the environment is everywhere at a uniform temperature and the radiometer is also at this same uniform temperature, then there is no net exchange of radiation between radiometer and environment. Under these conditions the tare is zero.

This condition for zero tare is approximated when the radiometer is in an ordinary room with everything (radiometer included) at a settled temperature. The tare is then small, being usually less than one milliwatt/cm². In the case of the radiometer in the space chamber, the conditions are far different when the space chamber is chilled by LN₂, and the radiometer is maintained at a constant temperature such as 25°C, the radiometer is emitting radiation characteristic of 25°C, but the chilled shrouds of the chamber are emitting almost no radiation. Hence the radiometer indicates a very large negative tare.

The magnitude of this tare is given by

$$\text{Watts/cm}^2 = A\epsilon F_{1-2} \sigma (T_{\text{walls}}^4 - T_{\text{rad.}}^4)$$

where

$$\text{Watts/cm}^2 = \text{watts/cm}^2 \text{ (sometimes designated as } W_L)$$

$$A = \text{area of radiometer aperture in cm}^2 = 1 \text{ cm}^2$$

ϵ = emissivity (or absorptivity) of radiometer cavity ≈ 1

F_{1-2} = view factor of radiometer. 0.36

σ = Stefan-Boltzmann constant. 5.6697×10^{-12}

T_{walls} = Kelvin temperature of space chamber shrouds. 80°K .

$T_{\text{rad.}}$ = Kelvin temperature of radiometer. 300°K .

Substituting the assumed numerical values given above, and applicable to the MK IV, in the above expression gives a tare of $-0.016 \text{ watts/cm}^2$, which is 12% of one solar constant.

With a tare value of $-0.016 \text{ watts/cm}^2$, a simulated solar irradiance of $+0.016 \text{ watts/cm}^2$ must be provided in the space chamber to make the radiometer indicate zero. Hence, the correct intensity is arrived at only when W_t (in this case = $+0.016 \text{ watts/cm}^2$) is added to the radiometer indication. In other words

$$W = W_{\text{rad.}} + W_L .$$

DIRECT READOUT CONTROL UNIT

Also developed at JPL is a direct readout control unit (shown in Figure 6) for use with the MK IV radiometer. The unit has a built-in DVM used for indicating values of irradiances measured by the MK IV radiometer. Also built into the control unit are all necessary circuits and controls for calibrating the radiometer and adjusting the circuits so that the readout of irradiance shown by the DVM is in one of the selected units of irradiance: KW/M^2 , watts/cm^2 , milliwatts/cm^2 , watts/Ft^2 , or in solar constants. An additional control makes it possible to allow for tare.

Making a calibration of the MK IV radiometer takes no more than two minutes. Once the radiometer is calibrated and the tare adjustment made, the DVM then continuously indicates the irradiance being measured. A BCD output from the DVM provides for continuous recording of the irradiance as a function of time.

CONCLUDING REMARK

The combination of the MK IV radiometer and the associated control unit provides an accurate and convenient means for making measurements of irradiance of total radiation. The MK IV radiometer has been in use in the JPL space chamber for several years, and has been used for monitoring simulated solar irradiances of all space crafts tested during this time.

REFERENCES

1. Kendall, J. M. Sr., Primary Absolute Cavity Radiometer, Technical Report 32-1396, Jet Propulsion Laboratory, Pasadena, Calif., July 1969.
2. Kendall, J. M. Sr., and Berdahl, C. M., "Two Blackbody Radiometers of High Accuracy," Applied Optics, Vol. 9, p. 1082, May 1970.
3. This paper presents the results of one phase of research carried out at the Jet Propulsion Laboratory, California Institute of Technology, under Contract No. NAS 7-100, sponsored by the National Aeronautics and Space Administration.

Fig. 1 - JPL MK IV Radiometer

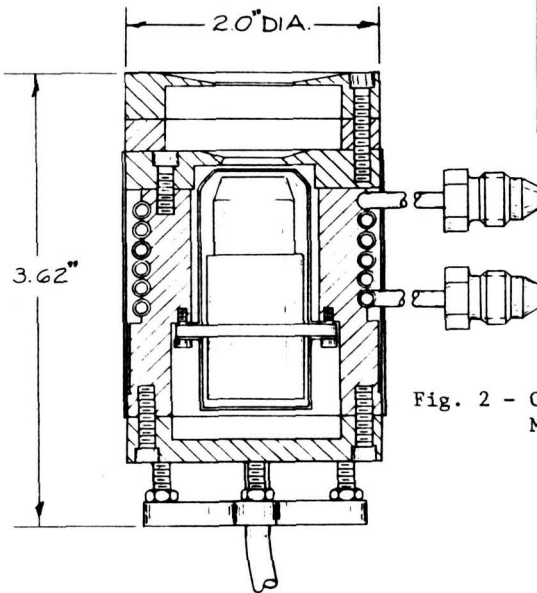


Fig. 2 - Cross section of the MK IV Radiometer

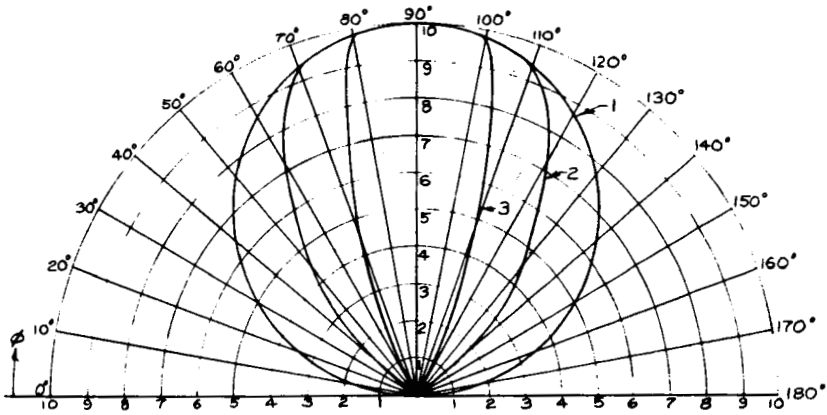


Fig. 3 - Relative response of the MK IV Radiometer with three different view limiters

- 1. - No view limiting (180°)
- 2. - View limiting as used in the JPL space chambers (80°)
- 3. - Smaller view limiting (40°)

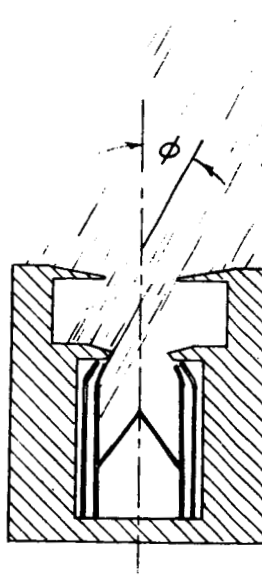


Fig. 4 - Angle of Incidence ϕ

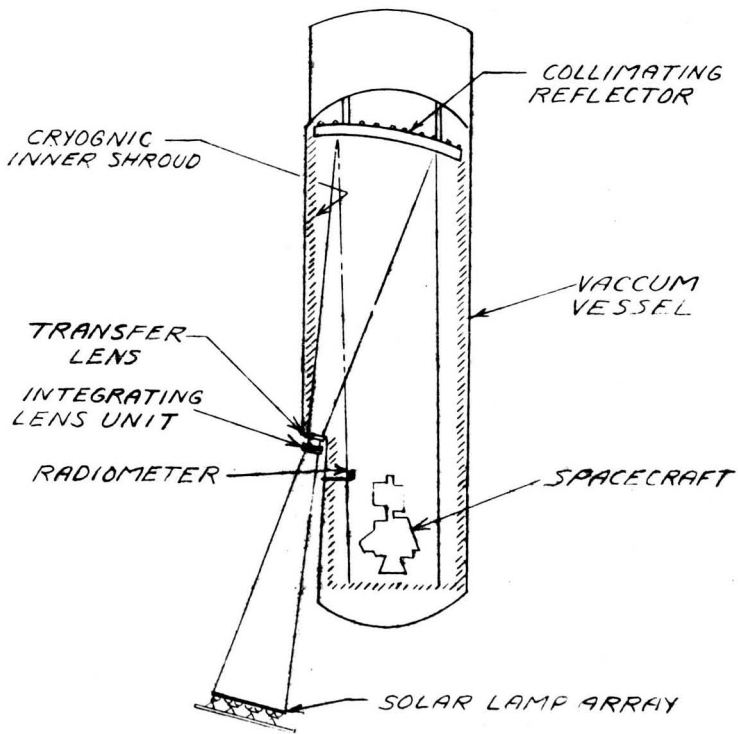


Fig. 5 - JPL Space Chamber, showing location of radiometer

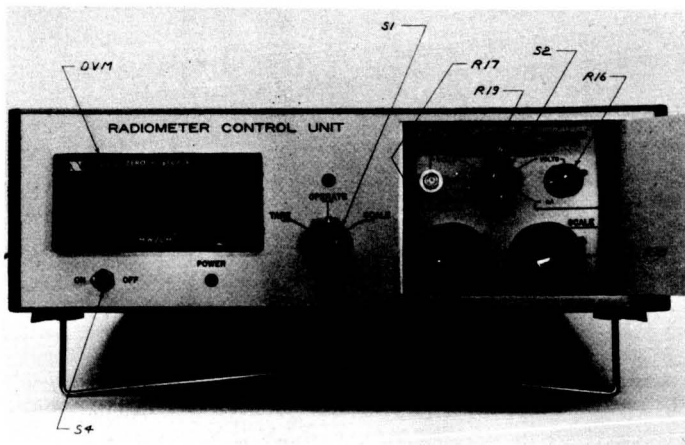


Fig. 6 - JPL Control Unit for use with the MK IV Radiometer

N74-10291

Paper No. 71

QUALIFICATION OF NONMETALLIC MATERIALS FOR THE VIKING MARS LANDER

W. K. Johnson and J. Y. K. Peng,
Martin Marietta Aerospace, Denver, Colorado

ABSTRACT

The Viking Mars mission has several unique environmental aspects that impose requirements on materials greatly surpassing those of previous space missions. Foremost among these requirements are: (1) the ability of all materials in the spacecraft to withstand exposures to 125°C for up to 100 hours without any deleterious effects; (2) a minimal or predictable change in material properties after 10 to 14 months exposure to the thermal vacuum environment of interplanetary space; (3) noninterference by materials of life detection and organic analysis experiments to be conducted on the surface of Mars. These requirements formed the basis for an elaborate materials qualification program. The elements of this program, including philosophy, test methods and facilities, are described.

INTRODUCTION

An extensive material qualification test program has been conducted to ensure the proper selection, processing, and application of nonmetallic materials in the design and construction of the Viking Mars Lander. As a part of the program, thousands of tests were conducted to derive basic thermochemical data, degassing data, and critical physical property data of nonmetallic materials ranging from marking inks to heat shield materials.

The vast amount of data obtained from this program will have significant value for both future aerospace programs and certain non-aerospace commercial activities.

Viking nonmetallic materials must be capable of withstanding the environmental conditions the probe will encounter before during and after its journey from earth to Mars. This includes sterilization temperatures of 125°C for periods of 100 hours or more, thermal vacuum exposures for periods of 14 months, and the ability to withstand the Martian environment without degradation or decomposition sufficient to interfere with the science package aboard the Viking Lander. Such areas as the soil sampling system, the organic analysis experiment, and the detection system have strict

requirements regarding the allowable organic contamination permissible as background in these systems.

A very significant aspect of the program described in this paper is in the discipline and controls employed. No other major hardware material qualification program to date has dictated the rigid control on facilities, methods, and materials as has occurred in the Viking Program. One reason for this strict discipline is that the qualification testing on any one material is extensive, and in comparing data from different lots and batches with the material originally qualified, no question should arise as to the methods or facilities employed. A second reason for the discipline in this program is the sheer magnitude of the effort. If careful recordings of each test were not maintained in an organized, disciplined fashion, the total volume of data would make it virtually impossible to reconstruct the test history associated with any single material. Finally, for any material tested, the material processing history and traceability up to the point of testing is of great significance since the chemical or physical behavior of polymers and other nonmetallics can be very dependent on prior treatment.

A significant fraction of the Viking Materials Program involves the selection of nonmetallic materials, since these materials as a class are considered most vulnerable to the Viking mission environment. This selection process for nonmetallics involves both chemical and physical property determinations. Considerable effort has been spent in the screening of candidate materials, the qualification of successfully screened materials, and the tracking or fingerprinting of qualified nonmetallics through hardware production.

MATERIAL SELECTION AND CONTROL

A candidate materials list was generated for the qualification program by using the following sources: 1) prior space vehicle history; 2) prior laboratory screening tests in other laboratories; and 3) preliminary in-house laboratory screening tests. Materials having little or no prior history for which a definite need was established on the program were screened in-house using vacuum thermogravimetric analysis combined with residual gas analysis. These specific tests, being relatively inexpensive and of short duration, give a good deal of information relating to material's thermal stability, degassing properties, cure effectiveness, resin content, etc. A further advantage of this technique is the small sample (12 to 20 mg) required for testing.

All candidate materials were assigned a specific identification number. Each material lot/batch was assigned a different number, even though the material may have been obtained from the same source and was supposed to be the same material type. Using

this method, it was possible to trace all the information regarding material, process, preparation, testing and qualification or rejection of any given lot or batch. Once the material had been subjected to all the necessary testing, a complete file of the test data was presented to a material review committee whose function it was to pass judgment on unlimited use, restricted use, or rejection for use on the Viking Lander.

A formal test report was generated for each material. This report contained a summary of the material history, test data compilation for both chemical and physical properties, and the conclusions reached by the review board. As a result of this action, material and process specifications were implemented to ensure the integrity of the materials used throughout the Viking Lander.

PROGRAM DESCRIPTION

Chemical Characterization

The chemical characterization phase of the qualification program consisted of the following tests: thermal degradation, mass spectral analysis, condensible outgassing, isothermal weight loss, and gas chromatograph-mass spectrometer analysis.

Thermal Degradation--Using thermogravimetric analysis (TGA), degradation testing from ambient temperature to 500°C or above was performed in a vacuum and, in some cases, nitrogen. The vacuum environment is representative of service, whereas the nitrogen simulates the sterilization environment.

Mass Spectral Analysis--To characterize the outgassing and degradation species during the TGA test, a residual gas analyzer was attached to the TGA apparatus to provide simultaneous mass spectral data during the vacuum TGA test.

Condensible Outgassing--The rate of deposition of condensibles from candidate materials was determined using a quartz crystal microbalance operating at -125°C in vacuum, the minimum temperature anticipated at the Martin surface.

Isothermal Weight Loss--To assess materials behavior during the sterilization cycle, isothermal weight loss tests were performed at 135°C for 100 hours in a nitrogen atmosphere.

Gas Chromatograph-Mass Spectrometer Analysis--For those materials used in the spacecraft in critical locations or in significant quantities, the material will be pyrolyzed and a gas chromatograph-mass spectrometer reference spectra generated. Testing of this type began in 1973.

A listing of the types of materials tested in this portion of the program is given in Table I. This table includes materials which did not get beyond the screening stage, but does not include "fingerprint" testing of different lot/batches of the same material.

Table I - Quantity of Nonmetallic Materials Chemically Tested

<u>Generic</u>	<u>Quantity</u>	<u>Application</u>	<u>Quantity</u>
Acrylics	2	Ablator	13
Butyl Rubber	6	Adhesive	127
Diallyl Phthalates	18	Coating	73
Epoxies	307	Elastomer	64
Ethylene Propylene Rubber	5	Electrical Insulation	110
Fluorocarbons	60	Encapsulant	65
Miscellaneous (principally inorganic nonmetallics)	92	Fabric	57
Phenolics	13	Film	25
Polyamides	20	Finish	12
Polycarbonates	1	Lubricant	24
Polychloro-P-Xylene	2	Marking	26
Polyester	43	Miscellaneous	20
Polyethylene	5	Molding Compound	9
Polyimide	45	Sealant	36
Polyolefin	2	Shock Insulation	10
Polypropylene	7	Structural Plastic	45
Polystyrene	5	Tape	18
Polyvinyl Chloride	1	Thermal Insulation	48
Polyvinyl Fluoride	6	Tubing	13
Silicone	123	Wire	18
Unknown	11		
Urethane	39		
Total	813	Total	813

Thermal Degradation TGA-RGA in Vacuum

A thermogravimetric analysis (TGA) combined with residual gas analysis (RGA) test is a short duration test which gives much information relating to the material's thermal stability, degassing properties, cure effectiveness, resin content, and the activation energy for thermal degradation. A further advantage of this technique is that only a very small sample (6 to 10 mg) is required for testing. Following sample conditioning, the specimen was heated in vacuum at a programmed rate of 10°C/minute to a maximum of 500°C or to the point at which decomposition is complete, whichever occurred first. Sample weight was continuously recorded throughout the heating cycle. Mass spectral data of evolved gases in the mass range m/e 2 to 250 was obtained at 10°C to 15°C intervals. RGA data from the screening test can be reduced in graphical form showing the change in relative peak heights

of significant m/e peaks (not present in background) versus sample temperature.

TGA-DTA in Nitrogen

In some cases, TGA-DTA tests were performed in a continuous nitrogen gas flow and other gaseous environments. In these tests Differential Thermal Analysis (DTA) was substituted for the RGA. This nitrogen testing was performed to determine whether the thermochemical behavior of the polymer is influenced by the presence of nitrogen (a common sealing gas). Samples were prepared, cleaned, and conditioned in the same manner as in the vacuum TGA screening test. TGA data can be reduced to a percentage weight loss as a function of temperature. DTA data can be reduced to give the temperature at which significant endothermic or exothermic reaction occurs.

Isothermal Weight Loss Prediction from TGA Data

Thermal degradation under vacuum, as measured by isothermal weight loss of polymers, has been studied for a variety of polymers by H. A. Papazian and his coworkers¹. Small samples of non-metallic materials have been used in the TGA tests. Isothermal studies, at much lower temperatures, have been made using larger samples (6.0 to 10.0 grams). Comparison of the two techniques has shown that the TGA result can accurately predict the isothermal kinetics.

Using the Arrhenius relation,

$$k = A e^{-\Delta E/RT} \quad (1)$$

and, accordingly,

$$\ln k = \ln A - \frac{\Delta E}{RT} \quad (2)$$

where k is the rate constant, A is known as the pre-exponential factor, and ΔE is the activation energy.

In the study of thermal stability of nonmetallic materials, the degradation reaction was found, in most cases, to be a first order reaction, and the degradation rate is directly proportional to concentration of the reacting substance,

$$-\frac{dc}{dt} = k c \quad (3)$$

where c is concentration of the reaction species, t is time. Let "a" be the initial weight of nonmetallics, and "x" the weight after time "t". The remaining weight is $(a - x)$, and

$$- \frac{d(a - x)}{dt} = k(a - x) \quad (4)$$

Therefore,

$$\frac{dx}{dt} = k(a - x) \quad (5)$$

From equation (1), the activation energy in Kcal/mole is

$$E = 4.574 \times 10^{-3} \frac{d(\log k)}{d\left(\frac{1}{T}\right)} \quad (6)$$

Integration of equation (5) yields

$$\frac{a - x}{a} = e^{-kt} \quad (7)$$

where a is the initial weight and $a - x/a$ is the fraction remaining. Therefore, if k is known for a given temperature, one can find the fraction of the polymer remaining for a predetermined time, t , or if the weight loss is desired,

$$(1 - e^{-kt}) \times 100 = \% \text{ weight loss} \quad (8)$$

Material Fingerprinting

To assure identity of materials used in the hardware phase of Viking with initial lot/batches of qualified materials, all later buys of most nonmetallics were subjected to a TGA-RGA "fingerprint" test as part of the receiving inspection function. In this manner, all new lots of material could be compared with the original qualification lot to ascertain that, chemically, the material and processing of that material were identical to the original qualification lot. This technique, put to test on over 800 materials to date, has proven to be an extremely sensitive tool in detecting small process variations.

Condensable Outgassing Tests

For measurement of outgassing, a standard method developed for use in the Viking Program is used. In this test, a quartz crystal microbalance is used to measure the rates of condensable degassing issuing from the sample. With the sample heated in an effusion cell, a cooled quartz crystal is located in close proximity to the orifice of the cell. As the degassed species issue from the cell and impinge on the surface of the quartz crystal, the condensable portion of the sample degassing

collects on the quartz, while the noncondensibles are pumped from the system. The sensitivity of this method permits condensible degassing rates as low as 1×10^{-5} percent/day to be accurately determined.

Nitrogen Weight Loss

The nitrogen isothermal weight loss tests were performed in accordance with a standard method developed for use to detect the material behavior during the heat sterilization cycle. The weight of the sample was measured before and after the 100 hours at 135°C with a 3 cc/minute nitrogen gas purge. The nitrogen purge outlet was cold trapped at -196°C during the test and then warmed up to room temperature while taking a residual gas analysis scan. For most materials, the condensibles were only air constituents.

GCMS Analysis

Those materials selected by the Viking Science Team to be used in the spacecraft in critical locations such as soil sampler assembly or in significant quantities will be pyrolyzed and a GCMS reference spectra determined. Tests of this type are to begin in the latter part of 1973.

Typical Qualification Test Summary (Chemical)

An example of a data summary of the thermochemical qualification testing of a typical nonmetallic, including TGA and DTA data (Figure 1) and mass spectral data (Table II) is as follows:

Material, EA934--EA 934 adhesive is a two part epoxy used for general purposes. This material is governed by MMA Viking Document TP 3720150 for all the control, specimen preparation and testing.

Vacuum, TGA--Onset of major degradation, $220^{\circ}\text{C} - 235^{\circ}\text{C}$ ($493^{\circ}\text{K} - 508^{\circ}\text{K}$). Weight loss at 135°C (408°K) ranges from 0.3 to 0.9% and consisted almost entirely of water loss. This loss occurred over the temperature range of $50^{\circ}\text{C} - 135^{\circ}\text{C}$ ($323^{\circ}\text{K} - 408^{\circ}\text{K}$). The highest water loss occurred in the specimen preconditioned at room temperature and 45% RH, while the lower water contents were observed in specimens preconditioned at 125°C (398°K) in nitrogen for 100 hours (3.6×10^7 sec).

Nitrogen, TGA--Onset of major degradation, $240^{\circ}\text{C} - 265^{\circ}\text{C}$ ($514^{\circ}\text{K} - 538^{\circ}\text{K}$). Weight loss at 135°C (408°K) was 0.45%. This loss occurred over the temperature range of $55^{\circ}\text{C} - 140^{\circ}\text{C}$ ($328^{\circ}\text{K} - 413^{\circ}\text{K}$). The specimen was preconditioned at room temperature and 45% RH for minimum of 24 hours prior to test.

Nitrogen Weight Loss--The weight loss in nitrogen after 100 hours

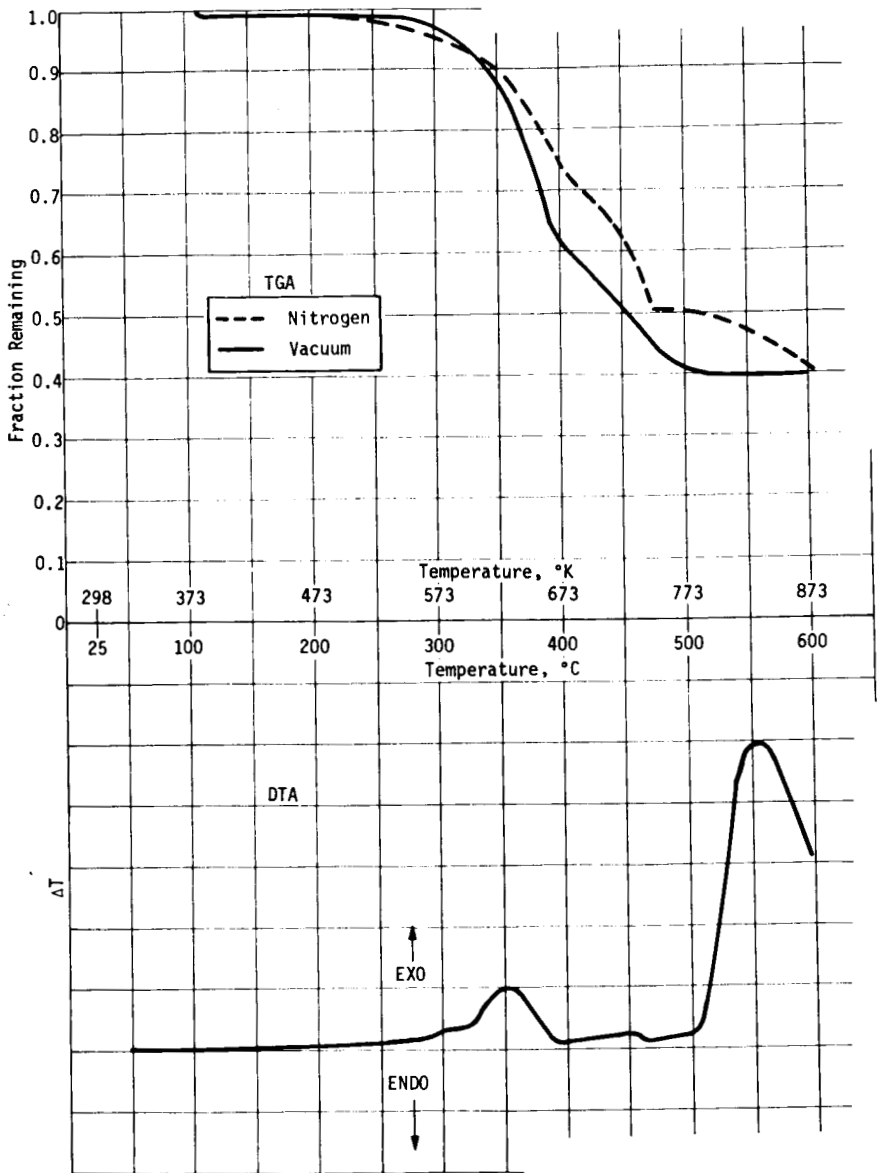


Figure 1 - TGA-DTA Curves for Epoxy Adhesive, EA 934

Table II

EA 934 Mass Number and Relative Peak Intensity

m/e	Temperature, °C						
	(298°K) 25	(573°K) 300	(623°K) 350	(673°K) 400	(723°K) 450	(773°K) 500	(823°K) 550
14	560	796	3 022	1 230	1 152	1 386	1 248
15	129	827	8 306	2 397	2 429	3 039	3 052
16	1 851	3 741	14 236	4 393	3 943	4 498	5 071
17	12 954	18 467	41 298	15 094	11 576	10 344	10 217
18	48 262	65 048	100 364	49 595	39 872	36 059	36 148
19	42	118	176	127	42	55	41
20	89	127	276	143	109	100	117
21							
22							
23							
24			422	100	108	117	41
25		95	1 952	663	580	564	191
26	44	993	13 180	4 443	4 366	4 043	1 479
27	76	1 044	16 218	6 197	7 465	6 903	2 053
28	10 230	13 538	36 439	18 124	17 149	16 609	13 172
29	106	776	7 677	2 938	5 325	4 851	821
30		154	9 887	1 916	873	736	349
31		127	2 837	399	109	64	105
32	2 530	2 546	2 844	2 420	2 258	2 319	2 188
33			51				
34							
35							
36			149	60	44	42	
37		46	1 946	509	290	273	72
38		106	4 043	1 464	795	606	152
39		420	13 088	4 760	5 291	4 850	919
40	996	1 594	8 671	3 407	2 761	2 600	1 557
41		262	6 449	3 182	7 262	7 060	724
42		372	9 859	2 182	3 379	3 037	370
43		571	6 056	2 672	6 071	4 318	326
44	155	2 544	9 614	1 810	1 219	743	286
45		101	1 572	192	58		45
46			118	41			
47			269	88			
48			72				
49			539	176	100	95	
50		78	3 204	1 550	792	522	142
51		95	3 616	1 998	1 091	768	188
52		110	2 867	1 049	469	329	117
53		84	3 193	1 613	1 134	828	128
54		42	1 375	456	501	427	68
55			2 255	1 398	2 430	2 440	165
56		50	1 853	699	1 937	1 718	155
57			1 185	585	1 678	1 365	67
58		54	1 889	177	149	100	
59			340	40			
60			88	50			
61			213	122	51		
62			549	224	75	59	
63			1 256	721	284	172	103
64			652	153	66	68	
65			3 294	1 630	566	280	101
66		54	4 366	1 686	365	210	94
67		111	2 853	326	529	634	73
68			353	128	173		
69			170	85	362	457	
70			230	126	553	487	
71			147	68	274	237	
72			139	42	52		
73			116				
74			204	76			
75			81	61			
76			127				
77			1 230	1 291	713	344	84
78			462	230	131	128	46
79			1 027	727	388	228	65
80		40	1 151	547	212	139	
81			377	105	134	163	
82			73	50	100	85	
83			52		60	97	
84			86		98	64	
85					73	73	
86							
87							
88							
89			54	56			
90			80	59			
91			209	242			
92			74		197	143	42
93			269	63	44	49	
94		48	4 030	1 230	202	84	
95			257	43			
96							
97							
98							
99							
100							
101			560	278	130		
102			315	182	54		
103							
104							
105							
106							
107							
108							
109			47				

(3.6×10^5 sec) exposure, at 135°C (408°K) was 0.75%.

Vacuum Condensible Degassing Rate--The steady-state vacuum condensible degassing rate for this material at 125°F (323°K) is 9.13×10^{-5} percent/day.

Activation Energy of Decomposition--In vacuum:

Over the range 233°C - 300°C (506°K - 573°K) -

$$A = 8.3 \times 10^{12}$$

$$\Delta E = 15.77 \text{ Kcal (75.77 Kjoules)/mole}$$

Over the range 300°C - 345°C (573°K - 628°K) -

$$A = 2.1 \times 10^{12}$$

$$\Delta E = 56.44 \text{ Kcal (225.35 Kjoules)/mole}$$

In nitrogen:

$$A = 5.6 \times 10^{12}$$

$$\Delta E = 17.27 \text{ Kcal (72.01 Kjoules)/mole}$$

Over the range 322°C - 370°C (596°K - 643°K) -

$$A = 2.56 \times 10^{12}$$

$$\Delta E = 46.84 \text{ Kcal (195.32 Kjoules)/mole}$$

Time for 1% Weight Loss at Temperature, T

<u>Temperature</u>	<u>Time (Minute)*</u>	
	<u>In Vacuum</u>	<u>In Nitrogen</u>
50°C (323°K)	782.2	52.5
100°C (373°K)	173.2	17.2
150°C (423°K)	54.8	7.1

*For larger sample applications, a factor of $\sim 10^2$ has to be applied to all the time in minutes.

Physical Properties Characterization

The qualification of the nonmetals used on the Viking Program with respect to their physical properties (mechanical, electrical, thermal, and optical) was a significant effort. Since there was a limited quantity of in-situ data available on the properties of materials after long term exposure in a high vacuum, it became necessary to institute an evaluation and qualification program

that would provide this necessary data after exposures to simulated space environments over extended periods of time up to 14 months. This meant that materials would have to be stored in vacuum chambers for extended periods of time and then tested in-situ. That is, the testing would be performed in a vacuum at the anticipated thermal conditions that could be expected during the flight to Mars as well as after landing on the planet.

The initial program identified a minimum of 75 different candidate materials. This amount increased during the program to over 800 materials. To evaluate these 75 materials could involve as many as 20,000 tests. However, as the program progressed, certain tests were eliminated for various reasons, such as testing for only those properties which were critical to the specific material application rather than all the physical properties of each material. In many cases, the long term testing was eliminated if the material showed little or no change over a 3 to 6 month vacuum exposure.

A sequence of testing was generated to provide a meaningful comparison of materials properties throughout the program. This sequence required the testing of materials as follows:

1. Baseline (as received);
2. Prelaunch (after receiving a heat sterilization);
3. Launch, cruise, and deorbit (after vacuum exposures of one, three, six and 14 months).

Once an acceptable program for material qualification was identified, the facilities required for this program were evaluated. The first two phases of testing (baseline and after-heat sterilization) required little more than conventional testing equipment and ovens. The third and fourth phases (vacuum soak and in-situ testing) presented severe problems. Conventional testing facilities were evaluated. Such techniques included a carousel fixture, where a quantity of specimens could be placed in a rotatable fixture and placed in a vacuum chamber. The disadvantages of this arrangement included price and long term reliability. Each test would require special fixtures for that test and, for instance, if flexure testing was required on 20 different materials, then 20 flexure rigs and vacuum chambers would be required and the testing machine would have to be physically transferred from chamber to chamber. If all the specimens were in one chamber, then a power failure or any equipment failure would ruin the entire set of specimens. If this occurred, let's say after five months of vacuum exposure, then it would be necessary to start the test sequence (including the heat compatibility cycle) over again.

The method selected for the vacuum soak and in-situ testing was to separate the two tasks. To accomplish this, 32 vacuum canisters were fabricated. The soak systems consisted of four

400 ℓ /sec ion pumps with a seven-canister manifold on each. Each canister was separated from the plenum with two vacuum valves. The remaining four canisters were connected to individual 50 ℓ /sec ion pumps. This provided the capability of using individual canisters for those materials that either had anticipated high outgassing loads, or the outgassing products were undesirable contaminants for other materials. Figure 2 shows one of the seven canister systems. Each of the canisters was fabricated from stainless steel with a double wall to provide thermal capabilities. A schematic of these canisters is shown in Figure 3. The top portion, or lid, was sealed with an O-ring compressed by a marman clamp. This sealing technique provided a full opening lid that required the tightening or loosening of only one nut to open or close the canister.

The test chamber was designed and fabricated to be used in conjunction with the soak systems. It is constructed of 300 series stainless steel and consists of two individual vacuum chambers separated by a 24 inch sliding gate valve (Figure 4). The main chamber is a nominal 5 feet in diameter and 7 feet long. The air lock chamber is 2 feet in diameter and 2 feet long.

The pumping portion of the main chamber consists of two 20-in. oil diffusion pumps with a multicoolant baffle and a valve isolating the pump from the chamber, and a 300 cfm roughing pump on the discharge side of the diffusion pumps. Fifteen cfm holding pumps are tied into the roughing manifold to enable the diffusion pumps to be exhausted while the main chamber is being roughed down. The net pumping speed for the main chamber is in excess of 10,000 ℓ /sec. The air lock pumping systems consist of a 6 inch diffusion pump with a multicoolant baffle and an isolation valve.

The 6 sq ft chamber window has three tempered glass sections, each laminated with two layers of 0.75 in. thick glass. Twenty-nine flanges on the main chamber range in size from 1.5 to 8 in. tube size. The flanges are fitted with feed-throughs for high voltage, coaxial, high current, instrumentation, liquid nitrogen and nude ion gages. A full opening door on one end provides easy access to the chamber. The air lock has four 1.5-in. tube size flanges and a sliding tray mounted on tracks within the air lock.

The unique feature of this system is the master/slave manipulation capability in the main chamber. The manipulators are similar to those used in nuclear installations and each consists of four major parts: the master arm, the slave arm, the seal tube assembly, and the tongs. Each slave arm contains over 70 bearings, lubricated with a dry film lubricant. Tong configurations can be changed remotely using a special fixture. The manipulators provide six degrees of freedom and have electric indexing in two axes for displacement of the master arm relative to the slave arm. All other motions are mechanical, with a one-to-one force ratio between the master arm and the slave arm except for

Figure 2 - Seven Canister Thermal Vacuum System

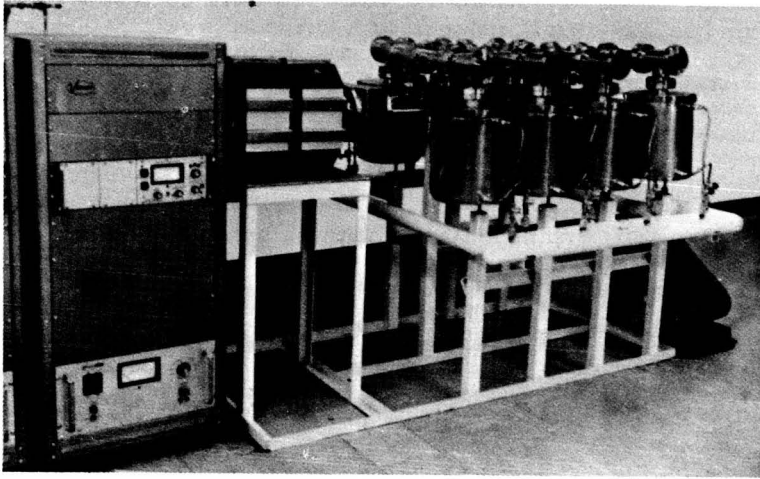


Figure 3 - Vacuum Canister

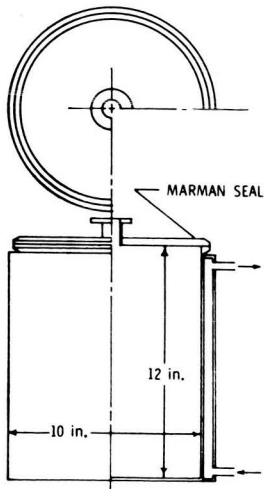
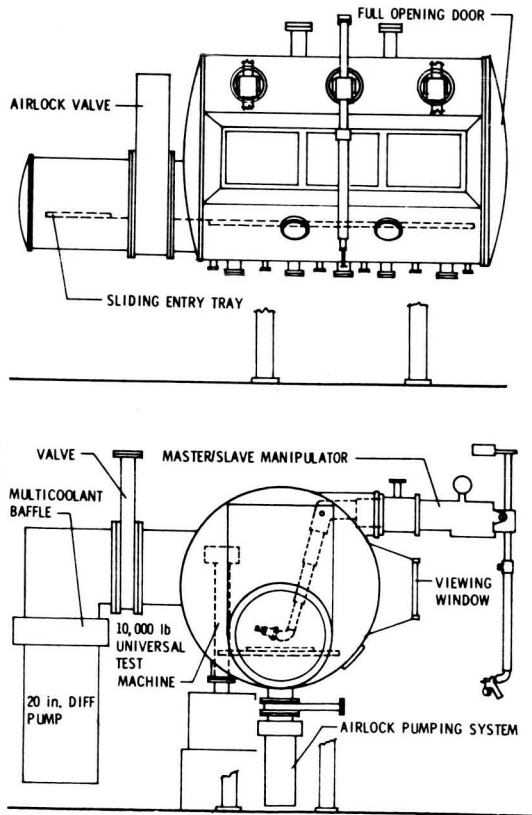


Figure 4 - Vacuum In-Situ Test Chamber



the friction of the motion rods within the seal tube assembly.

The linear motions of the master arm are converted to rotary motion at one end of the seal tube and then translated back to linear motion at the slave end of the seal tube assembly². This conversion enables the use of rotary seals to maintain a vacuum. Each end of the motion rods within the seal tube contains twin Viton seals, with the cavity between each set of seals filled with low pressure oil for lubrication. The chamber routinely can be evacuated to 10^{-6} to 10^{-7} torr.

A 10,000 lb universal test machine has been coupled to the main chamber. The columns are shock isolated from the chamber with bellows, and the moving crosshead pull rod is attached to a bellows with a 14-inch stroke capability. Heating and cooling of the test specimens is provided by radiant heaters (quartz lamps) and liquid nitrogen cooled shrouds. A typical sequence for the removal of a specimen from the soak system and the in-situ testing is as follows:

- Isolate the soak canister from the manifold by closing both the vacuum valves;
- Remove the canister and mount it on the sliding tray from the air lock;
- Install the sliding tray/canister in the air lock and evacuate the air lock;
- With the main chamber under vacuum, open the 24" gate valve that separates the air lock from the main chamber;
- Reach in the air lock with the master/slave manipulator and pull the sliding tray into the main chamber;
- Loosen the nut on the marman clamp and open the canister lid;
- Remove the specimens to be tested and close the lid;
- Push the canister back in the air lock, close the gate valve, and vent the air lock;
- Remove the canister and reinstall it on the soak system;
- Evacuate the area between the ion pump and the canister and open the canister isolation and ion pump isolation valves.

The test program required the capabilities and fixtures for performing over 40 different types of tests. Table III shows the different physical properties tests that were performed on the Viking program. Approximately 85% of these tests were performed in vacuum. These tests were performed generally according to ASTM test methods; however, in certain instances, modifications were made to the methods or special test methods were generated. The

Table III - Physical Properties Measured for Viking Materials

1. Tensile - (-150 to +600°F) - D412, D638, D882, D1000
2. Lap Shear - D1002, D1000
3. Flexure - D790, FTMS 141M6221
4. Peel Tests - D1876, D1867, D1000, D903
5. Bond Tension - D952
6. Tear Tests - D624
7. Dimensional Stability - C548, D1204, D2126
8. Compression Set - D395, FTMS 601M3311
9. Scratch Tests
10. Bend Tests } Adhesion - FTMS 141A Method 6304.1, D1000
11. Sand and Dust Abrasion Tests - STM*
12. Dielectric Constant - D150, D1673
13. Loss Tangent - D150, D1673
14. Surface and Volume Resistivity - D257, D1000
15. Dielectric Breakdown - D149, D1000
16. α_s , E Values for Thermal Control Coatings - STM
17. Insulation Resistance - D257
18. Compression Strength - D695, C165, D1621
19. Hardness - FTMS-M3021, D785, ASTM D2240
20. Thermal Expansion - D696
21. Specific Gravity - D792*
22. Solvent Resistance - D471*
23. Thermal Cond - C177
24. Creep - D674
25. Bearing Strength and Modification - FTMS 406M1051
26. Water Absorption - FTMS 406M7031*
27. Corona Resistance - D1868
28. Moisture Resistance - D570*

* Tests not performed in vacuum.

test method for surface and volume resistivity, for instance, called for the electrodes to be secured to the specimen by an adhesive or grease. The method was modified for use in the vacuum chamber and a constant force was applied to the specimen electrode configuration. By performing the entire sequence of tests using this method, a relative change could be determined between baseline and in-situ testing if one existed. Other test method modifications were required where measurements were needed on specimens at other than ambient temperatures. Because radiant heat transfer is the primary method of heating and cooling in a vacuum, it was necessary to fully enclose the test specimen within a cooling shroud to minimize temperature gradients on certain test specimens. Head travel was used to measure elongation on those tensile specimens where strain was a critical property. Again, this technique provided a relative change if one existed. Dielectric strength tests required reduced power testing due to corona discharge problems. A 50 KV machine was used for these tests, but corona discharge occurred in vacuum between 30 and 40 KV. This problem could have been corrected if time permitted. The corona occurred over the surface of the specimens and, if new specimens and fixtures were fabricated with a much larger surface area, it is felt this problem would have been corrected. This voltage was sufficient, however, to qualify the materials for the Viking program, since breakdown did not occur through the material.

In conclusion, it is felt that the materials qualification program performed was a meaningful one, and did categorize those materials that exhibited changes after extended periods of time in a vacuum. Most materials showed little or no change after this vacuum exposure, and those that did either were rejected from the program or it was determined the changes were not detrimental to the materials specific application. Teflon impregnated fiberglass lacing cord, for instance, showed a 41% increase in tensile strength after 3 months in vacuum. CR-124 (a potting compound) showed a change in the measured resistance from 10^{13} ohms to 10^4 ohms after heat compatibility. This change was sufficient to have the material rejected from the program.

DISCUSSION

In the chemical qualification of nonmetallic materials, the techniques employed most often from the material initial screening through qualification and in the final lot to lot fingerprinting were thermal gravimetric analysis (TGA), and combined residual gas analysis (RGA). The success of this program is due in large measure to the instruments used; namely, a Mettler Thermoanalyzer I, and Quadrupole Mass Spectrometer. The RGA data were obtained simultaneously with the TGA and read-out through an Infotronic CRS-160 Data Acquisition System.

Based on the experience of running more than 1500 tests, this method as a basic part for nonmetallic materials characterization

or qualification is highly recommended. For getting identical results from lot to lot samples, it is recommended that this tool become a part of the quality receiving/inspection process for nonmetallic materials.

In the physical properties portion of the qualification program, several conclusions can be reached. First, the testing of nonmetallic materials for obtaining relative changes after long term thermal vacuum exposures has categorized certain material groups as those most likely to be unaffected by the exposures and certain groups that will show changes in the properties, even though the effects may not be deleterious. For instance, dacron materials showed an average of 6.3% reduction in tensile properties after heat compatibility, but not after vacuum exposure which makes it acceptable for the specific application. Viton "A" MIL-R-25897 group exhibited a 35% compression set after one month thermal vacuum exposure, making it unacceptable for its specific application. In general, this qualification program has provided the necessary data to give assurance that nonmetallic materials, having passed a thermal screening, will undergo little significant changes of physical properties after long term vacuum exposure at moderate temperatures.

REFERENCES

1. Journal of Applied Polymer Science, Vol. 16, pp. 2503-2510, 1972.
2. Central Research Laboratory, Red Wing, Minnesota, Patent No. 3,507,163, dated 21 April 1970.

N 74-102 92

PRECEDING PAGE BLANK NOT FILMED

Paper No. 72

SPHERE FORMING IN ZERO GRAVITY*

W. Aubin, D. Larson, Jr., G. Busch and G. Geschwind,
*Research Department, Grumman Aerospace Corp.,
Bethpage, N.Y.*

ABSTRACT

Melting and solidification of melted spheres in zero-gravity were studied in the Marshall Space Flight Center's 300 foot drop tower. An apparatus to melt and solidify metals in the three seconds of zero-gravity time available is described.

INTRODUCTION

The exploitation of the space environment for materials processing is very attractive. This environment, unobtainable in laboratories on earth could allow development of new materials with unique properties and improve or reduce the cost of existing materials. The most unique feature of the space environment - zero gravity - has only been considered as a potential experimental variable by scientists and engineers for a few years (Ref. 1-3). Zero gravity is difficult to realize short of suborbital or orbital flights using rockets. To provide the scientific community with the opportunity to perform experiments in zero-gravity at low cost and with a rapid turn-around time, NASA/MSFC has made available its 300 foot drop tower as a testing facility. Using this equipment it is possible to get about three seconds of very low gravity ($\sim 10^{-5}g$) test time. In order to make full use of this facility to study the effect of zero gravity on the melting and solidification of metals, it is necessary to provide an experiment in which sufficient quantities of metal can be melted and solidified in the short time available. Thus analysis can be made on the solidified material. This paper describes such an apparatus and the results

*This work was partially supported by NASA under Contract NAS 8-28604

of both laboratory and drop tower tests.

PROCESS DESCRIPTION

A survey of the literature indicated that there is a process by which metal wires can be rapidly melted and as a result of surface tension forces will form and solidify as nearly perfect spheres. With sufficiently rapid cooling, the entire process can be accomplished in less than three seconds. In the experiment a low voltage, very high current is rapidly switched across a metal wire strung between two electrodes. If the rate of power input is sufficiently high, the solid wire will melt and form a liquid column, which is unstable. While still liquid, it will decay into a chain of non-connected liquid spheres as shown in Fig. 1. This sequence is from high speed movies taken of the process in the laboratory.

While the mechanism of sphere formation is not completely understood (Ref.4,5,6), the process has been termed "formation of unduloids". Most simply, the wires act in the same manner as does a fuse when the line it is protecting is overloaded.

Since, at present, almost all zero gravity experiments are time limited, it is instructive to consider what is the limiting size of sphere that will form and solidify during this experiment. Assuming the process to be the decay of a liquid column to a sphere, then the decay time for this process has been given by (Ref. 7, 8):

$$\tau = \left(\frac{\rho}{\sigma}\right)^{\frac{1}{2}} R^{3/2}$$

where

- ρ = density (Kg/m³)
- σ = surface tension (n/m)
- 2R = final sphere diameter (m).

A survey of the literature indicates that ρ/σ has a value of about 0.06 for many metals at their melting points. Using this value, we have plotted the time to form spheres of various sizes and this is shown in Fig. 2. The arrows indicate the limits on the sizes of spheres that could be formed in three seconds in the drop tower (5.1 cm) and in 12 seconds

in a KC-135 flight (~ 13 cm) if sufficient power is available.

It is next of interest to consider how large a sphere will solidify in the time available if we assume it is molten at the instant of achieving zero-g. This has been done for two cases (Ref. 9), both of which assume the sphere is a pure metal at its melting point. In the first case, all the heat of fusion is rejected by radiation and evaporation is neglected. The second case is for a very volatile element and assumes radiation heat transfer is small. Figure 3 presents some of the results for different metals. Consideration of Figs. 2 and 3 shows that in the time available in the drop tower, we can form very large molten spheres but they will not be completely solidified before the restoration of gravity. If large spheres are formed, then only the outer shell will have a chance to solidify before impact.

APPARATUS

Laboratory Experiments - The initial experiments in the laboratory were conducted using a bell jar vacuum system with the wire suspended from copper bus bars about one foot above the base plate. The free fall time following melting is therefore .25 seconds. AC power was supplied to the wire through a variac and a stepdown transformer; the power was switched on manually.

These experiments were carried out on several materials which were available in the laboratory. These are tabulated below with the wire diameter in centimeters. With sufficient power, it was possible to form spheres as shown in Fig. 4 from all these materials.

Metals	Alloys	Coated Wires	Other
Ag (0.025)	Nichrome (0.051)	Ni on Cu (0.015)	NiTi (0.160)
Ni (0.192)	Chromel (0.038)		
W (0.064)	Constatan (0.051)		
	SAE 1080 (0.102)		

The wide range of materials which were successfully formed into spheres indicates that the formation

of the unduloids and the resultant spheres is related to the process of power input and not the materials. Since even the highest melting metal, tungsten, formed spheres, it is expected that the wire melting experiment can be used to form spheres from any metallic conductor as long as it can be fabricated into wire or rod and sufficient power can be rapidly applied.

When performing the experiment in the laboratory, using AC heating, it was observed that a threshold voltage (or power) exists below which no spheres are formed. Figure 5 shows an example of this for chromel wire. As the power (or primary voltage) increases, the number of spheres formed rises rapidly. Since the sphere diameter remains relatively constant this result indicates that more of the length of the wire forms spheres. As expected, increasing the wire diameter increased this threshold voltage, however, the shape of the curve remains the same.

The results shown in Fig. 5 are for a vacuum of 10^{-4} torr. If the pressure in the chamber is increased using inert gas, the threshold voltage also increases, but the number of spheres formed increases more rapidly with voltage at the higher pressure.

Drop Tower Experiments - The experimental apparatus designed for the Drop Tower is also compatible with Aerobee rockets for longer zero-g testing. A stainless steel can 29 cm long by 28.5 cm diameter serves as the vacuum chamber. It is connected to a portable vacuum station through a shut off valve and a quick disconnect. One end of the chamber is removable and contains the electrical feed throughs, the specimen clamps, an observation lamp, a temperature reference wire and a mirror for observing the sphere formation in two planes. This is shown in Fig. 6. Color film at 300 frames/second was used to record the experiment from a movie camera mounted at the opposite end of the chamber. The electronics necessary for the proper sequencing of events in the drop tower is mounted with the can on a frame supplied by NASA.

The evacuated experiment can, on its frame was placed in a cylindrical chamber 2.44 m in diameter and 3.05 m long in the drop tower where it is allowed to float free during the 91.5 m drop. The chamber has a hemispherical cap on the bottom which

houses a bank of nickel-cadmium batteries used to provide power to the specimen, associated electronics and the telemetry transmitter during the drop. The top of the chamber is a cone and houses the pressure spheres used to thrust the entire chamber (called a drag shield) toward the ground. This thrust overcomes the air resistance of the drag shield and extends the length of zero-g test time.

Two series of drops were made one month apart using pure Ni wire as an example of a pure metal and SAE 1090 steel as an example of an important commercial alloy. The wire diameters and lengths were varied in an attempt to increase the size of the spheres.

In the first series of drops, spheres formed in four of the seven drops. When large diameter wire (.127 cm) was used at 28 volts or at 14.5 volts no spheres formed. In general, the spheres were bright and their surfaces appeared free from oxidation.

In only one drop of the second series of drops all with Ni wire were spheres successfully formed and many of the specimens appeared scaled. All of the runs made in the second series were simulated in the laboratory prior to entering the drop tower. Spheres were formed in most cases. In the section on Laboratory Experiments, the threshold power needed for sphere formation was mentioned. The laboratory tests were carried out in a vacuum of 10^{-4} torr and in an inert gas (argon) at atmospheric pressure. In both cases, there was a threshold power, but it was not markedly different.

Subsequent to the second series of drops, laboratory experiments were conducted using "Die Hard" batteries, .4 cm Ni wire five cm long, and three pressure levels: diffusion pump vacuum (1×10^{-4} torr), roughing pump vacuum ($\sim 5 \times 10^{-2}$ torr), and atmospheric pressure. At the highest and lowest pressures, spheres formed, although at atmospheric pressure they were oxidized. At the intermediate pressure, no spheres ever formed; the wire always broke into segments. The explanation for the non-formation of spheres in the second set of drops may have resulted from the outgassing or leaking of the chamber up to a critical pressure level between valve-off and dropping. This is currently under investigation.

TEMPERATURE MEASUREMENT

The temperature-time history of a sample in a melting and solidification experiment is of primary importance. In this experiment, temperature measurement is difficult because of the rapidity of heating and cooling and because of the movement of the sphere following its formation. To allow the specimen and record its temperature-time history, a photographic technique using a high speed movie camera and color film was developed (Ref. 10).

With color film it is impossible to make absolute temperature measurements without a standard. The use of a standard to produce reference temperatures in the apparatus allows for the necessary corrections on moving from the bench test calibration to the drop tower chamber.

In this technique only a single batch of film (Kodak Ektachrome EF film, type 7242) is used both for calibration and the experiments. The calibration involves photographing tungsten wires at a series of temperatures between 1173 and 2573 K in a vacuum bell jar. The temperature of wires was measured before and after exposure with an optical pyrometer. The appropriate corrections for change in wire emissivity with temperature and for bell jar absorption were made.

The film was analyzed with a microdensitometer to measure the optical density at three wavelengths corresponding to the three emulsions of the film, red ($.63 \mu\text{m}$), green ($.53 \mu\text{m}$) and blue ($.44 \mu\text{m}$). The optical density of the wire center, for each wavelength and frame, was then calculated and plotted as a function of Planck's black body radiation function, at the appropriate temperature. These calibration curves were then utilized, in conjunction with the internal reference wire set at 1773 K in the drop tower package, to yield specimen temperature data.

Figure 7 shows a typical temperature-time history for a drop tower experiment using .051 cm diameter, 6.03 cm long Ni wire. Shown are the results of calculations for the $0.530 \mu\text{m}$ and $0.630 \mu\text{m}$ wavelengths. These curves qualitatively follow the idealized time-temperature heating and cooling curves of a pure metal. The initial rapid temperature rise in Fig. 7 is due to heating of the solid and the

plateau, or thermal arrest, is a result of the time required to absorb the latent heat of fusion. At this time (.012 sec) the sample is now a liquid column and super-heating begins as the column goes unstable. Unduloids are formed and these in turn form spheres. At this point, the circuit is opened and cooling ensues. Cooling progresses until the melting point is reached and then there is a thermal arrest due to the release of the latent heat of fusion.

METALLOGRAPHIC INVESTIGATION

In general, it was found that the degree of sphericity of the drop tower samples was considerably greater than that of the laboratory samples. This reflects the increased solidification time in the drop tower before contact is made with the chamber walls. Consistent with this increased time, the samples were better able to withstand the wall contact. As the thermal contact with the wall was poorer due to enhanced sphericity, the samples likely had a slower solid state cooling rate.

The surface morphologies of those samples that had the highest degree of sphericity invariably exhibited an equiaxed surface grain morphology. These grains were not always representative of the interior grain structure. That is, they were not always carried through into the interior, and sometimes the interior grain structure could be seen in addition to the equiaxed surface morphology. This is shown in Fig. 8a and is reproduced schematically in Fig. 8b. Although the internal grains are likely to be related to specific surface grains which were favorably oriented for rapid growth from both the melt and in the solid state, their relationship to these "parent" grains is not obvious. This phenomenon may be a combination of a surface artifact and a solid state grain growth phenomenon.

Classical dendritic growth was also noted on a limited number of specimens, with the dendrite arms mutually perpendicular and corresponding to $\langle 100 \rangle$ directions in the face centered cubic lattice.

The one unique microstructure originating from the zero-gravity experiments appears to originate from those samples which have a solidified shell prior

to impact with the chamber wall. In this case, if the shell has sufficient strength to withstand the impact, the specimens will remain spherical or only be partially flattened and the solidification pattern will not emanate from the region of the flat. Figure 9 shows an example of this structure. The specimen has a large volume of internal porosity as predicted by solidification theories. The uniform distribution of void volume probably results from the simultaneous nucleation of a large number of grains throughout the interior of the sphere. These rapidly grow in place and the voids are a result of the volume difference between the liquid and solid states.

SUMMARY AND CONCLUSIONS

Direct resistance melting of wire specimens has proven to be a very effective way of preparing molten metal specimens in any limited time zero gravity facility. In the first series of experiments, both nickel and steel specimens were successfully melted and solidified during the three seconds of free fall. Although spheres were formed, their size was far smaller than predicted analytically. Larger spheres may result from better control of the heating circuit prior to drop or by increasing the rate at which energy is supplied to the specimens.

The effect of chamber pressure on sphere formation is complicated and may be related to the change from radiation heat transfer at low pressures to convection at some intermediate pressure. A good vacuum (10^{-4} torr) will insure sphere formation.

A film technique was developed for measuring the temperature of the wire during heating and the spheres during cooling. The temperature time history of the metal was shown to be similar to that observed in more conventional experiments.

The observed microstructures showed many of the features that would be expected when the solidification rate varies. A unique duplex structure, in which a thin shell of material solidifies first, followed by what appears to be simultaneously nucleation of the rest of the volume leaving a uniform distribution of small voids was observed.

ACKNOWLEDGEMENTS

The authors would like to thank William Poit and Cal Lottermoser of Grumman for their help in conducting the laboratory and drop tower experiments, and Lee Ramsey of NASA/MSFC for his expediting of the drop tower testing. In particular we would like to thank Mr. L. H. Berge our COR for his continued encouragement of this program.

REFERENCES

1. H.F. Wuenscher, "Unique Manufacturing Processes in Space Environment", NASA/MSFC ME-70-1, (4/70).
2. "Space Processing and Manufacturing", NASA/MSFC ME-69-1 (10/69).
3. "Manufacturing Technology Unique to Zero Gravity Environment", NASA/MSFC ME-68-1, (11/68).
4. W. Kleen, Ann. Phys., 11, 579, (1931).
5. W. G. Chace, Phy. Fluids, 2, 230, (1959).
6. J. Nasitowski in Exploding Wires, Vol. 3, p. 295, ed. by W. G. Chace and H. K. Moore, Plenum Press, N.Y. (1964).
7. H. L. Poynter, AIAA Jour., 2, 1624, (1964).
8. W. H. Steurer and D. J. Gorham, "Processes for Space Manufacturing - Definition of Criteria for Process Feasibility and Effectiveness", Final Report on our contract NAS 8-24979 (6/70).
9. J. Reichman, "Solidification of Molten Spheres in Vacuum", Grumman Research Department Memorandum, RM-544, (6/72).
10. G. Busch and T. Hilgeman, "Photographic Technique for Measuring Temperature" to be published as a Grumman Research Department Memorandum.
11. C. Li, Grumman Aerospace Corp., private communication.

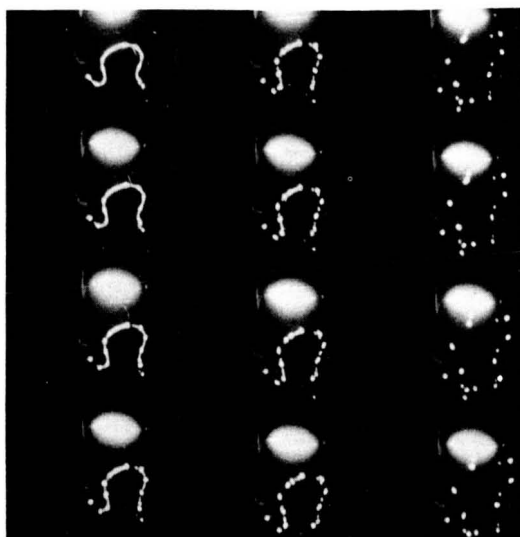


Fig. 1 Formation of Unduloids During Wire Melting

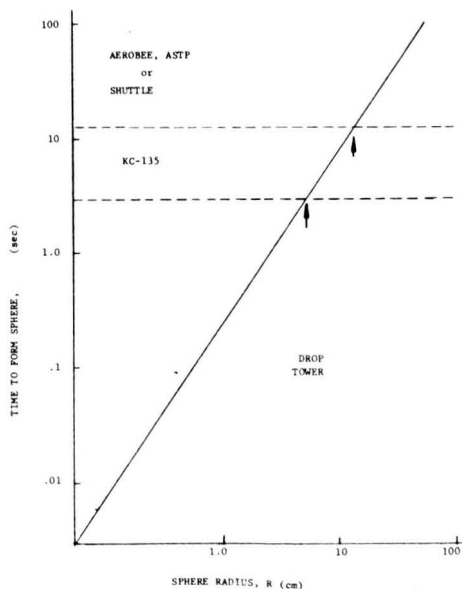


Fig. 2 Time to Form a Sphere of a Given Size

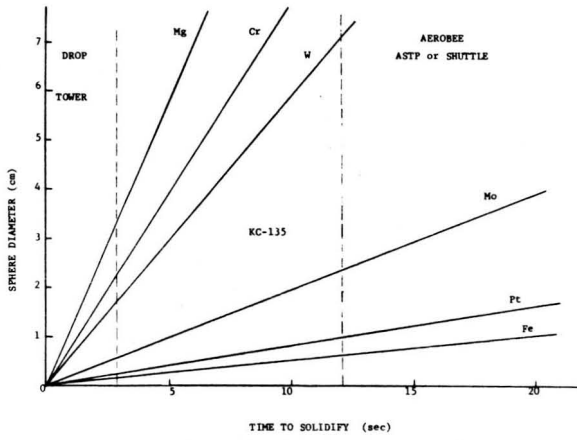


Fig. 3 Time to Solidify a Sphere of a Given Size

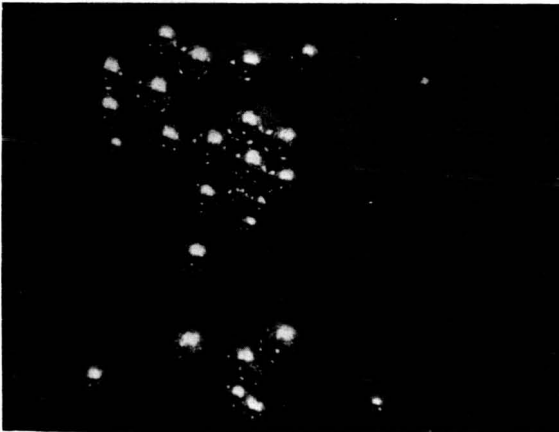


Fig. 4 Nickel Spheres Formed in Laboratory Experiments (8X)

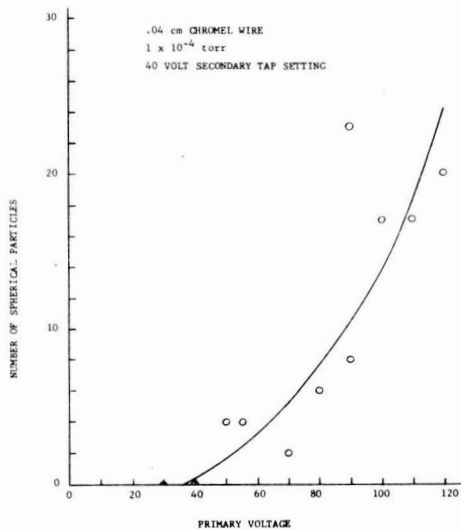


Fig. 5 Number of Spheres Formed as a Function of Power Input

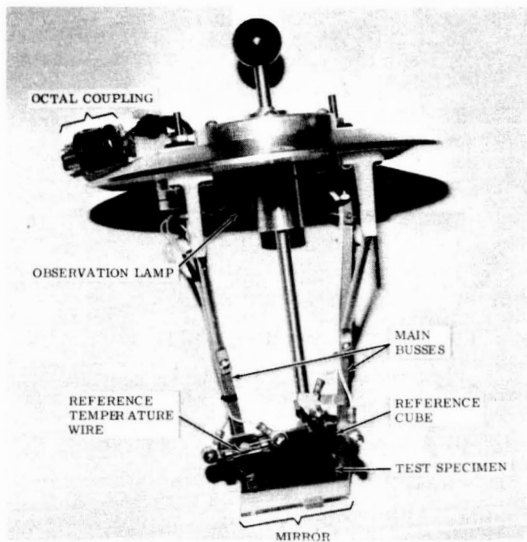


Fig. 6 Test Chamber Interior

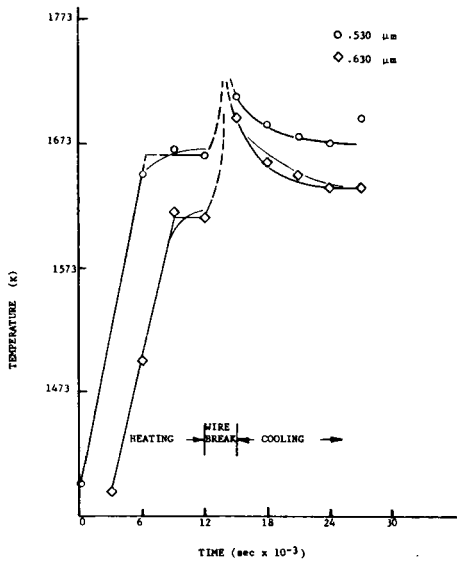
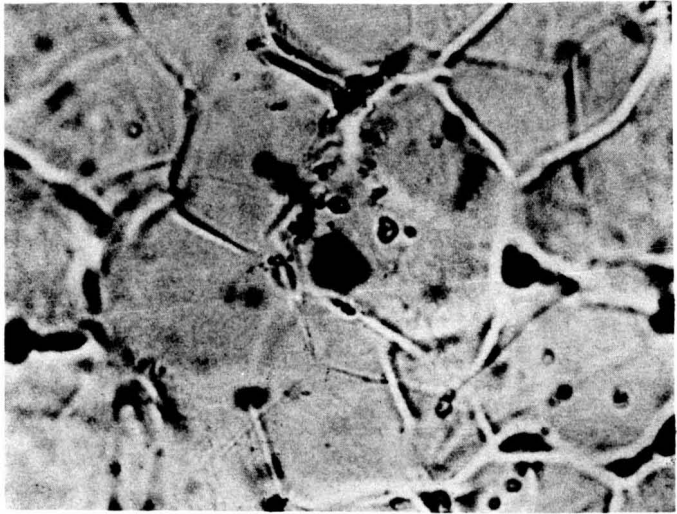
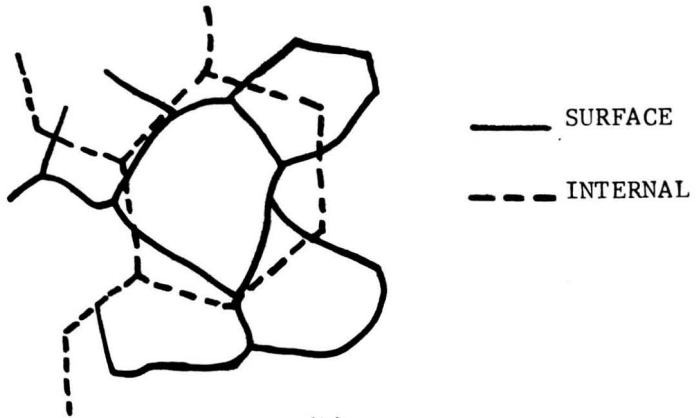


Fig. 7 Thermal History of Nickel Wire Melted in the Drop Tower



(a)



(b)

Fig. 8 Equiaxed Surface Grains and Interior Grain Structure. (a)Optical Micrograph Slightly Defocussed to Show Both Structures (375X)
(b)Schematic

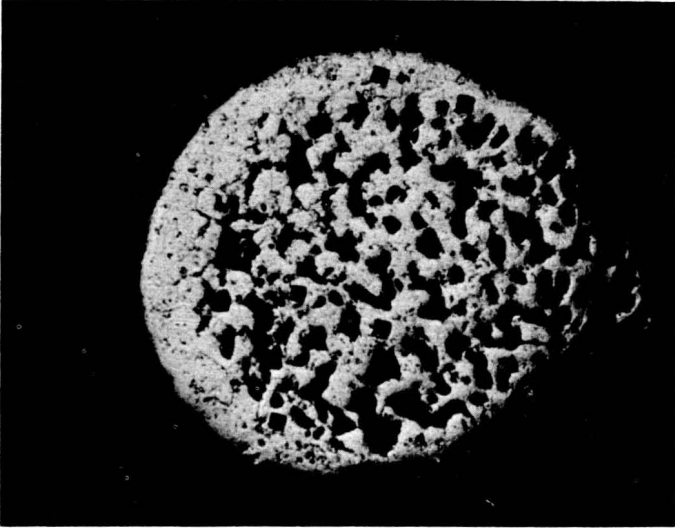


Fig.9 Internal Voids in Drop Tower
Nickel Specimen (100X)

PRECEDING PAGE BLANK NOT FILMED

Paper No. 73

A NEW METHOD FOR DETERMINING THE ABSORPTIVITY AND EMISSIVITY OF METAL WIRES

A. Lorenz and H. P. Schmidt, *Space Simulation Institute of DFVLR, 505 Porz-Wahn, F. R. Germany*

ABSTRACT

Special problems in connection with the high solar intensities affecting space probe HELIOS caused investigations of the real energy consumption of thin wires and the arising temperatures.

As the values for absorptivity and emissivity mentioned in literature must be considered as uncertain, especially for temperatures up to 700 °C, a direct measurement procedure became necessary. At the same time also the individual qualities of the wires, as for instance the influence of the surface quality, could thus be determined.

INTRODUCTION

The antenna reflector of space probe HELIOS consists of a supporting structure and a wire grid. While the supporting structure is coated with second surface mirrors for controlling the temperature, the wire grid is made of thin metal wires without surface protection against high temperatures. Simple calculations indicate that depending on the type of metal, these wires can take 500 to 800 °C. Due to reflections from the structure elements, part of the wires can be radiated by double or triple irradiance. One must bear in mind that space probe HELIOS will be facing an irradiance of 16 solar constants in perihelion.

From this situation result considerable problems when choosing suitable wires for the antenna reflector. Of course a wire material had to be selected, the high temperature strength of which is sufficient to guarantee the mechanical structural stability of the antenna grid when the probe passes the sun.

There were not sufficient details for absorptivity and emissivity to be found in literature re the materials and temperatures involved; thus it became necessary to develop a measuring procedure for determining these values. The procedure had to refer to wire dimensions of the original size in order to be able to consider also the surface qualities of this wire. Besides the mechanical stability it is also important to have a rather low

emissivity in order to keep the heat radiation from the antenna to the spacecraft as low as possible.

The test procedure described in the following is carried out in a smaller space chamber equipped with a solar simulator which generates 16 solar constants. Wires of various materials are irradiated, and the temperatures of these wires are measured by means of measurement of the electrical resistance of the wires. An exact determination of the temperature can be done from the known temperature coefficient. In a second consecutive procedure the wires are heated up to the same temperature without solar radiation by a current, the power of which is measured.

Description of the Experiments and Results

Wires of 0.2 mm diameter were used for the measurement. The measurement procedure is an absolute one. In order to obtain greater accuracy, various materials were simultaneously tested during each experiment so that the characteristics could be well compared. This is valid especially with respect to eventual deviations in the irradiance or in the spectral quality of the light.

Picture 1 shows a supporting frame to which the wires are fixed and where the electrical connectors are mounted. Each wire spans three times the length of 300 mm between the supporting fixtures. In this case, four wire materials are submitted to the test. The solar simulator irradiates the total area.

Behind the supporting frame a mirror is visible which was used for part of the tests, and which simulates reflections that are expected on the spacecraft under certain angles. Thus by this mirror a doubling of the intensity on the wires is practically produced by irradiating the wires also from behind.

The next picture shows a scheme of the chamber in order to demonstrate the location of the wires and the mirror inside the LN₂-cooled black wall. The resistance of the wires can be measured from outside by the normal method of resistance measurement with Wheatstone Bridge as well as by measuring current and voltage. The heat capacity of the wires is so small that the equilibrium is reached after a few minutes. This is the reason why the measurements at various irradiances can be carried out in a rather fast sequence.

Additionally it should be mentioned that the heat loss through the connections of the wire was considered as low. We realize that this means a certain inaccuracy, however, we consider that our assumption was permissible because of the small diameter of the wires of 0.2 mm on the one hand, and as we conducted comparison measurements of various materials which were subjected to the same condition on the other hand. It must also be pointed out that the heat loss occurred at the electrical connections only, and not at the other supporting points, which consist of small glass rods.

We conducted the measurements always twice, once with increasing and once with decreasing intensity. This enables us

1. to increase the measuring accuracy, and
2. to find out whether the characteristics of the wires have changed somewhat at the reached high temperature.

In some cases we found a certain change, especially in case the radiation took place for a prolonged period. We attributed this to the fact that the surface of the wire has changed by recrystallization, and thus the optical constants can also have been affected. The change of the surface was also proved in some cases by microphotographs of the wire (picture 3).

We have conducted two experiments. A scheme of experiments I and II is shown in picture 4. During the first experiment the wires were radiated and the temperatures were determined.

The optical constants α and ϵ and the arising temperature result from the equation

$$\alpha \cdot 1353 \cdot S \cdot \frac{A}{\pi} = \sigma \cdot \epsilon \cdot T_1^4 \cdot A \quad (1)$$

We thus obtain the ratio

$$\frac{\alpha}{\epsilon} = \frac{\pi \cdot \sigma \cdot T_1^4}{1353 \cdot S} \quad (1a)$$

α = absorptivity
 S = number of solar constants
 A = surface of the wire
 σ = Stefan-Boltzmann constant
 ϵ = emissivity

$$1 \text{ solar constant} = 1353 \text{ Watts} \cdot \text{m}^{-2}$$

Immediately after the irradiation procedure the wires were heated by an external source of current. The current was so adjusted that the same resistance was obtained for each material as it was found during experiment I, corresponding to the various measured irradiances.

Experiment II is described by the equation

$$U \cdot I = \sigma \cdot \epsilon \cdot T_1^4 \cdot A \quad (2)$$

This equation gives us the value of ϵ of the wire as a function of the temperature. It must be mentioned that this value does not only comprise the material characteristics, but also the surface condition of the wire. Therefore it is important to investigate that particular wire, which will be used later at the spacecraft, and not to investigate any other wire sample of that material.

By inserting equation 2 into equation 1, the absorptivity

$$\alpha = \frac{\pi \cdot U \cdot I}{1353 \cdot S \cdot A} \left[\frac{\text{Volt} \cdot \text{Amp.}}{\text{Watt} \cdot \text{m}^{-2} \cdot \text{m}^2} \right] \quad (3)$$

is obtained.

In our special example of application for project HELIOS we are interested to get a low value for the absorptivity, so that as little energy as possible is absorbed from the sun. At the perihelion of the HELIOS probe the total energy absorbed by the antenna grid amounts to approximately 30 Watts. It must be considered that an essential part of this energy is transferred by radiation into the central compartment through the louvers in the open position.

In picture 5 the measured values for the temperature are given for the metals gold, silver, and the alloy platinum 70/rhodium 30 with irradiances up to 16 solar constants. The resulting temperatures differ considerably. If reflections occur from the second surface mirrors of the spacecraft, as pointed out above, we have to expect about 800 °C for gold.

From the measurements it can be seen that silver has the most favorable values. Silver, however, cannot be used, as its high temperature strength is not sufficient. Therefore we have investigated a number of other materials, which for simplicity reasons are not contained in this graph. They are, however, mentioned in the following table (picture 6).

It points out the values of the absorptivity resulting from the calculation according to experiments 1 and 2. The absorptivity is mentioned for 100 °C, 300 °C, and 600 °C. At the first item there is no indication because the gold wire did not resist the full intensity, and it broke as it was too soft.

From the other materials we found that the alloys platinum/rhodium and platinum/iridium are most favorable, especially iridium. Thus we have recommended to use platinum/iridium. These materials have an ample high temperature strength.

Some peculiarities of the values may be caused by the surface condition of the wire. This is true especially for rhodium. That wire had an unfavorable surface which could be noticed at first sight. The rhodium wire was very interesting during the experiment because it taught us to recognize that a material for which the optical characteristics are very favorable in literature, was the worst case in the form of a wire. The reason is the manufacturing difficulty of this wire, due to its brittleness.

It is now important to say some words about the defining of temperature with the aid of the resistance. Because of the strong functional dependence between the contamination in the metals and the resistance, as well as of the temperature coefficient of the resistance, it is not possible to use the values mentioned in literature. These data are available for pure metals and for limited temperatures only.

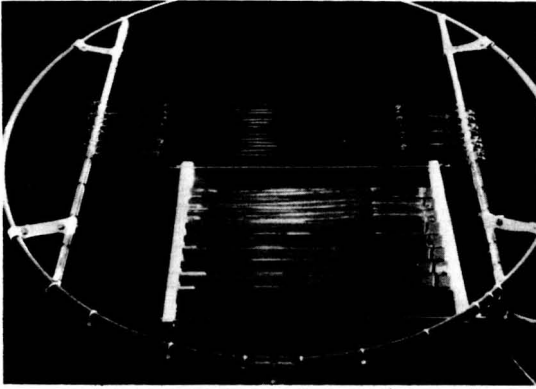
Therefore, in a simple apparatus, we have determined separately the resistance of the wire for the temperature concerned. To achieve this, the wire was heated in an evacuated tube furnace. The scheme of this apparatus is shown in picture 7 and should be understandable without further explanations. From the measured resistance values we have determined the coefficients A and B for the resistance equation

$$R_t = R_0 \cdot (1 + A \cdot t + B \cdot t^2) \quad (4)$$

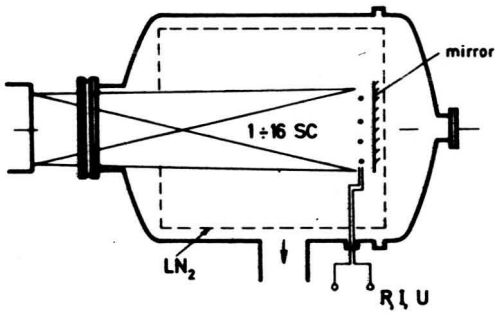
$$t = T - 273$$

We have used these coefficients to determine the temperatures pointed out above.

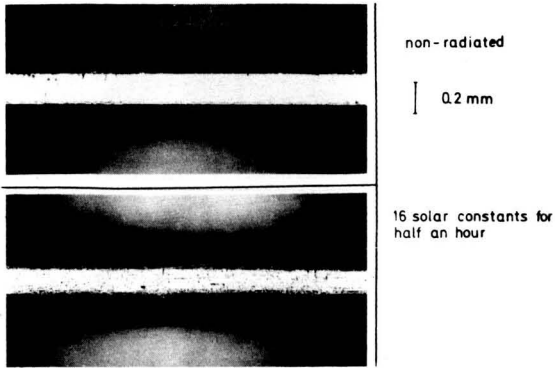
It seems to us that the mentioned method for determining the optical constants of wires can be easily performed in practice. In our case it was especially suitable in order to comprise the influence of the wire's surface. As the results have shown, it is important to consider the surface quality. The manufacturer of the wires should especially take care of the surface quality, that means he has to use very good drawing dies.



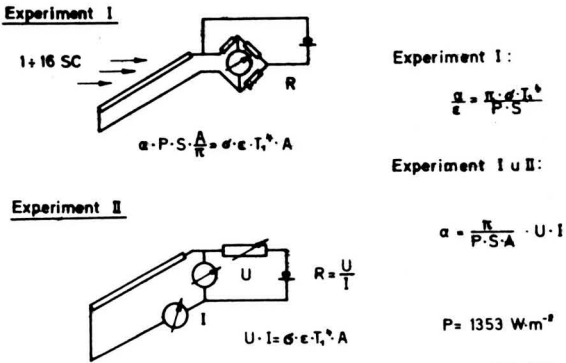
Picture 1: Supporting frame with 4 wire materials and mirror behind them



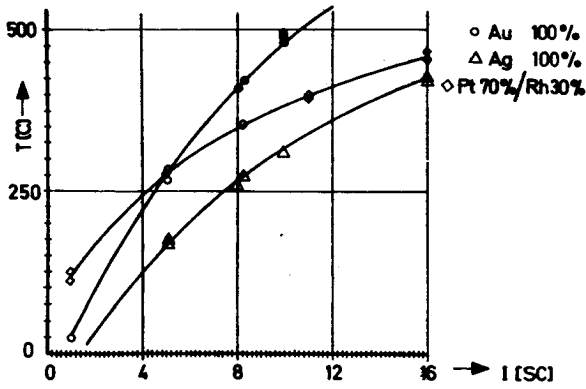
Picture 2: α & ϵ measurements on wires in a space chamber



Picture 3: Microphotographs of the Ag-wire



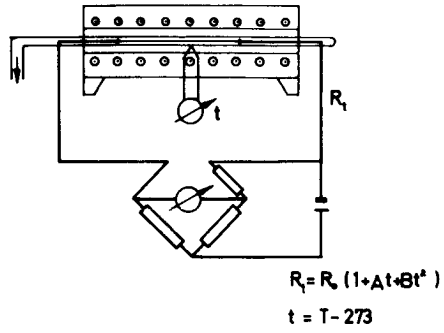
Picture 4: Scheme of the α & ϵ measurements



Picture 5: Wire temperatures in dependence of solar irradiance

Material	α (100°C)	α (300°C)	α (600°C)
Au	-	-	-
Ag	0,19	0,09	0,14
Au 50/Ag 50	0,21	0,17	0,19
Pt	0,37	0,35	0,29
Pt 90 / Ir 10	0,39	0,39	0,38
Pt 80 / Ir 20	0,16	0,13	0,13
Pt 70 / Ir 30	0,16	0,06	-
Rh	0,61	0,46	0,53
Pt 80 / Rh 20	0,26	0,31	0,29
Pt 80 / Rh 20 + Ag	0,11	0,10	0,11
Pt 70 / Rh 30	0,29	0,29	0,29

Picture 6: Absorptivity resulting from Experiment I and Experiment II



Picture 7: Determination of the temperature coefficient of the wire resistance

HEAT TRANSFER AT SUBATMOSPHERIC PRESSURES I.

Calvin M. Wolff, *Scientist*; Thakor J. Vyas, *Engineer*,
Northrop Services, Inc., Houston, Texas

ABSTRACT

A study was performed to measure heat transfer rates between surfaces at conditions experienced in space environment simulation chambers. Many of these conditions are also similar to those experienced in general cryogenic systems.

This study was performed to obtain data more directly applicable to space environment and cryogenic applications, using large temperature differentials and distances between surfaces of up to 40 cm. Previous investigations have been directed at determining the properties of the gases studied, mainly thermal conductivity. In those prior studies, hot wires in tubes and precision parallel plate and concentric cylinder devices were used. The data of this investigation was taken in a 1 meter diameter space environment simulation chamber examining heat transfer between 3.8 cm and also 10 cm diameter Boelter-Schmidt type heat flux meters at ambient temperature and a one meter by one meter square liquid nitrogen-cooled flat panel. The pressure range investigated was from 10^{-5} torr to one atmosphere. Two surfaces were investigated, matte black velvet and aluminized Kapton, to provide extreme cases. The distances between surfaces varied from 0.05 to 40 cm. The gas evaluated in this study was nitrogen.

INTRODUCTION

Investigations and studies have been made on thermal conductivity and heat transfer rates in rarified gases. In these investigations the mechanisms of heat (energy) transfer were studied and properties of the gases determined. These studies were necessarily

conducted at precisely controlled conditions selected to give data that required minimal mathematical complexity in interpreting. For example, three basic geometries were studied: parallel semi-infinite planes, concentric cylinders, and concentric spheres. Further, temperature differentials were kept minimal so error in assigning a mean temperature of the gas between the two heat transfer surfaces would be minimized. However, in space environment simulation and general cryogenic applications, heat transfer problems involving rarified gases (pressures one atmosphere or less) usually involve large temperature differentials, large distances and a variety of geometries. It is the purpose of this investigation to determine heat transfer rates for conditions encountered in the practice of space environment simulation testing and cryogenic systems. Included in the investigation are the large temperature differentials and nonideal geometries. It is hoped that useful and practical data are presented in this paper for ready use by those confronted with such problems.

THEORY

An introduction to gaseous heat transfer is given by Kennard (1). A survey and digest of heat transfer investigations is offered by Springer (2). A very thorough description of thermal conductivity measurements in gases is presented by Tseiderberg (3) except for the technique used in this investigation.

Depending upon the pressure of the gas and the distance between heat transfer surfaces, heat transfer in static gases can be considered to have four different modes. The condition of pressure and intersurface distance is described by the Knudsen number, λ/D , where λ is the mean free path of molecules of the gas colliding with one another and is a function of gas pressure, temperature, and molecular diameter, and D is the "characteristic dimension" of the heat transfer system closely describing the mean heat transfer path. The condition where the Knudsen number is greater than 10 is considered as the molecular heat transfer regime, where heat is transferred by single molecules colliding only (or in a great majority) with the walls. The Knudsen number range 10 to 0.01 is known as the "transition" range, wherein the mechanism is ill defined, being a combination of single molecular transfer between surfaces and a small number of intermolecular collisions before striking the second surface. When the Knudsen number is less than 0.01, heat conduction is said to take place by the laminar, viscous, or continuum regime. Heat is conveyed from a

surface to a layer of gas adjacent to it, and from that layer to the next, et cetera. An important characteristic to all modes of heat transfer, especially molecular, is the ability of a molecule of a gas to adjust its temperature toward that of the wall when it collides with the wall. This property, dependent upon the gas, gas temperature and the wall, is known as the accommodation coefficient (α). The accommodation coefficient is zero if the temperature of a gas molecule is unchanged by colliding with a surface of different temperature, and unity if the molecule achieves the temperature of the wall with one collision.

Molecular regime heat conduction increases linearly with density. A gas offers more carriers per unit area with increased density and also linearly with velocity, which is the rate of traverse of a single molecule from one surface to the other. Since density is proportional to the ratio of pressure over temperature, and velocity is proportional to the square root of kinetic energy, which, in turn, is proportional to temperature, heat conduction in the molecular regime is directly proportional to pressure and inversely proportional to the square root of the velocity. From a kinetic standpoint, the rate is inversely proportional to the square root of molecular weight of the gas and thermodynamically the heat transfer rate is directly proportional to the heat capacity of the gas. Free molecular conduction is proportional to the accommodation coefficient, but not as simply as might be suspected. A composite accommodation coefficient must be used if two different surfaces are involved:

$$\alpha = \frac{\alpha_1 \times \alpha_2}{\alpha_1 + \alpha_2 - \alpha_1 \alpha_2}$$

which reduces to $\alpha = \frac{\alpha_1}{2 - \alpha_1}$ when both surfaces are identical. A unique and important feature of molecular conduction is that it is independent of path length, providing that the mean free path exceeds ten times that path. This is evident when it is considered that molecular heat transfer is the product of number of molecules per unit area, velocity of the molecules, heat capacity of the molecule, and efficiency of the molecules to transfer heat with the surfaces.

Laminar or continuum heat conduction is dependent upon path length and independent of pressure. The dependency upon path length arises from the increased number of lamina which transfer heat from one to another as the path increases. The independence of

pressure exists because, although the number of molecular carriers per unit area increases with density, the number of lamina per unit length also increases and causes the effects to cancel each other. Due to the effect of velocity on the rate of energy transfer the heat transfer coefficient (thermal conductivity) of the gas in the continuum regime should be proportional to the square root of the gas temperature.

The fourth mode of heat transfer in a static gas is natural convection. This appears when the gas becomes dense enough that gases at higher temperature will decrease in density and tend to rise and those colder tend to fall. This phenomenon would not be expected in the absence of a gravity field. Because of gravity dependence we should expect natural convection to be highest for a warm horizontal surface facing up, lowest for a warm horizontal surface facing down (the surface hindering upflow of the gases it has heated), the opposite situation for a cold surface, and in the case of warm or cold surface, natural convection at a vertical surface would be in between those rates for upward and downward facing horizontal surfaces. A "warm" surface is a surface warmer than the gas, and a "cold" is a surface cooler than the gas.

All forms of heat conduction in static gases are also geometry dependent. For the continuum regime, the geometric problem is treated as is the Fourier relationship for isotropic solids. The effect of geometry is somewhat more subtle for molecular flow (ref. 1 and 2), and very complex for natural convection. For example, in convective transfer between a large and a small surface, the transfer rate would be determined mainly by the orientation of the small surface since the bulk of the gas may be considered as conditioned to the temperature of the large surface. This effect becomes ambiguous as the sizes of the two surfaces approach one another. Further, natural convection is dependent upon the distance between two surfaces. If the distance is small enough continuum conduction will dominate the heat transfer (since it is inversely proportional to path length), and as the distance increases natural convection will interfere and eventually dominate the heat transfer.

The investigation undertaken measured the actual heat transfer rates for simple geometries (two parallel vertical surfaces, the cold surface large and the warm surface small) in a common rarified gas (nitrogen). Due to the lack of ideal conditions, such as small temperature differentials and semi-infinite planes, the data obtained is difficult to relate to theory. On the other hand, the data is very practical since the conditions studied are similar to those en-

countered in cryogenic and space environment simulation practices.

INVESTIGATION

A unique calorimetric technique was used to obtain the heat transfer data. A windowless Hy-Cal P8400 radiometer was used as the heat transfer sensor. The radiometer diameter is 1.5-inch and has an aluminum body through which water flowed at a rate of 0.3 gallons per minute. The sensitivity of the radiometer was approximately 42 BTU/ft hr/millivolt. A copper-constantan thermocouple was mounted on the copper tubing water line within 1/2-inch of the radiometer. The water line was bent in a loop to permit translation of the radiometer without kinking the copper tubing. The water line was wrapped with aluminized Kapton film to isolate the water from the environment. The study was performed in a cylindrical vacuum chamber (Chamber N of the Space Environment Effects Laboratory, Johnson Space Center - see fig. 1) which contained a concentric cryogenically cooled shroud 36-inches in diameter and 36-inches long. The axis of the chamber is horizontal. A 36-inch square aluminum plate with an 8-inch diameter liquid nitrogen-cooled "wart" in its center was placed vertically in the chamber. The plate and the cryogenic walls were instrumented with thermocouples. The radiometer was mounted on a 0.5-inch diameter stainless steel rod that was supported by a "push-pull" feed-through. This penetration was located midway along the chamber horizontal (cylindrical) axis and along a horizontal radial line intercepting the center of the cylindrical cross section. The radiometer could be moved along a normal line through the vertical plate's center. The liquid nitrogen-cooled "wart" was on the side of the plate opposite the side facing the radiometer. The shroud was cooled with liquid nitrogen and all experiments were conducted with all plate and shroud temperatures of -280° F to -315° F. The radiometer water temperature was controlled by a cooling/heating servo-regulated circulating system of water-glycol.

Chamber pressures were measured by a Varian millitorr gage in the range of 10^{-6} to 10^{-2} torr, an alphatron gage in the range of 10^{-4} to 100 torr, and a Wallace and Tiernan Bourdon-type gage in the range of 0.3 to 760 torr. The distance between the radiometer face and the vertical plate was measured in the range of 0.05 to 2 cm with a cathetometer located at the front of the chamber, sighting through a glass viewport. Distances in the range 2 to 39 cm were measured

by a marker placed on the traversing rod which pointed to a fixed meter scale.

The gas selected was nitrogen because it is commonly used in space environment simulation and is the most common gas used in cryogenic engineering. Thermally, nitrogen is almost identical to air, except that problems involving partial condensation of oxygen at high pressures and liquid nitrogen temperatures can be avoided by using pure nitrogen. The nitrogen used for this investigation was water pumped and oil free.

Two radiometer surfaces were employed, first 3M Nextel 410C flat black and for a second study the radiometer surface was covered with aluminized Kapton film (aluminized side out) which was applied using 3M No. 467 tape adhesive. These coatings were selected to provide extremes in accommodation coefficients. The spongy black surface was expected to have a higher heat transfer rate than the specular aluminized surface

To isolate radiative transfer from conductive and convective, a series of data were taken at ultimate vacuum (less than 10^{-6} torr). The radiometer signal for various gas pressures was corrected by subtracting the radiometer output measured at high vacuum at the corresponding distances. The radiometer output stability was approximately 5 microvolts, corresponding to approximately 0.2 BTU/ft²-hr. Radiometer temperature was recorded for each reading.

The radiometer was calibrated when the high vacuum readings were taken for the flat black case. The technique of data interpretation is described in reference (4), and simply involves measuring radiometer output at a known temperature in a cryogenic environment of known temperature. The radiometer signal is proportional to the heat exchanged.

$$S = \frac{\epsilon\sigma[T_r^4 - T_w^4]}{mv}$$

where mv = radiometer millivolt output @ 1×10^{-5} torr or less

S = radiometer sensitivity

ϵ = emittance of 3M Nextel flat black paint = 0.89

σ = Stefan-Boltzmann constant, 0.173×10^{-8} btu/ft²-hr °R⁴

T_r = radiometer temperature ° R

T_w = wall temperature ° R

The calibration data was selected from the 20 cm distance readings to avoid effects of re-reflection of infrared radiation of close surfaces. Re-reflected radiation complicates the determination of heat exchange. This calibration is valid when the radiometer has the aluminized film applied to it because it pertains only to the heat passed through the sensing slab which is underneath the film of paint.

For all measurements, the following heat transfer paths were investigated: 0.05, 0.1, 0.2, 0.5, 1.0, 2.0, 5.0, 10.0, 20.0, and 39.0 cm. For the 3M black painted surface, sensor temperature was 90° F and pressure range studied was 10^{-4} to 3 torr. For the aluminized Kapton case, the pressure range was 10^{-4} to 10 torr for a 90° F sensor and 10^{-4} torr to 760 torr for a 30° F sensor.

RESULTS

The results of this study are tabulated in Tables I, II, and III and are depicted graphically in Figures 2, 3, and 4: The molecular regime, transition regime, and laminar or continuum regime boundaries are also illustrated in the figures, as defined according to the Knudsen number.

DISCUSSION

All three cases studies (3M black at 90° F, aluminized Kapton at 90° F, and aluminized Kapton at 30° F) appeared to demonstrate the same general behavior as a function of pressure and transfer path length. The heat transfer for the 30° F aluminized surface was disproportionately lower than that for the same surface at 90° F. The heat transfer for the aluminized surface at 90° F was higher than that of the 3M black surface at the same temperature but within the same order of magnitude. This result is unexpected, since it was assumed that a specular aluminized surface would have a low accommodation coefficient and a rough, spongy surface as 3M black would be much higher. Thus the heat transfer for the black surface should have been much greater than for the aluminized surface.

The results do demonstrate "textbook" style that the heat transfer is independent of distance in the molecular regime and is independent of pressure in the continuum regime. Figure 5 is a plot of heat transfer

versus distance in the continuum regime at fixed pressures and demonstrates that in this regime heat transfer is inversely proportional to the path and independent of pressure, providing the convective contribution is negligible. The convection causes the anomalies in the region of high pressure and large path length.

The very interesting case of natural convection is evidenced in figure 4. It is first evident at large distances, where conduction is subdued by the greater path, but as pressure increases, the convection increases so as to become evident even at 0.5 cm distance at 100 torr pressure. It is also evident from figure 4 that the actual amount of convective transfer is independent of the path and increases linearly with pressure. If the heat transfer curve for the 10 cm case in figure 4 is extrapolated horizontally from the incipience of the continuum to 760 torr and the difference between this pure conductive transfer and total transfer be attributed to natural convection, the natural convective heat transfer as a function of pressure would be the values presented in figure 6.

In figure 6, the values of heat transfer at distances of 5, 10, and 20 cm were averaged for each pressure, and 30 BTU/ft² hr was subtracted from the average for each pressure. The quantity 30 BTU/ft² hr is the value of conductive heat transfer just after which convective heat transfer becomes apparent (fig. 4). The lengths 5, 10, and 20 cm were selected because the convective component of transfer was apparent at pressures down to 10⁻¹ torr, giving seven data points for interpretation. The graph of figure 6 indicates that convective heat transfer Q_v is a function of pressure P according to the relationship $Q_v = aP^b$, where a and b are constants, and figure 4 indicates that Q_v is independent of length. A least squares solution for the constants from the seven data points is $a = 8.04$ and $b = 0.5669$, or $Q_v = 8.04 P^{0.5669}$, when Q_v is in BTU/ft² hr and P is in torr. The standard deviation of the data points from the values determined by the equation is 13.2 percent, which is ordinarily a poor fit, but considering we are quantitatively handling convection, this is quite good.

It should be pointed out again that this data is for specific geometries; a small warm surface and a very large cold surface, and some caution must be taken when applying this data to other conditions. The appearance of the data indicates, however, that in going from a parallel semi-infinite plane condition (0.05 to 0.5 cm) to a remote point source condition (10 to 39 cm) the heat transfer follows in parallel

patterns. This indicates that the error may not be too great in applying this data to a wide variety of conditions. The convective data, though, is strictly for the vertical warm surface case, and will certainly be different for horizontal surfaces, depending on their viewing up or down and being hot or cold.

Accommodation coefficients were calculated from the data, and showed for 3M velvet to be 0.35 and for the aluminized specular surface to be 0.374 and 0.408. The former value was calculated from the 90° F data and the latter value from the 30° F data. The values for the specular surface are larger than expected. No explanation is offered. The accommodation coefficient for the spongy, matte 3M black surface is lower than an expected value of near unity, but when adsorption and even entrainment of nitrogen molecules in the microscopically irregular surface is considered, low accommodation coefficient may be explained. In the case of adsorption or entrainment, the molecules are temporarily arrested at the painted surface, slowing their effective net heat transfer velocity, that velocity being the distance traversed divided by the sum of the time to traverse it at the mean velocity and the time the molecule is delayed at the surface.

Some useful heat transfer values were obtained for static nitrogen gas in the range 10^{-3} to 760 torr at path lengths ranging from 0.05 to 20 centimeters. The data demonstrated behavior agreed with theory concerning heat transfer in the molecular and continuum regimes. Exact calculations for comparison were not possible due to the uncertainty of mean gas temperature because temperature differentials were very large. Convective heat transfer for a vertical smooth surface in a nitrogen atmosphere was empirically correlated to pressure at a given large temperature differential, and was shown to be independent of path length.

CONCLUDING COMMENTS

It is evident from the limited number of cases studied and from the large number of important cases encountered that more data are necessary. Other gases should be investigated, including helium, argon and methane. Studies should be performed for temperatures ranging from -200° F to +250° F. Further, data should also be obtained for a surface facing up and a surface facing down. Structural metal surfaces should be studied, such as aluminum, stainless steel, and copper.

ACKNOWLEDGEMENTS

The authors are grateful to the Space Environment Test Division of the Lyndon B. Johnson Space Center for providing the facilities and permission to conduct this investigation. Mr. R. L. Anderson of the SETD Operations Engineering Section is acknowledged for suggesting this type of study. The authors are very grateful to the engineers and technicians of the Space Environment Effects Laboratory of Northrop Services, Inc., Houston, Texas who assisted in the test setup and taking of the measurements and, in particular, we wish to thank Mr. Gerry Udvardy of Northrop for his efforts.

REFERENCES

1. Kennard, E. H., Kinetic Theory of Gases, 1st Ed. McGraw-Hill, 1938.
2. Springer, G. S., Heat Transfer in Rarified Gases. Advances in Heat Transfer, vol. 7 Academic Press, 1971. pp 163-210.
3. Tsederberg, N. V., Thermal Conductivity of Gases and Liquids, MIT Press, 1965.
4. Wolff, C. M., Space Simulation, NASA SP-298 (1972) p 207.

TABLE I.- COMBINED CONDUCTIVE-CONVECTIVE HEAT FLUX IN BTU/FT HR FOR VERTICAL SPECULAR ALUMINIZED SURFACE AT 30 °F, -300 °F ENVIRONMENT, NITROGEN GAS

PRESSURE IN TORR d-DISTANCE IN cm	1.5 x 10 ⁻³	5 x 10 ⁻³	1.5 x 10 ⁻²	6.2 x 10 ⁻²	3.6 x 10 ⁻¹	1.0	3.0	10.0	30.0	100.0	300.0	500.0	760.0
0.05	13.7	50.7	146	399	-	-	-	-	-	-	-	-	-
0.1	14.1	54.5	134.	332	486	533	553	549	553	553	551	556	562
0.2	13.7	51.4	117.	249	323.	360.	360.	366.	370.	370.	389.	377.	394.
0.5	13.3	40.7	86.	145.	170.	177.	180.	181.	182.	203.	248.	270.	324.
1.0	12.6	35.0	67.	84.	102	105.	105.	107.	117.	156.	236.	294.	364
2.0	11.8	29.0	49.	57.	61.	61.	62.	69.	87.	151.	222.	279.	367
5.0	9.9	21.7	35.	37.	36.	43.	53.	61.	84.	141.	221.	278.	328
10.0	8.7	17.9	27.4	30.	28.	61.	63.	86.	102.	146.	212.	248.	301
20.0	7.2	14.1	22.	23.	24.	41.	59.	63.	81.	127.	198.	236.	308
39.0	6.8	14.1	21.7	19.	-	-	-	-	-	-	-	-	-

TABLE II.- COMBINED CONDUCTIVE-CONVECTIVE HEAT FLUX IN BTU/FT HR FOR VERTICAL MATTE BLACK SURFACE AT 90 °F, -300 °F ENVIRONMENT, NITROGEN GAS

PRESSURE IN TORR d-DISTANCE IN cm	5 x 10 ⁻⁴	1.5 x 10 ⁻³	5.3 x 10 ⁻³	1.2 x 10 ⁻²	4.2 x 10 ⁻²	1.1 x 10 ⁻¹	3.2 x 10 ⁻¹	9.4 x 10 ⁻¹	3.0				
0.05	7.1	12.7	48.	121.	384.	581.	881.	1164.	1633.				
0.1	5.4	12.6	47.	108.	323.	461.	583.	840.	926.				
0.2	7.9	14.7	46.	100.	249.	346.	466.	474.	473.				
0.5	5.1	13.	40.	77.	158.	203.	217.	225.	237.				
1.0	4.3	11.9	33.	56.	91.	103.	109.	112.	109.				
2.0	3.9	11.1	28.	44.	62.	67.	71.	71.	71.				
5.0	2.9	8.6	21.	31.	39.	41.	41.	43.	51.				
10.0	2.6	7.8	18.	24.	30.	29.	30.	40.	51.				
20.0	.9	7.1	15.	20.	23.	22.	27.	40.	54.				
39.0	.1	6.3	14.	20.	22.	22.	27.	39.	52.				

TABLE III.- COMBINED CONDUCTIVE-CONVECTIVE HEAT TRANSFER IN BTU/FT² HR FOR VERTICAL SPECULAR ALUMINIZED SURFACE AT 90 °F, -300 °F ENVIRONMENT, NITROGEN GAS

PRESSURE IN TORR d. DISTANCE IN cm	1.5 x 10 ⁻⁵	4.7 x 10 ⁻⁴	1.5 x 10 ⁻³	5 x 10 ⁻³	1.5 x 10 ⁻²	5 x 10 ⁻²	2.1 x 10 ⁻¹	4 x 10 ⁻¹	1.0	3.0	10.0		
0.05	1.9	4.9	15.2	51.1	180.6	493.3	1254	1540	1711	2290	2314		
0.1	1.5	4.6	14.5	50.4	161.3	407.2	919	1030	1177	1242	1234		
0.2	1.9	4.9	14.5	48.1	139.4	301.6	535	608	548	652	644		
0.5	1.9	4.9	14.1	41.9	102.4	172.5	236	248.3	277.7	263	251.6		
1.0	1.9	4.2	12.2	33.9	71.4	110.5	129	126.8	128.2	132.2	139.5		
2.0	1.5	4.2	11.4	29.0	54.1	71.7	76.2	77.4	76.6	79.7	91.9		
5.0	1.5	3.8	10.3	22.5	37.8	46.1	44.2	45.0	46.1	57.6	66.0		
10.0	1.1	3.8	9.51	18.7	28.9	33.9	32.7	33.9	38.5	58.4	68.9		
20.0	1.5	3.8	8.4	16.0	22.9	23.2	26.3	30.9	39.6	61.4	75.8		
39.0	1.5	3.4	5.0	15.6	22.1	22.4	27.1	31.6	39.5	59.1	77.0		
∞0.1	1.9	4.9	14.4	49.6	161.3	410.	935	1082	1169	1363	1524		

^a REPEAT TEST

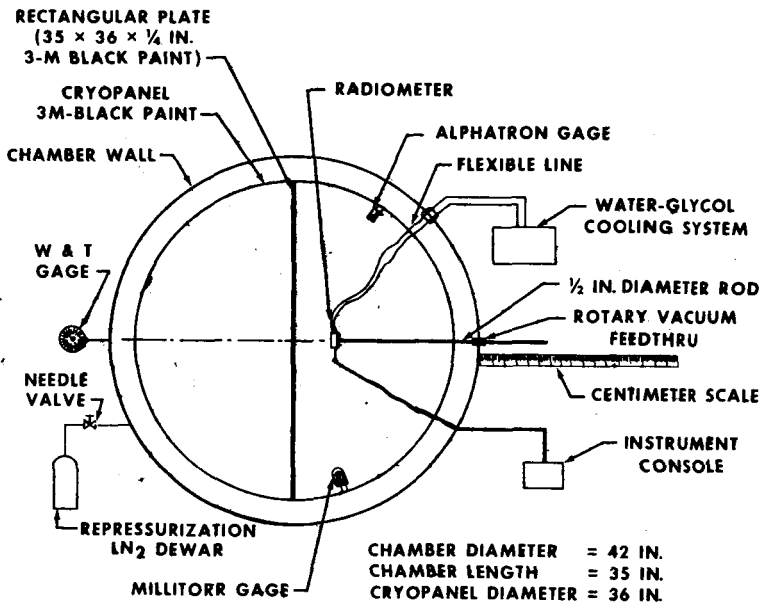


Figure 1.- Experimental configuration.

SURFACE TEMPERATURE = 90° F
 ENVIRONMENT TEMPERATURE = -300° F
 SURFACE: 3M - BLACK VELVET
 ATMOSPHERE: NITROGEN (GN₂)

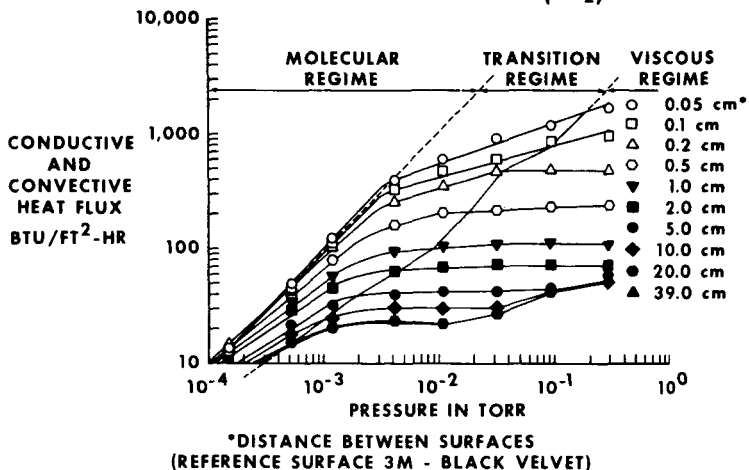


Figure 2

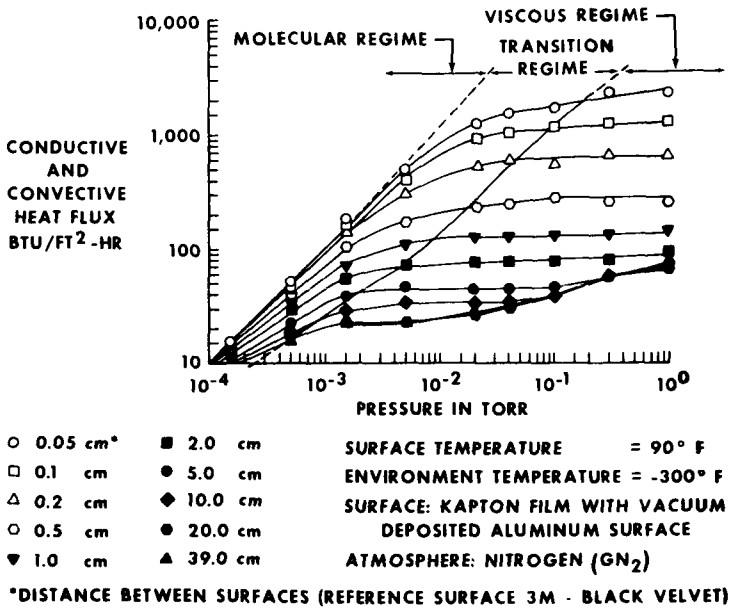


Figure 3

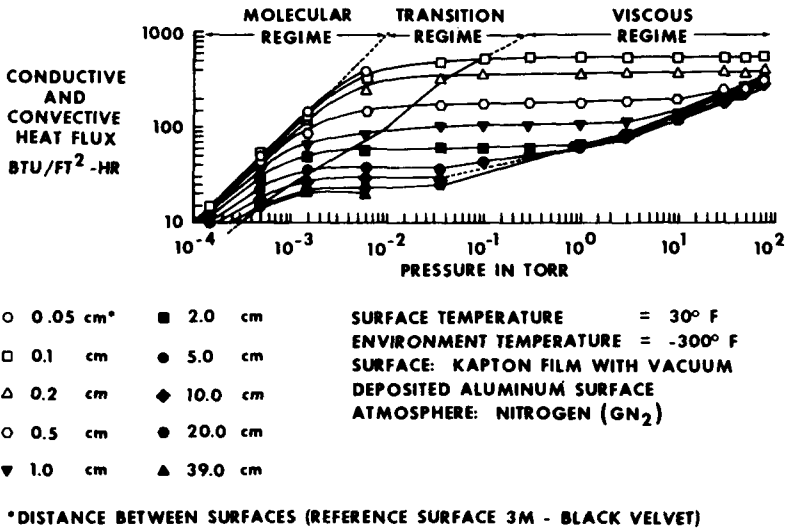


Figure 4

ALUMINIZED SPECULAR SURFACE AT 30° F
VIEWING -300° F MATTE BLACK
ENVIRONMENT, IN NITROGEN ATMOSPHERE

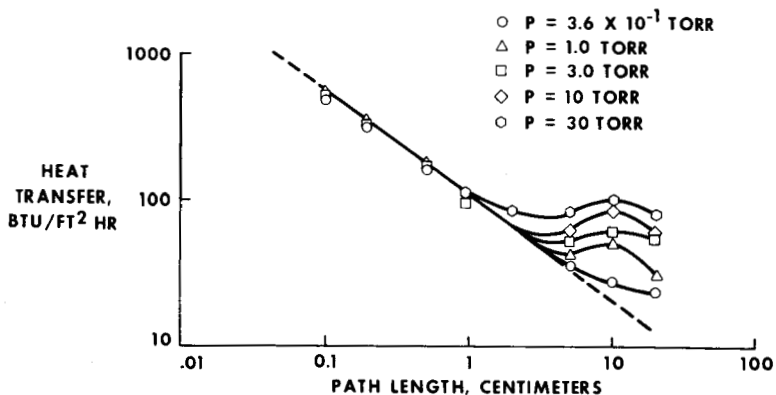


Figure 5.- Heat transfer as a function of distance between surfaces.

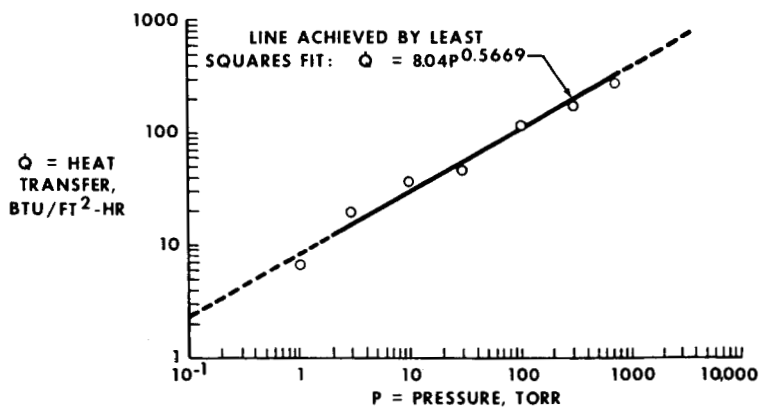


Figure 6.- Natural convective heat transfer as a function of a pressure vertical specular aluminized surface at 30 F in -300 F matte black environment, nitrogen gas.

N74-10295

A ROCKET-BORNE, LOW GRAVITY CRYOGENIC HEAT TRANSFER EXPERIMENT*

K. D. Williamson, Jr., F. J. Edeskuty and J. F. Taylor,
Los Alamos Scientific Laboratory of the University of California, Los Alamos, New Mexico 87544

ABSTRACT

In order to obtain steady state data on nucleate boiling heat transfer to liquid helium in a nearly zero gravity environment a rocket-borne experiment was designed, built and successfully flown. A description of the apparatus and flight is presented along with preliminary results.

INTRODUCTION

Although the space program is responsible for an interest in heat transfer to boiling cryogenics in a reduced gravitational field, this phenomenon is also of fundamental interest. Previous experiments have utilized drop tower (1-2 sec experiments) [1], parabolic airplane flights (15 sec experiments) [2] and magnetic levitation [3,4]. These experiments were devoted to studies using liquid oxygen, liquid nitrogen (LN₂), or liquid hydrogen. No reduced gravity data exists for liquid helium (LHe).

The Q/A vs ΔT curve for a normal gravitation field of 1 g is shown in Fig. 1 for helium where Q/A is the heat flux in watts/cm² and ΔT is the temperature difference between the surface and the fluid in Kelvins. Helmholtz instability occurs at the peak nucleate heat flux point and is the result of vapor flowing away from the surface at a rate which destabilizes the flow of liquid to the surface. The result of this instability is a jump, at constant Q/A, in ΔT of one or more orders of magnitude depending upon the fluid used. This phenomenon is referred to as burnout since, with the more conventional fluids, tube walls could reach temperatures above their melting points. This seldom occurs with cryogenic systems because of the temperature level at which they are operated. Taylor instability occurs at the minimum heat flux point and is the result of an instability in the interfacial gas film. Instead of vapor alone contacting the heated surface the overriding dense liquid phase comes in contact with it changing the heat transfer mechanism from film to nucleate boiling.

The vast majority of maximum heat flux theories [5,6,7,8, 9,10,11] and minimum heat flux theories [5,12,13,14] includes a

dependence of Q/A on $(a/g)^{1/4}$ where a is the component of acceleration in the direction of the gravitational field, g . In general the existing experimental data agrees with this dependence. One exception is the magnetic levitation work of Lyon et al. [4] using liquid oxygen. They found the $1/4$ power dependence for accelerations ranging from approximately 0.25 to 1 g but only a $1/14$ power dependence below 0.25 g.

Experimentally for LN_2 [1] and liquid hydrogen [2] it has been shown that nucleate boiling data (other than maximum heat flux) are not sensitive to gravity changes. From these results it has been concluded that buoyant forces are not significant in the process of nucleate boiling [1,2]. The primary influencing factor appears to be inertial forces. A Froude number criterion was introduced [15] to indicate the relative importance of inertial and buoyant forces. This number for nucleate boiling is the ratio of inertial to buoyant forces and is based upon bubble growth dynamics [16,17]. Values are given in Table 1 for helium, hydrogen, nitrogen and oxygen.

Table 1
FROUDE NO. AT 1 ATM AND 1 g

<u>Liquid</u>	<u>Froude No.</u>
Helium	0.020
Hydrogen	352
Nitrogen	452
Oxygen	546

For all of the fluids in Table 1, with the exception of helium, inertial forces far outweigh buoyant forces thus confirming theoretically the observations on hydrogen and nitrogen. In the case of helium, buoyant forces predominate at 1 g. As the g level decreases the Froude number increases reaching a value of 1 for He at 0.020 g's.

Because of this interesting difference of helium from other cryogenics, the lack of steady state reduced gravity data and the lack of any reduced gravity helium data an experiment was conceived to utilize a free fall rocket trajectory to obtain 5.5 minutes of a nearly zero-g environment.

DESCRIPTION OF THE EXPERIMENT

The purpose of the experiment was to obtain steady state near zero-g nucleate boiling heat transfer data on two cryogenic fluids, LN_2 and LHe . In addition, it was hoped that some information would be obtained on the location and movement of the vapor bubble in each fluid.

The LN_2 served two purposes. The first was to provide thermal shielding for the LHe thus minimizing boiloff as a result of thermal radiation and conduction heat leaks. The second was to provide a control medium for comparison to

existing, albeit nonsteady state data. Both cryogenic fluid containers were instrumented similarly. The heat transfer sensors (five in each container) consisted of 1/4-inch diameter cylindrical copper rods insulated on the sides and one end with 1/4-inch of polyurethane foam. A 100 ohm heater was wound around each rod at the end opposite the exposed end. Two thermistors were imbedded in the copper between the heater and the exposed end. The heat transfer surface temperature was obtained by extrapolating the measured temperatures to the exposed surface. Thermistors were also used to obtain bulk fluid temperatures at three locations in each vessel. The cryostat was equipped with a three axis accelerometer having a full scale reading of 0.05 g. Fluid pressures were obtained from one strain gage type pressure transducer on each vessel.

During the flight the Q/A values were stepped every 30 seconds for the first eight 30 sec time increments. From the ninth (last) step until the conclusion of the zero-g portion of the flight (90 sec) the Q/A values remained constant. The five values of Q/A for each fluid were chosen to cover the nucleate boiling region. The highest Q/A was chosen to be near the peak nucleate heat flux for 1 g. Typical Q/A values for the He and N₂ heat transfer sensors are shown in Table 2.

Table 2
TYPICAL POWER STEPS FOR TWO OF THE HELIUM AND TWO OF THE NITROGEN SENSORS

Programmer step	Q/A, W/cm ²			
	He (A)	He (B)	N ₂ (A)	N ₂ (B)
1	1.04	0.083	0.123	13.32
2	0.083	0.131	1.44	19.73
3	0.131	0.304	6.42	0.123
4	0.304	0.691	13.32	1.44
5	0.691	1.04	19.73	6.42
6	0.304	0.691	13.32	1.44
7	0.131	0.304	6.42	0.123
8	0.083	0.131	1.44	19.73
9	1.04	0.083	0.123	13.32

DESCRIPTION OF THE EQUIPMENT

A schematic diagram of the experimental package is shown in Fig. 2. The cryostat contained a LHe vessel within a thermal shield connected to a LN₂ vessel which was covered with multi-layer aluminized Mylar in the surrounding vacuum. Each vessel had a two liter capacity and was constructed of copper. The bottom closure on each vessel was removable and had attached to it all of the instrumentation for the given fluid. The closure was made vacuum tight by using Cerroseal O-rings

tightened to 35-inch-lb by a series of bolts on the circumference of the closure flange. The interior of each vessel contained longitudinal baffles which divided this space into eight equal volumes. These baffles performed two functions. One was to isolate the heat transfer sensors from one another and the second was to minimize residual fluid motion after despin of the rocket system.

Each of the vessels was equipped with two vents; one at the top which allowed venting on the ground prior to launch with the vessels full of cryogenic fluid and the second located in the geometric center of each vessel. An electronic circuit was developed based on carbon resistor level sensors and latching solenoid valves which opened the vent surrounded by the vapor bubble during the flight. This was to prevent venting of liquid regardless of the vapor bubble location.

Constant pressure was maintained on the cryogenic fluid by means of nominal 14.7 psia relief valves. The actual pressure was measured with strain gage pressure transducers located on each vessel.

The heat transfer sensors were located both parallel and perpendicular to the rocket axis. In each vessel they were located near the ends of the vessel close to the circumference.

The electronic circuitry utilized a 28 V battery supply. The thermistors were supplied with constant currents of 5 μ a in LN₂ and 2 μ a in LHe. The output voltages were amplified so that the maximum voltage measured was nearly five volts.

A mechanical commutator sampled the 126 amplified data channels ten times every second. Eight data channels were monitored continuously in real time during the flight. These channels provided complete data from helium heat sensor B as well as the bulk He temperature and pressure. The telemetered data were recorded on magnetic tape.

The 350 lb payload was launched in a 9-inch Nike-Tomahawk rocket. The payload was designed to withstand the launch loading of 30 g's and the deceleration of 5 g's between rocket stage firings. The payload was equipped with parachute and recovery beacon.

DESCRIPTION OF THE FLIGHT

The rocket and payload assembly were mounted on the launcher one day before the scheduled liftoff. The launch countdown began five hours before launch (T - 5 h) at 5:00 A.M. HST Wednesday, June 20, 1973, Barking Sands Missile Range, Kauai, Hawaii. At T - 90 minutes the filling of LN₂ and LHe commenced. The LHe fill was completed at approximately T - 45 minutes. On the launcher boiloff gases were vented through auxiliary solenoid valves held open with power supplied from the launcher. At liftoff this power was disconnected and these valves closed. At T + 62 sec (approximately 280,000 ft altitude) the on-board vent system was activated. Eighteen

seconds after despin, at $T + 82$ sec (385,000 ft), the experiment was started with the arming of the sensor heaters. An apogee of 753,000 ft was achieved at $T + 239$ sec. At $T + 412$ sec the zero-g environment was lost as the payload began to encounter measureable atmospheric resistance. At $T + 520$ sec all electrical power was turned off to minimize salt water corrosion after splash-down, the parachute was deployed, a recovery beacon activated and within one-half hour the payload had been recovered from the ocean. The recovered package was in excellent, reusable condition.

RESULTS

It should be emphasized that the flight data reported herein are limited and of a preliminary nature. This is necessary since all of the nitrogen data and most of the helium data are available only from magnetic tape recordings of the flight data. Computer processing of these tapes and data analysis will require several months. The flight data reported was obtained from real-time visicorder records which were not setup for maximum data resolution.

Prelaunch tests showed that the heat leak to the helium vessel was 0.13 watts and to the nitrogen vessel 4.2 watts. With these heat leaks complete vaporization of the helium required 11 h and the nitrogen 15 h. Thus at launch both vessels were approximately 90% full. Throughout the flight the helium bath temperature was constant at 4.2 K which corresponds to a pressure of slightly under 1 atm absolute. The g level on all three axes was less than 0.005 g's.

Preliminary heat transfer results for two of the helium sensors are shown in Fig. 3. The first sensor had its surface parallel to the axis of rocket (vertical in the 1 g environment) near the circumference of the helium vessel. The results from this sensor at 1 g (\blacktriangle) were in agreement with other helium data yielding a peak nucleate heat flux of approximately 1 W/cm^2 at a ΔT of approximately 0.6 K. At zero-g (\blacklozenge) the peak nucleate heat flux was reduced by nearly an order of magnitude to approximately 0.11 W/cm^2 . The second helium sensor had its surface perpendicular to the rocket axis (facing downward in the 1 g environment). It yielded a 1 g peak nucleate heat flux (\bullet) of approximately 0.25 W/cm^2 which is considerably lower than accepted literature values. This may be attributed to the fact that for helium at 1 g, buoyant forces (Froude number of 0.02) predominate. Because of its downward configuration the surface of this sensor vapor locks under 1 g conditions thus reducing the maximum in (Q/A) and approximating the zero-g data (\blacksquare). At 0.02 g the Froude number of helium has increased to one and inertia forces begin to dominate. In the region where buoyant forces dominate (greater than 0.02 g for helium) orientation of the surfaces is important with it apparently being possible to obtain zero-g data from a 1 g

experiment. The arrows on the film boiling data points of Fig. 3 indicate that these points should lie at higher values of ΔT than plotted. The exact position of these points will not be known until the recorded data are computer processed.

ACKNOWLEDGMENTS

From Sandia Laboratories (Albuquerque, New Mexico) we wish to thank P. K. Goen and L. W. Lathrop for their invaluable assistance throughout the experiment and P. Smelser and E. Niper for providing a successful rocket flight. We also wish to thank H. Merte of the University of Michigan for consultation on several aspects of the experiment.

REFERENCES

1. Merte, H., and J. A. Clark, *J. Heat Transfer*, 86, 351 (1964).
2. Sherley, J. E., *Advances in Cryogenic Engineering*, 8, 495 (1963).
3. Lyon, D. N., M. C. Jones, G. L. Ritter, C. I. Chiladakis, and P. S. Kosky, *AIChE J.*, 11, No. 5, 773 (1965).
4. Kirichenko, Yu. A. and A. I. Charkin, Fourth International Heat Transfer Conference, Paris-Versailles, Vol. 6, Paper B8.9, Elsevier Publishing Co., Amsterdam (1970).
5. Zuber, N., *Trans. Am. Soc. Mech. Engrs.*, 80, No. 3 711 (1958).
6. Kutateladze, S. S., *Izv. Akad. Nauk. SSSR Otd. Tekhn. Nauk.*, No. 4, 529 (1951).
7. Borishanskii, V. M., *Zh. Tekhn. Fiz.*, 26, 452 (1956); translated in *Soviet Phys. Tech. Phys.*, 1, 438 (1961).
8. Noyes, R. C., *J. Heat Transfer*, 85, No. 2, 125 (1963)
9. Chang, Y. P., and N. W. Snyder, *Chem. Eng. Progr. Symposium Ser. No. 30*, 56, 25 (1960).
10. Chang, Y. P., *J. Heat Transfer*, 85, No. 2, 89 (1963).
11. Moissis, R., and P. J. Berenson, *J. Heat Transfer*, 85, No. 3, 221 (1963).
12. Zuber, N., and M. Tribus, UCLA Report 58-5 (1958).
13. Berenson, P. J., *J. Heat Transfer*, 83, No. 3, 351 (1964).
14. Lienhard, J. H., and P. T. Y. Wong, *J. Heat Transfer*, 86, 220 (1964).
15. Clark, J. A., and H. Merte, "Advances in the Austro-nautical Sciences," 14, 177, Western Periodicals Co., North Hollywood, CA (1963).
16. Usiskin, C. M., and R. Siegel, *J. Heat Transfer*, 83, No. 3, (1961)
17. Forster, H. K., and N. Zuber, *AIChE, J.* 1, 532 (1955).

*Work performed under the auspices of the United States Atomic Energy Commission.

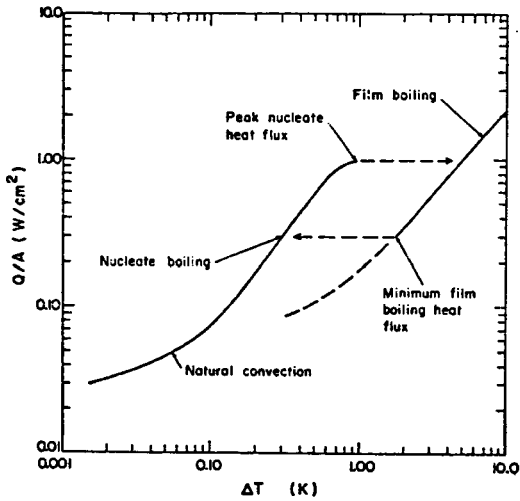


Fig. 1 - Q/A vs ΔT for helium at 1 g.

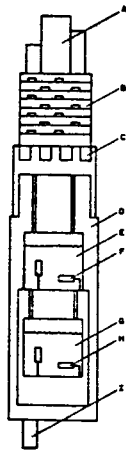


Fig. 2 - Schematic drawing of the experimental payload. A — programmer and commutator; B — printed circuit electronic boards; C — solenoid valves used for venting; D — vacuum space; E — liquid N_2 ; F — liquid N_2 heat transfer sensor; G — liquid He; H — liquid He heat transfer sensor; I — three axis accelerometer.

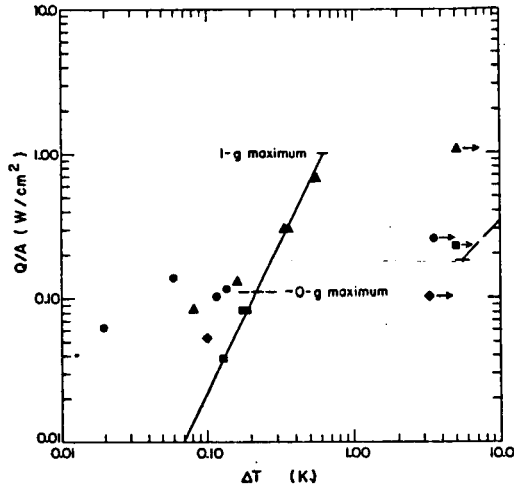


Fig. 3 - Preliminary experimental helium heat transfer. (\blacktriangle) 1 g data with sensor surface parallel to rocket axis; (\blacklozenge) zero-g data with sensor surface parallel to rocket axis; (\bullet) 1 g data with sensor surface perpendicular to rocket axis facing downward; (\blacksquare) zero-g data with sensor surface perpendicular to rocket axis facing downward. Solid lines represent typical 1 g helium data.

N74-10296

Paper No. 76

TEMPERATURE RISE FOR SPRING-LOADED PHASE CHANGE DEVICES

R. A. Farmer, *Staff Engineer, Martin Marietta Corporation,
Denver, Colorado*

ABSTRACT

Solid-to-liquid phase change materials (PCM) that may find use on planetary probes are examined. In this application, the PCM will perform only through the melting cycle to postpone the overheating of equipment within the probe. One way to minimize temperature rise is to maintain "solid phase contact melting". Resulting flow conditions in the liquid PCM film and temperature rise across the film are derived. The significance of the resulting equations, and ways suggested by them to reduce temperature rise, are discussed. The meager experimental data available is compared to results calculated by the equations.

NOMENCLATURE

d	Groove width
F	Force on solid PCM
g	Gravitational constant
ΔH	PCM heat of fusion
k	Liquid PCM thermal conductivity
L	Maximum dimension of heated surface
n	Number of zones between grooves in heated surface
P	Pressure in liquid PCM at ζ
PCM	Phase change material
p	Pressure in liquid PCM at x
\bar{P}	Pressure on solid PCM
∇p	Pressure gradient in liquid PCM
q	Heat flux \perp heated surface
\bar{q}	Average heat flux \perp heated surface
T	Heated surface temperature
T_m	PCM fusion temperature
ΔT	Temperature difference between heated surface and solid PCM
v	Mean liquid PCM exit velocity
v	Mean liquid PCM velocity at x
∇v	Velocity gradient in liquid PCM
W	Minimum dimension of heated surface
x	Coordinate in the plane of the heated surface with origin at ζ and parallel the minimum dimension
y	Liquid film thickness \perp heated surface
μ	Liquid PCM dynamic viscosity
ρ	Liquid PCM density
ρ_s	Solid PCM density

INTRODUCTION

Solid-to-liquid phase change materials (PCM) have been used since pre-historic times for temperature control, but only recently have they been applied to high technology systems. They have found use on the Lunar Rover and on Skylab, and probably will find use on planetary probes (see ref. 1). For the last application, the PCM will be called upon to perform only through the melting cycle to postpone the overheating of certain vulnerable equipment within the probe.

A container, enclosing a PCM, and comprising with it a phase change device, receives heat from the protected equipment, and melting begins at the fusion temperature. However, only the melting interface between liquid and solid PCM remains at the fusion temperature. All other parts closer to the heat source — liquid PCM, structure and the protected equipment — rise in temperature to maintain the necessary gradients for transfer of the heat. As the liquid PCM is typically a poor thermal conductor, means are often added to the device to minimize the thickness of liquid PCM and increase the area through which the heat must be transferred. Metal fins, honeycomb fillers and heat pipes have all been considered as means for enhancing heat transfer. One of

the most simple and effective means, at least for a device intended only for one melting cycle, is to maintain what has been called "solid phase contact melting". Of course, contact of solid PCM with the heated surface is not maintained at all, but the film of liquid PCM is dramatically reduced in thickness, and that is the desired effect.

Spring-loading of the solid PCM against the heated surface is only one of numerous ways of applying the necessary force. Motor drive, solenoid, pneumatic, hydraulic, vapor pressure, phase change expansion, thermal expansion, gravity or even inertial designs might all be competitive in certain applications. The following analysis is independent of the means of applying force.

ANALYSIS

Consider a rigid solid PCM inside a device of unspecified depth and of rectangular cross section parallel to the heated surface. The flat heated surface matches the device in area, being much longer than it is wide. A constant heat input is supplied to the heated surface. Specific heats of the solid and liquid PCM and structure will be neglected in comparison to the latent heat of fusion of the PCM. Spring-loading forces the solid PCM to move toward the heated surface, displacing the liquid PCM directly to the long edges of the heated surface. This, then, is a two-dimensional model of PCM melting, with heat flow in the direction perpendicular to the heated surface and liquid PCM flow parallel to the minimum dimension of the heated surface. See Figure 1.

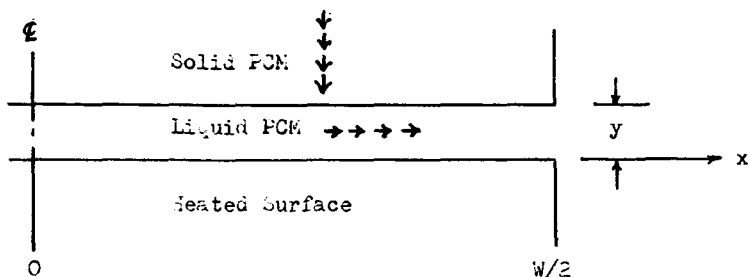


Figure 1. Phase Change Device Model

Because the solid PCM is rigid, no deformation of the solid PCM will occur. It moves as a body toward the heated surface. The rate of melting must be equal everywhere on its face. Its temperature is uniform at T_m , while the heated surface temperature is T , so ΔT from heated surface to solid PCM is equal everywhere. The heat flux at any point, if conduction dominates, is

$$Q = k \Delta T / y \quad (1)$$

Because the melting rate is uniform, and k and ΔT are uniform, y itself will be constant. The conclusion that the film of liquid PCM has a constant thickness makes an analytical treatment very convenient.

It should be noted that the constant film thickness between solid blocks of constant temperature is a very stable configuration. Perturbations to the film thickness cause local changes of opposite sign to the heat flux, a sort of negative feedback, which tend to tend to restore the quasi-equilibrium state.

The rate of motion of solid PCM will be $k \Delta T / y \rho_s \Delta H$, and rate of liquid volume production per unit area will be $k \Delta T / y \rho \Delta H$. Since all liquid PCM must travel in the x direction, the mean velocity must increase linearly from zero at the centerline of the heated surface to a maximum value at the edge. Flow will be laminar (justifying the conduction model), with plane parallel boundaries. For such a case,

$$-\nabla p = 12 \mu v / y^2 \quad (2)$$

Pressure will be its maximum value at the centerline, less the accumulated pressure drop:

$$\begin{aligned} p &= P - \int_0^x -\nabla p \, dx, \\ &= P - \int_0^x (12 \mu v / y^2) \, dx, \\ &= P - (12 \mu / y^2) \int_0^x v (2x / W) \, dx, \\ &= P - 12 \mu v x^2 / y^2 W \end{aligned}$$

Since $p = 0$ at $x = W/2$, $P = 12 \mu V (W/2)^2 / y^2 W$. Thus also $p = 12 \mu V [(W/2)^2 - x^2] / y^2 W$. All of the above illustrates in Figure 2.

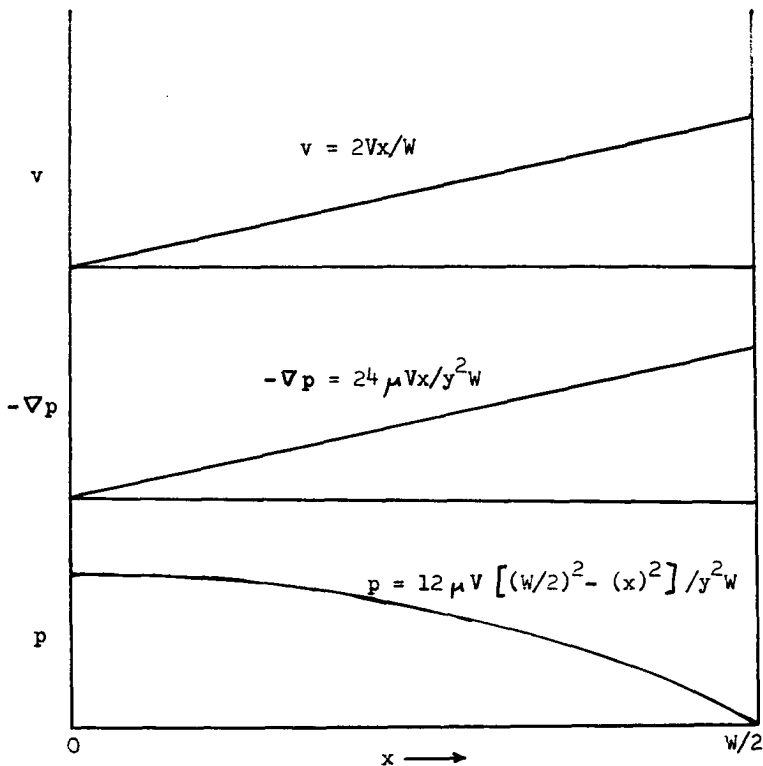


Figure 2. Velocity, Pressure Gradient and Pressure

Equation 2 is not strictly valid for this case because there is acceleration. Strictly speaking,

$$-\nabla p = 12 \mu v / y^2 + \rho \nabla v^2 / 2g, \text{ and}$$

$$p = 12 \mu V [(W/2)^2 - x^2] / y^2 W - \rho v^2 / 2g$$

It can be shown, however, that the second term is several orders of magnitude smaller than the first for all presently conceived PCM and device configurations. The temperature dependence of viscosity has been neglected in the first term (see ref. 2).

The pressure distribution is parabolic, and centerline pressure is $3 \mu VW / y^2$, so mean pressure is $2 \mu VW / y^2$. This can be equated to the force exerted on the solid PCM, divided by the area of that solid:

$$F / LW = 2 \mu VW / y^2, \text{ or}$$

$$V = \bar{p} y^2 / 2 \mu W \quad (3)$$

Also, since all liquid PCM is discharged at the edges:

$$k \Delta T W / 2 y \rho \Delta H = Vy, \text{ or}$$

$$V = k \Delta T W / 2 y^2 \rho \Delta H \quad (4)$$

From Equations 3 and 4,

$$\bar{p} y^2 / 2 \mu W = k \Delta T W / 2 y^2 \rho \Delta H, \text{ or}$$

$$y^4 = k \mu \Delta T W^2 / \bar{p} \rho \Delta H \quad (5)$$

From Equations 1 and 5,

$$q^4 = k^4 \Delta T^4 / y^4, \text{ or}$$

$$q^4 = k^4 \Delta T^4 \bar{p} \rho \Delta H / k \mu \Delta T W^2$$

Rearranging,

$$\Delta T = q^{4/3} W^{2/3} \mu^{1/3} / k \bar{p}^{1/3} (\rho \Delta H)^{1/3} \quad (6)$$

Equation 6 also gives scaling laws for devices for which this model is sufficiently approximate. ΔT is raised by increased heat flux, heated surface size and liquid PCM viscosity. All three factors increase the liquid PCM film thickness. ΔT is lowered by increased liquid PCM thermal conductivity more effectively than by increased loading on the PCM or increased PCM volumetric latent heat. However, it is evident that one could double the force and halve the size, and still retain the same ΔT at twice the heat flux with a given PCM. Furthermore, it is quite evident that reducing flux by increasing size will be only marginally effective in reducing ΔT . A much better approach would be to reduce effective size by cutting canals in the face of the heated surface to furnish easy paths to the edge. Recommendations on the proper means of fabricating the canals are discussed below.

Other results have been obtained. For a fully deformable

PCM with ∇p assumed as $4F/LW$ and using $q = (2/W) \int_0^{W/2} (K \Delta T / y) dx$, one gets

$$y^4 = 4 k \mu \Delta T W^2 / \bar{p} \rho \Delta H, \text{ and}$$

$$\Delta T = 0.86 \bar{q}^{4/3} W^{2/3} \mu^{1/3} / k \bar{p}^{1/3} (\rho \Delta H)^{1/3} \quad (7)$$

For a rigid cylindrical PCM heated on one circular end, with diameter D , one gets

$$y^4 = (3/8) k D^2 \mu \Delta T / \bar{p} \rho \Delta H, \text{ and}$$

$$\Delta T = 0.72 \bar{q}^{4/3} D^{2/3} \mu^{1/3} / k \bar{p}^{1/3} (\rho \Delta H)^{1/3} \quad (8)$$

DESIGN

It is suggested above that improving the drainage of melted PCM from the heated surface, in this particular kind of phase change device, reduces the amount of temperature rise of that surface above the PCM melting temperature for a given heat flux. In this way, the device can be made to approach more closely the ideal of a constant-temperature heat sink.

The analysis indicates that ΔT is proportional to the two-thirds power of the heated surface characteristic dimension. This is contingent on there being efficient drainage of the liquid PCM from the edges of the heated surface without appreciable back pressure. If the heated surface can be divided into (n) separately drained regions by ($n-1$) equally spaced grooves, then ΔT will be reduced by a factor of (n)^{-2/3}. Thus, seven grooves would reduce ΔT to 1/4 its former value. Shallow saw cuts in the face of the heated surface would suffice as grooves. Flow of the liquid PCM in these grooves would not require any significant part of the pressure drop, providing these grooves are large enough to be conveniently fabricated (equal to or larger than about 1 mm) and providing that larger cross grooves drain these grooves at frequent enough intervals. Figure 3 shows an arrangement of grooves on a heated surface which would reduce ΔT by nearly 75%.

More grooves would reduce ΔT even more, but the surface would be all grooves. In Figure 3, 8.3% of the area is lost for efficient transfer of the heat flux to solid PCM. If the loss of area is conservatively treated as an increase in heat flux, then heat flux is increased by a factor of $[1-(n-1)d/W]^{-1}$, neglecting cross grooves, or about $[1-(n+1)d/W]^{-1}$ with them. Here d is the groove width, and W is the heated surface width. The characteristic dimension is reduced also by a factor of $[1-nd/W]$. As ΔT is proportional to the four-thirds power of heat flux, minimum ΔT will be obtained by minimizing the expression $\Delta T_2 / \Delta T_1 = [n/(1-nd/W)]^{-2/3} [1-(n+1)d/W]^{-4/3}$.

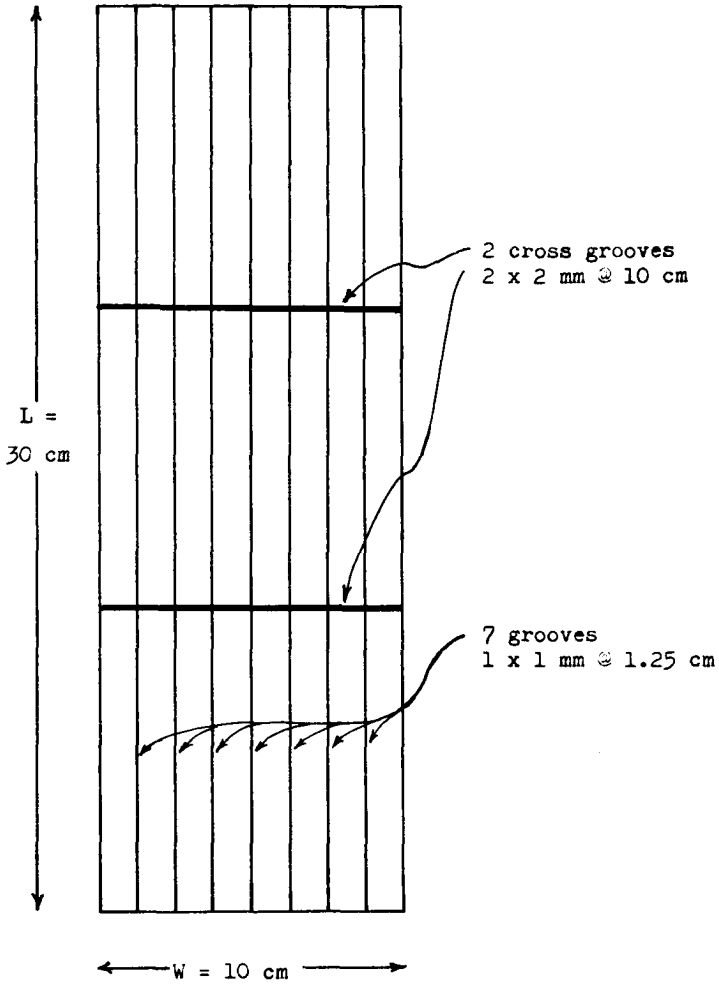


Figure 3. Typical Heated Surface Groove Pattern

ΔT_2 and ΔT_1 are temperature rises with and without the grooves. The ratio can analytically be determined to be a minimum when $n \approx W/2d$; that is, when half of the area is taken up with grooves. The expression for $\Delta T_2 / \Delta T_1$ is plotted in Figure 4, for the dimensions given in Figure 3. The difference between the $\Delta T_2 / \Delta T_1$ value and that for $(n)^{-2/3}$ represents the counter effect of area loss.

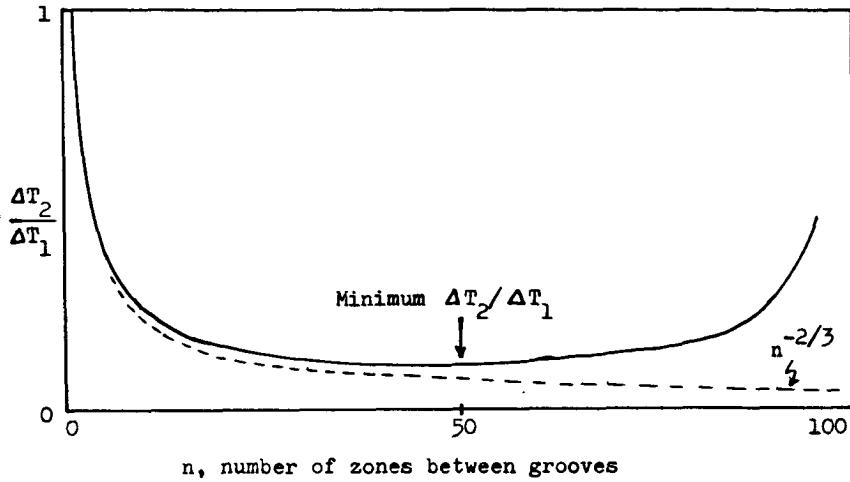


Figure 4. Effect of Grooves on Temperature

CORRELATIONS

There is at this time no data from spring-loaded devices with heated surfaces sufficiently long and narrow to approximate the model of Equation 6. Two devices have been operated with the same loaded PCM, octadecane (see refs. 3 and 4). One device had a heated surface 7.3 x 15.1 cm and was loaded with 25 lb. The other was 4.4 x 7.0 cm and was loaded manually, so that the applied force may have been in the neighborhood of 50 lb. The pressure ratio then may have been 25 / 7.3 (15.1) : 50 / 4.4 (7.0) or about 0.14. The ratio of heat fluxes imposed on the two devices was 1:1.73. Calculated ΔT ratio is

$$\begin{aligned} \Delta T_1 / \Delta T_2 &= (q_1 / q_2)^{4/3} (w_1 / w_2)^{2/3} (\bar{p}_1 / \bar{p}_2)^{-1/3} \\ &= (1/1.73)^{4/3} (7.3 / 4.4)^{2/3} (0.14)^{-1/3} \end{aligned}$$

$$= (0.48) (1.40) (1.92)$$

$$= 1.3$$

whereas measured ΔT ratio was $\frac{30}{3} = 10$. ΔT in the smaller device was somewhat larger than the model predicted, probably because of a thicker film due to appreciable increased viscosity of liquid in the film next to the melting interface. However, the larger device ΔT was very much larger than predicted, apparently due to reduced effective loading arising from appreciable back pressure in the liquid PCM at the edge of the heated surface. The larger device had a tighter fitting plunger exerting force on the solid PCM, which also was a deeper block than that in the smaller device. Increased viscosity was also undoubtedly at work, as suggested by the discrepancy between device heat capacity and total heat absorbed. PCM Volume $\times \rho \Delta H$ was greater than $q \times \text{area} \times \text{time}$ until the heated surface started continuously rising in temperature, implying in-complete melting of the block of solid PCM. If fragments of solid PCM were being carried away in the melt, then viscosity would be much higher than the value for a pure liquid PCM. Additional details of the calculation are shown in Table 1, which also lists data for the first device with another PCM.

Table 1. Sample ΔT Calculation

Device	Small	Large	Large
PCM (Properties from ref. 5)	Octadecane*	Octadecane*	LiNO ₃ · 3H ₂ O**
q, watts/cm ²	0.85	0.49	0.49
W, cm	4.4	7.3	7.3
\bar{p} , gm/cm ²	~ 736	103	103
Calculated y, cm	0.0015	0.0033	0.0022
V, cm/sec	6.7	2.9	1.9
Reynold's No.	≤ 0.3	≤ 0.3	≤ 0.2
ΔT , K	0.8	1.1	0.2
Measured ΔT , K	~ 3	30	~ 25-13***

CONCLUSIONS

The most that can be said is that Equation 6 remains unconfirmed by experiment. New experiments of proper design, appreciating the influences of the parameters in Equation 6, are needed to make any judgement of its validity. Even if the calculation of ΔT must be made with adjusted physical property data (such as viscosity) to match the experiments, the use of the equation as a scaling law may still be valid. At the very least, it suggests that there is considerable improvement available in the design of real devices.

REFERENCES

1. Schelden, B. G.: "Thermal Control of a Jovian Survivable Probe", Journal of Spacecraft and Rockets, June 1972.
2. Schlichting, H.: Boundary Layer Theory, McGraw-Hill, New York, 1960, p. 67.
3. Green, L. J.: "Liquid/Solid Phase Change Devices", IRAD Report No. D-70-48788-001, Martin Marietta Corporation, Denver, Colorado, 1970.
4. Reeves, P.: Private Communication, Martin Marietta Corporation, Denver, Colorado, 1972.
5. Hale, D. V., et al: "Phase Change Materials Handbook", NASA CR-61363, Lockheed Missile and Space Company, Huntsville, Alabama, 1971.

*A viscosity value for a few degrees above T_m was used.

**A viscosity value for water near the PCM melting temperature was used.

***This ΔT was decreasing with time, indicating what may be explained as a decreasing backpressure effect.

NATIONAL AERONAUTICS AND SPACE ADMINISTRATION
WASHINGTON, D.C. 20546

OFFICIAL BUSINESS
PENALTY FOR PRIVATE USE \$300

SPECIAL FOURTH-CLASS RATE
BOOK

POSTAGE AND FEES PAID
NATIONAL AERONAUTICS AND
SPACE ADMINISTRATION
451



POSTMASTER: If Undeliverable (Section 168
Postal Manual) Do Not Return

"The aeronautical and space activities of the United States shall be conducted so as to contribute . . . to the expansion of human knowledge of phenomena in the atmosphere and space. The Administration shall provide for the widest practicable and appropriate dissemination of information concerning its activities and the results thereof."

—NATIONAL AERONAUTICS AND SPACE ACT OF 1958

NASA SCIENTIFIC AND TECHNICAL PUBLICATIONS

TECHNICAL REPORTS: Scientific and technical information considered important, complete, and a lasting contribution to existing knowledge.

TECHNICAL NOTES: Information less broad in scope but nevertheless of importance as a contribution to existing knowledge.

TECHNICAL MEMORANDUMS: Information receiving limited distribution because of preliminary data, security classification, or other reasons. Also includes conference proceedings with either limited or unlimited distribution.

CONTRACTOR REPORTS: Scientific and technical information generated under a NASA contract or grant and considered an important contribution to existing knowledge.

TECHNICAL TRANSLATIONS: Information published in a foreign language considered to merit NASA distribution in English.

SPECIAL PUBLICATIONS: Information derived from or of value to NASA activities. Publications include final reports of major projects, monographs, data compilations, handbooks, sourcebooks, and special bibliographies.

TECHNOLOGY UTILIZATION PUBLICATIONS: Information on technology used by NASA that may be of particular interest in commercial and other non-aerospace applications. Publications include Tech Briefs, Technology Utilization Reports and Technology Surveys.

Details on the availability of these publications may be obtained from:

SCIENTIFIC AND TECHNICAL INFORMATION OFFICE
NATIONAL AERONAUTICS AND SPACE ADMINISTRATION
Washington, D.C. 20546